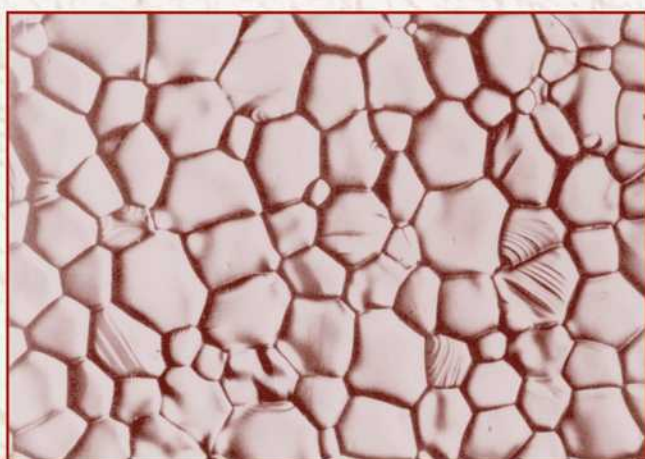


CERAMIC PROCESSING AND SINTERING

SECOND EDITION



M. N. RAHAMAN

1

Ceramic Fabrication Processes

An Introductory Overview

1.1 INTRODUCTION

The subject of ceramics covers a wide range of materials. Recent attempts have been made to divide it into two parts: *traditional ceramics* and *advanced ceramics*. The use of the term *advanced* has, however, not received general acceptance and other forms including technical, special, fine, and engineering will also be encountered. *Traditional ceramics* bear a close relationship to those materials that have been developed since the earliest civilizations. They are pottery, structural clay products, and clay-based refractories, with which we may also group cements and concretes and glasses. Whereas traditional ceramics still represent a major part of the ceramics industry, the interest in recent years has focused on *advanced ceramics*, ceramics that with minor exceptions have been developed within the last 50 years or so. Advanced ceramics include ceramics for electrical, magnetic, electronic, and optical applications (sometimes referred to as *functional ceramics*) and ceramics for structural applications at ambient as well as at elevated temperatures (*structural ceramics*). Although the distinction between traditional and advanced ceramics may be referred to in this book occasionally for convenience, we do not wish to overemphasize it. There is much to be gained through continued interaction between the traditional and the advanced sectors.

Chemically, with the exception of carbon, ceramics are nonmetallic, inorganic compounds. Examples are the silicates such as kaolinite [$\text{Al}_2\text{Si}_2\text{O}_5(\text{OH})_4$] and mullite ($\text{Al}_6\text{Si}_2\text{O}_{13}$), simple oxides such as alumina (Al_2O_3) and zirconia (ZrO_2), complex oxides other than the silicates such as barium titanate (BaTiO_3), and the superconducting material $\text{YBa}_2\text{Cu}_3\text{O}_{6+\delta}$ ($0 \leq \delta \leq 1$). In addition, there are nonoxides including carbides such as silicon carbide (SiC) and boron carbide

(B_4C), nitrides such as silicon nitride (Si_3N_4) and boron nitride (BN), borides such as titanium diboride (TiB_2), silicides such as molybdenum disilicide ($MoSi_2$) and halides such as lithium fluoride (LiF). There are also compounds based on nitride–oxide or oxynitride systems (e.g., β' -sialons with the general formula $Si_{6-z}Al_zN_{8-z}O_z$, where $0 < z < \sim 4$).

Structurally, all materials are either *crystalline* or *amorphous* (also referred to as *glassy*). The difficulty and expense of growing single crystals means that, normally, crystalline ceramics (and metals) are actually *polycrystalline*—they are made up of a large number of small crystals, or grains, separated from one another by grain boundaries. In ceramics as well as in metals, we are concerned with two types of structure, both of which have a profound effect on properties. The first type of structure is at the atomic scale: the type of *bonding* and the *crystal structure* (for a crystalline ceramic) or the *amorphous structure* (if it is glassy). The second type of structure is at a larger scale: the *microstructure*, which refers to the nature, quantity, and distribution of the structural elements or phases in the ceramic (e.g., crystals, glass, and porosity).

It is sometimes useful to distinguish between the intrinsic properties of a material and the properties that depend on the microstructure. The *intrinsic properties* are determined by the structure at the atomic scale and are properties that are not susceptible to significant change by modification of the microstructure, properties such as the melting point, elastic modulus, coefficient of thermal expansion, and whether the material is brittle, magnetic, ferroelectric, or semiconducting. In contrast, many of the properties critical to the engineering applications of materials are strongly dependent on the microstructure (e.g., mechanical strength, dielectric constant, and electrical conductivity).

Intrinsically, ceramics usually have high melting points and are therefore generally described as refractory. They are also usually hard, brittle, and chemically inert. This chemical inertness is usually taken for granted, for example, in ceramic and glass tableware and in the bricks, mortar, and glass of our houses. However, when used at high temperatures, as in the chemical and metallurgical industries, this chemical inertness is severely tried. The electrical, magnetic, and dielectric behavior covers a wide range—for example, in the case of electrical behavior, from insulators to conductors.

The applications of ceramics are many. Usually, for a given application one property may be of particular importance, but in fact, all relevant properties need to be considered. We are therefore usually interested in combinations of properties. For traditional ceramics and glasses, familiar applications include structural building materials (e.g., bricks and roofing tile), refractories for furnace linings, tableware and sanitaryware, electrical insulation (e.g., electrical porcelain and steatite), glass containers, and glasses for building and transportation vehicles. The applications for which advanced ceramics have been developed or proposed

are already very diverse and this area is expected to continue to grow at a reasonable rate. Table 1.1 illustrates some of the applications for advanced ceramics (1).

The important relationships between chemical composition, atomic structure, fabrication, microstructure, and properties of polycrystalline ceramics are illustrated in Fig. 1.1. The intrinsic properties must be considered at the time of materials selection. For example, the phenomenon of ferroelectricity originates in the perovskite crystal structure, of which BaTiO_3 is a good example. For the production of a ferroelectric material, we may therefore wish to select BaTiO_3 . The role of the fabrication process, then, is to produce microstructures with the desired engineering properties. For example, the measured dielectric constant of the fabricated BaTiO_3 will depend significantly on the microstructure (grain size, porosity, and presence of any secondary phases). Normally, the overall fabrication method can be divided into a few or several discrete steps, depending on the complexity of the method. Although there is no generally accepted terminology, we will refer to these discrete steps as *processing steps*. The fabrication of a ceramic body therefore involves a number of processing steps. In the next section, we examine, in general terms, some of the commonly used methods for the fabrication of ceramics.

1.2 CERAMIC FABRICATION PROCESSES

Ceramics can be fabricated by a variety of methods, some of which have their origins in early civilization. Our normal objective is the production, from suitable starting materials, of a solid product with the desired shape such as a film, fiber, or monolith and with the desired microstructure. As a first attempt, we divide the main fabrication methods into three groups, depending on whether the starting materials involve a gaseous phase, a liquid phase, or a solid phase (Table 1.2). In the following sections, we examine briefly the main features of the processing steps involved in these methods and, from the point of view of ease of processing, their main advantages and disadvantages.

1.2.1 Gas-Phase Reactions

By far the most important are vapor deposition methods, where the desired material is formed by chemical reaction between gaseous species. The reaction between a liquid and a gas is generally impractical but has been developed recently into an elegant technique, referred to as *directed metal oxidation*. Reaction between a gas and a solid, commonly referred to as *reaction bonding* (or reaction forming) has been used mainly for the production of Si_3N_4 but is now also being applied to the production of oxide ceramics. Reaction bonding (by a solid–liquid reaction) is also an important fabrication route for SiC .

TABLE 1.1 Application of Advanced Ceramics Classified by Function

Function	Ceramic	Application
Electric	Insulation materials (Al_2O_3 , BeO , MgO)	Integrated circuit substrate, package, wiring substrate, resistor substrate, electronics interconnection substrate
	Ferroelectric materials (BaTiO_3 , SrTiO_3)	Ceramic capacitor
	Piezoelectric materials (PZT)	Vibrator, oscillator, filter, etc. Transducer, ultrasonic humidifier, piezoelectric spark generator, etc.
	Semiconductor materials (BaTiO_3 , SiC , ZnO - Bi_2O_3 , V_2O_5 and other transition metal oxides)	NTC thermistor: temperature sensor, temperature compensation, etc. PTC thermistor: heater element, switch, temperature compensation, etc. CTR thermistor: heat sensor element Thick-film sensor: infrared sensor Varistor: noise elimination, surge current absorber, lightning arrestor, etc.
		Sintered CdS material: solar cell SiC heater: electric furnace heater, miniature heater, etc.
Magnetic	Ion-conducting materials ($\beta\text{-Al}_2\text{O}_3$, ZrO_2)	Solid electrolyte for sodium battery ZrO_2 ceramics: oxygen sensor, pH meter, fuel cells
	Soft ferrite	Magnetic recording head, temperature sensor, etc.
Optical	Hard ferrite	Ferrite magnet, fractional horse power motors, etc.
	Translucent alumina	High-pressure sodium vapor lamp
	Translucent Mg-Al spinel, mullite, etc.	Lighting tube, special-purpose lamp, infrared transmission window materials
	Translucent Y_2O_3 - ThO_2 ceramics	Laser materials
	PLZT ceramics	Light memory element, video display and storage system, light modulation element, light shutter, light valve

(Continued)

TABLE 1.1 *Continued*

Function	Ceramic	Application
Chemical	Gas sensor (ZnO, Fe ₂ O ₃ , SnO ₂)	Gas leakage alarm, automatic ventilation alarm; hydrocarbon, fluorocarbon detectors, etc.
	Humidity sensor (MgCr ₂ O ₄ -TiO ₂)	Cooking control element in microwave oven, etc.
	Catalyst carrier (cordierite)	Catalyst carrier for emission control
	Organic catalysts	Enzyme carrier, zeolites
	Electrodes (titanates, sulfides, borides)	Electrowinning aluminum, photochemical processes, chlorine production
Thermal	ZrO ₂ , TiO ₂	Infrared radiator
Mechanical	Cutting tools (Al ₂ O ₃ , TiC, TiN, others)	Ceramic tool, sintered CBN; cermet tool, artificial diamond; nitride tool
	Wear-resistant materials (Al ₂ O ₃ , ZrO ₂)	Mechanical seal, ceramic liner, bearings, thread guide, pressure sensors
	Heat-resistant materials (SiC, Al ₂ O ₃ , Si ₃ N ₄ , others)	Ceramic engine, turbine blade, heat exchangers, welding burner nozzle, high frequency combustion crucibles)
	Alumina ceramics implantation, hydroxyapatite, bioglass	Artificial tooth root, bone and joint.
Nuclear	UO ₂ , UO ₂ -PuO ₂	Nuclear fuels
	C, SiC, B ₄ C	Cladding materials
	SiC, Al ₂ O ₃ , C, B ₄ C	Shielding materials

Source: Ref. 1.

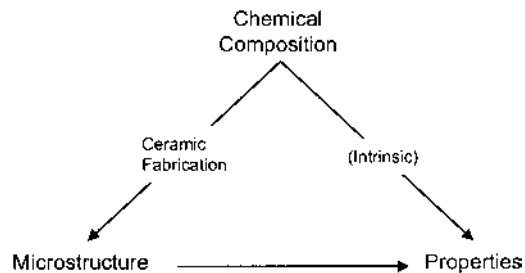


FIGURE 1.1 The important relationships in ceramic fabrication.

TABLE 1.2 Common Ceramic Fabrication Methods

Starting materials	Method	Product
Gases	Chemical vapor deposition	Films, monoliths
Gas–liquid	Directed metal oxidation	Monoliths
Gas–solid	Reaction bonding	Monoliths
Liquid–solid	Reaction bonding	Monoliths
Liquids	Sol–gel process	Films, fibers
	Polymer pyrolysis	Fibers, films
Solids (powders)	Melt casting	Monoliths
	Sintering of powders	Monoliths, films

1.2.1.1 Chemical Vapor Deposition

Chemical vapor deposition (CVD) is a process by which reactive molecules in the gas phase are transported to a surface at which they chemically react and form a solid film. It is a well-established technique that can be used to deposit all classes of materials, including metals, ceramics, and semiconductors, for a variety of applications. Large areas can be coated and the process is amenable to mass production. Thick films or even monolithic bodies can also be produced by basically prolonging the deposition process so that the desired thickness is achieved. Table 1.3 shows some of the important reactions used for the fabrication of ceramics together with the temperature range of the reactions and the applications of the fabricated articles.

There are several excellent texts on CVD and related processes covering the fundamental physics and chemistry, equipment, applications, and reaction chemistry for most materials (2); fundamental aspects of thermodynamics, kinetics, and transport phenomena (3,4); deposition of thin films (5); microelectronic applications (6,7); and common deposition strategies for Si_3N_4 , SiC and other materials (8).

The apparatus used for CVD depends on the reaction being used, the reaction temperature, and the configuration of the substrate. Figure 1.2 shows examples of reactors for the deposition of films on substrates such as Si wafers (9). The general objective for any design is to provide uniform exposure of the substrate to the reactant gases. CVD has a number of process variables that must be manipulated to produce a deposit with the desired properties. These variables include the flow rate of the reactant gases, the nature and flow rate of any carrier gases, the pressure in the reaction vessel, and the temperature of the substrate.

Substrate heating is required in CVD reactors because the films are produced preferably by endothermic reactions. The temperature of the substrate influences the deposition rate and is the main factor controlling the structure of the

TABLE 1.3 Some Important CVD Reactions for the Fabrication of Ceramics

Reaction	Temperature (°C)	Application
$2C_xH_y \rightarrow 2xC + yH_2$	900–2400	Pyrolytic carbon and graphite
$CH_3Cl_3Si \rightarrow SiC + 3HCl$	1000–1300	Composites
$W(CO)_6 \rightarrow WC + CO_2 + 4CO$	400–800	Coatings
$TiCl_4 + O_2 \rightarrow TiO_2 + 2Cl_2$	900–1200	Films for electronic devices
$SiCl_4 + 2CO_2 + 2H_2 \rightarrow$ $SiO_2 + 4HCl + 2CO$	800–1000	Films for electronic devices, optical fibers
$SiCl_4 + 2H_2O \rightarrow SiO_2 + 4HCl$	500–1000	Films for electronic devices, optical fibers
$SiCl_4 + 2H_2 \rightarrow Si + 4HCl$	500–800	Films for electronic devices
$TiCl_4 + 2BH_3 \rightarrow$ $TiB_2 + 4HCl + H_2$	1000–1300	Monoliths, composites
$SiH_4 + CH_4 \rightarrow SiC + 4H_2$	1000–1400	Coatings
$3SiH_4 + 4NH_3 \rightarrow$ $Si_3N_4 + 12H_2$	800–1500	Films for semiconductor devices
$3HSiCl_3 + 4NH_3 \rightarrow$ $Si_3N_4 + 9HCl + 3H_2$	800–1100	Composites
$BCl_3 + NH_3 \rightarrow BN + 3HCl$	700–1000	Monoliths

deposit. In general, high temperatures will yield crystalline deposits while low temperatures result in amorphous materials. Between these two extremes a polycrystalline deposit will be formed. The pressure in the reaction vessel influences the concentration of the reactant gases, the diffusion of reactants toward the substrate, and the diffusion of the products away from the surface. The higher diffusivity at lower pressure leads to the formation of films with better uniformity, so that most CVD reactors are operated in the pressure range of 1–15 kPa.

The reactant gases, also referred to as *precursor molecules*, are chosen to react and produce a specific film. Properties necessary for a good precursor include thermal stability at its vaporization temperature and sufficient vapor pressure (at least ~ 125 Pa) at a reasonable temperature ($\sim 300^\circ\text{C}$) for effective gas phase delivery to the growth surface. In addition, the molecules must be obtainable at high purity and must not undergo parasitic or side reactions which would lead to contamination or degradation of the film (10). Examples of the classes of precursor molecules (e.g., hydrides, halides, carbonyls, hydrocarbons, and organometallics) and the types of chemical reaction (pyrolysis, oxidation/hydrolysis, reduction, carbidization/nitridation, and disproportionation) are summarized in Table 1.3.

CVD technology has been attracting much interest recently for the production of diamond films or coatings (11). Diamond has several attractive properties

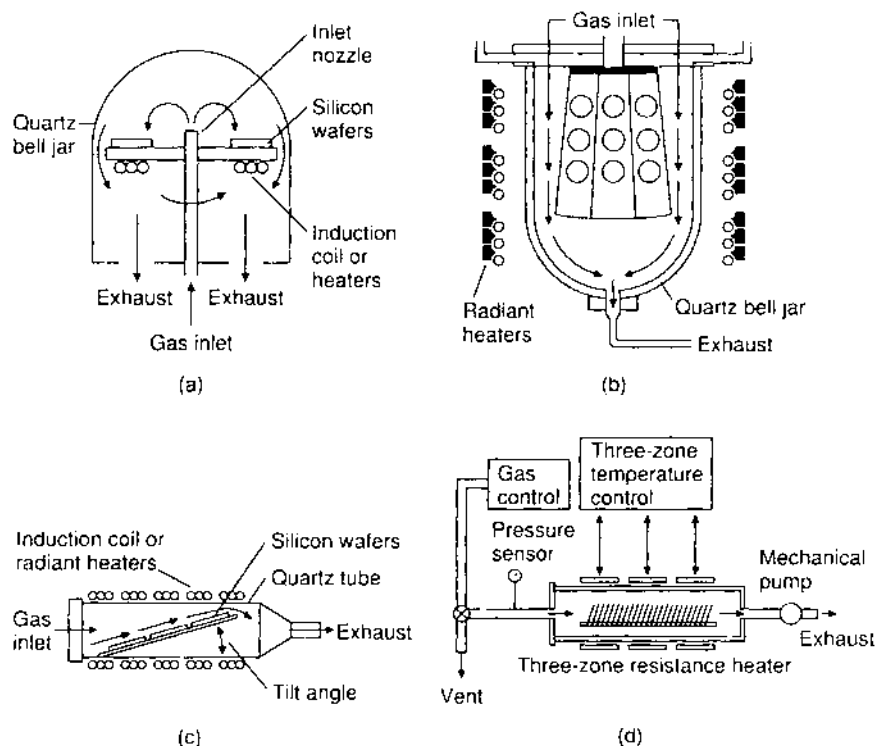


FIGURE 1.2 Typical reactors used in chemical vapor deposition: (a) pancake reactor; (b) barrel reactor; (c) horizontal reactor; (d) low-pressure (LPCVD) reactor. (From Ref. 9.)

but, in the past, high pressures and high temperatures have been required to produce synthetic diamond. In contrast, a plasma-assisted CVD process allows the production of diamond films at relatively low temperatures and low pressures (Fig. 1.3). The deposition process is complex and is not understood clearly at present. The basic reaction involves the pyrolysis of a carbon-containing precursor such as methane:



The typical process consists of the reactant gas at less than atmospheric pressure and containing $>95\%$ H_2 . The gas is activated by passing it through a plasma or past a heated filament (at $\sim 2000^\circ\text{C}$) before deposition on a substrate at $800\text{--}1000^\circ\text{C}$.

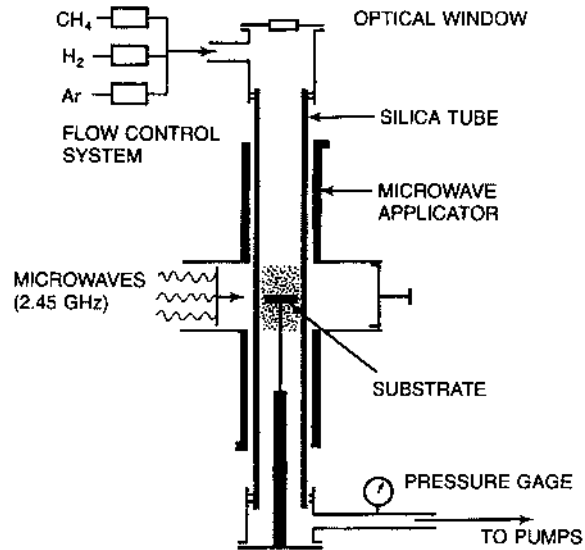


FIGURE 1.3 Schematic diagram of microwave-plasma-assisted chemical vapor deposition (MPACVD) diamond growth system. (From Ref. 11.)

CVD technology has also been attracting significant interest as a fabrication route for ceramic composites (12). For fiber-reinforced ceramics, one approach that has shown considerable promise is *chemical vapor infiltration* (CVI). The fibers, preformed into the shape and dimensions of the finished body, are placed into the reactant gases and held at the desired temperature so that the deposited material is formed in the interstices between the fibers. Significant effort has been devoted to SiC matrix composites reinforced with SiC or C fibers. The SiC matrix is typically deposited from methyltrichlorosilane, $\text{CH}_3\text{Cl}_3\text{Si}$, at temperatures of $\sim 1200^\circ\text{C}$ and pressures of ~ 3 kPa. The process is slow and a serious problem is the tendency for most of the reaction to occur near the surface of the fiber preform, leading to density gradients and the sealing off of the interior. A promising route involves the exploitation of forced flow of the reacting gas into the preform using pressure and temperature gradients (Fig. 1.4). Matrices with reasonably high density (typically $\sim 10\%$ porosity) have been produced. The CVI route has an inherent advantage over conventional ceramic powder processing routes that commonly require higher temperatures and high pressures for fabrication: mechanical and chemical degradation of the composite during fabrication is not severe. Composites containing as high as 45 vol% of fibers have been fabricated with an open porosity of $\sim 10\%$. The measured fracture toughness (13) remained

unchanged at $\sim 30 \text{ MPam}^{1/2}$ up to 1400°C , which is considerably better than unreinforced SiC with a fracture toughness of $\sim 3 \text{ MPam}^{1/2}$.

Table 1.3 indicates that the reaction temperatures for the CVD fabrication of most of the highly refractory ceramics listed are rather low. Therefore, CVD methods provide a distinct advantage of fairly low fabrication temperatures for ceramics and composites with high melting points that are difficult to fabricate by other methods or require very high fabrication temperatures. The low reaction temperatures also increase the range of materials that can be coated by CVD, especially for the highly refractory coatings. However, a major disadvantage is that the material deposition rate by CVD is very slow, typically in the range of $1\text{--}100 \text{ }\mu\text{m/h}$. The production of monolithic bodies can therefore be very time consuming and expensive. Another problem that is normally encountered in the fabrication of monolithic bodies by CVD is the development of a microstructure consisting of fairly large, columnar grains which leads to fairly low intergranular strength. These difficulties limit CVD methods primarily to the formation of thin films and coatings.

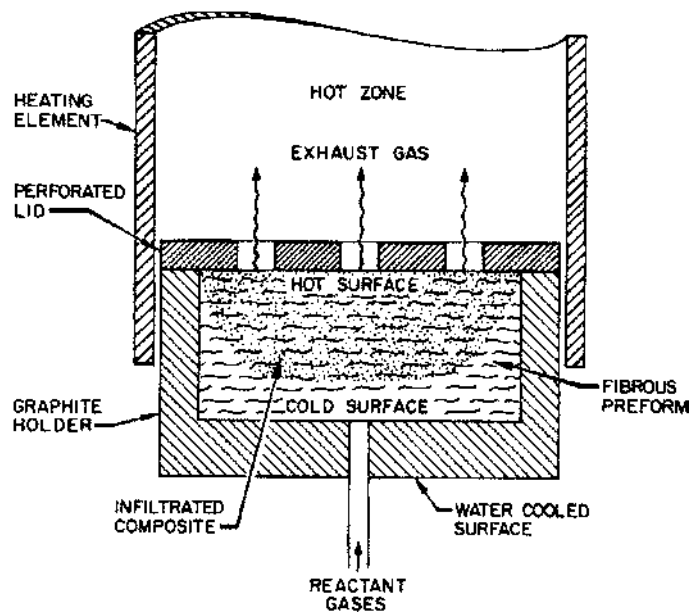


FIGURE 1.4 Schematic diagram of chemical vapor infiltration process exploiting forced flow of the infiltrating gas. (From Ref. 12.)

1.2.1.2 Directed Metal Oxidation

Fabrication routes involving reactions between a gas and a liquid are generally impractical for the production of ceramic bodies because the reaction product usually forms a solid protective coating, thereby separating the reactants and effectively stopping the reaction. However, a novel method employing directed oxidation of a molten metal by a gas has been developed by the Lanxide Corporation for the production of porous and dense materials as well as composites (14–19). Figure 1.5 shows a schematic of the reaction process. In Fig. 1.5a a molten metal (e.g., an aluminum alloy) is being oxidized by a gas (e.g., air). If the temperature is in the range of 900–1350°C and the aluminum alloy contains a few percent of Mg and a group IVA element (e.g., Si, Ge, Sn, or Pb), the oxide coating is no longer protective. Instead, it contains small pores through which molten metal is drawn up to the top surface of the film, thereby continuing the oxidation process. As long as the molten metal and the oxidizing gas are available to sustain the process and the temperature is maintained, the reaction product continues to grow at a rate of a few centimeters per day until the desired thickness is obtained. The material produced in this way consists of two phases: the oxidation product (e.g., Al_2O_3), which is continuous and interconnected, and unreacted metal (Al alloy). The amount of unreacted metal (typically 5–30 vol%) depends on the starting materials and processing parameters (e.g., the temperature).

For the production of composites, a filler material (e.g., particles, platelets, or fibers) is shaped into a preform of the size and shape desired of the product.

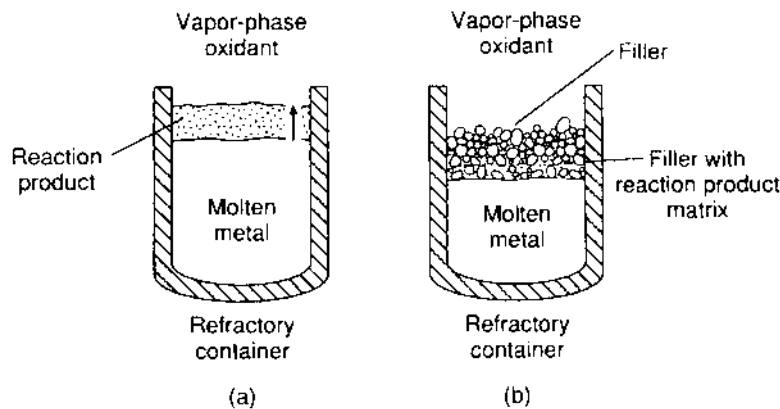


FIGURE 1.5 Schematic diagram of the formation of a matrix of oxide and unreacted metal by (a) directed oxidation of molten metal and (b) oxidation in the presence of a filler. (From Ref. 15.)

The filler and the metal alloy are then heated to the growth temperature where the oxidation process occurs outward from the metal surface and into the preform (Fig. 1.5b), such that the oxidation product becomes the matrix of the composite. A micrograph of a SiC fiber preform which has been filled with an $\text{Al}_2\text{O}_3/\text{Al}$ matrix by directed oxidation of molten aluminum is shown in Fig. 1.6.

The term *directed metal oxidation* is taken to include all reactions in which the metal gives up or shares its electrons. The method has been used to produce composites with not only matrices of oxides but also nitrides, borides, carbides, and titanates. Composite systems produced by the method include matrices of $\text{Al}_2\text{O}_3/\text{Al}$, AlN/Al , ZrN/Zr , TiN/Ti , and Zr and fillers of Al_2O_3 , SiC, BaTiO_3 , AlN , B_4C , TiB_2 , ZrN , ZrB_2 , and TiN . A distinct advantage of the method is that growth of the matrix into the preform involves little or no change in dimensions. The problems associated with shrinkage during densification in other fabrication routes (e.g., powder processing) are therefore avoided. Furthermore, large components can be produced readily with good control of the component dimensions.

1.2.1.3 Reaction Bonding

The term *reaction bonding* (or reaction forming) is commonly used to describe fabrication routes where a porous solid preform reacts with a gas (or a liquid) to produce the desired chemical compound and bonding between the grains.

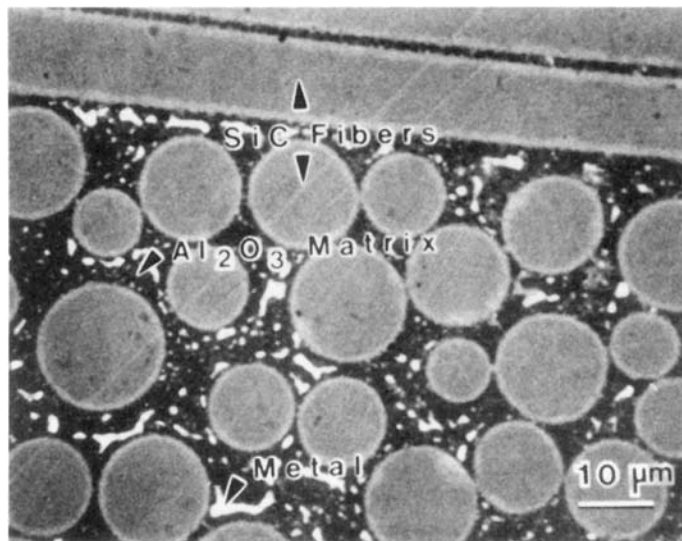


FIGURE 1.6 Optical micrograph of an $\text{Al}_2\text{O}_3/\text{Al}$ matrix reinforced with SiC fibers produced by directed metal oxidation. (From Ref. 15.)

Commonly, the process is accompanied by little or no shrinkage of the preform so that very close dimensional tolerances can be achieved for the finished component. Reaction bonding is used on a large scale as one of the fabrication routes for Si_3N_4 and SiC (20,21).

Silicon Nitride

Si_3N_4 is the most widely known reaction bonded system involving the reaction between a solid and a gas phase. A detailed review of the formation and properties of reaction bonded silicon nitride (RBSN) has been written by Moulson (22). In the formation of RBSN, silicon powder is consolidated by one of a variety of methods (e.g., pressing in a die, isostatic pressing, slip casting, and injection molding) to form a billet or a shaped body; this is then preheated in argon at $\sim 1200^\circ\text{C}$ after which it can be machined to the required component shape and dimensions. Finally, the component is heated, usually in N_2 gas at atmospheric pressure and at temperatures in the region of $1250\text{--}1400^\circ\text{C}$, when reaction bonding occurs to produce RBSN. While the mechanism is fairly complex, the overall reaction can be written:



The densities of Si and Si_3N_4 are 2.33 g/cm^3 and 3.18 g/cm^3 , respectively, so that the reaction of a silicon particle to form Si_3N_4 involves a volume expansion of 22%. However, very little size change occurs during the nitridation. This means that the nitridation occurs by a mechanism in which new mass being added to the body expands into the surrounding pore space (22). As the pore sizes and the number of pores decrease, the pore channels close off and the reaction effectively stops. In preforms with relatively high density, pore channel closure commonly occurs prior to complete reaction. The RBSN has a porosity of 15–20% and some residual, unreacted Si. The Si_3N_4 consists of 60–90 wt% of the α phase and the remainder being β - Si_3N_4 . Several factors influence the reaction kinetics and the resulting microstructure, including the Si particle size, the composition and pressure of the nitriding gas, the reaction temperature, and the impurities in the Si starting powder. Because of the high porosity, the strength of RBSN is inferior to that of dense Si_3N_4 produced by other methods (e.g., hot pressing). However, RBSN bodies with a high degree of dimensional accuracy and with complex shapes can be prepared fairly readily without the need for expensive machining after firing.

Oxides

A reaction bonding route involving both gas–solid and gas–liquid reactions is the reaction-bonded aluminum oxide (RBAO) process developed by Claussen and co-workers (23–27). The RBAO process utilizes the oxidation of powder

mixtures containing a substantial amount of Al (30–65 vol%). A mixture of Al (particle size $\sim 20\text{ }\mu\text{m}$), $\alpha\text{-Al}_2\text{O}_3$ (0.5–1.0 μm), and ZrO_2 ($\sim 0.5\text{ }\mu\text{m}$) is milled vigorously in an attrition mill, dried, and compacted to produce a green body (porosity $\sim 30\text{--}40\%$). During heat treatment in an oxidizing atmosphere (commonly air), the Al oxidizes to nanometer-sized $\gamma\text{-Al}_2\text{O}_3$ crystals below $\sim 900^\circ\text{C}$ which undergo a phase transformation to $\alpha\text{-Al}_2\text{O}_3$ up to $\sim 1100^\circ\text{C}$. The volume expansion (28 vol%) associated with the oxidation of Al to $\alpha\text{-Al}_2\text{O}_3$ is used to partially compensate for the shrinkage due to sintering, so that dense RBAO ceramics can be achieved with lower firing shrinkage than conventionally sintered Al_2O_3 ceramics. Figure 1.7 shows a micrograph of a reaction bonded $\text{Al}_2\text{O}_3/\text{ZrO}_2$ ceramic produced from a starting mixture of 45 vol% Al, 35 vol% Al_2O_3 , and 20 vol% ZrO_2 . Successful application of the RBAO process depends on several variables, including the characteristics of the starting powders, (e.g., particle size and volume fraction of the Al), the milling parameters, the green density of the compacted mixture, and the heating (oxidation) schedule. ZrO_2 is known to aid the microstructure development during sintering but its role is not clear. In addition to Al_2O_3 , the RBAO process has been applied to the fabrication of mullite ceramics (28) and composites (29).

A gas–solid reaction involving the oxidation of a combination of an alkaline earth metal and another metal has been used recently to produce ceramics contain-

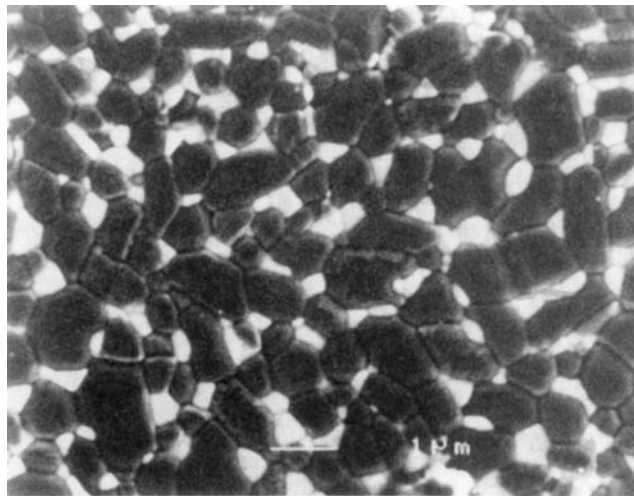


FIGURE 1.7 Scanning electron micrograph showing the microstructure of a reaction bonded aluminum oxide (RBAO) sample. The white phase is ZrO_2 ($\sim 20\text{ vol}\%$) and the dark phase is Al_2O_3 . (Courtesy of M. P. Harmer.)

ing an alkaline earth element (30–35). An unusual feature of most alkaline earth metals is the reduction in solid volume accompanying oxidation. For example, the molar volume of MgO is 19% smaller than that of Mg. In contrast, most other metals tend to expand during oxidation. The reduction in volume due to the oxidation of an alkaline earth metal can be used to offset the volume expansion accompanying the oxidation of another metal. In this way, dense ceramics containing an alkaline earth element can be produced with little change in dimensions from dense preforms of metal-bearing precursors.

Silicon Carbide

Reaction bonded silicon carbide (RBSC) represents the most important example of the fabrication route based on the reaction between a solid and a liquid (36,37). Commonly, a mixture of SiC particles (5–10 μm), carbon, and a polymeric binder is formed into a green body by pressing, extrusion or injection molding. In some variations, silicon carbide particles and a carbon-forming resin are used as the starting mixture. The binder or resin is burned off or converted to microporous carbon by pyrolysis, after which the porous preform is infiltrated with liquid Si at temperatures somewhat above the melting point of Si (1410°C). Reaction between the carbon and Si occurs according to



The reaction product crystallizes on the original SiC grains and bonds them together.

The infiltration and reaction processes occur simultaneously. Capillary pressure provides the driving force for infiltration, and good wetting of the surfaces by liquid Si is a key requirement. The kinetics of the infiltration are complex. However, if the pore structure of the preform is simplified as a set of parallel cylinders, the kinetics can be determined from Poiseuille's equation for viscous flow through a tube:

$$\frac{dV}{dt} = \frac{\pi r^4}{8\eta} \left(\frac{\Delta p}{l} \right) \quad (1.4)$$

where dV/dt is the rate of liquid flow, r is the radius of the tube with a length l , Δp is the pressure difference across the length of the tube, and η is the viscosity of the liquid. The height infiltrated in time t is found to be

$$h^2 = \left(\frac{r\gamma \cos \theta}{2\eta} \right) t \quad (1.5)$$

where γ is the surface tension of the liquid and θ is the contact angle for wetting. Equation (1.5) shows that the rate of infiltration is proportional to the pore size.

Since the pore size scales as the particle size, preforms made with larger particles are more readily infiltrated. However, the strength of the material decreases with larger grain sizes. The reaction given by Eq. (1.3) is exothermic and is accompanied by a large heat of reaction. The development of stresses due to thermal gradients can lead to cracking if the reaction kinetics are too fast.

Theoretically, it is possible to calculate the green density of the preform required to produce a fully dense RBSC, but in practice it is necessary to leave additional porosity to allow the infiltrating Si to move freely. Consequently, the fabricated material contains an interconnected network of unreacted Si. Commonly, there is no unreacted carbon or porosity, and the principal microstructural features are the original SiC grains coated with the SiC formed in the reaction and the residual Si (38,39). Figure 1.8 shows the microstructure of an RBSC. The optimum RBSC composition is ~ 90 vol% SiC and 10 vol% Si, but special products with 5–25 vol% Si are sometimes made. The presence of Si leads to a deterioration of the mechanical strength at temperatures above $\sim 1200^\circ\text{C}$ (40). The use of Si alloys (e.g., Si + 2 at% Mo), instead of pure Si, has been investigated to eliminate the residual Si in the fabricated body (41). The alloying elements form chemically stable, refractory silicides (e.g., MoSi_2) with the excess Si. The reaction bonding process has also been applied to the fabrication of composites where a reinforcing phase is incorporated into the preform prior to infiltration and reaction (42).

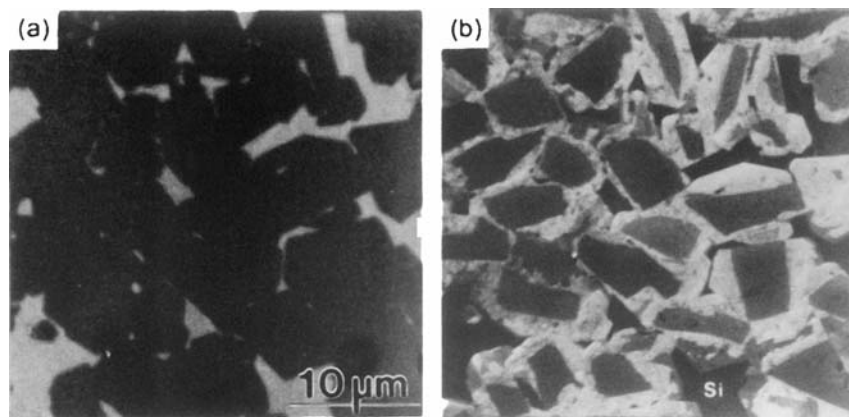


FIGURE 1.8 The same area of reaction bonded SiC observed with (a) reflected light showing the light Si phase due to its high reflectivity and (b) secondary electrons where the Si now appears black and the outer impure regions of SiC grains are lighter than the dark gray cores. (From Ref. 38.)

1.2.2 Liquid Precursor Methods

Fabrication routes in which a solution of metal compounds is converted into a solid body are sometimes referred to as *liquid precursor* methods. The sol–gel process has attracted considerable interest since the mid-1970s and forms the most important liquid precursor route for the production of simple or complex oxides. The pyrolysis of suitable polymers to produce ceramics (mainly nonoxides such as SiC and Si₃N₄) has attracted a fair degree of interest in the past 20 years. It is an important route for the production of SiC fibers.

1.2.2.1 Sol–Gel Processing

In the sol–gel process, a solution of metal compounds or a suspension of very fine particles in a liquid (referred to as a *sol*) is converted into a highly viscous mass (the *gel*). Two different sol–gel processes can be distinguished, depending on whether a sol or a solution is used (Fig. 1.9). Starting with a sol, the gelled material consists of identifiable colloidal particles that have been joined together by surface forces to form a network (Fig. 1.10a). When a solution is used, typically a solution of metal-organic compounds (such as metal alkoxides), the gelled material in many cases may consist of a network of polymer chains formed by hydrolysis and condensation reactions (Fig. 1.10b). This “solution sol–gel process” is receiving considerable research interest; however, the sol–gel process based on the gelling of suspensions sees more widespread industrial application. Several publications have been devoted to the sol–gel process, including an excellent text covering the physics and chemistry (43), a text on the applications (44), shorter review articles summarizing the science and technology (45), and proceedings of international conferences (46,47).

We shall consider the sol–gel process in more detail later (Chapter 5) but for the remainder of this section, we outline the main sequence of steps in the solution sol–gel route. As indicated above, the starting material normally consists of a solution of metal alkoxides in an appropriate alcohol. Metal alkoxides have the general formula M(OR)_x and can be considered as either a derivative an alcohol, ROH, where R is an alkyl group, in which the hydroxyl proton is replaced by a metal, M, or a derivative of a metal hydroxide, M(OH)_x. To this solution water is added, either in the pure state or diluted with more alcohol. Under constant stirring at temperatures slightly above room temperature (normally ~50–90°C) and with suitable concentration of reactants and pH of the solution, hydrolysis and condensation reactions may occur, leading to the formation of polymer chains. Taking the example of a tetravalent metal (e.g., M = Si), the reactions may be expressed as:

Hydrolysis



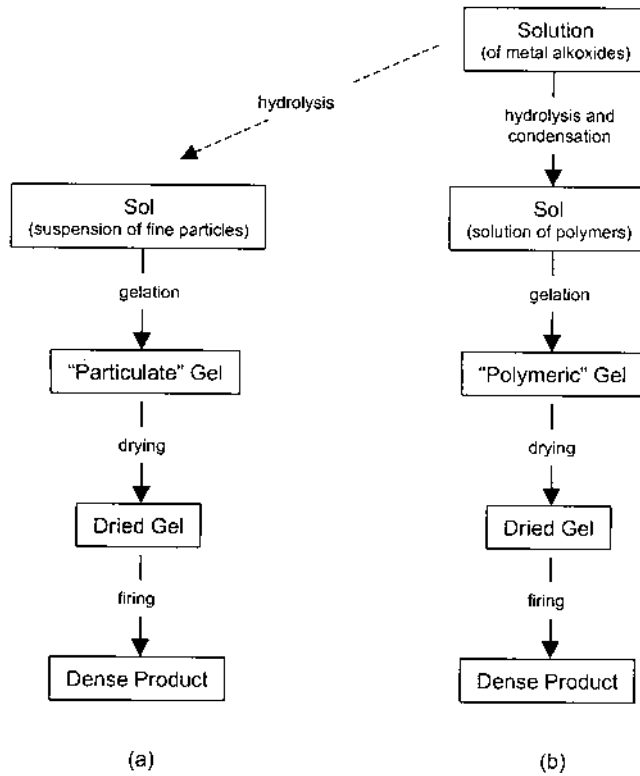


FIGURE 1.9 Basic flow charts for sol-gel processing using (a) a suspension of fine particles and (b) a solution.

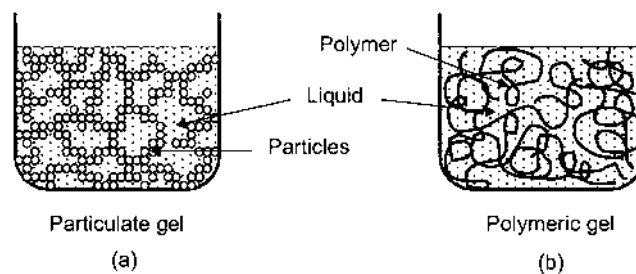


FIGURE 1.10 Schematic diagram of the structure of (a) a particulate gel formed from a suspension of fine particles and (b) a polymeric gel from a solution.

Condensation

Polymerization of the species formed by the hydrolysis and condensation reactions together with interlinking and cross-linking of the polymer chains eventually leads to a marked increase in the viscosity of the reaction mixture and the production of a gel. The gel has a continuous solid network and a finite shear modulus. Normally, excess water and alcohol are used in the reactions so that the amount of solid matter in the gel (i.e., the solids content of the gel) can be quite low, being <5–10 vol% in many cases. The remainder of the volume consists of liquid that must be removed prior to firing.

Drying of the gels can be the most time consuming and difficult step in the overall fabrication route, especially when a monolithic material is required directly from the gel. Normally, the liquid is present in fine channels, typically ~2–50 nm in diameter. Removal of the liquid by evaporation has two main consequences: large capillary stresses are generated, and the gel undergoes considerable shrinkage under the action of the capillary stress (48,49). If the liquid-filled pore channels in the gel are simplified as a set of parallel cylinders of radius a , then the maximum capillary stress exerted on the solid network of the gel is

$$p = \frac{2\gamma_{lv} \cos \theta}{a} \quad (1.8)$$

where γ_{lv} is the specific surface energy of the liquid/vapor interface and θ is the contact angle. For an alkoxide-derived gel with $\gamma_{lv} \cos \theta \approx 0.02$ – 0.07 J/m² and $a \approx 1$ – 10 nm, the maximum capillary stress is ~4–150 MPa, indicating that the gel can be subjected to quite large stresses. Remembering that the gelled material is fairly weak, unless special precautions are taken, cracking as well as warping of the dried gel can be a severe problem. If the evaporation is carried out slowly to control the vapor pressure of the liquid, drying can take weeks for a gel with a thickness of a few centimeters.

Aging before drying helps to strengthen the gel network and thereby reduce the risk of fracture (50). The addition of certain chemical agents to the solution prior to gelation has been reported to speed up the drying process considerably (51). These compounds, referred to as *drying control chemical additives* (DCCA), include formamide (NH₂CHO), glycerol (C₃H₈O₃), or oxalic acid (C₂H₂O₄). While their role in drying is not clear, it is known that they increase the hardness (and presumably the strength) of the gel. However, they can also cause serious problems during firing because they are difficult to burn off. Another approach is the use of supercritical drying where the problems associated with the capillary stresses are avoided by removing the liquid from the pores above the critical temperature and critical pressure (52,53).

Despite drying, the gel contains a small amount of adsorbed water and organic groups such as residual alkyl groups chemically attached to the polymer chains. These are removed below $\sim 500^\circ\text{C}$, prior to densification of the gels at a higher temperature. In general, this densification takes place at a much lower temperature than would be required to make an equivalent material by a more conventional fabrication route (e.g., sintering of powders). This densification at a lower temperature results, in general, from the amorphous nature of the gel and the very fine porosity. However, crystallization of the gel prior to significant densification can severely reduce the ease of sintering (see Chapter 12).

As a fabrication route for ceramics, the sol–gel process has a number of advantages. Because of the ease of purification of liquids (as the starting materials for the process), materials with high purity can be produced. Materials with exceptionally good chemical homogeneity, which is very desirable, especially in the case of complex oxides, can also be produced because the mixing of the constituents occurs at a molecular level during the chemical reactions. Another advantage is the lower densification temperature. However, the disadvantages are also real. The starting materials (e.g., the metal alkoxides) can be fairly expensive. We have already mentioned the difficulties of conventional drying, during which cracking, warping, and considerable shrinkage are common problems. Figure 1.11 illustrates the enormous amounts of shrinkage that may occur during the drying and sintering of a gel containing 5 vol% solids. Mainly because of these problems in drying, the sol–gel route has seen little use for the fabrication of monolithic ceramics. Instead it has seen considerable use for the fabrication of small or thin articles, such as films, fibers, and powders, and its use in this area is expected to grow substantially in the future.

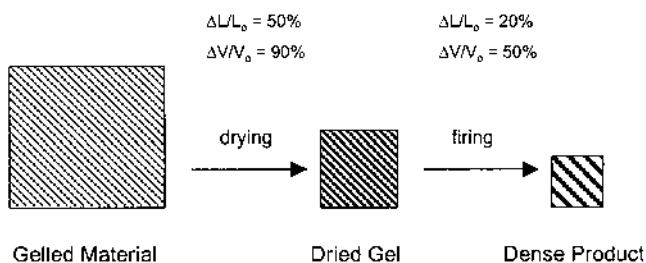


FIGURE 1.11 Schematic diagram illustrating the enormous shrinkages accompanying the drying by liquid evaporation and the firing of a polymeric gel ($\Delta L/L_0$ = linear shrinkage and $\Delta V/V_0$ = volumetric shrinkage). The solids content of the gelled material, the dried gel, and the final product are assumed to be 5, 50, and 100%, respectively.

1.2.2.2 Polymer Pyrolysis

Polymer pyrolysis refers to the pyrolytic decomposition of metal-organic polymeric compounds to produce ceramics. The polymers used in this way are commonly referred to as *preceramic polymers* in that they form the precursors to ceramics. Unlike conventional organic polymers (e.g., polyethylene), which contain a chain of carbon atoms, the chain backbone in preceramic polymers contains elements other than carbon (e.g., Si, B, and N) or in addition to carbon. The pyrolysis of the polymer produces a ceramic containing some of the elements present in the chain. Polymer pyrolysis is an extension of the well-known route for the production of carbon materials (e.g., fibers from pitch or polyacrylonitrile) by the pyrolysis of carbon-based polymers (54). It is also related to the solution sol-gel process described in the previous section where a metal-organic polymeric gel is synthesized and converted to an oxide.

The possibility of preparing ceramics from metal-organic polymers was recognized for many years (55). Heightened interest was generated in the mid-1970s when the formation of fibers with high SiC content was reported by Yajima et al. (56). While potentially a large field, the polymer pyrolysis route has been applied most effectively to the production of nonoxide ceramic fibers, in particular, fibers of two silicon-based ceramics, SiC and Si₃N₄, and to a more limited extent BN and B₄C. We shall therefore focus our attention on these nonoxide ceramics. Reviews have covered the general aspects of the precursor chemistry, polymer synthesis and pyrolysis of the polymers (57–61), the detailed precursor chemistry and synthesis (62), and the preceramic polymer routes to SiC fibers (63).

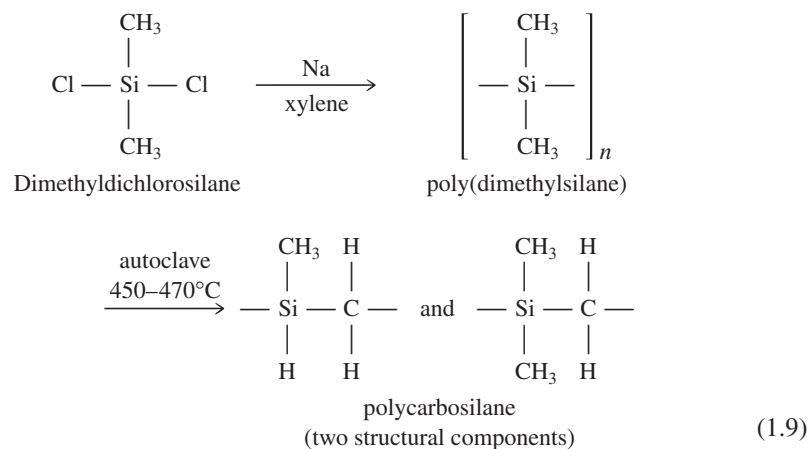
The characteristics of the ceramic product formed by polymer pyrolysis depend on the structure and composition of the polymer and on the pyrolysis conditions. The composition and structure of the polymer are dictated by the chemical synthesis of the monomers and their polymerization reactions. Furthermore, the usefulness of the polymer is determined by its processing characteristics, the ceramic yield on pyrolysis (percentage by weight of ceramic product formed from a given mass of polymer), the purity and microstructure of the ceramic product, and the manufacturing cost. Key requirements for the polymer include (a) synthesis from low-cost starting materials and polymerization reactions, (b) fusible at moderate temperatures or soluble in solvents for formation into the required shape (e.g., fibers), (c) high ceramic yield on pyrolysis (greater than ~75 wt%) to minimize volume changes, porosity, and shrinkage stresses, and (d) pyrolysis to give the desired chemical composition and crystalline microstructure of the ceramic product for property optimization (e.g., tensile strength and Young's modulus). Based on these requirements, only a limited number of synthetic routes have been developed. Examples of the types of polymers and the ceramics produced from them are shown in Table 1.4.

TABLE 1.4 Some Precursor Polymers and the Ceramics Produced by Their Pyrolysis

Polymer precursor	Ceramic yield		Ceramic product	Reference
	(wt%)	(Atmosphere)		
Polycarbosilanes	55–60	(N ₂ /vacuum)	SiC + amorphous SiC _x O _y	63
Polymethylsilanes	~80	(Ar)	SiC	67,68
Polysilazanes	80–85	(N ₂)	Amorphous SiC _x N _y	69
	60–65	(N ₂)	Amorphous Si ₃ N ₄ + carbon	70
Polysiladiazanes	~75	(N ₂)	Amorphous SiC _x N _y	71
	70–80	(Ar)	Amorphous Si ₃ N ₄ + SiC _x N _y	72
Polyborasilazanes	~90	(Ar)	Amorphous BSi _x C _y N _z	74
	~75	(NH ₃)	Amorphous BSi _x N _y	74

Silicon Carbide

Polymer precursor routes based on the synthesis of *polycarbosilanes* have been studied most extensively. The chain backbone of these polymers contains the Si–C bond. The polycarbosilane route was used by Yajima et al. (56) to produce fibers with high Si–C content and, as outlined above, formed an important contribution to the polymer pyrolysis route for Si-based ceramics. We shall use this system as an example to illustrate some basic steps in the process. The initial step [Eq. (1.9)] is the condensation reaction between Na and dimethyldichlorosilane, (CH₃)₂SiCl₂, in xylene to produce an insoluble poly(dimethylsilane), [(CH₃)₂Si]_n, where $n \approx 30$.



Poly(dimethylsilane) is not a useful preceramic polymer in that it gives a low ceramic yield on pyrolysis. When treated in an autoclave at 450–470°C, complex reactions take place and a new polymer is produced which no longer has a backbone consisting of just Si atoms. This polymer has Si–C–Si bonds in the chain and is referred to by the general term *polycarbosilane*. Alternatively, a catalyst (3–5 wt% polyborodiphenyl siloxane) allows the reaction to take place at lower temperatures ($\sim 350^\circ\text{C}$) and at atmospheric pressure. The purified polycarbosilanes have a complex structure with components consisting of the $\text{CH}_3(\text{H})\text{SiCH}_2$ unit and the $(\text{CH}_3)_2\text{SiCH}_2$ unit. The polycarbosilane structure suggested by Yajima (64) is shown in Fig. 1.12. Polycarbosilanes are glassy solids with a number average molecular weight M_n of 1000–2000 Da and, on pyrolysis in an inert atmosphere, give a ceramic yield of 55–60 wt%. They are soluble in common organic solvents, and the melt can be spun into fibers with small diameters (10–20 μm).

In the formation of fibers, after melt spinning at 250–350°C, the fibers undergo a rigidization step, referred to as *curing*, prior to conversion to the ceramic. Curing is accomplished by heating in air at 100–200°C to cross-link the polymer chains and serves to maintain geometrical integrity of the fibers. During pyrolysis in an inert atmosphere (e.g., N_2), an amorphous product is produced between 800 and 1100°C which crystallizes above $\sim 1200^\circ\text{C}$. The ceramic yield increases to ~ 80 wt% and this increase in the yield (when compared to the uncured material) correlates with cross-linking of the polymer chains by oxygen atoms during the curing step. The ceramic is not stoichiometric SiC but contains excess carbon and some oxygen (presumably from the curing step). In a variation of the process, Yajima et al. (65) heated the polycarbosilane with titanium tetrabutoxide, $\text{Ti}(\text{OC}_4\text{H}_9)_4$, to give a more highly cross-linked polymer, referred to as polytitanocarbosilane, containing Si, Ti, C, O, and H. Pyrolysis in an inert atmosphere produces a ceramic consisting mainly of SiC, a small amount of TiC, excess carbon and some oxygen. The ceramic yield is ~ 75 wt%.

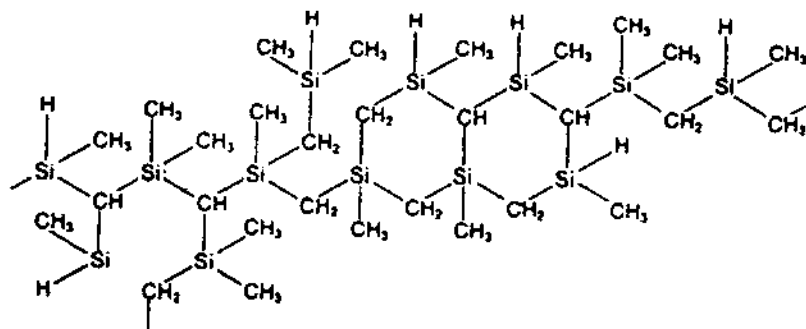


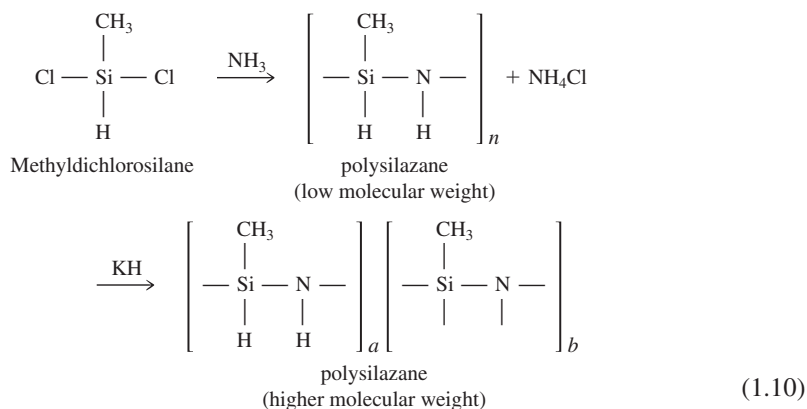
FIGURE 1.12 Constitutional chemical formula of polycarbosilane.

The procedures developed by Yajima et al. (56,65) form the basis for the industrial production of fibers with high SiC content. Fibers derived from polycarbosilane are produced by Nippon Carbon Company (Japan) under the trade name of *Nicalon*, while Ube Industries (Japan) produce fibers having the trade name *Tyranno* which are derived from polytitanocarbosilane. While nominally described as silicon carbide fibers, Nicalon fibers contain excess carbon and oxygen with a nominal composition of $\text{SiC}_{1.25}\text{O}_{0.33}$. The microstructure consists of microcrystalline β -SiC grains in an amorphous silicon oxycarbide matrix as well as significant microporosity. As the only high performance fibers available for several years, *Nicalon* fibers have been studied extensively and have been incorporated into more ceramic composites than any other fiber. The ceramic grade (CG) *Nicalon* fibers commonly used in ceramic composites have a tensile strength of ~ 3 GPa and a Young's modulus of ~ 200 GPa (66).

The nonstoichiometric composition coupled with the microporosity and amorphous phase in the microstructure reduces the thermal stability of the fibers. Depending on the magnitude and duration of the applied stress, the use of the fibers may be limited to temperatures lower than 1000°C . To overcome this deficiency, recent efforts have been devoted to producing dense, polycrystalline, stoichiometric SiC through modification of the synthesis and processing conditions or through the synthesis of more useful preceramic polymers (63,67,68).

Silicon Nitride

When compared to SiC, less work has been reported on the production of Si_3N_4 by the polymer pyrolysis route. Most efforts have focused on polymer precursors based on *polysilazanes*, a class of polymers having Si-N bonds in the main chain (58–61). The reactions to produce the Si-N bond in the chain backbone are based on the ammonolysis of methylchlorosilanes. A preceramic polymer can be prepared by the ammonolysis of methylchlorosilane, followed by the polymerization of the silazane product catalyzed by potassium hydride (69):



Polysilazanes with an average molecular weight of ~ 300 are produced in the first step. Pyrolysis of this material gives a ceramic yield of ~ 20 wt%. The second step results in the production of polysilazanes with molecular weight ranging from 600 to 1800. The suggested structure is shown in Fig. 1.13. Pyrolysis of these polysilazanes in N_2 at $\sim 1000^\circ C$ gives a ceramic yield of 80–85 wt%. The constitution of the product is not clear. Based on elemental chemical analysis, the constitution of the product has been suggested as an amorphous mixture of Si_3N_4 (~ 66 wt%), SiC (~ 27 wt%), C (~ 5 wt%), and possibly SiO_2 (~ 2 wt%). However, x-ray diffraction and nuclear magnetic resonance indicate that it may be an amorphous mixture of silicon-carbon-nitride and free carbon. Polysilazanes with a repeating unit of $[H_2SiNCH_3]$ that is isostructural and chemically identical with the $[CH_3HSiNH]$ repeating unit in Eq. (1.10) have also been studied as a precursor to silicon nitride (70). In this case, pyrolysis in N_2 at 1273K gives a ceramic yield of 63 wt% with the product consisting of predominantly of amorphous Si_3N_4 (77 wt%) and free carbon (18 wt%). These results indicate that the structure of the repeating unit in the preceramic polymer may have a significant influence on the composition and microstructure of the ceramic product.

Attempts have been made to improve the Si_3N_4 content and reduce the amount of carbon in the ceramic product through modification of the precursor chemistry. They include the synthesis of precursors based on hydridopolysilazane (71) and poly(methylsilyladiazane) (72).

Boron Nitride and Boron Carbide

While several routes exist for the preparation of polymer precursors to BN and B_4C (58–61,73), their usefulness is not clear. However, the reaction between

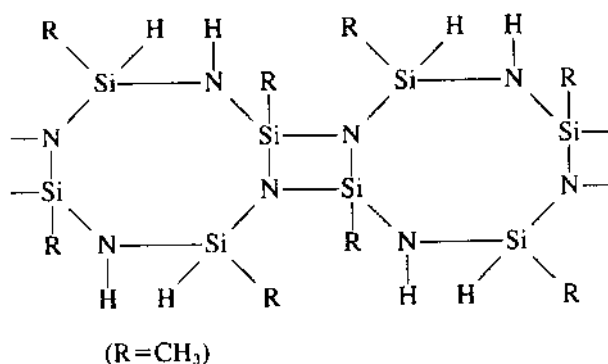


FIGURE 1.13 Example of the linkage of 8-membered rings via Si_2N_2 bridges in a polysilazane.

$\text{H}_3\text{B}-\text{S}(\text{CH}_3)_2$ and the silazane product $(\text{CH}_3\text{HSiNH})_n$ formed in the first step of Eq. (1.10) produces *borasilazane* polymers (molecular weight ~ 800) that are useful precursors to boron-containing ceramics (74). The polymers are soluble in many common organic solvents and can be processed into fibers. On pyrolysis in argon at 1000°C , polymers (formed with a Si/B reactant ratio of ~ 2) give a high yield (~ 90 wt%) of an amorphous “boron silicon carbon nitride” ceramic with a composition of $\text{B}_{1.0}\text{Si}_{1.9}\text{C}_{1.7}\text{N}_{2.5}$. Pyrolysis in NH_3 at 1000°C gives an amorphous “boron silicon nitride” ceramic with the composition BSi_3N_5 with a yield of ~ 75 wt%. For $\text{B}_4\text{C}/\text{BN}$ ceramics, high yield synthesis has been reported from polymer precursors synthesized by the reaction of decaborane ($\text{B}_{10}\text{H}_{14}$) with a diamine (e.g., $\text{H}_2\text{NCH}_2\text{CH}_2\text{NH}_2$) in an organic solvent (75).

The polymer pyrolysis route has key advantages such as ease of processing into the desired shape and relatively low conversion temperature to nonoxide ceramics. However, the pyrolysis step is accompanied by a large volume change. As an example, the pyrolysis of a polymer (density ~ 1 g/cm³) to give a ceramic yield of 75 wt% consisting of SiC or Si_3N_4 (density ~ 3.2 g/cm³) is accompanied by a decrease in volume of $\sim 75\%$. As outlined for the sol-gel process, such large volume changes make the fabrication of monolithic ceramics very difficult. The preceramic polymers have been investigated for use as binders in the processing of nonoxide ceramic powders (76–78), but they are very expensive and lead to a significant increase in the fabrication costs. The polymer pyrolysis route finds its most important use in the production of thin objects, in particular fibers and, to a more limited extent, coatings (79).

1.2.3 Fabrication from Powders

This route involves the production of the desired body from an assemblage of finely divided solids (i.e., powders) by the action of heat. It gives rise to the two most widely used methods for the fabrication of ceramics: (1) melting followed by casting (or forming) into shape, referred to simply as *melt casting*, and (2) firing of compacted powders. These two fabrication routes have their origins in the earliest civilizations.

1.2.3.1 Melt Casting

In its simplest form, this method involves melting a batch of raw materials (commonly in the form of powders), followed by forming into shape by one of several methods, including casting, rolling, pressing, blowing, and spinning. For ceramics that crystallize relatively easily, solidification of the melt is accompanied by rapid nucleation and growth of crystals (i.e., grains). Uncontrolled grain growth is generally a severe problem that leads to the production of ceramics with undesirable properties (e.g., low strength). Another problem is that many ceramics either have high melting points (e.g., ZrO_2 with a melting point of $\sim 2600^\circ\text{C}$) or decom-

pose prior to melting (e.g., Si_3N_4), so that obtaining a melt is rather difficult. The melt casting method is therefore limited to the fabrication of glasses. There are excellent texts covering the science and technology of glass manufacture by conventional melt casting routes (80–82) and by more specialized methods (83).

An important variation of glass processing is the *glass ceramic route* (84). Here, the raw materials are first melted and formed into shape in the glassy state by the conventional glass fabrication methods outlined above. The glass is then crystallized using a heat treatment consisting of two main steps: a lower temperature hold to induce nucleation of crystals followed by one or more higher temperature holds to promote growth of the crystals throughout the glass. Glass ceramics are by definition $\geq 50\%$ crystalline by volume and most are $>90\%$ crystalline. Other types of glass-based materials (e.g., opals and ruby glasses) that contain low levels of crystallinity are generally classified as glasses. The glass ceramic route has the advantage of economical fabrication by the conventional glass manufacturing methods. Furthermore, the composite structure, consisting of small crystals ($\sim 0.1\text{--}10\ \mu\text{m}$) held together in a glassy matrix, provides glass ceramics with improved properties when compared to the original glass. Generally, glass ceramics have higher strength, chemical durability, and electrical resistance and can be made with very low thermal expansion coefficients, giving excellent thermal shock resistance (85). The highest volume applications are cookware and tableware, architectural cladding, stove tops, and stove windows.

The potential range of glass ceramic compositions is fairly broad because the method depends only on the ability to form a glass and to control its crystallization. However, almost all glass ceramics developed so far are based on silicate glass compositions. They include

1. Simple silicates, e.g., compositions based on the $\text{Li}_2\text{O}\text{--}\text{SiO}_2$ system
2. Fluorosilicates
3. Aluminosilicates, e.g., compositions based on $\text{Li}_2\text{O}\text{--}\text{Al}_2\text{O}_3\text{--}\text{SiO}_2$ (LAS) and $\text{MgO}\text{--}\text{Al}_2\text{O}_3\text{--}\text{SiO}_2$ (MAS) systems

The most important glass ceramics in the LAS and MAS systems are compositions based on cordierite, β spodumene, and the structural derivatives of high quartz (β quartz). A typical commercial cordierite glass ceramic (Corning Code 9606) has the composition (in wt%): SiO_2 (56.0), Al_2O_3 (19.7), MgO (14.7), TiO_2 (9.0), CaO (0.11), and As_2O_3 (0.5). Compared to the stoichiometric cordierite composition ($2\text{MgO}\cdot 2\text{Al}_2\text{O}_3\cdot 5\text{SiO}_2$), this commercial composition has an excess of SiO_2 and utilizes 9 wt% TiO_2 for the nucleation of crystals. The phases produced by heat treatment above $\sim 1200^\circ\text{C}$ are cordierite, magnesium aluminum titanate, and cristobalite. The microstructure of a cordierite glass ceramic (Corning Code 9606) is shown in Fig. 1.14. The predominant phase with rounded grains is cordierite; the angular, needle-shaped crystals are magnesium aluminum titanate.

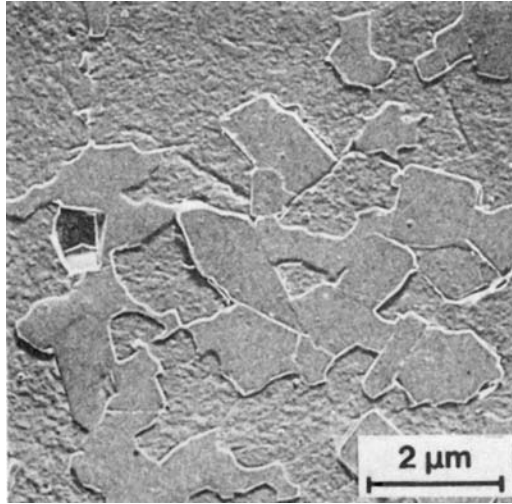


FIGURE 1.14 The microstructure of a commercial cordierite glass ceramic (Corning Code 9606). The predominant phase with somewhat rounded grains is cordierite and the angular, needle-shaped crystals are magnesium aluminum titanate. (From Ref. 85.)

1.2.3.2 Firing of Compacted Powders

Although in principle this route can be used for the production of both glasses and polycrystalline ceramics, in practice it is hardly ever used for glasses because of the availability of more economical fabrication methods (e.g., melt casting). It is, however, by far the most widely used method for the production of polycrystalline ceramics. The various processing steps are shown in Fig. 1.15. In its simplest form, this method involves the consolidation of a mass of fine particles (i.e., a *powder*) to form a porous, shaped powder (referred to as a *green body* or *powder compact*), which is then *fired* (i.e., heated) to produce a dense product. Because of its importance and widespread use, the fabrication of polycrystalline ceramics from powders will form the main focus of this book. In the next section, we provide an overview of the fabrication of polycrystalline ceramics from powders which will form the basis for the more detailed considerations in subsequent chapters.

1.3 PRODUCTION OF POLYCRYSTALLINE CERAMICS FROM POWDERS: AN OVERVIEW

In the flow chart shown in Fig. 1.15 for the fabrication of ceramics from powders, we can divide the processing steps into two parts: processes prior to the firing

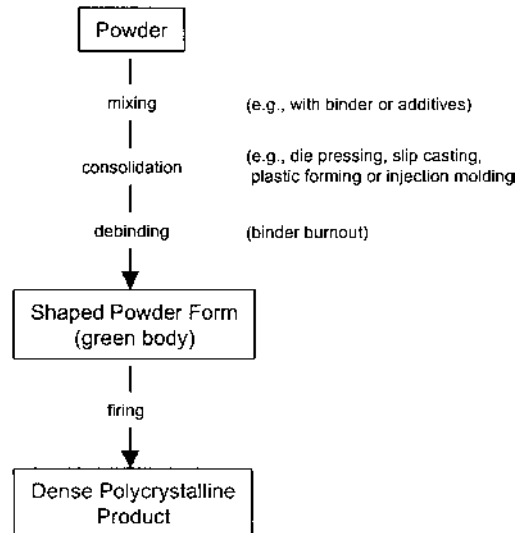


FIGURE 1.15 Basic flow chart for the production of polycrystalline ceramics by firing of consolidated powders.

of the green body and those that occur during firing. Until recently, most emphasis was placed on the processes that occur during firing, and the understanding gained from these studies is considerable. However, the increased attention given recently to powder synthesis and forming methods has yielded clear benefits. The most useful approach (and the one adopted in this book) requires that close attention be paid to each processing step in the fabrication route if the very specific properties required of many ceramics are to be achieved. Each step has the potential for producing undesirable microstructural flaws in the body that can limit its properties and reliability. The important issues in each step and how these influence or are influenced by the other steps are outlined in the following sections.

1.3.1 Powder Synthesis and Powder Characterization

In most cases, the fabrication process starts from a mass of powder obtained from commercial sources. Nevertheless, knowledge of powder synthesis methods is very important. Equally important are methods that can be used to determine the physical, chemical, and surface characteristics of the powder. The characteristics of the powder depend strongly on the method used to synthesize it, and these, in turn, influence the subsequent processing of the ceramic. The powder character-

istics of greatest interest are the size, size distribution, shape, degree of agglomeration, chemical composition, and purity.

Many methods are available for the synthesis of ceramic powders. These range from mechanical methods involving predominantly grinding or milling for the reduction in size of a coarse, granular material (referred to as *comminution*) to chemical methods involving chemical reactions under carefully controlled conditions. Some of the chemical methods, while often more expensive than the mechanical methods, offer unprecedented control of the powder characteristics. Figure 1.16 shows an example of a chemically synthesized powder consisting of spherical particles of approximately the same size (86).

One of the more troublesome issues in the production of ceramics is the effect of minor variations in the chemical composition and purity of the powder on processing and properties. These variations, produced by insufficient control of the synthesis procedure or introduced during subsequent handling, often go unrecorded or undetected. However, their effects on the microstructure and properties of the fabricated material can often be quite profound. For ceramics that must satisfy very demanding property requirements, one of the major advances made in the last 20 years has been the attention paid to powder quality. This has resulted in greater use of chemical methods for powder synthesis coupled with careful handling during subsequent processing.

A continuing trend is towards the preparation of fine powders. In principle, the enhanced activity of fine powders is beneficial for the attainment of high-density bodies at lower firing temperatures (87). A major problem, however, is that the benefits of fine powders are normally realized only when extreme care is taken in their handling and subsequent consolidation. Generally, as the size

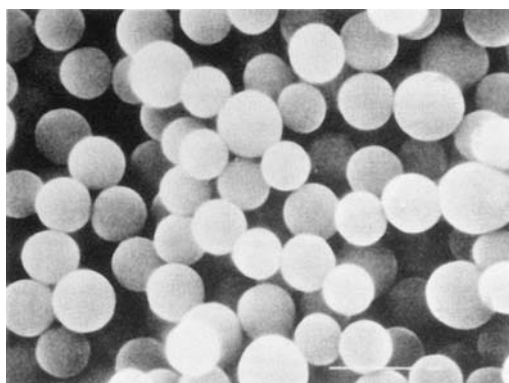


FIGURE 1.16 An example of a submicrometer TiO_2 powder prepared by controlled chemical precipitation from a solution. (From Ref. 86.)

decreases below $\sim 1\ \mu\text{m}$, the particles exhibit a greater tendency to interact, giving rise to the formation of *agglomerates*. One consequence of the presence of agglomerates is that the packing of the consolidated powder can be quite nonuniform. The overall effect is that, during the firing stage, little benefit is achieved over a coarse powder with a particle size corresponding to the agglomerate size of the fine powder. The use of fine powders therefore requires proper control of the handling and consolidation procedures in order to minimize the deleterious effects due to the presence of agglomerates. Such procedures may be quite demanding and expensive.

Along with the trend toward cleaner powders has been the growing use of analytical techniques for the characterization of the surface chemistry of the powders. These techniques include transmission electron microscopy (TEM), secondary ion mass spectroscopy (SIMS), Auger electron spectroscopy (AES), and x-ray photoelectron spectroscopy (XPS), also referred to as electron spectroscopy for chemical analysis (ESCA). The spectroscopic techniques have the capability for detecting constituents (atoms, ions, or molecules) down to the parts per million range.

1.3.2 Powder Consolidation

The consolidation of ceramic powders to produce a green body is commonly referred to as *forming*. The main forming methods include (1) dry or semidry pressing of the powder (e.g., in a die), (2) mixing of the powder with water or organic polymers to produce a plastic mass that is shaped by pressing or deformation (referred to as *plastic forming*), and (3) casting from a concentrated suspension or slurry (e.g., *slip casting* and *tape casting*). These methods have been in use for a long time and most have originated in the traditional ceramics industry for the manufacture of clay-based materials.

Perhaps the greatest advance made in the last 20 years has been the realization of the importance of the green body microstructure on the subsequent firing stage. If severe variations in packing density occur in the green body, then under conventional firing conditions, the fabricated body will usually have a heterogeneous microstructure that limits the engineering properties and reliability. This realization has led to the increasing use of colloidal techniques for the consolidation of powders from a suspension (88). This approach can be regarded essentially as a refinement of the slip casting technique used for many years in the traditional ceramics industry. The colloidal approach starts from powders with controlled characteristics which have been prepared by chemical methods or by fractionation of a commercial powder. The powders are dispersed in a liquid (normally water) and stabilized to prevent agglomeration through the use of electrolytes or polymers that are dissolved in the liquid. The suspension is then made to settle by itself, by filtration, or by centrifuging. The deposit forms the green body for

subsequent firing. Figure 1.17 shows an example of the uniform arrangement formed from almost spherical, nearly monosized particles (89). Whereas their benefits have been demonstrated, colloidal methods have not made inroads into many industrial applications where mass production is desired and fabrication cost is a serious consideration.

1.3.3 The Firing Process

In this stage of the fabrication route, the green body is heated to produce the desired microstructure. The changes occurring during this stage may be fairly complex, depending on the complexity of the starting materials. In the ceramics literature, two terms have been used to refer to the heating stage: firing and sintering. Generally, the term *firing* has been used when the processes occurring during the heating stage are fairly complex, as in many traditional ceramics produced from clay-based materials. In less complex cases, the term *sintering* has been used. We will distinguish between firing and sintering when this is convenient; however, we do not wish to attach much importance to this distinction.

The less complex nature of sintering allows it to be analyzed theoretically in terms of idealized models. The theoretical analyses combined with experimental

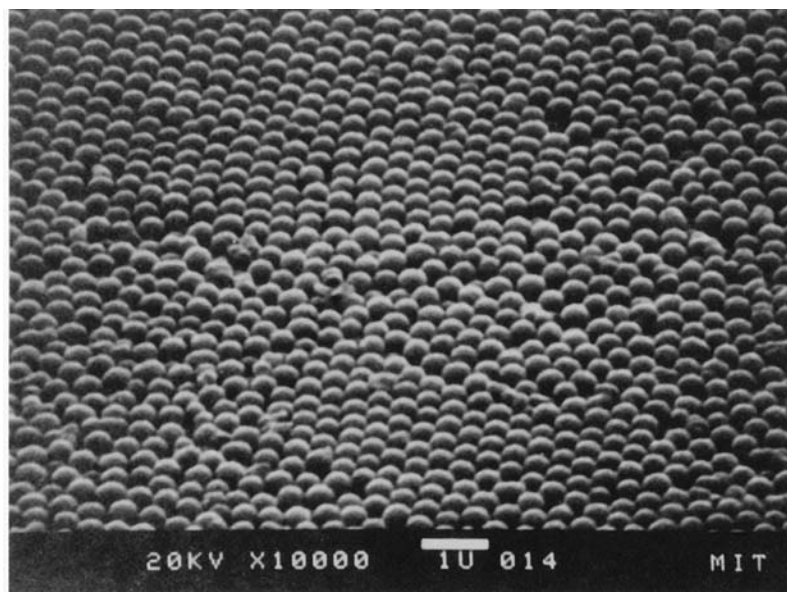


FIGURE 1.17 Uniformly packed submicrometer TiO_2 powder produced by consolidation from a stable suspension. (From Ref. 89.)

investigations during the last 50 years have provided a considerable understanding of sintering. The simplest case is that for a pure, single-phase material (e.g., Al_2O_3). The system is heated to a temperature that is in the range of 0.5–0.75 of the melting temperature. (For Al_2O_3 with a melting temperature of 2073°C, the sintering temperature is commonly 1400–1650°C.) The powder does not melt; instead, the joining together of the particles and the reduction in the porosity (i.e., densification) of the body, as required in the fabrication process, occurs by atomic diffusion in the solid state. This type of sintering is usually referred to as *solid-state sintering*. While solid state sintering is the simplest case of sintering, the processes occurring and their interaction can be fairly complex.

The driving force for sintering is the reduction in surface free energy of the consolidated mass of particles. This reduction in energy can be accomplished by atom diffusion processes that lead to either *densification* of the body (by transport matter from inside the grains into the pores) or *coarsening* of the microstructure (by rearrangement of matter between different parts of the pore surfaces without actually leading to a decrease in the pore volume). The diffusion paths for densification and coarsening are shown in Fig. 1.18 for an idealized situation of two spherical particles in contact (90). From the point of view of achieving high densities during sintering, a major problem is that the coarsening process reduces the driving force for densification. This interaction is sometimes expressed by the statement that sintering involves a competition between densification and coarsening. The domination of densifying diffusion processes will favor the production of a dense body (Fig. 1.19a). When coarsening processes dominate, the production of a highly porous body will be favored (Fig. 1.19b).

The effects of key material and processing parameters such as temperature, particle (or grain) size, applied pressure, and gaseous atmosphere on the densification and coarsening processes are well understood. The rates of these processes are enhanced by higher sintering temperature and by fine particle size. Densification is further enhanced by the application of an external pressure. A key issue that has received increasing attention in recent years is the effect of microstructural inhomogeneities present in the green body (e.g., density, grain size, and compositional variations). It is now well recognized that inhomogeneities can seriously hinder the ability to achieve high density and to adequately control the fabricated microstructure. As outlined earlier, a consequence of this realization has been the increased attention paid to powder quality and to powder consolidation by colloidal methods.

A common difficulty in solid-state sintering is that coarsening may dominate the densification process, with the result that high densities are difficult to achieve. This difficulty is especially common in highly covalent ceramics (e.g., Si_3N_4 and SiC). One solution is the use of an additive that forms a small amount of liquid-phase between the grains at the sintering temperature. This method is referred to as *liquid-phase sintering*. The liquid phase provides a high diffusivity

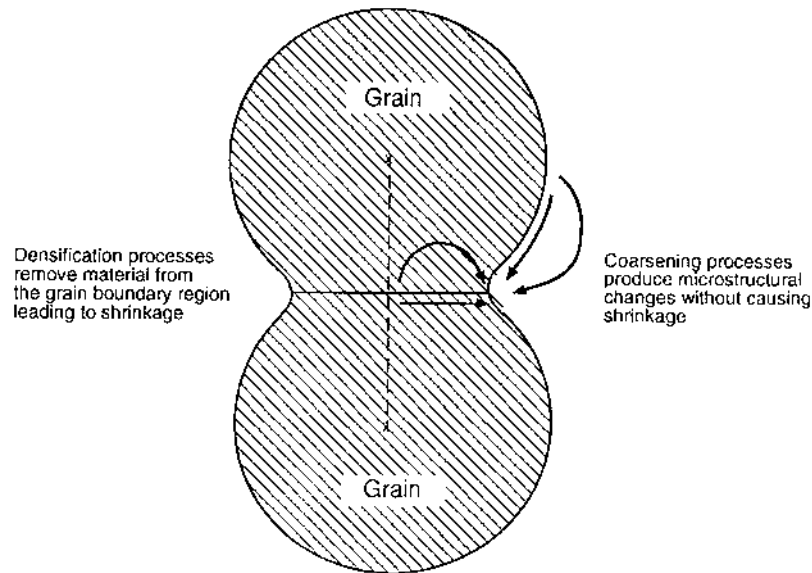


FIGURE 1.18 Schematic indication of the distinction between densifying and nondensifying microstructural changes resulting from atom transport during the firing of ceramic powders.

path for transport of matter into the pores to produce densification but is insufficient, by itself, to fill up the porosity. A classic example of liquid-phase sintering in ceramics is the addition of 5–10 wt% of MgO to Si_3N_4 (Fig. 1.20). The presence of the liquid phase adds a further complexity to the sintering process, but the benefits can be significant, as demonstrated by the widespread use of liquid phase sintering in industry. Another solution to the difficulty of inadequate densification is the application of an external pressure to the body during heating in either case of solid-state or liquid-phase sintering. This method is referred to as *pressure sintering* of which hot pressing and hot isostatic pressing are well-known examples. The applied pressure has the effect of increasing the driving force for densification without significantly affecting the rate of coarsening. However, a common drawback of pressure sintering is the increase in the fabrication costs.

A further type of sintering is *viscous sintering*. In this case, a viscous glass or liquid present at the sintering temperature flows under the action of the capillary forces of the pores to fill up the porosity of the body. A relatively simple example of viscous sintering is that of a porous glass body (e.g., consolidated glass particles). A more complex example is the fabrication of clay-based ceramics (e.g., porcelain) from a mixture of naturally occurring raw materials. Chemical reaction,

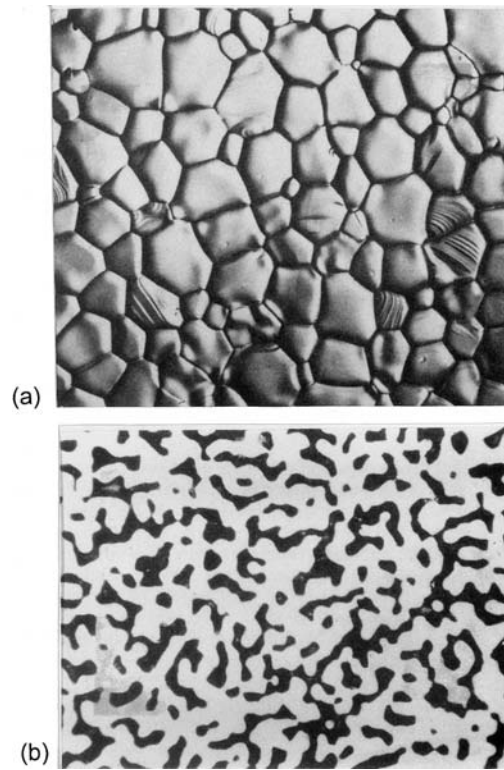


FIGURE 1.19 (a) The surface of an alumina ceramic from which all porosity has been removed during the firing of the powder; the microstructure consists of the crystalline grains and the boundaries (interfaces) between them. (b) The sintering of silicon results in the formation of a continuous network of solid material (white) and porosity (black); this microstructural change is not accompanied by any shrinkage. (From Ref. 90.)

liquid formation, and viscous flow of the liquid into the pores lead to a dense body that on cooling consists of a microstructure of crystalline grains and glassy phases. This rather complex case of viscous sintering in clay-based materials is referred to as *vitrification*.

1.3.4 Ceramic Microstructures

As outlined earlier, the microstructure of the fabricated article is significantly dependent on the processing methods. The examination of the microstructure may therefore serve as a test of successful processing. Equally important, micro-

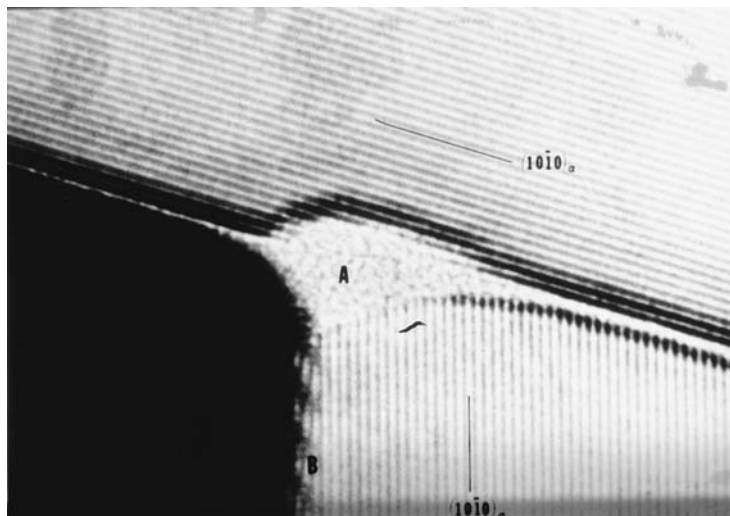


FIGURE 1.20 Microstructure produced by liquid-phase sintering, under an applied pressure, of Si_3N_4 with MgO additive. A continuous glassy phase, ~ 0.8 nm thick, separates the crystalline grains. (Courtesy of D. R. Clarke.)

structural observations may lead to inferences about the way in which the processing methods must be modified or changed to give the desired characteristics. As we have seen from the previous section, ceramic microstructures cover a wide range. For solid-state sintering in which all the porosity is successfully removed, a microstructure consisting of crystalline grains separated from one another by grain boundaries is obtained (Fig. 1.19a). However, most ceramics produced by solid-state sintering contain some residual porosity (Fig. 1.21). The use of liquid-phase sintering leads to the formation of an additional phase at the grain boundaries. Depending on the nature and amount of liquid, the grain boundary phase may be continuous, thereby separating each grain from the neighboring grains (Fig. 1.20), or may be discontinuous, e.g., at the corners of the grains.

Generally, the advanced ceramics that must meet exacting property requirements tend to have relatively simple microstructures. A good reason for this is that the microstructure is more amenable to control when the system is less complex. Even so, as outlined earlier, the attainment of these relatively simple microstructures in advanced ceramics can be a difficult task. For the traditional clay-based ceramics, for which the properties achieved are often less critical than the cost or shape of the fabricated article, the microstructures can be fairly complex, as shown in Fig. 1.22 for a ceramic used for sanitaryware (16).

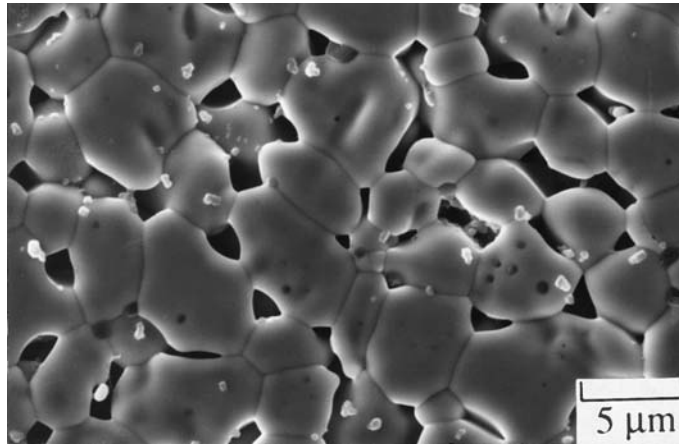


FIGURE 1.21 Incomplete removal of the porosity during solid-state sintering of CeO_2 results in a microstructure consisting of grains, grain boundaries, and pores.

Ceramic composites are a class of materials that have undergone rapid development in recent years because of their promising properties for structural applications at high temperatures (e.g., heat engines). A reinforcing phase (e.g., SiC fibers) is deliberately added to the ceramic (e.g., Al_2O_3) to make it mechanically tougher (i.e., reduce its brittleness). For these materials, the complexity of the microstructure is controlled by having an ordered distribution of the reinforcing phase in the ceramic matrix (see Fig. 1.6).

We discussed earlier the strong consequences of insufficient attention to the quality of the powder and to the consolidation of the powder in the production of the green body. Microstructural flaws that limit the properties of the fabricated body normally originate in these stages of processing. Large voids and foreign objects such as dust or milling debris are fairly common. The control of the powder quality such as the particle size distribution, the shape, and the composition, including minor constituents, has a major influence on the development of the microstructure. Impurities can lead to the presence of a small amount of liquid phase at the sintering temperature, which causes selected growth of large individual grains (Fig. 1.23). In such a case, the achievement of a fine uniform grain size would be impossible. The uniformity of the packing in the consolidated material is also very important. In general, any nonuniformity in the green body is exaggerated in the sintering process, leading to the development of cracklike voids or large pores between relatively dense regions (Fig. 1.24).

Assuming proper precautions were taken in the processing steps prior to firing, further microstructural manipulation must be performed during sintering.

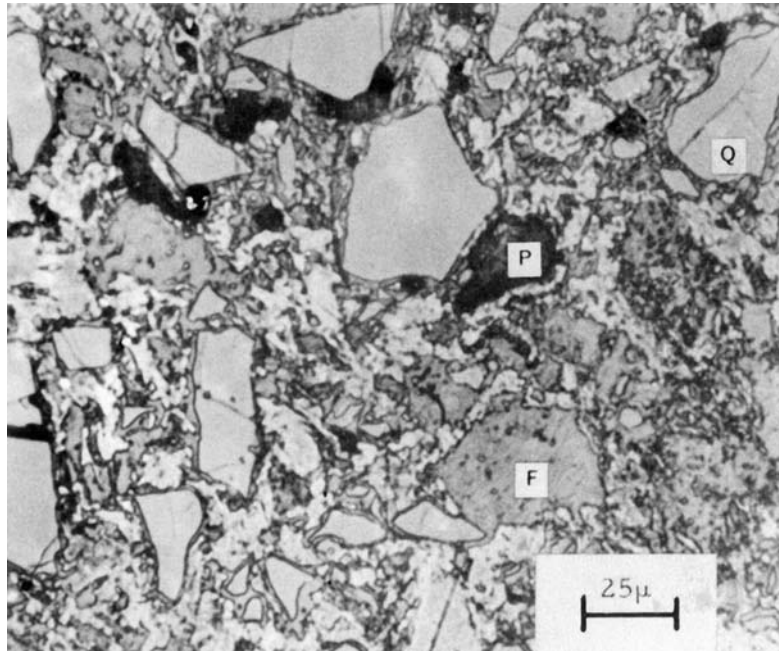


FIGURE 1.22 A commercial sanitaryware body produced by firing a mixture of clay, feldspar and quartz, showing a fairly complex microstructure containing some residual feldspar (F), porosity (P), and quartz (Q). (From Ref. 91.)

Unless high porosity is a deliberate requirement, we normally wish to achieve as high a density, as small a grain size, and as uniform a microstructure as possible. Insufficient control of the sintering conditions (e.g., sintering temperature, time at sintering temperature, rate of heating, and sintering atmosphere) can lead to defects and the augmentation of coarsening, which make attainment of the desired microstructure impossible. The sintering of many materials (e.g., Si_3N_4 , lead-based ferroelectric ceramics, and β -alumina) require control of the atmosphere in order to prevent decomposition or volatilization.

Most ceramics are not single-phase solids. For a material consisting of two solid phases, our general requirement is for a uniform distribution of one phase in a uniformly packed matrix of the other phase. Close attention must be paid to the processing steps prior to firing (e.g., during the mixing and consolidation stages) if this requirement is to be achieved in the fabricated body. The consequences of nonuniform mixing for the microstructure control of an Al_2O_3 powder containing fine ZrO_2 particles are illustrated in Fig. 1.25. As in the case for single-

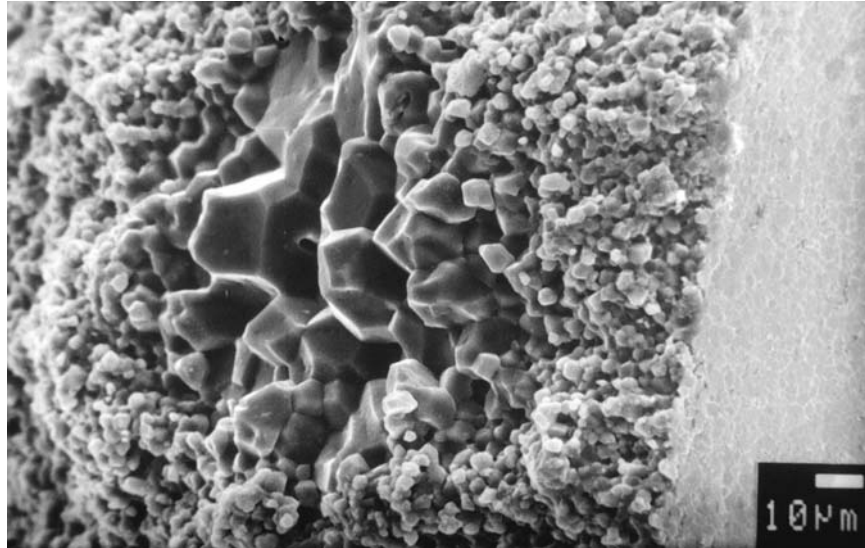


FIGURE 1.23 Large grained region of microstructural heterogeneity resulting from an impurity in hot pressed Al_2O_3 . (Courtesy of B. J. Dalglish.)

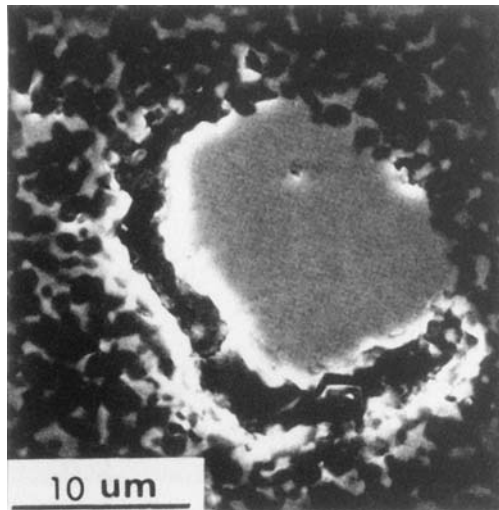


FIGURE 1.24 Cracklike void produced by a ZrO_2 agglomerate shrinking away from the surrounding $\text{Al}_2\text{O}_3/\text{ZrO}_2$ matrix during firing. (Courtesy of F. F. Lange.)

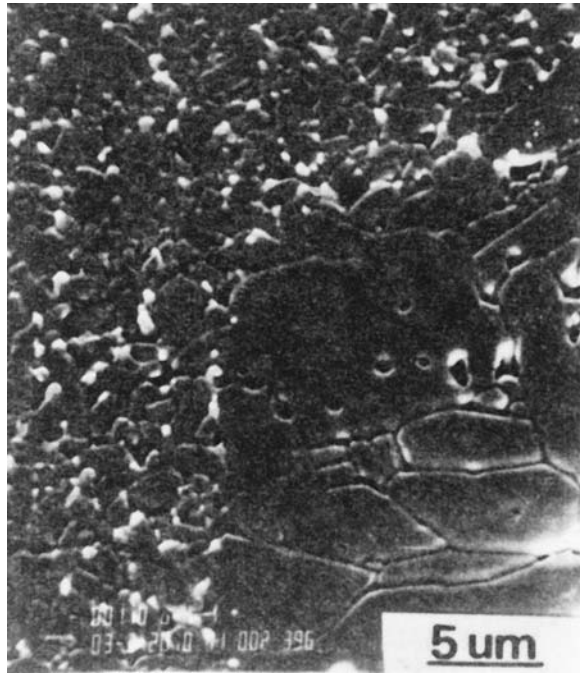


FIGURE 1.25 The nonuniform distribution of fine ZrO_2 particles (light phase) in Al_2O_3 (dark phase) is seen to result in a region of uncontrolled grain growth during firing. (Courtesy of F. F. Lange.)

phase ceramics, we must also pay close attention to the firing stage. An additional effect now is the possibility of chemical reactions between the phases. As outlined earlier, Al_2O_3 can be made mechanically tougher (i.e., less brittle) by the incorporation of SiC fibers. However, oxidation of the SiC fibers leads to the formation of an SiO_2 layer on the fiber surfaces. The SiO_2 can then react with the Al_2O_3 to form aluminosilicates with a consequent deterioration of the fibers. Prolonged exposure of the system to oxygen will eventually lead to the disappearance of the fibers. A primary aim therefore would be the control of the atmosphere during densification in order to prevent oxidation.

In summary, although sufficient attention must be paid to the firing stage, defects produced in the processing steps prior to firing cannot normally be reduced or eliminated. In most cases, these defects are enhanced during the firing stage. In general, properties are controlled by the microstructure (e.g., density and grain size), but the defects in the fabricated body have a profound effect on those properties that depend on failure of the material (e.g., mechanical strength, dielec-

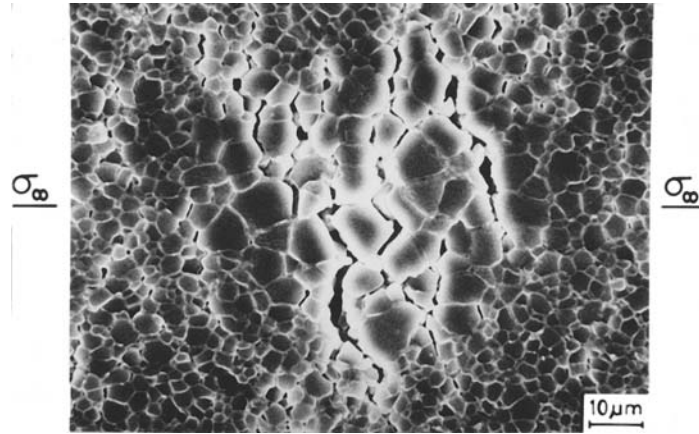


FIGURE 1.26 Crack nucleation at a large grained heterogeneity during deformation of a hot-pressed Al_2O_3 body. (Courtesy of B. J. Dalgleish.)

tric strength, and thermal shock resistance). Failure events are almost always initiated at regions of physical or chemical heterogeneity. An example is shown in Fig. 1.26 where mechanical failure originates at a large-grained heterogeneity (92).

1.4 A CASE STUDY IN PROCESSING: THE FABRICATION OF TiO_2 FROM POWDERS

Earlier, we outlined the potential benefits that may accrue from careful control of the powder quality and the powder consolidation method. To further illustrate these benefits, we consider the case of TiO_2 . One fabrication route for the production of TiO_2 bodies, referred to as the *conventional route* (93), is summarized in the flow diagram of Fig. 1.27a. Typically, TiO_2 powder available from commercial sources is mixed with small amounts of additives (e.g., Nb_2O_5 and BaCO_3) that aid the sintering process and is calcined for 10–20 h at $\sim 900^\circ\text{C}$ in order to incorporate the additives into solid solution with the TiO_2 . The calcined material is mixed with a small amount of binder (to aid the powder compaction process) and milled in a ball mill to break down agglomerates present in the material. The milled powder, in the form of a slurry, is sprayed into a drying apparatus (available commercially and referred to as a *spray dryer*). The spray drying process serves to produce a dried powder in the form of spherically shaped agglomerates. After

compaction, the powder is sintered for 10 h at $\sim 1400^{\circ}\text{C}$ to produce a body with a density of $\sim 93\%$ of the theoretical density of TiO_2 .

In the fabrication route used by Barringer and Bowen (89), powders with controlled characteristics are prepared and consolidated, by colloidal methods, into uniformly packed green bodies (e.g., similar to that shown in Fig. 1.17). An abbreviated flow diagram of the fabrication route is shown in Fig. 1.27b. Powders are prepared by controlled hydrolysis of titanium tetraisopropoxide (denoted powder I) or titanium tetraethoxide (powder II). The powder particles are nearly spherical and almost monosized. After washing, each powder is dispersed in a basic aqueous solution to produce a stable suspension. Consolidation of the suspension is accomplished by gravitational or centrifugal settling. The consolidated body is dried in a vacuum and sintered for ~ 90 min at 800°C (for powder

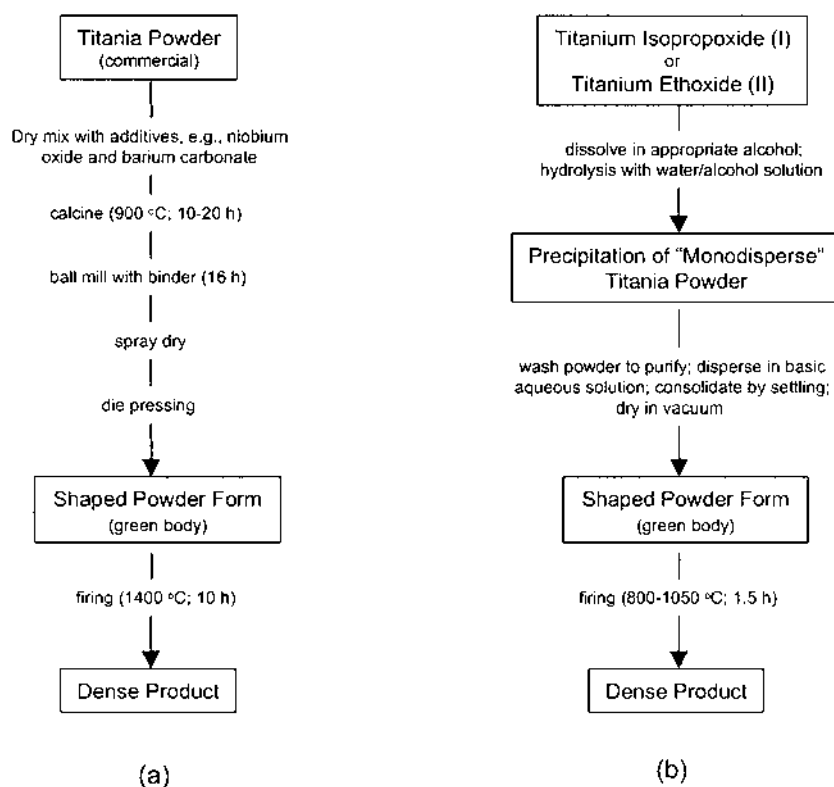


FIGURE 1.27 Flow chart for the production of TiO_2 by (a) a conventional powder route and (b) the powder route used by Barringer and Bowen (89).

TABLE 1.5 Processing Data for the Production of Titanium Dioxide by a Conventional Route (93) and by the Method of Barringer and Bowen (89)

Process parameter	Conventional	Barringer and Bowen
Powder particle size (μm)	1	0.1 (I) 0.4 (II)
Sintering temperature ($^{\circ}\text{C}$)	1400	800 (I) 1050 (II)
Sintering time (h)	10	1.5
Final relative density (%)	93	>99
Final grain size (μm)	50–100	0.15 (I) 1.2 (II)

I) or 1050 $^{\circ}\text{C}$ (for powder II) to produce bodies with a density greater than 99% of the theoretical.

Table 1.5 gives a summary of the main results of the two fabrication methods described above. It is easily recognized that the benefits achieved by the fabrication route of Barringer and Bowen are very extraordinary. These include a substantial reduction in sintering temperature (by 350–600 $^{\circ}\text{C}$) and sintering time, a higher final density, and a much smaller grain size. Furthermore since no milling, binder, or sintering aids are required, the purity of the fabricated bodies can be expected to be higher than for the conventional route.

In summary, the experiments of Barringer and Bowen demonstrate clearly that substantial benefits can be achieved in sintering and microstructure control when the powder quality is carefully controlled and the powder packing is homogeneous, i.e., when careful attention is paid to the processing steps that precede firing. However, this fabrication route is not currently used in many industrial applications where mass production and low cost are important considerations.

1.5 CONCLUDING REMARKS

In this chapter we have examined, in general terms, the common methods for the fabrication of ceramics. By far the most widely used method for the production of polycrystalline ceramics is the sintering of consolidated powders. Solution-based methods (e.g., sol–gel processing) are attracting significant research interest and their use is expected to grow substantially in the future. Although the powder processing route has its origins in early civilization, its use in the production of advanced ceramics with the desired microstructure can involve severe difficulties. Each processing step has the potential for producing microstructural flaws in the fabricated body, thereby causing a deterioration in properties. Careful attention

must therefore be paid to each processing step in order to minimize the microstructural flaws. Finally, we considered the fabrication of titania and showed the enormous benefits that can be achieved by careful attention to the processing.

PROBLEMS

- 1.1 Silicon powder is compacted to a density of 60% of the theoretical value and heated in N_2 to form reaction bonded silicon nitride (RBSN). If the reaction goes to completion and there is no change in the external dimensions of the compact, determine the porosity of the RBSN.
- 1.2 Consider the formation of Al_2O_3/ZrO_2 composites by the reaction bonded aluminum oxide (RBAO) process. An attrition-milled mixture of 45 vol% Al, 35 vol% Al_2O_3 , and 20 vol% ZrO_2 (monoclinic phase) is compacted to a green density of 65% of the theoretical value (35% porosity) and heated slowly to oxidize the Al prior to sintering. If the volume fraction of Al oxidized during the milling step is zero, determine the porosity of the compact after the oxidation step, assuming that the Al is completely oxidized. If the compact reaches full density during the sintering step, determine the linear shrinkage of the body. State any assumptions that you make.
 Repeat the calculations for the case when 10 vol% of the Al is oxidized during the milling step, assuming that the green density is the same.
- 1.3 One approach to the formation of mullite by the RBAO process uses a starting mixture of Al and SiC powders. After attrition milling, the mixture is compacted to form a green body with a relative density of ρ_o . Oxidation of the green body leads to the formation of a mixture of Al_2O_3 and SiO_2 , which is converted to mullite at higher temperatures. If the relative density of the final mullite body is ρ , derive a condition for zero shrinkage of the compact in terms of ρ_o , ρ , and the volume fractions of Al and SiC in the starting powder mixture (V_{Al} and V_{SiC} , respectively). Assume that the volume fraction of the starting powders oxidized during the attrition milling step is zero.
 Show the condition for zero shrinkage on a graph using axes corresponding to the final density and the green density.
- 1.4 Repeat the exercise in Prob. 1.3 for the case when the starting mixture consists of Si and Al_2O_3 powders.
- 1.5 Compare the production of dense $BaTiO_3$ tapes by the following two methods:
 - a. The oxidation of dense sheets of a solid metallic precursor consisting of Ba and Ti (See Ref. 94).
 - b. Tape casting of $BaTiO_3$ powder slurries (see Chapter 6).
- 1.6 Derive Eq. (1.5) for the height of a cylindrical pore infiltrated by a liquid.
- 1.7 Determine the linear and volume shrinkages that occur during the drying and sintering of a gel containing 5 vol% solids if the dried gel and the sintered gel have a solids content (relative density) of 50% and 100%, respectively. Compare the calculated values with the approximate values given in Fig. 1.11.

- 1.8 Assuming that a polycarbosilane consists of equal numbers of the two structural components given in Eq. (1.9), which on pyrolysis give SiC, estimate the ceramic yield (in wt%) on pyrolysis.
- 1.9 Taking 1 cm^3 of a polycarbosilane with a density of $\sim 1.2 \text{ g/cm}^3$, estimate the volume of SiC formed on pyrolysis if the ceramic yield is 60 wt%.
- 1.10 Discuss the key factors involved with using preceramic polymers for the following applications:
 - a. Production of high-strength ceramic fibers.
 - b. A binder in ceramic green bodies.
 - c. The formation of a fine reinforcing phase in ceramic composites.
 - d. The production of ceramic thin films.

REFERENCES

1. Kenney, G. B.; Bowen, H. K. *Am. Ceram. Soc. Bull.* 1983, Vol. 62 (5), 590.
2. Pierson, H. O. *Handbook of Chemical Vapor Deposition (CVD): Principles, Technology, and Applications*; Noyes: Park Ridge, NJ, 1992.
3. *Chemical Vapor Deposition: Principles and Applications*; Hitchman, M. L., Jensen, K. F. eds.; Academic Press: London, 1993.
4. Ohring, M. *The Materials Science of Thin Films*; Academic Press: San Diego, CA, 1992.
5. Schuegraf, K. L. *Handbook of Thin Film Deposition Processes and Techniques: Principles, Methods, Equipment, and Techniques*; Noyes: Park Ridge, NJ, 1998.
6. Sherman, A. *Chemical Vapor Deposition for Microelectronics*; Noyes: Park Ridge, NJ, 1987.
7. *Microelectronics Processing: Chemical Engineering Aspects*; Hess, D. W., Jensen, K. F. eds.; American Chemical Society: Washington, DC, 1989.
8. Galasso, F. S. *Chemical Vapor Deposited Materials*; CRC Press: Boca Raton, FL, 1991.
9. Hess, D. W.; Jensen, K. F.; Anderson, T. J. *Rev. Chem. Eng.* 1985, Vol. 3 (2), 130.
10. Aardahl, C. L.; Rogers, J. W., Jr. *Inorganic Reactions and Methods*; Atwood, J. D. ed.; Wiley-VCH: New York, 1999, Vol. 18, pp. 83–103.
11. Spear, K. E. *J. Am. Ceram. Soc.* 1989, Vol. 72 (2), 171.
12. Stinton, D. P.; Besmann, T. M.; Lowder, R. A. *Am. Ceram. Soc. Bull.* 1988, Vol. 67 (2), 350.
13. Lamicq, P. J.; Bernhart, G. A.; Dauchier, M. M.; Mace, J. G. *Am. Ceram. Soc. Bull.* 1986, Vol. 65 (2), 336.
14. Newkirk, M. S.; Urquhart, A. W.; Zwicker, H. R.; Breval, E. J. *Mater. Res.* 1986, Vol. 1 (1), 81.
15. Newkirk, M. S.; Leshner, H. D.; White, D. R.; Kennedy, C. R.; Urquhart, A. W.; Claar, T. D. *Ceram. Eng. Sci., Proc.* 1987, Vol. 8 (7,8), 879.
16. Claussen, N.; Urquhart, A. W. *Encyclopedia of Materials Science and Engineering*; Cahn, R. W. ed.; Pergamon: Oxford, U.K., 1990, Supplementary Vol. 2, pp. 1111–1115.

17. Urquhart, A. W. Engineered Materials Handbook. Ceramics and Glasses; ASM International, 1991, Vol. 4, pp. 232–235.
18. Antolin, S.; Nagelberg, A. S.; Creber, D. K. J. Am. Ceram. Soc. 1992, Vol. 75 (2), 447.
19. Nagelberg, A. S.; Antolin, A.; Urquhart, A. W. J. Am. Ceram. Soc. 1992, Vol. 75 (2), 455.
20. Washburn, M. E.; Coblenz, W. S. Am. Ceram. Soc. Bull. 1988, Vol. 67 (2), 356.
21. Haggerty, J. S.; Chiang, Y.-M. Ceram. Eng. Sci. Proc. 1990, Vol. 11 (7–8), 757.
22. Moulson, A. J. J. Mater. Sci. 1979, 14, 1017.
23. Claussen, N.; Le, T.; Wu, S. J. Eur. Ceram. Soc. 1989, 5, 29.
24. Claussen, N.; Wu, S.; Holz, D. J. Eur. Ceram. Soc. 1994, 14, 97.
25. Wu, S.; Holz, D.; Claussen, N. J. Am. Ceram. Soc. 1993, Vol. 76 (4), 970.
26. Holz, D.; Wu, S.; Scheppokat, S.; Claussen, N. J. Am. Ceram. Soc. 1994, Vol. 77 (10), 2509.
27. Claussen, N.; Janssen, R.; Holz, D. J. Ceram. Soc. Japan. 1995, Vol. 103 (8), 1.
28. Wu, S.; Claussen, N. J. Am. Ceram. Soc. 1991, Vol. 74 (10), 2460.
29. Wu, S.; Claussen, N. J. Am. Ceram. Soc. 1994, Vol. 77 (11), 2898.
30. Sandhage, K. H. U. S. Patent No. 5,318,725, June 7, 1994, U. S. Patent No. 5,447,291, Sept. 5, 1995.
31. Schmutzler, H. J.; Sandhage, K. H. Metall. Trans. B. 1995, Vol. 26B, 135.
32. Schmutzler, H. J.; Sandhage, K. H.; Nava, J. C. J. Am. Ceram. Soc. 1996, Vol. 79 (6), 1575.
33. Ward, G. A.; Sandhage, K. H. J. Am. Ceram. Soc. 1997, Vol. 80 (6), 1508.
34. Allameh, S. M.; Sandhage, K. H. J. Mater. Res. 1998, Vol. 13 (5), 1271.
35. Kumar, P.; Sandhage, K. H. J. Mater. Res. 1998, Vol. 13 (12), 3423.
36. Forrest, C. W.; Kennedy, P.; Shennan, J. V. Special Ceramics. 1972, Vol. 5, 99.
37. Kennedy, P. Non-Oxide Technical and Engineering Ceramics; Hampshire, S. Ed.; Elsevier: New York, 1986, pp. 301–317.
38. Sawyer, G. R.; Page, T. F. J. Mater. Sci. 1978, 13, 885.
39. Ness, J. N.; Page, T. F. J. Mater. Sci. 1986, 21, 1377.
40. Larsen, D. C.; Adams, J. W. Report # AFWAL-TR-83–4141; Wright Laboratory: Wright-Patterson AFB, OH, April 1984.
41. Messner, R. P.; Chiang, Y.-M. J. Am. Ceram. Soc. 1990, Vol. 73 (5), 1193.
42. Singh, M.; Levine, S. R. NASA-TM-107001; 1995.
43. Brinker, C. J.; Scherer, G. W. Sol-Gel Science. Academic Press, Inc.: New York, 1990.
44. Sol-Gel Technology for Thin Films, Fibers, Preforms, Electronics and Specialty Shapes; Klein, L. C. ed.; Noyes: Park Ridge, NJ, 1988.
45. Zelinski, B. J. J.; Uhlmann, D. R. J. Phys. Chem. Solids. 1984, Vol. 45, 1069.
46. Materials Research Society Symposium Proceedings: Better Ceramics Through Chemistry; Materials Research Society: Pittsburgh, PA.
47. American Ceramic Society. Ceram. Trans; 1995, Vol. 55, 1998, Vol. 81.
48. Scherer, G. W. J. Non-Cryst. Solids. 1989, Vol. 109, 171.
49. Scherer, G. W. J. Am. Ceram. Soc. 1990, Vol. 73 (1), 3.
50. Zarzycki, J.; Prassas, M.; Phalippou, J. J. Mater. Sci. 1982, Vol. 17, 3371.

51. Hench, L. L. Science of Ceramic Chemical Processing; Hench, L. L., Ulrich, D. R. eds.; Wiley: New York, 1986, pp. 52–64.
52. Kistler, S. S. J. Phys. Chem. 1932, Vol. 36, 52.
53. Tewari, P. H.; Hunt, A. J.; Lofftus, K. D. Mater. Lett. 1985, Vol. 3 (9,10), 363.
54. Jenkins, G. M.; Kawamura, K. Polymer Carbons—Carbon Fiber, Glass and Char; Cambridge Univ. Press: London, 1976.
55. Chantrell, P. G.; Popper, P. Special Ceramics 1964; Popper, P. ed.; Academic Press: New York, 1965, pp. 87–103.
56. Yajima, S.; Hayashi, J.; Omori, M.; Okamura, K. Nature. 1976, Vol. 261, 683.
57. Rice, R. W. Am. Ceram. Soc. Bull. 1983, Vol. 62 (8), 889.
58. Wynne, K. J.; Rice, R. W. Ann. Rev. Mater. Sci. 1984, Vol. 14, 297.
59. Baney, R.; Chandra, G. Encycl. Polym. Sci. Eng. 1985, Vol. 13, 312.
60. Pouskoulleli, G. Ceram. Int. 1989, Vol. 15, 213.
61. Toreki, W. Polymer News. 1991, Vol. 16, 6.
62. Inorganic and Organometallic Polymers, ACS Symposium Series; Zeldin, M., Wynne, K. J., Allcock, H. R. eds.; American Chemical Society: Washington, DC, 1988, Vol. 360.
63. Laine, R. M.; Babonneau, F. Chem. Mater. 1993, Vol. 5 (3), 260.
64. Yajima, S. Am. Ceram. Soc. Bull. 1983, Vol. 62 (8), 893.
65. Yajima, S.; Iwai, T.; Yamamura, T.; Okamura, K.; Hasegawa, Y. J. Mater. Sci. 1981, Vol. 16, 1349.
66. Mai, Y.-W. Compos. Sci. Technol. 1994, Vol. 51, 124.
67. Zhang, Z.-F.; Babonneau, F.; Laine, R. M.; Mu, Y.; Harrod, J. F.; Rahn, J. A. J. Am. Ceram. Soc. 1991, Vol. 74 (3), 670.
68. Zhang, Z.-F.; Scotto, C. S.; Laine, R. M. J. Mater. Chem. 1998, Vol. 8, 2715.
69. Seyferth, D.; Wiseman, G. H. J. Am. Ceram. Soc. 1984, Vol. 67 (7), C-132.
70. Laine, R. M.; Babonneau, F.; Blowhowiak, K. Y.; Kennish, R. A.; Rahn, J. A.; Exarhos, G. J.; Waldner, K. J. Am. Ceram. Soc. 1995, Vol. 78 (1), 137.
71. Legrow, G. E.; Lim, T. F.; Lipowitz, J.; Reaach, R. S. Am. Ceram. Soc. Bull. 1987, Vol. 66 (2), 363.
72. He, J.; Scarlete, M.; Harrod, J. E. J. Am. Ceram. Soc. 1995, Vol. 78 (11), 3009.
73. Paine, R. T.; Narula, C. K. Chem. Rev. 1990, Vol. 90, 73.
74. Seyferth, D.; Plenio, H. J. Am. Ceram. Soc. 1990, Vol. 73 (7), 2131.
75. Rees, W. R., Jr.; Seyferth, D. J. Am. Ceram. Soc. 1988, Vol. 71 (4), C-196.
76. Schwartz, K. B.; Rowcliffe, D. J.; Blum, Y. D. Adv. Ceram. Mater. 1988, Vol. 3, 320.
77. Schwab, S. T.; Blanchard-Ardis, C. R. Better Ceramics Through Chemistry III; Brinker, C. J., Clark, D. E., Ulrich, D. R. eds. ; 1989, Vol. 121, 345.
78. Mohr, D. L.; Desai, P.; Starr, T. L. Ceram. Eng. Sci. Proc. 1990, Vol. 11, 920.
79. Mucalo, M. R.; Milestone, N. B.; Vickridge, I. C.; Swain, M. V. J. Mater. Sci. 1994, Vol. 29, 4487.
80. The Handbook of Glass Manufacture; 3rd ed.; Tooley, F. V. (ed.); Ashlee Publishing Co.: New York, 1984, Vol. 1 and 2.
81. Advances in Ceramics. Commercial Glasses; Boyd, D. C., McDowell, J. F. eds.; The American Ceramic Society: Westerville, OH, 1986, Vol. 18.

82. Varshneya, A. K. *Fundamentals of Inorganic Glasses*; Academic Press: San Diego, CA, 1994, Chap. 20.
83. *Glass: Science and Technology*; Uhlmann, D. R., Kreidl, N. J. eds.; Academic Press: San Diego, CA, 1983, Vol. 1 Vol. 2, Pt. 1.
84. McMillan, P. W. *Glass Ceramics*; 2nd ed.; Academic Press: New York, 1979.
85. Grossman, D. G. *Concise Encyclopedia of Advanced Ceramic Materials*; Brook, R. J. ed.; The MIT Press: Cambridge, Massachusetts, 1990, pp. 170–176.
86. Matijevic, E. *Ultrastructure Processing of Ceramics, Glasses, and Composites*; Hench, L. L., Ulrich, D. R. eds.; John Wiley: New York, 1984, pp. 334–352.
87. Zhou, Y. C.; Rahaman, M. N. J. *Mater. Res.* 1993, Vol. 8 (7), 1680.
88. Lange, F. F. J. *Am. Ceram. Soc.* 1989, Vol. 72 (1), 3.
89. Barringer, E. A.; Bowen, H. K. J. *Am. Ceram. Soc.* 1982, Vol. 85 (12), C-199; *Am. Ceram. Soc. Bull.* 1982, 61, 336.
90. Brook, R. J. *Concise Encyclopedia of Advanced Ceramic Materials*; Brook, R. J. ed.; The MIT Press: Cambridge, Massachusetts, 1990, pp. 1–8.
91. Chu, G. P. K. *Ceramic Microstructures*; Fulrath, R. M., Pask, J. A. eds.; John Wiley: New York, 1968, p. 833.
92. Dalgleish, B. J.; Evans, A. G. J. *Am. Ceram. Soc.* 1985, Vol. 68 (1), 44.
93. Yan, M. F.; Rhodes, W. W. *Am. Ceram. Soc. Bull.* 1984, Vol. 63 (12), 1484.
94. Schmutzler, H. I. J. *Am. Ceram. Soc.* 1994, Vol. 77, 721.

2

Synthesis of Powders

2.1 INTRODUCTION

As outlined in Chapter 1, the characteristics of the powder have a remarkable effect on subsequent processing, such as consolidation of the powder into a green body and firing to produce the desired microstructure. As a result, powder synthesis is very important to the overall fabrication of ceramics. In this chapter we shall first define, in general terms, the desirable characteristics that a powder should possess for the production of successful ceramics and then consider some of the main methods used for the synthesis of ceramic powders. In practice, the choice of a powder preparation method will depend on the production cost and the capability of the method for achieving a certain set of desired characteristics. For convenience, we shall divide the powder synthesis methods into two categories: mechanical methods and chemical methods. Powder synthesis by chemical methods is an area of ceramic processing that has received a high degree of interest and has undergone considerable changes in the last 25 years. Further new developments in this area are expected in the future.

2.2 DESIRABLE POWDER CHARACTERISTICS

Traditional ceramics generally must meet less specific property requirements than advanced ceramics. They can be chemically inhomogeneous and can have complex microstructures. Unlike the case of advanced ceramics, chemical reaction during firing is often a requirement. The starting materials for traditional ceramics therefore consist of mixtures of powders with a chosen reactivity. For example, the starting powders for an insulating porcelain can, typically, be a

mixture of clay (~ 50 wt%), feldspar (~ 25 wt%), and silica (~ 25 wt%). Fine particle size is desirable for good chemical reactivity. The powders must also be chosen to give a reasonably high packing density that serves to limit the shrinkage and distortion of the body during firing. Clays form the major constituent and therefore provide the fine particle size constituent in the starting mixture for most traditional ceramics. Generally, low cost powder preparation methods are used for traditional ceramics.

Advanced ceramics must meet very specific property requirements and therefore their chemical composition and microstructure must be well controlled. Careful attention must be paid to the quality of the starting powders. For advanced ceramics, the important powder characteristics are the size, size distribution, shape, state of agglomeration, chemical composition, and phase composition. The structure and chemistry of the surface are also important.

The size, size distribution, shape, and state of agglomeration have an important influence on both the powder consolidation step and the microstructure of the fired body. A particle size greater than $\sim 1 \mu\text{m}$ generally precludes the use of colloidal consolidation methods because the settling time of the particles is fairly short. The most profound effect of the particle size, however, is on the sintering. As we shall show later, the rate at which the body densifies increases strongly with a decrease in particle size. Normally, if other factors do not cause severe difficulties during firing, a particle size of less than $\sim 1 \mu\text{m}$ allows the achievement of high density within a reasonable time (e.g., a few hours).

Whereas a powder with a wide distribution of particle sizes (sometimes referred to as a *polydisperse* powder) may lead to higher packing density in the green body, this benefit is usually vastly outweighed by difficulties in microstructural control during sintering. A common problem is that the large grains coarsen rapidly at the expense of the smaller grains, making the attainment of high density with controlled grain size impossible. Homogeneous packing of a narrow size distribution powder (i.e., a nearly *monodisperse* powder) generally allows greater control of the microstructure. A spherical or equiaxial shape is beneficial for controlling the uniformity of the packing.

Agglomerates lead to heterogeneous packing in the green body which, in turn, leads to differential sintering during the firing stage. Differential sintering occurs when different regions of the body shrink at different rates. This can lead to serious problems such as the development of large pores and cracklike voids in the fired body (see Fig. 1.24). Furthermore, the rate at which the body densifies is roughly similar to that for a coarse-grained body with a particle size equivalent to that of the agglomerates. An agglomerated powder therefore has serious limitations for the fabrication of ceramics when high density coupled with a fine-grained microstructure is desired. Agglomerates are classified into two types: *soft* agglomerates in which the particles are held together by weak van der Waals forces and *hard* agglomerates in which the particles are chemically bonded to-

gether by strong bridges. The ideal situation is the avoidance of agglomeration in the powder. However, in most cases this is not possible. In such cases, we would then prefer to have soft agglomerates rather than hard agglomerates. Soft agglomerates can be broken down relatively easily by mechanical methods (e.g., pressing or milling) or by dispersion in a liquid. Hard agglomerates cannot be easily broken down and therefore must be avoided or removed from the powder.

Surface impurities may have a significant influence on the dispersion of the powder in a liquid, but the most serious effects of variations in chemical composition are encountered in the firing stage. Impurities may lead to the formation of a small amount of liquid phase at the sintering temperature, which causes selected growth of large individual grains (Fig. 1.23). In such a case, the achievement of a fine uniform grain size would be impossible. Chemical reactions between incompletely reacted phases can also be a source of problems. We would therefore like to have no chemical change in the powder during firing. For some materials, polymorphic transformation between different crystalline structures can also be a source of severe difficulties for microstructure control. Common examples are ZrO_2 , for which cracking is a severe problem on cooling, and $\gamma\text{-Al}_2\text{O}_3$, where the transformation to the α phase results in rapid grain growth and a severe retardation in the densification rate. To summarize, the desirable powder characteristics for the fabrication of advanced ceramics are listed in Table 2.1.

2.3 POWDER SYNTHESIS METHODS

A variety of methods exist for the synthesis of ceramic powders. In this book, we divide them into two categories: *mechanical methods* and *chemical methods*. Mechanical methods are generally used to prepare powders of traditional ceramics from naturally occurring raw materials. Powder preparation by mechanical methods is a fairly mature area of ceramic processing in which the scope for new developments is rather small. However, in recent years, the preparation of fine

TABLE 2.1 Desirable Powder Characteristics for Advanced Ceramics

Powder characteristic	Desired property
Particle size	Fine ($< \sim 1 \mu\text{m}$)
Particle size distribution	Narrow or monodisperse
Particle shape	Spherical or equiaxial
State of agglomeration	No agglomeration or soft agglomerates
Chemical composition	High purity
Phase composition	Single phase

powders of some advanced ceramics by mechanical methods involving milling at high speeds has received a fair amount of interest.

Chemical methods are generally used to prepare powders of advanced ceramics from synthetic materials or from naturally occurring raw materials that have undergone a considerable degree of chemical refinement. Some of the methods categorized as chemical involve a mechanical milling step as part of the process. The milling step is usually necessary for the breakdown of agglomerates and for the production of the desired physical characteristics of the powder such as average particle size and particle size distribution. Powder preparation by chemical methods is an area of ceramic processing that has seen several new developments in the past 25 years and further new developments are expected in the future. Table 2.2 provides a summary of the common powder preparation methods for ceramics.

2.4 POWDER PREPARATION BY MECHANICAL METHODS

2.4.1 Comminution

The process in which small particles are produced by reducing the size of larger ones by mechanical forces is usually referred to as *comminution*. It involves operations such as crushing, grinding, and milling. For traditional, clay-based ceramics, machines such as jaw, gyratory, and cone crushers are used for coarse size reduction of the mined raw material, to produce particles in the size range of 0.1–1 mm. The equipment and the processes involved in the production of these coarse particles are well described elsewhere (1–3). Here we will assume that a stock of coarse particles (with sizes <1 mm) is available and consider the processes applicable to the subsequent size reduction to produce a fine powder. The most common way to achieve this size reduction is by milling. One or more of a variety of mills may be used, including high-compression roller mills, jet mills (also referred to as fluid energy mills), and ball mills (3,4). Ball mills are categorized into various types depending on the method used to impart motion to the balls (e.g., tumbling, vibration, and agitation).

For the following discussion, we define the *energy utilization* of the comminution method as the ratio of the new surface area created to the total mechanical energy supplied. The *rate of grinding* is defined as the amount of new surface area created per unit mass of particles per unit time. Obviously, there is a connection between the two terms. A comminution method that has a high energy utilization will also have a high rate of grinding, so that the achievement of a given particle size will take a shorter time. For a given method, we will also want to understand how the rate of grinding depends on the various experimental factors.

TABLE 2.2 Common Powder Preparation Methods for Ceramics

Powder preparation method	Advantages	Disadvantages
Mechanical		
Comminution	Inexpensive, wide applicability	Limited purity, limited homogeneity, large particle size
Mechanochemical synthesis	Fine particle size, good for nonoxides, low temperature route	Limited purity, limited homogeneity
Chemical		
Solid-state reaction		
Decomposition, reaction between solids	Simple apparatus, inexpensive	Agglomerated powder, limited homogeneity for multicomponent powders
Liquid solutions		
Precipitation or coprecipitation; solvent vaporization (spray drying, spray pyrolysis, freeze drying); gel routes (sol-gel, Pechini, citrate gel, glycine nitrate)	High purity, small particle size, composition control, chemical homogeneity	Expensive, poor for nonoxides, powder agglomeration commonly a problem
Nonaqueous liquid reaction	High purity, small particle size	Limited to nonoxides
Vapor-phase reaction		
Gas-solid reaction	Commonly inexpensive for large particle size	Commonly low purity, expensive for fine powders
Gas-liquid reaction	High purity, small particle size	Expensive, limited applicability
Reaction between gases	High purity, small particle size, inexpensive for oxides	Expensive for nonoxides, agglomeration commonly a problem

In the milling process, the particles experience mechanical stresses at their contact points due to compression, impact, or shear with the mill medium or with other particles. The mechanical stresses lead to elastic and inelastic deformation and, if the stress exceeds the ultimate strength of the particle, to fracture of the particles. The mechanical energy supplied to the particle is used not only to create new surfaces but also to produce other physical changes in the particle (e.g., inelastic deformation, increase in temperature, and lattice rearrangements within the particle). Changes in the chemical properties (especially the surface properties) can also occur, especially after prolonged milling or under very vigorous milling conditions. Consequently, the energy utilization of the process can be fairly low, ranging from <20% for milling produced by compression forces to <5% for milling by impact. Figure 2.1 summarizes the stress mechanisms and the range of particle sizes achieved with different types of mills for the production of fine powders.

2.4.1.1 High-Compression Roller Mills

In the high-compression roller mill, the material is stressed between two rollers. In principle, the process is similar to a conventional roller mill, but the contact pressure is considerably higher (in the range of 100–300 MPa). The stock of coarse particles is comminuted and compacted. This process must therefore be used in conjunction with another milling process (e.g., ball milling) to produce

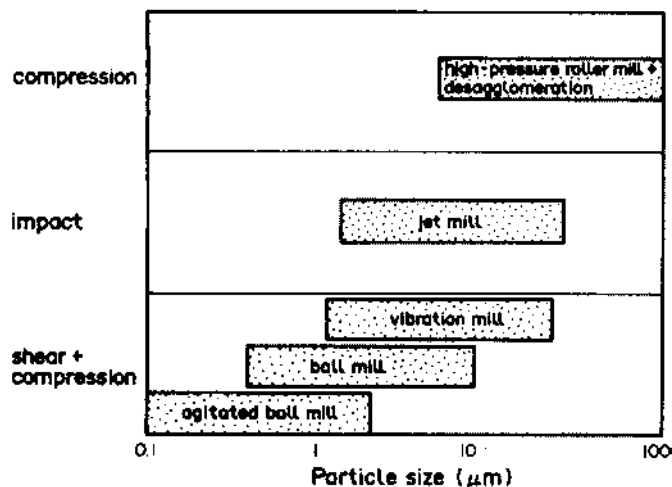


FIGURE 2.1 Range of particle sizes reached with different types of mills. (From Ref. 4.)

a powder. Although the process is unsuitable for the production of particle sizes below $\sim 10\text{ }\mu\text{m}$, it has two significant advantages. First, the energy utilization is fairly good because the mechanical energy supplied to the rollers goes directly into comminuting the particles. For the production of the same size of particles from a stock of coarse particles, the use of a high-energy roller mill in conjunction with a ball mill is more efficient than the use of a ball mill alone. A second advantage is that since only a small amount of material makes contact with the rolls, the wear can be fairly low (e.g., much lower than in ball milling).

2.4.1.2 Jet Mills

Jet mills are manufactured in a variety of designs. Generally, the operation consists of the interaction of one or more streams of high-speed gas bearing the stock of coarse particles with another high speed stream. Comminution occurs by particle–particle collisions. In some designs, comminution is achieved by collisions between the particles in the high speed stream and a wall (fixed or movable) within the mill. The milled particles leave the mill in the emergent fluid stream and are usually collected in a cyclone chamber outside the mill. The gas for the high-speed stream is usually compressed air, but inert gases such as nitrogen or argon may be used to reduce oxidation of certain nonoxide materials (e.g., Si). The average particle size and the particle size distribution of the milled powder depend on a number of factors, including the size, size distribution, hardness and elasticity of the feed particles, the pressure at which the gas is injected, the dimensions of the milling chamber, and the use of particle classification in conjunction with the milling.

Multiple gas inlet nozzles are incorporated into some jet mill designs in order to provide multiple collisions between the particles, thereby enhancing the comminution process. In some cases the flow of the particles in the high-speed gas stream can be utilized for their classification in the milling chamber. The feed particles remain in the grinding zone until they are reduced to a sufficiently fine size and then are removed from the milling chamber. An advantage of jet mills is that when combined with a particle classification device, they provide a rapid method for the production of a powder with a narrow size distribution for particle sizes down to $\sim 1\text{ }\mu\text{m}$. A further advantage is that for some designs, the particles do not come into contact with the surfaces of the milling chamber, so contamination is not a problem.

2.4.1.3 Ball Mills

The high-compression roller mills and jet mills just described achieve comminution without the use of grinding media. For mills that incorporate grinding media (balls or rods), comminution occurs by compression, impact, and shear (friction) between the moving grinding media and the particles. Rod mills are not suitable for the production of fine powders, whereas ball milling can be used to produce

particle sizes from $\sim 10\text{ }\mu\text{m}$ to as low as a fraction of a micrometer. Ball milling is suitable for wet or dry milling.

Ball milling is a fairly complex process that does not lend itself easily to rigorous theoretical analysis. The rate of grinding depends on a number of factors, including the mill parameters, the properties of the grinding media, and the properties of the particles to be ground (3). Generally, ball mills that run at low speeds contain large balls because most of the mechanical energy supplied to the particle is in the form of potential energy. Those mills that run at high speeds contain small balls because, in this case, most of the energy supplied to the particle is in the form of kinetic energy. For a given size of grinding medium, since the mass is proportional to the density, the grinding medium should consist of materials with as high a density as possible. In practice, the choice of the grinding medium is usually limited by cost.

The size of the grinding medium is an important consideration. Small grinding media are generally better than large ones. For a given volume, the number of balls increases inversely as the cube of the radius. Assuming that the rate of grinding depends on the number of contact points between the balls and the powder and that the number of contact points, in turn, depends on the surface area of the balls, then the rate of grinding will increase inversely as the radius of the balls. However, the balls cannot be too small since they must impart sufficient mechanical energy to the particles to cause fracture.

The rate of grinding also depends on the particle size. The rate decreases with decreasing particle size and, as the particles become fairly fine (e.g., about $1\text{ }\mu\text{m}$ to a few micrometers), it becomes more and more difficult to achieve further reduction in size. A practical grinding limit is approached (Fig. 2.2). This limit depends on several factors. An important factor is the increased tendency for the particles to agglomerate with decreasing particle size. A physical equilibrium is therefore set up between the agglomeration and comminution processes. Another factor is the decreased probability for the occurrence of a comminution event with decreasing particle size. Finally, the probability of a flaw with a given size existing in the particle decreases with decreasing particle size, i.e., the particle becomes stronger. The reduction of the limiting particle size may be achieved by wet milling as opposed to dry milling (Fig. 2.2), by using a dispersing agent during wet milling (Fig. 2.3), and by performing the milling in stages (3). For staged milling, as the particles get finer, they are transferred to another compartment of the mill or to another mill operating with smaller balls.

A disadvantage of ball milling is that wear of the grinding medium can be fairly high. For advanced ceramics, as discussed before, the presence of impurities in the powder is a serious concern. The best solution is to use balls with the same composition as the powder itself. However, this is only possible in very few cases and even for these, at fairly great expense. Another solution is to use a grinding medium that is chemically inert at the firing temperature of the body (e.g., ZrO_2

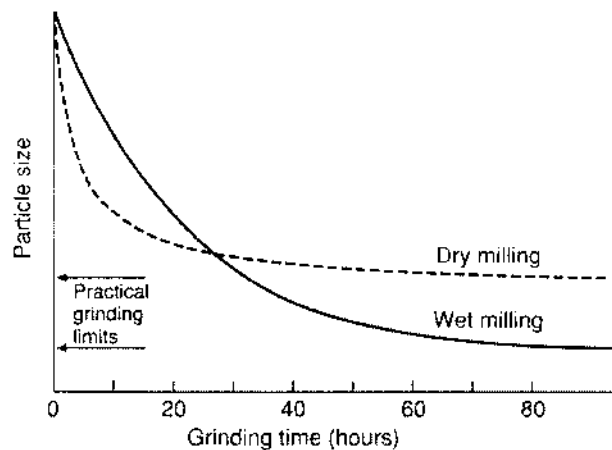


FIGURE 2.2 Particle size versus grinding time for ball milling. (From Ref. 3.)

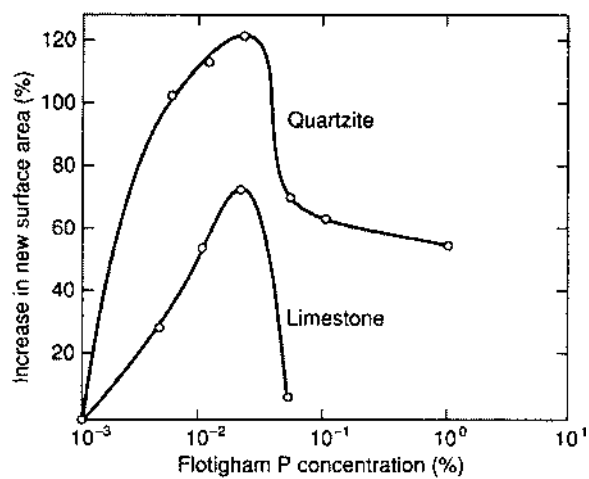


FIGURE 2.3 Effect of Flotigham P, an organic dispersing agent, on grinding of quartzite and limestone in a rod mill. (From Ref. 5.)

balls) or can be removed from the powder by washing (e.g., steel balls). A common problem is the use of porcelain balls or low-purity Al_2O_3 balls that wear easily and introduce a fair amount of SiO_2 into the powder. Silicate liquids normally form at the firing temperature and make microstructural control very difficult. A list of grinding balls available commercially and the approximate density of each is given in Table 2.3.

Tumbling ball mills, usually referred to simply as *ball mills*, consist of a slowly rotating horizontal cylinder that is partly filled with grinding balls and the particles to be ground. In addition to the factors discussed above, the speed of rotation of the mill is an important variable since it influences the trajectory of the balls and the mechanical energy supplied to the powder. Defining the *critical speed of rotation* as the speed required to just take the balls to the apex of revolution (i.e., to the top of the mill where the centrifugal force just balances the force of gravity), we find that the critical speed (in revolutions per unit time) is equal to $(g/a)^{1/2}/(2\pi)$, where a is the radius of the mill and g is the acceleration due to gravity. In practice, ball mills are operated at $\sim 75\%$ of the critical speed so that the balls do not reach the top of the mill (Fig. 2.4).

As we outlined earlier, the ball milling process does not lend itself easily to rigorous theoretical analysis. We therefore have to be satisfied with empirical relationships. One such empirical relationship is

$$\text{Rate of milling} \approx A a_m^{1/2} \frac{\rho d}{r} \quad (2.1)$$

where A is numerical constant that is specific to the mill being used and the powder being milled, a is the radius of the mill, ρ is the density of the balls, d

TABLE 2.3 Commercially Available Grinding Media for Ball Milling

Grinding media	Density (g/cm^3)
Porcelain	2.3
Silicon nitride	3.1
Silicon carbide	3.1
Alumina	
Lower than 95% purity	3.4–3.6
Greater than 99% purity	3.9
Zirconia	
MgO stabilized	5.5
High purity Y_2O_3 stabilized	6.0
Steel	7.7
Tungsten carbide	14.5

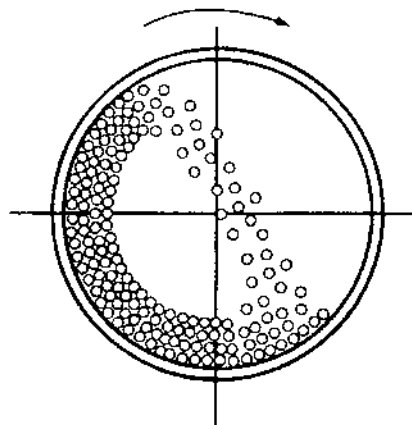


FIGURE 2.4 Schematic of a ball mill in cataracting motion. (From Ref. 4.)

is the particle size of the powder, and r is the radius of the balls. According to Eq. (2.1), the rate decreases with decreasing particle size; however, this holds up to a certain point since, as discussed earlier, a practical grinding limit is reached after a certain time. The variation of the rate of grinding with the radius of the balls must also be taken with caution; the balls will not possess sufficient energy to cause fracture of the particles if they are too small.

In the milling process, the objective is to have the balls fall onto the particles at the bottom of the mill rather than onto the mill liner itself. For a mill operating at $\sim 75\%$ of its critical speed, this occurs for dry milling for a quantity of balls filling $\sim 50\%$ of the mill volume and for a charge of particles filling $\sim 25\%$ of the mill volume. For wet milling, a useful guide is for the balls occupying $\sim 50\%$ of the mill volume and the slurry $\sim 40\%$ of the mill volume with the solids content of the slurry equal to $\sim 25\text{--}40\%$.

Wet ball milling has an advantage over dry milling in that its energy utilization is somewhat higher (by $\sim 10\text{--}20\%$). A further advantage, as we have mentioned earlier, is the ability to produce a higher fraction of finer particles. Disadvantages of wet milling are the increased wear of the grinding media, the need for drying of the powder after milling, and contamination of the powder by the adsorbed vehicle.

Vibratory ball mills or *vibro-mills* consist of a drum, almost filled with a well-packed arrangement of grinding media and the charge of particles, that is vibrated fairly rapidly ($10\text{--}20$ Hz) in three dimensions. The grinding medium, usually cylindrical in shape, occupies more than 90% of the mill volume. The amplitude of the vibrations is controlled so as not to disrupt the well-packed

arrangement of the grinding media. The three-dimensional motion helps in the distribution of the charge of particles and, in the case of wet milling, to minimize segregation of the particles in the slurry. The fairly rapid vibratory motion produces an impact energy that is much greater than the energy supplied to the particles in a tumbling ball mill. Vibratory ball mills therefore provide a much more rapid comminution process compared to the tumbling ball mills. They are also more energy efficient than tumbling ball mills.

Agitated ball mills, also referred to as *attrition mills* or *stirred media mills*, differ from tumbling ball mills in that the milling chamber does not rotate. Instead, the stock of particles and the grinding medium are stirred rather vigorously with a stirrer rotating continuously at frequencies of 1–10 Hz. The grinding chamber is aligned either vertically or horizontally (Fig. 2.5) with the stirrer located at the center of the chamber. The grinding media consist of small spheres (~ 0.2 –10 mm) that make up ~ 60 –90% of the available volume of the mill. Although it can be used for dry milling, most agitated ball milling is carried out with slurries. Most agitated ball milling is also carried out continuously, with the slurry of particles to be milled fed in at one end and the milled product removed at the other end. For milling where the agitation is fairly intense, considerable heat is produced, and a means of cooling the milling chamber is required.

Agitated ball mills have a distinct advantage over tumbling ball mills and vibratory ball mills in that the energy utilization is significantly higher. They also have the ability to handle a higher solids content in the slurry to be milled. Furthermore, as we have discussed earlier, the use of fine grinding media improves the rate of milling. The high efficiency of the process coupled with the short duration required for milling means that contamination of the milled powder is less serious than in the case for tumbling ball mills or vibratory ball mills. Contamination in agitated ball milling can be further reduced by lining the mill

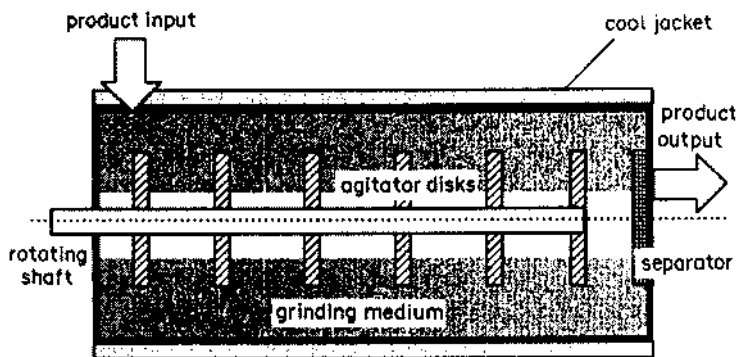


FIGURE 2.5 Schematic of an agitated ball mill. (From Ref. 4.)

chamber with a ceramic material or a plastic and by using ceramic stirrers and grinding media.

2.4.2 Mechanochemical Synthesis

In comminution, our interest lies mainly in achieving certain physical characteristics, such as particle size and particle size distribution. However, the exploitation of chemical changes during milling for the preparation of powders has received some interest in recent years. Grinding enhances the chemical reactivity of powders. Rupture of the bonds during particle fracture results in surfaces with unsatisfied valences. This, combined with the high surface area favors reaction between mixed particles or between the particles and their surroundings.

Powder preparation by high-energy ball milling of elemental mixtures is referred to by various terms, including *mechanochemical synthesis*, *mechanosynthesis*, *mechanical driven synthesis*, *mechanical alloying*, and *high energy milling*. While no term has received widespread acceptance, we shall use the term *mechanochemical synthesis* in this book. The method has attracted significant interest in the last 20 years or so for the production of powders of metals and alloys (6–8). While less attention has been paid to inorganic systems, the method has been investigated for the preparation of a variety of powders, including oxides, carbides, nitrides, borides, and silicides (9–12).

Mechanochemical synthesis can be carried out in small mills, such as the Spex mill, for synthesizing a few grams of powder or in attrition mills for larger quantities. In the Spex mill, a cylindrical vial containing the milling balls and the charge of particles undergoes large amplitude vibrations in three dimensions at a frequency of ~ 20 Hz. The charge occupies $\sim 20\%$ of the volume of the vial, and the amount of milling media (in the form of balls 5–10 mm in diameter) makes up 2–10 times the mass of the charge. The milling is normally carried out for a few tens of hours for the set of conditions indicated here. The method therefore involves high-intensity vibratory milling for very extended periods.

An advantage of mechanochemical synthesis is the ease of preparation of powders that can otherwise be difficult to produce, such as those of the silicides and carbides. For example, most metal carbides are formed by the reaction between metals or metal hydrides and carbon at high temperatures (in some cases as high as 2000°C). Furthermore, some carbides and silicides have a narrow compositional range that is difficult to produce by other methods. A disadvantage is the incorporation of impurities from the mill and milling medium into the powder.

The mechanism of mechanochemical synthesis is not clear. One possibility is the occurrence of the reaction by a solid-state diffusion mechanism. Since diffusion is thermally activated, this would require a significant lowering of the activation energy, a considerable increase in the temperature existing in the mill,

or some combination of the two. While considerable heating of the mill occurs, the temperature is significantly lower than that required for a true solid-state mechanism. A second possibility is that the reaction occurs by local melting during the milling process. While melting of the particles may accompany highly exothermic reactions, as outlined for the next mechanism, the evidence for compound formation by local melting is unclear.

A third possibility is the occurrence of the reaction by a form of self-propagating process at high temperature. In highly exothermic reactions, such as the formation of molybdenum and titanium silicides from their elemental mixtures, the heat that is liberated is often sufficient to sustain the reaction (13,14). However, for the reaction to first occur, a source of energy must be available to raise the adiabatic temperature of the system to that required for it to become self-sustaining. The surface energy of the very fine powders prior to extensive reaction is quite enormous.

For example, the average particle sizes of the Mo and Si powders prior to extensive formation of MoSi_2 have been reported as ~ 20 nm and ~ 10 nm, respectively (13). The surface energy of the particles alone is estimated as 5–10% of the heat of formation of MoSi_2 (131.9 kJ/mol at 298 K). This high surface energy, coupled with the stored strain energy (predominantly in the Mo particles), may provide such a source of energy for sustaining the reaction. A critical step for the formation reaction in mechanochemical synthesis appears to be the generation of a fine enough particle size so that the available surface and strain energy is sufficient to make the reaction self-sustaining.

Experimentally, the reaction for MoSi_2 and other silicides shows features that are characteristic of a self-propagating process. As shown in Fig. 2.6, following an induction period, the reaction occurs quite abruptly. It is likely that after a small portion of the elemental powders react during the milling process, the heat liberated by the reaction ignites the unreacted portion until the bulk of the elemental powders is converted to the product. It is not clear whether the formation of a liquid or the melting of the product occurs during the rapid reaction. Immediately following the reaction, the product is highly agglomerated. For MoSi_2 , the agglomerate size was found to be ~ 100 μm , made up of primary particles of ~ 0.3 μm in diameter (Fig. 2.7).

2.5 POWDER SYNTHESIS BY CHEMICAL METHODS

A wide range of chemical methods exist for the synthesis of ceramic powders and several reviews of the subject are available in the ceramic literature (15–20). For convenience, we will consider the methods in three fairly broad categories: (1) solid-state reactions, (2) synthesis from liquid solutions, and (3) vapor-phase reactions.

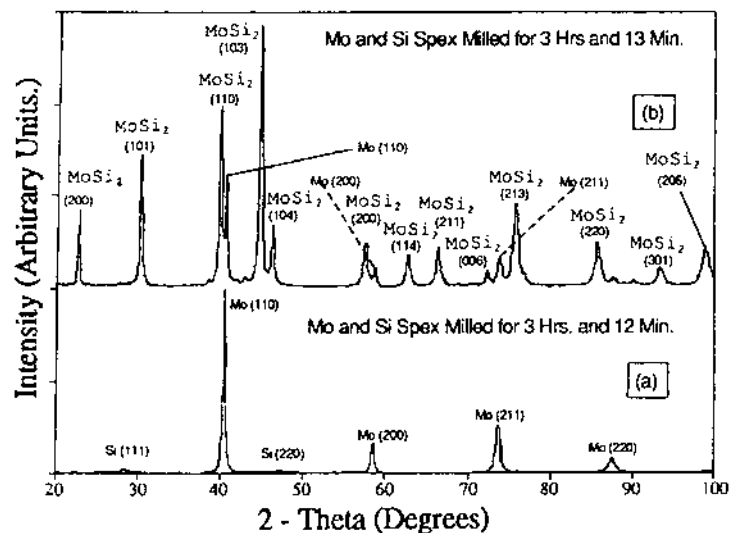


FIGURE 2.6 X-ray diffraction pattern of a stoichiometric mixture of Mo and Si powders after milling for (a) 3 h 12 min and (b) 3 h 13 min showing a fairly abrupt formation of MoSi₂. (From Ref. 13.)

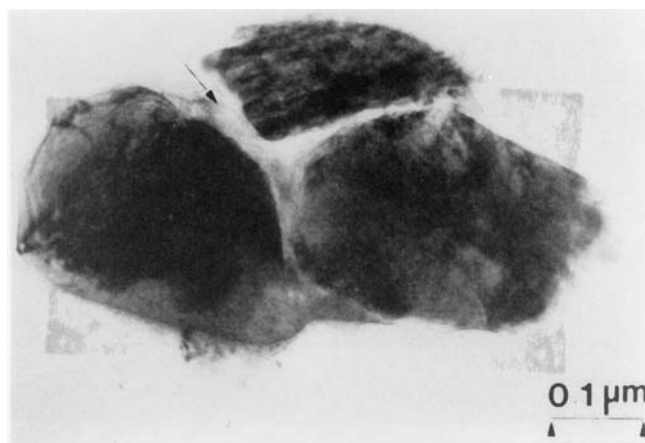


FIGURE 2.7 TEM image of MoSi₂ in the sample milled for 3 h 13 min showing three particles separated by Mo (arrow). (From Ref. 13.)

2.5.1 Solid-State Reactions

Chemical decomposition reactions, in which a solid reactant is heated to produce a new solid plus a gas, are commonly used for the production of powders of simple oxides from carbonates, hydroxides, nitrates, sulfates, acetates, oxalates, alkoxides, and other metal salts. An example is the decomposition of calcium carbonate (calcite) to produce calcium oxide and carbon dioxide gas:



Chemical reactions between solid starting materials, usually in the form of mixed powders, are common for the production of powders of complex oxides such as titanates, ferrites, and silicates. The reactants normally consist of simple oxides, carbonates, nitrates, sulfates, oxalates, or acetates. An example is the reaction between zinc oxide and alumina to produce zinc aluminate:



These methods, involving decomposition of solids or chemical reaction between solids are referred to in the ceramic literature as *calcination*.

2.5.1.1 Decomposition

Because of the industrial and scientific interest, a large body of literature exists on the principles, kinetics, and chemistry of decomposition reactions. Several comprehensive texts or reviews are available on the subject (21–23). The most widely studied systems are CaCO_3 , MgCO_3 , and $\text{Mg}(\text{OH})_2$. We will focus on the basic thermodynamics, reaction kinetics and mechanism, and process parameters pertinent to the production of powders.

Considering the thermodynamics, for the decomposition of CaCO_3 defined by Eq. (2.2), the standard heat (enthalpy) of reaction at 298K, ΔH_R° , is 44.3 kcal/mol (24). The reaction is strongly *endothermic* (i.e., ΔH_R° is positive), which is typical for most decomposition reactions. This means that heat must be supplied to the reactant to sustain the decomposition. The Gibbs free energy change associated with any reaction is given by:

$$\Delta G_R = \Delta G_R^\circ + RT \ln K \quad (2.4)$$

where ΔG_R° is the free-energy change for the reaction when the reactants are in their standard state, R is the gas constant, T is the absolute temperature, and K is the equilibrium constant for the reaction. For the reaction defined by Eq. (2.2),

$$K = \frac{a_{\text{CaO}} a_{\text{CO}_2}}{a_{\text{CaCO}_3}} = p_{\text{CO}_2} \quad (2.5)$$

where a_{CaO} and a_{CaCO_3} are the activities of the pure solids CaO and CaCO_3 , respectively, taken to be unity, and a_{CO_2} is the activity of CO_2 , taken to be the partial pressure of the gas. At equilibrium, $\Delta G_R = 0$, and combining Eqs. (2.4) and (2.5), we get

$$\Delta G_R^o = -RT \ln p_{\text{CO}_2} \quad (2.6)$$

The standard free energy for the decomposition of CaCO_3 , MgCO_3 , and $\text{Mg}(\text{OH})_2$ is plotted in Fig. 2.8, along with the equilibrium partial pressure of the gas for each of the reactions (25). Assuming that the compounds become unstable when the partial pressure of the gaseous product above the solid equals the partial pressure of the gas in the surrounding atmosphere, we can use Fig. 2.8 to determine the temperatures at which the compounds become unstable when heated in air. For example, CaCO_3 becomes unstable above $\sim 810\text{K}$, MgCO_3 above 480K , and depending on the relative humidity, $\text{Mg}(\text{OH})_2$ becomes unstable above $445\text{--}465\text{K}$. Furthermore, acetates, sulfates, oxalates, and nitrates have essentially zero partial pressure of the product gas in the ambient atmosphere so they are predicted to be unstable. The fact that these compounds are observed to be stable at much higher temperatures indicates that their decomposition is controlled by kinetic factors and not by thermodynamics.

Kinetic investigations of decomposition reactions can provide information about the reaction mechanisms and the influence of process variables such as temperature, particle size, mass of reactant, and the ambient atmosphere. They are conducted isothermally or at a fixed heating rate. In isothermal studies, the maintenance of a constant temperature represents an ideal that cannot be achieved in practice, since a finite time is required to heat the sample to the required temperature. However, isothermal decomposition kinetics are easier to analyze. The progress of the reaction is commonly measured by the weight loss and the data are plotted as the fraction of the reactant decomposed α versus time t with α defined as:

$$\alpha = \frac{\Delta W}{\Delta W_{\text{max}}} \quad (2.7)$$

where ΔW and ΔW_{max} are the weight loss at time t and the maximum weight loss according to the decomposition reaction, respectively.

There is no general theory of decomposition reactions. However, a generalized α versus time curve similar to that shown in Fig. 2.9 is often observed (22). The stage A is an initial reaction, sometimes associated with the decomposition of impurities or unstable superficial material. B is an induction period that is usually regarded as terminated by the development of stable nuclei, while C is the acceleratory period of growth of such nuclei, perhaps accompanied by further nucleation, which extends to the maximum rate of reaction at D. Thereafter, the

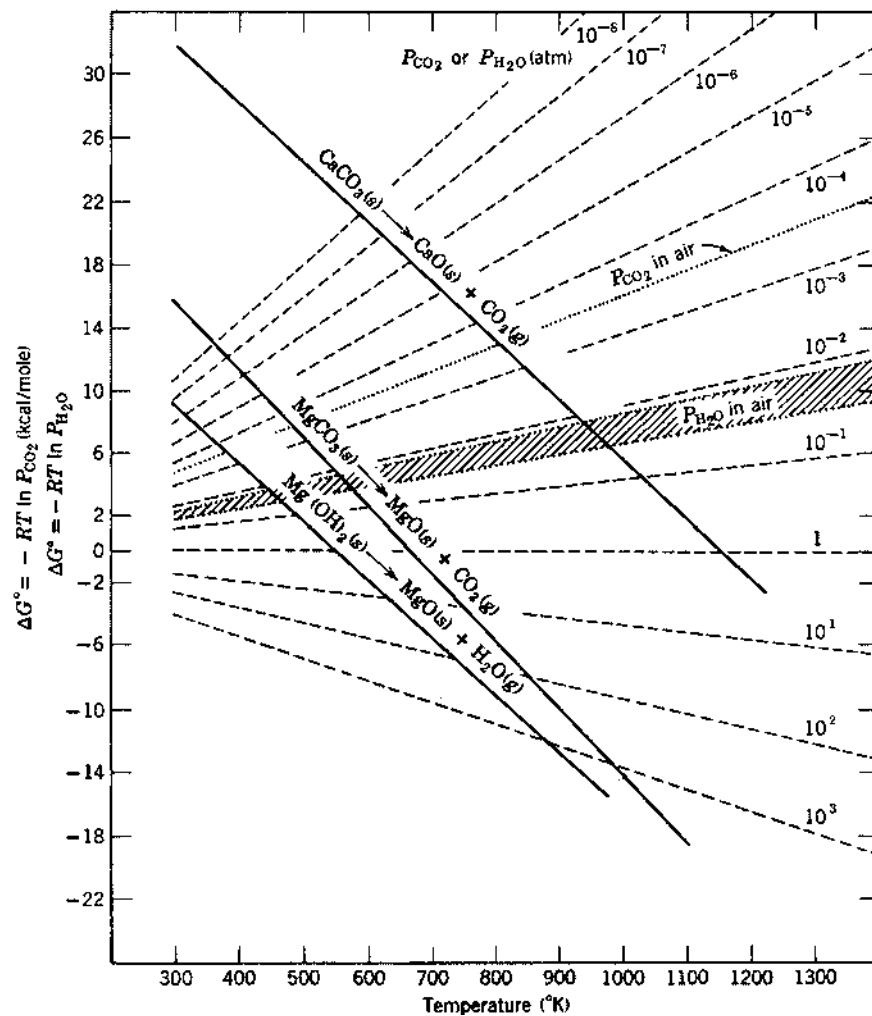


FIGURE 2.8 Standard free energy of reaction as a function of temperature. The dashed lines are the equilibrium gas pressure above the oxide/carbonate and oxide/hydroxide. (From Ref. 25.)

continued expansion of nuclei is no longer possible due to impingement and the consumption of the reactant, and this leads to a decay period, E, that continues until the completion of the reaction F. In practice, one or more of these features (except D) may be absent or negligible.

The molar volume of the solid product is commonly smaller than that for the reactant, so that very often, the product forms a porous layer around the nonporous core of reactant (Fig. 2.10). Like most solid-state reactions, the reaction is *heterogeneous* in that it occurs at a sharply defined interface. The kinetics may be controlled by any one of three processes: (1) the reaction at the interface between the reactant and the solid product, (2) heat transfer to the reaction surface, or (3) gas diffusion or permeation from the reaction surface through the porous product layer. As seen from Table 2.4, several expressions have been developed to analyze the reaction kinetics. It is generally assumed that the interface moves inward at a constant rate, so that for a spherical reactant of initial radius r_0 , the radius of the unreacted core at time t is given by

$$r = r_0 - Kt \quad (2.8)$$

where K is a constant. When the reaction at the interface is rate controlling, the different expressions reflect the different assumptions on the nucleation and growth of stable particles of the product from the reactant (*nucleation* equations in Table 2.4). If the nucleation step is fast, the equations depend only on the geometry of the model (*geometrical models*). The geometry for powder decompo-

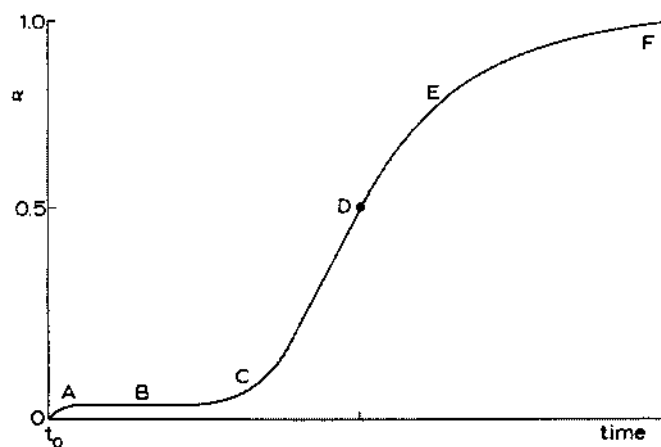


FIGURE 2.9 Generalized α versus time plot summarizing characteristic kinetic behavior observed for isothermal decomposition of solids. α represents the weight loss divided by the maximum weight loss.

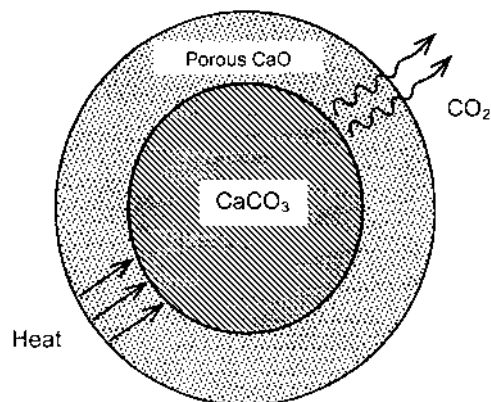


FIGURE 2.10 Schematic of the decomposition of calcium carbonate.

TABLE 2.4 Rate Equations for the Analysis of Kinetic Data in Decomposition Reactions

Equation ^a	Number
Nucleation	
Power law	$\alpha^{1/n} = Kt$ (1)
Exponential law	$\ln \alpha = Kt$ (2)
Avrami-Erofe'ev	$[-\ln(1 - \alpha)]^{1/2} = Kt$ (3)
	$[-\ln(1 - \alpha)]^{1/3} = Kt$ (4)
	$[-\ln(1 - \alpha)]^{1/4} = Kt$ (5)
Prout-Tompkins	$\ln \frac{\alpha}{1 - \alpha} = Kt$ (6)
Geometrical Models	
Contracting thickness	$\alpha = Kt$ (7)
Contracting area	$1 - (1 - \alpha)^{1/2} = Kt$ (8)
Contracting volume	$1 - (1 - \alpha)^{1/3} = Kt$ (9)
Diffusion	
One-dimensional	$\alpha^2 = Kt$ (10)
Two-dimensional	$(1 - \alpha) \ln(1 - \alpha) + \alpha = Kt$ (11)
Three-dimensional	$[1 - (1 - \alpha)^{1/3}]^2 = Kt$ (12)
Ginstling-Brounshtein	$(1 - \frac{2\alpha}{3}) - (1 - \alpha)^{2/3} = Kt$ (13)
Reaction Order	
First order	$-\ln(1 - \alpha) = Kt$ (14)
Second order	$(1 - \alpha)^{-1} = Kt$ (15)
Third order	$(1 - \alpha)^{-2} = Kt$ (16)

^aThe reaction rate constants K are different in each expression, and the times t are assumed to have been corrected for any induction period t_0 .

Source: From Ref. 22.

sition is complex. For thin CaCO_3 (calcite) crystals, Fig. 2.11 shows that the decomposition kinetics, measured under conditions such that the reaction interface advances in one dimension, follow a linear reaction equation in accordance with Eq. (7) in Table 2.4.

When large samples are used, the increasing thickness of the porous product layer may provide a barrier to the escape of the product gas. Kinetic equations for the decomposition of CaCO_3 controlled by the rate of removal of the product gas (CO_2) or the rate of heat transfer to the reaction interface have been developed by Hills (26). Table 2.4 includes equations for the reaction rate controlled by diffusion of the chemical components of the reactant.

The kinetics of chemical reactions are frequently classified with respect to reaction order. Taking the simple case where a reactant A is decomposed:



The rate of the reaction can be written:

$$-\frac{dC}{dt} = KC^\beta \quad (2.10)$$

where C is the concentration of the reactant A at time t , K is a reaction rate constant, and β is an exponent that defines the order of the reaction. The reaction is first order if $\beta = 1$, second order if $\beta = 2$, and so on. The kinetic equations for first-, second-, and third-order reactions are included in Table 2.4.

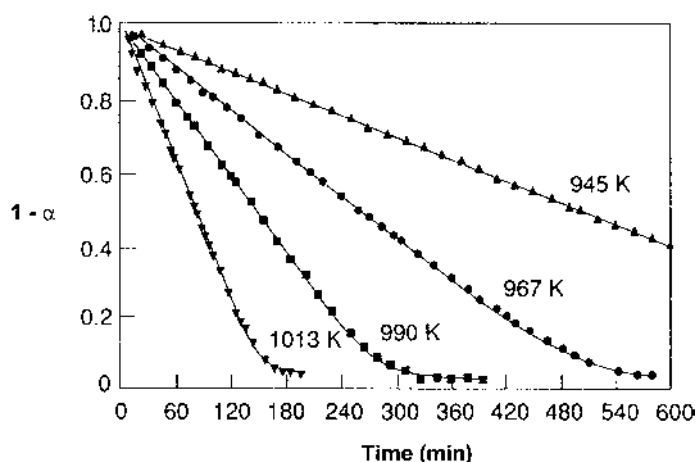


FIGURE 2.11 Isothermal decomposition kinetics of calcite (CaCO_3) single crystal. (From Ref. 27.)

When comparing experimental decomposition data with the theoretical equations, the best fit to a particular equation is consistent with, but not proof of, the mechanism on which the equation is based. It is often found that the data can be fitted with equal accuracy by two or more rate equations based on different mechanisms. In seeking mechanistic information, the kinetic analysis should commonly be combined with other techniques such as structural observations by electron microscopy.

The observed rate of decomposition and the characteristics of the powder produced by the decomposition reaction depend on a number of material and processing factors, including the chemical nature of the reactants, the initial size and size distribution of the reactant particles, the atmospheric conditions, the temperature, and the time. Isothermal rate data measured at several different temperatures show that the rate of decomposition obeys the Arrhenius relation: the rate constant K in the kinetic equations is given by:

$$K = A \exp \frac{-Q}{RT} \quad (2.11)$$

where A is a constant referred to as the *pre-exponential factor* or the *frequency factor*, Q is the activation energy, R is the gas constant, and T is the absolute temperature. Most reported activation energy values for CaCO_3 decompositions are close to the enthalpy of reaction (27). Equation (2.11) has been established for gas-phase processes by the collision theory of reaction rates. The reason why it should hold for decomposition reactions where a reactant is immobilized in the lattice of a solid phase has been the subject of some discussion (22).

Using the reaction described by Eq. (2.2) as an example, decomposition reactions are commonly carried out under conditions where the equilibrium is driven far to the right hand side. However, it is recognized that the decomposition kinetics of CaCO_3 will depend on the partial pressure of the CO_2 gas in the ambient atmosphere. High ambient CO_2 pressure drives the equilibrium to the left hand side. Studies of the effect of varying the ambient CO_2 pressure on the decomposition kinetics of CaCO_3 show that the reaction rate decreases as the partial pressure of CO_2 increases (28).

In addition to the kinetics, the microstructure of the solid product particles is also dependent on the decomposition conditions. A feature of decomposition reactions is the ability to produce very fine particle size from a normally coarse reactant when the reaction is carried out under controlled conditions. In vacuum, the decomposition reaction is often *pseudomorphic* (i.e., the product particle often maintains the same size and shape as the reactant particle). Since its molar volume is lower than that of the reactant, the product particle contains internal pores. Often the product particle consists of an aggregate of fine particles and fine internal pores. In the decomposition of 1–10 μm CaCO_3 particles performed at

$\sim 923\text{K}$ (29), the specific surface area of the CaO product formed in vacuum is as high as $\sim 100\text{ m}^2/\text{g}$ with particle and pore sizes smaller than 10 nm (Fig. 2.12a). If the reaction is carried out in an ambient atmosphere rather than in a vacuum, then high surface area powders are not produced. In 1 atmosphere N_2 , the surface area of the CaO particles is only $3\text{--}5\text{ m}^2/\text{g}$ (Fig. 2.12b).

Sintering of fine CaO particles during decomposition is also catalyzed by increasing partial pressure of CO_2 in the ambient atmosphere (30). The atmospheric gas catalyzes the sintering of the fine particles, leading to larger particles and a reduction of the surface area. The sintering of fine MgO particles produced by decomposition of MgCO_3 or $\text{Mg}(\text{OH})_2$ is catalyzed by water vapor in the atmosphere (31). High decomposition temperatures and long decomposition times promote sintering of the fine product particles, giving an agglomerated mass of low surface area powder. Although attempts are usually made to optimize the decomposition temperature and time schedule, agglomerates are invariably present so that a milling step is required to produce powders with controlled particle size characteristics.

2.5.1.2 Chemical Reaction Between Solids

The simplest system involves the reaction between two solid phases, A and B, to produce a solid solution C. A and B are commonly elements for metallic systems, while for ceramics they are commonly crystalline compounds. After the initiation of the reaction, A and B are separated by the solid reaction product C (Fig. 2.13). Further reaction involves the transport of atoms, ions, or molecules by several possible mechanisms through the phase boundaries and the reaction product. Reactions between mixed powders are technologically important for powder synthesis. However, the study of reaction mechanisms is greatly facilitated by the use of single crystals because of the simplified geometry and boundary conditions.

The spinel formation reaction $\text{AO} + \text{B}_2\text{O}_3 = \text{AB}_2\text{O}_4$ is one of the most widely studied reactions (32). Figure 2.14 shows a few of the possible reaction mechanisms. Included are: (1) mechanisms (Fig. 14a and b) in which O_2 molecules are transported through the gaseous phase and electroneutrality is maintained by electron transport through the product layer, (2) mechanism (Fig. 14c) involving counter diffusion of the cations with the oxygen ions remaining essentially stationary, and (3) mechanisms (Fig. 14d and e) in which O^{2-} ions diffuse through the product layer.

In practice, the diffusion coefficients of the ions differ widely. For example, in spinels, diffusion of the large O^{2-} ions is rather slow when compared to cationic diffusion so that the mechanisms in Fig. 2.14d and e can be eliminated. Furthermore, if ideal contact occurs at the phase boundaries so that transport of O_2 molecules is slow, then the mechanisms in Fig. 14a and b are unimportant. Under these conditions, the most likely mechanism is the counterdiffusion of

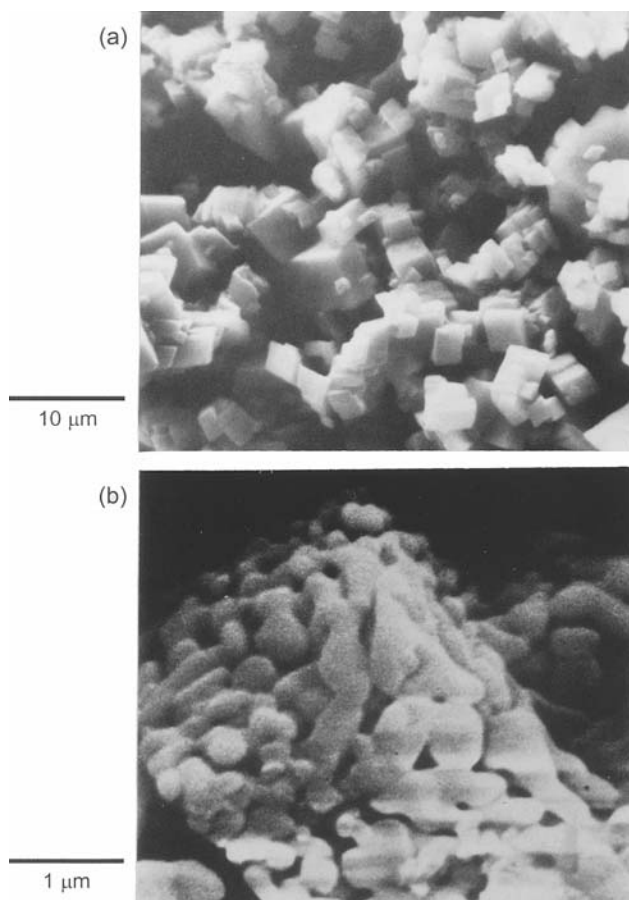


FIGURE 2.12 Scanning electron micrographs of CaO produced by decomposing CaCO_3 powder at 650°C in (a) vacuum (particles are same apparent size and shape as parent CaCO_3 particles) and (b) dry N_2 at atmospheric pressure. (From Ref. 29, used with permission.)

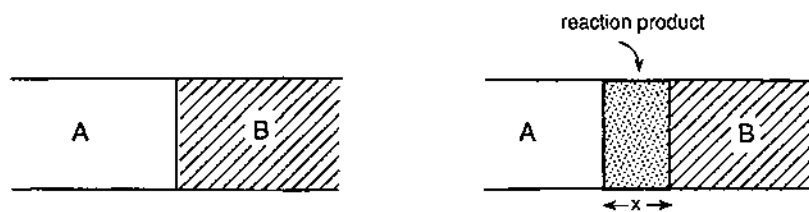


FIGURE 2.13 Schematic of solid-state reaction in single crystals.

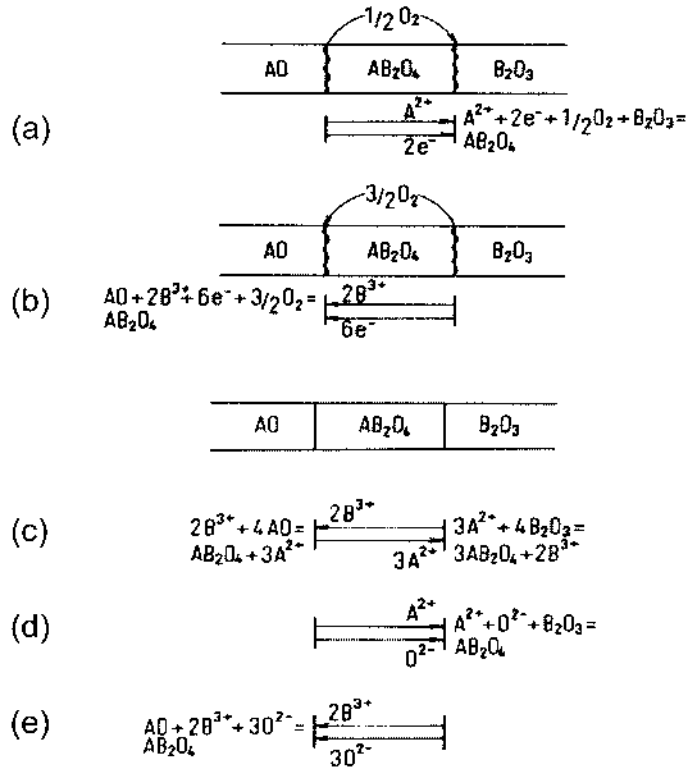


FIGURE 2.14 Reaction mechanisms and corresponding net phase boundary reactions for the spinel formation reaction $\text{AO} + \text{B}_2\text{O}_3 = \text{AB}_2\text{O}_4$. (From Ref. 32.)

cations (mechanism Fig. 14c), where the flux of the cations is coupled to maintain electroneutrality. When the rate of product formation is controlled by diffusion through the product layer, the product thickness is observed to follow a parabolic growth law:

$$x^2 = Kt \quad (2.12)$$

where K is a rate constant that obeys the Arrhenius relation.

Several investigations have reported a parabolic growth rate for the reaction layer, which is usually taken to mean that the reaction is diffusion controlled (32). The reaction between ZnO and Fe_2O_3 to form ZnFe_2O_4 is reported to occur by the counterdiffusion mechanism in which the cations migrate in opposite directions and the oxygen ions remain essentially stationary (33,34). The reaction

mechanism for the formation of ZnAl_2O_4 by Eq. (2.3) is not as clear. The reaction is reported to occur by a solid state mechanism in which the diffusion of zinc ions through the product layer controls the rate (35). However, as described below for reactions between powders, the reaction kinetics can also be described by a gas–solid reaction between ZnO vapor and Al_2O_3 .

For powder reactions (Fig. 2.15), a complete description of the reaction kinetics must take into account several parameters, thereby making the analysis very complicated. Simplified assumptions are commonly made in the derivation of kinetic equations. For isothermal reaction conditions, a frequently used equation has been derived by Jander (36). In the derivation, it is assumed that equal-sized spheres of reactant A are embedded in a quasi-continuous medium of reactant B and that the reaction product forms coherently and uniformly on the A particles. The volume of unreacted material at time t is

$$V = \frac{4}{3}\pi(r-y)^3 \quad (2.13)$$

where r is the initial radius of the spherical particles of reactant A and y is the thickness of the reaction layer. The volume of unreacted material is also given by

$$V = \frac{4}{3}\pi r^3(1-\alpha) \quad (2.14)$$

where α is the fraction of the volume that has already reacted. Combining Eqs. (2.13) and (2.14),

$$y = r[1 - (1-\alpha)]^{1/3} \quad (2.15)$$

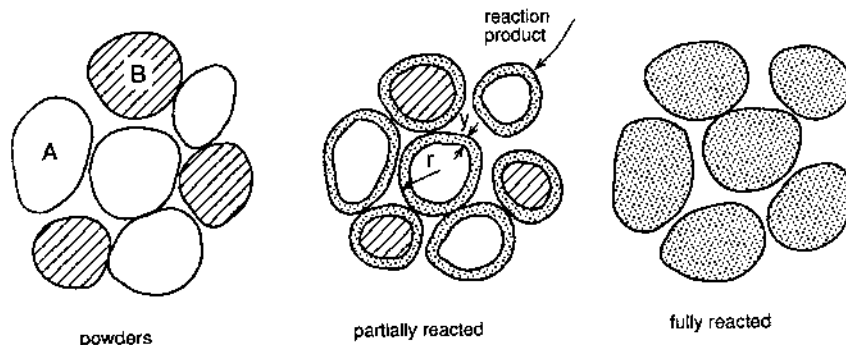


FIGURE 2.15 Schematic of solid-state reaction in mixed powders.

Assuming that y grows according to the parabolic relationship given by Eq. (2.12), then the reaction rate is

$$\left[1 - (1 - \alpha)^{1/3}\right]^2 = \frac{Kt}{r^2} \quad (2.16)$$

Equation (2.16), referred to as the *Jander equation*, suffers from two oversimplifications that limit its applicability and the range over which it adequately predicts reaction rates. First, the parabolic growth law assumed for the thickness of the reaction layer is valid for one-dimension reaction across a planar boundary and not for a system with spherical geometry. At best, it is expected to be valid only for the initial stages of the powder reaction when $y \ll r$. Second, any change in molar volume between the reactant and the product is neglected. These two oversimplifications have been taken into account by Carter (37), who derived the following equation:

$$\left[1 + (Z - 1)\alpha\right]^{2/3} + (Z - 1)(1 - \alpha)^{2/3} = Z + (1 - Z)\frac{Kt}{r^2} \quad (2.17)$$

where Z is the volume of the reaction product formed from unit volume of the reactant A. Equation (2.17), referred to as the *Carter equation*, is applicable to the formation of ZnAl_2O_4 by the reaction between ZnO and Al_2O_3 even up to 100% of reaction (Fig. 2.16).

For a solid-state diffusion mechanism, the growth of the reaction product in powder systems occurs at the contact points and for nearly equal-sized spheres, the number of contact points is small. Nevertheless, for many systems, the Jander equation and the Carter equation give a good description of the reaction kinetics for at least the initial stages of the reaction. It appears that rapid surface diffusion provides a uniform supply of one of the reactants over the other. Alternatively, if the vapor pressure of one of the reactants is high enough [e.g., ZnO in Eq. (2.3)], condensation on the surface of the other reactant can also provide a uniform supply of the other reactant. In this case, the powder reaction can be better described as a gas–solid reaction rather than a solid-state reaction (32).

In practical systems, solid state reaction in powder systems depends on several parameters. They include the chemical nature of the reactants and the product; the size, size distribution, and shape of the particles; the relative sizes of the reactant particles in the mixture; the uniformity of the mixing, the reaction atmosphere; the temperature; and the time. The reaction rate will decrease with an increase in particle size of the reactants because, on average, the diffusion distances will increase. For coherent reaction layers and nearly spherical particles, the dependence of the reaction kinetics on particle size is given by Eq. (2.16) or Eq. (2.17). The reaction rate will increase with temperature according to the Arrhenius relation. Commonly, the homogeneity of mixing is one of the most

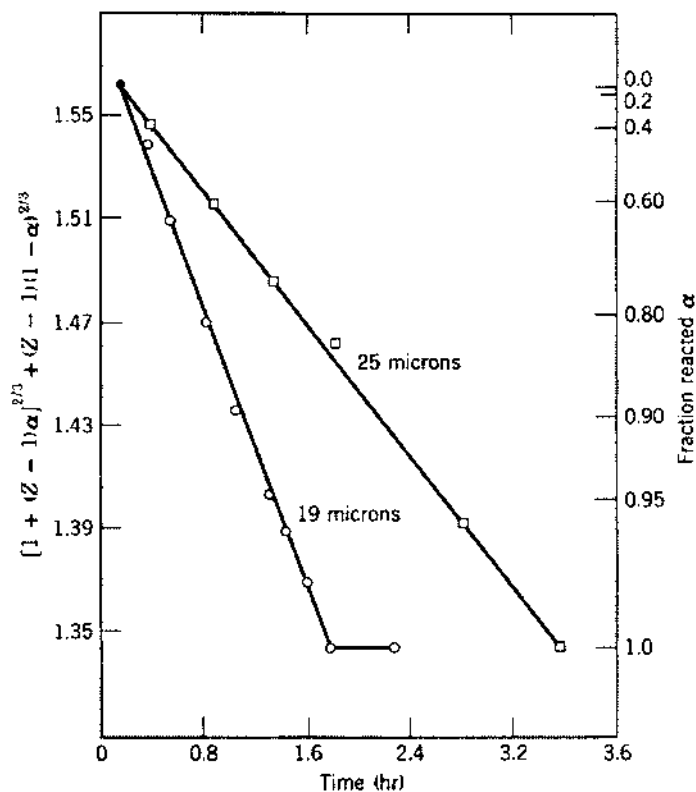


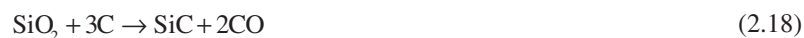
FIGURE 2.16 Kinetics of reaction between spherical particles of ZnO and Al_2O_3 to form ZnAl_2O_4 at 1400°C in air, showing the validity of the Carter equation. (From Ref. 32.)

important parameters. It influences the diffusion distance between the reactants and the relative number of contacts between the reactant particles, and thus the ability to produce homogeneous, single-phase powders.

Powder preparation by solid-state reactions generally has an advantage in terms of production cost, but as outlined earlier, the powder quality is also an important consideration for advanced ceramics. The powders are normally agglomerated and a grinding step is almost always required to produce powders with better characteristics. Grinding in ball mills leads to the contamination of the powder with impurities. Incomplete reactions, especially in poorly mixed powders, may produce undesirable phases. Furthermore, the particle shape of ground powders is usually difficult to control.

2.5.1.3 Reduction

The reduction of silica by carbon is used industrially to produce silicon carbide powders:



This reaction should occur somewhat above 1500°C but is usually carried out at much higher temperatures so that the SiO_2 is actually a liquid. The process is carried out on a large scale industrially and is generally referred to as the *Acheson* process. The mixture is self-conducting and is heated electrically to temperatures of ~2500°C. Side reactions occur so that the reaction is more complex than that indicated in Eq. (2.18). The product obtained after several days of reaction consists of an aggregate of black or green crystals. It is crushed, washed, ground, and classified to produce the desired powder sizes.

One disadvantage of the Acheson process is that powder quality is often too poor for demanding applications such as high-temperature structural ceramics. Because the reactants exist as mixed particles, the extent of the reaction is limited by the contact area and inhomogeneous mixing between reactant particles with the result that the SiC product contains unacceptably high quantities of unreacted SiO_2 and C. These limitations have been surmounted recently by a process in which the SiO_2 particles are coated with the C prior to reduction (38,39). Relatively pure SiC powders with fine particle sizes (<0.2 μm) are produced by this process. As described later, laboratory scale methods employing gas-phase reactions can also produce SiC powders with desirable powder characteristics, but the methods are expensive.

2.5.2 Liquid Solutions

There are two general routes for the production of a powdered material from a solution:

1. Evaporation of the liquid
2. Precipitation by adding a chemical reagent that reacts with the solution

The reader may be familiar with these two routes since they are commonly used in inorganic chemistry laboratories, e.g., the production of common salt crystals from a solution by evaporation of the liquid or of $\text{Mg}(\text{OH})_2$ by the addition of NaOH solution to MgCl_2 solution. An understanding of the principles of precipitation from solution is useful for achieving control of the particle size characteristics of the powder.

2.5.2.1 Precipitation from Solution

Principles

The kinetics and mechanism of precipitation are well covered in a textbook (40). Several review articles on the precipitation from solution are available, covering

the principles (41–44) and procedures (45,46) of synthesizing particles with controlled size characteristics. Precipitation from solution consists of two basic steps: (1) nucleation of fine particles and (2) their growth by addition of more material to the surfaces. In practice, control of the powder characteristics is achieved by controlling the reaction conditions for nucleation and growth and the extent of coupling between these two processes.

Nucleation

The type of nucleation we shall consider here is referred to as *homogeneous nucleation* because it takes place in a completely homogeneous phase with no foreign inclusions in the solution or on the walls of the reaction vessel. When these inclusions are present and act to assist the nucleation, the process is called *heterogeneous nucleation*. The occurrence of heterogeneous nucleation makes it difficult to obtain well-controlled particle sizes and must normally be avoided. As we shall see later, heterogeneous nucleation can be used to good advantage for the synthesis of coated particles.

Homogeneous nucleation of solid particles in solution is generally analyzed in terms of the classical theories developed for vapor-to-liquid and vapor-to-solid transformations which are described in detail by Christian (47). We shall briefly outline the main features of the classical theories for vapor-to-liquid transformation and then examine how they are applied to nucleation of solid particles from solution. In a supersaturated vapor consisting of atoms (or molecules), random thermal fluctuations give rise to local fluctuations in density and free energy of the system. Density fluctuations produce clusters of atoms referred to as *embryos*, which can grow by addition of atoms from the vapor phase. A range of embryo sizes will be present in the vapor with vapor pressures assumed to obey the Kelvin equation:

$$\ln \frac{p}{p_0} = \frac{2\gamma v_l}{kTr} \quad (2.19)$$

where p is the supersaturated vapor pressure, p_0 is the saturated vapor pressure, γ is the specific surface energy of the cluster, v_l is the volume per molecule in a liquid drop formed by condensation of the vapor, k is the Boltzmann constant, T is the absolute temperature, and r is the radius of the embryo (assumed to be spherical). Because of their higher vapor pressure, small embryos evaporate back to the vapor phase. Embryos with a radius r less than a critical radius r_c cannot grow whereas embryos with $r > r_c$ can. However, the formation of nuclei (i.e., embryonic droplets) requires an energy barrier to be surmounted. This may be illustrated by considering the free-energy change in forming a spherical nucleus of radius r . The increase in the free energy can be written as

$$\Delta G_n = 4\pi r^2 \gamma - \frac{4}{3} \pi r^3 \Delta G_v \quad (2.20)$$

The first term on the right is the intrinsically positive contribution of the surface free energy. The second term represents the contribution by the bulk free energy change. Considering unit volume of liquid, the free-energy decrease ΔG_v in going from vapor to liquid is given by (48)

$$\Delta G_v = \frac{kT}{v_l} \ln \frac{p}{p_0} \quad (2.21)$$

where v_l is the volume per molecule in the liquid. Substituting for ΔG_v in Eq. (2.20) gives

$$\Delta G_n = 4\pi r^2 \gamma - \frac{4}{3} \pi r^3 \frac{kT}{v_l} \ln \frac{p}{p_0} \quad (2.22)$$

For the limiting case when the supersaturation ratio $S = p/p_0 = 1$, the bulk term vanishes and ΔG_n increases monotonically as a parabola. For $S < 1$, the ΔG_n curve rises more steeply because a fractional S makes the second term on the right go positive, reinforcing the effect due to the surface free energy barrier. For $S > 1$, the second term is negative and this assures the existence of a maximum in ΔG_n at some critical radius r_c , as shown schematically in Fig. 2.17. The critical radius r_c is obtained by putting $d(\Delta G_n)/dr = 0$, giving

$$r_c = \frac{2\gamma_l}{kT \ln(p/p_0)} \quad (2.23)$$

Substituting for r_c in Eq. (2.22), the height of the free-energy activation barrier is

$$\Delta G_c = \frac{16\pi\gamma^3 v_l^2}{3[kT \ln(p/p_0)]^2} = \frac{4}{3} \pi r_c^2 \gamma \quad (2.24)$$

To summarize at this stage, sufficient increase in the supersaturation ratio $S = p/p_0$ finally serves to increase the atomic (molecular) bombardment rate in the vapor and to reduce ΔG_c and r_c to such an extent that the probability of subcritical embryo growing to supercritical size in a short time approaches unity. Homogeneous nucleation to form liquid droplets now becomes an effective process.

The nucleation rate I refers to the rate of formation of critical nuclei since only these can grow to produce liquid droplets. A pseudo-thermodynamic treatment of vapor-to-liquid transformation gives the result that I is proportional to $\exp(-\Delta G_c/kT)$, where k is the Boltzmann constant and ΔG_c is given by Eq.

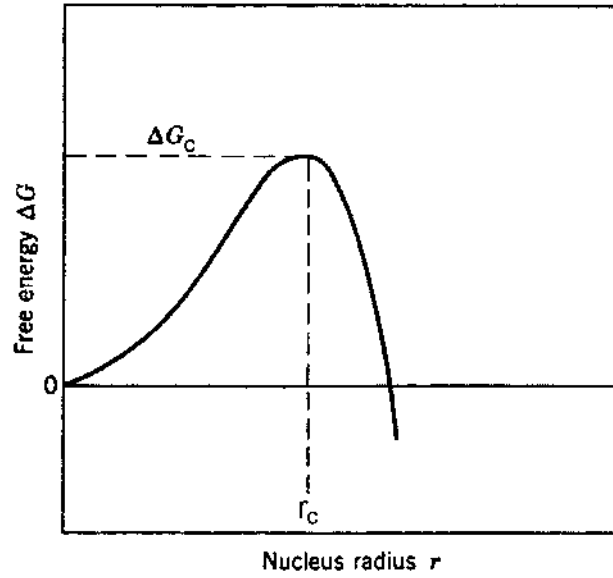


FIGURE 2.17 Schematic variation of the free energy versus radius for a spherical droplet. Some critical size must be exceeded before a nucleus becomes stable.

(2.24). The rate at which the nuclei grow will also depend on the frequency with which atoms join it, and this may be written as $[v \exp(-\Delta G_m/kT)]$, where v is the characteristic frequency and ΔG_m is the activation energy for atom migration. Putting $v = kT/h$, where h is Planck's constant, an approximate expression for the nucleation rate is (47):

$$I \approx \frac{NkT}{h} \exp \frac{-\Delta G_m}{kT} \exp \frac{-16\pi\gamma^3 v_i^2}{3kT [kT \ln(p/p_0)]^2} \quad (2.25)$$

where N is the number of atoms per unit volume in the phase undergoing transformation.

Homogeneous nucleation of particles from solution occurs in many techniques for the synthesis of ceramic powders. General aspects of nucleation from liquids and solutions are discussed by Walton (49). In aqueous solution, metal ions are hydrated (50). Embryos of hydrated metal ions are assumed to form by progressive addition of ions to one another by a polymerization process. These polynuclear ions are the precursors to nucleation. When the concentration of the polynuclear ions increases above some minimum supersaturation concentration,

homogeneous nucleation to form solid nuclei becomes an effective process. The nucleation rate of particles from solution can be expressed as (49)

$$I \approx \frac{2Nv_s (kT\gamma)^{1/2}}{h} \exp \frac{-\Delta G_a}{kT} \exp \frac{-16\pi\gamma^3 v_s^2}{3k^3 T^3 [\ln(C_{ss}/C_s)]^2} \quad (2.26)$$

where N is the number of ions per unit volume in the solution, v_s is the volume of a molecule in the solid phase, γ is the specific energy of the solid–liquid interface, ΔG_a is the activation energy for the transport of an ion to the solid surface, C_{ss} is the supersaturated concentration, and C_s is the saturated concentration of the ions in the solution. The nucleation rate is strongly dependent on the supersaturation ratio C_{ss}/C_s .

Particle Growth by Solute Precipitation

Nuclei are normally very small but even during a short nucleation stage they may have grown to somewhat different sizes. Therefore, the starting system for growth is not monodisperse. Nuclei formed in a supersaturated solution can grow by transport of solute species (ions or molecules) through the solution to the particle surface, desolvation, and alignment on the particle surface. The rate-determining step in the growth of the particles can be

1. Diffusion towards the particle
2. Addition of new material to the particle by a form of surface reaction

The occurrence of the specific mechanisms and their interplay control the final size characteristics of the particles.

Diffusion-controlled growth: Assuming that the particles are far apart so that each can grow at its own rate, the diffusion of solute species towards the particle (assumed to be spherical of radius r) can be described by Fick's first law. The flux J through any spherical shell of radius x is given by

$$J = 4\pi x^2 D \frac{dC}{dx} \quad (2.27)$$

where D is the diffusion coefficient for the solute through the solution and C is its concentration. Assuming that the saturation concentration C_s is maintained at the particle surface and that the concentration of the solute far from the particle is C_∞ , a concentration gradient is set up which approaches a stationary state in times of the order of r^2/D . In this stationary state, J does not depend on x , and integration of Eq. (2.27) gives

$$J = 4\pi r D (C_\infty - C_s) \quad (2.28)$$

The rate of growth of the particle radius is then:

$$\frac{dr}{dt} = \frac{JV_s}{4\pi r^2} = \frac{DV_s(C_\infty - C_s)}{r} \quad (2.29)$$

where V_s is the molar volume of the solid precipitating on the particle. Equation (2.29) can also be written:

$$\frac{d(r^2)}{dt} = 2DV_s(C_\infty - C_s) \quad (2.30)$$

showing that irrespective of the original size of the particle, the square of the radius of all particles increases at the same constant rate. The treatment leading to Eq. (2.30) is oversimplified. However, it has been shown more rigorously that for diffusion controlled growth, $d(r^2)/dt$ is the same for particles of any size but not necessarily constant in time (51).

If the absolute width of the particle size distribution is Δr for a mean radius r and Δr_0 for the mean radius r_0 of the initial system, we can deduce from Eq. (2.30) that

$$\frac{\Delta r}{\Delta r_0} = \frac{r_0}{r} \quad \text{and} \quad \frac{\Delta r}{r} = \left(\frac{r_0}{r}\right)^2 \frac{\Delta r_0}{r_0} \quad (2.31)$$

Equation (2.31) shows that the absolute width of the size distribution becomes narrower in the ratio r_0/r and the relative width decreases even faster in the ratio $(r_0/r)^2$.

Surface-reaction-controlled growth: Each new layer around the particle has to be nucleated first by a process that is different from the homogeneous nucleation discussed earlier. Two types of growth mechanism can be distinguished, referred to as *mononuclear* growth and *polynuclear* growth (Fig. 2.18). In the mononuclear growth mechanism, once a nucleation step is formed on the particle surface, a layer has the time to achieve its completion before a new step appears. Growth proceeds, therefore, layer by layer and the particle surface may appear faceted on a macroscopic scale. The following equation for particle growth has been derived (40):

$$\frac{dr}{dt} = K_1 r^2 \quad (2.32)$$

where K_1 is a constant. The relative width of the size distribution is given by

$$\frac{\Delta r}{r} = \frac{r}{r_0} \frac{\Delta r_0}{r_0} \quad (2.33)$$

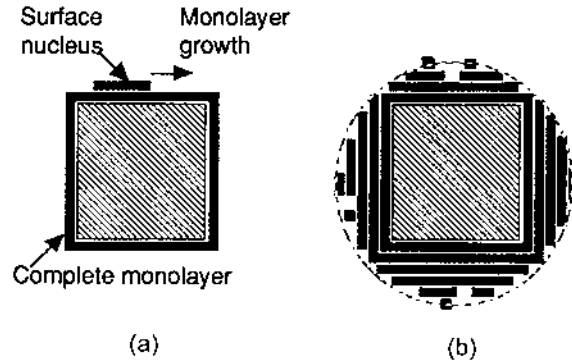


FIGURE 2.18 Nucleation of layers around a particle for (a) mononuclear growth and (b) polynuclear growth.

and increases in the ratio r/r_0 . In the *polynuclear* growth mechanism, formation of nucleation steps on the particle surface is fast enough to create a new layer before the previous one has been completed. The growth rate is independent of the surface area of the existing particles and is given by (40)

$$\frac{dr}{dt} = K_2 \quad (2.34)$$

where K_2 is a constant. In this case, the relative width of the distribution decreases according to

$$\frac{\Delta r}{r} = \frac{r_0}{r} \frac{\Delta r_0}{r_0} \quad (2.35)$$

Controlled Particle Size Distribution

The basic principles for obtaining particles with a fairly uniform size by precipitation from solution were put forward nearly 50 years ago by LaMer and Dinegar (52). The main features may be represented in terms of the diagram shown in Fig. 2.19, often referred to as the *LaMer diagram*. As the reaction proceeds, the concentration of the solute to be precipitated, C_x , increases to or above the saturation value C_s . If the solution is free of foreign inclusions and the container walls are clean and smooth, then it is possible for C_x to exceed C_s by a large amount to give a supersaturated solution. Eventually a critical supersaturation concentration C_{ss} will be reached after some time t_1 and homogeneous nucleation and growth of solute particles will occur, leading to a decrease in C_x to a value below

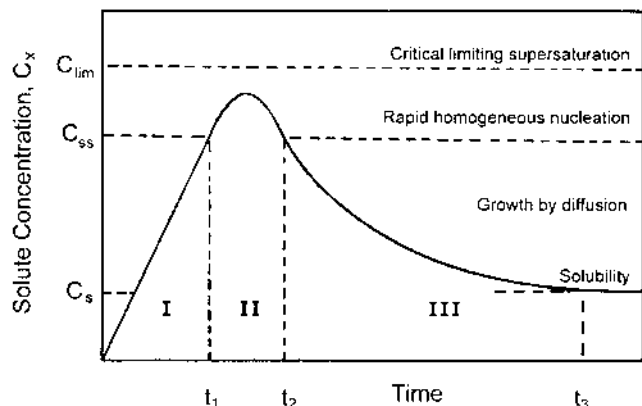


FIGURE 2.19 Schematic representation of the solute concentration versus time in the nucleation and growth of particles from a solution. (From Ref. 52.)

C_{ss} after a time t_2 . Further growth of the particles occurs by diffusion of solute through the liquid and precipitation on to the particle surfaces. Finally, particle growth stops after a time t_3 when $C_x = C_s$.

It is clear that if we wish to produce particles with a fairly uniform size, then one short burst of nucleation should occur in a short time interval, $t_2 - t_1$. One way of achieving this is through the use of a fairly low reactant concentration. Furthermore, uniform growth of the particles requires that the solute be released slowly to allow diffusion to the particles without buildup of the solute concentration and further bursts of nucleation. This mechanism of nucleation followed by diffusion-controlled growth does not apply to the formation of particles that are aggregates of finer primary particles. Instead, it may apply only to the primary particles.

Particle Growth by Aggregation

High-resolution electron micrographs of particles synthesized by several routes involving precipitation from solution show that the particles consist of aggregates of much finer primary particles. Titania particles prepared by the Stober process show primary particle features that are smaller than ~ 10 nm (Fig. 2.20a). The TEM of CeO_2 particles synthesized by hydrolysis of cerium nitrate salts in the presence of sulfate ions (53) show that the hexagonal particles consist of smaller primary particles with a spherical shape (Fig. 2.20b). Based on studies of SiO_2 particle synthesis by the Stober process, Bogush et al. (54,55) put forward a model in which particle growth occurs by aggregation of fine particles rather than by diffusion of solute to existing particles. Using the DLVO theory for

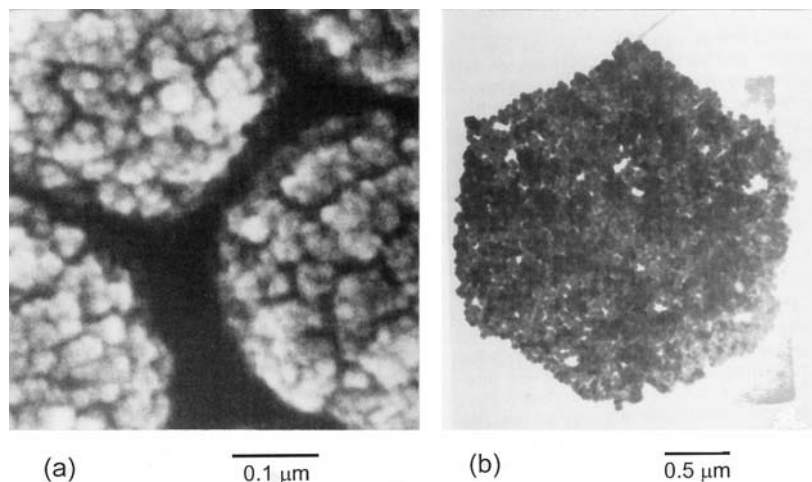


FIGURE 2.20 (a) Scanning electron micrograph of TiO_2 particles prepared by the Stober process showing that the particles consist of much finer primary particles. (Courtesy of A. M. Glaeser.) (b) Transmission electron micrograph of hexagonal CeO_2 particles synthesized by hydrolysis of cerium nitrate salts in the presence of sulfate ions showing that the hexagonal particles consist of much smaller primary particles with a spherical shape. (From Ref. 53.)

colloid stability (see Chapter 4), they showed that under identical surface charge densities, the barrier to aggregation increases with the size for two equal-size particles so that their rate of aggregation decreases exponentially. However, fine particles aggregate more quickly with large particles than they do with themselves. According to the model, during a precipitation reaction, the first nuclei grow rapidly by aggregation to a colloidally stable size. These particles then sweep through the suspension, picking up freshly formed nuclei and smaller aggregates. The formation of particles with uniform size is thus achieved through size-dependent aggregation rates.

Particle Growth by Ostwald Ripening

Particles in a liquid can also grow by a process in which the smaller particles dissolve and the solute precipitates on the larger particles. This type of growth, better described as *coarsening*, is referred to as *Ostwald ripening*. The coarsening of precipitates in a solid medium can occur by a similar process and the theory of Ostwald ripening, sometimes referred to as the Lifshitz-Slyozov-Wagner (LSW) theory, is described in detail in Chapter 10. Matter transport from the smaller particles to the larger particles can be controlled by (1) diffusion through the

liquid or (2) an interface reaction (dissolution of the solid or deposition of the solute onto the particle surfaces). The average radius $\langle r \rangle$ of the particles (assumed to be spherical) is predicted to increase with time t according to

$$\langle r \rangle^m = \langle r_0 \rangle^m + Kt \quad (2.36)$$

where $\langle r_0 \rangle$ is the initial average radius of the particles, K is a constant that obeys the Arrhenius relation, and m is an exponent that depends on the mechanism ($m = 2$ for interface reaction control and $m = 3$ for diffusion control). Regardless of the initial size distribution, the particle size distribution reaches a self-similar distribution since it depends only on $r/\langle r \rangle$ and is independent of time. The maximum radius of the distribution is $2\langle r \rangle$ for the interface reaction mechanism and $(3/2)\langle r \rangle$ for the diffusion mechanism. Ostwald ripening by itself cannot therefore lead to a monodisperse system of particles.

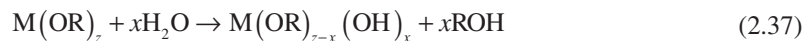
Procedures for Precipitation from Solution

The most straightforward use of precipitation is for the preparation of simple oxides or hydrous oxides (also referred to as hydroxides or hydrated oxides). Precipitation is commonly achieved by hydrolysis reactions. Two main routes can be distinguished:

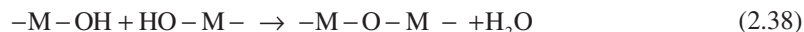
1. Hydrolysis of metal-organic compounds (e.g., metal alkoxides) in alcoholic solution, generally referred to as the *Stober process* and
2. Hydrolysis of aqueous solution of metal salts (where considerable work has been done by Matijevic)

Hydrolysis of Solutions of Metal Alkoxides

Metal alkoxides have the general formula $M(OR)_z$, where z is an integer equal to the valence of the metal M , and R is an alkyl chain (see Chapter 5). They can be considered as derivatives of either an alcohol, ROH , in which the hydrogen is replaced by the metal M , or of a metal hydroxide, $M(OH)_z$, in which the hydrogen is replaced by an alkyl group. The reactions involve hydrolysis:



followed by condensation and polymerization by dehydration:



Stober et al. (56) carried out a systematic study of the factors that control the preparation of fine, uniform SiO_2 particles by the hydrolysis of silicon alkoxides in the presence of NH_3 . The NH_3 served to produce pH values in the basic range. For the hydrolysis of silicon tetraethoxide, $Si(OC_2H_5)_4$, referred to commonly as TEOS, with ethanol as the solvent, the particle size of the powder was dependent

on the ratio of the concentration of H_2O to TEOS and on the concentration of NH_3 but not on the TEOS concentration (in the range of $0.02\text{--}0.50\text{ mol/dm}^3$). For a TEOS concentration of 0.28 mol/dm^3 , Fig. 2.21 shows the general correlation between particle size and the concentrations of H_2O and NH_3 . The particle sizes varied between 0.05 and $0.90\text{ }\mu\text{m}$ and were very uniform, as shown in Fig. 2.22. Different alcoholic solvents or silicon alkoxides were also found to have an effect. The reaction rates were fastest with methanol and slowest with *n*-butanol. Likewise, under comparable conditions, the particle sizes were smallest in methanol and largest in *n*-butanol. Fastest reactions (less than 1 min) and smallest sizes (less than $0.2\text{ }\mu\text{m}$) were obtained with silicon tetramethoxide, while silicon tetrapentoxide reacted slowly ($\sim 24\text{ h}$) and produced fairly large particles.

The controlled hydrolysis of metal alkoxides has since been used to prepare fine powders of several simple oxides. We mentioned in Chapter 1 the work of Barringer and Bowen (57) for the preparation, packing, and sintering of monodisperse TiO_2 powders. Later work (58) provided some insight into the mechanism of hydrolysis of $\text{Ti}(\text{OC}_2\text{H}_5)_4$. The alkoxide reacts with water to produce a monomeric hydrolysis species according to

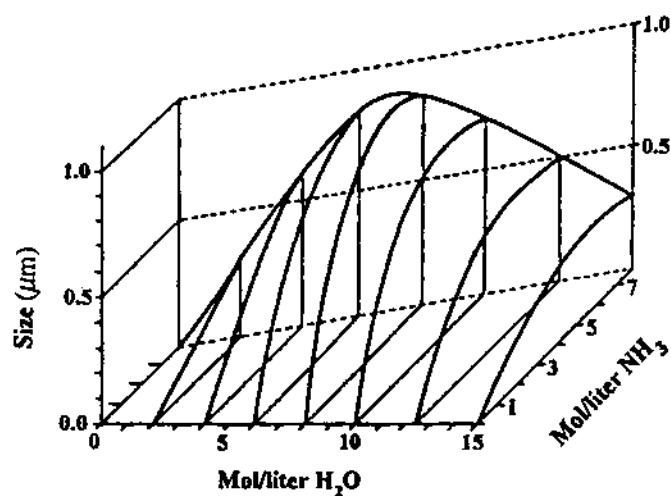
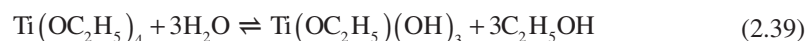


FIGURE 2.21 Correlation between particle size and the concentrations of water and ammonia in the hydrolysis of a solution of 0.28 mol/dm^3 silicon tetraethoxide in ethanol. (From Ref. 56.)

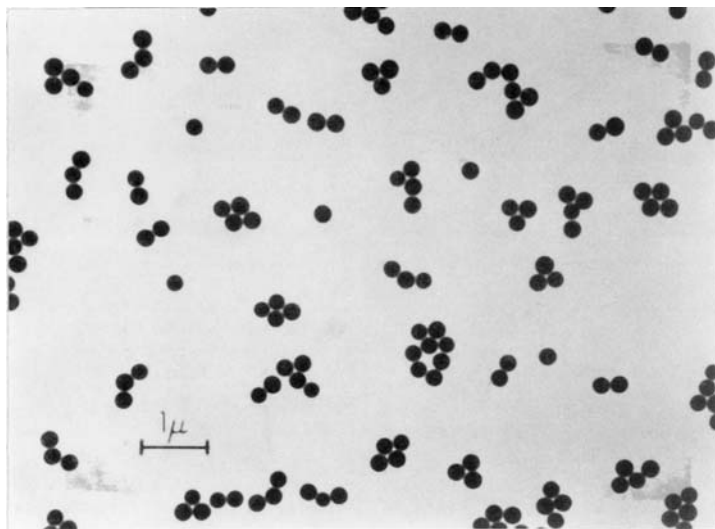
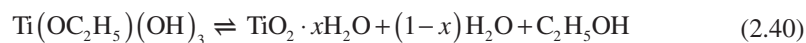
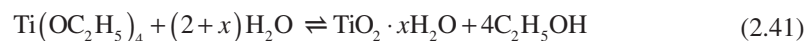


FIGURE 2.22 Silica spheres produced by the hydrolysis of a solution of silicon tetroxide in ethanol. (From Ref. 56.)

However, the presence of dimers and trimers of the hydrolysis species cannot be excluded. Polymerization of the monomer to produce the hydrated oxide is represented by



The overall reaction can therefore be represented as



The value of x was found by thermogravimetric analysis to be between 0.5 and 1.

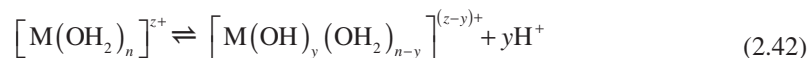
Most metal alkoxides hydrolyze readily in the presence of water, so that stringent conditions must be maintained to achieve powders with controlled characteristics. The reactions are sensitive to the concentration of the reactants, the pH, and the temperature. Oxide or hydrated oxide powders are produced. The precipitated particles are commonly amorphous and can be agglomerates of much finer particles (Fig. 2.20a).

Hydrolysis of Solutions of Metal Salts

Procedures for the preparation of uniform particles by the hydrolysis of metal salt solutions have been developed and reviewed by Maitjevic (45,46,59–61).

Compared to the hydrolysis of metal alkoxides, the method has the ability for producing a wider range of chemical compositions, including oxides or hydrous oxides, sulfates, carbonates, phosphates, and sulfides. However, the number of experimental parameters that must be controlled to produce uniform particles is generally higher. They include the concentration of the metal salts, the chemical composition of the salts used as starting materials, the temperature, the pH of the solution, and the presence of anions and cations that form intermediate complexes. While a variety of particle sizes and shapes can be produced (Fig. 2.23), the morphology of the final particles can rarely be predicted (59,60). Furthermore, while amorphous as well as crystalline particles can be produced, the factors that determine the crystalline versus amorphous structure of the product are not clear (61).

Metal ions, as indicated earlier, are normally hydrated in aqueous solution (50). The conditions for homogeneous precipitation of uniform particles can be achieved by a *forced hydrolysis* technique. This technique is based on promoting the *deprotonation* of hydrated cations by heating the solution at elevated temperatures (90–100°C). For a metal M with a valence z , the reaction can be written



The soluble hydroxylated complexes produced by the hydrolysis reaction form the precursors to the nucleation of particles. They can be generated at the proper rate to achieve nucleation and growth of uniform particles by adjustment of the temperature and pH. In principle, it is only necessary to age the solutions at elevated temperatures. In practice, however, the process is very sensitive to minor changes in conditions. In addition, anions other than hydroxide ions play a decisive role in the reaction. Some anions are strongly coordinated to the metal ions and thus end up in the precipitated solid of fixed stoichiometric composition. In other cases, the anions can be readily removed from the product by leaching. Finally, in some case the anions affect the particle morphology without being incorporated in the precipitated solid. The specific conditions for the precipitation of uniform particles must therefore be adjusted from case to case.

As an example of the sensitivity of the reactions to changes in conditions, we can consider the synthesis of spherical hydrated aluminum oxide particles with narrow size distribution (62). Solutions of $\text{Al}_2(\text{SO}_4)_3$, $\text{KAl}(\text{SO}_4)_2$, and a mixture of $\text{Al}(\text{NO}_3)_3$ and $\text{Al}_2(\text{SO}_4)_3$ or a mixture of $\text{Al}_2(\text{SO}_4)_3$ and Na_2SO_4 were aged in Pyrex tubes sealed with Teflon lined caps at $98 \pm 2^\circ\text{C}$ for up to 84 h. The pH of the freshly prepared solutions was 4.1, and after aging and cooling to room temperature was 3.1. Particles with uniform size were produced only when the Al concentration was between 2×10^{-4} and 5×10^{-3} mol/dm³ provided that the $[\text{Al}^{3+}]$ to $[\text{SO}_4^{2-}]$ molar ratio was between 0.5 and 1. For a constant Al concentration, the particle size increased with increasing sulfate concentration.

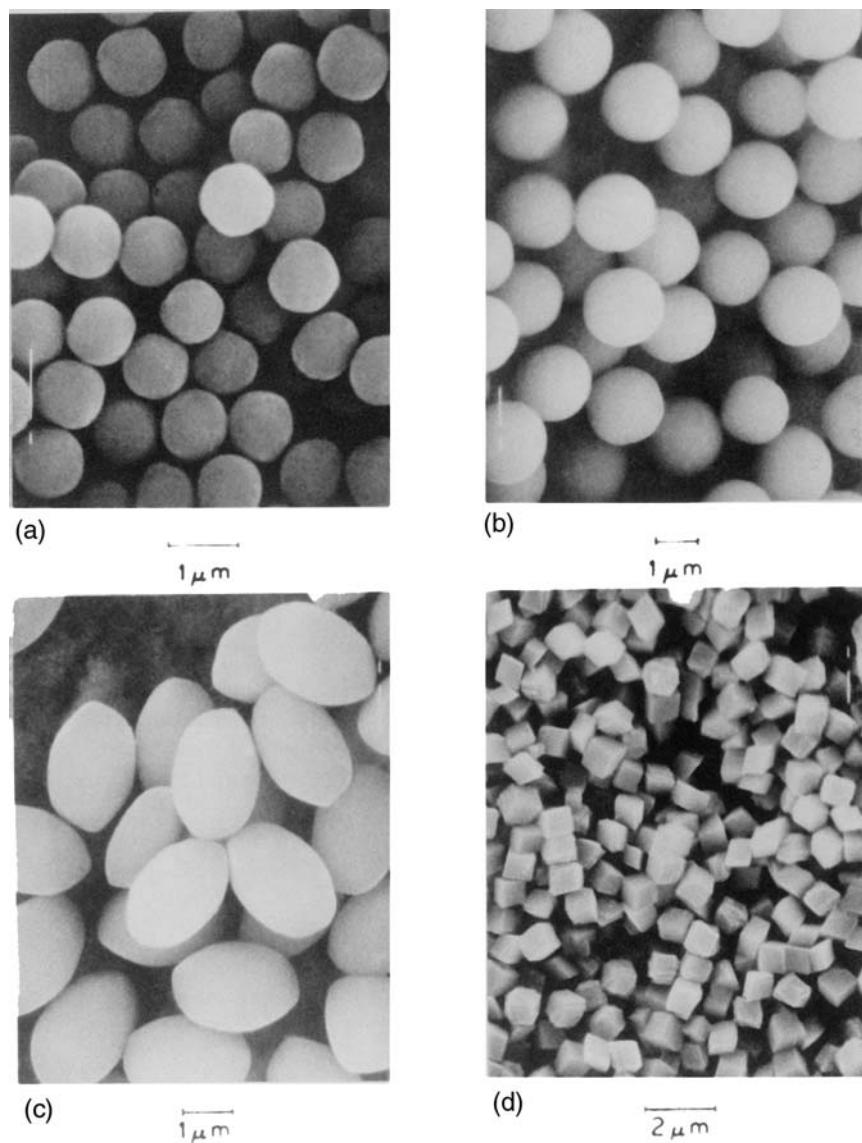


FIGURE 2.23 Examples of the sizes, shapes and chemical compositions for powders prepared by precipitation from metal salt solutions, showing particles of (a) hematite (α -Fe₂O₃), (b) cadmium sulfide, (c) iron (III) oxide, and (d) calcium carbonate. (From Ref. 59.)

The temperature of aging was a critical parameter; no particles were produced below 90°C, while the best results were obtained at 98°C. Finally, the particles had reasonably constant chemical composition, which indicates that one or more well-defined aluminum basic sulfate complexes were the precursors to the nucleation of particles.

The conditions for nucleation and growth of uniform particles in solution can also be met by the slow release of anions from organic molecules such as urea or formamide. An example is the precipitation of yttrium basic carbonate particles from a solution of yttrium chloride, YCl_3 , and urea, $(\text{NH}_2)_2\text{CO}$ (63). Particles of uniform size were produced by aging for 2.5 h at 90°C a solution of $1.5 \times 10^{-2} \text{ mol/dm}^3$ YCl_3 and 0.5 mol/dm^3 urea (Fig. 2.24a). However, solutions of YCl_3 containing higher urea concentrations yielded, on aging at 115°C for 18 h, rodlike particles somewhat irregular in size (Fig. 2.24b). At temperatures up to 100°C, aqueous solutions of urea yield ammonium and cyanate ions:



In acid solutions, cyanate ions react rapidly, according to

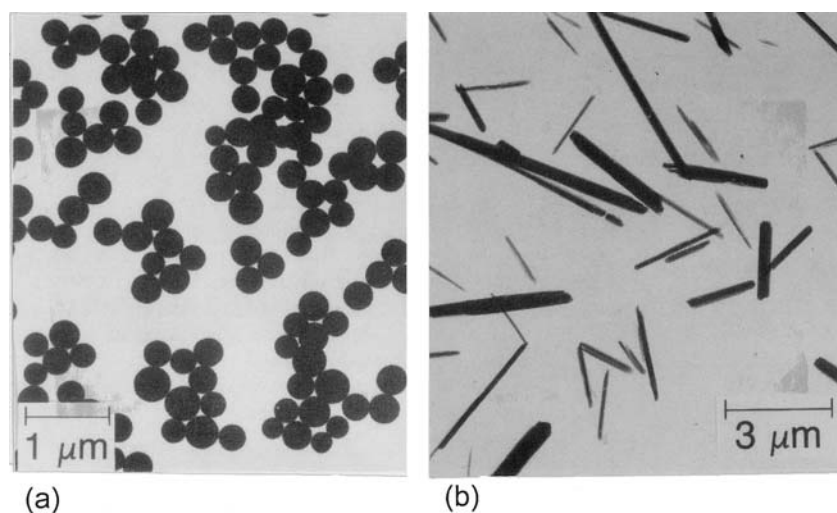
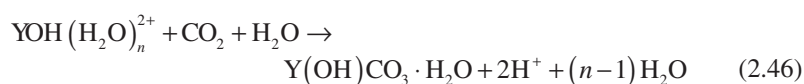


FIGURE 2.24 Particles obtained (a) by aging for 2.5 h at 90°C a solution of $1.5 \times 10^{-2} \text{ mol/dm}^3$ YCl_3 and 0.5 mol/dm^3 urea and (b) by aging for 18 h at 115°C a solution of $3.0 \times 10^{-2} \text{ mol/dm}^3$ YCl_3 and 3.3 mol/dm^3 urea. (From Ref. 63.)

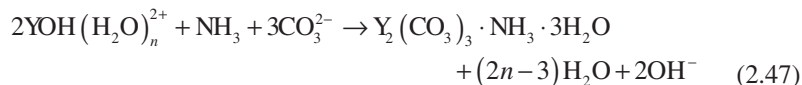
whereas in neutral and basic solutions, carbonate ions and ammonia are formed:



Yttrium ions are weakly hydrolyzed in water to $\text{YOH}(\text{H}_2\text{O})_n^{2+}$. The resulting release of hydronium ions accelerates urea decomposition according to Eq. (2.44). The overall reaction for the precipitation of the basic carbonate can, therefore, be written as



For the reaction at 115°C, the decomposition of excess urea ($>2 \text{ mol/dm}^3$) generates a large amount of OH^- ions, which change the medium from acidic to basic (pH 9.7). The reaction of cyanate ions proceeds according to Eq. (2.45). The precipitation of rodlike particles may therefore be represented as:



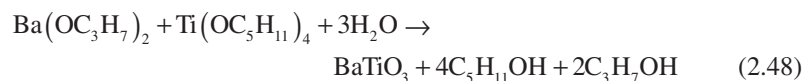
In addition to an excess of urea and a higher aging temperature, longer reaction times ($>12 \text{ h}$) are needed to generate a sufficient amount of free ammonia for reaction Eq. (2.47) to dominate.

Precipitation of Complex Oxides

Complex oxides are oxides such as titanates, ferrites, and aluminates that contain more than one type of metal in the chemical formula. We have already outlined the difficulties of solid-state reaction between a mixture of oxide powders when fine, stoichiometric, high-purity powders are required. Some of these difficulties may be alleviated by the use of *coprecipitation* from a solution (sometimes referred to as *cohydrolysis*). A solution of mixed alkoxides, mixed salts, or of a combination of salts and alkoxides is generally used. A common problem in coprecipitation is that the different reactants in the solution have different hydrolysis rates, which results in segregation of the precipitated material. Suitable conditions must therefore be found in order to achieve homogeneous precipitation. Consider the preparation of MgAl_2O_4 powders (64). Both Mg and Al are precipitated as hydroxides, but the conditions for their precipitation are quite different. $\text{Al}(\text{OH})_3$ is precipitated under slightly basic conditions (pH = 6.5–7.5), is soluble in the presence of excess ammonia, but is only slightly soluble in the presence of NH_4Cl . $\text{Mg}(\text{OH})_2$ is completely precipitated only in strongly basic solutions such as NaOH solution. In this case, an intimate mixture of $\text{Al}(\text{OH})_3$ and Mg-Al double hydroxide $2\text{Mg}(\text{OH})_2 \cdot \text{Al}(\text{OH})_3$ is produced when a solution of MgCl_2 and AlCl_3

is added to a stirred excess solution of NH_4OH kept at a pH of 9.5–10. Calcination of the precipitated mixture above $\sim 400^\circ\text{C}$ yields stoichiometric MgAl_2O_4 powder with high purity and fine particle size.

The co-precipitation technique generally produces an intimate mixture of precipitates. In many cases, the mixture has to be calcined at elevated temperature in order to produce the desired chemical composition. One serious consequence is the need for milling of the calcined powder, which can introduce impurities into the powder. The preparation of lead lanthanum zirconium titanate (PLZT) powders is a good example illustrating the combined use of co-precipitation, calcination, and milling (65). It is more desirable to produce a precipitate that does not require the use of elevated temperature calcination and subsequent milling. In a few cases, the precipitated powder may have the same cation composition as the desired product. An example is the preparation of BaTiO_3 by the hydrolysis of a solution of barium isopropoxide, $\text{Ba}(\text{OC}_3\text{H}_7)_2$, and titanium tertiary amoxide, $\text{Ti}(\text{OC}_5\text{H}_{11})_4$ by Mazdiyasi et al. (66). The overall reaction can be written as



The alkoxides are dissolved in a mutual solvent (e.g., isopropanol) and refluxed for 2 h prior to hydrolysis. While the solution is vigorously stirred, drops of deionized, triply distilled water are slowly added. The reaction is carried out in a CO_2 -free atmosphere to prevent the precipitation of barium carbonate. After drying the precipitate at 50°C for 12 h in a helium atmosphere, a stoichiometric BaTiO_3 powder with a purity of more than 99.98% and a particle size of 5–15 nm (with a maximum agglomerate size of $<1\ \mu\text{m}$) is produced. Dopants can be incorporated uniformly into the powders by adding a solution of the metal alkoxide prior to hydrolysis.

The hydrolysis of a mixture of metal alkoxides forms a fairly successful route for the synthesis of complex oxide powders (67). However, most metal alkoxides are expensive, and their hydrolysis requires carefully controlled conditions because of their sensitivity to moisture. The controlled hydrolysis of a mixture of salt solutions appears to be more difficult, but its use has been demonstrated by Matijevic (61) for a few systems, including barium titanate and strontium ferrite.

Precipitation Under Hydrothermal Conditions

Precipitation from solution under hydrothermal conditions has been known for decades as a method for synthesizing fine, crystalline oxide particles (68). Interest in the method has increased in recent years because of the need for fine, pure powders in the production of ceramics for electronic applications. The process involves heating reactants, often metal salts, oxide, hydroxide, or metal powder,

as a solution or a suspension, usually in water, at temperatures between the boiling and critical points of water (100–374°C) and pressures up to 22.1 MPa (the vapor pressure of water at its critical point). It is commonly carried out in a hardened steel autoclave, the inner surfaces of which are lined with a plastic (e.g., Teflon) to limit corrosion of the vessel.

Several types of reactions may be employed in hydrothermal synthesis (69). A common feature is that precipitation of the product generally involves forced hydrolysis under elevated temperature and pressure. The powders have several desirable characteristics, but they also suffer from a few disadvantages so that their benefits are normally not fully realized. In hydrothermal synthesis, the crystalline phase is commonly produced directly so that a calcination step is not required, as in the case of several other synthesis routes. The powders also have the characteristics of very fine size (10–100 nm), narrow size distribution, single-crystal particles, high purity, and good chemical homogeneity.

As an example, Fig. 2.25 shows CeO₂ powders (average particle size ~15 nm) produced from a suspension of amorphous, gelatinous cerium (hydrous) oxide under hydrothermal conditions (~300°C and 10 MPa pressure for 4 h). CeO₂ has a cubic crystal structure; the faceted nature of the particles is an indication that they are crystalline. High-resolution transmission electron microscopy also revealed that the particles are single crystals (70). A disadvantage of very fine powders is that they are difficult to consolidate to high packing density and are very prone to agglomeration, particularly in the dry state. Because of their high surface area, the powders may contain a high concentration of chemically bonded hydroxyl groups on their surfaces. Incomplete removal of the hydroxyl groups prior to sintering may limit the final density of the fabricated material.

Hydrothermal synthesis of BaTiO₃ powders was reported many years ago (71). Increased attention has been paid to the method in recent years because of the need for fine powders for the production of thin dielectric layers. One method involves the reaction between TiO₂ gels or fine anatase particles with a strongly alkaline solution (pH > 12–13) of Ba(OH)₂ at 150–200°C, which can be described by the equation



The reaction mechanisms have been discussed in detail elsewhere (72). Depending on the reaction time and temperature, particles with an average size in the range of 50–200 nm are produced. Another method involves crystallization of an amorphous barium-titanium-acetate gel in a strongly alkaline solution of tetramethylammonium hydroxide for 10–15 h at 150°C (73). Dissolution of the gel and precipitation of crystalline BaTiO₃ particles, coupled with Ostwald ripening of the particles, produced a weakly agglomerated powder with an average particle size in the range of 200–300 nm.

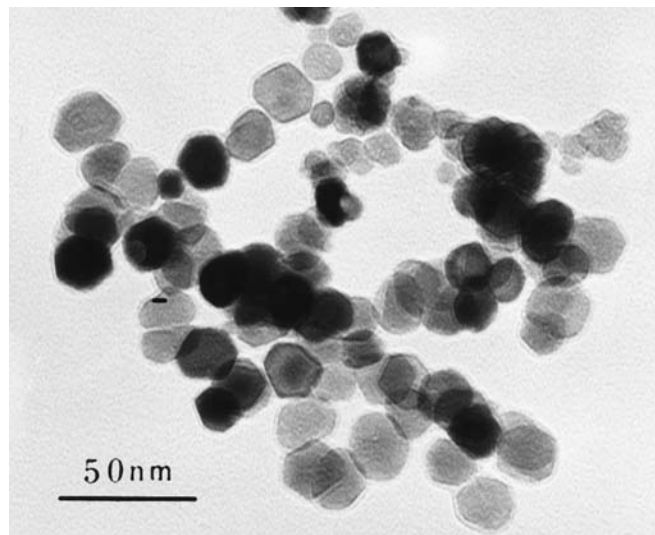


FIGURE 2.25 Powders of CeO₂ prepared by the hydrothermal method.

Hydrothermal BaTiO₃ powders, particularly very fine powders (less than ~100 nm) prepared at lower temperatures, show some structural characteristics that are not observed for coarser powders prepared by solid-state reaction at higher temperatures. X-ray diffraction reveals a cubic structure that is normally observed only at temperatures above the ferroelectric Curie temperature of 125–130°C. The possible causes for the apparent cubic and nonferroelectric structure are not clear and have been discussed in detail elsewhere (74). They include the idea of a critical size for ferroelectricity and, particularly for powders prepared by precipitation from solution, the presence of a high concentration of point defects due to hydroxyl groups in the structure.

Coated Particles

Coated particles, sometimes referred to as *composite particles*, consist of particles of a given solid coated uniformly with a thin or thick layer of another material. Reviews have considered the synthesis and use of coated particles for several applications (75–77). Their use can offer some interesting advantages in ceramic powder processing. Thin coatings are particularly useful for modifying the surface characteristics of colloidal dispersions and for uniformly incorporating additives such as sintering aids and dopants. Particles or inclusions coated with thick layers can serve to improve the sintering behavior of ceramic composites or compositions of complex oxides (Chapter 11).

Coated particles can be prepared by several techniques. Here we consider the precipitation from solution onto dispersed particles for the production of coated particles with thin or thick layers (Fig. 2.26). Successful coating of the particles requires control of several variables to produce the desired interaction between a particulate suspension A and the material that is to be precipitated out of solution, B (78). Several types of A-B interactions are possible:

1. B can nucleate *homogeneously* in the solution and grow to form particles that do not interact with A, giving simple mixtures of A and B.
2. Homogeneously nucleated particles of B grow and eventually heterocoagulate with particles of A, producing deposits that are rough and nonuniform, particularly if the B particles are large.
3. The homogeneously nucleated particles of B heterocoagulate with A at an early stage, and the growth of B continues on these aggregates, thereby producing a particulate coating of B on A. The coating would be more homogeneous than that formed in case (2), particularly if the B particles are very small compared to A.
4. B nucleates *heterogeneously* on the surface of A and growth produces a uniform layer of B on A. This may be the most desirable way to deposit smooth coatings on fine particles.

To produce coated particles in this way, a number of key requirements must be met:

Separation of the nucleation and growth steps: Figure 2.27 is a modified version of the LaMer diagram discussed earlier for the homogeneous precipitation

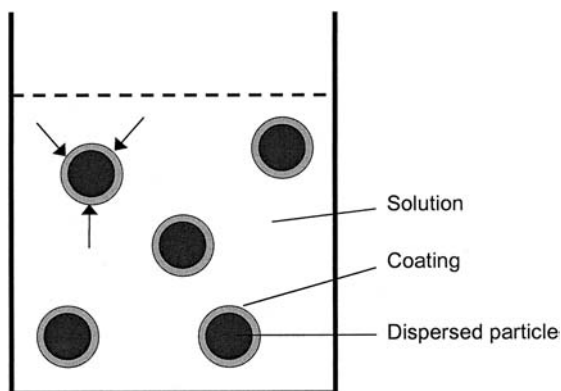


FIGURE 2.26 Schematic of the preparation of coated particles by the precipitation from solution onto dispersed particles.

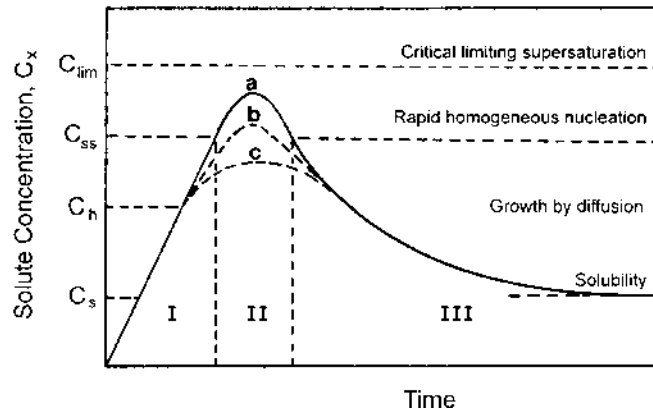


FIGURE 2.27 Modified La Mer diagram for the formation of coated particles by precipitation from solution.

of monodisperse particles (Fig. 2.19). The curve a in Fig. 2.27 represents the case of a single burst of homogeneous nucleation followed by growth. When the particles of A are present in the solution, heterogeneous nucleation can be initiated on their surfaces when the solute concentration reaches C_h , the critical concentration for heterogeneous nucleation. To produce uniformly coated particles, it is essential to have one rapid burst of heterogeneous nucleation (curve c) without reaching C_{ss} .

Colloidal stability of the dispersion: To obtain well-dispersed, coated particles, the dispersion must be stable against flocculation and settling during nucleation and growth. Agglomerates formed during these stages can get bonded by the newly formed surface layers and would be extremely difficult to disperse.

Surface area of the core particles: The surface area of the core particles A must be sufficient to prevent the solute concentration from reaching C_{ss} ; otherwise, a system of coated particles and free particles of B will result (curve b). The appropriate surface area of the core particles is linked to the rate of generation of the solute by the reaction r_g , and the rate of removal of the solute by precipitation, r_r . The minimum surface area of the core particles available for deposition, A_{min} , is associated with the maximum solute concentration, C_{max} , to avoid homogeneous precipitation. For a given r_g and assuming fairly concentrated suspensions so that the interface reaction is rate controlling, A_{min} is defined by

$$r_g = KA_{min}(C_{ss} - C_s) \quad (2.50)$$

where K is a constant and $C_{\max} = C_{ss}$. The maximum surface area for deposition, A_{\max} , should be such that the solute concentration exceeds C_h , otherwise only partial coating will result. Therefore, the following equation must also be satisfied:

$$r_g = KA_{\max}(C_h - C_s) \quad (2.51)$$

The maximum production rate and the latitude of the experimental conditions are then associated with the maximum value of the ratio A_{\max}/A_{\min} . By equating Eqs. (2.50) and (2.51) we get

$$\frac{A_{\max}}{A_{\min}} = 1 + \left[(C_{ss} - C_h)(C_h - C_s) \right] \quad (2.52)$$

The optimum conditions, i.e., permitting coating in suspensions with high particle concentration, high production rates, and ease of processing, depend critically on how close C_h is to C_s and on the separation between C_{ss} and C_h . Conditions should be found such that (1) C_h is close to C_s so that heterogeneous nucleation can begin soon after C_s is passed and (2) C_{ss} is much greater than C_s so that homogeneous precipitation is far removed from the onset of heterogeneous precipitation. In practice, A_{\min} can be found by trial and error for a given r_g and for particles with a known size by decreasing the concentration of the particles in the suspension until free precipitates appear. If A_{\min} is found to be low, then according to Eq. (2.50), $C_{ss} - C_s$ is relatively large, and coating of the particles in a suspension should be possible. Then if conditions for avoiding homogeneous precipitation are difficult to achieve, an approach may be to pretreat the particle surface with a nucleation catalyst.

Several examples of the conditions used in the preparation of coated particles by precipitation from solution can be found in the literature, including SiO_2 on Al_2O_3 (79), TiO_2 on Al_2O_3 (80), aluminum (hydrous) oxide on $\alpha\text{-Fe}_2\text{O}_3$, chromium (hydrous) oxide and TiO_2 (81), Al_2O_3 precursor on SiC whisker (82), Y_2O_3 or $\text{Y}_2\text{O}_3/\text{Al}_2\text{O}_3$ precursors on Si_3N_4 (78), yttrium basic carbonate, YOHCO_3 or Y_2O_3 on $\alpha\text{-Fe}_2\text{O}_3$ (83), and ZnO on ZrO_2 (84). The degree of crystallinity of the deposited material can have a marked effect on the morphology of the coating. In principle, the coating can be amorphous, polycrystalline or single crystal. Smooth and uniform coatings are obtained more easily for amorphous coatings (77,81) whereas somewhat rough layers are generated by polycrystalline deposits (85). Even for amorphous deposits, the morphology can depend on the reaction conditions, as illustrated in Fig. 2.28 for SiO_2 coatings deposited on YOHCO_3 at room temperature and at 80°C (86).

Industrial Preparation of Powders by Precipitation from Solution

The methods described earlier for the synthesis of monodisperse powders and coated particles have not made significant inroads into industrial production be-

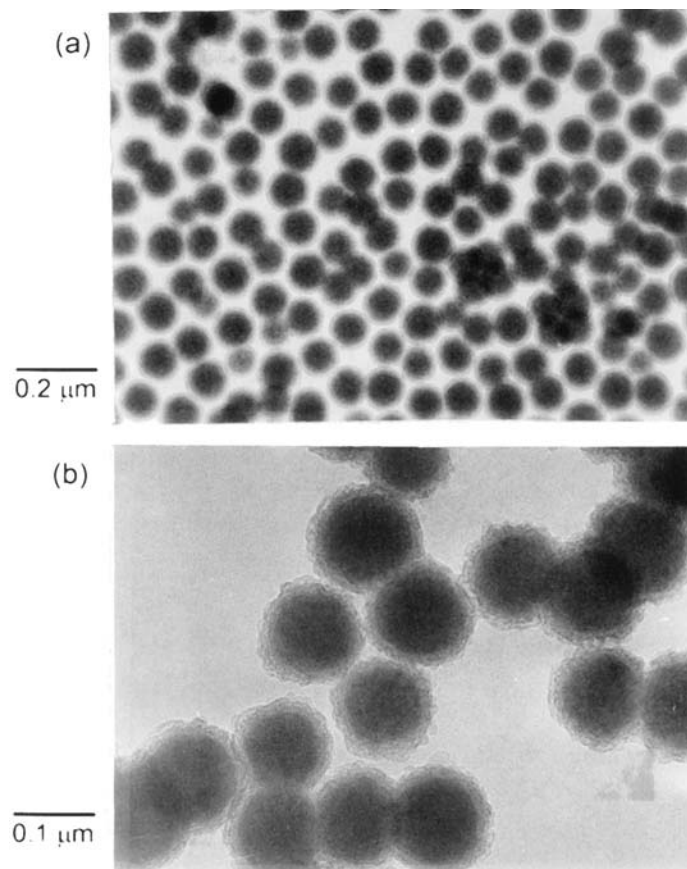
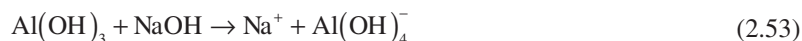


FIGURE 2.28 Transmission electron micrograph of yttrium basic carbonate (YOHCO_3) particles coated with SiO_2 showing (a) smooth SiO_2 coating when the reaction was carried out at room temperature and (b) rough SiO_2 coating formed at higher reaction temperature (80°C). (From Ref. 86.)

cause they are expensive. Co-precipitation and hydrothermal methods are seeing some use, particularly for the synthesis of multicomponent oxides (e.g., BaTiO_3) for electronic applications and for very fine powders.

The largest use of precipitation is the Bayer process for the industrial production of Al_2O_3 powders. The raw material bauxite is first physically beneficiated then digested in the presence of NaOH at an elevated temperature. During digestion, most of the hydrated alumina goes into solution as sodium aluminate:



and insoluble impurities are removed by settling and filtration. After cooling, the solution is seeded with fine particles of gibbsite, $\text{Al}(\text{OH})_3$. In this case, the gibbsite particles provide nucleating sites for growth of $\text{Al}(\text{OH})_3$. The precipitates are continuously classified, washed to reduce the Na, and then calcined. Powders of $\alpha\text{-Al}_2\text{O}_3$ with a range of particle sizes are produced by calcination at 1100–1200°C followed by grinding and classification. Tabular aluminas are produced by calcination at higher temperatures ($\sim 1650^\circ\text{C}$).

2.5.2.2 Evaporation of the Liquid

As we outlined earlier, evaporation of the liquid provides another method for bringing a solution to supersaturation, thereby causing the nucleation and growth of particles. The simplest case is a solution of a single salt. For the production of fine particles, nucleation must be fast and growth slow. This requires that the solution be brought to a state of supersaturation very rapidly so that a large number of nuclei are formed in a short time. One way of doing this is to break the solution up into very small droplets so that the surface area over which evaporation takes place increases enormously. For a solution of two or more salts, a further problem must be considered. Normally the salts will be in different concentrations and will have different solubilities. Evaporation of the liquid will cause different rates of precipitation, leading to segregation of the solids. Here again, the formation of very small droplets will limit the segregation to the droplets since no mass is transferred between individual droplets. Furthermore, for a given droplet size, the size of the particle becomes smaller for more dilute solutions. This means that we can further reduce the scale of segregation by the use of dilute solutions. We now consider some of the practical ways of producing powders by the evaporation of liquid solutions.

Spray Drying

In spray drying, a solution is broken up into fine droplets by a fluid atomizer and sprayed into a drying chamber (Fig. 2.29). Contact between the spray and drying medium (commonly hot air) leads to evaporation of moisture. The product, consisting of dry particles of the metal salt, is carried out in the air stream leaving the chamber and collected using a bag collector or a cyclone.

Spray drying principles, equipment, and applications are described in detail by Masters (87). A variety of atomizers are available and these are usually categorized according to the manner in which energy is supplied to produce the droplets. In rotary atomization (often referred to as centrifugal atomization), the liquid is centrifugally accelerated to high velocity by a spinning disk located at the top of the drying chamber before being discharged into the chamber. In pressure atomization, pressure nozzles atomize the solution by accelerating it through a

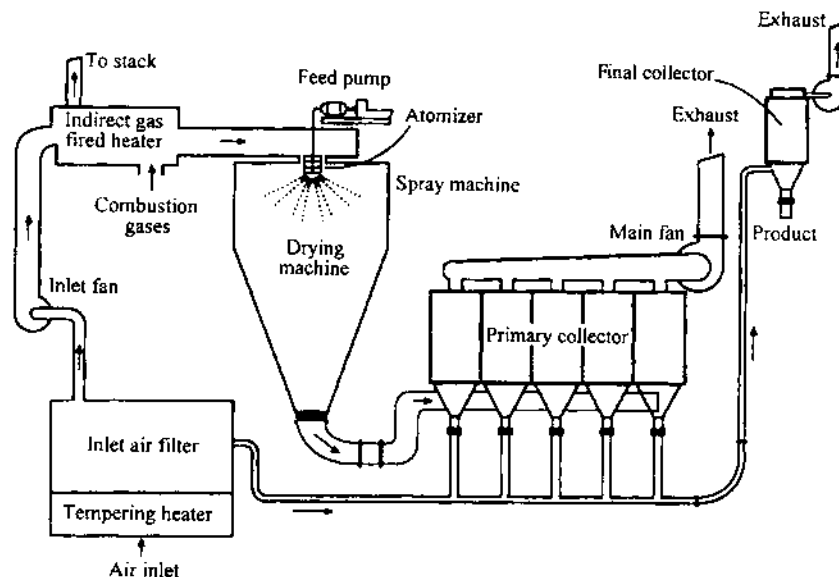


FIGURE 2.29 Schematic of a spray dryer for the production of powders. (Courtesy of L. C. De Jonghe.).

large pressure difference and injecting it into the chamber. Pneumatic atomization occurs when the solution is impacted by a stream of high-speed gas from a nozzle. Ultrasonic atomization involves passing the solution over a piezoelectric device that is vibrating rapidly. Droplet sizes ranging from less than $10\ \mu\text{m}$ to over $100\ \mu\text{m}$ can be produced by these atomizers.

The solutions in spray drying are commonly aqueous solutions of metal salts. Sulfates and chlorides are often used because of their high solubility. In the drying chamber, the temperature and flow pattern of the hot air as well as the design of the chamber determine the rate of moisture removal from the droplet and the maximum temperature (typically less than $\sim 300^\circ\text{C}$) that the particles will experience. The key solution parameters are the size of the droplet and the concentration and composition of the metal salt. These parameters control the primary particle size and the size and morphology of the agglomerate. The morphology of the agglomerate is not very critical in spray drying of solutions because the particle characteristics are largely determined by subsequent calcination and milling steps. Under suitable conditions, spherical agglomerates with a primary particle size of $\sim 0.1\ \mu\text{m}$ or less can be obtained. Because the temperature in the drying chamber is commonly insufficient to cause decomposition or solid-state

reaction, the spray-dried salt must be subjected to additional processing steps such as calcination and milling to achieve suitable characteristics for processing.

Spray drying of solutions has been found to be useful for the preparation of ferrite powders (88). For Ni-Zn ferrite, the solution of sulfates was broken up into droplets (10–20 μm) by a rotary atomizer. The powder obtained by spray drying was in the form of hollow spheres having the same size as the original droplets. Calcination at 800–1000°C produced a fully reacted powder consisting of agglomerates with a primary particle size of $\sim 0.2 \mu\text{m}$. The ground powder (particle size $< 1 \mu\text{m}$) was compacted and sintered to almost theoretical density.

Spray Pyrolysis

By using a higher temperature and a reactive (e.g., oxidizing) atmosphere in the chamber, solutions of metal salts can be dried and decomposed directly in a single step. This technique is referred to by many terms, including *spray pyrolysis*, *spray roasting*, *spray reaction*, and *evaporative decomposition of solutions*. In this book we shall use the term *spray pyrolysis*. A review covering the principles, process parameters and application of spray pyrolysis for the preparation of ceramic powders has been published by Messing et al. (89).

The idealized stages in the formation of a dense particle from a droplet of solution are shown schematically in Fig. 2.30. The droplet undergoes evaporation and the solute concentration in the outer layer increases above the supersaturation limit, leading to the precipitation of fine particles. Precipitation is followed by a drying stage in which the vapor must now diffuse through the pores in the precipitated layer. Decomposition of the precipitated salts produces a porous particle made up of very fine grains, which is finally heated to produce a dense particle. In practice, a variety of particle morphologies can be produced in the spray pyrolysis process, some of which are shown in Fig. 2.31. For the fabrication of advanced ceramics, dense particles are preferred over those with highly porous or hollow shell-like morphologies because a subsequent milling step is normally unnecessary. An understanding of the key processing conditions is useful for achieving the desired particle characteristics.

Figure 2.32 shows schematically how the conditions leading to precipitation in the droplet and the solution chemistry influence the particle morphology and microstructure. If dense particles are required, we must first achieve homogeneous nucleation and growth in the droplet (referred to as volume precipitation in Fig. 2.32a). This is facilitated by a small droplet size and slow drying to reduce gradients in solute concentration and temperature. A large difference between the supersaturation concentration C_{ss} and the saturation concentration C_s of the solute in solution increases the nucleation rate [see Fig. 2.19 and Eq. (2.26)]. It is also important to have a high C_s (i.e., a high solute solubility) and a positive temperature coefficient of solute solubility so that sufficient solute is available to form filled agglomerates of touching primary particles. Furthermore, the precip-

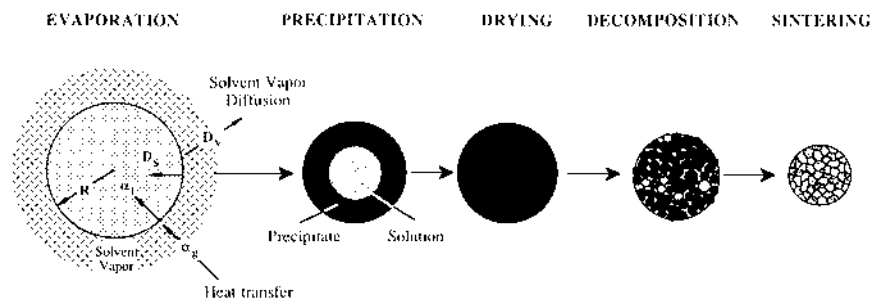


FIGURE 2.30 Schematic of the stages in the spray pyrolysis process. (From Ref. 89.)

itated solids should not be thermoplastic or melt during the decomposition stage. Figure 2.32b illustrates that there are a number of possibilities for synthesizing multicomponent and composite particles with a variety of microstructural characteristics.

The drying of a droplet containing fine precipitates is quite different from that of a liquid droplet. The fine precipitates provide a resistance to the mass transport of the solvent vapor, and if the temperature of the drying chamber is too high, boiling of the solution may occur leading to inflation or disintegration of the droplet. Furthermore, the combination of fine pores between the precipitates and rapid drying of the droplet can lead to high capillary stresses and fracture of the particle (see Chapter 5). It is important to achieve complete decomposition of the dried salts prior to sintering. For small-scale laboratory equipment in which the decomposition times are small, nitrates and acetates are preferable to sulfates because of their lower decomposition temperatures. However, acetates have a low solubility, while nitrates, acetates and sulfates can introduce impurities into the powder. Chlorides and oxychlorides are used industrially because of their high solubilities, but the corrosive nature of the gases produced during decomposition and the deleterious effect of residual chlorine on subsequent sintering can be problematic. The particles should be sintered *in situ* to take full advantage of the spray pyrolysis process. The fine pores between the primary particles and the short interparticle collision time in the process favor the formation of dense individual particles if exposure to a high enough temperature can be achieved.

Spray Drying of Suspensions

Suspensions of fine particles (sometimes referred to as *slurries*) can also be dried by spray drying. In this case, the liquid is removed in such a way as to limit the agglomeration of the dried powder to a scale equal to or less than the size of the droplet. Limiting the scale of the agglomeration should provide benefits in terms

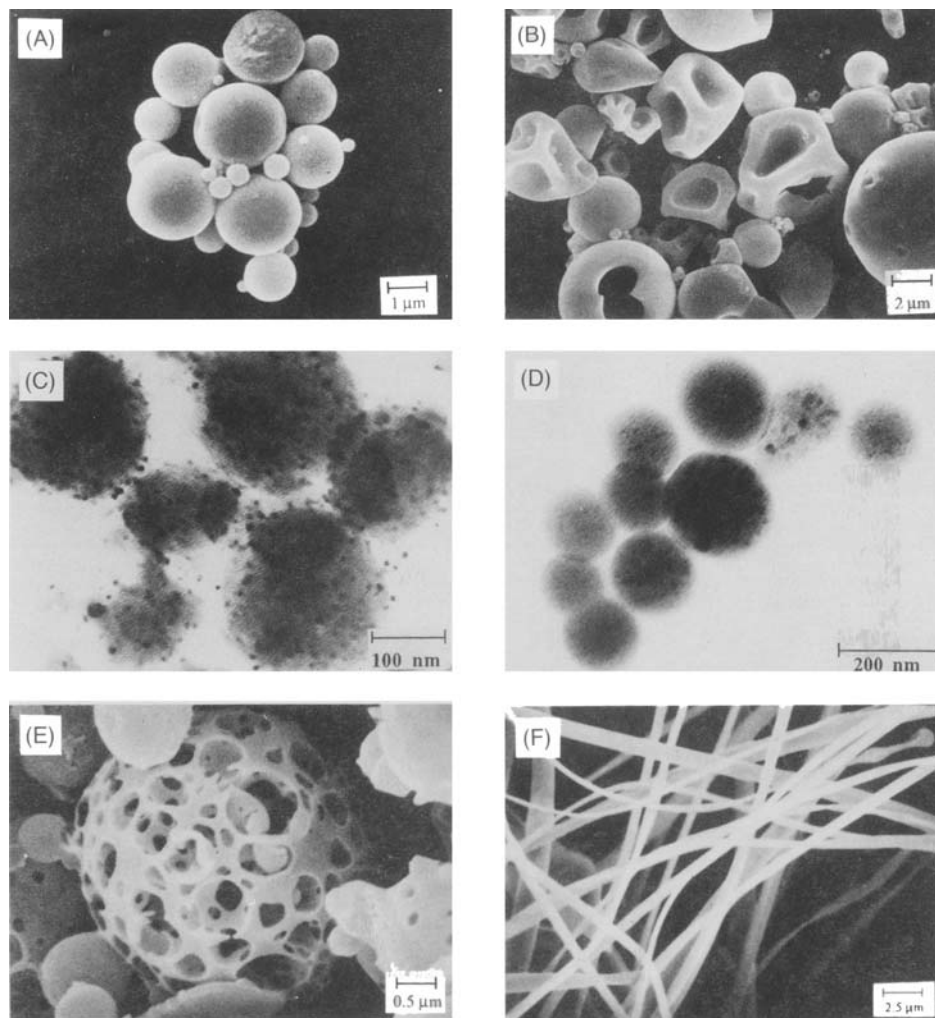


FIGURE 2.31 Examples of the particle morphologies produced in the spray pyrolysis process. (From Ref. 89.)

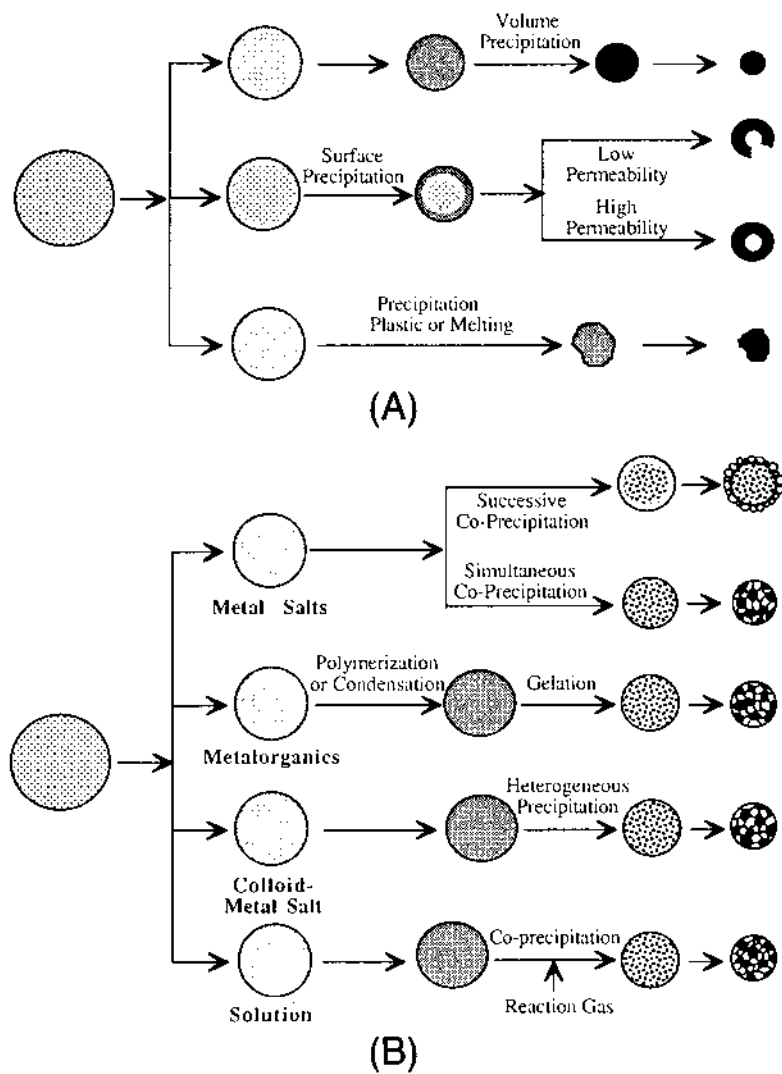


FIGURE 2.32 Effect of precipitation conditions and precursor characteristics on (A) particle morphology and (B) composite particle microstructure in spray pyrolysis. (From Ref. 89.)

of better overall uniformity of the compacted body, which in turn should also lead to benefits in sintering. An example of a powder produced by spray drying of a suspension is shown in Fig. 2.33 for fine lead zirconate titanate particles that were synthesized by precipitation from solution prior to the spray drying process (90). Spray drying of suspensions is used on a large scale industrially for granulating fine powders to control their flow and compaction characteristics during die pressing and is considered in Chapter 6. It is also used for numerous other applications in the food, chemical, and pharmaceutical industries (87).

Freeze Drying

In freeze drying, a solution of metal salt is broken up by an atomizer into fine droplets, which are then frozen rapidly by being sprayed into a cold bath of immiscible liquid such as hexane and dry ice or directly into liquid nitrogen. The frozen droplets are then placed in a cooled vacuum chamber and the solvent is removed, under the action of a vacuum, by sublimation without any melting. The system may be heated slightly to aid the sublimation. The technique produces spherical agglomerates of fine primary particles with the agglomerate size being the same size as that of the frozen droplets. The size of the primary particles (in the range of 10–500 nm) depends on the processing parameters such as the rate of freezing, the concentration of metal salt in the solution, and the chemical composition of the salt. After drying, the salt is decomposed at elevated temperatures to produce an oxide.

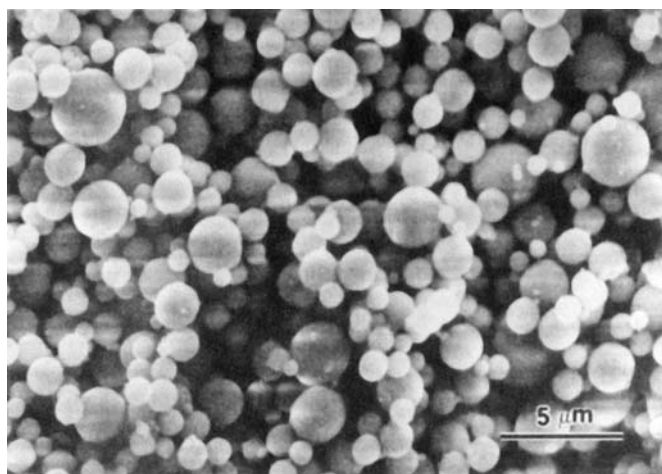


FIGURE 2.33 Scanning electron micrograph of a spray dried lead zirconate titanate powder prepared by spray drying of a suspension. (From Ref. 90.)

As we observed for spray drying, the breaking up of the solution into droplets serves to limit the scale of agglomeration or segregation to the size of the droplet. The solubility of most salts decreases with temperature and the rapid cooling of the droplets in freeze drying produces a state of supersaturation of the droplet solution very rapidly. Particle nucleation is therefore rapid and growth slow so that the size of the particles in the frozen droplet can be very fine. When compared to the evaporation of the liquid in spray drying, the approach to supersaturation is relatively faster so that freeze drying produces much finer primary particles with a higher surface area per unit mass. Surface areas as high as $60 \text{ m}^2/\text{g}$ have been reported for freeze-dried powders.

Freeze drying of solutions has been used on a laboratory scale for the preparation of ferrite and other oxide powders. Laboratory equipment and methods are described by Schnettler et al. (91). Lithium ferrite, LiFe_5O_8 , powders prepared by freeze drying a solution of oxalates were found to have lower sintering temperatures and afforded better control of the grain size when compared to similar powders prepared by spray drying (92). Finally, as we outlined for spray drying, the freeze drying technique is also used for drying slurries. Powders of Al_2O_3 produced from freeze dried slurries were found to consist of soft agglomerates that could be broken down easily (93). Pressing of such powders produced fairly homogeneous green bodies.

2.5.2.3 Gel Routes

A few methods utilize the formation of a semirigid gel or a highly viscous resin from liquid precursors as an intermediate step in the synthesis of ceramic powders, particularly for complex oxides when good chemical homogeneity is required. The powder is commonly obtained by decomposing the gel or resin followed by milling and calcination to control the particle characteristics. In the formation of the gel or resin, mixing of the constituents occurs on the atomic scale by a polymerization process. Provided none of the constituents are volatilized during the decomposition and calcination steps, then the cation composition of the powder can be identical to that of the original solution. Hence these methods have the ability to achieve good chemical homogeneity. A drawback is that the decomposition product is commonly not in the form of a powder but consists of charred lumps. These lumps have to be ground and calcined to achieve the desired powder characteristics. Gel routes to ceramic powders are currently used mainly at the laboratory scale. Key features of the methods are outlined in this section.

Sol–Gel Processing

The sol–gel route for the production of ceramics was outlined in Chapter 1 and will be discussed in greater detail in Chapter 5. The reader will recall that the process is best applied to the formation of films and fibers and, with careful drying, to a few monolithic ceramics. Here, we would like to point out that the

process, while expensive, can also be used for the production of powders. The procedure involves the formation of a polymeric gel by the hydrolysis, condensation, and gelation of a metal alkoxide solution, which is dried and ground to produce a powder. Carefully controlled drying is unnecessary in the production of a powder. Dried gels with lower viscosity are easier to grind, and the extent of contamination introduced during grinding is lower. Liquid removal under supercritical conditions produces almost no shrinkage so that a dried gel with low viscosity is obtained. Grinding can usually be carried out in plastic media. Powders with the stoichiometric mullite composition ($3\text{Al}_2\text{O}_3 \cdot 2\text{SiO}_2$) produced by supercritical drying of gels have been shown to have fairly high sinterability (94). The compacted powders sinter to nearly full density below $\sim 1200^\circ\text{C}$, which is considerably better than mullite prepared by reaction of mixed powders. The sintering benefits are due to the amorphous structure and high surface area of the gel-derived powders. However, crystallization of the powder prior to compaction or sintering can severely reduce the sintering benefits (see Chapter 11).

The Pechini Method

The Pechini method refers to an original process developed by Pechini (95) for the preparation of titanates and niobates for the capacitor industry. The method has since been applied to many complex oxide compositions (96,97). Metal ions from starting materials such as carbonates, nitrates, and alkoxides are complexed in an aqueous solution with α -carboxylic acids such as citric acid. When heated with a polyhydroxy alcohol, such as ethylene glycol, polyesterification occurs, and on removal of the excess liquid, a transparent resin is formed. The resin is then heated to decompose the organic constituents, ground, and calcined to produce the powder. The typical steps in the method are illustrated in Figure 2.34 for the preparation of SrTiO_3 powders (98).

The Citrate Gel Method

The citrate gel method was developed by Marcilly et al. (99) and can be illustrated by the synthesis of the ceramic superconductor $\text{YBa}_2\text{Cu}_3\text{O}_{7-x}$ (100). Nitrate solutions of Y, Ba, and Cu were added to citric acid solution, and the pH was kept at ~ 6 to prevent precipitation of barium nitrate. Heating the solution at 75°C in air produced a viscous liquid containing polybasic chelates. Further heating at 85°C in a vacuum produced an amorphous solid that was pyrolyzed in air at 900°C to produce a crystalline powder.

The Glycine Nitrate Process

The glycine nitrate process is one of a general class of combustion methods for the preparation of ceramic powders. A highly viscous mass formed by evaporation of a solution of metal nitrates and glycine is ignited to produce the powder (101). Glycine, an amino acid, forms complexes with the metal ions in solution which

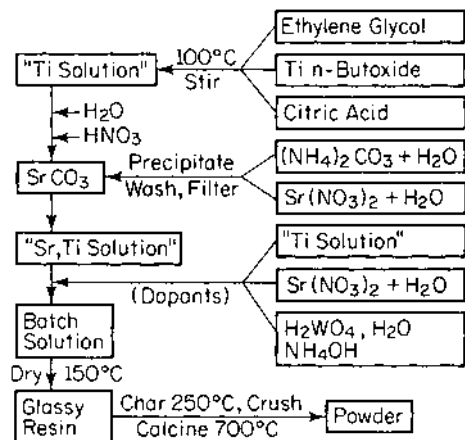


FIGURE 2.34 Flow chart for the preparation of strontium titanate powder by the Pechini method. (From Ref. 98.)

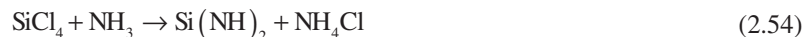
increases the solubility and prevents the precipitation of the metal ions as the water is evaporated. Good chemical homogeneity is therefore achieved, as outlined earlier. Glycine also serves another important function: it provides a fuel for the ignition step of the process since it is oxidized by the nitrate ions. The reactions occurring during ignition are highly explosive, and extreme care must be exercised during this step. Normally, only small quantities should be ignited at a time. Under well controlled conditions, a loose mass of very fine, crystalline powder (particle size less than a tens of nanometers) is obtained after ignition.

When compared to the Pechini method, grinding and calcination of the product are not required. The very fine size and crystalline nature of the powder is believed to be a direct result of the short exposure to high temperatures during the ignition step. With adequate process control, the glycine nitrate process offers a relatively inexpensive route to the preparation of very fine, chemically homogeneous powders. It has been used for the preparation of simple oxides as well as complex oxides (e.g., manganites, chromites, ferrites, and oxide superconductors).

2.5.2.4 Nonaqueous Liquid Reaction

Reactions involving nonaqueous liquids have been used for the synthesis of Si₃N₄ and other nonoxide powders (18). The advantage of these methods is the higher purity and finer particle size of the powder compared with methods that involve grinding of a solid product. The reaction between liquid SiCl₄ and liquid NH₃ has been used on an industrial scale by UBE Industries (Japan) to produce Si₃N₄.

powder. Initial products of the reaction are complex, and although the reaction can be written as



a more involved sequence of reactions occurs, involving the formation of polymeric silicon diimide and ammonium chloride triammoniate, $\text{NH}_4\text{Cl} \cdot 3\text{NH}_3$. Silicon diimide decomposes according to the overall reaction



In the UBE process, the products formed by the interfacial reaction between the SiCl_4 and NH_3 liquids are collected and washed with liquid NH_3 and calcined at 1000°C to produce an amorphous Si_3N_4 powder. Subsequent calcination at 1550°C in N_2 yields a crystalline powder with a particle size of $\sim 0.2 \mu\text{m}$ (Fig. 2.35). The characteristics of the powder are compared with those of other commercial Si_3N_4 powders in Table 2.5.

2.5.3 Vapor-Phase Reactions

Reactions involving the vapor phase have been used extensively for the production of oxide and nonoxide powders. We will outline these methods, paying

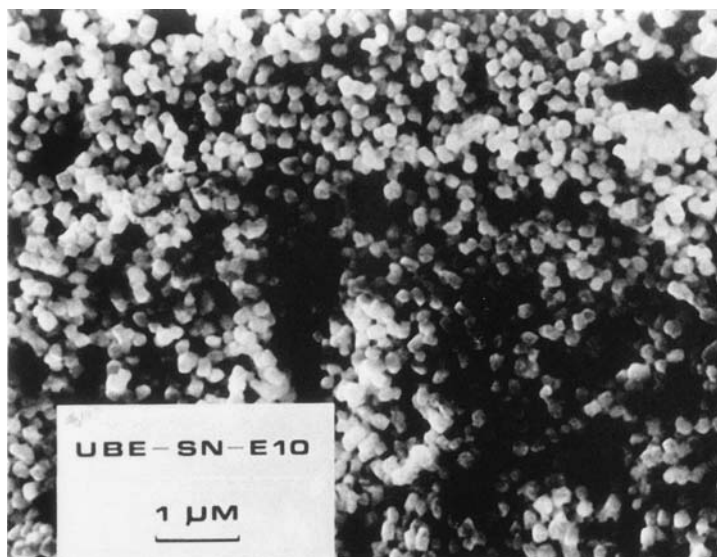


FIGURE 2.35 Scanning electron micrograph of a commercially available Si_3N_4 powder (UBE-SN-E10) produced by the reaction between SiCl_4 and NH_3 liquids. (Courtesy UBE, Japan.)

TABLE 2.5 Properties of Commercially Available Silicon Nitride Powders

	Method of preparation			
	Liquid-phase reaction of SiCl ₄ /NH ₃	Nitridation of Si in N ₂	Carbothermic reduction of SiO ₂ in N ₂	Vapor-phase reaction of SiCl ₄ /NH ₃
Manufacturer	UBE	H. C. Stark	Toshiba	Toya Soda
Grade	SN-E 10	H1	—	TSK TS-7
Metallic impurities (wt%)	0.02	0.1	0.1	0.01
Nonmetallic impurities (wt%)	2.2	1.7	4.1	1.2
α-Si ₃ N ₄ (wt%)	95	92	88	90
β-Si ₃ N ₄ (wt%)	5	4	5	10
SiO ₂ (wt%)	2.5	2.4	5.6	—
Surface area (m ² /g)	11	9	5	12
Average particle size (μm)	0.2	0.8	1.0	0.5
Tap density (g/cm ³)	1.0	0.6	0.4	0.8

particular attention to the preparation of Si₃N₄ and SiC powders. Crystalline Si₃N₄ exists in two different hexagonal polymorphs designated α and β, with the α form having the slightly higher free energy at the formation temperature. Powders of α-Si₃N₄ have a more equiaxial particle shape and sinter more readily than β-Si₃N₄, the particles of which grow in a more elongated shape. The preparation conditions are therefore selected to maximize the amount of the α-Si₃N₄ produced. SiC exist in many polytypes with the two major forms designated α and β. The β form is more stable at lower temperatures and transforms irreversibly to the α form at ~2000°C. Powders produced above ~2000°C therefore consist of α-SiC (e.g., the Acheson process described earlier). Powders of either the α form or the β form are used in the production of SiC materials. However, the sintering of β-SiC powders above ~1800–1900°C results in the transformation to the α-phase which is accompanied by growth of plate-like grains and a deterioration of mechanical properties. The use of β-SiC powder therefore requires very fine powders so that the sintering temperature can be kept below ~1800°C.

We consider vapor phase preparation methods in the following categories: (1) reactions between a gas and a solid, (2) reactions between a gas and a liquid, and (3) reactions between two or more gases.

2.5.3.1 Gas–Solid Reaction

A widely used method for the preparation of Si₃N₄ powders is by direct nitridation in which Si powder (particle size typically in the range 5–20 μm) is reacted with

N_2 at temperatures between 1200 and 1400°C for times in the range 10–30 h. The method is used commercially and a powder produced by H. C. Starck (Germany) is shown in Fig. 2.36. The nitridation process parameters and mechanisms are very similar to those described in Chapter 1 for the production of reaction bonded Si_3N_4 except that a loose bed of Si powder is used rather than a shaped article. The Si_3N_4 powder consists of a mixture of the α and β phases. Some control of the relative amounts of these two phases is achieved by controlling the reaction temperature, the partial pressure of the N_2 gas in the nitriding atmosphere, and the purity of the Si powder.

Silicon nitride powder is also produced by the carbothermic reduction of SiO_2 in a mixture of fine SiO_2 and C powders followed by nitridation between 1200 and 1400°C in N_2 . This process is used industrially by Toshiba (Japan). The widespread availability of pure, fine SiO_2 and C makes this method an attractive alternative to the nitridation of Si. While the overall reaction can be written



the mechanism is believed to involve the gaseous silicon monoxide, SiO , as follows:

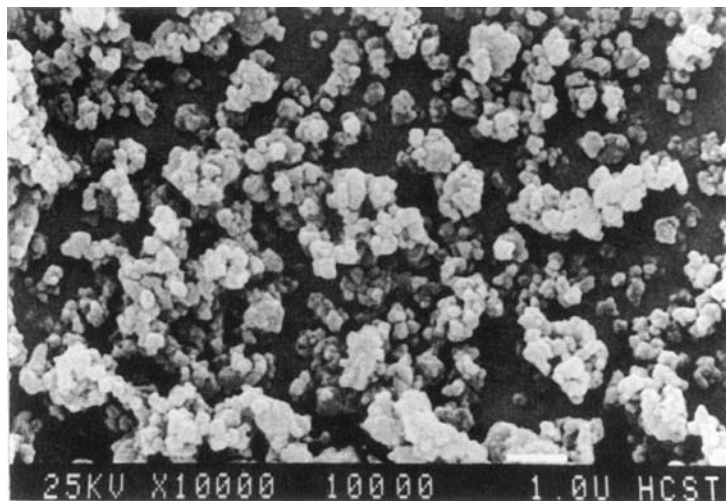
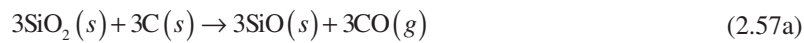
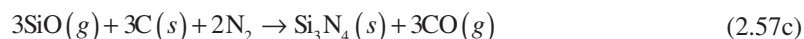


FIGURE 2.36 Scanning electron micrograph of a commercially available Si_3N_4 powder (LC 12) produced by the nitridation of silicon. (Courtesy H. C. Starck, Germany.)



Excess carbon is used as an oxygen sink to form gaseous CO and reduce the amount of oxygen on the powder surface. However, any C remaining after the reaction has to be burnt out in an oxidizing atmosphere, and this may cause some reoxidation of the Si_3N_4 surfaces.

The nitridation and carbothermic reduction methods produce a strongly agglomerated mass of Si_3N_4 that requires milling, washing, and classification. The impurities introduced into the powder during these steps can cause a significant reduction in the high-temperature mechanical properties of the fabricated material.

A two-step process, involving the production of fine metallic particles followed by their oxidation, has been used to synthesize oxide powders with sizes smaller than a few tens of nanometers (102,103). In the process, a metal (e.g., Ti) is evaporated into an inert atmosphere (e.g., He) with pressure of ~ 100 Pa. The particles that condense in the inert atmosphere are transported by convective gas flow to a cold shroud where they adhere. Oxygen gas at a pressure of ~ 5 kPa is then admitted to the chamber to produce oxidation of the metal particles. The particles are finally scraped off the cold shroud and collected. Starting with Ti, this process produces a highly oxygen deficient oxide $\text{TiO}_{1.7}$ with the rutile structure, but subsequent heating at $\sim 300^\circ\text{C}$ produces a nearly stoichiometric composition, $\text{TiO}_{1.95}$.

2.5.3.2 Reaction Between a Liquid and a Gas

Mazdiyasn and Cooke (104,105) showed that the reaction between liquid silicon tetrachloride SiCl_4 and NH_3 gas in dry hexane at 0°C can be used to prepare a fine Si_3N_4 powder with very low levels of metallic impurities (<0.03 wt%). As described earlier for the reaction between the two liquids, the reaction is complex but can be summarized by Eqs. (2.54) and (2.55). The powder obtained by the reaction is amorphous but crystallizes to $\alpha\text{-Si}_3\text{N}_4$ after prolonged heating between 1200 and 1400°C .

2.5.3.3 Reaction Between Gases

The types of deposits that can arise from reactions between heated gases are illustrated in Fig. 2.37 (106). Films, whiskers, and bulk crystals, as we described in Chapter 1, are produced by heterogeneous nucleation on a solid surface by the process known as chemical vapor deposition. The formation of particles occurs by homogeneous nucleation and growth in the gas phase and is governed by the same equations described earlier for the nucleation of liquid droplets from a supersaturated vapor [Eqs. (2.19)–(2.25)]. Several gas-phase reactions are used

to produce ceramic powders industrially as well as on a laboratory scale. The methods employ a variety of techniques for heating the reactant gases in the reactor, including flame, furnace, plasma, and laser heating.

Flame synthesis of TiO_2 and SiO_2 forms two of the largest industrial processes for synthesizing powders by gas phase reactions (107,108). The reactions can be written



and particle formation is illustrated in Fig. 2.38. In the formation of fumed SiO_2 , SiCl_4 reacts in an H_2 flame ($\sim 1800^\circ\text{C}$) to form single spherical droplets of SiO_2 . These grow by collision and coalescence for to form larger droplets. As the droplets begin to solidify, they stick together on collision but do not coalesce, forming solid aggregates, which in turn continue to collide to form agglomerates. A disadvantage of the process is the agglomerated nature of the particles, as shown in Fig. 2.39 for SiO_2 . The advantages include a high-purity product resulting from the use of high-purity gases, the simplicity of the reaction system, and scale up

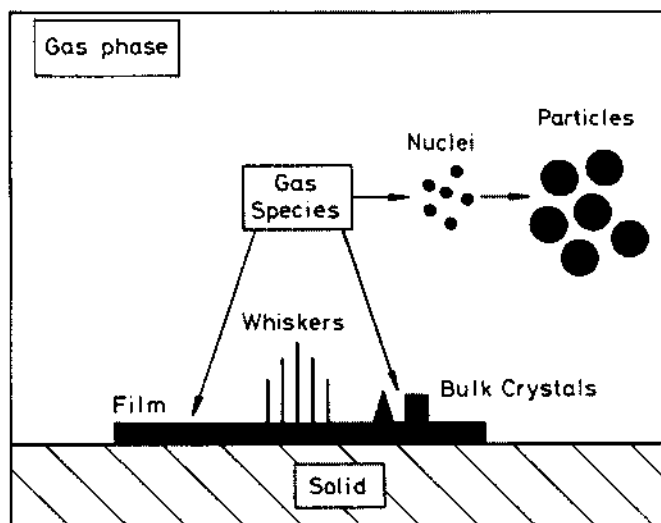
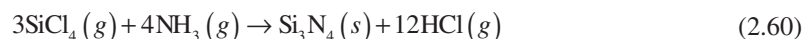


FIGURE 2.37 Schematic diagram illustrating the types of deposits that can form by the reaction between heated gases. (From Ref. 106.)

of the process, as demonstrated by the industrial production of TiO_2 and SiO_2 powders.

Furnace, plasma, and laser heating have been used to produce Si_3N_4 and SiC powders by several gas-phase reactions, including the following:



The use of silicon tetrachloride SiCl_4 leads to highly corrosive HCl as a by-product so that silane, SiH_4 , despite being expensive and flammable in air, is generally preferred as the reactant. For Si_3N_4 production, NH_3 is used because N_2 is fairly unreactive.

Prochazka and Greskovich (109) used the reaction between SiH_4 and NH_3 at temperatures between 500 and 900°C in an electrically heated silica tube to produce fine amorphous Si_3N_4 powders. Two main parameters were found to

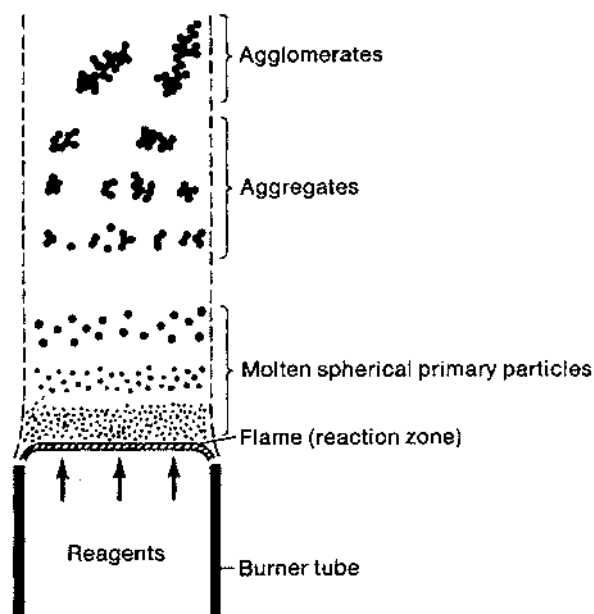


FIGURE 2.38 Schematic diagram illustrating the formation of primary particles, aggregates and agglomerates in gas phase reactions heated by a flame. (From Ref. 107.)

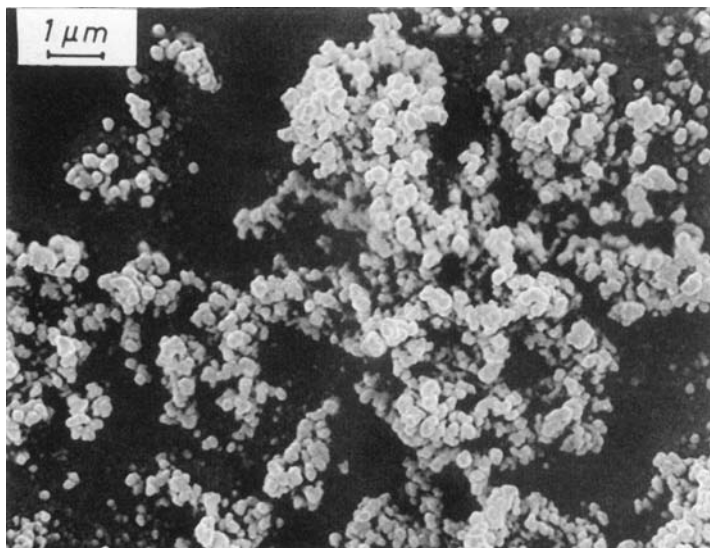


FIGURE 2.39 Scanning electron micrograph of flame-synthesized SiO₂. (Courtesy of Degussa Company.)

control the reaction: the temperature and the NH₃/SiH₄ molar ratio. For a molar ratio >10 and at temperatures between 500 and 900°C, nearly stoichiometric powders with a cation purity of >99.99%, surface area of 10–20 m²/g, and an oxygen content of <2 wt% were produced. Subsequent calcination above ~1350°C yielded crystalline α-Si₃N₄ powder. The reaction between SiCl₄ and NH₃ is used commercially by Toya Soda (Japan) for the production of Si₃N₄ powder. Table 2.5 summarizes the characteristics of the Toya Soda powder and the other commercial Si₃N₄ powders discussed in this chapter.

Thermal plasmas have been used for decades as a source of heat for gas-phase reactions. The use of a radiofrequency (RF) plasma has been investigated at a laboratory level for the production of very fine powders of oxides and to a greater extent for nonoxides such as nitrides and carbides (110). The process parameters that control the powder characteristics are the frequency and power level of the plasma source, the temperature of the plasma jet, the flow rate of the gases, and the molar ratio of the reactants. While powders with high purity and very fine particle size (e.g., 10–20 nm) can be produced by this method, a major problem is that the powders are highly agglomerated.

Haggerty and co-workers (111–113) used a CO₂ laser as the heat source for the gas phase synthesis of Si, Si₃N₄ and SiC powders. In addition to bringing the reactant gases to the required temperature, the laser heating serves another

useful purpose: the frequency of the radiation can be chosen to match one of the absorption frequencies of one or more of the reactants. A laser can therefore be a very efficient heat source. A laboratory scale reaction cell is shown in Fig. 2.40. The laser beam enters the cell through a KCl window and intersects the stream of reactant gases, usually diluted with an inert gas such as argon. The powders are captured on a filter located between the cell and a vacuum pump. An advantage of the method is that the reactions can be fairly well controlled by manipulation of the process variables such as the cell pressure, the flow rate of the reactant and dilutant gases, the intensity of the laser beam, and the reaction flame temperature. The reactions described by Eqs. (2.61) and (2.62) have been used for the production of Si_3N_4 and SiC powders. An advantage of using SiH_4 rather than SiCl_4 as a reactant is that it has a strong adsorption band near the wavelength of the laser ($10.6\text{ }\mu\text{m}$).

Table 2.6 summarizes the range of powder characteristics that are generally obtained for Si_3N_4 and SiC powders by this method. We see that most of the desirable powder characteristics outlined at the beginning of this chapter are achieved. The oxygen content of the powders maintained in an inert atmosphere is fairly low, but it can increase significantly if these fine powders are exposed excessively to oxidizing atmospheres. Although estimates indicate that the production cost can be very competitive with other methods (e.g., the Acheson process), particularly in the synthesis of submicron powders, the laser heating method has not seen industrial application.

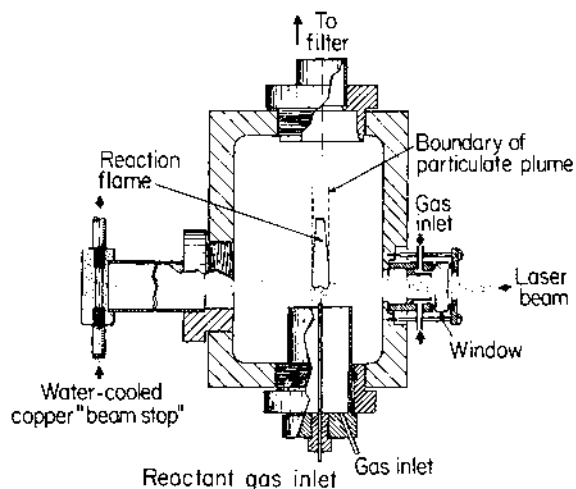


FIGURE 2.40 Laboratory scale reaction cell for the preparation of powders by laser heating of gases. (From Ref. 111.)

TABLE 2.6 Summary of the Range of Characteristics for Si_3N_4 and SiC Prepared by Laser-Heated Gas-Phase Reactions

Powder characteristic	Si_3N_4	SiC
Mean diameter (nm)	7.5–50	20–50
Standard deviation of diameters (% of mean)	2.3	~2.5
Impurities (wt%)		
Oxygen	0.3	0.33–1.3
Total others	<0.01	—
Major elements	Al, Ca	—
Stoichiometry (%)	0–60 (excess Si)	0–10 (excess C or Si)
Crystallinity	Amorphous-crystalline	Crystalline Si and SiC
Grain size: mean diameter	~0.5	0.5–1.0

Source: Ref. 111.

2.6 CONCLUDING REMARKS

In this chapter we have examined a wide range of methods commonly used for the preparation of ceramic powders. It will be recognized that scientifically, the methods are based on sound principles of physics and chemistry, which form a framework for understanding how the process variables influence the characteristics of the powder. Practically, the methods vary considerably in the quality of the powder produced and in the cost of production. Generally, higher powder quality is associated with higher production cost. For a given application, we will therefore need to examine whether the higher production cost is justified by the higher quality of the powder produced.

PROBLEMS

- 2.1 For a powder with the composition of TiO_2 , calculate and plot the surface area of 1 g of powder as a function of the particle size. Use a size range of 5 nm to 100 μm and assume that the particles are spherical. Estimate the percentage of TiO_2 molecules at the surface of the particle (relative to the total number of TiO_2 molecules in the volume of the particle) for the same size range and plot the results on a graph.
- 2.2 Show that the critical speed of rotation for a ball mill, defined as the speed required to take the balls just to the apex of revolution is equal to $(g/a)^{1/2}/2\pi$ revolutions per second, where a is the radius of the mill and g is the acceleration due to gravity. Determine the rotation speed for a ball mill with a radius of 5 cm which is operating at 75% of the critical rotation speed.

- 2.3 In an experiment to determine the kinetics of decomposition of MgCO_3 , a student weighs out 20.00 g of powder and finds that the mass of powder remaining in an isothermal experiment is as follows:

Time (min)	Mass of Powder (g)
0	20.00
10	16.91
20	14.73
30	13.19
50	11.35
80	10.16

Determine whether the following model equations provide a reasonable fit to the reaction kinetics:

- The Avrami-Erofe'ev equation
 - The geometrical model for a contracting spherical core
 - The Jander equation
 - A first order reaction
- 2.4 The calcination of CaCO_3 described by the equation:
- $$\text{CaCO}_3(\text{s}) \rightarrow \text{CaO}(\text{s}) + \text{CO}_2(\text{g})$$
- has a standard free energy given by
- $$\Delta G^\circ = 182.50 - 0.16T \quad (\text{kJ/mol})$$
- where T is the absolute temperature. The partial pressure of CO_2 in air is 3×10^{-3} atm.
- If the calcination is carried out in flowing air in an open tube furnace, at what temperature will CaCO_3 decompose to CaO ?
 - If the calcination is carried out in a tightly sealed tube furnace, explain qualitatively what will happen.
 - Will it help to calcine in a tightly sealed tube furnace backfilled with an inert gas such as argon or helium at 1 atm pressure?
 - If the calcination is carried out in a vacuum furnace with a pressure of 10^{-4} torr, at what temperature will the CaCO_3 decompose? What drawbacks, if any, do you see in vacuum calcination?
- 2.5 Consider the formation of NiCr_2O_4 from spherical particles of NiO and Cr_2O_3 when the reaction rate is controlled by diffusion through the product layer.
- Sketch an assumed geometry and derive a relation for the rate of formation early in the process.
 - What governs the particles on which the product layer forms?
 - At 1300°C , the diffusion coefficients in NiCr_2O_4 are as follows: $D_{\text{Cr}} > D_{\text{Ni}} > D_{\text{O}}$. Which controls the rate of formation of NiCr_2O_4 ? Explain why.
- 2.6 Outline the derivation of the Jander equation and discuss its limitations. How are the limitations corrected in the Carter equation? One-micron spheres of Al_2O_3 are surrounded by excess ZnO powder to observe the formation of zinc aluminate spinel ZnAl_2O_4 . It is found that 25% of the Al_2O_3 is reacted to form ZnAl_2O_4 during the first 30 min of an isothermal experiment. Determine how long it will take for all

the Al_2O_3 to be reacted on the basis of (a) the Jander equation and (b) the Carter equation.

- 2.7 In the preparation of TiO_2 powder by the Stober process, a student starts out with a solution containing 20 vol% of titanium isopropoxide in isopropanol. Assuming that the reaction is stoichiometric, how much water must be added?
- 2.8 Discuss the factors involved in the design of a continuous process for the preparation of narrow-sized, unagglomerated titania powder. (See Ref. 114.)
- 2.9 You wish to prepare approximately 50 g of a Y_2O_3 -stabilized ZrO_2 powder containing 8 mol% Y_2O_3 by the process of co-precipitation from solution. You start by dissolving $\text{ZrOCl}_2 \cdot 8\text{H}_2\text{O}$ and $\text{YCl}_3 \cdot 6\text{H}_2\text{O}$ in 300 cm^3 of deionized water and add the solution drop-wise into a stirred, excess solution of NH_4OH prepared by diluting a concentrated NH_4OH solution containing 30 wt% NH_3 . Determine the amount of each starting material and the volume of each solution required for the process, assuming that the reaction goes to completion.
- 2.10 Compare the key steps in the procedure and the expected particle characteristics for a Y_2O_3 -stabilized ZrO_2 powder (8 mol% Y_2O_3) synthesized by the following routes:
 - a. Calcination of a ball-milled mixture of submicron ZrO_2 and Y_2O_3 powders
 - b. Co-precipitation from solution
 - c. Combustion synthesis (e.g., glycine nitrate process).
- 2.11 Design a process for preparing ZnO powder that is uniformly coated with 0.5 mol% Bi_2O_3 . What would the thickness of the coating be if the particle size of the ZnO powder (assumed to be spherical in shape) is 100 nm?
- 2.12 A solution containing 0.1 mol/l of zinc acetate is spray roasted using a nozzle that produces 40- μm diameter droplets produce ZnO particles. If the particles are only 50% dense, estimate their diameter.
- 2.13 Surface oxidation produces an oxide layer (~ 3 nm thick) on SiC . Assuming the composition of the oxide layer to be that of SiO_2 , estimate the wt% of oxygen in SiC powders (assumed to be spherical) with a particle size of (a) 1 μm and (b) 50 nm.
- 2.14 Discuss the technical and economic factors that will favor the production of Si_3N_4 powders by laser heating of gases over the nitridation of Si . (See Ref. 111.)

REFERENCES

1. Perry, R. H.; Green, D. W.; Maloney, J. O. Perry's Chemical Engineers' Handbook; 6th ed.; McGraw-Hill: New York, 1984, Sec. 8.
2. Lowrinson, G. C. Crushing and Grinding; Butterworth: London, 1974.
3. Beddow, J. K. Particulate Science and Technology; Chemical Publishing Co.: New York, 1980.
4. Polke, R.; Stadler, R. In Concise Encyclopedia of Advanced Ceramic Materials; Brook, R. J. ed.; MIT Press: Cambridge, MA, 1991, pp. 187–193.
5. Somasundaran, P. In Ceramic Processing Before Firing; Onoda, G. Y., Hench, L.L. eds.; Wiley: New York, 1978, pp. 105–123.

6. Gilman, P. S.; Benjamin, J. S. *Ann. Rev. Mater. Sci.* 1983, Vol. 13, 279.
7. Sundaresan, R.; Froes, F. H. J. *Metals*. 1987, Vol. 39 (8), 22.
8. McCormick, P. G.; Froes, F. H. J. *Metals*. 1998, Vol. 50 (11), 61.
9. Lin, I. J.; Nadiv, S. *Mater. Sci. Eng.* 1979, Vol. 39, 193.
10. Kosmac, T.; Courtney, T. H. J. *Mater. Res.* 1992, Vol. 7 (6), 1519.
11. Le Caër, G.; Matteazzi, P.; Bauer Grosse, E.; Pinaelli, A.; Bouzy, E. J. *Mater. Sci.* 1990, Vol. 25, 4726.
12. El-Eskandarany, M. S.; Sumiyama, K.; Aoki, K.; Suzuki, K. J. *Mater. Res.* 1992, Vol. 7 (4), 888.
13. Patankar, S. N.; Xiao, S.-Q.; Lewandowski, J. J.; Heuer, A. H. J. *Mater. Res.* 1993, Vol. 8 (6), 1311.
14. Yen, B. K.; Aizawa, T. J. *Am. Ceram. Soc.* 1998, Vol. 81 (7), 1953.
15. Ganguli, D.; Chattergee, M. *Ceramic Powder Preparation: A Handbook*; Kluwer: Boston, 1997.
16. Segal, D. In *Materials Science and Technology*; Brook, R. J. ed.; VCH: New York, 1996, Vol. 17A, pp. 70–98.
17. Riman, R. E. In *Surface and Colloid Chemistry in Advanced Ceramics Processing*; Pugh, R. J., Bergström, L. eds.; Marcel Dekker: New York, 1994.
18. Segal, D. *Chemical Synthesis of Advanced Ceramic Powders*; Cambridge University Press: New York, 1989.
19. Johnson, D. W., Jr. In *Advances in Powder Technology*; Chin, G. Y. ed.; American Society for Metals: Metals Park, OH, 1982, pp. 22–37.
20. Johnson, D. W., Jr. *Am. Ceram. Soc., Bull.* 1981, Vol. 60 [2], 221.
21. Young, D. A. *Decomposition of Solids*; Pergamon: Oxford, 1966.
22. Bamford, C. H.; Tipper, C. F. H. *Reactions in the Solid State. Comprehensive Chemical Kinetics*; Elsevier: Oxford, 1980, Vol. 22.
23. Tompkins, F. C. *Reactivity of Solids. Treatise on Solid State Chemistry*; Plenum: New York, 1976, Vol. 4.
24. Kubaschewski, O.; Evans, E. L.; Alcock, C. B. *Metallurgical Thermochemistry*; 5th ed.; Pergamon Press: Oxford, 1979.
25. Kingery, W. D.; Bowen, H. K.; Uhlmann, D. R. *Introduction to Ceramics*; 2nd ed.; Wiley: New York, 1976, p. 415.
26. Hills, A. W. D. *Chem. Eng. Sci.* 1968, Vol. 23, 297.
27. Beruto, D.; Searcy, A. W. J. *Chem. Soc., Faraday Trans. I.* 1974, Vol. 70, 2145.
28. Hyatt, E. P.; Cutler, I. B.; Wadsworth, M. E. J. *Am. Ceram. Soc.* 1950, Vol. 41, 79.
29. Ewing, J.; Beruto, D.; Searcy, A. W. J. *Am. Ceram. Soc.* 1979, Vol. 62 (11–12), 580.
30. Beruto, D.; Barco, L.; Searcy, A. W. J. *Am. Ceram. Soc.* 1981, Vol. 67 (2), 74.
31. Beruto, D.; Botter, R.; Searcy, A. W. J. *Am. Ceram. Soc.* 1987, Vol. 70 (3), 155.
32. Schmalzried, H. *Solid State Reactions*; 2nd ed.; Verlag Chemie: Weinheim, Germany, 1981.
33. Linder, J. J. *Chem. Phys.* 1955, Vol. 23 (2), 410.
34. Kuczynski, G. C. In *Ferrites, Proceedings of the International Conference*; Hoshino, Y., Iida, S., Sugimoto, M. eds.; University Park Press: Baltimore, 1971, pp. 87–95.
35. Branson, D. L. J. *Am. Ceram. Soc.* 1965, Vol. 48 (11), 591.

36. Jander, W. Z. *Anorg. Allg. Chem.* 1927, Vol. 163, 1.
37. Carter, R. E. *J. Chem. Phys.* 1961, Vol. 34, 2010; 1961, Vol. 35, 1137.
38. Glatzmier, G.; Koc, R. U. S. Patent 5,324,494, 1994.
39. Koc, R.; Cattamanchi, S. V. *J. Mater. Sci.* 1998, Vol. 33, 2537.
40. Nielsen, A. E. *Kinetics of Precipitation*; MacMillan: New York, 1964.
41. Overbeek, J. Th. G. *Adv. Colloid Interface Sci.* 1982, Vol. 15, 251.
42. Sugimoto, T. *Adv. Colloid Interface Sci.* 1987, Vol. 28, 65.
43. Haruta, M.; Delmon, B. *J. Chim. Phys.* 1986, Vol. 83 (11–12), 859.
44. Pierre, A. C. *Am. Ceram. Soc. Bull.* 1991, Vol. 70 (8), 1281.
45. Matijevic, E. *Ann. Rev. Mater. Sci.* 1985, Vol. 15, 483.
46. Matijevic, E. *Langmuir.* 1986, Vol. 2, 12.
47. Christian, J. W. *The Theory of Transformations in Metals and Alloys*; Pergamon: Oxford, 1975.
48. McDonald, J. E. *Am. J. Phys.* 1962, Vol. 30 (12), 870.
49. Walton, A. G. In *Nucleation*; Zettlemoyer, A. C. ed.; Marcel Dekker: New York, 1969, pp. 225–307.
50. Mesmer, R. E., Jr. *The Hydrolysis of Cations*; Wiley: New York, 1976.
51. Reiss, H. *J. Chem. Phys.* 1951, Vol. 19 (1), 482.
52. LaMer, V. K.; Dinegar, R. H. *J. Am. Chem. Soc.* 1950, Vol. 72 (11), 4847.
53. Hsu, W. P.; Ronnquist, L.; Matijevic, E. *Langmuir.* 1988, Vol. 4, 31.
54. Bogush, G. H.; Zukoski, C. F. *J. Colloid Interf. Sci.* 1990, Vol. 142, 19.
55. Bogush, G. H.; Dickstein, G. L.; Lee, K. C.; Zukoski, C. F. *Mater. Res. Soc. Symp. Proc.* (1988), Vol. 121, 57.
56. Stober, W.; Fink, A.; Bohn, E. *J. Colloid Interf. Sci.* 1968, Vol. 26, 62.
57. Barringer, E. A.; Bowen, H. K. *J. Am. Ceram. Soc.* 1982, Vol. 65 (12), C-199.
58. Barringer, E. A.; Bowen, H. K. *Langmuir.* 1985, Vol. 1, 414.
59. Matijevic, E. In *Ultrastructure Processing of Ceramics, Glasses, and Composites*; Hench, L. L., Ulrich, D. R. eds.; Wiley: New York, 1984, pp. 334–352.
60. Matijevic, E. In *Ultrastructure Processing of Advanced Ceramics*; Mackenzie, J. D., Ulrich, D. R. eds.; Wiley: New York, 1988, pp. 429–442.
61. Matijevic, E. In *Chemical Processing of Advanced Ceramics*; Hench, L. L., West, J. K. eds.; Wiley: New York, 1992, pp. 513–527.
62. Brace, R.; Matijevic, E. *J. Inorg. Nucl. Chem.* 1973, Vol. 35, 3691.
63. Aiken, B.; Hsu, W. P.; Matijevic, E. *J. Am. Ceram. Soc.* 1988, Vol. 71 (10), 845.
64. Bratton, R. J. *Am. Ceram. Soc. Bull.* 1959, Vol. 48 (8), 759.
65. Haertling, G. H. In *Ceramic Materials for Electronics*; 2nd ed.; Buchanan, R. C.; Wiley: New York, 1991, pp. 129–205.
66. Mazdiasni, K. S.; Smith, J. S., Jr. *J. Am. Ceram. Soc.* 1969, Vol. 52 (10), 523.
67. Mah, T.-I.; Hermes, E. E.; Masdiasni, K. S. In *Chemical Processing of Ceramics*; Lee, B. I., Pope, E. J. A.; Marcel Dekker: New York, 1994.
68. Dawson, W. J. *Am. Ceram. Soc. Bull.* 1988, Vol. 67 (10), 1673.
69. Somiya, S. In *Concise Encyclopedia of Advanced Ceramic Materials*; Brook, R. J.; MIT Press: Cambridge, 1991, pp. 375–377.
70. Rahaman, M. N.; Zhou, Y. C. *J. Europ. Ceram. Soc.* 1995, Vol. 15, 939.
71. Peterson, J. H. U. S. Patent 2,216,655, Oct. 22, 1940.

72. Eckert, J. O.; Hung-Houston, C. C.; Gersten, B. L.; Lencka, M. M.; Riman, R. E. *J. Am. Ceram. Soc.* 1996, Vol. 79 (11), 2929.
73. Hennings, D.; Rosenstein, G.; Schreinemacher, H. J. *Europ. Ceram. Soc.* 1991, Vol. 8, 107.
74. Frey, M. H.; Payne, D. A. *Phys. Rev.* 1996, Vol. 54 (5), 3158.
75. Sparks, R. E. In *Encyclopedia of Chemical Technology*; Grayson, M., Eckroth, D.; Wiley: New York, 1981, Vol. 15, p. 470.
76. Matijevic, E. In *Science of Ceramic Chemical Processing*; Hench, L. L., Ulrich, D. R.; Wiley: New York, 1986, pp. 463–481.
77. Garg, A.; Matijevic, E. *Langmuir*. 1988, Vol. 4, 38.
78. Garg, A.; De Jonghe, L. C. J. *Mater. Res.* 1990, Vol. 5 (1), 136.
79. Sacks, M. D.; Bozkurt, N.; Scheiffle, G. W. J. *Am. Ceram. Soc.* 1991, Vol. 74 (10), 2428.
80. Okamura, H.; Barringer, E. A.; Bowen, H. K. J. *Am. Ceram. Soc.* 1986, Vol. 69 (2), C-22.
81. Kratochvil, S.; Matijevic, E. *Adv. Ceram. Mater.* 1987, Vol. 2 (4), 798.
82. Kapolnek, D.; De Jonghe, L. C. J. *Europ. Ceram. Soc.* 1991, Vol. 7, 345.
83. Aiken, B.; Matijevic, E. J. *Colloid Interface Sci.* 1988, Vol. 126 (2), 645.
84. Hu, C.-L.; Rahaman, M. N. J. *Am. Ceram. Soc.* 1992, Vol. 75 (8), 2066.
85. Gherardi, P.; Matijevic, E. J. *Colloid Interface Sci.* 1986, Vol. 109 (1), 57.
86. Giesche, H.; Matijevic, E. J. *Mater. Res.* 1994, Vol. 9 (2), 436.
87. Masters, K. *Spray Drying Handbook*; 5th ed.; Wiley: New York, 1991.
88. DeLau, J. G. M. *Am. Ceram. Soc. Bull.* 1970, Vol. 49 (6), 572.
89. Messing, G. L.; Zhang, S.-C.; Jayanthi, G. V. J. *Am. Ceram. Soc.* 1993, Vol. 76 (11), 2707.
90. Schwartz, R.; Eichart, D.; Payne, D. *Mater. Res. Soc. Symp. Proc.* 1986, Vol. 73, 123.
91. Schnettler, F. J.; Montforte, F. R.; Rhodes, W. W. In *Science of Ceramics*; Stewart, G. H. ed.; The British Ceramic Society, Stoke-on-Trent: UK, 1968, Vol. 4, pp. 79–90.
92. Gallagher, P. K., Jr.; Nitti, D. J.; Schrey, F. *Am. Ceram. Soc. Bull.* 1974, Vol. 53 (2), 167.
93. Real, M. W. *Proc. Brit. Ceram. Soc.* 1986, Vol. 38, 59.
94. Rahaman, M. N.; De Jonghe, L. C.; Shinde, S. L.; Tewari, P. H. J. *Am. Ceram. Soc.* 1988, Vol. 71 (7), C-338.
95. Pechini, M. U. S. Patent 3,330,697, 1967.
96. Eror, N. G.; Anderson, H. U. *Mater. Res. Soc. Symp. Proc.* 1986, Vol. 73, 571.
97. Lessing, P. A. *Am. Ceram. Soc. Bull.* 1989, Vol. 68 (5), 1002.
98. Budd, K. D.; Payne, D. A. *Mater. Res. Soc. Symp. Proc.* 1984, Vol. 32, 239.
99. Marcilly, C.; Courty, P.; Delmon, B. J. *Am. Ceram. Soc.* 1970, Vol. 53 (1), 56.
100. Chu, C.-T.; Dunn, B. J. *Am. Ceram. Soc.* 1987, Vol. 70 (12), C-375.
101. Chick, L. A.; Pederson, L. D.; Maupin, G. D.; Bates, J. L.; Thomas, L. E.; Exarhos, G. J. *Mater. Lett.* 1990, Vol. 10 (12), 6.
102. Birringer, R.; Gleiter, H.; Klein, H.-P.; Marquard, P. *Phys. Lett.* 1984, Vol. 102A, 365.
103. Siegel, R. W.; Ramasamy, S.; Hahn, H.; Zongquan, L.; Ting, L. J. *Mater. Res.* 1988, Vol. 3, 1367.

104. Mazdiasni, K. S.; Cooke, C. M. J. Am. Ceram. Soc. 1973, Vol. 56, 628.
105. Mazdiasni, K. S.; Cooke, C. M. U. S. Patent 3,959,446, 1976.
106. Kato, A.; Hojo, J.; Okabe, Y. Memoirs of the Faculty of Engineering, Kyushu University. 1981, Vol. 41, 319.
107. Ulrich, G. D. Chem. Eng. News. 1984, Vol. 62 (32), 22.
108. George, A. P.; Murley, R. D.; Place, E. R. Faraday Symp. Chem. Soc. 1973, Vol. 7, 63.
109. Prochazka, S.; Greskovich, C. Am. Ceram. Soc. Bull. 1978, Vol. 57 (6), 579.
110. Hollabaugh, C. M.; Hull, D. E.; Newkirk, L. R.; Petrovic, J. J. J. Mater. Sci. 1983, Vol. 18, 3190.
111. Haggerty, J. S. In Ultrastructure Processing of Ceramics, Glasses and Composites; Hench, L. L., Ulrich, D. R.; Wiley: New York, 1984, pp. 353–366.
112. Cannon, W. R.; Danforth, S. C.; Flint, J. H.; Haggerty, J. S.; Marra, R. A. J. Am. Ceram. Soc. 1982, Vol. 65 (7), 324.
113. Cannon, W. R.; Danforth, S. C.; Haggerty, J. S.; Marra, R. A. J. Am. Ceram. Soc. 1982, Vol. 65 (7), 330.
114. Jean, J. H.; Goy, D. M.; Ring, T. A. Am. Ceram. Soc. Bull. 1987, Vol. 66, 1517.

3

Powder Characterization

3.1 INTRODUCTION

Chapter 2 reviewed the important methods for the preparation of ceramic powders. You may have observed that the quality of the powder depends on the preparation method. You will also recall that the powder characteristics have a significant influence on the packing homogeneity of the consolidated body and on the microstructural evolution of the fired body. Knowledge of the powder characteristics serves two key purposes:

- Quality control of the starting material
- Ability to control the microstructure of the fabricated material

The extent to which the characterization process is taken depends on the application. In the case of traditional ceramics, which do not have to meet exacting property requirements, a fairly straightforward observation, with a microscope, of the size, size distribution, and shape of the powders may be sufficient. For advanced ceramics, however, detailed knowledge of the powder characteristics is required for adequate control of the microstructure and properties of the fabricated material. Commercial powders are used in most applications. Normally, the manufacturer has carried out most of the characterization experiments and provides the user with the results, generally referred to as *powder specifications*. The manufacturer's specifications combined with a straightforward observation of the powder with a microscope are sufficient for many applications.

For a powder prepared in the laboratory, a detailed set of characterization experiments may have to be carried out. Minor variations in the chemical composition and purity of the powder, as we have seen, can have profound effects on

the microstructure and properties of advanced ceramics. This realization has led to a growing use of analytical techniques that have the capability of detecting constituents, especially on the surfaces of the particles, at concentrations down to the parts-per-million level.

The important characteristics of a powder can be categorized into four groups: physical characteristics, chemical composition, phase composition, and surface characteristics. For each group, the main powder properties that have a significant influence on processing are summarized in Table 3.1. A vast number of techniques have been developed for the characterization of solids (1). In this chapter, we concentrate only on those techniques that have broad applications to ceramic powders. The experimental details in performing the characterization will, in general, not be covered as they are usually discussed at length in the manuals supplied by the manufacturers of the equipment. Instead, we concentrate on the principles of the methods, the range of information that can be obtained with them, and some of their limitations.

3.2 PHYSICAL CHARACTERIZATION

Powders consist of an assemblage of small units with certain distinct physical properties. These small units, loosely referred to as particles, can have a fairly complex structure. A variety of terms have been used to describe them and this has led to some confusion in the literature. In this book we adopt, with minor modifications, the terminology proposed by Onoda and Hench (2).

TABLE 3.1 Powder Characteristics that Have a Significant Influence on Ceramic Processing

Physical characteristics	Chemical composition	Phases	Surface characteristics
Particle size and distribution	Major elements	Structure (crystalline or amorphous)	Surface structure
	Minor elements		Surface composition
Particle shape	Trace elements	Crystal structure	
Degree of agglomeration		Phase composition	
Surface area			
Density and porosity			

3.2.1 Types of Particles

3.2.1.1 Primary Particles

A primary particle is a discrete, low-porosity unit that can be either a single crystal, a polycrystalline particle, or a glass. If any pores are present, they are isolated from each other. A primary particle cannot, for example, be broken down into smaller units by ultrasonic agitation in a liquid. It may be defined as the smallest unit in the powder with a clearly defined surface. For a polycrystalline primary particle, the crystals have been referred to variously as crystallites, grains, or domains. In this book, we shall use the term *crystal*.

3.2.1.2 Agglomerates

An agglomerate is a cluster of primary particles held together by surface forces, by liquid, or by a solid bridge. Figure 3.1 is a schematic diagram of an agglomerate consisting of dense, polycrystalline primary particles. Agglomerates are porous, with the pores being generally interconnected. They are classified into two types: soft agglomerates and hard agglomerates. *Soft agglomerates* are held together by fairly weak surface forces and can be broken down into primary particles by ultrasonic agitation in a liquid. *Hard agglomerates* consist of primary particles that are chemically bonded by solid bridges; they therefore cannot be broken down into primary particles by ultrasonic agitation in a liquid. Hard agglomerates, as outlined in Chapter 2, are undesirable in the production of advanced ceramics because they commonly lead to the formation of microstructural defects.

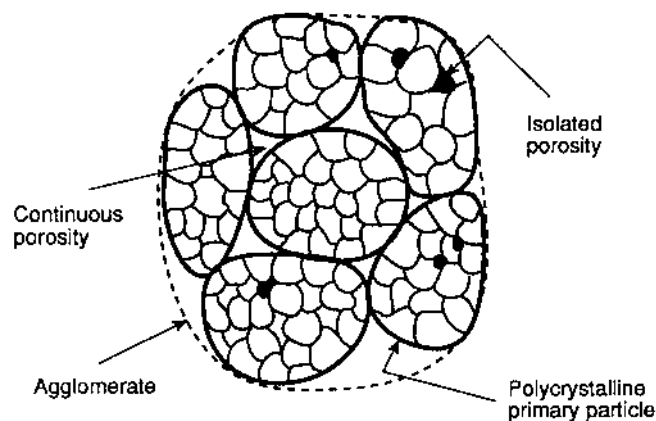


FIGURE 3.1 Schematic diagram of an agglomerate consisting of dense, polycrystalline primary particles.

3.2.1.3 Particles

When no distinction is made between primary particles and agglomerates, the term *particles* is used. Particles can be viewed as small units that move as separate entities when the powder is dispersed by agitation and can consist of primary particles, agglomerates, or some combination of the two. Most particle size analysis techniques would refer to such particles.

3.2.1.4 Granules

The term *granules* refers to large agglomerates (~ 100 – $1000\ \mu\text{m}$ in size) that are deliberately formed by the addition of a granulating agent (e.g., a polymer-based binder) to the powder, followed by tumbling or spray drying. These large, nearly spherical agglomerates improve the flowability of the powder during filling and compaction in die pressing.

3.2.1.5 Flocs

Flocs are clusters of particles in a liquid suspension. The particles are held together weakly by electrostatic forces or by organic polymers and can be redispersed by appropriate modification of the interfacial forces through alteration of the solution chemistry. The formation of flocs is undesirable because it decreases the packing homogeneity of the consolidated body.

3.2.1.6 Colloids

A *colloid* is any system consisting of a finely divided phase in a fluid. A colloidal suspension (or sol) consists of fine particles dispersed in a liquid. The particles, referred to as *colloidal particles*, undergo Brownian motion and have a slow (often negligible) sedimentation rate under normal gravity. The size range for colloidal particles is approximately 1 nm to $1\ \mu\text{m}$.

3.2.1.7 Aggregates

An *aggregate* is a coarse constituent in a mixture, which usually also contains a fine constituent called the *bond*. Pebbles in concrete are an example, with the fine cement particles forming the bond.

The approximate size ranges of the types of particles considered above are summarized in Table 3.2.

3.2.2 Particle Size and Particle Size Distribution

We have seen from Chapter 2 that ceramic powders generally consist of particles of different sizes distributed over a certain range. Some powders may have a very narrow distribution of sizes (e.g., those prepared by chemical precipitation under controlled conditions), whereas for others the distribution in sizes may be

TABLE 3.2 Size Range for Particles in Ceramic Processing

Type of particle	Size range
Powder	
Colloidal particle	1 nm–1 μm
Coarse particle	1 μm –100 μm
Granule	100 μm –1 mm
Aggregate	>1 mm

very broad (e.g., an unclassified powder prepared by milling). Some particles are spherical or equiaxial (i.e., with the same length in each direction), but many are irregular in shape. Often we are required to characterize the particle size and particle size distribution of the powder because as discussed earlier, these two characteristics (along with the particle shape) have a key effect on the consolidation and sintering of the powders.

3.2.2.1 Definition of Particle Size

For a spherical particle, the diameter is taken as the size. However, the size of an irregularly shaped particle is a rather uncertain quantity. We therefore need to define what the “particle size” represents. One simple definition of the size of an irregularly shaped particle is the diameter of the sphere having the same volume as the particle. This is not much help because in many cases the volume of the particle is ill-defined or difficult to measure. Usually, the particle size is defined in a fairly arbitrary manner in terms of a number generated by one of the measuring techniques described later. A particle size measured by one technique may therefore be quite different from that measured by another technique, even when the measuring instruments are operating properly.

If an irregularly shaped particle is allowed to settle in a liquid, its terminal velocity may be compared with that for a sphere of the same density settling under similar conditions. For laminar flow, the sphere diameter can be calculated from Stokes law and is commonly referred to as the *Stokes diameter*. Using a microscope, individual particles are observed and measured. In this case, the particle size is commonly determined from the projected area of the particles (*projected area diameter*) or a linear dimension measured parallel to some fixed direction (*Feret’s diameter* or *Martin’s diameter*). Some definitions of particle size are given in Table 3.3.

3.2.2.2 Average Particle Size

Bearing in mind the uncertainty in defining the size of an irregularly shaped particle, we will now attempt to describe the average particle size of the powder.

TABLE 3.3 Some Definitions of Particle Size

Symbol	Name	Definition
x_S	Surface diameter	Diameter of a sphere having the same surface area as the particle
x_V	Volume diameter	Diameter of a sphere having the same volume as the particle
x_{SV}	Surface volume diameter	Diameter of a sphere having the same surface area to volume ratio as the particle
x_{STK}	Stokes diameter (or equivalent spherical diameter)	Diameter of a sphere having the same sedimentation rate as the particle for laminar flow in a liquid
x_{PA}	Projected area diameter	Diameter of a circle having the same area as the projected area of the particle
x_C	Perimeter diameter	Diameter of a circle having the same perimeter as the projected outline of the particle
x_A	Sieve diameter	Width of the minimum square aperture through which the particle will pass
x_F	Feret's diameter	Mean value of the distance between pairs of parallel tangents to the projected outline of the particle
x_M	Martin's diameter	Mean chord length of the projected outline of the particle

As a start, let us assume that the powder consists of N particles with sizes $x_1, x_2, x_3, \dots, x_N$, respectively. We can calculate a mean size \bar{x} and the standard deviation in the mean s according to the equations:

$$\bar{x} = \sum_{i=1}^N \frac{x_i}{N} \quad (3.1)$$

$$s = \left(\sum_{i=1}^N \frac{(x_i - \bar{x})^2}{N} \right)^{1/2} \quad (3.2)$$

The value of \bar{x} is taken as the particle size of the powder, and s gives a measure of the spread in the particle size distribution. In a random (Gaussian) distribution, approximately two out of every three particles will have their sizes in the range of $\bar{x} \pm s$.

Most likely the characterization technique will sort the particles into a small number n of size categories, where n is much smaller than N . The technique may

also produce a count of the number of particles within each category, so that there would be n_1 particles in a size category centered about x_1 , n_2 of size x_2 , etc., and n_n of size x_n . Alternatively, the mass or the volume of particles within each size category may be obtained. We will consider the number of particles within a size category giving rise to a *number-weighted* average; the representation of the data in terms of the mass or volume of particles within a size category will follow along similar lines. The mean size and the standard deviation can be determined from the data according to the equations:

$$\bar{x}_N = \frac{\sum_{i=1}^n n_i x_i}{\sum_{i=1}^n n_i} \quad (3.3)$$

$$s = \left(\frac{\sum_{i=1}^n n_i (x_i - \bar{x})^2}{\sum_{i=1}^n n_i} \right)^{1/2} \quad (3.4)$$

For comparison, the volume-weighted average size is

$$\bar{x}_V = \frac{\sum_{i=1}^n v_i x_i}{\sum_{i=1}^n v_i} = \frac{\sum_{i=1}^n n_i x_i^4}{\sum_{i=1}^n n_i x_i^3} \quad (3.5)$$

The reader will recognize that the mean particle size determined from Eq. (3.3) is the arithmetic mean. This is not the only mean size that can be defined, but it is the most significant when the particle size distribution is normal. The geometric mean \bar{x}_g is the n th root of the product of the diameter of the n particles and is given by

$$\log \bar{x}_g = \frac{\sum_{i=1}^n n_i \log x_i}{\sum_{i=1}^n n_i} \quad (3.6)$$

It is of particular value when the distribution is lognormal. The harmonic mean, \bar{x}_h is the number of particles divided by the sum of the reciprocals of the diameters of the individual particles:

$$\bar{x}_h = \frac{\sum_{i=1}^n n_i}{\sum_{i=1}^n \frac{n_i}{x_i}} \quad (3.7)$$

It is related to the specific surface area and is of importance when the surface area of the sample is concerned.

The mean particle size determined from Eq. (3.3) is sometimes referred to as the *linear mean diameter* and denoted as \bar{x}_{NL} when it is required to distinguish it from the surface mean diameter, \bar{x}_{NS} , and the volume mean diameter \bar{x}_{NV} . The surface and volume mean diameters are defined by

$$\bar{x}_{NS} = \frac{\left(\sum_{i=1}^n n_i x_i^2 \right)^{1/2}}{\sum_{i=1}^n n_i} \quad (3.8)$$

$$\bar{x}_{NV} = \frac{\left(\sum_{i=1}^n n_i x_i^3 \right)^{1/3}}{\sum_{i=1}^n n_i} \quad (3.9)$$

3.2.2.3 Representation of Particle Size Data

A simple and widely used way to describe the data is in terms of a histogram. A rectangle is constructed over each interval, with the height of the rectangle being proportional to the percent or fraction of particles within a size interval. Using the data given in Table 3.4, a histogram is shown in Fig. 3.2. A variation of this representation is to construct the rectangles of the histogram such that their areas are proportional to the number of particles in the intervals. The total area under the histogram is equal to the number of particles counted. To aid the comparison of histograms for different powders, it is useful to reduce this number to 100 by making the areas of the rectangles equal to the percentages of the particles in the intervals.

It is commonly more useful to plot the data as a cumulative size distribution by summing the percent (or fraction) of particles finer than a given size, defined as the *cumulative number percent finer* (CNPF), or larger than a given size, defined as the *cumulative number percent larger* (CNPL). Using the data in Table 3.4, the CNPF is also shown in Fig. 3.2, where a smooth curve is drawn through the data points.

TABLE 3.4 Particle Size Distribution Data

Size range	Number in size range, n_i	Size, x_i (μm)	Number fraction	CNPF ^a	$q_N(x)$ ^b ($1/\mu\text{m}$)
<10	35	5	0.005	0.5	0.001
10–12	48	11	0.007	1.2	0.003
12–14	64	13	0.009	2.1	0.004
14–16	84	15	0.012	3.3	0.005
16–18	106	17	0.015	4.8	0.007
18–20	132	19	0.019	6.7	0.009
20–25	468	22.5	0.067	13.4	0.012
25–30	672	27.5	0.096	23.0	0.019
30–35	863	32.5	0.124	35.4	0.025
35–40	981	37.5	0.141	49.5	0.028
40–45	980	42.5	0.141	63.6	0.028
45–50	865	47.5	0.124	76.0	0.025
50–55	675	52.5	0.097	85.7	0.020
55–60	465	57.5	0.067	92.4	0.006
60–70	420	65	0.060	98.4	0.006
70–80	93	75	0.013	99.7	0.001
80–90	13	85	0.002	99.9	0.001
90–100	1	95	0	99.9	—
>100	4	—	0.001	100	—

^a CNPF = cumulative number percent finer.^b $\bar{x}_N = 40 \mu\text{m}$ [Eq. (3.3)]; $s = 14 \mu\text{m}$ [Eq. (3.4)].

Source: Ref. 5.

In many cases it is necessary to provide a more complete description of the particle size data in terms of a mathematical equation, the parameters of which can be used to compare different powders. If the number of particles were fairly large and the size intervals Δx were small enough, then we would be able to fit a reasonably smooth curve through the particle size distribution data. Normally, the cumulative size distribution data is used as the starting point (rather than the histogram) and a smooth curve is fitted through the data. We are now assuming that the cumulative size distribution is some smoothly varying function of x , which we denote as $Q_N(x)$. The fractional size distribution function, $q_N(x)$, is then obtained from $Q_N(x)$ by taking the derivative:

$$q_N(x) = \frac{d}{dx} Q_N(x) \quad (3.10)$$

where $q_N(x) dx$ is the fraction of particles with sizes between x and $x + dx$.

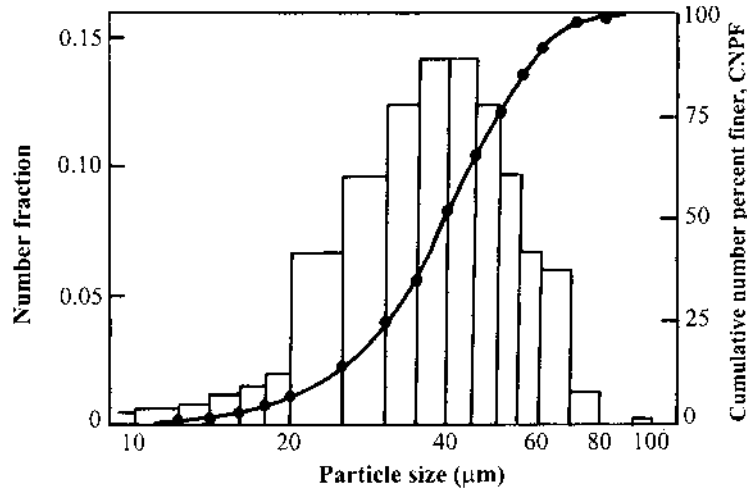


FIGURE 3.2 Particle size distribution data of Table 3.4 represented in terms of a histogram and the cumulative number percent finer (CNPF) than a given size.

The function $q_N(x)$ represents the measured size distribution, and this is used for the description of the data in terms of a mathematical equation. Figure 3.3 shows the measured size distribution determined from the data plotted in Fig. 3.2. Usually, the measured size distribution is fitted in terms of an expected size distribution, such as the normal distribution:

$$q_N(x) = \frac{1}{s\sqrt{2\pi}} \exp \left[-\frac{(x - \bar{x})^2}{2s^2} \right] \quad (3.11)$$

where \bar{x} is the mean particle size and s is the standard deviation in the mean particle size. In practice, the values of \bar{x} and s are adjusted in a curve-fitting routine until the best fit to the data is obtained. Since we are assuming the data are smoothly varying functions, the mean size and standard deviation must now be defined in terms of equations appropriate to the normal distribution:

$$\bar{x} = \frac{\int_{-\infty}^{\infty} x q_N(x) dx}{\int_{-\infty}^{\infty} q_N(x) dx} \quad (3.12)$$

$$s = \left[\frac{\int_{-\infty}^{\infty} q_N(x) (x - \bar{x})^2 dx}{\int_{-\infty}^{\infty} q_N(x) dx} \right]^{1/2} \quad (3.13)$$

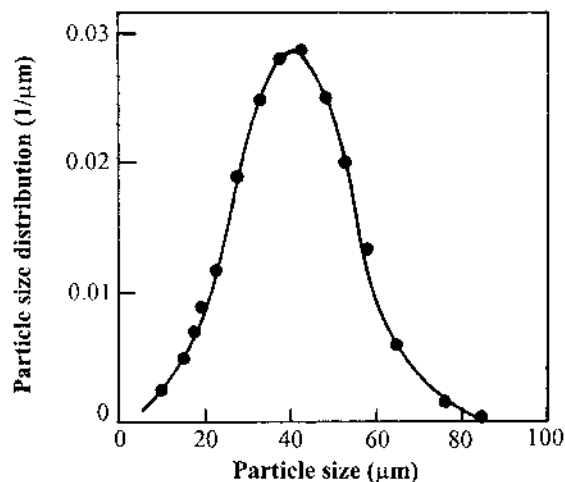


FIGURE 3.3 Particle size distribution data of Fig. 3.2 fitted to a smooth curve.

A serious problem with the normal distribution is that it predicts a finite fraction of particles with sizes less than zero. Furthermore, the largest particle size does not have a limit and is infinite. Therefore, the normal distribution seldom gives a good fit to real particle size data.

A better equation that has been found to give a good approximation to the size distribution of powders prepared by spray drying or by mechanical milling is the lognormal distribution:

$$q_N(\ln x) = \frac{1}{s\sqrt{2\pi}} \exp \left[-\frac{(\ln x - \bar{x})^2}{2s^2} \right] \quad (3.14)$$

where \bar{x} is now the mean of the natural logarithm of the particle sizes and s is the standard deviation of the natural logarithm of the particle sizes. Unlike the normal distribution, the lognormal distribution accounts for particle sizes greater than zero; however the largest size is still unlimited.

An empirical function that has been observed to describe the particle size distribution of milled powders is the Rosin–Rammler equation. The equation has undergone a number of modifications; one form is

$$Q_M(x) = \alpha b x^{\alpha-1} \exp(-bx^\alpha) \quad (3.15)$$

where $Q_M(x)$ is the mass fraction of particles with sizes between x and $x + dx$, and α and b are empirical constants for the powder being analyzed. The value

of α is typically found to be between 0.4 and 1.0. Another empirical distribution function that has been used to describe the size distribution of milled powders is the Gates–Gaudin–Schuhman equation:

$$Q_M(x) = \alpha \frac{x^{\alpha-1}}{x_{\max}^{\alpha}} \quad (3.16)$$

where x_{\max} is the maximum particle size and α is an empirical constant for the powder. Unlike the lognormal distribution, both the Rosin–Rammler and Gates–Gaudin–Schuhman equations have a finite size for the largest particle.

3.2.3 Particle Shape

Particle shape influences the flow properties and packing of powders as well as their interaction with fluids (e.g., viscosity of a suspension). Qualitative terms are sometimes used to give an indication of the nature of particle shape (e.g., spherical, equiaxial, acicular, angular, fibrous, dendritic, and flaky). However, except for the fairly simple geometries such as a sphere, cube, or cylinder, the quantitative characterization of particle shape can be fairly complex. The shape of a particle is commonly described in terms of a *shape factor*, which provides some measure of the deviation from an idealized geometry, such as a sphere or a cube. For elongated particles, the most common way of representing the shape is in terms of the *aspect ratio*, defined as the ratio of the longest dimension to the shortest dimension. For powders, the sphere is used as a reference, and the shape factor is defined as:

$$\text{Shape factor} = \frac{1}{\psi} = \frac{\text{surface area of the particle}}{\text{surface area of a sphere with the same volume}} \quad (3.17)$$

where ψ is referred to as the *sphericity*. According to Eq. (3.17), the shape factor of a sphere is unity, and the shape factor for all other shapes is greater than unity [e.g., $(6/\pi)^{1/3}$ or 1.24 for a cube]. Unfortunately, the use of a shape factor (or sphericity) is ambiguous; radically different shapes can have the same shape factor.

Shape *coefficients* have also been used to characterize particle shape. They relate the measured size, x , determined by one of the techniques described later, and the measured particle surface area A or volume V :

$$A = \alpha_A x^2 \quad (3.18a)$$

$$V = \alpha_V x^3 \quad (3.18b)$$

where α_A is the area shape coefficient and α_V is the volume shape coefficient. According to this definition, the area and volume shape coefficients for the sphere

are π and $\pi/6$, respectively, whereas for the cube, the area and volume shape coefficients are 6 and 1, respectively.

Because of its complexity, a detailed quantification of the shapes of irregularly shaped particles may not provide significant practical benefits. The trend in ceramic processing is toward increasing use of spherical or equiaxial particles because they produce better packing homogeneity in the consolidated body. The use of these spherical or equiaxial particles combined with the direct measurement of the surface area of the particles provides a far more effective approach.

3.2.4 Measurement of Particle Size and Size Distribution

Excellent accounts of the principles and practice of particle size measurement are given in Refs. 3 and 4. Table 3.5 shows the common methods used for the measurement of particle size and particle size distribution, together with their approximate size range of applicability. The main features of these methods are described below.

3.2.4.1 Microscopy

Microscopy is a fairly straightforward technique that offers the advantage of direct measurement of the particle size coupled with simultaneous observation of the individual particles, their shape, and the extent of agglomeration. It usually forms the first step in the characterization of ceramic powders. Optical microscopes can be used for particle sizes down to $\sim 1 \mu\text{m}$, while electron microscopes

TABLE 3.5 Common Methods for the Measurement of Particle Size and Their Approximate Range of Applicability

Method	Range (μm)
Microscopy	
Optical	> 1
Scanning electron	> 0.1
Transmission electron	> 0.001
Sieving	20–10000
Sedimentation	0.1–100
Coulter counter	0.5–400
Light scattering	
Scattering intensity	0.1–1000
Brownian motion	0.005–1
X-ray line broadening	< 0.1

can extend the range down to ~ 1 nm. Commonly, the sample is prepared by adding a small amount of the powder to a liquid to produce a dilute suspension. After suitable agitation (e.g., with an ultrasonic probe), a drop of the suspension is placed on a glass slide or a microscope stub. Evaporation of the liquid leaves a deposit that is viewed in the microscope. Good separation of the particles must be achieved. Because of the small amount of powder used in the measurements, care must also be taken to ensure that the deposit is representative of the original powder batch.

Particle size measurements are usually made from micrographs. The method is extremely tedious if it is done manually. Automatic image analysis of micrographs or an electronic display can reduce the amount of work considerably. Normally a large number of particles (a few hundred) need to be measured. As would be apparent, microscopy produces a particle size distribution based on the number of particles within an appropriate size range.

The image of a particle seen in a microscope (or micrograph) is two-dimensional and from this image an estimate of the particle size has to be made. Some of the more common measurements of the size are the following (Fig. 3.4):

1. Martin's diameter (x_M) is the length of a line that bisects the area of the particle image. The line can be drawn in any direction but the same direction must be maintained for all of the measurements.
2. Feret's diameter (x_F) is the distance between two tangents on opposite sides of the particle, parallel to some fixed direction.

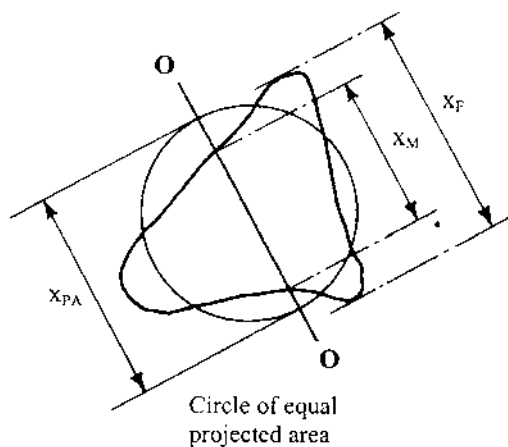


FIGURE 3.4 Representative two-dimensional diameters of particles observed in a microscope.

3. The projected area diameter (x_{PA}) is the diameter of a circle having the same area as the two-dimensional image of the particle.
4. The perimeter diameter (x_C) is the diameter of the circle having the same circumference as the perimeter of the particle.
5. The longest dimension is equal to the maximum value of Feret's diameter.

3.2.4.2 Sieving

The use of sieves for separating particles into fractions with various size ranges is the oldest and one of the most widely used classification methods. The particles are classified in terms of their ability or inability to pass through an aperture with a controlled size. Sieves with openings between approximately 20 μm and 10 mm are constructed with wire mesh and are identified in terms of a mesh size and a corresponding aperture size. The wire mesh has square apertures, the size of which depends on the number of wires per linear dimension and the diameter of the wire. The mesh size is equal to the number of wires per linear inch of the sieve screen, which is the same as the number of square apertures per inch (Fig. 3.5). The mesh number M , aperture width a , wire diameter w , and the open area A are related by the following equations:

$$M = \frac{1}{a + w} \quad (3.19a)$$

$$a = \frac{1}{M} - w \quad (3.19b)$$

$$A = \frac{a^2}{(a + w)^2} = (Ma)^2 \quad (3.19c)$$

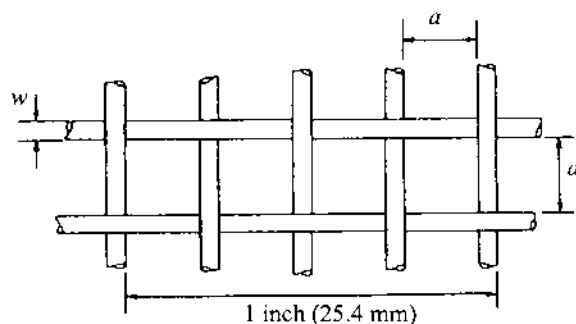


FIGURE 3.5 Dimensions of woven wire cloth in sieves.

For example, a 400 mesh sieve with an aperture of $38\text{ }\mu\text{m}$ has a wire diameter of $25.5\text{ }\mu\text{m}$ and an open area of 36%. The use of special metal sieves can extend the range of sieving to $5\text{ }\mu\text{m}$ or lower, while punched plate sieves can extend the upper range to $\sim 125\text{ mm}$.

Summaries of sieve apertures according to the American standard (ASTM E 11–87) and the British standard (BS 410) are given in the Appendix. The American standard apertures are in the progression of $\sqrt[4]{2}$. Originally the apertures were determined taking $75\text{ }\mu\text{m}$ as the reference value, but the current international standard (ISO) uses $45\text{ }\mu\text{m}$ as the reference value.

Sieving may be carried out in the dry or wet state by hand or by a machine. However, most sieving is done in the dry state on a machine designed to impart the necessary shaking, rotating, or vibrating motion to the material on the screens. Several sieves are stacked together, with the coarsest mesh aperture at the top and the smallest at the bottom and with the powder placed on the top sieve. A closed pan is placed at the bottom of the stack to collect the fines, and a lid is placed on the top sieve to prevent loss of material. A stack commonly consists of four to six sieves arranged in a $\sqrt{2}$ progression of sizes. The stack is vibrated for a fixed time, and the residual mass of powder on each sieve is measured. For routine classification, sieving is commonly carried out for 20 to 30 min. Reference should be made to the American or British standard for a complete description of the procedure. Agglomeration of the powder and clogging of the screens during sieving of a dry powder can lead to significant problems below $\sim 40\text{ }\mu\text{m}$. The use of pulsed jets of air to reduce clogging or wet sieving in which the particles are dispersed in a liquid can alleviate the problems. Wet sieving is also required when the powder to be tested is already suspended in a liquid.

Adequate separation of the particles into their true size fractions requires a fairly long time. Since it is normally too time-consuming to sieve for such a long time, the particle size distribution, obtained from most sieving operations is only approximate. However, this approximate size characterization can be quite useful for the selection or verification of raw materials in the traditional ceramic industry. The various fractions produced by sieving are weighed so that a particle distribution based on mass is obtained. For elongated particles, the method generally favors measurement of the longer particle dimension. Sieving is not feasible for powders of advanced ceramics, where the particle size is normally less than $1\text{ }\mu\text{m}$. Furthermore, it should not be used for clean powders because of the expected contamination with metallic impurities from the sieves.

3.2.4.3 Sedimentation

A spherical particle falling in a viscous liquid with a sufficiently small velocity soon reaches a constant velocity called the *terminal velocity*, where the effective weight of the particle is balanced by the frictional force exerted on it by the liquid. The frictional force F on the particle is given by Stokes law:

$$F = 6\pi\eta av \quad (3.20)$$

where η is the viscosity of the liquid, a is the radius of the particle, and v is the terminal velocity. Equating F to the effective weight of the particle gives

$$x = \left[\frac{18\eta v}{(d_s - d_L)g} \right]^{1/2} \quad (3.21)$$

where x is the diameter of the sphere, g is the acceleration due to gravity, and d_s and d_L are the densities of the particle and the liquid, respectively. Equation (3.21) is normally referred to as *Stokes equation*, which is not to be confused with Stokes law [Eq. (3.20)]. Measurement of the sedimentation rate can therefore be used to determine the sphere diameter from Stokes equation. When particle shapes other than spheres are tested, the measured particle size is referred to as the *Stokes diameter* x_{STK} , or the equivalent spherical diameter.

Determination of particle size from Eq. (3.21) has a limited range of validity. Stokes law is valid for laminar or streamline flow (i.e., where there is no turbulent flow) and assumes that there are no collisions or interactions between the particles. The transition from laminar to turbulent flow occurs at some critical velocity, v_c , given by

$$v_c = \frac{N_R \eta}{d_L x} \quad (3.22)$$

where N_R is a dimensionless number called the *Reynolds number*. The transition from laminar to turbulent flow occurs when its value is ~ 0.2 . Therefore,

$$\frac{v d_L x}{\eta} < 0.2 \quad \text{laminar flow} \quad (3.23a)$$

$$\frac{v d_L x}{\eta} > 0.2 \quad \text{turbulent flow} \quad (3.23b)$$

The maximum particle size for laminar flow can be found by substituting for v from Eq. (3.21) into Eq. (3.23). For Al_2O_3 particles dispersed in water at room temperature, $x_{\text{max}} \approx 100 \mu\text{m}$.

For sufficiently small particles undergoing sedimentation under gravity, Brownian motion resulting from collisions with the molecules of the liquid may displace the particle by a measurable amount. This effect puts a lower limit to the use of gravitational settling in water at $\sim 1 \mu\text{m}$. Faster settling can be achieved by centrifuging the suspension, thereby extending the size range down to $\sim 0.1 \mu\text{m}$.

In the sedimentation method, the powder may be introduced as a thin layer on top of a column of clear liquid (sometimes referred to a two-layer or line-start technique), or it may be uniformly dispersed in the liquid (the homogeneous suspension technique). The particle size distribution is determined by measuring the change in concentration (or density) of the suspension as a function of time, height along the suspension, or both. A light beam or an x-ray beam is projected at a known height through a glass cell containing the suspension and the intensity of the transmitted beam is measured by a photocell or an x-ray detector located at the opposite side. According to Eq. (3.21), particles with a larger velocity will settle first, followed by successively smaller particles. The intensity I of the transmitted beam will increase according to the equation:

$$I = I_o \exp(-KACy) \quad (3.24)$$

where I_o is the intensity of the incident beam, K is a constant called the extinction coefficient, A is the projected area per unit mass of particles, C is the concentration by mass of the particles, and y is the length of the light path through the suspension. The particle size distribution [e.g., the cumulative mass percent finer (CMPF) versus the Stokes diameter] is deconvoluted from the measured intensity ratio, I/I_o , coupled with Eq. (3.21).

3.2.4.4 Electrical Sensing Zone Techniques (the Coulter Counter)

In the Coulter counter, the number and size of particles suspended in an electrolyte are measured by causing them to flow through a narrow orifice on either side of which an electrode is immersed (Fig. 3.6). As a particle passes through the orifice, it displaces an equivalent volume of the electrolyte and causes a change in the electrical resistance, the magnitude of which is proportional to the volume of the particle. The changes in resistance are converted to voltage pulses, which are amplified, sized, and counted to produce data for the particle size distribution of the suspended particles. Since the number and volume of the particles are measured in this technique, the particle size distribution will consist of the CNPF (or CNPL) versus the volume diameter x_v .

The effect of particle shape on the data is subject to some doubt. While it has been claimed that particle shape, roughness, and the nature of the material have little effect on the analysis, there is considerable evidence that the measured size parameter corresponds to the overall envelope of the particle (3). The technique is suitable for dense particles with sizes in the range 1–100 μm , but with care and the use of multiple orifices, the range can be extended to 0.5–400 μm . It is most sensitive when the particle size is close to the diameter of the orifice. However, blocking of the orifice by larger particles can be a tedious problem.

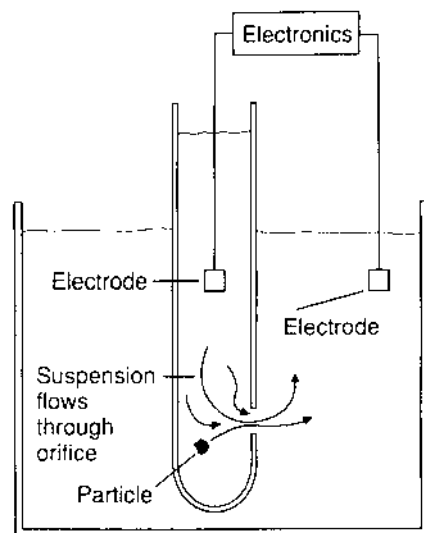


FIGURE 3.6 Electrical sensing zone apparatus (Coulter counter).

Originally applied to the counting of blood cells, the technique has become fairly popular for particle size analysis of ceramic powders.

3.2.4.5 Light Scattering

A light beam with an intensity I_o entering one end of a column of smoke will emerge from the other end with an intensity I that is less than I_o . However, most of the decrease in the intensity of I in this case is not due to absorption by the smoke particles (which represents an actual disappearance of light) but to the fact that some light is scattered to one side by the smoke particles and thus removed from the direct beam. A considerable intensity, I_s , of scattered light may easily be detected by observing the column from the side in a darkened room.

For a system of fine particles dispersed in a liquid or gas, measurement of I_s provides a versatile and powerful technique for determining particle size data. Large particles tend to reflect light back toward the source in much the same way as this page “backscatters” light towards the reader’s eyes. However, as the particle size is decreased towards the wavelength of the light, there is a greater tendency for the light to be scattered in the forward direction, i.e., at small angles to the direction of the incident beam (Fig. 3.7). Many instruments are based on measuring I_s of this forward-scattered light as a function of the scattering angle. The dependence of I_s on the size of the particles is governed by rigorous diffraction theory. Because of the complexity of the general theory, three limiting cases,

stated in terms of the ratio of the particle size x to the wavelength λ of the incident light, are commonly considered:

1. $x \ll \lambda$, Rayleigh scattering theory
2. $x \approx \lambda$, Mie theory
3. $x \gg \lambda$, Fraunhofer diffraction theory

The first quantitative study of scattering by small particles was made in 1871 by Rayleigh. The theory shows that I_s is proportional to the square of the volume of the particle. For larger particles ($x \gg \lambda$), Fraunhofer diffraction theory applies and the distribution of I_s is similar to that for diffraction from a single slit, where the size of the scattering particle takes the place of the slit width. In the Fraunhofer theory, I_s is proportional to the square of the slit width, so that for scattering from particles, I_s is proportional to the projected area of the particle. Based on diffraction theory, the scattering angle, θ , is inversely proportional to the particle size and is given by

$$\sin \theta \approx \frac{1.22\lambda}{x} \quad (3.25)$$

Smaller particles scatter a small amount of light, but according to Eq. (3.25), they scatter the light through a larger angle.

In recent years, because of the ready availability of the laser for providing an intense, monochromatic source of light (e.g., He-Ne laser emitting light with a wavelength of $0.63 \mu\text{m}$) and the reduced cost of computers for data analysis, light scattering has become an important technique for particle size measurement.

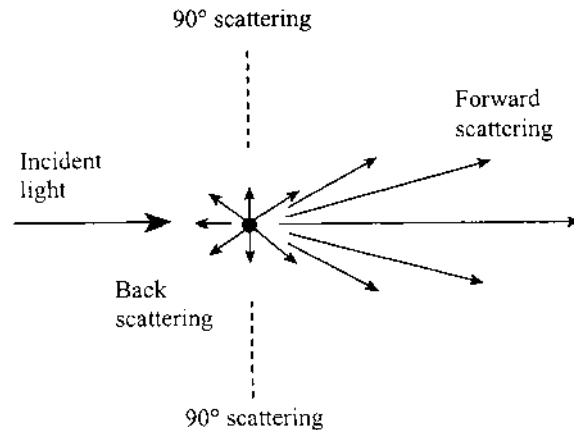


FIGURE 3.7 Illustration of forward scattering of light by small particles.

The powder can be analyzed in the dry state or, more commonly, as a dilute suspension. The measurements can be made accurately and fairly rapidly. For instruments based on the Fraunhofer diffraction theory, a reliable size range is $\sim 2\text{--}100\text{ }\mu\text{m}$. However, the use of special light collection systems and the Mie theory can extend the range to $\sim 0.1\text{--}1000\text{ }\mu\text{m}$.

Particles smaller than $\sim 1\text{ }\mu\text{m}$ display Brownian motion when dispersed in a liquid due to collisions with the molecules of the liquid. The motion increases with temperature (increase in momentum of the colliding molecules) and with a decrease in particle size (greater probability of the collision on one side of the particle not matching that on the other size and the enhanced response of a smaller particle to the unbalanced collision). Brownian motion leads to scattering of the incident light and to fluctuations in the average intensity. A light detector (often arranged at right angles to the incident light) records these fluctuations, and the data are used to determine particle size data based on the Stokes–Einstein equation:

$$a = \frac{kT}{3\pi\eta D} \quad (3.26)$$

where a is the radius of the particle (assumed spherical), k is the Boltzmann constant, T is the absolute temperature, η is the viscosity of the liquid, and D is the diffusion coefficient. This technique, sometimes referred to as dynamic light scattering or photo correlation spectroscopy, can be used for particle size measurements in the range of $\sim 5\text{ nm}$ to $\sim 1\text{ }\mu\text{m}$.

3.2.4.6 x-ray Line Broadening

The broadening of x-ray diffraction peaks provides a convenient method for measuring particle sizes below $\sim 0.1\text{ }\mu\text{m}$ (6-8). As the crystal size decreases, the width of the diffraction peak (or the size of the diffraction spot) increases. An approximate expression for the peak broadening is given by the Scherer equation:

$$x = \frac{C\lambda}{\beta \cos\theta} \quad (3.27)$$

where x is the crystal size, C is a numerical constant (~ 0.9), λ is the wavelength of the x-rays, β is the effective broadening as a full width at half maximum (FWHM) in radians, and θ is the diffraction angle for the peak. The effective broadening β is the measured broadening corrected for the broadening due to (1) the instrument and (2) residual stress in the material. Broadening due to the instrument is most accurately determined by using a single crystal with a calibrated broadening. Residual stress arises from cooling or heating the sample which can trap compressive or tensile stresses in the material due to inhomogene-

ous or anisotropic thermal expansion. Depending on the magnitude and sign of the stresses, a broadening of the peaks occurs which increases as $\tan \theta$. Since the broadening due to crystal size [Eq. (3.27)] varies as $1/(\cos \theta)$, the broadening due to residual stress can be separated. Computerized software available with most modern diffractometers allow for fairly rapid and accurate determination of the crystal size by the line broadening technique.

The reader may have noticed that we have used the term *crystal size* to describe the size obtained by x-ray line broadening. This is because the technique gives a measure of the size of the crystals regardless of whether the particles consist of single crystals, polycrystals, or agglomerates. If the primary particles consist of single crystals, then the crystal size determined by x-ray line broadening will be comparable to the particle size determined by other methods such as electron microscopy. For polycrystalline primary particles or agglomerates, it will be much smaller than the size determined by other methods.

3.2.5 Surface Area

The surface area of powders is important in its own right but can also be used to determine the average particle size when certain assumptions are made concerning the particle shape and the presence or absence of pores. Techniques for measuring the surface area are based on the phenomenon of gas adsorption (3,9). The term *adsorption*, in the present context refers to condensation of gases (*adsorbate*) on the free surfaces of the solid (*adsorbent*) and should be distinguished from *absorption*, where the gas molecules penetrate into the mass of the absorbing solid. Adsorption is commonly divided into two categories:

1. Physical adsorption in which the adsorption is brought about by physical forces between the solid and the gas molecules (similar in nature to the weak van der Waals forces that bring about condensation of a vapor to a liquid)
2. Chemical adsorption or chemisorption where the adsorbed gases will have developed strong chemical bonds with the surface

In the present section we are concerned with physical adsorption, the type of adsorption that is the basis for the common techniques for surface area measurement.

In the determination of the surface area, the amount of gas adsorbed by a fixed mass of solid at a fixed temperature is measured for different gas pressures p . Commonly, a known volume of gas is contacted with the powder, and the amount of gas adsorbed is determined from the fall in gas pressure by application of the gas laws. A graph of amount of gas adsorbed versus p (or p/p_o , if the gas is at a pressure below its saturation vapor pressure p_o), referred to as the *adsorption isotherm*, is plotted. In the literature, there are thousands of adsorption isotherms

measured for a wide variety of solids. However, the majority of these isotherms can be conveniently grouped into five classes (Fig. 3.8): Types I to V of the original classification proposed by Brunauer, et al. (10), referred to as the Brunauer, Emmett, and Teller (BET) classification (11) or simply the Brunauer classification (12). The Type VI isotherm, referred to as the *stepped isotherm*, is relatively rare but is of particular theoretical interest. The adsorption of gases by nonporous solids in the vast majority of cases gives rise to a Type II isotherm. From this isotherm, it is possible to determine a value for the monolayer capacity of the solid, defined as the amount of gas required to form a monolayer coverage on the surface of unit mass of the solid. From this monolayer capacity, the specific surface area of the solid can be calculated.

A kinetic model for adsorption was put forward almost a century ago by Langmuir (13) in which the surface of the solid was assumed to be an array of

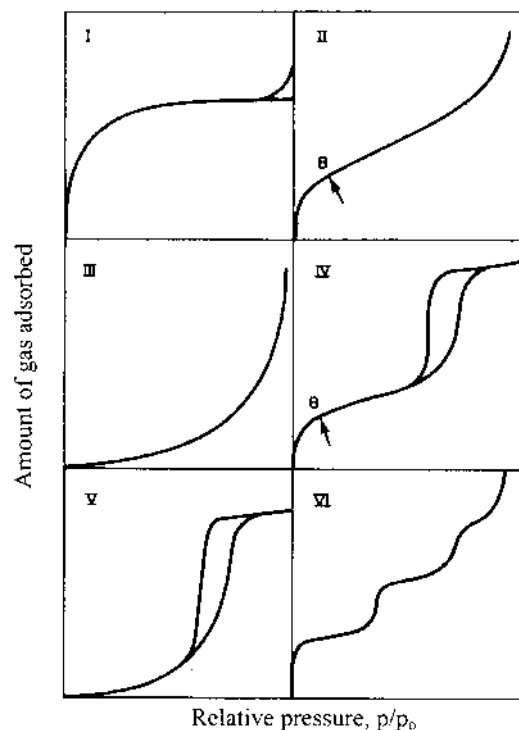


FIGURE 3.8 The five types of adsorption isotherms consisting of Types I to V of the original classification proposed by Brunauer et al. (10), together with Type VI, the stepped isotherm.

adsorption sites. He postulated a state of dynamic equilibrium in which the rate of condensation of gas molecules on the unoccupied surface sites is equal to the rate of evaporation of gas molecules from the occupied sites. The analysis leads to the equation:

$$\frac{V}{V_m} = \frac{bp}{1+bp} \quad (3.28)$$

where V is the volume of gas adsorbed per unit mass of solid at a gas pressure p , V_m is the volume of gas required to form one monolayer, and b is an empirical constant. Equation (3.28) is the familiar Langmuir adsorption equation for the case when adsorption is confined to a monolayer. It is more appropriate to Type I isotherms.

By adopting the Langmuir mechanism and introducing a number of simplifying assumptions, Brunauer et al. (11) were able to derive an equation to describe multilayer adsorption (Type II isotherm) which forms the basis for surface area measurement. The equation, commonly referred to as the BET equation, can be expressed in the form

$$\frac{p/p_o}{V(1-p/p_o)} = \frac{1}{V_m c} + \frac{c-1}{V_m c} \frac{p}{p_o} \quad (3.29)$$

where c is a constant and the other terms are as defined earlier. When applied to experimental data, a plot of the left-hand side of Eq. (3.29) versus p/p_o should yield a straight line with a slope s and an intercept i given by

$$s = \frac{c-1}{V_m c} \quad (3.30a)$$

$$i = \frac{1}{V_m c} \quad (3.30b)$$

The monolayer volume V_m can therefore be obtained from

$$V_m = \frac{1}{s+i} \quad (3.31)$$

We can now use V_m to calculate the specific surface area of the solid from:

$$S_w = \frac{N_A \sigma V_m}{V_o} \quad (3.32)$$

where the symbols, expressed in their most commonly used units, are defined as follows:

S_w = the specific surface area (m^2/g)
 N_A = the Avogadro number ($6.023 \times 10^{23} \text{ mol}^{-1}$)
 σ = area of an adsorbed gas molecule ($16.2 \times 10^{-20} \text{ m}^2$ for nitrogen)
 V_m = monolayer volume (in cm^3/g)
 V_o = the volume of 1 mol of the gas at STP ($22,400 \text{ cm}^3/\text{mol}$)

Substituting these values in Eq. (3.27) gives, for nitrogen adsorption,

$$S_w = 4.35V_m \quad (3.33)$$

Assuming that the powder is unagglomerated and that the particles are spherical and dense, the particle size can be estimated from the equation

$$x = \frac{6}{S_w d_s} \quad (3.34)$$

where d_s is the density of the solid.

The validity of the BET equation is commonly stated to extend over the range of relative pressures (p/p_o values) of ~ 0.05 and ~ 0.3 , but there are numerous examples where the BET plot departs from linearity at relative pressures below ~ 0.2 . Although several gases have been used as the adsorbate, the standard technique is the adsorption of nitrogen at the boiling point of liquid nitrogen (77K). The molecular area $\sigma = 16.2 \times 10^{-20} \text{ m}^2$ (16.2 \AA^2) has gained widespread acceptance for the determination of surface area from Type II isotherms. Argon ($\sigma = 16.6 \times 10^{-20} \text{ m}^2$) is a good alternative because it is chemically inert, it is composed of spherically symmetrical, monatomic molecules, and its adsorption is relatively easy to measure at the boiling point of liquid nitrogen. Nitrogen or argon works well for powders with a specific surface area greater than $\sim 1 \text{ m}^2/\text{g}$. For powders with lower surface areas, the use of krypton ($\sigma = 19.5 \times 10^{-20} \text{ m}^2$) at the boiling point of liquid nitrogen is recommended.

3.2.6 Porosity of Particles

Depending on the method used to synthesize them, many powders may consist of agglomerates of primary particles which are highly porous. Commonly, it is necessary to quantitatively characterize the porosity and pore size distribution of the agglomerates. For pores that are accessible (i.e., pores that are not completely isolated from the external surface), two methods have been used: gas adsorption (sometimes referred to as *capillary condensation*) and mercury intrusion porosimetry (referred to simply as *mercury porosimetry*). The characteristic pore feature of interest is the size, taken as the diameter, radius, or width. A classification of pores according to their size is given in Table 3.6. Although there is considerable overlap in the range of applicability, gas condensation is applicable to pore

size measurement in the mesopore range, while mercury porosimetry is better applied to the macropore range.

3.2.6.1 Gas Adsorption

At lower gas pressures, ($p/p_o < \sim 0.3$), the adsorbed gas produces multilayer coverage of the solid surface, and as described earlier, this forms the basis for the BET method. At higher pressures, the gas may condense to a liquid in the capillaries of a porous solid and this condensation can be used to determine the pore size and pore size distribution. When condensation occurs, the isotherm (Fig. 3.9) is commonly found to possess a hysteresis loop between the adsorption and the desorption branches, which is characteristic of Type IV isotherms.

Assuming cylindrical capillaries with a radius r , the relative gas pressure in the capillaries when condensation occurs is governed by the Kelvin equation:

$$\ln \frac{p}{p_o} = \frac{-2\gamma_{LV}V_L \cos \theta}{RT r} \quad (3.35)$$

where p is the gas pressure over a meniscus with radius r , p_o is the saturation gas pressure of the liquid having a plane surface, γ_{LV} is the surface tension of the liquid–vapor interface, V_L is the molar volume of the liquid, θ is the contact angle between the liquid and the pore wall, R is the gas constant and T is the absolute temperature. From the Kelvin equation it follows that the vapor pressure p over a *concave* meniscus must be less than p_o . Consequently, capillary condensation of a vapor to a liquid should occur within a pore at some pressure p determined by the radius r for the pore and less than p_o .

The determination of the pore size distribution by application of the Kelvin equation to the capillary condensation part of the Type IV isotherms is almost entirely restricted to the use of nitrogen as the adsorbing gas. This is largely a reflection of the widespread use of nitrogen for surface area measurements so that both surface area and pore size distribution can be obtained from the same isotherm. If the volume of gas adsorbed on the external surface of the solid is

TABLE 3.6 Classification of Pores
According to Their Size (Diameter or Width)

Category	Pore Size (nm)
Micropores	<2
Mesopores	2–50
Macropores	>50

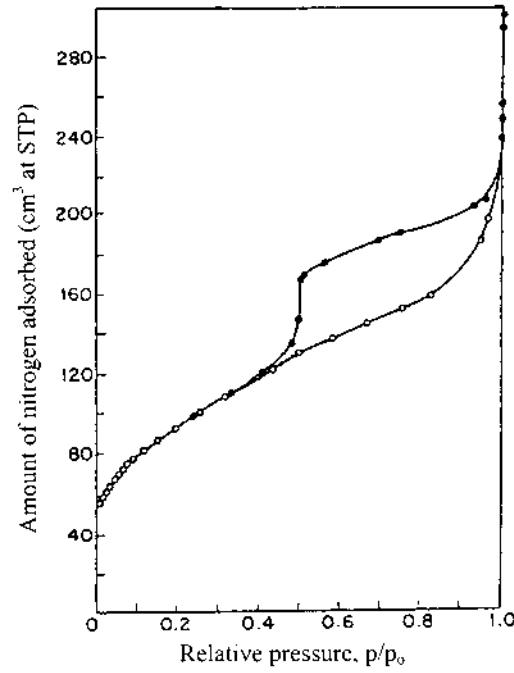


FIGURE 3.9 Nitrogen adsorption (open circles) and the desorption data (filled circles) used in the determination of pore size distribution. (From Ref. 3.)

small compared to that adsorbed in the pores, then the volume of gas adsorbed V_g , when converted to a liquid (condensed) volume V_c , gives the pore volume. The relationship between V_g and V_c is

$$V_c = \frac{M_w V_g}{\rho_L V_o} \quad (3.36)$$

where M_w is the molecular weight of the adsorbate, ρ_L is the density of the liquefied gas at its saturated vapor pressure, and V_o is the molar gas volume at STP ($22,400 \text{ cm}^3$). For nitrogen: $M_w = 28 \text{ g}$ and $\rho_L = 0.808 \text{ g/cm}^3$, so that

$$V_c = 1.547 \times 10^{-3} V_g \quad (3.37)$$

For nitrogen adsorption at the boiling point of liquid nitrogen (77K), $\gamma_{LV} = 8.72 \times 10^{-3} \text{ N/m}$, $V_L = 34.68 \times 10^{-6} \text{ m}^3$, and θ is assumed to be zero, so that Eq. (3.35) becomes

$$r = \frac{-4.05 \times 10^{-1}}{\log(p/p_o)} \text{ nm} \quad (3.38)$$

Typical values for p/p_o are in the range 0.5–0.95; so the gas adsorption is appropriate to pore radius values in the range of ~ 1 –20 nm.

For any relative pressure p/p_o on the isotherm, V_{ci} gives the cumulative volume of the pores having pore radius values up to and equal to r_i , where V_{ci} and r_i are determined from Eqs. (3.37) and (3.38), respectively. The pore size distribution curve, $v(r)$, versus r is obtained by differentiating the cumulative pore volume curve with respect to r [i.e., $v(r) = dV_c/dr$]. This analysis does not take into account that when capillary condensation occurs, the pore walls are already covered with an adsorbed layer of gas. Thus the capillary condensation occurs not directly in the pore itself but in the inner core. The calculated values for the pore size are therefore appropriate to the inner core.

As outlined earlier, a characteristic feature of Type IV isotherms is its hysteresis loop. The exact shape of the loop varies from one adsorption system to another, but as seen from Fig. 3.9, at any given relative pressure, the amount adsorbed is always greater along the desorption branch than along the adsorption branch. Ink-bottle pores, consisting of a cylindrical pore closed at one end and with a narrow neck at the other end (Fig. 3.10a), have played a prominent role in the explanation of the hysteresis. It is easily shown that the adsorption branch of the loop corresponds to values of the pore radius of the body and the desorption branch corresponds to values of the pore radius of the neck. The representation of a pore as narrow-necked bottle is overspecialized, and in practice a series of interconnected pore spaces (Fig. 3.10b) rather than discrete bottles is more likely.

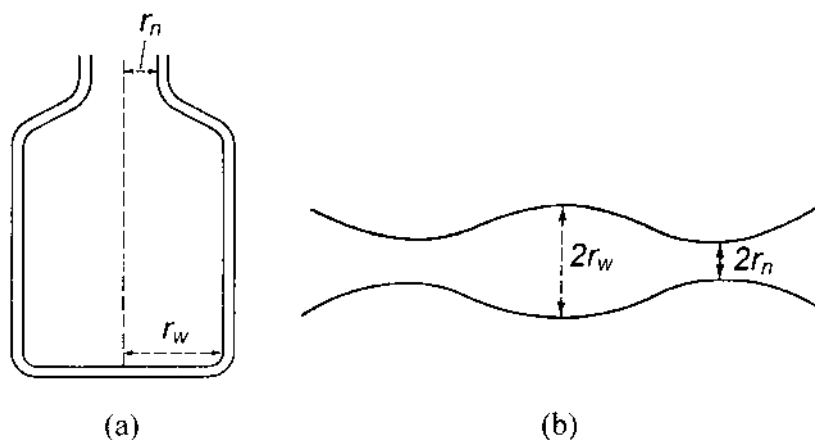


FIGURE 3.10 (a) Ink-bottle pores associated with hysteresis in capillary condensation, and (b) more practical interconnected pore spaces.

3.2.6.2 Mercury Porosimetry

In ceramics, mercury porosimetry is more widely used than gas adsorption because pore sizes in the macropore range are more common. The technique is based on the phenomenon of capillary rise (Fig. 3.11). A liquid that wets the walls of a narrow capillary (contact angle, $\theta < 90^\circ$) will climb up the walls of the capillary. However, the level of a liquid that does not wet the walls of a capillary ($\theta > 90^\circ$) will be depressed. For a nonwetting liquid, a pressure must be applied to force the liquid to flow up the capillary to the level of the reservoir. For a capillary with principal radii of curvature r_1 and r_2 in two orthogonal directions, this pressure is given by the equation of Young and Laplace:

$$p = -\gamma_{LV} \left(\frac{1}{r_1} + \frac{1}{r_2} \right) \cos \theta \quad (3.39)$$

where γ_{LV} is the surface tension of the liquid–vapor interface. For a cylindrical capillary of radius r , Eq. (3.39) becomes

$$p = \frac{-2\gamma_{LV} \cos \theta}{r} \quad (3.40)$$

For mercury, depending on its purity and the type of sample surface, γ_{LV} and θ vary slightly. The average values found in the literature are $\gamma_{LV} = 0.480$ N/m and $\theta = 140^\circ$. Then for p in units of megapascals (MPa) and r in micrometers (μm), Eq. (3.40) becomes

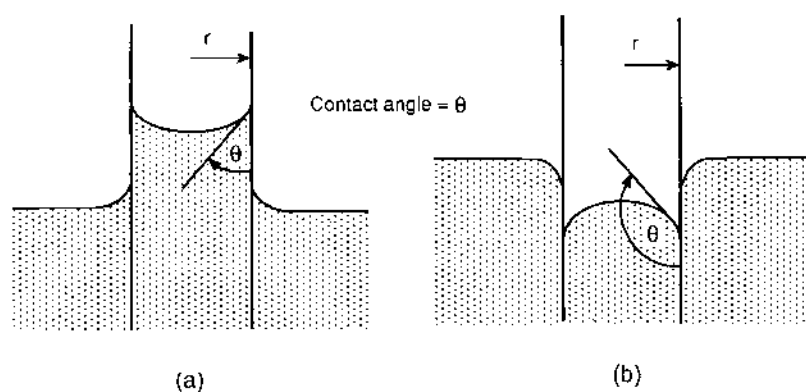


FIGURE 3.11 Capillary rise phenomena for (a) a wetting liquid (contact angle $< 90^\circ$) and (b) a nonwetting liquid (contact angle $> 90^\circ$).

$$r = \frac{0.735}{p} \quad (3.41)$$

In mercury porosimetry, a sample holder is partially filled with the powder, evacuated, and then filled with mercury. The volume of mercury intruded into the sample, V_m , is measured as a function of the applied pressure p . An example of this type of data is shown in Fig. 3.12. Assuming that the pores are cylindrical, the value V_{mi} at any value of the applied pressure p_i gives the cumulative volume of all pores having a radius *equal to or greater than* r_i . This designation is the converse of that in gas adsorption where the cumulative pore volume is the volume of the pores having a radius *less than or equal to* r_i . Thus in mercury porosimetry, the cumulative pore volume decreases as r increases (Fig. 3.13), while in gas adsorption the cumulative pore volume increases as r increases. In both techniques, however, the pore size distribution $v(r)$ is obtained by differentiating the cumulative pore volume curve with respect to r . The pore size distribution can also be obtained directly from the data for V_m versus p (Fig. 3.12) using

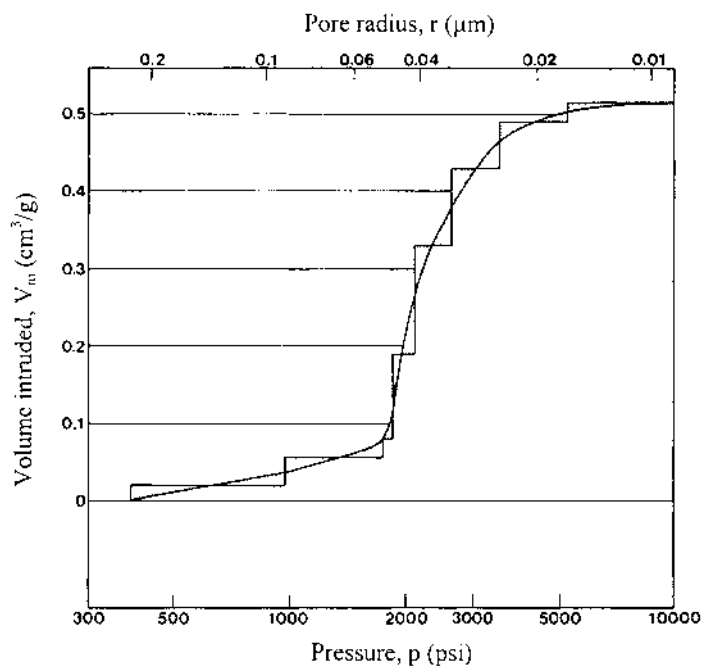


FIGURE 3.12 Mercury porosimetry data showing the intruded volume V_m versus pressure. (From Ref. 3.)

$$v(r) = \frac{dV_m}{dp} \frac{p}{r} \quad (3.42)$$

The pressures available in mercury porosimeters are such that pore sizes in the range of ~ 5 nm to $200 \mu\text{m}$ can be measured, but the technique becomes increasingly uncertain as the lower end of the range is approached. It should be remembered that Eq. (3.40) assumes that the pores are circular in cross section, which is hardly the case in practice. Furthermore, for ink-bottle pores (Fig. 3.10) or pores with constricted necks opening to large volumes, the use of Eq. (3.40) gives a measure of the neck size which is not truly indicative of the actual pore size. These types of pores can also give rise to hysteresis because they fill at a pressure characteristic of the neck size but they empty at a pressure characteristic of the larger volume of the pore. Finally, the compressibilities of the mercury and of the porous sample are assumed to be independent of the applied pressure, which may not be the case at the lower end of the pore size range involving fairly high pressures.

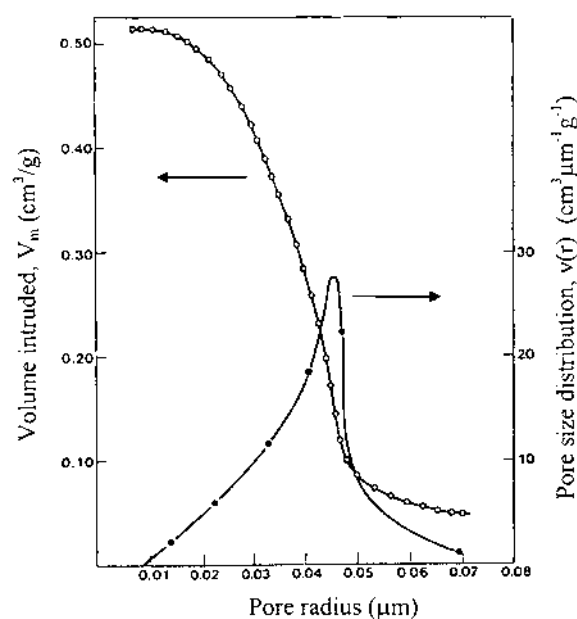


FIGURE 3.13 Mercury porosimetry data of Fig. 3.12 replotted to show the intruded volume V_m (open circles) and the pore size distribution $v(r)$ (filled circles) versus pore radius r . (From Ref. 3.)

3.2.6.3 Pycnometry

Pycnometry can be used to determine the isolated porosity in particles. In practice, the apparent density of the particles d_a , defined as

$$d_a = \frac{\text{mass of solid}}{\text{volume of solid} + \text{volume of isolated pores}} \quad (3.43)$$

is measured. If d_t is the theoretical density of the particles (i.e., the density of the pore-free solid), the amount of isolated porosity is equal to $1 - d_a/d_t$. Commonly, d_t is obtained from a handbook of physical and chemical data. For crystalline materials, it can also be obtained from the crystal structure and the dimensions of the unit cell determined by x-ray diffraction.

For coarser powders (particle size $> \sim 10 \mu\text{m}$), a liquid pycnometer is used. A calibrated bottle is weighed (mass m_o) and the powder is added (total mass m_1). A liquid of known density, d_L , is then added (total mass m_2). In a separate run, the pycnometer bottle containing the liquid only (i.e., no powder) is weighed (mass m_3). The apparent density of the particles d_a is found from

$$d_a = \frac{m_1 - m_o}{(m_3 - m_o) - (m_2 - m_1)} (d_L - d_{air}) + d_{air} \quad (3.44)$$

where d_{air} is the density of air. Care must be taken to achieve good wetting of the particle surfaces by the liquid and to remove trapped air (by boiling the liquid).

Helium gas pycnometry is commonly used for powders finer than $\sim 10 \mu\text{m}$. The small size of the helium molecule enables it to penetrate into very fine pores. The volume occupied by the solid is measured from the volume of gas displaced. The apparent density is then calculated from the mass of the powder used and its measured volume.

3.3 CHEMICAL COMPOSITION

The major, minor, and trace elements present in a powder can all have a significant influence on the subsequent processing and microstructural development of the material. Changes in the concentration of the major elements may result from different powder synthesis methods or from changes in the synthesis conditions. Small concentrations of dopants (~ 0.1 to $10 \text{ at}\%$) are commonly added to improve processing and properties. Trace impurity elements at concentrations less than a few hundred parts per million are invariably present even in the cleanest powders.

Several techniques are currently available for the quantitative analysis of chemical composition, including (1) optical atomic spectroscopy (atomic absorption, atomic emission, and atomic fluorescence), (2) x-ray fluorescence spectroscopy,

copy, (3) mass spectrometry, (4) electrochemistry, and (5) nuclear and radioisotope analysis. The principles, instrumentation, and procedures for these and other techniques used in chemical analysis are described in a recent text (14). For ceramic powders, the most widely used technique is optical atomic spectroscopy involving atomic absorption (AA) or atomic emission (AE). High precision of analysis coupled with low detection limits make the technique very valuable for the determination of major and minor elements as well as for the analysis of trace elements.

X-ray fluorescence spectroscopy (XRF) has been used for many years for the measurement of major and minor elemental concentrations. Improvements made in the sensitivity in recent years now allow the technique to be applied to the analysis of trace elements. A problem is that the sensitivity of XRF decreases dramatically for lower atomic number elements so the technique cannot be used for quantification of elements with atomic number $Z < 9$. When compared to XRF, modern AA or AE instruments are simpler to use, less expensive, have similar precision of analysis and have better sensitivity. Optical atomic spectroscopy is ideally suited to the analysis of solutions so the method requires complete dissolution of the powder in a liquid. In comparison, XRF is ideally suited to the analysis of solid samples, and this can be a distinct advantage for ceramic powders that are commonly difficult to dissolve. Table 3.7 includes a summary of the main features of optical atomic spectroscopy and XRF.

TABLE 3.7 Common Techniques for the Chemical Analysis of Ceramic Powders

Feature	Flame AA	ICP-AE	Furnace AA	XRF	XRD
Range	Metals and metalloid elements	Metals and metalloid elements	Metals and metalloid elements	$Z > 8$	Crystalline materials
Common state of specimen	Liquid	Liquid	Liquid	Solid	Solid
Detection limit ^a (ppm)	10^{-3} – 10^{-1}	10^{-3} – 10^{-1}	10^{-5} – 10^{-2}	>10	10^3 – 10^4
Precision ^b (%)	0.2–1	0.5–2	1–2	0.1–0.5	0.2–0.5
Accuracy ^c (%)	1–2	2–5	5–10	0.1–1	0.5–5

^aMinimum concentration or mass of element that can be detected at a known confidence level

^bRelative standard deviation

^cRelative error

Legend: AA = atomic absorption; ICP-AE = inductively coupled plasma atomic emission; XRF = x-ray fluorescence; XRD = x-ray diffraction; Z = atomic number

Source: Refs. 14–17.

3.3.1 Optical Atomic Spectroscopy: Atomic Absorption and Atomic Emission

Optical atomic spectroscopy is based on transitions of electrons between the outer energy levels in atoms. For a multielectron atom, there are many energy levels in the ground state of an atom, i.e., the state of lowest energy. There are also a large number of unoccupied energy levels into which electrons may be excited. In an excited state of an atom, some of the electrons go to the higher energy levels. In the simplest case, we shall consider two energy levels only, one in the ground state of the atom with energy E_g and one in the excited state with energy E_e (Fig. 3.14). The frequency of radiation absorbed or emitted during the transition is given by Planck's law,

$$\nu = \frac{E_e - E_g}{h} \quad (3.45)$$

where h is Planck's constant. The transitions that are useful in optical atomic spectroscopy involve fairly low energy transitions such that the wavelength of the radiation given by Eq. (3.45) occurs in range of ~ 10 nm to $400 \mu\text{m}$. Typically, these transitions will occur between the outer energy levels of the atom.

For atoms at thermal equilibrium at a temperature T , the number of atoms in the excited state n_e is related to the number in the ground state, n_g by the Boltzmann equation:

$$\frac{n_e}{n_g} = \exp \left[\frac{-(E_g - E_e)}{kT} \right] \quad (3.46)$$

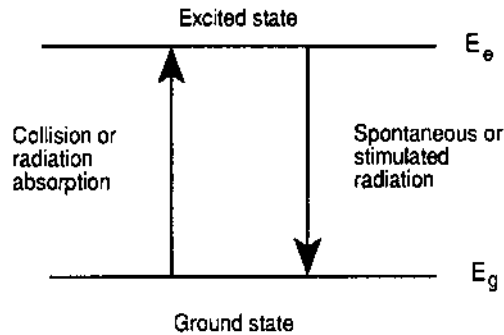


FIGURE 3.14 Schematic showing the transitions in optical atomic spectroscopy.

where k is the Boltzmann constant. The number of atoms in the ground state will be less than the total number n due to the excitation of n_e atoms. However, unless the temperature is very high, n_g will be approximately equal to n . From Eq. (3.46), the number of excited atoms n_e will be proportional to n . The intensity of the absorbed or emitted radiation, which is proportional to n_e , will therefore be proportional to the total number of atoms n . Since each element has its own characteristic energy levels, the elemental composition can be identified from the wavelength (frequency) of the absorbed or emitted radiation, while the intensity of the radiation can be used to determine its concentration.

The relationship between intensity of the absorbed or emitted radiation and the concentration of the atoms can be rigorously derived (15), but it is rarely used practically in quantitative analysis. Instead, standard samples with known concentrations are made up and the intensities are determined for these standards. The concentration of the unknown sample, C_u , is determined from a calibration curve or more simply from the relation

$$C_u = C_s \frac{I_u}{I_s} \quad (3.47)$$

where C_s is the concentration of a standard and I_u and I_s are the measured intensities of the unknown and standard samples, respectively.

For the analysis of ceramic powders by optical atomic spectroscopy, a portion of the powder has to be converted into individual atoms. In practice, this is achieved by dissolving the powder in a liquid to form a solution, which is then broken into fine droplets and vaporized into individual atoms by heating. The precision and accuracy of optical atomic spectroscopy are critically dependent on this step. Vaporization is most commonly achieved by introducing droplets into a flame (referred to as flame atomic absorption spectrometry or flame AA). Key problems with flame AA include incomplete dissociation of the more refractory elements (e.g., B, V, Ta, and W) in the flame and difficulties in determining elements that have resonance lines in the far ultraviolet region (e.g., P, S, and the halogens). While flame AA is rapid, the instruments are rarely automated to permit simultaneous analysis of several elements.

Several types of plasmas have been considered for vaporizing the solution, but by far the most widely used is the inductively coupled plasma (ICP). Elements that are only partially dissociated in the flame are usually completely dissociated by the higher temperatures achieved by ICP. In addition, a valuable feature of ICP is the capability for simultaneous analysis of several elements. Vaporization in a graphite furnace (furnace AA or electrothermal AA) provides better detection limits than flame AA or ICP in the analysis of trace elements but the analysis is slow. Commonly, it is used only when flame AA or ICP provides inadequate

detection limits. Figure 3.15 gives a comparison of the detection limits for flame AA, ICP-AE, and furnace AA in the analysis of trace elements (16).

3.3.2 X-ray Fluorescence Spectroscopy

Atomic x-ray fluorescence spectroscopy (17,18), referred to simply as x-ray fluorescence spectroscopy (XRF), is a technique for qualitatively or quantitatively determining elemental composition by measurement of the wavelength and intensities of the electron transitions from the outer to the inner energy levels of the atom. The energy associated with these transitions ($\sim 0.6\text{--}60\text{ keV}$) is significantly greater than that associated with the transitions in optical atomic spectroscopy (approximately a few electron volts). The emitted x-ray spectrum does not depend on the way in which the atomic excitation is produced, but in XRF, a beam of energetic x-rays is used.

When a primary beam of monochromatic x-rays falls on a specimen, the x-rays may be absorbed or scattered. Coherent scattering of x-rays from an ordered arrangement of scattering centers (such as the environment present in crystals) leads to diffraction. The use of x-ray diffraction for characterizing powders is described in the next section. The absorption of x-rays leads to electronically excited atoms (ions) due to the ejection of electrons (i.e., the *photoelectric effect*) or to the transition of electrons to higher energy levels (Fig. 3.16a). (The ejected electrons, as described later, form the basis for the surface characterization technique of *x-ray photoelectron spectroscopy*.)

As the excited atoms readjust to their ground state, two processes may occur. The first involves a rearrangement of the electrons which leads to the ejection of other electrons (referred to as *Auger electrons*) from higher energy levels (Fig. 3.16b). The second process leads to the emission of x-rays when the electrons undergo transitions from the outer levels to fill the vacant electron sites in the inner energy levels (Fig. 3.16c). This secondary beam of x-rays emitted from the specimen, resulting from the interaction of the primary x-ray beam, forms the basis of XRF. It is characteristic of the elements in the specimen and can therefore be used to identify the elements. The relationship between the wavelength λ of the emitted x-rays and the atomic number Z of the element was first established by Moseley (1913) and is given by

$$\frac{1}{\lambda} = A(Z - \alpha)^2 \quad (3.48)$$

where A is a constant for each series of spectral lines and $\alpha \approx 1$.

In XRF, the polychromatic beam of radiation emitted from the specimen is diffracted through a single crystal to isolate narrow wavelength bands (*wavelength dispersive spectroscopy*) or analyzed with a proportional detector to isolate narrow energy bands (*energy dispersive spectroscopy*). Because the relationship between

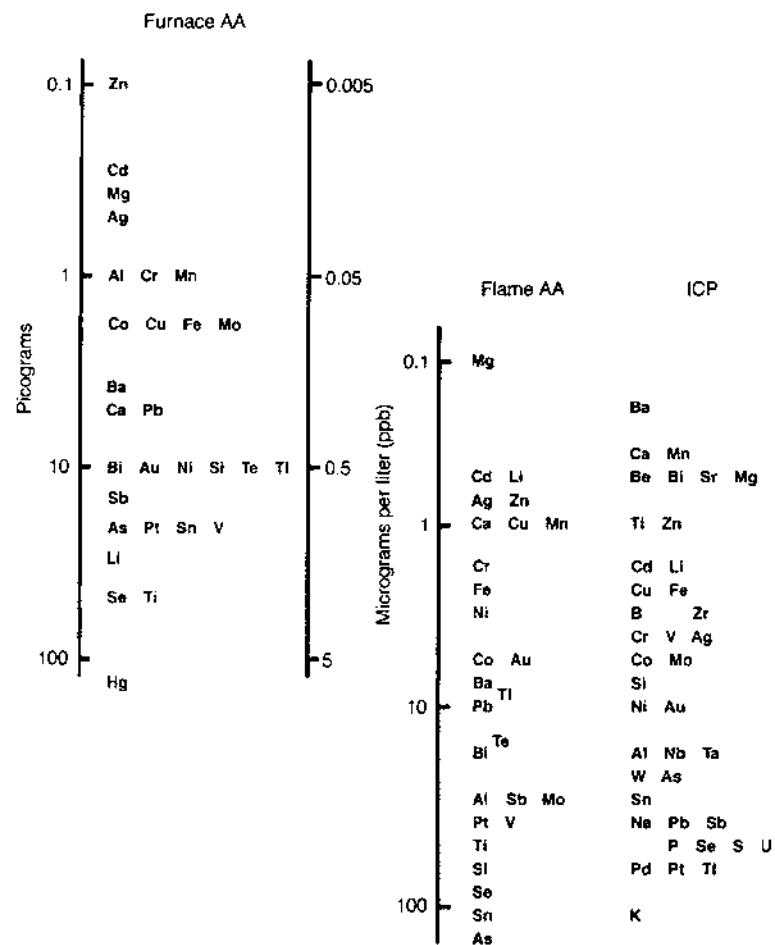


FIGURE 3.15 Comparison of detection limits for trace element analysis by flame atomic absorption, ICP-atomic emission, and furnace atomic absorption, plotted on a logarithmic scale of concentration in micrograms per liter (parts per billion). Because furnace detection limits are inherently in units of mass (picograms), they have been converted to concentration by assuming a 20 μL sample. (From Ref. 16.)

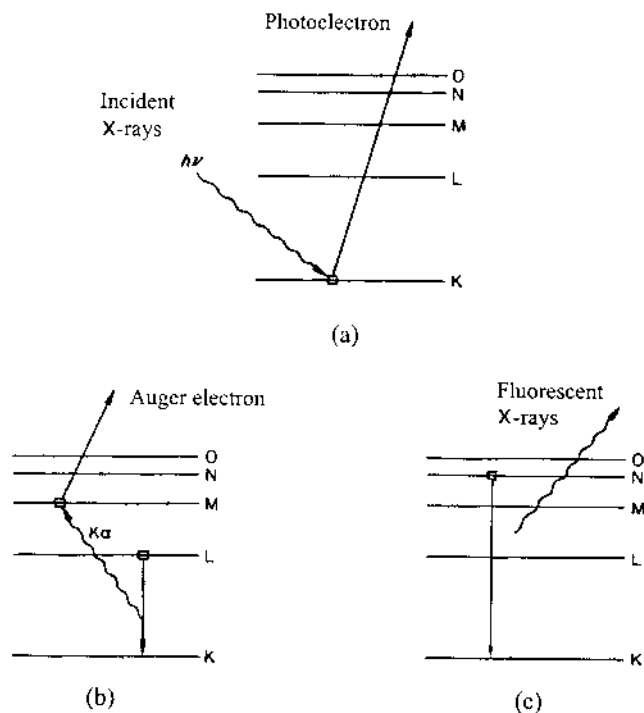


FIGURE 3.16 (a) Interaction of x-rays with a solid producing atomic excitation with the emission of a photoelectron, (b) followed by de-excitation with the emission of an Auger electron, (c) or by the emission of characteristic x-ray photons.

wavelength and atomic number is known [Eq. (3.48)], isolation of individual characteristic lines allows the identification of the element. The elemental concentrations are found from the intensity of the spectral lines (e.g., by comparing with the intensities of standards).

3.4 CRYSTAL STRUCTURE AND PHASE COMPOSITION

Coherent scattering of x-rays from crystalline materials, as outlined earlier, leads to diffraction. Since its discovery in 1912 by von Laue, x-ray diffraction (XRD) has provided a wealth of information about the structure and chemical composition of crystalline materials. For compositional analysis, the technique is unique in that it is the only analytical method capable of providing qualitative and quanti-

tative information about the crystalline *compounds* (phases) present in a solid. For example, the technique can determine the percentage of ZnO and Al₂O₃ present in a mixture of the two compounds, whereas other analytical techniques can only give the percentage of the elements Zn, Al, and O in the mixture. A detailed description of the XRD technique is available in several excellent texts [6–8,19].

The requirements for x-ray diffraction are (1) the atomic spacing in the solid must be comparable with the wavelength of the x-rays and (2) the scattering centers must be spatially distributed in an ordered way (e.g., the environment present in crystals). The diffraction of x-rays by crystals (Fig. 3.17) was treated by Bragg in 1912. The condition for constructive interference, giving rise to intense diffraction maxima, is known as Bragg's law:

$$2d \sin \theta = n\lambda \quad (3.49)$$

where d is the spacing between the lattice planes of the crystal, θ is the angle of incidence (or reflection), n is an integer (sometimes referred to as the order of diffraction), and λ is the wavelength of the x-rays (0.15406 nm for Cu K_α radiation). When the reflection angle θ does not satisfy Eq. (3.49), destructive interference occurs.

In recent years, computer automation has greatly reduced the amount of work required for x-ray analysis of structure and composition so that much of the data analysis is now commonly performed by software and computerized search programs. Structural analysis involves the measurement of the lattice parameters of the crystal (the unit cell dimensions) and the structural model of the crystal (the crystal structure). While the use of single crystals is the preferred

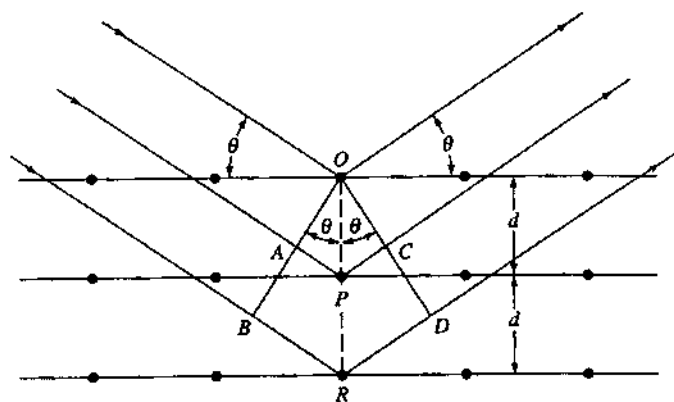


FIGURE 3.17 Diffraction of x-rays by a crystal.

method for structural analysis whenever possible, powder diffraction in which the sample consists of a random orientation of a large number of fine particles (polycrystals) can also be used. Determination of the unit cell requires finding a set of unit cell parameters that index all of the observed reflections. Lattice parameter measurements are important for doped powders and solid solutions where data on compositional effects on the lattice parameters are required (e.g., Y_2O_3 -stabilized ZrO_2).

Compositional analysis is based on the fact that an x-ray diffraction pattern is unique for each crystalline material. Thus, if an exact match can be found between the pattern of the unknown material and an authentic sample, chemical identity can be assumed. The International Center for Diffraction Data (ICDD-JCPDS) publishes a database containing powder diffraction patterns for several thousands of materials. Commonly, it is possible to identify an unknown material by searching the ICDD-JSPDS database for a matching pattern.

For a physical mixture, the powder diffraction pattern is the sum of the patterns of the individual materials. The diffraction pattern can therefore be used to identify the crystalline phases in a mixture. The concentrations of the crystalline phases can be determined by methods based on comparing the intensities of the diffraction peaks with standards (6-8). If the crystal structures of the phases are known, the concentration of each phase can be determined by Rietveld analysis (20,21). In the Rietveld method, a theoretical diffraction pattern is computed and the difference between the theoretical and observed patterns is minimized. For quantitative analysis, some care should be taken with specimen preparation if accurate and reliable results are to be obtained. The effects of factors such as preferred orientation, texturing, and particle size broadening must be minimized.

X-ray diffraction, as indicated in Table 3.7, has a detection limit of 0.1–1 wt% so that crystalline phases present in concentrations below this limit will not be detected. Furthermore, amorphous phases are not directly measured but their presence may be quantified by comparing the pattern with a standard that is known to contain no amorphous phase (22).

3.5 SURFACE CHARACTERIZATION

As the particle size of a powder decreases below 1 μm , the surface area of the powder and the volume fraction of the outermost layer of ions on the surface increase quite significantly. We would therefore expect the surface characteristics to play an increasingly important role in the processing of fine powders as the particle size decreases. The surface area (described earlier) and the surface chemistry are the surface characteristics that have the most profound influence on processing. Another characteristic, the surface structure, while having only a limited role in processing, may nevertheless have an important influence on surface phenomena (e.g., vaporization, corrosion, and heterogeneous catalysis).

Although the characterization of the powder surface area and its role in processing have received considerable attention for decades, it is only within recent years that the importance of surface chemistry in ceramic processing has begun to be recognized. As we have outlined in Chapter 1, the consolidation of fine ceramic powders from liquid suspensions to produce more uniform green bodies has been shown to produce significant benefits in fabrication. In this case, the quality of the microstructure of the consolidated body is controlled by the dispersion behavior of the powder and the interaction between the particles in the liquid, which, in turn, are controlled by the surface chemistry.

The powder surface chemistry can also have a direct influence on densification and microstructural evolution during the firing process, regardless of the powder consolidation method. The surfaces of the particles become interfaces and grain boundaries that act as sources and sinks for the diffusion of matter. Densification and coarsening processes will therefore be controlled by the structure and composition of the interfaces and grain boundaries. Impurities on the surfaces of the powder, for example, will alter the grain boundary composition and, in turn, the microstructure of the fabricated body. In many ceramics (of which Si_3N_4 is a classic example), controlling the structure and chemistry of the grain boundaries through manipulation of the powder surface chemistry forms one of the most important considerations in processing.

With the enormous and increasing importance of surfaces to modern technological processes, a large number of techniques have been developed to study various surface properties. Here we consider only those techniques that have emerged to be most widely applicable to ceramic powders. Readers interested in the more specialized techniques are referred to texts devoted to surface analysis (23-25).

In general, the surface characterization techniques rely on the interaction of atomic particles (e.g., atoms, ions, neutrons, and electrons) or radiation (e.g., x-rays and ultraviolet rays) with the sample. The interaction produces various emissions that can be used to analyze the sample, as shown in Fig. 3.18 for the principal emissions produced by the interaction of an electron beam with a solid. Depending on the thickness of the solid and the energy of the electron beam, a certain fraction of electrons will be scattered in the forward direction, another fraction will be absorbed and the remaining fraction will be scattered in the backward direction. The forward scattered electrons consist of electrons that have undergone elastic scattering (i.e., interactions with the atoms of the sample that result in a change in direction but virtually no loss in energy) and electrons that have undergone inelastic scattering (i.e., interactions that result in a change in direction and a reduction in the energy of the incident electrons). The elastically scattered electrons are much greater in number than the inelastically scattered electrons. They are used in the transmission electron microscope to produce diffraction effects in the determination of the structure of the sample. The backscat-

tered electrons are highly energetic electrons that have been scattered in the backward direction. The majority of these will also have undergone elastic collisions with the atoms of the sample.

The incident electron beam can also generate secondary effects in the sample. One of these effects is that the incident electrons can knock electrons out of their orbits around an atom. If the ejected electrons are near the surface of the sample (within ~ 20 nm), they may have enough energy to escape from the sample and become what are called secondary electrons. These secondary electrons are used in the scanning electron microscope to produce an image. A second type of effect occurs when an electron undergoes a transition from a higher energy level to fill a vacant site in the lower energy level of an excited atom. As we observed earlier (Fig. 3.16), radiation in the form of x-rays or light can be produced in the transition and used to obtain information about the chemical composi-

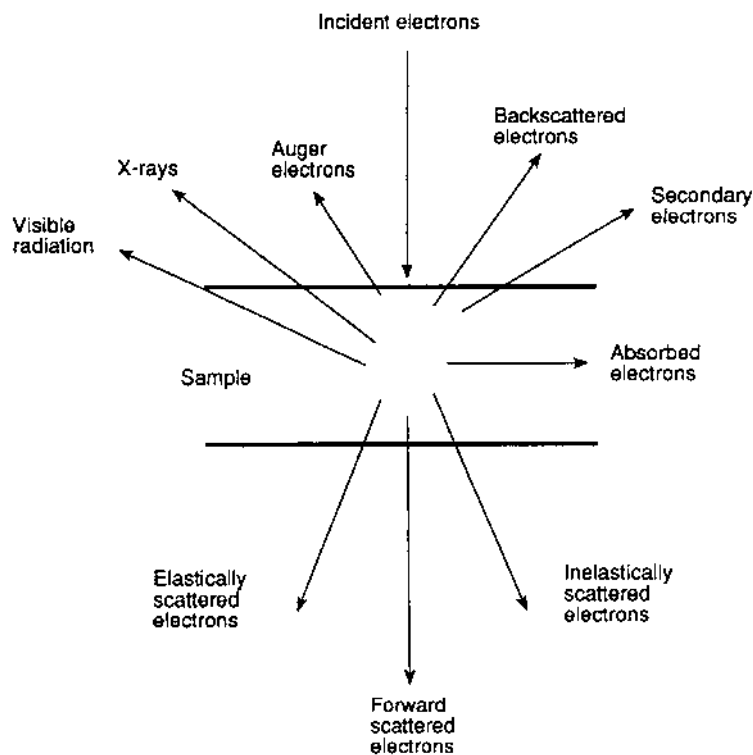


FIGURE 3.18 Emissions produced by the interaction of an electron beam with a solid sample.

tion of the sample. Furthermore, some of the x-rays can be absorbed by electrons in the outer orbitals around the atoms. If these electrons are very close to the surface of the sample, they may escape. These electrons, called Auger electrons, can also provide chemical information about the near-surface region.

The depth to which the incident electron beam penetrates into the sample depends on the energy of the beam and the nature of the sample. For electron energies of 1 MeV, the penetration depth is $\sim 1\ \mu\text{m}$. However, for energies in the range 20–1000 eV, the penetration depth is only $\sim 1\ \text{nm}$. An incident electron beam with energy below $\sim 1\ \text{keV}$ can therefore be used to probe surface layers one to two monolayers thick. Ions and x-rays can also be used to produce diffraction effects and to eject electrons. They too can be used as incident beams to probe the surfaces of materials.

3.5.1 Surface Structure

When viewed on a microscopic or submicroscopic scale, the surface of a particle is not smooth and homogeneous. Various types of irregularities are present. Most ceramic particles, as we observed in Chapter 2, are agglomerates of finer primary particles. Features such as porosity and boundaries between the primary particles will be present on the surface. For nonoxide particles, a thin oxidation layer will cover the surfaces of the particles. Even for single-crystal particles, the surface can be fairly complex. Figure 3.19 shows an atomic-scale model of the surface structure of solids which has been constructed on the basis of information obtained from a few techniques (26). The surface has several atomic irregularities that are distinguishable by the number of nearest neighbors (coordination number). The atoms in terraces are surrounded by the largest number of nearest neighbors. Atoms located in steps have fewer neighbors and atoms in kink sites have even fewer. Kink, step, and terrace atoms have large equilibrium concentrations on any real surface. On a rough surface, 10–20% of the atoms are in step sites, with $\sim 5\%$ in kink sites. Steps and kinks are also referred to as *line defects*. Atomic vacancies and adatoms, referred to as *point defects*, are also present in most surfaces. While their concentrations are small ($<1\%$ of a monolayer even at temperatures close to the melting point), they are important participants of atomic transport along the surface.

The most widely applicable techniques for characterizing the surface structure of solids include electron diffraction and scanning probe microscopy. The most prominent techniques, low energy electron diffraction (LEED), scanning tunneling microscopy (STM), and atomic force microscopy (AFM) have limitations for characterizing powder surfaces since they require a fairly flat surface with sufficient coherency over a relatively large area. Readers interested in these techniques are referred to treatments elsewhere on LEED (25,27), STM (28,29) and AFM (29,30).

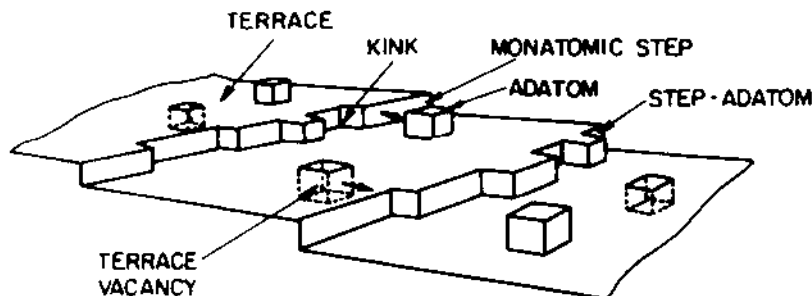


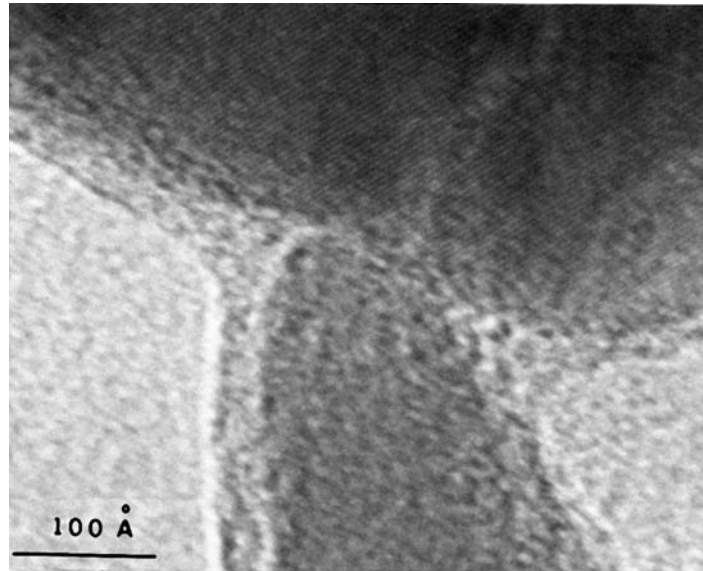
FIGURE 3.19 Model of a heterogeneous solid surface showing different surface sites. (From Ref. 26.)

Modern scanning electron microscopes provide a very simple method for observing the powder structure with a point-to-point resolution of ~ 2 nm. Finer details of the structure can be observed by TEM. Figure 3.20a shows a high-resolution TEM micrograph of a Si_3N_4 powder having an amorphous layer (3–5 nm thick) on the surface (31). This surface layer, with the composition of a silicon oxynitride, has a significant effect on the sintering and high temperature mechanical properties of Si_3N_4 . A micrograph of another Si_3N_4 powder observed in a high voltage TEM (1.5 MeV) shows that the particles are connected by a strong amorphous bridge, presumably a silicon oxynitride (Fig. 3.20b). Such hard agglomerates, as we observed earlier, can have a detrimental effect on the packing of the powder.

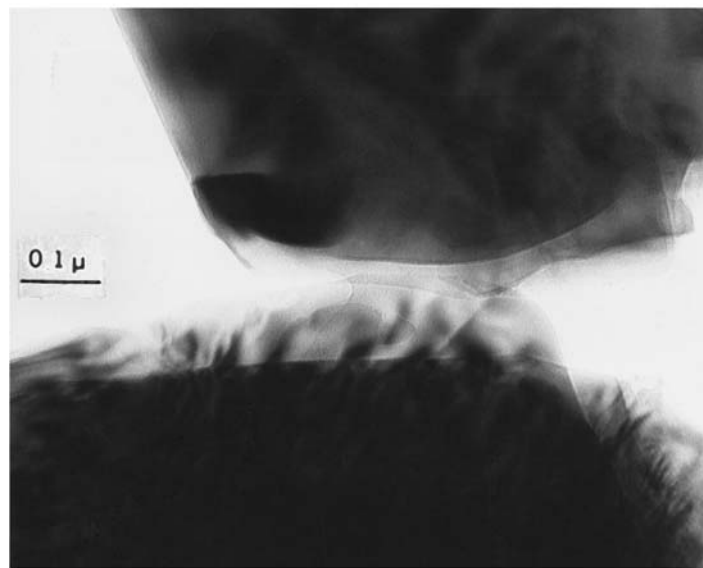
3.5.2 Surface Chemistry

Electron, ion, and photon emissions from the outermost layers of the surface can be used to provide qualitative or quantitative information about the chemical composition of the surface. The most widely applicable techniques for characterizing the surface chemistry of ceramic powders are Auger electron spectroscopy (AES), x-ray photoelectron spectroscopy (XPS), which is also referred to as electron spectroscopy for chemical analysis (ESCA), and secondary ion mass spectrometry (SIMS). Table 3.8 provides a summary of the main measurement parameters for these three techniques.

All surface analytical techniques (with the exception of Rutherford back-scattering) require the use of ultrahigh vacuum environment. The analysis conditions are therefore rather limited and do not correspond to those normally used in ceramic processing where the powder experiences fairly prolonged exposure to the atmosphere. Although the techniques described here derive their usefulness from being truly surface sensitive, they can also be used to provide information



(a)



(b)

FIGURE 3.20 Surface structure of a Si_3N_4 powder as revealed by (a) high resolution TEM and (b) high voltage TEM.

TABLE 3.8 Common Methods for the Surface Chemical Analysis of Ceramic Powders

Measurement parameter	Auger electron spectroscopy (AES)	X-ray photoelectron spectroscopy (XPS)	Secondary ion mass spectrometry (SIMS)
Incident particle	Electrons (1–20 keV)	X-rays (1254 eV and 1487 eV)	Ions (He^+ , Ne^+ , Ar^+) (100 eV–30 keV)
Emitted particle	Auger electrons (20–2000 eV)	Photoelectrons (20–2000 eV)	Sputtered ions (~ 10 eV)
Element range	$>\text{Li}$ ($Z = 3$)	$>\text{Li}$ ($Z = 3$)	$>\text{H}$ ($Z = 1$)
Detection limit	10^{-3}	10^{-3}	10^{-6} – 10^{-9}
Depth of analysis	2 nm	2 nm	1 nm
Lateral resolution	>20 nm	>150 μm	50 nm–10 mm

Source: Ref. 23.

from much deeper layers. This is normally done by sequential (or simultaneous) removal of surface layers by ion beam sputtering and analysis. This mode of analysis in which the composition can be found layer by layer is referred to as *depth profiling*. It is probably one of the most important modes of surface analysis because the composition of the surface is usually different from that of the bulk. The ability to perform composition-depth profiling, therefore, is often a measure of the effectiveness of a technique.

3.5.2.1 Auger Electron Spectroscopy

Auger electron spectroscopy (AES) is based on a two-step process as shown schematically in Fig. 3.21a. When an electron is emitted from the inner atomic orbital through collision with an incident electron beam, the resulting vacant site is soon filled by another electron from an outer orbital. The energy released in the transition may appear as an x-ray photon (the characteristic x-rays used in electron microprobe techniques for compositional analysis) or may be transferred to another electron in an outer orbital which is ejected from the atom with a kinetic energy E_K given by

$$E_K = E_1 - E_2 - E_3^* \quad (3.50)$$

where E_1 and E_2 are the binding energies of the atom in the singly ionized state and E_3^* is the binding energy for the doubly ionized state. The ejected electron (referred to as the *Auger* electron) moves through the solid and soon loses its energy through inelastic collision with bound electrons. However, if the Auger electron is emitted sufficiently close to the surface, it may escape from the surface and be detected by an electron spectrometer. The number of electrons (or the derivative of the counting rate) is commonly plotted as a function of the kinetic

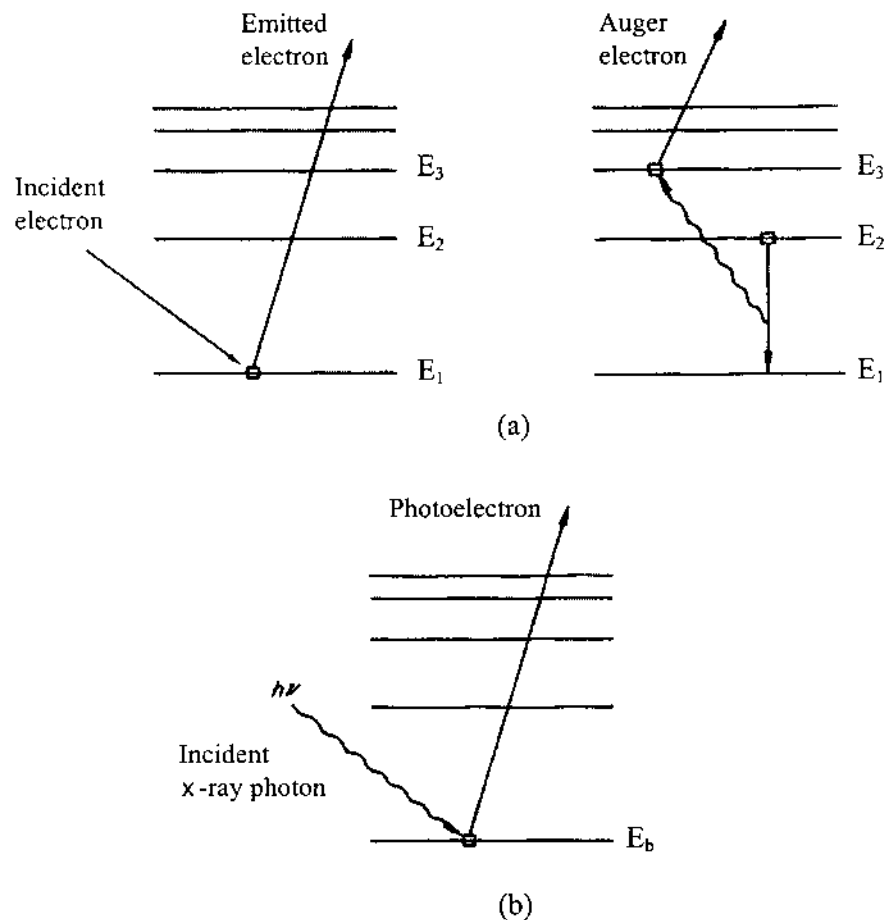


FIGURE 3.21 Schematic showing the electron emissions in (a) Auger electron spectroscopy and (b) x-ray photoelectron spectroscopy.

energy of the electron. Since each type of atom has its own characteristic electron energy levels, the peaks in the observed Auger spectrum can be used to determine the elemental composition by comparison with standard Auger spectra for the elements.

The technique is fairly rapid and provides high reproducibility of the results. When calibration standards are used, quantitative elemental composition can be obtained to better than $\pm 10\%$. While AES in principle can provide information on the chemical composition, it is largely used for elemental analysis only. For

ceramic powders, which are mostly insulating, electrostatic charging of the surface may occur, and this leads to large shifts in the energies of the Auger electrons, making reliable analysis of the spectra difficult.

3.5.2.2 X-ray Photoelectron Spectroscopy

In x-ray photoelectron spectroscopy (XPS), the sample is irradiated by a source of low-energy x-rays that leads to the emission of electrons from the lower energy atomic orbitals by the well-known photoelectric effect (Fig. 3.21b). The kinetic energy of the emitted photoelectrons E_K is given by

$$E_K = h\nu - E_b - W \quad (3.51)$$

where $h\nu$ is the frequency of the incident x-ray photon, E_b is the binding energy of the photoelectron, and W is the work function of the spectrometer, a factor that corrects for the electrostatic environment in which the electron is produced and measured. By measuring E_K in a spectrometer with a known W , the binding energy can be determined from Eq. (3.51). The data is commonly plotted as the number of emitted electrons versus the binding energy. The binding energy of an electron is characteristic of the atom and orbital from which the electron was emitted. In addition to the valence electrons that take part in chemical bonding, each atom (except hydrogen) possesses core electrons that do not take part in bonding. We are generally concerned with the core electrons in XPS.

XPS is a fairly versatile technique that can be used for qualitative or quantitative analysis of the elemental composition of the surface as well as for determining the chemical bonding (or oxidation state) of the surface atoms. For qualitative analysis, a low-resolution, wide-scan spectrum (often referred to as a survey scan) covering a wide energy range (typically binding energy values of 0 to 1250 eV) serves as the basis for determining the elemental composition of the surface. Every element in the periodic table has one or more energy levels that will result in the appearance of peaks in this range. The position of each peak in the spectrum is compared with standard spectra to determine the elements present. A survey scan for a commercial Si_3N_4 powder, prepared by a gas phase reaction between SiCl_4 and NH_3 is shown in Fig. 3.22. The presence of residual chlorine and accompanying fluorine, as well as oxygen from the oxide layer, are revealed.

For quantitative analysis, the principal peak for each element is selected and its intensity (peak area after removal of the background) is measured. The fractional atomic concentration of an element A is given by

$$C_A = \frac{I_A/S_A}{\sum_i I_i/S_i} \quad (3.52)$$

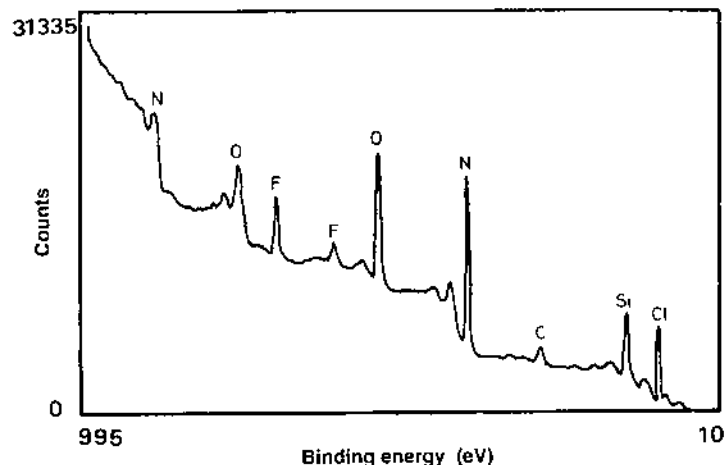


FIGURE 3.22 Survey scan of the surface chemistry of a commercial Si_3N_4 powder by x-ray photoelectron spectroscopy.

where I_i is the measured peak intensity of the element i and S_i is the atomic sensitivity factor for that peak. The atomic sensitivity factors, which can be calculated theoretically or derived empirically, are usually provided in the reference manuals supplied by the manufacturer of the instrument. The accuracy of the quantitative analysis (less than $\pm 10\%$) is similar to that for AES.

Information about the chemical bonding and oxidation state of the surface atoms can be determined from the chemical shifts in the peak positions in the XPS spectrum. When one of the peaks of a survey scan is examined at a higher resolution, the binding energy of the maximum is found to depend to a small degree on the chemical environment of the atom responsible for the peak. Variations in the number of valence electrons, and the types of bonds they form, influence the binding energy of the core electrons to produce a measurable shift (of a few eV) in the measured electron energy. Figure 3.23 illustrates the nature of the chemical shift for the $2p$ peak in Si and in SiO_2 . In the practical determination of the chemical bonding, the measured peak position is compared with reference values for the corresponding peak in different compounds.

Unlike AES in which, especially for insulating samples, electron beam damage may occur, the damage to the sample in XPS is minimal. Furthermore, electrostatic charging of commonly insulating ceramic powders is not a severe problem. AES and XPS provide similar information about the elemental composition, and the methods tend to be complementary rather than competitive. It is

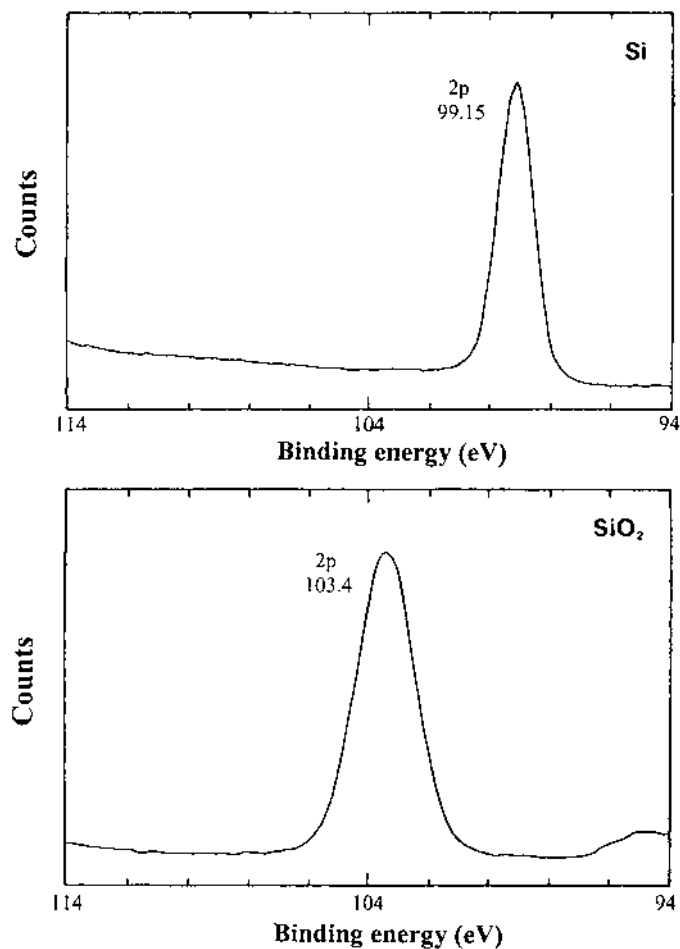


FIGURE 3.23 Peak positions for the silicon $2p$ peak in Si and in SiO_2 , showing the chemical shift produced by the formation of SiO_2 . (Courtesy Perkin-Elmer Corporation, Eden Prairie, MN.)

therefore not uncommon to find instruments that incorporate both techniques, as sketched in Figure 3.24 for a combined AES/XPS instrument.

3.5.2.3 Secondary Ion Mass Spectrometry

Secondary ion mass spectrometry (SIMS) consists of bombarding a surface with a primary beam of ions (He^+ , Ne^+ , or Ar^+ in the energy range of a few hundred



There are two distinct modes of analysis. In static SIMS, an ion beam of low current density is used so that the analysis is confined to the outermost layers. In dynamic SIMS, a high current density beam is used to erode successive atomic layers at a relatively fast rate. While the sensitivity of the technique is improved to the parts-per-billion range, the analytical conditions in dynamic SIMS are not suitable for surface analysis. Here we limit our attention more specifically to static SIMS.

Ion beam sputtering is the primary process in SIMS, but as remarked earlier, it is also important in depth profiling, a method widely used in AES, XPS, SIMS, and many other techniques to study subsurface composition with quite fine depth resolution. When an energetic ion strikes a surface, it dissipates some of its energy into the surface. In the simplest case when the ion is scattered back out of the surface, the energy transferred to a surface atom after a binary collision is sufficient to cause substantial local damage. However, when the incident ion is scattered into the solid, the result is a *collision cascade* leading to the emission of sputtered particles (ions, ionized clusters, atoms, and atomic clusters) from the

top one or two atomic layers of the surface (Fig. 3.25). Analysis of the sputtered particles in SIMS provides a method, albeit intrinsically destructive, of surface composition analysis.

SIMS has the advantages of high spatial resolution, high sensitivity for qualitative elemental analysis, and the ability to provide a detailed analysis of the chemical composition of the surface. Quantitative analysis can be performed only with a certain degree of difficulty. Figure 3.26 shows the positive and negative secondary ion mass spectra of a pressed pellet of the Si_3N_4 powder referred to in Fig. 3.22. In addition to oxygen from the native oxide layer, the surface is contaminated with hydroxyl groups as well as small amounts of Cl, F, Na. The presence of Li and K is also detected.

3.6 CONCLUDING REMARKS

In this chapter we have examined a variety of techniques with broad application to the characterization of ceramic powders. In addition to ceramic processing, powders are also important in several other technologies (e.g., powder metallurgy, catalysis, and pollution control) so that the techniques described here have broader

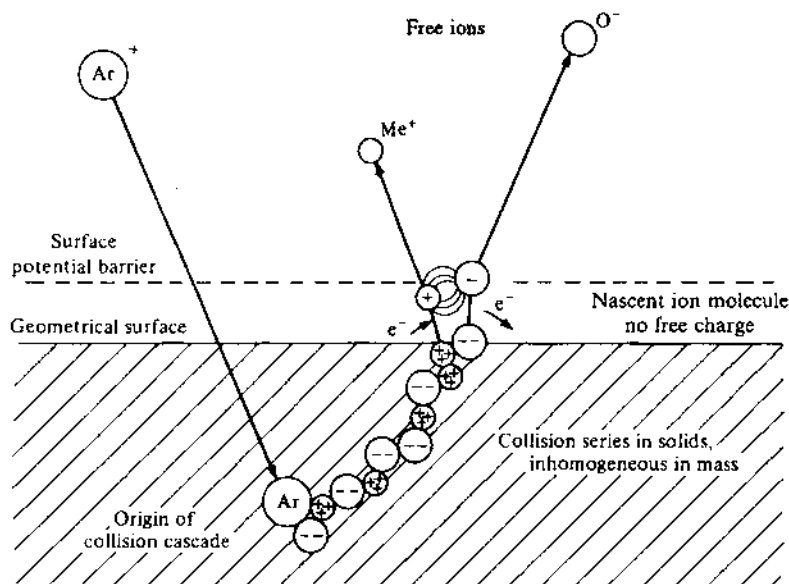


FIGURE 3.25 Model for the emission of secondary ions produced by ion beam sputtering. (From Ref. 23.)

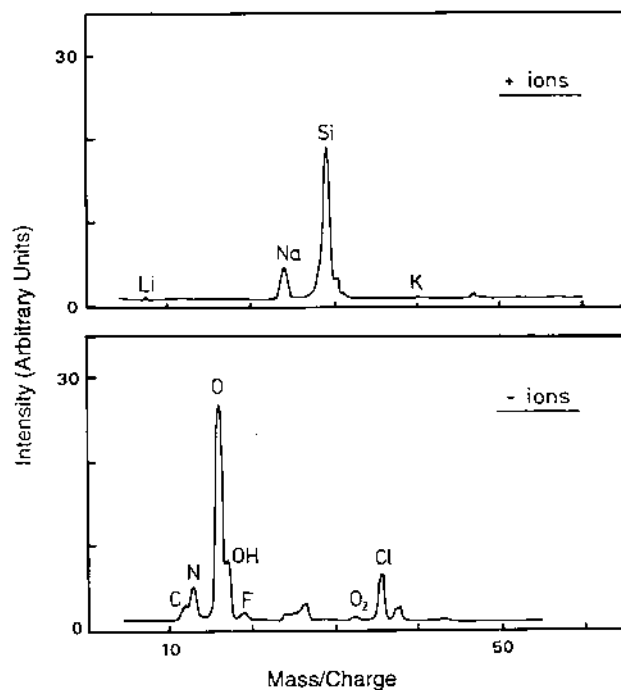


FIGURE 3.26 Positive and negative secondary ion mass spectra of the Si_3N_4 powder referred to in Fig. 3.22.

applicability. Some of the techniques (e.g., gas adsorption and mercury porosimetry) are also important for characterizing porous compacts, while others (e.g., techniques for phase analysis, chemical composition, and surface analysis) are very important for solids also. We shall encounter the use of these techniques again when we consider powder consolidation and the microstructural characterization of solids produced by firing. Finally, as stated earlier, proper characterization of the starting powders is essential for understanding their behavior during subsequent processing.

PROBLEMS

3.1 The particle size distribution of a powder is as follows:

Mean size (μm):	4	6	9	12	18	25
Number of particles:	10	16	20	25	15	7

Calculate the arithmetic, geometric, and harmonic mean sizes.

- 3.2 Discuss what methods you would use to measure the particle sizes of the following powders:
- A powder with particles less than 50 μm .
 - A nanoscale powder with particles less than 20 nm.
 - A submicrometer powder.
 - A powder with particles in the range 20–85 μm which must be analyzed dry.
 - A powder with particles less than 50 μm where the surface area is the important property.
- 3.3
- Plot the shape factor for a cylinder as a function of the length to diameter ratio.
 - Calculate the shape factor for a tetrahedron, an octahedron, and a dodecahedron.
 - An agglomerate consists of n spherical particles of the same size in point contact. Calculate and plot the shape factor as a function of n , for n in the range 2–100.
- 3.4 In a nitrogen adsorption experiment at the boiling point of liquid N_2 , the volume V of gas adsorbed at a pressure p were measured as follows:

p (mm Hg):	80	100	125	140	200
V (cm^3/g):	0.420	0.439	0.464	0.476	0.534

Determine the surface area of the powder.

- 3.5 The following data were obtained in a liquid pycnometry experiment performed at 20°C: mass of pycnometer = 35.827 g; mass of pycnometer and powder = 46.402 g; mass of pycnometer and water = 81.364 g; mass of pycnometer, powder, and water = 89.894 g. If the theoretical density of the solid is 5.605 g/cm^3 , determine the amount of closed porosity in the powder.
- 3.6 Discuss how you would measure the following:
- The solid solubility limit of Ca in ZrO_2 .
 - The effect of Ca concentration on the theoretical density of Ca-doped ZrO_2 .
 - The Ba/Ti atomic ratio in BaTiO_3 powder.
 - The presence of the cubic or tetragonal phase in BaTiO_3 powder.
 - The concentration of SiO_2 impurities in BaTiO_3 powder.
 - The concentration of the α and β phases in a Si_3N_4 powder.
 - The temperature at which ZnO and Al_2O_3 powders react to form ZnAl_2O_4 .
 - The amount of ZnAl_2O_4 formed by the reaction between ZnO and Al_2O_3 powders.
- 3.7 In an x-ray photoelectron spectrum, would you expect the C 1s peak to be at a higher or lower binding energy compared to that for the O 1s peak? Would the F 1s peak occur at a higher or lower binding energy compared to that for the O 1s peak? Explain your answer.
- 3.8 The chemical composition of the oxide layer on Si_3N_4 particles varies as a function of the thickness of the layer. How would you confirm this? What methods would you use to measure the composition as a function of the thickness of the oxide layer?

REFERENCES

1. Wachtman, J. B. *Characterization of Materials*; Butterworth-Heinemann: Boston, 1991.
2. Onoda, G. Y., Jr.; Hench, L. L. *Ceramic Processing Before Firing*; Onoda, G. Y., Jr., Hench, L. L. eds.; Wiley: New York, 1978, pp. 35–37.
3. Allen, T. *Particle Size Measurement*; 4th ed.; Chapman and Hall: London, 1990.
4. Beddow, J. K. *Particulate Science and Technology*; Chemical Publishing Co.: New York, 1980.
5. Evans, J. W.; De Jonghe, L. C. *The Production of Inorganic Materials*; Macmillan: 1991, p. 131.
6. Cullity, B. D. *Elements of X-ray Diffraction*; 2nd ed.; Addison-Wesley: 1978.
7. Klug, H. P.; Alexander, L. F. *X-ray Diffraction Procedures for Polycrystalline and Amorphous Materials*; Wiley: New York, 1974.
8. Jenkins, R.; Snyder, R. L. *Introduction to X-ray Powder Diffractometry*; Wiley: New York, 1996.
9. Gregg, S. J.; Sing, K. S. W. *Adsorption, Surface Area and Porosity*; 2nd ed.; Academic Press: New York, 1982.
10. Brunauer, S.; Deming, L. S.; Deming, W. S.; Teller, E. J. *Am. Chem. Soc.* 1940, Vol. 62, 1723.
11. Brunauer, S.; Emmett, P. H.; Teller, E. J. *Am. Chem. Soc.* 1938, Vol. 60, 309.
12. Brunauer, S. *The Adsorption of Gases and Vapours*; Oxford University Press: Oxford, 1945.
13. Langmuir, I. J. *Am. Chem. Soc.* 1916, Vol. 38, 2221.
14. Skoog, D. A.; Holler, F. J.; Nieman, T. A. *Principles of Instrumental Analysis*; 5th ed.; Harcourt Brace: Philadelphia, PA, 1998.
15. Winefordner, J. D.; Epstein, M. S. *Physical Methods of Chemistry: Vol. IIIA, Determination of Chemical Composition and Molecular Structure*; Wiley: New York, 1987, pp. 193–327.
16. Slavin, W. *Anal. Chem.* 1986, Vol. 58, 589A.
17. Jenkins, R. *X-ray Fluorescence Spectrometry*; 2nd ed.; Wiley: New York, 1999.
18. Jenkins, R.; Gould, R. W.; Gedcke, D. *Quantitative X-ray Spectrometry*; 2nd ed.; Marcel Dekker: New York, 1995.
19. Stout, G. H.; Jensen, L. H. *X-Ray Structure Determination*; Wiley: New York, 1989.
20. Rietveld, H. M. J. *Appl. Cryst.* 1969, Vol. 2, 65–71.
21. *The Rietveld Method*; Young, R. A. ed.; Oxford University Press: New York, 1993.
22. Von Dreele, R. B.; Kline, J. P. *Advances in X-ray Analysis: Vol. 38*; Plenum Press: New York, 1995, pp. 59–69.
23. Walls, J. M. *Methods of Surface Analysis*; Cambridge University Press: Cambridge, 1989.
24. Hudson, J. B. *Surface Science: An Introduction*; Butterworth-Heinemann: Boston, 1992.
25. Woodruff, D. P.; Delchar, T. A. *Modern Techniques of Surface Analysis*; 2nd ed.; Cambridge University Press: Cambridge, 1994.
26. Somorjai, G. A.; Salmeron, M. *Ceramic Microstructures '76*; Fulrath, R. M., Pask, J. A. eds.; Westview Press: Boulder, CO, 1977, pp. 101–128.

27. van Hove, M. A. *Proc. R. Soc. Lond.A.* 1993, Vol. 442, 61.
28. van de Leemput, L. E. C.; van Kempen, H. *Rep. Prog. Phys.* 1992, Vol. 55, 165.
29. Hansma, P. K.; Elings, V. B.; Marti, O.; Bracker, C. E. *Science*. 1988, Vol. 242, 157.
30. Meyer, E. *Prog. Surf. Sci.*. 1992, Vol. 41, 1.
31. Rahaman, M. N.; Boiteux, Y.; De Jonghe, L. C. *Am. Ceram. Soc. Bull.* 1986, Vol. 65, 1171.

4

Science of Colloidal Processing

4.1 INTRODUCTION

A colloid consists of two distinct phases: a continuous phase (referred to as the *dispersion medium*) and a fine, dispersed particulate phase (the *disperse phase*). In general, the two phases may be either solids, liquids, or gases, giving rise to various types of colloidal systems as listed in Table 4.1. The dispersed particles generally have dimensions ranging between 1 and 1000 nm, sometimes referred to as the *colloidal size range*.

In the processing of ceramics, colloidal suspensions (also referred to as *sols*), consisting of a dispersion of solid particles in a liquid, are of particular interest. They are being used increasingly in the consolidation of ceramic powders to produce the green body. Compared to powder consolidation in the dry or semidry state (e.g., pressing in a die), colloidal methods can lead to better packing uniformity in the green body which, in turn, leads to a better microstructural control during firing. Colloidal solutions consist of polymer molecules dissolved in a liquid. The size of the polymer molecules in solution falls in the colloidal size range so that these systems are considered part of colloid science. Polymer solutions are relevant to the fabrication of ceramics by the solution sol–gel route, which we shall consider in the next chapter. For the present chapter, we concentrate on colloidal suspensions.

A basic problem with which we shall be concerned is the stability of colloidal suspensions. Clearly the particles must not be too large otherwise gravity will produce rapid sedimentation. The other important factor is the attractive force between the particles. Attractive van der Waals forces exist between the particles regardless of whether other forces may be involved. If the attractive force is large

TABLE 4.1 Types of Colloidal Systems with Some Common Examples

Disperse phase	Dispersion medium	Technical name	Examples
Solid	Gas	Aerosol	Smoke
Liquid	Gas	Aerosol	Mist; fog
Solid	Liquid	Suspension or sol	Paint; printing ink
Liquid	Liquid	Emulsion	Milk; mayonnaise
Gas	Liquid	Foam	Fire-extinguisher foam
Solid	Solid	Solid dispersion	Ruby glass (Au in glass); some alloys
Liquid	Solid	Solid emulsion	Bituminous road paving; ice cream
Gas	Solid	Solid foam	Insulating foam

enough, the particles will collide and stick together, leading to rapid sedimentation of particle clusters (i.e., to flocculation or coagulation). Although in principle the reduction in the attractive force can also be used, the techniques employed to prevent flocculation rely on the introduction of repulsive forces. Repulsion between electrostatic charges (*electrostatic stabilization*), repulsion between polymer molecules (*steric stabilization*), or some combination of the two (*electrosteric stabilization*) are the basic techniques used. The stability of colloidal suspensions must be understood at a basic level because it controls the packing uniformity of the consolidated body. A stable colloidal suspension may be consolidated into a densely packed structure; however, an unstable suspension may lead to a loosely packed structure or, under certain conditions, to a particulate gel with a fairly high volume.

Colloidal suspensions exhibit several interesting properties that are important for controlling their stability and consolidation. The motion of the particles when subjected to an electric field (*electrophoresis*) can be a source of valuable information for determining the surface charge of the particles. Colloidal suspensions, especially concentrated suspensions, also have remarkable rheological properties. A good paint must flow easily when applied to the surface to be painted but then must become rigid enough to prevent it from flowing off a vertical surface. In ceramic processing, the rheological behavior of the suspension can be used as a direct process parameter to control and optimize the structure of the green body produced as a result of the consolidation process.

There are several excellent texts that provide an extensive description of the principles of colloid science, of which Refs. 1 to 3 are recommended for further reading.

4.2 TYPES OF COLLOIDS

Colloids consisting of particles dispersed in a liquid are generally divided into two broad classes: *lyophilic* colloids and *lyophobic* colloids. When the liquid is specifically water, the colloids are described as *hydrophilic* and *hydrophobic*. Lyophilic (i.e., liquid-loving) colloids are those in which there is a strong affinity between the dispersed particle and the liquid. The liquid is strongly adsorbed on to the surfaces of the particle so that the interface between the particle and the liquid is very similar to the interface between the liquid and itself. This system will be intrinsically stable because there is a reduction in the Gibbs free energy when the particles are dispersed. Polymer solutions and soap solutions are good examples of lyophilic colloids.

Lyophobic (liquid-hating) colloids are those in which the liquid does not show affinity for the particle. The Gibbs free energy increases when the particles are distributed through the liquid so that if attractive forces exist between the particles, there will be a strong tendency for the particles to stick together when they come into contact. This system will be unstable and flocculation will result. A lyophobic colloid can, therefore, only be dispersed if the surface is treated in some way to cause a strong repulsion to exist between the particles. Suspensions of insoluble particles in a liquid (e.g., most ceramic particles dispersed in a liquid) are well-known examples of lyophobic colloids. We therefore need to understand the attractive forces that lead to flocculation and how they can be overcome by repulsive forces to produce colloids with the desired stability.

4.3 ATTRACTIVE SURFACE FORCES

Attractive surface forces, generally referred to as *van der Waals* forces, exist between all atoms and molecules regardless of what other forces may be involved. They have been discussed in detail by Isrealachvili (4). We shall first examine the origins of the van der Waals forces between atoms and molecules and later consider the attractive forces between macroscopic bodies such as particles.

4.3.1 Van der Waals Forces Between Atoms and Molecules

The van der Waals forces between atoms and molecules can be divided into three groups (5):

1. Dipole-dipole forces (Keesom forces). A molecule of HCl, because of its largely ionic bonding, has a positive charge and a negative charge separated by a small distance (~ 0.1 nm), i.e., it consists of a minute electric dipole. A polar HCl molecule will interact with another polar HCl molecule and produce a net attractive force.

2. Dipole-induced dipole forces (Debye forces). A polar molecule, e.g., HCl, can induce a dipole in a nonpolar atom or molecule, e.g., an argon atom, causing an attractive force between them.
3. Dispersion forces (London forces). This type of force exists between nonpolar atoms or molecules (e.g., between argon atoms).

To understand the origin of dispersion forces, consider an argon atom. Although the argon atom has a symmetrical distribution of electrons around the nucleus so that it has no dipole, this situation is only true as an average over time. At any instant, the electron cloud undergoes local fluctuations in charge density, leading to an instantaneous dipole. This instantaneous dipole produces an electric field that polarizes the electron distribution in a neighboring argon atom so that the neighboring atom itself acquires a dipole. The interaction between the two dipoles leads to an attractive force.

The attractive dispersion force can be calculated as follows (6). Suppose the first atom has a dipole moment μ at a given instant in time. The electric field E at a distance x along the axis of the dipole is

$$E = \frac{1}{4\pi\epsilon_o} \left(\frac{2\mu}{x^3} \right) \quad (4.1)$$

where ϵ_o is the permittivity of free space and x is much greater than the length of the dipole. If there is another atom at this point (Fig. 4.1), it becomes polarized and acquires a dipole moment μ' given by

$$\mu' = \alpha E \quad (4.2)$$

where α is the polarizability of the atom. A dipole μ' in a field E has a potential energy V given by

$$V = -\mu'E \quad (4.3)$$

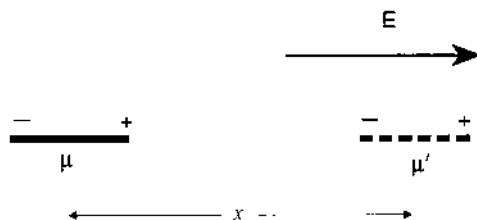


FIGURE 4.1 Polarization of a molecule by the field E due to a dipole, giving rise to mutual attraction.

Substituting for μ' and E gives

$$V = -\left(\frac{1}{4\pi\epsilon_o}\right)^2 \left(\frac{4\alpha\mu^2}{x^6}\right) \quad (4.4)$$

A rigorous derivation by London (1930) using quantum mechanics gives

$$V = -\frac{3}{4}\left(\frac{1}{4\pi\epsilon_o}\right)^2 \left(\frac{\alpha^2 h\nu}{x^6}\right) \quad (4.5)$$

where h is Planck's constant and ν is the frequency of the polarized orbital. The force between the atoms has a magnitude

$$F = \frac{\partial V}{\partial x} = \frac{B}{x^7} \quad (4.6)$$

where B is a constant. The Keesom and Debye forces are also proportional to $1/x^7$ and lead to a potential energy proportional to $1/x^6$. For dispersion forces, the dependence of V on $1/x^6$ is strictly applicable to separation distances that are small enough (less than a few tens of nanometers) that the interactions between the dipoles can be considered to be instantaneous. In this case, the forces are referred to as *nonretarded* forces. For larger separations, when the forces are described as *retarded* forces, V varies as $1/x^7$. Unless otherwise stated, we shall assume that nonretarded forces operate for the remainder of this chapter.

4.3.2 Van der Waals Forces Between Macroscopic Bodies

To determine the van der Waals forces between macroscopic bodies (e.g., two particles), we assume that the interaction between one molecule and a macroscopic body is simply the sum of the interactions with all the molecules in the body. We are therefore assuming simple additivity of the van der Waals forces and ignore how the induced fields are affected by the intervening molecules.

In the computation due to Hamaker (1937), individual atoms are replaced by a smeared-out, uniform density of matter (Fig. 4.2). An infinitesimally small volume Δv_1 in the first body exerts an attractive potential on an infinitesimally small volume Δv_2 according to the equation

$$V' = -\frac{C}{x^6} \rho_1 \Delta v_1 \rho_2 \Delta v_2 \quad (4.7)$$

where C is a constant and ρ_1 and ρ_2 are the numbers of molecules per unit volume in the two bodies. Of course, $\rho_1 = \rho_2$ if the two bodies consist of the same material.

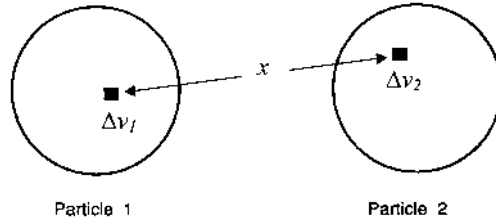


FIGURE 4.2 Additivity of the van der Waals force between macroscopic bodies. The total interaction is taken as the sum of the interactions between infinitesimally small elements in the two bodies.

The additivity of the forces now becomes an integration, with the total potential energy being

$$V_A = \int -\frac{C}{x^6} \rho_1 \rho_2 \, dv_1 \, dv_2 \quad (4.8)$$

Hamaker showed that Eq. (4.8) can be expressed as

$$V_A = -\frac{A}{\pi^2} \int \frac{dv_1 dv_2}{x^6} \quad (4.9)$$

where A , called the *Hamaker constant*, is equal to $C\pi^2\rho_1\rho_2$. According to Eq. (4.9), V_A is the product of a material-specific constant A and a geometrical term.

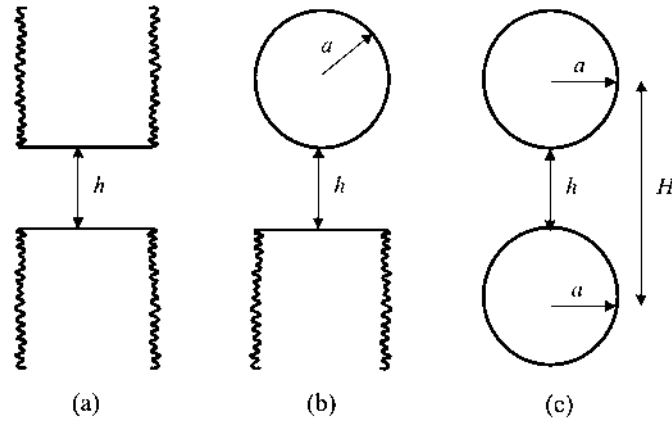
We will now consider some specific cases of interest in colloid science where analytical solutions to the geometric term in Eq. (4.9) may be obtained. For two semi-infinite parallel surfaces separated by a distance h (Fig. 4.3a), the potential energy is infinite. However, it is possible to define a finite interaction energy per unit area of one semi-infinite surface as

$$V_A = -\frac{A}{12\pi h^2} \quad (4.10)$$

For a sphere of radius a at a distance h from a flat semi-infinite solid (Fig. 4.3b), V_A is given by

$$V_A = -\frac{Aa}{6h} \left(1 + \frac{h}{2a+h} + \frac{h}{a} \ln \frac{h}{2a+h} \right) \quad (4.11)$$

Finally, the potential energy between two spheres of radius a that are separated by a distance h (Fig. 4.3c) is given by



$$V_A = -\frac{A}{12\pi h^2}$$

$$V_A = -\frac{Aa}{6h}$$

$$V_A = -\frac{Aa}{12h}$$

FIGURE 4.3 The potential energy of attraction between two bodies with specified geometries: (a) two semi-infinite parallel surfaces, (b) a sphere and a semi-infinite surface, (c) two spheres.

$$V_A = -\frac{A}{6} \left(\frac{2a^2}{H^2 - 4a^2} + \frac{2a^2}{H^2} + \ln \frac{H^2 - 4a^2}{H^2} \right) \quad (4.12)$$

where the distance between the centers of the spheres is equal to $h + 2a$. For small separations, where $h \ll a$, Eq. (4.12) gives

$$V_A = -\frac{Aa}{12h} \quad (4.13)$$

showing that V_A is proportional to $1/h$. In the case of large separations where $h \gg a$, the potential energy is

$$V_A = -\frac{16Aa^6}{9h^6} \quad (4.14)$$

showing that V_A is proportional to $1/h^6$.

4.3.3 Determination of the Hamaker Constant

We start by making an estimate of A for a simple model. The value of C is given by Eq. (4.5) if the x^6 term is removed from the denominator. For identical interacting systems, $A = C\pi^2\rho^2$, so that

$$A = -\frac{3}{4} h\nu \left(\frac{\alpha}{4\pi\epsilon_o} \right)^2 \pi^2 \rho^2 \quad (4.15)$$

The polarizability of an atom (or molecule) with a spherical shape of radius a is given by

$$\alpha = 4\pi\epsilon_o a^3 \quad (4.16)$$

For a cubic array of atoms, $\rho = (1/2a)^3$. Substituting for α and ρ in Eq. (4.15) gives

$$A = -\frac{3}{4} \frac{h\nu\pi^2}{64} \approx -\frac{h\nu}{8} \quad (4.17)$$

Taking the quantity $h\nu$ to be comparable with the first ionization potential (of the order 5–10 eV),

$$A \approx 1.5 \times 10^{-19} \text{ J} \quad (4.18)$$

For a large number of solids (Table 4.2), A has values in a fairly narrow range between 10^{-20} and 10^{-19} J (~ 2.5 – 25 kT , where k is the Boltzmann constant and T is room temperature in degrees Kelvin).

The method of pair-wise addition, sometimes referred to as the *microscopic* approach, was originally used by Hamaker (7) to calculate A from the polarizabilities and number densities of the atoms in the two interacting bodies. However, the method suffers from several problems. For example, it neglects many-body interactions between the atoms. It is evident that if an atom X in Particle 1 exerts a force on atom Y in Particle 2 (Fig. 4.2), then the presence of neighboring atoms in Particle 1 and Particle 2 is bound to influence the interaction between atoms X1 and Y2. It is also not clear how the addition needs to be modified if the intervening medium between Particles 1 and 2 is not vacuum or air but another dielectric medium. A solution to these problems was provided by Lifshitz (8), who treated the bodies and the intervening medium in terms of their bulk properties, specifically their dielectric constants. The Lifshitz theory, sometimes referred to as the *macroscopic* approach, is fairly complex and has been reviewed in a number of textbooks and articles at various levels of sophistication (9–12). Various methods for calculating A from the Lifshitz theory have been described (13,14) and calculated values for several ceramic materials are given in Table 4.2.

The Hamaker constant can be determined experimentally by direct measurement of the surface forces as a function of separation for bodies separated by vacuum, air, or liquids. Differences between the calculated and measured values depend on the complexity of the theoretical calculations and the accuracy of the physical data used in the models (15). The first measurements down to separations

TABLE 4.2 Nonretarded Hamaker Constants at 298K for Ceramic Materials
When the Intervening Medium is Vacuum or Water

Material	Crystal structure	Hamaker constant (10^{-20} J)	
		Vacuum	Water
α -Al ₂ O ₃	Hexagonal	15.2	3.67
BaTiO ₃	Tetragonal	18	8
BeO ^a	Hexagonal	14.5	3.35
C (diamond)	Cubic	29.6	13.8
CaCO ₃ ^a	Trigonal	10.1	1.44
CaF ₂	Cubic	6.96	0.49
CdS	Hexagonal	11.4	3.40
CsI	Cubic	8.02	1.20
KBr	Cubic	5.61	0.55
KCl	Cubic	5.51	0.41
LiF	Cubic	6.33	0.36
MgAl ₂ O ₄	Cubic	12.6	2.44
MgF ₂	Tetragonal	5.87	0.37
MgO	Cubic	12.1	2.21
Mica	Monoclinic	9.86	1.34
NaCl	Cubic	6.48	0.52
NaF	Cubic	4.05	0.31
PbS	Cubic	8.17	4.98
6H-SiC	Hexagonal	24.8	10.9
β -SiC	Cubic	24.6	10.7
β -Si ₃ N ₄	Hexagonal	18.0	5.47
Si ₃ N ₄	Amorphous	16.7	4.85
SiO ₂ (quartz)	Trigonal	8.86	1.02
SiO ₂	Amorphous	6.5	0.46
SrTiO ₃	Cubic	14.8	4.77
TiO ₂ ^a	Tetragonal	15.3	5.35
Y ₂ O ₃	Hexagonal	13.3	3.03
ZnO	Hexagonal	9.21	1.89
ZnS	Cubic	15.2	4.80
ZnS	Hexagonal	17.2	5.74
ZrO ₂ /3 mol% Y ₂ O ₃	Tetragonal	20.3	7.23

^a Average value calculated using a weighted procedure.

Source: Ref. 14.

of 2 nm or less were performed by Tabor and Winterton (16) and by Israelachvili and Tabor (17) using a cantilever spring to measure the force between molecularly smooth surfaces of mica and a piezoelectric crystal to control the separation. By fitting the measured surface force to the theoretical expression for the appropriate geometry, they found that nonretarded forces operate for separations less than ~ 10 nm and the nonretarded Hamaker constant $A = 10^{-19}$ J. More recently, the relatively new technique of atomic force microscopy (18,19) has seen considerable use (20–23).

4.3.4 Effect of the Intervening Medium

The Lifshitz theory, as outlined earlier, is fairly difficult, and we provide here only approximate relations for the effect of the intervening medium. If we consider two bodies with dielectric constants ϵ_1 and ϵ_2 separated by a medium with dielectric constant ϵ_3 , the theory predicts that the Hamaker constant A is proportional to a term given by the equation

$$A \propto \left(\frac{\epsilon_1 - \epsilon_3}{\epsilon_1 + \epsilon_3} \right) \times \left(\frac{\epsilon_2 - \epsilon_3}{\epsilon_2 + \epsilon_3} \right) \quad (4.19)$$

According to Eq. (4.19), if $\epsilon_1 > \epsilon_3 > \epsilon_2$, the value of A is negative, that is, there is a repulsive force. It is difficult to explain this in terms of the Hamaker method of pair-wise interactions. One might say that the intervening medium with dielectric constant ϵ_3 likes itself more than the two bodies.

In colloidal systems, the bodies 1 and 2 are identical so that

$$A = c \left(\frac{\epsilon_1 - \epsilon_3}{\epsilon_1 + \epsilon_3} \right)^2 \quad (4.20)$$

where c is a constant. We see that A is always positive, that is, the van der Waals force is always attractive, whether ϵ_3 is greater or smaller than ϵ_1 . The intervening medium always leads to a reduction in the attractive force when compared to the force when the medium is air or vacuum ($\epsilon_3 = 1$). Table 4.2 also gives the Hamaker constants calculated from the Lifshitz theory for several ceramic materials when the intervening medium is water.

4.4 STABILIZATION OF COLLOIDAL SUSPENSIONS

Consider a suspension of colloidal particles. The particles undergo Brownian motion (similar to the motion of pollen in a liquid) and will eventually collide. The potential energy of attraction V_A between two particles with radius a and a

distance h apart is given by Eq. (4.13). Assuming that this equation is valid down to contact between the particles, then we can calculate V_A by putting $h \approx 0.3$ nm. Taking $A \approx 10^{-20}$ J, for particles with a radius $a = 0.2$ μm , V_A has a value of $\sim 5 \times 10^{-19}$ J. The thermal energy of the particles is kT , where k is the Boltzmann constant and T is the absolute temperature. Near room temperature ($T \approx 300\text{K}$), kT is of the order of 4×10^{-21} J and this value is much smaller than V_A for the particles in contact. Thus the particles will stick together on collision because the thermal energy is insufficient to overcome the attractive potential energy. Flocculation will therefore occur unless some method is found to produce a repulsion between the particles which is sufficiently strong to overcome the attractive force. There are several ways for achieving this, but the most commonly used are (Fig. 4.4)

1. *Electrostatic stabilization* in which the repulsion between the particles is based on electrostatic charges on the particles
2. *Steric stabilization* in which the repulsion is produced by uncharged polymer chains adsorbed onto the particle surfaces
3. *Electrosteric stabilization*, consisting of a combination of electrostatic and steric repulsion, achieved by the adsorption of charged polymers (polyelectrolytes) onto the particle surfaces.

4.5 ELECTROSTATIC STABILIZATION

Electrostatic stabilization, as outlined above, is said to occur when the repulsion between the particles is achieved by electrostatic charges on the particles. The repulsion is not, however, a simple case of repulsion between charged particles. An electrical double layer of charge is produced around each particle, and the repulsion occurs as a result of the interaction of the double layers. By way of an introduction to the analysis of the electrical double layer, we consider how particles acquire an electrostatic charge in an aqueous liquid (water) and the general principle of the double layer.

4.5.1 The Development of Charges on Oxide Particles in Water

The main processes by which particles dispersed in a liquid can acquire a surface charge are (1) preferential adsorption of ions, (2) dissociation of surface groups, (3) isomorphic substitution, and (4) adsorption of charged polymers (polyelectrolytes). Preferential adsorption of ions from solution is the most common process for oxide particles in water, whereas isomorphic substitution is commonly found in clays. The adsorption of polyelectrolytes is the main charging mechanism in electrosteric stabilization and will be discussed later. The dissociation of ionizable

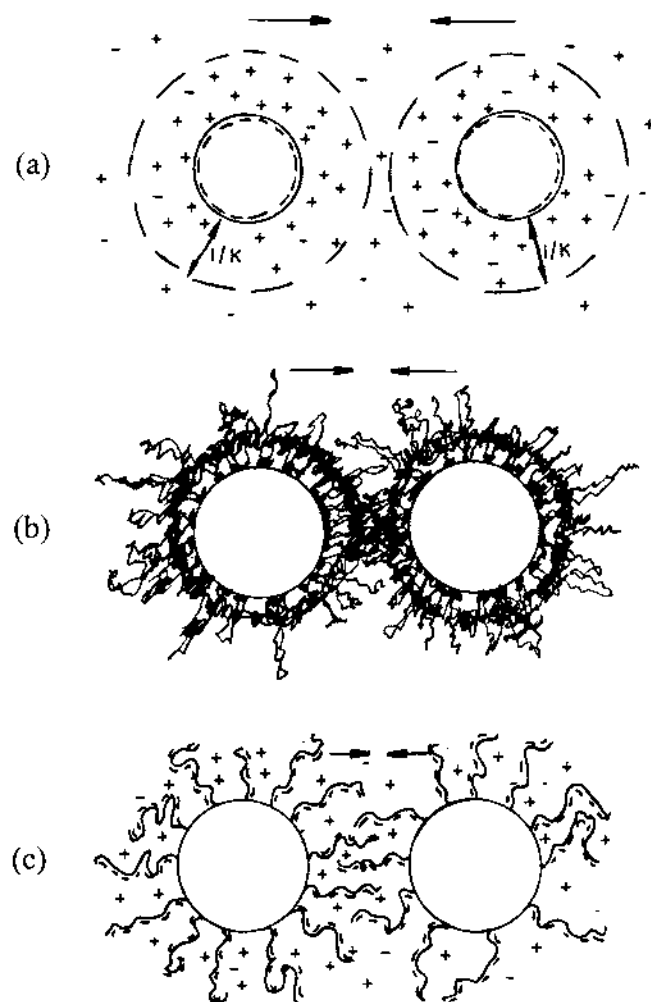


FIGURE 4.4 Schematic representation of (a) electrostatic stabilization for negatively charged particles, (b) steric stabilization, and (c) electrosteric stabilization. (From Ref. 34.)

surface groups such as sulfate, sulfonate, carboxyl, and amino groups is reviewed in Ref. 24.

4.5.1.1 Isomorphic Substitution

In the crystal lattice of clay minerals, some of the cations are replaced by other cations of lower valence without altering the crystal structure; e.g., Si^{4+} ions are replaced by Al^{3+} or Mg^{2+} ions, and Al^{3+} ions by Mg^{2+} ions. This substitution leads to a deficit of positive charges, which is balanced by other positive ions (e.g., Na^+ , K^+ , or Ca^{2+}) adsorbed on the basal surfaces (the larger flat surfaces) of the platelike clay particles. The process occurs naturally in the weathering of clays. In the case of the clay mineral pyrophyllite, $\text{Al}_2(\text{Si}_2\text{O}_5)_2(\text{OH})_2$, isomorphic substitution in which Mg^{2+} replaces some of the Al^{3+} ions in the lattice leads to montmorillonite, $\text{Na}_{0.33}(\text{Al}_{1.67}\text{Mg}_{0.33})(\text{Si}_2\text{O}_5)_2(\text{OH})_2$, another mineral with the same crystal structure in which the charge deficit is balanced by Na^+ ions on the particle surfaces. When the clay mineral montmorillonite is dispersed in water, the Na^+ ions pass freely into solution, leaving negatively charged basal surfaces (Fig. 4.5).

The extent of isomorphic substitution is dictated by the nature of the clay, and this is expressed by the cation exchange capacity (CEC). The CEC of a clay is the number of charges on the clay (expressed in coulombs per kilogram) which can be replaced in solution. It is typically in the range of 10^3 to 10^5 C/kg and for a given clay is not sensitive to variables such as pH or concentration of the electrolyte in solution.

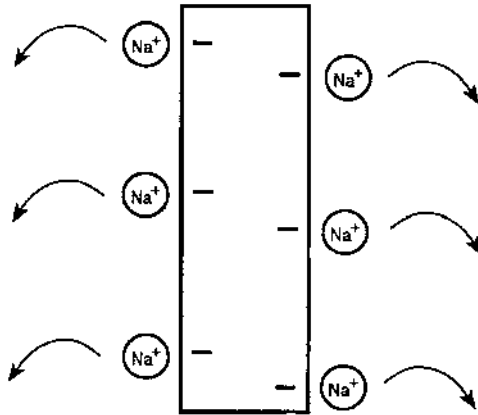
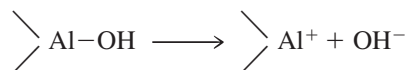


FIGURE 4.5 The production of charges on the basal surfaces of clay particles (e.g., montmorillonite) in aqueous liquids.

The edges of clay particles, where imperfections occur due to bond breakage, carry a positive charge in water at low pH, and this decreases to zero as the pH is raised to ~ 7 . The charge is not due to isomorphic substitution but is generally considered to be due to dissociation of OH groups from aluminum octahedra:



The plasticity of clay suspensions results in part from the “house of cards” structure formed by the attraction of the oppositely charged basal surfaces and edges (Fig. 4.6).

4.5.1.2 Adsorption of Ions from Solution

In the process of preferential adsorption of ions from solution, an electrolyte such as an acid, a base, or a metal salt is added to the aqueous liquid. Ions preferentially adsorb onto the surface of the dispersed particles leading to a charge on the particle surface. Because the system consisting of the particle and the electrolyte must be electrically neutral, an equal and opposite countercharge exists in the solution. Most oxide surfaces are hydrated; for an oxide of a metal M, there will be MOH groups on the surface, as illustrated in Fig. 4.7 for SiO_2 . In acidic solutions, adsorption of H^+ ions (or hydronium ions, H_3O^+) produces a positively charged surface, while in basic solutions, adsorption of OH^- ions (or the dissociation of H^+ ions) leads to a negatively charged surface. Thus oxide surfaces are positively charged at low pH and negatively charged at high pH. At some intermediate pH, the adsorption of H^+ ions will balance that of the OH^- ions, and the

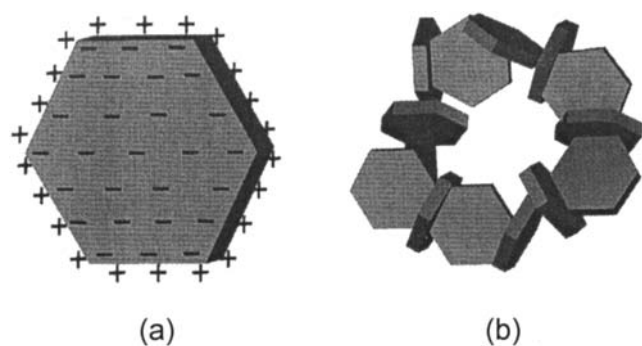


FIGURE 4.6 Schematic illustration of clay particles in water showing (a) surface charges on an individual particle and an (b) aggregated particle network formed by the attraction of oppositely charged faces and edges.

particle surface will be effectively neutral. The pH value where the particle surface has a net charge of zero (denoted as pH_0) is defined as the *point of zero charge* (PZC). The acid-base properties of oxide surfaces are commonly characterized by the PZC. The more “acidic” oxides such as SiO_2 have a low PZC while the more “basic” oxides such as MgO have a high PZC.

The PZC is measured by potentiometric acid-base titrations (25). As discussed later, it is usually more convenient to measure the ζ -potential of the particles, which corresponds to the electrostatic potential at a short distance from the particle surface (at the surface of the Stern layer). The pH where the ζ -potential is zero is called the *isoelectric point* (IEP). For oxides, commonly $\text{PZC} \approx \text{IEP}$. However, when the ζ -potential measurements are carried out in the presence of surface active species such as multivalent ions and charged dispersant molecules, the PZC may be somewhat different from the IEP. Table 4.3 gives the approximate IEP values for several oxides (26,27).

The PZC of pure oxides can be calculated in two ways. In the Parks theory (27), hydroxyl groups on the surface of the oxide are considered to act as acids or bases, according to the equilibria



and

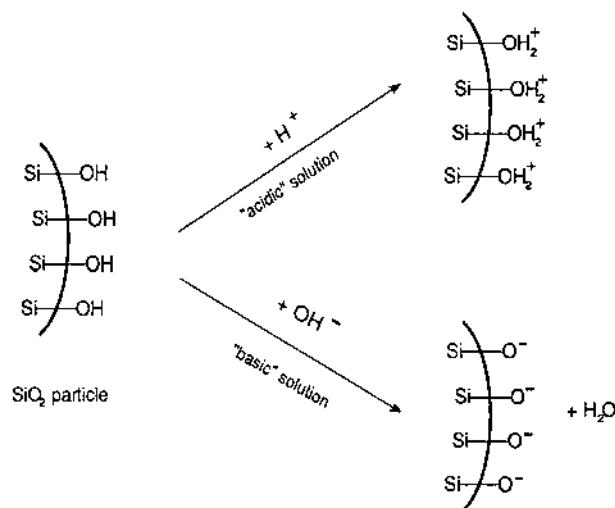


FIGURE 4.7 The production of surface charges on SiO_2 particles by adsorption of ions from acidic or basic solutions.

TABLE 4.3 Nominal Isoelectric Points (IEPs) of Some Oxides

Material	Nominal composition	IEP
Quartz	SiO ₂	2–3
Soda-lime-silica glass	1.0Na ₂ O·0.6CaO·3.7SiO ₂	2–3
Potassium feldspar	K ₂ O·Al ₂ O ₃ ·6SiO ₂	3–5
Zirconia	ZrO ₂	4–6
Tin oxide	SnO ₂	4–6
Titania	TiO ₂	4–6
Bariun titanate	BaTiO ₃	5–6
Kaolin	Al ₂ O ₃ ·SiO ₂ ·2H ₂ O	5–7
Mullite	3Al ₂ O ₃ ·2SiO ₂	6–8
Ceria	CeO ₂	6–7
Chromium oxide	Cr ₂ O ₃	6–7
Hydroxyapatite	Ca ₁₀ (PO ₄) ₆ (OH) ₂	7–8
Haematite	Fe ₂ O ₃	8–9
Alumina	Al ₂ O ₃	8–9
Zinc oxide	ZnO	9
Calcium carbonate	CaCO ₃	9–10
Nickel oxide	NiO	10–11
Magnesia	MgO	12

Source: Refs. 26 and 27.

so that the equilibrium between the positive and negative charges on the surface can be written



with an equilibrium constant K given by

$$K = \frac{[\text{MOH}_2^+]}{[\text{MO}^-][\text{H}^+]^2} \quad (4.23)$$

where the quantities in the square brackets represent the concentrations of the species. At the PZC, $[\text{MOH}_2^+] = [\text{MO}^-]$, so that

$$\text{PZC} = \frac{1}{2} \log K \quad (4.24)$$

By relating K to the free energy change due to the approach of the 2H^+ ions to the MO^- ion, Park showed that

$$PZC = A_1 - B_1 \frac{Z}{r} \quad (4.25)$$

where A_1 and B_1 are constants, Z is the ionic charge of the cation, and $r = 2r_o + r_+$, where r_o and r_+ are the ionic radii of the oxygen ion and the cation, respectively. A good correlation between the measured PZC values and those calculated from Eq. (4.25) is shown in Figure 4.8. Yoon et al. (28) have developed an improved version of the Parks relationship.

The second method considers the surface acidity to result from the electron acceptor character of the oxide surface (29). This is related to the Lewis acid-base concept where, for an ionic oxide, the acid entity is the cation with the base being the oxygen anions. For an oxide M_xO_y , the surface acidity has been shown to be related to the ionization potential (IP) of the metal M according to

$$PZC = A_2 + B_2 (IP) \quad (4.26)$$

where A_2 and B_2 are constants. The correlation between PZC data and Eq. (4.26) is also found to be good (29).

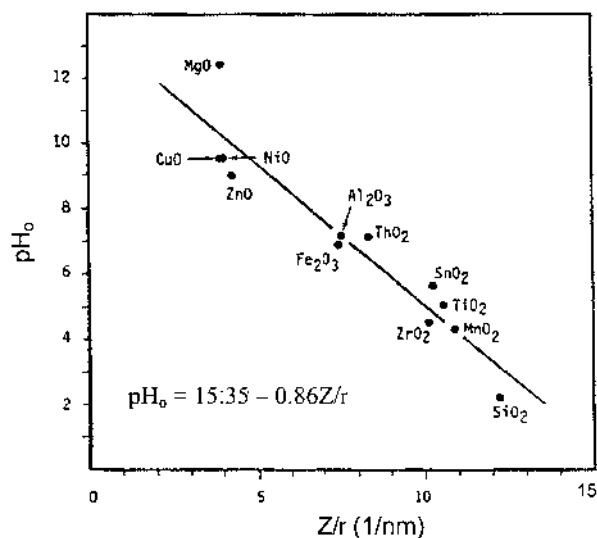


FIGURE 4.8 The Parks relationship between the point of zero charge pH_o and Z/r , where Z is the ionic charge of the cation and r is the sum of the cation radius and the oxygen ion diameter. (From Ref. 27.)

4.5.2 Origins of the Electrical Double Layer

For electrostatically stabilized colloidal suspensions, the charges, as we have seen, consist of a surface charge on the particles and an equal and opposite countercharge in the solution. Suppose the particle has a positive surface charge due to preferential adsorption of positive ions. In the complete absence of thermal motion an equal number of negative ions (counterions) would adsorb onto the positive charge and neutralize it. However, such a compact double layer does not form because of thermal motion. Instead, the counterions are spread out in the liquid to form an diffuse double layer as shown in Fig. 4.9. There is a fairly rapid change in the concentration of the positive and negative ions as we move away from the surface (Fig. 4.10a). As a result, the electrical potential also falls off rapidly with distance from the surface (Fig. 4.10b).

As two particles approach one another in the liquid, the diffuse double layers will start to overlap. It is the interaction between the double layers that gives rise to the repulsion between the particles. If the repulsion is strong enough, it can overcome the van der Waals attractive force, thereby producing a stable colloidal suspension. As a prelude to examining the interactions between double layers, we start with an isolated double layer associated with a single particle.

4.5.3 Isolated Double Layer

The electrical properties of an isolated double layer can be described in terms of the variation of the electrical charge or the electrical potential (Fig. 4.10). The two are related through the capacitance so that if one is known, the other can be found. We shall consider the potential mainly. We shall also consider the analysis in one dimension (the x direction) and make a number of simplifying assumptions:

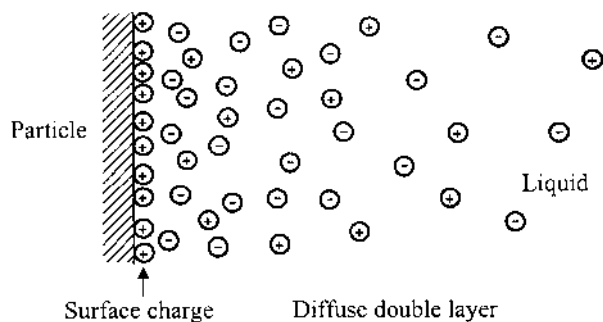


FIGURE 4.9 The distribution of positive and negative charges in the electrical double layer associated with a positively charged surface in a liquid.

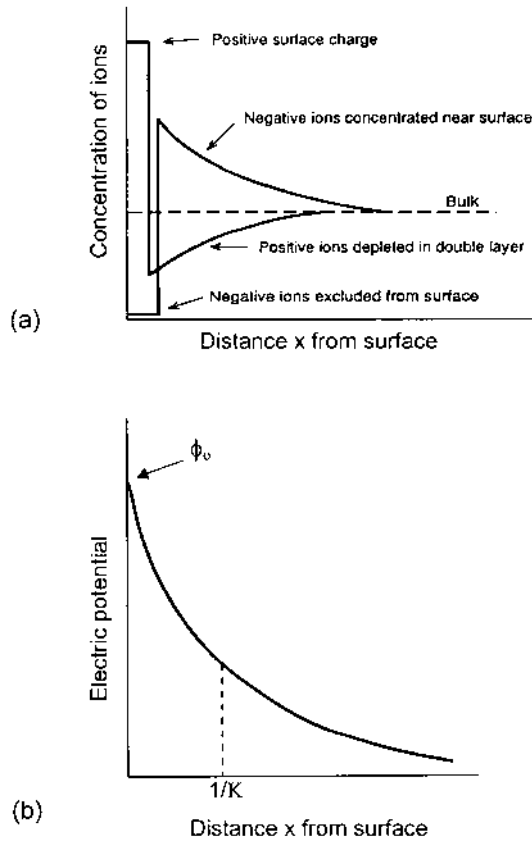


FIGURE 4.10 (a) Concentration of positive and negative ions as a function of distance from the particle surface. (b) The electrical potential ϕ as a function of distance from the particle surface. The distance equal to $1/K$ is the Debye length.

(1) the particle surface is taken to be flat and (2) the electrolyte is symmetrical (e.g., HCl) in that the valence of the positive ions is equal in magnitude to the valence of the negative ions.

The variation in the electrical potential ϕ with distance x is governed by Poisson's equation:

$$\nabla^2 \phi(x) = -\frac{\rho(x)}{\epsilon \epsilon_0} \quad (4.27)$$

where $\rho(x)$ is the charge density at a distance x from the surface, ϵ is the dielectric constant of the liquid medium, and ϵ_0 is the permittivity of vacuum. The charge density is obtained from the sum of the contributions of the individual ions:

$$\rho(x) = \sum_i c_i z_i F \quad (4.28)$$

where c_i is the concentration and z_i is the valence of the i ions, and the summation is over the positive and negative ions in the solution. The concentration c_i is given by the Boltzmann distribution:

$$c_i = c_{\infty i} \exp\left(\frac{-z_i F \phi(x)}{RT}\right) \quad (4.29)$$

where $c_{\infty i}$ is the concentration of the i ions very far from the particle surface, F is the Faraday constant, R is the gas constant, and T is the absolute temperature. Equations (4.27) to (4.29) give

$$\nabla^2 \phi(x) = -\frac{1}{\epsilon \epsilon_0} \sum_i c_{\infty i} z_i F \exp\left(\frac{-z_i F \phi(x)}{RT}\right) \quad (4.30)$$

Summing over the positive (+) and negative (-) ions and putting $z_+ = -z_- = z$ (symmetrical electrolyte) and $c_{\infty +} = c_{\infty -} = c_{\infty}$ (the concentrations of the positive and negative ions far from the surface are equal), Eq. (4.30) reduces to

$$\nabla^2 \phi(x) = \frac{2czF}{\epsilon \epsilon_0} \sinh\left(\frac{zF \phi(x)}{RT}\right) \quad (4.31)$$

For low surface potential, referred to as the *Debye-Hückel approximation*, such that

$$zF\phi \ll RT \quad (4.32)$$

and making the substitution

$$K^2 = \frac{2cz^2 F^2}{\epsilon \epsilon_0 RT} \quad (4.33)$$

Equation (4.31) becomes

$$\nabla^2 \phi(x) = K^2 \phi(x) \quad (4.34)$$

With the appropriate boundary conditions:

$$\phi = \phi_o \text{ at } x = 0 \quad \phi = 0 \text{ at } x = \infty \quad (4.35)$$

where ϕ_o is the potential at the surface of the particle, the solution of Eq. (4.34) is

$$\phi = \phi_o \exp(-Kx) \quad (4.36)$$

The term K occurs frequently in the analysis of the electrical double layer, and $1/K$ has the dimensions of length. At a distance $x = 1/K$ the potential ϕ has fallen to $1/e$ of its value at the surface of the particle, and beyond this the change in ϕ is small. Thus $1/K$ may be considered the *thickness* of the double layer and is usually referred to as the *Debye length*. According to Eq. (4.33) the thickness of the double layer depends on a number of experimental parameters. As we shall see later, these parameters can be varied to control the magnitude of the repulsion between two double layers and thereby the stability of the suspension.

Equation (4.31) can be integrated twice to give (30)

$$\tanh\left(\frac{zF\phi(x)}{4RT}\right) = \tanh\left(\frac{zF\phi_o}{4RT}\right) \exp(-Kx) \quad (4.37)$$

Equation (4.37), referred to as the *Gouy-Chapman equation*, is valid for any value of the surface potential ϕ_o . However, for ϕ_o less than ~ 50 mV, the difference in the ϕ values found from the Debye-Hückel approximation and the Gouy-Chapman equation is insignificant (Fig. 4.11).

A more rigorous analysis shows that the electrical double layer consists of a compact layer (about a few molecular diameters thick) referred to as the *Stern*

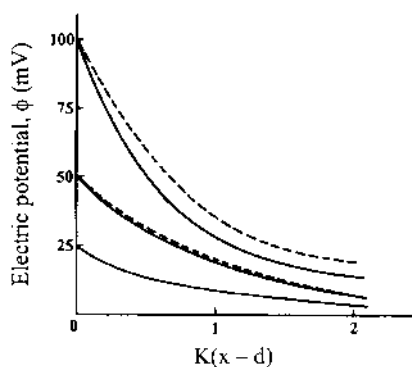


FIGURE 4.11 Comparison of the predictions of the Debye-Hückel and Gouy-Chapman equations for the potential ϕ in the electrical double layer. The Debye-Hückel equation can be used with insignificant error up to ~ 50 mV. (From Ref. 3.)

layer and a more diffuse layer referred to as the *Gouy-Chapman layer*. The electrical potential in the Gouy-Chapman layer decreases exponentially with distance according to Eq. (4.36) or (4.37) but decreases less steeply in the Stern layer (Fig. 4.12). However, this refinement in the double-layer theory will not be considered any further in this book.

4.5.4 Surface Charge

For electroneutrality, the surface charge density (charge per unit area) must be equal to the integrated charge density in the solution; that is,

$$\sigma_o = - \int_0^{\infty} \rho \, dx \quad (4.38)$$

Substituting for ρ from Eq. (4.27), then

$$\sigma_o = \int_0^{\infty} \epsilon \epsilon_o \nabla^2 \phi(x) \, dx = \left(\epsilon \epsilon_o \frac{d\phi}{dx} \right)_0^{\infty} = -\epsilon \epsilon_o \left(\frac{d\phi}{dx} \right)_{x=0} \quad (4.39)$$

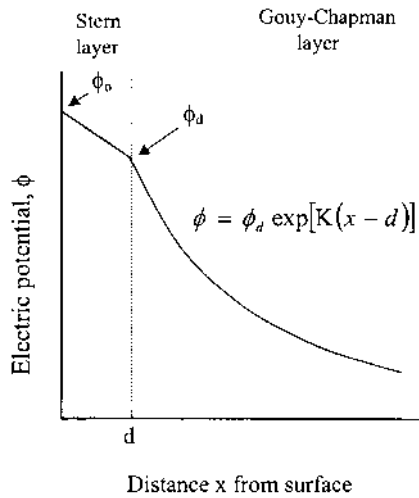


FIGURE 4.12 The electrical double layer consists of a compact Stern layer and a more diffuse Gouy-Chapman layer.

Equation (4.31) can be integrated once to give

$$\left(\frac{d\phi}{dx}\right)_{x=0} = -\left(\frac{8RTc}{\epsilon\epsilon_o}\right)^{1/2} \sinh\left(\frac{zF\phi_o}{2RT}\right) \quad (4.40)$$

Substituting in Eq. (4.39) gives

$$\sigma_o = (8\epsilon\epsilon_o RTc)^{1/2} \sinh\left(\frac{zF\phi_o}{2RT}\right) \quad (4.41)$$

For low potential (Debye-Huckel approximation), Eq. (4.41) becomes

$$\sigma_o = \epsilon\epsilon_o K\phi_o \quad (4.42)$$

The capacitance is defined as the charge divided by the voltage, and for a parallel plate capacitor the capacitance is equal to $\epsilon\epsilon_o/t$, where t is the distance between the plates. We can therefore see from Eq. (4.42) that the electrical double layer can be treated as a parallel plate capacitor with a thickness of $1/K$.

4.5.5 Repulsion Between Two Double Layers

Two colloid particles will begin to interact as soon as their double layers overlap. We consider the simplest case of two parallel surfaces at a distance h apart in an electrolyte. The electrical potential within the double layers consists of two symmetrical curves resembling that shown in Fig. 4.10b, and the net effect is roughly additive (Fig. 4.13). As the distance h decreases the overlap of the double layers causes the potential to increase, giving rise to a repulsive force that tends to oppose further approach.

The general theory of the interaction between electrical double layers is known as the DLVO theory (after Derjaguin, Landau, Verwey, and Overbeek). It applies to the diffuse Gouy-Chapman layer. The theory is beyond the scope of this book, but if we consider the particles to be two parallel surfaces, the repulsion can be approximated by a fairly simple method, called the *Langmuir force method*. The interaction between the particles can be analyzed in terms of a repulsive force or a repulsive potential energy (i.e., the work done in bringing the particles from infinity to the desired distance apart). Normally, the repulsive potential energy is used.

The ionic concentration at a point midway between the two charged surfaces (at A in Fig. 4.14) will be greater than that far away from the surfaces (at B). This gives rise to an excess osmotic pressure Π that acts to push the surfaces apart. The excess osmotic pressure at A is given by (1)

$$\Pi = 2RTc \left[\cosh\left(\frac{zF\phi_m}{RT}\right) - 1 \right] \quad (4.43)$$

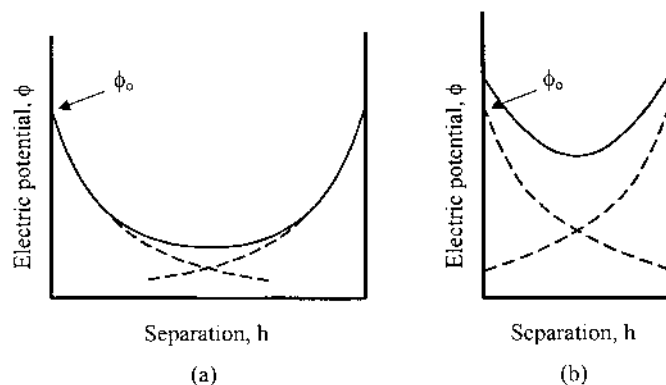


FIGURE 4.13 (a) The electrical potential in the electrolyte solution between two parallel surfaces for (a) large separation and (b) small separation. As the separation is decreased, the potential is increased, implying a repulsion.

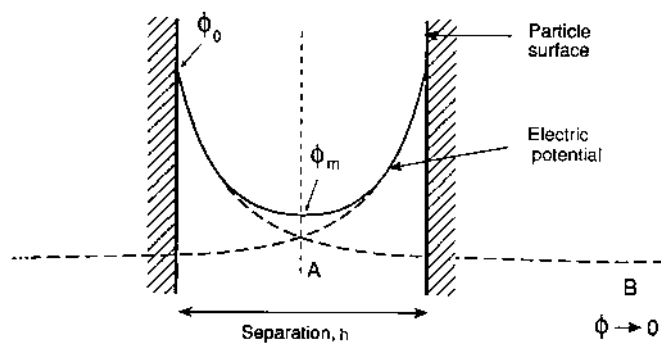


FIGURE 4.14 Overlap of the electrical double layers associated with two parallel surfaces leads to an increase in the ionic concentration. The osmotic pressure that results from the increased concentration acts to push the surfaces apart.

where ϕ_m is the net electrostatic potential at A arising from the overlap of the double layers. For large separation h , the net potential is roughly additive so

$$\phi_m = 2\phi \quad (4.44)$$

where ϕ is the potential of an isolated double layer at A. When ϕ_m is small, that is, $zF\phi_m \ll RT$, Eq. (4.43) reduces to

$$\Pi = \frac{cz^2 F^2 \phi_m^2}{RT} \quad (4.45)$$

For low surface potential ϕ_o , the Debye-Hückel approximation can be used:

$$\phi = \phi_o \exp\left(-\frac{Kh}{2}\right) \quad (4.46)$$

The repulsive potential energy V_R between the charged surfaces at a separation h is the work done in bringing the surfaces from ∞ to a distance h apart, so that

$$V_R = \int_h^\infty \Pi dh \quad (4.47)$$

Using Eqs. (4.44)–(4.46) and integrating,

$$V_R = 2\varepsilon\varepsilon_o K \phi_o^2 \exp(-Kh) \quad (4.48)$$

Equation (4.48) is valid for low ϕ_o and for large separations when the plates interact under conditions of constant potential or constant charge.

For large ϕ_o , the Gouy-Chapman equation must be used [Eq. (4.37)]. Using Eq. 4.45 (valid for low ϕ_m) and integrating (1), we obtain

$$V_R = 2\varepsilon\varepsilon_o K \left(\frac{4RT\gamma}{zF}\right)^2 \exp(-Kh) \quad (4.49)$$

where γ is defined by

$$\gamma = \tanh\left(\frac{zF\phi_o}{4RT}\right) \quad (4.50)$$

For two spherical particles of radius a at a distance h apart (see Fig. 4.3c), when the double layer around the particles is very extensive such that $Ka < 5$, V_R is given approximately by (2)

$$V_R \approx 2\pi a \varepsilon \varepsilon_o \phi_o^2 \exp(-Kh) \quad (4.51)$$

Equation (4.51) is valid for low ϕ_o and for constant potential or constant charge. For large values of Ka (> 10) and for low ϕ_o , V_R is given by

$$V_R = 2\pi a \varepsilon \varepsilon_o \phi_o^2 \ln[1 + \exp(-Kh)] \quad (4.52)$$

4.5.6 Stability of Electrostatically Stabilized Colloids

We now consider what happens when two colloid particles approach one another. As the double layers start to overlap, the resulting repulsion opposes the attraction from van der Waals interactions. The total potential energy V_T is given by

$$V_T = V_A + V_R \quad (4.53)$$

Using the convention that repulsive potentials are positive and attractive potentials are negative, Fig. 4.15 shows an example of V_A for the van der Waals attraction and V_R for the double layer repulsion. The resultant curve for V_T shows a deep minimum at M_1 corresponding approximately to contact between the particles, a secondary minimum at M_2 , and a maximum between M_1 and M_2 . For two particles initially far apart approaching one another to a separation M_2 , if the thermal energy (kT) of the particles is small compared to the depth of M_2 , the particles will not be able to escape from one another. Flocculation will result, leading to a sediment of loosely packed particles. Restabilization of the colloid can be achieved by heating (increasing kT), by changing the electrolyte concentration to increase the double layer repulsion, or a combination of the two. This process of restabilizing a flocculated suspension is referred to as *peptization*.

In practice, the resultant curve for V_T depends on the relative magnitudes of V_A and V_R . For a given system (e.g., a suspension of Al_2O_3 particles in water),

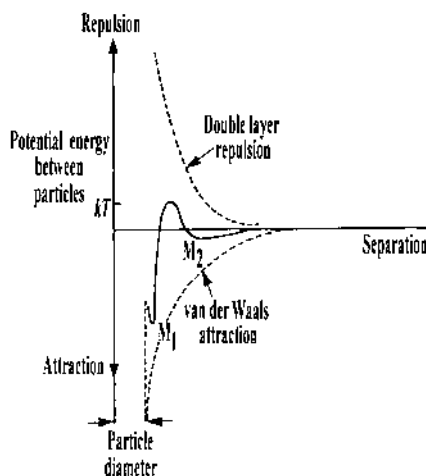


FIGURE 4.15 The potential energy between two particles in a liquid resulting from the effects of the van der Waals attraction and the double layer repulsion.

V_A is approximately constant, but V_R can be changed significantly by changing the concentration and the valence of the ions in solution [see Eq. (4.51)]. These two experimental parameters provide a useful way for controlling the stability of the colloid. Figure 4.16 summarizes four main types of curves for V_T . In curve A, the repulsion is weak and V_T is not significantly different from the curve for the van der Waals attraction. The particles attract one another and reach equilibrium at the primary minimum M_1 . A sediment consisting of clusters of particles almost in contact is produced. This is known as *coagulation*, in contrast to flocculation in which, as we have outlined above, the particles are loosely held together at relatively large separations.

In curve B the repulsion is increased, and this leads to a secondary minimum at M_2 which is shallow compared to kT . There is therefore little chance for flocculation. However, the height of the maximum at P_1 is comparable to kT so that particles may be able to surmount the energy at P_1 and fall into the primary minimum at M_1 . Irreversible coagulation will result because the depth of M_1 is much greater than kT .

The double-layer repulsion has become so large in curve C that there is no secondary minimum at M_2 . Furthermore, the height of the maximum P_1 is much

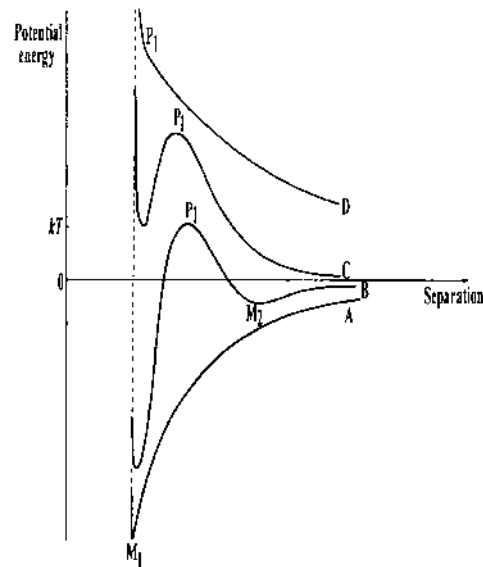


FIGURE 4.16 Four examples of the resultant potential energy between two particles. The repulsion between the particles increases in going from curve A to curve D.

greater than kT so that the particles have almost no chance of surmounting the energy barrier. Curve C therefore represents the situation for a stable colloid.

Finally, in curve D, the attraction is much smaller than the repulsion over all separations so that there is no minimum in the curve. An extremely stable colloid will be produced under these conditions, but the strong repulsion limits the concentration of particles in suspension. Addition of a salt can lead to compression of the double layer and a reduction in the viscosity.

Some general features of the DLVO theory have been confirmed (31) by direct measurement of the surface forces between two sapphire platelets immersed in an aqueous solution of NaCl at pH values from 6.7 to 11 using a surface force apparatus (32). Measurements of the electrical double layer and van der Waals forces were found to fit the theoretical predictions.

4.5.7 Kinetics of Flocculation

Flocculation is a kinetic process and the rate at which a colloidal suspension flocculates forms one of its most important characteristics. Smoluchowski (1917) distinguished between *rapid flocculation* and *slow flocculation* and developed a theory based on the rate of collision between the particles (2). Rapid flocculation is considered to take place in the absence of a potential barrier and is limited only by the rate of diffusion of the particles towards one another. The flocculation time, defined as the time $t_{1/2}$ required for the number of particles to be reduced by one-half of the initial value is given by

$$t_{1/2} = \frac{3\eta}{4kTn_o} \quad (4.54)$$

where η is the viscosity of the liquid, k is the Boltzmann constant, T is the absolute temperature, and n_o is the particle concentration (number per unit volume). For particles of radius a in water, Eq. (4.54) becomes

$$t_{1/2} \approx \frac{2 \times 10^{11}}{n_o} \text{ seconds} \quad (4.55)$$

where n_o is expressed in units of number per cm^3 . The particle volume fraction f is related to n_o by the relation $n_o = f/(4\pi a^3/3)$; so Eq. (4.55) can also be written

$$t_{1/2} \approx \frac{a^3}{f} \text{ seconds} \quad (4.56)$$

where a is expressed in microns (μm).

For slow flocculation in the presence of a potential barrier, analysis leads to

$$R_s = \frac{R_f}{W} \quad (4.57)$$

where R_s and R_f are the rates of slow and rapid flocculation, respectively, and W is a factor known as the *stability ratio*. For a repulsive potential energy barrier with a maximum V_{\max} , the stability ratio is given by

$$W = \frac{1}{2Ka} \exp\left(\frac{V_{\max}}{kT}\right) \quad (4.58)$$

showing that W depends exponentially on V_{\max} and linearly as the normalized double layer thickness $(Ka)^{-1}$.

4.5.8 Electrokinetic Phenomena

Electrokinetic phenomena involve the combined effects of motion and an electric field. When an electric field is applied to a colloidal suspension, the particles move with a velocity that is proportional to the applied field strength. The motion is called *electrophoresis*. It is a valuable source of information on the sign and magnitude of the charge and on the potential associated with the double layer. The measured potential, called the ζ potential, is an important guide to the stability of lyophobic colloids (25). The most widely used method for measuring the ζ potential is the microelectrophoretic technique, in which the motion of individual particles is followed in a microscope. The technique is used with very dilute suspensions. Modern instrumentation provides for automated, rapid measurements and for the use of concentrated suspensions.

4.5.8.1 Microelectrophoretic Technique

A schematic of a particle electrophoresis apparatus is shown in Fig. 4.17. The suspension is placed in a cell, and a dc voltage V is applied to two electrodes at a fixed distance l apart. The sign of the particle charge is obtained directly since it is opposite to that of the electrode toward which the particle is migrating. The particle velocity is measured by using a microscope, and the velocity per unit field strength (the electrophoretic mobility) is used to determine the ζ -potential and the surface charge.

A particle with a charge q in an electric field E experiences a force directed towards the oppositely charged electrode given by

$$F = qE \quad (4.59)$$

In a viscous medium, the terminal velocity v is reached rapidly, so Stoke's law can be used to account for the force on the particle:

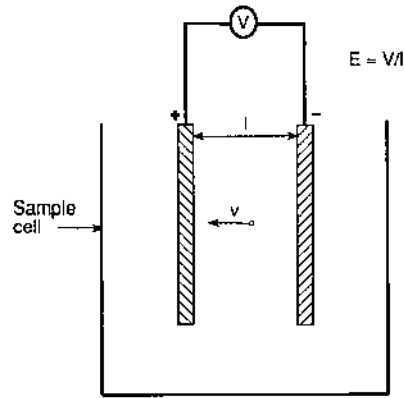


FIGURE 4.17 Schematic of a particle electrophoresis cell.

$$F = 6\pi\eta av \quad (4.60)$$

where η is the viscosity of the medium and a is the radius of the particle. From these two equations, the electrophoretic mobility is obtained:

$$u = \frac{v}{E} = \frac{q}{6\pi\eta a} \quad (4.61)$$

For particles in a dilute electrolyte solution (i.e., for $Ka < 0.1$), the potential on the surface of the particle can be taken as that of an isolated particle, that is,

$$\zeta = \frac{q}{4\pi\epsilon\epsilon_o a} \quad (4.62)$$

Substituting for q in Eqs. (4.61) and (4.62) gives

$$u = \frac{2\epsilon\epsilon_o \zeta}{3\eta} \quad (4.63)$$

For concentrated electrolyte solutions ($Ka > 200$), the Helmholtz-Smoluchowski equation can be used:

$$u = \frac{\epsilon\epsilon_o \zeta}{\eta} \quad (4.64)$$

For values of Ka between 0.1 and 200, Henry's equation applies:

$$u = \frac{2\varepsilon\varepsilon_o\zeta}{3\eta} [1 + f(Ka)] \quad (4.65)$$

where $f(Ka)$ has the values

Ka	0	0.1	1	5	10	50	100	∞
$f(Ka)$	0	0.0001	0.027	0.16	0.239	0.424	0.458	0.5

4.5.8.2 Significance of the ζ -Potential

The ζ -potential determined from the electrophoretic mobility represents the potential at the surface of the electrokinetic unit moving through the solution. It is not the potential at the surface of the particle but must correspond to a surface removed from the particle surface by at least one hydrated radius of the counterion (sometimes referred to as the shear plane). The ζ -potential is close to the Stern potential (ϕ_d in Fig. 4.12). It is the appropriate potential to be used in effects that depend on the diffuse double layer (e.g., the double-layer repulsion discussed earlier) provided that a reasonable guess can be made as to the distance of the ζ -potential from the surface of the particle.

The surface charge calculated from the ζ -potential is the charge within the shear surface. If the particle surface is assumed to be planar, the surface charge density σ_d may be determined approximately from Eq. (4.41) or (4.42). Since the ζ -potential and σ_d depend only on the surface properties and the charge distribution in the electrical double layer, they are independent of the particle size.

Typical data are shown in Fig. 4.18 for the electrophoretic mobility and surface charge density of TiO_2 (rutile) as a function of pH in aqueous solutions of potassium nitrate (33). The ζ -potential will show the same variation with pH since it is proportional to the mobility. For many oxides, ζ -potential values determined from the mobility generally fall within the range of +100 to -100 mV.

The ζ -potential plays an important role in that it is widely used as a measure of the stability of colloidal suspensions. Suspensions prepared at pH values close to the isoelectric point (IEP) may flocculate fairly rapidly because the repulsion may not be sufficient to overcome the van der Waals attraction. Farther away from the IEP, we should expect the rate of flocculation to be slower. In practice, for good stability, suspensions are often prepared at pH values comparable to those of the plateau regions of the ζ -potential or electrophoretic mobility curve. For the data shown in Fig. 4.18, this corresponds to pH values of <5 or >7.

4.6 STERIC STABILIZATION

Steric stabilization is the term used to describe the stabilization of colloidal particles which results from the interaction between uncharged polymer chains ad-

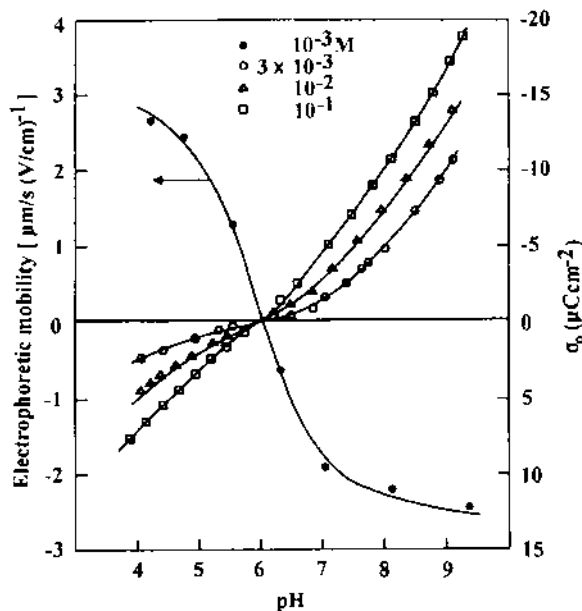


FIGURE 4.18 Surface charge density and electrophoretic mobility as functions of pH for rutile in aqueous solutions of potassium nitrate. (From Ref. 33.)

sorbed onto the particle surfaces (Fig. 4.4b). The interactions between the polymer chains are fundamentally different from those between the charged ions in electrostatic stabilization and are dominated by the configurational entropy of the chains. Steric stabilization is commonly associated with suspensions in organic liquids, but it is also effective for aqueous solvents. Exploited for over 4500 years since the Egyptians applied the principle empirically in the production of ink for writing on papyrus, steric stabilization is today exploited in a wide range of industrial products such as paints, inks, coatings, and pharmaceuticals. In ceramics processing, it is widely used for the production of stable suspensions in the consolidation of ceramic powders by casting methods such as slip casting and tape casting.

Steric stabilization is treated by Napper in detail in a textbook (34) and in a more condensed manner in a review article (35). For effective stabilization, the adsorbed polymer chains must be well anchored to the particle surfaces to minimize the risk of desorption, and the adsorbed layer must be reasonably thick to provide sufficient repulsion when the particles approach one another.

4.6.1 Adsorption of Polymers from Solution

Polymer chains existing freely in solution can adopt a large number of different configurations, and in thermal equilibrium this leads to a large configurational

entropy contribution to their free energy (36). Because of the mutual van der Waals attraction between the monomer units, the chains have a tendency to collapse to a small solid ball, but this is resisted by the reduction in configurational entropy that it would entail. Polymer chains in solution therefore tend to adopt an open, random coil structure (Fig. 4.19). The diameter of the coil is a difficult parameter to calculate. It can be taken as approximately the root-mean-square (rms) end-to-end distance $\langle r^2 \rangle^{1/2}$ of the polymer chain, given by

$$\langle r^2 \rangle^{1/2} = l\sqrt{N} \quad (4.66)$$

where l is the length of a monomer unit and N is the number units in the chain (i.e., the degree of polymerization). We see that for $l \approx 0.1$ nm and $N \approx 10^4$, then $\langle r^2 \rangle^{1/2} \approx 10$ nm.

Homopolymers, such as polystyrene and polyethylene oxide, consisting of a single type of monomer in the polymer chain, adsorb physically on the particle surfaces by weak van der Waals forces. Individual monomer segments are weakly attracted to the particle surface, but a large number of segments may contact the surface at any given time so that the sticking energy of each chain is still much greater than its thermal energy ($\approx kT$, where k is the Boltzmann constant and T is the absolute temperature). The result is irreversible adsorption. Under these conditions, the adsorbed polymer chain adopts a different conformation from the coil conformation in free solution but has a similar characteristic size when

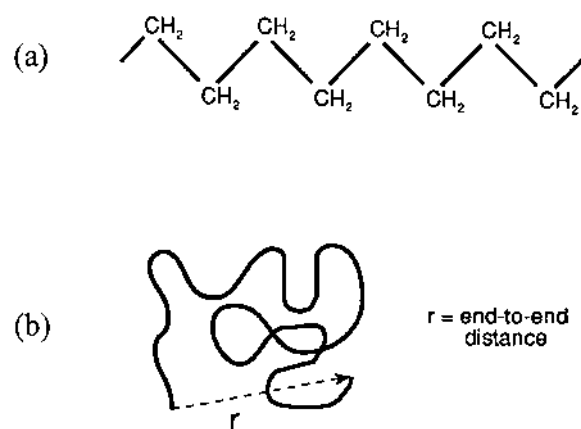


FIGURE 4.19 Two configurations of a polymer chain: (a) an extended chain in a highly extended polymer, (b) a coiled chain in a solution. The end-to-end distance of the coil is r .

“trains” of adsorbed segments act as anchor points between “loops” and “tails” of segments extending into solution (Fig. 4.20a). Strong segmental attraction to the particle surface is undesirable because it leads to a flattened conformation.

Steric stabilization by adsorbed homopolymers suffers from the conflicting requirements that the liquid be a poor solvent to ensure strong adsorption but a good solvent to impart a strong repulsion when the adsorbed polymer chains overlap. At low polymer concentrations, an individual polymer chain can become simultaneously adsorbed on two (or more) surfaces, resulting in an attractive interaction known as *bridging flocculation* (see Sect. 4.6.4).

A more effective approach is to use polymer chains consisting of two parts (graft or block copolymers). Figures 4.20b and 4.20c show these two types of copolymers in which one part is nominally insoluble and anchors (chemically or physically) onto the particle surface and the other is soluble in the liquid and extends into the liquid (37). Examples of commonly chosen block copolymers in organic solvents (e.g., toluene) are poly(vinyl pyrrolidone)/polystyrene (PVP/PS) or poly(ethylene oxide)/polystyrene (PEO/PS).

The incorporation of a single polar group to the end of the polymer chain can help to strengthen the anchoring to the particle surface by the formation

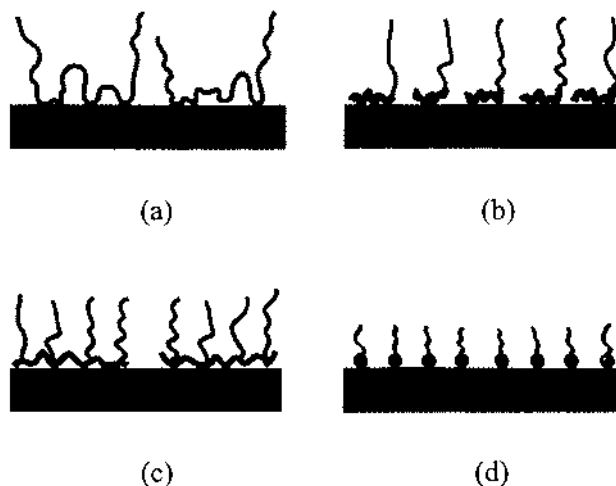


FIGURE 4.20 Schematic illustration of the adsorbed polymer conformation on a ceramic surface as a function of the chemical structure and composition: (a) homopolymer consisting of tails, loops, and trains; (b) block copolymer consisting of a short anchoring block and an extended chain block; (c) copolymer consisting of extended segments attached to anchored backbone; and (d) short-chain polymer (surfactant) consisting of an anchoring functional head group and an extended tail. (From Ref. 37.)

of hydrogen bonds (in aqueous solvents) or coordinate bonds (in aqueous or nonaqueous solvents). A useful way to describe the polar interactions is by the Lewis acid-base concept or the more general donor–acceptor concept (38). In the original form of the concept, a Lewis acid is defined as a substance capable of accepting a pair of electrons from another species, while a Lewis base is a substance capable of donating a pair of electrons. A basic functional group, for example, attaches itself to acidic functional sites on the particle surface, while an acidic functional attaches itself to basic functional group. The resulting polymer-coated surface has a brushlike structure with the chains attached at one end while the nonadsorbing chain protrudes into the solvent (Fig. 4.20d). An example is the polyisobutene succinamide (OLOA-1200), one of the most widely used dispersants in nonaqueous solvents, in which the nitrogen atom in the basic succinamide group can form a coordinated bond with a Lewis acid site (e.g., an electron-deficient metal atom) on the particle surface (see Chapter 6).

Another way of achieving strong anchoring is to chemically attach the polymer chain to the particle surface via functional groups that react with specific sites (39,40), thereby eliminating the need for anchoring segments on the chain. One type of approach involves the reaction of surface hydroxyl groups with chlorosilane or alkoxy silane groups of the polymers. This is illustrated in Fig. 4.21 by a silane terminated polymer chain with silica.

4.6.2 Origins of Steric Stabilization

Let us consider what happens when two particles covered with polymer molecules come within range of one another (Fig. 4.22a). The polymer chains will start to interact when the distance between the particles is equal to $2L$, where L is the

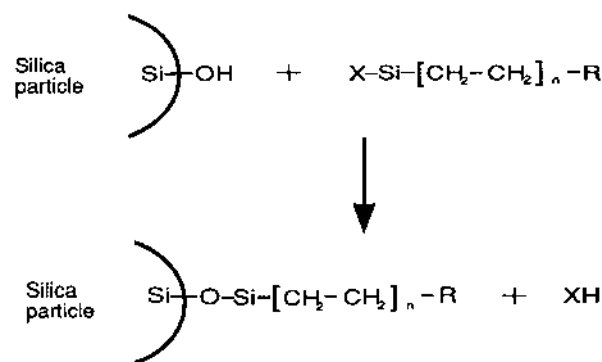


FIGURE 4.21 Schematic illustration of the formation of a chemically bonded polymer chain on the surface of an oxide particle (e.g., SiO_2).

thickness of the adsorbed polymer layer (see Fig. 4.20). For a long chain homopolymer, $L \approx \langle r^2 \rangle^{1/2}$. On further approach such that the interparticle distance is between L and $2L$ (Fig. 4.22b), the polymer chains may interpenetrate. The concentration of the polymer is increased in the interpenetration region, and in certain solvents, this can lead to a repulsion. The repulsion is said to arise from a mixing (or rather a demixing) effect due to the need of the polymer chains to avoid other chains in the interpenetration region of increased concentration. The repulsion can also be thought of as corresponding to an osmotic pressure (i.e., due to the increased concentration in the interpenetration region) and is sometimes described in these terms.

In some solvents, as discussed below, the interpenetration of the coils can lead to an attraction, thereby causing flocculation. As the distance of approach between the particles decreases further to less than L (Fig. 4.22c), not only does interpenetration occur, but the polymer chain on one particle may be compressed by the rigid surface of the other particle. This compression generates an elastic contribution to the stabilization that always opposes flocculation. The elastic contribution to the repulsion is sometimes described as an entropic effect or a volume restriction effect. At these separations, there are regions of space which are no longer accessible to a given chain. Conformations that would otherwise have been accessible are excluded so that there is a loss of configurational entropy. The loss in entropy is given by the Boltzmann equation:

$$\Delta S = k \ln \Omega \quad (4.67)$$

where k is the Boltzmann constant and Ω is the loss in the number of configurations of the polymer chain. The free-energy change due to the loss in entropy is

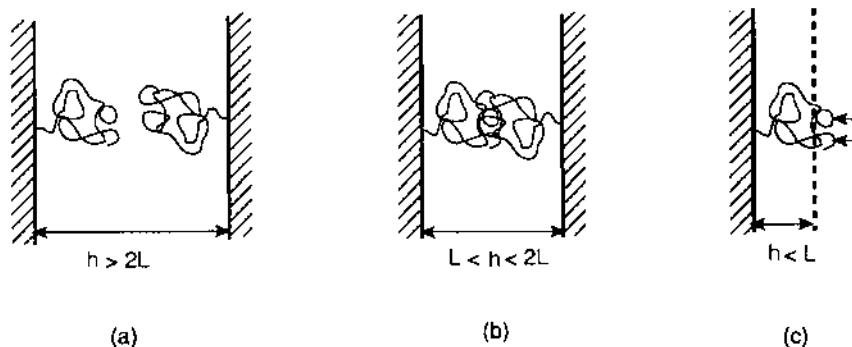


FIGURE 4.22 The range of steric repulsion in polymeric stabilization. (a) There is no interpenetration for large separations. (b) When the particles become close enough, interpenetration of the coils leads to a repulsion in good solvents or an attraction in poor solvents. (c) For small separations, compression of the coils always leads to a repulsion.

$$\Delta G_{en} = -T\Delta S \quad (4.68)$$

where T is the absolute temperature. The term ΔG_{en} is always positive (because ΔS is negative), and this is equivalent to a repulsion.

To summarize at this stage, the interactions between the adsorbed polymer chains may be separated into (1) a mixing effect that produces either a repulsion or an attraction and (2) an elastic effect that is always repulsive (Table 4.4). The mixing effect is also described as an osmotic effect whereas the elastic effect is described as an entropic effect or a volume restriction effect. The free energy of the polymeric interaction can be written

$$\Delta G_{steric} = \Delta G_{mix} + \Delta G_{elastic} \quad (4.69)$$

where ΔG_{mix} and $\Delta G_{elastic}$ are the free energy change due to the mixing and elastic effects, respectively.

4.6.3 Effects of Solvent Quality and Temperature

A key difference between electrostatic and steric stabilization is the significant influence that the solvent quality and the temperature can have in steric stabilization. As we saw above, interpenetration of the polymer chains gives rise to a mixing effect. At a certain temperature, referred to as the Θ (theta) temperature, the interpenetration of the polymer chains does not lead to a change in the free energy of mixing ($\Delta G_{mix} = 0$), and a system of the polymer dissolved in the solvent behaves like an ideal solution. The solvent is referred to as a Θ solvent.

At temperatures greater than the Θ temperature, the interpenetration of the polymer chains leads to an increase in the free energy of mixing ($\Delta G_{mix} > 0$), that is to say that the polymer chains prefer contact with the solvent rather than contact with one another. The solvent is referred to now as a *good solvent* (or a better than Θ solvent). The repulsion between the chains leads to stability of the suspension. Below the Θ temperature, the polymer chains prefer contact with one another rather than contact with the solvent ($\Delta G_{mix} < 0$), and in this case the solvent is

TABLE 4.4 Interactions Between Adsorbed Polymer Chains in Steric Stabilization

Interaction	Nature of Force
Mixing effect (osmotic effect)	Repulsive (good solvent) Attractive (poor solvent)
Elastic effect (entropic effect or volume restriction effect)	Repulsive (always)

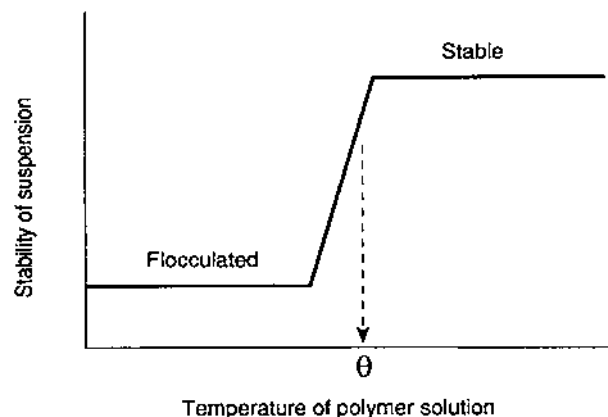


FIGURE 4.23 Schematic representation of the stability of a suspension as a function of the temperature of the polymer solution. The stability changes dramatically within a few degrees of the Θ temperature of the solution.

referred to as a *poor solvent* (or a worse than Θ solvent). The attraction between the chains may lead to flocculation of the suspension. As shown schematically in Fig. 4.23, we would therefore expect the stability of the suspension to change very markedly within a few degrees of the Θ temperature for the polymer solution. In practice, for many sterically stabilized suspensions, the temperature at which the stability changes dramatically [referred to as the *critical flocculation temperature* (CFT)] correlates very well with the Θ temperature of the solution (Table 4.5).

TABLE 4.5 Comparison of the Theta (Θ) Temperature of Solutions of Steric Stabilizers with the Critical Flocculation Temperatures (CFT) of Suspensions

Stabilizer	Molecular weight	Dispersion medium	Θ (K)	CFT (K)
Poly(ethylene oxide)	10,000	0.39 M MgSO ₄	315 ± 3	318 ± 2
Poly(acrylic acid)	51,900	0.2 M HCl	287 ± 5	283 ± 2
Poly(vinyl alcohol)	57,000	2 M NaCl	300 ± 3	310 ± 3
Polyisobutylene	760,000	2-methylbutane	318	327
Polyisobutylene	760,000	cyclopentane	461	455
Polystyrene	110,000	cyclopentane	410	427
Polystyrene	110,000	cyclopentane	280	293

Source: Ref. 35.

4.6.4 Stability of Sterically Stabilized Suspensions

The total energy of interaction V_T for sterically stabilized suspensions is now the sum of the steric interaction ΔG_{steric} , given by Eq. (4.69), and the van der Waals energy of attraction V_A ; that is,

$$V_T = \Delta G_{\text{steric}} + V_A \quad (4.70)$$

Napper (34) gives theoretical expressions for ΔG_{mix} and $\Delta G_{\text{elastic}}$. For interactions between adsorbed homopolymers in the region $L < h < 2L$ (see Fig. 4.22), where chain conformations from only trains and loops are taken into consideration, ΔG_{mix} is given by (41,42)

$$\Delta G_{\text{mix}} = \frac{32\pi akT}{5v_1} \frac{(\bar{\Phi}_2^a)^2}{L^4} \left(\frac{1}{2} - \chi \right) \left(L - \frac{h}{2} \right)^6 \quad (4.71)$$

where a is the radius of the particle, k is the Boltzmann constant, T is the absolute temperature, $\bar{\Phi}_2^a$ is the average volume fraction of segments in the adsorbed layer (measured as ~ 0.37), v_1 is the molar volume of the solvent, and χ is the Flory-Huggins parameter ($\chi > 0.5$ for a poor solvent and $\chi < 0.5$ for a good solvent). At smaller interparticle separations, $h < L$, the polymer segment density is assumed to be uniform, and the contributions from the elastic and mixing interactions are given by

$$\begin{aligned} \Delta G_{\text{mix}} &= \frac{4\pi a L^2 kT}{v_1} (\bar{\Phi}_2^a)^2 \left(\frac{1}{2} - \chi \right) \left(\frac{h}{2L} - \frac{1}{4} - \ln \frac{h}{L} \right) \\ \Delta G_{\text{elastic}} &= \frac{2\pi a L^2 kT \rho_2 \bar{\Phi}_2^a}{M_2^a} \left\{ \frac{h}{L} \ln \left[\frac{h}{L} \left(\frac{3-h/L}{2} \right)^2 \right] \right. \\ &\quad \left. - 6 \ln \left(\frac{3-h/L}{2} \right) + 3(1-h/L) \right\} \end{aligned} \quad (4.72)$$

where ρ_2 is the density and M_2^a the molecular weight of the adsorbed polymer.

The interaction energy in sterically stabilized systems has been measured (43,44) using the surface force apparatus described earlier, and the variation in V_T can be illustrated with the results shown in Fig. 4.24 for the interaction between mica surfaces in the presence of a solution of polystyrene in cyclopentane. The degree of polymerization of the polymer (i.e., the number of segments in the chain) is 2×10^4 , which gives $\langle r^2 \rangle^{1/2} \approx 15$ nm. In the absence of polymer molecules there is simply a short-range van der Waals attraction (curve a). This is replaced by a deep, long-ranged attractive well at low coverage of the surface

by the polymer chains (curve b). At progressively increasing surface coverage, the attractive well becomes shallower and the range of the final repulsive potential increases (curves b and c). Finally, when equilibrium coverage of the mica surfaces is attained, the interaction is repulsive at all separations (curve d).

The results shown in Fig. 4.24 serve to illustrate the influence of two important effects in steric stabilization: the relative unimportance of van der Waals attraction in steric stabilization, especially at fairly high coverage, and the significance of the surface coverage by the adsorbed polymer chains. In certain cases, low coverage may actually lead to flocculation. This occurs when the particle has usable anchoring sites that are not occupied and for homopolymers having a large number of segments that can contact the particle surface. Polymers from a neighboring particle can then attach themselves and form bridges, leading to flocculation. This type of flocculation is referred to as *bridging flocculation*. As outlined earlier, the use of block or graft copolymers or polymers with functional end-groups can alleviate this type of flocculation.

4.6.5 Stabilization by Polymers in Free Solution

It has been suggested that polymers in free solution can also impart stability to colloidal suspensions. To understand how this type of stabilization might occur,

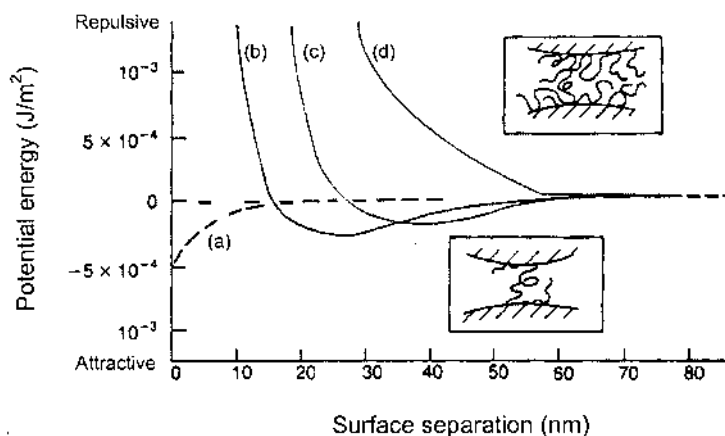


FIGURE 4.24 Interaction energy between mica surfaces in the presence of a solution of polystyrene in cyclopentane. In the absence of polymer molecules (a), there is a simple van der Waals attraction. At low surface coverage bridging (lower inset) dominates. As more polymer adsorbs (b) and (c), the steric repulsion counteracts the attraction until at high surface coverage (d), the interaction is repulsive at all separations. (From Ref. 43.)

let us consider the approach of two particles from a large separation (Fig. 4.25). Closer approach of the particles must be accompanied by demixing of the polymer molecules and the solvent in the interparticle region. Consequently, work must be done to make the polymer molecules leave the interparticle region. This corresponds to a repulsion between the particles that, if high enough, can lead to stabilization of the suspension. This type of stabilization is referred to as *depletion stabilization*.

If the repulsion is not high enough, the particles can approach closer, and when the separation becomes smaller than the size of the polymer chain in solution (i.e., approximately $\langle r^2 \rangle^{1/2}$), all of the polymer chains would have been excluded from the interparticle region (Fig. 4.25b). Closer approach of the particles will

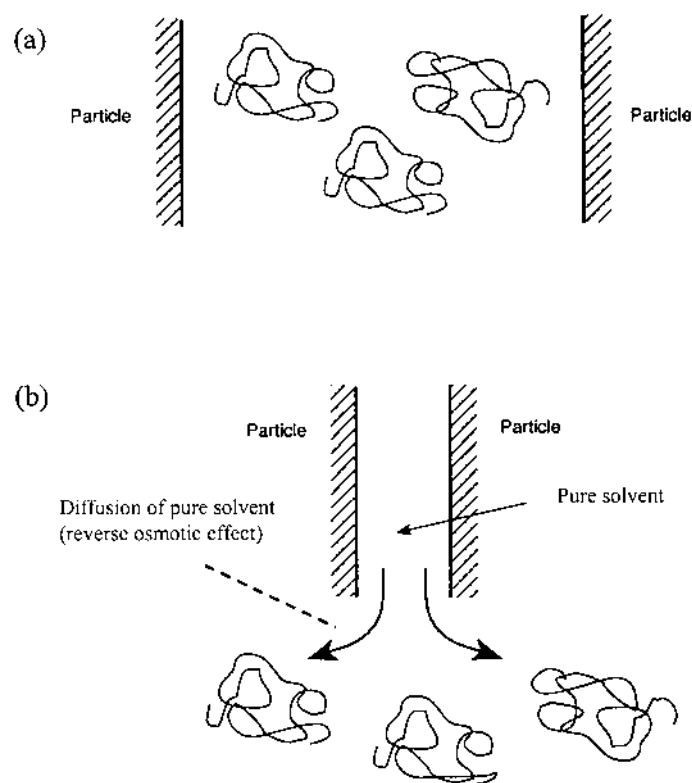


FIGURE 4.25 Polymeric stabilization by free polymer molecules in solution: (a) depletion stabilization at separations greater than the diameter of the polymer coil and (b) depletion flocculation at small separations.

be favored because we have now created a type of reverse osmotic effect. The pure solvent between the particles will diffuse into the surrounding region in an attempt to lower the concentration of the polymer. This reverse osmotic effect is equivalent to an attraction between the particles and flocculation occurs. This type of flocculation is referred to as *depletion flocculation*.

The important effects in the stabilization of suspensions with uncharged polymer chains are summarized in Fig. 4.26 (45).

4.7 ELECTROSTERIC STABILIZATION

As outlined earlier, suspensions can also be stabilized by *electrosteric repulsion*, involving a combination of electrostatic repulsion and steric repulsion (Fig. 4.4c). Electrosteric stabilization requires the presence of adsorbed polymers and a significant double layer repulsion. It is commonly associated with suspensions in aqueous liquids, but several studies have indicated that electrostatic effects can be important in some nonaqueous systems (46). A common way of achieving electrosteric stabilization in aqueous liquids is through the use of polyelectrolytes, i.e., polymers that have at least one type of ionizable group (e.g., carboxylic or

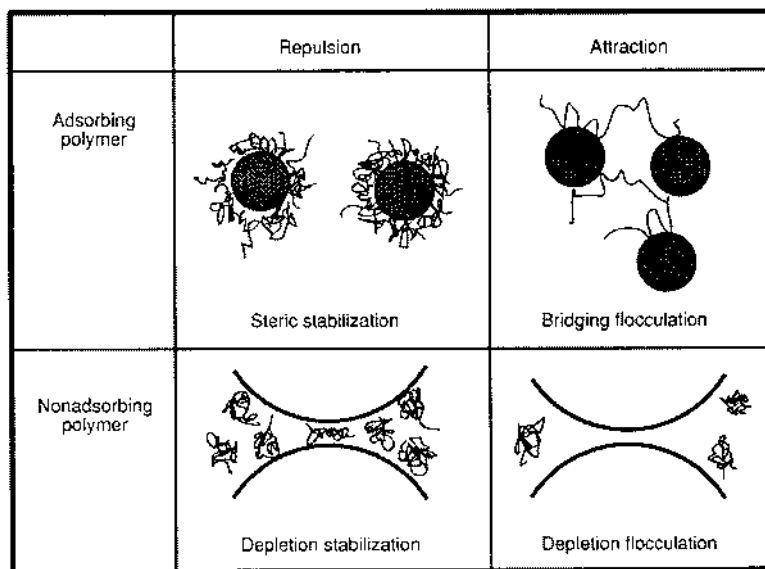


FIGURE 4.26 Summary of the most important effects occurring in the stabilization of suspensions with uncharged polymer chains. (From Ref. 45.)

sulfonic acid group) that dissociates to produce charged polymers. The polymers can be homopolymers such as poly(acrylic acid), block copolymers, or graft copolymers. Polyelectrolytes are widely used industrially in the preparation of highly concentrated ceramic suspensions (>50 vol% particles) which are subsequently consolidated and fired to produce dense articles.

4.7.1 Dissociation of Polyelectrolytes in Solution

In aqueous solvents, polymers with ionizable groups develop electrostatic charges by dissociation. The dissociation of the polymers as well as their adsorption is strongly influenced by the properties of the solvent and the particle surfaces (47–50). Figure 4.27 shows schematically the structure of two common homopolymers used for electrosteric stabilization: poly(methacrylic acid) (PMAA) and poly(acrylic acid) (PAA) having a carboxylic acid (COOH) functional group. The sodium or ammonium salts of these polymers, where the H in the COOH group is replaced by Na or NH₄, are also commonly used in electrosteric stabilization. The molecular weight of the polymers can vary between ~1000 and ~50,000. These polymers are examples of *anionic polyelectrolytes* in that they dissociate to give negatively charged species. *Cationic polyelectrolytes* are positively charged on dissociation.

The functional groups of PMAA and PAA can exist as COOH or dissociated to COO[−]. The dissociation reaction can be written in a general form as



Depending on the pH and the ionic concentration of the solution, the fraction of the functional groups which is dissociated (i.e., COO[−]) and which is not dissociated (i.e., COOH) will vary. As the fraction α of COOH groups dissociated increases from 0 to 1, the charge on the polymer varies from neutral to highly

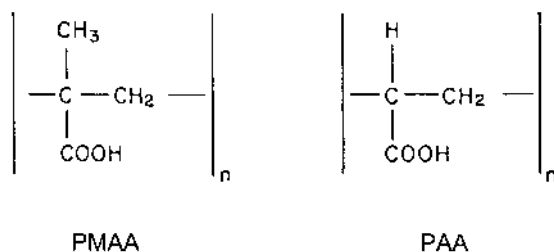


FIGURE 4.27 Schematic diagram showing the polymer segments of poly(methacrylic acid) (PMAA) and poly(acrylic acid) (PAA).

negative. Figure 4.28 shows how α varies as a function of the pH and NaCl salt concentration for the sodium salt of PMAA with a molecular weight of $\sim 15,000$. As the pH and salt concentration increases, the extent of dissociation and the negative charge of the polymer increase. At a pH greater than ~ 8.5 , the polymer is highly negative with $\alpha \approx 1$. Under these conditions, the free polymer is in the form of relatively large expanded random coils (diameter ~ 10 nm) due to the repulsion between the charges segments. As the pH decreases, the number of negative charges decreases, with the polymer being effectively neutral at a pH of ~ 3.5 . In the neutral condition, the polymer forms small coils (diameter ~ 3 nm) or clumps.

4.7.2 Adsorption of Polyelectrolytes from Solution

Adsorption of polyelectrolyte onto the particle surface is commonly dominated by electrostatic interactions and is often strongly favored if the particle surface and the polyelectrolyte have opposite charges. As discussed earlier, the surface charge of the oxide particles dispersed in aqueous solvents depends on the pH of the suspension. For example, Fig. 4.29 shows the surface charge density σ_0 of Al_2O_3 particles (Sumitomo AKP-15) as a function of pH for two NaCl salt concentrations. By comparing the data in Figs. 4.28 and 4.29, we see that considerable electrostatic attraction should occur between the negatively charged polyelectrolyte and the positively charged Al_2O_3 , particularly in the pH range of ~ 3.5 to 8.5.

Figure 4.30 shows the measured adsorption isotherms for the sodium salt of PMAA (PMAA-Na) on the Al_2O_3 particles at various pH values. The results

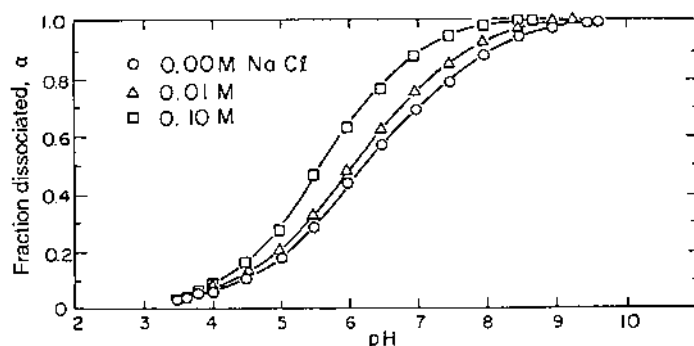


FIGURE 4.28 Fraction of acid groups dissociated versus pH for the sodium salt of poly(methacrylic acid), PMAA-Na, in water containing three different salt concentrations. (The molecular weight of the polyelectrolyte is 15,000.) (From Ref. 47.)

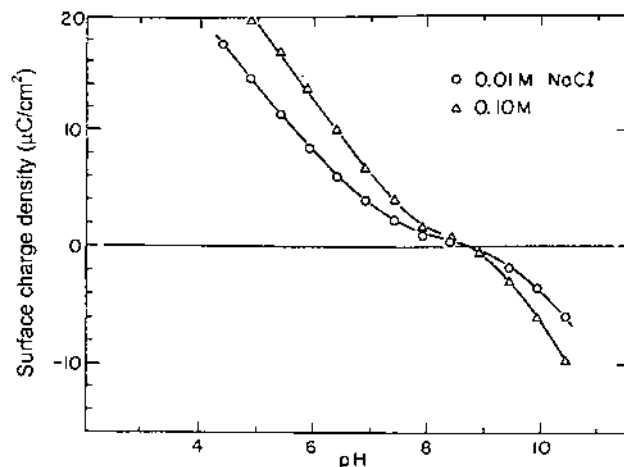


FIGURE 4.29 Surface charge density versus pH for α - Al_2O_3 powder (Sumitomo AKP-30) in water containing two different salt concentrations. (From Ref. 47.)

are plotted in the form of milligrams of PMAA adsorbed per square meter of the Al_2O_3 surface versus the initial amount of PMAA-Na added [as a percent of the dry weight of Al_2O_3 , i.e., on a dry weight basis (dwb)]. The solid diagonal line represents the adsorption behavior that would occur if 100% of the PMAA added were to adsorb. It is clear that the amount of PMAA adsorbed increases with decreasing pH. At low pH values ($\alpha \rightarrow 0$), the polymer chain adopts a fairly compact conformation and adsorbs in a dense layer with a small thickness (Fig. 4.31). The projected area per adsorbed chain is relatively small, and more adsorbed chains are required to establish a monolayer. When fully ionized ($\alpha \rightarrow 1$) at higher pH values, the polyelectrolyte adsorbs in an open layer with a large thickness, and fewer chains are needed to form a monolayer.

4.7.3 Stability of Electrosterically Stabilized Suspensions

At low concentration of adsorbed polyelectrolyte, flocculation can occur by charge neutralization between the oppositely charged polyelectrolyte and the particle surface, so that interparticle repulsion is limited. Bridging flocculation can also occur when a charged homopolymer adsorbs on a neighboring particle. At higher concentration of adsorbed polyelectrolyte, the stability of the suspension improves because of the long-range repulsion resulting from electrostatic and

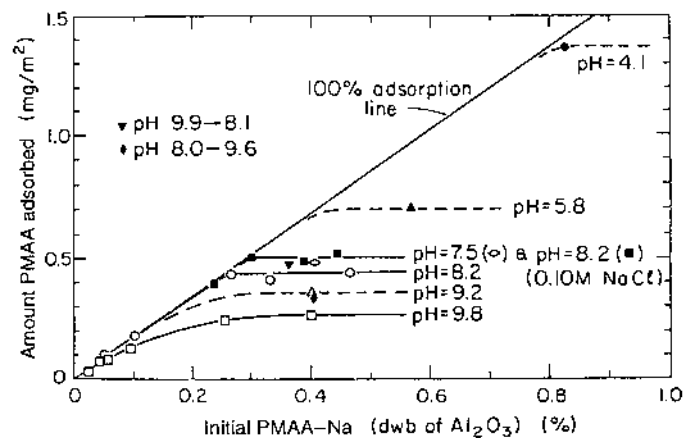


FIGURE 4.30 Amount of PMAA salt adsorbed on α - Al_2O_3 powder as a function of the initial amount of PMAA-Na added to the suspension. (From Ref. 47.)

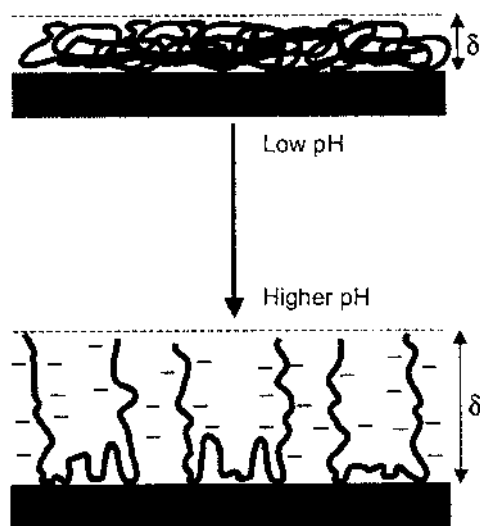


FIGURE 4.31 Schematic illustration of the conformation of an anionic polyelectrolyte on a ceramic surface as a function of pH. (δ is the thickness of the adsorbed polymer layer.) (From Ref. 37.)

steric interactions (51). The electrostatic repulsion dominates at larger particle separation, whereas the steric repulsion becomes more pronounced at shorter separation.

By studying the sedimentation behavior of Al_2O_3 suspensions stabilized with PMAA-Na, the conditions for stability have been determined as a function of pH and polyelectrolyte concentration. The observations can be conveniently plotted on a map, called a *colloid stability map* (Fig. 4.32). The map shows, for a given concentration of Al_2O_3 particles (20 vol%), the regions of stability and instability (tendency towards flocculation). Regions below the curve are unstable. Regions near and slightly above the curve are stable and dispersed as a result of electrosteric repulsion due to the adsorbed polyelectrolyte. For a given pH value, the concentration of adsorbed polyelectrolyte at the stability boundary corresponds to the saturation concentration of the adsorption isotherm (Fig. 4.30). Regions further above the curve have appreciable amounts of free polymer in solution. At pH values below ~ 3.5 , the adsorbed polymer is essentially neutral so that the electrostatic repulsion results from the *surface charge* of the particles.

4.8 STRUCTURE OF CONSOLIDATED COLLOIDS

So far in this chapter we have been concerned mainly with the principles of colloid stability. The key factors and how they can be manipulated to influence

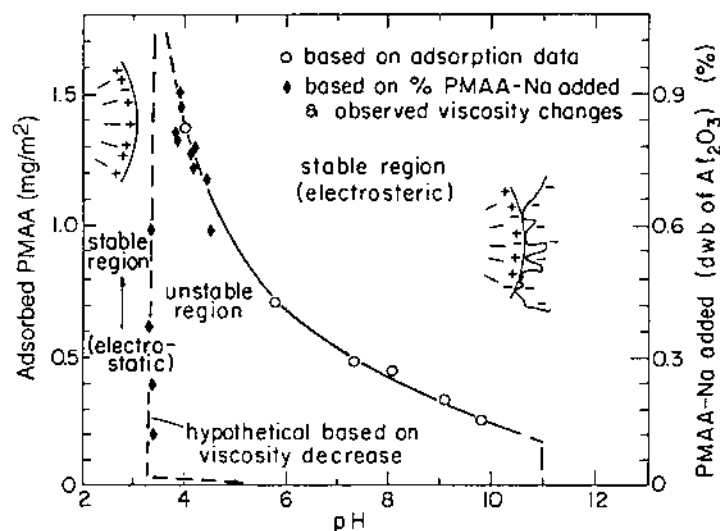


FIGURE 4.32 Colloid stability map for suspensions of $\alpha\text{-Al}_2\text{O}_3$ powder (20 vol %) as a function of adsorbed PMAA and pH. (From Ref. 47.)

the stability of the suspensions have been discussed. The next step, which is of great practical importance to ceramic processing, is to relate the stability of the suspension to the structure of the consolidated colloid. As we have outlined earlier, the structure of the consolidated body has a significant influence on the quality of the fired microstructure. The objective, therefore, is to understand how the colloidal properties of the suspension can be manipulated to produce the desired structure in the consolidated body.

An initial step in the colloidal processing of most ceramic powders may involve the removal of hard agglomerates and large particles (if present) from the suspension by sedimentation. After this, consolidation of the suspension is achieved by a variety of methods. For suspensions with a low concentration of particles, methods such as gravitational settling, centrifuging, and filtration can be used, whereas the casting methods such as pressure casting, slip casting, tape casting and gel casting are suitable for concentrated suspensions. Stable suspensions of submicron particles are known to settle very slowly under normal gravity; the settling rate is normally increased by centrifuging or by filtration. The consolidated colloid has a densely packed structure (Fig. 4.33a). Because the particles flocculate while settling, unstable suspensions settle faster and produce a loosely packed structure (Fig. 4.33b).

The structure of the consolidated colloid formed is actually more complex than the arrangements illustrated in Fig. 4.33. The microstructures of nearly monodisperse SiO_2 particles shown in Fig. 4.34 indicate that the difference in structure formed from the stable suspension and the unstable suspension is not controlled by the way in which the individual particles arrange themselves in the sediment but rather the way they group themselves to form densely packed multiparticle units called *domains* (52). Figure 4.34c shows that the domains in a consolidated

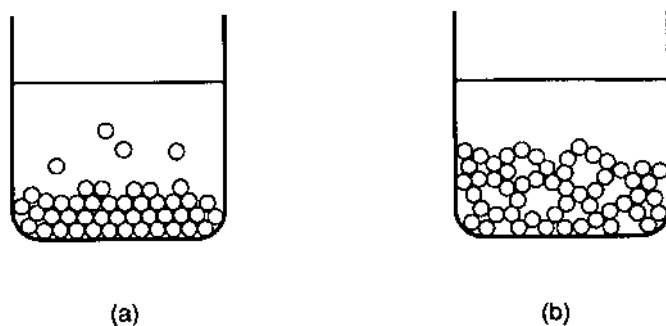


FIGURE 4.33 Schematic of a consolidated colloid formed from (a) a stable suspension and (b) a flocculated suspension.

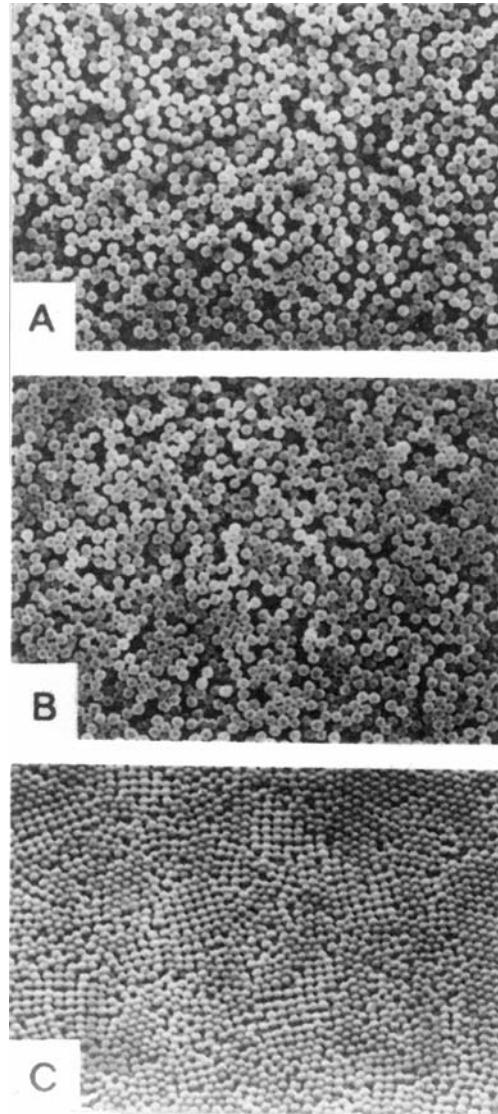


FIGURE 4.34 Microstructures of particle domains formed by centrifugal consolidation of SiO_2 colloidal suspensions at (A) $\zeta = 0$ mV, (B) $\zeta = 68$ mV and (C) $\zeta = 110$ mV. The average particle diameter is $0.7 \mu\text{m}$. (From Ref. 52.)

colloid formed from a stable suspension of spherical, nearly monodisperse powders are arranged in a periodic pattern not unlike that found in crystalline grains. Domains are also formed if the particles are irregular in shape, but the periodic arrangement of the domains is lost.

The microstructures of Fig. 4.34 also show that the size of the domains can be altered through manipulation of the interparticle forces. The size of the domains increases for higher double-layer repulsion. Furthermore, the efficiency of the packing of the domains increases, leading to high packing density in the consolidated colloid (Fig. 4.34C). As the repulsion decreases (or equivalently, as the attraction increases), the domain size decreases and the interdomain pore size increases. The interdomain porosity is therefore the main cause of the low packing density of flocculated colloids.

We can attempt to describe the structure of the consolidated colloid in terms of the particle interactions. For highly attractive forces, the particle will “stick” on contact with another particle, leading to the formation of a highly disordered system (Fig. 4.34A). As the repulsion increases, the particle will be able to undergo a certain amount of rearrangement into low-energy positions leading to an increase in the domain size and a reduction of the interdomain pore size (Fig. 4.34B). Finally, when the repulsion becomes dominant, each additional particle can interact with the others to produce larger domains with small interdomain pores (Fig. 4.34C). A problem, however, is that the domain boundaries constitute defects that interfere with sintering. As discussed later (Chapter 11), sintering of the domains leads to differential stresses that produce an enlargement of the defects at the domain boundaries, thereby limiting the final density and the properties of the sintered material.

We have discussed the structure of consolidated colloids formed from electrostatically stabilized suspensions, but the same principles apply to sterically stabilized suspensions. For example, studies with polystyrene spheres stabilized with polymers have yielded structures similar to those shown in Fig. 4.34.

4.9 RHEOLOGY OF COLLOIDAL SUSPENSIONS

The term *rheology* refers to the deformation and flow characteristics of matter. Rheological measurements monitor changes in flow behavior in response to an applied stress (or strain). The viscosity of the suspension is the key rheological parameter of interest in ceramic processing, but other parameters such as the yield stress in compression (or shear) and the viscoelastic properties (e.g., storage modulus and the loss modulus) under an oscillatory stress are also important in many systems.

Rheological measurements are widely used to characterize the properties of colloidal suspensions (53,54). They can be used as a method of analysis as,

for example, in determining the optimum concentration of dispersant required to stabilize a suspension by measuring the viscosity of the suspension as a function of the concentration of dispersant added. Rheological measurements are also used commonly as a quality control technique to minimize the batch-to-batch variation of suspension properties prior to consolidation (e.g., by spray drying, slip casting or tape casting). Furthermore, rheological measurements can be used as a direct processing parameter. For example, when the suspension is consolidated by casting methods (e.g., slip or tape casting), we require, on the one hand, that the suspensions contain the highest possible fraction of particles. This is because a concentrated suspension serves to reduce the shrinkage during drying of the cast and to produce a green body with high packing density. On the other hand, we also want the suspension to have a low enough viscosity so that it can be cast into the desired shape. Rheological measurements provide an important means of optimizing these requirements.

4.9.1 Rheological Properties

In simple shear, which is the most common way of determining the rheological properties, the shear stress τ is related to the shear strain rate $\dot{\gamma}$ by

$$\tau = \eta \dot{\gamma} \quad (4.75)$$

where η is the viscosity. In general, the stress and the strain are tensors with each having nine components. If η is independent of the shear rate (or the shear stress), the liquid is said to be Newtonian. Many simple liquids (e.g., water, alcohols, and some oils) as well as many molten glasses show Newtonian behavior. For more complex systems such as polymer solutions and colloidal suspensions, η is not independent of the shear rate and the behavior is said to be non-Newtonian. We must now write

$$\eta(\dot{\gamma}) = \frac{d\tau}{d\dot{\gamma}} \quad (4.76)$$

where $\eta(\dot{\gamma})$, the viscosity at a given strain rate, is found from the slope of curve of shear stress versus strain rate.

The viscosity of colloidal suspensions often shows a dramatic dependence on the shear rate, and this dependence is used as a means to classify the rheological behavior. Figure 4.35 shows the curves for Newtonian behavior and types of non-Newtonian behavior found with colloidal suspensions. When the viscosity increases with increasing shear rate, the behavior is described as *shear thickening* (or *dilatant*). Suspensions containing a high concentration of nearly equiaxial

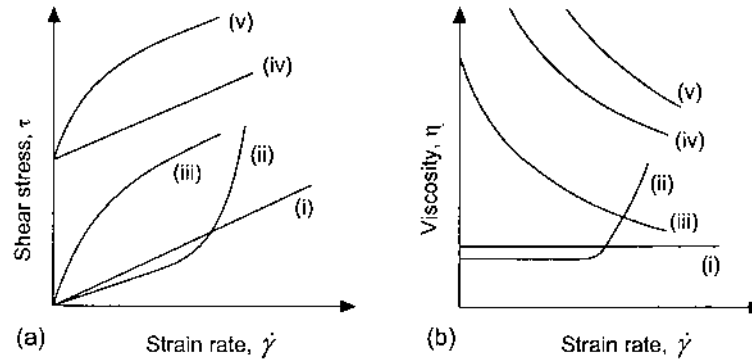


FIGURE 4.35 Typical rheological behavior of colloidal suspensions: (i) Newtonian, (ii) shear thickening or dilatant, (iii) shear thinning or pseudoplastic, (iv) Bingham plastic, (v) pseudoplastic with a yield stress.

particles may show shear thickening. Moderately concentrated suspensions of small, elongated particles may show *shear thinning* or *pseudoplasticity*, where the viscosity decreases with increasing shear rate. Shear thickening or shear thinning behavior is sometimes described by an empirical relation of the form

$$\tau = K\dot{\gamma}^n \quad (4.77)$$

where K is called the consistency index and n is an exponent that indicates the deviation from Newtonian behavior. If $n = 1$, the suspension is Newtonian; when $n < 1$, the suspension shows shear thinning or pseudoplastic flow; and when $n > 1$, the flow is described as shear thickening or dilatant.

For systems where the viscosity decreases with increasing shear rate after an initial threshold stress called the *yield stress* τ_y , the flow behavior is described as plastic. Concentrated suspensions of clay particles commonly exhibit plastic behavior. A material obeying the equation

$$\tau - \tau_y = \eta\dot{\gamma} \quad (4.78)$$

where η is independent of the shear rate, is said to show Bingham-type behavior. The viscosity of most plastic materials, however, is dependent on the shear rate, and the flow behavior is often described by a power law relation,

$$\tau - \tau_y = K\dot{\gamma}^n \quad (4.79)$$

where K and n were defined earlier in Eq. (4.77).

The rheological properties of concentrated suspensions often depend not only on the shear rate but also on the time. When the viscosity decreases with time under shear but recovers to its original value after flow ceases, the behavior is known as *thixotropic* (Fig. 4.36). This type of behavior is more often observed in flocculated suspensions and colloidal gels. When the suspension is sheared, the flocs are broken down leading a distribution of floc sizes. Often the regeneration of the flocs is slow which causes the resistance to flow to decrease. The opposite behavior, when the viscosity increases with shear rate and is also time dependent, is known as *rheopectic*.

In practice, dilatant and rheopectic behavior are often undesirable because at high shear rates the suspension becomes too stiff to flow smoothly. Plastic behavior is desirable for many ceramic forming methods because the suspension will flow under high stress but will retain its shape when the stress is removed after forming. Pseudoplastic (shear thinning) behavior is often an acceptable compromise.

For the range of values encountered with colloidal suspensions, a concentric cylinder rotating viscometer is often used to measure the viscosity. Less often used are the cone and plate viscometer and the parallel plate viscometer. For liquids and solutions, a capillary viscometer is often used. Information on several types of viscometers can be found in Ref. 55.

4.9.2 Factors Influencing the Rheology of Colloidal Suspensions

The interparticle forces discussed earlier in this chapter have a significant influence on the rheological behavior and the stability of the suspension can often be

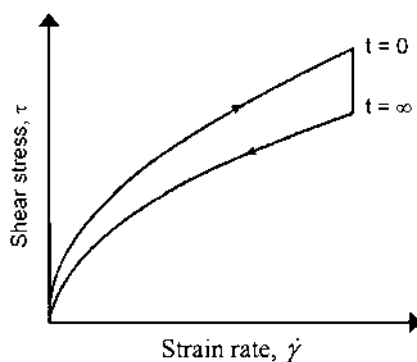


FIGURE 4.36 Thixotropic behavior in which the rheology depends not only on the strain rate but also on time.

inferred from the observed behavior. The particle characteristics, particularly the particle concentration, can also have a significant effect on the suspension rheology. Commonly, the influence of the liquid medium is small unless an excess concentration of dissolved polymer is present.

4.9.2.1 Influence of Interparticle Forces

Hard Sphere Systems

Hard sphere colloidal systems do not experience interparticle interactions until they come into contact, at which point the interaction is infinitely repulsive. Such systems represent the simplest case, where the flow is affected only by hydrodynamic (viscous) interactions and Brownian motion. Hard sphere systems are not often encountered in practice, but model systems consisting of SiO₂ spheres stabilized by adsorbed stearyl alcohol layers in cyclohexane (56,57) and polymer latices (58,59) have been shown to approach this behavior. They serve as a useful starting point for considering the more complicated effects when interparticle forces are present.

In a quiescent suspension, the particles are moving continuously in a random manner with Brownian motion. The time t_B taken for a particle to diffuse a distance equal to its radius a is given by the relation

$$a^2 \approx Dt_B \quad (4.80)$$

with the diffusion coefficient D given by the Stokes-Einstein equation

$$D = \frac{kT}{6\pi\eta_o a} \quad (4.81)$$

where k is the Boltzmann constant, T is the absolute temperature, and η_o is the viscosity of the liquid medium. From Eqs (4.80) and (4.81),

$$t_B = \frac{6\pi\eta_o a^3}{kT} \quad (4.82)$$

We can take t_B to represent a characteristic time required to restore the structure of the suspension from a disturbance caused by Brownian motion. The time scale t_S for viscous flow due to a shear stress can be taken as the reciprocal of the strain rate $\dot{\gamma}$. The dimensionless parameter equal to the ratio t_B/t_S , which is referred to as the *Peclet number* (or the reduced strain rate)

$$P_e = \frac{6\pi\eta_o a^3 \dot{\gamma}}{kT} \quad (4.83)$$

gives the relative importance of Brownian motion and viscous forces.

For hard sphere systems, experimental data for the relative viscosity η_r (equal to the viscosity of the suspension η divided by the viscosity of the liquid medium η_0) versus P_e lie on curves of the form illustrated in Fig. 4.37. At low strain rates when P_e is $\ll 1$, the structure of the suspension is not significantly altered by the shear because Brownian motion dominates over the viscous forces. At higher strain rates, the viscous forces start to affect the suspension structure, and shear thinning occurs. At very high strain rates, i.e., when P_e is $\gg 1$, the viscous forces dominate and the plateau region represents the viscosity of a suspension with a hydrodynamically controlled structure.

In the limit of infinite dilution when all interactions between the particles are neglected, the relative viscosity of hard sphere suspensions is given by the Einstein equation

$$\eta_r = 1 + 2.5f \quad (4.84)$$

where f is the volume fraction of the particles. Equation (4.84) can be used with negligible error for $f < 0.01$. At low strain rates ($P_e \ll 1$), when two-particle interactions are taken into account,

$$\eta_r = 1 + 2.5f + 6.2f^2 \quad (4.85)$$

Equation (4.85) has been shown to provide an adequate fit to experimental data for $f < 0.15$.

As f is increased above 0.15, interactions involving multiple particles become important and no rigorous hydrodynamic theory exists. The problem is treated empirically, and several equations are available in the literature. One of the most useful is the Krieger-Dougherty equation (60)

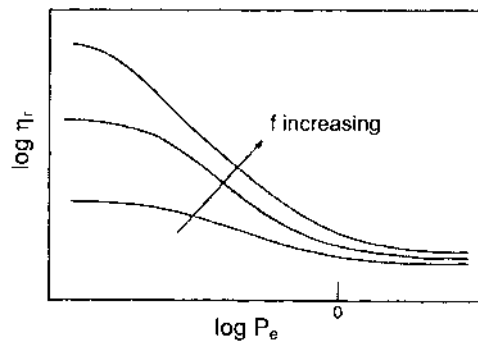


FIGURE 4.37 Schematic representation of the relative viscosity versus the Peclet number for suspensions with different particle concentration f . (From Ref. 53.)

$$\eta_r = \left(1 - \frac{f}{f_m}\right)^{-[\eta]f_m} \quad (4.86)$$

where $[\eta]$ is the intrinsic viscosity of the suspension, equal to 2.5 for a suspension of hard spheres, and f_m is the volume fraction of particles at which the viscosity becomes practically infinite. For sterically stabilized SiO_2 spheres in cyclohexane, Fig. 4.38 shows that the relative viscosity at low and high strain rates can be well fitted by Eq. (4.86), with $f_m = 0.63$ at low strain rate and $f_m = 0.71$ at high strain rate (61).

Soft Sphere Systems

Colloidal suspensions can be classified as soft sphere systems because the repulsive interactions occur at some characteristic distance from the particle surface. For electrostatic and steric stabilization, this distance is the Debye length ($1/K$) and the thickness of the adsorbed polymer layer, respectively. For sterically stabilized suspensions, the adsorbed polymer layer leads to an increase in the hydrodynamic radius of the particle. When the adsorbed layer is densely packed, the principles described above for hard sphere systems are applicable, provided that the volume fraction of particles f is replaced by an effective volume fraction f_{eff} given by

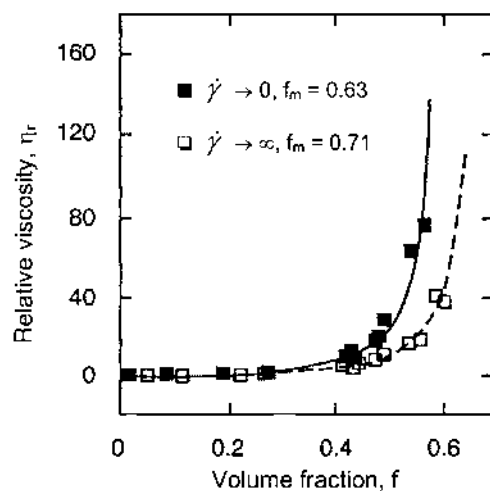


FIGURE 4.38 Relative viscosity versus volume fraction of particles for sterically stabilized suspensions of silica spheres (radius = 110 nm) in cyclohexane. The data are for low and high strain rates, $\dot{\gamma}$. (From Ref. 61.)

$$f_{eff} = f \left(1 + \frac{\delta}{a} \right)^3 \quad (4.87)$$

where δ is the thickness of the polymer layer and a is the particle radius (62–64). The use of Eq. (4.87) with hard sphere scaling principles is successful only when the ratio δ/a is small (less than ~ 0.1). With increasing thickness of the adsorbed polymer layer, the experimental data deviate from the predicted behavior, particularly at high volume fraction of particles. In principle, it should also be possible to scale electrostatically stabilized suspensions in a similar manner. For these systems, the Debye length $1/K$ is a reasonable estimate for the parameter δ in Eq. (4.87).

Flocculated Systems

Flocculated suspensions are dominated by attractive interparticle interactions and form disordered, metastable structures. Because of these nonequilibrium structures, the rheological behavior is difficult to characterize. It is common to distinguish between two types of flocculated systems which are dependent on the magnitude of the interparticle attraction: weakly flocculated and strongly flocculated. Weakly flocculated suspensions are characterized by a shallow minimum having a total potential energy of interaction in the range $1 < -V_T^{min}/kT < 20$. This state can be achieved by adding a nonadsorbing polymer to an otherwise stable suspension (65) or by controlling the repulsion between the particles (66) to achieve flocculation into a secondary minimum of the DLVO potential (see Fig. 4.15). Weakly flocculated suspensions exhibit reversible flocculation, which facilitates deformation of the structure during shear and its reformation in a short time after removal of the stress. With increasing shear stress, the links between individual particles or particle clusters are broken down, allowing significant shear thinning to occur at low stresses and particle concentration (54). Strongly flocculated suspensions are characterized by a deep minimum in the total potential energy ($-V_T^{min}/kT > 20$) and an irreversible rheological behavior during shear. They exhibit significant shear thinning and a significant yield stress.

Influence of Particle Interactions on the Viscosity

The interactions between the particles have a dramatic effect on the viscosity of the suspension, as illustrated in Fig. 4.39 for Al_2O_3 suspensions containing 50 vol% particles which are stabilized with the polyelectrolyte poly(acrylic acid) (see Sect. 4.7). The viscosity decreases dramatically as the concentration of PAA is increased and, at some critical PAA concentration corresponding to the amount required to form a complete monolayer on particle surface, reaches a low plateau region that is almost independent of the PAA concentration. This dramatic change

in viscosity reflects the change from a flocculated suspension at low PAA concentration to an electrosterically stabilized system above the critical PAA concentration. Figure 4.39 also shows that the critical PAA concentration required to achieve monolayer coverage of the particle surface is dependent on the molecular weight. After the critical concentration is reached, further additions of PAA serve mainly to produce excess polymer in the solution, and the viscosity of the suspension starts to increase again at high concentration.

A significant decrease in the viscosity is also found for systems stabilized by electrostatic or steric mechanisms by moving from conditions where the suspension is flocculated to those where it is stable. Data for the viscosity of aqueous suspensions of nearly monodisperse SiO_2 particles (20 vol%) stabilized electrostatically by varying the pH or sterically by adsorbed layers of poly(vinyl alcohol) (PVA) serve to illustrate some of the effects (67). The adsorption behavior of PVA onto the SiO_2 particle surfaces is shown in Fig. 4.40 for a suspension prepared at a pH value (3.7) that is close to the isoelectric point. Initially, all of the PVA added to the suspension is adsorbed on to the particle surfaces. As the PVA concentration increases, the particle surfaces become saturated and a plateau region occurs in the adsorption isotherm. This first plateau is believed to be due to the development of monolayer coverage of PVA on the particle surfaces. Further increases in the PVA concentration lead to an increase in the adsorption and the occurrence of a second plateau region, believed to be due to the develop-

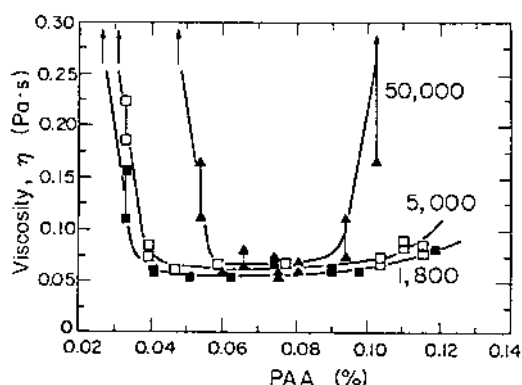


FIGURE 4.39 Viscosity versus the amount of poly(acrylic acid) (PAA) added (as a percent of the dry weight of Al_2O_3) for various PAA molecular weights. The suspensions, prepared at a pH of 9, contained 50 vol% $\alpha\text{-Al}_2\text{O}_3$ particles (Sumitomo AKP-20). The unfilled data points are the initial values and the filled points are the values after 10 min. (From Ref. 48.)

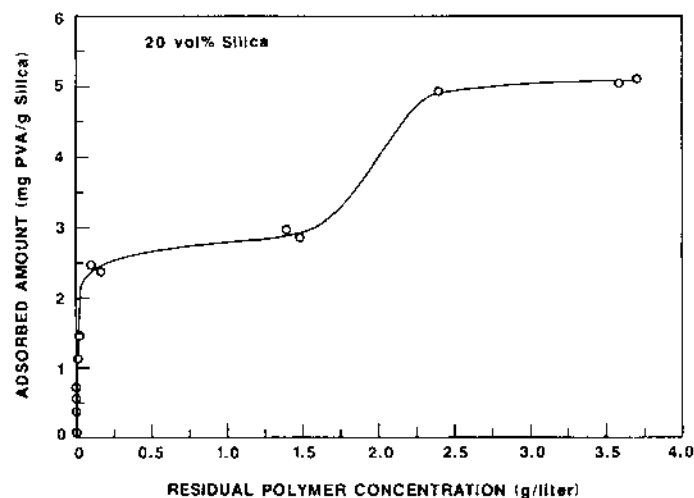


FIGURE 4.40 Adsorption isotherm for suspensions containing 20 vol% SiO_2 particles in solutions of poly(vinyl alcohol). (From Ref. 67.)

ment of a denser packing of the adsorbed polymer molecules or to the occurrence of multilayer adsorption.

Figure 4.41 shows the effect of the adsorbed PVA on the relative viscosity of the suspension for suspensions prepared at a pH of 3.7. The data also show the viscosity for an electrostatically stabilized suspension prepared at a pH of 7.0 without any PVA. For the suspensions containing no PVA, we see that the stabilized suspension (pH = 7.0) has a fairly low viscosity and shows Newtonian behavior, while the unstabilized suspension (pH = 3.7) has a much higher viscosity and shows a high degree of shear thinning.

Considering now the effect of the PVA, we see that initially, the viscosity increases as the amount of adsorbed PVA increases from 0 to 1.1 mg/g of SiO_2 and a high degree of shear thinning occurs. The increase in the viscosity is most likely due to bridging flocculation discussed earlier (see Sect. 4.6.4). When the amount of adsorbed PVA becomes greater than 1.1 mg/g of SiO_2 , the trend is reversed, and the viscosity decreases with increasing amount of adsorbed PVA. For an amount of adsorbed PVA equivalent to that near the end of the first plateau of the adsorption isotherm of Fig. 4.40 (~ 2.9 mg/g SiO_2), the viscosity is fairly low and the behavior is almost Newtonian. For higher PVA concentrations (5.1 mg/g SiO_2), the viscosity shows a small further decrease, but it is still higher than that for the electrostatically stabilized suspension (pH = 7.0).

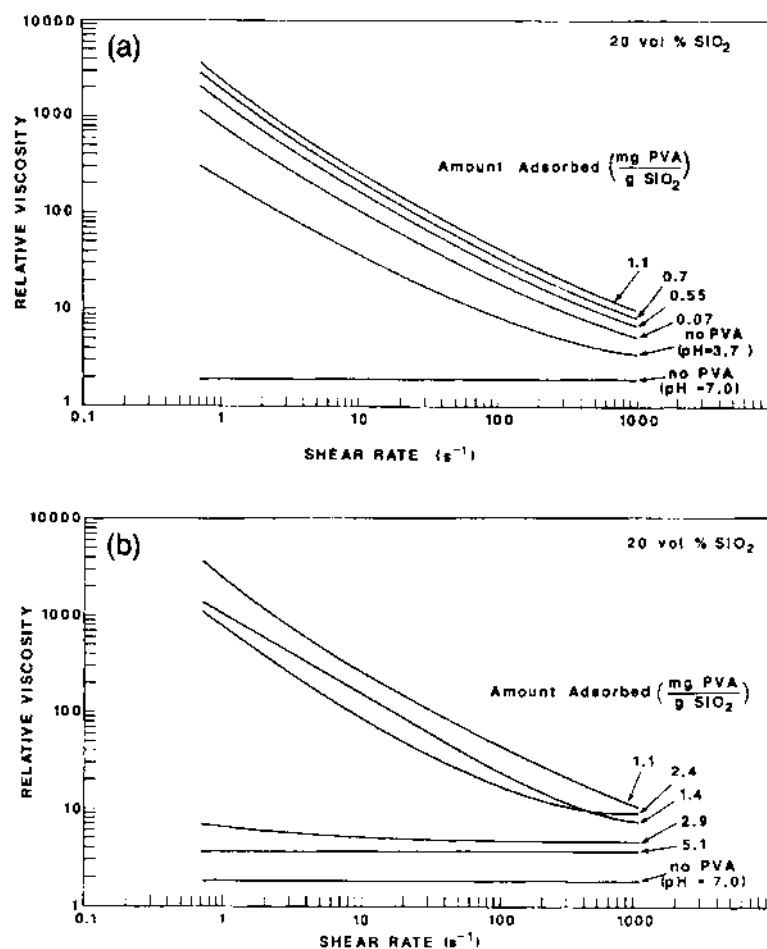


FIGURE 4.41 The relative viscosity versus shear rate for suspensions containing 20 vol% SiO_2 particles. The suspensions prepared at pH = 3.7 (the isoelectric point of the SiO_2) and pH = 7.0 contained no poly(vinyl alcohol). All of the suspensions containing poly(vinyl alcohol) were prepared at pH = 3.7. (From Ref. 67.)

4.9.2.2 Influence of Particle Characteristics

In addition to the interparticle forces discussed above, the particle concentration also has a significant effect on the rheological properties of the suspension. At the same level of stability, the viscosity of the suspension increases with increasing volume fraction of particles, as illustrated by the results Fig. 4.38. The viscosity increases rapidly as the particle concentration approaches f_m , the maximum volume fraction of particles that can be accommodated in the suspension before flow ceases.

For electrostatically and sterically stabilized suspensions (soft sphere systems), the presence of an electrical double layer or an adsorbed polymer layer, as discussed earlier, leads to an increase in the hydrodynamic radius of the particle and a consequent reduction in f_m with decreasing particle size [Eq. (4.87)].

As discussed later (Chapter 6), the packing of particles can be significantly improved by mixing spheres of two different sizes (bimodal distribution) or by using a broad, continuous particle size distribution. The packing of particles can also have a significant effect on the rheological properties of a suspension. Several studies have shown how the use of a bimodal or a broad, continuous particle size distribution can lower the viscosity and increase f_m , but in many cases, large particles ($> 5\text{--}10\text{ }\mu\text{m}$) have been used where colloidal effects play no significant role (68). For electrostatically stabilized suspensions of bimodal polymer particles, Fig. 4.42 shows how the relative viscosity varies with the composition of the mixture and the ratio of the particle sizes (69). The data are also compared with a theoretical model proposed by Farris (70). For even a small size ratio of 2.5, the viscosity of the suspension decreases significantly, and increasing the size ratio to 3.2 produces a further decrease. However, the decrease in the viscosity due to a further increase in the size ratio from 3.2 to 6.8 is far less than expected, and this has been attributed to the enhanced importance of the Debye length with decreasing particle size. For a constant Debye length, δ/a increases with decreasing particle size and, as can be seen from Eq. (4.87), f_{eff} increases.

The shape of the particles also has an effect on the viscosity. Most advanced ceramics are fabricated using nearly equiaxial particles, but the effect of shape would be important, for example, in the colloidal processing of ceramic composites reinforced with whiskers (short single crystal fibers) or platelets. Figure 4.43 shows the results of theoretical calculations for the intrinsic viscosity $[\eta]$ as a function of the axial ratio for particles with the shape of prolate ellipsoids. For an axial ratio of 15–20, which may be relevant to the use of whiskers or platelets in ceramic composites, the results show that $[\eta]$ has a value of ~ 4.5 compared to 2.5 for spherical particles.

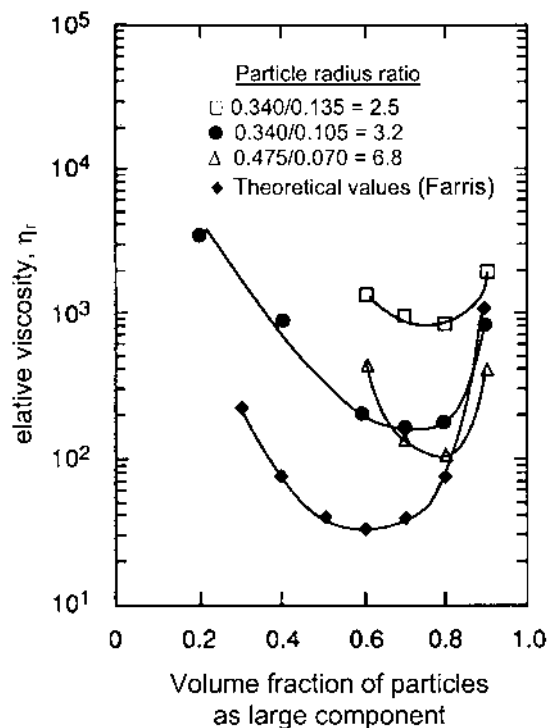


FIGURE 4.42 Effect of particle size ratio on the relative viscosity of stable suspensions of bimodal polymer particles. The data were obtained at a shear stress = 1 dyne/cm² and for suspensions with a particle concentration $f = 0.65$. (From Ref. 69.)

4.10 CONCLUDING REMARKS

In this chapter we outlined the basic principles of electrostatic, steric, and electrosteric stabilization of colloidal suspensions. A considerable gap still exists in our understanding of many aspects of colloid stability, particularly in the case of steric stabilization. Nevertheless, the principles outlined in this chapter provide a basis for manipulating the experimental parameters in order to produce a suspension of the desired stability. Colloidal methods have been used for a long time in the forming of traditional, clay-based ceramics, and they are now being used increasingly in the advanced ceramics sector. The use of colloidal methods for improving the packing uniformity of the green body has yielded clear benefits in the control of the fired microstructure. Finally, many of the principles outlined

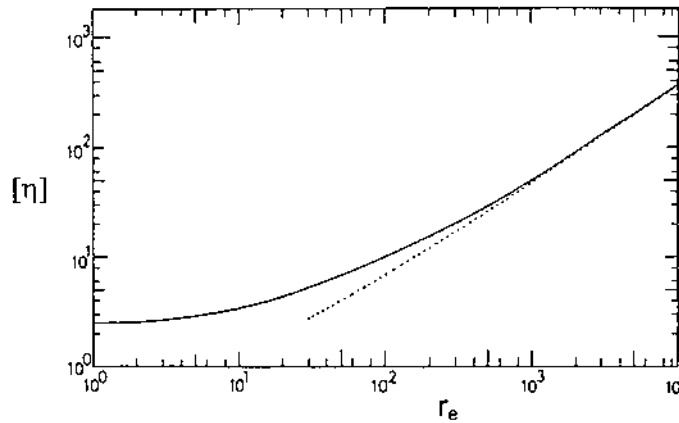


FIGURE 4.43 Intrinsic viscosity as a function of axial ratio for prolate ellipsoids. (From Ref. 53.)

in this chapter will be encountered again in Chapter 6 when we consider the methods used to consolidate ceramic powders.

PROBLEMS

- 4.1 Calculate the van der Waals potential energy V_A , the electrostatic repulsive potential energy V_R , the gravitational potential energy V_G , and the total potential energy V_T between two colloidal particles of radius $a = 0.2 \mu\text{m}$ separated by a distance $h = 10 \text{ nm}$ in a dilute hydrochloric acid solution at 27°C , given that the Hamaker constant $A = 10^{-20} \text{ J}$, the surface potential of the particles $\phi_0 = 25 \text{ mV}$, the dielectric constant of the solution $\epsilon = 80$, the concentration of hydrochloric acid $c = 5 \text{ mmol/l}$, and the density of the particles $d = 4.0 \text{ g/cm}^3$.
- 4.2 Compare the mechanism by which clay mineral particles (e.g., kaolinite) acquire a surface charge in water with the mechanism by which oxide particles (e.g., SiO_2) acquire a surface charge in water.
- 4.3 The clay mineral montmorillonite has the formula



Assuming that all of the Na^+ ions pass into solution, determine the ion exchange capacity (in C/kg) of montmorillonite.

- 4.4 Stable suspensions of Al_2O_3 particles and SiO_2 particles are prepared separately at a $\text{pH} = 6$. If the two suspensions are mixed, discuss the colloidal stability of the resulting suspension.

- 4.5 Derive Eq. (4.37). Hence show that for a high surface potential, the double layer potential at a large distance from a flat surface decays as

$$\phi = \frac{4RT}{zF} \exp(-Kx)$$

- 4.6 Calculate the free energy of repulsion V_R between two double layers, each having an area of 1 cm^2 at a surface potential $\phi_o = 4RT/F$, in a monovalent electrolyte giving a Debye length $1/K$ equal to 10^{-6} cm and a distance of separation equal to 10 nm .
- 4.7 The surface potential of a flat surface in dilute HCl solution at 27°C is 50 mV . If the acid concentration is 5 mmol/L , calculate the surface charge density. The dielectric constant of the solution can be assumed to be equal to that of water (i.e., 78).
- 4.8 a. How does the double-layer repulsion change if the medium water is replaced by methanol, assuming that the surface potential and the ionic concentration remain the same?
 b. If a monovalent electrolyte is replaced by a bivalent electrolyte but the Debye length $1/K$ remains the same, how would the concentration of the electrolyte have to change?
- 4.9 In a particle electrophoresis experiment, the particles in a dilute suspension are observed to travel an average distance of 1 mm in 25 s when a potential difference of 100 V is applied to the electrodes that are 5 cm apart. Determine the ζ -potential of the particles.
- 4.10 Derive Eq. (4.66) for the root mean square end-to-end distance $\langle r^2 \rangle^{1/2}$ of a polymer chain. Derive expressions for the average end-to-end distance $\langle r \rangle$ and the most probable end-to-end distance r_{mp} in terms of $\langle r^2 \rangle^{1/2}$.
 Determine $\langle r^2 \rangle^{1/2}$ for polystyrene molecules in cyclopentane given that the degree of polymerization of polystyrene is 2×10^4 .
- 4.11 Determine the van der Waals potential energy V_A , the free energy due to the mixing effect ΔG_{mix} , and the free energy due to the elastic effect $\Delta G_{\text{elastic}}$, between two mica particles of radius $a = 0.2 \text{ }\mu\text{m}$ separated by a distance $h = 2L/3$ in a solution of polystyrene in cyclopentane at 27°C , given that the Hamaker constant $A = 5 \times 10^{-20} \text{ J}$, the Flory-Huggins parameter $\chi = 0.25$, the degree of polymerization of the polystyrene molecules $= 2 \times 10^4$, and $L = \langle r^2 \rangle^{1/2}$, the root-mean-square end-to-end distance of the polystyrene molecules in the solvent. State any assumptions that you make.
- 4.12 Using Eq. (4.87), plot the effective volume fraction of particles f_{eff} versus the volume fraction of solid particles f for particles with radii of $10, 1, 0.1, \text{ and } 0.01 \text{ }\mu\text{m}$ and assuming an adsorbed layer with a constant thickness of 10 nm .
- 4.13 Assuming that the suspension viscosity can be described by the Krieger-Dougherty equation, determine the relative viscosity for suspensions containing 40 vol\% of solid spherical particles when
 a. The particles are hard spheres with a radius of $1 \text{ }\mu\text{m}$. Assume $[\eta] = 2.5$ and $f_m = 0.63$.

- b. The particles with a radius of $1\text{ }\mu\text{m}$ have an adsorbed surfactant layer with a thickness of 5 nm .
- c. The particles with a radius of $0.1\text{ }\mu\text{m}$ have an adsorbed surfactant layer with a thickness of 5 nm .
- d. The particles are elongated. Assume $[\eta] = 4.5$ and $f_m = 0.5$.

REFERENCES

1. Overbeek, J. Th. G. Colloid and Surface Chemistry: A Self-Study Course; Massachusetts Institute of Technology: Cambridge, MA, 1972, Parts 1–4.
2. Hunter, R. J. Foundations of Colloid Science; Oxford University Press: Oxford, 1986, Vol. 1, 1989, Vol. 2.
3. Colloidal Dispersions; Goodwin, J. W. ed.; The Royal Society of Chemistry: London, 1982.
4. Israelachvili, J. N. Intermolecular and Surface Forces; 2nd ed.; Academic Press: London, 1992.
5. Tabor, D. In Colloidal Dispersions; Goodwin, J. W. ed.; The Royal Society of Chemistry: London, 1982, Chap. 2.
6. Tabor, D. Gases, Liquids and Solids; 3rd ed.; Cambridge University Press: Cambridge, 1991, Chap. 12.
7. Hamaker, H. C. Physica. 1937, Vol. 4, 1058.
8. Lifshitz, E. M. Soviet Phys. JETP. 1956, Vol. 2, 73.
9. Mahanty, J.; Ninham, B. W. Dispersion Forces; Academic Press: New York, 1976.
10. Margenau, H.; Kestner, N. R. Theory of Intermolecular Forces; Pergamon Press: Oxford, 1971.
11. Israelachvili, J. N.; Tabor, D. Prog. Surface Membrane Sci. 1973, Vol. 7, 1.
12. Israelachvili, J. N. Quarterly Reviews of Biophysics. 1974, Vol. 6, 341.
13. French, R. H. J. Am. Ceram. Soc. 2000, Vol. 83, 2117.
14. Bergström, L. Adv. Colloid Interface Sci. 1997, Vol. 70, 125.
15. Ackler, H. D.; French, R. H.; Chiang, Y.-M. J. Colloid Interface Sci. 1996, Vol. 179, 460.
16. Tabor, D.; Winterton, R. H. S. Proc. Roy. Soc. 1969, Vol. A312, 435.
17. Israelachvili, J. N.; Tabor, D. Proc. Roy. Soc. 1972, Vol. A331, 19.
18. Hansma, P. K.; Elings, V. B.; Marti, O.; Bracker, C. E. Science. 1988, Vol. 242, 157.
19. Meyer, E. Prog. Surf. Sci. 1992, Vol. 41, 1.
20. Ducker, W. A.; Senden, T. J.; Pashley, R. M. Langmuir. 1992, Vol. 8, 1831.
21. Larson, I.; Drummond, C. J.; Chan, D. Y. C.; Grieser, F. J. Am. Ceram. Soc. 1993, Vol. 115, 11885.
22. Biggs, S.; Mulvaney, P. J. Chem. Phys. 1994, Vol. 100, 8501.
23. Senden, T. J.; Drummond, C. J.; Kékicheff, P. Langmuir. 1994, Vol. 10, 358.
24. Healey, T. W.; White, L. R. Adv. Colloid Interface Sci. 1978, Vol. 9, 303.
25. Hunter, R. J. Zeta Potential in Colloid Science; Academic Press: New York, 1981.
26. Reed, J. S. Introduction to the Principles of Ceramic Processing; Wiley: New York, 1988, p. 134.
27. Parks, G. A. Chem. Rev. 1965, Vol. 65, 177.

28. Yoon, R. H.; Salman, T.; Donnay, G. J. *Colloid Interface Sci.* 1979, Vol. 70, 483.
29. Carre, A.; Roger, F.; Varinot, C. J. *Colloid Interface Sci.* 1992, Vol. 154, 174.
30. Shaw, D. J. *Introduction to Colloid and Surface Chemistry*; 3rd ed.; Butterworth: London, 1980.
31. Horn, R. G.; Clarke, D. R.; Clarkson, M. T. J. *Mater. Res.* 1988, Vol. 3, 413.
32. Israelachvili, J. N.; Adams, G. E. J. *Chem. Soc. Faraday Trans.*, 1. 1978, Vol. 74, 975.
33. Jang, H. M.; Fuerstenau, D. W. *Colloids Surf.* 1986, Vol. 21, 238.
34. Napper, D. H. *Polymeric Stabilization of Colloidal Dispersions*; Academic press: New York, 1983.
35. Napper, D. H. In *Colloidal Dispersions*; Goodwin, J. W. ed.; The Royal Society of Chemistry: London, 1982, Chap. 5.
36. Flory, P. J. *Statistical Mechanics of Chain Molecules*; Hanser Publishers: New York, 1969.
37. Lewis, J. A. J. *Am. Ceram. Soc.* 2000, Vol. 83, 2341.
38. Jensen, W. B. *The Lewis Acid-Base Concepts*; Wiley: New York, 1980.
39. Laible, R.; Hamann, K. *Adv. Colloid Interface Sci.* 1980, Vol. 13, 65.
40. Green, M.; Kramer, T.; Parish, M.; Fox, J.; Lalanandhan, R.; Rhine, W.; Barclay, S.; Calvert, P.; Bowen, H. K. *Advances in Ceramics.* 1987, Vol. 21, 449.
41. Vincent, B.; Luckham, P. F.; Waite, F. A. J. *Colloid Interface Sci.* 1980, Vol. 73, 508.
42. Vincent, B.; Edwards, J.; Emmett, S.; Jones, A. *Colloids Surf.* 1986, Vol. 18, 261.
43. Klein, J. *Physics World*; June 1989, pp. 35–38.
44. Patel, S. S.; Tirrell, M. *Ann. Rev. Phys. Chem.* 1989, Vol. 40, 597.
45. Horn, R. G. J. *Am. Ceram. Soc.* 1990, Vol. 73, 1117.
46. Fowkes, F. M. *Advances in Ceramics.* 1987, Vol. 21, 412.
47. Cesarano, J., III.; Aksay, I. A.; Bleier, A. J. *Am. Ceram. Soc.* 1988, Vol. 71, 250.
48. Cesarano, J., III.; Aksay, I. A. J. *Am. Ceram. Soc.* 1988, Vol. 71, 1062.
49. Biggs, S.; Healy, T. W. J. *Chem Soc. Faraday Trans.* 1994, Vol. 90, 3415.
50. Rojas, D. J.; Claesson, P. M.; Muller, D.; Neuman, R. D. J. *Colloid Interface Sci.* 1998, Vol. 205, 77.
51. Marra, J.; Hair, M. L. J. *Phys. Chem.* 1988, Vol. 92, 6044.
52. Aksay, I. A. *Advances in Ceramics.* 1984, Vol. 9, 94.
53. Goodwin, J. W. In *Colloidal Dispersions*; Goodwin, J. W. ed.; The Royal Society of Chemistry: London, 1982, Chap. 8.
54. Bergström, L. In *Surface and Colloid Chemistry in Advanced Ceramic Processing*; Pugh, R. J., Bergström, L. eds.; Marcel Dekker: New York, 1994, Chap. 5.
55. Barnes, H. A.; Hutton, J. F.; Walters, K. *An Introduction to Rheology*; Elsevier Science: Amsterdam, 1989.
56. Jones, D. A. R.; Leary, B.; Boger, B. V. J. *Colloid Interface Sci.* 1991, Vol. 147, 479.
57. de Hek, H.; Vrij, A. J. *Colloid Interface Sci.* 1981, Vol. 84, 409.
58. Krieger, I. M. *Adv. Colloid Interface Sci.* 1972, Vol. 3, 111.
59. Frith, W. J.; Strivens, T. A.; Russel, W. B. J. *Colloid Interface Sci.* 1990, Vol. 139, 55.
60. Krieger, I. M.; Dougherty, T. J. *Trans. Soc. Rheol.* 1959, Vol. 3, 137.

61. van der Werff, J. C.; de Kruif, C. G. J. *Rheol.* 1989, Vol. 33, 421.
62. Choi, G. N.; Krieger, I. M. J. *Colloid Interface Sci.* 1986, Vol. 113, 101.
63. Jones, D. A. R.; Leary, B.; Boger, B. V. J. *Colloid Interface Sci.* 1991, Vol. 150, 84.
64. Mewis, J.; Frith, W. J.; Strivens, T. A.; Russel, W. B. *AIChE J.* 1989, Vol. 35, 415.
65. Reynolds, P. A.; Reid, C. A. *Langmuir.* 1991, Vol. 7, 89.
66. Velamakanni, B. V.; Chang, J. C.; Lange, F. F.; Pearson, D. S. *Langmuir.* 1990, Vol. 6, 1323.
67. Sacks, M. D.; Khadilkar, C. S.; Scheiffele, G. W.; Shenoy, A. V.; Dow, J. H.; Sheu, R. S. *Adv. Ceram.* 1987, Vol. 21, 495.
68. Smith, P. L.; Haber, R. A. J. *Am. Ceram. Soc.* 1992, Vol. 75, 290.
69. Hoffmann, R. L. J. *Rheol.* 1992, Vol. 36, 947.
70. Farris, R. J. *Trans. Soc. Rheol.* 1968, Vol. 12, 281.

5

Sol-Gel Processing

5.1 INTRODUCTION

The term *sol-gel* is used broadly to describe the preparation of ceramic materials by a process that involves the preparation of a sol, the gelation of the sol, and the removal of the liquid. A *sol* is a suspension of colloidal particles in a liquid or a solution of polymer molecules. The term *gel* refers to the semirigid mass formed when the colloidal particles are linked to form a network or when the polymer molecules are cross-linked or interlinked. Two different sol-gel processing routes are commonly distinguished: the *particulate* (or *colloidal*) gel route in which the sol consists of dense colloidal particles (1 to 1000 nm) and the *polymeric* gel route in which the sol consists of polymer chains but has no dense particles >1 nm. In many cases, particularly when the particle size approaches the lower limit of the colloidal size range, the distinction between a particulate and a polymeric system may not be very clear.

The subject of sol-gel science is covered in great depth in Ref. 1. We outlined the basic steps in sol-gel processing in Chapter 1 when we surveyed the common methods used for the production of ceramics. This chapter provides a more detailed examination of the science and practice of the process for the fabrication of ceramics and glasses. We shall pay particular attention to the sol-gel processing of silica glass not only because of its practical interest but also because of the heightened understanding of the process mechanisms and structural evolution developed from numerous studies.

Figure 5.1 shows a schematic illustration of the routes that can be followed in sol-gel processing. The starting compounds (*precursors*) for the preparation of the sol consist of inorganic salts or metal-organic compounds, but we shall

focus mainly on the *metal alkoxides*, a class of metal-organic precursors that are most widely used in sol-gel research. The chemical reactions that occur during the conversion of the precursor solution to the gel have a significant influence on the structure and chemical homogeneity of the gel. A basic problem therefore is understanding how the rates of the chemical reactions are controlled by the processing variables such as chemical composition of the precursor, concentration of reactants, pH of the solution, and temperature. The problem becomes more complex when a solution of two or more alkoxides is used in the fabrication of *multicomponent* gels (i.e., gels containing more than one metal cation). There will be a loss of chemical homogeneity if steps are not taken to control the reaction.

After preparation, the gel contains a large amount of liquid existing in fine interconnected channels, and it must be dried prior to conversion to a useful material. Drying by evaporation under normal conditions gives rise to capillary pressure that causes shrinkage of the gel network. The resulting dried gel is called a *xerogel*. The capillary pressure can be quite large in polymeric gels because the pores are normally much finer than those in colloidal gels; consequently, severe problems can be encountered with warping and cracking of the gel. Two general approaches have been used to circumvent these problems. The use of chemicals added to the precursor solution prior to gelation, referred to as *drying control chemical additives* (DCCAs), permit relatively rapid drying, but the mechanism by which they operate is not very clear. The removal of the liquid under *supercritical* conditions eliminates the liquid-vapor interface and thereby pre-

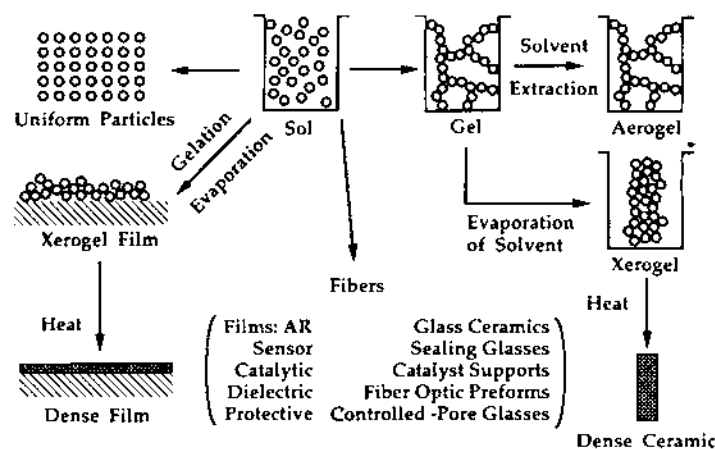


FIGURE 5.1 Schematic illustration of the routes that could be followed in sol-gel processing. (From Ref. 1.)

vents the development of capillary stresses; thus, the gel undergoes relatively little shrinkage. The dried gel, called an *aerogel*, is therefore fragile and may shrink considerably during firing.

Most gels have an amorphous structure even after drying and contain fine pores, which in many cases can be fairly uniform in size. If a dense ceramic is required as the end product, these characteristics are very favorable for good densification during *sintering*. When compared to the production of similar ceramics by traditional processing routes involving the compaction and sintering of crystalline particles, a reduction in the sintering temperature, particularly in the case of polymeric gels, forms a characteristic advantage of the sol–gel route. In some cases, crystallization of the gel prior to full densification may limit the sintering rate for compositions that are crystallizable. The competition between densification and crystallization during sintering is discussed in Chapter 11.

Applications sol–gel processing can provide substantial benefits, such as the various special shapes that can be obtained directly from the gel state (e.g., monoliths, films, fibers, and particles), control of the chemical composition and microstructure, and low processing temperatures. However the disadvantages are also real. Many metal alkoxides are fairly expensive, and most are very sensitive to moisture so that they must be handled in a dry environment (e.g., an inert atmosphere glove box). The large shrinkage of the gel during drying and sintering makes dimensional control of large articles difficult. It is often difficult to dry monolithic gels thicker than a few millimeters or films thicker than $\sim 1\text{ }\mu\text{m}$ without cracking. The sol–gel process is therefore seldom used for the production of thick articles. Instead, it has seen considerable use for the production of small or thin articles such as films, fibers, and powders, and its use in this area is expected to grow substantially in the future.

5.2 TYPES OF GELS

5.2.1 Particulate Gels

Particulate gels consist of a skeletal network of essentially anhydrous particles held together by surface forces, with the structure of the particles normally corresponding to that of the bulk solid with the same composition. For example, colloidal SiO_2 particles have the same structure as bulk silica glass produced by melting. Hydroxyl groups are present only on the surface of the particles. The pores in particulate gels are much larger than in polymeric gels, and the capillary stress developed during drying is therefore lower; thus less shrinkage occurs. Because of the larger pores, the permeability of colloidal gels is higher, and this, combined with the lower capillary pressure, means that colloidal gels are less likely to crack during drying. The structure of the dried gel is characterized by a relatively high porosity ($\sim 70\text{--}80\%$) and pores that are relatively large compared

with the size of the particles (i.e., the average pore size is typically 1–5 times the particle size).

In Chapter 4, we discussed the factors that influence the stability of colloidal suspensions. Particulate gels are commonly prepared by taking a stable colloidal suspension and reducing its volume by evaporating some of the liquid or reducing its stability through the addition of an electrolyte such as an acid, a base, or a metal salt. The attractive van der Waals forces dominate, and the particles stick on contact, forming a skeletal network. Methods for the preparation of SiO_2 gels from fine particles ($\sim 0.05\text{--}0.2\ \mu\text{m}$) made by flame oxidation (sometimes referred to as fumed silica) has been described by Rabinovitch et al. (2,3) and by Scherer and Luong (4). This class of gels provides an interesting contrast with the properties of polymeric gels prepared from silicon alkoxides.

The structure of the dried gel has important consequences for its sintering and conversion to the final article. Densification of amorphous materials during sintering occurs by viscous flow. Because of the larger pores (hence lower driving force for densification), particulate gels sinter at temperatures well above the glass transition temperature T_g . In contrast, polymeric gels with their much finer pores sinter near T_g . For particulate SiO_2 gels (particle size $\approx 50\ \text{nm}$), sintering is performed in the range of $1200\text{--}1500^\circ\text{C}$.

The particulate gel route is not effective for the production of dense ceramics from crystalline particles because the large pore size relative to the particle size is thermodynamically unfavorable for achieving densification in crystalline systems (see Chapter 9). The trend in the production of crystalline ceramics, as we have indicated earlier, is towards the use of fine particles that are consolidated uniformly from stable colloidal suspensions (Fig. 5.2).

While polymeric gels are the subject of considerable research and publication, the particulate systems include some of the most successful industrial applications of sol-gel technology. An early application was in the nuclear fuels

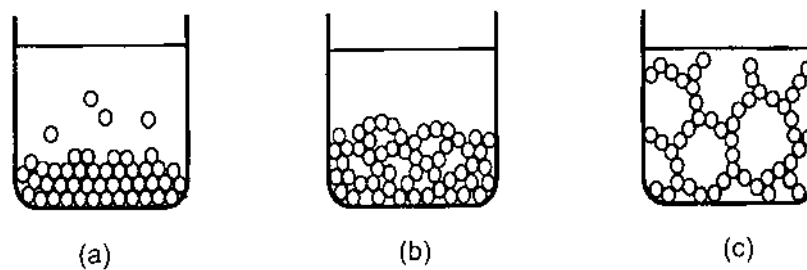


FIGURE 5.2 Sediments formed from (a) a stable colloid and (b) a flocculated colloid compared with (c) a colloidal gel

industry in the late 1950s (5). The goal of the work was to prepare small spheres (several tens of micrometers) of radioactive oxides [(Th,U)O₂] as fuels for nuclear reactors. The advantage of the sol–gel process was that it avoided the generation of harmful dust, which would be produced in conventional ceramic processing methods, and allowed the formation of spheres. The spherical shape was achieved by dispersing an aqueous sol in an immiscible organic liquid so that the sol would form into small droplets, each of which would subsequently gel. The particulate sol–gel route has also been applied to the fabrication of porous oxides for catalyst supports (6) and chromatographic columns (7).

For the formation of multicomponent gels that contain more than one metal cation (e.g., SiO₂ doped with TiO₂), the particulate gel route typically involves the mixing of two or more sols (e.g., sols of SiO₂ and TiO₂) or the addition of a metal (e.g., Ti) salt solution to the sol (e.g., SiO₂) followed by gelling. The range of chemical homogeneity in the gelled material can, at best, be of the order of the particle size containing between 10³ and 10⁹ molecules. When the dopant concentration is small (i.e., less than a few percent), the production of good chemical homogeneity becomes difficult. The polymeric gel route commonly provides exceptional chemical homogeneity because the mixing can be achieved at a molecular level rather than at the colloidal level.

5.2.2 Polymeric Gels

Polymeric gels consist of a skeletal network of polymer chains that form by the entanglement and cross-linking of growing polymer chains or polymer clusters resulting from the hydrolysis, condensation and polymerization of precursors in solution. Our main focus will be on polymeric gels formed from metal alkoxide precursors. Depending on the conditions used in the preparation, the structure of the polymer chains can vary considerably. The polymerization of silicon alkoxide, for example, can lead to complex branching of the polymer as shown in Fig. 5.3, but under certain conditions (e.g., low water concentration), little branching will occur.

Gelation is accompanied by a sharp increase in the viscosity that essentially “freezes-in” the polymer structure at the point of gelling. At this stage, the gel consists of a weak amorphous solid structure and an interconnected network of very fine pores filled with liquid. The volume of the liquid-filled pores is very high, typically 90–95% of the total volume, and the diameters of the pore channels are typically of the order of 2 to 10 nm. The frozen-in structure can change appreciably during subsequent aging of the gel and during removal of the liquid from the gel (drying). Under certain conditions, the aging gel can shrink considerably while expelling liquid. Because of the very fine pores, huge capillary stresses are developed during normal evaporation of the liquid so that polymeric gels are very prone to cracking. The capillary stresses are equivalent to the application

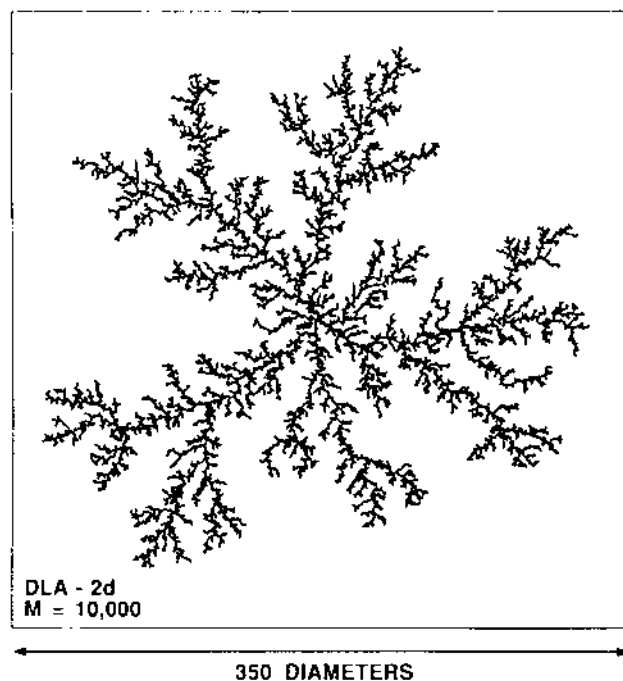


FIGURE 5.3 Fractal polymer made by branching of polyfunctional monomer. (Computer simulation of two-dimensional aggregation.) (From Ref. 8.)

of external compressive stresses on the gel. Removal of the liquid by evaporation therefore collapses the weak polymer network and results in additional cross-linking of the polymer structure. Cross-linking and collapse of the gel continues until the structure can withstand the compressive action of the capillary stresses. Depending on the structure of the gel, the porosity of the dried gel can be anywhere between ~30 and 70%.

Compared to the particulate gel case, structural effects of the dried gel on sintering are more pronounced as well as more complex. The average pore size of polymeric gels is usually much finer than that of colloidal gels so that the driving force for sintering (which varies inversely as the radius of the pore) is usually much higher. The result is a lowering of the sintering temperature for polymeric gels. For example, in the case of SiO_2 , viscous sintering of polymeric gels occurs generally between 800 and 1000°C.

The local chemical structure also has an important influence on the sintering of polymeric gels. While there is some collapse of the gel structure during drying,

the solid skeletal phase that makes up the dried gel is not identical to the corresponding bulk glass produced, for example, by melting. Evidence suggests that the gel structure contains fewer cross-links and additional free volume compared to the melted glass (9). This means that during the firing process, the gel structure will change to become more highly cross-linked with a corresponding reduction in its free volume and its surface area.

While there are many potential applications of the polymeric gel route, the preparation of thin films is by far the most important use. As discussed later, thin films benefit from most of the advantages of the method while avoiding most of the disadvantages. However, even films suffer from problems (e.g., cracking) if attempts are made to prepare films thicker than 1 μm .

5.3 SOL-GEL PROCESSING OF AQUEOUS SILICATES

The chemistry of silica in aqueous systems (e.g., sodium silicate) is discussed in detail by Iler (10). Silicon is hydrolyzed even in dilute acid and as shown in Fig. 5.4, silicic acid [$\text{Si}(\text{OH})_4$], often referred to as monosilicic acid, orthosilicic acid, or soluble silica, is the dominant mononuclear species in solution below pH values of ~ 7 (11). The Si-OH group is called a *silanol* group, indicating that $\text{Si}(\text{OH})_4$ contains four silanol groups. Above $\text{pH} \approx 7$, further hydrolysis produces anionic species:

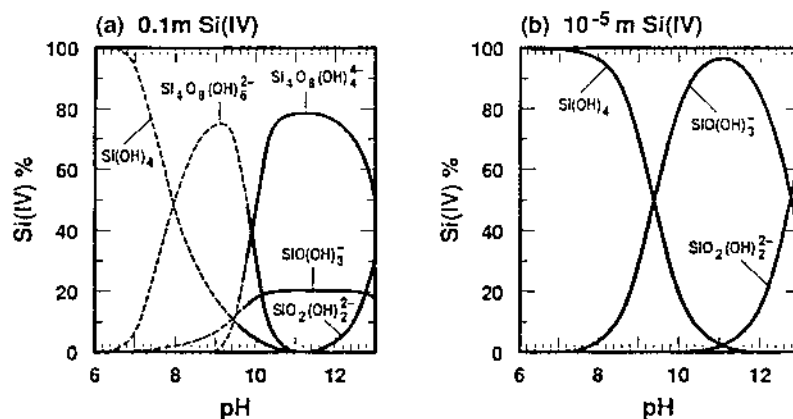
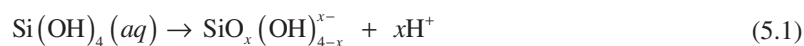


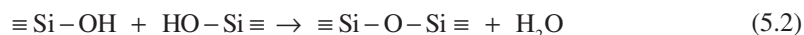
FIGURE 5.4 Distribution of aqueous silicate species at 25°C in (a) 0.1 m Si(IV) and (b) 10^{-5} m Si(IV). Ionic strength $I = 3$ m. (From Ref. 11.)

where $\text{SiO}(\text{OH})_3^-$ [$x = 1$ in Eq. (5.1)] is the dominant mononuclear species. Because $\text{SiO}(\text{OH})_3^-$ is a very weak acid, $\text{SiO}_2(\text{OH})_2^{2-}$ is observed in appreciable quantities only above pH values of ~ 12 (Fig. 5.4).

Solutions of silicic acid thicken slowly and finally form a gel. Since the gel appears outwardly like organic gels, it was generally thought that $\text{Si}(\text{OH})_4$ polymerized into siloxane chains (i.e., chains with $\text{Si}-\text{O}-\text{Si}$ bonds) that branched and crosslinked like many organic polymers. However, in his book, Iler (10) clearly states that silicic acid polymerizes into discrete *particles* that in turn aggregate into chains and networks. Polymerization occurs in three stages:

1. Polymerization of monomers to form particles
2. Growth of particles
3. Linking of particles into chains, then networks that extend throughout the liquid medium, finally thickening into a gel.

In aqueous silicate chemistry, the term *polymerization* is commonly used in its broadest sense to include reactions that result in an increase in molecular weight of silica. It includes the condensation of silanol groups



to give molecularly coherent units of increasing size, whether these are polymeric species, particles, or particle networks. Condensation reactions take place in such a way as to maximize the number of $\text{Si}-\text{O}-\text{Si}$ bonds and minimize the number of terminal hydroxyl groups through internal condensation. Thus rings are formed quickly to which monomers add, giving particles that in turn condense to the more compact state, leaving OH groups on the outside. The particles serve as nuclei for further growth, which occurs by an Ostwald ripening process (see Chapter 9). The smaller, more soluble particles dissolve and precipitate on the larger, less soluble particles, so that the number of particles decreases but the average particle size increases. Because of the greater solubility, particle growth is enhanced at higher temperatures, particularly at pH values > 7 . After the gel network has formed, the structure becomes stronger as the necks between the particles become thicker due to solution of silica and its reprecipitation at the necks. A schematic of the polymerization process for aqueous silica is shown in Fig. 5.5.

5.3.1 Effect of pH

The polymerization of aqueous silica is divided into three approximate pH domains (1,10): $\text{pH} < \sim 2$, $\text{pH} \approx 2-7$, and $\text{pH} > \sim 7$ (Fig. 5.6). The pH value of 2 occurs as a boundary in that the point of zero charge (PZC), where the surface charge is zero, and the isoelectric point (IEP), where the electrophoretic mobility is zero, both occur close to this pH value (Chapter 4). The pH of 7 forms another

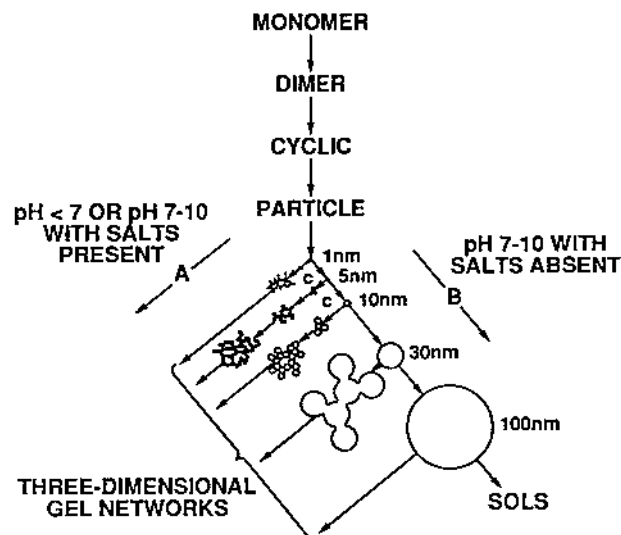
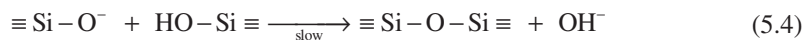


FIGURE 5.5 Polymerization behavior of silica. In basic solution (B) particles in sol grow in size with decrease in numbers; in acid solution or in presence of flocculating salts (A), particles aggregate into three-dimensional networks and form gels. (From Ref. 10.)

boundary because the solubility and dissolution rates of silica are maximized at or above this pH value and because the appreciable surface charge creates a significant repulsion so that particle growth occurs without aggregation or gelation. Silica sols have a maximum stability at $\text{pH} \approx 2$ and a minimum stability with rapid gelling at $\text{pH} \approx 6$.

5.3.1.1 Polymerization in the pH range of 2 to 7

Since the gelation times decrease with increasing pH values between 2 and 6, it is generally assumed that above the IEP the gelation rate is proportional to $[\text{OH}^-]$. The base-catalyzed polymerization occurs by a nucleophilic mechanism according to the following reaction sequence:



The surface silanols will be deprotonated depending on their acidity. The acidity depends on the other substituents on the silicon atom. When basic OR and OH groups are replaced by O—Si, the reduced electron density on Si increases the

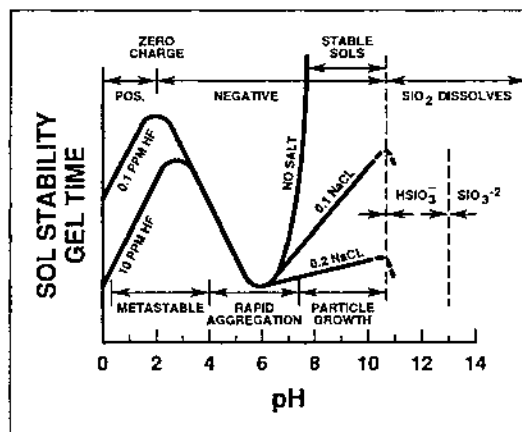


FIGURE 5.6 Effect of pH in the colloidal silica-water system. (From Ref. 10)

acidity of the protons on the remaining silanols. In any given distribution of silicate species, the most acidic silanols are the ones contained in the most highly condensed species, and these will be most likely to be deprotonated according to Eq. (5.3). Therefore, condensation according to Eq. (5.4) occurs preferentially between the more highly condensed species and the less highly condensed, neutral species. The formation of dimers is slow [Eq. (5.4)], but once formed, dimers react with monomers to form trimers which, in turn, react with monomers to form tetramers. Cyclization (to form rings) is rapid due to the proximity of the chain ends and the rapid depletion of monomers. Cyclic trimers may also form, but the strain resulting from the reduced Si—O—Si bond angles makes them much less stable in this pH range. (As described later, they are, however, quite stable at pH values above ~ 12 .)

Further growth occurs by continued addition of lower molecular weight species to more highly condensed species (by conventional polymerization or by Ostwald ripening) and by aggregation of the condensed species to form chains and networks. Near the IEP, where there is no electrostatic repulsion, growth and aggregation occur together and may be indistinguishable. However, particle growth becomes negligible when the particles reach a size of 2–4 nm because of low solubility of silica in this pH range and the greatly reduced size-dependent solubility (Fig. 5.7). The gels consist of chains and networks of very fine particles. The presence of a salt (e.g., NaCl) has little effect on the gelation in this pH range.

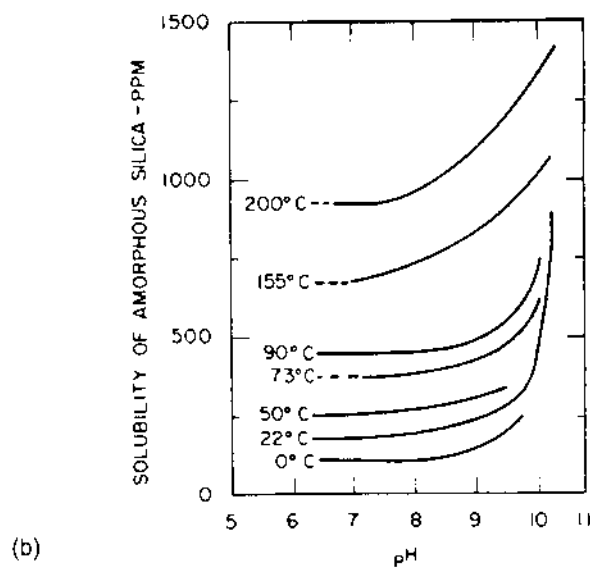
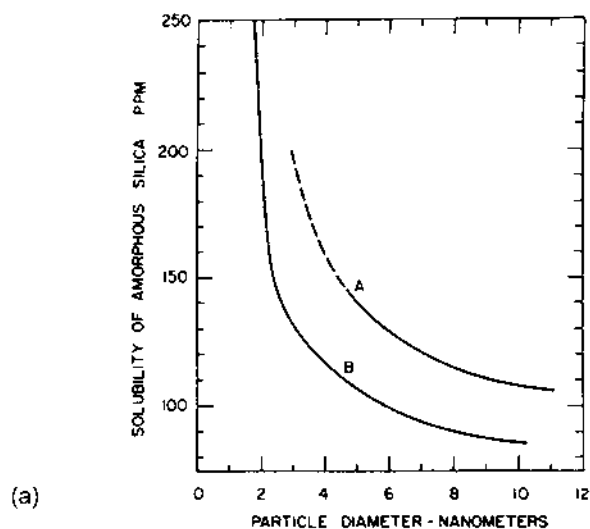


FIGURE 5.7 (a) Relation between solubility of amorphous silica in water at 25°C and particle diameter. Particles A made at 80–100°C at pH 8. Particles B made at 25–50°C at pH 2.2. (b) Solubility of amorphous silica versus pH at different temperatures. (From Ref. 10.)

5.3.1.2 Polymerization above pH ≈ 7

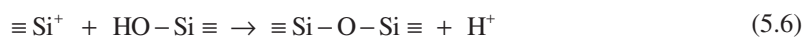
Polymerization occurs by the same nucleophilic mechanism described by Eqs. (5.3) and (5.4). In this pH range, however, all the condensed species are likely to be ionized and therefore mutually repulsive. Growth occurs by the addition of monomers to the highly condensed particles rather than by aggregation. Particles with diameters of 1 to 2 nm are formed in a few minutes. Above pH values of ~ 12 , where most of the silanols are deprotonated, the condensed species are cyclic trimers and tetramers. Cyclic trimers are stable in this pH range because the planar, cyclic configuration permits the greatest separation of charge between the deprotonated sites.

Because of the greater solubility of silica in this pH range and the greater size-dependence of solubility (Fig. 5.7), growth of the primary particles occurs by Ostwald ripening. Particles grow rapidly to a size (5–10 nm) that depends on the temperature. Since the ripening process occurs by the dissolution of the smaller particles and reprecipitation on the larger particles, the growth rate depends on the particle size distribution.

In the absence of any salt, the electrostatic repulsion between the particles leads to stable sols without the formation of chains or aggregates. The addition of salt (e.g., NaCl) leads to a reduction in the thickness of the electrical double layer (Chapter 4), thereby reducing the stability of the sol and producing a dramatic reduction of the gelation time (Fig. 5.6).

5.3.1.3 Polymerization below pH ≈ 2

Since the gelation times decrease with decreasing pH below ≈ 2 , the polymerization rate is proportional to $[H^+]$. The acid-catalyzed polymerization mechanism is not clear. Iler and others propose a mechanism that involves a *siliconium ion* intermediate ($\equiv Si^+$):



However, in the polymerization of silicon alkoxides discussed in the next section, Brinker and Scherer (1) suggest that the condensation process more likely proceeds via an associative $\equiv SiOHR(OH_2)^+$ intermediate.

In the absence of fluoride ion, the solubility of silica in this pH range is very low, and for moderate acidities (pH = 0–2), the silicate species should not be highly ionized. Therefore it is likely that the formation and aggregation of the primary particles occur together and that Ostwald ripening contributes little to the growth after the particles exceed a diameter of ~ 2 nm. As a result, the gel networks are composed of exceedingly fine particles. Traces of F^- or the addition of HF lead to a reduction of the gelation times and produce gels similar to those

formed above $\text{pH} \approx 2$. Because F^- and OH^- have a similar size, they have the same influence on the polymerization behavior.

5.4 METAL ALKOXIDES

Metal alkoxides are the most common precursors used in sol–gel processing because they react readily with water. We recall that these compounds are also used in the synthesis of fine oxide particles (e.g., the Stober process discussed in Chapter 2). Metal alkoxides are a class of metal-organic compounds which have the general formula $\text{M}(\text{OR})_z$, where M is a metal of valence z and R is an alkyl group. They can be considered as derivatives either of an alcohol in which the hydroxylic hydrogen is replaced by the metal or of metal hydroxide in which the hydrogen is replaced by an alkyl group. Accordingly, the chemistry of the metal alkoxides involves the metal-oxygen-carbon bond system. Metal alkoxides have also been referred to in the literature as *organometallic* compounds, but it is not correct to call alkoxides organometallic. An organometallic has a metal-carbon (M—C) bond (unlike most alkoxides), whereas a metal-organic need not have M and C directly bonded.

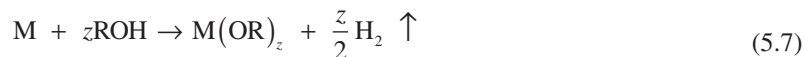
The synthesis and properties of metal alkoxides have been considered in detail by Bradley et al. (12), while several important synthesis reactions are described in a review article (13). Here we consider only a few of the main features relevant to the sol–gel processing of ceramics and glasses.

5.4.1 Preparation

The method used for the preparation of a metal alkoxide depends, in general, on the electronegativity of the metal. The main methods may be divided into two groups: (1) reactions between metals and alcohols for the more electropositive metals (i.e., those with relatively low electronegativity values) and (2) reactions involving metal chlorides for the less electropositive metals or electronegative elements (i.e., those with relatively high electronegativity values). In addition, there are miscellaneous methods that are useful for the synthesis of some alkoxides. These include alcohol interchange or alcoholysis reactions, transesterification reactions between alkoxides and esters, and esterification reactions between oxides or hydroxides and alcohols.

Reactions Between Metals and Alcohols

The alkoxides of the more electropositive metals with valences up to 3 can be prepared by the simple reaction:



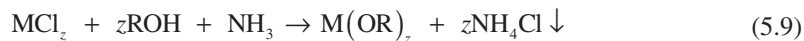
The nature of the alcohol also has a significant effect on these reactions. For example, sodium reacts vigorously with methanol and ethanol, but the reaction rate is considerably slower with isopropanol and extremely slow in *tert*-butanol. For the alkali metals (e.g., Li, Na, K) and the alkali earth metals (e.g., Ca, Sr, Ba), the reaction proceeds without the use of a catalyst. However, beryllium, magnesium, aluminum, the lanthanides, and yttrium require catalysts to cause them to react with alcohols. Depending on the metal, various catalysts have been used, including I₂, HgCl₂, and BeCl₂. Although the mechanism of these catalytic reactions is not well understood, one suggestion is that the catalyst aids the removal of the surface oxide layer that acts as a passivating layer on the metal.

Reactions Involving Metal Chlorides

For less electropositive metals or electronegative elements, the alkoxides are obtained via the anhydrous metal chloride. For some highly electronegative elements such as boron, silicon, and phosphorus, the direct reaction between metal chlorides and alcohols is effective:



However, for most metals the reaction must be forced to completion by using bases such as ammonia:



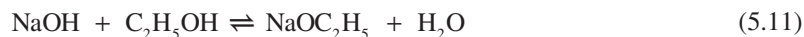
The reaction described by Eq. (5.9) forms the most useful procedure for the preparation of many alkoxides (including Zr, Hf, Si, Ti, Fe, Nb, Ge, V, Ta, Th, Sb, U, and Pu) and is used widely for commercial production. The reaction between anhydrous metal chlorides and sodium alkoxide in the presence of excess alcohol and an inert solvent such as benzene or toluene is also a useful method:



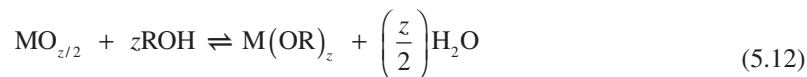
The nature of the alcohol has a significant influence on the preparation of alkoxides by the reaction involving metal chlorides and alcohols. For the lower straight chain alcohols such as methanol and ethanol, the alcohol undergoes a relatively straightforward reaction with the metal chloride and the base. However, for other alcohols, side reactions may assume a dominant role so that the yield of the alkoxide product is usually low.

Miscellaneous Methods

The alkoxides of the alkali metals may also be prepared by dissolving the metal hydroxide in the alcohol. For example, sodium ethoxide may be produced from sodium hydroxide and ethanol:

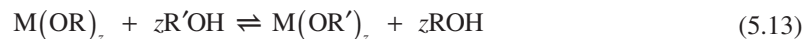


Alkoxides of some highly electronegative elements (e.g., B, Si, Ge, Sn, Pb, As, Se, V, and Hg) can be prepared by an *esterification* reaction involving an oxide and an alcohol:

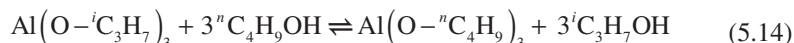


The reactions described by Eqs. (5.11) and (5.12) are reversible so that the water produced must be removed continually. In practice, this is usually done by using solvents such as benzene or xylene, which form *azeotropes* with the water. The azeotropic mixture behaves like a single substance in that the vapor produced by distillation has the same compositions as the liquid, and it can be easily fractionated out by distillation.

Metal alkoxides have the ability to exchange alkoxide groups with alcohols, and this has been used in the preparation of new alkoxides for a variety of metals, including Zn, Be, B, Al, Si, Sn, Ti, Zr, Ce, Nb, Nd, Y, and Yb. The reaction is called *alcoholic interchange* or *alcoholysis*. The general reaction can be written:

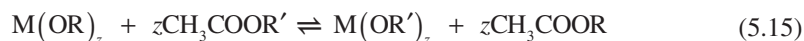


To complete the reaction, the alcohol ROH produced in the reaction is removed by fractional distillation. Benzene or xylene, which forms azeotropes with alcohol, is used to aid the removal of the alcohol by fractional distillation. As an example, the alcoholysis of aluminum isopropoxide with *n*-butanol can be used to prepare aluminum *n*-butoxide:

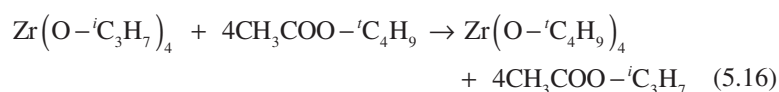


where the superscripts *i* and *n* refer to the secondary (or iso) and normal alkyl chains, respectively.

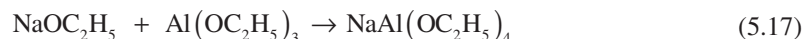
Metal alkoxides undergo *transesterification* with carboxylic esters, and this affords a method of conversion from one alkoxide to another. The reaction is reversible and can be written:



Fractional distillation of the more volatile ester CH₃COOR in Eq. (5.15) is required to complete the reaction. Transesterification reactions have been used for the preparation of alkoxides of various metals including Zr, Ti, Ta, Nb, Al, La, Fe, Ga, and V. For example, zirconium *tert*-butoxide has been prepared from the reaction between zirconium isopropoxide and *tert*-butyl ester followed by distillation of isopropyl acetate:



Double alkoxides are metal alkoxides with two different metal cations chemically combined within each molecule or molecular species. They have an advantage over the use of a mixture of individual alkoxides for the preparation of gels where the difference in the hydrolysis rates of the individual alkoxides can cause a reduction in chemical homogeneity. Double alkoxides are not easy to prepare in a ceramic laboratory, but a few are available commercially at relatively high cost. Their stability can vary considerably, depending on the nature of the two metals and the alkoxide group. Bradley et al. (12) provides a summary of the methods used to synthesize double alkoxides. One of these involves dissolving each alkoxide in a mutual solvent, mixing the solutions and refluxing at elevated temperatures. An example is the synthesis of the double alkoxide, $\text{NaAl}(\text{OC}_2\text{H}_5)_4$ by the reaction between sodium ethoxide and aluminum ethoxide:



Mah et al. (14) provides an overview of several double alkoxides for the preparation of multicomponent ceramics.

5.4.2 Basic Properties

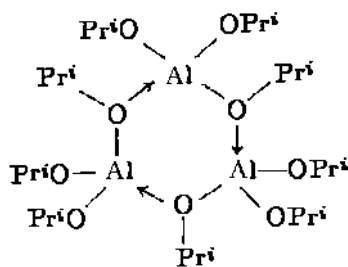
Physical Properties

The physical properties of metal alkoxides depend primarily on the characteristics of the metal (e.g., the electronegativity, valence, atomic radius, and coordination number) and secondarily on the characteristics of the alkyl group (e.g., the size and shape). There is a change from the solid, nonvolatile ionic alkoxides of some of the alkali metals to the volatile covalent liquids of elements of valence 3, 4, 5, or 6 (e.g., Al, Si, Ti, Zr, Sb, and Te), whereas alkoxides of metals with intermediate electronegativities, such as La and Y, are mainly solids (Table 5.1).

The alkyl group has a striking effect on the volatility of metal alkoxides. Many metal methoxides are solid, nonvolatile compounds (e.g., sodium methoxide). However, as the number of methyl groups increases and the size of the metal atom decreases, methoxides become sublimable solids or fairly volatile liquids (e.g., silicon tetramethoxide). Many metal alkoxides are strongly associated by intermolecular forces that depend on the size and shape of the alkyl group. The degree of association of metal alkoxides is sometimes described by the term *molecular complexity*, which refers to average number of empirical units in a complex. Figure 5.8 shows a schematic of a coordination complex of aluminum isopropoxide with a molecular complexity of 3.

TABLE 5.1 Physical State of the Alkoxides of Some Metals with Different Electronegativities

Alkoxide	State
Na(OC ₂ H ₅)	Solid (decomposes above ~530K)
Ba(O- ^{<i>i</i>} C ₃ H ₇) ₂	Solid (decomposes above ~400K)
Al(O- ^{<i>i</i>} C ₃ H ₇) ₃	Liquid (bp 408K at 1.3 kPa)
Si(OC ₂ H ₅) ₄	Liquid (bp 442K at atmospheric pressure)
Ti(O- ^{<i>i</i>} C ₃ H ₇) ₄	Liquid (bp 364.3K at 0.65 kPa)
Zr(O- ^{<i>i</i>} C ₃ H ₇) ₄	Liquid (bp 476K at 0.65 kPa)
Sb(OC ₂ H ₅) ₃	Liquid (bp 367K at 1.3 kPa)
Te(OC ₂ H ₅) ₄	Liquid (bp 363K at 0.26 kPa)
Y(O- ^{<i>i</i>} C ₃ H ₇) ₃	Solid (sublimes at ~475K)

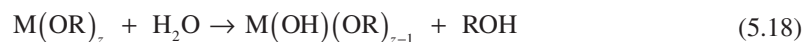
**FIGURE 5.8** Coordination complex of aluminum isopropoxide consisting of three molecules

The physical properties of the alkoxides are determined by two opposing tendencies. One tendency is for the metal to increase its coordination number by utilizing the bridging property of the alkoxo groups. The opposite tendency is the screening or steric effect of the alkyl groups, which interfere with the coordination process. The degree of the screening depends on the size and shape of the alkyl group. The result is that alkoxides with a wide variety of properties, ranging from nonvolatile polymeric solids to volatile monomeric liquids can be achieved depending on the nature of the alkyl group. Table 5.2 shows the boiling point and molecular complexity of some titanium alkoxides. In spite of the large increase in molecular weight, the boiling point decreases dramatically from 138.3°C for the ethoxide to 93.8°C for the *tert*-butoxide. For the same molecular weight, there

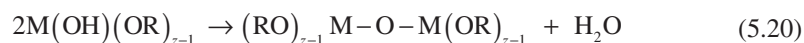
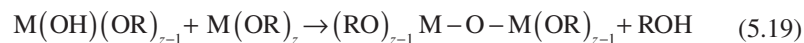
is also a dramatic reduction in the boiling point for the branched isopropoxide compared to the linear *n*-propoxide.

Chemical Properties

Metal alkoxides are characterized by the ease with which they undergo hydrolysis. In many cases, the alkoxides are so sensitive to traces of moisture that special precautions must be taken in their handling and storage. The use of an inert, dry atmosphere (e.g., normally available in a glove box) and dehydrated solvents is essential in most experiments. Hydrolysis in excess water leads to the formation of insoluble hydroxides or hydrated oxides. However, when restricted amounts of water are added, metal alkoxides undergo partial hydrolysis reactions, yielding soluble species that can take part in polymerization reactions. The initial step involves a *hydrolysis reaction* in which alkoxide groups (OR) are replaced by hydroxyl groups (OH):



Subsequent *condensation reactions* involving the hydroxy metal alkoxide produces polymerizable species with M—O—M bonds plus alcohol (ROH) or water as a by-product:



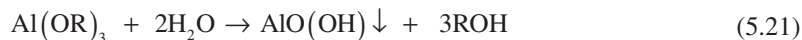
Since most metal alkoxides containing lower aliphatic alkyl groups are actually coordinated complexes and not single molecules (Fig. 5.8), the reactions described by Eqs. (5.18) to (5.20) must be considered to be somewhat simplified. The rate of hydrolysis of metal alkoxides depends on the characteristics of the metal and those of the alkyl group. In general, silicon alkoxides are among the slowest to

TABLE 5.2 Boiling Point and Molecular Complexity of Some Titanium Alkoxides

Alkoxide	Molecular weight	Boiling point (K) at 0.65 kPa	Molecular complexity
Ti(OCH ₃) ₄	172	(Solid)	—
Ti(OC ₂ H ₅) ₄	228	411.3	2.4
Ti(O- ⁿ C ₃ H ₇) ₄	284.3	410	(Unknown)
Ti(O- ⁱ C ₃ H ₇) ₄	284.3	364.3	1.4
Ti(O- ^t C ₄ H ₉) ₄	340.3	366.8	1.0

hydrolyze and, for a given metal alkoxide, the hydrolysis rate increases as the length of the alkyl group decreases.

In excess water, aluminum alkoxides (15) initially form the monohydroxide (boehmite), which later may convert to the trihydroxide (bayerite):



Boron alkoxides form the oxide or boric acid when reacted with excess water. Oxide formation can be written as



As discussed later, the formation of insoluble precipitates as represented by Eqs. (5.21) to (5.23) makes it impossible for polymerization reactions to occur and must be prevented if good chemical homogeneity is to be achieved by the polymeric gel route.

Silicon alkoxides show a different type of reaction. They form soluble *silanols* in excess water rather than an insoluble oxide or hydroxide. The hydrolysis reaction may be written:



Complete hydrolysis leading to the formation of the silicic acid monomer Si(OH)_4 generally does not occur except at low pH and high water concentration. Under most conditions, condensation of the silanol groups occurs prior to the replacement of all the OR groups by hydroxyl groups, leading to the formation of polymeric species, as in Eqs. (5.19) and (5.20), for example.

Metal alkoxides are soluble in their corresponding alcohols. In practice, dissolution of solid alkoxides or dilution of liquid alkoxides is normally performed in the corresponding alcohol. As outlined below for the case of silicon alkoxides, the alcohol may also serve an additional function as a mutual solvent for the alkoxide and water when they are immiscible. Metal alkoxides also have the ability to exchange alkoxide groups with alcohols, as in Eq. (5.13), for example.

5.5 SOL-GEL PROCESSING OF SILICON ALKOXIDES

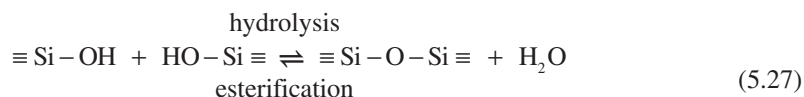
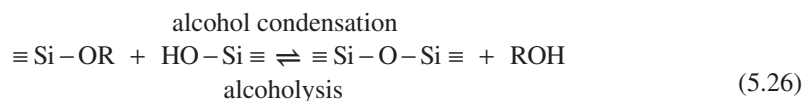
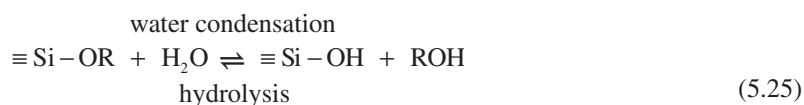
5.5.1 Precursors

The most commonly used precursors for the sol-gel processing of silica are *tetraethoxysilane*, $\text{Si(OC}_2\text{H}_5)_4$, abbreviated TEOS, which is also referred to as

tetraethylorthosilicate or silicon tetraethoxide, and *tetramethoxysilane*, $\text{Si}(\text{OCH}_3)_4$, abbreviated TMOS, which is also referred to as tetramethoxyorthosilicate or silicon tetramethoxide. The physical properties of these two precursors are given in Table 5.3.

5.5.2 Hydrolysis and Condensation

Following Eqs. (5.18) to (5.20), the hydrolysis and condensation reactions for silicon alkoxides can be written as:



where R represents the alkyl group and the reverse reactions have also been included. The alkoxysilanes and water are immiscible, so a mutual solvent, commonly the corresponding alcohol of the alkoxy group, is used to homogenize the mixture, as shown in Fig. 5.9 for TEOS (16). The alcohol can also take part in *esterification* and *alcoholysis* reactions [Eqs. (5.25) and (5.26)].

Silica gels are often synthesized by employing an acid (e.g., HCl) or a base (e.g., NH_3) as a catalyst. Gels have been prepared under a wide range of catalyst concentration (0.01 to 7 M) and reactant concentration ($\text{H}_2\text{O}:\text{Si}$ ratio w of <1 to >50). Table 5.4 gives examples of the conditions used to synthesize gels in the form of monoliths, fibers, films, and particles.

TABLE 5.3 Physical Properties of the Commonly Used Silicon Alkoxides

Name	Molecular weight	Boiling point (K)	Specific gravity (at 293K)	Refractive index (at 293K)	Solubility
$\text{Si}(\text{OC}_2\text{H}_5)_4$, tetraethoxysilane	208.33	442	0.934	1.3818	Alcohols
$\text{Si}(\text{OCH}_3)_4$, tetramethoxysilane	152.22	394	1.032	1.3688	Alcohols

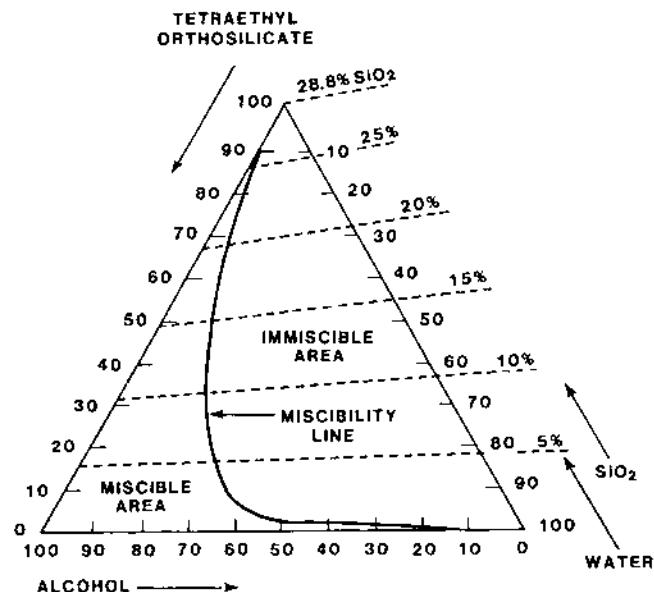


FIGURE 5.9 TEOS, H₂O, and Synasol (95% EtOH, 5% water) ternary phase diagram at 25°C. For pure ethanol, the miscibility line is shifted slightly to the right. (From Ref. 16.)

TABLE 5.4 Sol-Gel Silicate Compositions for Bulk Gels, Fibers, Films, and Powders

SiO ₂ gel types	Mole percent (mol %)					
	TEOS	EtOH	H ₂ O	HCl	NH ₃	H ₂ O/Si (w)
Bulk						
1-step acid	6.7	25.8	67.3	0.2	—	10
1-step base	6.7	25.8	67.3	—	0.2	10
2-step acid-base						
1st step, acid	19.6	59.4	21.0	0.01	—	1.1
2nd step, acid (A2)	10.9	32.8	55.7	0.6	—	5.1
2nd step, base (B2)	12.9	39.2	47.9	0.01	0.016	3.7
Fibers	11.31	77.26	11.31	0.11	—	1.0
Films	5.32	36.23	58.09	0.35	—	10.9
Monodisperse spheres	0.83	33.9	44.5	—	20.75	53.61

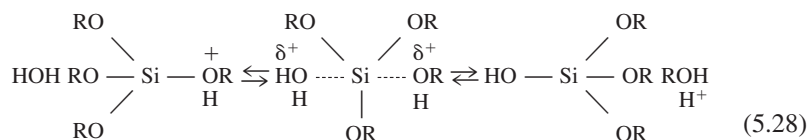
Source: Ref. 1.

It is found that the synthesis conditions have a significant influence on the structural evolution of the sol-gel silicate, which in turn affects the behavior of the gel during drying and subsequent sintering. The synthesis conditions are often divided into acid catalyzed conditions and base catalyzed conditions. Three broad categories of synthesis conditions can be identified. Under conditions of acid catalysis and low w , the sols consist of weakly branched polymers. With base catalysis and high w , highly condensed particulate sols are formed. In conditions that are intermediate between these two extremes (acid catalysis/high w or base catalysis/low w), the sols have intermediate structures (branched to highly branched polymers).

The structure of the sol-gel silicate depends on the relative rates of the hydrolysis and condensation reactions, as well as on the reverse reactions [Eqs. (5.25)–(5.27)]. The influence of the reaction conditions on the mechanism and kinetics of the reactions forms a key issue in understanding the structural evolution.

Acid-Catalyzed Conditions

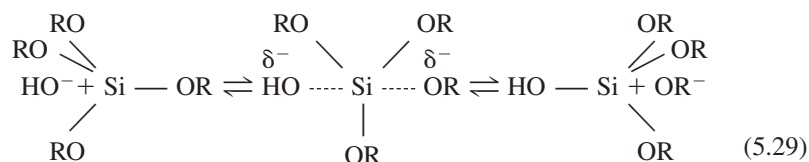
Hydrolysis and condensation occur by bimolecular nucleophilic displacement reactions involving protonated alkoxide groups (1). In the first step, it is likely that an OR group bonded to Si is rapidly protonated. Electron density is withdrawn from Si, making it more electrophilic and thus more susceptible to attack by water. The H₂O molecule attacks from the rear and acquires a small positive charge while the positive charge on the protonated alkoxide is correspondingly reduced, making alcohol a better leaving group. The transition state decays by displacement of alcohol accompanied by inversion of the Si tetrahedron:



Condensation to form siloxane bonds occurs by either an alcohol-producing reaction [Eq. 5.26] or a water-producing reaction [Eq. (5.27)]. The most basic silanol species, namely silanols contained in monomers or weakly branched *oligomers* (very short chain polymers), are most likely to be protonated so that condensation reactions are likely to occur between neutral species and protonated silanols situated on monomers and the end groups of chains.

Base-Catalyzed Conditions

Under basic conditions, hydrolysis and condensation also occurs by a bimolecular nucleophilic substitution reaction. It is likely that water dissociates to produce hydroxyl anions in a rapid first step. The hydroxyl anion then attacks Si directly, displacing OR[−], followed by inversion of the Si tetrahedron:



The most widely accepted condensation mechanism involves the attack of a nucleophilic deprotonated silanol on a neutral silicate species, as outlined earlier for the condensation in aqueous silicates [Eq. (5.4)]. This condensation mechanism pertains above the PZC (or IEP) of silica ($\text{pH} > \sim 2$) because the surface silanols are deprotonated (i.e., they are negatively charged) and the mechanism changes with the charge on the silanol. Condensation between larger, more highly condensed species, which contain more acidic silanols, and smaller, less weakly branched species is favored. The condensation rate is maximized near neutral pH where significant concentrations of both protonated and deprotonated silanols exist. A minimum rate is observed near the PZC (or IEP).

5.5.3 Polymer Growth

Structural evolution of sol–gel silicates in solution has been investigated on scales of several lengths using a variety of techniques, such as nuclear magnetic resonance (NMR), Raman and infrared spectroscopy, and x-ray, neutron, and light scattering. Reference 1 provides an excellent account of the information obtained with these techniques and the models proposed to describe polymer growth and gelation in silicate systems. On a length scale of 1–200 nm, the evolving structures are not uniform objects described by Euclidean geometry but tenuous structures called *fractal* structures (an example of which is given in Fig. 5.3). Fractal geometry is discussed in a classic text by Mandelbrot (17), the inventor of the concept and the connection of fractals to problems in materials science is discussed by Feder (18).

A *mass fractal* is defined as an object whose mass m increases with its radius r according to

$$m \propto r^{d_m} \quad (5.30)$$

where d_m is called *mass fractal dimension* of the object. For a Euclidean object, $m \propto r^3$, whereas for a fractal $d_m < 3$, so that the density of the fractal ($\rho \propto m/r^3$) decreases as the object gets bigger. A surface fractal has a surface area S that increases faster than r^2 :

$$S \propto r^{d_s} \quad (5.31)$$

where d_s is called the *surface fractal dimension*.

Euclidean objects (dense spherical particles) are most likely to form in systems (e.g., aqueous silicates) in which the particle is slightly soluble in the solvent. In this case, monomers can dissolve and reprecipitate until the equilibrium structure (having a minimum surface area) is obtained. In nonaqueous systems (e.g., silicon alkoxide–alcohol–water solutions), the solubility of the solid phase is so limited that condensation reactions are virtually irreversible. Bonds form at random and cannot convert to the equilibrium configuration, thereby leading to fractal polymeric clusters.

5.5.3.1 Polymer Growth Models

The models put forward to describe polymer growth in silicate systems are divided into two types: classical (or equilibrium) growth models and kinetic growth models (1,19,20).

Classical Growth Models

The first theory of polymer growth accompanying gelation was put forward more than 50 years ago by Flory (21) and by Stockmayer (22). In their model, bonds are formed at random between adjacent nodes on an infinite Cayley tree or Bethe lattice (Fig. 5.10). The model is qualitatively successful in correctly describing the emergence of an infinite cluster at some critical extent of reaction and in providing good predictions of the gel point. However, it has come under some criticism because it does not provide an entirely realistic picture of polymer growth. Because of the unphysical nature of the Cayley tree, cyclic configurations of the growing polymers are avoided in the model. The purely branched clusters formed on the Cayley tree have a mass fractal dimension $d_m = 4$. Since the volume of the cluster increases as r^3 , where r is the radius of the cluster, the theory predicts that the density ρ increases in proportion to r . This result is physically unrealistic because the density cannot increase indefinitely as the cluster grows.

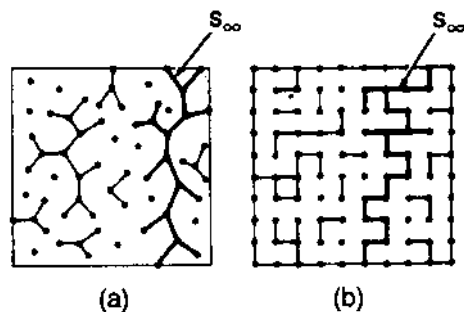


FIGURE 5.10 Gelation theories (Schematic). (a) Flory's model (molecular functionality $f = 3$). (b) Percolation on a square lattice. In each case, a spanning s_∞ gel molecule is embedded in the sol. (From Ref. 23.)

Kinetic Growth Models

The kinetic models avoid the unrealistic assumptions of the classical theory and make predictions about the growth and fractal structure of the simulated structures that are in good agreement with experimental observations. They are based on Smoluchowski's equation describing the rate at which the number of clusters of a given size changes with time during an aggregation process. Most kinetic growth models produce objects with self-similar fractal properties, i.e., they look self-similar under transformation of scale, as would be achieved, for example, by changing the magnification of a microscope. Depending on the conditions, growth in silicate systems may occur predominately by the condensation of monomers with growing clusters (referred to as *monomer-cluster* growth) or by condensation reactions of clusters with either monomers or other clusters (*cluster-cluster* growth). The simulated structures resulting from these two types of growth processes are illustrated in Fig. 5.11 (19,24).



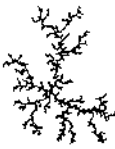
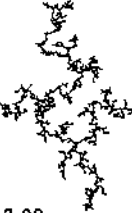
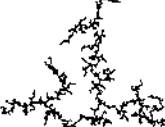
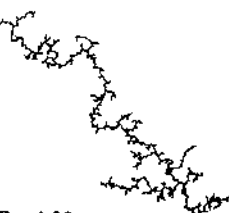
	REACTION-LIMITED	BALLISTIC	DIFFUSION-LIMITED
MONOMER-CLUSTER	EDEN  $D = 3.00$	VOLD  $D = 3.00$	WITTEN-SANDER  $D = 2.50$
CLUSTER-CLUSTER	RLCA  $D = 2.09$	SUTHERLAND  $D = 1.95$	DLCA  $D = 1.80$

FIGURE 5.11 Simulated structures resulting from various kinetic growth models. Fractal dimensions are listed for three-dimensional clusters even though their two-dimensional analogs are displayed. Each cluster contains 1000 primary particles. Simulations by Meakin (24). (From Ref. 20.)

Monomer-cluster or cluster-cluster growth can be limited by diffusion or by reaction. In *diffusion-limited monomer-cluster aggregation* (DLMCA), simulated by the Witten and Sander model (25) in Fig. 5.11, it is assumed that monomers are released one by one from sites arbitrarily far from a central cluster. The monomers travel by a random walk diffusion mechanism and stick irreversibly at first contact with the growing cluster. Because of this trajectory, the monomers cannot penetrate deeply into a cluster without intercepting a cluster arm and the arms effectively screen the interior of the cluster from incoming monomers. Growth occurs preferentially at exterior sites, resulting in objects in which the density decreases radially from the center of mass (in three dimensions $d_m = 2.45$).

Reaction-limited monomer-cluster aggregation (RLMCA) is distinguished from DLMCA in that there is an energy barrier to bond formation. The effect of this barrier is to reduce the condensation rate because many collisions can occur before the monomer and cluster form a bond. In this process, all potential growth sites are sampled by the monomers. The probability of attachment to a particular site per encounter is dictated by the local structure rather than the large-scale structure, which governs the probability that a monomer will encounter a given site. RLMCA is simulated by the Eden model (26), originally developed to simulate cell colonies. In the model, unoccupied perimeter sites are selected randomly and occupied with equal probability. Because all sites are accessible and filled with equal probability, the Eden model leads to compact, smooth clusters ($d_m = 3$). The “poisoned” Eden growth model (26) represents a modification of the Eden model, whereby a certain fraction of sites is prohibited from being occupied, i.e., these sites do not undergo polymerization. Depending on the number of poisoned sites and their distribution, the poisoned Eden growth model generates structures that vary from being uniformly nonporous (nonfractal) to surface fractals to mass fractals.

Cluster-cluster aggregation models (27) describe growth that results when a “sea” of monomers undergoes random walks, forming a collection of clusters that continue to grow by condensation reactions with each other and with remaining monomers. Under diffusion-limited conditions (DLCA), clusters stick irreversibly on contact, whereas under reaction-limited conditions (RLCA), the sticking probability is less than unity. Compared to monomer-cluster growth, the strong mutual screening of colliding clusters creates very open structures even under reaction-limited conditions. It is also evident from Fig. 5.11 that in contrast to monomer-cluster growth, cluster-cluster growth produces objects with no obvious centers.

5.5.3.2 Structural Evolution of Sol-Gel Silicates

In silicates, the condensation rate is sufficiently small that *reaction-limited aggregation* is assumed to occur under both acid and base catalysis. The cross-linking

between the polymer chains is much higher at high pH and high $\text{H}_2\text{O}:\text{Si}$ ratio (w) so that highly branched clusters are formed under these conditions, whereas more weakly branched clusters are formed at low pH. Based on our description of the hydrolysis and condensation mechanisms and the polymer growth models, we can now summarize the structural evolution of sol–gel silicates and its description by the kinetic models.

$$\text{pH} < \sim 2$$

Both hydrolysis and condensation occur by a bimolecular nucleophilic displacement mechanism involving protonated alkoxide groups. The rate of hydrolysis is large compared to the rate of condensation. For w greater than ~ 4 , hydrolysis is expected to be completed at an early stage of the reaction prior to any significant condensation. After monomers are depleted, condensation between completely hydrolyzed species occurs by reaction-limited cluster-cluster aggregation, leading to weakly branched structures with a mass fractal dimension $d_m \approx 2$.

Under low water conditions ($w < 4$), condensation occurs prior to the completion of hydrolysis. Condensation between the incompletely hydrolyzed species is also expected to occur by reaction-limited cluster-cluster aggregation, but because the OR groups effectively reduce the functionality of the condensing species, the structures will be more weakly branched when compared to the high water conditions.

$$\text{pH} > \sim 7$$

Hydrolysis and condensation occur by bimolecular nucleophilic displacement reactions involving OH^- and Si-O^- anions. For $w > 4$, the hydrolysis of all polymeric species is expected to be complete. Dissolution reactions provide a continual source of monomers. Because condensation occurs preferentially between weakly acidic species that tend to be protonated and strongly acidic species that are deprotonated, growth occurs primarily by reaction-limited monomer-cluster aggregation (equivalent to nucleation and growth), leading to compact, nonfractal structures.

For $w \ll 4$, unhydrolyzed sites are incorporated into the growing cluster. The probability of condensation at these sites is less than at hydrolyzed sites. Under these conditions, growth is described by a “poisoned” Eden model. Depending on the number and distribution of the poisoned sites, mass fractals, surface fractals or uniformly porous objects can result. The addition of more water in a second hydrolysis step is expected to completely hydrolyze the clusters and further growth should be described by the Eden model.

$$\text{pH} \approx 2-7$$

Hydrolysis occurs by an *acid-catalyzed* mechanism involving a basic, protonated alkoxy substituent. Condensation occurs by a *base-catalyzed* mechanism involv-

ing a deprotonated silanol. Hydrolysis will therefore occur on monomers and weakly branched oligomers that subsequently condense preferentially with clusters (monomer-cluster growth). However, the availability of monomers at later stages in the reaction decreases with decreasing pH. The predominant growth mechanism therefore changes from monomer-cluster to cluster-cluster with decreasing pH and increasing time of reaction. A wide range of structures, from weakly branched to highly branched, might be expected in this pH range of ~ 2 – 7 .

5.5.3.3 Rheological Measurements

Rheological measurements are most often used to characterize the bulk properties of a solution (e.g., the viscosity), but the dependence of the rheological properties on the concentration, molecular weight, and shear rate can be used to infer structural information.

Figure 5.12 shows the changes in the solution viscosity for acid-catalyzed and base-catalyzed TEOS systems described in Table 5.5. The sudden increase in viscosity is generally used to identify the gel point in a crude way. The gel point is often defined as the time at which the viscosity is observed to increase rapidly or the time to reach a given viscosity (e.g., 1000 Pa·s).

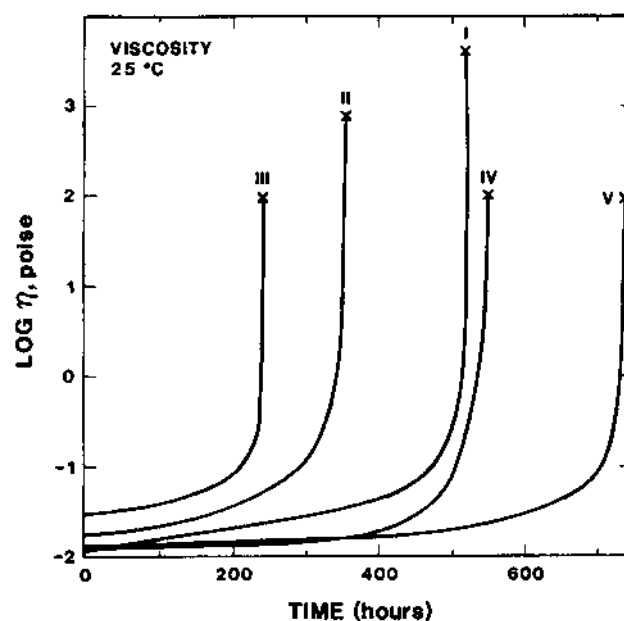


FIGURE 5.12 Temporal changes in solution viscosity for acid- and base-catalyzed TEOS systems. Crosses indicate gel points. Samples I–V are identified in Table 5.5. (From Ref. 28.)

TABLE 5.5 Compositions and Behavior of Sol–Gel Systems Investigated by Sakka et al. (28–30)

Solution	Si(OC ₂ H ₅) ₄ (g)	H ₂ O (g)	C ₂ H ₅ OH (g)	Mole ratio (w) of H ₂ O to Si(OC ₂ H ₅) ₄	Catalyst ^a	Time for gelling (h)	Spinnability
I	169.5	14.7	239.7	1	HCl	525	Yes
II	382.0	33.0	83.4	1	HCl	360	Yes
III	169.5	292.8	37.5	20	HCl	248	No
IV	50	3.8	47.6	1	NH ₄ OH	565	No
V	50	7.6	47.6	2	NH ₄ OH	742	no

^a Mole ratio of HCl or NH₄OH to the Si(OC₂H₅)₄ is 0.01.

Source: Ref. 1.

The rheology of silicate systems prepared from TEOS (Table 5.5) was studied by Sakka and coworkers (28–30) and correlated with the observed ability of certain compositions for fiber formation (spinnability). They measured the dependence of the reduced viscosity η_{sp} [equal to $\eta_r - 1$ in Eq. (4.84)] on silica concentration C and the dependence of the intrinsic viscosity $[\eta]$ on the number-averaged molecular weight M_n for acid-catalyzed and base-catalyzed systems prepared with w values in the range of 1–20. Figure 5.13 compares the concentration dependence of η_{sp}/C for composition 1 (Table 5.5) after various periods of aging (t/t_{gel}) with that for Ludox[®] (sol of silica particles) and for sodium metasilicate (chainlike silicates). As discussed in Chapter 4, η_{sp} for a sol of noninteracting spherical particles (e.g., Ludox[®]) is given the Einstein relation, which can be expressed as

$$\frac{\eta_{sp}}{C} = \frac{K_1}{\rho} \quad (5.32)$$

where K_1 is a constant equal to 2.5 and ρ is the density of the particles. The silicate species present at $t/t_{gel} = 0.34$ can therefore be inferred to be compact and noninteracting.

As t/t_{gel} increases, there is a progressively larger dependence of η_{sp}/C on C . According to the Huggins equation (31), the reduced viscosity of solutions of chainlike or linear polymers (e.g. metasilicate) is given by

$$\frac{\eta_{sp}}{C} = [\eta] + K_2 [\eta]^2 C \quad (5.33)$$

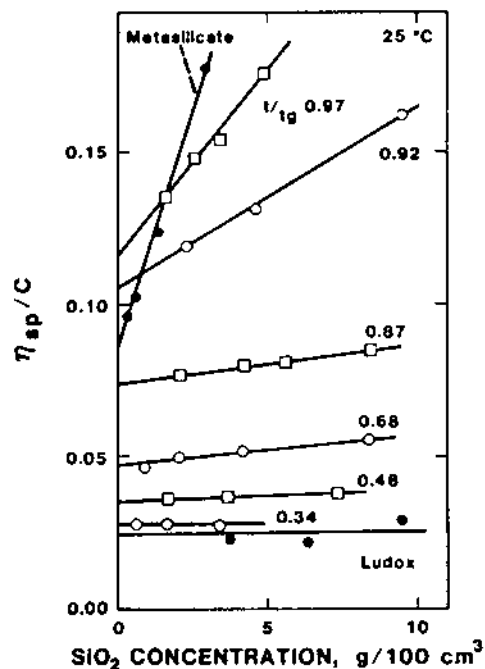


FIGURE 5.13 Dependence of the reduced viscosity of solution I (see Table 5.5) on concentration for various values of t/t_{gel} . Data for LUDOX® (sol of silica particles) and for sodium metasilicate (chainlike silicates) are shown for comparison. (From Ref. 28.)

where K_2 is a constant. The larger dependence of η_{sp}/C on C with aging time may be explained in terms of a change in the silicate structure from small noninteracting species to extended, weakly branched polymers.

Figure 5.14 shows plots of $\log [\eta]$ versus the $\log M_n$ for acid-catalyzed TEOS systems in which w was varied from 1 to 20. For organic polymer solutions, $[\eta]$ is related to M_n by the expression

$$[\eta] = K_3 M_n^\alpha \quad (5.34)$$

where K_3 is a constant that depends on the type of polymer, the solvent and the temperature. The exponent α depends on the structure of the polymer: $\alpha = 0$ for rigid spherical particles; $\alpha = 0.5-1.0$ for flexible, chainlike, or linear polymers; and $\alpha = 1.0-2.0$ for rigid, rodlike polymers (32). The results of Fig. 5.14 indicate that spinnable systems ($w = 1$ or 2) are composed of flexible chainlike or linear polymers ($\alpha = 0.64-0.75$) whereas the nonspinnable systems are composed of more highly branched structures.

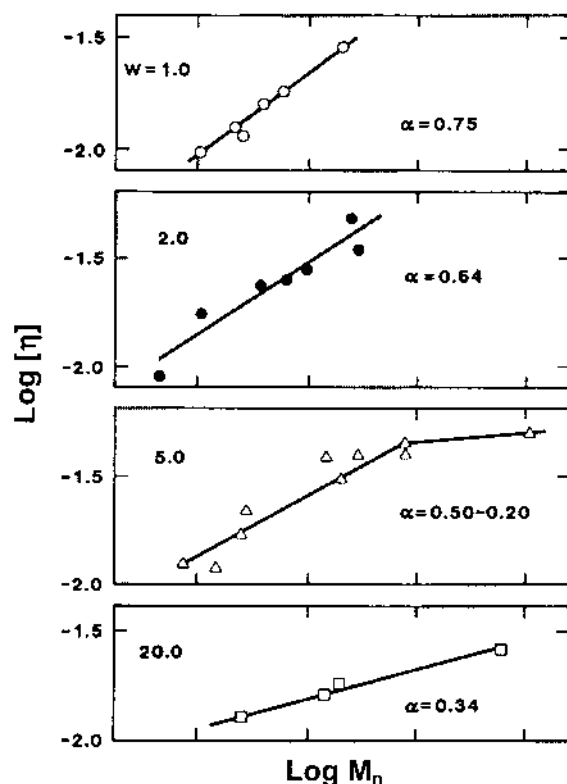


FIGURE 5.14 Log intrinsic viscosity $[\eta]$ versus log number averaged molecular weight M_n for acid-catalyzed hydrolysis of TEOS and $w = 1-20$. The parameter α is defined in Eq. (5.34). (From Ref. 29.)

5.5.4 Gelation

The clusters grow until they begin to impinge on one another and gelation occurs by a linking of these clusters by a *percolation* process. Near the gel point, bonds form at random between the nearby clusters, linking them into a network. The gel point corresponds to the *percolation threshold*, when a single cluster (called the *spanning cluster*) appears that extends throughout the sol (Fig. 5.10). The spanning cluster coexists with the sol containing many smaller clusters, which gradually become attached to the network. It reaches across the vessel that contains it so the sol does not pour when the vessel is tipped. By creating a continuous solid network, the spanning cluster is responsible for an abrupt rise in the viscosity and the appearance of an elastic response to stress.

Reference 1 gives an excellent review of the theories that have been proposed to explain gelation. The theories can be divided into three main classes: classical theory, percolation theory, and kinetic models. *Classical theory* is based on the theory of Flory and Stockmeyer mentioned earlier. The classical theory provides a good description of the gel point; however, as we outlined earlier, it provides an unrealistic description of polymer growth in sol-gel silicates. *Percolation theory* avoids the unrealistic assumptions of the classical theory and makes predictions of the gelling systems that are in good accord with experimental observations. A disadvantage is that only a few results can be obtained analytically, so that these models must be studied by computer simulations. Reviews of percolation theory and its relation to gelation can be found in Refs. 33 and 34.

The *kinetic models*, as described earlier, are based on Smoluchowski's analysis of cluster growth. They are reviewed by Meakin (8). The geometry of the clusters is not considered specifically in the theory, but the size distribution and shape of the clusters determined by computer simulation are in good agreement with experiment. The predictions of polymer growth and fractal structure are also in good agreement with experimental observations. The growing clusters eventually overlap and become immobile, so that further bonding involves a percolation process. The evolution of the properties in the vicinity of the gel point is generally in agreement with the critical behavior predicted by percolation theory.

5.5.5 Aging of Gels

The condensation reactions that cause gelation continue long after the gel point, leading to strengthening, stiffening, and shrinkage of the network. These changes have a significant effect on the subsequent drying and sintering processes. If the gel is aged in the original pore liquid, small clusters continue to diffuse and attach to the main network. As these new links form, the network becomes stiffer and stronger. Many gels exhibit the phenomenon of *syneresis*, shown in Fig 5.15, where the gel network shrinks and expels the liquid from the pores (35). Shrinkage most likely results from condensation between neighboring groups on the surface of the solid network, as illustrated in Fig. 5.16.

Studies of syneresis in silica gels show that the rate depends on the processing conditions in much the same way as the condensation reactions leading to gelation. The shear modulus of the gel increases with aging time and the rate of increase of the modulus is larger at higher temperatures. However, when compared to drying where evaporation of the liquid is allowed to take place, the shrinkage and the shear modulus of the gel increase much less rapidly with time.

5.5.6 Drying of Gels

After preparation, polymeric gels typically consist of a weak amorphous solid structure containing an interconnected network of very fine pores filled with

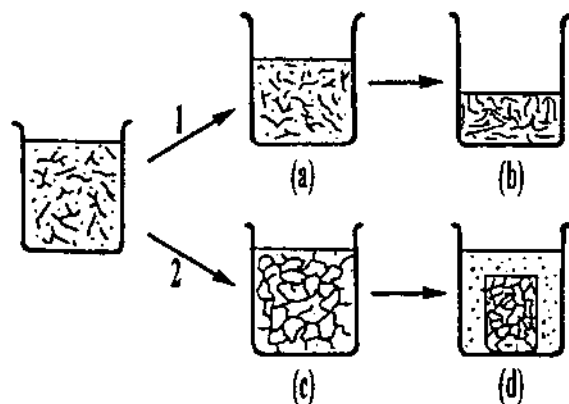


FIGURE 5.15 Two modes of shrinkage of a wet gel: shrinkage produced when the liquid is allowed to evaporate (route 1) and expulsion of liquid from the gel giving rise to shrinkage without evaporation (syneresis) (route 2). (From Ref. 35.)

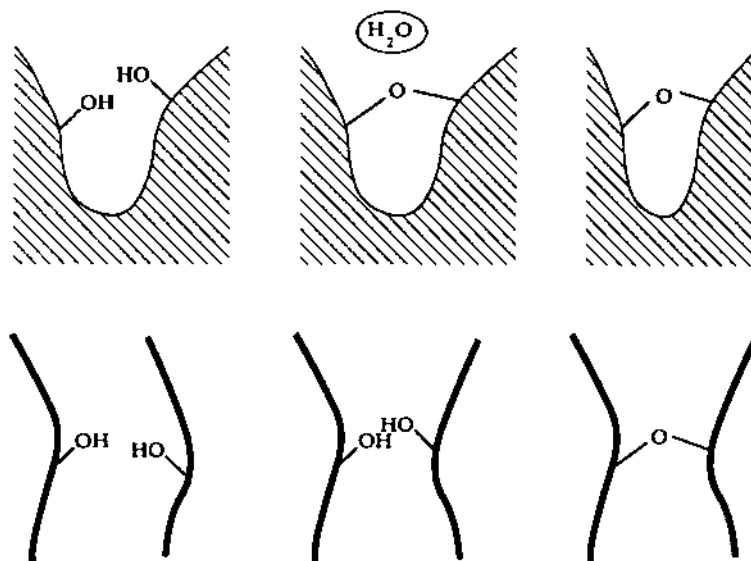


FIGURE 5.16 (Top) Shrinkage results from condensation between neighboring groups on a surface as the strain in the new bond relaxes. (Bottom) Movement of flexible chains may permit new bonds to form that prevent the chains from returning to their original position; this permits extensive shrinkage as long as the network remains flexible. (From Ref. 1.)

liquid. Often an excess volume of alcohol is used as a common solvent, so that the liquid composition is predominantly an alcohol. The gel is sometimes referred to as an *alcogel*. Particulate gels consist of a network in which the pores are filled with an aqueous liquid, and in this case the gel is sometimes referred to as an *aquagel* (or a *hydrogel*). The gel must be dried prior to its conversion to the final article by sintering. The simplest method, referred to as *conventional* drying, is to remove the liquid by evaporation in air or in a drying chamber such as an oven. Drying must be carried out slowly and under carefully controlled conditions, especially in the case of polymeric gels, if monolithic crack-free bodies are to be obtained. The gel produced by conventional drying is referred to as a *xerogel*. Alternatively, the gel may be dried by removal of the liquid under *supercritical* conditions. In the ideal case, no shrinkage occurs during supercritical drying so that the dried gel is highly porous (e.g., typically ~90–95% porosity in polymeric gels). The gel produced by supercritical drying is referred to as an *aerogel*.

In practice, the drying stage often presents one of the major difficulties of the sol–gel process. It is often difficult to dry polymeric gels thicker than 1 mm or films thicker than 1 μm . We will examine some of the main factors that control the drying process so that a better understanding of the problems and their solution may be achieved.

5.5.6.1 Conventional Drying

Drying is a complex process involving the interaction of three independent processes: (1) evaporation, (2) shrinkage, and (3) fluid flow in the pores. As in most complex physical phenomena, an insight into the problem is best achieved through a combination of theoretical modeling and experimental investigations. A detailed analysis of the drying process has been carried out by Scherer (36). Although special attention is given to the drying of gels, the theory is fairly general that it can also be applied to the drying of ceramics formed by other methods (e.g., slip casting and extrusion) described in the next chapter.

Stages in Drying

As shown in Fig. 5.17, the drying process can be divided into two major stages: (1) a constant rate period (CRP) where the evaporation rate is nearly constant and (2) a falling rate period (FRP) where the evaporation rate decreases with time or the amount of liquid remaining in the body. In some materials it is possible to further separate the FRP into two parts. In the first falling rate period (FRP1), the evaporation rate decreases approximately linearly with time, while in the second falling rate period (FRP2), the rate decreases in a curvilinear manner.

The drying process is illustrated schematically in Fig. 5.18. During the CRP, the liquid–vapor meniscus remains at the surface of the gel. Evaporation occurs at a rate close to that of a free liquid surface (e.g., an open dish of liquid).

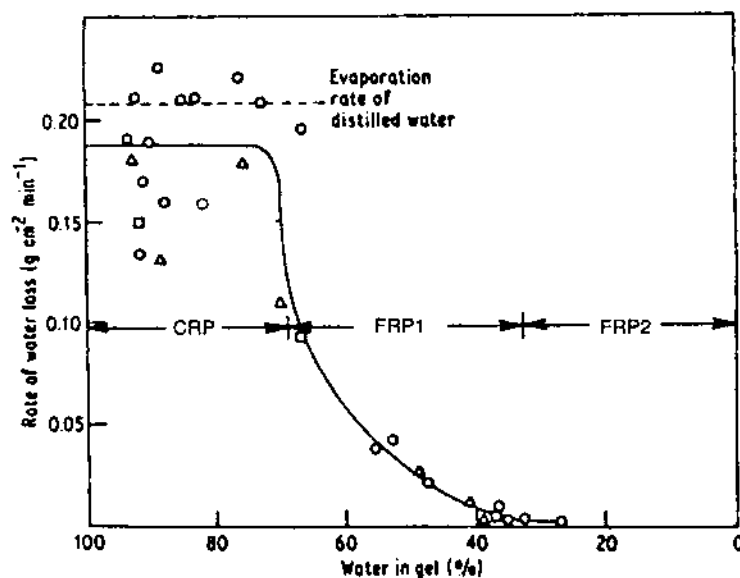


FIGURE 5.17 Rate of water loss from alumina gel versus water content of the gel for various initial thicknesses [(○) 7.5, (◊) 3.0, (◻) 1.8, (Δ) 0.8 mm]. During the first stage (CRP) the evaporation rate from the gel is about the same as from a dish of water. (From Ref. 37.)

For every unit volume of liquid that evaporates, the volume of the gel decreases by one unit volume. This stage of constant evaporation rate accompanied by shrinkage lasts until the end of the CRP when shrinkage stops and the FRP begins. At the end of the CRP, the gel may shrink to as little as one-tenth of its original volume. During the FRP, the liquid recedes into the gel.

Driving Force for Shrinkage: Decrease in Interfacial Energy

Consider a tube of radius a held vertically in a reservoir of liquid which wets it (Fig. 5.19). If the contact angle is θ , the negative pressure under the liquid–vapor meniscus in the capillary is

$$p = -\frac{2\gamma_{LV} \cos \theta}{a} \quad (5.35)$$

where γ_{LV} is the specific surface energy (surface tension) of the liquid–vapor interface. Assuming for simplicity that $\theta = 0$, the liquid is drawn up the tube to a height h , given by

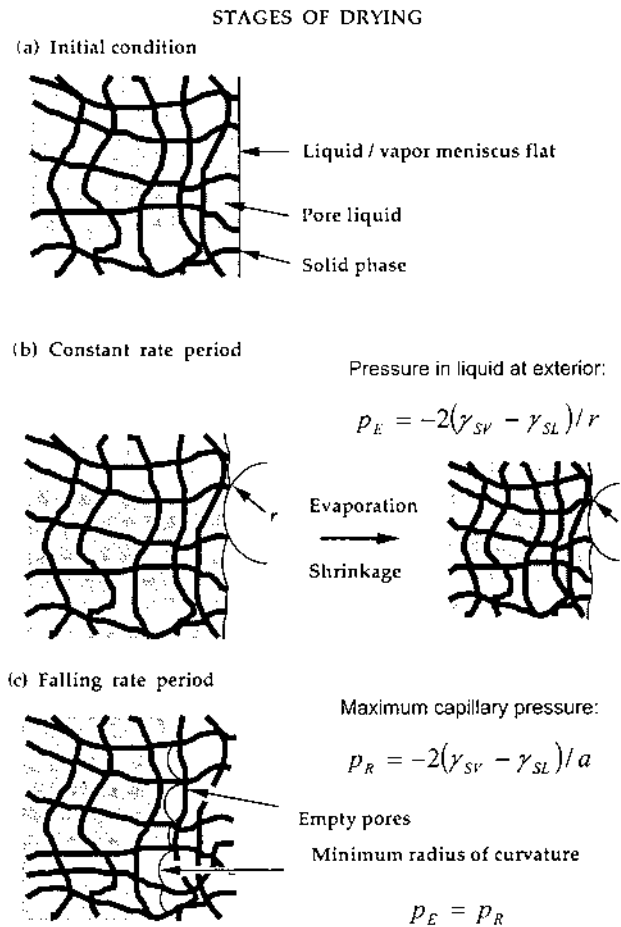


FIGURE 5.18 Schematic illustration of the drying process. (a) before evaporation occurs, the meniscus is flat. (b) Capillary tension develops in liquid as it “stretches” to prevent exposure of the solid phase, and network is drawn back into liquid. The network is initially so compliant that little stress is needed to keep it submerged, so the tension in the liquid is low, and the radius of the meniscus is large. As the network stiffens, the tension rises, and at the critical point (end of the constant rate period), the radius of the meniscus drops to equal the pore radius. (c) During the falling rate period, the liquid recedes into the gel. (From Ref. 36.)

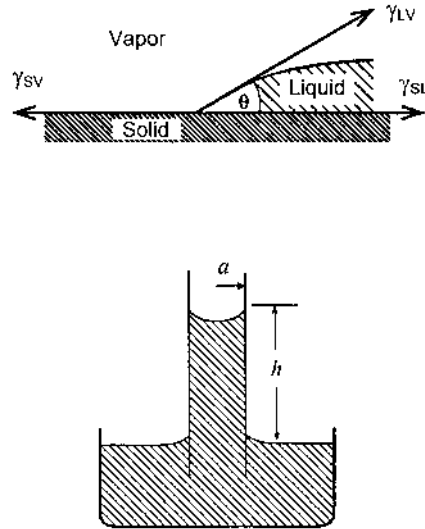


FIGURE 5.19 Capillary rise phenomenon for a wetting liquid with a contact angle θ

$$h = \frac{2\gamma_{LV}}{a\rho_L g} \quad (5.36)$$

where ρ_L is the density of the liquid and g is the acceleration due to gravity. The potential energy (PE) gained by the liquid is equivalent to raising a mass of liquid $\pi a^2 h \rho_L$ through a height $h/2$. Hence,

$$PE = \pi a^2 h^2 \frac{\rho_L g}{2} \quad (5.37)$$

This energy comes from the wetting of the walls of the tube by the liquid. We may describe the process in the following way. The surface energy of a solid arises from the asymmetric forces at the free surface. If we cover the surface with another material (e.g., a liquid), we reduce this asymmetry and hence reduce the surface energy. The energy liberated in the process is available for pulling the liquid up the tube. The energy liberated can also be thought of as giving rise to a *capillary pressure* or *capillary force* which acts on the liquid to pull it up the tube.

Quantitatively, if the liquid rises up the tube to cover 1 m^2 of the surface, then we destroy 1 m^2 of solid–vapor interface and create 1 m^2 of solid–liquid interface. The energy given up by the system is then

$$\Delta E = \gamma_{SV} - \gamma_{SL} \quad (5.38)$$

where γ_{SV} and γ_{SL} are the specific surface energies of the solid–vapor and solid–liquid interfaces, respectively.

Consider now a wet gel with pores that are assumed, for simplicity, to be cylindrical. If evaporation occurs to expose the solid phase, a solid–liquid interface is replaced by a solid–vapor interface. If the liquid wets the solid (i.e., the contact angle $\theta < 90^\circ$), then as seen from Fig. 5.19, $\gamma_{SV} > \gamma_{SL}$. The exposure of the solid phase would lead to an increase in the energy of the system. To prevent this, liquid tends to spread from the interior of the gel to cover the solid–vapor interface. (This is analogous to the example of liquid flow up a capillary tube discussed earlier.) Since the volume of the liquid has been reduced by evaporation, the meniscus must become curved, as indicated in Fig. 5.20. The hydrostatic tension in the liquid is related to the radius of curvature r of the meniscus by

$$p = -\frac{2\gamma_{LV}}{r} \quad (5.39)$$

The negative sign in this equation arises from the sign convention for stress and pressure. The stress in the liquid is positive when the liquid is in tension; the pressure follows the opposite sign convention, so tension is negative pressure.

The maximum capillary pressure p_R in the liquid occurs when the radius of the meniscus is small enough to fit into the pore. For liquid in a cylindrical pore of radius a , the minimum radius of the meniscus is

$$r = -\frac{a}{\cos \theta} \quad (5.40)$$

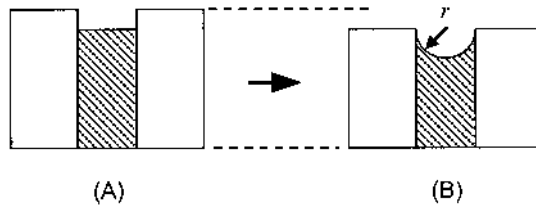


FIGURE 5.20 To prevent exposure of the solid phase (A), the liquid must adopt a curved liquid–vapor interface (B). Compressive forces on the solid phase cause shrinkage. (From Ref. 36.)

The maximum tension is

$$p_R = -\frac{2(\gamma_{SV} - \gamma_{SL})}{a} = -\frac{2\gamma_{LV} \cos \theta}{a} \quad (5.41)$$

It is equal to the tension under the liquid–vapor meniscus [Eq. (5.35)]. The capillary tension in the liquid imposes a compressive stress on the solid phase, causing contraction of the gel. As outlined later, the capillary tension is smaller than the maximum value during most of the drying process.

It is observed that for silica gels, shrinkage proceeds faster when evaporation is allowed to take place, indicating that capillary pressure is the dominant factor driving the shrinkage. However, other factors can make a contribution to the driving force, and these can be significant in other systems.

Osmotic Pressure

Osmotic pressure (Π) is produced by a concentration gradient. A common example is the diffusion of pure water through a semipermeable membrane to dilute a salt solution on the other side. A pressure Π would have to be exerted on the salt solution or a tension $-\Pi$ must be exerted on the pure water to prevent it from diffusing into the salt solution. As discussed earlier, gels prepared by the hydrolysis of metal alkoxides contain a solution of liquids (e.g., water and alcohol) that differ in volatility. Evaporation creates a composition gradient, and liquid diffuses from the interior to reduce the gradient. If the pores are large, a counter-flow of liquid to the interior occurs and no stress is developed. However, if the pores are small enough to inhibit flow, diffusion away from the interior can produce a tension in the liquid. The balancing compression on the solid phase (which, in principle can approach the value of Π) can cause shrinkage of the gel.

Disjoining Forces

Disjoining forces are short range forces resulting from the presence of solid–liquid interfaces. An example of such forces is the repulsion between electrostatically charged double layers discussed in Chapter 4. Short range forces in the vicinity of a solid surface can also induce some degree of structure in the adjacent liquid. The molecules in the more ordered regions adjacent to the solid surface have reduced mobility compared with those in the bulk of the liquid. Disjoining forces are important in layers that are within ~ 1 nm of the solid surface. They would be expected to be important in gels with very fine pores. For gels with relatively large pore sizes, disjoining forces will be important only in the later stages of drying.

Transport of Liquid

Transport of liquid during drying can occur by (1) flow if a pressure gradient exists in the liquid and (2) diffusion if a concentration gradient exists. According

to Fick's first law (see Chapter 7), the flux J , caused by a concentration gradient ∇C , is given by

$$J = -D\nabla C \quad (5.42)$$

where D is the diffusion coefficient. The flux J is defined as the number of atoms (molecules or ions) diffusing across unit area per second down the concentration gradient. In one dimension (e.g., the x direction), $\nabla C = dC/dx$. As discussed earlier, diffusion may be important during drying if the liquid in the pores consists of a solution and a concentration gradient develops by preferential evaporation of one component of the solution. In general, however, diffusion is expected to be less important than flow.

As in most porous media, liquid (or fluid) flow obeys Darcy's law:

$$J = -\frac{K\nabla p}{\eta_L} \quad (5.43)$$

where J is the flux of liquid (the volume flowing across unit area per unit time down the pressure gradient), ∇p is the pressure gradient (equal to dp/dx in one dimension), η_L is the viscosity of the liquid, and K is the permeability of the porous medium. As in Fick's law where the physics of the diffusion process is subsumed in the diffusion coefficient, in Darcy's law the parameters of the porous medium that control the liquid flow are accounted for in terms of the permeability. A variety of models, based on the representation of pores by arrays of tubes, has been put forward for the permeability of porous media. One of the most popular, based on its simplicity and accuracy, is the *Carman-Kozeny* equation:

$$K = \frac{P^3}{5(1-P)^2 S^2 \rho_s^2} \quad (5.44)$$

where P is the porosity, S is the specific surface area (i.e., per unit mass of the solid phase), and ρ_s is the density of the solid phase. For a silica gel prepared from an alkoxide, $S \approx 400\text{--}800 \text{ m}^2/\text{g}$, $P \approx 0.9$, and $\rho_s \approx 1.5\text{--}1.8 \text{ g/cm}^3$. Substituting these values in Eq. (5.44) gives K in the range of 10^{-13} to 10^{-14} cm^2 (i.e., very low). While Eq. (5.44) is fairly successful for many types of porous materials, it also fails often, so it must therefore be used with caution.

Darcy's law, as outlined earlier, is obeyed by many materials, including some with very fine pores ($\leq 10 \text{ nm}$ in size). Figure 5.21 shows the data for silica gel where the flux is indeed proportional to the pressure gradient (38). The experiment was performed by casting a sheet of gel ($\sim 2 \text{ mm}$ thick) onto a Teflon® filter, then imposing a pressure drop across it and measuring the rate of flow through it.

Physical Process of Drying

Particulate gels and polymeric gels show the same general behavior in drying: a constant rate period followed by a falling rate period (Fig. 5.17). However, because of the profound difference in structure, the gels respond differently to the compressive stresses imposed by capillary forces. Initially, colloidal gels show a very small elastic contraction, but this is insignificant compared to the total drying shrinkage (typically 15–30 vol%) that occurs predominantly by rearrangement of the particles. Sliding of the particles over one another leads to denser packing and an increase in the stiffness of the gel. Eventually the network is stiff enough to resist the compressive stresses and shrinkage stops. Rearrangement processes are difficult to analyze; as a result, theoretical equations for the strain rate and shrinkage during drying have not been developed for particulate gels.

Polymeric gels are highly deformable. As for other materials with a polymeric structure, the response to a stress is viscoelastic, i.e., a combination of an instantaneous elastic deformation and a time-dependent viscous deformation. The elastic deformation arises from stretching and bending of the polymer chains, whereas the viscous deformation arises from reorientation and relaxation of polymer chains (or clusters) into lower energy configurations. Assuming the gel to be a continuum, constitutive equations relating the strain to the imposed stress have been developed. As a result of such analysis, considerable insight has been gained into the stress development in the gel and the shrinkage during drying. In the following discussion, particular attention will therefore be paid to the drying of polymeric gels.

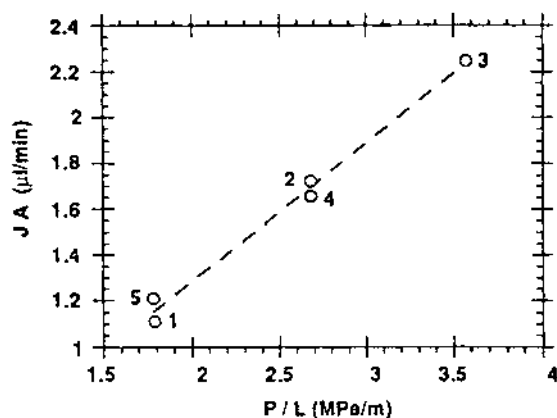


FIGURE 5.21 Flow rate JA (where J is the flux and A is the area of sheet of gel) versus pressure gradient in a silica gel is linear, in accordance with Darcy's law, Eq. (5.43); numbers next to points indicate order of experiments. (From Ref. 38.)

The Constant Rate Period

In the constant rate period, the rate of evaporation is constant. When evaporation starts, the temperature at the surface of the gel drops because of a loss of heat due to the latent heat of vaporization of the liquid. However, heat flow to the surface from the atmosphere quickly establishes thermal equilibrium where transfer of heat to the surface balances the heat loss due to the latent heat of vaporization. The temperature at the surface becomes steady and is called the *wet-bulb* temperature (T_w). The surface of the gel is therefore at the wet-bulb temperature during the CRP. The rate of evaporation, \dot{V}_E is proportional to the difference between the vapor pressure of the liquid at the surface p_w and the ambient vapor pressure p_A :

$$\dot{V}_E = H(p_w - p_A) \quad (5.45)$$

where H is a factor that depends on the temperature, the velocity of the drying atmosphere, and the geometry of the system. Since \dot{V}_E increases as p_A decreases, T_w decreases with a decrease in ambient humidity. For polymeric gels, the ambient vapor pressure must be kept high to avoid rapid drying so that the temperature of the sample remains near the ambient.

Let us consider a wet gel in which some liquid suddenly evaporates. As outlined earlier, the liquid in the pores stretches to cover the dry region and a tension develops in the liquid. The tension is balanced by compressive stresses on the solid phase of the gel. Since the network is compliant, the compressive forces cause it to contract into the liquid, and the liquid surface remains at the exterior surface of the gel (Fig. 5.18b). In a polymeric gel, it does not take much force to submerge the solid phase, so that initially the capillary tension of the liquid is low and the radius of the meniscus is large. As drying proceeds, the network becomes stiffer because new bonds are forming (e.g., by condensation reactions) and the porosity is decreasing. The meniscus also deepens (i.e., the radius decreases), and the tension in the liquid increases [Eq. (5.39)]. When the radius of the meniscus becomes equal to the pore radius in the gel, the liquid exerts the maximum possible stress [Eq. (5.41)]. This point marks the end of the CRP; beyond this the tension in the liquid cannot overcome the further stiffening of the network. The liquid meniscus recedes into the pores, and this marks the start of the FRP (Fig. 5.18c). Thus, the characteristic features of the CRP are

1. the shrinkage of the gel is equal to the rate of evaporation.
2. the liquid meniscus remains at the surface.
3. the radius of the liquid meniscus decreases.

At the end of the CRP, shrinkage virtually stops. According to Eq. (5.41), for an alkoxide gel with $\gamma_L \cos \theta \approx 0.02$ to 0.07 J/m² and $a \approx 1$ – 10 nm, the capillary

tension, p_R , at the critical point is $\approx 4\text{--}150$ MPa. This shows that the gel can be subjected to enormous pressures at the critical point. The amount of shrinkage that precedes the critical point depends on p_R , which, according to Eq. (5.41), increases with the interfacial energy γ_{LV} and with decreasing pore size a . If additives (e.g., surfactants) are added to the liquid to reduce γ_{LV} , then p_R decreases; as a result, less shrinkage occurs and the porosity of the dried gel increases.

Falling Rate Period

When shrinkage stops, further evaporation forces the liquid meniscus into the pores, and the evaporation rate decreases (Fig. 5.18c). This stage is called the *falling rate period*. As outlined earlier, the FRP can be divided into two parts. In the first falling rate period (FRP1), most of the evaporation is still occurring at the exterior surface. The liquid in the pores near the surface exists in channels that are continuous with the rest of the liquid. (The liquid is said to be in the funicular state.) These continuous channels provide pathways for liquid flow to the surface (Fig. 5.22a). At the same time, some liquid evaporates in the pores and the vapor diffuses to the surface. In this stage of drying, as air enters the pores, the surface of the gel may lose its transparency.

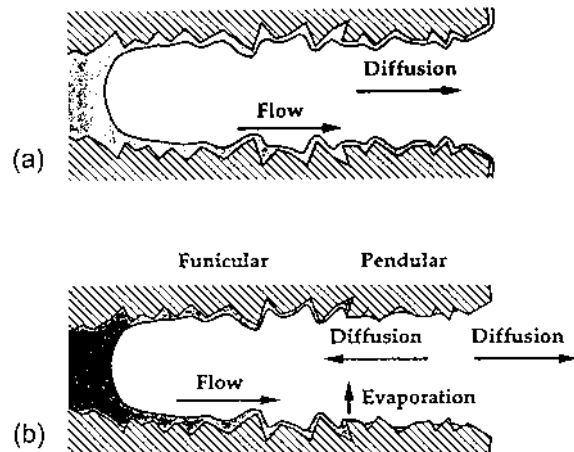


FIGURE 5.22 Schematic diagram illustrating fluid transport during the falling rate period. After the critical point, the liquid–vapor meniscus retreats into the pores of the body. (a) In the first falling rate period, liquid is in the funicular state, so transport by liquid flow is possible. There is also some diffusion in the vapor phase. (b) During the second falling rate period evaporation occurs inside the body, at the boundary between the funicular (continuous liquid) and pendular (isolated pockets of liquid) regions. Transport in the pendular region occurs by diffusion of vapor. (From Ref. 36.)

As the distance between the liquid–vapor interface (the drying front) and the surface increases, the pressure gradient decreases and the flux of liquid also decreases. If the gel is thick enough, eventually a stage is reached where the flux becomes so slow that the liquid near the surface is in isolated pockets. (The liquid is now said to be in the pendular state.) Flow to the surface stops, and the liquid is removed from the gel by diffusion of the vapor. This marks the start of the second falling rate period (FRP2), where evaporation occurs inside the gel (Fig. 5.22b).

Drying from One Surface

In many cases the wet gel is supported so that liquid evaporates from one surface only (Fig. 5.23). As evaporation occurs, capillary tension develops first on the drying surface. This tension draws liquid from the interior to produce a uniform hydrostatic pressure. If the permeability of the gel is high, liquid flow is produced by only a small pressure gradient. However, if the permeability is low (or the gel is fairly thick), a significant pressure gradient is developed. The solid network is therefore subjected to a greater compression on the drying surface. This causes the gel to warp upwards (Fig. 5.23a). Later in the drying process the liquid–vapor interface moves into the interior of the gel, and the pores are filled with air. The gel network surrounding the air-filled pores is relieved of any compressive stress, but the lower part of the gel still contains liquid so that it is subjected to compression due to capillary forces. This causes the gel to warp in the opposite direction (Fig. 5.23b).

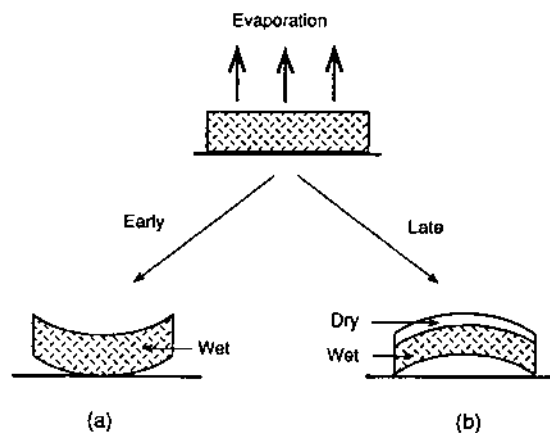


FIGURE 5.23 Warping of plate of gel dried by evaporation from upper surface. Plate warps upward initially then reverses curvature after top surface becomes dry. (Adapted from Ref. 36.)

Drying Stresses

During the CRP, the pores remain full of incompressible liquid. The change in liquid content must be equal to the change in pore volume, which is related to the volumetric strain rate \dot{V} . Equating these changes, we obtain

$$\dot{V} = -\nabla \cdot J = -\nabla \cdot \left(\frac{K}{\eta_L} \nabla p \right) \quad (5.46)$$

The flux of liquid to the surface also matches the evaporation rate (i.e., $J = \dot{V}_E$); so Eq. (5.43) requires that

$$\dot{V}_E = \frac{K}{\eta_L} \nabla p|_{\text{surface}} \quad (5.47)$$

To calculate the drying stresses, Eq. (5.46) must be solved using Eq. (5.47) as a boundary condition. The methods for solving the equation are discussed in Ref. 36. For a viscoelastic flat plate (including one that is purely elastic or viscous), the stress in the solid phase of the gel in the plane of the plate (xy plane) is given by

$$\sigma_x = \sigma_y = \langle p \rangle - p \quad (5.48)$$

where p is the negative pressure (tension) in the liquid and $\langle p \rangle$ is the average pressure in the liquid. According to this equation, if the tension in the liquid is uniform, $p = \langle p \rangle$, and there is no stress on the solid phase. However, when p varies through the thickness, the network tends to contract more where p is high and this differential strain causes warping or cracking. The situation is analogous to the stress produced by a temperature gradient: cooler regions contract relative to warmer regions, and the differential shrinkage causes the development of stresses.

If the evaporation rate is high, p can approach its maximum value, given by Eq. (5.41), while $\langle p \rangle$ is still small so that the total stress at the surface of the plate is

$$\sigma_x \approx \frac{2\gamma_{LV} \cos \theta}{a} \quad (5.49)$$

For slow evaporation, the stress at the drying surface of the plate is

$$\sigma_x \approx \frac{L\eta_L \dot{V}_E}{3K} \quad (5.50)$$

where the half-thickness of the plate is L and evaporation occurs from both faces of the plate.

Cracking During Drying

It is commonly observed that cracking is more likely to occur if the drying rate is high or the gel is thick. It is also observed that cracks generally appear at the critical point (the end of the CRP) when shrinkage stops and the liquid/vapor meniscus moves into the body of the gel. In the theoretical analysis developed by Scherer (36), cracking is attributed to stresses produced by a pressure gradient in the liquid. However, the stress that causes failure is not the macroscopic stress σ_x acting on the network. If the drying surface contains flaws, such as that sketched in Fig. 5.24, the stress is concentrated at the tip of the flaw. The stress at the tip of a flaw of length c is proportional to

$$\sigma_c = \sigma_x (\pi c)^{1/2} \quad (5.51)$$

Fracture occurs when $\sigma_c > K_{IC}$, where K_{IC} is the critical stress intensity of the gel. Assuming that the flaw size distribution is independent of the size and drying rate of the gel, the tendency to fracture would be expected to increase with σ_x . According to Eq. (5.50), σ_x increases with the thickness L of the sample and the drying rate \dot{V}_E . Scherer's analysis therefore provides a qualitative explanation for the dependence of cracking on L and \dot{V}_E .

In another explanation, it has been proposed that cracking in gels occurs as a result of local stresses produced by a distribution of pores sizes (39). As sketched in Fig. 5.25, after the critical point, liquid is removed first from the largest pores. It has been suggested that the tension in the neighboring small

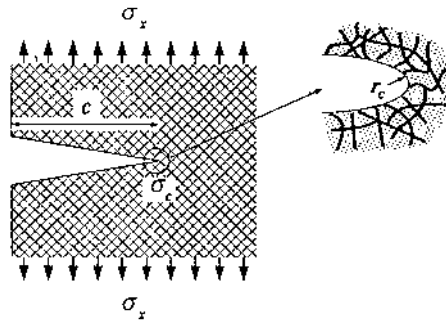


FIGURE 5.24 Surface flaw of length c and tip radius r_c acted upon by far-field stress σ_x creates amplified stress σ_c at the crack tip. Insert indicates that r_c is on the scale of the mesh size of the network. (From Ref. 38.)

pores deforms the pore wall and causes cracking. As discussed in Ref. 36, this explanation does not appear to be valid. The drying stresses are macroscopic in that the pressure gradient extends through the thickness of the gel, i.e., the stresses are not localized. If the stresses were localized on the scale of the pores, the gel would be expected to crumble to dust as the drying front advanced. Instead, gels crack into only a few pieces. However, flaws that lead to failure may be created by local stresses (resulting, for example, from nonuniform pore sizes) and then propagated by the macroscopic stresses.

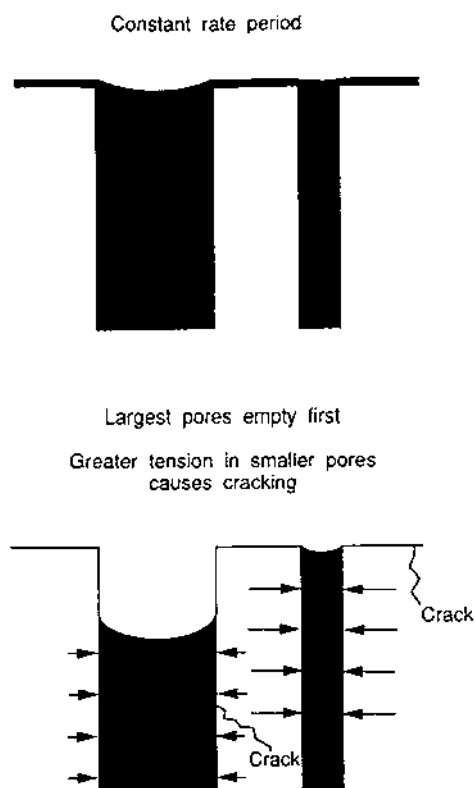


FIGURE 5.25 Illustration of microscopic model: during the constant rate period, meniscus has same radius of curvature for pores of all sizes; after the critical point, the largest pores are emptied first. The capillary tension compressing the smaller pores causes local stresses that crack the network. (After Ref. 39.)

Avoidance of Cracking

Scherer's theory of drying provides useful guidelines for controlling stress development and therefore for avoiding fracture. Cracking is attributed to macroscopic stresses produced by a pressure gradient ∇p in the liquid. Fast evaporation leads to a high ∇p and hence to large differential strain. To avoid cracking, the gel must be dried slowly. However, the "safe" drying rates are so slow that gels thicker than ~ 1 cm require uneconomically long drying times. A number of procedures may be used to increase the safe drying rates.

The boundary condition at the surface of the gel [Eq. (5.47)] shows that high \dot{V}_E leads to high ∇p . Furthermore, low permeability (low K) leads to high ∇p for a given \dot{V}_E . From Eq. (5.44), it can be shown that K increases roughly as the square of the pore size. An obvious strategy is to increase the pore size of the gel. One approach that has been used for silica gels involves mixing colloidal silica particles with the alkoxide (TEOS). In addition to producing gels with large pores, the silica particles also strengthen the gel. Another approach is to use colloidal particles to produce gels that are easier to dry (e.g., particulate silica gel). However, as outlined later, gels with larger pores require higher sintering temperatures for densification so that some compromise between ease of drying and ease of sintering is made.

The capillary pressure sets a limit on the magnitude of the drying stresses, i.e., $\sigma_x \leq p_R$, and is probably responsible for the creation of critical flaws. The probability of fracture can therefore be reduced by reducing the capillary pressure through (1) increasing the pore size (discussed above) and (2) decreasing the liquid-vapor interfacial tension, [see Eq. (5.41)]. The interfacial tension can be reduced by using a solvent with a lower volatility than water that, in addition, has a low γ_{LV} . The surface tension of a liquid can also be reduced by raising the temperature. Beyond the critical temperature and pressure, there is no tension. Since $p = 0$, ∇p must also be zero so that no drying stresses can be produced. This approach forms the basis of supercritical drying described in the next section.

Another approach is to strengthen the gel so that it is better able to withstand the drying stresses. For example, aging the gel in the pore liquid at slightly elevated temperatures stiffens the gel network and also reduces the amount of shrinkage in the drying stage.

For gels prepared from metal alkoxides, certain organic compounds added to the alkoxide solution have been claimed to speed up the drying process considerably while avoiding cracking of the gel. It has been reported that with the use of these compounds, gels thicker than 1 cm can be dried in ~ 1 day. These compounds, referred to as *drying control chemical additives* (DCCA) include formamide (NH_2CHO), glycerol ($\text{C}_3\text{H}_8\text{O}_3$), and oxalic acid ($\text{C}_2\text{H}_2\text{O}_4$). While the role of these compounds during drying is not clear, it is known that they increase

the hardness (and presumably the strength) of the wet gel. However, they also cause serious problems during sintering because they are difficult to burn off. Decomposition leading to bloating of the gel and chemical reaction (e.g., the formation of carbonates) severely limit the effectiveness of these compounds.

5.5.6.2 Supercritical Drying

In *supercritical* drying (sometimes referred to as *hypercritical* drying), the liquid in the pores is removed above the critical temperature T_c and the critical pressure p_c of the liquid. Under these conditions, there is no distinction between the liquid and the vapor states. The densities of the liquid and vapor are the same, there is no liquid–vapor meniscus and no capillary pressure, and so there is no drying stresses.

In supercritical drying, the wet gel is placed in an autoclave and heated fairly slowly (less than $\sim 0.5^\circ\text{C}/\text{min}$) to a temperature and pressure above the critical point. The temperature–pressure path during the drying process is sketched in Fig. 5.26. The temperature and pressure are increased in such a way that the liquid–vapor phase boundary is not crossed. After equilibration above the critical point, the fluid is released slowly.

Table 5.6 shows the critical points of some fluids. The critical temperature and pressure for ethanol are 516 K and 6.4 MPa (~ 63 atm). The need to cycle an autoclave through such high temperature and pressure makes the process time consuming, expensive, and somewhat dangerous. The total drying time can be as long as 2–3 days for a large gel. An alternative is to replace the liquid in the pores with a fluid having a much lower critical point. Carbon dioxide has a T_c of 304 K and a p_c of 7.4 MPa. The low T_c means that the drying process can be carried out near ambient temperatures. Carbon dioxide is also relatively cheap. In supercritical drying with CO_2 , the liquid (e.g., alcohol) in the pores of the gel must first be replaced. This is accomplished by placing the gel in the autoclave

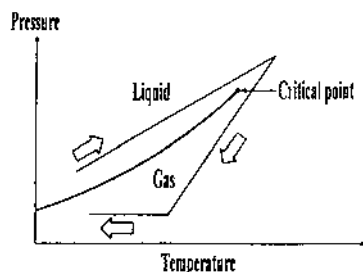


FIGURE 5.26 Schematic illustration of the pressure-temperature schedule during supercritical drying

and flowing liquid CO₂ through the system until no trace of alcohol can be detected. Following this, the temperature and pressure of the autoclave are raised slowly to ~40°C and ~8.5 MPa. After maintaining these conditions for ~30 min, the CO₂ is slowly released. The step where the liquid in the pores is replaced with CO₂ can take several hours so that supercritical drying with CO₂ is not much faster overall.

With supercritical drying, monolithic gels as large as the autoclave can be produced. Very little shrinkage (< 1% linear shrinkage) occurs during supercritical drying so that the aerogel is very porous and fragile. The solid phase occupies less than 10 vol% of the aerogel. Because of the low density, the sintering of aerogels to produce dense polycrystalline articles is impractical. Considerable shrinkage (> 50% linear shrinkage) would have to take place, and this makes dimensional control of the article difficult. As discussed in Chapter 11, a common problem is the crystallization of the gel prior to the attainment of high density which severely limits the final density. Because of these problems, supercritical drying is better suited to the fabrication of porous materials and powders. Monolithic aerogels are of interest because of their exceptionally low thermal conductivity. Powders with good chemical homogeneity can be easily produced by grinding the fragile aerogel.

5.5.6.3 Structural Changes During Drying

We saw earlier that there are fundamental differences in structure between particulate gels and polymeric gels, and within polymeric gels, between gels prepared by acid-catalyzed and base-catalyzed reactions. During conventional drying, we would expect the structure of these gels to evolve differently under the compressive action of the capillary stresses. Polymeric gels will gradually collapse and

TABLE 5.6 Critical Points of Some Fluids

Fluid	Formula	Critical temperature (K)	Critical pressure (MPa)
Carbon dioxide	CO ₂	304.1	7.36
Nitrous oxide	N ₂ O	309.8	7.24
Freon-13	CClF ₃	301.9	3.86
Freon-23	CHF ₃	298.9	4.82
Freon-113	CCl ₂ F-CClF ₂	487	3.40
Freon-116	CF ₃ -CF ₃	292.7	2.97
Methanol	CH ₃ OH	513	7.93
Ethanol	C ₂ H ₅ OH	516	6.36
Water	H ₂ O	647	22.0

cross-link as unreacted OH and OR groups come into contact with each other (see Fig. 5.16). When the structure becomes stiff enough to resist the capillary stresses, residual porosity will be formed. For gels produced by acid-catalyzed reactions, in which the polymer chains are weakly cross-linked, the structure can be highly compacted before it is sufficiently cross-linked to produce residual porosity (Fig. 5.27a). The xerogel will be characterized by a relatively high density and very fine pores. In contrast, after drying, base-catalyzed gels will have a relatively low density and larger pores because the structure of polymeric clusters will be more difficult to collapse (Fig. 5.27b). Silica gels prepared by acid-catalyzed reactions can lead to xerogels with porosities as low as 35–40% compared to values as high as 60–70% for similar xerogels produced by the base-catalyzed route.

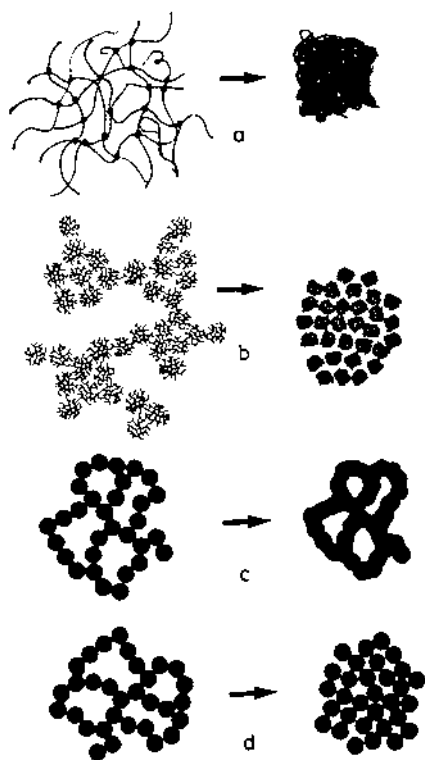


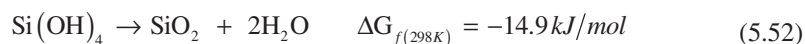
FIGURE 5.27 Schematic representation of the structural evolution during drying for (a) acid-catalyzed gels, (b) base-catalyzed gels, (c) colloidal gel aged under conditions of high silica solubility, and (d) colloidal gel composed of weakly bonded particles. (From Ref. 40.)

For particulate gels, the structure will fold or crumple under the action of the capillary stresses. Neck formation or an increase in the coordination number of the gel will continue until the structure is strong enough to resist the capillary stresses, at which point residual porosity is formed. Because the particulate structure of the gel can better withstand the smaller capillary stresses (arising from the larger pores), the shrinkage for particulate gels will be significantly smaller than that for polymeric gels. The structure of the xerogel will be a somewhat contracted and distorted version of the original structure (Fig. 5.27c and d). The porosity is typically in the range of 70–80%.

5.5.7 Gel Densification During Sintering

Particulate gels, as discussed above, contract slightly during drying. Since the solid phase is composed of a fully cross-linked network that is similar in structure to that of the corresponding melted glass, the drying process does not alter the structure of the solid skeletal phase of the gel. Polymeric gels undergo significant contraction and further polymerization by condensation reactions during drying. Even so, the resulting polymer structure of the solid skeletal phase of the xerogel is still less highly cross-linked than the corresponding melted glass. For example, the number of nonbridging oxygen atoms (i.e., those ending in OH and OR groups) has been estimated in the range of 0.33 to 1.48 for every silicon atom in polymeric silica xerogels as compared to a value of ~ 0.003 for a melted silica glass with 0.05 wt% water. One effect of the lower crosslink density is that the solid skeletal phase of the gel has a lower density than that of the corresponding melted glass. This is equivalent to saying that the skeletal phase has extra *free volume* when compared to the corresponding glass produced by melting.

The structure of the xerogel has important implications for densification. Compared to the corresponding dense glass prepared by melting, xerogels have a high free energy that will act as a powerful driving force for densification during firing. Three characteristics contribute to this high free energy (40). The surface area of the solid/vapor interface makes the largest contribution, estimated at 30–300 J/g (which corresponds to 100–1000 m²/g of interfacial area). The reduction of the surface area provides a high driving force for densification by viscous flow. The two other contributions to the high free energy result from the reduced cross-link density of the polymer chains compared to the corresponding melted glass. Polymerization reactions can occur according to



More weakly cross-linked polymers containing more non-bridging oxygen atoms will therefore make a greater contribution to the free energy. For silica gels containing 0.33–1.48 OH groups per silicon atom, the contribution to the free

energy resulting from the reaction described by Eq. (5.52) is estimated to range from ~ 20 to 100 J/g. The free volume of the solid skeletal phase is also expected to provide a contribution to the free energy. Figure 5.28 summarizes the free energy versus temperature relations for polymeric and particulate gels, glass, and an ideal supercooled liquid of the same oxide composition.

The densification of gels during sintering has been studied extensively by Scherer and co-workers (41)–(43). Figure 5.29 shows data for the linear shrinkage of three silica gels during firing at a constant heating rate of $2^\circ\text{C}/\text{min}$. The particulate gel (curve C) shrinks only at elevated temperatures ($\sim 1200^\circ\text{C}$), and its densification behavior can be accurately described by models for viscous sintering of porous melted glass. We shall examine these models in Chapter 8. The shrinkage of the polymeric gels differs markedly from that of the particulate gel. Starting from fairly low temperatures, continuous shrinkage occurs, and the extent of the shrinkage depends on the method used to prepare the gel. At any temperature, the shrinkage of the acid-catalyzed gel (curve A) is significantly greater than that of the base-catalyzed gel (curve B). The results indicate that the sintering of polymeric gels is not as simple as that of particulate gels. Furthermore the densifi-

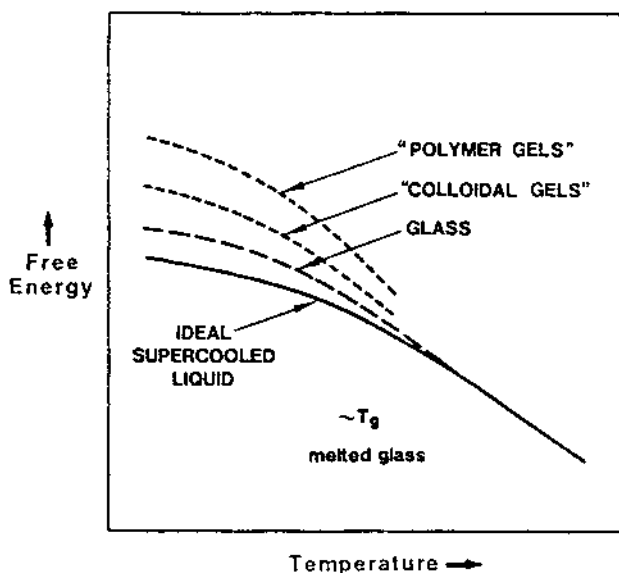


FIGURE 5.28 Schematic representation of free energy versus temperature relations between dried polymeric gels, dried colloidal gels, glass, and an ideal supercooled liquid of the same oxide composition. (From Ref. 40.)

cation behavior of polymeric gels cannot be explained on the basis of viscous sintering alone.

For polymeric gels, four mechanisms can operate during the conversion of the dried gel to a dense glass: (1) capillary contraction of the gel, (2) condensation polymerization leading to an increase in the cross-link density, (3) structural relaxation by which the structure approaches that of a supercooled liquid, and (4) viscous sintering. The temperature range in which each of these mechanisms contribute to the densification depends on the structure of both the porous and solid phases of the gel (e.g., pore size and skeletal density) as well as the rate of heating and the previous thermal history. A good illustration of the temperature range in which each of these mechanisms operate is provided in Fig. 5.30, which shows the shrinkage and weight loss of a borosilicate gel during heating at a constant rate of $0.5^\circ\text{C}/\text{min}$. Three regions have been identified corresponding to the following trends:

Region I: Weight loss without shrinkage ($25\text{--}150^\circ\text{C}$)

Region II: Weight loss with concurrent shrinkage ($150\text{--}525^\circ\text{C}$)

Region III: Shrinkage without weight loss ($>525^\circ\text{C}$)

Region I

The weight loss in region I is due to the desorption of physically adsorbed water and alcohol. A very small shrinkage is observed and this occurs as a result of

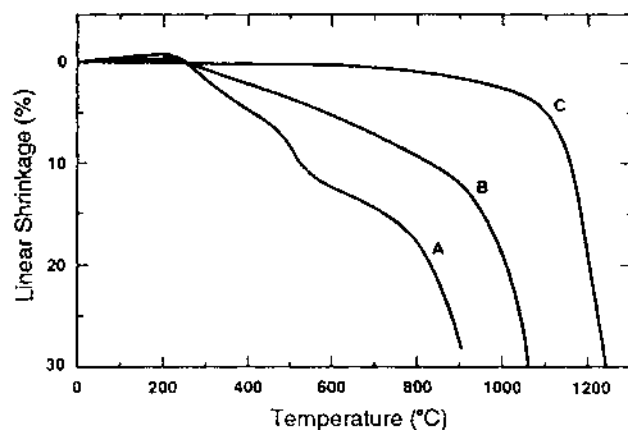


FIGURE 5.29 Linear shrinkage versus temperature during constant heating rate sintering at $2^\circ\text{C}/\text{min}$ for an acid-catalyzed silica gel (A), a base-catalyzed silica gel (B) and a colloidal silica gel. The acid- and base-catalyzed gels were prepared with a water concentration of 4 mol H_2O per mole of TEOS. (From Ref. 43.)

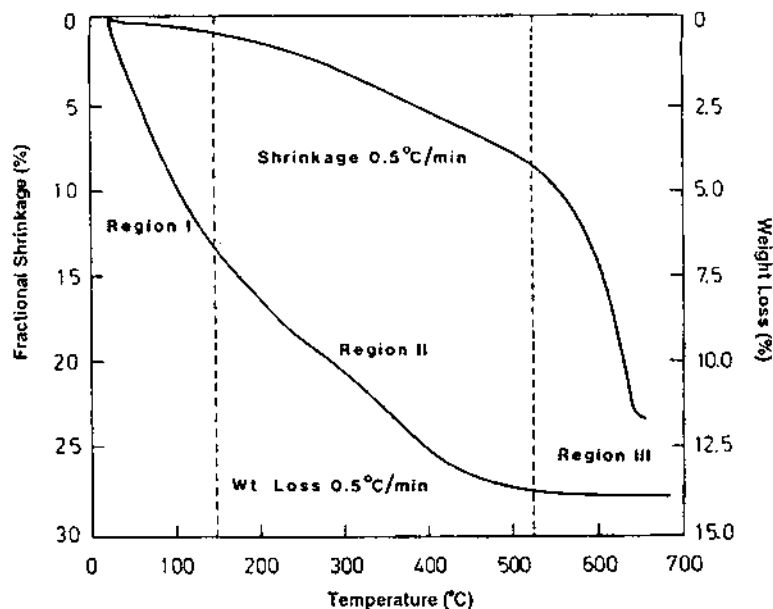
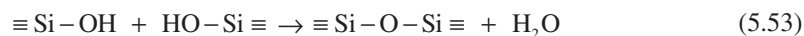


FIGURE 5.30 Linear shrinkage and weight loss for a borosilicate gel during heating at a constant rate of 0.5°C/min. (From Ref. 41.)

the increase in the surface energy due to the desorption process. The surface energy increases from $\sim 0.03 \text{ J/m}^2$ for a surface saturated with water and alcohol to $\sim 0.15 \text{ J/m}^2$ for a pure silanol surface (i.e., produced after desorption). This increase in surface energy is equivalent to an increase in the capillary pressure.

Region II

Weight loss in this region is attributed to two processes. Water is removed as a by-product of polycondensation reactions:



The reaction described by Eq. (5.53) may occur within the skeletal phase or on the surface of the skeletal phase. The second process is the oxidation of carbonaceous residues present originally as unhydrolyzed alkoxy groups. Experiments indicate that the removal of carbon is essentially complete by 400°C but that hydrogen is continuously removed over the whole temperature range (150–525°C).

The shrinkage in region II can be attributed solely to densification of the solid skeletal phase of the gel. Alternatively, the removal of very fine pores by

viscous sintering may be postulated, but the pore size would have to be less than ~ 0.4 nm. Pores of this size would, however, be indistinguishable from free volume in the skeletal phase. Two mechanisms have been identified for the densification of the skeletal phase: (1) polymerization reactions (e.g., Eq. 5.53), which lead to a higher cross-link density of the polymer chain, and (2) structural relaxation of the polymeric network as the structure approaches the configuration of the melt-prepared glass. Structural relaxation occurs by diffusive motion of the polymer network without the expulsion of water and other products. The relative contribution of each mechanism to the overall densification in region II is difficult to quantify.

We would expect skeletal densification to be insignificant for particulate gels in which the solid network has the same structure as the corresponding melt-prepared glass and to make the greatest contribution to shrinkage for weakly cross-linked gels. This is fully borne out by the results of Fig. 5.29.

Region III

The large, fairly fast shrinkage in this region is consistent with a mechanism of densification by viscous flow. The pores in the gel that were formed after the removal of the liquid in the drying stage are removed in this process. The driving force for densification is the reduction in the solid/vapor interfacial area associated with the pores. While the weight loss in this region is low, studies indicate that polymerization reactions and structural relaxation can have a strong influence on the kinetics of densification.

Table 5.7 summarizes the dominant shrinkage mechanisms and their relative contribution to the overall shrinkage for the borosilicate gel described in Fig. 5.30. The significant contribution due to skeletal densification by condensation polymerization and structural relaxation should not go unnoticed.

TABLE 5.7 Dominant Mechanisms of Shrinkage During the Sintering of a Borosilicate Gel and Their Relative Contributions to the Total Shrinkage

Region	Temperature range (°C)	Mechanism	Relative contribution (%)
I	25–150	Capillary contraction	3
II	150–525	Condensation polymerization and structural relaxation	33
III	>525	Viscous flow	63

Source: Ref. 42.

So far, we have discussed the sintering of gels under the influence of the available driving forces. Other factors must also be considered because they can have a significant influence on the sintering process. Densification involves transport of matter so that it is limited by the *kinetics* of the process. The kinetics determine how long the process will take and depend not only on the physical and chemical structure of the gel but also on the time–temperature schedule of heating. The rate of heating, for example, may have a significant effect on the densification. Increased heating rate reduces the time spent at each increment of temperature and therefore reduces the amount of viscous flow that can occur in a given temperature interval. However, increased heating rate also reduces the amount of cross-linking and structural relaxation that can occur over the same temperature interval, so the viscosity of the gel at each temperature is reduced. Under certain conditions, the rate of viscous sintering can increase at sufficiently high heating rates (41).

Even after drying, the gel structure normally contains a fairly large amount of unhydrolyzed alkoxy groups. These are oxidized and removed as gases below $\sim 400^{\circ}\text{C}$. Two major problems may arise if the firing process is not carried out carefully. One is trapped gases in the pores leading to bloating of the gel at higher temperatures. This may occur, for example, if the heating rate is so fast that the pores become isolated prior to complete oxidation of the alkoxy groups. Further heating to higher temperatures causes an increase in the pressure of the gas in the pores, resulting in enlargement of the pores and bloating. The other problem is the presence of carbon residues in the gel due to incomplete oxidation. In some cases, the gel may turn black around 400°C . Generally, for this part of the sintering process, the temperature must be high enough to oxidize the alkoxy groups but at the same time low enough to prevent the pores from sealing off.

We have assumed that a dense glass is produced at the end of the firing process. This is not always so. For crystallizable compositions such as ceramics, crystallization may occur prior to full densification. A crystalline body is generally more difficult to densify than the corresponding amorphous body so crystallization prior to full densification will, in general, hinder densification. If full densification is achieved prior to crystallization, a controlled heating step is necessary to nucleate and grow the crystalline grains. We shall examine this point in more detail in Chapter 11, where we consider viscous sintering concurrently with crystallization.

In the production of a glass by the polymeric gel route, the network structure evolves very differently from that of the corresponding glass prepared by conventional melting. An important question is whether the structure and properties of the fabricated sol–gel-derived glass is any different from that for the corresponding melt-prepared glass. Current indications are that for gels densified *above* the glass transition temperature, the structure and properties can be indistinguishable from those for the corresponding melt-prepared glass.

5.6 SOL-GEL PREPARATION TECHNIQUES

Having considered some of the basic physics and chemistry of the sol-gel method, we come now to some of the practical issues involved in the preparation of gels. For the production of simple oxides (e.g., SiO_2), the preparation techniques are fairly straightforward. Further considerations must be taken into account for the production of complex oxides, for we must ensure that the desired chemical composition and uniformity of mixing are achieved during the sol-gel processing. Gel compositions with one type of metal cation (such as silica or alumina gel) yield simple oxides on pyrolysis and are referred to as single-component gels. Multicomponent gels have compositions with more than one type of metal cation and yield complex oxides on pyrolysis.

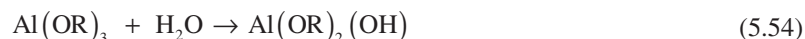
A wide range of ceramic and glass compositions have been prepared by sol-gel processing and details of the experimental procedure can be found in the literature (see, for example, Ref. 44 for a partial list). We will not repeat the procedure for the preparation of specific gel compositions. Instead, the common techniques will be outlined with the aid of a few specific examples. To keep the discussion at a suitable level, we shall limit the consideration of multicomponent gels mainly to the case of gels containing two metal cations only.

5.6.1 Particulate Gels

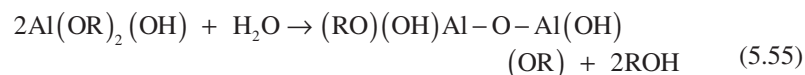
5.6.1.1 Single-Component Gels

For single-component gels, colloidal particles are dispersed in water and peptized with acid or base to produce a sol. Two main methods can be employed to achieve gelation: (1) removal of water from the sol by evaporation to reduce its volume or (2) changing the pH to slightly reduce the stability of the sol.

Earlier in this chapter we discussed the sol-gel processing of aqueous silicates and mentioned the preparation of SiO_2 gels from fine particles made by flame oxidation (2)–(4). The preparation of alumina sols from alkoxides has been characterized by Yoldas (45). Aluminum alkoxides such as aluminum *sec*-butoxide and aluminum isopropoxide are readily hydrolyzed by water to form hydroxides. Which hydroxide is formed depends on the conditions used in the hydrolysis. The initial hydrolysis reaction of aluminum alkoxides can be written



The reaction proceeds rapidly with further hydrolysis and condensation:



Assuming the formation of polymers that are not too highly cross-linked, the incorporation of n aluminum ions into the chain is given by the formula $\text{Al}_n\text{O}_{n-1}(\text{OH})_{(n+2)-x}(\text{OR})_x$. As the reaction proceeds, the number of OR groups (i.e., x) relative to n should decrease to a value that depends on the hydrolysis temperature and the concentration of OR groups in the solvent. [It should be kept in mind, as we mentioned earlier, that Eqs. (5.54) and (5.55) are not exact formulas but merely represent simplifications.]

Hydrolysis by cold water (20°C) results in the formation of a monohydroxide that is predominantly amorphous. The structure contains a relatively high concentration of OR groups. It is believed that the presence of the OR groups is directly related to the structural disorder in the amorphous phase since their removal (e.g., by aging in the solvent) inevitably leads to conversion of the amorphous hydroxide to a crystalline hydroxide, boehmite [$\text{AlO}(\text{OH})$], or bayerite [$\text{Al}(\text{OH})_3$]. Aging at room temperature leads to the formation of bayerite by a process involving the solution of the amorphous hydroxide and subsequent precipitation as the crystalline phase. Aging of the amorphous hydroxide above 80°C leads to rapid conversion to boehmite. Since the conversion of the amorphous hydroxide to boehmite or bayerite is accompanied by the liberation of OR groups, the rate of conversion is inhibited by the presence of alcohol in the solvent during the aging process. Hydrolysis of aluminum alkoxides by hot water (80°C) results in the formation of boehmite, which is relatively unaffected by aging.

Using aluminum alkoxides as the starting material, the production of alumina by the colloidal gel route involves the following main steps:

1. Hydrolysis of the alkoxide to precipitate a hydroxide
2. Peptization of the precipitated hydroxide (e.g., by the addition of acids) to form a clear sol
3. Gelation (e.g., by evaporation of solvent)
4. Drying of the gel
5. Sintering of the dried gel

The formation of the sol can be a critical part of the process. While boehmite and the amorphous hydroxide prepared by cold water hydrolysis can be peptized to a clear sol, bayerite will not form a sol and its formation during hydrolysis should therefore be avoided. In addition, the nature of the acid has a significant effect on the peptization step. Table 5.8 shows the peptizing effect of various acids on the precipitate formed by hydrolysis of aluminum *sec*-butoxide. The results are similar when aluminum isopropoxide is used. It appears that only strong or fairly strong acids, which do not form chemical complexes (or form only very weak complexes) with aluminum ions, are effective for achieving peptization. For these acids, the concentration of the acid also has an effect. Peptization

requires the addition of at least 0.03 mole of acid per mole of alkoxide (followed by heating at $\sim 80^\circ\text{C}$ for a sufficient time).

The amount of acid used in the peptization step also has a significant influence on the gelation of the sol and on the properties of the fabricated aluminum oxide. There is a critical acid concentration at which the volume of the gel is a minimum. For nitric acid, this critical concentration is ~ 0.07 mol/mol of alkoxide. At this minimum volume, the gel contains an equivalent of 25 wt% of Al_2O_3 . Deviation from the critical acid concentration, to higher or lower values, causes a sharp increase in the volume of the gel (Fig. 5.31). At higher acid concentration, the gels may contain an equivalent of only 2 to 3 wt % Al_2O_3 . Because of the large shrinkages that occur, gels containing an equivalent of less than ~ 4 wt% of Al_2O_3 do not retain their integrity after drying and firing.

5.6.1.2 Multicomponent Gels

In the case of multicomponent particulate gels, a primary concern is the prevention of segregation of the individual components so that uniform mixing may be achieved. Various routes have been used for their preparation, including (1) coprecipitation of mixed oxides or hydroxides, (2) mixing of sols of different oxides

TABLE 5.8 Peptizing Effect of Various Acids on the Precipitate Formed by the Hydrolysis of Aluminum *sec*-Butoxide

Acid	Formula	Condition of Precipitate ^a
Nitric	HNO_3	Clear sol
Hydrochloric	HCl	Clear sol
Perchloric	HClO_4	Clear sol
Hydrofluoric	HF	Unpeptized
Iodic	HIO_4	Unpeptized
Sulfuric	H_2SO_4	Unpeptized
Phosphoric	H_3PO_4	Unpeptized
Boric	H_3BO_3	Unpeptized
Acetic	CH_3COOH	Clear sol
Trichloroacetic	CCl_3COOH	Clear sol
Monochloroacetic	CH_2ClCOOH	Clear to cloudy
Formic	HCOOH	Clear to cloudy
Oxalic	$\text{H}_2\text{C}_2\text{O}_4 \cdot 2\text{H}_2\text{O}$	Unpeptized
Phthalic	$\text{C}_8\text{H}_4\text{O}_3$	Unpeptized
Citric	$\text{H}_3\text{C}_6\text{H}_5\text{O}_7 \cdot \text{H}_2\text{O}$	Unpeptized
Carbolic	$\text{C}_6\text{H}_5\text{OH}$	Unpeptized

^aAfter 7 days at 95°C .

Source: Ref. 45.

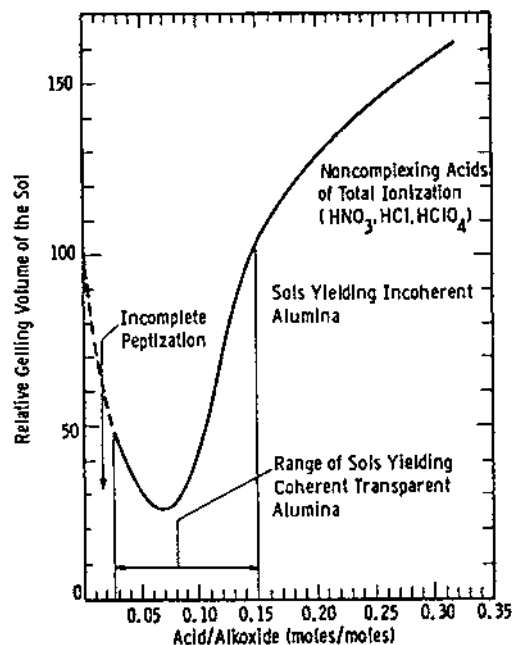


FIGURE 5.31 Effect of acid concentration on the volume of the gel formed from a peptized boehmite sol. (From Ref. 35.)

or hydroxides, and (3) mixing of sols and solutions. In the co-precipitation technique, the general approach is to mix different salt solutions or alkoxide solutions to give the required composition, followed by hydrolysis with water. The precipitated material is usually referred to as a gel but unlike the gels produced from dispersions of colloidal particles, it is not normally dispersible in water. The success of the method depends on controlling the concentration of the reactants and the pH and temperature of the solution to produce mixed products with the desired chemical homogeneity. The co-precipitation technique was considered in Chapter 2 for the preparation of powders of complex oxides.

When gels are formed by mixing sols of different oxides or hydroxides, the uniformity of mixing is, at best, of the order of the colloidal particle size. The chemical homogeneity will therefore be worse than that obtained in the coprecipitation method assuming ideal coprecipitation (i.e., without aggregation). An example of this technique is the preparation of alumino-silicate gels, for example one with the mullite composition ($3\text{Al}_2\text{O}_3 \cdot 2\text{SiO}_2$) by the mixing of boehmite sol and silica sol (46,47). Although these sols can be prepared in the

laboratory (by, for example, the hydrolysis of alkoxides), they are also available commercially. In the pH range of ~ 2.5 –8, the surfaces of the boehmite particles are positively charged while those of the silica particles are negatively charged. If the mixture of the two sols is gelled within this pH range, then a fairly homogeneous colloidal gel can be obtained because of the attraction and intimate contact between the oppositely charged boehmite and silica particles.

The alumino-silicate system can also be used to illustrate the third method of mixing sols and solutions. In one case, boehmite sol is mixed with a solution of TEOS in ethanol (46). Gelling is achieved by heating the mixture to evaporate some solvent. Alternatively, silica sol is mixed with a solution of aluminum nitrate and the mixture is gelled by heating.

5.6.2 Polymeric Gels

For single-component gels such as silica gel, we have considered in detail the conditions that lead to the formation of polymeric gels. Turning now to the preparation of multicomponent gels, further considerations must be taken into account. As an example, consider the formation of silica-titania glasses. A convenient starting point for the preparation of the gel is the hydrolysis and condensation of a mixed solution of a silicon alkoxide (e.g., TEOS) and a titanium alkoxide (e.g., titanium tetraethoxide). From our earlier discussion of the properties of alkoxides, we would expect the hydrolysis of the titanium alkoxide to be much faster than that of the silicon alkoxide. Uncontrolled additions of water to the mixture of the two alkoxides would lead to vigorous hydrolysis of the titanium alkoxide and the formation of precipitates that are useless for polymerization. The problem of mismatched hydrolysis rates must therefore be considered when gels with good chemical homogeneity are required.

In general, five different approaches can be used to prepare multicomponent gels:

1. Use of double alkoxides.
2. Partial hydrolysis of the slowest reacting alkoxide.
3. Use of a mixture of alkoxides and metal salts.
4. Slow addition of small amounts of water.
5. Matching the hydrolysis rates of the individual alkoxides.

Of these, methods (2), (3), and (4) are more commonly used.

5.6.2.1 Use of Double Alkoxides

The use of double alkoxides as the starting material for sol-gel processing seeks to eliminate the problem of mismatched hydrolysis rates by forming a molecule or molecular species in which the metal cations are mixed in the desired ratio. The double alkoxide is hydrolyzed and polymerized in the same way described

earlier for simple alkoxides containing one metal cation and the gel has the same ratio of the two metals as the double alkoxide. The homogeneity of mixing therefore extends to the atomic level. The mechanisms of hydrolysis and condensation of double alkoxides are however unclear because the topic has been studied thoroughly in only a few cases (48,49).

The high degree of homogeneity obtained by this route is illustrated by the work of Dislich (50), who prepared magnesium aluminum spinel (MgAl_2O_4) from a double alkoxide formed by reacting magnesium methoxide with aluminum *sec*-butoxide (Fig. 5.32). On heating the dried gel, the major x-ray reflections of spinel started to appear at $\sim 250^\circ\text{C}$, and crystallization was completed by $\sim 400^\circ\text{C}$. In comparison, particulate gels of the same material prepared by Bratton (51) using a co-precipitation technique still contained gibbsite [$\text{Al}(\text{OH})_3$] at temperatures below $\sim 400^\circ\text{C}$.

Despite the high degree of chemical homogeneity obtainable by the double alkoxide route, the method is used only on a limited basis because many double alkoxides are difficult to prepare or are unstable. Furthermore, for a given two-component gel, changing the chemical composition of the gel by changing the atomic ratios of the two metal cations becomes a tedious task because a new double alkoxide has to be synthesized in each case.

5.6.2.2 Partial Hydrolysis of the Slowest Reacting Alkoxide

This method, involving partial hydrolysis of the slowest reacting alkoxide prior to adding the other alkoxide, was invented by Thomas (52) and popularized by the work of Yoldas (15,53). The idea is that the newly added, unhydrolyzed alkoxide will condense with the partially hydrolyzed sites formed by the previous

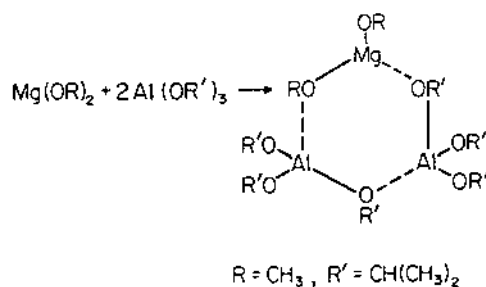
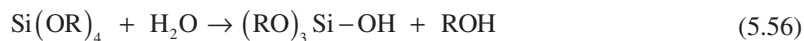


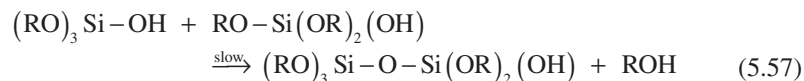
FIGURE 5.32 Magnesium aluminum double alkoxide formed by the reaction of a solution containing 1 mol magnesium methoxide to 2 mol aluminum *sec*-butoxide in alcohol. (From Ref. 50.)

hydrolysis (*heterocondensation*) rather than with itself (*homocondensation*). Unlike the method involving the use of double alkoxies where molecular-level homogeneity is predicted, the chemical homogeneity of the gel will depend on the size of the polymeric species to which the last component is added.

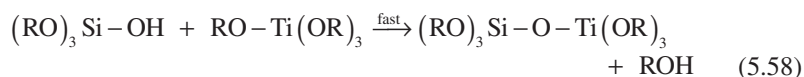
As an example, consider the SiO_2 - TiO_2 system, for which the starting materials are commonly TEOS and titanium tetraethoxide $\text{Ti}(\text{OEt})_4$. The hydrolysis rate of TEOS, we recall, is much slower than that for the titanium ethoxide. If the TEOS is diluted with ethanol (e.g., 1 mol of ethanol to 1 mol of TEOS) and partial hydrolysis of the solution is carried out with the addition of 1 mol of water per mole of TEOS, the majority of the silanol species will contain one OH group:



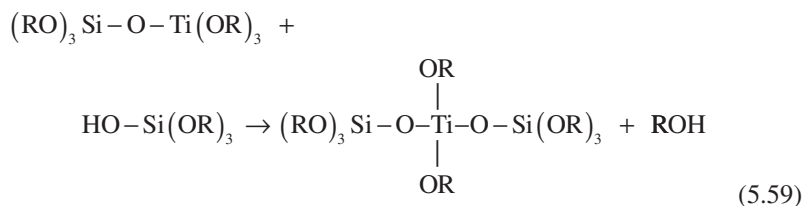
As noted earlier, these soluble silanols will undergo condensation reactions on aging. For the present situation where the number of OH groups in the silanol is limited to about 1 per molecule and the system is diluted, the condensation rate is slow during the first few hours if the temperature is reasonably low (e.g., room temperature):



If titanium ethoxide is introduced into the solution with vigorous stirring, heterocondensation occurs:



Further condensation with, e.g., other silanols, occurs with aging:



The heterocondensation reactions described by Eqs. (5.58) and (5.59) occur at a faster rate than the self-condensation reaction described by Eq. (5.57), so dissimilar constituents (i.e., molecular species of silicon and titanium rather than those of silicon alone) tend to become neighbors. Therefore, a gel with good chemical homogeneity can be expected. Furthermore, the product remains in solution be-

cause there are too few hydroxyl groups to cause precipitation. After the silicon and titanium have been incorporated into the polymeric network, further addition of water completes the hydrolysis and condensation reactions to produce a single-phase gel. Figure 5.33 summarizes the application of the method to the preparation of a five-component borosilicate glass (54).

5.6.2.3 Use of a Mixture of Alkoxides and Metal Salts

For some metals it is inconvenient to use alkoxides because they are not available, difficult to prepare or use, or too expensive. This is particularly the case with Group 1 and Group II elements whose alkoxides are solid, nonvolatile, and in many cases of low solubility. Metal salts are a viable alternative provided they are readily converted to the oxide by thermal or oxidative decomposition (55,56). The salt should preferably be soluble in alcohol so that it can be mixed with

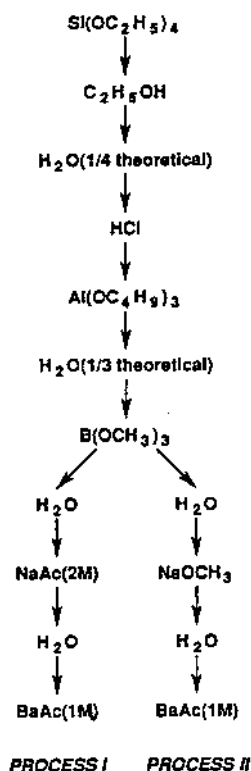


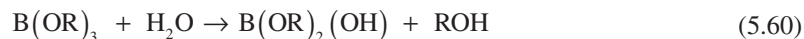
FIGURE 5.33 Synthesis of a five-component oxide by sequential additions of alkoxides (or salts) to partially hydrolyzed condensates. (From Ref. 54.)

alkoxide solutions without premature hydrolysis of the alkoxide. Salts of organic acids, in particular acetates, but also citrates, formates, and tartrates are potential candidates. Nitrates are possibly the only suitable inorganic salts because others, such as chlorides or sulfates, are more thermally stable and their anions are difficult to remove. However, nitrates are highly oxidizing, and care should be taken during heating of the gel to reduce the risk of explosions. A problem that is often encountered with this method is that the salt often crystallizes during the drying of the gel, leading to a loss of chemical homogeneity.

Little is known about the reaction mechanism by which the polymerizing alkoxide incorporates the ions of the metal salt into the gel structure. The normal method of preparation (54)–(57) is first to form a solution of all components that are to be added as alkoxides, as described in the previous method, and then add one or more salts as solutions in alcohol or, if this is not possible, in the water to be used for further hydrolysis (Fig. 5.33). All components are then uniformly dispersed and subsequent gelation should then incorporate the elements into a gel network.

5.6.2.4 Slow Addition of Small Amounts of Water

For most metal alkoxides, hydrolysis with excess water yields insoluble oxide or hydroxide precipitates that are useless for further polymerization reactions [Eqs. (5.21)–(5.23)]. However, if small amounts of water are added slowly to a sufficiently dilute solution, it is possible to form polymerizable molecular species from these alkoxides also. For example, when a dilute solution of boron alkoxide in alcohol is exposed to water, soluble transient molecular species such as $B(OR)_2(OH)$ and $B(OR)(OH)_2$, representing various degrees of hydrolysis, form initially, e.g.,



These species can undergo condensation reactions leading to the formation of a polymer network, as discussed earlier for the silanols.

For the SiO_2 - B_2O_3 system, Yoldas (15) investigated the effect of water additions on the homogeneity of a solution of TEOS and boron methoxide $[B(OCH_3)_3]$. His results are shown in Fig. 5.34. For a given solution, if the water content exceeds a certain value, solution homogeneity is lost due to precipitation. Boron methoxide hydrolyzes much faster than TEOS and precipitates as B_2O_3 . For lower water content, the partially hydrolyzed molecular species are soluble, so a clear solution is obtained. Condensation reactions between the partially hydrolyzed species lead to the production of a homogeneous gel. The line separating the clear solution from that containing precipitates can be represented by

$$M_{\text{water}} = A(M_{BE}) + B(M_{\text{TEOS}}) \quad (5.61)$$

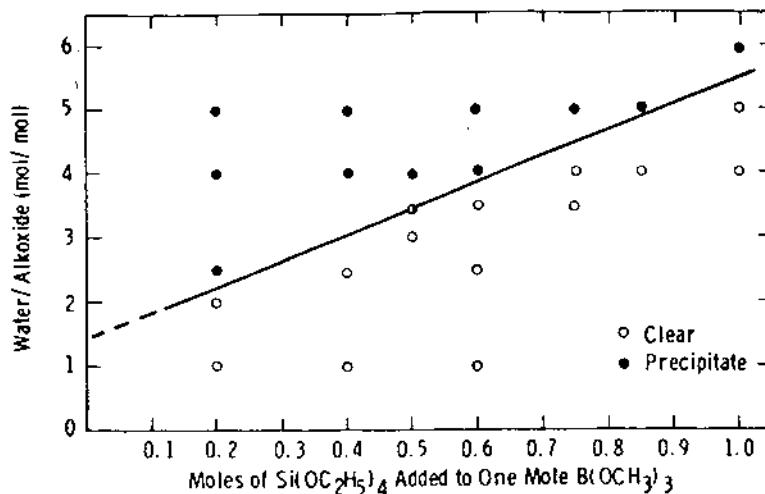


FIGURE 5.34 Regions of precipitate and clear solution formation for the hydrolysis of a solution containing various ratios of TEOS and boron methoxide. (From Ref. 15.)

where M_{water} , M_{BE} , and M_{TEOS} are the number of moles of water, boron ethoxide, and TEOS, respectively. For $M_{\text{BE}} = 1$, the results of Fig. 5.34 give $A \approx 1.5$ and $B \approx 4$. These values indicate that, to cause precipitation by the addition of water slowly, ~ 1.5 mol of water is required for 1 mol of boron ethoxide [in accordance with Eq. (5.23)] and an additional 4 mol of water is required for each mole of TEOS added to the system.

5.6.2.5 Matched Hydrolysis Rates

We noted earlier that for a given metal M, the hydrolysis rate of the alkoxide M(OR)_x depends on the length of the alkyl group R. This suggests that it may be possible to match the hydrolysis rates of the alkoxides of different metals by careful choice of the alkoxide group. As an example, consider the SiO_2 - TiO_2 system. Silicon alkoxides are among the slowest to hydrolyze, but of these, tetramethoxysilane (TMOS) has the fastest hydrolysis rate. By selecting a titanium alkoxide with a sufficiently long alkyl group, it may be possible to match its hydrolysis rates with that of TMOS. Yamane et al. (58) found that the hydrolysis of a mixed solution of TMOS and titanium *tert*-amyloxide $\{\text{Ti}[\text{OC}(\text{CH}_3)_2\text{C}_2\text{H}_5]_4\}$ produced a homogeneous gel.

In general, this method is rarely used because of the difficulties in matching the hydrolysis rates closely or in obtaining alkoxides with the desired hydrolysis rates. A more promising approach has been described by Livage et al. (59,60)

who showed that chelating agents such as acetylacetone can react with alkoxides at a molecular level, giving rise to new molecular precursors. The whole hydrolysis-condensation process can therefore be modified. For example, with the use of chelating agents, the hydrolysis of transition metal alkoxides can be slowed so that better chemical homogeneity can be achieved in multicomponent gels.

Comparison of the Preparation Methods

To compare the homogeneity of multicomponent gels prepared by different methods, Yamane et al. (58) produced gels by methods (2), (4) and (5) outlined above for a composition corresponding to 93.75 mol% SiO_2 and 6.25 mol% TiO_2 . Each gel was melted to form a glass and the optical transmission of the glass was used as a measure of the homogeneity of the gel. In this way, it was found that the homogeneity of the three glasses did not differ significantly. The homogeneity of the glasses was also compared with that of a glass produced by melting a mechanically mixed gel. To produce the mixed gel, SiO_2 and TiO_2 gels were prepared separately by hydrolysis of the individual alkoxides, after which they were mixed mechanically. The three gels prepared from mixtures of alkoxides gave glasses with a homogeneity that was far better than that for the glass produced from the mechanically mixed gel.

5.7 APPLICATIONS OF SOL-GEL PROCESSING

Applications of sol-gel processing are discussed in a book (61) and a review of the topic with an extensive listing of references to the technology is given in Ref. 1. The applications of sol-gel processing derive from the specialty shapes obtained directly from the gel state (e.g., films, fibers, monoliths and particles), coupled with compositional and microstructural control, and low temperature processing. Sol-gel processing also has its problems. Many alkoxides are expensive and most require special handling in a dry inert atmosphere (e.g., in a glove box.). Drying is often a limiting step for articles thicker than ~ 1 mm, and the shrinkage during drying and sintering are large. Some advantages and disadvantages of the process are summarized in Table 5.9.

Although potential applications of sol-gel processing are numerous, the actual number of successful applications is rather few. Thin films (and coatings) benefit from most of the advantages of sol-gel processing while avoiding the disadvantages. They represent one of the few successful commercial applications. However, even films suffer from cracking problems when attempts are made to prepare thick films ($> 1 \mu\text{m}$). Sol-gel processing allows fibers to be drawn from viscous sols and is used to prepare continuous, refractory fibers with high strength, stiffness and chemical durability for the reinforcing phase in composites. For the production of monolithic ceramics and glasses, it is unlikely that the process will be a successful alternative to conventional fabrication methods (glass melting or

TABLE 5.9 Polymeric Gel Route Compared with Conventional Fabrication Methods for Ceramics and Glasses

Advantages	Disadvantages
1. High purity.	1. Expensive raw materials.
2. High chemical homogeneity with multicomponent systems.	2. Large shrinkage during fabrication.
3. Low temperature of preparation.	3. Drying step leads to long fabrication times.
4. Preparation of ceramics and glasses with novel compositions.	4. Limited to the fabrication of small articles.
5. Ease of fabrication for special products such as films and fibers.	5. Special handling of raw materials usually required.

powder processing) unless novel compositions with unique properties are the result. Powder synthesis by the sol–gel route was discussed in Chapter 2.

5.7.1 Thin Films and Coatings

Prior to gelation, the sol or solution can be used for preparing thin films by common methods such as dipping, spinning, and spraying. We shall consider the techniques of (1) dip coating, where the object to be coated is lowered into the solution and withdrawn at a suitable speed, and (2) spin coating, where the solution is dropped onto the object, which is spinning at a high speed. In practice, dip coating is currently the more widely used.

One requirement is that the contact angle between the solution and the surface of the object be low so that the solution wets and spreads over the surface. Usually water is present in the sol, but moisture from the atmosphere is also sufficient to cause hydrolysis and condensation reactions. The final film is obtained after sintering. There are various advantages and disadvantages inherent in each coating technique. Dip coating does not require any specialized apparatus. Both internal and external surfaces wetted by the solution are coated. The solution must not be too sensitive to moisture because it commonly undergoes some exposure to the atmosphere during the coating process. Spin coating leads to coating of one side of the object only, and the coating solution can be kept away from moisture prior to being dropped onto the object. Edge effects may occur for objects that are not axisymmetric. Because the spinning of large objects is impractical, the objects to be coated are commonly in the shape of small, flat disks.

5.7.1.1 Dip Coating

The physics of dip coating has been reviewed by Scriven (62) who divided the batch dip coating process into five stages: immersion, start up, deposition, drain-

age, and evaporation (Fig. 5.35). With volatile solvents such as alcohols, evaporation normally accompanies start-up, deposition, and drainage. The continuous dip coating process (Fig. 5.35f) is simpler because it separates immersion from the other stages, essentially eliminates start-up, hides drainage in the deposited film, and restricts evaporation to the deposition stage and afterward.

The thickness of the film in the deposition region (position 3 in Fig. 5.35f) is controlled by a competition between as many as 6 forces:

1. Viscous drag upward on the liquid by the moving substrate
2. Force of gravity
3. Resultant force of surface tension in the concavely curved meniscus,
4. Inertial force of the boundary layer liquid arriving at the deposition region
5. Surface tension gradient
6. Disjoining or conjoining pressure, important for films less than $1\ \mu\text{m}$ thick.

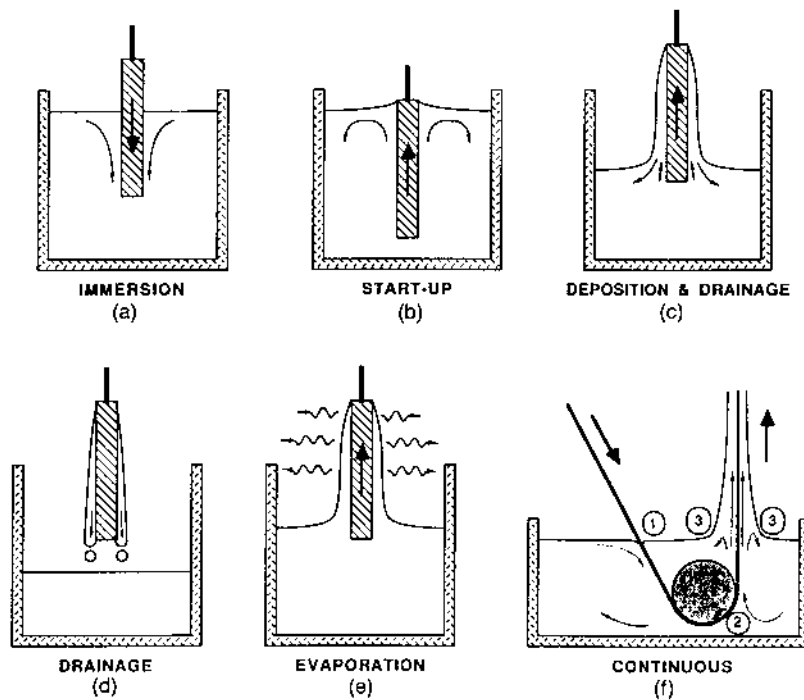


FIGURE 5.35 Stages of the dip coating process: (a)–(e) batch; (f) continuous. (From Ref. 62.)

When the liquid viscosity η and substrate speed U are high enough to hold the meniscus curvature down, then the deposited film thickness h is governed by a balance between the viscous drag (proportional to $\eta U/h$) and gravity force (proportional to ρgh , where ρ is the density of the liquid and g is the acceleration due to gravity). Thus

$$h = c_1 \left(\frac{\eta U}{\rho g} \right)^{1/2} \quad (5.62)$$

where the constant of proportionality c_1 is ~ 0.8 for Newtonian liquids (63). When the liquid viscosity and substrate speed are not high enough, as in sol–gel processing, this balance of forces is modulated by the ratio of viscous drag to the liquid–vapor surface tension γ_{LV} , according to the following relationship derived by Landau and Levich (64):

$$h = 0.944 \left(\frac{\eta U}{\gamma_{LV}} \right)^{1/6} \left(\frac{\eta U}{\rho g} \right)^{1/2} \quad (5.63)$$

Rearranging the terms in Eq. (5.63) gives

$$h = 0.944 \frac{(\eta U)^{2/3}}{\gamma_{LV}^{1/6} (\rho g)^{1/2}} \quad (5.64)$$

so the thickness of the film is predicted to vary as $(\eta U)^{2/3}$.

The applicability of Eqs. (5.62)–(5.64) to film deposition in sol–gel processing has been tested in only a few studies. Strawbridge and James (65) investigated the relationship between film thickness and viscosity for an acid-catalyzed TEOS solution (H_2O : TEOS ratio = 1.74) deposited on glass substrates at substrate withdrawal speeds U in the range of 5–15 cm/min. Significant deviations from a modified form of Eq. (5.62) were observed as the speed is increased. For silica sols in which the precursor structures varied from weakly branched polymers to highly condensed particles, the results of Brinker and Ashley reported in Ref. 1 indicate that for polymeric sols, h varies approximately as $U^{2/3}$, in accordance with Eqs. (5.63) and (5.64) and with previous results of Dislich and Hussmann (66).

5.7.1.2 Spin Coating

As illustrated in Fig. 5.36, spin coating can be divided into four stages: deposition, spin-up, spin-off, and evaporation (62,67). As in dip coating, evaporation may occur throughout the process. Initially, an excess of liquid is deposited on the surface, which is at rest or rotating slowly. In the spin-up stage, liquid flows

radially outward, driven by the centrifugal force generated by the rotating substrate. In the spin-off stage, excess liquid flows to the perimeter of the substrate, leaving as droplets. As the film gets thinner, the rate of removal of excess liquid by spin-off becomes slower because of the greater resistance to flow and the greater effect of evaporation in raising the viscosity by concentrating the nonvolatile component of the solution. In the fourth stage, evaporation becomes the primary mechanism of thinning.

The key stage in spin coating is spin-off. Apart from edge effects, a film of liquid tends to become uniform in thickness as it gets thinner and, once uniform, tends to remain so with further thinning, provided the viscosity is insensitive to shear and does not vary over the substrate. The reason for the strong tendency towards uniformity is the way the two main forces balance, i.e., the rotation-induced centrifugal force, which drives radially outward flow, and the resisting viscous force, which acts radially inward.

The thickness of an initially uniform film during spin-off is given by (62)

$$h(t) = \frac{h_0}{(1 + 4\rho\omega^2 h_0^2 t / 3\eta)^{1/2}} \quad (5.65)$$

where h_0 is the initial thickness, t is the time, ρ is the density of the liquid, and ω is the angular velocity. In the theory, both ω and ρ are assumed to be constant. Even films that are initially nonuniform tend strongly towards uniformity following Eq. (5.65).

The spinning substrate creates a steady forced convection in the vapor above the substrate such that the mass transfer coefficient κ is uniform. The evaporation

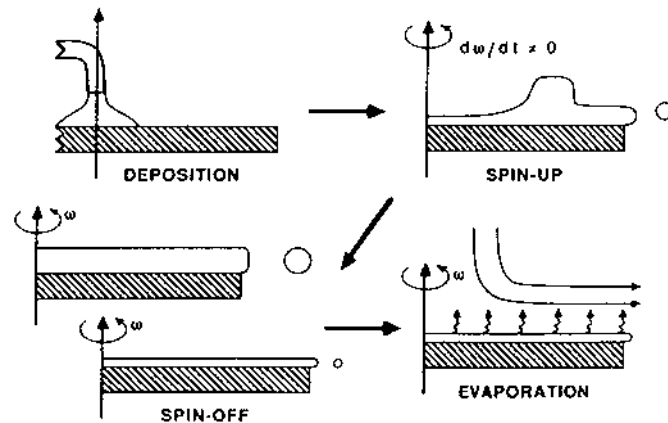


FIGURE 5.36 Stages of the spin coating process. (From Ref. 62.)

rate all over the substrate is therefore quite uniform also. Assuming a crude model in which evaporation occurs only after the rate of thinning by flow falls to a certain rate $e\rho_A/\rho_A^0$, where ρ_A is the mass of volatile solvent per unit volume, ρ_A^0 is the initial value, and e is the evaporation rate that depends on the gas-phase mass transfer coefficient, Meyerhofer (68) found that the final thickness and the total elapsed time to achieve this thickness are

$$h_{final} = \left(1 - \frac{\rho_A^o}{\rho_A}\right) \left(\frac{3\eta e}{2\rho_A^o \omega^2}\right)^{1/3} \quad (5.66)$$

$$t_{final} = t_{spin-off} + h_{spin-off} \left(\frac{\rho_A^o}{e\rho_A}\right) \quad (5.67)$$

According to Eq. (5.66), the final thickness of the film varies inversely as $\omega^{2/3}$ and as $\eta^{1/3}$.

5.7.1.3 Structural Evolution in Films

The physics and chemistry governing polymer growth and gelation in films are essentially the same as those discussed earlier for bulk gels but certain factors distinguish the structural evolution in films (1). The overlap between the deposition and evaporation stages establishes a competition between evaporation (which compacts the structure) and condensation reactions (which stiffen the structure, thereby increasing the resistance to compaction). We recall that the gelation, and drying stages are normally separated in bulk systems. The aggregation, gelation, and drying in films deposited by dipping or spinning occur in seconds to minutes compared with days or weeks for bulk gels. Films therefore undergo considerably less aging so the result is a more compact dried structure. Fluid flow by draining, evaporation, or spin-off coupled with the attachment of the precursors to the substrate impose a shear stress within the film during deposition. After gelation, drying and further condensation lead to *tensile* stresses in the film. Bulk gels are generally not constrained in any dimension.

Current and potential applications of films prepared by sol–gel processing are numerous (1,61) and they are expected to grow in the future. Table 5.10 summarizes some possible applications of films and coatings prepared from metal alkoxide solutions (69).

5.7.2 Fibers

Fibers can be produced by two sol–gel routes. In one route, a dense monolithic perform is produced by sol–gel processing, drying, and sintering, followed by

TABLE 5.10 Applications of Films Prepared from Metal Alkoxide Solutions

Application	Example	Composition
Mechanical	Protection	SiO ₂
Chemical	Protection	SiO ₂
Optical	Absorbing	TiO ₂ -SiO ₂ ; SiO ₂ -R _m O _n oxides of Fe, Cr and Co
	Reflecting	In ₂ O ₃ -SnO ₂
	Anti-reflecting	Na ₂ O-B ₂ O ₃ -SiO ₂
Electrical	Ferroelectric	BaTiO ₃ ; KTaO ₃ ; PLZT
	Electronic conductor	In ₂ O ₃ -SnO ₂ ; SnO ₂ -CdO
	Ionic conductor	β-alumina
Catalytic	Photocatalyst	TiO ₂
	Catalyst carrier	SiO ₂ ; TiO ₂ ; Al ₂ O ₃

Source: Ref. 69.

conventional fiber drawing above the glass softening temperature. The preparation of monolithic SiO₂ gels from fine particles made by flame oxidation is described by Rabinovitch et al. (2,3) and by Scherer and Luong (4). Compared to fibers drawn from the melt, the monolithic gel route does not require a melting step, thereby avoiding the introduction of impurities from the crucible. However, the route suffers from long processing times and the fiber quality for optical applications is inferior to that prepared from CVD performs. Therefore the monolithic gel route does not appear to have any technological or commercial advantage over current CVD processes.

The other sol-gel route is to draw the fibers directly from a viscous sol near room temperature and then convert them into dense glass or ceramic fibers by sintering. The advantage of this route is that very refractory and chemically durable fibers can be produced at relatively low temperatures which would be difficult to prepare by conventional drawing from a melt. The preparation of SiO₂ fibers from TEOS precursors is reviewed by Sakka (70). The solution conditions for fiber formation (spinnability) are acid catalysis and low water content, which means that the polymeric species in the solution are more weakly branched polymers. Under these conditions, the drawn fibers are microporous and contain a significant amount of residual organics that are difficult to remove completely prior to sintering. Many compositions also produce fibers with nonuniform cross sections. The influence of the starting composition on spinnability and fiber cross section are summarized in Fig. 5.37. The fibers produced by this sol-gel route are not suitable for optical applications but have current or potential applications

as the reinforcing phase in composites and as refractory textiles. In addition to SiO_2 , examples of high strength, refractory fibers produced commercially by the sol-gel route include compositions in the $\text{SiO}_2\text{-Al}_2\text{O}_3$, $\text{SiO}_2\text{-ZrO}_2$, and $\text{SiO}_2\text{-B}_2\text{O}_3\text{-Al}_2\text{O}_3$ systems (1,70).

5.7.3 Monoliths

Monoliths are defined as bulk gels (smallest dimension ≥ 1 mm) cast into shape and processed without cracking. The ability to form complex shapes by casting the gel coupled with relatively low temperature sintering are attractive features of the route, but cracking during drying and the significant shrinkage during sintering can present significant challenges in achieving the final shape. The good applications of monolithic gels take advantage of the process advantages, such as purity, chemical homogeneity, porosity, low temperature fabrication, and the ability to produce novel chemical compositions. The main applications are optical components, graded refractive index (GRIN) glasses, and transparent aerogels used as Cherenkov detectors and as insulation (1).

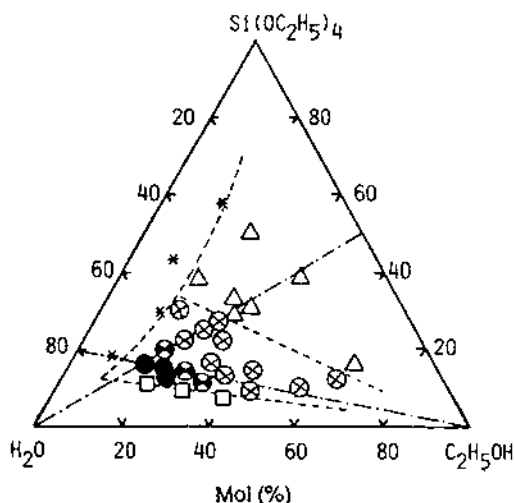


FIGURE 5.37 Relation between fiber drawing behavior and composition of TEOS-water-ethanol solutions after hydrolysis at 80°C with an acid concentration of 0.01 mol HCl per mole of TEOS: (*) immiscible, (\square) not spinnable, (Δ) no gel formation, (\bullet) circular cross section, (\otimes) noncircular cross section, (\odot) circular and noncircular cross section. (From Ref. 69.)

5.7.4 Porous Materials

Sol-gel processing is an attractive route for the production of porous ceramics and glasses because the characteristic properties of gels such as high surface area, high porosity, and small pore size are not easily attainable by more conventional methods. In addition to the transparent aerogel applications mentioned above, these unique properties are exploited in a variety of applications, which include filtration, separation, catalysis, and chromatography (1,61,71).

5.8 CONCLUDING REMARKS

In this chapter, we have examined the physics and chemistry of sol-gel processing and the ways in which these relate to the practical fabrication of ceramics and glasses. It is apparent that sol-gel processing offers considerable opportunities in both science and technology. An understanding of the scientific issues provides the most useful basis for successful application of the method. While sol-gel processing offers considerable advantages as a fabrication method, its disadvantages are also very real. Potential applications of sol-gel processing are numerous, but the successful applications (e.g., films, fibers, porous membranes) benefit from most of advantages of the process while avoiding the disadvantages. Although the successful applications are expected to grow substantially, the method cannot compete with the more conventional fabrication methods for the mass production of monolithic ceramics and glasses.

PROBLEMS

- 5.1 Summarize the polymerization and growth mechanisms of aqueous silicates in the pH range of (a) <2 , (b) $2-7$, and (c) >7 .
- 5.2 Summarize the structural evolution of sol-gel silicates in the pH range of (a) <2 , (b) $2-7$, and (c) >7 .
- 5.3 Estimate the surface free energy of 1 g of a silica gel that is 50% porous with pores (assumed spherical) of 5 nm in diameter. Compare your answer with the surface free energy of 1 g of silica glass spheres with a diameter of 10 μm . The specific surface energy of both materials can be assumed to be 0.25 J/m^2 .
- 5.4 You wish to prepare approximately 50 g of SiO_2 by the sol-gel process under the following conditions: You start with a solution of 50 mol% TEOS in ethanol and you add 10 mol of H_2O per mole of alkoxide. Determine the volume of each starting material required for the process, assuming that the reaction goes to completion.
- 5.5 A silica gel prepared from an alkoxide has a surface area $S \approx 500 \text{ m}^2/\text{g}$, a porosity $P \approx 0.9$, and a density $\rho \approx 1.5 \text{ g/cm}^3$. Estimate the permeability K of the gel.

- 5.6 Compare the estimated value of K with the value determined from the data in Fig. 5.21.
- 5.7 An alcogel contains 5 vol% of solid. Careful drying leads to the production of a xerogel that is approximately 50% porous. Estimate the linear shrinkage during drying. On sintering, a fully dense solid is obtained but there is a weight loss of 20%. Estimate the linear shrinkage during sintering.
- 5.8 In another experiment, the alcogel in Problem 5.7 is dried supercritically with negligible shrinkage. Sintering in this case also produces a fully dense solid with a 20% weight loss. Estimate the linear shrinkage during sintering.
- 5.9 Explain the meaning of the term *drying control chemical additive* (DCCA). Briefly describe the role of DCCAs in drying. What drawbacks do you see with the use of DCCAs?
- 5.10 Compare the drying and sintering characteristics of SiO_2 gels prepared by the following two methods:
 - a. Particulate gel route by gelling of fumed SiO_2 particles
 - b. Polymeric gel route by hydrolysis of silicon ethoxide.
- 5.11 Describe three methods for the preparation of BaTiO_3 by the sol–gel process and comment on the chemical homogeneity of the gel produced by each method.
- 5.12 In a dip-coating experiment, a student uses a solution of TEOS in ethanol with a viscosity $\eta = 2 \text{ mPa}\cdot\text{s}$ and a density $\rho = 1.0 \text{ g/cm}^3$, a withdrawal speed $U = 10 \text{ cm/min}$. Assuming a surface tension of the solution $\gamma_{lv} = 0.04 \text{ J/m}^2$, use Eq. (5.64) to estimate the thickness of the liquid film deposited on the substrate.
- 5.13 If the film is dried and sintered to full density ($\rho_f = 2.2 \text{ g/cm}^3$), determine the thickness of the final film. If required, the density of the solvent $\rho_s = 0.8 \text{ g/cm}^3$.
- 5.14 Compare the key steps in the production of 1- μm -thick TiO_2 films on an Al_2O_3 substrate by the following two methods:
 - a. Spin coating of a solution of titanium alkoxide
 - b. Spin coating of a suspension of flame-synthesized TiO_2 particles.

REFERENCES

1. Brinker, C. J.; Scherer, G. W. *Sol–Gel Science*; Academic Press: New York, 1990.
2. Rabinovich, E. M.; Johnson, D. W.; MacChesney, J. B.; Vogel, E. M. J. *Non-Cryst. Solids*. 1982, Vol. 47, 435.
3. Rabinovich, E. M.; MacChesney, J. B.; Johnson, D. W.; Stimpson, J. R.; Meagher, B. W.; Dimarcelto, F. V.; Wood, D. L.; Sigety, E. A. J. *Non-Cryst. Solids*. 1984, Vol. 63, 155.
4. Scherer, G. W.; Luong, J. C. J. *Non-Cryst. Solids*. 1984, Vol. 63, 163.
5. Segal, D. *Chemical Synthesis of Advanced Ceramic Materials*; Cambridge University Press: Cambridge, 1989, Chap. 4.
6. Cairns, J. A.; Segal, D. L.; Woodhead, J. L. *Mater. Res. Soc. Symp. Proc.* 1984, Vol. 32, 135.

7. Ramsay, J. D. F. In *Chromatography of Synthetic and Biological Polymers*, Vol. 1; Epton, R. ed.; Ellis Horwood: Chichester, UK, pp. 339–343.
8. Meakin, P. *Ann. Rev. Phys. Chem.* 1988, Vol. 39, 237.
9. Brinker, C. J.; Scherer, G. W. J. *Non-Cryst. Solids*. 1985, Vol. 70, 301.
10. Iler, R. K. *The Chemistry of Silica*; Wiley: New York, 1979.
11. Baes, C. F.; Messmer, R. E. *The Hydrolysis of Cations*; Wiley: New York, 1976.
12. Bradley, D. C.; Mehrotra, R. C.; Gaur, D. P. *Metal Alkoxides*; Academic Press: London, 1978.
13. Okamura, H.; Bowen, H. K. *Ceramics International*. 1986, Vol. 12, 161.
14. Mah, T.-I.; Hermes, E. E.; Masdiyasi, K. S. In *Chemical Processing of Ceramics*; Lee, B. I., Pope, E. J. A. eds.; Marcel Dekker: New York, 1994, Chap. 4.
15. Yoldas, B. E. *J. Mater. Sci.* 1979, Vol. 14, 1843.
16. Cogan, H. D.; Setterstrom, C. A. *Chem. and Eng. News*. 1946, Vol. 24, 2499.
17. Mandelbrot, B. B. *The Fractal Geometry of Nature*; W. H. Freeman: New York, 1983.
18. Feder, J. *Fractals*; Plenum Press: New York, 1988.
19. Schaefer, D. W. *MRS Bulletin*. 1988, Vol. 8, 22.
20. Martin, J. E. In *Proceedings of Atomic and Molecular Processing of Electronic and Ceramic Materials: Preparation, Characterization, Properties*; Aksay, I. A., McVay, G. L., Stoebe, T. G., Wager, J. F. eds.; Materials Research Society: Pittsburgh, PA, 1987, pp. 79–89.
21. Flory, P. J. *J. Am. Chem. Soc.* 1941, Vol. 63, 3083; *J. Phys. Chem.* 1942, Vol. 46, 132.
22. Stockmayer, W. H. *J. Chem. Phys.* 1943, Vol. 11, 45.
23. Zarzycki, J. In *Science of Ceramic Chemical Processing*; Hench, L. L., Ulrich, D. R. eds.; Wiley: New York, 1986, pp. 21–36.
24. Meakin, P. In *On Growth and Form*; Stanley, H. E., Ostrowsky, N. eds.; Martinus-Nijhoff: Boston, 1986, pp. 11–135.
25. Witten, T. M.; Sander, L. M. *Phys. Rev. Lett.* 1981, Vol. 47, 1400.
26. Keefer, K. D. In *Better Ceramics Through Chemistry II*; Brinker, C. J., Clarke, D. E., Ulrich, D. R. eds.; Materials Research Society: Pittsburgh, PA, 1986, pp. 295–304.
27. Meakin, P. *Phys. Rev. Lett.* 1983, Vol. 51, 1119.
28. Sakkam, S.; Kamiya, Y. J. *Non-Cryst. Solids*. 1982, Vol. 48, 31.
29. Sakka, S. In *Better Ceramics Through Chemistry*; Brinker, C. J., Clarke, D. E., Ulrich, D. R. eds.; Materials Research Society: Pittsburgh, PA, 1984, pp. 91–99.
30. Sakka, S.; Kamiya, K.; Makita, K.; Yamamoto, Y. J. *Non-Cryst. Solids*. 1984, Vol. 63, 223.
31. Huggins, M. L. *J. Am. Chem. Soc.* 1942, Vol. 64, 2716.
32. Tsuchida, H. *Science of Polymers*; Baikukan Publishing: Tokyo, 1975.
33. Zallen, R. *The Physics of Amorphous Solids*; Wiley: New York, 1983.
34. Stauffer, D.; Coniglio, A.; Adam, M. *Advances in Polymer Science*. 1982, Vol. 44, 103.
35. Partlow, D. P.; Yoldas, B. E. *J. Non-Cryst. Solids*. 1981, Vol. 46, 153.
36. Scherer, G. W. J. *Non-Cryst. Solids*. 1989, Vol. 109, 171; *J. Am. Ceram. Soc.* 1990, Vol. 73, 3.
37. Dwivedi, R. K. *J. Mater. Sci. Lett.* 1986, Vol. 5, 373.

38. Scherer, G. W. In *Drying '92*; Mujumdar, A. S. ed.; Elsevier: New York, 1992, pp. 92–113.
39. Zarzycki, J.; Prassas, M.; Phalippou, J. J. *Mater. Sci.* 1982, Vol. 17, 3371.
40. Brinker, C. J.; Scherer, G. W. *J. Non-Cryst. Solids*. 1985, Vol. 70, 301.
41. Brinker, C. J.; Scherer, G. W.; Roth, E. P. *J. Non-Cryst. Solids*. 1984, Vol. 70, 345.
42. Scherer, G. W.; Brinker, C. J.; Roth, E. P. *J. Non-Cryst. Solids*. 1985, Vol. 72, 369.
43. Brinker, C. J.; Roth, E. P.; Tallant, D. R.; Scherer, G. W. In *Science of Ceramic Chemical Processing*; Hench, L. L., Ulrich, D. R. eds.; Wiley: New York, 1986, Chap. 3.
44. James, P. F. *J. Non-Cryst. Solids*. 1988, Vol. 100, 93.
45. Yoldas, B. E. *Am. Ceram. Soc. Bulletin*. 1975, Vol. 54, 286, 289; *J. Mater. Sci.* 1975, Vol. 10, 1856; *J. Appl. Chem. Biotechnol.* 1973, Vol. 23, 803.
46. Komarneni, S.; Suwa, Y.; Roy, R. J. *Am. Ceram. Soc.* 1986, Vol. 69, C-155.
47. Ishmail, M. G. M. U.; Nakai, Z.; Minegishi, K.; Somiya, S. *Int. J. High Technol. Ceram.* 1986, Vol. 3, 123.
48. Riman, R. E. Ph.D. Thesis, Massachusetts Institute of Technology; Cambridge: MA, 1987.
49. Jones, K.; Davies, T. J.; Emblem, H. G.; Parkes, P. In *Better Ceramics Through Chemistry III*; Brinker, C. J., Clarke, D. E., Ulrich, D. R.; Materials Research Society: Pittsburg, PA, 1988, pp. 111–116.
50. Dislich, H. *Angewandte Chemie International Edition*. 1971, Vol. 10, 363.
51. Bratton, R. J. *Am. Ceram. Soc. Bulletin*. 1969, Vol. 48, 759.
52. Thomas, I. M. U. S. Patent No. 3,791,808, February 12, 1974.
53. Yoldas, B. E. *J. Mater. Sci.* 1977, Vol. 12, 1203.
54. Brinker, C. J.; Mukherjee, S. P. *J. Mater. Sci.* 1981, Vol. 16, 1980.
55. Roy, R. J. *Am. Ceram. Soc.* 1969, Vol. 52, 344.
56. Levene, L.; Thomas, I. M. U. S. Patent No. 3,640,093, February 8, 1972.
57. Phalippou, J.; Prassa, M.; Zarzycki, J. J. *Non-Cryst. Solids*. 1982, Vol. 48, 17.
58. Yamane, M.; Inoue, S.; Keiichi, N. *J. Non-Cryst. Solids*. 1982, Vol. 48, 153.
59. Livage, J.; Henry, M.; Sanchez, C. *Progress in Solid State Chemistry*. 1988, Vol. 18, 259.
60. Sanchez, C.; Livage, J.; Henry, M.; Babonneau, F. *J. Non-Cryst. Solids*. 1988, Vol. 100, 65.
61. *Sol–Gel Technology for Thin Films, Fibers, Preforms, Electronics and Specialty Shapes*; Klein, L. C. ed.; Noyes Publications: Park Ridge, NJ, 1988.
62. Scriven, L. E. In *Better Ceramics Through Chemistry III*; C. J., Brinker, D. E., Ulrich, D. R. eds.; Materials Research Society: Pittsburg, PA, 1988, pp. 717–729.
63. Spiers, R. P.; Subbaraman, C. V.; Wilkinson, W. L. *Chem. Eng. Sci.* 1974, Vol. 29, 389.
64. Landau, L. D.; Levich, B. G. *Acta Physicochim. U.R.S.S.* 1942, Vol. 17, 42.
65. Strawbridge, I.; James, P. F. *J. Non-Cryst Solids*. 1986, Vol. 86, 381.
66. Dislich, H.; Hussmann, E. *Thin Solid Films*. 1981, Vol. 98, 129.
67. Bornside, D. E.; Macosko, C. W.; Scriven, L. E. *J. Imaging Tech.* 1987, Vol. 13, 122.
68. Meyerhofer, D. J. *Appl. Phys.* 1978, Vol. 49, 3993.
69. Sakka, S. *Am. Ceram. Soc. Bulletin*. 1985, Vol. 64, 1463.

70. Sakka, S. In Sol-Gel Technology for Thin Films, Fibers, Preforms, Electronics and Specialty Shapes; Klein, L. C. ed.; Noyes Publications: Park Ridge, NJ, 1988, pp. 140-161.
71. Ceramic Trans. Vol. 31. Porous Materials; Ishizaki, K., Sheppard, L., Okada, S., Hamasaki, T., Huybrechts, B. eds; The American Ceramic Society: Westerville, OH, 1993.

6

Powder Consolidation and Forming of Ceramics

6.1 INTRODUCTION

The common methods for the consolidation of ceramic powders are described in this chapter. We recall that the microstructure of the green body has a significant effect on the subsequent firing stage. If severe variations in packing density occur in the green body, the fired body will, in general, contain heterogeneities that will limit the engineering properties. The *homogeneous packing* of particles in the green body is the desired goal of the consolidation step. Since the packing density controls the amount of shrinkage during firing, the achievement of high *packing density* is also desirable. Geometrical particle packing concepts provide a useful basis for understanding how the structure of the consolidated powder comes about. An important practical consideration is the extent to which the parameters of the consolidation process can be manipulated to control the packing uniformity and packing density of the green body.

The colloidal techniques described in Chapter 4 provide considerable benefits for the control of the packing uniformity of the green body. The production of green bodies with uniform microstructure from a fully stabilized colloidal suspension of spherical, fine, monodisperse particles has not been incorporated into industrial applications where mass production is desired and fabrication cost is a serious consideration. Colloidal techniques, however, play an important role in the low-cost forming methods of *slip casting* and *tape casting*, as well as in the less commonly used methods of *electrophoretic deposition* and *gel casting*.

Mechanical compaction of dry or semidry powders in a die is one of the most widely used forming operations in the ceramic industry. In general the applied pressure is not transmitted uniformly because of friction between the

particles and the die walls as well as between the particles themselves. The stress variations lead to density variations in the green body, thereby placing considerable limits on the degree of packing uniformity that can be achieved. Although the density variations can be reduced significantly by *isostatic pressing*, mechanical compaction provides far less control in the manipulation of the green body microstructure than the casting methods.

Plastic forming methods in which a mixture of the ceramic powder and additives is deformed plastically through a nozzle or in a die provide a convenient route for the mass production of ceramic green bodies. *Extrusion* is used extensively in the traditional ceramics industry and to a lesser extent in the advanced ceramics sector. *Injection molding* has been the subject of intense investigation in recent years, but it has not yet made any significant inroads in the forming of ceramics for industrial applications.

The common forming methods are summarized in Table 6.1. The specific method to be used will depend in each case on the shape and size of the green body as well as the cost of fabrication. More recently, considerable interest has been devoted to a group of forming methods referred to as *solid free-form fabrication* which allow the formation of objects by computer-assisted techniques.

Additives (commonly polymeric in nature) play an important role in the production of the green body. In many cases, the selection of the additives can be vital to the success of the forming process. The additives must however be

TABLE 6.1 Feed Materials and Shapes of the Green Body for the Common Ceramic Forming Methods

Forming method	Feed material	Shape of green body
Dry or semidry pressing		
Die compaction	Powder or free-flowing granules	Small simple shapes
Isostatic pressing	Powder or fragile granules	Larger, more intricate shapes
Casting of a slurry		
Slip casting	Free-flowing slurry with low binder content	Thin intricate shapes
Tape casting	Free-flowing slurry with high binder content	Thin sheets
Deformation of a plastic mass		
Extrusion	Moist mixture of powder and binder solution	Elongated shapes with uniform cross section
Injection molding	Granulated mixture of powder and solid binder	Small intricate shapes

removed from the green body prior to firing. For consolidation techniques such as tape casting and injection molding where a considerable amount of additives are used, binder removal can be one of the limiting steps in the overall fabrication process.

6.2 PACKING OF PARTICLES

The packing of particles is treated in texts by German (1) and Cumberland and Crawford (2). Particle packing is commonly divided into two types: (1) *regular* (or ordered) packing and (2) *random* packing. The commonly used ceramic forming methods produce random packing arrangements, but regular packing is typically the first structure encountered in models, partly because of their similarity to crystalline atomic structure. Several parameters can be used to characterize the packing arrangement, but two of the most widely used are

1. *Packing density* (also referred to as the packing fraction or the fractional solids content), defined as

$$\text{Packing density} = \frac{\text{volume of solids}}{\text{total volume of the arrangement (solids + voids)}} \quad (6.1)$$

2. *Coordination number*, which is the number of particles in contact with any given particle.

The packing density is an easily measured parameter that provides much insight about the behavior of a powder.

6.2.1 Regular Packing of Monosize Spheres

The reader would be familiar with the packing of atoms in crystalline solids to produce regular, repeating, three-dimensional patterns such as the simple cubic, body-centered cubic, face-centered cubic, and hexagonal close-packed structures. The packing density and coordination number of these crystal structures for a pure metal are listed in Table 6.2.

TABLE 6.2 Packing Density and Coordination Number of Some Common Crystal Structures for a Pure Metal

Crystal structure	Packing density	Coordination number
Simple cubic	0.524	6
Body-centered cubic	0.680	8
Face-centered cubic	0.740	12
Hexagonal close-packed	0.740	12

In order to build up a three-dimensional packing pattern of particles we can begin conceptually by (1) packing spheres in two dimensions to form layers and then (2) stacking the layers on top of one another. Two types of layers are shown in Fig. 6.1, where the angle of intersection between the rows has limiting values of 90° (referred to a square layer) and 60° (simple rhombic or triangular layer). Although other types of layers that have angles of intersection between these two values are possible, only the square layer and the simple rhombic layer will be considered here. There are three geometrically simple ways of stacking each type of layer on top of one another, giving rise to six packing arrangements altogether. However, examination of the arrangements will show that, neglecting the difference in orientation in space, two of the ways of stacking the square layers are identical to two of the ways of stacking the simple rhombic layers (2). Therefore there are only four different regular packing arrangements shown in Fig. 6.2. The packing densities and coordination numbers of these arrangements are summarized in Table 6.3.

The rhombohedral packing arrangement, which has the highest packing density, is the most stable packing arrangement. Even for monosized spherical powders, such dense packing arrangements have been achieved over only very small regions (called *domains*) of the green body when rather special consolidation procedures have been used. An example is the slow sedimentation of monosize SiO_2 particles from a stable suspension shown earlier in Fig. 4.34. The domains are separated from one another by boundaries of disorder much like the granular microstructure of polycrystalline materials. Figure 6.3 shows one problem that can arise when the green body is fired: cracklike voids open at the domain boundaries (3). The commonly used ceramic forming methods produce more random packing arrangements in the green body.

6.2.2 Random Packing of Particles

Two different states of random packing have been distinguished. If the particles are poured into a container that is then vibrated to settle the particles, the resulting

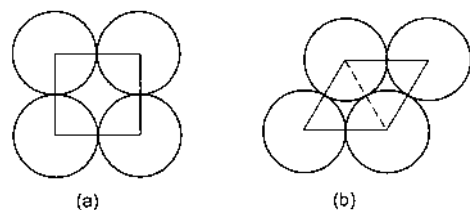


FIGURE 6.1 Two types of layers for the regular packing of monosize spheres: (a) square and (b) rhombic or triangular.

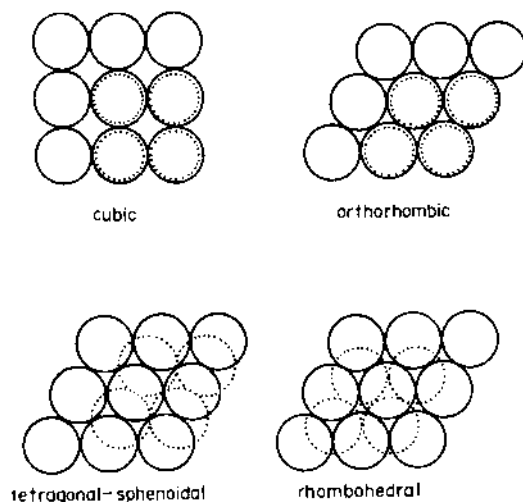


FIGURE 6.2 The four packing arrangements produced by stacking square and triangular layers of monosize spheres.

TABLE 6.3 Packing Density and Coordination Number for Regular Packing of Monosize Spheres

Packing arrangement	Packing density	Coordination number
Cubic	0.524	6
Orthorhombic	0.605	8
Tetragonal-sphenoidal	0.698	10
Rhombohedral	0.740	12

packing arrangement reaches a state of highest packing density (or minimum porosity) referred to as *dense random packing*. On the other hand, if the particles are simply poured into the container so that they are not allowed to rearrange and settle into as favorable a position as possible, the resulting packing arrangement is referred to as *loose random packing*. An infinite number of packing arrangements may exist between these two limits. The packing densities of a powder after pouring and after being vibrated are commonly referred to as the *poured density* and the *tap density*, respectively.

6.2.2.1 Monosize Particles

Dense random packing of *monosized spheres* has been studied experimentally by shaking hard spheres in a container. The upper limit of the packing density

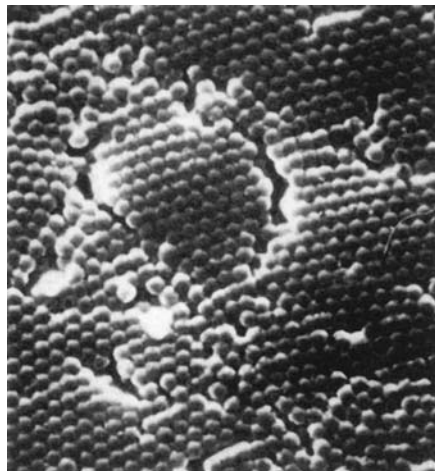


FIGURE 6.3 Partial densification of a periodically packed, multilayered arrangement of polymer spheres. Note the opening displacements at the domain boundaries. (From Ref. 3.)

consistently ranges from 0.635 to 0.640 (4). Computer simulations give a value of 0.637 (5). The maximum packing density for random packing of monosize spheres is predicted to be independent of the sphere size, and this prediction has been verified experimentally. For loose random packing of monosize spheres, theoretical simulations as well as experiments give values in the range 0.57–0.61 for the packing density.

In the case of dense random packing of monosize spheres, calculations show that fluctuations in the packing density become weak beyond a distance of three sphere diameters from the center of any given sphere. For density fluctuations existing over such a small scale, uniform densification may be achieved during sintering of the green body. Therefore, the production of regular, crystal-like particle packing, achievable at present only over very small domains, may after all be unnecessary from the point of view of fabrication.

Powders used in the industrial production of ceramics very rarely have spherical particles. The surfaces of the particles are also rarely smooth. Particles with rough surface textures or shapes suffer from agglomeration because of increased interparticle friction, and the packing density decreases as the particle shape departs from that of a sphere. Figure 6.4 shows the packing density for various irregular particle shapes. Spherical particles are normally desirable when a high packing density is required. However, the use of nonspherical particles does not always lead to a reduction in the packing density if the particles have

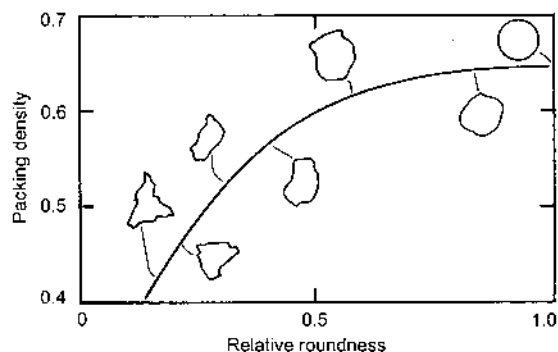


FIGURE 6.4 Packing density versus relative roundness for randomly packed monosized particles. (From Ref. 1.)

a regular geometry. The highest packing density and most isotropic structures are obtained with spheres and with particles having simple, equiaxial shapes (e.g., cubes). Anisotropic particles can be packed to high packing density if they are ordered, but in random packing, the packing density can be quite low. Table 6.4 shows a comparison of the dense random packing density for various particle shapes.

6.2.2.2 Bimodal Mixtures of Spheres

The packing density of an arrangement of spheres in dense random packing can be increased by filling the interstitial holes with spheres that are smaller than

TABLE 6.4 Dense Random Packing Density for Various Particle Shapes

Particle shape	Aspect ratio	Packing density
Sphere	1	0.64
Cube	1	0.75
Rectangle	2:5:10	0.51
Plate	1:4:4	0.67
Plate	1:8:8	0.59
Cylinder	5	0.52
Cylinder	15	0.28
Cylinder	60	0.09
Disk	0.5	0.63
Tetrahedron	1	0.5

Source: Ref. 1.

those of the original structure (Fig. 6.5a). For this type of random packing of a binary mixture of spheres, the packing density is a function of (1) the ratio of the sphere diameters and (2) the fraction of the large (or small) spheres in the mixture.

By filling the interstitial holes with a large number of very fine spheres, we can maximize the packing density of the binary mixture. Starting with an aggregate of large (coarse) spheres in dense random packing, as we add fine spheres the packing density of the mixture increases along the line CR in Fig. 6.6. A stage will be reached when the interstitial holes between the large spheres are filled with fine spheres in dense random packing. Further additions of fine spheres will only serve to expand the arrangement of large spheres, leading to a reduction in the packing density. Assuming a packing density of 0.637 for dense random packing, the volume fraction of interstitial holes in the original aggregate of large spheres is $1 - 0.637$, or 0.363. At the maximum packing density of the binary mixture, the interstitial holes are filled with a large number of fine spheres in dense random packing. The maximum packing density is therefore $0.637 + 0.363 \times 0.637 = 0.868$. The fractional volumes occupied by the large spheres and fine spheres are 0.637 and $0.868 - 0.637$, respectively. The fraction (by weight or volume) of large spheres in the binary mixture is therefore $0.637/0.868$, or 0.733.

In an alternative approach, we can increase the packing density of an aggregate of fine spheres in dense random packing by replacing some of them and their interstitial holes by large spheres (Fig. 6.5b). In this case, the packing density of the mixture will increase along the line FR in Fig. 6.6. The intersection at R of the two curves CR and FR represent the state of optimum packing. Figure 6.6 also shows the experimental data of McGeary (6) for binary mixtures of spherical steel particles with different size ratios. (McGeary assumed a packing density of

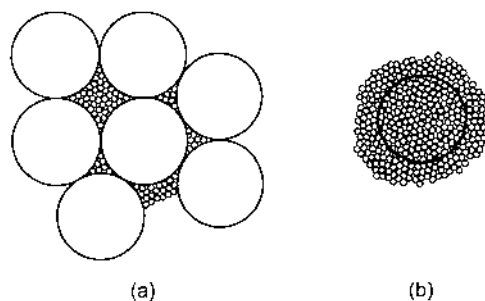


FIGURE 6.5 Increase in packing density achieved by (a) filling the interstices between large spheres with small spheres and (b) replacing small spheres and their interstitial porosity by large spheres.

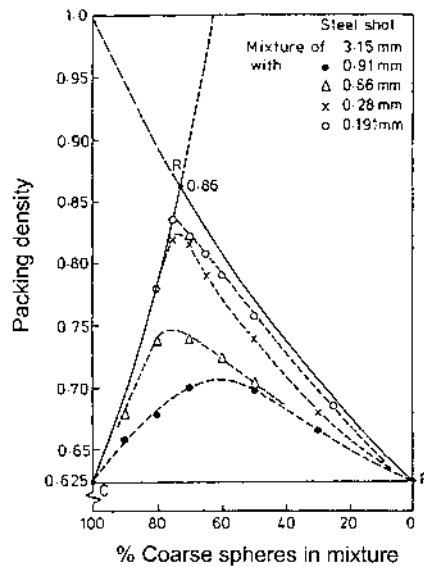


FIGURE 6.6 Binary packing of spheres showing the packing density as a function of the composition of the mixture. CRF represents the theoretical predictions for dense random packing when the ratio of the large sphere diameter to the small sphere diameter approaches infinity. The data of McGeary (6) for the mechanical packing of steel shot are also shown.

0.625 for dense random packing of monosize spheres.) As the ratio of the diameter of the large sphere to the small sphere increases, the data move closer to the theoretical curve. This is illustrated more clearly in Figure 6.7, which shows McGeary's data for dense random packing of binary mixtures of spheres. The packing density increases as the size ratio increases to ~ 15 but is relatively unchanged at higher size ratios. A change of behavior is apparent for a size ratio of ~ 7 , which corresponds to the size of a small particle just filling the triangular pore between the large particles.

The packing of binary mixtures of spheres is also commonly represented in terms of the apparent volume (i.e., total volume of the solid phase and porosity) occupied by unit volume of solid (7). The apparent volume is defined as

$$V_a = \frac{1}{1-P} \quad (6.2)$$

where P is the fractional volume of the voids (i.e., the porosity). As shown in Fig. 6.8, the line CRF represents the theoretical curve for the packing of a binary

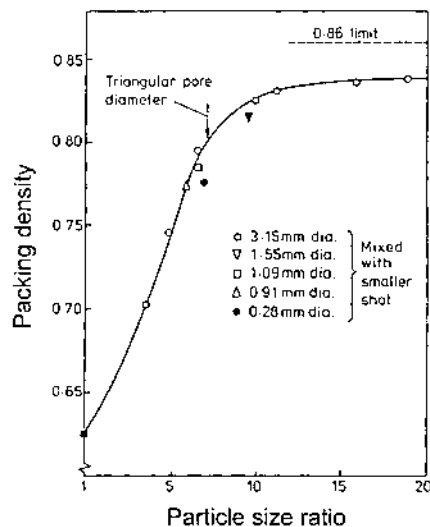


FIGURE 6.7 The data of McGeary (6) shows the effect of particle size ratio on the maximum packing density for bimodal powder mixtures.

mixture in which the size of the large spheres is very much greater than that of the small spheres.

Instead of filling the interstitial holes between the large spheres with a large number of very small spheres, another approach is to insert into each hole a single sphere with the largest possible diameter that would fit into the hole. For an aggregate of monosize spheres in dense random packing, computer simulations reveal that with this approach the maximum packing density of the binary mixture is 0.763 (5). This value is smaller than the maximum packing density (0.868) obtained earlier by filling the interstices with a large number of fine spheres, but it may represent a more realistic upper limit to the packing of real powder mixtures.

6.2.2.3 Binary Mixtures of Nonspherical Particles

The mixing of different sizes of nonspherical particles also leads to an increase in the packing density, but the packing density is generally lower than for spherical particles. The greater the surface roughness, shape irregularity, and the aspect ratio of the particles, then the lower the packing density. As in the case of spherical particles, the packing density of a mixture of nonspherical particles increases with increasing size ratio of the two powders and is dependent on the composition (i.e., the fraction of large to small particles). The composition that gives the maximum packing density is sensitive to the particle shape.

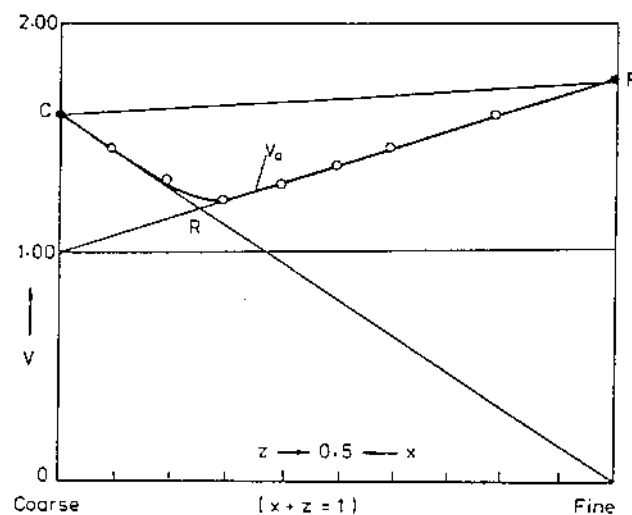


FIGURE 6.8 Binary packing of spheres plotted in terms of the apparent volume occupied by unit volume of the solid phase. In this representation, straight lines are obtained for the theoretical case CRF when the ratio of large sphere diameter to the small sphere diameter approaches infinity. The data of Westman and Hugill (7) for a diameter ratio of 50 are also shown.

The packing of model mixtures consisting of cylindrical rods and spherical particles has been studied experimentally by Milewski (8). The results provide useful insight into the key factors controlling the packing of short single crystal fibers or whiskers (e.g., SiC and Si₃N₄) and powders (e.g., Al₂O₃) for the production of ceramic matrix composites. Packing uniformity and a high enough density remain our basic requirements for the green composite. We require a uniform distribution of the whiskers and the elimination of large voids in the composite.

As shown in Fig. 6.9, experiments with cylindrical rods indicate that short fibers pack to very low densities, with the packing density decreasing with increasing aspect ratio. Whiskers with high aspect ratio (>50–100) also tend to tangle and to form bundles or loose clumps, leading to poor distribution of the whiskers and large voids spanned by whiskers in the green composite. Whiskers with high aspect ratios therefore should not be used in the production of ceramic composites.

The results of Milewski for the packing of cylindrical rods and spherical particles are shown in Table 6.5. The parameter R represents the ratio of the diameter of the particle to the diameter of the rod. Efficient packing of the mixture is promoted by low volume fraction of whiskers which have low aspect ratio and which are thin compared to the particle size of the matrix powder.

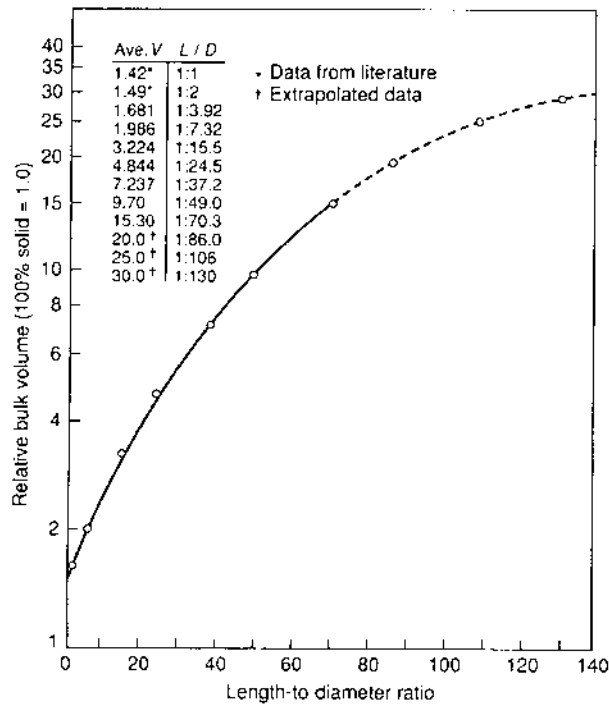


FIGURE 6.9 Packing curve for fibers with varied length-to-diameter (L/D) ratios. (From Ref. 8.)

For whisker reinforced ceramic composites, theoretical models and experimental investigations indicate that very little enhancement in the mechanical properties is achieved for whisker aspect ratios above ~ 15 – 20 . Whiskers with aspect ratios less than ~ 20 – 30 flow fairly easily and show behavior close to that of a powder. A suitable whisker aspect ratio for the production of ceramic composites is therefore ~ 15 – 20 . Most commercial whiskers, however, contain a large fraction with aspect ratios greater than this value. Normally, ball milling is used to reduce the aspect ratio. For closer control of the aspect ratio, the ball milled whiskers can be fractionated to produce fractions with the desired range. Good mixing of the whiskers and the matrix powder is achieved by ball milling for several hours or by colloidal dispersion techniques.

6.2.2.4 Ternary and Multiple Mixtures

The packing density of binary mixtures of spheres can be increased further by going to *ternary* mixtures, *quaternary* mixtures, and so on. For example if each

TABLE 6.5 Experimental Packing Densities at 25%, 50%, and 75% Fiber Loading for Fiber-Sphere Packing

Fiber L/D	Percent fibers	<i>R</i> value									
		0	0.11	0.45	0.94	1.95	3.71	6.96	14.30	17.40	∞
3.91	25	68.5	68.5	65.4	61.7	61.0	64.5	70.0	74.6	76.4	82.0
	50	76.4	74.6	67.2	61.7	60.2	64.1	67.5	72.5	74.5	75.7
	75	78.2	69.5	64.5	61.0	59.5	62.5	64.4	66.7	67.2	67.1
7.31	25	68.5	68.5	64.5	61.0	58.5	59.9	64.5	73.5	74.6	80.6
	50	76.4	71.4	67.5	58.8	55.5	56.6	58.8	65.4	67.1	67.1
	75	66.3	61.7	60.0	55.0	52.8	53.5	54.6	57.2	58.2	57.4
15.52	25	68.5	66.7	63.7	59.9	54.6	50.3	50.5	54.1	57.5	65.0
	50	61.7	55.6	51.8	50.7	45.5	42.0	42.4	44.3	44.3	48.1
	75	41.0	40.4	37.9	38.2	37.3	35.7	35.5	36.0	36.8	38.2
24.50	25	68.5	66.5 ^a	61.5 ^a	55.5 ^a	47.5	45.5	40.2	42.7	44.7	50.5
	50	40.0	39.0 ^a	38.0 ^a	36.0 ^a	34.0 ^a	32.7	30.3	31.8	31.8	33.5
	75	26.4	26.3 ^a	26.2 ^a	25.8 ^a	25.5 ^a	25.2	24.3	25.0	25.6	26.2
37.10	25	50.0	48.0 ^a	45.0 ^a	42.0 ^a	39.4	37.7	33.8	33.1	39.2	41.3
	50	25.7						22.6	22.6	22.6	25.6
	75										

^a Estimated values (extrapolated data).

Source: Ref. 8, reprinted with permission.

interstitial hole in the binary mixture (packing density = 0.868) is filled with a large number of very fine spheres in dense random packing, the maximum packing density becomes 0.952. Using the same approach, the maximum packing density of quaternary mixtures is 0.983. Following this packing scheme, McGeary (6) experimentally achieved packing densities of 0.90 for a ternary mixture and 0.95 for quaternary mixture of steel spheres that were compacted by vibration.

In practice, little is gained beyond the use of ternary mixtures because the finer particles do not locate into their ideal positions to maximize the packing density. Additional practical problems may arise as the number of size classes in the mixture increases. As described earlier, a particle size ratio of at least 7 is required for optimum packing. For a ternary mixture of fine, medium and large particles, assuming that the fine particles are 1 μm in size, then the medium, and large particles will be 7 μm and 49 μm , respectively. The ability to produce some advanced ceramic powders with such widely different sizes is limited.

Although less severe in ternary or quaternary mixtures than in the case of powders with a wide particle size distribution, the problem of the packing uniformity of the green body still needs to be considered seriously. Two requirements must be satisfied for this approach to be successful. First, uniform mixing of the

powder fractions by mechanical or colloidal methods must be achieved. Second, the mixture must be consolidated to produce uniform packing. The objective is a green body in which the small pores are fairly uniformly spaced and the large voids are eliminated.

6.2.2.5 Continuous Particle Size Distributions

Most powders used for the fabrication of ceramics have a continuous distribution of particle sizes between some minimum and maximum size. For mixtures with discrete sizes, we found that as long as the particles are very different in size, the packing density increases as the number of components in the mixture increases. Extending this concept to continuous distributions, a wide particle size distribution gives a higher packing density than a narrow particle size distribution.

The development of particle size distributions with optimum packing density has received considerable attention. As an example, Fig. 6.10 shows the results for the packing of particles with a lognormal distribution of sizes (9,10). The packing density increases as the standard deviation of the distribution S increases (i.e., as the spread in the distribution of sizes increases) and reaches fairly high values for a wide distribution of particle sizes. The data in Fig. 6.10 can be approximated by an equation of the form

$$\text{Packing density} = a - \frac{b}{S} \quad (6.3)$$

where a and b are constants for a given powder. For the spherical lead glass beads (sphericity $\psi = 1$), $a = 0.96$, which is equal to the value predicted by Bierwagen and Saunders (11). There is also a particle shape effect, illustrated by the data for sand, showing that the packing density decreases for the more irregular particles.

Furnas (12) considered the use of discrete particle fractions (produced by sieving) that differ in size by a constant factor of 1.414 and predicted optimum packing density when each fraction has 1.10 times the amount of powder in the lower-sized sieved fraction. Although based on the use of discrete particle size fractions, the work of Furnas provides a first estimate of the shape of the particle size distribution curve that gives the optimum packing. At approximately the same time, Andreasen (13) was developing an approach to particle packing based on the use of continuous particle size distributions. In this approach, optimum packing occurs when the particle size distribution can be described by a power-law equation commonly known as the *Andreasen equation*:

$$W = \left(\frac{D}{D_L} \right)^n \quad (6.4)$$

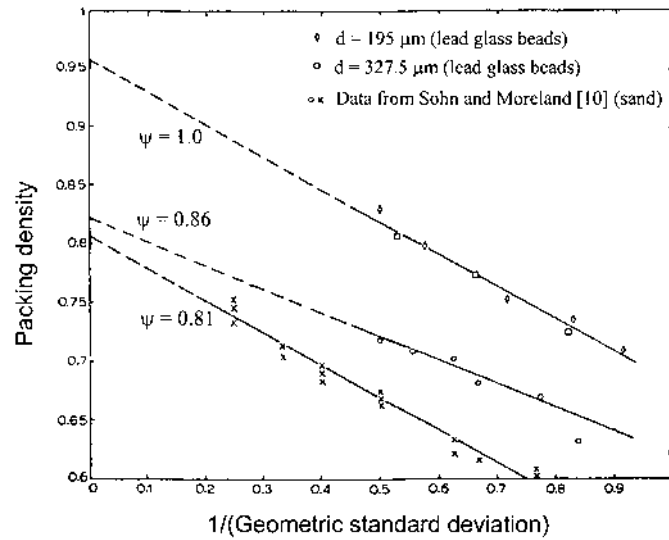


FIGURE 6.10 Packing density versus the reciprocal of the standard deviation for particles with a log normal size distribution. The parameter ψ is a measure of the sphericity of the particles and is equal to the reciprocal of the shape factor. (From Ref. 9.)

where W is the cumulative mass fraction of particles finer than a size D , D_L is the largest particle size in the distribution, and n is an empirical constant used to fit the experimental particle size distribution. From experimental studies of many particle size distributions, Andreassen concluded that the highest packing density occurs when n has values between $1/3$ and $1/2$.

The Andreassen equation assumes that all particle sizes below D_L exist, including infinitely small particles. Dinger and Funk (14) modified the equation to account for the more realistic case of a distribution with a finite minimum particle size D_S :

$$W = \frac{D^n - D_S^n}{D_L^n - D_S^n} \quad (6.5)$$

where the exponent n is the same as that in the Andreassen equation.

Continuous particle size distributions can be mixed to improve the packing density. Generally, the mean particle size of the two distributions should be very different and the particle size distribution of the smaller powder should be wider than the larger powder. For a wide particle size distribution where the packing density is already high, little benefit is achieved by mixing with another distribution.

In view of the high packing densities that can be achieved, it seems that we may be better off, as far as the green body is concerned, with powders having a wide distribution of particle sizes. However, the packing density by itself is a misleading parameter for predicting the densification behavior and microstructural evolution during sintering. A more important consideration for advanced ceramics is the *packing uniformity* or, equivalently, the spatial scale over which density fluctuations occur in the green body. Computer simulations (15) show that as the width of the particle size distribution increases, the scale over which density fluctuations occur also increases (Fig. 6.11). As discussed later in this book, it is this increasing scale of density fluctuations that causes many of the problems in the sintering stage.

Commercial powders that have a wide distribution of particle sizes can be classified to provide fractions with the desired size range. One approach is to use the colloidal techniques described in Chapter 4 to disperse the powder and to remove hard agglomerates and large particles by sedimentation (16). The supernatant can then be decanted and fractionated into various size fractions. Although in many cases this approach may not be economical for industrial production, Fig. 6.12 shows that significant improvement in the packing homogeneity can be achieved. The unclassified powder contains large agglomerates that produce

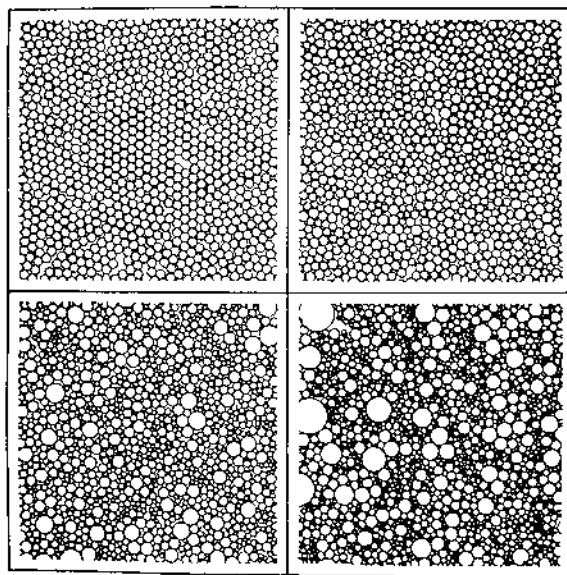


FIGURE 6.11 Four typical packings of multisized circles. (From Ref. 15.)

regions with very nonuniform packing, but the classified powder shows fairly homogeneous packing with a high packing density.

6.3 ADDITIVES AND CERAMIC FORMING

In the forming of ceramics, the use of certain additives, sometimes in concentrations as low as a fraction of a percent by weight, is often vital for controlling the characteristics of the feed material, for achieving the desired shape, and for controlling the packing uniformity of the green body. In methods such as tape casting and injection molding, the selection of suitable additives forms one of the most vital parts of the forming process. The additives are either *organic* or *inorganic* in composition. Organic additives, which can be *synthetic* or *natural* in origin, find greater use in the forming of advanced ceramics because they can be removed almost completely (e.g., by pyrolysis) prior to the sintering step. Therefore the presence of residues that can degrade the microstructure of the final product is largely eliminated. Organic additives can also be synthesized with a wide variety of compositions so they provide a large number of chemicals

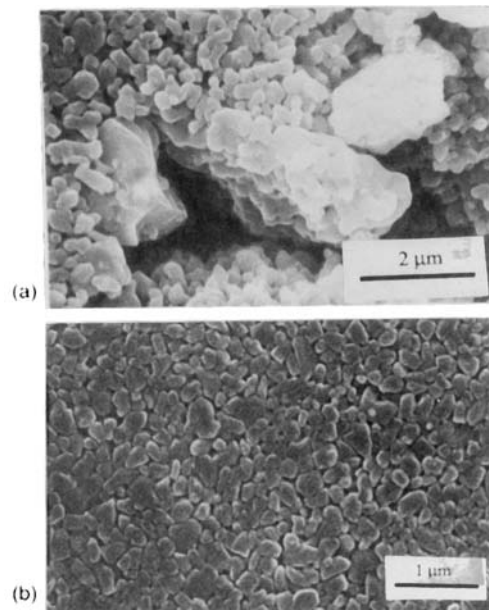


FIGURE 6.12 Scanning electron micrographs of (a) an unclassified alumina powder and (b) the powder after classification by sedimentation in water. (From Ref. 16.)

for specialized applications. Inorganic additives cannot generally be removed after the forming step and are used in applications, particularly in the traditional ceramics industry, where the residues do not have an adverse effect on the properties of the final product.

The additives serve a variety of specialized functions, which may be divided into four main categories: (1) solvents, (2) dispersants (also referred to as defloculants), (3) binders, and (4) plasticizers. Some forming methods may require, in addition, the use of other additives such as lubricants and wetting agents. Chemical principles and practical guidelines for the selection of additives for a given process can be formulated. However, because of the wide range of available chemicals and the incomplete knowledge of the chemical structure and process mechanisms, there is often no simple way of selecting additives for a given system. Most successful additives have been found by a trial-and-error approach.

Organic additives employed in ceramic processing form the subject of a text (17) in which the chemical principles and applications are described. Review papers have been published on the use of organic binders in ceramic forming (18) and on the role of additives in tape casting (19).

6.3.1 Solvents

Liquids serve two major functions:

1. Provide fluidity for the powder during forming.
2. Serve as solvents for dissolving the additives to be incorporated into the powder, thereby providing a means for uniformly dispersing the additives throughout the powder.

The selection of a solvent involves basically a choice between water and an organic liquid. Organic solvents generally have higher vapor pressure, lower latent heat of vaporization, lower boiling point, and lower surface tension than water, due in a large part to the strong hydrogen bonding of the water molecules (Table 6.6). Several common organic solvents also have a lower viscosity than water. The actual choice of a liquid for a given application often involves the consideration of a combination of several properties from the following list: (1) the ability to dissolve other additives, (2) evaporation rate, (3) ability to wet the powder, (4) viscosity, (5) reactivity towards the powder, (6) safety, and (7) cost.

Generally, solubility of the solid in the liquid is enhanced if the chemicals have similar functional groups [e.g., poly(vinyl alcohol) and water, which contain OH groups] or similar molecular polarity [e.g., poly(vinyl butyral) and ethanol]. Evaporation rate is an important factor in industrial tape casting where the tape is often cast, dried, peeled off from the carrier film, and rolled up for storage in a continuous operation. Fast drying solvents such as toluene and methyl ethyl

TABLE 6.6 Physical Properties of Some Liquids (at 20°C where applicable)

Liquid	Density (g/cm ³)	Dielectric constant	Surface tension (10 ⁻³ N/m)	Viscosity (10 ⁻³ Pas)	Latent heat of vaporization (kJ/g)	Boiling point (°C)	Flash point (°C)
Water	1.0	80	73	1.0	2.26	100.0	None
Methanol	0.789	33	23	0.6	1.10	64.6	18
Ethanol	0.789	24	23	1.2	0.86	78.4	20
Isopropanol	0.785	18	22	2.4	0.58	82.3	21
Acetone	0.781	21	25	0.3	0.55	56.0	-17
Methyl ethyl ketone	0.805	18	25	0.4	0.44	80	-1
Toluene	0.867	2.4	29	0.6	0.35	111	3
Xylene (ortho)	0.881	2	28	0.7	0.33	140	32
Trichloroethylene	1.456	3	25	0.4	0.24	87	None
n-Hexane	0.659	1.9	18	0.3	0.35	68.7	-23
Cyclohexanone	0.947	18	35	0.8	0.43	155	46
Mineral spirits	0.752					179–210	57

ketone (2-butanone) are commonly used for tape casting, particularly for thick tapes. Water is used occasionally for thin tapes. The evaporation rate of a liquid is determined by its latent heat of vaporization, but the boiling point is sometimes used as a rough guide. A mixture of solvents (e.g., trichloroethylene and ethanol) is sometimes used in tape casting to control the solubility and evaporation rate.

Wetting of a solid by a liquid is defined in terms of the contact angle θ (see Fig. 5.19), given by

$$\cos \theta = \frac{\gamma_{SV} - \gamma_{SL}}{\gamma_{LV}} \quad (6.6)$$

where γ_{SV} , γ_{SL} , and γ_{LV} are the surface tensions of the solid–vapor, solid–liquid, and liquid–vapor interfaces, respectively. Good wetting (low θ) is desirable in practice and, according to Eq. (6.6), is promoted by a low value of γ_{LV} (if γ_{SL} is not changed considerably). This is often achieved by using an organic solvent (low γ_{LV}) or by adding a *surfactant* (or *wetting agent*) to water to reduce its surface tension. The chemistry of surfactants and the mechanisms by which they operate are discussed in the next section. Poor wetting can lead to undesirable effects such as foaming of the liquid during milling and an increase in the suspension viscosity. The high surface tension of water makes it more difficult for air bubbles to escape to the surface, so that when compared to the use of organic liquids (e.g., toluene), water-based slurries have a greater tendency towards foam-

ing during milling. Trapped bubbles have a detrimental effect in that they generate flaws in the green body. A reduction in γ_{LV} , by the methods outlined above, can alleviate the problem.

Water has a relatively high viscosity, and its tendency to form hydrogen bonds with hydroxyl groups on the surfaces of oxide powders can often steepen the effect of particle concentration on the suspension viscosity. The result is often a reduction in the solids content of the suspension for the maximum usable viscosity when compared to the use of an organic solvent such as toluene. This difficulty with aqueous slurries is no longer so severe, due in large part to recent advances in the understanding and use of dispersants for aqueous media (20), but very high solids content appear to be easier to achieve reproducibly in organic liquids.

The surfaces of many powders (e.g., BaTiO_3 , AlN , and Si_3N_4) can be chemically attacked by water, leading to a change in composition and properties. For these powders, the use of an organic solvent is recommended because approaches to reducing the chemical attack in water, such as the use of a thin protective coating, are currently expensive or ineffective. Another approach (21) that has been shown to prevent chemical attack of AlN in aqueous media is to control the pH at a value of ~ 6 , but wider applicability of the approach is unclear.

Water has a distinct advantage over organic solvents when safety, cost, and waste disposal are considered. Despite the disadvantages of water outlined above, problems with the disposal and toxicity of organic solvents are leading to a shift towards greater use of aqueous solvents. Two main areas of safety are flammability and toxicity. A commonly used indicator of flammability is the flash point which gives the temperature at which there is sufficient vapor, generated by evaporation, so that an already existing flame can cause a fire to start. Organic solvents such as toluene and methyl ethyle ketone, which are commonly used in tape casting, have very low flash points (Table 6.6), so precautions must be taken to avoid explosions. Many organic liquids used in ceramic forming are toxic. Human exposure to these chemicals and waste disposal are important concerns. Trichloroethylene or a mixture of trichloroethylene and ethanol has been widely used in the tape casting industry because of its good solubility for many organic additives and inflammability. However, trichloroethylene and toluene, another solvent widely used in tape casting, are suspected of being carcinogens.

6.3.2 Dispersants

Dispersants, also referred to as deflocculants, serve to stabilize a slurry against flocculation by increasing the repulsion between the particles. While normally used in very small concentrations (e.g., a fraction of a percent by weight), the dispersant plays a key role in maximizing the particle concentration for some usable viscosity of the slurry. The principles that control the stabilization of

colloidal suspensions (i.e., electrostatic, steric, and electrosteric stabilization) were discussed in Chapter 4. Here we provide more practical information concerned with the main types of dispersants and how they operate to produce stabilization.

Dispersants cover a wide range of chemical composition (22), and for many of them the composition is considered to be proprietary information by the manufacturers. We will divide dispersants into three main classes, based on their chemical structure, as follows:

1. Simple ions and molecules
2. Short chain polymers with a functional head (or end) group, commonly referred to as *surfactants*
3. Low to medium molecular weight polymers

6.3.2.1 Simple Inorganic Ions and Molecules

Dispersants consisting of simple ions and molecules are effective in aqueous solvents. They are formed by dissociation of dissolved inorganic compounds such as salts, acids, and bases, often referred to as electrolytes. Examples are sodium silicate (Na_2SiO_3) commonly used for clays, tetrasodium pyrophosphate ($\text{Na}_4\text{P}_2\text{O}_7$), sodium hexametaphosphate ($\text{Na}_6\text{P}_6\text{O}_{18}$), sodium carbonate (Na_2CO_3), and hydrochloric acid (HCl) for oxides.

Preferential adsorption of one type of ions onto the particle surface coupled with the formation of a diffuse layer of the counterions (ions of opposite charge) leads to *electrostatic stabilization* due to repulsion between the double layers (Chapter 4). The valence and radius of the counterions can modify the repulsion between the particles and so can influence the stability of the suspension. Counterions with higher valence are more effective for causing flocculation (*Schulze-Hardy rule*), while for ions of the same valence, the smaller ions are more effective. For monovalent cations, the effectiveness of flocculation is in the order $\text{Li}^+ > \text{Na}^+ > \text{K}^+ > \text{NH}_4^+$, while for divalent cations, $\text{Mg}^{2+} > \text{Ca}^{2+} > \text{Sr}^{2+} > \text{Ba}^{2+}$. This sequence is known as the *Hofmeister series*. For common anions, the effectiveness of flocculation is in the order $\text{SO}_4^{2-} > \text{Cl}^- > \text{NO}_3^-$.

Sodium silicate forms one of the most effective dispersants for clays. As illustrated in Fig. 6.13, replacement of bivalent Ca^{2+} ions (or Mg^{2+} ions) more commonly present on the clay particle surfaces by monovalent Na^+ ions produces less screening of the surface charge and, hence, to a greater repulsion between the clay particles. For advanced ceramics that must meet very specific property requirements, the use of inorganic dispersants may leave residual ions (e.g., sodium or phosphate), which even in very small concentrations can lead to the formation of liquid phases during sintering, thereby making microstructural control more difficult.

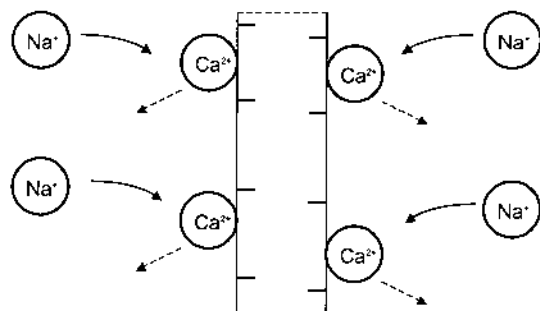


FIGURE 6.13 Schematic illustrating the stabilization of clay particles with sodium silicate.

6.3.2.2 Short-Chain Polymers with a Functional Head Group (Surfactants)

Surfactants contain a short-chain organic tail (containing up to 50–100 carbon atoms) and a functional head group that is nonionic or ionic in nature (Fig. 6.14a). For *nonionic surfactants*, the head group may be polar but does not ionize to produce charged species, so nonionic surfactants are commonly effective in *organic* solvents. Adsorption onto the particle surfaces occurs either by van der Waals attraction or, more effectively, by stronger coordinate bonding. As illustrated in Fig. 6.14b, using the Lewis acid-base concept, an atom in the surfactant functional group which has an unshared pair of electrons (e.g., N or O) may act as a Lewis base and form a coordinate bond with an atom (e.g., Al) on the particle surface which has an incomplete shell of electrons (Lewis acid). Stabilization most likely occurs by steric repulsion between the organic tails or micelles that are stretched out in the organic solvent (Fig. 6.14c and d). Examples of some commonly used nonionic surfactants are given in Fig. 6.15. In addition, menhaden fish oil is a widely used dispersant for Al_2O_3 , BaTiO_3 , and several other oxides. It consists of a mixture of several short-chain fatty acids with the alkyl chain containing some $\text{C}=\text{C}$ double bonds and the functional end group being a carboxylic acid (COOH). Polyisobutylene succinamide (OLOA-1200) is commonly used for dispersing carbon particles in organic solvents.

Ionic surfactants are described as either *anionic*, when the functional head group ionizes to form a negatively charged species, or *cationic*, when a positively charged head group is formed (Fig. 6.16a). They are effective in *aqueous* solvents. Usually, negatively charged *oxygen* species are formed on dissociation of anionic surfactants. Adsorption of the surfactant commonly occurs by electrostatic attrac-

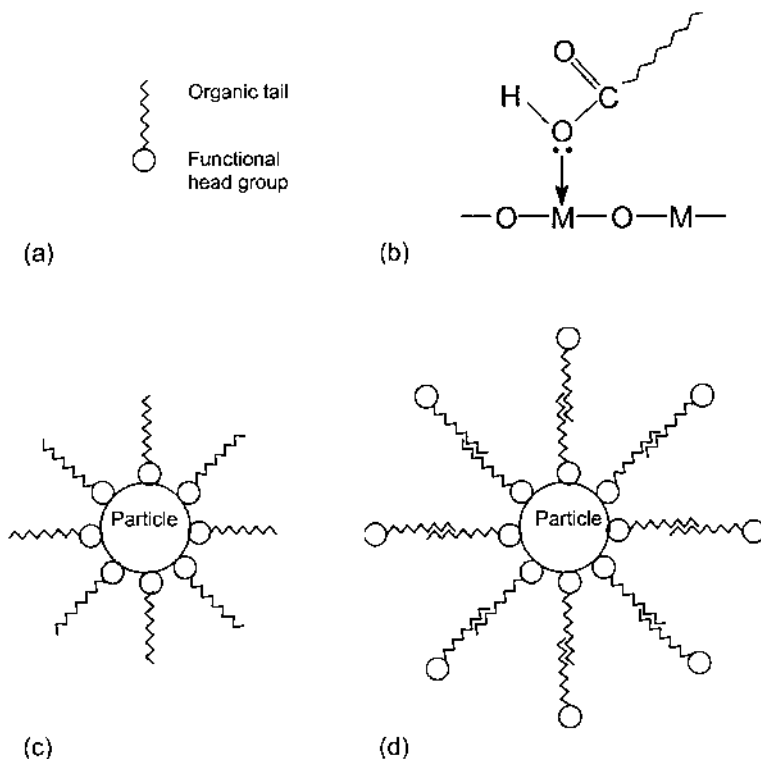


FIGURE 6.14 (a) Schematic of a surfactant molecule. (b) Illustration of surfactant adsorption onto an oxide particle surface by coordinate bonding. (c) Stabilization by steric repulsion between organic tails of the surfactant molecules. (d) Stabilization by micelles.

tion with positively charged particle surfaces. Stabilization of the suspension occurs essentially by electrostatic repulsion between the negative charges due to the adsorbed surfactant molecules (Fig. 6.16b) or micelles (Fig. 6.16c). Cationic surfactants commonly consist of positively charged *nitrogen* species on dissociation. Except for the reversal in the sign of the charges on the surfactant and the particle surface, the mechanisms of adsorption and stabilization are similar to the anionic surfactant case.

6.3.2.3 Low to Medium Molecular Weight Polymers

These dispersants, with a molecular weight in the range of several hundred to several thousand, are also classified into nonionic and ionic types. Common *non-ionic* polymeric dispersants are poly(ethylene oxide) (PEO), or poly(ethylene

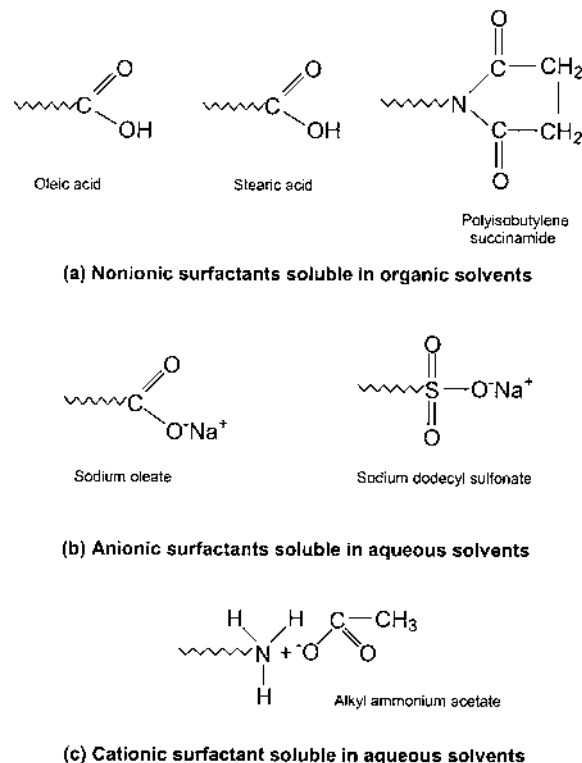


FIGURE 6.15 Functional head groups of some common surfactants.

glycol) (PEG), poly(vinyl pyrrolidone) (PVP), poly(vinyl alcohol) (PVA), polystyrene (PS), and block copolymers of PEO/PS. With a higher molecular weight, many of these polymers are effective as binders; their chemical compositions are given in the next section (see Fig. 6.18). When the chain segment contains OH groups or polar species the dispersants are effective in water; otherwise they are effective in organic solvents. In organic or aqueous solvents, adsorption of the polymers can occur by the weaker van der Waals bonding or more effectively by coordinate bonding (see Fig. 6.14b). In aqueous solvents, hydrogen bonding can also produce very effective adsorption. Because they are uncharged, nonionic polymeric dispersants provide stabilization by steric repulsion.

Also referred to as *polyelectrolytes*, ionic polymeric dispersants consist of chain segments that carry ionized groups and are therefore effective in aqueous solvents. On dissociation, the ionized groups in the chain segment can produce negatively charged species (anionic polymers) or positively charged species (ca-

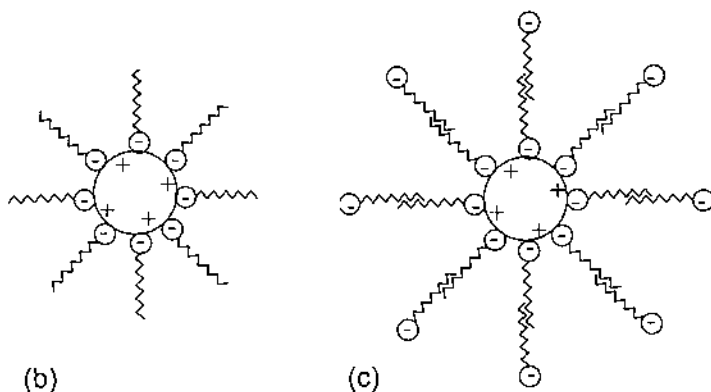
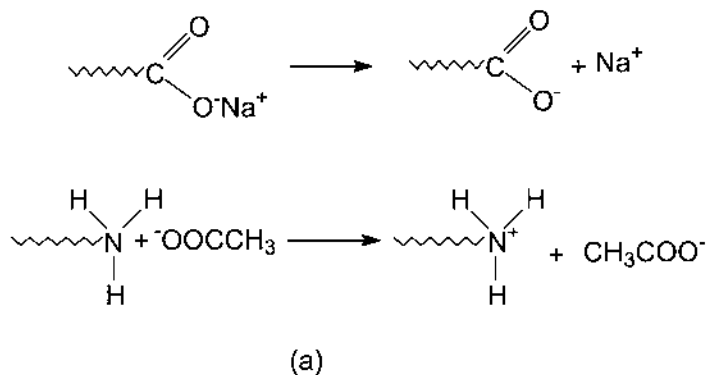
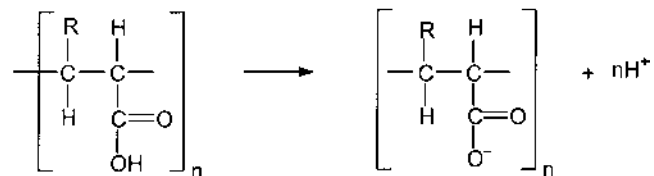
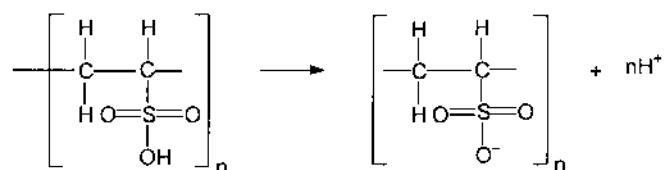


FIGURE 6.16 (a) Dissociation of anionic and cationic surfactants to form negatively charged and positively charged head groups, respectively. (b) Stabilization by negatively charged surfactant. (c) Stabilization by negatively charged micelles.

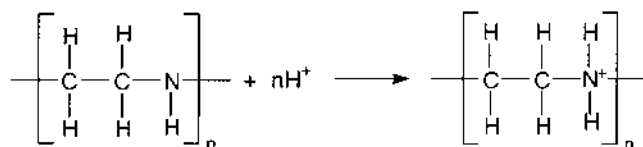
tionic polymers). Some common anionic polymers are given in Fig. 6.17. The sodium or ammonium salts of the polyacrylic acids have been used successfully with aqueous slurries of several oxide powders and their use is increasing. For advanced ceramics, the use of the sodium salt of these acids is not recommended because residual Na ions, even in very small concentrations, can create problems for microstructural control during sintering. An example of a cationic polymer is poly(ethylene imine), which becomes positively charged in acidic conditions but remains an undissociated weak base in basic conditions. The mechanisms of adsorption (electrostatic attraction) and stabilization (electrosteric) for polyelectrolytes were described in Chapter 4.



(a) Poly(acrylic acid): R = H; poly(methacrylic acid): R = CH₃



(b) Poly(vinyl sulfonic acid)



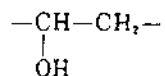
(c) Poly(ethylene imine)

FIGURE 6.17 Examples of common anionic and cationic polymers used as dispersants.

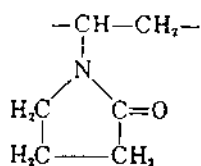
6.3.3 Binders

Binders are typically long chain polymers that serve the primary function of providing strength to the green body by forming bridges between the particles. In some forming methods (e.g., injection molding), they also provide plasticity to the feed material to aid the forming process. A large number of organic substances can be utilized as binders, some of which are soluble in water, while others are soluble in organic liquids. The monomer formulas of some common *synthetic* binders are shown in Fig. 6.18. They include the vinyls, acrylics, and the ethylene oxides (glycols). The vinyls have a linear chain backbone in which the side group is attached to every other C atom. The acrylics have the same backbone structure but may have one or two side groups attached to the C atom.

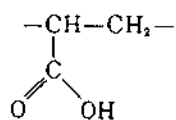
The cellulose derivatives are a class of *naturally occurring* binders. The polymer molecule is made up of a ring-type monomer unit having a modified α -

Soluble in water


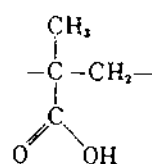
Poly(vinyl alcohol)



Polyvinylpyrrolidone



Poly(acrylic acid)



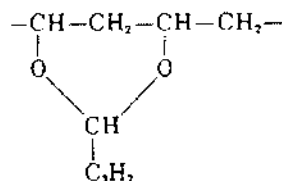
Poly(methacrylic acid)

Poly(ethylene glycol) and
poly(ethylene oxide)

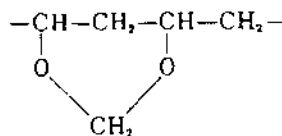
Polyethylenimine

Soluble in organic solvents
Vinyls

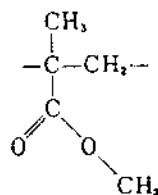
Poly(vinyl butyral)



Poly(vinyl formol)

**Acrylics**

Poly(methyl methacrylate)

**FIGURE 6.18** Monomer formulas of some synthetic binders.

glucose structure (Fig. 6.19). The modifications to the polymer occur by changes in the side groups R. The degree of substitution (DS) is the number of sites on which modifications are made in the monomer. Substitutions occur first at the C-5 site, followed by the C-2 site, and finally at the C-3 site. The formulas of the R groups in some common cellulose derivatives are shown in Fig. 6.20.

The selection of a binder for a given forming process involves the consideration of several factors that include (1) binder burnout characteristics, (2) molecular weight, (3) glass transition temperature, (4) compatibility with the dispersant, (5) effect on the viscosity of the solvent, (6) solubility in the solvent, and (7) cost. It is clear that low cost is a key consideration in industry.

The binder as well as the other additives used to aid the forming of the green body must normally be removed as completely as possible (commonly by pyrolysis) prior to sintering. The concentration of the binder is commonly much greater than that of the other additives, so the burnout characteristics is of primary importance in the selection of the binder. As discussed in detail later, the burnout characteristics depend primarily on the binder chemistry and the atmosphere (oxidizing or nonoxidizing).

In general, a high molecular weight is required to enhance the binder strength. However, the glass transition temperature T_g (i.e., the temperature that marks the transition from a rubbery state to a glassy state) of the polymer must be relatively low (e.g., near room temperature) to aid the deformation of the binder during forming. A reduction in T_g involves essentially reducing the resistance to motion of the polymer chains. This can be achieved by the use of polymers with less rigid side groups, less polar side groups, or a lower molecular weight but, as discussed later, is most commonly achieved by reducing the intermolecular bonding between the chains through the use of a plasticizer. If a dispersant is used in the forming process, then the binder should be compatible with it. In general, the binder should not displace the dispersant from the particle surface which, for oxides, commonly means that the binder molecule should be less polar than the dispersant.

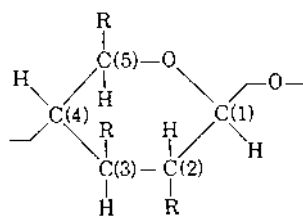


FIGURE 6.19 The modified α -glucose structure.

Binder	R Group	DS
Soluble in water		
Methylcellulose	$-\text{CH}_2-\text{O}-\text{CH}_3$	2
Hydroxypropylmethylcellulose	$-\text{CH}_2-\text{O}-\text{CH}_2-\underset{\text{OH}}{\text{CH}}-\text{CH}_3$	2
Hydroxyethylcellulose	$-\text{CH}_2-\text{O}-\text{C}_2\text{H}_4-\text{O}-\text{C}_2\text{H}_4-\text{OH}$ $-\text{CH}_2-\text{O}-\text{C}_2\text{H}_4-\text{OH}$	0.9-1.0
Sodium carboxymethylcellulose	$-\text{CH}_2-\text{O}-\text{CH}_2-\underset{\text{ONa}}{\overset{\text{O}}{\text{C}}}$	
Starches and dextrans	$-\text{CH}_2-\text{OH}$	
Sodium alginate	$-\underset{\text{ONa}}{\overset{\text{O}}{\text{C}}}$	
Ammonium alginate	$-\underset{\text{ONH}_2}{\overset{\text{O}}{\text{C}}}$	
Soluble in organic solvents		
Ethyl cellulose	$-\text{CH}_2-\text{O}-\text{CH}_2-\text{CH}_3$	

FIGURE 6.20 Formulas of the side groups in some cellulose derivatives.

The effect of the binder on the rheology of the solvent is a key consideration. Organic binders increase the viscosity and change the flow characteristics of the liquid. Some can even lead to the formation of a gel. In the casting methods (e.g., tape casting), the binder should not produce a rapid increase in the viscosity of the solvent with increasing concentration because this will limit the amount of powder that can be incorporated into the suspension for some usable viscosity. On the other hand, a rapid increase is generally desirable in extrusion to provide good green strength with a small concentration of binder.

Binders are often arbitrarily classified into low, medium, and high viscosity grades based on how effectively they increase the viscosity of the solution. The

scheme shown in Fig. 6.21 has been proposed by Onoda (18) and the classification of several water-soluble binders according to this scheme is shown in Table 6.7. The binder grade depends to a large extent on the structure of the polymer chain. Polymer molecules in solution, as discussed in Chapter 4, take up the conformation of a coil. Smaller coils exert less viscous drag on the molecules of the liquid and lead to a smaller increase in the viscosity with concentration. Linear chains with good flexibility in which the bonds can easily rotate [e.g., vinyl, acrylic, and poly(ethylene oxide) binders] are expected to form smaller coils and should have a lower viscosity grade than chains based on ring molecules or with large, rigid side groups (e.g., some cellulose binders). Although the molecular weights of the binders shown in Table 6.7 are not known accurately, the viscosity grades appear to be consistent with this line of reasoning.

In most of the forming methods (injection molding being a well-known exception), the binder is commonly added as a solution, so its solubility in the liquid is an important factor. The backbone of the molecule consists of covalently bonded atoms such as carbon, oxygen, and nitrogen. Attached to the backbone are side groups located at frequent intervals along the length of the molecule.

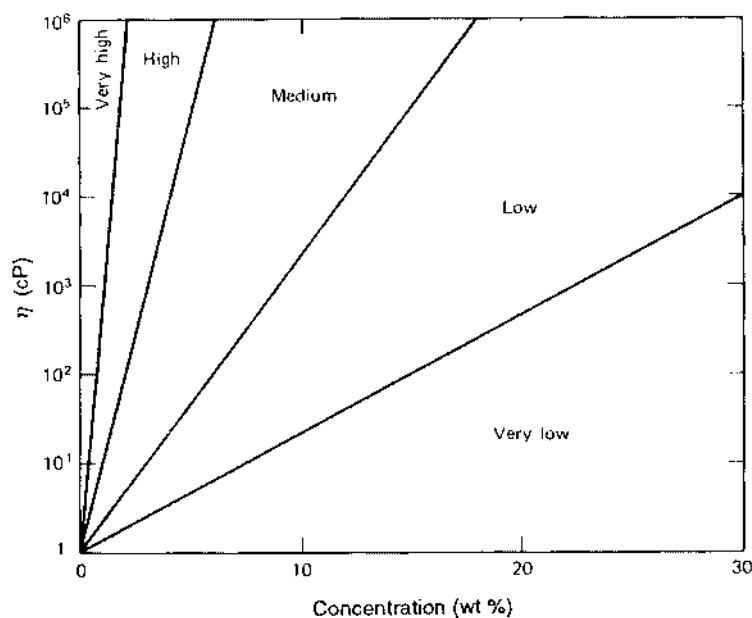


FIGURE 6.21 Criterion for viscosity grades based on viscosity–concentration relationship. (From Ref. 18.)

TABLE 6.7 Viscosity Grades for Some Water-Soluble Binders

Binder	Viscosity grade					Electrochemical type			
	Very low	Low	Medium	High	Very high	Nonionic	Anionic	Cationic	Biodegradable
Gum arabic	•						X		X
Lignosulfonates	•						X		X
Lignin liquor	•						X		X
Molasses	•					X			X
Dextrins	•—•					X			X
Polyvinylpyrrolidone	•—•					X			
Poly(vinyl alcohol)	•—•					X			
Poly(ethylene oxide)		•—•				X			
Starch		•—•				X			X
Acrylics		•—•					X		
Polyethylenimine (PEI)		•—•						X	
Methycellulose			•—•			X			X
Sodium carboxymethylcellulose			•—•				X		X
Hydroxypropylmethylcellulose			•—•			X			X
Hydroxyethylcellulose			•—•			X			X
Sodium alginate				•—•			X		X
Ammonium alginate				•—•			X		X
Polyacrylamide				•—•		X			
Scleroglucan				•		X			X
Irish moss				•			X		X
Xanthan gum				•					X
Cationic galactomanan					•			X	X
Gum tragacanth					•	X			X
Locust bean gum					•	X			X
Gum karaya					•	X			X
Guar gum					•—•	X	X	X	

Source: Ref. 18.

The chemical nature of the side groups determines, in part, what liquids will dissolve the binder. As outlined earlier, solubility of the binder in the liquid is enhanced if they have similar functional groups or similar molecular polarity.

Sodium silicate is an inorganic binder that finds considerable use in the forming of some traditional ceramics whose properties are not deleteriously affected by Na and Si residues. The compositions used as a binder have a $\text{Na}_2\text{O}:\text{SiO}_2$ ratio in the range of ~ 2 to 4. Hydrolysis leads to the formation of fine SiO_2 particles that gel and form a strong bonding phase between the ceramic particles.

6.3.4 Plasticizers

Plasticizers are generally organic substances with a lower molecular weight than the binder. The primary function of the plasticizer is to soften the binder in the dry state (i.e., reduce the T_g of the binder), thereby increasing the flexibility of the green body (e.g., tapes formed by tape casting). For forming processes in which the binder is introduced as a solution, the plasticizer must be soluble in the same liquid used to dissolve the binder. In the dry state, the binder and plasticizer are homogeneously mixed as a single substance. The plasticizer molecules get between the polymer chains of the binder, thereby disrupting the chain alignment and reducing the van der Waals bonding between adjacent chains. This leads to softening of the binder but also reduces the strength. Some commonly used plasticizers are listed in Table 6.8.

6.3.5 Other Additives

The number of additives used in a given forming process should be kept to a minimum because the potential for undesirable interactions between the components increases with their number. However, small amounts of other additives

TABLE 6.8 Common Plasticizers Used in Ceramic Processing

Plasticizer	Melting point (°C)	Boiling point (°C)	Molecular weight
Water	0	100	18
Ethylene glycol	−13	197	62
Diethylene glycol	−8	245	106
Triethylene glycol	−7	288	150
Tetraethylene glycol	−5	327	194
Poly(ethylene glycol)	−10	>330	300
Glycerol	18	290	92
Dibutyl phthalate	−35	340	278
Dimethyl phthalate	1	284	194

are sometimes used to serve special functions. *Wetting agents*, as outlined earlier, are *surfactants* added primarily to reduce the surface tension of liquids (particularly water), thereby improving the wetting of the particles by the liquid. *Lubricants* are commonly used in die compaction, extrusion, and injection molding to reduce the friction between the particles themselves or between the particles and the die walls. Under the application of an external pressure, the particles rearrange more easily, leading to a higher and more uniform packing density. Common lubricants are stearic acid, stearates, and various waxy substances. *Homogenizers* such as cyclohexanone are sometimes used in tape casting to increase the mutual solubility of the components, thereby improving the homogeneity of the mixture.

6.4 FORMING OF CERAMICS

The common ceramic forming methods were summarized in Table 6.1. We will now describe the key factors in each method and how they can be manipulated to optimize the microstructure of the green body.

6.4.1 Dry and Semidry Pressing

Uniaxial pressing in a die and isostatic pressing are commonly used for the compaction of dry powders, which typically contain <2 wt% water, and semidry powders, which contain ~ 5 – 20 wt% water (23,24). Die compaction is one of the most widely used operations in the ceramics industry. It allows the formation of relatively simple shapes rapidly and with accurate dimensions. The agglomeration of dry powders combined with the nonuniform transmission of the applied pressure during compaction leads to significant variations in the packing density of the green body. To minimize the density variations, die pressing is used for the production of relatively simple shapes (e.g., disks) with a height-to-diameter ratio of <0.5 – 1.0 . Isostatic pressing produces better uniformity in the packing density and can be used for the production of green bodies with complex shapes and with much higher height-to-diameter ratios. The green body has irregularities in both shape and surface quality and often requires considerable machining.

6.4.1.1 Die Compaction

In die compaction, the powder or a granular material undergoes simultaneous uniaxial compaction and shaping in a rigid die. The overall process consists of three steps: filling of the die, powder compaction, and ejection of the compacted powder. There are three main modes of compaction, which are defined in terms of the relative motion of the die and the punches. In the single-action mode, the top punch moves but the bottom punch and the die are fixed, whereas in the double-action mode both punches move but the die is fixed. In the floating die mode the top punch and the die move but the bottom punch is fixed. The double-

action mode is capable of providing better packing homogeneity and is commonly used in industry.

Feed Material: Powders and Granules

Powders, often mixed with a small amount of binder (less than 5 vol%), are commonly used as the feed material in laboratory experiments. In industrial practice, the flow properties of the feed material become an important factor when efficient die filling, fast pressing rates, and reproducible green body properties are required. Fine powders do not flow very well and are difficult to compact homogeneously, so it is often necessary to granulate them, commonly by spray drying of a slurry (see Chapter 2). The formulation of the slurry for spray drying typically involves the use of a dispersant (e.g., ammonium polyacrylate), a *binder* [e.g., poly(vinyl alcohol)], a *plasticizer* [e.g., poly(ethylene glycol)], and a lubricant [e.g., ammonium stearate). Figure 6.22 shows a commercial spray-dried Al_2O_3 powder.

Several factors control the granule characteristics. They include the particle size distribution of the initial powder, the degree of flocculation of the slurry, the type of additives, and the spray-drying conditions. The key granule characteristics are

1. *Size, size distribution, and shape:* Granules prepared by spray drying in commercial equipment have nearly spherical shape and sizes in the range of $\sim 50\text{--}400\ \mu\text{m}$, with the average size in the range of $\sim 100\text{--}200\ \mu\text{m}$.

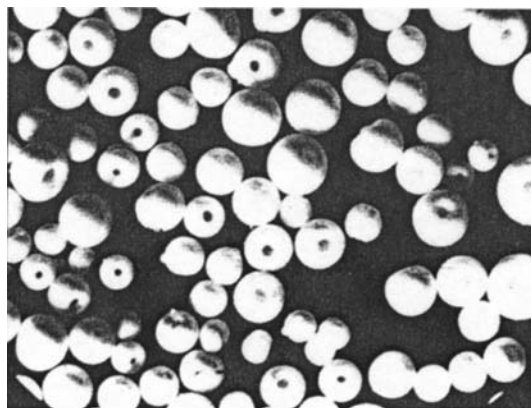


FIGURE 6.22 Example of a commercial spray-dried Al_2O_3 powder. (Magnification = $50\times$) (Courtesy of Niro Inc., Columbia, MD.)

2. *Particle packing*: The particle packing density in the granule is controlled by the particle size distribution of the powder as well as on the particle concentration and colloidal stability of the slurry prior to spray drying (25). Particle packing densities of $\sim 45\text{--}55\%$ are common for granules.
3. *Particle packing homogeneity*: The particle packing homogeneity in the granule depends on the colloidal stability of the suspension and on the drying step during spray drying. Granules are commonly prepared from a partially flocculated slurry so the particle packing is not very homogeneous. In addition, if the binder segregates to the granule surface during spray drying, the outer region of the granule will have a low packing density (26).
4. *Hardness*: The hardness of the granule is controlled by the particle packing density and by the nature of the binder used in the slurry formulation. A high particle packing density or a hard binder (e.g., with a high glass transition temperature) leads to the formation of hard granules. On the other hand, soft granules have a lower packing density or contain a soft binder.
5. *Surface friction*: Smooth granule surfaces reduce the friction between the granules themselves and between the granules and the die walls.

Die Filling

The flow of the granules during die filling is improved by a wide distribution of sizes, a spherical shape, and a smooth surface (14). The uniformity of the die filling must also be considered because it will affect the packing homogeneity of the green body. In addition to the filling method and the geometry of the die, the die filling uniformity depends on the ratio of the granule size to the die diameter. Narrower dies lead to a lower overall packing density in the compact because the packing density near the die walls is lower. Simulations indicate that the effect of the die walls becomes insignificant when the die diameter is greater than ~ 250 times the granule diameter (23). For particle packing densities of $45\text{--}55\%$ in the granules and assuming loose random packing of the granules ($\sim 60\%$), the actual particle packing density during die filling is $\sim 25\text{--}35\%$.

The Compaction Step

After die filling, the structure of a system of granules contains large voids on the order of the granule size and voids that are smaller than the granule size (Fig. 6.23). The compaction of this system can be divided into two stages. The first stage of compaction involves reduction of the large voids by *rearrangement* of the granules, while in the second stage, the small voids are reduced by *deformation* of the granules.

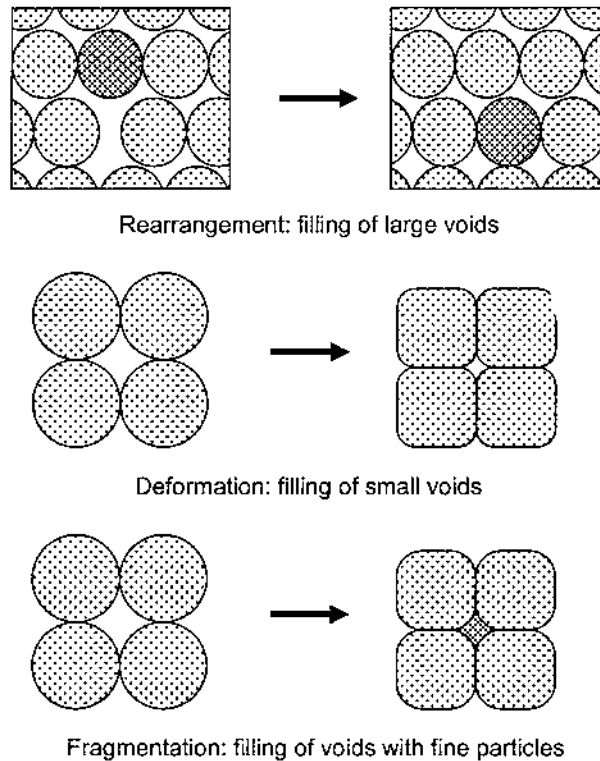


FIGURE 6.23 Schematic diagram showing the stages of compaction for granules.

The compaction of a system of particles will depend on the amount and type of agglomerates in the powder. For a system of primary particles with monomodal pores, the compaction will essentially consist of one stage involving sliding and rearrangement (with some fracture at higher pressures) to reduce the voids under the action of the applied pressure. If the powder contains low-density, weak agglomerates, then two stages of compaction may be observed: rearrangement and sliding in the first stage to reduce the larger voids followed by fracture of the agglomerates and further rearrangement and sliding in the second stage to reduce the smaller voids. For powders or granules, the particles also undergo elastic compression, which, as we shall see later, influences the ejection of the compact from the die and the creation of crack-like defects in the green body.

While it provides only a limited representation, the density of the compact as a function of the applied pressure is commonly used to characterize the compaction behavior. The data can be easily measured and find use in process optimization.

tion and quality control. When the density is plotted versus the logarithm of the pressure, the compaction data for granules often show two straight lines separated by a break point (Fig. 6.24). Compaction is interpreted to occur by rearrangement in the low-pressure linear region and by deformation in the high-pressure linear region. The break point scales as the hardness (or the strength) of the granules. Powders consisting of primary particles show a single line, whereas an agglomerated powder may show two lines, with the break point determined by the strength of the agglomerates.

The compaction process is a complex many-body problem, and theoretical analysis to produce a predictive model is difficult (28). In view of this difficulty, several empirical equations have been developed to account for the experimental data. None have been found to be generally applicable. One equation that has the advantage of simplicity and is as good as any of the others is

$$p = \alpha + \beta \ln \left(\frac{1}{1-\rho} \right) \quad (6.7)$$

where p is the applied pressure, ρ is the relative density, and α and β are constants that depend on the initial density and the nature of the material. The empirical expressions have often been criticized as being merely curve fitting, but they

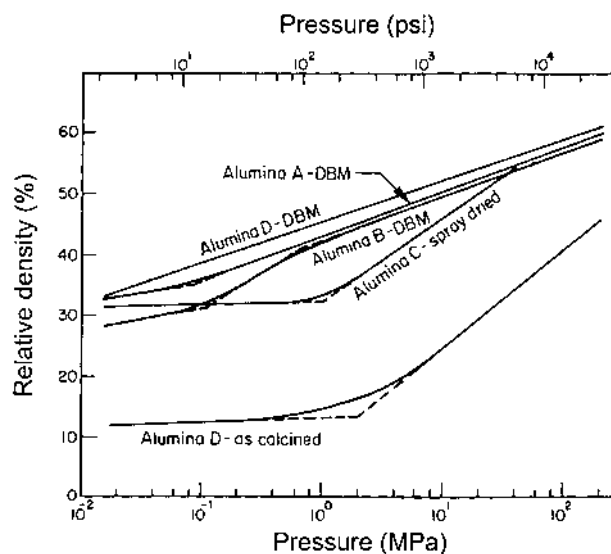


FIGURE 6.24 Compaction behavior of fine Al_2O_3 powders and spray-dried granules. (DBM refers to dry ball milling.) (From Ref. 27.)

have served to focus attention on the complexity of the variables and mechanisms of the process.

The behavior of a powder is changed dramatically when it is converted to granules, so the key factors influencing the compaction of particles and granules are considered separately.

Factors Influencing the Compaction of Particles

A severe problem in die compaction is that the applied pressure is not transmitted uniformly to the powder due mainly to friction between the powder and the die wall. The pressure gradients produce density gradients in the powder compact. The application of a uniaxial pressure p_z to the powder leads to the generation of a radial stress p_r and a shear (or tangential) stress τ at the die wall. The radial and shear stresses vary with distance along the die, so the resultant stress in the compact is nonuniform. Strijbos and co-workers (29) have made extensive studies of the stresses occurring during die compaction using equipment designed to measure the *radial pressure coefficient* (equal to the ratio p_r/p_z) and the *powder-wall friction coefficient* (equal to the ratio τ/p_r). The parameters investigated included the mean powder particle size d_p , the roughness of the wall R_w , the hardness of the powder H_p , the hardness of the wall H_w , and the use of lubricants.

For ferric oxide powder (Vickers hardness ≈ 600) and walls of tungsten carbide and hardened and nonhardened tool steels (Vickers hardness ≈ 1300 , 600, and 200, respectively), some data for the friction coefficient f_{dyn} as a function of d_p/R_w for the three values of H_p/H_w are shown in Fig. 6.25. For particles smaller than the roughness, f_{dyn} is as high as 0.6. A layer of the fine particles sticks to the die wall so that there is no direct contact between the stationary powder compact and the moving wall in the friction coefficient apparatus. In this case, R_w and H_w have no effect on f_{dyn} , and the high value of f_{dyn} is a reflection of the friction between the powder particles. Failure occurs within the powder compact and not at the die wall. For particles larger than the wall roughness, f_{dyn} is between 0.2 and 0.4 and is dependent on both the powder parameters and the die wall parameters. The low values of f_{dyn} are a reflection of the friction between the particles and the relatively smooth wall. Failure in this case occurs at the powder-wall interface. The influence of the particle size on the friction coefficient is summarized schematically in Fig. 6.26. The higher friction coefficient, reduced uniformity of die filling, and greater tendency for agglomeration are largely responsible for the more severe density gradients obtained in die compaction of fine powders.

The friction coefficient between the powder and a rough wall is also dependent on the direction of the grooves in the wall. The friction is lower if the grooves run in the direction of relative motion between the powder and the die wall. The effect of die-wall lubricants (e.g., stearic acid) can be fairly complex. For fine particles ($d_p/R_w < 1$), the coefficient of friction decreases gradually as the thick-

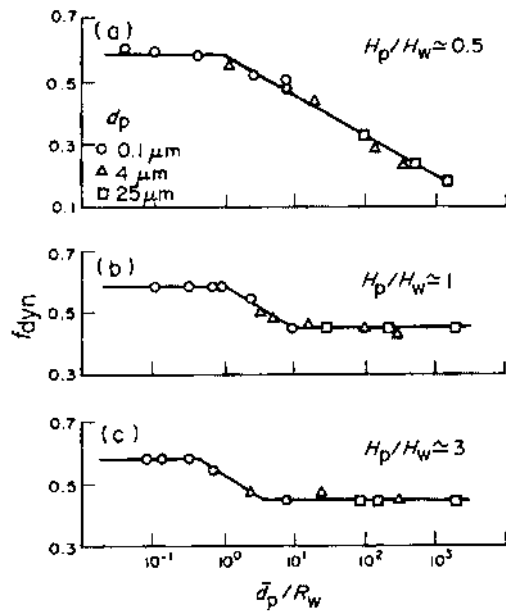


FIGURE 6.25 Dynamic powder-wall friction coefficient versus the ratio of powder particle size to wall roughness, for three values of the ratio of particle hardness to wall hardness (H_p/H_w). The powder is ferric oxide and the walls are (a) tungsten carbide, (b) hardened tool steel and (c) non-hardened tool steel. (From Ref. 29b.)

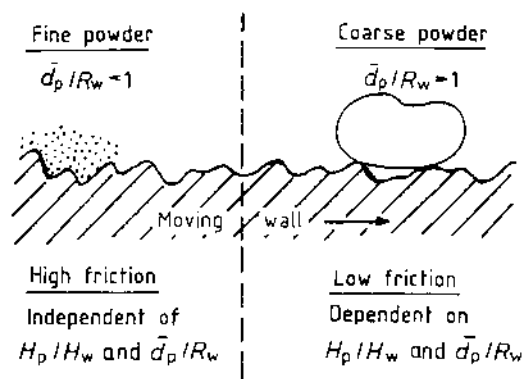


FIGURE 6.26 Sliding friction between a stationary powder compact and a moving wall. (From Ref. 29d.)

ness of the lubricant increases, and the magnitude of the decrease can be fairly significant when the thickness of the lubricating layer becomes larger than the particle size. For coarse particles ($d_p/R_w > 1$), the presence of a lubricant causes only a small reduction in the die-wall friction, and almost no dependence on the thickness of the lubricating layer is observed.

Density variations in powder compacts have been characterized by several techniques, including microscopy, microhardness, x-ray tomography, x-ray radiography, ultrasonic, and nuclear magnetic resonance (30). Figure 6.27 shows the density variations in a section of a cylindrical manganese–zinc ferrite powder compact (diameter = 14 mm) produced by die compaction in the single-action mode of pressing. The large density difference in the upper and lower corners due to die-wall friction is very noticeable.

The particle size distribution also has an effect on the compaction behavior. For a powder with a wide distribution of sizes, a plot of the compact density versus the logarithm of the applied pressure has a steeper slope than that for a narrow size distribution (Fig. 6.28), indicating that the deformation process occurs more easily. As outlined earlier (Fig. 6.24), the type and amount of agglomerates in the powder influence its compaction behavior. The effect of the particle shape can sometimes be difficult to predict. The spherical (or equiaxial) shape is the commonly desired geometry, but flat particles with smooth surfaces can provide a higher compact density if they become aligned.

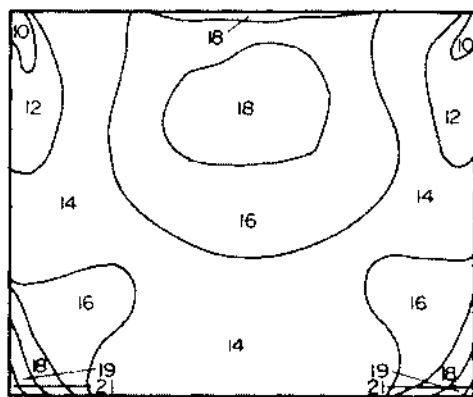


FIGURE 6.27 Density variation in a cross section of manganese ferrite powder compact produced by single-action die pressing from the top. High numbers correspond to low density while low numbers correspond to high density. The numbers are the optical density of the x-ray transmission photographs of the compact. (From Ref. 31.)

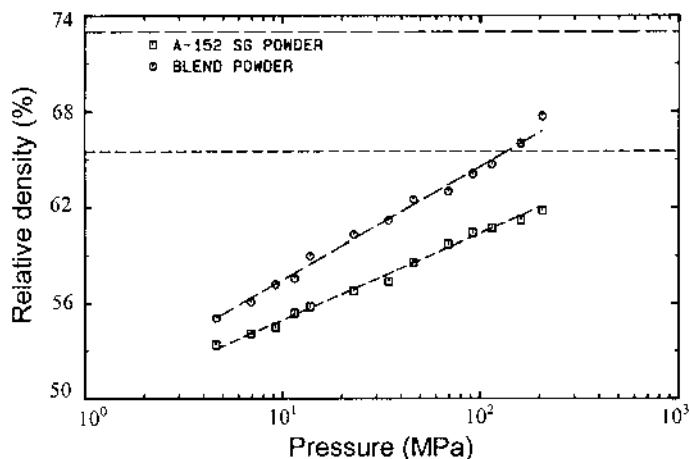


FIGURE 6.28 Density versus pressure for powders having a different maximum particle packing density. (From Ref. 32.)

Factors Influencing the Compaction of Granules

The key granule characteristics that influence compaction are the *hardness*, which is controlled by the particle packing and type of binder in the granule, the *size*, and the *size distribution*. As outlined earlier, the compaction process can be divided into two stages: rearrangement of the granules at low pressure and deformation at higher pressure. Nominally *hard* granules rearrange easily but, if too hard, are difficult to deform, thereby producing a green body with large *intergranular* pores. These large pores are difficult to remove during sintering, so they limit the final density and produce microstructural flaws in the sintered article (Fig. 6.29). Nominally *soft* granules deform readily under pressure but, if too soft, will not rearrange sufficiently at low pressure to eliminate large packing flaws present after die filling, so a compact with large density gradients is formed. The density gradients become magnified during sintering, often resulting in a limited final density and cracking. The requirement is therefore for granules with a nominal *medium hardness* which can undergo rearrangement as well as deformation during compaction.

The granule hardness depends on the particle packing in the granule and on the properties of the binder. Since the particle packing in the granule is dependent on the properties of the slurry used in spray drying, control of the granule hardness actually requires an understanding of the relationship between the suspension characteristics and the granule characteristics. A stable colloidal suspension with a high particle concentration leads to nominally hard granules with a

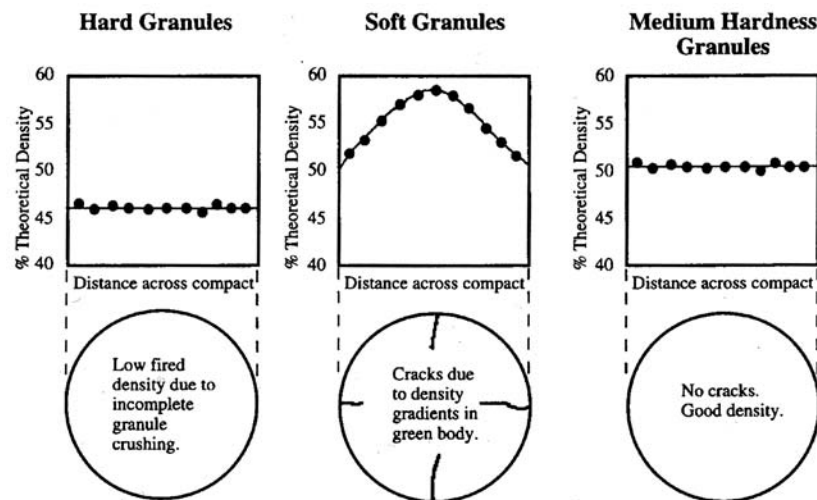


FIGURE 6.29 Qualitative results from experiments with nominally hard, soft, and medium hardness Al_2O_3 granules compacted uniaxially after irregular die filling. The upper set of graphs show density across the diameter of the green compact while the lower set of illustrations are schematics showing the appearance of the sintered pellets (top view). Granule hardness was modified by granulating the Al_2O_3 powder with different organic binders. (From Ref. 24.)

dense particle packing (25). A *partially flocculated* slurry, leading to a lower particle packing density in the granules is therefore desirable for spray drying.

The effect of granule density on compaction behavior is shown in Fig. 6.30. Because the granules themselves pack to the same density during die filling, compacts formed from the denser granules have a higher green density at any pressure. However, the compact density is lower than the granule density, indicating that the large intergranular pores remain in the compact. In contrast, while the density of the compact produced from low-density granules is lower, it is higher than the granule density at any pressure above ~ 12 MPa, which suggests that the large intergranular porosity in the compacts have been eliminated.

The hardness of the organic binders is determined by the glass transition temperature T_g . If the compaction temperature (commonly room temperature) is well below T_g , the binder is hard and brittle, so the granule is difficult to deform. On the other hand, if the temperature is well above T_g , the binder is soft and rubbery. If the binder is too soft, rearrangement at lower pressure is inefficient, resulting in density gradients. Methods for altering the T_g of organic binders were outlined earlier in this chapter. Water is a good plasticizer for poly(vinyl alcohol),

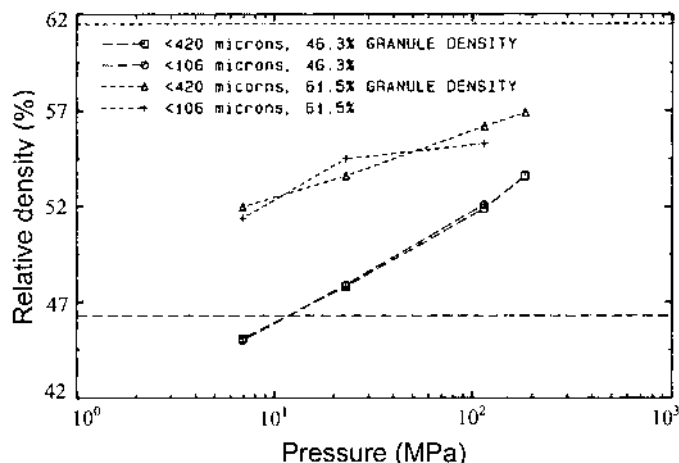


FIGURE 6.30 Density versus pressure for a powder prepared at two granule densities. (From Ref. 32.)

a commonly used binder in spray drying, so the hardness of the granules can change with the humidity of the atmosphere (33,34).

Provided that it is much smaller than the die diameter, granule size does not have a significant effect on the compact density (Fig. 6.30). The granule size distribution influences the packing and the compaction behavior. A wider size distribution produces a higher packing density after die filling, but a narrow size distribution is found to produce a higher compact density after pressing (24). Binder segregation to the granule surface and macroscopic flaws in the granule (e.g., holes) produce packing heterogeneities in the compact which normally remain as microstructural flaws in the sintered body.

Ejection of the Powder Compact

As outlined earlier, the powder undergoes elastic compression during the compaction process. The stored elastic energy leads to an expansion of the compact when the applied pressure is released. This expansion is referred to as *springback*, *strain recovery*, or *strain relaxation*. Springback is almost instantaneous on release of the pressure. The amount of springback depends on several factors, including the powder, the organic additives, the applied pressure, the rate of pressing, and the gas permeability of the powder compact. Generally, it is higher for higher amounts of organic additives and for higher applied pressure. While a small amount of strain recovery is desirable to cause the compact to separate from the punch, an excessive amount can lead to flaws. Ejection of the powder compact from the

die is resisted by friction between the compact and the die wall. Lubricants added to reduce die-wall friction during the compaction process have an additional benefit in that they reduce the pressure required for ejection.

Compaction Defects

After the completion of the die compaction process, we require that the green body be free of macroscopic defects and that density gradients be as low as possible. Density gradients lead to the development of cracklike voids in the sintered body and can also lead to cracking and warping of the body during sintering. They also enhance the formation of defects in the compact on ejection from the die. Several factors can be controlled to reduce the extent of density gradients in the powder compact. Uniform die filling reduces the amount of internal movement of the powder during the compaction process. The use of lubricants to reduce the internal friction between the particles and die-wall friction can lead to significant improvements. Stress gradients (and hence, density gradients) due to die-wall friction are enhanced with increasing ratio of the length to diameter (L/D) of the compact. For the single-action mode of die compaction, L/D should be less than 0.5, while for the double-action mode, it should be less than 1.

The common defects in compacts formed by die pressing are illustrated in Fig. 6.31. They are caused by springback and by friction at the die walls. The use of a binder to increase the compact strength, reduction of the applied pressure to reduce the extent of the springback, and the use of a lubricant to reduce die wall friction can significantly reduce the tendency for defect formation.

6.4.1.2 Isostatic Compaction

Isostatic pressing involves the application of a uniform hydrostatic pressure to the powder contained in a flexible rubber container. There are two modes of isostatic pressing: wet-bag pressing and dry-bag pressing (Fig. 6.32). In wet-bag pressing, a flexible rubber mold is filled with the powder, which is then submerged into a pressure vessel filled with oil and pressed. After pressing, the mold is removed from the pressure vessel and the green body is retrieved. Wet-bag press-

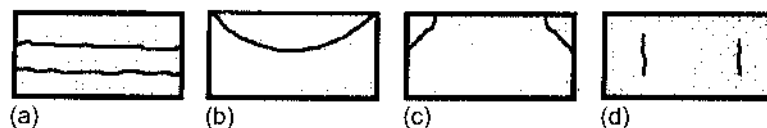


FIGURE 6.31 Illustrations of typical defects in die compaction of dry or semidry powders: (a) delamination, (b) end capping, (c) ring capping, and (d) vertical cracks.

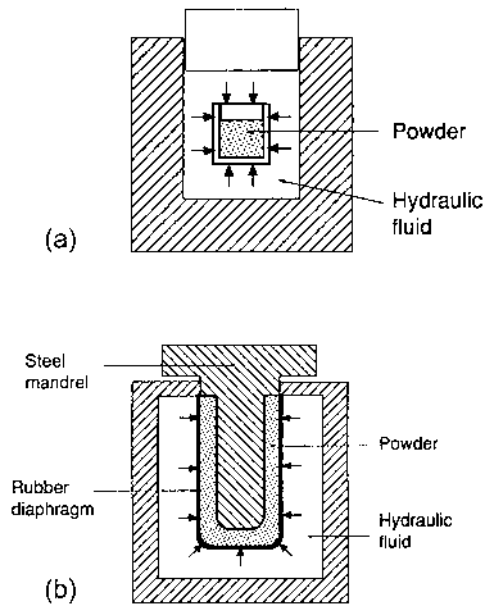


FIGURE 6.32 Two modes of isostatic pressing: (a) wet bag and (b) dry bag.

ing is used for the formation of complex shapes and for large sizes. In dry-bag pressing, the mold is fixed in the pressure vessel and need not be removed. The pressure is applied to the powder situated between a fairly thick rubber mold and a rigid core. After release of the pressure, the powder compact is removed from the mold. Dry-bag pressing is easier to automate than wet-bag pressing. It has been used for the formation of spark plug insulators by compressing a porcelain powder mixture around a metal core as well as for plates and hollow tubes. Compared to die compaction, the formation of defects in isostatically pressed compacts is much less severe, but delamination and fracture (caused by springback) can still occur if the pressure is released too rapidly after compaction.

6.4.2 Casting Methods

The common casting methods are *slip casting*, *pressure casting*, and *tape casting*. They are based on colloidal systems in which removal of the liquid is used to consolidate particles suspended in a slurry. In slip casting and pressure casting, consolidation of the particles is accomplished as the liquid flows through a porous medium under a pressure gradient. In tape casting, consolidation is accomplished by evaporation of the liquid. *Gel casting* is a recently introduced method in which

the particles in a slurry are immobilized by polymerization and cross-linking of a monomer solution to form a gel prior to evaporation of the liquid. *Electrophoretic deposition* is a process in which ceramic bodies are deposited on an electrode by applying a direct current (dc) electric field to a colloidal suspension.

The ideal requirements for the green body (the cast) are homogeneous particle packing and a green density that is as high as possible. The slurry that is used to produce these characteristics must have a high particle concentration but must also have the rheological properties to flow easily during the casting process and to allow a high enough casting rate for economical production. The attainment of the slurry characteristics in a controlled manner requires an understanding of (1) the colloidal interactions between particles in a suspension and (2) the factors that control the rheological behavior of suspensions, both of which were considered in Chapter 4. An understanding of particle packing concepts and the use of organic additives in processing, described earlier in this chapter, are also important.

The casting methods have the capability for producing a fairly homogeneous particle packing in the green body, but they are generally limited to the production of relatively thin articles. Slip casting offers a route for the production of complex shapes and is widely used in the traditional clay-based industry, for example, for the manufacture of pottery and sanitary ware. It has been steadily introduced over the past 50 years to the production of advanced ceramics. Tape casting is widely used for the production of thin sheets, substrates, and multilayer components for the electronic packaging industry.

6.4.2.1 Slip Casting

A recent review of slip casting is given by Fries and Rand (35) and much practical details of the process can be found in a set of earlier articles (36). In the process, a slurry is poured into a microporous plaster of Paris mold. The porous nature of the mold provides a capillary suction pressure, estimated to be of the order of $\sim 0.1\text{--}0.2$ MPa, which draws the liquid from the slurry into the mold. A consolidated layer of solids, referred to as a *cast* (or *cake*), forms on the walls of the mold (Fig. 6.33). After a sufficient thickness of the cast is formed, the surplus slip is poured out and the mold and cast are allowed to dry. Normally, the cast shrinks away from the mold during drying and can be easily removed. Once fully dried, the cast is heated to burn out the binder and sintered to produce the final article. Examples of slip casting compositions are given in Table 6.9.

Slip Casting Mechanics

Some of the early analyses incorrectly treated the mechanics of slip casting in terms of a *diffusion* process. The slip casting process involves the *flow* of liquid through a porous medium, which is described by Darcy's law. In one dimension, Darcy's law can be written as

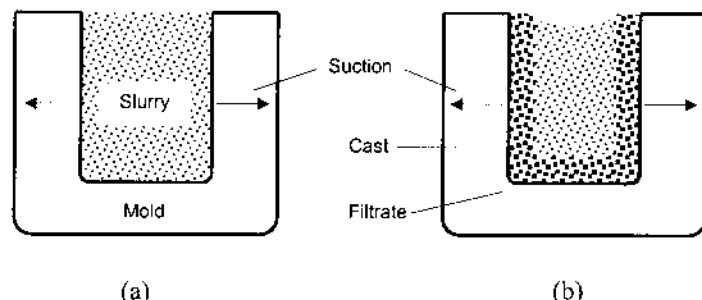


FIGURE 6.33 Schematic diagram of the slip-casting system: and (a) initial system (b) after the formation of a thin cast.

$$J = \frac{K(dp/dx)}{\eta_L} \quad (6.8)$$

where J is the flux of liquid, K is the permeability of the porous medium, dp/dx is the pressure gradient in the liquid, and η_L is the viscosity of the liquid. In slip casting, the pressure gradient that causes flow arises from the capillary suction pressure of the mold. As the consolidation of the particles proceeds, the filtrate (i.e., the liquid) passes through two types of porous media: (1) the consolidated layer and (2) the mold (Fig. 6.33).

Many authors have adopted the model of Adcock and McDowall (37) which neglects the resistance of the mold to liquid flow and treats the process in terms

TABLE 6.9 Examples of Slip Casting Compositions

Whiteware		Alumina	
Material	Concentration (vol %)	Material	Concentration (vol %)
Clay, silica, feldspar	45–50	Alumina	40–50
Water	50	Water	50–60
Sodium silicate, polyacrylate, or lignosulfate (dispersant)	<0.5	Ammonium polyacrylate (dispersant)	0.5–2
Calcium carbonate (flocculant, if required)	<0.1	Ammonium alginate or methyl cellulose (binder)	0–0.5

of liquid flow through the porous consolidated layer. In this case, an application of Darcy's law leads to a parabolic relation for the increase in the thickness of the cast L_c with time t :

$$L_c^2 = \frac{2K_c p t}{\eta_L (V_c/V_s - 1)} \quad (6.9)$$

where K_c is the permeability of the cast, p is the pressure difference across the cast (assumed to be constant and equal to the suction pressure of the mold), V_c is the volume fraction of solids in the cast (assumed to be incompressible), and V_s is the volume fraction of solids in the slurry. The *rate* of consolidation decreases with time, and this limits the slip casting process to a certain thickness of the cast. Above this value, further increases in the thickness are very time consuming.

Models in which the resistance of both media to flow is taken into account have been developed more recently (38,39). The capillary suction pressure p is given by

$$p = \Delta p_c + \Delta p_m \quad (6.10)$$

where Δp_c and Δp_m are the hydraulic pressure drops in the cast and in the mold, respectively (Fig. 6.34). If η_L , V_c , V_s , K_c , and the porosity P_m and permeability K_m of the mold do not change with time, the pressure drops Δp_c and Δp_m are linear. The flux of the liquid must be the same in the cast and in the mold; so for this case

$$J = \frac{K_c}{\eta_L L_c} \Delta p_c = \frac{K_m}{\eta_L L_m} \Delta p_m \quad (6.11)$$

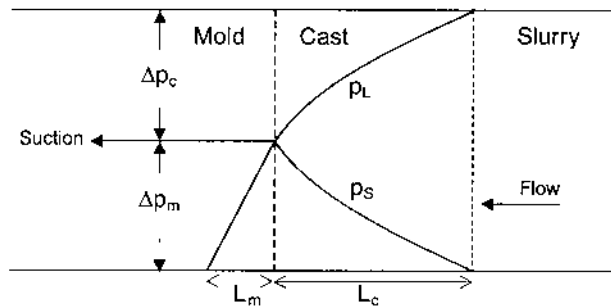


FIGURE 6.34 Hydraulic pressure distribution across the cast and the mold in slip casting.

where L_c is the thickness of the cast and L_m is the thickness of the mold saturated with liquid. Integration of Eq. (6.11) subject to the appropriate boundary conditions also gives a parabolic equation (39):

$$L_c^2 = \frac{2Hpt}{\eta_L} \quad (6.12)$$

where the function H depends on the properties of both the cast and the mold and is given by

$$H = \left[\left(\frac{V_c}{V_s} - 1 \right) \left(\frac{1}{K_c} + \frac{V_c/V_s - 1}{P_m K_m} \right) \right]^{-1} \quad (6.13)$$

When the resistance to liquid flow in the mold can be neglected, Eq. (6.9) is recovered from Eqs. (6.12) and (6.13). This situation applies when the term $(V_c/V_s - 1)/P_m K_m$ in Eq. (6.13) is very small compared to the term $1/K_c$, i.e., when

$$\frac{K_c (V_c/V_s - 1)}{P_m K_m} \ll 1 \quad (6.14)$$

According to Eq. (6.14), the hydraulic resistance of the mold can be neglected when the mold porosity P_m is high, the volume fraction of solids in the slurry V_s is high, and the ratio of the cast permeability to the mold permeability K_c/K_m is high.

Effect of Permeability of the Cast

For a given system, Eq. (6.9) predicts that the rate of consolidation increases with an increase in the permeability of the cast K_c . Various models have been put forward to account for the permeability of porous media. One of the most popular, based on its simplicity and its ability to outline the key parameters, is the *Carman-Kozeny* equation:

$$K = \frac{P^3}{\alpha(1-P)^2 S^2 \rho_s^2} \quad (6.15)$$

where P is the porosity, S is the specific surface area (i.e., per unit mass of the solid phase), ρ_s is the density of the solid phase, and α is a constant (equal to 5 for many systems) that defines the shape and tortuosity of the channels. For a cast consisting of spherical, monodisperse particles with a diameter D , the permeability can be expressed as

$$K_c = \frac{D^2 (1 - V_c)^3}{180 V_c^2} \quad (6.16)$$

It is clear that in order to increase K_c , we should increase D or reduce V_c . For advanced ceramics, an increase in D may not be desirable because this leads to a rapid decrease in the sintering rate. On the other hand, varying V_c can provide an effective method for controlling the consolidation rate. As discussed in Chapter 4, this can be achieved by controlling the colloidal stability of the slurry.

Effect of Mold Parameters

Equations (6.9) and (6.12) indicate that the consolidation rate increases with the capillary suction pressure p of the mold. If there were no other effects, an increase in p would always lead to a shorter time for a given thickness of the cast. The capillary suction pressure varies inversely as the pore radius of the mold, and it may be thought that a decrease in the pore radius would lead to an increase in the casting rate. However, the permeability of the mold K_m also decreases with a decrease in the pore radius of the mold, so there should be an optimum pore size to give the maximum rate of casting (39).

Effect of Slurry Parameters

The colloidal stability of the slurry has the strongest influence on the microstructure of the cast. A flocculated slurry leads to a cast with a fairly high porosity. Moreover, in this case, the effective pressure in the cast (p_s in Fig. 6.34) decreases rapidly and nonlinearly from the mold–cast interface. The compressible nature of the highly porous cast coupled with the variation in p_s leads to a rapid reduction in the density of the cast as it builds up and to an almost constant high porosity region in the bulk of the cast (37). Heterogeneities in the green body microstructure, as we will recall, hinder microstructural control during the firing process. A well dispersed slip containing no agglomerates and stabilized by electrostatic or steric repulsion leads to the formation of a fairly dense cast with better microstructural uniformity. In practice, the fairly dense cast formed from a well-dispersed slip has a low permeability, and the rate of casting is therefore low. For industrial operations where such low casting rates are uneconomical, the slip is only partially deflocculated.

Equation (6.9) indicates that the consolidation rate increases with the solids concentration of the slurry V_s . For monodisperse particles, V_s is not expected to have a significant effect on the resulting green density of the cast. In the case of a wide distribution of particle sizes, however, the effect of V_s on the green density is somewhat more complex. When V_s is low, a reduction in the green density may be expected if the sedimentation rate of the particles is significant compared to the casting rate, leading to segregation of particles of different size. For more concentrated suspensions, the sedimentation rate is diminished significantly, and high green densities can be achieved if the fine particles fill the interstices between the large.

Other parameters such as the size, size distribution, and shape of the particles can also influence the compressibility and, hence, the packing density of the cast. Figure 6.35 summarizes the effects of particle size, particle shape, and the degree of flocculation of the slurry on the packing density of the cast. For fairly coarse particles (greater than $\sim 10\text{--}20\text{ }\mu\text{m}$), colloidal effects are insignificant and the degree of dispersion of the particles has no effect on the packing density. Large spheres of the same size produce casts with a packing density of $\sim 0.60\text{--}0.65$, close to that for dense random packing whereas irregular particles produce casts with a lower packing density. As the particle size decreases below $\sim 10\text{ }\mu\text{m}$, colloidal effects control the packing density. At one extreme, well-dispersed slips produce casts with high packing density while at the other extreme, flocculated slips yield a low packing density. As outlined above, particles with a distribution in sizes may produce casts with a packing density that is higher than that for monodisperse particles if segregation does not take place.

The rate of consolidation also increases with a decrease in the viscosity of the filtrate η_L [Eq. (6.9)]. A reduction in η_L is achieved by increasing the temperature of the slurry or, in a less practical way, by using a liquid with a lower viscosity. For aqueous slips, an increase in the temperature improves the stability of the slip and leads to a cast with a higher packing density. This decreases the consolidation rate because the permeability of the cast K_c decreases. However,

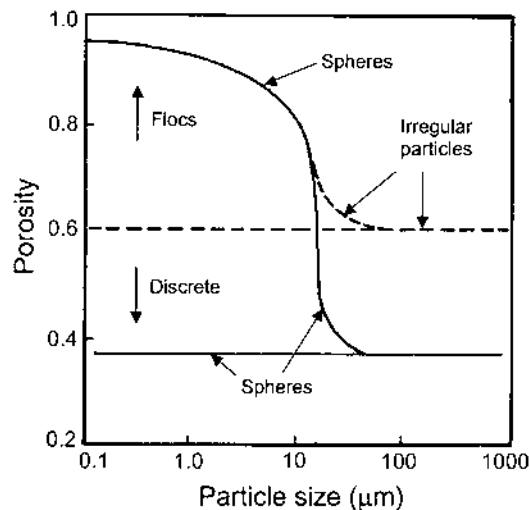


FIGURE 6.35 Schematic diagram showing the effects of particle size, shape, and degree of flocculation on the porosity of the cast produced in slip casting. (From Ref. 39.)

the reduction in η_L with increasing temperature has a far greater effect, and the overall result is an increase in the casting rate.

Microstructural Defects in Slip-Cast Green Bodies

Several types of microstructural defects can be present in green articles formed by slip casting. They arise during the casting operation and are generally related to the properties of the slurry. *Large voids* due to air bubbles in the slurry are a common occurrence. They can be avoided by improving the wetting characteristics of the particles by the liquid, proper de-airing of the slurry, and the avoidance of turbulent flow of the slurry during the casting operation. Elongated (anisometric) particles can be *preferentially aligned* along certain directions, usually parallel to the mold surface. *Segregation*, in which the larger particles settle faster than the smaller, can be alleviated by improving the colloidal stability of the slurry.

6.4.2.2 Pressure Casting

Equation (6.9) indicates that for a given slurry, as the filtration pressure p increases, the time taken to produce a given thickness of cast L decreases. The casting can therefore be speeded up by the application of an external pressure to the slurry. This is the principle of *pressure casting*, also referred to as *pressure filtration* or *filter pressing*. The plaster of Paris molds used in slip casting are, however, weak and cannot withstand pressures greater than ~ 0.5 MPa; so plastic or metal molds must commonly be used in pressure casting.

A schematic of the main features of a laboratory scale pressure casting device is shown in Fig. 6.36. Particles in the slurry form a consolidated layer (the cast) on the filter as the liquid is forced through the system. The cast provides a much greater resistance to flow of the liquid when compared to the filter, so the kinetics of pressure casting can be described by Eq. (6.9).

The kinetics and mechanics of pressure casting have been studied by Fennelly and Reed (40) and more recently by Lange and Miller (41). As observed for slip casting, the colloidal stability of the slurry has the strongest influence on the microstructure of the cast. Figure 6.37 shows that the highest packing density is obtained with well-dispersed slurries and for these slurries the packing density obtained is independent of the applied pressure above ~ 0.5 MPa. Dynamic models for particle packing which incorporate rearrangement processes have not been developed so far. However, the high packing densities obtained with dispersed slurries at such low applied pressures indicate that the repulsive forces between the particles must facilitate rearrangement. For flocculated slurries, the packing density is dependent on the applied pressure, and the approximate linear relationship between the relative density and the logarithm of the applied pressure shows the same trend observed earlier for the die compaction of dry powders.

Problems have been observed with pressure-cast bodies of advanced ceramics produced from either a dispersed or a flocculated slurry. As the last portion

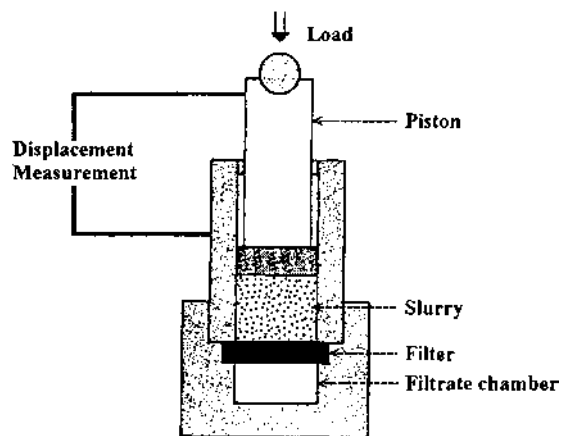


FIGURE 6.36 A laboratory-scale pressure casting apparatus.

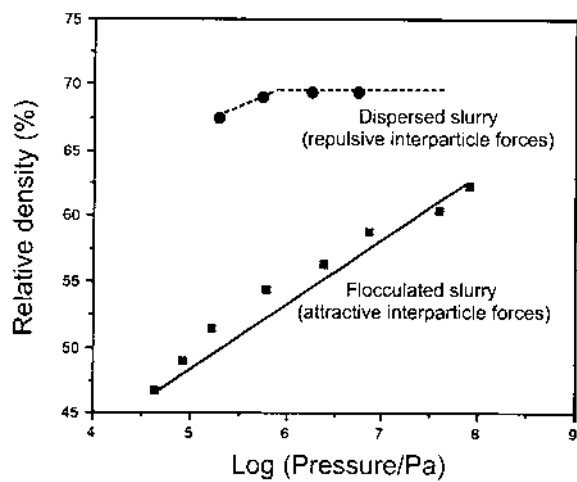


FIGURE 6.37 Relative density of different bodies produced from the same Al_2O_3 powder by filtration at different applied pressures. Bodies were consolidated from either dispersed ($\text{pH} = 2$) or flocculated ($\text{pH} = 8$) aqueous slurries containing 20 vol % solids. (From Ref. 3.)

of the slurry is consolidated during pressure casting, the pressure gradient across the cast becomes zero, and the total applied pressure is transferred onto the cast. On removal of the applied pressure, the cast expands, i.e., undergoes strain recovery, due to the stored elastic energy. The nature of the strain recovery is, however, different from that observed in the die compaction of dry powders. The strain recovery for compacts produced by pressure casting is time dependent. This phenomenon of time dependent strain recovery arises because fluid (liquid or gas) must flow into the compact to allow the particle network to expand and relieve the stored strain. The magnitude of the recovered strain increases with increasing consolidation pressure in a nonlinear manner and can be described by a Hertzian elastic stress-strain relation of the form

$$p = \beta \epsilon^{3/2} \quad (6.17)$$

where p is the stress, ϵ is the strain, and β is constant for a given particulate system. For Al_2O_3 , the recovered strain can be fairly large (2–3%) for moderately low pressures in the range 50–100 MPa. A consequence of the fairly large strain recovery is the tendency for cracking to occur in the compact. This can be relieved to some extent by reducing consolidation pressure and by using a small amount of binder (<2 wt %). None of these problems have been reported for pressure-cast clay-based bodies, presumably because of the significant plasticity of the green bodies.

Compared to slip casting, pressure casting offers the advantages of greater productivity through shorter consolidation times and the requirement of a smaller amount of floor space for setting up the molds. However, the pressure casting molds are more expensive. Slip casting will remain an important forming method for ceramics, but the trend is towards increasing use of pressure casting, particularly for fine powders of advanced ceramics.

6.4.2.3 Tape Casting

The principles and practice of tape casting are covered in a recent text (42) and the process also forms the subject of several review articles (43–46). In tape casting, sometimes referred to as the *doctor-blade process*, the slurry is spread over a surface covered with a removable sheet of paper or plastic using a carefully controlled blade referred to as a doctor blade. For the production of long tapes, the blade is stationary and the surface moves (Fig. 6.38), whereas for the production of short tapes in the laboratory, the blade is pulled over a stationary surface. Drying occurs by evaporation of the solvent to produce a tape, which adheres to the carrier surface, consisting of particles bonded by the polymeric additives. The flexible green tape can be stored on take-up reels or stripped from the carrier surface and cut into the desired lengths for subsequent operations. Sheets with thicknesses from as low as 10 μm to as thick as 1 mm are prepared by tape

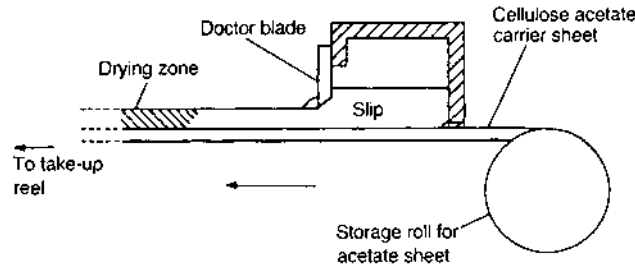


FIGURE 6.38 Schematic diagram of the tape casting process.

casting. The steps in the production of an MgO-doped Al_2O_3 component by tape casting are summarized in Fig. 6.39.

Slurry (Slip) Preparation

The preparation of the slurry is a critical step in the tape casting process. The factors that govern the selection of solvent, dispersant, binder, plasticizer, and other additives were described earlier in this chapter. Most tape casting operations currently use organic solvents, but the trend is towards aqueous-based systems. Other considerations in the selection of a solvent are the thickness of the tape to be cast and the surface on which the cast is to be made. Thin tapes are cast from highly volatile solvent systems (e.g., acetone or methyl ethyl ketone), whereas

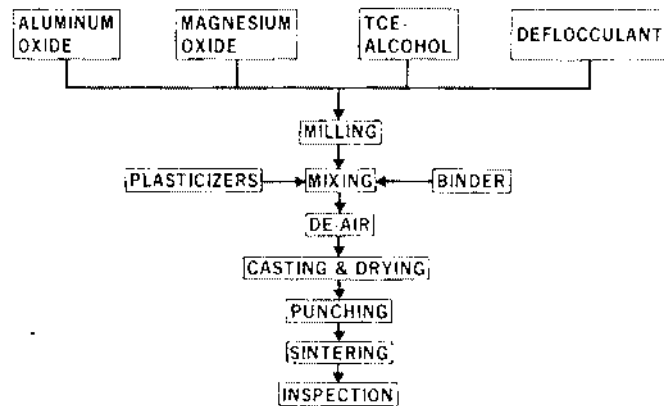


FIGURE 6.39 Schematic flow diagram for the tape casting of an alumina substrate material.

thicker tapes (>0.25 mm) have to be cast from slower drying solvents (e.g., toluene).

The dispersant may be the most important organic additive in that it serves to lower the viscosity of the slurry, thereby allowing the use of a high particle concentration. Another important selection to be made is that of the binder–plasticizer combination because the concentration used in tape casting slurries is high. It must provide the required strength and flexibility of the green tape and must also be easily burnt out prior to sintering of the tape. Many organic systems can easily satisfy this criterion if the binder burnout process is carried out in an oxidizing atmosphere at reasonably high temperatures. However, several ceramic systems require the use of a binder–plasticizer system that can be removed in a nonoxidizing atmosphere. Typical slurry formulations for tape casting are given in Table 6.10.

The Tape Casting Process

As illustrated in Fig. 6.38, the key component of the tape casting equipment is the doctor blade assembly. It consists of an adjustable doctor blade mounted in a frame with a reservoir to hold the slurry (or slip) before it is metered out under the blade to form the thin layer of slurry on the carrier surface. The flow behavior of the slurry during the casting of the tape has been analyzed theoretically to estimate the influence of the casting parameters on the thickness of the tape (47).

TABLE 6.10 Examples of Tape-Casting Compositions (Concentration in wt%)

Powder	Solvent	Binder	Plasticizer	Dispersant	Other additives
Nonaqueous formulation for use in oxidizing atmospheres					
Al ₂ O ₃ (59.5)	Ethanol (8.9)	PVB (2.4)	Octylphthalate (2.2)	Fish oil (1.0)	
MgO (0.1)	TCE (23.2)		PEG (2.6)		
Nonaqueous formulation for use in nonoxidizing atmospheres					
BaTiO ₃ (69.9)	MEK (7.0)	30 wt% solution of acrylic in MEK (9.3)	PEG (2.8) Butyl benzyl phthalate (2.8)	Fish oil (0.7)	Cyclohexanone (homogenizer) (0.5)
Aqueous formulation					
Al ₂ O ₃ (69.0)	Deionized water (14.4)	Acrylic emulsion (cross-linkable) (6.9)	Acrylic emulsion (low T_g) (9.0)	Ammonium polyacrylate (0.6)	Poly (oxyalkylene- diamine) (0.1)

Source: Refs. 42, 44, and 45.

Assuming a Newtonian viscous slurry and laminar flow in a simple casting unit (Fig. 6.40), the thickness of the dry tape, h_d is given by

$$h_d = \frac{\alpha\beta}{2} \frac{\rho_w}{\rho_d} h_o \left(1 + \frac{h_o^2 \Delta p}{6\eta UL} \right) \quad (6.18)$$

where α (<1) and β (<1) are correction factors, ρ_w and ρ_d are the densities of the slurry and the dry tape, respectively, h_o and L are the height and thickness of the doctor blade, respectively, Δp is the pressure difference (determined by the height of the slurry in the reservoir), η is the viscosity of the slurry, and U is the velocity of the doctor blade relative to the casting surface.

According to Eq. (6.18), the thickness of the dried tape would simply be proportional to the height h_o of the doctor blade if the second term in the brackets is much smaller than unity. For values of h_o smaller than $\sim 200 \mu\text{m}$, this can be achieved if the parameters η , U , L , and Δp are kept within certain ranges. Large values of h_o can lead to significant deviations from this simple relationship. The effect is more pronounced for small values of η , U , and L . A knife-edged doctor blade (very small value of L) appears to be unsuitable for tape-casting. While a variety of blade designs and shapes are used in the tape casting sector, a flat-bottomed doctor blade is effective practically and has some theoretical support based on Eq. (6.18). A double doctor blade is often found to be useful when a uniform thickness must be maintained over a long length of tape.

In practice, the casting speed is largely determined by the type of casting process: continuous or batch. For a continuous process, the speed is determined by the length of the casting machine, the thickness of the tape, and the volatility of the solvent. Typical casting speeds can vary from 15 cm/min for a continuous process to 50 cm/min for a batch process. Several carrier surfaces have been used in tape casting, ranging from glass plates in laboratory machines employing a moving doctor blade to polyester and coated polyester carriers in continuous industrial machines. The type of carrier surface to be used is determined by the

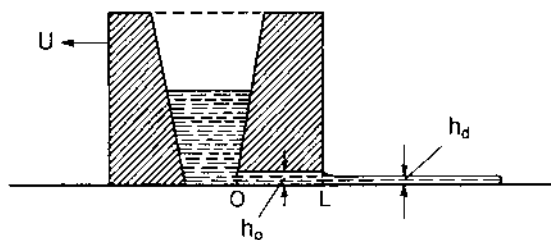


FIGURE 6.40 Section of a tape casting unit.

interaction of the solvent–binder system with the carrier surface and by how well the dried tape can be peeled off.

Drying occurs by evaporation of the solvent from the surface and the tape adheres to the carrier surface, so the shrinkage during drying occurs in the thickness of the tape. Typically, the dried tape has a thickness equal to approximately half the doctor blade height and consists of approximately 50 vol% ceramic particles, 30 vol% organic additives, and 20 vol% porosity. Despite the relatively low density of the tape after binder burnout, the fired tape can reach nearly full density. However, the binder burnout step can provide significant difficulties due to the large amount of organic additives that must be removed. Drying of granular ceramics and binder burnout are considered later in this chapter.

Microstructural Defects in Green Tapes

The main types of microstructural defects in green tapes are similar to those outlined earlier for slip-cast bodies. *Large voids* are caused by air bubbles in the slurry or by rapid evaporation of the liquid during drying and can be avoided by proper de-airing of the slurry or controlling the drying rate. *Segregation* due to differential settling of particles with different sizes is not a severe problem unless the tape is thick, the rate of drying is slow, or the colloidal stability of the slurry is poor. Because of the high concentration of binder in the slurry, binder segregation to the surface of the tape during drying can lead to a gradient in the packing density. The effect of particle or binder segregation is to produce warping (or even cracking) of the tape during sintering. If the particles in the slurry are elongated (anisometric), flow under the doctor blade produces *preferential alignment* of the particles along the direction of flow. As outlined later (Chapter 9), this effect can be used to produce ceramics with aligned microstructures. However, it is undesirable in tapes for electronic applications because the resulting anisotropic shrinkage during sintering makes it difficult to achieve the normally required small dimensional tolerances.

6.4.2.4 Gel Casting

Gel casting is a recently introduced process that is based on ideas taken from the traditional ceramics industry and the polymer industry (48–51). As summarized in Fig. 6.41, a slurry of ceramic particles dispersed in a monomer solution is poured into a mold, and the monomer is polymerized to immobilize the particles and to form a gel-like bonding phase (i.e., a binder). The system is removed from the mold while still wet, dried by evaporation of the liquid, heated to burn out the organic additives, and finally sintered.

Gel casting commonly employs aqueous solvents (although organic solvents can also be used), dispersants, and processing methods (e.g., ball milling) similar to those used in traditional slip casting to produce the commonly desired slurry properties for casting: stability against flocculation, high particle concentra-

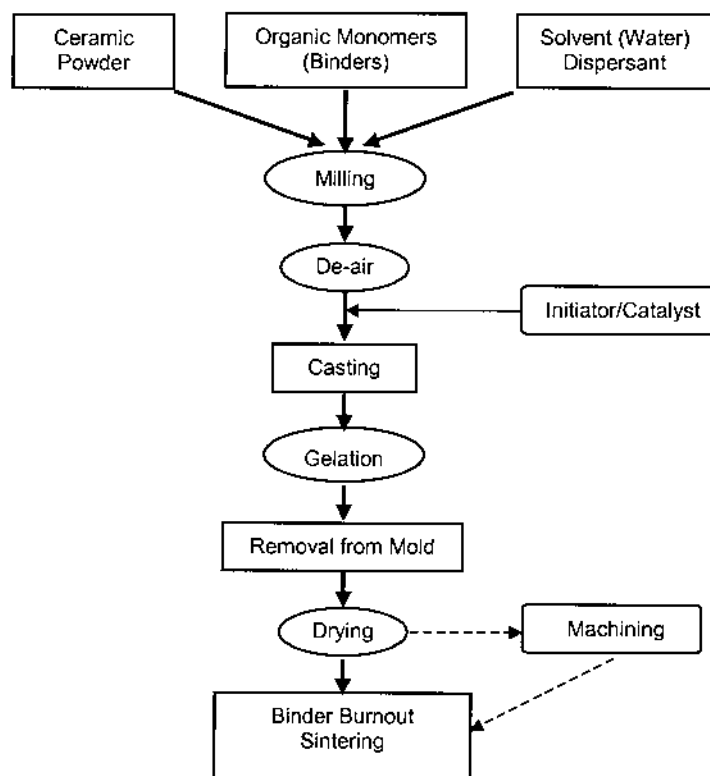


FIGURE 6.41 Schematic flow diagram of the gel casting process.

tion (~ 50 vol% for gel casting), and a low viscosity. The key element of the process is the addition of an organic monomer to the solution which is polymerized in situ to form a strong, cross-linked gel. In addition to preventing segregation or settling of the particles, the gel provides strength to the body to withstand capillary stresses during drying so that thick as well as thin parts can be formed. There is only 2–4 wt% of polymeric material in the dried body, a value that is comparable to the amount of organic additives in die-pressed bodies formed from spray-dried granules and in slip-cast bodies, so binder burnout is not normally a limiting step.

Monomers and Polymerization

The monomer solution consists of the solvent (commonly water), a chain-forming monomer, a chain-branching (cross-linking) monomer, and a free radical initiator.

Commonly used chain formers are methacrylamide (MAM), hydroxymethacrylamide (HMAM), N-vinyl pyrrolidone (NVP), and methoxy poly(ethylene glycol) monomethacrylate (MPEGMA). Sometimes two monomers may be used in combination (e.g., MAM and NVP, or MPEGMA and HMAM). The cross-linkers commonly used are methylene bisacrylamide (MBAM) and poly(ethylene glycol) dimethacrylate (PEGDMA). The free radical initiator used most often is ammonium persulfate (APS) with tetramethylethylenediamine (TEMED) used as a catalyst.

The choice of the monomer system depends on several factors, such as the reactivity of the system (including the reaction temperature), the strength, stiffness and toughness of the gel, and the strength and machinability of the green body. One system used for several ceramics is MAM-MBAM in which the total monomer concentration in the solution is 10–20 wt% and the MAM to MBAM ratio is 2–6. Another system is MAM-PEGDMA in which the monomer concentration is also 10–20 wt% but the MAM to PEGDMA ratio is 1–3. Examples of gel casting compositions are given in Table 6.11.

The formation of the gel occurs in two stages: initiation and polymerization. In the initiation stage, the viscosity does not change and no heat is generated. The addition of the initiator at room temperature allows a reasonable time (30–120 min) for de-airing of the slurry and mold filling. The polymerization step is often conducted at an elevated temperature (40–80°C), and the faster reaction rate produces gelation in a short time. Because the reaction is exothermic, its progress can be followed by monitoring the temperature of the system.

Mold Materials

The commonly used mold materials for gelcasting are aluminum, glass, polyvinylchloride, polystyrene, and polyethylene. Aluminum and especially anodized alu-

TABLE 6.11 Examples of Compositions for Gel Casting

Ceramic powder ^a	Dispersant	Monomer solution ^c	Initiator
Al ₂ O ₃	Ammonium polyacrylate ^b	MAM-MBAM or MAM-PEGDMA	APS/TEMED
Si ₃ N ₄	Poly(acrylic acid) ^b	MAM-MBAM or MAM-PEGDMA	APS/TEMED
SiC	Tetramethyl ammonium hydroxide (pH > 11)	MAM-MBAM or MAM-PEGDMA	APS/TEMED

^aApproximately 50 vol%;

^b0.5–2 vol%;

^cApproximately 50 vol% (monomer concentration in the solution = 10–20 wt%); MAM-MBAM ratio = 2–6; MAM-PEGDMA ratio = 1–3.

Source: Refs. 50, 51.

minum are used widely for permanent production molds, while glass and the polymeric materials are useful for laboratory experiments. The gel-casting system can react with the contact surfaces of the mold so the mold surfaces are often coated with mold release agents, such as the commercial mold releases employed in the polymer processing industry.

6.4.2.5 Electrophoretic Deposition

The method of electrophoretic deposition (EPD) is shown schematically in Fig. 6.42. A dc electric field causes the charged particles in a colloidal suspension to move toward and deposit on the oppositely charged electrode. EPD involves a combination of electrophoresis (described in Chapter 4) and particle deposition on the electrode. Successful EPD to form a deposit with high packing density requires a stable suspension. Agglomerated particles in an unstable suspension move toward the oppositely charged electrode and form a low-density deposit. Therefore, an understanding of colloidal interactions in a suspension (Chapter 4) is important to EPD.

A recent review of EPD discusses the mechanisms and kinetics of the deposition process and includes a detailed list of references to the application of EPD to ceramics (52). EPD is a facile forming technique that has the additional

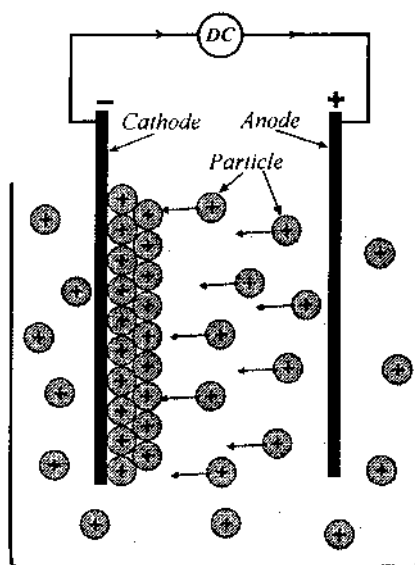


FIGURE 6.42 Schematic drawing of an electrophoretic deposition cell showing the process.

benefit of controllability because the rate and extent of deposition are manipulated electrically. It is best used for depositing coatings and thin objects.

Kinetics and Mechanisms of Deposition

Whereas electrophoresis is well understood, the deposition mechanism of the particles on the electrode has been the subject of much controversy, and several explanations have been put forward to explain the phenomenon. A recent explanation given in Ref. 52 is illustrated in Fig. 6.43. As a positively charged oxide particle with its surrounding double layer of counterions (the *lyosphere*) moves towards the cathode in an EPD cell, the electric field coupled with motion of the charged particle through the liquid causes a distortion of the double-layer envelope: the envelope becomes thinner ahead of and thicker behind the particle. Compared to a particle far away from the electrode, the ζ -potential is greater for the leading hemisphere of the particle and smaller for the trailing hemisphere. Cations in the liquid also move to the cathode with the positively charged particles. The counterions in the trailing lyosphere tails tend to react with the high concentration of cations surrounding them, leading to a thinning of the double layer around the trailing surface of the particle. The next incoming particle, which has a thin double layer around the leading surface, can approach close enough so that van der Waals attractive forces dominate. The result is coagulation and deposition on the electrode.

The kinetics of EPD is important for controlling the thickness of the deposited layer. There are two modes of operating the system. In *constant-voltage* EPD, the voltage between the electrodes is maintained constant. Because deposition requires a steeper electric field than electrophoresis, as the deposition thickness (and consequently the electrical resistance) increases, the electric field decreases. The particle motion and, hence, the rate of deposition decreases. Under *constant-current* EPD, on the other hand, the electric field is maintained constant by increasing the total potential difference between the electrodes, so the limited deposition in constant-voltage EPD is avoided.

Assuming that the suspension is homogeneous and the change in concentration is due to EDP only, the mass of particles m deposited on the electrode is equal to that removed from the suspension; therefore,

$$\frac{dm}{dt} = AvC \quad (6.19)$$

where A is the area of the electrode, v is the velocity of the particle, C is the concentration of particles in the suspension, and t is the deposition time. For a concentrated suspension, the velocity of the particles is given by the Helmholtz-Smoluchowski equation (Chapter 4):

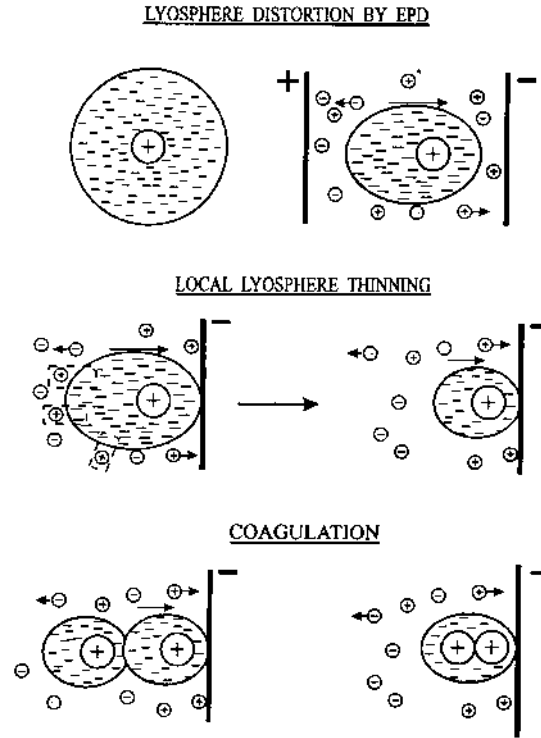


FIGURE 6.43 Schematic illustration of the electrophoretic deposition mechanism by lyosphere distortion and thinning. (From Ref. 52.)

$$v = \frac{\epsilon \epsilon_0 \zeta E}{\eta} \quad (6.20)$$

where ϵ is the dielectric constant of the liquid, ϵ_0 is the permittivity of free space, ζ is the zeta-potential of the particles, E is the applied electric intensity, and η is the viscosity of the liquid. If m_0 is the initial mass of the particles in the suspension, then

$$m = m_0 - VC \quad (6.21)$$

where V is the volume of the suspension. Combining Eqs. (6.19) and (6.20) subject to the boundary condition of Eq. (6.21), we get

$$m = m_0 (1 - e^{-at}) \quad (6.22)$$

$$\frac{dm}{dt} = m_0 \alpha e^{-\alpha t} \quad (6.23)$$

where $\alpha = Av/V$. According to Eq. (6.23), the rate of deposition decreases exponentially with time and is controlled by the parameter α .

6.4.3 Plastic Forming Methods

Plastic deformation of a moldable powder–additive mixture is employed in several forming methods for ceramics. *Extrusion* of a moist clay–water mixture is used extensively in the traditional ceramics sector for forming components with a regular cross section (e.g., solid and hollow cylinders, tiles, and bricks). The method is also used to form some oxide ceramics for advanced applications (e.g., catalyst supports, capacitor tubes and electrical insulators). A recent development is the repeated *co-extrusion* of a particle-filled thermoplastic polymer to produce textured microstructures or fine-scale structures. *Injection molding* of a ceramic–polymer mixture is a potentially useful method for the mass production of small ceramic articles with complex shapes. However, the method has not yet materialized into a significant forming process for ceramics mainly because of two factors:

1. High tooling costs relative to other common forming methods.
2. Removal of the high concentration of binder prior to sintering remains a limiting step for thicknesses greater than ~ 1 cm.

The application of extrusion and injection molding to the forming of ceramic powders has benefited considerably from the principles and technology developed in the plastics industry. Extruders and molding machines used in the plastics industry are employed but some modification of the machines is required for ceramic systems (e.g., hardening of the contact surfaces).

Two basic requirements must be satisfied for plastic forming to be successful:

1. The mixture must flow plastically (above a certain yield stress) for the formation of the desired shape.
2. The shaped article must be strong enough to resist deformation under the force of gravity or under stresses associated with handling.

The selection of additives and the formulation of the mixture are critical steps in meeting these requirements.

6.4.3.1 Extrusion

In extrusion, a powder mixture in the form of a stiff paste is compacted and shaped by forcing it through a nozzle in a piston extruder or a screw-fed extruder

(53). The piston extruder is simple in design, consisting of a barrel, a piston, and a die. In contrast, as illustrated by Fig. 6.44, the screw extruder is complex, and considerable attention goes into the design of the extruder barrel and screw (54). The screw has to mix the powder and other additives into a homogeneous mass and generate enough pressure to transport the mixture against the resistance of the die. Shaping of the extruded body is achieved with the head of the extruder screw and the die. The extruder screw head changes the rotational flow of the mixture produced by the screw into an axial flow for extrusion and to produce uniform flow in the die. In the release of the body from the extruder, the die must generate the required cross section, allow uniform flow across the entire cross section, and ensure a smooth surface.

The main approaches for imparting the required plastic properties to the feed material are (1) manipulating the characteristics of the powder–water system, commonly used for clays and (2) adding a binder solution to the powder, commonly used for advanced ceramics. Clay particles develop desirable plastic characteristics when mixed with a controlled amount of water (15–30 wt% depending on the type of clay). The plasticity arises from two main factors: (1) particle to particle bonding due to the charged particle surfaces and intervening charges (“house of cards” structure described in Chapter 4) and (2) surface tension effects due to the presence of water. Surface charge and surface tension do not play a significant role in coarse ceramic powders, but some degree of plasticity may be

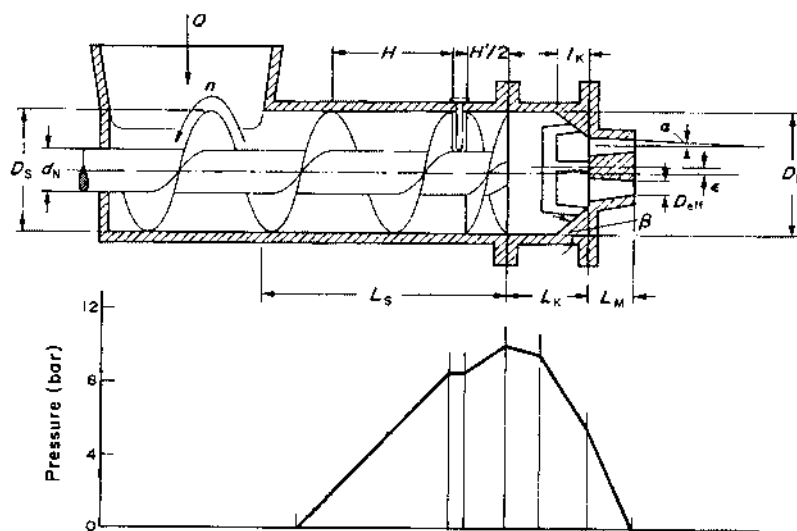


FIGURE 6.44 Pressure variation along a screw extrusion press. (From Ref. 54.)

developed by adding fine particles (such as clay or boehmite) provided that they are chemically compatible with the coarse powder.

The powders of advanced ceramics, when mixed with water, do not possess the desirable plastic characteristics found in the clay–water system. For this reason, they are mixed with a viscous solution containing a few weight percent of an organic binder to provide the desired plastic characteristics. The solvent is commonly water, but nonaqueous solvents (e.g., alcohols; mineral spirits) can also be used. Since the extruded body must also have sufficient green strength, the binder is generally selected from the medium to high viscosity grades, e.g., methylcellulose, hydroxyethyl cellulose, poly(acrylimides), or poly(vinyl alcohol). Methylcellulose undergoes *thermal gelation*, a property that offers considerable benefits for extrusion of ceramics (55).

Examples of compositions used in extrusion are given in Table 6.12. Aqueous systems are often flocculated using a small concentration of an additive (such as MgCl_2 , AlCl_3 , or MgSO_4). In addition, lubricants (e.g., stearates, silicones, or petroleum oils) are commonly used to reduce die-wall friction.

Extrusion Mechanics

The flow pattern of the feed material through the extruder influences the quality of the shaped article. The rheology of concentrated ceramic suspensions can be divided into four classes: ideal plastic, Bingham, shear thinning, and shear thickening (see Chapter 4). Bingham-type behavior is widely observed and forms a useful approximation for theoretical analysis (56,57). A characteristic feature of the velocity profile is the occurrence of *differential flow* with a central plug (Fig. 6.45). The velocity is constant with radius in the central plug but decreases with radius between the central plug and the inner wall of the tube. In more

TABLE 6.12 Examples of Compositions Used in Extrusion

Whiteware		Alumina	
Material	Concentration (vol %)	Material	Concentration (vol %)
Kaolin	16	Alumina	45–50
Ball clay	16	Water	40–45
Quartz	16	Ammonium polyacrylate (dispersant)	1–2
Feldspar	16	Methyl cellulose (binder)	5
Water	36	Glycerin (plasticizer)	1
CaCl_2 (flocculant)	<1	Ammonium stearate (lubricant)	1

extreme situations, *slippage flow* or *complete plug flow* can occur in which the velocity of the material through the extruder is independent of the radius of the tube.

Extrusion Defects

A variety of defects can occur in the extruded body (58). The common *macroscopic defects* are laminations, tearing, and segregation (Fig. 6.46). Laminations are cracks that generally form a pattern or orientation, particularly in a screw-fed extruder, because of incomplete re-knitting of the feed material around the auger. Tearing consists of surface cracks that form as the material leaves the die and is caused by poor die design or by low plasticity of the mixture. Segregation involves separation of the liquid and the solid phases of the mixture during extrusion and is often caused by poor mixing. *Microscopic defects* such as pores (caused by trapped air) and inclusions (due to contamination) can also occur.

6.4.3.2 Co-extrusion

A method based on repeated co-extrusion of a powder-filled thermoplastic polymer has been developed recently to form ceramics with a textured microstructure (59) or with fine-scale features (60). A schematic of the method is shown in Fig. 6.47. A mixture of ceramic particles (e.g., Al_2O_3), thermoplastic polymer (e.g., ethylene vinyl acetate), and processing aid (e.g., low molecular weight polyethylene glycol as a plasticizer) containing ~ 50 vol% particles is formed into a rodlike feed material (the feed rod) with the required arrangement of the ceramic phase by extrusion in a piston extruder or by lamination. Extrusion of the feed rod,

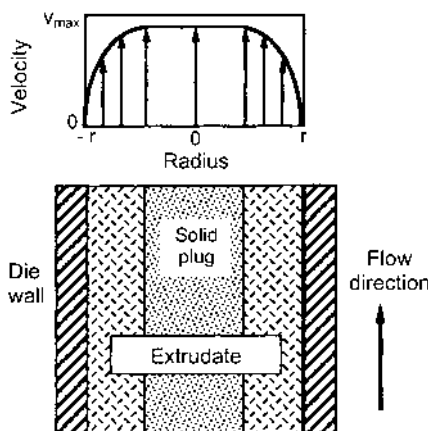


FIGURE 6.45 Differential flow with a central plug commonly observed in extrusion.

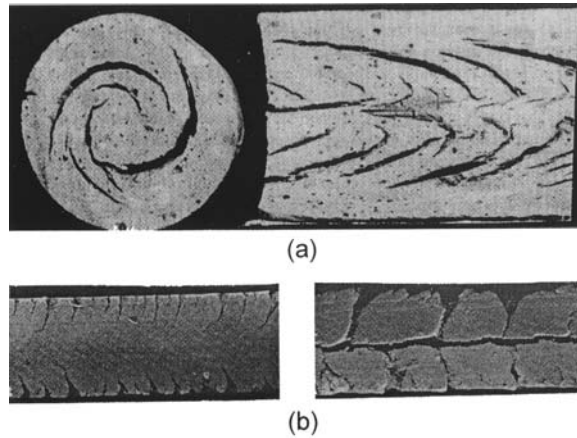


FIGURE 6.46 Typical defects observed in extrusion: (a) lamination cracks in longitudinal (left) and transverse (right) section; (b) edge tearing. (From Ref. 58.)

commonly at temperatures in the range of 100–150°C, through a die in a piston extruder produces an extrudate with a smaller cross section (e.g., a diameter that is ~ 5 times smaller than the diameter of the feed rod), and with a corresponding reduction in the scale of the structural features. The material produced after the first extrusion is cut into suitable lengths and reassembled to form a new feed rod. After repeated extrusion, an extrudate with the required small-scale structural features is produced.

A requirement for successful co-extrusion is the control of the rheological properties of the feed material and of the extrusion parameters to produce an extrudate with the required uniformity of structural features. After the final extru-

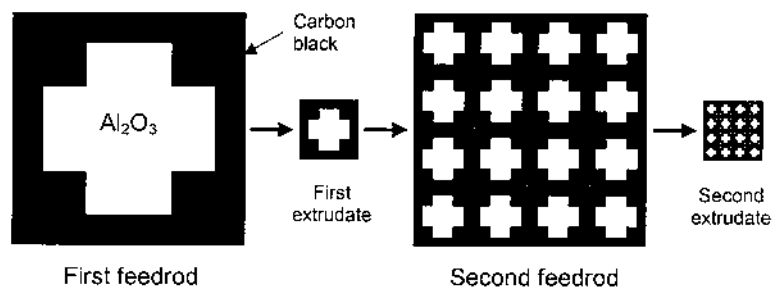


FIGURE 6.47 Illustration of the formation of fine-scale features by co-extrusion.

sion, the extrudate is compacted into the required shape, heated to decompose the binder and other additives, and sintered to produce the final article.

6.4.3.3 Injection Molding

Two recent texts cover the principles and practice of injection molding of metals and ceramics (61,62). The subject is also considered in several review articles (63–65). The production of a ceramic article by injection molding involves the following steps: selection of the powder and the binder; mixing the powder with the binder, production of a homogeneous feed material in the form of granules, injection molding of the green body, removal of the binder (debinding) at lower temperatures and, finally, sintering at higher temperatures to produce a dense, final article. The debinding step involves features that are common to other forming methods (e.g., tape casting) and is considered later in this chapter. Here, we shall consider the key factors in powder and binder selection, preparation of the feed material, and injection molding of the green body.

Powder Characteristics

When the forming step is considered in combination with other processing steps such as debinding and sintering, the desirable powder characteristics for injection molding are generally no different from those described in Chapter 2 for powder processing. A small *particle size* is beneficial for shape retention during debinding and for ease of sintering, but the viscosity of the powder/binder mixture is higher and binder removal from the molded article is slower. A wide *distribution of particle sizes* gives a higher packing density, higher green strength, and lower shrinkage during sintering. On the other hand, the rate of binder removal is slower, the system is prone to segregation, and microstructural evolution during sintering is inhomogeneous. A spherical (or equiaxial) *shape* leads to higher packing density, lower viscosity of the powder–binder mixture, and improved flow during forming but also produces a lower green strength and leads to slumping during binder removal. Generally, an equiaxial powder, free from agglomeration and having an average particle size smaller than 10 μm , a narrow or wide particle size distribution, and a packing density greater than $\sim 60\%$, is often suitable for most ceramic injection molding operations.

Binder System

Although the binder plays a transient role in the overall fabrication route, careful selection of a binder is vital to the success of the injection molding operation. The binder must provide the desired rheological properties to the feed material so that the powder can be formed into the desired shape and then must be removed completely from the shaped article prior to firing, without the disruption of the particle packing or any chemical reaction with the powder. A good binder must

therefore have desirable rheological, chemical, and debinding characteristics. In addition, it must possess many qualities suitable for manufacturing such as environmental safety and low cost.

A single binder cannot provide all the desirable characteristics and, in practice, the binder system is generally a blend of at least three components: a major binder, a minor binder, and a processing aid. The *major binder* controls the rheology of the feed material during injection molding to produce a body free from defects and also controls the strength of the green body and the debinding behavior. The *minor binder* is used to modify the flow properties of the feed material for good filling of the mold. It may also provide benefits in the debinding stage by extending the range of conditions over which the binder is removed. The removal of the minor binder (by dissolution or by pyrolysis) creates a network of porosity through which the decomposition products of the major binder can be removed more easily. The processing aid may include small concentrations of one or all of the following: a plasticizer to reduce the glass transition temperature of thermoplastic binders, a surfactant to improve the wetting between the particle surfaces and the polymer melt, and a lubricant to reduce interparticle and die-wall friction.

Many binder systems are used in ceramic injection molding, and they can be classified into five types, based on the composition of the major binder phase: (1) thermoplastic compounds, (2) thermosetting compounds, (3) water-based systems, (4) gelation systems, and (5) inorganics. Of these, the thermoplastic compounds are the most widely used and understood. They include most of the common commercial polymers, such as polystyrene, polyethylene, polypropylene, poly(vinyl acetate), and poly(methyl methacrylate). Examples of materials used for thermoplastic binder systems are given in Table 6.13.

Powder–Binder Mixture

The ratio of powder to binder is a key parameter for successful injection molding. Too little binder in the mixture leads to a high viscosity and to the formation of

TABLE 6.13 Thermoplastic Binder Systems for Ceramic Injection Molding

Major Binder	Minor binder	Plasticizer	Other additives
Polypropylene	Microcrystalline wax	Dimethyl phthalate	Stearic acid
Polyethylene	Paraffin wax	Diethyl phthalate	Oleic acid
Polystyrene	Carnauba wax	Dibutyl phthalate	Fish oil
Poly(vinyl acetate)		Dioctyl phthalate	Organo silane
Poly(methyl methacrylate)			Organo titanate

trapped air pockets, both of which make molding difficult. On the other hand, too much binder leads to microstructural heterogeneities in the molded article and to slumping during binder burnout.

If f_m is the maximum packing density of the particles, defined as the volume fraction at which the particles touch so that flow is not possible, then the actual particle volume fraction f used in injection molding is 5–10 vol% lower than f_m . The remainder of the mixture consists of the binder and other additives. This means that for a well-dispersed powder, the particles are separated from their neighbors by a thin layer of polymer (~ 50 nm thick) during molding, which is required to achieve flow of the mixture. The volume fraction of particles f incorporated into the binder therefore depends on the particle size distribution, the particle shape, and for particles finer than ~ 1 μm , on the particle size. For equiaxial particles greater than ~ 1 μm , f is the range 0.60–0.75.

The volume fraction of powder that can be reasonably incorporated into the mixture is best determined from viscosity measurements using a capillary rheometer over the range of conditions expected in the forming operation. Data for the relative viscosity (the viscosity of the mixture divided by the viscosity of the unfilled polymer) versus particle concentration can be well fitted by the equation (66)

$$\eta_r = \left(\frac{1 - 0.25 f/f_m}{1 - f/f_m} \right)^2 \quad (6.24)$$

Inhomogeneous mixing and incomplete breakdown of the powder agglomerates influence the viscosity and provide serious problems in the molding step. The use of high shear stress mixers can serve to remove residual agglomeration during mixing. After the mixing step, the cooled mixture is passed through a cutting mill where it is converted into granules (a few millimeters in diameter) that form the feed material for molding. Two examples of the composition of the feed material are given in Table 6.14.

TABLE 6.14 Examples of Ceramic Injection Molding Feed Materials

Component	Composition (wt%)	
Powder	1 μm Al_2O_3 (85)	20 μm Si (82)
Major binder	Paraffin wax (14)	Polypropylene (12)
Minor binder	—	Microcrystalline wax (4)
Other additives	Oleic acid (1)	Stearic acid (2)

Molding

When compared to injection molding of plastics, control of the molding process in ceramics is more difficult because of the higher density, viscosity, thermal conductivity, and elastic modulus associated with the particle-filled polymer. The higher modulus and faster cooling rate (due to the higher thermal conductivity) coupled with the lower fracture toughness of the particle-filled polymer means that the molded article is prone to cracking due to the development of residual stress during the solidification process. Attempts have been made to model the residual stress development in ceramic injection molding, but a more practical approach, involving a systematic variation of the process variables, is often used to optimize the molding conditions.

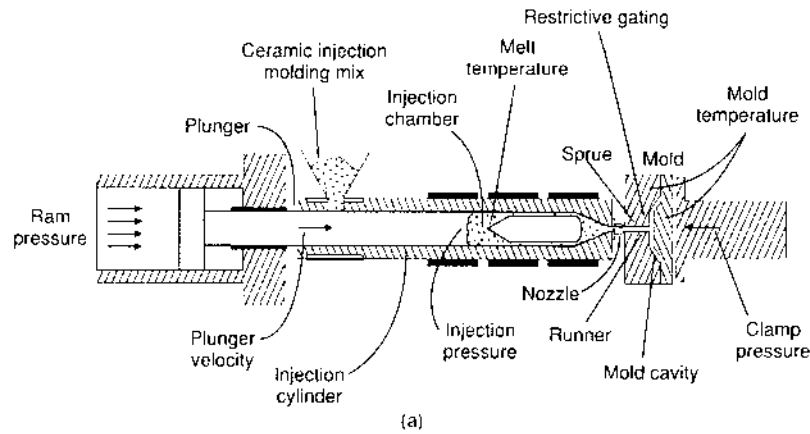
Figure 6.48 illustrates the principle of operation of an injection molding machine and some of the parameters that influence its functioning. The feed material in the form of granules is fed into the machine, transported by a screw or plunger to the injection chamber where it is heated to produce a viscous mass, and then injected under pressure into the mold cavity. When the cavity is filled, the mold is cooled and the green body is ejected. It is obvious from Fig. 6.48b that a given machine variable can influence more than one of the fundamental variables. This, combined with the large number of variables, makes optimization of the process a considerable task. In general, injection molding is best applied selectively to the forming of small articles with complex shapes.

6.4.4 Solid Free-form Fabrication

Solid free-form fabrication (SFF) is a term used to describe processing technologies that allow the production of parts with the required geometrical complexity directly from a computer-aided design (CAD) file without the use of traditional tools such as molds. There is no general agreement on the term, and several other terms have been used, including *solid free-form manufacturing*, *rapid prototyping*, *desktop manufacturing*, and *layer manufacturing*. The last 10–15 years have seen a rapid development and application of SFF technology.

SFF technology is not intended to replace traditional manufacturing technologies. A key benefit is the rapid production of hard prototypes of the object to be copied or developed for evaluation of design, limited testing, and improvement in the manufacturing process. A key aspect of the SFF techniques is the layer-wise deposition of material only where it is required, so the methods also provide significant flexibility for the production of small, complex-shaped components with unique structural features that are not achievable with other ceramic forming methods.

The basic approach of SFF is illustrated in Fig. 6.49. A prototype which represents the physical component to be built is modeled on a CAD system. The model is next converted into a format that is analyzed by a computer, which slices



Fundamental Variable	Machine Variable
Material temperature	Melt temperature Injection pressure Plunger velocity Mold geometry Mold temperature
Flow rate (shear rate)	Plunger velocity Mold geometry Injection pressure
Cavity pressure	Injection pressure Melt temperature Plunger velocity Mold geometry
Cooling rate	Melt temperature Mold temperature

(b)

FIGURE 6.48 (a) Schematic of a plunger injection molding machine identifying the principal machine variables. (b) Relation of fundamental injection molding variables to plunger machine variables. (From Ref. 65.)

the model into cross sections. The cross sections are systematically recreated in the computer-aided manufacturing step, employing suitable equipment and materials, to produce an actual three-dimensional prototype.

A wide variety of techniques, employing liquids, powders, and laminates, is available for SFF. The main features of the techniques and details of the available commercial equipment are described in recent texts (67,68). The more mature

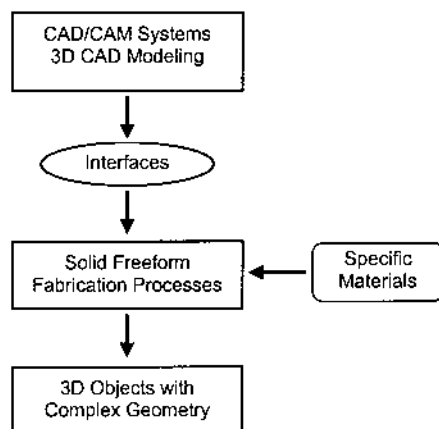


FIGURE 6.49 Basic principle of solid free-form fabrication.

techniques are (1) stereolithography, (2) laminated object manufacturing, (3) fused deposition modeling, and (4) selected laser sintering. The techniques have commonly been used to fabricate plastic components but in the last few years they have been rapidly extended to the production of ceramic (and metal) components. Other techniques based on ink-jet printing and on the extrusion of highly concentrated suspensions are also being investigated for SFF of ceramics. Recent developments in the application of these techniques are described in the proceedings of recent topical meetings (69,70).

The ceramic SFF techniques generally provide the methods for assembling the complex-shaped objects from common starting materials such as concentrated suspensions, powders, and particle-filled polymers. Many of the processing issues (e.g., particle packing, polymeric additives, colloidal interactions, and rheological behavior) discussed earlier for the common forming methods such as slip casting, tape-casting, and extrusion are therefore applicable to SFF of ceramics. Drying and binder removal, to be discussed later in this chapter, also form key steps in some methods.

6.4.4.1 Stereolithography

A schematic of the stereolithography technique is shown in Fig. 6.50. A laser beam is scanned on the surface of a highly concentrated suspension of ceramic particles in a monomer solution, and the monomer is cured to form a polymer layer that binds the particles together. When the first layer is completed, the support platform is lowered by a depth equal to the layer thickness, and the suspension flows over the polymerized layer. The laser is scanned over the new

surface to form the second layer, and the process is repeated until the component is completed. Ceramic components are obtained after binder removal and sintering (71).

If a dense ceramic object is the goal of the fabrication process, then the green body and the starting suspension must have many of the desirable characteristics discussed earlier for the casting methods: e.g., the suspension must have a high concentration of particles (≥ 50 vol%) to produce a high packing density in the green body and a low viscosity for ease of flow during the stereolithography process. Thus, low-viscosity monomer solutions and effective dispersants to control the colloidal interactions between the particles (and hence the viscosity of the suspension) are important requirements for successful processing. The layer depth of curing during stereolithography is also an important parameter. With currently available equipment an individual layer thickness of 100–200 μm is required to achieve successful lamination and adhesion of the layers. The presence of ceramic particles in the monomer solution enhances photon scattering and leads to a reduction in the mean transport length of the photons through the solution. Thus, maximizing the curing depth in the monomer solution (e.g., through the use of appropriate monomers and photoinitiators) is important for achieving the required layer thickness.

6.4.4.2 Laminated Object Manufacturing

In laminated object manufacturing (LOM), layers of a thin sheet are sequentially bonded to each other and cut by a laser according to a computer-generated model (Fig. 6.51). A modified form of the process, referred to as *computer-aided manufacturing of laminated engineering materials* (CAM-LEM), has been developed to produce complex shapes directly from tape-cast ceramics (72). In CAM-LEM, individual slices are cut from the tape-cast sheet using a laser and stacked to

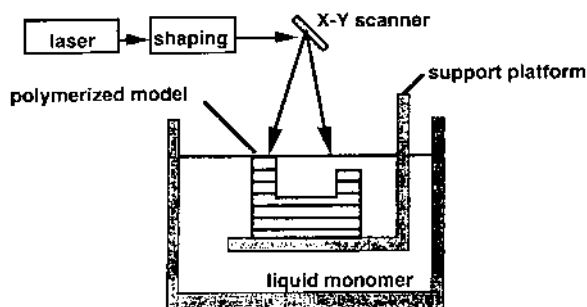


FIGURE 6.50 Diagram of the stereolithography apparatus.

assemble the object. Following lamination of the slices and binder removal, the body is sintered to produce a ceramic component.

6.4.4.3 Fused Deposition Modeling

Fused deposition modeling (FDM) is a technique that builds plastic objects by extrusion of a polymer–wax filament through a nozzle (Fig. 6.52). A modification of the technique, referred to as *fused deposition of ceramics* (FDC), has been developed to create ceramic components from particle-filled polymer filaments (73). Ceramic–polymer mixtures used in FDC are similar to those described earlier for injection molding of ceramics. The mixture is first extruded to form filaments with a diameter of ~ 2 mm, after which the spooled filaments are fed into a computer-controlled extrusion head. Extrusion of the plastic mixture through a nozzle is used to form the object layer by layer. Subsequent processing steps follow those described for injection molded bodies.

6.4.4.4 Selective Laser Sintering

In selective laser sintering (SLS), components are built layer by layer by scanning a laser beam over a thin layer of powdered material (74). For polymers and some metals, interaction of the laser beam with the powder raises the temperature to the point of melting, resulting in particle bonding and fusion of the particles to themselves as well as to the previous layer to form a solid object. Crystalline

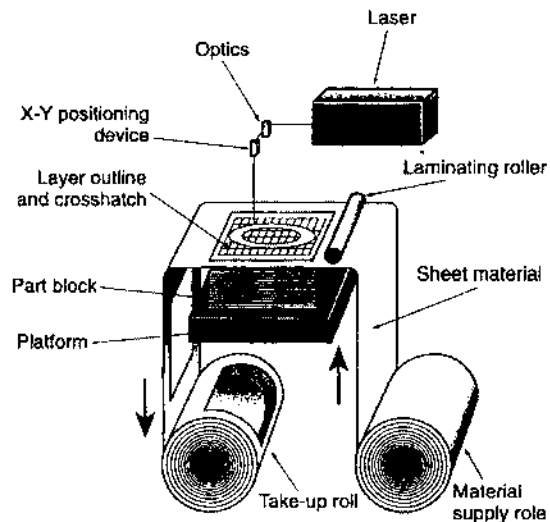


FIGURE 6.51 Illustration of laminated object manufacturing.

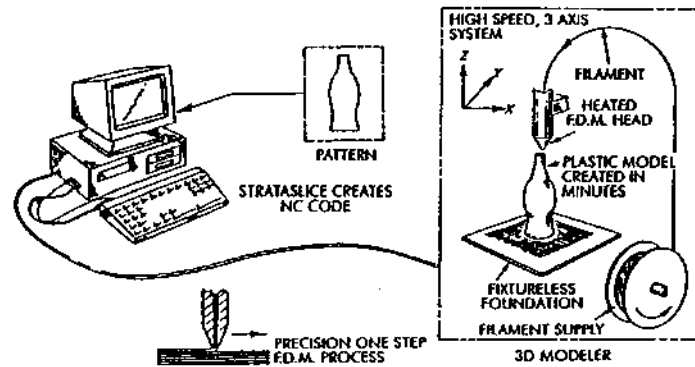


FIGURE 6.52 Illustration of the fused deposition modeling process.

ceramics cannot be formed directly by SLS because matter transport by solid state diffusion is insignificant during the short time of laser scanning. An alternative way is to use a polymeric binder mixed with the ceramic powder which provides the bonding phase for forming by SLS. Following binder removal, the body is sintered to produce a dense object.

6.4.4.5 Printing and Casting Techniques

In one type of technique, referred to as *three-dimensional printing* (3DP), complex-shaped parts are formed by sequentially depositing a thin layer of ceramic powder followed by ink-jet printing of a binder solution to fix the powder in place and to selectively define the geometry of the part (75). The thin layer of powder can be formed by roll compaction, but more homogeneous particle packing and higher packing density are obtained by deposition from a well-dispersed suspension (e.g., through a nozzle 100–200 μm in diameter) followed by drying. After application of the binder solution to fix the powder, the layer is heated to remove excess liquid (water). Once a single layer is complete, the sequential slurry and binder deposition processes are repeated until the part is completed. The binder is then cured to develop adequate strength, and the unwanted powder is re-dispersed in a liquid to recover the part. Finally, the shaped part is heated to decompose the binder and sintered to produce a ceramic object. Three key aspects of the 3DP process can be identified. First, the colloidal properties of the suspension and the drying of the deposited layer control the structure of the deposited powder layer (76). Second, the interaction of the binder solution with the powder layer must be optimized to control the shape uniformity of the printed part. Third, the re-dispersion of the unwanted powder to retrieve the printed part is controlled by the chemistry and colloidal properties of the suspension (77).

In another printing technique, referred to as *direct ceramic ink-jet printing* (DCIJP), the ceramic powder is contained in an ink, which is cast through a printer nozzle (78). The ink is essentially a well-dispersed, fairly concentrated suspension of the powder in a liquid (~ 30 vol % particles). Typically, the nozzle diameter is $50\text{ }\mu\text{m}$, and the suspension is deposited in the form of drops with a diameter of $\sim 100\text{ }\mu\text{m}$. Successful forming by DCIJP is critically dependent on the preparation of a suitable ink (79,80). In addition to the common powder requirements (e.g., fine particle size, narrow particle size distribution, and no strong agglomeration), the effective use of polymeric additives (dispersants, binders, and, if necessary, plasticizers) to control the colloidal and rheological properties of the suspension is a key factor in the development of the ink. In addition, drying of the drops can influence the structure of the deposit.

Robocasting is a method based on the extrusion of highly concentrated ceramic suspensions through a narrow orifice (81). The orifice openings can range from a few tenths to a few millimeters, while a typical suspension contains 50–65 vol% particles, 35–50 vol% solvent (commonly water), and 1–5 vol% organic additives. In the process, individual layers are sequentially deposited after the previous layer has had sufficient time to dry. Key processing aspects are the rheological properties of the suspension and the drying of the deposited layers.

6.5 DRYING OF GRANULAR CERAMICS

Moist granular ceramics produced by the common forming methods such as tape casting and extrusion must be dried prior to binder burnout and sintering. Drying is also a key step in solid free-form fabrication techniques that involve layer-by-layer deposition of colloidal suspensions.

6.5.1 Drying of Granular Layers

Investigations of the drying of liquid drops containing a dilute concentration of colloidal particles (particle concentration = 10^{-4}) show considerable migration of the particles (82), leading to the deposition of a ring (Fig. 6.53). Ring formation has also been observed during the drying of SiO_2 films ($\sim 40\text{ }\mu\text{m}$ thick) deposited from more concentrated colloidal suspensions (83). In the initial stage of drying, particles at the outer edge of the film undergo consolidation to form a ring (Fig. 6.54). As drying proceeds, liquid flows to the outer region to maintain a saturated state, a process driven by the capillary suction pressure of the ring. Particles in the liquid are deposited at the interface between the saturated ring and the supersaturated suspension. As Fig. 6.54 illustrates, the drying of the film is analogous to consolidation by slip casting. On completion of the drying process, a dimple or depression is commonly observed in the center of the film, which reflects the depletion of particles arising from the migration. In practice, such

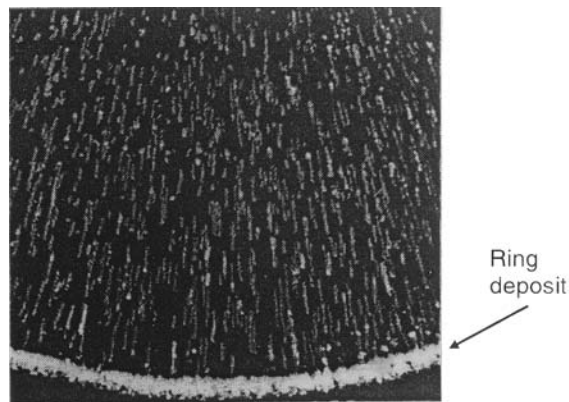


FIGURE 6.53 Colloidal particle migration during drying of a liquid drop containing a dilute concentration of colloidal particles. Arrow denotes the ring deposit that forms at the edge of the drop and the background streaks denote the migration of individual particles to the edge as a result of capillary-induced fluid flow. (From Ref. 82.)

dimpling of the film can be suppressed by hindering the motion of the particles in the suspension, by increasing the particle concentration, or by decreasing the colloidal stability.

Films deposited on a rigid substrate experience biaxial tensile stresses during drying because they cannot shrink in the plane of the film. The biaxial tensile stress develops during drying as a result of the capillary tension in the pore liquid as it stretches to cover the dried surface exposed by the evaporation of the liquid (see Chapter 5). The capillary tension in the liquid would cause the film to shrink except the rigid substrate prevents the shrinkage in the plane of the film. Films

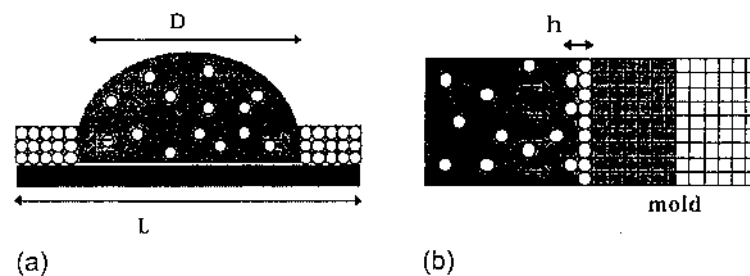


FIGURE 6.54 Illustration of (a) drying of a granular film and (b) the slip-casting process. Arrows indicate the direction of fluid flow. (From Ref. 83.)

produced from electrostatically stabilized, binder-free suspensions (0.5 μm Al_2O_3 particles) are observed to crack spontaneously regardless of the drying rate (84) when the film thickness is above a certain critical value ($\sim 50 \mu\text{m}$). The existence of a critical cracking thickness can be explained by a linear elastic fracture model (85) which states that a constrained film will crack when subjected to a stress only if the strain energy released in the process exceeds the energy required to form the crack. The critical cracking thickness depends on the capillary tension in the liquid: it increases with increasing particle size and with decreasing surface tension of the liquid. It also increases for a flocculated suspension but at the expense of a lower particle packing density in the dried film. The use of a binder provides an effective way for improving the critical cracking thickness.

6.5.2 Drying of Granular Solids

While important differences exist between gels and granular solids, the general principles of drying discussed in Chapter 5 are also applicable to granular solids. It is assumed that the reader is familiar with the discussion presented in Chapter 5 and we shall only briefly outline the application of the principles to the drying of cast or plastically formed articles. Cast or extruded articles contain considerably less water than gels so that the shrinkage during drying is considerably less. The pores in granular ceramics are also much larger, so the permeability is higher. Drying problems in granular solids are therefore not as severe as in gels. However, inhomogeneities in the body produced by inadequate processing or forming operations provide an additional source of problems in granular solids.

6.5.2.1 Physical Process of Drying

The drying curves for cast or extruded articles show the same general features as those described in Chapter 5 for gels. The evaporation rate shows a constant rate period (CRP) followed by a falling rate period (FRP) (Fig. 5.17). In some cases, two parts can be distinguished in the FRP: the first falling rate period (FRP1) and the second falling rate period (FRP2). Drying curves for clay-based and other granular ceramics are often plotted as a function of the *moisture content* of the body, expressed as a percentage of the dry weight of the solid (dry basis):

$$\text{Moisture content (\%)} = \frac{(\text{wet weight} - \text{dry weight}) \times 100}{\text{dry weight}} \quad (6.25)$$

The moisture content of articles produced by casting or extrusion is typically 20–35%.

In the CRP, the rate of evaporation is independent of the moisture content. As evaporation starts, a dry surface region is created, and the liquid stretches to cover the dry region. A tension develops in the liquid, and this is balanced by

compressive stresses on the solid phase. The compressive stresses cause the body to contract, and the liquid meniscus remains at the surface. As drying proceeds, the particles achieve a denser packing, and the body becomes stiffer. The liquid meniscus at the surface deepens, and the tension in the liquid increases. Eventually, the particles, surrounded by a thin layer of bound water, touch and shrinkage stops. The moisture content at this point is sometimes referred to as the *leatherhard moisture content*.

When shrinkage stops, further evaporation drives the meniscus into the body and the rate of evaporation falls. The point at which the rate starts to fall is the *critical moisture content*. In practice, the critical moisture content and the leatherhard moisture content are approximately equal. In the FRP1, the liquid is still evaporating from the surface. Contiguous pathways exist along which liquid can flow to the surface. Eventually, the liquid near the outside of the body becomes isolated into pockets. Flow to the surface stops, and the liquid is removed predominantly by diffusion of the vapor. At this stage, drying enters the FRP2.

6.5.2.2 Cracking and Warping

Cracking and warping during drying are caused by differential strain due to (1) pressure gradients in the liquid and (2) inhomogeneities in the body produced by inadequate processing or forming operations. As discussed in Chapter 5, a tension develops in the liquid as it stretches to cover the dry region exposed by evaporation of the liquid. If the tension p in the liquid is uniform, there is no stress in the solid phase [Eq. (5.48)]. However, when p varies through the thickness, the body tends to contract more where p is high, and the differential strain causes warping or cracking.

If the evaporation rate is very high, the tension in the liquid can reach its maximum value given by Eq. (5.41), and the total stress at the surface of the body is given by Eq. (5.49):

$$\sigma_x \approx \frac{2\gamma_{LV} \cos \theta}{a} \quad (5.49)$$

where γ_{LV} is the surface tension of the liquid, θ is the contact angle, and a is the pore radius. For clay–water mixtures with a particle size in the range 0.5–1 μm , assuming that $\theta = 0$, $\gamma_{LV} = 0.07 \text{ J/m}^2$, and the pore size is equal to half the particle size, gives $\sigma_x \approx 0.5 \text{ MPa}$. Unfired granular ceramics containing little binder are very weak and this stress is sufficiently high to cause cracking.

During the CRP, the boundary condition at the surface of the body is given by Eq. (5.47):

$$\dot{V}_E = \frac{K}{\eta_L} \nabla p|_{\text{surface}} \quad (5.47)$$

where \dot{V}_E is the evaporation rate, K is the permeability of the body, η_L is the viscosity of the liquid, and ∇p is the pressure gradient in the liquid. According to Eq. (5.47), fast evaporation rate leads to high ∇p . To avoid cracking or warping the body must be dried slowly. However, the “safe” drying rates may be so slow that uneconomically long drying times are needed.

To increase the safe drying rates, a few procedures can be used. According to Eq. (5.47), for a given \dot{V}_E , ∇p decreases with higher K and lower η_L . The permeability K increases roughly as the square of the particle (or pore) size. One approach is to use a larger particle size or to mix a coarse filler with the particles. This approach is often impractical because it can lead to a reduction in densification rate during sintering. Another approach, based on a decrease in η_L is used practically in *high humidity drying* where the process is carried out at slightly elevated temperatures ($\sim 70^\circ\text{C}$) and high ambient humidity in the drying atmosphere. Increasing the temperature leads to a decrease in η_L (by a factor of ~ 2 at 70°C) and to an increase in the rate of drying. However, the increase in the drying rate is counteracted by increasing the ambient humidity [see Eq. (5.45)]. In this way a reasonable drying rate is achieved while keeping ∇p small. The sequence of operation in a high humidity dryer involves increasing the ambient humidity followed by increasing the temperature and, after drying, decreasing the humidity, followed by decreasing the temperature.

Even if the moist body were dried uniformly and at a safe rate, inhomogeneities produced by inadequate processing or forming operations can still lead to cracking and warping. Regions of the body with higher moisture content (above the critical value) undergo higher shrinkage. Differential shrinkage due to moisture gradients is a common source of cracking and warping. Gradients in the particle size caused, for example, by preferential settling can also lead to differential shrinkage. Figure 6.55 summarizes the effects of differential shrinkage caused by (a) pressure gradients in the liquid, (b) moisture gradients, and (c) preferential settling.

6.6 BINDER REMOVAL

The organic additives and other processing aids (referred to in this section simply as the binder) must be removed from the green body prior to sintering. This process of binder removal is commonly referred to as *debinding*. Ideally, we would like to remove the binder completely without disrupting the particle packing or producing any new microstructural defects in the green body. Residual contaminants (e.g., carbon and inorganic ions) and defects (e.g., cracks and large voids) generally have an adverse effect on the microstructural evolution during sintering and hence on the properties of the fabricated body. Debinding can be a critical step in ceramic processing, especially in the case of the forming methods where the binder content in the green body is relatively high. Debinding can be

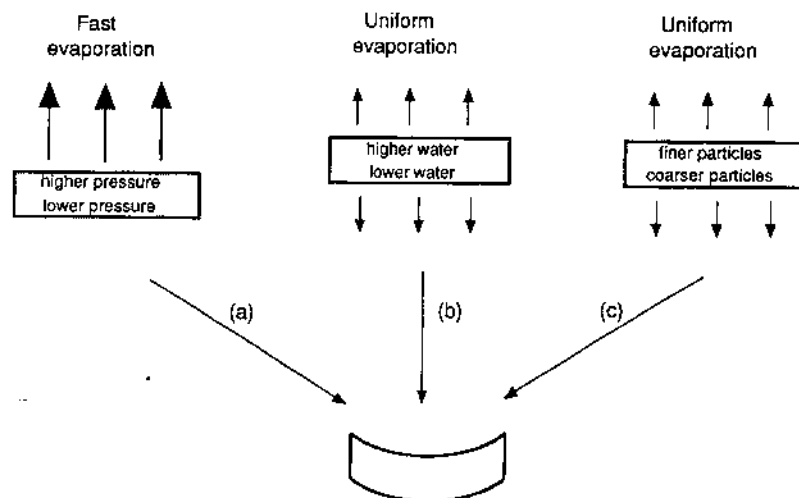


FIGURE 6.55 Diagram illustrating warping during drying due to (a) pressure gradient in the liquid, (b) a moisture gradient in the body, and (c) segregation of particles.

accomplished by three methods: (1) extraction by capillary flow into a porous surrounding material, (2) solvent extraction, and (3) thermal decomposition, but by far the most commonly used method is thermal decomposition (referred to as *thermal debinding*). Reference 61 provides a discussion of the techniques for debinding of injection-molded articles.

6.6.1 Extraction by Capillary Flow

In extraction by capillary flow, also referred to as *wicking*, the green body is heated in a packed powder bed or on a porous substrate that absorbs the molten binder. The net time t for binder removal by wicking is given by (61)

$$t \approx \frac{5L^2\eta V_s^2 D_w}{\gamma_{LV} (1-V_s)^3 D(D-D_w)} \quad (6.26)$$

where L is the thickness of the body, η and γ_{LV} are the viscosity and specific surface energy, respectively, of the molten binder, V_s is the particle packing density of the body, D is the particle size of the body, and D_w is the particle size of the powder bed. Rapid binder removal by wicking is promoted by small D_w and small L . Because the viscosity of the binder increases with molecular weight, wicking is generally useful for waxes but not for high molecular weight polymers.

The amount of binder removed scales as the square root of time. However, not all the binder can be removed by wicking. When the molten binder enters the pendular state (i.e., when it becomes trapped in isolated pockets), binder removal stops.

6.6.2 Solvent Extraction

Solvent extraction involves immersing the component in a liquid that dissolves at least one binder phase, leaving an open pore structure for subsequent binder burnout. Full debinding is possible but not practical because the resulting powder mass will have almost no strength. The time t for debinding is given by (61)

$$t = \frac{L^2}{\alpha} \ln \left(\frac{V_B}{1 - V_s} \right) \exp \left(\frac{q}{kT} \right) \quad (6.27)$$

where L is the thickness of the body, α is a factor that depends on the solubility of the binder in the solvent, V_B is the fraction of the binder to be removed, V_s is the particle packing density of the body, q is the activation energy for the dissolution of the binder in the solvent, k is the Boltzmann constant, and T is the absolute temperature.

Binder systems for solvent extraction consist of at least two components, one soluble in the solvent and the other insoluble to hold the particles in place after extraction of the soluble component. The soluble component must be at least ~ 30 vol% of the binder system in order to have sufficient interconnectivity for extraction. Interaction between the solvent and the binder can involve both swelling and dissolution, so it is necessary to choose a *good* solvent and perform the extraction above the *theta* temperature to reduce swelling (see Chapter 4).

6.6.3 Thermal Debinding

In thermal debinding, the binder is removed as a vapor by heating at ambient pressure in an oxidizing or nonoxidizing atmosphere or under a partial vacuum. The process is influenced by both chemical and physical factors. Chemically, the composition of the binder determines the decomposition temperature and the decomposition products. Physically, the removal of the binder is controlled by heat transfer into the body and mass transport of the decomposition products out of the body. In practice, binder systems consist of a mixture of at least two components that differ in volatility and chemical decomposition. The ceramic powder may alter the decomposition of the pure polymer. In view of the complexity of real systems, we first consider the basic features of thermal debinding for a simplified system consisting of a powder compact with a single binder, e.g., a thermoplastic polymer such as poly(methyl methacrylate) or polyethylene. Later,

the key practical factors related to the use of a mixture of binders and to the influence of the powder will be outlined.

6.6.3.1 Stages and Mechanisms

In the case of a thermoplastic binder, thermal debinding can be roughly divided into three stages. Stage 1 involves the initial heating of the binder to a point where it softens ($\sim 150\text{--}200^\circ\text{C}$). Chemical decomposition and binder removal are negligible in this stage, but the occurrence of several other processes such as shrinkage, deformation, and bubble formation can seriously affect the ability to control the shape and structural uniformity of the body. Shrinkage occurs by a rearrangement process as the particles try to achieve a denser packing under the action of the surface tension of the polymer melt, and its magnitude increases with decreasing particle packing density in the green body. Deformation is enhanced by a lower particle packing density, higher binder content, and lower melt viscosity. Bubble formation results from the decomposition of the binder as well as from residual solvent, dissolved air, or air bubbles trapped within the green body during forming, and it provides a possible source of failure or defect formation during thermal debinding (86).

In stage 2, typically covering a temperature range of $200\text{--}400^\circ\text{C}$ most of the binder is removed by chemical decomposition and evaporation. Appreciable capillary flow of the molten binder can accompany the evaporation process. The nature of the decomposition reactions depends on the chemical composition of the binder and on the atmosphere. In inert atmospheres such as nitrogen or argon, polymers such as poly(ethylene) undergo thermal degradation by chain scission at random points in the main chain to form smaller segments (Fig. 6.56a), which leads to a reduction in the polymer viscosity. With continued thermal degradation, the chain segments become small enough (i.e., their volatility increases) that evaporation is promoted. Other polymers such as poly(methyl methacrylate) undergo depolymerization reactions to produce a high percentage of volatile monomers (Fig. 6.56b).

In oxidizing atmospheres, degradation by oxidation occurs in addition to thermal degradation. Oxidative degradation commonly occurs by a free radical mechanism to produce decomposition products that contain a high percentage of volatile, low molecular weight compounds such as water, carbon dioxide, and carbon monoxide. Compared to thermal degradation, oxidation reactions generally lead to decomposition at lower temperatures and lead to an increase in the rate at which the binder is removed.

Finally, in stage 3, the small amount of binder still remaining in the body is removed by evaporation and decomposition at temperatures above $\sim 400^\circ\text{C}$. Binder removal is facilitated by the highly porous nature of the body, but the atmosphere must be carefully chosen to avoid the retention of an excessive amount of binder residue.

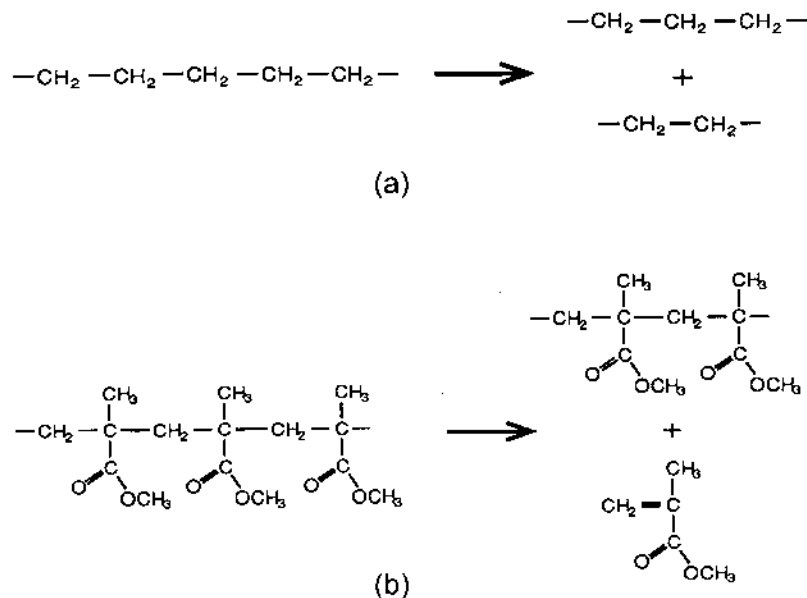


FIGURE 6.56 Mechanisms of thermal degradation of polymers showing (a) chain scission at random points in the chain, e.g., polyethylene, and (b) depolymerization (unzipping) to produce monomers, e.g., poly(methyl methacrylate).

6.6.3.2 Models for Thermal Debinding

As described above for a high molecular weight thermoplastic binder, thermal debinding occurs by evaporation of low molecular weight species produced by thermal or oxidative degradation. Low molecular weight binders simply undergo evaporation without the need for any significant degradation. There are therefore three models for thermal debinding: (1) evaporation, (2) thermal degradation followed by evaporation, and (3) oxidative degradation followed by evaporation. However, the evaporation model differs from the thermal degradation model only as far as the concentration of the volatile species is concerned. In the evaporation model, the volatile species are present in the binder at some initial concentration and the concentration decreases as debinding proceeds, whereas in the thermal degradation model, the volatile species have a concentration that is initially zero but increases with degradation of the binder and then decreases as the volatile species evaporate. The thermal degradation model is therefore expected to describe the main features of the evaporation of low molecular weight binders.

Assuming that the temperature is uniform, thermal degradation produces volatile, low molecular weight species throughout the molten binder. Removal

of the binder occurs by evaporation of these volatile species. The rate of evaporation at the surface and the rate of transport of the degradation products through the body determine the concentration profile of the products. Volatile products present, for example, in the center of the body must not be allowed to reach temperatures above their boiling point since this will lead to the formation of bubbles and hence, microstructural defects.

Binder removal during thermal degradation has features that are similar to those encountered in the drying of a moist granular material. Let us consider a model in which interconnected pores of two different radii are present (Fig. 6.57a). Even though the pores have different radii (r_L and r_S), initially liquid evaporates from them at the same rate so that the radii of the menisci (r_m) are equal. The capillary tension in the liquid is given by the equation of Young and Laplace:

$$p = \frac{2\gamma_{LV}}{r_m} \quad (6.28)$$

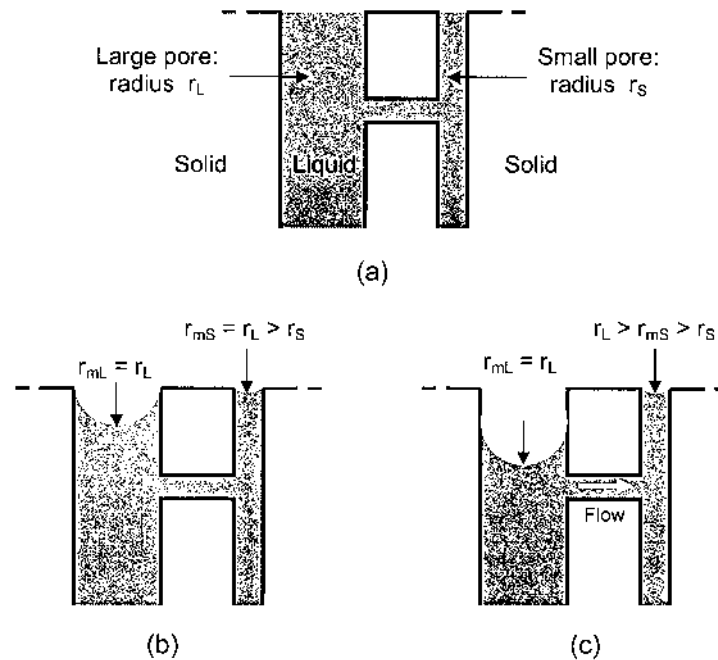


FIGURE 6.57 Illustration of evaporation and liquid flow during binder removal by thermal degradation. The large pore empties first while the meniscus is maintained at the surface of the small pore, then the small pore empties. (r_m is the radius of the meniscus.)

where γ_{LV} is the surface tension of the liquid. If the radii of the menisci were different, the capillary tension given by Eq. (6.28) would also be different, and liquid would flow from one pore to the other until the menisci became equal again.

As evaporation from the surface proceeds, the radius of the menisci decreases. However, almost no shrinkage of the body occurs because the particles are practically touching. A point is reached where the radius of the menisci is equal to the radius of the large pore, i.e., $r_m = r_L$ (Fig. 6.57b). Further evaporation forces the liquid to retreat into the large pore. However, the radius of the meniscus, r_m , will continue to decrease in the small pore, and the capillary tension will suck liquid from the large pore (Fig. 6.57c). In this way the large pore empties first and the small pore remains full of liquid. After the large pore has been emptied, the small pore starts to empty. In practice, we will have a distribution of pore sizes and pore shapes, but the same principles will apply. Considerable redistribution of the liquid would therefore be expected to occur during thermal degradation. Furthermore, the evaporation front is not expected to move uniformly into the body. Instead, pore channels first develop deep into the body as liquid from the larger pores is drawn into the smaller pores. These trends in porosity development and liquid redistribution have been observed in binder burnout studies (87).

In oxidative degradation, the reaction occurs at the polymer–gas interface that recedes into the body as degradation proceeds. As outlined earlier, most debinding occurs after the binder melts. The gaseous reaction products can be removed at ambient pressure via permeation or under partial vacuum via diffusion through the porous outer layer (Fig. 6.58). Whether diffusion or permeation is rate controlling depends essentially on the mean free path of the gas molecules. In diffusion control, the collisions are mainly with the pore structure whereas in permeation control the collisions are mainly with other gas molecules. For the model shown in Fig. 6.58, and assuming that the binder is removed isothermally as a single-component, low molecular weight vapor, theoretical analysis indicates that the debinding time t for the diffusion controlled process is given by (88)

$$t \approx \frac{L^2}{2D(1-V_s)^2(p-p_0)} \frac{(M_w kT)^{1/2}}{V_M} \quad (6.29)$$

where L is the thickness of the body, D is the particle size, V_s is the particle packing density, p is the pressure in the pores, p_0 is the ambient pressure, M_w is the molecular weight, V_M is the molecular volume of the vapor, k is the Boltzmann constant, and T is the absolute temperature. For the case of permeation control, the debinding time is given by

$$t \approx \frac{20L^2\eta}{D^2F} \frac{V_s^2}{(1-V_s)^3} \frac{p}{(p^2 - p_o^2)} \quad (6.30)$$

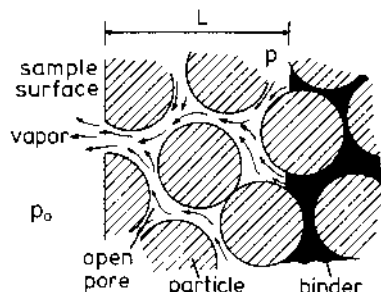


FIGURE 6.58 Schematic diagram of the model for thermal debinding by oxidative degradation where the binder–vapor interface is at a distance L from the surface of the compact. (From Ref. 88.)

where η is the viscosity of the vapor, F is the volume change associated with the burnout of the binder, and the other terms were defined in Eq. (6.29).

For both diffusion and permeation control, the debinding time varies as the square of the component thickness. Small particle size and high particle packing density reduce the rate of binder removal, but on the other hand they are beneficial for the subsequent sintering step. A conflict therefore exists between rapid removal of the binder and the achievement of high density during sintering. Process optimization or the use of a sintering aid that enhances the densification process can provide a solution to the conflicting requirements. Equations (6.29) and (6.30) also indicate that a low ambient pressure or a vacuum serves to reduce the time for binder removal. A vacuum, however, does not lead to oxidative degradation. Furthermore, temperature control and transport of heat are poor in a vacuum. The use of an oxidizing gas at reduced ambient pressure may provide adequate degradation as well as good thermal transport.

6.6.3.3 Thermal Debinding in Practice

For green bodies containing less than ~ 5 vol% binder, binder removal can be accomplished relatively fast and is not a critical step in the overall fabrication process. Our discussion of thermal debinding is therefore most closely identified with green bodies formed by tape casting, injection molding, and some solid free-form fabrication routes which have a relatively high binder content, making debinding a critical processing step.

Practical binder systems, particularly in the case of injection molding, consist of at least two components that differ in their volatility and decomposition behavior. A key to efficient debinding is to select components that do not have a significant overlap between the temperature ranges for removal. In this case,

removal of the first binder at lower temperature creates a network of porosity through which the decomposition products of the second component can be removed more easily. Oils and waxes have lower melting temperatures than most high molecular weight thermoplastic polymers, and they form a useful minor component in thermoplastic binder mixtures.

The decomposition of the polymeric binder in a ceramic green body is more complex than that of the pure binder. In the case of poly(vinyl butyral), Fig. 6.59 shows that oxide powders can catalyze the reaction, leading to a decrease in the decomposition temperature (89). Cerium oxide (CeO_2), for example, reduces the temperature for the greatest weight loss by $\sim 200^\circ\text{C}$. Binders that normally burn out completely in the pure state may leave a small amount of residue that cannot be easily removed from the particle surfaces. For a given binder composition, the amount of residue depends on several factors, such as the powder composition, the gaseous atmosphere, and the structure and chemistry of the powder surface.

It is essential to achieve some balance between the time for debinding and the prevention of defects during debinding. Normally, this is achieved by controlling the heating cycle. A very slow heating rate makes the thermal debinding process time-consuming, whereas a fast heating rate leads to bubble formation, rapid melting of the binder, and distortion of the body. Initially the heating rate should be slow (less than $\sim 1^\circ\text{C}/\text{min}$) and isothermal stages should be appropriately incorporated until the pores are partially opened, after which the heating rate can be increased. In some cases, the use of solvent extraction to partially open

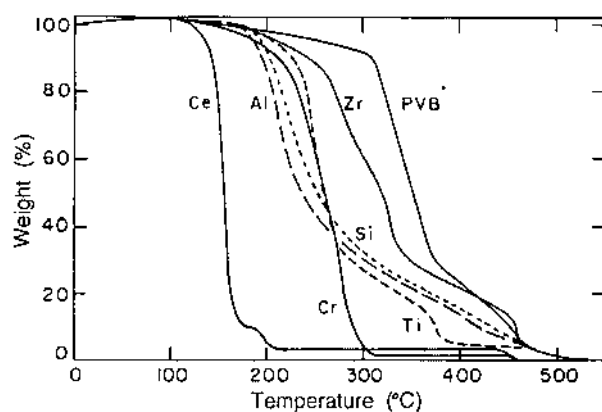


FIGURE 6.59 Thermogravimetric plots of the decomposition of poly(vinyl butyral) from films containing 2 wt% poly(vinyl butyral) and 98 wt% of various oxides during heating in air at $5^\circ\text{C}/\text{min}$. (From Ref. 89.)

the pores, followed by thermal debinding, can serve to improve the efficiency of the debinding step.

6.7 GREEN MICROSTRUCTURES AND THEIR CHARACTERIZATION

The microstructure of the green body, as noted earlier, has a significant influence on the microstructural evolution during sintering, so some degree of characterization is often essential. For a compact formed from a given powder, the important green body characteristics are the relative density (or porosity) and the pore size distribution, which is used as a measure of the packing homogeneity. As mentioned earlier, the density alone is a misleading parameter for predicting the sintering characteristics of a powder compact.

The density is measured from the mass and external volume. For a body with a regular shape, the external volume can be measured from the dimensions. Porosity and pore size distribution are normally measured by *mercury porosimetry* or, for very fine pores, by *gas adsorption*. *Scanning electron microscopy* (SEM) of a fracture surface provides a rough visual guide of the packing homogeneity and is also easy to perform. The techniques of mercury porosimetry, gas adsorption, and SEM are also commonly used for powder characterization and have been described in Chapter 3.

Additional information can be obtained by using other techniques (90). Impregnation of the green body with epoxy resin, followed by sectioning, polishing, and observation in the SEM provides quasi-three-dimensional information of the green microstructure (91), but the method is time-consuming and only the features present on the polished surface are observed. A liquid immersion technique has been developed to characterize the internal structure of granules (26) and green bodies (92). In this technique, the specimens are made transparent by immersion in a liquid with a matching refractive index and observed in an optical microscope under transmitted light. The technique is well suited to the observation of low concentrations of microstructural defects (1 to tens of microns in size). Techniques for characterizing density variations in a green compact were mentioned earlier in this chapter.

6.8 CONCLUDING REMARKS

In this chapter we considered the common ceramic forming methods and briefly described the solid free-form fabrication routes applicable to ceramics. Powder consolidation forms the last major processing step prior to the sintering process in which the microstructure of the final article is developed. Heterogeneities present in the green body cannot be easily removed during sintering, so control of

the green body microstructure provides considerable benefits for microstructural control in the final article. The selection of a forming method depends on the size and shape of the article, as well as on the cost. However, for a given forming method, careful manipulation of the powder characteristics and the consolidation parameters provides a useful approach for optimizing the uniformity of the green microstructure. Particle packing and polymeric additives play an important role in powder consolidation. After forming, drying and debinding must be carefully controlled to limit further creation of microstructural defects.

PROBLEMS

- 6.1 Find the radius r of a spherical particle that would fit precisely in the interstices of a hexagonal close-packed arrangement of spheres of radius a . Determine the density of a compact of spherical Al_2O_3 particles if 25 wt% of the particles fits precisely in the interstices of the hexagonal close-packed larger fraction.
- 6.2 Show that the representation of the random packing of binary mixtures of spheres in terms of the packing density (Fig. 6.6) is equivalent to the representation in terms of the apparent volume (Fig. 6.8).
- 6.3 For each of the surfactants sodium stearate, oleic acid, and alkyl ammonium acetate
 - a. Draw the structure of the functional end group, indicating whether the surfactant is nonionic, cationic, or anionic.
 - b. State whether the surfactant is soluble in aqueous or organic solvents.
 - c. Sketch and briefly explain the mechanism of adsorption of the surfactant onto the surfaces of Al_2O_3 particles.
 - d. State and briefly explain the dominant mechanism by which the surfactant can stabilize a suspension of Al_2O_3 particles.
- 6.4 Draw the structure of the repeating unit in the dispersants poly(acrylic acid) and poly(ethylene imine).
 - a. State whether each dispersant is soluble in aqueous solvents or organic solvents.
 - b. State whether each polymer is nonionic, cationic, or anionic.
 - c. Which of the two dispersants would be more effective for stabilizing a suspension of SiO_2 particles? Explain why.
- 6.5 Sodium silicate is commonly used as a dispersant for clays and for some oxide ceramics. It is also used as a binder in some ceramic forming methods. Compare and explain the mechanism by which sodium silicate functions as a dispersant and as a binder.
- 6.6 Draw the structure of the repeating unit in ethyl cellulose and hydroxyethyl cellulose. Ethyl cellulose is not soluble in aqueous solvents but hydroxyethyl cellulose is. Suggest an explanation for the difference in solubility of these two binders.
- 6.7 Explain what is meant by the term *viscosity grade* of a binder. Draw the structure of repeating unit in poly(vinyl pyrrolidone) and ammonium alginate. In Table 6.7, poly(vinyl pyrrolidone) is listed as a low viscosity binder whereas ammonium alginate is listed as a high-viscosity grade binder. Suggest an explanation for the difference in viscosity grade of these two binders.

- 6.8 Menhaden fish oil and poly(vinyl butyral) are often used as a dispersant and binder combination for Al_2O_3 particles.
- Draw the structure of the functional end group in Menhaden fish oil and the repeating unit in poly(vinyl butyral).
 - Is this dispersant and binder combination soluble in aqueous or organic solvents?
 - Suggest an explanation why this dispersant and binder combination is effective for Al_2O_3 .
- 6.9 Explain what is meant by the term *glass transition temperature* of an organic binder. Poly(vinyl alcohol) and poly(ethylene glycol) are often used as a binder and plasticizer combination for oxide particles.
- Draw the structure of the repeating unit in poly(vinyl alcohol) and poly(ethylene glycol).
 - Is this combination of binder and plasticizer soluble in aqueous or organic solvents?
 - Suggest an explanation why poly(ethylene glycol) is an effective plasticizer for poly(vinyl alcohol).
- 6.10 Discuss how the viscosity of an Al_2O_3 suspension would change depending on the order in which poly(acrylic acid) and poly(vinyl alcohol) are added to the suspension.
- 6.11 The particle packing density in spray-dried granules is 50%, and the granules themselves achieve a packing density of 55% after die filling. Determine the particle packing density of the material after die filling. During compaction the granules rearrange to a packing density of 62.5% prior to any significant deformation. Estimate the particle packing density of the material after the rearrangement stage. After compaction, the particle packing density of the green body is 65%. Assuming the original granules are spherical and of the same size, estimate the degree of flattening of the granules during compaction, giving the answer as a ratio of the diameters along the axial and radial directions of the die.
- 6.12 What would be the effect on slip casting behavior when using
- A cold mold and a warm slip?
 - A warm mold and a cold slip?
 - A warm mold and a warm slip?
- 6.13 An aqueous Al_2O_3 slip has a density of 2.5 g/cm^3 . Estimate the concentration of Al_2O_3 in the slip on a weight basis and on a volume basis. The slip is pressure-cast under an applied pressure of 1.5 MPa. Assuming that the density of the cast is equal to that for dense random packing of monosize spheres and the particle size of the powder is $1 \text{ }\mu\text{m}$, use Eqs. (6.9) and (6.16) to estimate the time required for the formation of a 1 cm thick cast.
- 6.14 A slip for tape casting contains, on a weight basis, 100 parts Al_2O_3 , 10 parts nonvolatile organics, and 35 parts toluene. After drying, the adherent tape is 60% of the original thickness of the cast. Estimate the porosity of the tape after drying and after binder burnout. After sintering, there is a shrinkage of 7.5% in the thickness of the tape, and the relative density of the tape is 95.0 %. Estimate the linear shrinkage in the plane of the tape, assuming homogeneous shrinkage in the plane.

- 6.15 Consider an injection-molded article consisting of ceramic powder and polymeric binder:
- Develop a relationship between the ceramic solids content of the article and its linear shrinkage when sintered to a specific end-point density, assuming that the binder is removed completely and that the shrinkage is homogeneous.
 - Repeat the calculation assuming that on pyrolysis, the binder produces an 85% yield of ceramic powder with the same composition as the starting powder.
 - Assuming a sintered density equal to the theoretical density of the ceramic, plot the linear shrinkage versus solids content for the cases considered in parts a and b. (The density of the binder and the theoretical density of the ceramic can be assumed as 1.2 and 4.0 g/cm³, respectively.)

REFERENCES

- German, R. M. Particle Packing Characteristics; Metal Powder Industries Federation: Princeton, NJ, 1989.
- Cumberland, D. J.; Crawford, R. J. The Packing of Particles; Elsevier: New York, 1987.
- Lange, F. F. J. Am. Ceram. Soc. 1989, Vol. 72, 3.
- Scott, G. D. Nature. 1960, Vol. 188, 908.
- Frost, H. J.; Raj, R. J. Am. Ceram. Soc. 1982, Vol. 65, C19.
- McGeary, R. K. J. Am. Ceram. Soc. 1961, Vol. 44, 513.
- Westman, A. E. R.; Hugill, H. R. J. Am. Ceram. Soc. 1930, Vol. 13, 767.
- Milewski, J. V. Adv. Ceram. Mater. 1986, Vol. 1, 1.
- Wakeman, R. J. Powder Technol. 1975, Vol. 11, 297.
- Sohn, H. Y.; Moreland, C. Can. J. Chem. Eng. 1968, Vol. 46, 162.
- Bierwagen, G. P.; Saunders, T. E. Powder Technol. 1974, Vol. 10, 111.
- Furnas, C. C. Indust. Eng. Chem. 1931, Vol. 23, 1052.
- Andreasen, A. H. M.; Andersen, J.; Kolloid, Z. 1930, Vol. 50, 217.
- Funk, J. E.; Dinger, D. R. Predictive Process Control of Crowded Particulate Suspensions; Kluwer Academic Publishers: Boston, MA, 1994.
- Burk, R.; Apte, P. Am. Ceram. Soc. Bulletin. 1987, Vol. 66, 1390.
- Roosen, A.; Bowen, H. K. J. Am. Ceram. Soc. 1988, Vol. 71, 970.
- Shanefield, D. J. Organic Additives and Ceramic Processing; 2nd ed.; Kluwer Academic Publishers: Boston, MA, 2000.
- Onoda, G. Y., Jr. In Ceramic Processing Before Firing; Onoda, G. Y., Jr., Hench, L. L. eds.; Wiley: New York, 1978, pp. 235–251.
- Moreno, R. Am. Ceram. Soc. Bulletin. 1992, Vol. 71, 1521; 1992, Vol. 71, 1647.
- 20a. Cesarano, J., III.; Aksay, I. A.; Bleier, A. J. Am. Ceram. Soc. 1988, Vol. 71, 250.
- 20b. Cesarano, J., III.; Aksay, I. A. J. Am. Ceram. Soc. 1988, Vol. 71, 1062.
- Howard, K. E. U. S. Patent 5,234,712, 1993.
- Bernhardt, C. Adv. Colloid Interface Sci. 1988, Vol. 29, 79.
- Bortzmeyer, D. In Materials Science and Technology; Vol. 17A: Processing of Ceramics, Part I; Brook, R. J. ed.; VCH: New York, 1996, pp. 127–152.
- Glass, S. J.; Ewsuk, K. G. MRS Bulletin. 1997, Vol. 22 (12), 24.

25. Takahashi, H.; Shinobara, N.; Okumiya, M.; Uematsu, K.; Junichiro, T.; Iwamoto, Y.; Kamiya, H. *J. Am. Ceram. Soc.* 1995, Vol. 78, 903.
26. Uematsu, K. *Powder Technol.* 1996, Vol. 88, 291.
27. Niesz, D. E.; McCoy, G. L.; Wills, R. R. In *Materials Science Research*, Vol. 11: *Processing of Crystalline Ceramics*; Palmour, H., III., Davis, R. F., Hare, T. M.; Plenum: New York, 1978, pp. 41–48.
28. Aydin, I.; Briscoe, B. J.; Ozkan, N. *MRS Bulletin.* 1997, Vol. 22 (12), 45.
- 29a. Strijbos, S.; van Groenou, A. B.; Vermeer, P. A. *J. Am. Ceram. Soc.* 1979, Vol. 62, 57.
- 29b. van Groenou, A. B. *Powder Metallurgy Int.* 1978, Vol. 10, 206.
- 29c. Strijbos, S.; Rankin, P. J.; Klein Wassink, R. J.; Bannink, J.; Oudemans, G. *Powder Technol.* 1977, Vol. 18, 187.
- 29d. Strijbos, S. *Powder Technol.* 1977, Vol. 18, 209.
30. Lannutti, J. J. *MRS Bulletin.* 1997, Vol. 22 (12), 38.
31. Welzen, J. T. A. M. In *Concise Encyclopedia of Advanced Ceramic Materials*; Brook, R. J. ed.; Pergamon: Oxford, 1991, pp. 112–120.
32. Zheng, J.; Reed, J. S. *J. Am. Ceram. Soc.* 1988, Vol. 71, C456.
33. Nies, C. W.; Messing, G. L. *J. Am. Ceram. Soc.* 1984, Vol. 67, 301.
34. Di Milia, R. A.; Reed, J. S. *J. Am. Ceram. Soc.* 1983, Vol. 66, 667.
35. Fries, R.; Rand, B. In *Materials Science and Technology*, Vol. 17A: *Processing of Ceramics*, Part I; Brook, R. J. ed.; VCH: New York, 1996, pp. 153–187.
36. *Ceramic Fabrication Processes*; Kingery, W. D. ed.; MIT Press: Cambridge, MA, 1958, pp. 5–51.
37. Adcock, D. S.; McDowall, I. S. *J. Am. Ceram. Soc.* 1957, Vol. 40, 355.
38. Aksay, I. A.; Schilling, C. H. In *Advances in Ceramics*, Vol. 9: *Forming of Ceramics*; The American Ceramic Society: Columbus, OH, 1984, pp. 85–93.
39. Tiller, F. M.; Tsai, C.-D. *J. Am. Ceram. Soc.* 1986, Vol. 69, 882.
40. Fennelly, T. J.; Reed, J. S. *J. Am. Ceram. Soc.* 1972, Vol. 55, 264.
41. Lange, F. F.; Miller, K. T. *Am. Ceram. Soc. Bulletin.* 1987, Vol. 66, 1498.
42. Mistler, R. E.; Twiname, E. R. *Tape Casting—Theory and Practice*; The American Ceramic Society: Westerville, OH, 2000.
43. Williams, J. C. In *Treatise on Materials Science and Technology*, Vol. 9; Wang, F. F. Y. ed.; Academic Press: New York, 1976, pp. 331–364.
44. Mistler, R. E.; Shanefield, D. J.; Runk, R. B. In *Ceramic Processing Before Firing*; Onoda, G. Y., Jr., Hench, L. L. eds.; Wiley: New York, 1978, pp. 411–448.
45. Mistler, R. E. In *Ceramic Processing*; Terpstra, R. A., Pex, P. P. A. C., DeVries, A. H. eds.; Chapman & Hall: London, 1995, pp. 147–173.
46. Hellebrand, H. In *Materials Science and Technology*, Vol. 17A: *Processing of Ceramics*, Part I; Brook, R. J. ed.; VCH: New York, 1996, pp. 189–265.
47. Chou, Y. T.; Ko, Y. T.; Yan, M. F. *J. Am. Ceram. Soc.* 1987, Vol. 70, C280.
48. Janney, M. A. U. S. Patent No. 4,894,194, January 16, 1990.
49. Janney, M. A.; Omatete, O. O. U. S. Patent No. 5,028,362, July 2, 1991, U. S. Patent No. 5,145,908, September 8, 1992.
50. Omatete, O. O.; Janney, M. A.; Strehlow, R. A. *Am. Ceram. Soc. Bulletin.* 1991, Vol. 70, 1641.

51. Young, A. C.; Omatete, O. O.; Janney, M. A.; Menchhofer, P. A. J. *Am. Ceram. Soc.* 1991, Vol. 74, 612.
52. Sarkar, P.; Nicholson, P. S. J. *Am. Ceram. Soc.* 1996, Vol. 79, 1987.
53. Janney, M. A. In *Ceramic Processing*; Terpstra, R. A., Pex, P. P. A. C., DeVries, A. H. eds.; Chapman & Hall: London, 1995, pp. 174–211.
54. Pels Leusden, C. O. In *Concise Encyclopedia of Advanced Ceramic Materials*; Brook, R. J. ed.; Pergamon: Oxford, 1991, pp. 131–135.
55. Schuetz, J. E. *Am. Ceram. Soc. Bulletin.* 1986, Vol. 65, 1556.
56. Buckingham, E. *Proc. Am. Soc. Test. Mater.* 1921, Vol. 21, 1154.
57. Reiner, M. *Kolloid Z.* 1926, Vol. 39, 80.
58. Robinson, G. C. In *Ceramic Processing Before Firing*; Onoda, G. Y., Jr., Hench, L. L. eds.; Wiley: New York, 1978, pp. 391–407.
59. Brady, G. A.; Hilmas, G. E.; Halloran, J. W. *Ceram. Trans.* 1995, Vol. 51, 301.
60. Van Hoy, C.; Barda, A.; Griffith, M.; Halloran, J. W. J. *Am. Ceram. Soc.* 1998, Vol. 81, 152.
61. German, R. M.; Bose, A. *Injection Molding of Metals and Ceramics*; Metal Powder Industries Federation: Princeton, NJ, 1997.
62. Mutsuddy, B. C.; Ford, R. G. *Ceramic Injection Molding*; Chapman & Hall: New York, 1995.
63. Evans, J. R. G. In *Materials Science and Technology*, Vol. 17A: *Processing of Ceramics, Part I*; Brook, R. J. ed.; VCH: New York, 1996, pp. 267–311.
64. German, R. M.; Hens, K. F.; Lin, S.-T. P. *Amer. Ceram. Soc. Bulletin.* 1991, Vol. 70, 1294.
65. Mangels, J. A.; Trela, W. In *Advances in Ceramics*, Vol. 9: *Forming of Ceramics*; The American Ceramic Society: Columbus, OH, 1984, pp. 220–233.
66. Chong, J. S.; Christianson, E. B.; Baer, A. D. J. *Appl. Polym. Sci.* 1971, Vol. 15, 2007.
67. Kochan, D. *Solid Freeform Manufacturing*; Elsevier: New York, 1993.
68. Kai, C. C.; Fai, L. K. *Rapid Prototyping*; Wiley: New York, 1997.
69. Dimos, D.; Danforth, S. C.; Cima, M. J. eds. *Solid Freeform and Additive Fabrication. Mater. Res. Soc. Symp. Proc.* 1999, Vol. 542.
70. Danforth, S. C.; Dimos, D.; Prinz, F. B. eds. *Solid Freeform and Additive Fabrication. Mater. Res. Soc. Symp. Proc.* 2000, Vol. 625.
71. Griffith, M. L.; Halloran, J. W. J. *Am. Ceram. Soc.* 1996, Vol. 79, 2601.
72. Cawley, J. D.; Heuer, A. H.; Newman, W. S.; Mathewson, B. B. *Am. Ceram. Soc. Bulletin.* 1996, Vol. 75, 75.
73. Agarwala, M. K.; Bandyopadhyay, A.; van Weeren, R.; Safari, A.; Danforth, S. C.; Lagrana, N. A.; Jamalabad, V. K.; Whalen, P. J. *Am. Ceram. Soc. Bulletin.* 1996, Vol. 75, 61.
74. Beaman, J. J. *Solid Freeform Fabrication*; Kluwer Academic Publishers: Boston, MA, 1997.
75. Sachs, E.; Cima, M.; Cornie, J.; Brancazio, D.; Bredt, J.; Curodeau, A.; Fan, T.; Khanuja, S.; Lauder, A.; Lee, J.; Michaels, S. *Ann. CIRP.* 1993, Vol. 42, 257.
76. Grau, J. E.; Uhland, S. A.; Moon, J.; Cima, M. J.; Sachs, E. M. J. *Am. Ceram. Soc.* 1999, Vol. 82, 2080.

77. Moon, J.; Grau, J. E.; Cima, M. J.; Sachs, E. M. J. *Am. Ceram. Soc.* 2001, Vol. 83, 2401.
78. Blazdell, P. F.; Evans, J. R. G.; Edirisinghe, M. J.; Shaw, P.; Binstead, M. J. J. *Mater. Sci. Lett.* 1995, Vol. 14, 1562.
79. Teng, W. D.; Edirisinghe, M. J.; Evans, J. R. G. J. *Am. Ceram. Soc.* 1997, Vol. 80, 486.
80. Teng, W. D.; Edirisinghe, M. J. J. *Am. Ceram. Soc.* 1998, Vol. 81, 1033.
81. Cesarano, J.; Segalman, R.; Calvert, P. *Ceram. Industry.* 1998, Vol. 148, 94.
82. Deegan, R. D.; Bakajin, O.; Dupont, T. F.; Huber, G.; Nagel, S. R.; Witten, T. A. *Nature.* 1997, Vol. 389, 827.
83. Guo, J. J.; Lewis, J. A. J. *Am. Ceram. Soc.* 1999, Vol. 82, 2345.
84. Chiu, R. C.; Cima, M. J. J. *Am. Ceram. Soc.* 1993, Vol. 76, 2557; 1993, Vol. 76, 2769.
85. Hu, M. S.; Thouless, M. D.; Evans, A. G. *Acta Metall.* 1988, Vol. 36, 1301.
86. Dong, C.; Bowen, H. K. J. *Am. Ceram. Soc.* 1989, Vol. 72, 1082.
- 87a. Cima, M. J.; Dudziak, M.; Lewis, J. A. J. *Am. Ceram. Soc.* 1989, Vol. 72, 1087.
- 87b. Cima, M. J.; Lewis, J. A.; Defoe, A. D. J. *Am. Ceram. Soc.* 1989, Vol. 72, 1192.
88. German, R. M. *Int. J. Powder Metall.* 1987, Vol. 23, 237.
89. Masia, S.; Calvert, P. D.; Rhine, W. E.; Bowen, H. K. J. *Mater. Sci.* 1989, Vol. 24, 1907.
90. Bonekamp, B. C.; Veringa, H. J. In *Materials Science and Technology*, Vol. 17A: Processing of Ceramics, Part I; Brook, R. J. ed.; VCH: New York, 1996, pp. 343–387.
91. Weeks, M. J.; Laughner, J. W. *Adv. Ceram.* 1987, Vol. 21, 793.
92. Uematsu, K.; Miyashita, M.; Kim, J.-Y.; Kato, Z.; Uchida, N. J. *Am. Ceram. Soc.* 1991, Vol. 74, 2170.

7

Sintering of Ceramics

Fundamentals

7.1 INTRODUCTION

Almost all ceramic bodies must be sintered to produce a microstructure with the required properties. This widespread use of the sintering process has led to a variety of approaches to the subject. In practice, the ceramist, wishing to prepare a material with a particular set of properties, identifies the required microstructure and tries to design processing conditions that will produce this required microstructure. The key objective of sintering studies is therefore to understand how the processing variables influence the microstructural evolution. In this way, useful information can be provided for the practical effort of designing processing conditions for producing the required microstructure.

One approach to developing an understanding of sintering is to connect the behavior or changes in behavior during sintering to controllable variables and processes. This can be achieved empirically by measuring the sintering behavior under a set of controlled conditions or theoretically by modeling the process. The theoretical analyses and experimental studies performed over the last 50 years have produced an excellent qualitative understanding of sintering in terms of the driving forces, the mechanisms, and the influence of the principal processing variables such as particle size, temperature, and applied pressure. However, the database and models are far less successful at providing a quantitative description of sintering for most systems of interest. For this shortcoming, the sintering models have received some criticism.

Table 7.1 lists some of the important parameters in sintering that may serve to illustrate the scope of the problem (1). In general, the processing and material parameters provide a useful set of variables for model experimental and theoretic-

TABLE 7.1 Some Important Parameters in the Sintering of Ceramics

<i>Behavior:</i>	<i>Processing and Material Parameters:</i>
General morphology	Powder preparation: particle size, shape, and size distribution
Pore evolution: size, shape, interpore distance	Distribution of dopants or second phases
Grain evolution: size and shape	Powder consolidation: density and pore size distribution
Density: function of time and temperature	Firing: heating rate and temperature
Grain size: function of time and temperature	Applied pressure
Dopant effects on densification and grain growth	Gaseous Atmosphere
<i>Models:</i>	<i>Characterization Measurements:</i>
Neck growth	Neck growth
Surface area change	Shrinkage, density, and densification rate
Shrinkage	Surface area change
Densification in the later stages	Grain size, pore size, and interpore distance
Grain growth: porous and dense systems, solute drag, pore drag, pore breakaway	Dopant distribution
Concurrent densification and grain growth	Strength, conductivity, and other microstructure-dependent properties
<i>Data Base:</i>	
Diffusion coefficients: anion and cation, lattice, grain boundary and surface	
Surface and interfacial energies	
Vapor pressure of components	
Gas solubilities and diffusivities	
Solute diffusivities	
Phase equilibria	

cal studies. Some parameters, such as the sintering temperature, applied pressure, average particle size, and gaseous atmosphere, can be controlled with sufficient accuracy. Others, such as the powder characteristics and particle packing, are more difficult to control but have a significant effect on sintering. While partial information exists in the other areas of behavior, characterization measurements, and the data base, much critically needed information is severely lacking. This is especially serious in the data base for the fundamental parameters such as the surface and grain boundary energies and the diffusion coefficients. This lack of information coupled with the complexity of practical ceramic systems makes

quantitative predictions of the sintering behavior very difficult even for the simplest systems.

Some fundamental concepts in sintering will be examined in this chapter. For sintering to occur, there must be a decrease in the free energy of the system. The *curvature* of the free surfaces and, when used, the applied pressure provide the main motivation or *driving force* for sintering to occur. However, to accomplish the process within a reasonable time, we must also consider the *kinetics* of matter transport. In crystalline ceramics, matter transport occurs predominantly by *diffusion* of atoms, ions, or other charged species. Solid-state diffusion can occur by several paths that define the *mechanisms of diffusion* and, hence, the mechanisms of sintering. The rate of diffusion depends on the type and concentration of *defects* in the solid, so an understanding of the defect structure and the changes in the defect concentration (the defect chemistry) is important. We must also understand how the defect chemistry is controlled by key variables in the sintering process such as temperature, gaseous atmosphere, and solutes (dopants).

In order to predict how the rate of sintering depends on the primary processing variables, equations for the flux of matter must be formulated and solved subject to the appropriate boundary conditions. Matter transport can be viewed in terms of the flux of atoms (ions) or, equivalently, in terms of the counterflow of vacancies. Following Fick's laws of diffusion, the flux can be analyzed in terms of the concentration gradient of the diffusing species, but the equations take a more generalized form when expressed in terms of the *chemical potential* (the molar Gibbs free energy). In this view, matter transport occurs from regions of higher chemical potential to regions of lower chemical potential. In inorganic solids, the different ions or charged species diffuse at different rates but matter transport must take place in such a way that the stoichiometry and electroneutrality of the solid are preserved. The diffusion of the ions is therefore coupled and this coupled diffusion is referred to as *ambipolar diffusion*.

7.2 DRIVING FORCE FOR SINTERING

As with all other irreversible processes, sintering is accompanied by a lowering of the free energy of the system. The sources that give rise to this lowering of the free energy are commonly referred to as the *driving forces for sintering*. Three possible driving forces are

1. the curvature of the particle surfaces
2. an externally applied pressure, and
3. a chemical reaction.

7.2.1 Surface Curvature

In the absence of an external stress and a chemical reaction, surface curvature provides the driving force for sintering (Fig. 7.1). To see why this is so, let us

consider, for example, one mole of powder consisting of spherical particles with a radius a . The number of particles is

$$N = \frac{3M}{4\pi a^3 \rho} = \frac{3V_m}{4\pi a^3} \quad (7.1)$$

where ρ is the density of the particles, which are assumed to contain no internal porosity, M is the molecular weight, and V_m is the molar volume. The surface area of the system of particles is

$$S_A = 4\pi a^2 N = \frac{3V_m}{a} \quad (7.2)$$

If γ_{sv} is the specific surface energy (i.e., the surface energy per unit area) of the particles, then the surface free energy associated with the system of particles is

$$E_s = \frac{3\gamma_{sv} V_m}{a} \quad (7.3)$$

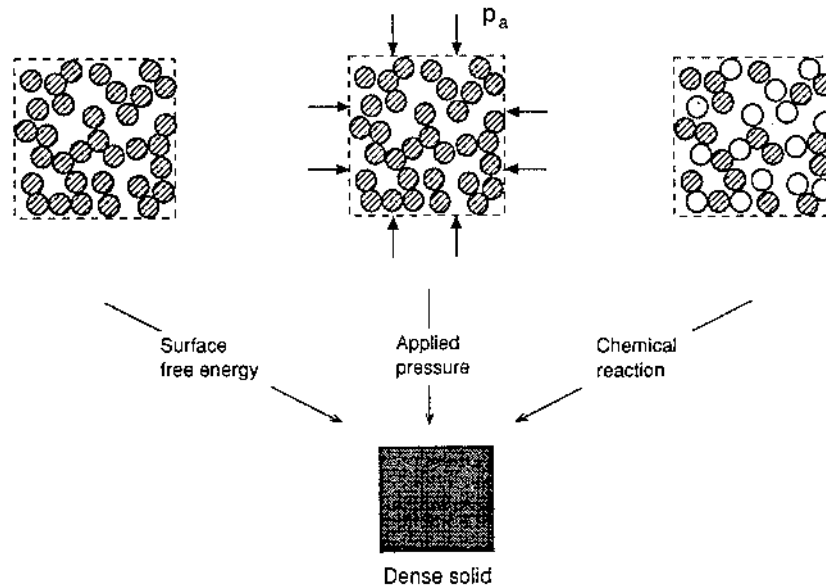


FIGURE 7.1 Schematic diagram illustrating three main driving forces for sintering: surface free energy, applied pressure, and chemical reaction.

E_s represents the decrease in surface free energy of the system if a fully dense body were to be formed from the mole of particles and provides a motivation for sintering. Taking $\gamma_{sv} = 1 \text{ J/m}^2$, $a = 1 \text{ }\mu\text{m}$, and $V_m = 25 \times 10^{-6} \text{ m}^3$, then $E_s = 75 \text{ J/mol}$ of material.

7.2.2 Applied Pressure

In the absence of a chemical reaction, an externally applied pressure normally provides the major contribution to the driving force when the pressure is applied over a significant part of the heating process as in hot pressing and hot isostatic pressing (Fig. 7.1). Surface curvature also provides a contribution to the driving force, but for most practical situations it is normally much smaller than that provided by the external pressure. The external pressure does work on the system of particles and, for 1 mol of particles, the work done can be approximated by

$$W = p_a V_m \quad (7.4)$$

where p_a is the applied pressure and V_m is the molar volume. W represents the driving force for densification due to the application of an external pressure. For $p_a = 30 \text{ MPa}$, which is a typical value of the stress applied in hot pressing, and $V_m = 25 \times 10^{-6} \text{ m}^3$, then $W = 750 \text{ J}$.

7.2.3 Chemical Reaction

A chemical reaction can, in principle, provide a driving force for sintering if it can be used to aid the densification process (Fig. 7.1). The change in free energy accompanying a chemical reaction is given by

$$\Delta G^\circ = -RT \ln K_{eq} \quad (7.5)$$

where R is the gas constant (8.3 J/mol), T is the absolute temperature, and K_{eq} is the equilibrium constant for the reaction. Taking $T = 1000\text{K}$ and $K_{eq} = 10$, then $\Delta G^\circ \approx 20,000 \text{ J/mol}$. This decrease in energy is significantly greater than the driving force due to an applied stress. In practice, a chemical reaction is hardly ever used deliberately to drive the densification process in advanced ceramics because microstructure control becomes extremely difficult when a chemical reaction occurs concurrently with sintering (see Chapter 11).

7.3 DEFECTS IN CRYSTALLINE SOLIDS

The driving forces provide a motivation for sintering but the actual occurrence of sintering requires transport of matter, which in crystalline solids occurs by a process of diffusion involving atoms, ions, or molecules. Crystalline solids are not ideal in structure. At any temperature they contain various imperfections

called *defects*. It is the presence of these defects that allow diffusional mass transport to take place. Because they control the rate at which matter is transported, defects control the rates of processes such as sintering, grain growth, and creep.

Defects in crystalline solids occur for structural reasons, because the atoms (or ions) are not arranged ideally in the crystal when all the lattice sites are occupied, and for chemical reasons, because inorganic compounds may deviate from the fixed composition determined by the valence of the atoms. There are different types of structural defects in a crystalline solid which are normally classified into three groups: (1) *point* defects, (2) *line* defects, and (3) *planar* defects. Point defects are associated with one lattice point and its immediate vicinity. They include missing atoms or *vacancies*, *interstitial* atoms occupying the interstices between atoms, and *substitutional* atoms sitting on sites that would normally be occupied by another type of atom. These point defects are illustrated in Fig. 7.2 for an elemental solid (e.g., a pure metal). The point defects that are formed in pure crystals (i.e., vacancies and interstitials) are sometimes referred to as intrinsic or native defects.

Most of our discussion will be confined to point defects in ionic solids (ceramics). Line defects, commonly referred to as *dislocations*, are characterized by displacements in the periodic structure of the lattice in certain directions. They play their most important role in the plastic deformation of metals. Planar defects include free surfaces, grain boundaries, stacking faults, and crystallographic shear planes.

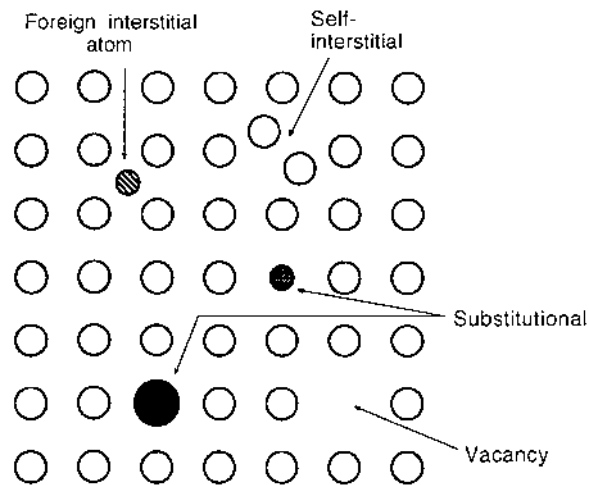


FIGURE 7.2 Point defects in an elemental solid.

7.3.1 Point Defects and Defect Chemistry

A key distinction between point defects in ceramics and those in metals is that in ceramics, the defects can be electrically charged. For a pure ionic compound with the stoichiometric formula MO consisting of a metal M (with a valence of $+2$) and oxygen O (valence -2), the types of point defects that may occur are vacancies and interstitials of both M and O . These *ionic* defects may be either charged or neutral. In addition to the single defects, it is possible for one or more defects to associate with one another, leading to the formation of defect clusters. There may also be *electronic* (or valence) defects consisting of quasi-free electrons or holes (missing electrons). If the compound contains a small amount of solute (or impurity) atoms M_f , substitutional or interstitial defects of M_f will also occur, and these may be either charged or neutral.

Another important distinction between ceramic and metallic systems is that the composition of the ceramic may become nonstoichiometric by annealing in a suitable gaseous atmosphere (e.g., a controlled oxygen partial pressure). The compound seeks to equilibrate itself with the partial pressure of one of its components in the surrounding atmosphere. This equilibration leads to a change in the composition and a change in the type and concentration of the defects. For example, annealing the compound MO in an atmosphere with a low oxygen partial pressure may lead to an oxygen-deficient oxide, MO_{1-x} , in which oxygen vacancies predominate. On the other hand, annealing in an atmosphere with a higher oxygen partial pressure may lead to a metal deficient oxide, $M_{1-y}O$, in which metal vacancies predominate.

Charged defects in solids can interact with one another in an analogous way to the interactions between ions (or between ions and electrons) in a solution. In the solid-state situation, the crystal may be viewed as a neutral medium into which the charged defects are dissolved. This similarity between solution chemical interactions and defect interactions in the solid state has resulted in the field of *defect chemistry*, which provides basic methods for studying the effects of point defects in solids. The methods are normally applicable to fairly low defect concentrations. Generally, a broad distinction is made between *intrinsic defects* that are thermally generated in pure compounds and *extrinsic defects* produced by external influences such as impurities and gaseous atmospheres. References 2 and 3 provide a detailed discussion of point defects and defect chemistry in metal oxides.

7.3.2 Kroger-Vink Notation

A standard notation, referred to as the *Kroger-Vink notation*, is used for the description of point defects in ionic solids. In this notation, the defect is defined with respect to the perfect lattice and is described by three parts: the main symbol, a subscript, and a superscript. For example, in the notation, M_L^C , the main symbol

M denotes the particular type of atom, or in the case of a vacancy, the main symbol is V . The subscript L denotes the site in the perfect lattice at which the defect is located. The superscript C gives the *effective charge* (or relative charge) of the defect, equal to the difference in valence between the species on the L site and the valence of the atom that occupies the L site in the perfect lattice. The effective charge is represented as follows:

Positive effective charge: $C = \bullet$

Negative effective charge: $C = /$

Neutral effective charge: $C = x$

Electronic defects are specified as follows: a quasi-free electron is represented as e' , while a missing electron or hole is represented as h^\bullet . The use of the Kroger-Vink notation is demonstrated in Table 7.2 for some possible defects in Al_2O_3 .

The *concentration* of defects is denoted by square brackets, for example, $[V_O^{\bullet\bullet}]$ and $[Ti_{Al}^\bullet]$. The concentration of electrons and holes, $[e']$ and $[h^\bullet]$, is commonly written n and p , respectively.

7.3.3 Defect Reactions

The formation of defects can be viewed as a chemical reaction, and by this analogy, we can write defect reactions in a way similar to chemical reactions once the following three conservation rules are observed:

1. *Conservation of mass*: A mass balance must be maintained so that mass is neither created nor destroyed in the defect reaction. Vacancies have zero mass, while electronic defects are considered to have no effect on the mass balance.
2. *Electroneutrality*: The crystal must remain electrically neutral. This means that for the overall reaction, the sum of the positive effective charges must be equal to the sum of the negative effective charges.

TABLE 7.2 Kroger-Vink Notation for Some Possible Defects in Al_2O_3

Notation	Defect
$Al_T^{\bullet\bullet\bullet}$	Aluminum ion in the interstitial lattice site
$V_O^{\bullet\bullet}$	Oxygen vacancy
Mg'_{Al}	Magnesium dopant on the normal Al lattice site
Ti_{Al}^\bullet	Ti dopant on the normal Al lattice site
e'	Quasi-free electron
h^\bullet	Missing electron or hole

3. *Site ratio conservation*: The ratio of the number of regular cation sites to the number of regular anion sites in the crystal remains constant. For example, in the compound MO, the ratio of the regular M and O sites must remain in the ratio of 1:1. Sites may be created or destroyed in the defect reaction, but they must occur in such a way that the site ratio in the regular lattice is maintained.

To see how these rules apply, let us consider the incorporation of MgO into Al_2O_3 . Based on the ionic radii of Mg^{2+} and Al^{3+} in sixfold coordination, the Mg ions may enter the solid solution *substitutionally*. In the corundum structure, one-third of the octahedral sites between the close-packed O ions are vacant, so it is possible that the Mg ions can also enter the solid solution *interstitially*. It is not clear which incorporation reaction has the lower energy. In Al_2O_3 , there are two cation sites to every three anion sites. Considering the substitutional process, if we incorporate two Mg atoms on cation sites we must use two Al sites as well as two O sites. Since we have only two O sites, we can tentatively assume that the third O site for site conservation may be vacant. At this stage, on the basis of mass and site balance, we may write

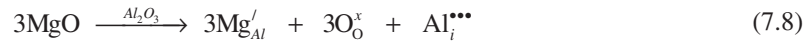


Assuming that the defects are fully ionized, which is believed to be a more realistic solid solution process, conservation of electroneutrality gives

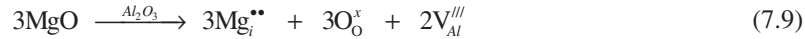


and we have mass, charge, and site ratio balance.

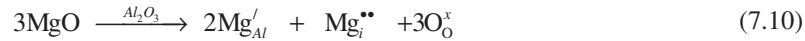
Another possibility is the formation of Al interstitials (instead of O vacancies), for which we may write



This equation is, however, invalid because mass and site ratio are not conserved. If the Mg ions are incorporated interstitially, we can write



It is also possible that the Mg is self-compensating and forms both substitutional and interstitial defects:



The reader will verify the conservation of mass, electroneutrality, and site ratio in Eqs. (7.9)–(7.10). The formation of interstitials does not create new crystal sites but must be taken into account for mass and charge conservation.

7.3.4 Defect Concentration

The concentration of defects can be determined by a statistical thermodynamics approach, but an equivalent way is to view the formation of defects as a chemical reaction in which there is an equilibrium constant governed by the law of mass action. For a general reaction in which the reactants A and B lead to products C and D:



where a , b , c , and d are the number of moles of the reactants and products. At equilibrium at a fixed temperature, the law of mass action applies, and assuming that the activities of the reactants and products are equal to their concentrations, the law gives

$$K = \frac{[C]^c [D]^d}{[A]^a [B]^b} \quad (7.12)$$

where the brackets denote the concentrations and K , the *equilibrium constant*, is given by the Arrhenius equation

$$K = \exp\left(\frac{-\Delta G}{RT}\right) \quad (7.13)$$

In this equation, ΔG is the free energy change for the reaction, R is the gas constant, and T is the absolute temperature. For defect reactions, the use of Eqs. (7.12) and (7.13) requires that the concentration of the defects be expressed as site *fractions*. For low defect concentrations, the concentration of ions in their regular lattice sites is assigned a value of unity. For reactions involving gaseous species, the concentration of a gas is taken as its partial pressure. The application of the law of mass action is illustrated in the next two sections.

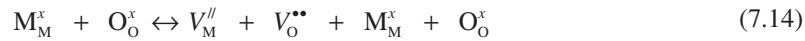
7.3.5 Intrinsic Defects

Two of the more common types of intrinsic defects in ionic crystals are the *Schottky defect* and the *Frenkel defect*.

7.3.5.1 Schottky Defect

The formation of a Schottky defect can be viewed as the transfer of a cation and an anion from their regular lattice sites to an external surface, thereby creating extra perfect crystal, and leaving behind vacancies (Fig. 7.3). To preserve electro-neutrality of the crystal, vacancies must be formed in the stoichiometric ratio.

For the compound MO and assuming that the defects are fully ionized, the defect formation reaction can be written



In this equation, M_M^x and O_O^x on both sides of the equation can be canceled, so the net reaction is written



where null (also written nil or zero) denotes the creation of defects from a perfect lattice. Assuming that the reaction has reached equilibrium, applying the law of mass action gives

$$K_s = [V_M''] [V_O^{\bullet\bullet}] = \exp\left(\frac{-\Delta G_s}{RT}\right) \quad (7.16)$$

where K_s is the equilibrium constant and ΔG_s is the free-energy change for the creation of Schottky defects as defined by Eq. (7.15). For electroneutrality we must have $[V_M''] = [V_O^{\bullet\bullet}]$, so we obtain

$$[V_M''] = [V_O^{\bullet\bullet}] = \exp\left(\frac{-\Delta G_s}{2RT}\right) \quad (7.17)$$

7.3.5.2 Frenkel Defect

A Frenkel defect is formed when an ion leaves its regular lattice site and occupies an interstitial site, leaving behind a vacant site (Fig. 7.4). For the compound MO

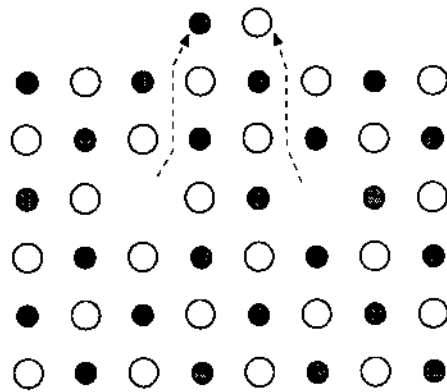


FIGURE 7.3 Schematic diagram for the formation of a Schottky defect.

and assuming fully ionized defects, the creation of a Frenkel defect at the cation site can be written



The equilibrium constant for the reaction is

$$K_F = [M_i^{\bullet\bullet}][V_M^{\prime\prime}] = \exp\left(\frac{-\Delta G_F}{RT}\right) \quad (7.19)$$

By invoking the electroneutrality condition $[M_i^{\bullet\bullet}] = [V_M^{\prime\prime}]$, we obtain

$$[M_i^{\bullet\bullet}] = [V_M^{\prime\prime}] = \exp\left(\frac{-\Delta G_F}{2RT}\right) \quad (7.20)$$

Corresponding equations can be written for the formation of Frenkel defects on the anion sites. It should be noted that the formation of cation and anion Frenkel defects are not linked through an electroneutrality condition, so the cation interstitial concentration need not be equal to the anion interstitial concentration.

7.3.6 Extrinsic Defects

Extrinsic defects, as outlined earlier, are caused by external influences such as the gaseous atmosphere (which may lead to nonstoichiometry) and solutes (or dopants).

7.3.6.1 Nonstoichiometry

Equilibration of ionic solids (e.g., an oxide MO) with an ambient gas that is also a constituent of the solid (e.g., O₂) can have a significant effect on the defect

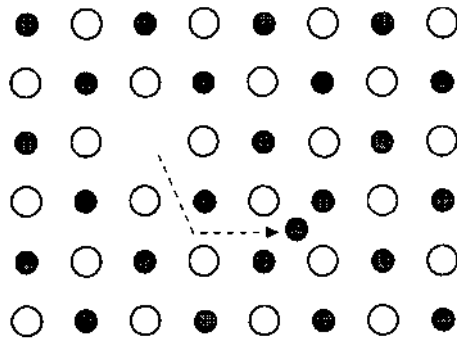


FIGURE 7.4 Schematic diagram for the formation of a Frenkel defect.

structure. Oxides of elements tending to show fixed valency (e.g., MgO, Al₂O₃, and ZrO₂) have negligible deviation from stoichiometry, whereas those of elements with variable valence (e.g., NiO, CoO, FeO, and TiO₂) can display a large departure from stoichiometry.

At any fixed temperature and composition, the oxide must be in equilibrium with a specific oxygen partial pressure. If not, the crystal will give up or take up oxygen until equilibrium has been reached. When the oxide gives up oxygen, in a *reduction* reaction, it will do so by creating *oxygen vacancies* in the lattice, with the electrons that were associated with the O²⁻ ions in the reaction being liberated within the solid. The overall reaction can be written as



The creation of the vacant oxygen sites leads to a change in the cation to anion ratio, i.e., to *nonstoichiometry*. The equilibrium constant for the reaction is

$$K_R = n^2 [V_\text{o}^{\bullet\bullet}] p_{\text{O}_2}^{1/2} = K_R^o \exp\left(\frac{-\Delta G_R}{RT}\right) \quad (7.22)$$

where the concentration of the oxygen gas is taken as its partial pressure, K_R^o is a constant, and ΔG_R is the free energy change for the reduction. For electroneutrality, $n = 2[V_\text{o}^{\bullet\bullet}]$, and substituting in Eq. (7.22) gives

$$[V_\text{o}^{\bullet\bullet}] = \left(\frac{K_R}{4}\right)^{1/3} p_{\text{O}_2}^{-1/6} \quad (7.23)$$

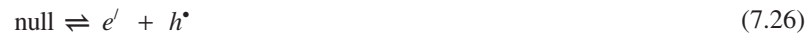
When the oxide takes up oxygen, the *oxidation* reaction can be written as the consumption of oxygen vacancies, with the charge neutralized by combining with an electron, thus creating a missing electron or *hole* in the valence band:



The equilibrium constant is

$$K_\text{O} = \frac{p^2}{[V_\text{o}^{\bullet\bullet}] p_{\text{O}_2}^{1/2}} = K_\text{O}' \exp\left(\frac{-\Delta G_\text{O}}{RT}\right) \quad (7.25)$$

It is important to note that since oxidation and reduction are the same thermodynamic process simply reversed, the reactions written to describe them are not independent. For example, taking the reduction reaction [Eq. (7.21)] in combination with the intrinsic electronic defect equilibrium



yields the oxidation reaction [Eq. (7.24)]. In fact, there are a number of ways of writing the oxidation and reduction reactions, which we may choose for convenience to show the formation or removal of particular defects. For example, oxidation can also be viewed as the buildup of the oxygen lattice and creating cation vacancies that take their charge by combining with an electron, thus creating a hole in the valence band. For an oxide MO, the reaction can be written as



Equation (7.27) can be obtained by adding the Schottky reaction to (7.24).

7.3.6.2 Influence of Solutes

Solutes (also referred to as *dopants*), present in concentrations as low as a fraction of a mole percent, have a significant influence on sintering. They refer to compounds that are incorporated into solid solution to modify the microstructure and properties of ceramics. The term *aliovalent* dopant is sometimes used to describe a solute in which the cation valence is different from that of the host cation, whereas a solute in which the cation valence is the same as that of the host is sometimes called an *isovalent* dopant. For aliovalent dopants, when the valence of the solute cation is *greater* than that of the host cation, the solute is referred to as a *donor* dopant. On the other hand, an *acceptor* dopant refers to a solute in which the cation valence is smaller than that of the host cation. For example, TiO_2 and MgO are donor and acceptor dopants, respectively, for Al_2O_3 (the host).

Let us now consider the incorporation of Al_2O_3 solute into MgO . Based on the similarity in ionic radii, we may assume that the Al will substitute for Mg, with charge compensation achieved by the simultaneous creation of a vacant Mg site:



As the incorporation reaction proceeds, the other defect equilibria such as the creation of Schottky or Frenkel defects are still present. Supposing that the intrinsic defects in MgO consist of Schottky disorder, then following Eq. (7.16), we can write

$$[V_\text{O}^{\bullet\bullet}][V_{\text{Mg}}''] = K_s \quad (7.29)$$

The electroneutrality condition is

$$[\text{Al}_{\text{Mg}}^\bullet] + 2[V_\text{O}^{\bullet\bullet}] = 2[V_{\text{Mg}}''] \quad (7.30)$$

For very low Al_2O_3 concentration, $[\text{Al}_{\text{Mg}}^\bullet] \ll [V_{\text{Mg}}'']$, so

$$\left[V_{\text{O}}^{\bullet\bullet} \right] = \left[V_{\text{Mg}}^{\prime\prime} \right] = K_s^{1/2} \quad (7.31)$$

indicating that the concentration of the intrinsic defects are independent of the Al_2O_3 concentration.

As the incorporation reaction described by Eq. (7.28) proceeds, the concentration of the Al in solid solution increases and the extrinsic defects begin to dominate. The electroneutrality condition now becomes

$$\left[\text{Al}_{\text{Mg}}^{\bullet} \right] = 2 \left[V_{\text{Mg}}^{\prime\prime} \right] \quad (7.32)$$

Assuming that the Al_2O_3 has been completely incorporated in the reaction, the concentration of Al in solid solution is equal to the total atomic concentration of Al, so

$$\left[\text{Al}_{\text{Mg}}^{\bullet} \right] = [\text{Al}] \quad (7.33)$$

Since Eq. (7.29) must apply for the cation and anion vacancies, combination of Eq. (7.29) with Eqs. (7.32) and (7.33) yields

$$\left[V_{\text{O}}^{\bullet\bullet} \right] = \frac{2K_s}{[\text{Al}]} \quad (7.34)$$

Furthermore, Eqs. (7.32) and (7.33) give

$$\left[V_{\text{Mg}}^{\prime\prime} \right] = \frac{[\text{Al}]}{2} \quad (7.35)$$

7.3.6.3 Brouwer Diagram

The changes in defect concentration as a function of temperature, oxygen partial pressure, or dopant concentration are sometimes described semi-quantitatively in terms of a double logarithmic plot known as a *Brouwer diagram*. Figure 7.5 shows a Brouwer diagram for the effect of Al_2O_3 dopant on the defect chemistry of MgO that was considered above. Similar principles will apply for the variation of the defect concentration with temperature or oxygen partial pressure.

As illustrated for the Al_2O_3 -doped MgO system, the Brouwer diagram gives the net effect when the different defect reactions are considered simultaneously. In principle, the number of defect reactions that can be written for a given system is nearly limitless, but in practice, the number of defects that must be included to describe a given defect-related property (e.g., electrical conductivity or sintering) is small. The majority defects are always important, but in addition, certain minority defects may be relevant to a property of interest. The defect formation reactions will typically include those for

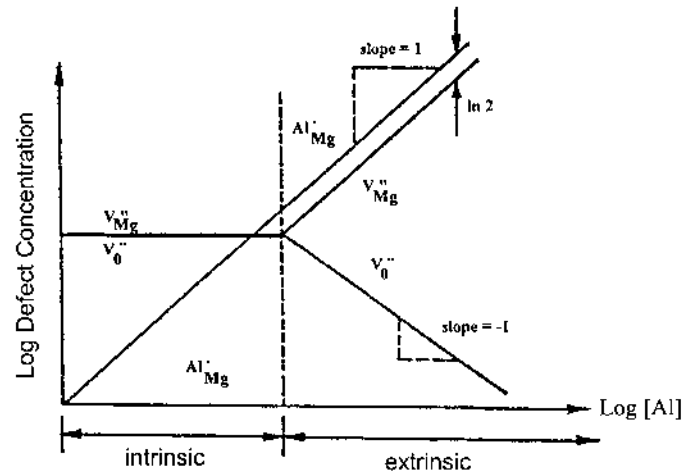


FIGURE 7.5 Brouwer diagram for MgO doped with Al_2O_3 . The defect concentrations are shown as a function of the concentration of Al.

1. Predominant intrinsic ionic defects (Schottky or Frenkel)
2. Intrinsic electronic defects
3. Oxidation and reduction
4. Solute incorporation

In addition, an equation for the electroneutrality condition for the bulk crystal is always necessary. Problems requiring the construction of Brouwer diagrams are given at the end of the chapter.

7.3.7 Defect Chemistry and Sintering

To summarize at this stage, the point defect concentration and hence the rate of matter transport through the crystal lattice can be altered by manipulating three accessible variables: the temperature, the oxygen partial pressure (the gaseous atmosphere), and the concentration of dopants. Taking the Al_2O_3 -doped MgO system as an example, if the sintering rate of MgO is controlled by the diffusion of oxygen vacancies, then Eq. (7.34) indicates that the addition of Al_2O_3 acts to inhibit the sintering rate. On the other hand, if the diffusion of magnesium vacancies is the rate-controlling mechanism, then the addition of Al_2O_3 will increase the sintering rate [Eq. (7.35)]. In practice, control of the sintering rate through manipulation of the defect structure is not as straightforward as this example may indicate. A major problem is that the rate-controlling mechanism for sintering in most systems is not clear. Another problem is that more than one mechanism

may operate during sintering, and the relative rates of transport by the different mechanisms may change with the conditions. Furthermore, other factors such as the particle packing homogeneity have a considerable influence on the sintering rate and may actually overwhelm the effects produced by changes in the defect structure.

7.4 DIFFUSION IN CRYSTALLINE SOLIDS

Solid-state diffusion is discussed in detail in many texts, including a treatment of the concepts by Shewmon (4) and a mathematical treatment by Frank (5). Review articles by Howard and Lidiard (6) and Atkinson (7) provide a condensed treatment of key concepts.

7.4.1 Fick's Laws of Diffusion

In an elementary view of diffusion, the movement of the diffusing species is considered to be driven by gradients in the concentration without taking into account the atomic nature of crystal structure and atomic defects. This *continuum approach* to diffusion is quite similar to heat transfer. The concentration can vary as a function of distance and time. When the concentration is independent of time, the mathematics of the diffusion process is described by *Fick's first law*, which states that the flux of the diffusing species J (number crossing unit area, normal to the direction of flux, per second) is proportional to the concentration gradient dC/dx and occurs in the direction of decreasing concentration. Fick's first law (in one dimension) is

$$J_x = -D \frac{dC}{dx} \quad (7.36)$$

The constant of proportionality D is called the *diffusion coefficient* or *diffusivity* and has SI units of m^2/s (but is more commonly expressed in cm^2/s). The diffusion coefficient is a material property and is the most useful parameter for characterizing the rate of diffusive mass transport. It is usually a strong function of temperature and is also a function of composition, although in certain limiting cases, such as a dilute concentration of the diffusing species, it can be taken to be independent of the composition.

A concentration that is independent of time is often experimentally difficult to establish in a solid. It is more often convenient to measure the change in concentration as a function of time t . This is given by *Fick's second law*, which in one dimension is

$$\frac{dC}{dt} = D \frac{d^2C}{dx^2} \quad (7.37)$$

Fick's second law can be derived from his first law and an application of the principle of conservation of matter. For the one-dimensional case, consider the region between the two planes $[x_1, (x_1 + dx)]$ shown in Fig. 7.6. The solute concentration C is shown schematically as a function of distance x in Fig. 7.6a. Since dC/dx at x_1 is greater than dC/dx at $(x_1 + dx)$, $J(x_1)$ will be greater than $J(x_1 + dx)$, as shown in Fig. 7.6b. If $J(x_1) > J(x_1 + dx)$ and matter is conserved, the solute concentration in the region between x_1 and $x_1 + dx$ must increase. Considering a volume element of unit area normal to the x axis and dx in thickness, the rate of change of concentration is

$$\left(\frac{dC}{dt} \right)_{x_1} dx = J(x_1) - J(x_1 + dx) \quad (7.38)$$

If dx is small, $J(x_1 + dx)$ can be related to $J(x)$ by

$$J(x_1 + dx) = J(x_1) + \left(\frac{dJ}{dx} \right)_{x_1} dx \quad (7.39)$$

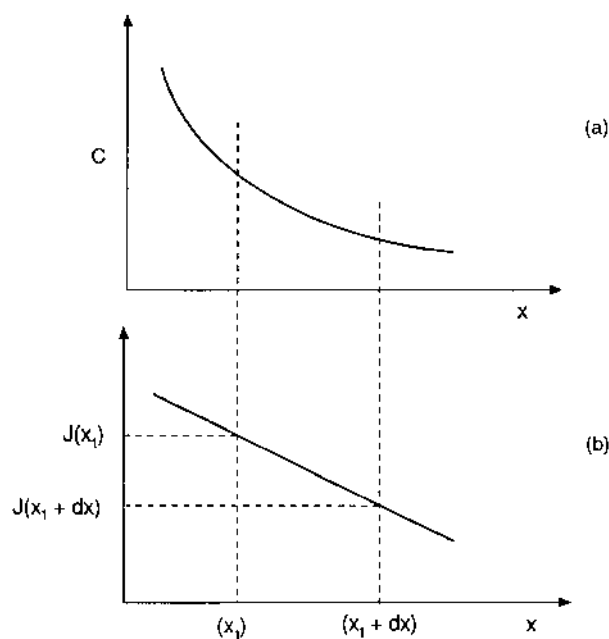


FIGURE 7.6 (a) Concentration C versus distance x and (b) the resulting flux J versus distance.

Substituting Eq. (7.39) into Eq. (7.38) and using Eq. (7.36) for J gives

$$\frac{dC}{dt} = -\frac{dJ}{dx} = -\frac{d}{dx}\left(-D\frac{dC}{dx}\right) = D\frac{d^2C}{dx^2} \quad (7.40)$$

Equation (7.37) can be solved for certain boundary conditions that can be approximated experimentally. For example, a common technique to measure D is to deposit a very thin film of a radioactive isotope (or mass isotope) on a plane surface of a thick sample and, after annealing for fixed times, determine the concentration of the diffusing species as a function of distance. Our experimental system approximates to the case of diffusion of a thin planar source in a semi-infinite solid. If the initial thickness of the layer of radioisotope is small compared to the distance over which the radioisotope diffuses, the solution of Eq. (7.37) is

$$C = \frac{C_0}{(\pi D^* t)^{1/2}} \exp\left(\frac{-x^2}{4D^* t}\right) \quad (7.41)$$

where C is the concentration at a distance x from the surface, t is the annealing time, and C_0 is the initial concentration (moles per unit area) of the radioisotope (i.e., at $t = 0$). D^* is the diffusion coefficient of the radioisotope, which, as we see later, is referred to as the *tracer diffusion coefficient*. Graphical representation of Eq. (7.41) is shown in Fig. 7.7. A plot of the data for $\ln C$ versus x^2 yields a straight line with a slope of $-1/(4D^*t)$ from which D^* can be found. Solutions to Eq. (7.37) for several geometries and boundary conditions can be found in Ref. 5 as well as in Ref. 8 (by converting the solutions for heat transfer).

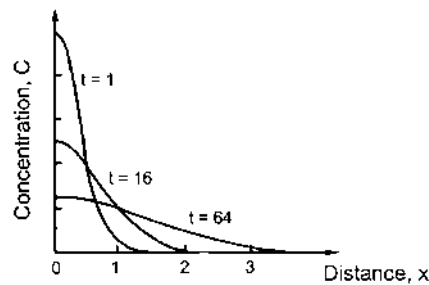


FIGURE 7.7 Graphical representation of the solution to Fick's second law for a thin planar source diffusing into a semi-infinite solid. The curves show concentration versus distance after various times and the units have been chosen arbitrarily.

7.4.2 Atomistic Diffusion Processes

At the atomic level, diffusion may be viewed as the periodic jumping of atoms from one lattice site to another via an intermediate stage of higher energy that separates one site from another (Fig. 7.8). The energy barrier that must be surmounted in the intermediate state before the jump can occur is called the *activation energy*. This periodic jumping of the atoms, in which the atom diffuses by a kind of Brownian motion or random way over the lattice sites, is sometimes referred to as *random diffusion*. It can be treated as a random-walk problem that allows us to determine a relationship between the observed macroscopic diffusion coefficients and the jump frequencies and jump distances of the atoms.

Let us consider two adjacent planes, denoted *A* and *B*, a distance λ apart, in a crystalline solid that has a concentration gradient along the *x* axis (Fig. 7.9). Let there be n_A diffusing atoms per unit area in plane *A* and n_B in plane *B*. We consider only jumps to the left and right, that is, those giving a change in position along the *x* axis. The probability P that an atom will have, at any instant, sufficient energy to surmount the energy barrier q is

$$P = \exp\left(\frac{-q}{kT}\right) \quad (7.42)$$

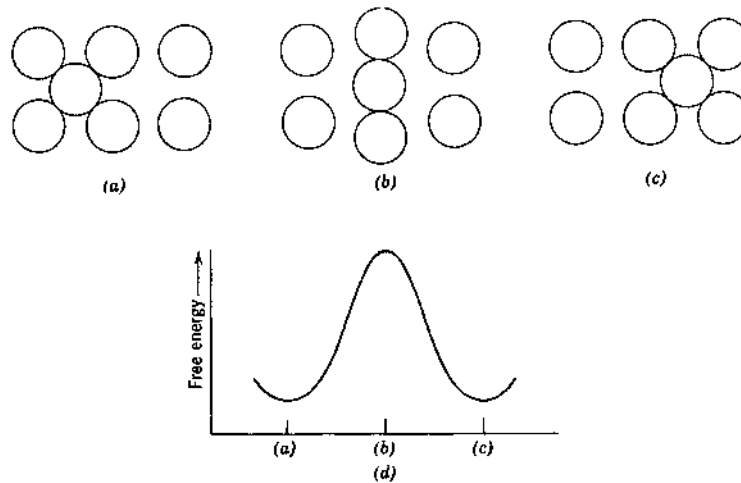


FIGURE 7.8 Schematic diagram showing the sequence of configurations when an atom jumps from one lattice site to another (a)–(c) and the corresponding change in the free energy of the lattice (d).

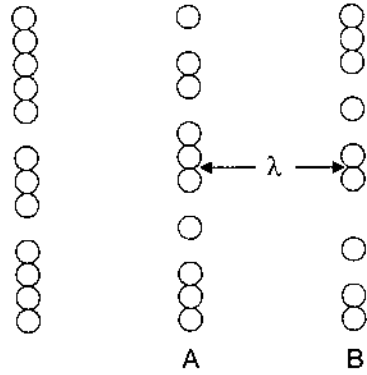


FIGURE 7.9 Planes of atoms with a gradient in concentration.

where k is the Boltzmann constant and T is the absolute temperature. The number of atoms (per unit area of plane A) that have sufficient energy to surmount the energy barrier from A to B at any instant is $n_A P = n_A \exp(-q/kT)$. If the atoms vibrate (or oscillate) about their mean positions with a frequency ν , and assuming that the vibration frequency is the same in all six orthogonal directions, then the *flux* of atoms (that is, the number jumping across unit area per second) from A to B is $(\nu/6)n_A \exp(-q/kT)$. Similarly the flux of atoms from B to A is $(\nu/6)n_B \exp(-q/kT)$. The net flux of atoms from A to B is therefore

$$J = \frac{\nu}{6}(n_A - n_B) \exp\left(\frac{-q}{kT}\right) \quad (7.43)$$

If λ is the distance between adjacent planes, then $n_A - n_B$ can be related to the concentration (that is, the number of atoms per unit volume) by observing that $n_A/\lambda = C_A$ and $n_B/\lambda = C_B$, giving

$$J = \frac{\nu\lambda}{6}(C_A - C_B) \exp\left(\frac{-q}{kT}\right) \quad (7.44)$$

Assuming that C changes slowly enough so that $C_A - C_B = \lambda(dC/dx)$, Eq. (7.44) becomes

$$J = -\frac{\nu\lambda^2}{6} \exp\left(\frac{-q}{kT}\right) \frac{dC}{dx} \quad (7.45)$$

This equation is identical to Fick's first law, with the diffusion coefficient D given by

$$D = \frac{v\lambda^2}{6} \exp\left(\frac{-q}{kT}\right) \quad (7.46)$$

For most diffusing atoms, q is an inconveniently small quantity and it is better to use the larger quantities $Q = N_A q$ and $R = N_A k$, where Q is the activation energy per mole, N_A is the Avogadro number, and R is the gas constant. In addition, the term $v\lambda^2/6$ is usually written as D_0 , giving

$$D = D_0 \exp\left(\frac{-Q}{RT}\right) \quad (7.47)$$

This method of writing D emphasizes the exponential dependence of D on temperature and gives a conveniently sized activation energy (in units of J/mol). Data for the diffusion coefficients of some common ceramics are given in Fig. 7.10.

Taking the activation energy q as equal to $\Delta h - T\Delta s$, where Δh is the enthalpy and Δs is the entropy for atomic diffusion, then Eq. (7.46) becomes

$$D = \frac{v\lambda^2}{6} \exp\left(\frac{\Delta s}{k}\right) \exp\left(\frac{-\Delta h}{kT}\right) \quad (7.48)$$

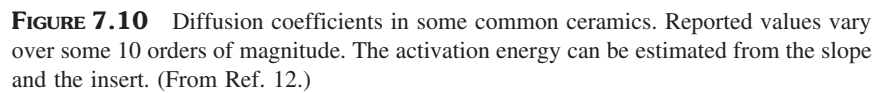
and comparing this equation with Eq. (7.47) indicates that

$$D_0 = \frac{v\lambda^2}{6} \exp\left(\frac{\Delta s}{k}\right) \quad (7.49)$$

The vibration frequency of atoms about their mean positions (the Debye frequency) is $10^{13} - 10^{14} \text{ s}^{-1}$ and $\lambda \approx 0.2 \text{ nm}$, so $v\lambda^2/6 \approx 10^{-7} \text{ m}^2/\text{s}$. Data indicate that D_0 for diffusion by the interstitial and vacancy mechanisms is in the range of 10^{-7} to $10^{-3} \text{ m}^2/\text{s}$. It has been shown that for a given class of materials, the data for D_0 and Q/RT_m (where T_m is the melting temperature) are nearly constant (9). For the alkali halides (NaCl, LiF, etc.), the data give $D_0 \approx 2.5 \times 10^{-3} \text{ m}^2/\text{s}$ and $Q/RT_m \approx 22.5$, whereas for oxides (MgO, Al_2O_3 , etc.), $D_0 \approx 3.8 \times 10^{-4} \text{ m}^2/\text{s}$ and $Q/RT_m \approx 23.4$.

7.4.3 Mechanisms of Diffusion

The different types of defects determine the path of matter transport and diffusion along the major paths gives rise to the major mechanisms of matter transport: lattice diffusion (also referred to as volume or bulk diffusion), grain boundary diffusion, and surface diffusion.



7.4.3.1 Lattice Diffusion

Lattice diffusion takes place by the movement of point defects through the bulk of the lattice. Depending on the type of defects (vacancy or interstitial), lattice diffusion can occur by the *vacancy* mechanism or the *interstitial* mechanism. Vacancy and interstitial diffusion are by far the most important lattice diffusion mechanisms.

Vacancy Mechanism

An atom on a normal lattice site exchanges its place with a vacant site (Fig. 7.11a). The movement of the atom is opposite to that of the vacancy, so we can track the movement of the atom (i.e., atom diffusion) or, equivalently, the motion of the vacancy (i.e., vacancy diffusion). Whereas the diffusion coefficients of the atoms and the vacancies are related, they are not equal. We can see this as follows. An atom can only jump if a vacancy is located on an adjacent lattice site, but a vacancy can jump to any of the occupied nearest neighbor sites. The number of atomic jumps will therefore be proportional to the fraction of sites occupied by vacancies, C_v . The atomic (or self-) diffusion coefficient D_a and the vacancy diffusion coefficient D_v are related by

$$D_a = C_v D_v \quad (7.50)$$

The vacancy concentration, as outlined earlier, is determined by the temperature, solute, and atmosphere. It should be noted that in vacancy diffusion, the flux of vacancies must be compensated by an equal and opposite flux of atoms; otherwise, vacancies would accumulate in the crystal and produce pores. Pore formation can actually occur during the interdiffusion of two atoms that have very different diffusion coefficients.

Interstitial Mechanism

If they are small enough, solute or regular atoms are often found in the interstitial sites of the lattice and move to neighboring interstitial sites (Fig. 7.11b). A relationship analogous to Eq. (7.50) will hold:

$$D_a = C_i D_i \quad (7.51)$$

where D_i is now the interstitial diffusion coefficient and C_i is the concentration of the interstitial atoms.

Interstitialcy Mechanism

If the distortion of the lattice becomes too large for interstitial diffusion to be favorable, then movement of the interstitial atoms may occur by the interstitialcy

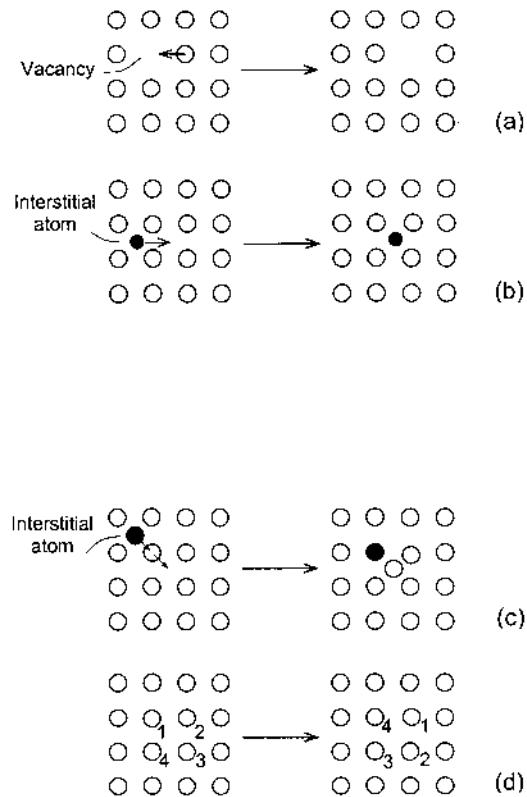


FIGURE 7.11 Lattice diffusion by (a) the vacancy mechanism, (b) the interstitial mechanism, (c) the interstitialcy mechanism, and (d) the ring mechanism.

mechanism. An atom on the regular lattice site exchanges position with a neighboring interstitial atom (Fig. 7.11c). The two need not be the same type of atom.

Direct Exchange or Ring Mechanism

Atoms exchange places by rotation in a circle without the participation of a defect (Fig. 7.11d). Several atoms can participate in a simultaneous exchange. The significant momentary distortion coupled with the large energy changes arising from electrostatic repulsion makes this mechanism improbable in ionic solids.

7.4.3.2 Grain Boundary Diffusion

In polycrystalline materials, the crystals or grains are separated from one another by regions of lattice mismatch and disorder called *grain boundaries*. Because of

the highly defective nature of the grain boundary, we would expect grain boundary diffusion to be more rapid than lattice diffusion in the adjacent grains. Although not known accurately, the width of the grain boundary region is assumed to be 0.5–1 nm. For a constant grain boundary width, the fraction of the solid that is occupied by the grain boundary increases with decreasing grain size, so the rate of grain boundary diffusion averaged over several grains is dependent on grain size.

7.4.3.3 Surface Diffusion

The free surface of a crystalline solid is not perfectly flat (Fig. 3.19). It contains some vacancies (as in the bulk of the crystal), terraces, kinks, edges, and adatoms. The migration of vacancies and the movement of adatoms provide the main mechanisms of surface diffusion. The diffusion process is assumed to be confined to a thin surface layer having a thickness of 0.5–1 nm.

7.4.3.4 Trends in Diffusion Coefficients

Since the atoms on the surface have fewer neighbors than those in the bulk of the lattice and are less tightly bound, we would expect the activation energy for surface diffusion to be less than that for lattice diffusion. This appears to be the case, judging from the limited data available. Because of the lower activation energy, the relative importance of surface diffusion increases with decreasing temperature. As we shall see in the next chapter, this has important consequences for sintering.

It has often been stated that the diffusion coefficients for lattice diffusion D_l , grain boundary diffusion D_{gb} , and surface diffusion D_s increase in the order $D_l < D_{gb} < D_s$, and that the corresponding activation energies vary as $Q_l > Q_{gb} > Q_s$. However, these relations may not always be correct.

7.4.4 Types of Diffusion Coefficients

Several terminologies are used in the literature for specifying diffusion coefficients. They may describe the diffusion of a particular species (e.g., atom, interstitial, or vacancy), a particular diffusion path (e.g., lattice, grain boundary, or surface diffusion), or a particular process (e.g., chemical diffusion or ambipolar diffusion).

Self-diffusion coefficient: The self-diffusion coefficient D_{self} refers to the diffusion coefficient for the host atoms (or ions) in random diffusion and is the important diffusion coefficient in sintering. For lattice diffusion by the vacancy or interstitial mechanism, D_{self} is given by Eq. (7.50) or (7.51).

Tracer diffusion coefficient: Direct measurement of D_{self} is often difficult. As outlined earlier, it is more common to measure the diffusion coeffi-

cient for a radioactive or mass isotope. The tracer diffusion coefficient D^* measured in this type of experiment is close to but not identical to D_{self} because the motion of the tracer atom is not completely random. Successive jumps are, to a certain extent, correlated and dependent on previous jumps. D_{self} and D^* are related by

$$D^* = fD_{\text{self}} \quad (7.52)$$

where f is a correlation factor that depends on the crystal structure and the diffusion mechanism (4). The calculated values for f are in the range 0.6–1.0 (e.g., for the fcc lattice, $f = 0.78$ for the vacancy mechanism).

Lattice diffusion coefficient: The lattice diffusion coefficient D_l refers to any diffusion process in the lattice of the solid.

Grain boundary diffusion coefficient: The grain boundary diffusion coefficient D_{gb} (or D_b) refers to diffusion along the grain boundary.

Surface diffusion coefficient: The surface diffusion coefficient D_s refers to diffusion along a free surface.

Diffusion coefficients for defects: The diffusion coefficients for defects refer to a particular type of defect. We can, for example, specify the diffusion coefficient for a vacancy D_v or for an interstitial D_i . The diffusion coefficient of a defect is independent of its concentration and is given by Eq. (7.46) or (7.48).

Chemical, effective, or interdiffusion coefficient: The chemical, effective, or interdiffusion coefficient \tilde{D} refers to diffusion in a chemical composition (or chemical potential) gradient. A chemical composition gradient can, for example, be established experimentally by a gradient in oxygen activity, leading to migration of ions in response to the chemical gradient. Interdiffusion occurs when two components of a solid solution migrate in opposite directions down their coupled chemical potential gradient.

7.5 CHEMICAL POTENTIAL

Matter transport, as outlined earlier, can be analyzed in terms of Fick's first law by considering the flux of atoms or vacancies driven by gradients in the *concentration*. This is however a special case of mass transport. We should allow for the possibility that an atom is acted on by other types of driving forces such as gradients in pressure, electric potential, and so on. One way to do this is to regard diffusion as driven by gradients in the *chemical potential* rather than gradients in concentration. The gradient in chemical potential could then arise from gradients in pressure, or electric potential, for example, as well as from concentration gradients.

7.5.1 Definition of the Chemical Potential

Consider a phase with fixed mass and composition but under conditions of variable temperature T and pressure p . For an infinitesimal reversible process, the change in the Gibbs free energy is

$$dG = \left(\frac{\partial G}{\partial T} \right)_p dT + \left(\frac{\partial G}{\partial p} \right)_T dp = -S dT + V dp \quad (7.53)$$

where S is the entropy and V the volume of the system. For a phase of variable composition consisting of m chemical constituents of which there are n_1 moles of the substance A_1 , n_2 moles of A_2 , ..., n_m moles of A_m , the change in the Gibbs free energy is now given by

$$\begin{aligned} dG = & \left(\frac{\partial G}{\partial T} \right)_{p, n_1, n_2, \dots, n_m} dT + \left(\frac{\partial G}{\partial p} \right)_{T, n_1, n_2, \dots, n_m} dp \\ & + \left(\frac{\partial G}{\partial n_1} \right)_{p, T, n_2, n_3, \dots, n_m} dn_1 + \dots + \left(\frac{\partial G}{\partial n_m} \right)_{p, T, n_1, n_2, \dots, n_{m-1}} dn_m \end{aligned} \quad (7.54)$$

Since the first two terms on the right-hand side of this equation are at constant mass and composition, we can use Eq. (7.53). Now if a small amount of one constituent (e.g., dn_k moles of the k th constituent) is introduced into the phase, with T , p , and the other n 's remaining constant, the effect on the Gibbs free energy can be expressed as

$$\mu_k = \left(\frac{\partial G}{\partial n_k} \right)_{T, p, n_1, n_2, \dots, n_{k-1}, n_{k+1}, \dots, n_m} \quad (7.55)$$

where μ_k is called the *chemical potential* of the k th constituent. Equation (7.54) can now be written as

$$dG = -S dT + V dp + \sum_{i=1}^m \mu_i dn_i \quad (7.56)$$

Suppose we increase the number of moles of a phase while keeping T , p , and the composition constant, then Eq. (7.56) becomes

$$dG_{T,p} = \sum_i \mu_i dn_i \quad (7.57)$$

Since the μ_i depend only on T , p , and composition, they must remain constant; so Eq. (7.57) can be integrated to give

$$G = \sum_i \mu_i n_i \quad (7.58)$$

For a *pure substance*, Eq. (7.58) reduces to

$$G = \mu n \quad (7.59)$$

so the chemical potential is the *Gibbs free energy per mole* at the temperature and pressure in question. We now go on to relate the chemical potential of other systems to more familiar variables.

7.5.2 Chemical Potential of a Mixture of Gases

For 1 mol of an ideal gas at constant temperature T ,

$$\left(\frac{\partial G}{\partial p} \right)_T = V = \frac{RT}{p} \quad (7.60)$$

where R is the gas constant and p is the pressure. On integration we obtain

$$G(T, p) = G_o(T) + RT \ln p \quad (7.61)$$

where G_o is a reference value. We can therefore write

$$\mu(T, p) = \mu_o(T) + RT \ln p \quad (7.61a)$$

For a mixture of ideal gases at constant T and for a constant total pressure, following Eq. (7.61a), we can write for each component:

$$\mu_i(T, p) = \mu_{oi}(T) + RT \ln p_i \quad (7.62)$$

where p_i is the pressure of the i th component. It is more useful to relate the Gibbs free energy or the chemical potential of a particular component to its concentration defined by

$$C_i = \frac{n_i}{\sum n_i} = \frac{p_i}{p} \quad (7.63)$$

where n_i is the number of moles of each component in the mixture and p is the total gas pressure. Equation (7.62) can now be written

$$\mu_i(T, p, C_i) = \mu_{oi}(T, p) + RT \ln C_i \quad (7.64)$$

Real gases, as the reader will be aware, do not show ideal behavior. The deviation from ideal behavior is, however, not too large over a fairly wide range of pressures, so Eqs. (7.62) to (7.64) provide a good approximation to the chemical potential of real gases.

7.5.3 Chemical Potential of Solids and Liquids

For solid and liquid solutions, the chemical potential is defined by an expression similar to Eq. (7.62) in which the p_i is replaced by a quantity a_i , called the *activity*:

$$\mu_i = \mu_{oi} + RT \ln a_i \quad (7.65)$$

The activity of pure liquids and solids under some specified standard conditions of temperature and pressure is taken as unity. For other systems, the activity is written

$$a_i = \alpha_i C_i \quad (7.66)$$

where α_i is called the activity coefficient and C_i is the concentration, usually expressed as a mole fraction. The chemical potential of the i th species in liquid or solid solution can now be written as

$$\mu_i = \mu_{oi} + RT \ln(\alpha_i C_i) \quad (7.67)$$

In the case of ideal solutions, $\alpha_i = 1$.

7.5.4 Chemical Potential of Atoms and Vacancies in a Crystal

Consider a crystal of a pure element that is perfect except for the presence of vacancies. If there are N_a atoms and n_v vacancies, the total number of lattice sites in the crystal is $N = N_a + n_v$, so the Gibbs free energy of the crystal can be expressed as

$$G = U + n_v g + pV - TS \quad (7.68)$$

where U is the internal energy of the crystal and g is the energy of formation of a vacancy. The configurational entropy of the crystal is given by the Boltzmann relation, which for the present system can be written

$$S = k \ln \frac{(N_a + n_v)!}{N_a! n_v!} \quad (7.69)$$

where k is the Boltzmann constant. The chemical potential of the atoms is defined by

$$\mu_a = \left(\frac{\partial G}{\partial N_a} \right)_{T,p,n_v} \quad (7.70)$$

Using the Stirling approximation to express the factorials in Eq. (7.69) and applying Eq. (7.70) gives

$$\mu_a = \mu_{0a} + p\Omega_a + kT \ln \left(\frac{N_a}{N_a + n_v} \right) \quad (7.71)$$

where μ_{0a} is a reference value and Ω_a is the volume of an atom defined by

$$\left(\frac{\partial V}{\partial N_a} \right)_{T,p,n_v} = \Omega_a \quad (7.72)$$

If C_a is the fraction of lattice sites occupied by the atoms in the crystal, then Eq. (7.71) can be written

$$\mu_a = \mu_{0a} + p\Omega_a + kT \ln C_a \quad (7.73)$$

This equation shows that the chemical potential of atoms in a crystal depends on the pressure and on the atomic concentration. It is also worth noting that for small vacancy concentration, the last term on the right-hand side of Eqs. (7.71) and (7.73) is negligible.

The chemical potential of the vacancies is defined by

$$\mu_v = \left(\frac{\partial G}{\partial n_v} \right)_{T,p,N_a} \quad (7.74)$$

and following a procedure similar to that used for μ_a , we find that

$$\mu_v = \mu_{0v} + p\Omega_v + kT \ln C_v \quad (7.75)$$

where C_v is the vacancy concentration (i.e., the fraction of lattice sites occupied by the vacancies). The volume of a vacancy Ω_v , may be greater or smaller than Ω_a , but from now on we will use the rigid lattice approximation and assume that $\Omega_a = \Omega_v = \Omega$.

7.5.5 Chemical Potential of Atoms and Vacancies Beneath a Curved Surface

The atoms and vacancies beneath a curved surface will have their chemical potentials altered by the curvature of the surface, and this difference in chemical poten-

tial drives the diffusional flux of atoms to reduce the free energy of the system. Surfaces and interfaces play a dominant role in sintering and other diffusion-controlled processes, so the dependence of the chemical potential on curvature is vital to the analysis and understanding of sintering.

Consider a solid consisting of a pure element with adjoining convex and concave surfaces (Fig. 7.12), and let us assume that vacancies are the only type of point defects present. For the convex surface, the surface can be decreased by reducing the volume of the region beneath it. This can be achieved by reducing the concentration of vacancies. Since a decrease in the surface area leads to a decrease in the surface contribution to the free energy, it is expected that the vacancy concentration will be below normal (e.g., relative to a flat surface). Following a similar type of argument, it is expected that the concentration of vacancies will be above normal beneath the concave surface. The difference in vacancy concentration leads to a diffusional flux of vacancies from the concave to the convex region or, equivalently, a diffusional flux of atoms from the convex to the concave region.

A method for determining the dependence of the chemical potential on the surface curvature is described by Herring (10). Consider a smoothly curved surface as shown in Fig. 7.13. Suppose we build an infinitesimal hump on the surface by taking atoms from beneath the surface and adding them to the surface. The change in surface free energy, to a good approximation, is given by

$$\delta\left(\int \gamma_{sv} dS\right) = \int \delta(\gamma_{sv}) dS_o + \int \gamma_{sv} \delta(dS) \quad (7.76)$$

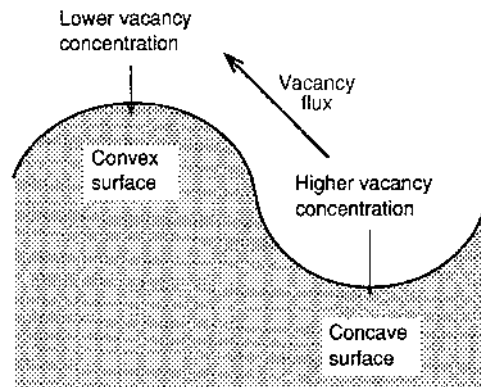


FIGURE 7.12 Schematic diagram showing the direction of flux for vacancies in a curved surface. The flux of atoms is equal and opposite to that of the vacancies.

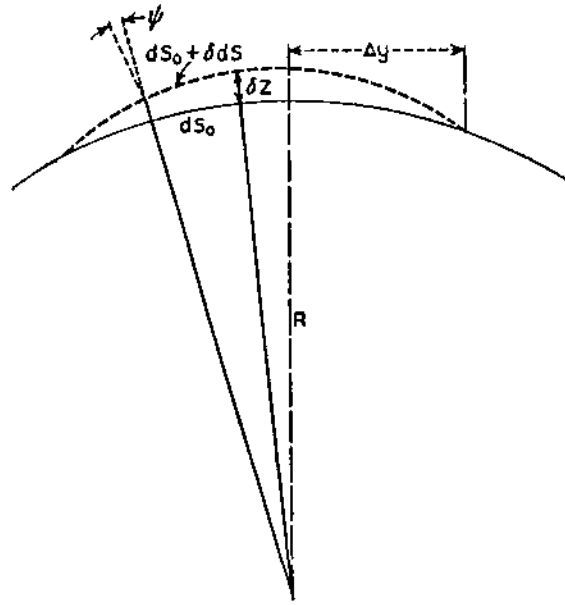


FIGURE 7.13 Infinitesimal hump formed by building up a curved surface. Full curve: original surface; dashed curve: built-up surface. (From Ref. 10.)

where δ represents a small change in a quantity, γ_{sv} is the specific surface energy, and dS is the change in surface area. We will assume that the surface is uniform and isotropic so the first term on the right-hand side of Eq. (7.76) is zero. Referring to Fig. 7.13, the term $\delta(dS)$ is given by

$$\delta(dS) = (\sec \psi - 1)dS_0 + \delta z \left(\frac{1}{R_1} + \frac{1}{R_2} \right) dS_0 \quad (7.77)$$

where R_1 and R_2 are the two principal radii of curvature at dS_0 . If Δy is small, then R_1 and R_2 may be taken as constant over the hump. The first term on the right-hand side of Eq. (7.77) can be neglected and substituting in Eq. (7.76) gives

$$\delta \left(\int \gamma_{sv} dS \right) = \gamma_{sv} \left(\frac{1}{R_1} + \frac{1}{R_2} \right) \delta v \quad (7.78)$$

where δv is the volume of the hump.

The change in the volume term of the free energy due to the creation of the small hump is

$$\delta G_v = -p\delta v + \mu_v \frac{\delta v}{\Omega} \quad (7.79)$$

where p is the mean hydrostatic pressure in the crystal just beneath the surface, μ_v is the chemical potential of a vacancy, and $\delta v/\Omega$ represents the number of vacancies created by the transfer of atoms to the hump. In equilibrium, the sum of the energy changes defined by Eqs. (7.78) and (7.79) must vanish, so

$$\mu_v = p\Omega + \gamma_{sv} \left(\frac{1}{R_1} + \frac{1}{R_2} \right) \Omega \quad (7.80)$$

The curvature K of the surface is defined by

$$K = \frac{1}{R_1} + \frac{1}{R_2} \quad (7.81)$$

where $K > 0$ for a convex surface. Substituting for K in Eq. (7.80) gives

$$\mu_v = (p + \gamma_{sv}K)\Omega \quad (7.82)$$

In general, the chemical potential is measured relative to some reference value μ_{v0} , and as found earlier, μ_v contains a vacancy concentration term. An expression for μ_v that incorporates not only curvature but also pressure and concentration effects can therefore be written as

$$\mu_v = \mu_{ov} + (p + \gamma_{sv}K)\Omega + kT \ln C_v \quad (7.83)$$

Using a similar procedure, the chemical potential of the atoms can be shown to be

$$\mu_a = \mu_{oa} + (p + \gamma_{sv}K)\Omega + kT \ln C_a \quad (7.84)$$

As pointed out earlier, the last term containing C_a in this equation is normally small and can be put equal to zero.

Equations (7.83) and (7.84) describe two important relations in sintering. Since the terms containing C_a and C_v are normally very small, they show that μ_a and μ_v depend primarily on the hydrostatic pressure in the solid and on the curvature of the surface. The curvature term $\gamma_{sv}K$ has the units of pressure or stress, so that curvature and applied pressure effects can therefore be treated by the same formulation. This concept will be used in the next chapter when the sintering models are considered.

7.6 DIFFUSIONAL FLUX EQUATIONS

The theoretical analysis of sintering requires the formulation of equations for diffusional mass transport and their solution subject to the appropriate boundary conditions. There are two equivalent formulations: sintering can be viewed in terms of the diffusion of atoms or the diffusion of vacancies.

For an elemental solid, if the influence of the flux of the neutral atoms upon one another is neglected, then the flux of the atoms (in one dimension) can be expressed in a general form as (6):

$$J_x = -L_{ii} \frac{d\mu}{dx} \quad (7.85)$$

where the coefficients L_{ii} are called *transport coefficients* and μ is the chemical potential. By comparing this equation with Fick's first law [Eq. (7.36)], it is found that

$$L_{ii} = D \frac{dC}{d\mu} \quad (7.86)$$

Using the relation between chemical potential and concentration [Eq. (7.67)]:

$$\mu = \mu_o + kT \ln(\alpha C) \quad (7.87)$$

where α is the activity coefficient, we obtain by differentiating to find $dC/d\mu$ and substituting in Eq. (7.86)

$$L_{ii} = \frac{D_i C}{kT} \quad (7.88)$$

where D_i is given by

$$D_i = D \left(1 + \frac{d \ln \alpha}{d \ln C} \right)^{-1} \quad (7.89)$$

For an ideal system, α is independent of the concentration, so $\ln \alpha$ does not vary with $\ln C$, and the second term in the brackets in Eq. (7.89) is zero. By substituting Eq. (7.88) into Eq. (7.85) we can write the atomic flux equation

$$J_x = - \frac{D_i C}{kT} \frac{d\mu}{dx} \quad (7.90)$$

where, in the general case, D_i is given by Eq. (7.89).

7.6.1 Flux of Atoms

For a pure elemental solid in which the point defects consist of vacancies, diffusion of atoms or vacancies from one region to another does not produce a change in the total number of lattice sites. In a given region, the number of atoms and the number of vacancies change by equal and opposite amounts. The diffusional flux is determined by gradients in $\mu_a - \mu_v$ and following Eq. (7.90) is given by

$$J_a = -\frac{D_a C_a}{\Omega kT} \frac{d(\mu_a - \mu_v)}{dx} \quad (7.91)$$

where D_a is the atomic self diffusion coefficient, k is the Boltzmann constant, and it must be remembered that C_a is the *fraction* of lattice sites occupied by the atoms. The diffusion response can therefore be found from Eq. (7.91) subject to the appropriate boundary conditions.

7.6.2 Flux of Vacancies

When the flux of vacancies is considered, the atomic flux in sintering is taken as equal and opposite to the vacancy flux, that is,

$$J_a = -J_v \quad (7.92)$$

where J_v is given by

$$J_v = -\frac{D_v C_v}{\Omega kT} \frac{d\mu_v}{dx} = -\frac{D_v}{\Omega} \frac{dC_v}{dx} \quad (7.93)$$

where D_v is the vacancy diffusion coefficient. Determination of J_v requires an expression for C_v . Normally C_v is taken as the *equilibrium* vacancy concentration, determined from the condition

$$\left(\frac{\partial G}{\partial n_v} \right)_{T,p,N_a} = 0 \quad (7.94)$$

so that $\mu_v = 0$. Assuming that externally applied pressure effects are absent, and putting $\mu_v = 0$ in Eq. (7.83) gives

$$C_v = C_{ov} \exp\left(-\frac{\gamma_{sv} K \Omega}{kT}\right) \quad (7.95)$$

where C_{ov} is a reference value, normally taken as the vacancy concentration under a flat surface. For $\gamma_{sv} K \Omega \ll kT$, Eq. (7.91) becomes

$$C_v = C_{ov} \left(1 - \frac{\gamma_{sv} K \Omega}{kT} \right) \quad (7.96)$$

For the equilibrium condition, we therefore have

$$J_a = \frac{D_v}{\Omega} \frac{dC_v}{dx} \quad (7.97)$$

where C_v is given by Eq. (7.96). Here again it should be remembered that C_v is the *fraction* of lattice sites occupied by vacancies.

7.7 VAPOR PRESSURE OVER A CURVED SURFACE

In sintering, matter transport by evaporation and condensation is normally treated alongside the solid-state diffusion mechanisms. The rate of transport is taken as proportional to the equilibrium vapor pressure over the surface, which can be related to the value of $\mu_a - \mu_v$ beneath the surface. Suppose a number dN_a of atoms is removed from the vapor and added to the surface with an accompanying decrease in the number of vacancies beneath the surface. The free energy change for this virtual operation must be zero, so that

$$\mu_{vap} = \mu_a - \mu_v \quad (7.98)$$

where μ_{vap} is the chemical potential of the atoms in the vapor phase. The vapor pressure is proportional to $\exp(\mu_{vap}/kT)$, so we can write

$$p_{vap} = p_o \exp \left(\frac{\mu_a - \mu_v - \mu_o}{kT} \right) \quad (7.99)$$

where p_o is a reference value of the vapor pressure corresponding to some standard value of the chemical potential, μ_o , and is normally taken as the value over a flat surface. Equations (7.83), (7.84), and (7.95) give

$$\mu_a - \mu_v = \mu_o + \gamma_{sv} K \Omega \quad (7.100)$$

and substituting into Eq. (7.99) yields

$$p_{vap} = p_o \exp \left(\frac{\gamma_{sv} K \Omega}{kT} \right) \quad (7.101)$$

This equation is commonly known as the Kelvin equation. For $\gamma_{sv}K\Omega \ll kT$, it becomes

$$p_{vap} = p_o \left(1 + \frac{\gamma_{sv}K\Omega}{kT} \right) \quad (7.102)$$

For a given system under isothermal conditions, the vapor pressure increases with the curvature of the surface.

7.8 DIFFUSION IN IONIC CRYSTALS: AMBIPOLAR DIFFUSION

In much of our discussion so far in this chapter, we have purposely considered the diffusing species to be uncharged atoms (or vacancies) so that electrostatic effects on the diffusing species have been avoided. However, the reader will know that in most crystalline ceramics, matter transport occurs by the motion of charged species (e.g., ions). For compounds containing more than one type of ion, it would be expected that the different ions will have different diffusion rates. Matter transport from a given source to a given sink must occur in such a way that the stoichiometry and electroneutrality of the solid are preserved in the different regions of the solid (Fig. 7.14). Other effects must also be taken into account. For example, if an external electric field is applied to the system, in addition to diffusion down a concentration gradient, the ions will migrate in response to the field. Even in the absence of an external field, the ions themselves can generate an internal field that will influence the motion.

Consider a diffusing species with a charge z_i (i.e., $z_i = 1$ for a sodium ion or $z_i = -2$ for a doubly charged oxygen ion). In a region where the electric

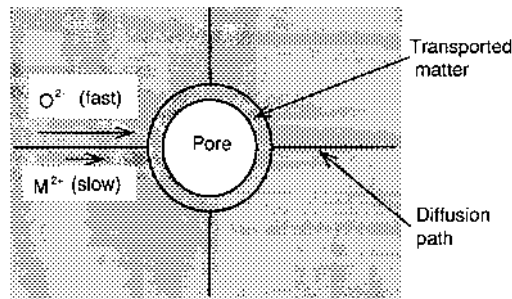


FIGURE 7.14 Schematic diagram illustrating that the diffusion of ions in an ionic solid must be coupled to preserve the stoichiometry and electroneutrality of the solid.

potential is ϕ , the chemical potential of an ion is increased by an amount $z_i e \phi$, where e is the magnitude of the electron charge. In the absence of an externally applied pressure, from Eq. (7.73) we can write the chemical potential of an ion as

$$\mu_i = \mu_{oi} + kT \ln C_i + z_i e \phi \quad (7.103)$$

where C_i is the fraction of sites occupied by the ions in the crystal. Differentiating with respect to x and substituting into Eq. (7.90) for the flux gives

$$J_{ix} = -D_i \frac{dC_i}{dx} - B_i C_i z_i e E \quad (7.104)$$

where D_i is the diffusion coefficient for the ions, E is the electric field strength (equal to $d\phi/dx$), and $B_i = D_i/kT$ is the ionic mobility. The first term on the right hand side of Eq. (7.104) is the familiar diffusion term given by Fick's first law whereas the second term arises from ion migration in the electric field.

Let us now apply Eq. (7.104) to a system consisting of two different types of diffusing ions. One type has a charge z_+ (a positive number) and the other type has a charge z_- (a negative number), so this system may correspond to diffusion of metal and oxygen ions in a metal oxide. If no net current passes through the system, the electric current density must be zero; so

$$z_+ J_+ = -z_- J_- \quad (7.105)$$

Substituting for J_+ and J_- from Eq. (7.104) gives

$$-z_+ D_+ \frac{dC_+}{dx} - B_+ C_+ z_+^2 e E = z_- D_- \frac{dC_-}{dx} + B_- C_- z_-^2 e E \quad (7.106)$$

After rearrangement, we can find an equation for E :

$$E = -\frac{1}{e(B_+ C_+ z_+^2 + B_- C_- z_-^2)} \left(z_+ D_+ \frac{dC_+}{dx} + z_- D_- \frac{dC_-}{dx} \right) \quad (7.107)$$

For electroneutrality we must have

$$C_+ z_+ = -C_- z_- \quad (7.108)$$

Differentiating this equation and multiplying by D_+ gives

$$z_+ D_+ \frac{dC_+}{dx} = -z_- D_+ \frac{dC_-}{dx} \quad (7.109)$$

Substituting into Eq. (7.107) we obtain

$$E = - \frac{z_-}{e(-B_+ z_+ C_- z_- + B_- z_- C_+ z_+)} (D_- - D_+) \frac{dC_-}{dx} \quad (7.110)$$

Substituting for E in Eq. (7.104) gives for the flux of the negative ions

$$J_- = - \frac{B_- z_- D_+ - B_+ z_+ D_-}{B_- z_- - B_+ z_+} \frac{dC_-}{dx} \quad (7.111)$$

Replacing the ionic mobility B_i by D_i/kT , Eq. (111) becomes

$$J_- = - \frac{D_+ D_- (z_+ - z_-)}{D_+ z_+ - D_- z_-} \frac{dC_-}{dx} \quad (7.112)$$

Finally, applying Eqs. (7.105) and (7.108) to Eq. (7.112) gives

$$J_+ = - \frac{D_+ D_- (z_+ - z_-)}{D_+ z_+ - D_- z_-} \frac{dC_+}{dx} \quad (7.113)$$

By analogy with Fick's first law we can define an effective diffusion coefficient given by

$$\tilde{D} = \frac{D_+ D_- (z_+ - z_-)}{D_+ z_+ - D_- z_-} \quad (7.114)$$

To illustrate the use of Eq. (7.114), consider the case of Al_2O_3 . Assuming that the ions are fully ionized, the diffusing species are Al^{3+} and O^{2-} , and the effective diffusion coefficient is

$$\tilde{D} = \frac{5D_{\text{Al}^{3+}} D_{\text{O}^{2-}}}{3D_{\text{Al}^{3+}} + 2D_{\text{O}^{2-}}} \quad (7.115)$$

It is instructive to consider two limiting cases. In the first case, if

$$D_{\text{O}^{2-}} \gg D_{\text{Al}^{3+}} \quad \text{then} \quad \tilde{D} = \frac{5}{2} D_{\text{Al}^{3+}} \quad (7.116)$$

In the second case, if

$$D_{\text{Al}^{3+}} \gg D_{\text{O}^{2-}} \quad \text{then} \quad \tilde{D} = \frac{5}{3} D_{\text{O}^{2-}} \quad (7.117)$$

We see from Eqs. (7.116) and (7.117) that the more slowly diffusing ion determines the rate of matter transport, but the effect of the faster diffusing species

is to accelerate the motion of the slower ion. Physically, the faster diffusing ion reduces its concentration gradient more rapidly than the slower diffusing ion. However, only a small amount of such diffusion is necessary before a large potential gradient is set up. The potential gradient has the same sign as the concentration gradient so it retards the transport of the faster ions and enhances the transport of the slower ions. The buildup of the potential occurs to the point where the fluxes are related by Eq. (7.105).

The coupled diffusion of charged species is referred to as *ambipolar diffusion*. It has important consequences not only for sintering but also for other mass transport processes such as creep and the formation of oxide layers on materials. The slower (or slowest) diffusing species, as observed above, will control the rate of matter transport. A further complication arises when each ion may have more than one diffusion path (e.g., lattice diffusion and grain boundary diffusion). It is expected that matter transport will occur predominantly along the fastest path so the rate controlling mechanism becomes the *slowest diffusing species along its fastest path*. Differences in the effective area and path length for mass transport must also be taken into account when considering the rate-controlling mechanism of a process.

As an example, Fig. 7.15 shows a schematic plot of the log(creep rate) versus log(grain size) at constant temperature and applied stress for Al_2O_3 , a system for which the relative values of the grain boundary and lattice diffusion coefficients are known: $D_l^{\text{Al}} > D_l^{\text{O}}$ and $D_b^{\text{O}} > D_b^{\text{Al}}$. The two lines with slope = -2 show the creep rate by lattice diffusion if Al and O are the rate-limiting ions, whereas the two lines with slope = -3 give the corresponding creep rate by grain boundary diffusion. The controlling species and path are given by the dotted line. We notice that each combination of species and path is controlling over a specific grain size range and that in each of these regimes, it is not the topmost line (giving the highest creep rate) that is rate controlling. The rate controlling species and path is given by the second line, representing the other ion along its fastest path.

If the lattice and grain boundary coefficients are additive, then for a pure binary compound M_xO_y , the effective (or ambipolar) diffusion coefficient is given by (11)

$$\tilde{D} = \frac{(x + y) \left[D_l^{\text{M}} + \pi \delta_{gb} D_{gb}^{\text{M}} / G \right] \left[D_l^{\text{O}} + \pi \delta_{gb} D_{gb}^{\text{O}} / G \right]}{y \left[D_l^{\text{M}} + \pi \delta_{gb} D_{gb}^{\text{M}} / G \right] + x \left[D_l^{\text{O}} + \pi \delta_{gb} D_{gb}^{\text{O}} / G \right]} \quad (7.118)$$

where δ_{gb} is the width of the grain boundary region and G is the grain size. Each of the terms in square brackets represents the effective diffusion coefficient for one of the species when both transport paths are taken into account. Examination of Eq. (7.118) indicates that the slowest effective diffusion coefficient is rate controlling, but within each term, it is the faster of the two paths that dominates,

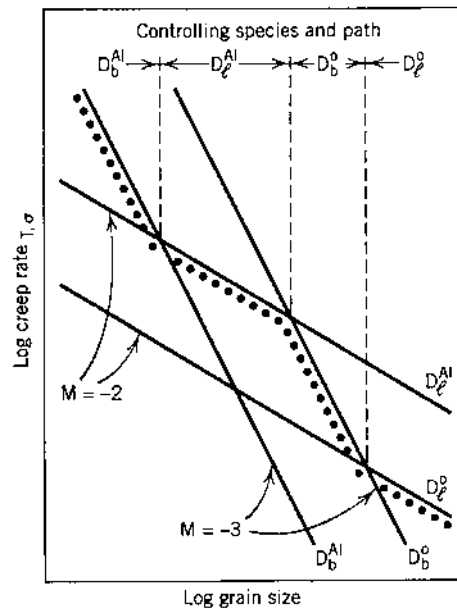


FIGURE 7.15 Diffusional creep in Al_2O_3 (schematic). The solid lines show the creep rate dependence on grain size for each assumed species and path. The dotted line traces the rate-limiting mechanism, given by the slower diffusing species along its fastest path. (From Ref. 1.)

confirming that the rate controlling mechanism is the slowest diffusing species along its fastest path.

7.9 CONCLUDING REMARKS

In this chapter we considered several topics that form the basis for understanding the sintering process. The concepts introduced will be used extensively in the next chapter dealing with the sintering models and in subsequent chapters. Matter transport during the sintering of polycrystalline ceramics occurs by diffusion, a thermally activated process, which can occur along different paths in the solid, giving rise to the different mechanisms of diffusion: lattice, grain boundary, and surface diffusion. The rate of atomic (or ionic) diffusion depends on the temperature and on the concentration of defects in the solid. The defect concentration can be manipulated by changing the temperature, the oxygen partial pressure (or atmosphere), and the concentration of dopants or impurities. Matter transport during sintering can be viewed in terms of the flux of atoms (ions) or, equivalently,

in terms of the counterflow of vacancies. The flux of the diffusing species is driven by gradients in the concentration or, in the more general case, by gradients in the chemical potential. The diffusion of charged species (ions) in ceramics is coupled in such a way that stoichiometry and electroneutrality of the solid is maintained and as a result of this coupling, the rate of sintering and other mass transport processes is controlled by the slowest diffusing species along its fastest path.

PROBLEMS

- 7.1 Assuming that a powder has a surface energy of 1 J/m^2 , estimate the maximum amount of energy that is available for densification for spherical particles with a diameter of $1 \text{ }\mu\text{m}$ compacted to a green density of 60% of the theoretical density. Assume that there is no grain growth and the grain boundary energy is 0.5 J/m^2 .
- 7.2 Assuming a constant grain boundary width of 0.5 nm , plot the fractional volume of a polycrystalline solid occupied by the grain boundaries as a function of the grain size for grain sizes in the range of 10 nm to $10 \text{ }\mu\text{m}$. To simplify the calculation, the grains may be assumed to have a cubic shape.
- 7.3 Write formally correct defect reactions and the corresponding mass action equilibrium constants for the following cases. If more than one reaction is possible, give the different possibilities and briefly discuss why.
 - a. Solid solution of CaCl_2 in NaCl
 - b. Solid solution of Y_2O_3 in ZrO_2
 - c. Reduction of CeO_2
 - d. Solid solution of Nb_2O_5 in TiO_2
 - e. Solid solution of Al_2O_3 in TiO_2
 - f. Solid solution of SrTiO_3 in BaTiO_3
 - g. Solid solution of Nb_2O_5 in BaTiO_3
 - h. Solid solution of Al_2O_3 in BaTiO_3
 - i. Solid solution of Y_2O_3 in BaTiO_3
- 7.4 The densification of a metal oxide MO is controlled by the diffusion of oxygen vacancies. The oxide has a native defect structure of oxygen vacancies. Develop equations for the defect equilibria and discuss how the densification rate can be enhanced.
- 7.5 Nickel oxide NiO is metal deficient with cation vacancies predominating. If it is doped with Li , which goes into solid solution on the regular Ni lattice sites, develop equations for the defect equilibria and construct the Brouwer diagram.
- 7.6 A pure oxide MO forms predominantly Schottky defects at the stoichiometric composition. It is oxygen deficient under reducing conditions and metal deficient under oxidizing conditions.
 - a. Develop equations for the defect equilibria and construct the Brouwer diagram.
 - b. If the oxide is doped with acceptor or donor dopants, develop the new equations for the defect equilibria and construct the Brouwer diagram.

- 7.7 List all possible mechanisms of diffusion in a polycrystalline ceramic.
- Which mechanism is expected to have the highest activation energy? The lowest activation energy? Explain.
 - Which mechanism is expected to be the fastest? The slowest?
 - Which mechanism is expected to dominate at lower temperatures? At higher temperatures?
- 7.8 The measured diffusion coefficient in ZnO is $5.0 \times 10^{-5} \text{ cm}^2/\text{s}$ at 600°C and $2.0 \times 10^{-5} \text{ cm}^2/\text{s}$ at 500°C . What would the diffusion coefficient be at 700°C ?
- 7.9 The self-diffusion coefficient of a metal is $10^{-10} \text{ cm}^2/\text{s}$ at 800°C . A thin film of a radioactive isotope of the metal is evaporated onto a plane surface of the metal. Assuming that the concentration of the isotope is described by Eq. (7.41)
- Plot the surface concentration as a function of time.
 - Show that the average diffusion distance after an annealing time t is $(D^*t)^{1/2}$.
 - Calculate the average diffusion distance after 10 h annealing at 800°C .
- 7.10 Estimate the difference in equilibrium vapor pressure for two spherical particles, one with a diameter of $0.1 \text{ }\mu\text{m}$ and the other with a diameter of $10 \text{ }\mu\text{m}$, assuming a temperature of 500°C , an atomic radius of 10^{-10} m , and a surface energy of 1 J/m^2 . Discuss what would happen if the two particles were placed in the same closed box at 500°C .
- 7.11 Determine the diffusional creep rate for a dense, fine-grained Al_2O_3 (average grain size = $1 \text{ }\mu\text{m}$) at 1400°C and under an applied pressure of 150 MPa . At this temperature, the following diffusion coefficients have been measured for Al_2O_3 :

$$\begin{aligned} D_{gb}^{\text{Al}} &= 5.6 \times 10^{-17} \text{ cm}^2/\text{sec} \\ D_{gb}^{\text{O}} &= 7.0 \times 10^{-14} \text{ cm}^2/\text{sec} \\ D_l^{\text{Al}} &= 4.0 \times 10^{-14} \text{ cm}^2/\text{sec} \\ D_l^{\text{O}} &= 1.0 \times 10^{-17} \text{ cm}^2/\text{sec} \end{aligned}$$

The diffusional creep equations are given in Chapter 8, Eqs. (8.78) and (8.79).

REFERENCES

- Coble, R. L.; Cannon, R. M. In *Processing of Crystalline Ceramics*, Mater. Sci. Res. Vol. 11. Palmour, H., III., Davis, R. F., Hare, T. M. eds.; Plenum: New York, 1978, pp. 151–170.
- Kroger, F. A. *The Chemistry of Imperfect Crystals*; North-Holland: Amsterdam, 1964.
- Kofstad, Per *Nonstoichiometry, Diffusion and Electrical Conductivity in Binary Metal Oxides*; Krieger Publishing Company: Malabar, FL, 1983.
- Shewmon, P. G. *Diffusion in Solids*; The Metals Society: Warrendale, PA, 1989.
- Crank, J. *The Mathematics of Diffusion*; 2nd ed.; Oxford Univ. Press: 1975.
- Howard, R. E.; Lidiard, A. B. *Rept. Prog. Phys.* 1964, Vol. 27, 161.
- Atkinson, A. In *Materials Science and Technology*, Vol. 11: *Structure and Properties of Ceramics*; Swain, M. V. ed.; VCH: New York, 1994, pp. 295–337.
- Carlsaw, H. S.; Jaeger, J. C. *Conduction of Heat in Solids*; 2nd ed.; Clarendon Press: Oxford, 1959.

9. Brown, A. M.; Ashby, M. F. *Acta Metall.* 1980, Vol. 28, 1085.
10. Herring, C. In *The Physics of Powder Metallurgy*; Kingston, W. ed.; McGraw Hill: New York, 1951, pp. 143–179.
11. Gordon, R. S. *J. Am. Ceram. Soc.* 1973, Vol. 56, 147.
12. Chiang, Y.-M.; Birnie, D., III.; Kingery, W. D. *Physical Ceramics*; Wiley: New York, 1997.

8

Theory of Solid-State and Viscous Sintering

8.1 INTRODUCTION

The reader will recall from Chapter 1 the basic types of sintering processes: solid-state sintering, liquid-phase sintering, viscous sintering, and vitrification. This chapter is devoted to a theoretical analysis of *densification* in solid-state and viscous sintering. The analysis of the densification process, by itself, is not very useful. We must also understand how the microstructure of the powder system evolves during sintering, which forms the subject of Chapter 9. To complete the picture of the basic theory and principles of sintering, liquid-phase sintering, and vitrification are considered in Chapter 10.

The sintering phenomena in polycrystalline materials are considerably more complex than those in viscous sintering of amorphous materials because of the availability of several matter transport paths and the presence of grain boundaries. Matter transport in solid-state sintering can occur by at least six different paths which define the *mechanisms of sintering*. In practice, more than one mechanism may operate during any given regime of sintering, and the occurrence of multiple mechanisms makes analysis of sintering rates and the determination of the sintering mechanisms difficult. Perhaps the most important consequence of the grain boundaries is the occurrence of grain growth and pore growth during sintering, a process normally referred to as *coarsening*. The coarsening process provides an alternative route by which the free energy of the powder system can be reduced, therefore, it reduces the driving force for densification. The interplay between the two processes, sometimes referred to as a competition between sintering (densification) and coarsening, is discussed in Chapter 9.

In contrast to solid-state sintering, the analysis of viscous sintering appears relatively simple in principle. Matter transport occurs by a viscous flow mecha-

nism, but the path along which matter flows is not specified. Instead the equations for matter transport are derived on the basis of an *energy balance* concept put forward by Frenkel (1), in which the rate of energy dissipation by viscous flow is put equal to the rate of energy gained by reduction in surface area. The models based on this energy balance concept are generally successful in describing the sintering kinetics of amorphous materials.

A comprehensive theory of sintering should be capable of describing the entire sintering process as well as the evolution of the microstructure (i.e., grain size, pore size, and the distribution of the grain and pore sizes). However, in view of the complex nature of the process, it is unlikely that such a theory will be developed. A more realistic approach, which is adopted in this book, is to first develop an understanding of the densification and coarsening phenomena separately and then explore the consequences of their interaction.

Several theoretical approaches have been used to analyze the densification process during sintering, including the use of analytical models, scaling laws, and numerical simulations. These approaches, particularly the analytical models, have been criticized because the drastic simplifications assumed in the models make them unsuitable for quantitatively predicting the sintering behavior of real powder systems. Commonly, the models assume uniform packing of monosize spherical particles, the occurrence of a single mass transport mechanism, and no grain growth. At best, they provide only a qualitative understanding of sintering. In spite of these shortcomings, the role of the theoretical models in the development of our understanding of sintering should not be overlooked. Other approaches, such as phenomenological equations and sintering maps, attempt to represent sintering data in terms of equations or diagrams but provide very little insight into the process.

8.2 MECHANISMS OF SINTERING

Sintering of polycrystalline materials occurs by diffusional transport of matter along definite paths that define the *mechanisms of sintering*. We will recall that matter is transported from regions of higher chemical potential (referred to as the *source* of matter) to regions of lower chemical potential (referred to as the *sink*). There are at least six different mechanisms of sintering in polycrystalline materials, as shown schematically in Fig. 8.1 for a system of three sintering particles. They all lead to bonding and growth of necks between the particles, so the strength of the powder compact increases during sintering. Only certain mechanisms, however, lead to shrinkage or densification, and a distinction is commonly made between *densifying* and *nondensifying* mechanisms. Surface diffusion, lattice diffusion from the particle surfaces to the neck, and vapor transport (mechanisms 1, 2, and 3) lead to neck growth without densification and are referred to as nondensifying mechanisms. Grain boundary diffusion and lattice

diffusion from the grain boundary to the pore (mechanisms 4 and 5) are the most important densifying mechanisms in polycrystalline ceramics. Diffusion from the grain boundary to the pore permits neck growth as well as densification. Plastic flow by dislocation motion (mechanism 6) also leads to neck growth and densification but is more common in the sintering of metal powders. The nondensifying mechanisms cannot simply be ignored because when they occur, they reduce the curvature of the neck surface (i.e., the driving force for sintering) and so reduce the rate of the densifying mechanisms.

In addition to the alternative mechanisms, there are additional complications arising from the diffusion of the different ionic species making up the compound. As discussed in Chapter 7, the flux of the different ionic species is coupled to preserve the stoichiometry and electroneutrality of the compound. As a result, it

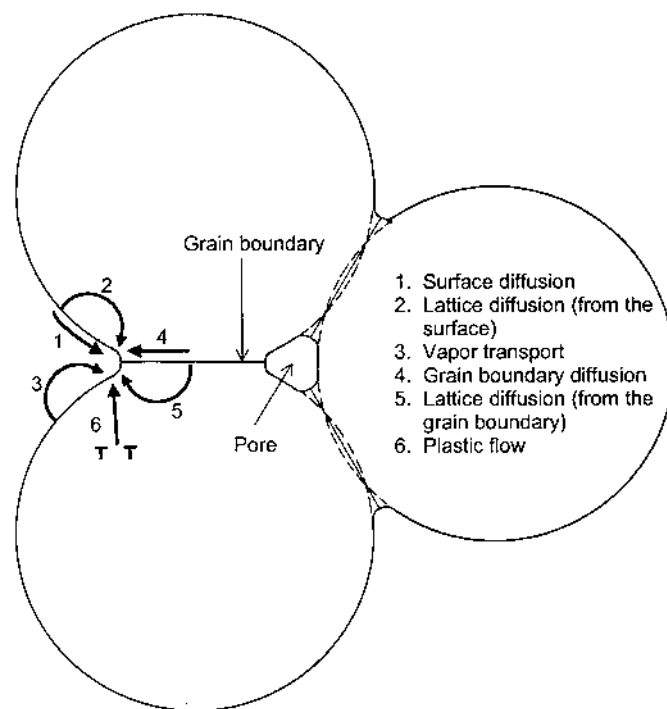


FIGURE 8.1 Six distinct mechanisms can contribute to the sintering of a consolidated mass of crystalline particles: (1) surface diffusion, (2) lattice diffusion from the surface, (3) vapor transport, (4) grain boundary diffusion, (5) lattice diffusion from the grain boundary, and (6) plastic flow. Only mechanisms 1 to 3 lead to densification, but all cause the necks to grow and so influence the rate of densification.

is the slowest diffusing species along its fastest path that controls the rate of densification.

For amorphous materials (glasses), which cannot have grain boundaries, neck growth and densification occur by viscous flow involving deformation of the particles. Figure 8.2 shows as an example the sintering of two glass spheres by viscous flow. The path by which matter flows is not clearly defined. The geometrical changes that accompany viscous flow are fairly complex, and as we shall see later, severe simplifying assumptions are made in formulating the equations for matter transport. For the sintering of spheres, Fig. 8.3a shows a schematic of two possible flow fields for viscous sintering (2). While the form shown on the left-hand side may be expected in real systems, the results of recent simulations (Fig. 8.3b) show good agreement with the flow field on the right (see Sec. 8.7). Table 8.1 summarizes the sintering mechanisms in polycrystalline and amorphous solids.

8.3 EFFECTS OF GRAIN BOUNDARIES

One important respect in which polycrystalline and amorphous materials differ is the presence of grain boundaries in the polycrystalline material. The presence of the grain boundaries dictates the equilibrium shapes of the pores and the grains

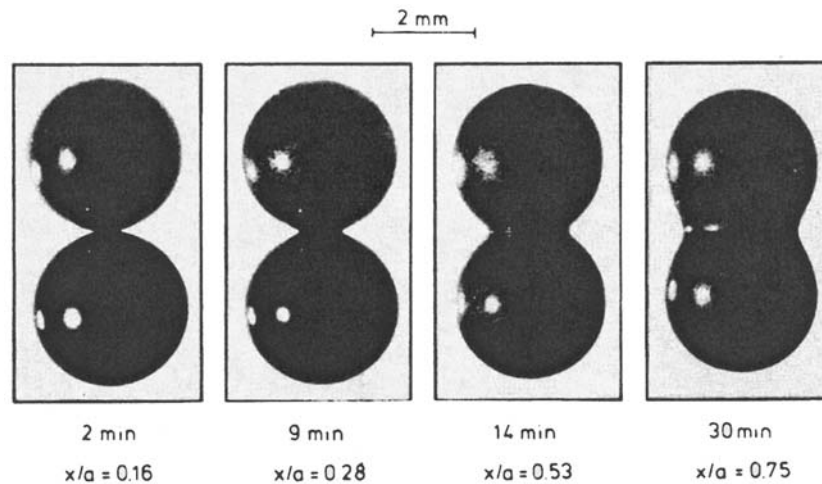


FIGURE 8.2 Two-particle model made of glass spheres (3 mm diameter) sintered at 1000°C. (x and a represent the radius of the neck and the sphere, respectively.). (From Ref. 66.)

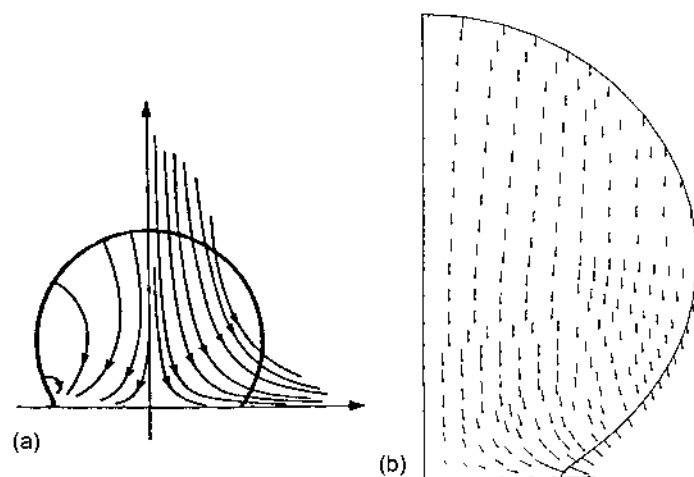


FIGURE 8.3 Densification of glass powders occurs by viscous flow. The matter transport paths are not clearly defined as for crystalline powders. (a) Two possible flow fields for viscous sintering of spheres are illustrated. (From Ref. 1.) (b) Simulations by finite-element analysis indicate that the flow field on the right-hand side is more realistic. (From Ref. 31, with permission.)

TABLE 8.1 Mechanisms of Sintering in Polycrystalline and Amorphous Solids

Type of solid	Mechanism	Source of matter	Sink of matter	Densifying	Non densifying
Polycrystalline	Surface diffusion	Surface	Neck		x
	Lattice diffusion	Surface	Neck		x
	Vapor transport	Surface	Neck		x
	Grain boundary diffusion	Grain boundary	Neck	x	
	Lattice diffusion	Grain boundary	Neck	x	
	Plastic flow	Dislocations	Neck	x	
	Viscous flow			x	
Amorphous		Unspecified	Unspecified	x	

in a polycrystalline material. Consider a hypothetical pore surrounded by three grains in Fig. 8.4. The forces must balance at the junction where the surfaces of the pores meet the grain boundary. They are normally represented by the tension in the interface, i.e., the tension in the solid–vapor interface and the tension in the grain boundary. By analogy with the surface tension of a liquid, a tension arises because an increase in the area of the interface leads to an increase in energy. At the junction, the tension in the solid–vapor interface is tangential to that interface, while that in the grain boundary is in the plane of the boundary. The balance of forces leads to

$$\gamma_{gb} = 2\gamma_{sv} \cos \frac{\psi}{2} \quad (8.1)$$

where ψ is the dihedral angle. A few sintering models (3) include the dihedral angle, but most assume that the pores have a circular cross section, which is equivalent to assuming that $\psi = 180^\circ$ or $\gamma_{gb} = 0$.

In the sintering of polycrystalline materials, part of the energy decrease due to the elimination of free surface area goes into creating new grain boundary area (Fig. 8.1), so the driving force for sintering will be somewhat lower than that calculated by Eq. (7.3) when the grain boundaries were neglected. If ΔA_{sv}

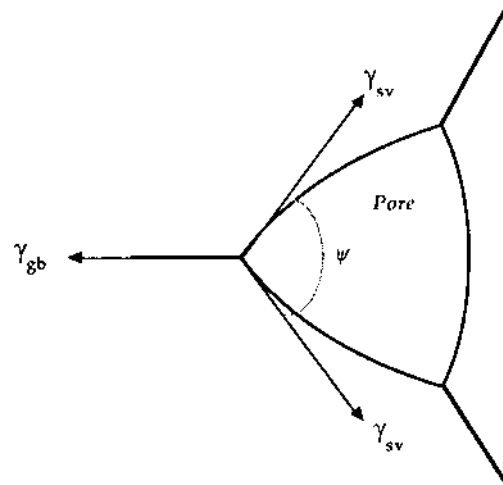


FIGURE 8.4 The equilibrium shapes of the pores in polycrystalline solids are governed by the balance between the surface and interfacial forces at the point where the grain boundary intersects the pore. γ_{sv} is the surface tension, γ_{gb} is the grain boundary tension, and ψ is the dihedral angle.

and ΔA_{gb} are the changes in the free surface area and grain boundary area, respectively, then the change in energy of the system is

$$\Delta E = \gamma_{sv} \Delta A_{sv} + \gamma_{gb} \Delta A_{gb} \quad (8.2)$$

where γ_{sv} is the specific surface energy and γ_{gb} is the specific grain boundary energy. The system will evolve towards a provisional equilibrium governed by the condition $|\gamma_{gb} \Delta A_{gb}| = |\gamma_{sv} \Delta A_{sv}|$. It is also worth noting that when, $|\gamma_{gb} \Delta A_{gb}| > |\gamma_{sv} \Delta A_{sv}|$, the change in energy ΔE in Eq. (8.1) is actually positive. Under these conditions, there would be an incentive for the solid–vapor surface area to increase, i.e., for the pores to grow. The sintering models commonly assume a uniformly packed powder system in which the pores decrease in size during sintering. We therefore postpone an analysis of pore growth until the next chapter when we consider the interactions of pores with grain boundaries.

Perhaps one of the most important consequences of the presence of the grain boundaries is that grain growth provides an alternative process by which the powder system can decrease its energy (by reducing the total grain boundary energy). Grain growth is normally accompanied by pore growth, the overall process being described as *coarsening*. Coarsening therefore occurs concurrently with sintering. A theory of sintering which rigorously analyzes the three-dimensional arrangement of particles, interaction between the particles, and concurrent densification and coarsening by the active transport mechanisms does not exist yet. The common approach therefore is to analyze sintering and grain growth separately. The understanding gained from the separate analyses is then used to explore the consequences of their interaction.

8.4 THEORETICAL ANALYSIS OF SINTERING

The main approaches that have been used in the theoretical analysis of sintering are summarized in Table 8.2. The development of the *analytical models*, starting about 1945–1950 (1,4), represents the first real attempt at a quantitative modeling of the sintering process. Whereas the analytical models assume an unrealistically simple geometry and often the occurrence of only a single mechanism, they have received the most attention and provide the basis for the present understanding of sintering. The *scaling laws*, formulated at about the same time as the early analytical models (5), have received little attention in the sintering literature but provide one of the most reliable guides for understanding the particle-size (i.e., scale) dependence of the sintering mechanisms. *Numerical simulations* offer a potentially powerful method because of their ability to analyze more realistic geometries than the analytical models as well as the occurrence of multiple mechanisms. They have not achieved the popularity of the analytical models presumably because the calculations normally require some advanced techniques in numerical

methods. The *topological models* make limited predictions of the sintering kinetics and are more appropriate to the understanding of the evolution of the microstructure (6). They will be outlined in the next chapter. The *statistical models* (7) have received little attention since they were originally put forward and will not be considered any further. The *phenomenological equations* are used to fit sintering data but add almost no insight into the process. Sintering maps show changes in the sintering behavior and mechanisms under different conditions of temperature and particle size. Because the maps are based on the predictions of the analytical models, they suffer from the same limitations.

8.5 SCALING LAWS

The scaling laws, formulated by Herring (5) in 1950, consider the effect of change of scale on microstructural phenomena during sintering. For a powder compact undergoing sintering, perhaps the most fundamental scaling parameter is the particle size. The scaling laws attempt to answer the following important question: How does the change in scale (i.e., the particle size) influence the rate of sintering?

The scaling laws do not assume a specific geometrical model. Instead, the main assumptions in the model are that during sintering (1) the particle size of

TABLE 8.2 Main Approaches Used for the Theoretical Analysis of Sintering

Approach	Comments	Ref.
Scaling laws	Not dependent on specific geometry. Effects of change of scale on the rate of single mechanism derived.	5
Analytical models	Greatly oversimplified geometry. Analytical equations for dependence of sintering rate on primary variables derived for single mechanism.	1, 10–14
Numerical simulations	Equations for matter transport solved numerically. Complex geometry and concurrent mechanisms analyzed.	26–32
Topological models	Analysis of morphological changes. Predictions of kinetics limited. More appropriate to microstructural evolution.	6
Statistical models	Statistical methods applied to the analysis of sintering. Simplified geometry. Semi-empirical analysis.	7
Phenomenological equations	Empirical or phenomenological derivation of equations to describe sintering data. No reasonable physical basis.	34, 35

any given powder system remains the same and (2) the geometrical changes remain similar. Two systems are defined as being geometrically similar if the linear dimension of all of the features (e.g., grains, pores) of one system (system 1) is equal to a numerical factor times the linear dimension of the corresponding features in the other system (system 2):

$$(\text{Linear dimension})_1 = \lambda (\text{Linear dimension})_2 \quad (8.3)$$

where λ is a numerical factor. Geometrically similar systems therefore involve simply a magnification of one system relative to the other (Fig. 8.5).

8.5.1 Derivation of the Scaling Laws

To illustrate the derivation of the scaling laws, let us now consider a simple system consisting of two spheres in contact (Fig. 8.6). We are not restricted to this geometry. It is chosen to simplify the illustration. Suppose it takes a time Δt_1 to produce a certain microstructural change (e.g., the growth of a neck to a certain radius X_1) in system 1. The question we must attempt to answer is: How long (Δt_2) does it take to produce a geometrically similar change in system 2? For geometrically similar changes, the initial radius of the particle and the neck radius of the two systems are related by

$$R_2 = \lambda R_1 \quad X_2 = \lambda X_1 \quad (8.4)$$

The time taken to produce a certain change by diffusional flow of matter can be expressed as

$$\Delta t = \frac{V}{JA\Omega} \quad (8.5)$$

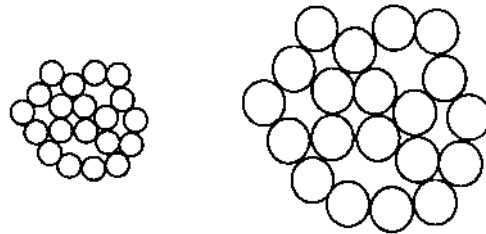


FIGURE 8.5 An example of two geometrically similar systems consisting of a random arrangement of circles. The systems differ only in scale and involve a simple magnification of one relative to the other.

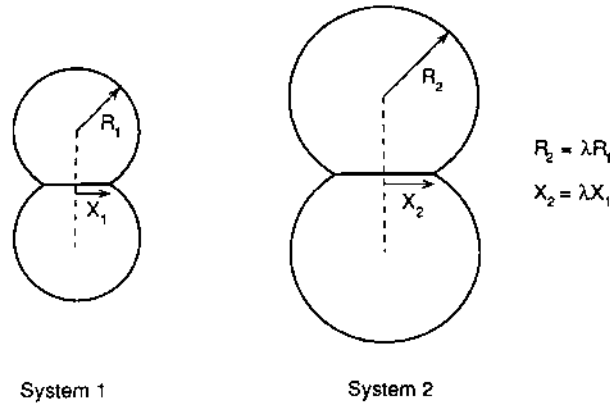


FIGURE 8.6 Geometrically similar models consisting of two spheres in contact. The linear dimensions of system 2 are a factor λ times those of system 1.

where V is the volume of matter transported, J is the flux, A is the cross-sectional area over which matter is transported, and Ω is the atomic volume. We can therefore write

$$\frac{\Delta t_2}{\Delta t_1} = \frac{V_2 J_1 A_1}{V_1 J_2 A_2} \quad (8.6)$$

As an example of the application of Eq. (8.6), consider matter transport by volume diffusion.

Scaling Law for Lattice Diffusion

The volume of matter transported is proportional to R^3 , where R is the radius of the sphere (see Fig. 8.6). Therefore V_2 is proportional to $(\lambda R)^3$, or $V_2 = \lambda^3 V_1$. For lattice diffusion, the area over which matter diffuses is proportional to R^2 . Therefore A_2 is proportional to $(\lambda R)^2$, or $A_2 = \lambda^2 A_1$. The flux J , as we outlined in the previous chapter, is proportional to $\nabla \mu$, the gradient in the chemical potential. For a curved surface with a radius of curvature r , μ varies as $1/r$. Therefore J varies as $\nabla(1/r)$ or as $1/r^2$. Now J_2 is proportional to $1/(\lambda r)^2$ so that $J_2 = J_1/\lambda^2$. To summarize, the parameters for lattice diffusion are

$$V_2 = \lambda^3 V_1 \quad A_2 = \lambda^2 A_1 \quad J_2 = \frac{J_1}{\lambda^2} \quad (8.7)$$

and substituting in Eq. (8.6) gives

$$\frac{\Delta t_2}{\Delta t_1} = \lambda^3 = \left(\frac{R_2}{R_1} \right)^3 \quad (8.8)$$

According to Eq. (8.8), the time taken to produce geometrically similar changes by a lattice diffusion mechanism increases as the cube of the particle size.

The scaling laws for the other mass transport mechanisms can be derived using a procedure similar to that outlined above for lattice diffusion, as described in detail by Herring (5). The laws can be written in the general form

$$\frac{\Delta t_2}{\Delta t_1} = \lambda^m = \left(\frac{R_2}{R_1} \right)^m \quad (8.9)$$

where m is an exponent that depends on the mechanism of sintering. Table 8.3 gives the values of m for the different sintering mechanisms.

8.5.2 Application and Limitation of the Scaling Laws

An important application of the scaling laws is the determination of how the relative rates of sintering by the different mechanisms depend on the particle size of the powder system. This type of information is useful, for example, in the fabrication of ceramics with controlled microstructure. As we observed earlier, some mechanisms lead to densification while others do not, so the achievement of high density requires that the rates of the densifying mechanisms be enhanced over those for the nondensifying mechanisms.

Relative Rates of Sintering Mechanisms

To determine the relative rates of the different mechanisms, it is more useful to write Eq. (8.9) in terms of a rate. For a given change, the rate is inversely proportional to the time so that Eq. (8.9) can be written

TABLE 8.3 Exponents for Herring's Scaling Laws Described by Eq. (8.9)

Sintering Mechanism	Exponent (m)
Surface diffusion	4
Lattice diffusion	3
Vapor transport	2
Grain boundary diffusion	4
Plastic flow	1
Viscous flow	1

$$\frac{(\text{Rate})_2}{(\text{Rate})_1} = \lambda^{-m} \quad (8.10)$$

In a given powder system, let us suppose that grain boundary diffusion and vapor transport (evaporation/condensation) are the dominant mass transport mechanisms. Then the rates of sintering by these two mechanisms vary with the scale of the system according to

$$(\text{Rate})_{gb} \sim \lambda^{-4} \quad (8.11)$$

and

$$(\text{Rate})_{ec} \sim \lambda^{-2} \quad (8.12)$$

The variation of the rates of sintering with λ for the two mechanisms is illustrated in Fig. 8.7. The crossover point for the two lines is arbitrary but this does not affect the validity of the results. We see that for small λ , i.e., as the particle size becomes smaller, the rate of sintering by grain boundary diffusion is enhanced compared to that for vapor transport. Conversely, the rate of sintering by vapor transport dominates for larger λ , i.e., for larger particle sizes. According to the scaling laws, smaller particle size is beneficial for densification when grain boundary diffusion and vapor transport are the dominant mechanisms. For the case where surface diffusion and lattice diffusion are the dominant mechanisms, we can use a similar procedure to show that surface diffusion is enhanced as the particle size decreases. It is left as an exercise for the reader to consider other combinations, for example, (1) lattice diffusion versus grain boundary diffusion and (2) surface diffusion versus grain boundary diffusion.

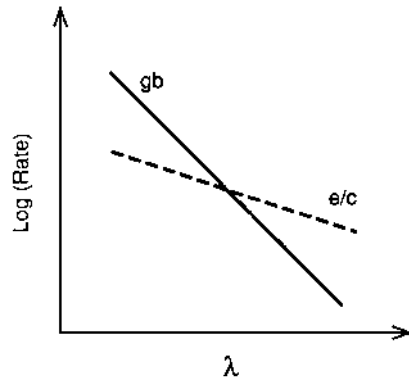


FIGURE 8.7 Schematic diagram of the relative rates of sintering by grain boundary diffusion and by evaporation/condensation as a function of the scale (i.e., particle size) of the system.

Limitation of the Scaling Laws

Due to the general approach and the simple physical principles employed in the derivation, the scaling law approach overcomes several key limitations of the analytical models. Because the geometric details of the powder system do not enter into the derivation, the laws can be applied to particles of any shape and to all stages of the sintering process. On the other hand, we must remember the conditions that govern the validity of the laws. The derivation assumed that the particle size of each powder system did not change during sintering and that the microstructural changes remained geometrically similar in the two systems. This requirement of geometrically similar microstructural changes is a key limitation of the scaling laws because it is difficult to maintain in real powder systems. The scaling laws also require that the two systems be identical in chemical composition so that the mass transport coefficients (e.g., the diffusion coefficients) are the same.

Since the exponent m in Eq. (8.9) or (8.10) depends on the mechanism of sintering, it may seem that the measurement of m would provide information on the mechanism of sintering. In practice, several factors can complicate the task of determining the mechanism. A major problem is the simultaneous occurrence of more than one mechanism. In such a case, the measured exponent may correspond to a mechanism that is entirely different from those operating. As outlined above, it is difficult to maintain the geometrically similar microstructure assumed in the derivation of the scaling laws. Furthermore, the sintering mechanism may change with the size of the particles.

Whereas the scaling laws appear to be obeyed reasonably well in simple metallic systems, e.g., nickel wires, copper spheres, and silver spheres, the application of the laws to the sintering of Al_2O_3 produced unexpected results (8). For powders with a narrow size distribution, high nonintegral values of the exponent m were found. The value of the exponent also varied with the extent of densification, especially in the early stages of sintering.

To summarize, the use of the scaling laws for the determination of the mechanism of sintering does not appear to be a worthwhile exercise. The laws are, however, useful for understanding the particle size dependence of the sintering mechanisms and for determining how the relative rates of the different mechanisms are influenced by the particle size.

8.6 ANALYTICAL MODELS

The analytical models assume a relatively simple, idealized geometry for the powder system, and for each mechanism, the mass transport equations are solved analytically to provide equations for the sintering kinetics. A problem is that the microstructure of a real powder compact changes continuously as well as drasti-

cally during sintering. It is therefore difficult to find a single geometrical model that can adequately represent the entire process yet still provide the degree of simplicity for the mass transport equations to be solved analytically. To overcome this problem, the sintering process is conceptually divided into separate *stages*, and for each stage, an idealized geometry that has a rough similarity with the microstructure of the powder system is assumed.

8.6.1 Stages of Sintering

Sintering is normally thought to occur in three sequential stages referred to as (1) the *initial* stage, (2) the *intermediate* stage, and (3) the *final* stage. In some analyses of sintering, an extra stage, stage 0, is considered which describes the instantaneous contact between the particles, when they are first brought together due to elastic deformation in response to surface energy reduction at the interface (9). However, we shall not consider this refinement. A stage represents an interval of time or density over which the microstructure is considered to be reasonably well defined. For polycrystalline materials, Fig. 8.8 shows the idealized geometrical structures that were suggested by Coble (10) as representative of the three stages. For amorphous materials, the geometrical models assumed for the intermediate and final stages are very different from those for the polycrystalline case and will be described appropriately later.

8.6.1.1 Initial Stage

The initial stage consists of fairly rapid interparticle neck growth by diffusion, vapor transport, plastic flow, or viscous flow. The large initial differences in surface curvature are removed in this stage, and shrinkage (or densification) accompanies neck growth for the densifying mechanisms. For a powder system consisting of spherical particles, the initial stage is represented as the transition between Figs. 8.8a and 8.8b. It is assumed to last until the radius of the neck between the particles has reached a value of ~ 0.4 – 0.5 of the particle radius. For a powder system with an initial density of 0.5 – 0.6 of the theoretical density, this corresponds to a linear shrinkage of 3 to 5% or an increase in density to ~ 0.65 of the theoretical when the densifying mechanisms dominate.

8.6.1.2 Intermediate Stage

The intermediate stage begins when the pores have reached their equilibrium shapes as dictated by the surface and interfacial tensions (see Sec. 8.3). The pore phase is still continuous. In the sintering models, the structure is usually idealized in terms of a spaghetti-like array of porosity sitting along the grain edges as illustrated in Fig. 8.8c. Densification is assumed to occur by the pores simply shrinking to reduce their cross section. Eventually, the pores become unstable and pinch off, leaving isolated pores; this constitutes the beginning of the final

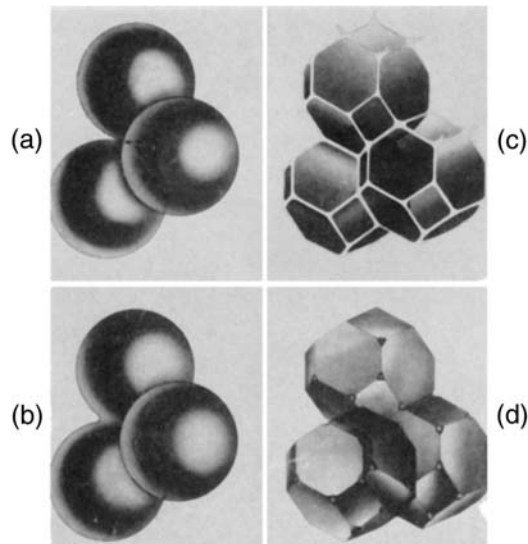


FIGURE 8.8 Idealized models for the three stages of sintering. (a) Initial stage: Model structure represented by spheres in tangential contact. (b) Near the end of the initial stage: Spheres have begun to coalesce. The neck growth illustrated is for center-to-center shrinkage of 4%. (c) Intermediate stage: Dark grains have adopted the shape of a tetrakaidecahedron, enclosing white pore channels at the grain edges. (d) Final stage: Pores are tetrahedral inclusions at the corners where four tetrakaidecahedra meet. (From Ref. 10.)

stage. The intermediate stage normally covers the major part of the sintering process, and it is taken to end when the density is ~ 0.9 of the theoretical.

8.6.1.3 Final Stage

The microstructure in the final stage can develop in a variety of ways, and we shall consider this in detail in Chapter 9. In one of the simplest descriptions, the final stage begins when the pores pinch off and become isolated at the grain corners, as shown by the idealized structure in Fig. 8.8d. In this simple description, the pores are assumed to shrink continuously and may disappear altogether. As outlined in Chapter 1, the removal of almost all of the porosity has been achieved in the sintering of several real powder systems.

Some of the main parameters associated with the three idealized stages of sintering are summarized in Table 8.4, and examples of the microstructures (planar section) of real powder compacts in the initial, intermediate, and final stages are shown in Fig. 8.9.

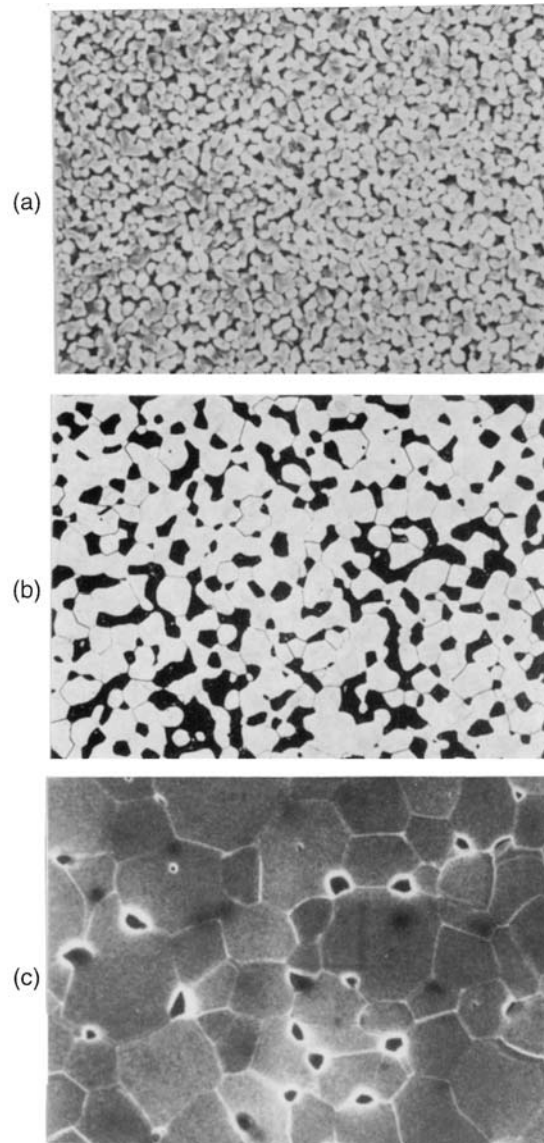


FIGURE 8.9 Examples of real microstructures (planar sections) for (a) initial stage of sintering, (b) intermediate stage, and (c) final stage.

TABLE 8.4 Parameters Associated with the Stages of Sintering for Polycrystalline Solids

Stage	Typical microstructural feature	Relative density range	Idealized model
Initial	Rapid inter-particle neck growth	Up to ~0.65	Two monosize spheres in contact
Intermediate	Equilibrium pore shape with continuous porosity	~0.65–0.90	Tetrakaidecahedron with cylindrical pores of the same radius along the edges
Final	Equilibrium pore shape with isolated porosity	>~0.90	Tetrakaidecahedron with spherical monosize pores at the corners

8.6.2 Modeling the Sintering Process

The analytical models, as outlined earlier, commonly assume that the particles in the initial powder compact are spherical and of the same size and that they are uniformly packed. With these assumptions, a unit of the powder system, called the *geometrical model*, can be isolated and analyzed. By imposing the appropriate boundary conditions, the remainder of the powder system can be considered as a continuum having the same macroscopic properties (e.g., shrinkage and densification rate) as the isolated unit. The derivation of the equations for the sintering kinetics follows a simple procedure: for the assumed geometrical model, the mass transport equations are formulated and solved under the appropriate boundary conditions.

8.6.3 Initial Stage Models

8.6.3.1 Geometrical Parameters

The model for the initial stage consists of two equal-sized spheres in contact, referred to as the *two-sphere model*. Two slightly different geometries can be considered, depending on whether the mechanisms are nondensifying (Fig. 8.10a) or densifying (Fig. 8.10b). The two-sphere model for the densifying mechanisms accounts for interpenetration of the spheres (i.e., shrinkage) as well as neck growth. The neck formed between the particles is assumed to be circular with a radius X and with a surface having a circular cross section with a radius r . A circular cross section for the neck surface is tantamount to assuming that the grain boundary energy is zero. The main geometrical parameters of the model

are the principal radii of curvature of the neck surface r and X , the area of the neck surface A , and the volume of material transported into the neck V . These parameters are summarized in Fig. 8.10 and it is left as an exercise for the reader to derive them. It will be noticed that the parameters for the densifying model differ by only a small numerical factor compared to those for the nondensifying model.

8.6.3.2 Kinetic Equations

Diffusional transport of matter, as described in Chapter 7, can be analyzed in terms of the flux of atoms or equivalently in terms of the counterflow of vacancies. In the early development of sintering theory, the approach based on the counterflow of vacancies driven by a vacancy concentration gradient was used predominantly. We will adopt this approach in the present section, but later in the chapter we will outline a more general approach based on the flux of atoms driven by a

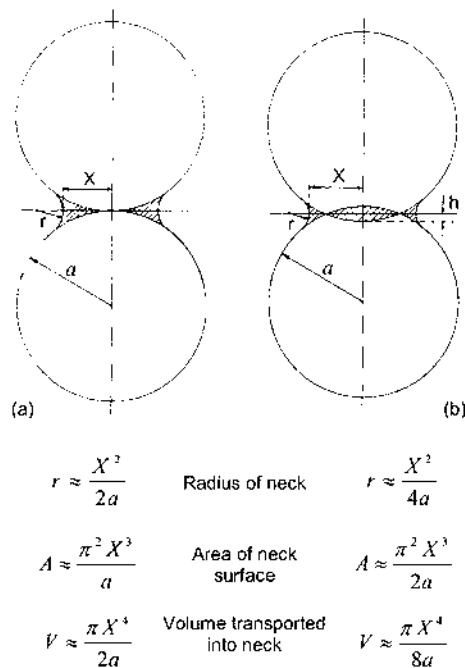


FIGURE 8.10 Geometrical parameters for the two-sphere model used in the derivation of the initial stage sintering equations for crystalline particles. The geometries shown correspond to those for (a) the nondensifying mechanisms and (b) the densifying mechanisms.

chemical potential gradient. As an illustration of the derivation of the initial stage sintering equations, let us start with the mechanism of grain boundary diffusion.

Grain Boundary Diffusion

According to Eq. (7.97), the flux of atoms into the neck is

$$J_a = \frac{D_v}{\Omega} \frac{dC_v}{dx} \quad (8.13)$$

where D_v is the vacancy diffusion coefficient, Ω is the volume of an atom or vacancy, and dC_v/dx is the vacancy concentration gradient (in one dimension). As outlined in Chapter 7, C_v is the *fraction* of sites occupied by the vacancies. The volume of matter transported into the neck per unit time is

$$\frac{dV}{dt} = J_a A_{gb} \Omega \quad (8.14)$$

where A_{gb} is the cross-sectional area over which diffusion occurs. Grain boundary diffusion is assumed to occur over a constant thickness δ_{gb} so that $A_{gb} = 2\pi X \delta_{gb}$, where X is the radius of the neck. Combining Eqs. (8.13) and (8.14) and substituting for A_{gb} gives

$$\frac{dV}{dt} = D_v 2\pi X \delta_{gb} \frac{dC_v}{dx} \quad (8.15)$$

Since the neck radius increases radially in a direction orthogonal to a line joining the centers of the spheres, a one-dimensional solution is adequate. Assuming that the vacancy concentration between the neck surface and the center of the neck is constant, then $dC_v/dx = \Delta C_v/X$, where ΔC_v is the difference in vacancy concentration between the neck surface and the center of the neck. The vacancy concentration at the center of the neck is assumed to be equal to that under a flat, stress-free surface C_{vo} , so according to Eq. (7.96) we can write

$$\Delta C_v = C_v - C_{vo} = \frac{C_{vo} \gamma_{sv} \Omega}{kT} \left(\frac{1}{r_1} + \frac{1}{r_2} \right) \quad (8.16)$$

where r_1 and r_2 are the two principal radii of curvature of the neck surface. From Fig. 8.10, $r_1 = r$ and $r_2 = -X$, and it is assumed that $X \gg r$. Substituting into Eq. (8.15) gives

$$\frac{dV}{dt} = \frac{2\pi D_v C_{vo} \delta_{gb} \gamma_{sv} \Omega}{kTr} \quad (8.17)$$

Using the relations given in Fig. 8.10b for V and r , and putting the grain boundary diffusion coefficient D_{gb} equal to $D_v C_{v0}$ we obtain

$$\frac{\pi X^3}{2a} \frac{dX}{dt} = \frac{2\pi D_{gb} \delta_{gb} \gamma_{sv} \Omega}{kT} \left(\frac{4a}{X^2} \right) \quad (8.18)$$

Rearranging this equation gives

$$X^5 dX = \frac{16 D_{gb} \delta_{gb} \gamma_{sv} \Omega a^2}{kT} dt \quad (8.19)$$

After integration and application of the boundary conditions $X = 0$ at $t = 0$, Eq. (8.19) becomes

$$X^6 = \frac{96 D_{gb} \delta_{gb} \gamma_{sv} \Omega a^2}{kT} t \quad (8.20)$$

We may also write Eq. (8.20) in the form

$$\frac{X}{a} = \left(\frac{96 D_{gb} \delta_{gb} \gamma_{sv} \Omega}{kT a^4} \right)^{1/6} t^{1/6} \quad (8.21)$$

Equations (8.20) and (8.21) predict that the ratio of the neck radius to the sphere radius increases as $t^{1/6}$.

For this densifying mechanism, the linear shrinkage, defined as the change in length ΔL divided by the original length L_0 , can also be found. As a good approximation (see Fig. 8.10b) we can write

$$\frac{\Delta L}{L_0} = - \frac{h}{a} = - \frac{r}{a} = - \frac{X^2}{4a^2} \quad (8.22)$$

where h is half the interpenetration distance between the spheres. Using Eq. (8.21) we obtain

$$\frac{\Delta L}{L_0} = - \left(\frac{3 D_{gb} \delta_{gb} \gamma_{sv} \Omega}{2 kT a^4} \right)^{1/3} t^{1/3} \quad (8.23)$$

so the shrinkage is predicted to increase as $t^{1/3}$.

Viscous Flow

As another example, let us consider the mechanism of viscous flow. We will recall that for this mechanism, matter transport is assumed to be governed by Frenkel's energy balance concept, which can be stated as

$$\begin{array}{l} \text{Rate of energy dissipation} \\ \text{by viscous flow} \end{array} = \begin{array}{l} \text{rate of energy gained by} \\ \text{reduction in surface area} \end{array} \quad (8.24)$$

The equation for neck growth between two spheres by viscous flow was derived by Frenkel (1). The original derivation by Frenkel contained an extra factor of π that is omitted in the version given here. For the parameters shown in Fig. 8.11 and assuming that the radius of the sphere remains roughly constant during the viscous flow, the decrease in the surface area of the two spheres is

$$S_0 - S = 8\pi a^2 - 4\pi a^2 (1 + \cos \theta) \quad (8.25)$$

Note that this means that the material removed from the plane of contact is uniformly distributed over the surface of the sphere, rather than accumulating at the neck. For small values of θ , i.e., for small neck radius, $\cos \theta \approx 1 - \theta^2/2$, so that Eq. (8.25) becomes

$$S_0 - S = 2\pi a^2 \theta^2 \quad (8.26)$$

The rate of change of energy due to the reduction in surface area can be written

$$\dot{E}_s = - \gamma_{sv} \frac{dS}{dt} = 4\pi a^2 \gamma_{sv} \frac{d}{dt} \left(\frac{\theta^2}{2} \right) \quad (8.27)$$

where γ_{sv} is the specific surface energy of the solid–vapor interface. According to Frenkel, the rate of energy dissipation by viscous flow between the two spheres is

$$\dot{E}_v = \frac{16}{3} \pi a^3 \eta \dot{u}^2 \quad (8.28)$$

where η is the viscosity of the glass and \dot{u} is the velocity of motion for the viscous flow given by

$$\dot{u} = \frac{1}{a} \frac{d}{dt} \left(\frac{a\theta^2}{2} \right) = \frac{d}{dt} \left(\frac{\theta^2}{2} \right) \quad (8.29)$$

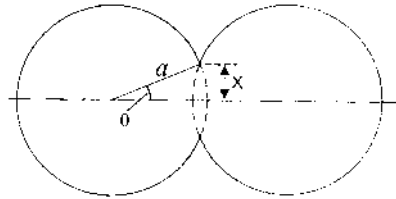


FIGURE 8.11 Geometrical parameters of the two-sphere model used in the derivation of the initial stage equation for viscous sintering by Frenkel.

This equation is based on the assumption that flow occurs uniformly along the axis joining the centers of the spheres, rather than being concentrated near the neck. Substituting for \dot{u} in Eq. (8.28) and putting $\dot{E}_s = \dot{E}_v$ gives

$$\frac{16}{3} \pi a^3 \eta \dot{u} \frac{d}{dt} \left(\frac{\theta^2}{2} \right) = 4 \pi a^2 \gamma_{sv} \frac{d}{dt} \left(\frac{\theta^2}{2} \right) \quad (8.30)$$

Rearranging Eq. (8.30) gives

$$\dot{u} = \frac{3}{4} \frac{\gamma_{sv}}{\eta a} \quad (8.31)$$

Substituting for \dot{u} in Eq. (8.29) and integrating subject to the boundary conditions of $\theta = 0$ at $t = 0$, we obtain

$$\theta^2 = \frac{3}{2} \left(\frac{\gamma_{sv}}{\eta a} \right) t \quad (8.32)$$

Since $\theta = X/a$, where X is the neck radius, Eq. (8.32) gives

$$\frac{X}{a} = \left(\frac{3\gamma_{sv}}{2\eta a} \right)^{1/2} t^{1/2} \quad (8.33)$$

It is left as an exercise for the reader to determine the equation for the shrinkage by this densifying mechanism.

8.6.3.3 Summary and Limitations of the Initial Stage Sintering Equations

The original derivations of the initial stage sintering equations can be found in publications by Kuczynski (11), Kingery and Berg (12), Coble (13), and Johnson and Cutler (14). The equations for neck growth and, for the densifying mechanisms, shrinkage can be expressed in the general form

$$\left(\frac{X}{a} \right)^m = \frac{H}{a^n} t \quad (8.34)$$

$$\left(\frac{\Delta L}{L_0} \right)^{m/2} = -\frac{H}{2^m a^n} t \quad (8.35)$$

where m and n are numerical exponents that depend on the mechanism of sintering and H is a function that contains the geometrical and material parameters of the powder system. Depending on the assumptions made in the models, a range of

values for m , n , and the numerical constant in H have been obtained. The values given in Table 8.5 represent the most plausible values for each mechanism (15).

The form of the neck growth equations indicates that a plot of $\log(X/a)$ versus $\log t$ yields a straight line with a slope equal to $1/m$, so by fitting the theoretical predictions to experimental data, the value of m can be found. A similar procedure can be applied to the analysis of shrinkage if it occurs during sintering. Data for validating the models are commonly obtained by measuring the neck growth in simple systems (e.g., two spheres, a sphere on a plate, or two wires) or the shrinkage in a compacted mass of spherical particles. Since m is dependent on the mechanism of sintering, at first sight it may seem that the measurement of m would provide information on the mechanism of sintering. However, the basic assumption in the models of a single dominant mass transport mechanism is not valid in most powder systems.

When more than one mechanism operates simultaneously, the measured exponent may correspond to an entirely different mechanism. As an example consider the initial sintering of copper. Kingery and Berg (12) showed that the neck growth and shrinkage data of copper spheres gave exponents characteristic of *lattice diffusion* as the dominant mechanism (Fig. 8.12). Later analysis (see Sect. 8.9) showed that *surface diffusion* was the dominant mechanism with a significant contribution from lattice diffusion (which gave shrinkage). In the case

TABLE 8.5 Plausible Values for the Constants Appearing in Eqs. (8.34) and (8.35) for the Initial Stage of Sintering

Mechanism	m	n	H^b
Surface diffusion ^a	7	4	$\frac{56D_s\delta_s\gamma_{sv}\Omega}{kT}$
Lattice diffusion from the surface ^a	4	3	$\frac{20D_l\gamma_{sv}\Omega}{kT}$
Vapor transport ^a	3	2	$\frac{3p_0\gamma_{sv}\Omega}{(2\pi mkT)^{1/2}kT}$
Grain boundary diffusion	6	4	$\frac{96D_{gb}\delta_{gb}\gamma_{sv}\Omega}{kT}$
Lattice diffusion from the grain boundary	5	3	$\frac{80\pi D_l\gamma_{sv}\Omega}{kT}$
Viscous flow	2	1	$\frac{3\gamma_{sv}}{2\eta}$

^aDenotes nondensifying mechanism, i.e., $\Delta L/L_0 = 0$.

^b D_s , D_l , D_{gb} , diffusion coefficients for surface, lattice, and grain boundary diffusion. δ_s , δ_{gb} , thickness for surface and grain boundary diffusion. γ_{sv} , specific surface energy; p_0 , vapor pressure over a flat surface; m , mass of atom; k , Boltzmann constant; T absolute temperature; η , viscosity.

of glass, sintering is dominated by viscous flow, and Frenkel's neck growth equation is well verified by the data of Kuczynski (16).

The other simplifying assumptions of the models must also be remembered. The extension of the two-sphere geometry to real powder compacts is valid only if the particles are spheres of the same size arranged in a uniform pattern. In practice, this system is, at best, approached only by the uniform consolidation of monodisperse powders by colloidal methods (see, for example, the work of Barringer and Bowen discussed in Chapter 1). Coble (17) considered the effect of a particle size distribution on the initial stage of sintering by considering a linear array of spheres.

Johnson (3) included the dihedral angle in his sintering model, but most models assume that the crosssection of the neck surface is circular, which is

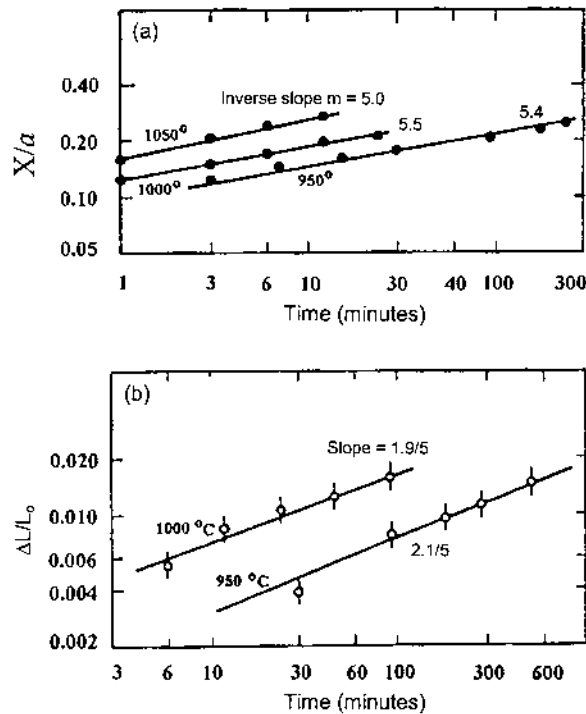


FIGURE 8.12 Data for (a) neck growth and (b) shrinkage of copper spheres. The exponents are characteristic of those for lattice diffusion. (From Ref. 12.) Later analysis of the data showed that surface diffusion was the dominant mechanism with a major contribution from lattice diffusion that gave shrinkage (see Fig. 8.23).

equivalent to assuming that the dihedral angle is 180° or that the grain boundary energy is zero. As we shall describe later, numerical simulations indicate that this circular neck cross section is grossly simplified. However, Johnson's results indicate that the neglect of the grain boundary energy is insignificant if the dihedral angle is greater than 150° .

The models also make simplifying assumptions about the way in which matter transported into the neck is redistributed over the surface. Matter transported into the neck by grain boundary diffusion must be redistributed over the neck surface to prevent buildup on the grain boundary groove (18). The models assume that surface diffusion is fast enough to cause redistribution, but this assumption has been questioned from time to time in the sintering literature.

8.6.4 Intermediate Stage Models

The geometrical model for the intermediate stage sintering of polycrystalline systems differs from that proposed for amorphous systems, so we will consider the two systems separately.

8.6.4.1 Geometrical Model for Polycrystalline Systems

The geometrical model commonly used for the intermediate stage was proposed by Coble (10). The powder system is idealized by considering it to consist of a space-filling array of equal-sized *tetrakaidecahedra*, each of which represents one particle. The porosity is cylindrical, with the axis of the cylinder coinciding with the edge of the tetrakaidecahedra (Fig. 8.8c). The unit cell of the structure is taken as a tetrakaidecahedron with cylindrical pores along its edges.

A tetrakaidecahedron is constructed from an octahedron by trisecting each edge and joining the points to remove the six edges (Fig. 8.13). The resulting structure has 36 edges, 24 corners, and 14 faces (8 hexagonal and 6 square). The volume of the tetrakaidecahedron is

$$V_t = 8\sqrt{2}l_p^3 \quad (8.36)$$

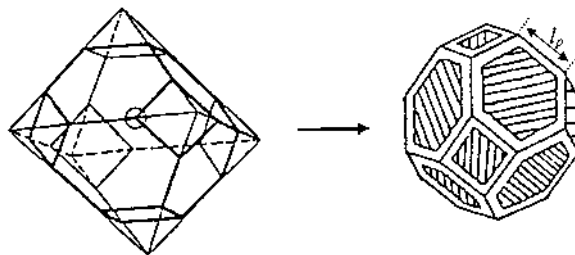


FIGURE 8.13 Sketch illustrating the formation of a tetrakaidecahedron from a truncated octahedron.

where l_p is the edge length of the tetrakaidecahedron. Each pore is shared by three tetrakaidecahedra, and if r is the radius of the pore, then the total volume of the porosity per unit cell is

$$V_p = \frac{1}{3}(36\pi r^2 l_p) \quad (8.37)$$

The porosity of the unit cell, V_p/V_t , is therefore

$$P_c = \frac{3\pi}{2\sqrt{2}} \left(\frac{r^2}{l_p^2} \right) \quad (8.38)$$

8.6.4.2 Mechanisms

Since the model assumes that the pore geometry is uniform, the nondensifying mechanisms cannot operate. This is because the chemical potential is the same everywhere on the pore surface. We are left with the densifying mechanisms: lattice diffusion and grain boundary diffusion. Plastic flow is not expected to operate in any significant way for ceramic systems.

8.6.4.3 Sintering Equations

Following the analysis by Coble (10), we shall outline the derivation of the kinetic equations for sintering by lattice diffusion and grain boundary diffusion.

Lattice Diffusion

Figure 8.14a shows that the cylindrical pores along the edges enclose each face of the tetrakaidecahedron. Because the vacancy flux from the pores terminates on the boundary faces (Fig. 8.14b), Coble assumed radial diffusion from a circular vacancy source and neglected the shape effects on the corner of the tetrakaidecahedron. For the boundary to remain flat, the vacancy flux per unit area of the boundary must be the same over the whole boundary. The diffusion flux field can be approximated to that of the temperature distribution in a surface-cooled, electrically heated cylindrical conductor.

The flux per unit length of the cylinder is given by

$$\frac{J}{l} = 4\pi D_v \Delta C \quad (8.39)$$

where D_v is the vacancy diffusion coefficient and ΔC is the difference in vacancy concentration between the pore (source) and the boundary (sink). Coble also made several other assumptions, including the following:

1. The convergence of the flux to the boundary does not qualitatively change the flux equation with regards to its dependence on the pore radius.

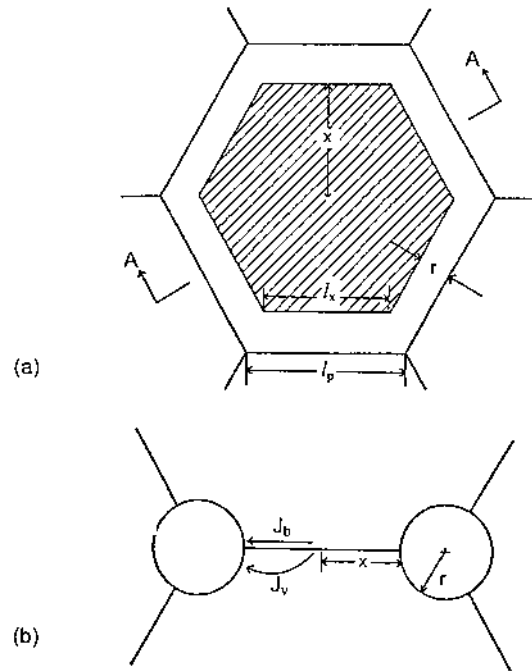


FIGURE 8.14 (a) The intermediate stage sintering equations for polycrystalline solids are based on a hexagonal neck. (b) The section (on A–A) shows a cut through the neck with the atomic flux paths for grain boundary and lattice diffusion.

2. The width of the flux field, i.e., the equivalence of l in Eq. (8.39), is equal to the pore diameter.
3. The flux is increased by a factor of 2 due to the freedom of the vacancy diffusion flux to diverge initially, thereby providing additional available area.

With these assumptions, Eq. (8.39) becomes

$$J = 2(4\pi D_v \Delta C) 2r \quad (8.40)$$

Since there are 14 faces in a tetrakaidecahedron and each face is shared by 2 grains, the volume flux per unit cell is

$$\frac{dV}{dt} = \frac{14}{2} J = 112\pi D_v \Delta C \quad (8.41)$$

For the cylindrical pore in the intermediate stage, the two principal radii of curvature are r and ∞ , so ΔC is given by

$$\Delta C = \frac{C_{v0} \gamma_{sv} \Omega}{kTr} \quad (8.42)$$

Substituting into Eq. (8.41) and putting $D_l = D_v C_{v0}$, where D_l is the lattice diffusion coefficient, we obtain

$$dV = \frac{112\pi D_l \gamma_{sv} \Omega}{kT} dt \quad (8.43)$$

The integral of dV is equal to the porosity given by Eq. (8.37), that is,

$$\int dV = 12\pi r^2 l_p \int_{r_0}^r \quad (8.44)$$

Combining with Eq. (8.43) gives

$$r^2 \Big|_r^0 \approx -10 \frac{D_l \gamma_{sv} \Omega}{l_p kT} t \Big|_t^{t_f} \quad (8.45)$$

where t_f is the time when the pore vanishes. Dividing both sides of this equation by l_p^2 and evaluating the integrand yields

$$P_c \approx \frac{r^2}{l_p^2} \approx \frac{10 D_l \gamma_{sv} \Omega}{l_p^3 kT} (t_f - t) \quad (8.46)$$

In view of the many approximations used by Coble, this equation can only be considered as an order-of-magnitude calculation. The model applies until the pores pinch off and become isolated.

The sintering equations are commonly expressed in terms of the densification rate. Using the relation between porosity P and relative density ρ , that is, $P = 1 - \rho$, and differentiating Eq. (8.46) with respect to time, we obtain

$$\frac{d}{dt}(P_c) = - \frac{d\rho}{dt} \approx - \frac{10 D_l \gamma_{sv} \Omega}{l_p^3 kT} \quad (8.47)$$

Taking l_p as approximately equal to the grain size G , and writing the densification rate in the form of a volumetric strain rate, Eq. (8.47) becomes

$$\frac{1}{\rho} \frac{d\rho}{dt} \approx \frac{10 D_l \gamma_{sv} \Omega}{\rho G^3 kT} \quad (8.48)$$

According to this equation, the densification rate at a fixed density is predicted to depend inversely as the cube of the grain size, in agreement with the prediction from Herring's scaling law.

Grain Boundary Diffusion

Using the same geometrical model described above for lattice diffusion and modifying the flux equations to account for grain boundary diffusion, Coble derived the following equation

$$P_c \approx \frac{r^2}{l_p^2} \approx \left(\frac{2D_{gb}\delta_{gb}\gamma_{sv}\Omega}{l_p^4 kT} \right)^{2/3} t^{2/3} \quad (8.49)$$

Using the procedure outlined above, Eq. (8.49) can be expressed as

$$\frac{1}{\rho} \frac{d\rho}{dt} \approx \frac{4}{3} \left[\frac{D_{gb}\delta_{gb}\gamma_{sv}\Omega}{\rho(1-\rho)^{1/2} G^4 kT} \right] \quad (8.50)$$

At a fixed density, the densification rate for grain boundary diffusion is predicted to vary inversely as the fourth power of the grain size, as also predicted by the scaling law.

Models for the intermediate stage of sintering have also been developed by Johnson (19) and Beeré (20). These models can be considered as refinements of Coble's model. Johnson derived equations for the shrinkage in terms of the average values of the neck radius and the pore radius. His model cannot be used to predict the rate of sintering. Instead, they are meant to help the analysis of sintering data. From the measured values of the average neck radius and pore radius, the boundary and lattice diffusion coefficients and the relative flux of matter due to the two mechanisms can be inferred. Beeré extended the model of Coble by allowing the pores to relax to a minimum free energy configuration. The pores have a fairly complex curvature and meet the grain boundary at a constant dihedral angle satisfying the balance of interfacial tensions (see Sec. 8.3). Beeré's model shows the same dependence on grain size and temperature as Coble's model but contain additional terms that involve the dihedral angle and the grain boundary area.

8.6.4.4 Geometrical Model for Amorphous Systems

The structure shown in Fig. 8.15 has been proposed by Scherer (21) as a model for the intermediate stage sintering of amorphous materials. It consists of a cubic array formed by intersecting cylinders and densification is assumed to be brought about by the cylinders getting shorter and thicker. The model can be viewed as

an idealized structure in which the cylinders represent strings of spherical particles joined together by necks.

The structure is represented by a unit cell consisting of 12 quarter cylinders (Fig. 8.15a). The volume of the solid phase in the unit cell is

$$V_s = 3\pi a^2 l - 8\sqrt{2}a^3 \quad (8.51)$$

where l is the length of the side of the unit cell and a is the radius of the cylinder. Since the total volume of the cell is l^3 , the density of the cell d is equal to $d_s V_s / l^3$, where d_s is the theoretical density of the solid phase. The relative density ρ , defined as d/d_s is given by

$$\rho = 3\pi x^2 - 8\sqrt{2}x^3 \quad (8.52)$$

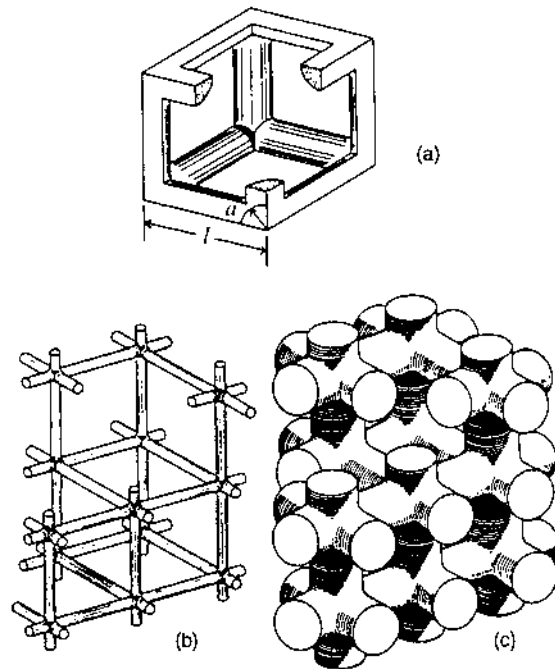


FIGURE 8.15 Scherer's model for viscous sintering. (a) Unit cell of the structure with edge length l and cylinder radius a . (b) Microstructure with a relative density of ~ 0.1 . (c) Microstructure with a relative density of ~ 0.5 . (From Ref. 21.)

where $x = a/l$. According to this equation, ρ is a function of a/l only. The inverse of Eq. (8.52) is

$$x = \frac{\pi\sqrt{2}}{8} \left[\frac{1}{2} + \cos \left(\Theta + \frac{4\pi}{3} \right) \right] \quad (8.53)$$

where

$$\Theta = \frac{1}{3} \cos^{-1} \left[1 - \left(\frac{4}{\pi} \right)^3 \rho \right] \quad (8.54)$$

The volume of solid phase in the unit cell is ρl^3 . This volume does not change and can also be put equal to $\rho_0 l_0^3$, where ρ_0 and l_0 are the initial values of the relative density and length, respectively, of the unit cell. Each cell contains one pore, so the number of pores per unit volume of the solid phase is

$$N = \frac{1}{\rho_0 l_0^3} \quad (8.55)$$

The model should be valid until the adjacent cylinders touch, thereby isolating the pores. This occurs when $a/l = 0.5$, i.e., when $\rho = 0.94$.

The derivation of the sintering equations for Scherer's model is quite similar to that outlined earlier for Frenkel's initial stage model. The result is (21)

$$\int_{t_0}^t \frac{\gamma_{sv} N^{1/3}}{\eta} dt = \int_{x_0}^x \frac{2dx}{(3\pi - 8\sqrt{2}x)^{1/3} x^{2/3}} \quad (8.56)$$

where γ_{sv} is the specific surface energy of the solid-vapor interface and η is the viscosity of the solid phase. By making the substitution

$$y = \left(\frac{3\pi}{x} - 8\sqrt{2} \right)^{1/3} \quad (8.57)$$

the integral on the right-hand side of Eq. (8.56) can be evaluated. The result can be written as

$$\frac{\gamma_{sv} N^{1/3}}{\eta} (t - t_0) = F_s(y) - F_s(y_0) \quad (8.58)$$

where

$$F_s(y) = -\frac{2}{\alpha} \left[\frac{1}{2} \ln \left(\frac{\alpha^2 - \alpha y + y^2}{(\alpha + y)^2} \right) + \sqrt{3} \arctan \frac{2y - \alpha}{\alpha\sqrt{3}} \right] \quad (8.59)$$

and $\alpha = (8\sqrt{2})^{1/3}$

The predictions of the model are normally expressed in terms of a curve of ρ versus $(\gamma_{sv}N^{1/3}/\eta)(t - t_0)$, referred to as the *reduced time*. The curve is obtained as follows: For a chosen value of ρ the parameter y is found from Eqs. (8.53) and (8.57). The function $F_s(y)$ is then found from Eq. (8.59) and the reduced time is obtained from Eq. (8.58). The procedure is repeated for other values of ρ . The predictions of the model are shown by the full curve in Fig. 8.16. The curve has the characteristic sigmoidal shape observed for the density versus time data in many sintering experiments. The model has been extended by considering a Gaussian or a bimodal distribution of pore sizes (21).

The predictions of Scherer's model have been well validated by the data for many amorphous materials such as colloidal gels, polymeric gels and consolidated glass particles (22). In the comparison with experimental data, the predictions of the model are plotted versus reduced time, while the data are obtained as function of measured time (e.g., seconds). To construct such a plot, one must first find the reduced time corresponding to the measured density as described above. A plot of the reduced time versus the measured time would be a straight line with a slope of $\gamma_{sv}N^{1/3}/\eta$. Multiplying that slope by the measured time gives the average reduced time interval for each density. The data points in Fig. 8.16 show a comparison of the sintering results for low density bodies formed from SiO_2 soot with the predictions of Scherer's model (23).

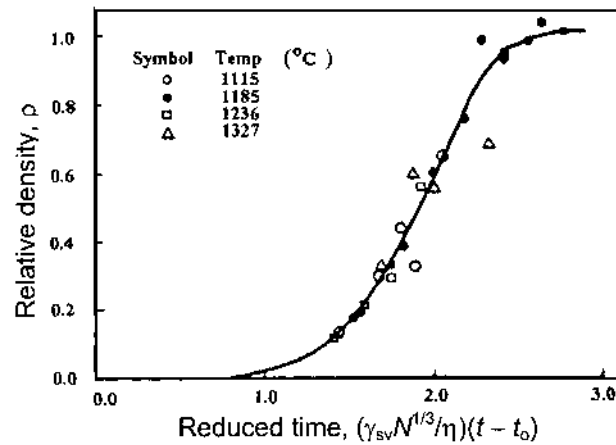


FIGURE 8.16 Comparison of the sintering data for silica soot preform sintered in air with the predictions of Scherer's model. (From Ref. 23.)

8.6.5 Final Stage Models

8.6.5.1 Geometrical Model for Polycrystalline Systems

For the final stage sintering of polycrystalline materials, the powder system is idealized in terms of an array of equal-sized tetrakaidecahedra with spherical pores of the same size at the corners (Fig. 8.8d). The tetrakaidecahedron has 24 pores (one at each corner), and each pore is shared by four tetrakaidecahedra, so the pore volume associated with a single tetrakaidecahedron is $V_p = (24/4)(4/3)\pi r^3$, where r is the radius of a pore. Making use of Eq. (8.36), the porosity in a single tetrakaidecahedron is

$$P_s = \frac{8\pi r^3}{8\sqrt{2}l_p^3} = \frac{\pi}{\sqrt{2}} \left(\frac{r^3}{l_p^3} \right) \quad (8.60)$$

A more convenient unit cell of the idealized structure can be chosen as a thick-walled spherical shell of solid material centered on a single pore of radius r (Fig. 8.17). The outer radius b of the spherical shell is defined such that the average density of the unit cell is equal to the density of the powder system, that is,

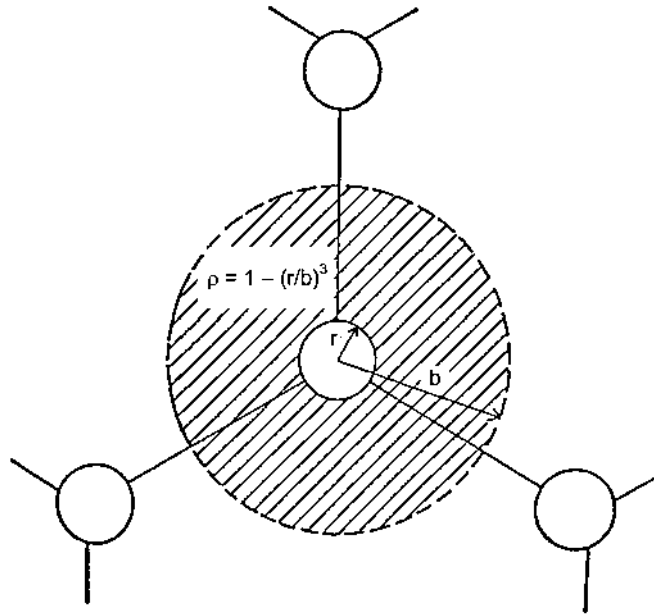


FIGURE 8.17 A porous solid during the final stage of sintering can be modeled by constructing a spherical shell centered on a single pore. The outer radius b is chosen such that the density of the shell matches that of the porous solid.

$$\rho = 1 - \left(\frac{r}{b}\right)^3 \quad (8.61)$$

The volume of the solid phase in the unit cell is $(4/3)\pi(b^3 - r^3)$. Since a unit cell contains a single pore, the number of pores per unit volume of the solid phase is

$$N = \frac{3}{4\pi} \left(\frac{1 - \rho}{r^3} \right) \quad (8.62)$$

8.6.5.2 Sintering Equations

As in the intermediate stage, the uniform pore geometry assumed in the models precludes the occurrence of nondensifying mechanisms. Final stage sintering models have been developed by Coble (10) and Coleman and Beeré (24).

Lattice Diffusion

Coble (10) used a procedure similar to that outlined earlier for the intermediate stage, but the atomic flux equation was approximated to that corresponding to diffusion between concentric spherical shells. The final result is

$$P_s = \frac{6\pi}{\sqrt{2}} \left(\frac{D_l \gamma_{sv} \Omega}{l_p^3 k T} \right) (t_f - t) \quad (8.63)$$

where P_s is the porosity at a time t , D_l is the lattice diffusion coefficient, γ_{sv} is the specific energy of the solid–vapor interface, Ω is the atomic volume, l_p is the edge length of the tetrakaidecahedron (taken as approximately equal to the grain size), k is the Boltzmann constant, T is the absolute temperature, and t_f is the time when the pore vanishes.

Because of the approximations made in the flux field, Eq. (8.63) is believed to be valid for porosities less than about 2%. For higher porosities (2–5%), a more complex equation was derived by Coble, but in view of the drastic approximations made, little benefit may be gained from the more complex expression. Except for a small difference in the value of the numerical constant, Eq. (8.63) is identical to the corresponding equation for the intermediate stage [Eq. (8.46)].

Grain Boundary Diffusion

A final stage sintering equation for grain boundary diffusion was not derived by Coble, but apart from a difference in the numerical constant, the equation may be expected to be identical to Eq. (8.49). As we shall see later in Sec. 8.10, Coble later developed models for diffusional sintering with an applied pressure from

which sintering equations for both the intermediate and final stages can be extracted.

8.6.5.3 Geometrical Model for Amorphous Systems

A model consisting of the spherical shell shown in Fig. 8.17 but without the grain boundaries was used by Mackenzie and Shuttleworth (25) to derive final stage sintering equations for viscous flow of an amorphous solid. The use of the model means that the real system is idealized in terms of a structure consisting of spherical pores of the same size in a solid matrix. The concentric shell maintains its spherical geometry during sintering. Unlike the initial stage, exact equations can be derived in Frenkel's energy balance concept for the rate of reduction of surface area and the rate of dissipation of energy by viscous flow. The result is

$$\int_{t_0}^t \frac{\gamma_{sv} N^{1/3}}{\eta} dt = \frac{2}{3} \left(\frac{3}{4\pi} \right)^{1/3} \int_{\rho_0}^{\rho} \frac{d\rho}{(1 - \rho)^{2/3} \rho^{1/3}} \quad (8.64)$$

where ρ is the relative density at time t , ρ_0 is the initial relative density at time t_0 , γ_{sv} is the specific energy of the solid-vapor interface, N is the number of pores per unit volume [see Eq. (8.62)], and η is the viscosity of the solid phase. Equation (8.64) can be written

$$\frac{\gamma_{sv} N^{1/3}}{\eta} (t - t_0) = F_{MS}(\rho) - F_{MS}(\rho_0) \quad (8.65)$$

where

$$F_{MS}(\rho) = \frac{2}{3} \left(\frac{3}{4\pi} \right)^{1/3} \left[\frac{1}{2} \ln \left(\frac{1 + \rho^3}{(1 - \rho)^3} \right) - \sqrt{3} \arctan \left(\frac{2\rho - 1}{\sqrt{3}} \right) \right] \quad (8.66)$$

The form of Eq. (8.65) is similar to that for Scherer's intermediate stage model [Eq. (8.58)], and the predictions for the sintering kinetics can be analyzed in a way similar to that outlined for Scherer's model.

A comparison of the predictions of Mackenzie and Shuttleworth's model with those of Scherer's model is shown in Fig. 8.18. Despite the large difference in the geometry of the models, the agreement is excellent over a wide density range. Significant deviations begin to occur only when ρ falls below ~ 0.2 . Although the Mackenzie and Shuttleworth model is strictly valid for ρ greater than ~ 0.9 , the predictions are applicable over a much wider range. A similar situation exists for Scherer's model. The predictions show excellent agreement not only with Mackenzie and Shuttleworth's model but also with Frenkel's initial stage model. The conclusion we can draw is that unlike the case of polycrystalline

materials, the sintering behavior of amorphous materials is not sensitive to structural details.

8.6.6 Application and Limitation of the Analytical Models

A feature that arises from our consideration of the analytical models is the difference in complexity between the sintering phenomena in polycrystalline materials and amorphous materials. The analysis of viscous sintering on the basis of Frenkel's energy balance concept appears relatively simple in principle. The idealization of the structure of amorphous materials leads to analytical solutions that describe the sintering behavior in a very satisfactory manner.

For polycrystalline materials, the sintering phenomena are considerably more dependent on the structural details of the powder system. Because of the drastic simplifications made in the models, they do not provide an adequate *quantitative* representation of the sintering behavior of real powder systems. The models do, however, provide a good *qualitative* understanding of the different sintering mechanisms and the dependence of the sintering kinetics on key processing parameters such as particle size, temperature, and, as we shall see later, applied pressure.

The assumptions made in the models must be remembered. The models assume a geometry that is a drastic simplification of a real powder system. They also assume that each mechanism operates separately. Although attempts have been made to develop analytical models with more realistic neck geometries [e.g.,

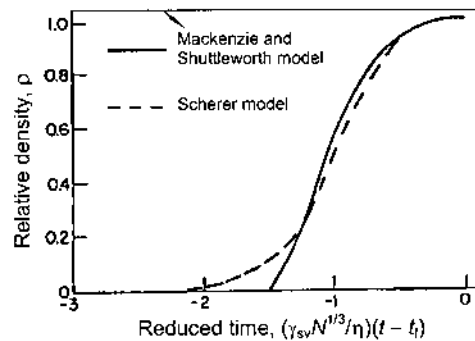


FIGURE 8.18 Relative density versus reduced time for the Mackenzie and Shuttleworth model and the Scherer model. For relative densities >0.942 , the Mackenzie and Shuttleworth model applies. The curves have been shifted to coincide at the time t_f when sintering is complete. (From Ref. 21.)

a catenary (a hyperbolic cosine function)] and with simultaneous mechanisms (e.g., surface diffusion and grain boundary diffusion), these more complex analyses do not provide any significant advances in the understanding of sintering when compared to the simple models. The analytical models assume that the powder particles are spherical and of the same size, a regular packing arrangement in the green body, and no grain growth. These assumptions are almost never reproduced in real powder systems.

8.7 NUMERICAL SIMULATION OF SINTERING

In view of the drastic simplifications made in the analytical models, attempts have been made to use numerical simulations to provide a better description of some of the complexities of sintering, such as more realistic neck geometries and the occurrence of simultaneous mechanisms. The analytical models, as described earlier, generally assume that the cross section of the neck surface is a circle (sometimes referred to as the circle approximation) that is tangential to both the grain boundary and to the spherical surface of the particle. Physically, this neck geometry is unsatisfactory because the surface curvature is forced to change discontinuously at the point of tangent between the neck surface and the spherical surface of the particle, which would require an abrupt change in the chemical potential. The use of a circular neck surface is also at odds with experimental observations. Undercutting of the neck surface occurs so that the surface has the cross section of a bulb rather than that of a circle. When more than one mechanism operates simultaneously, the rate of one mechanism influences that of another, but this effect cannot be easily treated by the analytical models.

8.7.1 Sintering by Diffusion Mechanisms

Numerical simulations of sintering have been performed by Nicholls and Mullins (26) for surface diffusion and by Bross and Exner (27) for surface diffusion and grain boundary diffusion operating simultaneously. In general, the three dimensional situation of real powder systems is reduced to a two-dimensional problem by choosing a geometrical model that can be described by one cross section only, e.g., two cylinders or a row of cylinders. The cylinders need not have the same radius. The differential equations for the flux of matter are then transformed into suitable equations for finite differences, i.e., employing small increments in time and small surface elements. The simulations are carried out using a computer to yield results for the neck growth or shrinkage.

For a model consisting of a row of cylinders of the same radius, Fig. 8.19 shows the results of Bross and Exner for the neck contours. Two situations were considered: (1) matter transport by surface diffusion only (Fig. 8.19a) and (2) the simultaneous occurrence of surface diffusion and grain boundary diffusion

(Fig. 8.19b). The results for the surface diffusion mechanism are in agreement with those of Nicholls and Mullins. The circle approximation used in the analytical models differs from the contours found by the numerical simulation approach which predicts undercutting and a continuous change in the curvature of the neck surface. The region of the neck surface influenced by matter transport also extends far beyond that given by the circle approximation, but the extension is less pronounced when surface diffusion and grain boundary diffusion occur simultaneously.

Numerical simulation of the initial stage of sintering of two spheres for the simultaneous occurrence of grain boundary, lattice, and surface diffusion was performed by Johnson (28). Although the simulation gave results for the neck size versus shrinkage that showed good agreement with experimental data for the sintering of spherical iron particles, the analysis included two approximations that are unsatisfactory: (1) the circle approximation for the neck surface and (2) the equality of the chemical potential gradient for grain boundary diffusion and for lattice diffusion.

The formation of a neck between two spherical particles by the simultaneous occurrence of surface diffusion and grain boundary diffusion was modeled by Svoboda and Riedel (29) using three independent methods: an accurate numerical solution, an exact similarity solution valid for short times in the limiting cases

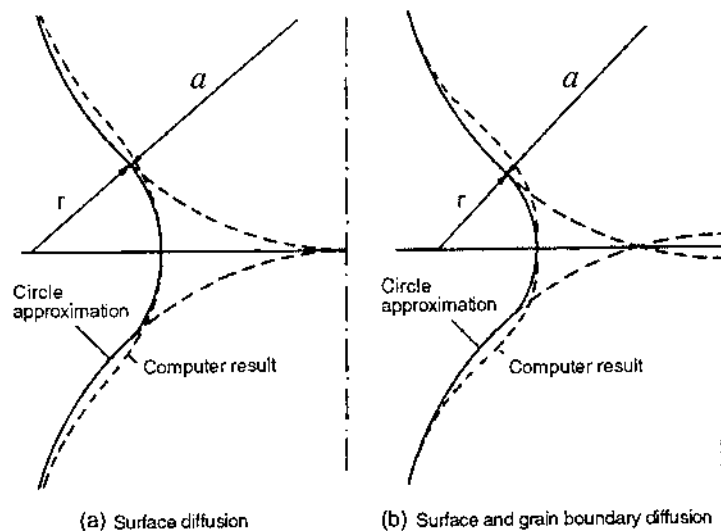


FIGURE 8.19 Contours of necks between cylinders for sintering by (a) surface diffusion and (b) simultaneous surface and grain boundary diffusion. (From Ref. 27.)

of small and large values of D_s/D_{gb} , and an approximate analytical solution based on a thermodynamic variational principle. Figure 8.20 shows the predictions of the analysis for the normalized neck radius (X/a) versus normalized time when the dihedral angle ψ is equal to 120° . Although the analysis confirms the occurrence of a power-law dependence of the neck radius on time, the exponent m in Eq. (8.34) increases from $11/2$ for high values of D_s/D_{gb} to 7 for low D_s/D_{gb} values. This trend in the value of m is opposite to that predicted by the analytical models (see Table 8.5).

8.7.2 Sintering by Viscous Flow

Finite element modeling was applied by Ross et al. (30) to numerically simulate the viscous sintering of an infinite line of cylinders, but the method has been used more effectively in recent years to simulate the viscous sintering of two spherical particles (31,32). Simulations by Jagota and Dawson (30) show that the viscous flow field assumed in the Frenkel model is qualitatively correct: the flow is axially downward and radially outward near the neck, with most of the energy dissipation occurring near the neck (see Fig. 8.3b). However, the Frenkel model is quantitatively in error. The common observation that the Frenkel model does not match experimental data for the linear shrinkage above $\sim 5\%$ is attributed more to the inaccuracy of the model rather than the inapplicability of the two-sphere model as such. According to the simulations, the two-sphere model is in

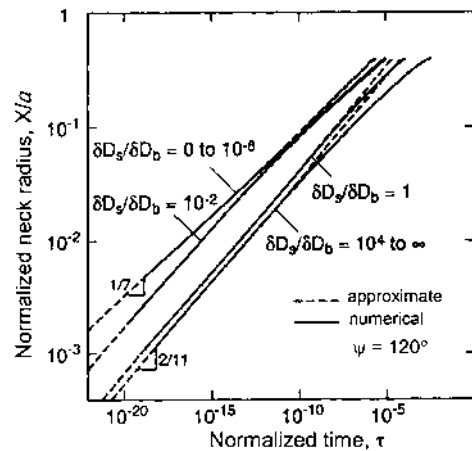


FIGURE 8.20 Results of numerical simulations for the normalized neck radius versus reduced time for sintering of two spherical particles by the simultaneous occurrence of surface and grain boundary diffusion. (From Ref. 29.)

good agreement with the Mackenzie and Shuttleworth model and the Scherer model for linear shrinkages of up to 15%.

Jagota (33) has used finite element modeling to simulate the sintering of a pair of rigid particles coated with an amorphous layer (Fig. 8.21a). As discussed in Chapter 11, the use of such *coated particles* can alleviate the difficulties encountered in the sintering of mixtures consisting of rigid inclusions and sinterable particles. Figure 8.21b shows the predicted change in the relative density of a packing of coated particles (initial relative density = 0.60) as a function of reduced time for different coating thicknesses and for the Mackenzie-Shuttleworth model. With sufficiently thick coatings (in this case s greater than ~ 0.2 of the particle radius), full density is predicted at a rate comparable to a packing that consists of particles without a rigid core.

8.7.3 Summary of the Numerical Simulation Approach

When compared to the analytical models, the numerical simulations can be fairly complex, and in many cases the results cannot be easily cast into a useful form showing the dependence of the sintering kinetics on key parameters. On the other hand, the simulations provide good insight into how matter is transported and

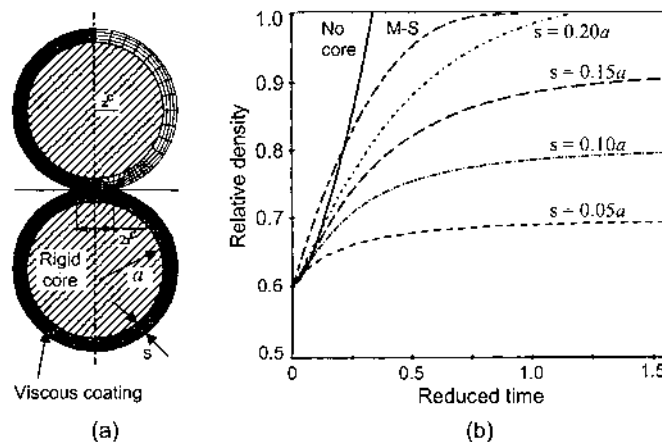


FIGURE 8.21 Finite element simulation of viscous sintering of two rigid particles coated with an amorphous layer: (a) Rigid particles of radius a coated with a viscous layer of thickness s and showing the finite element mesh; (b) predictions for the relative density versus reduced time for different coating thicknesses, and for the Mackenzie and Shuttleworth (M-S) model. (From Ref. 33.)

how the geometry of the structure changes. This, coupled with the ability to analyze more realistic particle geometries and the occurrence of simultaneous mechanisms, gives the approach great potential for elucidating many of the complexities of sintering. As discussed later in the book, numerical simulations also provide significant insight into grain growth and the sintering of composites. With the wider availability of more powerful computers, the approach is expected to see increasing use in the future.

8.8 PHENOMENOLOGICAL SINTERING EQUATIONS

In the phenomenological approach, empirical equations are developed to fit sintering data, usually in the form of density (or shrinkage) versus time. Although the equations provide little or no help in understanding the process of sintering, they may serve a useful function in some numerical models that require the incorporation of explicit equations for the densification of a powder system.

A simple expression that is found to be very successful in fitting sintering and hot pressing data is

$$\rho = \rho_0 + K \ln \frac{t}{t_0} \quad (8.67)$$

where ρ_0 is the density at an initial time t_0 , ρ is the density at time t , and K is a temperature-dependent parameter. Equation (8.67) is sometimes referred to in the sintering literature as the *semilogarithmic law*, but the use of the word *law* does not appear to be justified. Coble (10) attempted to provide some theoretical justification for the expression in the following way. Using the rate equation for Coble's intermediate or final stage model for sintering by lattice diffusion [for example, Eq. (8.48)], we can write

$$\frac{d\rho}{dt} = \frac{AD_l\gamma_{sv}\Omega}{G^3kT} \quad (8.68)$$

where A is a constant that depends on the stage of sintering, and assuming that the grains grow according to a cubic law of the form

$$G^3 = G_0^3 + \alpha t \approx \alpha t \quad (8.69)$$

and that $G^3 \gg G_0^3$, Eq. (8.68) becomes

$$\frac{d\rho}{dt} = \frac{K}{t} \quad (8.70)$$

where $K = AD_1\gamma_{sv}/(\alpha kT)$. On integrating Eq. (8.70) we obtain Eq. (8.67) which is expected to be valid in both the intermediate and final stages because Eq. (8.68) has the same form in both of these stages.

When grain growth is fairly limited, shrinkage data over a large part of the sintering process can usually be fitted by the equation

$$\frac{\Delta L}{L_0} = Kt^{1/\beta} \quad (8.71)$$

where K is a temperature-dependent parameter and β is an integer. This equation has the same form as the initial stage shrinkage equations for the analytical models.

Other empirical equations in the sintering literature include one due to Tikkanen and Makiipirtti (34):

$$\frac{V_0 - V_t}{V_0 - V_f} = Kt^n \quad (8.72)$$

where V_0 is the initial volume of the powder compact, V_t is the volume after sintering for time t , V_f is the volume of the fully dense solid, and K is a temperature-dependent parameter. Depending on the material, n has values between 0.5 and 1.0. Another equation due to Ivensen (35) is

$$\frac{V_t^P}{V_o^P} = (1 + C_1 mt)^{-1/m} \quad (8.73)$$

where V_o^P is the initial pore volume of the body, V_t^P is the pore volume after sintering for time t , and C_1 and m are constants.

Attempts have sometimes been made to attach physical significance to parameters in the empirical equations, but the difficulties of doing this have been demonstrated by Pejovnik et al. (36), who showed that sintering data for UO_2 could be well fitted by any of the following four equations: Eqs. (8.67), (8.72), (8.73), and a simple hyperbolic equation of the form $V_t^P/V_o^P = K_1/(K_2 + t) + K_3$. The conclusion is that more than one empirical equation can provide a good fit to any given set of sintering data. In practice, the choice of any one of the equations appears to be fairly arbitrary. Coble's semilogarithmic relationship has the advantage of simplicity and is very successful in fitting many sintering and hot pressing data, an example of which is shown in Fig. 8.22.

8.9 SINTERING DIAGRAMS

As discussed earlier, more than one mechanism commonly operates simultaneously during the sintering of polycrystalline systems. Numerical simulations pro-

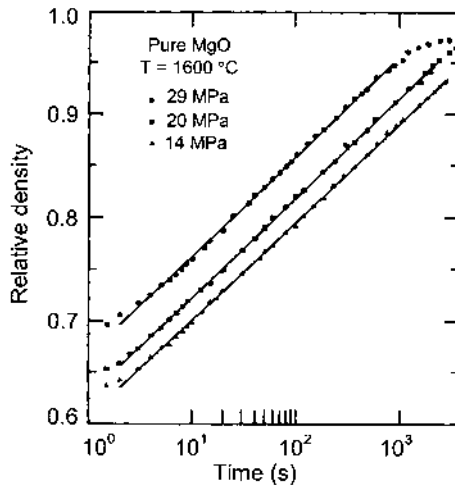


FIGURE 8.22 Semilogarithmic dependence of the density on time during the hot pressing of high purity MgO. (From Ref. 46.)

vide a theoretical framework for the analysis of sintering with simultaneous mechanisms, but a more practical approach, involving the construction of *sintering diagrams*, has been developed by Ashby (37) and Swinkels and Ashby (38). The earlier diagrams show, for a given temperature and neck size, the dominant mechanism of sintering and the net rate of neck growth or densification. Later, a second type of diagram was put forward in which the density rather than the neck size is evaluated, but the principles used for the construction of the density diagrams are similar to those for the neck size diagrams.

The form that a sintering diagram can take is shown in Fig. 8.23 for the sintering of copper spheres with a radius of $57\text{ }\mu\text{m}$. The axes are the neck radius X , normalized to the radius of the sphere a , and the homologous temperature T/T_M , where T_M is the melting temperature of the solid. The diagram is divided into various fields, and within each field, a single mechanism is dominant, i.e., it contributes most to neck growth. Figure 8.23, for example, is divided into three fields corresponding to surface diffusion, grain boundary diffusion, and lattice diffusion (from the grain boundary). At the boundary between two fields (shown as solid lines), two mechanisms contribute equally to the sintering rate. Superimposed on the fields are contours of constant sintering time.

Some diagrams, especially those developed more recently, may contain additional information. For example, broken lines roughly parallel to the temperature axis (not shown in Fig. 8.23) represent the transition between the stages of

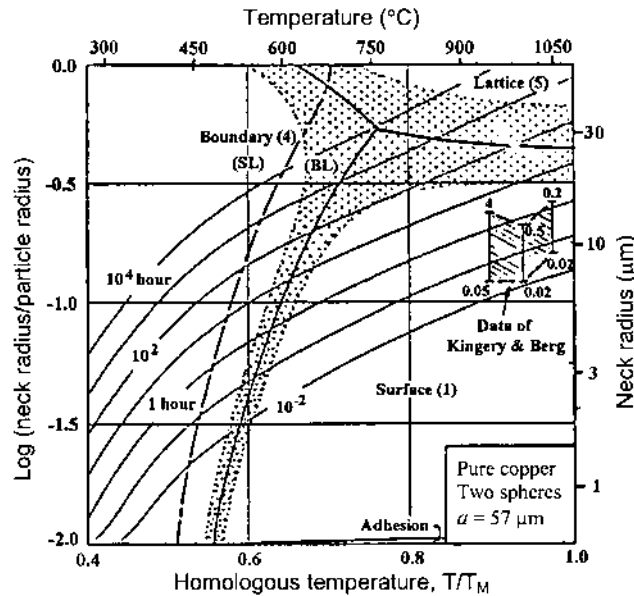


FIGURE 8.23 Neck size sintering diagram for copper spheres. The data of Kingery and Berg (12) are also shown. (From Ref. 37.)

sintering. On either side of the field boundaries is a shaded band, and outside this band, a single mechanism contributes more than 55% of the total neck growth. Within the shaded band, two or more mechanisms contribute significantly, but none contributes more than 55%. The shaded band provides an idea of the width of the field boundaries. A dashed line running roughly parallel to the field boundary between surface diffusion and grain boundary diffusion shows where redistribution of the matter transported by grain boundary diffusion controls the rate of this mechanism. As discussed earlier, matter transported into the neck by grain boundary diffusion requires another mechanism (e.g., surface diffusion) for redistribution over the neck surface. On the side labeled SL, redistribution by surface diffusion controls the rate; on the side labeled BL, boundary diffusion controls the rate.

8.9.1 Construction of the Diagrams

The construction of the diagrams is described in detail by Ashby (37). It requires neck growth equations for specified geometrical models and data for the material constants (e.g., diffusion coefficients, surface energy, and atomic volume) that

appear in the equations. The geometrical models are commonly the analytical models that were discussed earlier. The diagrams are constructed by numerical methods, and it is assumed that the total neck growth rate is the sum of all the neck growth rates for the individual mechanisms. The field boundaries at which one mechanism contributes 50% of the neck growth rate is then calculated. The procedure is carried out incrementally for small increases on X/a and T/T_M . The time interval between the steps is calculated and added to give the total time, which is used to plot the time contours. Refinements such as the width of the boundaries between the fields are added by modification of the same procedure.

8.9.2 Limitations of the Diagrams

Because the diagrams are based on approximate geometrical models and data for the material parameters which appear in them, they are no better than the analytical models discussed earlier. Furthermore, the material parameters (particularly for ceramics) are often not known with sufficient accuracy, so small changes in the values of the parameters can produce significant changes in the nature of the diagrams. Sintering diagrams have so far been constructed for several pure metals and a few simple ceramics (e.g., NaCl and Al_2O_3). For practical ceramic systems, small changes in the characteristics of the powders (e.g., purity) can produce significant changes in the material parameters (e.g., diffusion coefficients), so diagrams would have to be constructed for each system, thereby involving an enormous amount of work. In spite of these limitations, the diagrams have proved to be useful in visualizing conceptual relationships between the various mechanisms and changes in sintering behavior under different temperature and particle size regimes.

8.10 SINTERING WITH AN EXTERNALLY APPLIED PRESSURE

A common difficulty that often arises in the sintering of ceramics is that of inadequate densification. One solution to this difficulty is the application of an external stress or pressure to the powder system during heating, giving rise to the techniques of hot pressing, hot isostatic pressing, and hot forging. The theory and principles of such pressure-assisted sintering are considered here, while the practical application of the techniques are described in Chapter 12.

Models for hot pressing by diffusional mass transport under the driving forces of surface curvature and applied stress were formulated by Coble (39,40). In one approach, the analytical models for sintering were adapted to include the effects of an applied stress, while in a second approach, hot pressing is viewed in a manner analogous to that of creep in dense solids and the creep equations

are modified to account for the porosity and the surface curvature appropriate to powder systems.

8.10.1 Hot Pressing Models

8.10.1.1 Adaptation of the Analytical Sintering Models

Consider the idealized models for the three stages of sintering (Fig. 8.8). The vacancy concentration under the neck surface is not affected by the applied stress so that it is still given by Eq. (8.16); that is,

$$\Delta C_v = C_v - C_{v0} = \frac{C_{v0} \gamma_{sv} \Omega}{kT} \left(\frac{1}{r_1} + \frac{1}{r_2} \right) = \frac{C_{v0} \gamma_{sv} \Omega K}{kT} \quad (8.74)$$

where K is the curvature of the pore surface. For the initial stage of sintering, $K = 1/r = 4a/X^2$, whereas for the intermediate and final stages $K = 1/r$ and $2/r$, respectively, where r is the pore radius, a is the particle radius, and X is the neck radius. The stress p_a applied to the powder system leads to a stress p_e on the grain boundary, and because of the porosity, p_e is greater than p_a . Let us assume that

$$p_e = \phi p_a \quad (8.75)$$

where ϕ is a factor, referred to as the *stress intensification factor*, which we shall define in more detail later. The compressive stress on the grain boundary means that the vacancy concentration is less than that of a flat, stress-free boundary; that is,

$$\Delta C_{vb} = -\frac{C_{v0} p_e \Omega}{kT} = -\frac{C_{v0} \phi p_a \Omega}{kT} \quad (8.76)$$

For the two-sphere model appropriate to the initial stage of sintering (Fig. 8.10), Coble assumed that ϕ is equal to the area of the sphere projected onto the punch of the hot pressing die divided by the cross sectional area of the neck, i.e., $\phi = 4a^2/\pi X^2$, whereas for both the intermediate and final stages, Coble argued that $\phi = 1/\rho$, where ρ is the relative density of the body.

Using the parameters for K and ϕ , the variation of ΔC_{vp} and ΔC_{vb} is shown schematically in Fig. 8.24. For hot pressing, the difference in the vacancy concentration between the neck surface and the grain boundary is given by $\Delta C = \Delta C_{vp} - \Delta C_{vb}$, so for the initial stage

$$\Delta C = \frac{C_0 \Omega 4a}{kT X^2} \left(\gamma_{sv} + \frac{p_a a}{\pi} \right) \quad (8.77)$$

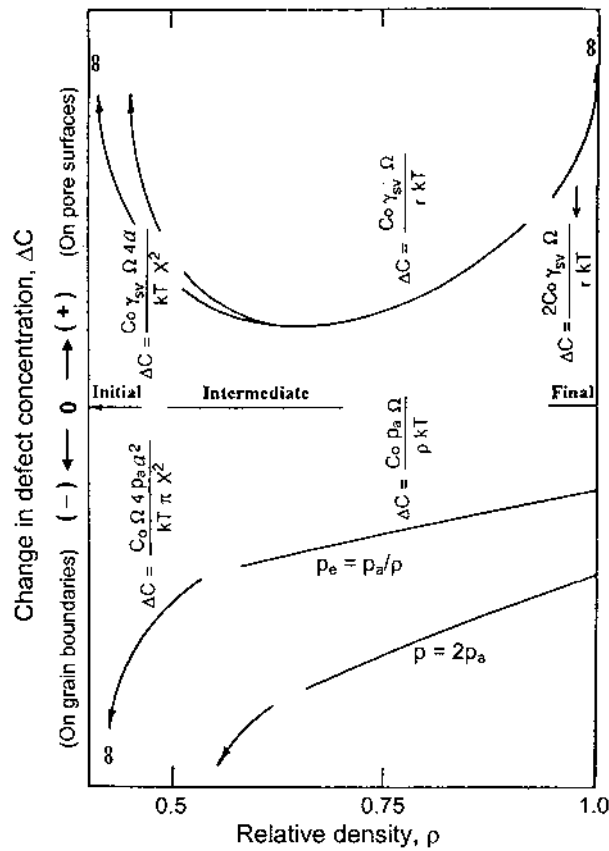


FIGURE 8.24 The driving force for hot pressing as a function of relative density. (From Ref. 40.)

This equation shows that for the initial stage, ΔC for hot pressing is identical to that for sintering except that γ_{sv} is replaced by $\gamma_{sv} + p_a a/\pi$. Since p_a and a are constant, it follows that the hot pressing equations can be obtained from the sintering equations by simply replacing γ_{sv} by $\gamma_{sv} + p_a a/\pi$.

Coble did not specifically adapt the intermediate and final stage sintering models to account for hot pressing, but as described below, he used a different approach based on a modification of creep equations. However, as we shall show later, if the differential equations for matter transport are formulated with the proper dependence of the chemical potential on surface curvature and applied

stress, then the sintering and hot pressing equations can be derived by the same analysis.

8.10.1.2 Modification of the Creep Equations

Let us consider matter transport during creep of a dense solid and the form that the creep equations can take. We start with a single crystal of a pure solid with the cubic structure that has the shape of a rod with a cross section of length L . Let normal stresses p_a act on the sides of the rod as shown in Fig. 8.25a. Nabarro (41) and Herring (42) argued that self-diffusion within the crystal will cause the solid to deform (i.e., creep) in an attempt to relieve the stresses. The creep is caused by atoms diffusing from interfaces subjected to a compressive stress (where they have a higher chemical potential) towards those subjected to a tensile stress (lower chemical potential). Extending this idea of creep to a polycrystalline solid, self-diffusion within the individual grains will cause atoms to diffuse from grain boundaries under compression towards those boundaries under tension (Fig. 8.25b). Creep by lattice diffusion is commonly referred to as *Nabarro-Herring creep*. An analysis of the atomic flux by Herring gave the following equation for the creep rate:

$$\dot{\epsilon}_c = \frac{40}{3} \frac{D_l \Omega p_a}{G^2 kT} \quad (8.78)$$

where D_l is the lattice diffusion coefficient, Ω is the atomic volume, p_a is the applied stress, G is the grain size, k is the Boltzmann constant, and T is the absolute temperature. The creep rate is, by definition, a linear strain rate equal to $(1/L) dL/dt$, where L is the length of the solid and t is the time.

Creep in a polycrystalline solid can also occur by diffusion along the grain boundaries (Fig. 8.25c), commonly referred to as *Coble creep*, and for this mechanism, the creep equation is (43)

$$\dot{\epsilon}_c = \frac{47.5 D_{gb} \delta_{gb} \Omega p_a}{G^3 kT} \quad (8.79)$$

where D_{gb} is the grain boundary diffusion coefficient and δ_{gb} is the grain boundary width. Equations (8.78) and (8.79) have the same linear dependence on p_a but differ in terms of the grain size dependence and the numerical constants.

The application of a high enough stress may, in some ceramics, activate matter transport by dislocation motion. For this mechanism, the creep rate is given by

$$\dot{\epsilon}_c = \frac{AD\mu b}{kT} \left(\frac{p_a}{\mu} \right)^n \quad (8.80)$$

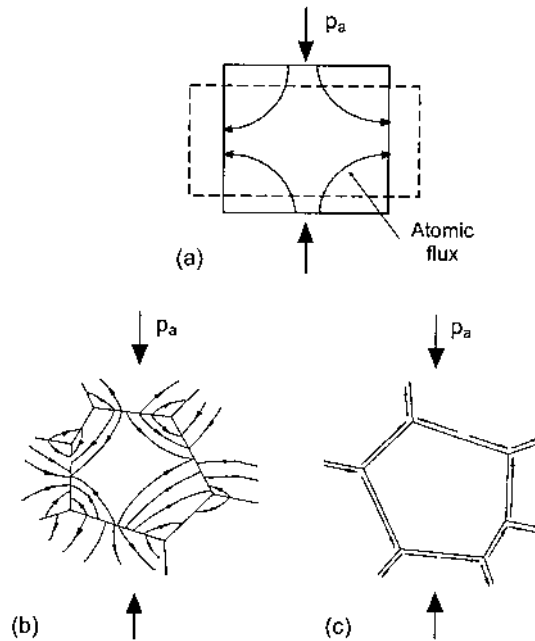


FIGURE 8.25 (a) A single crystal subjected to a uniaxial stress, showing the direction of the atomic flux. (b) and (c) A typical grain in a polycrystalline solid, showing the expected atomic flux by lattice diffusion (b) and by grain boundary diffusion (c).

where A is a numerical constant, D is a diffusion coefficient, μ is the shear modulus, and b is the Burgers vector. The exponent n depends on the mechanism of the dislocation motion and has values in the range 3–10.

8.10.1.3 Hot Pressing Equations

In the hot pressing of powders, the data are normally acquired in the form of density versus time from which the densification rate can be determined. Furthermore, considerable porosity is present over a large part of the process. The modification of the creep equations derived for dense solids therefore attempt to incorporate these two factors: (1) relating the creep rate (a linear strain rate) to the densification rate (a volumetric strain rate) and (2) compensating for the presence of porosity.

In hot pressing, the mass M of the powder and the cross sectional area A of the die, are constants. As the density D of the sample increases, the sample thickness L decreases. The variables D and L are related by

$$\frac{M}{A} = LD = L_0 D_0 = L_f D_f \quad (8.81)$$

where the subscripts 0 and f refer to the initial and final values. Differentiating this equation with respect to time gives

$$L \frac{dD}{dt} + D \frac{dL}{dt} = 0 \quad (8.82)$$

Rearranging this equation, we obtain

$$-\frac{1}{L} \frac{dL}{dt} = \frac{1}{D} \frac{dD}{dt} = \frac{1}{\rho} \frac{d\rho}{dt} \quad (8.83)$$

where ρ is the relative density. Equation (8.83) relates the linear strain rate of the body during hot pressing to its densification rate. As discussed in Chapter 12, the linear strain rate is commonly obtained by measuring the distance traveled by the punch of the hot pressing die as a function of time.

In compensating for the presence of porosity in the powder system, we recall from our discussion of Coble's initial stage hot pressing model that the effective stress on the grain boundaries p_e is related to the externally applied stress p_a by Eq. (8.75). To account for the effects of the applied stress and the surface curvature on the densification rate, Coble argued that the total driving force (DF) is a linear combination of the two effects; that is,

$$DF = p_e + \gamma_{sv} K = p_a \phi + \gamma_{sv} K \quad (8.84)$$

where K is the curvature of the pore, equal to $1/r$ for the intermediate stage sintering model and $2/r$ for the final stage model. To get the equation appropriate to hot pressing, DF given by Eq. (8.84) is substituted for the applied stress p_a in the creep equations for dense solids. The hot pressing equations obtained by the modification of the creep equations are summarized in Table 8.6.

TABLE 8.6 Hot Pressing Equations Obtained by Modification of the Creep Equations

Mechanism	Intermediate stage	Final stage
Lattice diffusion	$\frac{1}{\rho} \frac{d\rho}{dt} = \frac{40}{3} \left(\frac{D_l \Omega}{G^2 kT} \right) \left(p_a \phi + \frac{\gamma_{sv}}{r} \right)$	$\frac{1}{\rho} \frac{d\rho}{dt} = \frac{40}{3} \left(\frac{D_l \Omega}{G^2 kT} \right) \left(p_a \phi + \frac{2\gamma_{sv}}{r} \right)$
Grain boundary diffusion	$\frac{1}{\rho} \frac{d\rho}{dt} = \frac{95}{2} \left(\frac{D_{gb} \delta_{gb} \Omega}{G^3 kT} \right) \left(p_a \phi + \frac{\gamma_{sv}}{r} \right)$	$\frac{1}{\rho} \frac{d\rho}{dt} = \frac{15}{2} \left(\frac{D_{gb} \delta_{gb} \Omega}{G^3 kT} \right) \left(p_a \phi + \frac{2\gamma_{sv}}{r} \right)$
Dislocation motion ^a	$\frac{1}{\rho} \frac{d\rho}{dt} = A \left(\frac{D \mu b}{kT} \right) \left(\frac{p_a \phi}{\mu} \right)^n$	$\frac{1}{\rho} \frac{d\rho}{dt} = B \left(\frac{D \mu b}{kT} \right) \left(\frac{p_a \phi}{\mu} \right)^n$

^aA and B are numerical constants; n is an exponent that depends on the mechanism of dislocation motion.

Coble's modification of the creep equations can provide only an approximation to the densification rate during hot pressing. A more rigorous analysis would require additional modifications to the creep models to better represent the situation present in powder systems, such as differences in the atomic flux field and in the path length for diffusion. In the creep models, the atomic flux terminates at the boundaries under tension, whereas in hot pressing, the flux terminates at the pore surfaces. The grain boundary area, which is related to the grain size, remains constant during creep, but both the grain boundary area and the path length for diffusion increase during hot pressing.

8.10.2 Hot Pressing Mechanisms

The mechanisms discussed earlier for sintering also operate during hot pressing, but the nondensifying mechanisms can be neglected because they are not enhanced by the applied stress, whereas the densifying mechanisms are significantly enhanced. Because of this enhancement of the densifying mechanisms relative to the nondensifying mechanisms, hot pressing provides an effective technique for determining the mechanism of densification. However, new mechanisms can be activated by the applied stress and may provide complications, so their occurrence needs to be recognized.

Particle rearrangement contributes to the densification during the initial stage but it is difficult to analyze. Grain boundary sliding is necessary to accommodate the diffusion-controlled shape changes that occur during the intermediate and final stages. As shown in Fig. 8.26 for a cross section, a representative element of the system (e.g., three idealized grains with a hexagonal shape) must mimic the overall shape change of the powder compact. Since the diameter of the hot pressing die is fixed, powder compaction occurs predominantly in the direction of the applied pressure, so the grains will be flattened. This shape change must be accommodated by sliding of the grains over one another. Grain boundary sliding and diffusional mass transport are not independent mechanisms. They occur sequentially so that the slower mechanism controls the rate of densification. To summarize, the major mechanisms that commonly operate during hot pressing are lattice diffusion, grain boundary diffusion, plastic deformation by dislocation motion, viscous flow, rearrangement, and grain boundary sliding.

According to Table 8.6, when the applied stress is much greater than the driving force due to curvature (which corresponds to the common practical situation), the densification rate during hot pressing can be written

$$\frac{1}{\rho} \frac{d\rho}{dt} = \frac{HD\phi^n}{G^m kT} P_a^n \quad (8.85)$$

where H is a numerical constant, D is the diffusion coefficient of the rate-controlling species, ϕ is the stress intensification factor, G is the grain size, k is the

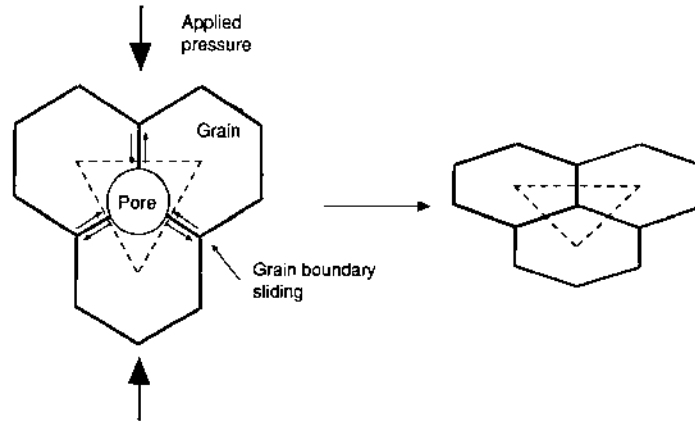


FIGURE 8.26 Sketch illustrating the change in grain shape that occurs during hot pressing. The grains are flattened in the direction of the applied pressure. When matter transport occurs by diffusion, grain boundary sliding is necessary to accommodate the change in grain shape.

Boltzmann constant, T is the absolute temperature, and the exponents m and n depend on the mechanism of densification. Table 8.7 gives the values of m and n , as well as the appropriate diffusion coefficient for the various mechanisms.

Because the densifying mechanisms are enhanced and grain growth is limited, hot pressing provides an effective technique for investigating the mechanism of densification. According to Eq. (8.85) and Table 8.7, a plot of the densification

TABLE 8.7 Hot Pressing Mechanisms and the Associated Exponents and Diffusion Coefficients

Mechanism	Grain size exponent, m	Stress exponent, n	Diffusion coefficient ^a
Lattice diffusion	2	1	D_l
Grain boundary diffusion	3	1	D_{gb}
Plastic deformation	0	≥ 3	D_l
Viscous flow	0	1	—
Grain boundary sliding	1	1 or 2	D_l or D_{gb}
Particle rearrangement			

^a D_l = lattice diffusion coefficient; D_{gb} = grain boundary diffusion coefficient.

rate (at a fixed density) versus p_a allows the exponent n and thus the mechanism of densification to be determined. For the commonly used hot pressing pressures (typically 10–50 MPa), data for many ceramics give $n \approx 1$, suggesting that a diffusion mechanism is responsible for densification (44,45). This finding is not surprising in view of the strong bonding in ceramics (which limit dislocation motion) and the tendency for the use of fine powders (which favor diffusion mechanisms). However, higher values of n characteristic of dislocation mechanisms are observed for a few ceramics (46).

The dominant densification mechanism may change depending on the applied pressure, temperature, and grain size. For example, because of the larger grain size exponent ($m = 3$) and the generally lower activation energy, finer powders and lower temperatures favor grain boundary diffusion over lattice diffusion ($m = 2$). By careful selection of the process variables, the dominant mechanism under a given set of conditions can be identified and the results are commonly displayed in the form of a map, referred to as a *hot pressing map* or a *deformation mechanism map*, analogous to a sintering map discussed earlier. Figure 8.27 shows a hot pressing map for α - Al_2O_3 , plotted in the form of temperature versus grain size, showing the relationships between the mechanisms and hot pressing parameters (44).

8.11 THE STRESS INTENSIFICATION FACTOR

In the hot pressing models, we found that the factor ϕ defined by Eq. (8.75) arose every time we needed to relate the mean stress on the grain boundary

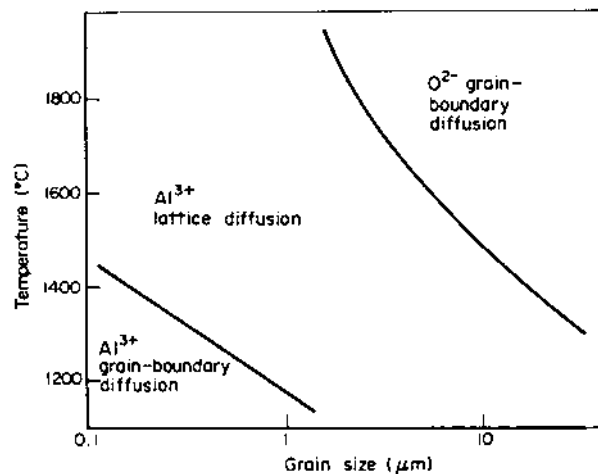


FIGURE 8.27 Hot pressing (deformation) map for pure α -alumina. (From Ref. 44.)

p_e to the externally applied stress, p_a . The factor ϕ is referred to as the *stress intensification factor* (or the stress multiplication factor). It should not be confused with a nearly similar term, the stress intensity factor, which has a different meaning in fracture mechanics. The significance of ϕ is such that while p_a is the stress that is measured, p_e is its counterpart that influences the rate of matter transport. The factor ϕ is geometrical in origin and would be expected to depend on the porosity and the shape of the pores.

Consider a hydrostatic pressure p_a applied to the external surface of a powder system, a model of which is shown schematically in Fig. 8.28a. The applied pressure exerts on the surface of the solid an applied load $F_a = A_T p_a$, where A_T is the total external cross-sectional area of the solid, including such areas as may be occupied by pores. The presence of porosity located at the grain boundaries makes the actual grain boundary area A_e lower than the total external area. Assuming a force balance across any plane of the solid, we obtain

$$p_a A_T = p_e A_e \quad (8.86)$$

Therefore,

$$\phi = \frac{p_e}{p_a} = \frac{A_T}{A_e} \quad (8.87)$$

For spherical pores randomly distributed in a porous solid, ϕ can be easily found. Taking a random plane through the solid, the area fraction of porosity in the plane is equal to the volume fraction of porosity. If A_T is assumed to be unity,

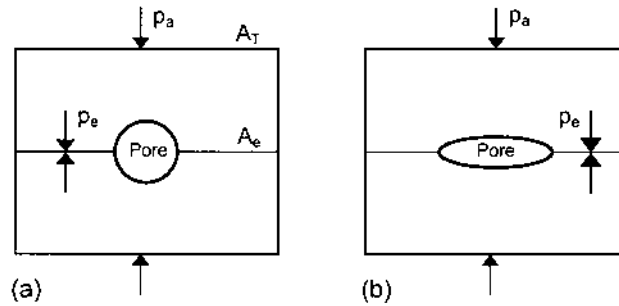


FIGURE 8.28 (a) The effective stress on the grain boundary p_e is greater than the externally applied stress p_a due to the presence of pores on the grain boundary. The stress intensification factor ϕ is defined as the ratio of the total external area to the actual grain boundary area. (b) ϕ depends on the porosity as well as the pore shape, having a stronger dependence on porosity for pores with smaller dihedral angles, e.g., elliptical pores.

then A_e is equal to $1 - P$, where P is the porosity of the solid. Since $(1 - P)$ is also equal to the relative density, we can write

$$\phi = \frac{1}{\rho} \quad (8.88)$$

This expression would be applicable to a glass containing isolated, nearly spherical pores or to a polycrystalline solid in which the equilibrium shapes of the isolated pores are roughly spherical (i.e., for dihedral angles greater than $\sim 150^\circ$). When the pores deviate significantly from a spherical shape, this simple expression will no longer hold and in fact, ϕ may be expected to be quite complex. As illustrated in Fig. 8.28 for pores with the same volume but different shapes, we may expect ϕ to depend not only on the porosity but also on the shape of the pores. As the pore shape deviates from a spherical geometry (i.e., as the dihedral angle decreases), the actual area of the grain boundary decreases, so ϕ would therefore be expected to increase.

Computer simulation of the equilibrium shapes of a continuous network of pores has been performed by Beeré (20). An analysis of Beeré's results by Vieira and Brook (46) showed that ϕ can be approximated by the expression

$$\phi = \exp(\alpha P) \quad (8.89)$$

where α is a factor that depends on the dihedral angle and P is the porosity. A semilogarithmic plot of Beeré's results is shown in Fig. 8.29 for several dihedral angles from which the factor α can be determined. Equation (8.89) has been verified by recent experimental data (see Section 8.13), but this does not imply that it is the most accurate or appropriate model. As summarized in Table 8.8, other expressions have been proposed for ϕ , and depending on the powder characteristics and packing, one may be appropriate to fit the data (47–49). A plot of ϕ versus ρ for several expressions (Fig. 8.30) shows large differences between the values (50). Except for the model based on monosize spheres, all of the results can be represented by an exponential function of the form given by Eq. (8.89).

8.12 THE SINTERING STRESS

According to Table 8.6, the densification rate for the diffusion-controlled mechanisms may be written in the general form

$$\frac{1}{\rho} \frac{d\rho}{dt} = -\frac{3}{L} \frac{dL}{dt} = \frac{3}{\eta_p} (p_a \phi + \sigma) \quad (8.90)$$

where $(1/L) dL/dt$ is the linear strain rate of the sintering solid, η_p has the dimensions of a viscosity and can be called the densification viscosity, and σ is the

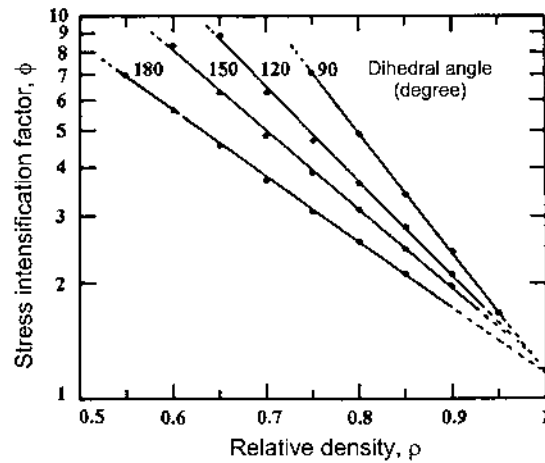


FIGURE 8.29 Stress intensification factor represented by an exponential function of the porosity. (From Ref. 46.)

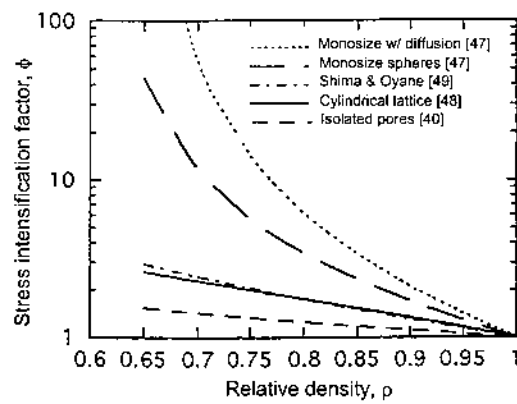


FIGURE 8.30 Stress intensification factor versus relative density for various idealized powder geometries and for the data of Shima and Oyane (49). (From Ref. 50.)

TABLE 8.8 Stress Intensification Factors for Various Powder Geometries

Stress intensification factor, ϕ	Model	Ref.
$(1 - \rho_0)/\rho^2 (\rho - \rho_0) \quad \rho < 0.90$	Monosize spherical powder	47
$(1 - \rho_0)^2/\rho (\rho - \rho_0)^2 \quad \rho < 0.90$	Monosize spherical powder, including neck growth due to diffusion	47
$1/\rho \quad \rho > 0.90$	Random distribution of isolated pores	39, 40
$\exp [\alpha(1 - \rho)] \quad \rho < 0.90$	Free energy minimization for equilibrium shapes of continuous pores	20, 46
$(3 - 2\rho/\rho) \quad \rho < 0.95$	Cubic array of intersecting cylindrical particles	21, 48
$1/\rho^{5/2} \quad \rho < 1.00$	Empirical equation developed to fit sintering data of spherical Cu particles	49

effective stress on the atoms under the pore surface given by the equation of Young and Laplace:

$$\sigma = \gamma_{sv} \left(\frac{1}{r_1} + \frac{1}{r_2} \right) \quad (8.91)$$

where r_1 and r_2 are the two principal radii of curvature of the pore surface. The quantity σ is the thermodynamic driving force for sintering. It has the units of a pressure (or stress) and is sometimes referred to as the *sintering pressure* or the *sintering potential*. The equation for σ is actually more complex for a polycrystalline ceramic where the pores are in contact with the grain boundaries and consists of two contributions, one attributed to the pores and the other attributed to the grain boundaries (51). For example, for an idealized final stage microstructure where the pores and grains are assumed to have a spherical shape, σ is given by (52)

$$\sigma = \frac{2\gamma_{gb}}{G} + \frac{2\gamma_{sv}}{r} \quad (8.92)$$

where γ_{gb} is the specific energy of the grain boundary, G is the grain size, and r is the pore radius. The driving force for sintering is also influenced by the dihedral angle and the mass transport mechanism, and has been calculated for a simple geometry consisting of a line of spherical particles (53).

Equation (8.90) can also be written

$$\frac{1}{\rho} \frac{d\rho}{dt} = \frac{3\phi}{\eta_p} (p_a + \Sigma) \quad (8.93)$$

where $\Sigma = \sigma/\phi$ has the units of stress and is referred to as the *sintering stress*. Because Σ occurs in a linear combination with the externally applied stress p_a , it can be taken to represent the *equivalent externally applied stress* that has the same effect on sintering as the curved surfaces of the pores and grain boundaries. The formulation of the driving force for sintering in terms of a fictitious externally applied stress is advantageous in the analysis of sintering where mechanical stress effects arise, such as in pressure sintering and constrained sintering. It also provides a conceptual basis for designing experiments to measure the driving force for sintering.

8.13 MEASUREMENT OF THE SINTERING STRESS AND STRESS INTENSIFICATION FACTOR

8.13.1 Zero-Creep Technique

A relatively straightforward technique for measuring the sintering stress is similar to the zero-creep technique suggested by Gibbs (54) for the determination of surface energies. The powder formed into the shape of a wire or a tape is clamped at one end and a load is suspended from the other end. The creep of the sample is monitored, and the load required to produce zero creep is determined. The sintering stress is taken as the applied stress at the zero-creep condition because the creep may be assumed to stop when the applied stress just balances the sintering stress. Gregg and Rhines (55) used this technique for copper powder in the form of a wire and found that the sintering stress increased with relative density up to a value of ~ 0.95 after which it decreased (Fig. 8.31). The increase in the sintering stress with density can be attributed to a decrease in the pore size, and it is likely that significant coarsening of the microstructure (grain growth and pore growth) caused the observed decrease at values of the relative density above ~ 0.95 (56). Gregg and Rhines also found that the sintering stress at a given density of the system scaled inversely as the initial particle size of the powder, which is consistent with Eq. (8.92) if the average pore size is assumed to be proportional to the average particle size.

8.13.2 Sintering Under a Uniaxial Load

The technique of loading dilatometry, in which a small, controlled uniaxial stress p_z is applied to a powder compact during sintering has been used to investigate the simultaneous occurrence of densification and creep, as well as their interaction (57,58). Parameters such as the stress intensity factor ϕ and the sintering stress Σ can be determined from the data. In the experiments, simultaneous measurement of the time-dependent axial and radial strains allows the determination of the

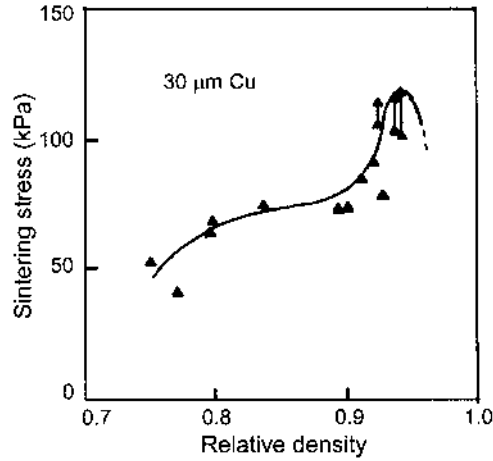


FIGURE 8.31 Data of Gregg and Rhines (55) for the sintering stress versus relative density for 30 μm copper particles, determined by the zero-creep technique.

densification (volumetric) strain rate $\dot{\epsilon}_p$ and the creep strain rate $\dot{\epsilon}_c$ using the following relations:

$$\dot{\epsilon}_c = \frac{2}{3}(\dot{\epsilon}_z - \dot{\epsilon}_r) \quad (8.94)$$

$$\dot{\epsilon}_p = \frac{1}{3\rho} \frac{d\rho}{dt} = -\frac{1}{3}(\dot{\epsilon}_z + 2\dot{\epsilon}_r) \quad (8.95)$$

where $\dot{\epsilon}_z$ and $\dot{\epsilon}_r$ are the measured axial and radial strain rates. In the loading dilatometer experiments, the hydrostatic component of the applied uniaxial stress (equal to $p_z/3$) is small compared to Σ , so the sintering mechanism of the loaded powder compact is expected to be identical to that for a freely sintered compact. Furthermore, the hydrostatic component of the applied uniaxial stress can be neglected, and under these conditions, Eq. (8.93) can be written

$$\dot{\epsilon}_p = \frac{1}{\eta_p} \Sigma \phi \quad (8.96)$$

Similarly, the creep rate can be expressed as

$$\dot{\epsilon}_c = \frac{1}{\eta_c} p_z \phi \quad (8.97)$$

where η_c can be described as the creep viscosity. The ratio of the densification rate to the creep rate can be found from Eqs. (8.96) and (8.97) as

$$\frac{\dot{\epsilon}_p}{\dot{\epsilon}_c} = \frac{F\Sigma}{p_z} \quad (8.98)$$

where F is a parameter equal to η_c/η_p . As shown in Fig. 8.32, measurement of the simultaneous densification and creep rates at a fixed value of p_z indicates that the ratio $\dot{\epsilon}_p/\dot{\epsilon}_c$ is fairly constant over a wide density range for several materials (59). The ratio is also found to be fairly constant over a wide temperature range, but for a given system, it decreases with the green density (60)

Making the assumption that $F \approx 1$, which is equivalent to assuming that the atomic flux fields in sintering and creep of porous ceramics at low stress are not significantly different, the value of Σ can be determined from the measured values of $\dot{\epsilon}_p/\dot{\epsilon}_c$ and p_z . The sintering stress determined in this way is shown in Fig. 8.33 for CdO. It is of the order of 1–2 MPa and, for a given green density, appears to be relatively constant over a large part of the densification process. Based on the sintering model of Coble (40), it might be expected that Σ would increase with density after the initial stage of sintering. The observed decrease may have its origins in processes such as coarsening and differential densification that are not taken into account in the models. For glass particles in which grain

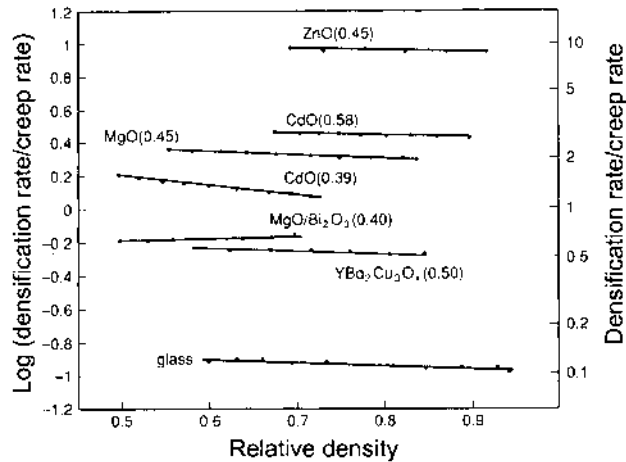


FIGURE 8.32 Ratio of the densification rate to the creep rate versus relative density at a constant uniaxial applied stress of 200 kPa. The numbers in parenthesis represent the relative green density. (From Ref. 59.)

boundaries are absent, Σ is observed to increase with density, in agreement with theoretical predictions (61).

According to Eq. (8.97), a plot of the creep rate determined at a constant value of p_z and η_c (i.e., constant grain size) versus the relative density ρ gives the functional dependence of the stress intensity factor ϕ on ρ . Data for the creep rates of some porous compacts measured in the loading dilatometry experiments (58,62) yield values for ϕ that can be well fitted by Eq. (8.89). An example of such data is shown in Fig. 8.34.

In experiments when the applied uniaxial stress is not insignificant compared with the sintering stress (63), Eq. (8.93) must be used for the densification rate, and p_a represents the hydrostatic component of the applied uniaxial stress, equal to $p_z/3$. A plot of the densification rate at a given density versus the hydrostatic component of the applied stress yields Σ by extrapolation to zero densification rate.

8.14 ALTERNATIVE DERIVATION OF THE SINTERING EQUATIONS

The sintering equations can be derived in an alternative manner to the earlier derivations for the analytical models by solving the differential equations for the atomic flux subject to the appropriate boundary conditions. The method is outlined for grain boundary diffusion, and the sintering stress concept is incorporated into the derivation (64).

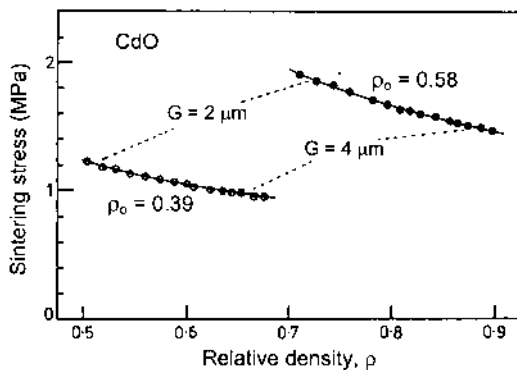


FIGURE 8.33 The sintering stress for CdO powder determined by the technique of loading dilatometry. (From Ref. 58.)

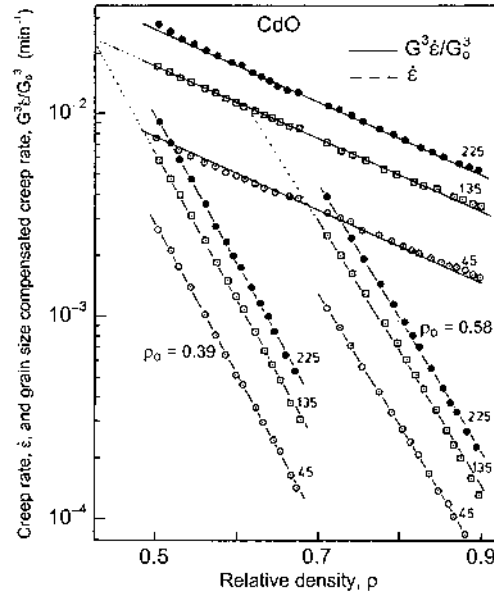


FIGURE 8.34 Dependence of the creep rate and the grain size compensated creep rate on relative density for CdO powder compacts with initial densities of 0.39 and 0.58, subjected to the uniaxial stresses shown in kPa. (From Ref. 58.)

8.14.1 Grain Boundary Diffusion

To simplify the derivation, we consider a geometrical model consisting of spherical particles with a diameter a arranged in a simple cubic pattern (Fig. 8.35a). It is assumed that the grain boundary remains flat, with a constant width δ_{gb} (Fig. 8.35b). Following Eq. (7.91), the flux of atoms as a function of distance along the neck is

$$j(x) = -\frac{D_{gb}}{\Omega kT} \nabla \mu \quad (8.99)$$

where D_{gb} is the grain boundary diffusion coefficient, Ω is the atomic volume, k is the Boltzmann constant, T is the absolute temperature, and μ is the chemical potential of the atoms. The total number of atoms crossing the neck at a radius x per unit time is

$$J(x) = 2\pi x \delta_{gb} j(x) = -\frac{2\pi x D_{gb} \delta_{gb}}{\Omega kT} \nabla \mu \quad (8.100)$$

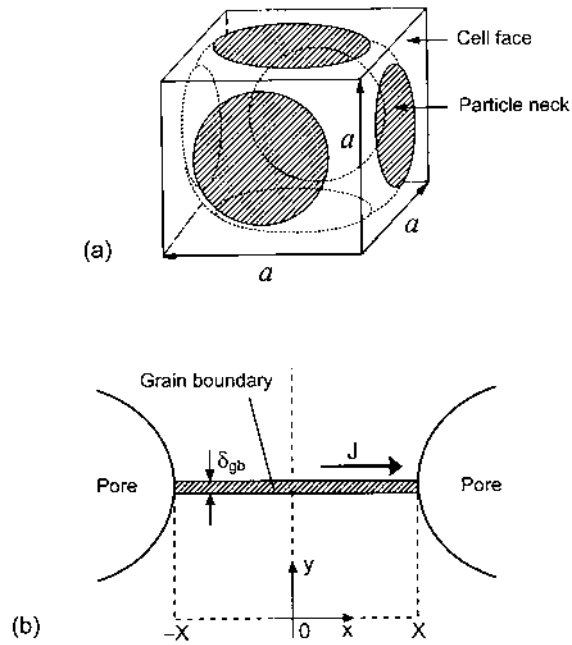


FIGURE 8.35 (a) Schematic of cell surrounding a spherical particle showing the neck (grain boundary) section with an adjoining particle. (b) Geometrical parameters for matter transport by grain boundary diffusion.

Since the displacement of the boundary must be independent of x , the rate of approach of the particle centers, dy/dt , is related to $J(x)$ by

$$J(x) = \frac{\pi x^2}{\Omega} \frac{dy}{dt} \quad (8.101)$$

From Eqs. (8.100) and (8.101), we obtain

$$\frac{d\mu}{dx} = -2Ax \quad (8.102)$$

where

$$A = \frac{kT}{4D_{gb}\delta_{gb}} \frac{dy}{dt} \quad (8.103)$$

Integrating Eq. (8.102) gives

$$\mu(x) = -Ax^2 + B \quad (8.104)$$

where B is a constant. The chemical potential μ is related to the normal stress on the boundary σ by $\mu = \sigma\Omega$, so Eq. (8.104) can be written

$$\sigma(x) = \frac{-Ax^2 + B}{\Omega} \quad (8.105)$$

where the constants A and B can be found from the boundary conditions. The first boundary condition is that the stresses must balance at $x = X$ and at $x = -X$. We will recall that according to the definition of the sintering stress, the effects of the pores and grain boundaries were artificially set at zero and replaced by an equivalent external stress equal to Σ . In this representation, the stress acting at the surface of the pore must be equal to zero. Therefore our second boundary condition is $\sigma = 0$ at $x = \pm X$, and substituting either of these into Eq. (8.105) gives

$$B = AX^2 \quad (8.106)$$

The second boundary condition is that the average stress on the grain boundary is equal to $\phi\Sigma$, where ϕ is the stress intensification factor. This condition can be expressed as

$$\frac{1}{\pi X^2} \int_0^{2\pi} \int_0^X \sigma(x) x \, dx \, d\theta = \phi\Sigma \quad (8.107)$$

Substituting for $\sigma(x)$ and integrating gives

$$-\frac{AX^2}{2} + B = \Omega\phi\Sigma \quad (8.108)$$

and using Eq. (8.106) we obtain

$$A = \frac{2\Omega\phi\Sigma}{X^2} \quad B = 2\Omega\phi\Sigma \quad (8.109)$$

Using Eq. (8.100), the total flux at the surface of the neck between two particles is given by

$$J(X) = \frac{8\pi D_{gb} \delta_{gb} \phi\Sigma}{kT} \quad (8.110)$$

To relate $J(X)$ to the shrinkage of the system, the total volume transported out of one neck in a time Δt is given by

$$\Delta V = -J(X)\Omega\Delta t = \pi X^2 \Delta a \quad (8.111)$$

where Δa is the corresponding change in the center-to-center distance between the particles. The total volumetric shrinkage in all three orthogonal directions is

$$\frac{\Delta V}{V} = \frac{3\Delta a}{a} \quad (8.112)$$

and since $V = a^3$, the rate of change of the cell volume is

$$\frac{dV}{dt} = \frac{\Delta V}{\Delta t} = 3a^2 \left(\frac{\Delta a}{\Delta t} \right) \quad (8.113)$$

Substituting for $\Delta a/\Delta t$ from Eq. (8.111), we have

$$\frac{dV}{dt} = -3a^2 \frac{J(X)\Omega}{\pi X^2} \quad (8.114)$$

By definition, $\phi = a^2/(\pi X^2)$, so the instantaneous volumetric strain rate is given by

$$\frac{1}{V} \frac{dV}{dt} = -\frac{3J(X)\Omega\phi}{a^3} \quad (8.115)$$

The linear densification strain rate $\dot{\epsilon}_p$ is equal to $(-1/3V) dV/dt$, and substituting for $J(X)$ from Eq. (8.110), we obtain

$$\dot{\epsilon}_p = \frac{8\pi D_{gb} \delta_{gb} \Omega}{a^3 kT} \phi^2 \Sigma \quad (8.116)$$

8.14.2 Lattice Diffusion

The derivation of the sintering equation for lattice diffusion follows a procedure similar to that described above for grain boundary diffusion. The linear densification strain rate can also be obtained from Eq. (8.116) by replacing $\pi D_{gb} \delta_{gb}$ with $2XD_l$, where D_l is the lattice diffusion coefficient (65). Remembering that $\phi = a^2/(\pi X^2)$, these substitutions give

$$\dot{\epsilon}_p = \frac{16D_l \Omega}{\pi^{1/2} a^2 kT} \phi^{3/2} \Sigma \quad (8.117)$$

8.14.3 General Isothermal Sintering Equation

For matter transport by diffusion, a general equation for the linear densification strain rate may be written as

$$\dot{\epsilon}_p = \frac{H_1 D \Omega \phi^{(m+1)/2}}{G^m k T} (\Sigma + p_h) \quad (8.118)$$

where H_1 is a numerical constant that depends on the geometry of the model, p_h is the hydrostatic component of an externally applied stress, G is the particle (or grain) size, k is the Boltzmann constant, T is the absolute temperature, Ω is the atomic volume, and

$$\begin{aligned} D &= D_{gb} \delta_{gb} & m &= 3 & \text{for grain boundary diffusion} \\ D &= D_l & m &= 2 & \text{for lattice diffusion} \end{aligned}$$

Compared with Coble's hot pressing equations (Table 8.5), Eq. (8.118) has the same dependence on the material and physical parameters except for the value of the exponent for ϕ . The difference in the exponents arises because Coble assumed that $X = G$, whereas the present derivation related X to G , through ϕ .

8.14.4 General Isothermal Creep Equation for Porous Solids

The procedure used in the derivation of Eq. (8.116) can also be used to analyze diffusional creep of porous solids under an applied uniaxial stress p_z . In this case, the mean stress on the grain boundary is ϕp_z , and the general creep equation has the form

$$\dot{\epsilon}_c = \frac{H_2 D \Omega \phi^{(m)+1/2}}{G^m k T} p_z \quad (8.119)$$

where H_2 is a numerical constant and the other parameters are the same as those defined by Eq. (8.118).

8.15 CONCLUDING REMARKS

In this chapter, we considered the main theoretical approaches for describing solid-state sintering and viscous sintering. The models for the densification of glasses by viscous flow assume Frenkel's energy balance concept in the derivation of the sintering rate equations. The predictions of the models give good agreement with the data for real powder compacts of glass particles and for other porous amorphous systems. The sintering phenomena in polycrystalline ceramics are considerably more complex. Matter transport can occur by at least six different

paths that define the mechanisms of sintering and a distinction is often made between the densifying mechanisms and the nondensifying mechanisms. Analytical models yield explicit expressions for the dependence of the sintering rate on the primary variables, such as particle size, temperature, and applied pressure, but in view of the drastic simplification used in their development, the models provide only a qualitative description of sintering. Numerical simulations can provide significant benefits for analyzing the complexities of sintering, and the approach is expected to see more use in the future. The stress intensification factor and the sintering stress are fundamental parameters in the understanding of sintering. The physical meaning of these parameters and methods for their measurement were discussed. The analysis of the sintering rate is, by itself, not very useful. We must also understand how the microstructure of the powder system evolves during sintering. The results of the present chapter must therefore be combined with those of the next chapter in order to develop a clearer understanding of solid-state sintering.

PROBLEMS

- 8.1 The dihedral angles for two oxides are 150° and 90° . If the oxides have the same surface energy, which would you expect to densify more readily? Explain why.
- 8.2 Show that in Eq. (8.9) relating the scaling laws, $m = 4$ for grain boundary diffusion and $m = 2$ for vapor transport.
- 8.3 Sintering is a continuous process but in the models, the process is divided into stages. Explain why. For the idealized solid state sintering theory, make a table of the three stages of sintering and for each stage give the approximate density range of applicability and the mechanisms of sintering, indicating which mechanisms lead to densification and which do not.
- 8.4 For the two-sphere sintering model, derive the equations given in Fig. 8.10 for the neck radius X , the surface area of the neck A , and the volume of material transported into the neck V .
- 8.5 For the two-sphere model, derive the equations given in Table 8.5 for sintering by
 - a. Lattice diffusion from the grain boundary
 - b. Vapor transport
 - c. Surface diffusion
- 8.6 The lattice diffusion coefficient for Al^{3+} ions in Al_2O_3 is $4.0 \times 10^{-14} \text{ cm}^2/\text{sec}$ at 1400°C and the activation energy is 580 kJ/mol . Assuming that sintering is controlled by lattice diffusion of Al^{3+} ions, estimate the initial rate of sintering for an Al_2O_3 powder compact of $1 \text{ }\mu\text{m}$ particles at 1300°C .
- 8.7 Consider a pore with constant volume. Assuming that the pore takes on the shape of an ellipsoid of revolution, calculate the surface area of the pore as a function of the ratio of the short axis to the long axis.
- 8.8 Derive Eq. (8.51) for the volume of the solid phase in a unit cell of Scherer's model for viscous sintering.

- 8.9 Consider the sintering of a spherical pore in an infinite viscous matrix. Derive an expression for the radius of the pore as a function of the sintering time. For a borosilicate glass, the viscosity at 800°C is measured to be 10^9 Pas. Assuming that the surface energy of the glass is ~ 0.35 J/m², estimate the time it will take for an isolated pore of diameter 10 μm to be removed from a large block of the glass by sintering at 800°C.
- 8.10 A ZnO powder compact is formed from particles with an average size of 3 μm . Assuming that densification occurs by a lattice diffusion mechanism with an activation energy of 250 kJ/mol, estimate the factor by which the densification rate will change if
- The particle size is reduced to 0.3 μm .
 - The compact is hot pressed under an applied pressure of 40 MPa.
 - The sintering temperature is raised from 1000 to 1200°C.
- The specific surface energy of ZnO can be assumed to be 1 J/m².
- 8.11 Zinc oxide has a fairly high vapor pressure for commonly-used sintering temperatures above half the melting point, so that coarsening due to vapor transport can reduce the densification rate. Discuss how the changes in the particle size, applied pressure, and temperature described in Problem 8.10 will influence the rate of vapor transport.
- 8.12 For MgO-doped Al₂O₃, the average dihedral angle is found to be approximately 120°. Assuming that the stress intensification factor ϕ is given by Eq. (8.89), determine the value of the parameter α in Eq. (8.89) using the values for ϕ given in Fig. 8.29.
- 8.13 Explain the meaning of the term *sintering stress*. Briefly describe the methods that can be used to measure the sintering stress, indicating the principles on which each method is based, and the advantages and disadvantages of each method.

REFERENCES

1. Frenkel, J. J. Phys. (Moscow). 1945, Vol. 5, 385.
2. Uhlmann, D. R.; Klein, L. C.; Hopper, R. W. In The Moon; Reidel, D. ed.; : Dordrecht, Holland, 1975, pp. 277–284.
3. Johnson, D. L. J. Appl. Phys. 1969, Vol. 40, 192.
4. Shaler, A. J. Metals Trans. 1949, Vol. 185, 796.
5. Herring, C. J. Appl. Phys. 1950, Vol. 21, 301.
6. Rhines, F. N.; DeHoff, R. T. Mater. Sci. Res. 1984, Vol. 16, 49.
7. Kuczynski, G. C. Z. Metallkunde. 1976, Vol. 67, 606.
8. Song, H.; Coble, R. L.; Brook, R. J. Mater. Sci. Res. 1984, Vol. 16, 63.
9. Johnson, K. L.; Kendall, K.; Roberts, A. D. Proc. Roy. Soc. A. 1971, Vol. 324, 301.
10. Coble, R. L. J. Appl. Phys. 1961, Vol. 32, 787; 1961, Vol. 32, 793.
11. Kuczynski, G. C. Trans. AIME. 1949, Vol. 185, 169.
12. Kingery, W. D.; Berg, M. J. Appl. Phys. 1955, Vol. 26, 1206.
13. Coble, R. L. J. Am. Ceram. Soc. 1958, Vol. 41, 55.
14. Johnson, D. L.; Cutler, I. B. J. Am. Ceram. Soc. 1963, Vol. 46, 541.

15. Coblenz, W. S.; Dynys, J. M.; Cannon, R. M.; Coble, R. L. *Mater. Sci. Res.* 1980, Vol. 13, 141.
16. Kuczynski, G. C. *J. Appl. Phys.* 1949, Vol. 20, 1160.
17. Coble, R. L. *J. Am. Ceram. Soc.* 1973, Vol. 56, 461.
18. Swinkels, F. B.; Ashby, M. F. *Powder Metall.* 1980, Vol. 23, 1.
19. Johnson, D. L. *J. Am. Ceram. Soc.* 1970, Vol. 53, 574.
20. Beeré, W. *Acta Metall.* 1979, Vol. 23, 131; 1979, Vol. 23, 139.
21. Scherer, G. W. *J. Am. Ceram. Soc.* 1977, Vol. 60, 236; 1977, Vol. 60, 243; 1984, Vol. 67, 709.
22. Brinker, C. J.; Scherer, G. W. *Sol-Gel Science*; Academic: New York, 1990, Chap. 11.
23. Scherer, G. W.; Bachman, D. L. *J. Am. Ceram. Soc.* 1977, Vol. 60, 239.
24. Coleman, S.; Beeré, W. *Phil. Mag.* 1975, Vol. 31, 1403.
25. Mackenzie, J. K.; Shuttleworth, R. *Proc. Phys. Soc. (London)*. 1949, Vol. 62, 833.
26. Nicholls, F. A.; Mullins, W. W. *J. Appl. Phys.* 1965, Vol. 36, 1826.
27. Bross, P.; Exner, H. E. *Acta metall.* 1979, Vol. 27, 1013.
28. Johnson, D. L. *J. Appl. Phys.* 1969, Vol. 40, 192.
29. Svoboda, J.; Riedel, H. *Acta Metall. Mater.* 1995, Vol. 43, 1.
30. Ross, J. W.; Miller, W. A.; Weatherly, C. J. *J. Appl. Phys.* 1981, Vol. 52, 3884.
31. Jagota, A.; Dawson, P. R. *Acta Metall.* 1988, Vol. 36, 2551; *J. Am. Ceram. Soc.* 1990, Vol. 73, 173.
32. Martínez-Herrera, J. I.; Derby, J. J. *J. Am. Ceram. Soc.* 1995, Vol. 78, 645.
33. Jagota, A. *J. Am. Ceram. Soc.* 1994, Vol. 77, 2357.
34. Tikkanen, M. H.; Mäkipirtti, S. A. *Int. J. Powder Metall.* 1965, Vol. 1, 15.
35. Ivensen, V. A. *Densification of Metal Powders During Sintering*; Consultants Bureau: New York, 1973.
36. Pejovnik, S.; Smolej, V.; Susnik, D.; Kolar, D. *Powder Metall. Int.* 1979, Vol. 11, 22.
37. Ashby, M. F. *Acta Metall.* 1974, Vol. 22, 275.
38. Swinkels, F. B.; Ashby, M. F. *Acta Metall.* 1981, Vol. 29, 259.
39. Coble, R. L. In *Sintering and Related Phenomena*; Kuczynski, G. C., Hooton, N. A., Gibbon, C. F. eds.; Gordon and Breach: New York, 1967, pp. 329–347.
40. Coble, R. L. *J. Appl. Phys.* 1970, Vol. 41, 4798.
41. Nabarro, F. R. N. In *Report of a Conference on the Strength of Solids*; Physical Society: London, 1948, p. 75.
42. Herring, C. *J. Appl. Phys.* 1950, Vol. 21, 437.
43. Coble, R. L. *J. Appl. Phys.* 1963, Vol. 34, 1679.
44. Harmer, M. P.; Brook, R. J. *J. Mater. Sci.* 1980, Vol. 15, 3017.
45. Beeré, W. *J. Mater. Sci.* 1975, Vol. 10, 1434.
46. Vieira, J. M.; Brook, R. J. *J. Am. Ceram. Soc.* 1984, Vol. 67, 245.
47. Helle, A. S.; Easterling, K. E.; Ashby, M. F. *Acta Metall.* 1985, Vol. 33, 2163.
48. Scherer, G. W. *J. Non-Cryst. Solids.* 1979, Vol. 34, 239.
49. Shima, S.; Oyane, M. *Int. J. Mech. Sci.* 1976, Vol. 18, 285.
50. Dutton, R. E.; Shamasundar, S.; Semiatin, S. L. *Metall. Mater. Trans. A* 1995, Vol. 26, 2041.

51. De Jonghe, L. C.; Rahaman, M. N. *Acta Metall.* 1988, Vol. 36, 223.
52. Raj, R. J. *Am. Ceram. Soc.* 1987, Vol. 70, C-210.
53. Cannon, R. M.; Carter, W. C. J. *Am. Ceram. Soc.* 1989, Vol. 72, 1550.
54. Gibbs, J. W. In *The Scientific Papers of J. Willard Gibbs*; Dover Press: New York, 1961.
55. Gregg, R. A.; Rhines, F. N. *Metall. Trans.* 1973, Vol. 4, 1365.
56. Aigeltinger, A. *Int. J. Powder Metall. Powder Technol.* 1975, Vol. 11, 195.
57. De Jonghe, L. C.; Rahaman, M. N. *Rev. Sci. Instrum.* 1984, Vol. 55, 2007.
58. Rahaman, M. N.; De Jonghe, L. C.; Brook, R. J. J. *Am. Ceram. Soc.* 1986, Vol. 69, 53.
59. Chu, M.-Y.; De Jonghe, L. C.; Rahaman, M. N. *Acta Metall.* 1989, Vol. 37, 1415.
60. Rahaman, M. N.; De Jonghe, L. C.; Chu, M.-Y. J. *Am. Ceram. Soc.* 1991, Vol. 74, 514.
61. Rahaman, M. N.; De Jonghe, L. C. J. *Am. Ceram. Soc.* 1990, Vol. 73, 707.
62. Rahaman, M. N.; De Jonghe, L. C. J. *Mater. Sci.* 1987, Vol. 22, 4326.
63. Venkatachari, K. R.; Raj, R. J. *Am. Ceram. Soc.* 1986, Vol. 69, 499.
64. Chu, M.-Y.; Rahaman, M. N.; De Jonghe, L. C.; Brook, R. J. J. *Am. Ceram. Soc.* 1991, Vol. 74, 1217.
65. Raj, R.; Ashby, M. F. *Acta Metall.* 1975, Vol. 23, 653.
66. Exner, H. E. *Reviews on Powder Metallurgy and Physical Ceramics*; 1979, Vol. 1, pp. 1–251.

9

Grain Growth and Microstructure Control

9.1 INTRODUCTION

The engineering properties of ceramics, as outlined in Chapter 1, are strongly dependent on the microstructure, the important features of which are the size and shape of the grains, the amount of porosity, the pore size, the distribution of the pores in the body, and the nature and distribution of any second phases. For most applications, microstructural control usually means the achievement of as high a density, as small a grain size, and as homogeneous a microstructure as possible. We recall that the microstructure of the fabricated article is influenced to a significant extent by the structure of the green body, which in turn depends strongly on the powder characteristics and the forming method. However, even if proper procedures are employed in the production of the green body (which is rarely the case), further manipulation of the microstructure is necessary during sintering.

The densification of a polycrystalline powder compact is normally accompanied by *coarsening* of the microstructure: the average size of the grains and of the pores becomes larger. In Chapter 8 we considered the densification process. We must now address the coarsening process and the interplay between densification and coarsening for microstructural control.

To achieve a basic understanding of how grains grow and how such growth can be controlled, it is often convenient to first consider a fully dense, single-phase solid where the complicating effects of pores are absent. In ceramics, grain growth is divided into two main types: normal and abnormal. In *normal* grain growth the grain sizes and shapes occur within a fairly narrow range, and except for a magnification factor, the grain size distribution at a later time is similar to that at an earlier time. *Abnormal* grain growth is characterized by the rapid growth

of a few larger grains at the expense of the smaller ones. Simple models have been developed to predict the kinetics of normal grain growth, but many of them analyze an isolated grain boundary or a single grain and neglect the topological requirements of space filling. In recent years, computer simulation has begun to play an important role in exploring the complexities of grain growth.

Sintering of porous powder compacts involves the interaction between pores and grain boundaries that move as a result of grain growth. A common approach is to analyze how the average sizes of the grains and the pores increase with time, but a broader understanding of microstructural development also requires an understanding of how the pore network evolves. The interaction between spherical, isolated pores, and the grain boundaries can be analyzed in terms of simple models, and since grain growth is more pronounced in the final stage of sintering, this interaction plays a critical role in determining the limits of densification. A key result is that the separation of the boundaries from the pores (a condition which is symptomatic of abnormal grain growth in porous solids) must be prevented if high density is to be achieved. Coarsening also occurs in the earlier stages of sintering, and this process influences microstructural evolution in the later stages, so the coarsening of very porous compacts is also important.

The densification process and the coarsening process are by themselves very complex and a detailed theoretical analysis of the interplay between the two processes does not appear to be a fruitful approach. Simple analyses indicate that the achievement of high density and controlled grain size in the fabricated article is dependent on reducing the grain growth rate, increasing the densification rate, or some combination of these two. Fabrication approaches that satisfy one or both of these conditions include the use of dopants or fine, inert, second-phase particles, homogeneous packing of fine particles with a narrow size distribution, sintering with an externally applied pressure, rapid heating rates, and second phases that form a liquid at the firing temperature.

9.2 GENERAL FEATURES OF GRAIN GROWTH

Before we consider the details of grain growth in dense and porous ceramics, we outline some common terms and general features associated with the process.

9.2.1 Grain Growth and Coarsening

Grain growth is the term used to describe the increase in the grain size of a single-phase solid or in the matrix grain size of a solid containing second-phase particles. Grain growth occurs in both dense and porous polycrystalline solids at sufficiently high temperatures. For the conservation of matter, the sum of the individual grain sizes must remain constant; so an increase in the average grain size is accompanied by the disappearance of some grains, usually the smaller

ones. In porous solids, both the grains and the pores commonly increase in size while decreasing in number. Because of the considerable interaction between the grains and the pores, microstructural evolution is considerably more complex than for dense solids. Frequently, the term *coarsening* is used to describe the process of grain growth coupled with pore growth.

9.2.2 Occurrence of Grain Growth

In the widely accepted picture, the grain boundary is considered to be a region of disorder between two crystalline regions (the grains), as sketched in Fig. 9.1 for a section across two grains. High-resolution transmission electron microscopy indicates that the thickness of the grain boundary region is 0.5–1 nm. Grain growth occurs as atoms (or ions) diffuse less than an interatomic distance from one side of the boundary to new positions on the other side, resulting in one grain growing at the expense of another. The atoms move from the “convex” surface on one side of the grain boundary to the “concave” surface on the other side more readily than in the reverse direction because the chemical potential of the atoms under the convex surface is higher than that for the atoms under the concave surface (see Chapter 7). The result of this net flux is that the boundary moves toward its center of curvature (Fig. 9.2).

9.2.3 Driving Force for Grain Growth

It will be recalled that the atoms in the grain boundary have a higher energy than those in the bulk of the crystalline grain, so the grain boundary is characterized

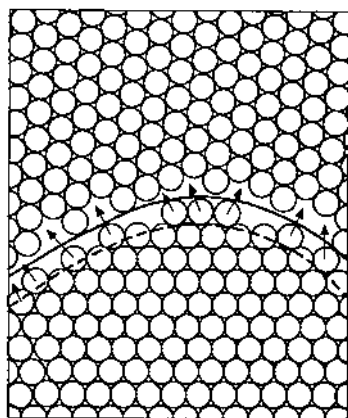


FIGURE 9.1 Classic picture of a grain boundary. The boundary migrates downward as atoms move less than an interatomic spacing from the convex side of the boundary to the concave side.

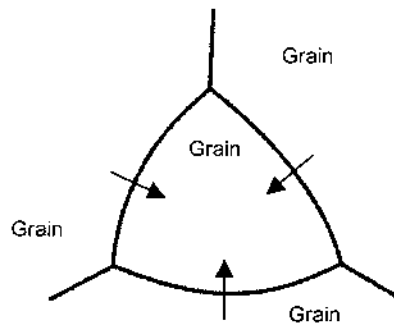


FIGURE 9.2 Movement of the grain boundary toward its center of curvature.

by a specific energy (denoted γ_{gb} in this book), typically on the order of 0.2–1.0 J/m². The *driving force* for grain growth is the decrease in free energy that accompanies reduction in the total grain boundary area.

9.2.4 Normal and Abnormal Grain Growth

Grain growth in ceramics is generally divided into two types: (1) *normal* grain growth and (2) *abnormal* grain growth, which is sometimes referred to as exaggerated grain growth, discontinuous grain growth, or in the case of metals, secondary crystallization. In normal grain growth, the average grain size increases but the grain sizes and shapes remain within a fairly narrow range, so the grain size distribution at a later time is fairly similar to that at an early time (Fig. 9.3a). The form of the grain size distribution is therefore time invariant, and this characteristic is sometimes expressed as the grain size distribution having the property of *scaling* or *self-similarity*. In abnormal grain growth, a few large grains develop and grow relatively faster than the surrounding matrix of smaller grains. The grain size distribution may change significantly, giving rise to a bimodal distribution (Fig. 9.3b), so in this case the property of time invariance of the distribution is lost. Eventually, the large grains impinge and may revert to a normal distribution of sizes.

Grain growth in *porous* ceramics is also described by the terms normal and abnormal grain growth, but the interaction of the pores with the grains is also taken into account. Thus, normal grain growth in porous ceramics is, in addition, characterized by the pores remaining at the grain boundaries. When the boundaries break away from the pores, leaving them inside the grains, the situation is usually indicative of abnormal grain growth. While ceramic microstructures commonly show nearly *equiaxial* grain shapes, it is sometimes observed that the normal or abnormal grains grow in an anisotropic manner, resulting in grains that have

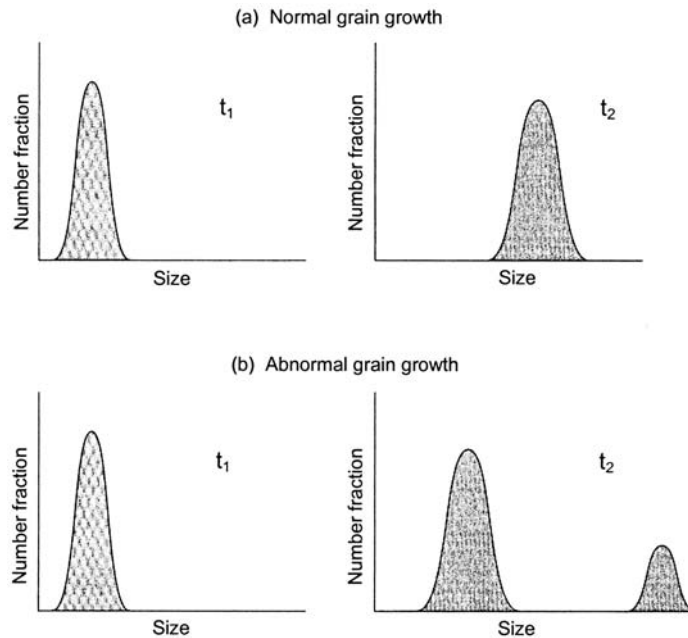


FIGURE 9.3 For an initial microstructure consisting of a unimodal distribution of grain sizes (a) normal grain growth results in an increase in the average grain size whereas the grain size distribution remains almost self-similar; (b) abnormal grain growth is characterized by a few large grains growing rapidly at the expense of the surrounding matrix grains and may lead to a bimodal distribution of grain sizes.

an elongated or platelike morphology. In this case, the growth is described as *anisotropic* grain growth.

Figure 9.4 shows some examples of normal and abnormal grain growth in dense and porous ceramics. A dense Al_2O_3 structure with normal grains is shown in Fig. 9.4a, and if the structure is heated further, a few abnormal grains may start to develop (Fig. 9.4b), subsequently growing rapidly and eventually consuming the smaller grains. Figure 9.4c shows a combination of normal and abnormal grain growth in a nickel-zinc ferrite. The pores deep inside the large, abnormal grain to the left are characterized by long diffusion distances for matter transport into them from the grain boundary. As discussed below, these pores are difficult to remove, so they limit the final density that can be achieved during sintering. In comparison, the pores in the fine-grained array to the right lie almost exclusively on the grain boundaries, so these pores are less difficult to remove during sintering because of the short diffusion distances. Figure 9.4d shows a sample of Al_2O_3 that has undergone considerable abnormal grain growth.

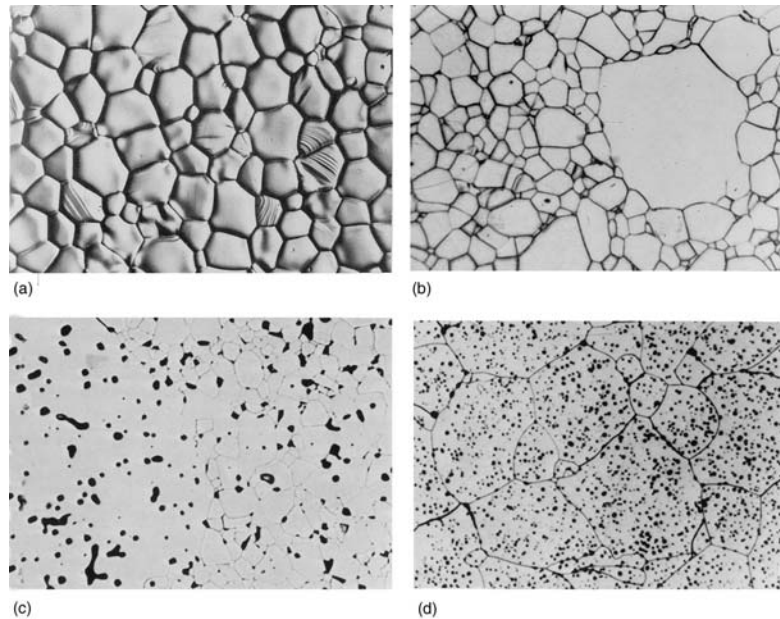


FIGURE 9.4 Microstructures illustrating (a) normal grain size distribution in an alumina ceramic, (b) initiation of abnormal grain growth in an alumina ceramic, (c) normal and abnormal grain growth in a porous nickel-zinc ferrite, and (d) an alumina ceramic that has undergone considerable abnormal grain growth. [(a) and (b) from Ref. 1; (c) and (d) from Ref. 2.)

9.2.5 Importance of Controlling Grain Growth

The control of grain growth during sintering forms one of the most important considerations in the fabrication of ceramics for two key reasons. First, many engineering properties of ceramics are dependent on the grain size, so grain growth control is directly related to the achievement of the desired properties. Second, grain growth increases the diffusion distance for matter transport, thereby reducing the rate of densification, so grain growth control forms an important approach for achieving the normally required high density.

9.2.5.1 Effect of Grain Size on Properties

Few properties are completely independent of grain size and the subject of grain size effects on properties is well covered in several texts and review articles, including Kingery et al. (3). Generally most properties are enhanced by smaller grain size, a notable exception being the creep resistance which increases with larger grain size. For example, the fracture strength of many ceramics is often

found to increase with grain size G according to $1/G^{1/2}$. A wide range of electrical and magnetic phenomena are affected by grain size, and it is in this area that grain size control has been used most effectively to produce ceramics with properties suitable for a variety of applications. For example, the electrical breakdown strength of ZnO varistors used in electrical surge suppressors increases as $1/G$, while the dielectric constant of BaTiO₃ capacitors is found to increase with decreasing grain size down to $\sim 1 \mu\text{m}$.

9.2.5.2 Attainment of High Density

As described in Chapter 8, densification occurs by the flux of matter from the grain boundaries (the source) to the pores (the sink). For sintering by diffusion mechanisms, the dependence of the densification rate on the grain size G can be written

$$\frac{1}{\rho} \frac{d\rho}{dt} = \frac{K}{G^m} \quad (9.1)$$

where K is a temperature-dependent constant and the exponent $m = 3$ for lattice diffusion and $m = 4$ for grain boundary diffusion. Rapid densification requires that the diffusion distance between the source of matter and the sink be kept small, that is, the grain size must remain small (Fig. 9.5a). According to Eq. (9.1), rapid grain growth causes a drastic reduction in the densification rate, so prolonged sintering times are needed to achieve the required density, which increases the possibility for abnormal grain growth to occur. When abnormal grain growth occurs, the pores become trapped inside the grains and become difficult or almost impossible to remove because the transport paths become large in the case of lattice diffusion, or they are eliminated in the case of grain boundary diffusion (Fig. 9.5b). The attainment of high density therefore requires the control of normal grain growth as well as the avoidance of abnormal grain growth.

9.3 OSTWALD RIPENING: THE LSW THEORY

Ostwald ripening refers to the coarsening of precipitates (particles) in a solid or liquid medium. Its relevance to microstructural control is that many features of grain growth and pore growth during sintering are shared by the Ostwald ripening process. Let us consider a system consisting of a dispersion of spherical precipitates with different radii in a medium in which the particles have some solubility (Fig. 9.6). We will recall from Chapter 7 that the chemical potential of the atoms under the surface of a sphere of radius a is given by

$$\mu = \mu_0 + \frac{2\gamma\Omega}{a} \quad (9.2)$$

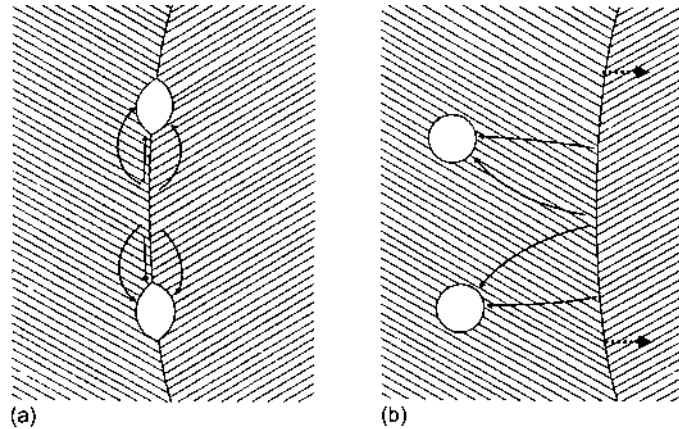


FIGURE 9.5 (a) Densification mechanisms for porosity attached to a grain boundary. The arrows indicate paths for atom diffusion. (b) Densification mechanisms for porosity separated from a grain boundary. The solid arrows indicate paths for atom diffusion, and the dashed arrows indicate the direction of boundary migration. (From Ref. 1.)

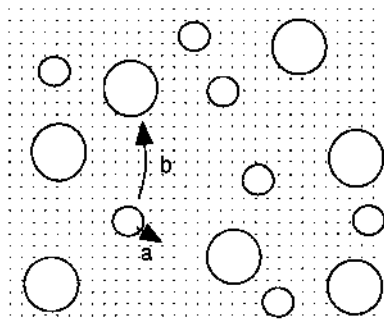


FIGURE 9.6 Coarsening of particles in a medium by matter transport from the smaller to the larger particles. Two separate mechanisms can control the rate of coarsening: (a) reaction at the interface between the particles and the medium and (b) diffusion through the medium.

where μ_0 is the chemical potential of the atoms under a flat surface, γ is the specific energy of the interface between the sphere and the medium, and Ω is the atomic volume. Due to their higher chemical potential, the atoms under the surface of the sphere have a higher solubility in the surrounding medium than the atoms under a flat surface. Making use of the relation between chemical potential and concentration [Eq. (7.67)] and assuming ideal solutions, we can write

$$kT \ln \left(\frac{C}{C_0} \right) = \mu - \mu_0 = \frac{2\gamma\Omega}{a} \quad (9.3)$$

where C is the concentration of solute surrounding a particle of radius a , C_0 is the concentration over a flat surface, k is the Boltzmann constant, and T is the absolute temperature. If $\Delta C = C - C_0$ is small, then $\ln(C/C_0) \approx \Delta C/C_0$, and Eq. (9.3) becomes

$$\frac{\Delta C}{C_0} = \frac{2\gamma\Omega}{kTa} \quad (9.4)$$

The higher solute concentration around a precipitate with smaller radius gives rise to a net flux of matter from the smaller precipitates to the larger ones, so the dispersion coarsens by a process in which the smaller precipitates dissolve and the larger ones grow. This type of coarsening process is referred to as *Ostwald ripening*, in honor of the work of Ostwald in this area around 1900. The driving force for the process is the reduction in the interfacial area between the precipitates and the medium.

9.3.1 The LSW Theory

The basic theory of Ostwald ripening was developed independently by Greenwood (4), Wagner (5), and Lifshitz and Slyozov (6). It is often referred to as the LSW theory. The idealized system considered in the LSW theory is required to satisfy three conditions during the coarsening process:

1. The growth rate of a precipitate is equal to the atomic flux at the precipitate surface.
2. The distribution of precipitate sizes is continuous.
3. Mass conservation in which the total volume (mass) of the precipitates is conserved.

There are also several idealized assumptions, including the following: (1) the precipitate and the medium are isotropic fluids, (2) the precipitates are spherical in shape, (3) the number of precipitates is sufficiently large for the distribution of the precipitate radii to be represented as a continuous function, (4) the solute

concentration at the surface of the precipitate is determined only by the radius of the precipitate, (5) nucleation and precipitate coalescence are neglected, and (6) the total volume of the system is infinite.

As illustrated in Fig. 9.6, two different mechanisms can control the rate of coarsening. In one case, the solubility of the particles into the medium or the deposition of the solute onto the particle surfaces may be the slowest step, and under these conditions, Ostwald ripening is said to be controlled by the *interface reaction*. In the other case, the diffusion of atoms through the medium may be the slowest step, and the process is said to be *diffusion-controlled*.

9.3.2 Ostwald Ripening Controlled by the Interface Reaction

In his analysis, Wagner assumed that the rate of transfer of atoms is proportional to the difference between the solute concentration around a precipitate of radius a given by Eq. (9.4) and an average concentration of the solute, C^* , defined as the concentration that is in equilibrium with a precipitate of radius a^* that neither grows nor shrinks. It is also assumed that the change in C^* with increasing a^* can be neglected. The rate of change of the precipitate radius can be written

$$\frac{da}{dt} = -\alpha_T \Omega (C_a - C^*) \quad (9.5)$$

where α_T is a transfer constant and the negative sign is included to indicate that for smaller precipitates $C_a - C^*$ is positive but the radius a decreases with time. If the total volume of the precipitates is constant, then

$$4\pi \sum_i a_i^2 \frac{da_i}{dt} = 0 \quad (9.6)$$

where the summation is taken over all the precipitates in the system. Writing Eq. (9.5) as

$$\frac{da}{dt} = \alpha_T \Omega [(C^* - C_o) - (C_a - C_o)] \quad (9.7)$$

and substituting into Eq. (9.6) gives

$$\sum_i a_i^2 (C^* - C_o) = \sum_i a_i^2 (C_{a_i} - C_o) \quad (9.8)$$

Putting $C_{a_i} - C_o = \Delta C$ and using Eq. (9.4) for ΔC , Eq. (9.8) becomes

$$C^* - C_o = \frac{2\gamma\Omega C_o}{kT} \left(\frac{\sum_i a_i}{\sum_i a_i^2} \right) \quad (9.9)$$

Substituting Eq. (9.9) into Eq. (9.7) gives

$$\frac{da}{dt} = \frac{2\alpha_r \gamma \Omega^2 C_o}{kT} \left(\frac{\sum a_i}{\sum a_i^2} - \frac{1}{a} \right) \quad (9.10)$$

Putting $a^* = (\sum a_i^2) / (\sum a_i)$, Eq. (9.10) can be written

$$\frac{da}{dt} = \frac{2\alpha_r \gamma \Omega^2 C_o}{kT} \left(\frac{1}{a^*} - \frac{1}{a} \right) \quad (9.11)$$

According to Eq. (9.11), the rate of change of the precipitate radius is proportional to the difference between the critical precipitate curvature and the actual precipitate curvature.

The evolution of a system of precipitates is described by a distribution function $f(a, t)$ such that $f(a, t) da$ represents the fractional number of precipitates between a and $a + da$. The distribution function must satisfy the continuity equation

$$\frac{df}{dt} + \frac{\partial}{\partial a} \left[f \left(\frac{da}{dt} \right) \right] = 0 \quad (9.12)$$

The solution of the coupled differential equations (9.11) and (9.12) shows that after a sufficient amount of time, coarsening proceeds in a steady-state manner such that the precipitate size distribution remains stationary in time. If the precipitate radius is expressed as a reduced size $s = a/a^*$, the distribution function takes the form (5)

$$f(s, t) \begin{cases} \approx s \left(\frac{2}{2-s} \right)^5 \exp \frac{-3s}{2-s} & \text{for } 0 < s < 2 \\ = 0 & \text{for } s > 2 \end{cases} \quad (9.13)$$

This asymptotic distribution is independent of the initial distribution at the start of coarsening. In this distribution, the average radius \bar{a} , taken as the arithmetic mean radius, is given by $\bar{a} = (8/9)a^*$, and the maximum particle radius is $2a^*$. The distribution function f is shown in Fig. 9.7. The critical radius in this steady-state coarsening regime increases parabolically according to

$$(a^*)^2 - (a_o^*)^2 = \left(\frac{\alpha_r C_o \gamma \Omega^2}{kT} \right) t \quad (9.14)$$

9.3.3 Ostwald Ripening Controlled by Diffusion

The solution of the coarsening problem when diffusion is rate controlling follows along the same lines as that for reaction control. The rate of change of the particle radius, equated to the diffusive flux at the precipitate surface, is

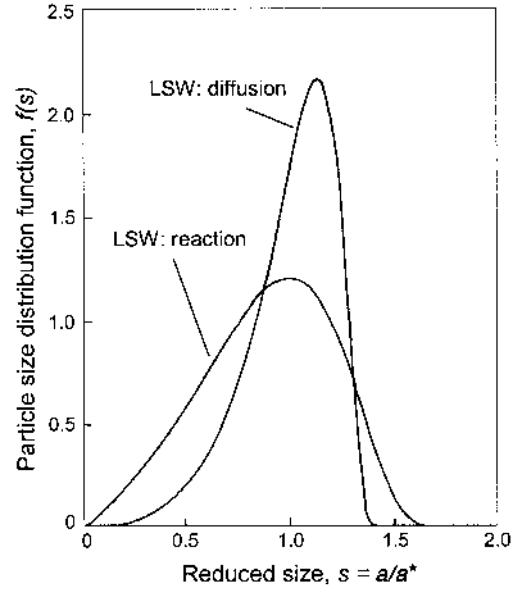


FIGURE 9.7 The particle size distribution function plotted versus the reduced size for Ostwald ripening controlled by interface reaction or diffusion.

$$\frac{da}{dt} = -D\Omega \frac{dC}{da} \quad (9.15)$$

where D is the diffusion coefficient for the solute atoms in the medium. For a dilute dispersion of particles in the medium, Eq. (9.15) can be written

$$\frac{da}{dt} = D\Omega \frac{(C^* - C_a)}{a} = \frac{2DC_o\gamma\Omega^2}{kTa} \left(\frac{1}{a^*} - \frac{1}{a} \right) \quad (9.16)$$

Solution of the coupled differential equations (9.12) and (9.16) gives the distribution function for steady-state coarsening as (5)

$$f(s, t) = \begin{cases} \approx s^2 \left(\frac{3}{3+s} \right)^{7/3} \left(\frac{3/2}{3/2-s} \right)^{11/3} \exp\left(\frac{-s}{3/2-s} \right) & \text{for } 0 < s < 3/2 \\ = 0 & \text{for } s > 3/2 \end{cases} \quad (9.17)$$

The distribution function is also independent of the initial size distribution, but the average radius \bar{a} is now equal to a^* and the maximum particle radius is equal to $3a^*/2$. It is compared with the function for reaction control in Fig. 9.7. In the case of diffusion control, the critical (or average radius) in the steady-state coarsening regime increases according to a cubic law:

$$(a^*)^3 - (a_o^*)^3 = \left(\frac{8DC_o\gamma\Omega^2}{9kT} \right) t \quad (9.18)$$

9.3.4 Modifications to the LSW Theory

Despite the idealized and restrictive set of assumptions, the LSW theory provides a remarkably successful description of many coarsening observations. However, for diffusion-controlled coarsening, it is often found that real systems exhibit a broader and more symmetric steady-state distribution. Furthermore, while the average precipitate size is usually observed to increase qualitatively with the predicted $t^{1/3}$ dependence, the rate constant is generally found to be different from that predicted by the LSW theory. For purely reaction-controlled coarsening where the mechanism is strictly a surface phenomenon, the process should be independent of the volume fraction of precipitates as long as the precipitates do not touch. On the other hand, for diffusion control, the interaction of the diffusion fields of the precipitates must be taken into account, and there have been several attempts to incorporate volume fraction effects into the LSW theory (7).

A volume fraction modification to the LSW theory was investigated by Ardell (8), who assumed that a random spatial arrangement of different sized precipitates can be related through a mean free diffusion path that is a function of the volume fraction. On repeating the LSW analysis, the results showed that as the volume fraction increases, the rate constant increases and the size distribution function broadens. However, the precipitate size increases as $t^{1/3}$ at all volume fractions. Figure 9.8 shows the predicted size distribution for several values of the volume fraction ϕ . In the limit of $\phi = 0$, the results reduce to those of the LSW theory, but for $\phi = 1$, the distribution function is formally identical to the LSW function for *reaction control*.

Modifications to the LSW theory has also been made by Davies et al. (9), who included the effect of direct contact between the precipitates, and by Brailsford and Wynblatt (10), who considered a precipitate embedded in a random array of precipitates with different sizes. Both modifications give the $t^{1/3}$ coarsening dependence and reduce to the LSW results at zero volume fraction. The analysis of Davies et al. shows that the rate constant increases as a result of the encounters between the precipitates and the steady-state distribution function broadens and becomes more symmetric with increasing volume fraction. The results of Brails-

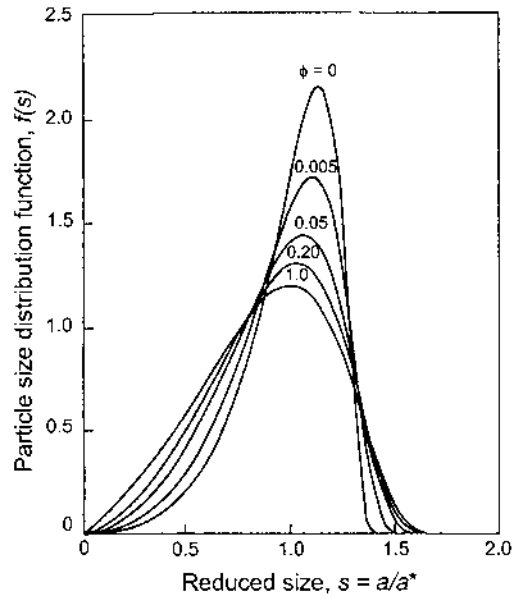


FIGURE 9.8 Dependence of the particle size distribution on the particle volume fraction for diffusion-controlled Ostwald ripening. (From Ref. 8.)

ford and Wynblatt show that the broadening of the steady-state distribution is less than that found by Ardell and by Davies et al. The modifications by Davies et al. and by Brailsford and Wynblatt provide reasonable agreement with most experimental data.

9.3.5 Time-Dependent Ostwald Ripening

The LSW theory and its modifications described in the previous section apply to the limit of long time, sometimes referred to as the *scaling regime*, when the precipitate size distribution function is time invariant. Prior to reaching this scaling regime, the distribution function is time dependent, and the approach to the steady-state distribution is an interesting problem that was addressed by Enomoto et al. (11). For precipitates with a modified Gaussian distribution of sizes given as

$$Y(a) = a^2 \exp\left(-\frac{(a - a_m)^2}{2a_w^2}\right) \quad (9.19)$$

where the parameters a_m and a_w correspond approximately to the position of the maximum and width of the distribution, respectively, Enomoto et al. chose distributions with varying a_m and a_w (Fig. 9.9a) and analyzed the changes in the properties of the distribution with time. The results show that for distributions with a broad width, the standard deviation of the distribution decreases to the characteristic steady-state value, while for systems with a narrow width, the standard deviation increases to the steady-state value (Fig. 9.9b). We may interpret this behavior during the transient regime to mean that the scaling regime acts as a strong attractor for the evolution of the precipitate size distribution.

9.4 TOPOLOGICAL AND INTERFACIAL TENSION REQUIREMENTS

A dense polycrystalline solid consists of a space-filling array of grains. Whereas many theories of grain growth analyze the interfacial tension requirements of an isolated grain boundary or an isolated grain, certain topological requirements of space filling and the local requirements for equilibrium of the interfacial tensions must be satisfied, as recognized many years ago by Smith (12). Consider a two-dimensional section through a dense polycrystalline solid (Fig. 9.10). The structure consists of vertices joined by edges (also called sides) that surround faces. Provided that the face at infinity is not counted, the number of faces F , edges E , and vertices V , obey Euler's equation

$$F - E + V = 1 \quad (9.20)$$

For stable topological structures, i.e., those for which the topological features are unchanged by small deformations, the number of edges that intersect at a vertex is equal to 3. For isotropic grain boundary energies (i.e., γ_{gb} is the same for all grain boundaries), balance of the grain boundary tensions requires that the edges meet at an angle of 120° . Let us now consider polygons in which the sides intersect at 120° . Taking N as the number of sides, under such conditions a hexagon ($N = 6$) has plane sides, whereas a polygon with $N > 6$ has concave sides and one with $N < 6$ has convex sides (Fig. 9.11). Since the grain boundary migrates toward its center of curvature, grains with $N > 6$ tend to grow, while those with $N < 6$ tend to shrink.

In three dimensions, the faces surround cells, and provided the cell at infinity is not counted, we have

$$F - E + V - C = 1 \quad (9.21)$$

where C is the number of cells. Assuming isotropic interfacial energies, balance of interfacial tension requires that the surfaces meet in groups of three at angles of 120° , along lines which themselves meet in groups of four mutually at an angle

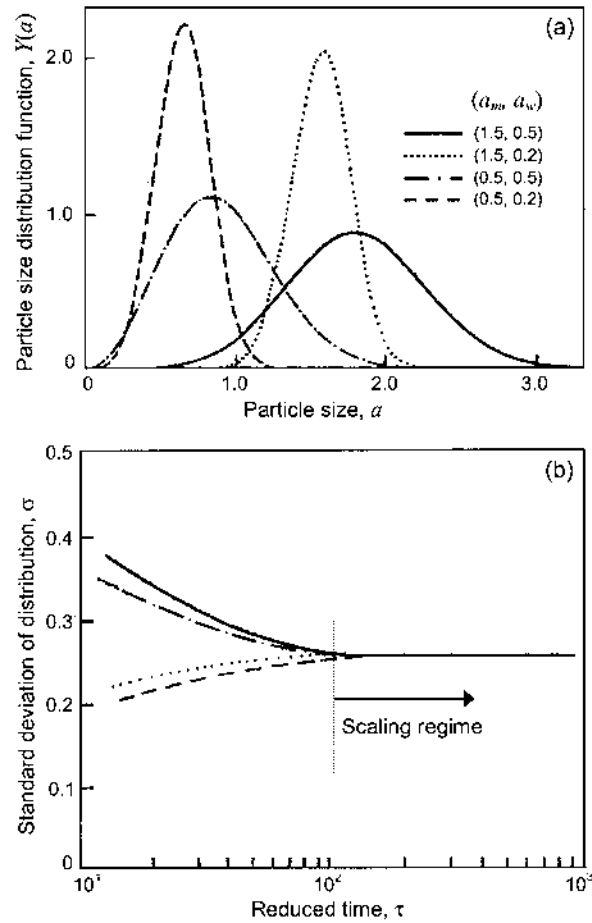


FIGURE 9.9 Effect of the initial particle size distribution shown in (a) on the time variation of the standard deviation of the distribution function (b). (From, Ref. 11.)

of 109.5° . This is the angle subtended by straight lines joining the corners of a regular tetrahedron. No regular polyhedron with plane sides has exactly this angle between its edges. The nearest approach to space filling by a regular plane-sided polyhedron is obtained with tetrakaidecahedra arranged on a body-centered cubic lattice (Fig. 9.12a), but even with this structure, the angles are not exactly those required and the boundaries must become curved to satisfy local equilibrium at the vertices. In general, real grains are arranged randomly and also have different sizes (Fig. 9.12b).

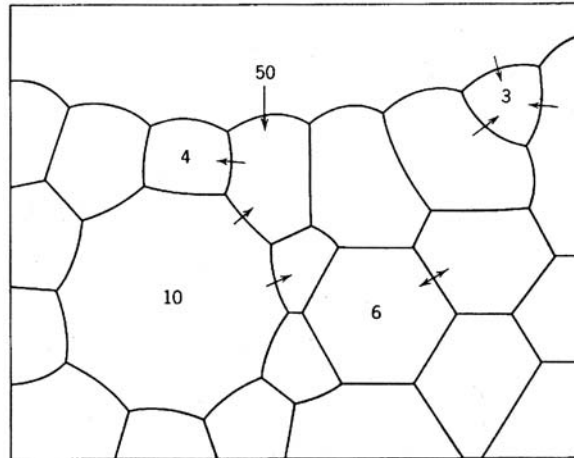


FIGURE 9.10 Sketch of a section through a dense polycrystalline solid. The sign of the curvature changes as the number of sides increases from less than six to more than six. The arrows indicate the direction in which the boundaries migrate. (Courtesy of J. E. Burke.)

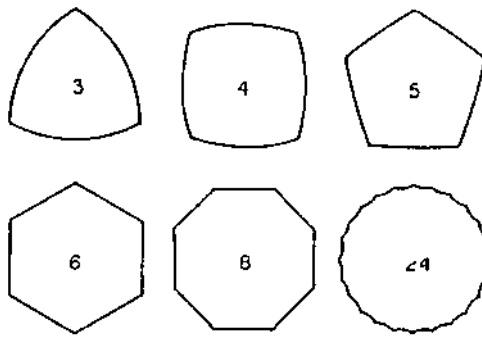


FIGURE 9.11 Polygons with curved sides meeting at 120° .

9.5 NORMAL GRAIN GROWTH IN DENSE SOLIDS

Starting from the early 1950s, the theoretical analysis of normal grain growth in dense polycrystalline solids has received considerable attention, and a review of the subject is given in Ref. 13. Here we provide a discussion of the main ap-

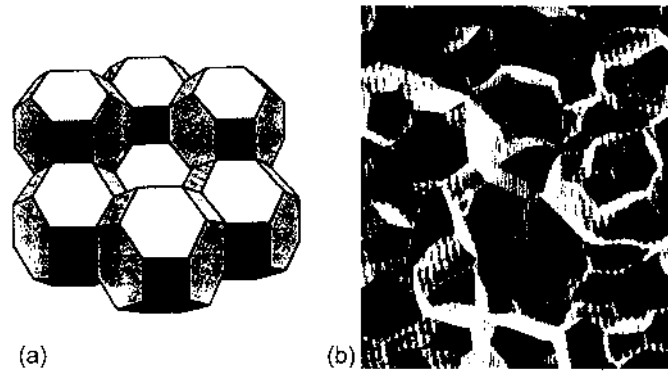


FIGURE 9.12 (a) A group of regular tetrakaidecahedra and (b) grains in an almost fully dense ZnO material.

proaches that have had a key impact on advancing our understanding of the grain growth process.

9.5.1 The Model of Burke and Turnbull

In one of the earliest analyses, Burke and Turnbull (14) modeled the grain growth process as occurring by transport of atoms across the grain boundary under the driving force of the *pressure gradient* across the grain boundary. More correctly, the *chemical potential gradient* across the boundary should be used. Burke and Turnbull considered an isolated part of the grain boundary and assumed that the grain growth equation derived in the analysis represents the average behavior of the whole system. In addition, the grain boundary energy γ_{gb} is assumed to be isotropic and independent of the crystallographic direction, and the grain boundary width δ_{gb} is assumed to be constant.

If the average rate of grain boundary migration v_b (sometimes called the *grain boundary velocity*) is taken to be approximately equal to the instantaneous rate of grain growth, we can write

$$v_b \approx \frac{dG}{dt} \quad (9.22)$$

where G is the average grain size. It is also assumed that v_b can be represented as the product of the driving force for boundary migration F_b and the boundary mobility M_b , so

$$v_b = M_b F_b \quad (9.23)$$

where M_b includes effects arising from the mechanism of migration. The pressure difference across the boundary is given by the equation of Young and Laplace

$$\Delta p = \gamma_{gb} \left(\frac{1}{r_1} + \frac{1}{r_2} \right) \quad (9.24)$$

where γ_{gb} is the specific grain boundary energy (energy per unit area) and r_1 and r_2 are the principal radii of curvature of the boundary. Assuming that the radius of the boundary is proportional to G , then

$$\frac{1}{r_1} + \frac{1}{r_2} = \frac{\alpha}{G} \quad (9.25)$$

where α is a geometrical constant that depends on the shape of the boundary. Taking the driving force for atomic diffusion across the boundary to be equal to the gradient in the chemical potential, we have

$$F_b = \frac{d\mu}{dx} = \frac{d}{dx}(\Omega \Delta p) = \frac{1}{\delta_{gb}} \frac{\Omega \gamma_{gb} \alpha}{G} \quad (9.26)$$

where Ω is the atomic volume and $dx = \delta_{gb}$ is the grain boundary width. From Eq. (7.91), the flux of atoms across the boundary is

$$J = \frac{D_a}{\Omega kT} \frac{d\mu}{dx} = \frac{D_a}{\Omega kT} \frac{\Omega \gamma_{gb} \alpha}{\delta_{gb} G} \quad (9.27)$$

where D_a is the diffusion coefficient for atomic motion across the grain boundary. The boundary velocity becomes

$$v_b \approx \frac{dG}{dt} = \Omega J = \frac{D_a}{kT} \frac{\Omega}{\delta_{gb}} \frac{\alpha \gamma_{gb}}{G} \quad (9.28)$$

In many analyses, the driving force is taken as the pressure difference across the boundary, $\alpha \gamma_{gb}/G$, and v_b is given by

$$v_b \approx \frac{dG}{dt} = M_b \left(\frac{\alpha \gamma_{gb}}{G} \right) \quad (9.29)$$

Comparing Eqs. (9.28) and (9.29), M_b is defined as

$$M_b = \frac{D_a}{kT} \left(\frac{\Omega}{\delta_{gb}} \right) \quad (9.30)$$

Integrating Eq. (9.29) gives

$$G^2 - G_o^2 = Kt \quad (9.31)$$

where G_o is the initial grain size ($G = G_o$ at $t = 0$) and K is a temperature-dependent growth factor given by

$$K = 2\alpha\gamma_{gb}M_b \quad (9.32)$$

Equation (9.31) is the parabolic grain growth law that has the same form as the LSW equation for interface reaction-controlled Ostwald ripening [Eq.(9.14)]. The growth factor K has an Arrhenius dependence on temperature T , given by $K = K_o \exp(-Q/RT)$, where K_o is a constant, R is the gas constant, and Q is the activation energy for grain growth.

The boundary mobility M_b depends on the diffusion coefficient D_a for the atomic jumps across the boundary of the pure material and is termed the *intrinsic* boundary mobility. For an ionic solid, in which both cations and anions must diffuse, D_a represents the diffusion coefficient of the rate-limiting (or slowest) species. In ceramics, the experimentally determined boundary mobility is rarely as high as M_b given by Eq. (9.30) because as described later, segregated solutes, inclusions, pores, and second-phase films can also exert a drag force on the boundary.

9.5.2 Mean Field Theories

The next major advance in the theoretical analysis of grain growth was made by Hillert (15). His approach was to consider the change in size of an isolated grain embedded in an environment that represented the average effect of the whole array of grains. Theories based on this type of approach are often referred to in the grain growth literature as *mean field theories*. Hillert's analysis formed the first significant application of the LSW theory of Ostwald ripening to grain growth. He deduced an expression for the growth rate of grains with radius a of the form

$$\frac{da}{dt} = \alpha_1\gamma_{gb}M_b\left(\frac{1}{a^*} - \frac{1}{a}\right) \quad (9.33)$$

where α_1 is a geometrical factor equal to 1/2 in two dimensions (2-D) and 1 in three dimensions (3-D), a is the radius of the circle (2-D) or sphere (3-D) having the same area or volume as the grain, and a^* is a critical grain size such that if $a > a^*$, the grain will grow and if $a < a^*$, the grain will shrink. It is expected that a^* would be related to the average grain size of the system, but the exact relation was not derived.

Equation (9.33) has the same form as the LSW equation [Eq. (9.11)] for the rate of change of the particle radius in Ostwald ripening controlled by the interface reaction. By following the LSW analysis, Hillert derived an equation for the rate of change of the critical radius given by

$$\frac{d(a^*)^2}{dt} = (1/2)\alpha_1\gamma_{gb}M_b \quad (9.34)$$

Assuming that the terms on the right-hand side of this equation are constant with time, then integration leads to parabolic grain growth kinetics, similar in form to the equation of Burke and Turnbull. Hillert also derived an equation for the size distribution during steady-state grain growth given by

$$f(s, t) = (2e)^\beta \frac{\beta s}{(2 - s)^{2+\beta}} \exp\left(\frac{-2\beta}{2 - s}\right) \quad (9.35)$$

where s is the reduced size equal to a/a^* , e is the base of the natural logarithm (equal to 2.718), and $\beta = 2$ in two dimensions or 3 in three dimensions. The distribution is sharply peaked when compared to a lognormal distribution (Fig. 9.13).

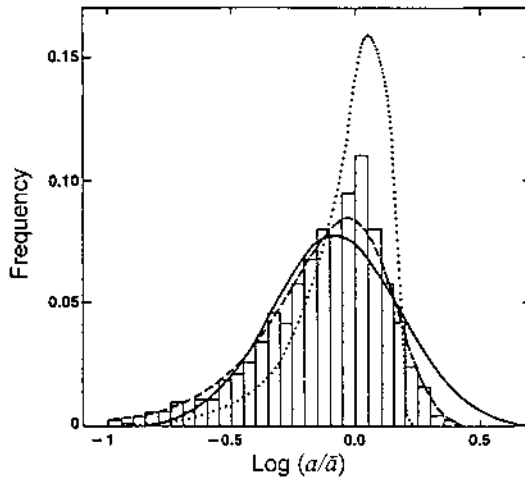


FIGURE 9.13 The grain size distribution function for three theoretical distributions and that obtained from a computer simulation employing the Monte Carlo procedure: log-normal distribution (solid curve), Hillert's model (dotted curve), Louat's model (dashed curve), and computer simulation (histogram). (From Ref. 22.)

Other theories that employ the mean field approach include those of Feltham (16) and Louat (17). Feltham assumed that the grain size distribution is lognormal and time invariant if plotted as a function of the reduced size $s = a/\bar{a}$, where \bar{a} is the average grain size. Using an approach similar to that of Hillert, he obtained parabolic growth kinetics. Louat assumed that the grain boundary motion can be modeled as a random walk process in which the fluctuation of the grain size is the cause of the drift to larger average sizes. He deduced that the grain growth kinetics is parabolic and derived a time-invariant grain size distribution function given by

$$f(s, t) = A s \exp\left(-\frac{s^2}{2}\right) \quad (9.36)$$

where A is a constant. A plot of this distribution function is shown in Fig. 9.13.

To summarize at this stage, in spite of the different assumptions, the theories considered so far all predict a parabolic law for normal grain growth which is formally similar to the LSW equation for interface reaction-controlled Ostwald ripening. The grain size distribution functions predicted by the theories also show the property of time invariance found in the LSW theory. Because of these similarities, normal grain growth in dense polycrystalline solids is sometimes considered as a special case of interface-controlled Ostwald ripening.

In practice, the grain growth data of dense polycrystalline solids do not follow the predicted parabolic law very well. Writing the grain growth equation as

$$G^m - G_0^m = Kt \quad (9.37)$$

the exponent m is often found to be between 2 and 4 and may also depend on the temperature. In ceramics, the value $m = 3$ has been reported most often, but as discussed later (see Table 9.3), this value can be indicative of any of five separate mechanisms. Deviations from $m = 2$ are often explained away in terms of additional factors not considered in the models. One common explanation is the segregation of impurities to the grain boundaries, but the grain growth kinetics of very pure, zone-refined metals also show deviations from $m = 2$. Other explanations that have been suggested include the presence of second-phase particles and anisotropy in the grain boundary energy.

9.5.3 Topological Analysis of Grain Growth

A difficulty with the grain growth theories considered so far is that they neglect the topological requirements of space filling. The most detailed analysis of the topological features of grain growth was carried out by Rhines and Craig (18), who argued that the volume of a shrinking grain must be shared with the grains

throughout the whole structure. Similarly, changes in the topological parameters, e.g., the number of faces, edges, and vertices, must also be shared with the other grains. Rhines and Craig introduced two constants of grain growth, the *sweep constant* θ and the *structure gradient* σ , which have been the subject of some debate. The sweep constant is defined as the number of grains lost when grain boundaries throughout the whole grain structure sweep through the equivalent of unit volume of the solid. There is some doubt about whether the sweep constant is indeed constant (19). The structure gradient is defined as

$$\sigma = \frac{M_v S_v}{N_v} \quad (9.38)$$

where M_v , S_v , and N_v are the curvature, surface area, and number of grains, respectively, per unit volume of the solid. From a limited amount of experimental data, Rhines and Craig found that σ was constant.

In the analysis of the grain growth kinetics, the mean boundary velocity is taken as the product of the boundary mobility and the force on the boundary, that is,

$$v_b = M_b \gamma_{gb} M_v \quad (9.39)$$

Considering unit volume of the solid, the volume swept out per unit time is $v_b S_v$, and from the definition of the sweep constant, the number of grains lost per unit time is $\theta v_b S_v$. The total volume transferred from the disappearing grains to the remaining grains per unit time is $\theta v_b S_v V_G$, where V_G is the average volume of a grain. The rate of increase in the average volume per grain can be written

$$\frac{dV_G}{dt} = \frac{\theta v_b S_v V_G}{N_v} \quad (9.40)$$

where N_v , the number of grains per unit volume, is equal to $1/V_G$. Substituting for S_v and v_b from Eqs. (9.38) and (9.39) gives

$$\frac{dV_G}{dt} = \frac{M_b \gamma_{gb} \theta \sigma}{N_v} \quad (9.41)$$

and assuming that the terms on the right-hand side of this equation are constant, integration leads to

$$V_G - V_{G0} = \left(\frac{M_b \gamma_{gb} \theta \sigma}{N_{v0}} \right) t \quad (9.42)$$

where V_{G0} and N_{v0} are the average grain volume and the average number of grains at $t = 0$. For the grain growth of aluminum at 635°C, the data in Fig. 9.14

show a linear dependence of V_G (measured as $1/N_V$) on time, in agreement with the predictions of Eq. (9.42). N_V was measured directly by serial sectioning.

Since V_G is proportional to G^3 , where G is the average grain size, and assuming self-similarity of the grain size distribution, Eq. (9.42) indicates that the growth exponent m in Eq. (9.37) is equal to 3, in contrast to the theories described earlier where m is equal to 2. Most investigations conventionally use the mean grain intercept length from 2-D sections as a measure of G and as outlined earlier, the m values found in this way are in the range 2–4. A puzzling aspect of Rhines and Craig's experiments is that when the conventional intercept lengths were determined from the samples that were previously examined by serial sectioning, they found that the mean intercept length increased as $t^{0.43}$, i.e., $m = 2.3$. Rhines and Craig used this difference in their measured m values to cast doubt on the use of mean grain intercept lengths determined from 2-D sections. However, a possible source for the discrepancy in the two measured m values may be the presence of anisotropy in the grain shapes.

9.5.4 Computer Simulation of Normal Grain Growth

Since the 1980s, computer simulations have played a key role in exploring some of the complexities of grain growth. Several models have been developed and

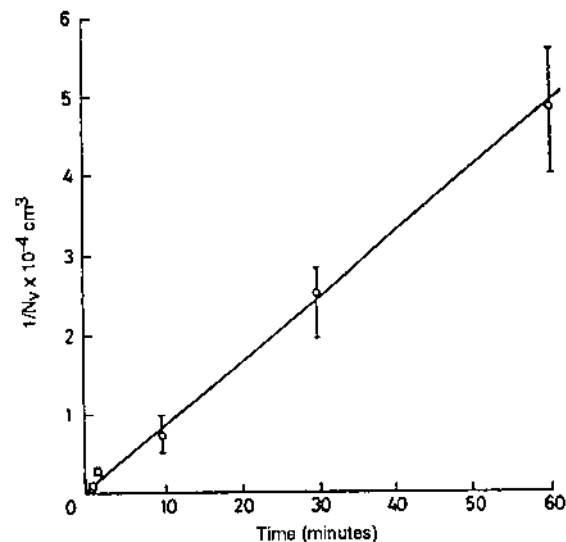


FIGURE 9.14 Plot of the grain volume ($1/N_V$) versus time of annealing for aluminum, showing a linear relationship. (From Ref. 18.)

these are reviewed in Ref. 13. As summarized in Fig. 9.15, the models simulate grain growth in two dimensions for a soap froth (20) or a polycrystal (21,22). The models can employ either a *direct simulation* where the boundary network is constructed and operated on in the computer program or a *statistical* approach in which ensemble probabilities for a collection of grains are determined from a series of interrelated equations so as to find the behavior of typical grain types. Whereas the statistical models do not take into account the topological constraints of space filling, the direct simulations do, and they can be divided into *deterministic* and *probabilistic* models. *Deterministic* in this context means that each subsequent configuration of the boundary network is exactly defined by a previous configuration whereas *probabilistic*, which is used synonymously with the terms *stochastic* or *random*, relates to probabilities of events on a microscopic scale.

The probabilistic models of Srolovitz et al. (21,22), which employ a Monte Carlo procedure, have the advantage that both the topological requirements of space filling and the detailed local effects of grain boundary curvature can be incorporated into the simulations. To analyze the complexity of the grain boundary topology, the microstructure is mapped out onto a discrete lattice (Fig. 9.16). Each lattice site is assigned a number between 1 and Q , corresponding to the orientation of the grain in which it is embedded and commonly a sufficiently large value of Q (>30) is chosen to limit the impingement of grains of the same orientation. The grain boundary segment is defined to lie between two sites of unlike orientation and the grain boundary energy is specified by defining the interaction between nearest neighbor lattice sites in terms of a Hamiltonian opera-

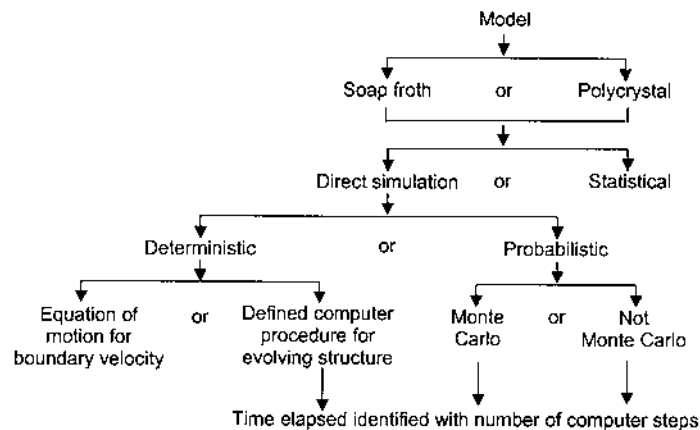


FIGURE 9.15 Classification of computer simulation models for soap froth and grain boundary evolution. (From Ref. 13.)

tor. The unit of time for the simulations is defined as 1 Monte Carlo step (MCS) per site, which corresponds to N microtrials or re-orientation attempts, where N is the total number of sites in the system.

In the two-dimensional analysis, the average area per grain \bar{A} is monitored, and this can be related to the average grain size G . An initial simulation of a shrinking circular grain embedded in an infinite matrix ($Q = 2$), i.e., a structure equivalent to the mean field approximation, showed that the size of the circular grain increases uniformly with time according to the equation

$$\bar{A} - \bar{A}_0 = Kt \quad (9.43)$$

where \bar{A}_0 is the initial area and K is a constant. The grain growth kinetics of the isolated grain are therefore parabolic, in agreement with the mean field theories and the theory of Burke and Turnbull.

For an interconnected network of polycrystalline grains, the kinetics are not parabolic. Large Q values and long times give grain structures (Fig. 9.17) that resemble those of real systems (see Fig. 9.3a and b). After an initial transient, the grain growth exponent, m , obtained from the simulations is equal to 2.44. Srolovitz et al. (21) attempted to justify the m value found in their simulations by comparing it with measured m values determined from data for six very pure metals. Whereas the m value obtained from their simulations is in good agreement with the average experimental value for the six metals, the limited number of

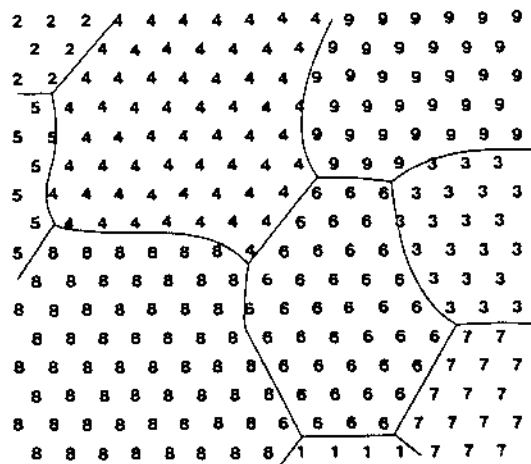


FIGURE 9.16 Sample microstructure on a triangular lattice where the integers denote orientation and the lines represent grain boundaries. (From Ref. 21.)

samples and the wide variation of measured m values (2–4) for this sampling should be recognized.

Reasons for the deviation between the grain growth exponent obtained in the simulations ($m = 2.44$) and the value predicted by the mean field theories ($m = 2$) were discussed by Srolovitz et al. (21). In the mean field approach, the driving force for grain growth, as outlined earlier, is the reduction of the curvature (or area) of the boundary. In the lattice model used in the simulations, the curvature is discretely allocated as kinks on the boundary. Such kinks can be eliminated by two mechanisms: (1) the meeting and annihilation of two kinks of identical orientation (as defined by the lattice) but opposite sign and (2) adsorption of a kink at a vertex where more than two grains meet. The first mechanism corresponds to grain growth driven purely by curvature, as in the case of the simulation of a circular grain embedded in the infinite matrix. However, the second mechanism can only operate when vertices are present. By absorbing kinks, vertices are capable of decreasing the curvature without causing grain growth. Effectively, the growth is slowed relative to the case of the circular grain in the infinite matrix, resulting in a higher m value.

In a subsequent analysis, Srolovitz et al. (22) showed that when the grain size is normalized to the average grain size, then the size distribution function becomes time invariant, as also predicted by the mean field theories. A comparison of the distribution function obtained from the computer simulations with the lognormal distribution, and the distribution functions derived by Hillert and that by Louat are shown in Fig. 9.13. As shown in Fig. 9.18, the distribution function can also provide an excellent fit to some experimental data.

To summarize at this stage, the computer simulations employing the Monte Carlo procedure show a remarkable ability to provide realistic pictures of normal grain growth process and to provide a good fit to some experimental data. On the other hand, the physical significance of some of the results may need to be considered more fully. Nevertheless, Srolovitz et al. (22) suggest that the true

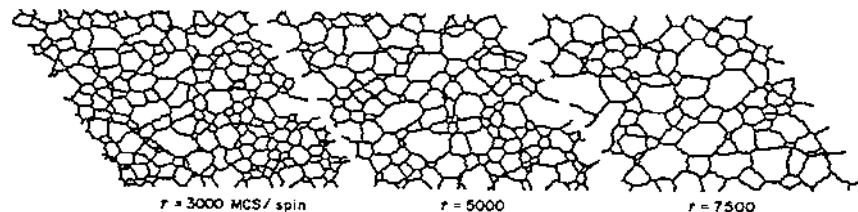


FIGURE 9.17 The evolution of the microstructure for a $Q = 64$ mel on a triangular lattice. (From Ref. 21.)

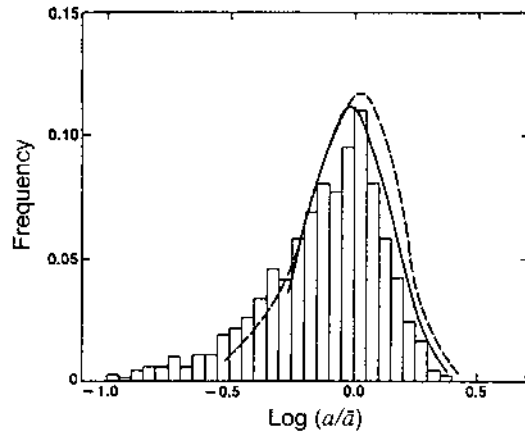


FIGURE 9.18 The grain size distribution function obtained from a computer simulation (histogram) compared with a lognormal fit to grain growth data for aluminum (solid curve) and with grain growth data for MgO (dashed curve). (From Ref. 22.)

nature of the grain growth process may lie somewhere between growth driven by the grain boundary curvature and a random walk process.

9.6 ABNORMAL GRAIN GROWTH IN DENSE SOLIDS

Microstructures of polycrystalline ceramics that have been heated for some time often show very large grains in a fine-grained matrix. The large grains, as outlined earlier, are referred to as abnormal grains, and they are said to have developed as a result of abnormal or runaway grain growth in which the large grains have a much faster growth rate relative to the surrounding fine-grained matrix. A well-known microstructure in the ceramic literature involves the growth of a relatively large single-crystal Al_2O_3 grain in a fine-grained Al_2O_3 matrix, which appears to show the single-crystal grain growing much faster than the matrix grains (Fig. 9.19). It is important to understand abnormal grain growth and to be able to control it for the two key reasons discussed earlier: the large grains limit the attainment of high density and can be detrimental to the material's engineering properties.

9.6.1 Causes of Abnormal Grain Growth

Abnormal grain growth has often been explained in terms of the grain size distribution in the starting material. According to the Hillert theory discussed earlier,

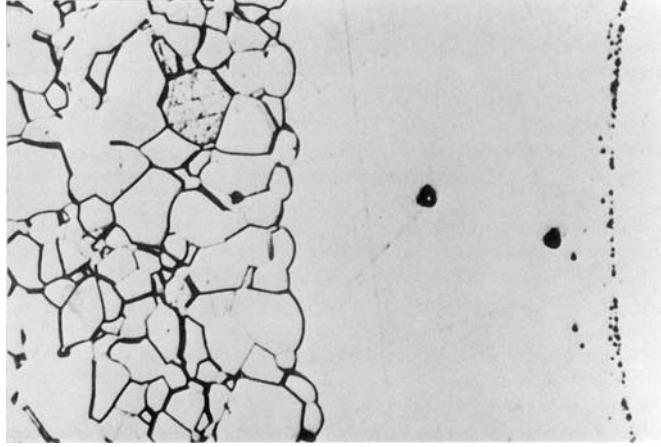


FIGURE 9.19 Example of abnormal grain growth: a large Al_2O_3 crystal growing into a matrix of uniformly sized grains (magnification 495x). (Courtesy of R. L. Coble.)

a steady-state normal grain size distribution has a maximum or cut-off grain size [see Eq. (9.35)]. It was inferred that a grain larger than twice the average size (in two dimensions) would be outside the maximum sustainable size and would grow abnormally. Surprisingly, when the evolution of large grains in a fine grained matrix is analyzed theoretically, it is found that large grains do not undergo abnormal or run-away grain growth.

Using the Monte Carlo procedure outlined in the previous section, Srolovitz et al. (23) simulated the growth of large grains in a matrix of fine (normal) grains in two dimensions. They found that for isotropic systems with uniform grain boundary energy and mobility, although the large grains did grow, they did not outstrip the normal grains. The normal grains grew at a faster relative rate so that the large (abnormal) grains eventually returned to the normal size distribution (Fig. 9.20). The growth of large grains in a matrix of fine grains can also be treated analytically (24). Consider a large grain of radius a in a matrix of fine, normal grains. By analogy with Eq. (9.11) we can write

$$\frac{da}{dt} = 2M_b\gamma_{gb}\left(\frac{1}{a^*} - \frac{1}{a}\right) \quad (9.44)$$

where a^* is the critical radius at which a grain neither grows nor shrinks. The *relative* growth rate of the large grain can be defined as

$$\frac{d\left(\frac{a}{a^*}\right)}{dt} = \frac{1}{(a^*)^2}\left(a^* \frac{da}{dt} - a \frac{da^*}{dt}\right) \quad (9.45)$$

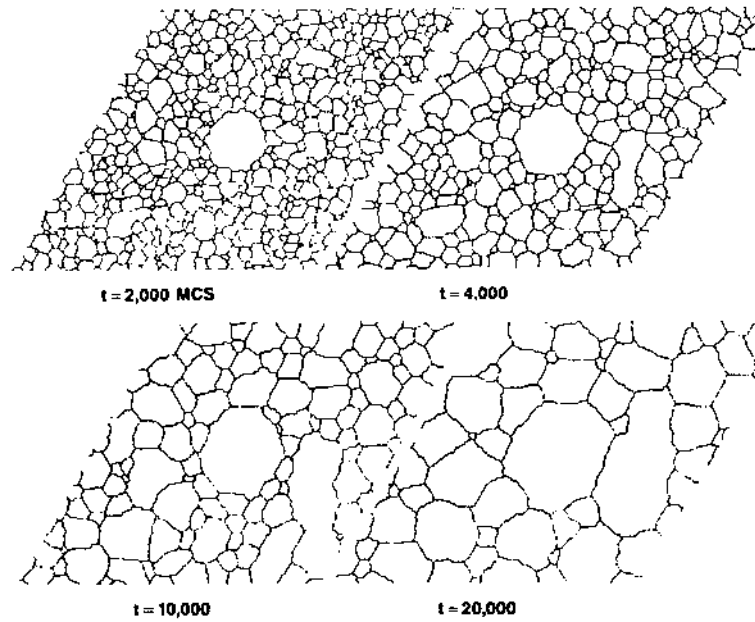


FIGURE 9.20 Computer simulation of the growth of a large grain in an otherwise normal grain growth microstructure for an isotropic system. The microstructure was produced by running the normal grain growth simulation procedure for 1000 MCS, and the large grain was then introduced as a circular grain with an initial size equal to 5 times the average grain size of the matrix grains. (From Ref. 23.)

Since the number of fine, normal grains is much greater than that (one) of the abnormal grain, the time dependence of a^* is still described by Eq. (9.14) which, in differential form is

$$\frac{da^*}{dt} = \frac{M_b \gamma_{gb}}{2a^*} \quad (9.46)$$

Substituting Eqs. (9.44) and (9.46) into Eq. (9.45) gives

$$\frac{d}{dt} \left(\frac{a}{a^*} \right) = - \frac{M_b \gamma_{gb}}{2aa^*} \left(\frac{a}{a^*} - 2 \right)^2 \quad (9.47)$$

This equation shows that the relative growth rate of the large grains is always negative, except for $a = a^*$, in which case it is zero. Abnormal grains (i.e., with $a > 2a^*$) therefore do not outstrip the normal grain population but rejoin it at

the upper limit of $2a^*$. Furthermore, due to irregularities in their shape and to fluctuations, they cannot remain at exactly $2a^*$ after they rejoin the population. They eventually continue to decrease in relative size and are eventually incorporated into the normal distribution. Therefore, for isotropic systems, size difference alone is not a sufficient criterion for initiating abnormal grain growth.

Computer simulations and theoretical analysis show that true abnormal grain growth can occur as a result of variable (or anisotropic) grain boundary energy or mobility (25–27). Abnormal grain growth is favored for grains with boundaries that have a higher mobility or a lower energy than the surrounding matrix grains. Figure 9.21 shows the results of simulations in which the single abnormal grain embedded in a fine-grained matrix has a size that is 6 times the average size and a mobility that is 7.5 times the mobility of the fine grains. The abnormal grain is predicted to grow faster than the average size of the surrounding matrix.

There are several ways in which variable grain boundary properties can arise in practice. One factor is the structure and misorientation of the grain boundary. *Special* or *low-angle* grain boundaries, which result when two grains have only a slight misorientation relative to one another, possess a *lower energy* than general boundaries that may have high misorientation angles. Transfer of matter from the surrounding grains to the low-energy boundaries results in abnormal grain growth. Alternatively, low-energy grain boundaries are generally believed to have low mobility, so growth is slow normal to and rapid parallel to the low-

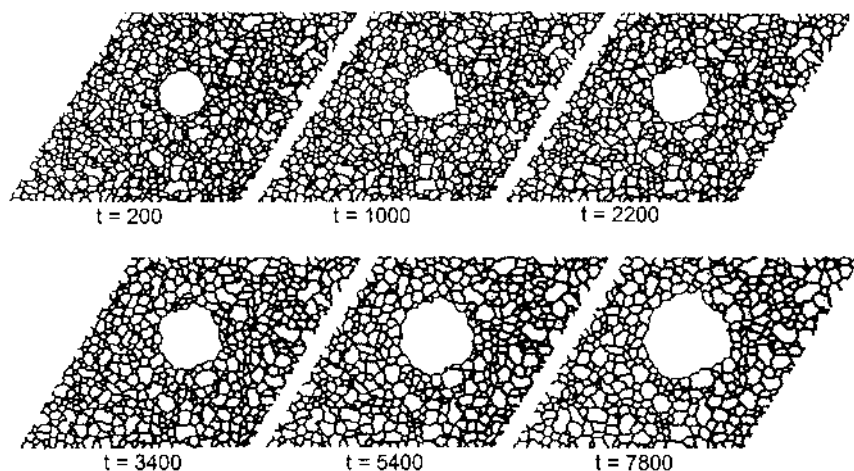


FIGURE 9.21 Computer simulation of the microstructural evolution in which a large grain embedded in a fine-grained matrix has a size that is 6 times the average size and a mobility that is 7.5 times the mobility of the fine grains. (From Ref. 25.)

energy boundaries, often resulting in faceting and anisotropic abnormal growth (Fig. 9.22).

Preferential segregation of dopants and impurities to different types of boundaries can also change the relative grain boundary mobility or energy. Considerable attention has been paid to the Al_2O_3 system, largely based on attempts to understand the role of MgO in suppressing abnormal grain growth in this system (28). While the single most important role of MgO is the reduction in the grain boundary mobility (29), it is also recognized that MgO plays an important role in reducing anisotropies in the surface and grain boundary energies and mobilities (30,31). On the other hand, doping of Al_2O_3 with TiO_2 is observed to enhance anisotropic abnormal grain growth (32,33), presumably due to preferential segregation to some types of boundaries which changes the relative boundary energies and mobilities or the formation of a liquid phase that selectively wets certain boundaries.

The release of solutes, second-phase particles, and pores from moving grain boundaries leads to a sudden increase in the boundary mobility, and this has been

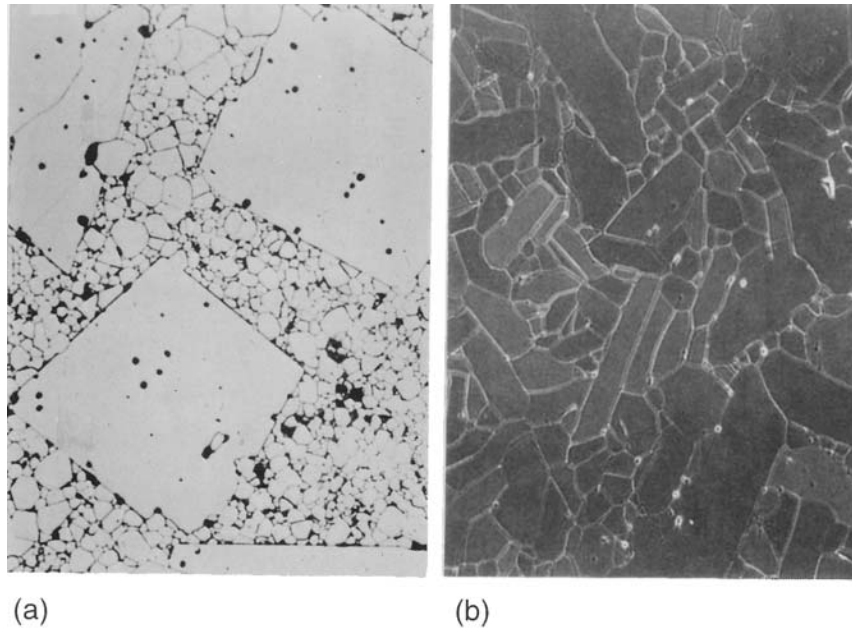


FIGURE 9.22 (a) Large faceted grains in a polycrystalline spinel. The straight boundaries of the large grains suggest a crystallographic orientation of low energy, possibly with a wetting liquid (magnification $350\times$). (Courtesy of R. L. Coble.) (b) Faceted grain growth in TiO_2 -doped Al_2O_3 (500 ppm Ti) (magnification $650\times$). (Courtesy of A. M. Glaeser.)

suggested as a cause of abnormal grain growth. Liquid phases have long been cited as a major cause of abnormal grain growth. The formation of liquid films at grain boundaries often has the effect of significantly enhancing the mobility. In the Al_2O_3 system, a small amount of SiO_2 impurity is often present in the material and this, together with other impurities, may form a liquid phase at high temperatures. It has been observed that the liquid tends to selectively wet the low-energy boundaries whereas a small fraction of the other types of boundaries are not wetted (34). The large mobility difference between the nonwetted, fast-moving boundaries and the wetted, low-energy boundaries has been claimed to predispose the system toward anisotropic abnormal grain growth.

Physical and chemical inhomogeneities, such as inhomogeneous packing and nonuniform distribution of dopants and second-phase particles, commonly lead to local variation in the microstructure, and this has often been considered as a major cause of abnormal grain growth. The local microstructural variations produce inequalities in the boundary mobility or energy, leading to the initiation of abnormal growth.

9.6.2 Controlled Use of Abnormal Grain Growth

Whereas the suppression of abnormal grain growth is commonly a key goal in sintering, the ability to exploit abnormal grain growth in a *controlled* manner can provide significant benefits for several ceramic systems. For example, seeding a fine-grained polycrystalline ceramic with a very large grain does have the effect that this grain will become very large before the slower growing matrix will have developed an average size even comparable to the seed grain. Some single crystal ferrites are actually made in this way (35). The procedure involves consolidating and sintering nearly monodisperse ferrite particles to form a fine-grained matrix with a narrow distribution of grain sizes, bonding a large seed crystal to the matrix, and annealing the system to make the boundary of the seed crystal migrate into the matrix, converting virtually the entire sample into a single grain. The procedure has also proved successful for BaTiO_3 , Al_2O_3 , and lead magnesium niobate–lead titanate (36–38) and an example of a BaTiO_3 single crystal grown by the procedure is shown in Fig. 9.23.

The in situ growth of a controlled distribution of anisotropic abnormal grains in a fine-grained matrix (Fig. 9.24a) has been used to enhance the fracture toughness of Si_3N_4 , SiC , and mullite (39–41). Preferential alignment of growing anisotropic grains leads to *texturing* of the microstructure (Fig. 9.24b), which may cause the development of anisotropic properties in some ceramics. For example, the dielectric constant of bismuth titanate, a ceramic with a layered crystal structure, is significantly higher in the direction of alignment than in the perpendicular direction. Such anisotropy in dielectric properties may be beneficial for several applications in the electronic ceramic industry. Alignment can be achieved

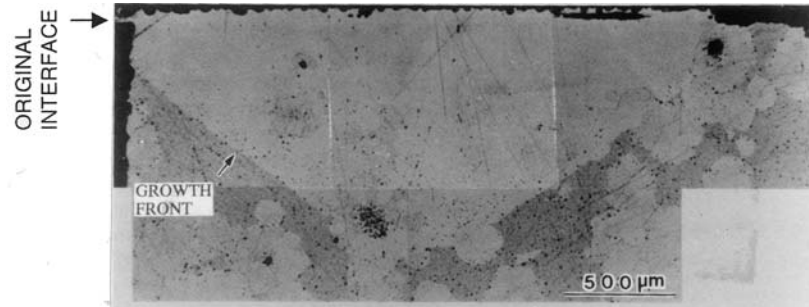


FIGURE 9.23 Optical micrograph of a barium titanate single crystal growing into a polycrystalline matrix after annealing for 20 h at 1300°C. (From Ref. 36.)

by applying a unidirectional pressure during densification of the powder compact, as for example in hot pressing or sinter forging. A more elegant procedure developed by Messing and co-workers (42,43), referred to as *templated grain growth*, involves the use of large, elongated seed crystals that are mixed with a fine equiaxial powder and aligned during the forming of the green body by, for example, tape casting. The aligned seed crystals act as templates to pattern the growth of the matrix during sintering, leading to microstructural texturing.

9.7 MECHANISMS CONTROLLING THE BOUNDARY MOBILITY

So far we have limited our analysis of grain growth to the case of single-phase solids in which the boundary mobility M_b , termed the *intrinsic* boundary mobility defined by Eq. (9.30), is controlled by the diffusion of the atoms of the grain across the boundary. While dopants, impurities, fine second-phase particles, and porosity are commonly present in ceramics, they have been assumed to produce no effect on the basic rate of atom diffusion across the boundary, so their effect on the boundary mobility has been neglected. However, boundary mobilities determined from grain growth data for dense or nearly dense ceramics are often found to be significantly lower than the calculated intrinsic mobility (44). Figure 9.25 shows selected grain boundary mobilities for a few common ceramics, where it is assumed that $\gamma_{gb} = 0.3 \text{ J/m}^2$ for each material and the mobilities are normalized to that for a fixed grain size of $90 \text{ } \mu\text{m}$. While recognizing the uncertainty in the calculated intrinsic mobility due to the lack of definitive data for the diffusion coefficient of the rate-controlling ion, trends in the mobility values are clear. First, the measured mobilities of the oxides are well below the calculated intrinsic values. Second, dense samples containing dopants or second-phase pre-

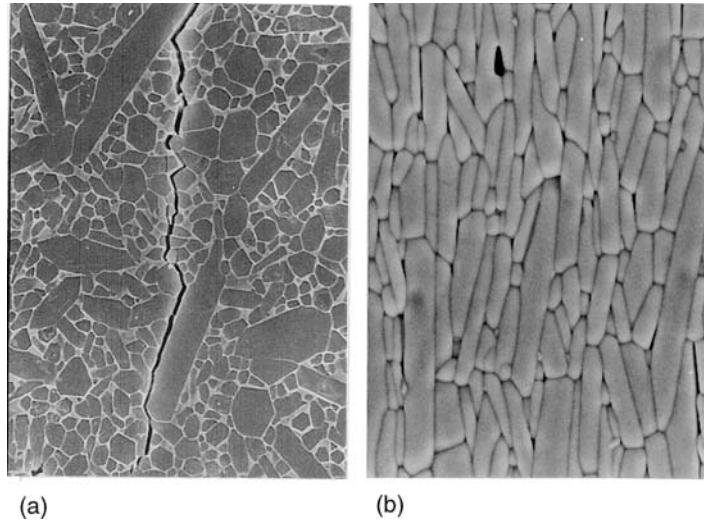


FIGURE 9.24 Exploitation of controlled anisotropic abnormal grain growth: (a) Self-reinforced silicon nitride, showing the interaction of a propagating crack with the microstructure (magnification $2000\times$). (Courtesy of M. J. Hoffmann.) (b) Bismuth titanate with a microstructure of aligned anisotropic grains, giving anisotropic dielectric properties. (magnification $1000\times$).

precipitates have low mobilities, while the mobilities for porous samples are much lower than those for the dense samples. Third, when liquid phases are present, the mobilities are higher than those for porous samples but often not much higher than for dense samples.

Because of their influence on the boundary mobility, the use of fine second-phase particles and, in particular, the use of dopants form two of the most effective approaches for controlling grain size during solid-state sintering. Prior to considering their practical use, we examine the mechanism by which they influence M_b .

9.7.1 Effect of Fine Second-Phase Particles

Let us consider a system of fine second-phase particles (also referred to as fine inclusions or precipitates) dispersed randomly in a polycrystalline solid in which they are insoluble and immobile. If a grain boundary moving under the driving force of its curvature encounters an inclusion, it will be held up by the particle until the motion elsewhere has proceeded sufficiently far for it to break away. If

there are a sufficient number of particles, we might expect that the boundary will be pinned when it encounters the particles and boundary migration will therefore cease. Two basic models have been put forward to describe this situation, but recent studies indicate that both models suffer from inconsistencies.

9.7.1.1 The Zener Model

The first quantitative model to describe particle inhibited grain growth was developed by Zener, as communicated by Smith (45). Zener assumed that the inclusion particles are monosize, spherical, insoluble, immobile, and randomly distributed in the polycrystalline solid. Taking a grain boundary with principal radii of curvature a_1 and a_2 , the driving force (per unit area) for boundary motion is

$$F_b = \gamma_{gb} \left(\frac{1}{a_1} + \frac{1}{a_2} \right) \quad (9.48)$$

Assuming that a_1 and a_2 are proportional to the grain size G , then

$$F_b = \frac{\alpha \gamma_{gb}}{G} \quad (9.49)$$

where α is a geometrical shape factor (e.g., $\alpha = 2$ for a spherical grain). When the grain boundary intersects an inclusion, its further movement is hindered (Fig. 9.26a and b). A dimple is formed in the grain boundary, and compared to the inclusion-free boundary, extra work must be performed for the equivalent motion of the boundary. This extra work manifests itself as a retarding force on the boundary. If r is the radius of the inclusion (Fig. 9.26c), then the retarding force exerted by the inclusion on the boundary is

$$F_r = (\gamma_{gb} \cos \theta)(2\pi r \sin \theta) \quad (9.50)$$

i.e., the retarding force is the grain boundary tension, resolved in the direction opposite to that of the grain boundary motion, times the perimeter of contact. The retarding force is a maximum when $\theta = 45^\circ$; so $\sin \theta \cos \theta = 1/2$, and

$$F_r^{\max} = \pi r \gamma_{gb} \quad (9.51)$$

If there are N_A inclusions per unit area of the grain boundary, then the maximum retarding force (i.e., per unit area of the boundary) is

$$F_d^{\max} = N_A \pi r \gamma_{gb} \quad (9.52)$$

N_A is difficult to determine but is related to N_V , the number of inclusions per unit volume, by

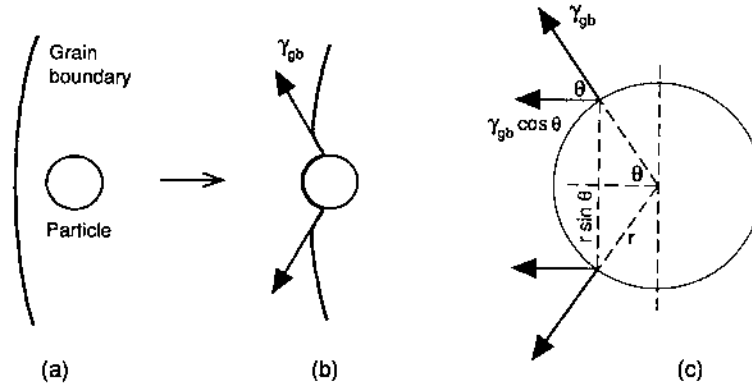


FIGURE 9.26 Interaction of a grain boundary with an immobile particle. (a) Approach of the boundary toward the particle. (b) Interaction between the grain boundary and the particle leading to a retarding force on the boundary. (c) Detailed geometry of the particle–grain boundary interaction.

$$N_A = 2rN_V \quad (9.53)$$

If the volume fraction of the inclusions in the solid is f , then

$$N_V = \frac{f}{(4/3)\pi r^3} \quad (9.54)$$

Substituting for N_A in Eq. (9.52) gives

$$F_d^{\max} = \frac{3f\gamma_{gb}}{2r} \quad (9.55)$$

The net driving force per unit area of the boundary is

$$F_{net} = F_b - F_d^{\max} = \gamma_{gb} \left(\frac{\alpha}{G} - \frac{3f}{2r} \right) \quad (9.56)$$

When $F_{net} = 0$, boundary migration will cease, and this occurs when

$$G_L = \frac{2\alpha r}{3f} \quad (9.57)$$

where G_L is the limiting grain size. Equation (9.57) is sometimes referred to as the *Zener relationship*. It indicates that a limiting grain size will be reached, the magnitude of which is proportional to the inclusion size and inversely proportional

to the inclusion volume fraction. Changes in temperature would not affect this equilibrium relationship but would affect only the *rate* at which the system approaches the equilibrium condition. While it may be difficult to achieve in practice, if a limiting grain size is reached, further grain growth can only occur if (1) the inclusions coarsen by Ostwald ripening, (2) the inclusions go into solid solution into the matrix, or (3) abnormal grain growth occurs.

There have been several refinements to the Zener analysis by modifying the simple assumptions used in the model but the approach has remained essentially the same (46–49). The refinements lead to a different geometrical constant in Eq. (9.57) but do not affect the dependence of G_L on f .

9.7.1.2 Computer Simulations of Particle-Inhibited Grain Growth

A completely different approach was used by Srolovitz and co-workers (50–52) who modified their Monte Carlo computer simulation technique outlined earlier for normal grain growth in single-phase solids to include a dispersion of fine second-phase particles that are assumed to be monosize, spherical, insoluble, immobile, and randomly distributed (Fig. 9.27). The temporal evolution of the microstructure for a system undergoing grain growth in the presence of second-phase particles shows that the grains grow and finally reach a pinned, limiting grain size. In the growing regime, simulated microstructures show several features that are characteristic of normal grain growth. The grain growth exponent and the grain size distribution are found to be identical with or without the presence of the inclusions.

Figure 9.28 shows the pinned microstructures for two different volume (or areal) fractions f of the inclusions. When compared to the simulated microstructures for normal grain growth without the presence of inclusions (see Fig. 9.17), a few grains with highly irregular shapes are observed in the pinned microstructures. The simulations predict that the time taken to reach the limiting grain size as well as the value of the limiting grain size decreases with increasing values of f . The simulations also reveal that while the total number of inclusions remains constant, the fraction of inclusions ϕ_p that are located at the boundaries decreases with time, and the effect becomes more significant for smaller values of f . The limiting grain size G_L is predicted to follow an expression of the form

$$G_L = K_s \frac{r}{(\phi_p f)^{1/3}} \quad (9.58)$$

where K_s is a constant and r is the radius of the inclusions.

In comparison to the Zener relationship, the different dependence of G_L on f given by Eq. (9.58) should be noted. It is sometimes claimed that the Zener analysis overestimates the driving force for grain growth because it neglects the

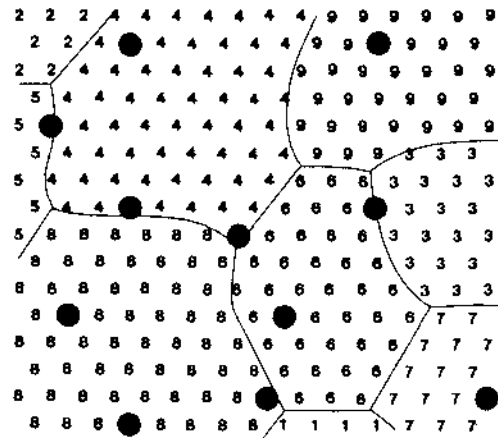


FIGURE 9.27 Sample microstructure on a triangular lattice where the integers denote crystallographic orientation, the lines represent boundaries, and the solid circles represent second-phase particles. (From Ref. 50.)

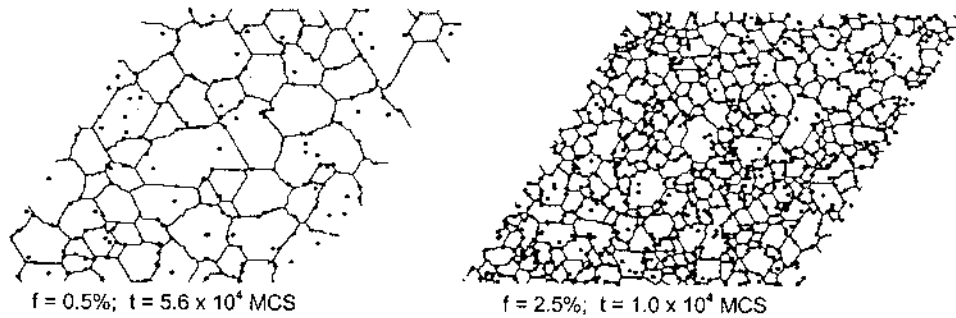


FIGURE 9.28 Pinned microstructures for two different inclusion concentrations. (From Ref. 50.)

effect of the inclusions on the *curvature* of the boundary and considers only the work involved in dragging the inclusion. As a result, for a given value of f , the Zener relationship predicts more grain growth and a larger limiting grain size. On the other hand, in the computer simulations, when the boundary intersects an inclusion, the inclusion becomes a new vertex that has the effect of reducing the boundary curvature. Furthermore, the boundaries deform to maximize the number of pinning inclusion intersections, so the pinning effect is strong, leading to smaller limiting grain sizes.

9.7.1.3 Comparison with Experimental Results

Alumina containing fine ZrO_2 particles is the most widely studied ceramic system for particle-inhibited grain growth (53–58), but the experimental conditions often differ from the assumptions of the models. For example, ZrO_2 particles are quite mobile at Al_2O_3 grain boundaries and they migrate with the boundaries. The particles also tend to coalesce, so that the particle size does not remain constant. Zirconia containing fine Al_2O_3 particles is another widely studied system (57,59) but the Al_2O_3 particles coarsen faster than the ZrO_2 grains grow. Thus, the model assumptions of immobile inclusions and fixed inclusion size are not met in these systems.

Grain growth in Al_2O_3 containing fine SiC particles has been investigated by Sterns and Harmer (60), and it is claimed that this system closely fulfils the criteria for an ideal pinning experiment. A plot of the Al_2O_3 grain size versus the SiC volume fraction after annealing dense, hot pressed samples for 100 hours at 1700°C indicated that the data are not consistent with the Zener model or the computer simulations (Fig. 9.29). The fraction of SiC particles at the grain boundaries ϕ_p is found to decrease with increasing grain size G during thermal annealing in a predictable manner. By relaxing the assumption of totally random distribution of the particles at the grain boundaries and incorporating the observed relation between ϕ_p and G into the Zener analysis, good agreement between the limiting grain size G_L and the volume fraction of particles f is achieved.

9.7.2 Effect of Dopants: Solute Drag

Let us consider a system in which a small amount of a dopant (also referred to as the *solute*) is dissolved in solid solution in a polycrystalline solid (sometimes referred to as the *host*). If the solute is attracted to (or repelled from) the grain boundary due to an interaction potential, the solute ions will tend to have a nonuniform distribution in the grain boundary. The interaction between the boundary and the solute can arise from lattice strain energy due to size mismatch between the solute and host ions and, for aliovalent solutes, from electrostatic potential energy.

For a hypothetical stationary boundary, the concentration profile of the solute ions will be symmetrical (Fig. 9.30a). The force of interaction due to the solute ions to the right of the boundary balances that due to the ions to the left of the boundary, so that the net force of interaction is zero. If the boundary now starts to move, the dopant concentration profile becomes asymmetric, since the diffusivity of the solute ions across the boundary is expected to be different from that of the host (Fig. 9.30b). This asymmetry results in a retarding force or drag on the boundary which reduces the driving force for migration. If the driving force for boundary migration is high enough, the boundary will break away from the high concentration of solute (sometimes called a solute cloud), and when this

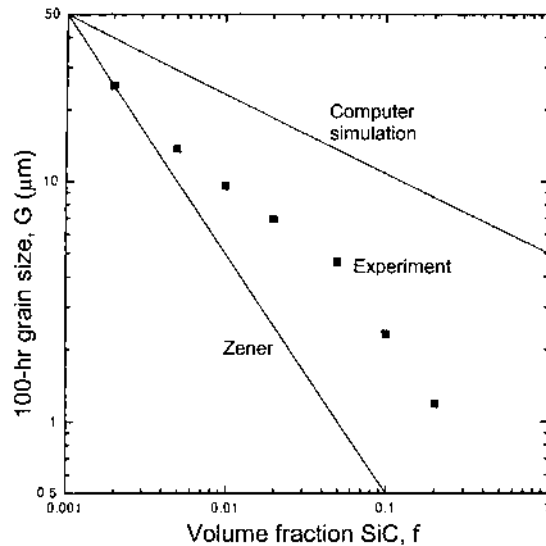


FIGURE 9.29 Data for grain size of Al_2O_3 (after annealing for 100 hour at 1700°C) as a function of SiC inclusion volume fraction, compared with the predictions of the Zener model and computer simulations. (From Ref. 60.)

occurs (Fig. 9.30c), its mobility will approach the intrinsic value, given by Eq. (9.30).

Models for grain boundary migration controlled by solute drag have been developed by Cahn (61), Stuwe (62), Hillert and Sundman (63), and others. We shall outline the model of Cahn which is more quantitative and concise than the others and has the advantage that the boundary mobility can be more directly related to the physical parameters of the process. The model analyzes the problem in one dimension and makes the following assumptions:

1. The solute concentration C , expressed as a fraction of the host atoms, is fairly dilute, so the chemical potential of the solute can be expressed as $\mu = \mu_0 + kT \ln C$, where k is the Boltzmann constant and T is the absolute temperature.
2. An interaction potential energy U exists between the solute atoms and the grain boundary which is independent of the boundary velocity and the dopant concentration but is a function of the distance x from the grain boundary.
3. The Einstein relation between mobility M and diffusivity D is obeyed (i.e., $M = D/kT$).
4. Steady-state conditions exist; so the boundary velocity v_b is constant.

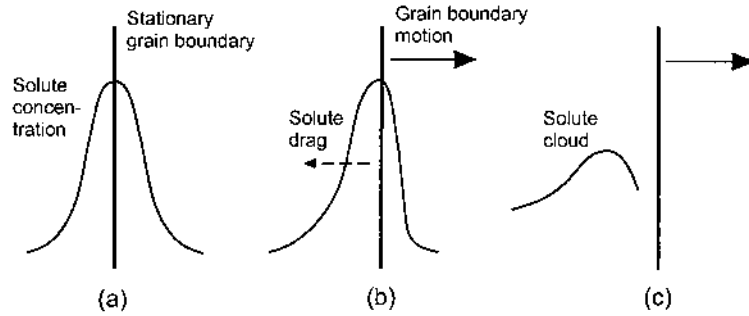


FIGURE 9.30 Sketch of the solute drag effect produced by the segregation of dopants to the grain boundaries. (a) Symmetrical distribution of the dopant in the region of a stationary grain boundary. (b) For a moving boundary, the dopant distribution becomes asymmetric if the diffusion coefficient of the dopant atoms across the boundary is different from that of the host atoms. The asymmetric distribution produces a drag on the boundary. (c) Breakaway of the boundary from the dopant leaving a solute cloud behind.

The chemical potential of the solute atoms in the near grain boundary region is assumed to be given by

$$\mu = kT \ln C(x) + U(x) + U_0 \quad (9.59)$$

where $C(x)$ and $U(x)$ are functions of x and U_0 is a constant chosen such that $U(\infty) = 0$. For steady state conditions, the composition profile of the solute satisfies the equation

$$\frac{dC}{dt} = -v_b \frac{dC}{dx} \quad (9.60)$$

Following Eq. (7.91), the flux of the solute atoms is given by

$$J = -\frac{D_b C}{\Omega kT} \frac{d\mu}{dx} \quad (9.61)$$

where D_b is the diffusion coefficient for the solute atoms across the boundary. Using Eq. (9.59), we can also write Eq. (9.61) as

$$J = -\frac{D_b}{\Omega} \frac{dC}{dx} + \frac{D_b C}{\Omega kT} \frac{dU}{dx} \quad (9.62)$$

The concentration profile of the solute can now be calculated from the continuity equation

$$\frac{dJ}{dx} + \frac{1}{\Omega} \frac{dC}{dt} = 0 \quad (9.63)$$

and the boundary conditions: $dC/dx = 0$, $dU/dx = 0$, and $C(x) = C_\infty$ at $x = \infty$. The concentration C_∞ can be taken as that in the bulk of the grain. Thus $C(x)$ must satisfy the equation

$$D_b \frac{dC}{dx} + \frac{D_b C}{kT} \frac{dU}{dx} + v_b (C - C_\infty) = 0 \quad (9.64)$$

The solute atom exerts a force $-(dU/dx)$ on the boundary, so the net force exerted by all the solute atoms is

$$F_s = -N_v \int_{-\infty}^{\infty} [C(x) - C_\infty] \frac{dU}{dx} dx \quad (9.65)$$

where N_v is the number of host atoms per unit volume. In the analysis, the $C(x)$ that satisfies Eq. (9.64) is used to calculate F_s from Eq. (9.65). An approximate solution that is valid for both low and high boundary velocities is

$$F_s = \frac{\alpha C_\infty v_b}{1 + \beta^2 v_b^2} \quad (9.66)$$

where the parameters α and β are given by

$$\alpha = 4N_v kT \int_{-\infty}^{\infty} \frac{\sinh^2 [U(x)/2kT]}{D_b(x)} dx \quad (9.67)$$

and

$$\frac{\alpha}{\beta^2} = \frac{N_v}{kT} \int_{-\infty}^{\infty} \left(\frac{dU}{dx} \right)^2 D_b(x) dx \quad (9.68)$$

Physically, α is the solute drag per unit velocity and per unit dopant concentration in the low boundary velocity limit, whereas $1/\beta$ is the drift velocity with which an impurity atom moves across the grain boundary. From the form of Eq. (9.67), solutes with either an attractive or repulsive interaction energy of the same magnitude will exert a similar drag force.

The total drag force on the boundary is the sum of the intrinsic drag F_b and the drag due to the dopant atoms F_s ; that is,

$$F = F_b + F_s = \frac{v_b}{M_b} + \frac{\alpha C_\infty v_b}{1 + \beta^2 v_b^2} \quad (9.69)$$

where M_b is the intrinsic boundary mobility defined by Eq. (9.30). In the low boundary velocity limit, the term $\beta^2 v_b^2$ in Eq. (9.69) can be neglected, so

$$v_b = \frac{F}{1/M_b + \alpha C_\infty} \quad (9.70)$$

Initially the mobility due to solute drag is constant, but as the velocity increases, the boundary continually sheds solute and for sufficiently high velocity is able to break away from the solute cloud and migrate at the intrinsic velocity. As is shown in Fig. 9.31 for the theoretical relationship between velocity and driving force, transitions are predicted to occur from the solute drag limited velocity to the intrinsic velocity over a range of driving forces. Direct observations indicate that the grain boundary motion is often not uniform but starts and stops as if making transitions between the solute drag and intrinsic regimes (64).

According to Eq. (9.70), the boundary mobility M'_b equal to v_b/F can be written in terms of the intrinsic component M_b and the solute drag component M_s :

$$M'_b = \left(\frac{1}{M_b} + \frac{1}{M_s} \right)^{-1} \quad (9.71)$$

where $M_s = 1/\alpha C_\infty$. For situations where the solute segregates to the grain boundary and the center of the boundary contributes most heavily to the drag effect, α can be approximated by

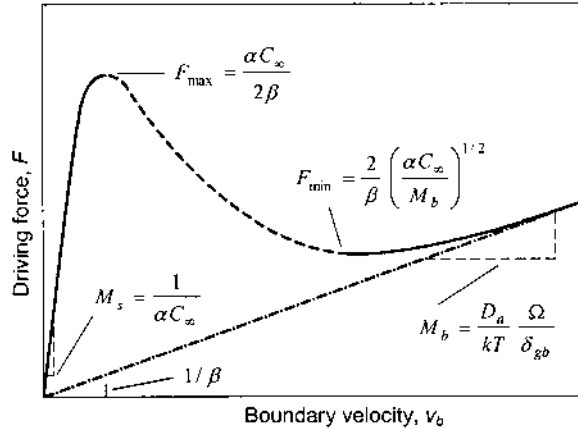


FIGURE 9.31 Driving force–velocity relationship for boundary migration controlled by solute drag and in the intrinsic regime. (From Ref. 44.)

$$\alpha = \frac{4N_v kT \delta_{gb} Q}{D_b} \quad (9.72)$$

where Q is a partition coefficient (>1) for the dopant distribution between the boundary region and the bulk of the grain such that the solute concentration in the boundary region is QC_∞ . The mobility due to solute drag is therefore

$$M_s = \frac{D_b}{4N_v kT \delta_{gb} QC_\infty} \quad (9.73)$$

According to Eq. (9.73), dopants are predicted to be most effective for reducing the boundary mobility when the diffusion coefficient of the rate-limiting species D_b is low and the segregated solute concentration QC_∞ is high. While some systems may show behavior consistent with this prediction, for example, CeO_2 doped with trivalent solutes (65,66), in general the selection of an effective dopant is complicated because of the multiplicity of the dopant role (see Chapter 11). Some examples of systems where the dopant approach has been used successfully for inhibiting grain growth are given in Table 9.1.

9.8 GRAIN GROWTH AND PORE EVOLUTION IN POROUS SOLIDS

Grain growth data for many porous ceramic systems during sintering follow trends similar to those shown in Fig. 9.32 for the sintering of TiO_2 (73). In the early stage of sintering, grain growth is limited, but some coarsening of the microstructure can occur by processes such as surface diffusion and vapor transport. The changes that occur in this early stage have a significant influence on the microstructural evolution in the later stages. Grain growth increases as the

TABLE 9.1 Examples of Dopants Used for Grain Growth Control in Some Common Ceramics

Host	Dopant	Concentration (atomic %)	Reference
Al_2O_3	Mg	0.025	28,67
BaTiO_3	Nb,Co	0.5–1.0	68,69
ZnO	Al	0.02	70
CeO_2	Y, Nd, Ca	3–5	65,66
Y_2O_3	Th	5–10	71
SiC	(B + C)	0.3B + 0.5C	72

body densifies, but frequently, grain growth does not become pronounced until the final stage of sintering when the pores pinch off and become isolated. A region of significant densification with limited grain growth is followed by one of reduced densification but with significant grain growth. Generally, coarsening becomes prominent in the late intermediate and final stages of sintering. Gupta (74) found that the average grain size increases slowly and roughly linearly with density up to relative densities of 0.85 to 0.90 but then it increases much more rapidly above this density value (Fig. 9.33). Migration of the boundaries leads to coalescence of the pores, so the average pore size increases (Fig. 9.34a). It is believed that this process of grain growth and pore coalescence contributes to coarsening in the later stages of sintering. Figure 9.34b shows an example of coarsening by such a process in UO_2 (75).

9.8.1 Pore Evolution During Sintering

Microstructural coarsening during sintering is commonly considered in terms of how fast the grains grow. However, a more realistic view of the sintering compact may be that of a network of contacting grains interpenetrated by a network of porosity, so an understanding of the evolution of the porous network is also necessary for a broader understanding of microstructure evolution in porous sys-

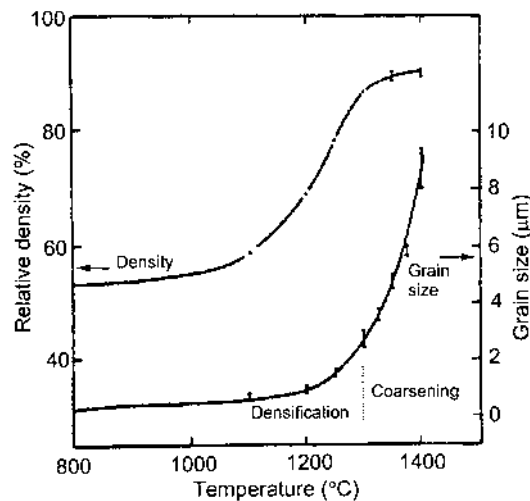


FIGURE 9.32 The density and grain size of a TiO_2 powder compact as a function of the sintering temperature. Rapid densification with limited grain growth occurs at lower temperatures followed by rapid grain growth with little densification at higher temperatures. (From ref. 73.)

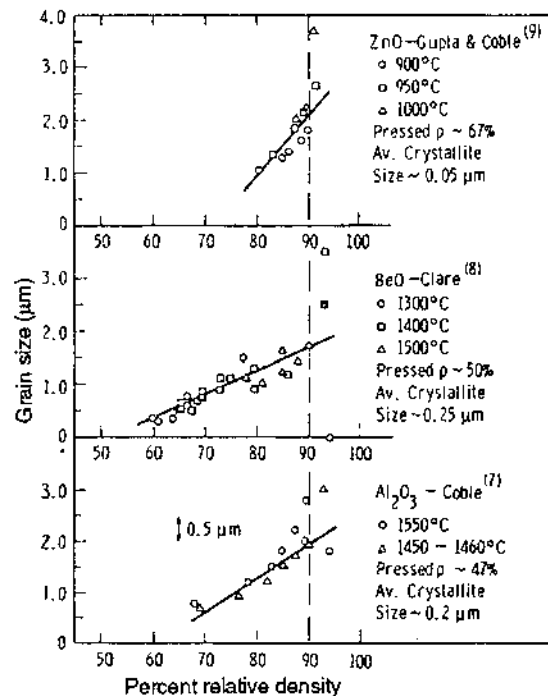


FIGURE 9.33 Simultaneous plots of density versus grain size for Al_2O_3 , BeO , and ZnO . (From Ref. 74.)

tems. Figure 9.35 shows an example of a pore network in a partially sintered compact of ZnO with a relative density of 0.73. The pictures are a stereo pair of an epoxy resin replica of the network. The replica was obtained by forcing the epoxy resin, under high pressure, into the partially sintered compact, and after curing of the resin, the ZnO was dissolved away in an acid solution. While the closed porosity cannot be viewed by this method, the complexity of the pore network in a real powder compact is readily apparent.

We may expect that for a compact formed from fully dense particles, the porosity is initially all connected. As sintering proceeds, more and more of the open porosity is converted to closed porosity. The conversion is, however, dependent on the packing uniformity of the structure. For a heterogeneously packed structure, the variation of the open and closed porosity may show trends similar to those of Fig. 9.36 for a UO_2 powder compacted in a die (76). Initially, the total porosity of the UO_2 compact was 0.37, made up of an open porosity of 0.36 and closed porosity of 0.01. During sintering at 1400°C , the open porosity

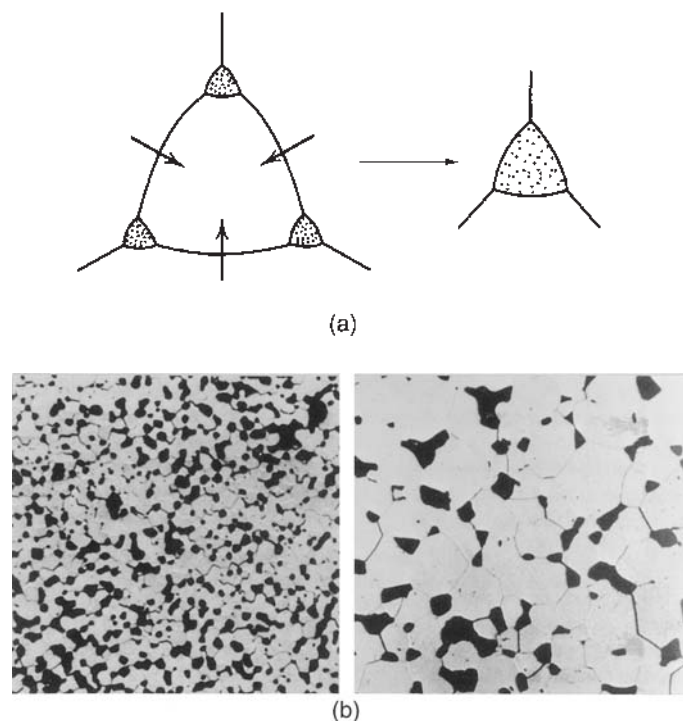


FIGURE 9.34 (a) Schematic illustration of grain growth accompanied by pore coalescence. (b) Grain growth and pore coalescence in a sample of UO_2 after 2 min, 91.5% dense and 5 h, 91.9% dense, at 1600°C (magnification $400\times$). (From Ref. 75.)

decreased continuously, whereas the closed porosity increased initially to 0.04 but returned to the value of 0.01. This initial variation in the closed porosity may be due to the sintering of fairly dense agglomerates. When the open porosity had decreased to 0.15, the closed porosity began to increase again and reached a maximum value of 0.05, after which it decreased with further sintering. For a homogeneously packed powder, we may expect the conversion to closed porosity to occur later and more suddenly. Compared to the UO_2 results in Fig. 9.36, a greater fraction of the total porosity may remain as an open network even after the compact has reached relative densities as high as 0.90.

The evolution of the pore network is difficult to analyze quantitatively. Experimentally, very few attempts have been made to produce a detailed stereological characterization of the evolution of the network. Such characterization is very time-consuming, requiring detailed quantitative microscopy of a series of

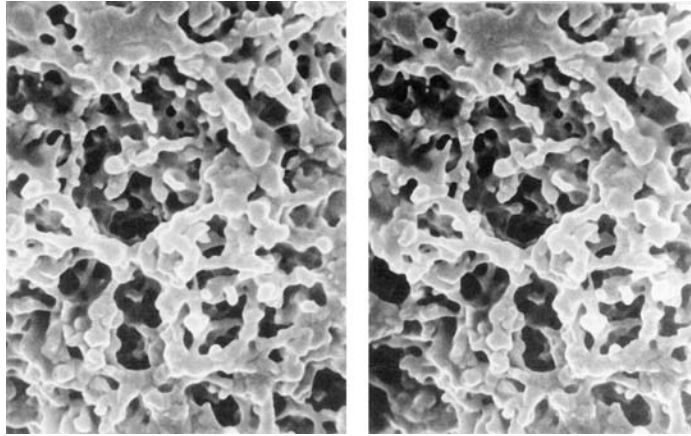


FIGURE 9.35 Stereographic pair of a replica of the pore space in a partially densified ZnO powder compact (density 73% of the theoretical). (Courtesy of M-Y. Chu.)

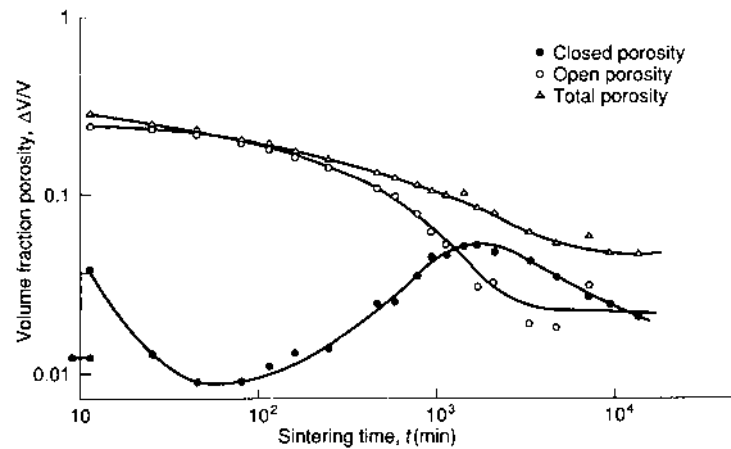


FIGURE 9.36 Change in porosity during the sintering of a UO_2 powder compact at 1400°C . (From Ref. 76.)

partially sintered samples. On the basis of such stereological observations, Rhines and DeHoff (77) deduced that the evolution of the pore network contained features which were comparable to those of other topological decay processes, such as grain growth in fully dense polycrystalline solids (see Sec. 9.5.3). The pore network, consisting of channels and junctions, changes by the collapse of pore channels and the reforming of a new network of lower connectivity (Fig. 9.37). While providing a more realistic picture of the evolution of the pore network, the topological model does not provide information on the kinetics of the coarsening process or how such coarsening can be controlled.

9.8.2 Thermodynamics of Pore-Boundary Interactions

As discussed in Chapter 8, whether a pore shrinks or not is dependent on the free energy change that accompanies the change in pore size. If the pore shrinks,

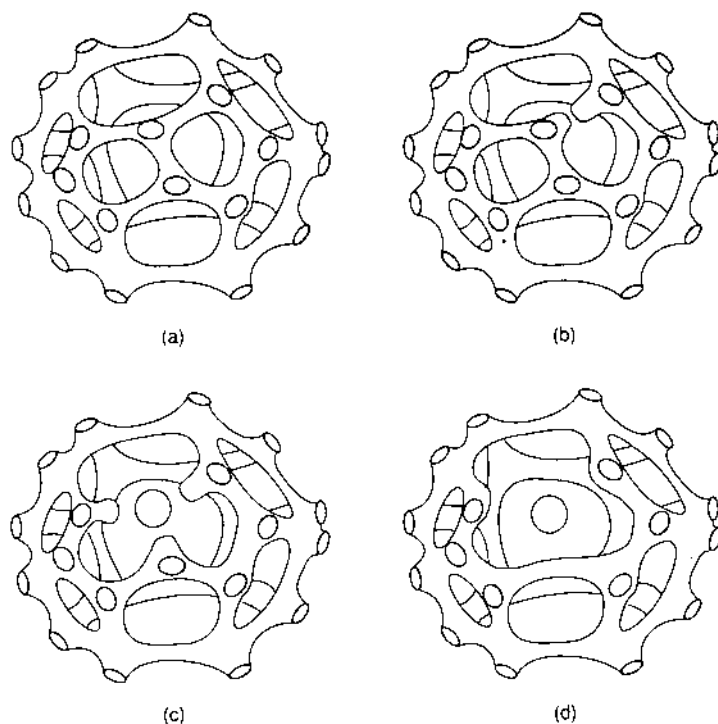


FIGURE 9.37 Sequence of pore channel collapse in a porous sintering solid. The sequential collapse can be envisioned as the coarsening process leaving a larger pore network as well as isolated pores. (From. Ref. 77.)

there will be a *decrease* in the free energy resulting from the decrease in the pore surface area but also an *increase* due to the increase in the grain boundary area. For the pore to shrink, the former (decrease) must be greater than the latter (increase). It will also be recalled (see Fig. 8.4) that the equilibrium shape of the pore is dictated by the dihedral angle ψ defined by

$$\cos \frac{\Psi}{2} = \frac{\gamma_{gb}}{2\gamma_{sv}} \quad (9.74)$$

where γ_{sv} and γ_{gb} are the interfacial tensions at the pore surface and in the grain boundary interface, respectively.

Let us consider, in two dimensions, a pore with a dihedral angle $\psi = 120^\circ$ which is surrounded by N grains. The number N is called the *pore coordination number*. Following our earlier discussion for the case of a grain surrounded by other grains, the pore has straight sides if $N = 6$, convex sides for $N < 6$ and concave sides for $N > 6$ (Fig. 9.38). The surface of the pore will move towards its center of curvature, so the pore with $N < 6$ will shrink, whereas the one with $N > 6$ will grow. The pore is metastable for $N = 6$, and this number is called the *critical pore coordination number*, denoted N_c . In fact, it can be shown that for the pore with convex sides ($N < 6$), the decrease in the pore surface energy is greater than the increase in the grain boundary energy, whereas for the pore with concave sides ($N > 6$), the decrease in pore surface energy is smaller than the increase in grain boundary energy. For the metastable situation ($N = 6$), the decrease in pore surface energy exactly balances the increase in grain boundary energy. We can go on to consider other dihedral angles; for example, $N_c = 3$ for $\psi = 60^\circ$. The general result is that N_c decreases with the dihedral angle. The two parameters are connected by a simple geometrical relationship given by $\Psi = (180N_c - 360)/N_c$.

The geometrical considerations can be extended to three dimensions, in which case the pore is a polyhedron. The analysis has been carried out by Kingery and Francois (78). Taking r_s as the radius of curvature of the circumscribed sphere around a polyhedral pore surrounded by grains, the ratio of the radius of curvature of the pore, r to r_s depends both on the dihedral angle and the pore coordination number, as shown in Fig. 9.39. When the surfaces of the pore become flat ($r = \infty$), the pore is metastable and there is no tendency for the pore to grow or shrink. The ratio r_s/r is zero, and this condition defines N_c . The value of N_c as a function of the dihedral angle is plotted in Fig. 9.40. As an example, for a pore with a dihedral angle of 120° , we find that $N_c = 12$, so a pore with $N < 12$ will shrink, whereas one with $N > 12$ will grow. A refinement of the analysis by Cannon (79) indicates that the pore with $N > N_c$ may not grow continuously but may reach some limiting size.

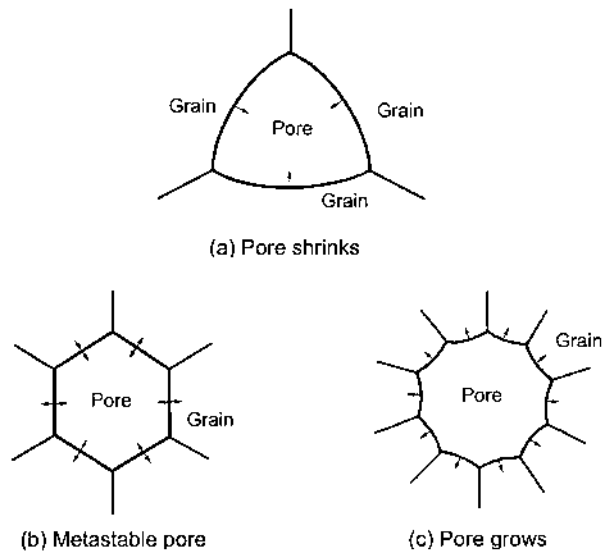


FIGURE 9.38 Pore stability in two dimensions for a dihedral angle of 120° .

From this discussion, we see that a poorly compacted powder containing pores that are large compared to the grain size, would be difficult to densify, especially if the dihedral angle is low, because the pore coordination number is large. One practical solution to the difficulty of densification is to prepare compacts with reasonably high green density and a fairly uniform pore size distribution by cold isostatic pressing or by colloidal methods, so that the fraction of pores with $N > N_c$ is minimized.

9.8.3 Kinetics and Mechanisms of Grain Growth in Porous Solids

Grain growth in porous ceramics is complex, but a few limiting cases can be discussed. Grain growth in very porous ceramics characteristic of the early stage of sintering is limited, but because of the complexity of the microstructure, a detailed analysis of the coarsening process has not been performed. Instead, our understanding of the process is at a qualitative level. In less porous ceramics characteristic of the later stage of sintering, grain growth has been commonly analyzed in terms of an idealized microstructure consisting of a nearly spherical pore on an isolated grain boundary.

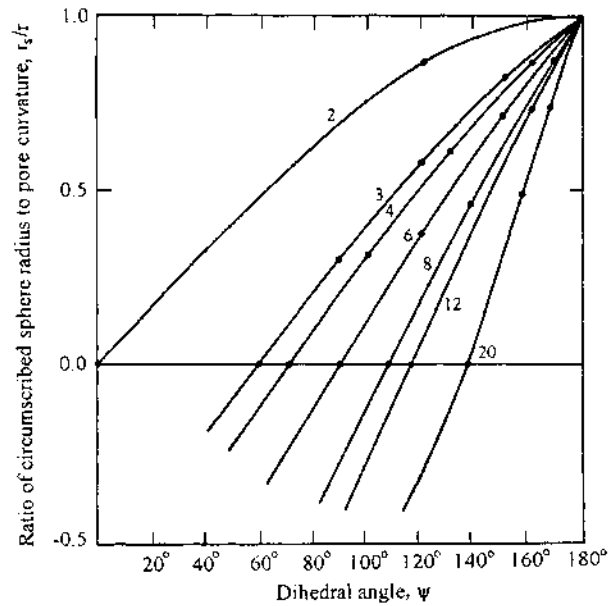


FIGURE 9.39 Change in the ratio r_s/r with dihedral angle for pores surrounded by different numbers of grains as indicated on the individual curves. (From Ref. 78.)

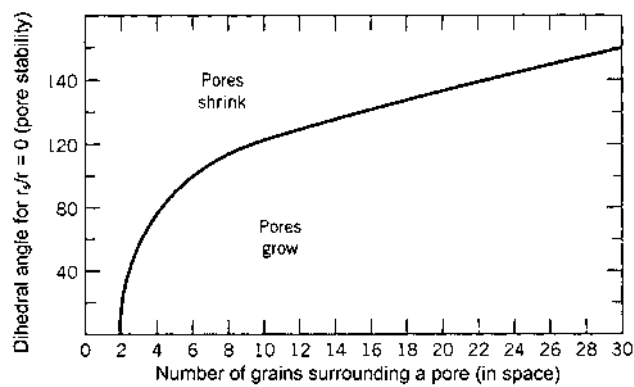


FIGURE 9.40 Conditions for pore stability in three dimensions as a function of pore coordination number. (From Ref. 78.)

9.8.3.1 Grain Growth in Very Porous Solids

For a model consisting of two originally spherical particles separated by a grain boundary, which can be taken as a rough approximation to the microstructure in the initial stage of sintering, migration of the boundary is difficult. As sketched in Fig. 9.41, the balance of interfacial tensions requires that the equilibrium dihedral angle of the grain boundary groove at the surface of the sphere be maintained. Migration of the boundary would actually involve a significant *increase* in the grain boundary area. The occurrence of grain growth is energetically unfavorable unless other processes that significantly reduce this energy barrier come into play.

One way in which grain growth can occur was suggested by Greskovich and Lay (80) on the basis of observations of the coarsening of Al_2O_3 powder compacts. Figure 9.42 illustrates the development of the porous Al_2O_3 microstructure during sintering at 1700°C . The green compact (Fig. 9.42a) consists of individual grains with a large amount of open porosity. In going from Fig. 9.42a to Fig. 9.42b, the relative density increased from 0.31 to 0.40, but even in such very porous structures, the average grain size has nearly doubled.

The model put forward by Greskovich and Lay is shown in Fig. 9.43 for two particles and for a cluster of particles. For two particles that differ in size, surface diffusion is assumed to assist in the rounding of the particles and the growth of the necks between the particles. Whether the boundary can migrate depends on whether the structure permits it, i.e., there must be a decrease in the total energy of the system for an incremental movement of the boundary. As sketched for the two particles, it is assumed that surface diffusion produces the structural changes for the movement of the boundary to be favorable. The rate of migration of the boundary depends on the difference in initial size between

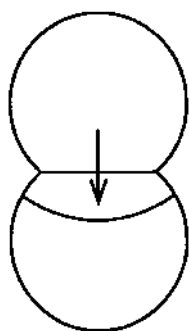


FIGURE 9.41 For an idealized initial stage microstructure, grain growth increases the total grain boundary area between two spheres. The dihedral angle constraint at the surface of the sphere creates a boundary curvature that opposes grain growth.

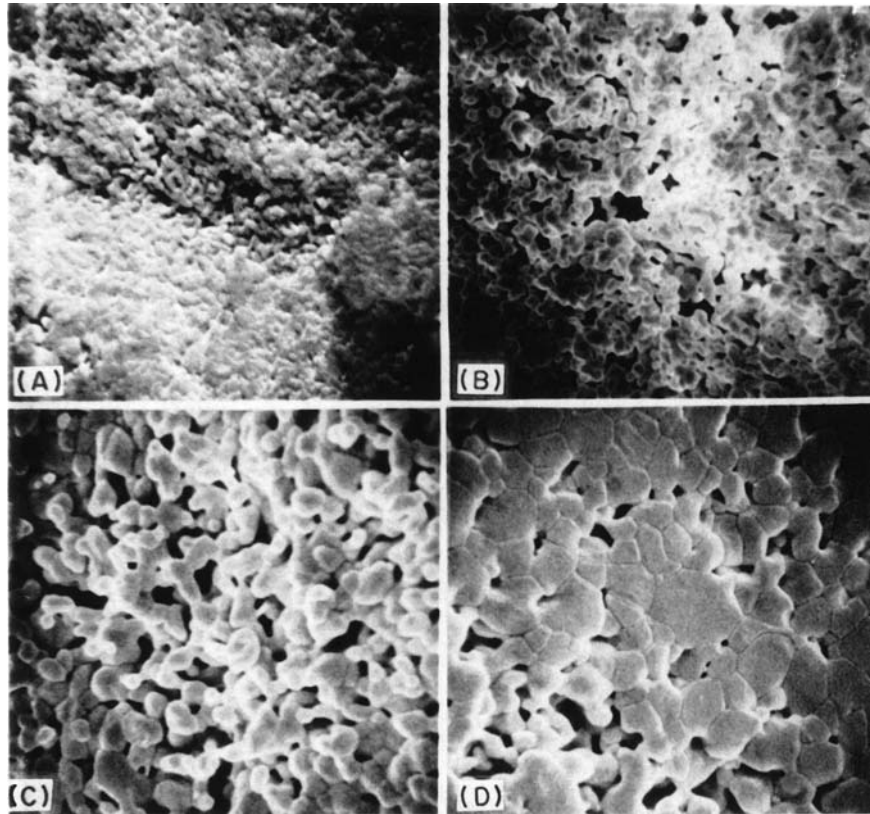


FIGURE 9.42 Development of the microstructure of an MgO-doped Al_2O_3 powder compact during sintering at 1700°C . (A) Green compact, (B) 1 min, (C) 2.5 min, and (D) 6 min (magnification $5000\times$). (From Ref. 80.)

the particles: the greater the difference in size, the greater the curvature of the boundary and the greater the driving force for the boundary to sweep through the smaller grain. Neck growth between the grains is likely to be much slower than the migration of the boundary so that it controls the rate of the overall coarsening process.

While Greskovich and Lay considered surface diffusion to be the dominant neck growth mechanism, vapor transport may also be important in systems with fairly high vapor pressures. Furthermore, coarsening controlled by neck growth is not expected to be the only process operating in fairly porous systems. A heterogeneously packed powder compact will, after some sintering, contain fairly

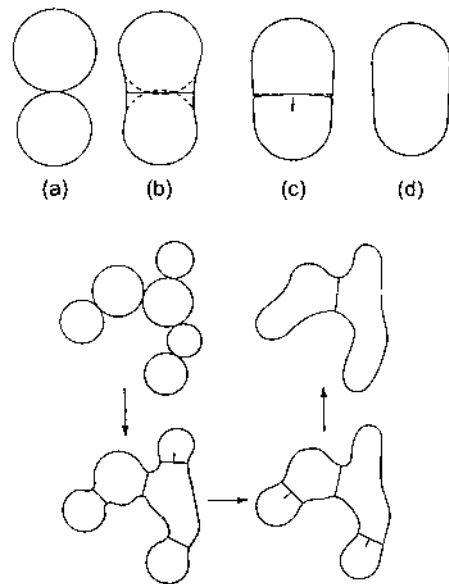


FIGURE 9.43 Qualitative mechanism for grain growth in porous powder compacts. *Top:* Two particles. (a) Particles of slightly different size in contact; (b) neck growth by surface diffusion between the particles; (c) grain boundary migrating from the contact plane; and (d) grain growth. *Bottom:* A cluster of particles. Arrows on the grain boundaries indicate the direction of boundary movement. (From Ref. 80.)

porous regions as well as fairly dense regions (Fig. 9.42d). For this type of structure, coarsening is likely to be controlled by two separate mechanisms: (1) neck growth in the fairly porous regions and (2) curvature-driven boundary migration in the fairly dense regions.

Another way in which grain growth can occur in porous compacts was described by Edelson and Glaeser (81). As sketched in Fig. 9.44a, if large grain size differences exist at the necks between the particles, elimination of grain boundaries by the advancing boundary releases enough energy to make the overall process favorable. In this way, the finer neighboring grains can be consumed in an incremental growth process. Figure 9.44b shows that the growing grain can also entrap porosity, a process that can limit the density of the final article. However this process is less likely to occur in the earlier stages of sintering because the fairly large, continuous pores that are closely spaced provide a significant drag on the boundary and limit its mobility.

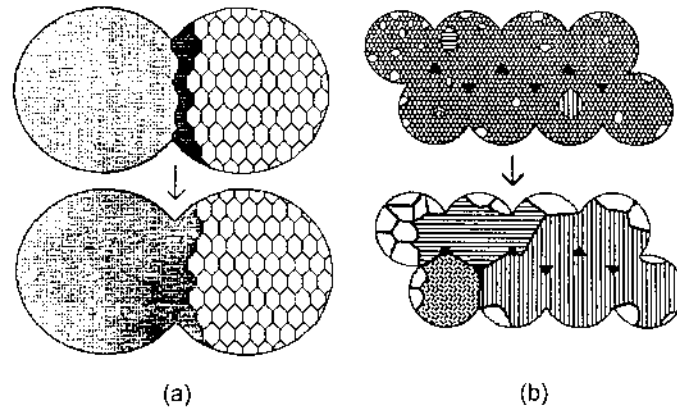


FIGURE 9.44 Growth of intra-agglomerate grains through polycrystalline necks. (a) Growth of a large grain proceeds across a neck by incremental consumption of smaller grains. (b) Exaggerated intra-agglomerate crystalline growth results in the development of large grains in the early stage of sintering. The resulting grain structure may contain some large grains that grow abnormally during inter-agglomerate sintering. (From Ref. 81.)

9.8.3.2 Grain Growth in Less Porous Solids

Grain growth in the later stages of sintering is often discussed in terms of an idealized final stage sintering model consisting of small, isolated spherical pores situated at the grain boundaries. In the analysis of the grain growth, the approach is to consider an isolated region of the grain boundary containing a single pore and assume that the kinetic equations derived for the model represents the average behavior of the whole system. By adopting this approach, we are assuming that the microstructure is homogeneous. The approach may be viewed as being equivalent to that of Burke and Turnbull for dense solids but with the added complication of the interaction of a pore and the grain boundary.

Two cases may be distinguished depending on whether the pores are either *immobile* or *mobile*. The case of immobile pores on the grain boundary can be described in terms of the Zener analysis discussed earlier for pinning particles. In principle, if the drag exerted by the pores is sufficiently high, the boundary will be pinned and boundary migration will stop. A limiting grain size, G_L will be reached, given by

$$G_L = \frac{2\alpha}{3} \frac{r}{P} \quad (9.75)$$

where r is now the pore radius, P is the porosity, and α is a geometrical factor that depends on the pore shape. If the drag exerted by the pores is insufficient, the boundary will break away, leaving the pores trapped in the grains. Observations of ceramic microstructures do not provide convincing evidence for Eq. (9.75). Instead much of the evidence is in favor of mobile pores.

9.8.3.3 Pore Mobility

Small, isolated pores situated at the grain boundary can be dragged along by the moving grain boundary. The reason is that the boundary moving under the influence of its curvature applies a force on the pore causing the pore to change its shape, as illustrated in Fig. 9.45. The leading surface of the pore becomes less strongly curved than the trailing surface. The difference in curvature leads to a chemical potential difference that drives matter flux from the leading surface to the trailing surface. The result is that the pore moves forward in the direction of the boundary motion. Matter transport from the leading surface to the trailing surface can occur by three separate mechanisms: vapor transport (evaporation/condensation), surface diffusion, and lattice diffusion.

The flux of matter from the leading surface to the trailing surface of the pore can be analyzed to derive an equation for the pore mobility M_p . By analogy with the case of a moving boundary, the pore velocity v_p is defined by a force-mobility relationship,

$$v_p = M_p F_p \quad (9.76)$$

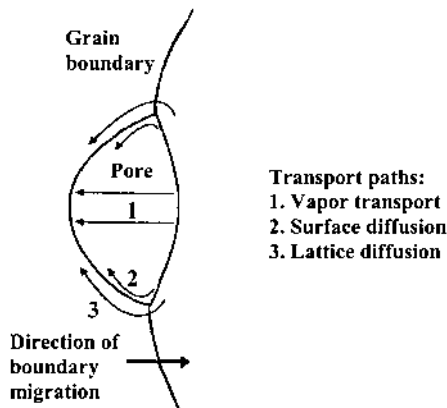


FIGURE 9.45 Possible transport paths for a pore moving with a grain boundary: (1) vapor transport (evaporation and condensation); (2) surface diffusion; (3) lattice diffusion.

where F_p is the driving force acting on the pore. Let us consider a pore of average radius r in which matter transport occurs by surface diffusion from the leading surface to the trailing surface (82). The net atomic flux is

$$J_s A_s = \left(\frac{D_s}{\Omega k T} F_a \right) 2\pi r \delta_s \quad (9.77)$$

where J_s is the flux of atoms, A_s is the area over which surface diffusion occurs, D_s is the surface diffusion coefficient, Ω is the atomic volume, F_a is the driving force on an atom, δ_s is the thickness for surface diffusion, k is the Boltzmann constant, and T is the absolute temperature. If the pore moves forward a distance dx in a time dt , the volume of matter which must be moved per unit time is $\pi r^2 dx/dt$. Equating the number of atoms moved to the net flux gives

$$\frac{\pi r^2}{\Omega} \frac{dx}{dt} = - \frac{D_s 2\pi r \delta_s}{\Omega k T} F_a \quad (9.78)$$

where the negative sign is inserted because the flux is opposite to the direction of motion. The work done in moving the pore a distance dx is equal to that required to move $\pi r^2 dx/\Omega$ atoms a distance $2r$, so

$$F_p dx = -F_a \frac{\pi r^2 dx}{\Omega} 2r \quad (9.79)$$

Substituting for F_a from Eq. (9.78) and rearranging gives

$$F_p = \frac{\pi r^4 k T}{D_s \delta_s \Omega} \frac{dx}{dt} \quad (9.80)$$

Putting the velocity of the pore v_p equal to dx/dt , the pore mobility is given by

$$M_p = \frac{D_s \delta_s \Omega}{\pi k T r^4} \quad (9.81)$$

The pore mobility for matter transport by vapor transport or by lattice diffusion can be derived by a similar procedure, and the formulae are summarized in Table 9.2. For all three mechanisms, M_p is found to have a strong dependence on r , decreasing rapidly with increasing r . Fine pores are highly mobile and therefore better able to remain attached to the moving boundary during grain growth. In practice, strategies for avoiding breakaway of the boundary from the pore (abnormal grain growth) are based mainly on suppressing M_b by the solute drag mechanism discussed earlier.

TABLE 9.2 Pore and Boundary Parameters

A. Mobilities ^a		
M_p	Mobility of spherical pore; migration by faster of	
	(a) Surface diffusion	$\frac{D_s \delta_s \Omega}{kT\pi r^4}$
	(b) Lattice diffusion	$\frac{D_l \Omega}{fkT\pi r^3}$
	(c) Vapor transport	$\frac{D_g d_g \Omega}{2kTd_s \pi r^3}$
M_b	Mobility of boundary Pure system	$\frac{D_a \Omega}{kT\delta_{gb}}$
	Solute drag	$\frac{\Omega}{kT\delta_{gb}} \left(\frac{1}{D_a} + \frac{4N_V \Omega Q C_\infty}{D_b} \right)^{-1}$
B. Forces ^b		
F_p	Maximum drag force of pore	$\pi r \gamma_{gb}$
F_b	Force per unit area of pore- free boundary	$\frac{\alpha \gamma_{gb}}{G}$

^a f = correlation factor; d_g = density in the gas phase of the rate-controlling species; d_s = density in the solid phase of the rate-controlling species.

^b α = geometrical constant depending on the grain shape (e.g., $\alpha = 2$ for spherical grains).

Source: Adapted from Ref. 1.

9.8.4 Kinetics of Pore-Boundary Interactions

The definition of the pore mobility allows us to go on to analyze how the interactions between the pores and the grain boundaries influence the kinetics of grain growth. There are two cases that can be considered: (1) the pore becomes separated from the boundary and (2) the pore remains attached to the boundary.

Pore separation will occur when $\nu_p < \nu_b$, and this condition can also be written as

$$F_p M_p < F M_b \quad (9.82)$$

where F is the effective driving force on the boundary. If F_d is the drag force exerted by a pore, then a balance of forces requires that F_d is equal and opposite to F_p . Considering unit area of the boundary in which there are N_A pores, Eq. (9.82) can be written

$$F_p M_p < (F_b - N_A F_p) M_b \quad (9.83)$$

where F_b is the driving force on the pore-free boundary due to its curvature. Rearranging Eq. (9.83), the condition for pore separation can be expressed as

$$F_b > N_A F_p + \frac{M_p F_p}{M_b} \quad (9.84)$$

The condition for pore attachment to the boundary is $v_p = v_b$, which can also be written as

$$F_p M_p = (F_b - N_A F_p) M_b \quad (9.85)$$

Putting $v_p = F_p M_p = v_b$ and rearranging gives

$$v_b = F_b \frac{M_p M_b}{N_A M_b + M_p} \quad (9.86)$$

Two limiting conditions can be defined. When $N_A M_b \gg M_p$, then

$$v_b = \frac{F_b M_p}{N_A} \quad (9.87)$$

The effective driving force on the boundary is $F = F_b - N_A F_p$, and using Eq. (9.85) gives $F = v_p / M_b$. Putting $v_p = v_b = F_b M_p / N_A$ gives $F = F_b M_p / N_A M_b \ll F_b$. The driving force on the boundary is nearly balanced by the drag of the pores, and the boundary motion is limited by the pore mobility. This condition is referred to as *pore control*. The other limiting condition is when $N_A M_b \ll M_p$, in which case

$$v_b = F_b M_b \quad (9.88)$$

The drag exerted by the pores is $N_A F_p = N_A (F_b M_b / M_p) \ll F_b$. The presence of the pores has almost no effect on the boundary velocity, a condition referred to as *boundary control*.

9.8.5 Grain Growth Kinetics

For the simplified model consisting of nearly spherical isolated pores on the grain boundary, we can derive equations for the grain growth kinetics. Consider the

situation of grain growth controlled by the pore mobility (pore control). If pore migration occurs by surface diffusion, then Eqs. (9.81) and (9.87) give

$$v_b \approx \frac{dG}{dt} = \frac{F_b}{N_A} \frac{D_s \delta_s \Omega}{\pi k T r^4} \quad (9.89)$$

Taking $F_b \sim 1/G$, $N_A \sim 1/X^2 \sim 1/G^2$, where X is the interpore distance, and assuming coarsening by grain growth and pore coalescence so that $r \sim G$, after some rearranging, Eq. (9.89) becomes

$$\frac{dG}{dt} = \frac{K_1}{G^3} \quad (9.90)$$

where K_1 is a constant at a given temperature. After integration we obtain

$$G^4 = G_0^4 + K_2 t \quad (9.91)$$

where G_0 is the grain size at $t = 0$ and K_2 is a constant. Grain growth equations can be derived by the same procedure for the other mechanisms.

Using the general form of the grain growth equation as $G^m = G_0^m + Kt$, the exponent m for the various mechanisms are summarized in Table 9.3. Except for the mechanism involving solution of second phase particles ($m = 1$), the m values lie in the range 2 to 4. In many ceramics, the value $m = 3$ has often been reported, and it is seen that this value can correspond to at least five different mechanisms. Attaching physical significance to the m values determined from grain growth data can therefore be very dubious. Furthermore, the fitting of experimental data to produce m values that are exact whole numbers may not be realistic because the occurrence of simultaneous mechanisms is likely to give m values that are not integers. We must also remember the many approximations used in the derivation of the equations, including a structurally homogeneous compact, isotropic grain boundary energy, and isolated spherical pores at the grain boundary interfaces. These conditions are rarely achieved in real powder compacts.

9.9 SIMULTANEOUS DENSIFICATION AND GRAIN GROWTH

In our consideration of solid state sintering, we have so far treated the processes of densification and grain growth (coarsening) separately. However, as sketched in Fig. 9.46 for a final stage microstructure, the two processes occur simultaneously, and the extent of one process will influence the rate at which the other can proceed. To be able to understand and control the sintering process, both densification and coarsening must be considered and the interaction between them addressed. In addressing this interaction, we should remember that each process by itself is fairly complex and that the models provide only a qualitative under-

TABLE 9.3 Grain Growth Exponent m in the Equation $G^m = G_0^m + Kt$ for Various Mechanisms

Mechanism ^a	Exponent m
Pore control	
Surface diffusion	4
Lattice diffusion	3
Vapor transport (vapor pressure $p = \text{constant}$)	3
Vapor transport ($p = 2\gamma_{sv}/r$)	2
Boundary control	
Pure system	2
System containing second-phase particles	
Coalescence of second phase by lattice diffusion	3
Coalescence of second phase by grain boundary diffusion	4
Solution of second phase	1
Diffusion through continuous second phase	3
Doped system	
Solute drag (low solubility)	3
Solute drag (high solubility)	2

^aThe pore control kinetics are given for the situation where the pore separation is related to the grain size, i.e., the number of pores per unit area of the boundary $N_A \sim 1/G^2$. Changes in distribution during growth would change the kinetics.

Source: Ref. 1.

standing of each process in practical systems. Faced with this situation, it appears unlikely that a detailed theoretical analysis of the coupling of densification and coarsening would provide any significant advantage for understanding and controlling sintering. A simpler approach that seeks to provide a qualitative understanding of the interaction may be more useful in practice.

9.9.1 Brook Model

A treatment of the simultaneous densification and grain growth processes and the transition to abnormal grain growth was developed by Brook (83). Assuming an idealized final stage microstructure consisting of a nearly spherical pore on an isolated grain boundary, it involves the determination of the transition from pore drag controlled boundary migration to intrinsic or solute drag boundary migration with the pores either attached or separated from the boundary as functions of grain size G and pore size $2r$. As discussed earlier, the conditions for attachment of the pore to the boundary fall into two limiting cases: *pore control* and *boundary control*. The conditions that separate these two cases are represented

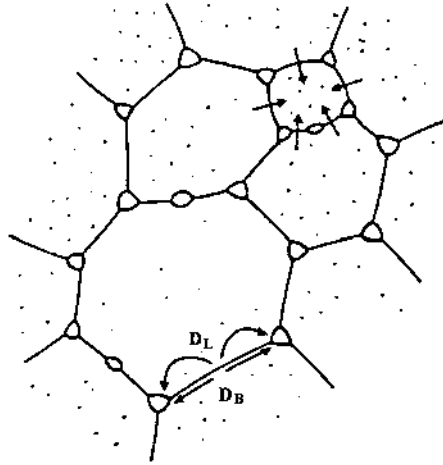


FIGURE 9.46 Late stage sintering of a powder compact. The two contributions to free energy reduction are (1) densification (lower part of figure) where the arrows show the direction of atom flow and (2) coarsening or grain growth (top right) where the arrows show the direction of boundary movement. (From Ref. 90.)

by a curve, called the *equal mobility curve*, defined by the condition that the pore mobility is equal to the boundary mobility, that is,

$$N_A M_b = M_p \quad (9.92)$$

Assuming that pore migration occurs by *surface diffusion*, the appropriate relations for M_b and M_p can be found in Table 9.2. Using the approximation that $N_A \approx 1/X^2$, where X is the interpore distance, and taking $X \approx G$, Eq. (9.88) gives

$$G_{em} = \left(\frac{D_a \pi}{D_s \delta_s \delta_{gb}} \right)^{1/2} r^2 \quad (9.93)$$

where G_{em} is the grain size defined by the equal mobility condition. Using logarithmic axes for a plot of G versus $2r$ (Fig. 9.47), the equal mobility condition is represented by a straight line with a slope of 2.

In determining the conditions for separation of the boundary from the pore, we recall that the maximum force exerted by the grain boundary on a pore to drag it along is given by Eq. (9.51), that is

$$F_p^{\max} = \pi r \gamma_{gb} \quad (9.94)$$

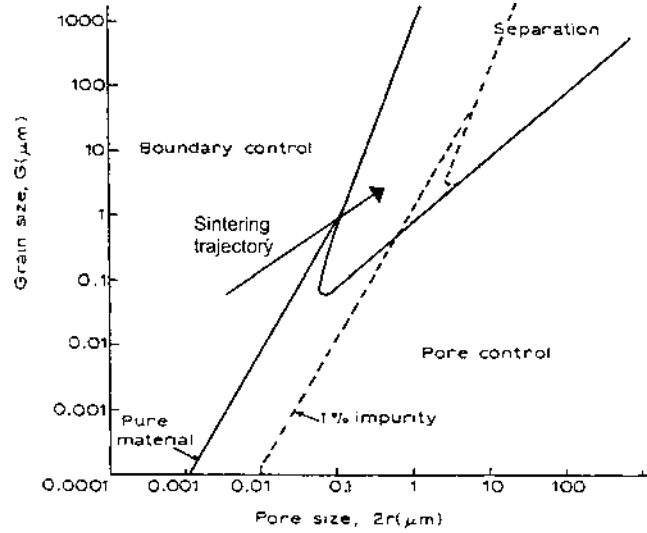


FIGURE 9.47 The dependence of the type of pore-boundary interaction on microstructural parameters when pores migrate by surface diffusion. The interpore spacing is assumed to be equal to the grain size. (From Ref. 83.)

The maximum velocity that the pore can attain is therefore

$$v_p^{\max} = M_p F_p^{\max} \quad (9.95)$$

If the velocity of the boundary with the attached pore were to exceed v_p^{\max} , then separation will occur. The limiting condition for separation can therefore be written as

$$v_b = v_p^{\max} \quad (9.96)$$

Substituting for v_b from Eq. (9.86), we obtain

$$\frac{M_b M_p}{N_A M_b + M_p} F_b = M_p F_p^{\max} \quad (9.97)$$

Putting $N_A \approx 1/X^2$ and substituting for the other parameters from Table 9.2, after some rearranging Eq. (9.97) gives

$$G_{sep} = \left(\frac{\pi r}{X^2} + \frac{D_s \delta_s \delta_{gb}}{D_a r^3} \right)^{-1} \quad (9.98)$$

where G_{sep} is the grain size when the boundary separates from the pore. Assuming that $X \approx G$, Eq. (9.98) can be written

$$\left(\frac{D_s \delta_s \delta_{gb}}{D_a r^3} \right) G_{sep}^2 - G_{sep} + \pi r = 0 \quad (9.99)$$

The solution to this quadratic equation determines the *separation curve* shown in Fig. 9.47.

To allow for the use of quantitative axes for the G versus $2r$ diagram in Fig. 9.47, Brook used realistic values taken from the literature for the parameters in Eqs. (9.93) and (9.99). Qualitatively, three basic types of pore-boundary interactions are found in the diagram. For larger, less mobile pores that are closely separated, the pores remain attached to the boundary and control the motion. In another region of the diagram, smaller, more mobile pores remain attached to the boundary, and they do not exert a significant drag on the boundary; the boundary migration is therefore controlled by the boundary mobility. The third region occurs for larger pores that are widely separated, where boundary-controlled migration occurs with pores separated. For the achievement of high density with controlled grain size, this separation region must be avoided.

Dopants, as discussed earlier, have the effect of reducing M_b . In the G versus $2r$ diagram, this has the effect of extending the region of pore attachment (Fig. 9.47). In terms of this diagram, a possible explanation of the effectiveness of dopants is that they delay the onset of abnormal grain growth (pore separation) beyond the grain size at which final densification is achieved.

Possible trajectories for sintering can be identified on the basis of the G -versus- $2r$ diagram. As outlined earlier, grain growth and pore coalescence often contribute to the coarsening of porous ceramics, particularly in the later stages of sintering, thereby resulting in an increase in both the average grain size and the average pore size during sintering. For this situation, a possible trajectory for the microstructural evolution runs diagonally upward from left to right (Fig. 9.47). According to this representation, it is likely that the interaction changes from boundary control (with possibly a small region of pore control) to separation.

The kinetic analysis of the pore-boundary interactions and its representation in terms of the G -versus- $2r$ diagram provide a qualitative basis for understanding microstructural evolution during the later stages of sintering, but because of the considerable simplifying assumptions in the geometry and microstructure, the treatment may be inadequate for describing the microstructural evolution of real systems. It is to be expected that factors such as grain size distribution, the number of pores at the grain boundaries, and the dihedral angle will affect the simple relationships between grain boundary curvature and pore size assumed in the analysis for the separation condition (84).

A refinement to Brook's basic treatment was introduced by Carpay (85), who observed that when pore separation occurs, the assumption $X \approx G$ is no longer valid. By solving Eq. (9.99) for fixed values of X (in the range of 1–4 μm), the most significant result of this refinement is that after a region of separation, the boundary may again become attached to the pores. Hsueh et al. (86,87) considered the effect of dihedral angle. As shown in Fig. 9.48, the effective area of the boundary intersected by a pore of constant volume increases as the dihedral angle decreases, resulting in greater pore drag and less likelihood of the boundary separating from the pore. The effects of a grain size distribution and solute drag were incorporated into the basic model by Yan et al. (88). Compared to a powder with a narrow size distribution, the critical density at which pore separation occurs is found to be significantly lower for powder compacts with a wide distribution of particle size. The statistical nature of the separation process must also be recognized. Separation of only a fraction of the pores from the boundary is sufficient to cause abnormal grain growth as opposed to the assumption in the simple analysis that all pores separate from the boundaries. In this case, the separation region in the G -versus- $2r$ diagram becomes larger as the fraction of pores required to separate from the boundary decreases.

9.9.2 Yan, Cannon, and Chowdhry Model

Another treatment of simultaneous densification and grain growth was developed by Yan, Cannon, and Chowdhry, as reported in Ref. 73. Assuming an idealized final stage microstructure consisting of tetrakaidecahedral grains with spherical pores at the grain corners, the treatment determines how the achievable final density and the extent of coarsening depend on the ratio of the coarsening rate

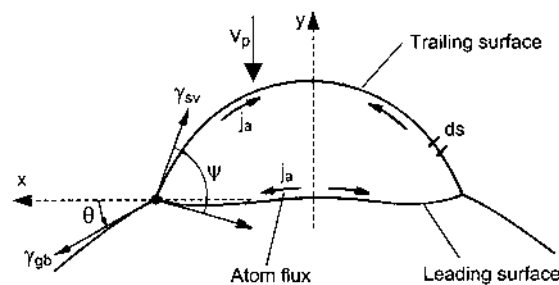


FIGURE 9.48 Schematic of the distortion that accompanies the motion of pores attached to grain boundaries and the atomic flux from the leading surface to the trailing surface. (From Ref. 87.)

to the densification rate. The instantaneous rate of change of the pore radius r is given by

$$\frac{dr}{dt} = \left(\frac{dr}{dt} \right)_p + \left(\frac{dr}{dt} \right)_G \quad (9.100)$$

where the first term on the right-hand side gives the rate of change of the pore size at constant porosity due to the coarsening process (a positive value) and the second term gives the rate of change at constant grain size due to the densification process (a negative value). For a coarsening process involving grain growth and pore coalescence, we can write

$$\frac{dr}{dt} = \frac{r}{G} \left(\frac{dG}{dt} \right)_p + \left(\frac{dr}{dt} \right)_G \quad (9.101)$$

Since $dG/dr = (dG/dt)/(dr/dt)$,

$$\frac{dG}{dr} = \frac{(dG/dt)}{(r/G)(dG/dt) + (dr/dt)_G} \quad (9.102)$$

This equation can be written

$$\frac{d \ln G}{d \ln r} = \frac{\Gamma}{\Gamma - 1} \quad (9.103)$$

where Γ is the ratio of the coarsening rate to the densification rate given by

$$\Gamma = - \frac{(r/G)(dG/dt)}{(dr/dt)_G} \quad (9.104)$$

The term Γ is calculated by assuming specific models for densification and grain growth, and it is necessary to consider simple cases where only one densification mechanism and one coarsening mechanism are dominant.

As an example, assuming the Coble model for final stage densification by grain boundary diffusion (see Chapter 8) to calculate the change in pore size with time at constant grain size, and the change in grain size with time is controlled by grain boundary migration limited by surface diffusion-controlled pore drag [see Eq. (9.87)], then

$$\Gamma = \frac{3}{176} \frac{D_s \delta_s \gamma_{gb}}{D_{gb} \delta_{gb} \gamma_{sv}} \xi \quad (9.105)$$

where D_s and D_{gb} are the surface and grain boundary diffusion coefficients, respectively, δ_s and δ_{gb} are the effective widths for surface and grain boundary

diffusion, respectively, γ_{sv} and γ_{gb} are the surface and grain boundary energies, respectively, and ξ is function of the porosity. The equations for Γ for different combinations of densification and coarsening mechanisms are given in Table 9.4.

Selection of the initial values for G and r , followed by the use of Eqs. (9.103) to (9.105) and iteration allows the calculation of the grain size versus density trajectory. Figure 9.49 shows the calculated results for different values of Γ assuming densification by grain boundary diffusion and coarsening by surface diffusion. If $\Gamma > 1$, grain growth predominates and the approach to the final density is asymptotic, so a high density may be unachievable in a realistic time. However, little grain growth occurs during densification if $\Gamma < 1$ and theoretical density is achievable.

A refinement of the treatment of simultaneous densification and grain growth was introduced by Bennison and Harmer (89) who modified the analysis of Yan, Cannon, and Chowdhry to include the conditions under which separation of the boundary from the pore occurs. The calculated results for Al_2O_3 , where densification is controlled by lattice diffusion and grain growth (coarsening) is controlled by surface diffusion-controlled pore drag, are shown in Fig. 9.50. The combined features of grain size versus density trajectory and the conditions for separation make the treatment particularly effective for discussing the influence of dopants, temperature, and other variables on microstructural evolution. Figure 9.50 indicates that the separation region is shifted to higher grain sizes by the use of MgO as a dopant which lowers the grain boundary mobility, thereby making it easier for the grain size versus density trajectory to bypass the separation

TABLE 9.4 Simultaneous Densification-Coarsening Equations for Various Rate-Controlling Mechanisms

Mechanisms		Ratio of coarsening rate/densification rate Γ
Densification	Coarsening	
Grain boundary diffusion	Surface diffusion	$\frac{3}{176} \frac{D_s \delta_s}{D_{gb} \delta_{gb}} \frac{\gamma_{gb}}{\gamma_{sv}} \xi$
Lattice diffusion	Surface diffusion	$\frac{1}{32} \frac{D_s \delta_s}{D_l r} \frac{\gamma_{gb}}{\gamma_{sv}} \xi$
Grain boundary diffusion	Boundary control	$\frac{3}{11} \frac{M_b k T r^4}{D_{gb} \delta_{gb} \Omega G^2} \frac{\gamma_{gb}}{\gamma_{sv}} \xi$

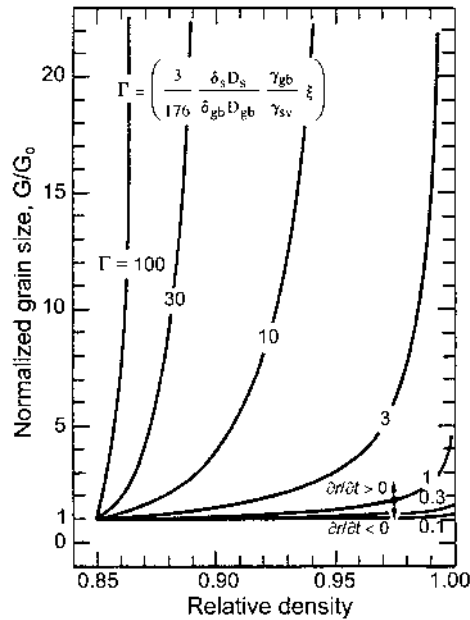


FIGURE 9.49 Grain size–density evolution during final stage sintering for different values of the ratio of the coarsening rate to the densification rate Γ , assuming coarsening by surface diffusion and densification by grain boundary diffusion. (From ref. 73.)

region. Flattening of the trajectory, that is, increasing the densification rate relative to the grain growth rate, is also beneficial and can be achieved, for example, by the use of a dopant that increases the rate of densification or reduces the boundary mobility. As described later, the trajectory can also be flattened by controlling the heating cycle during sintering, for example, by rapidly heating to a temperature where densification dominates over grain growth.

Whereas the treatment by Yan, Cannon, and Chowdhry and the refined treatment by Bennison and Harmer provide significant benefits for predicting microstructural evolution during sintering, their limitations for application to real systems must also be recognized. The treatments assume an idealized final stage microstructure and the sintering and grain growth equations derived for these idealized geometries. They also rely on the use of data for material parameters such as diffusion coefficients which may have a doubtful reliability or may have widely different values in the literature.

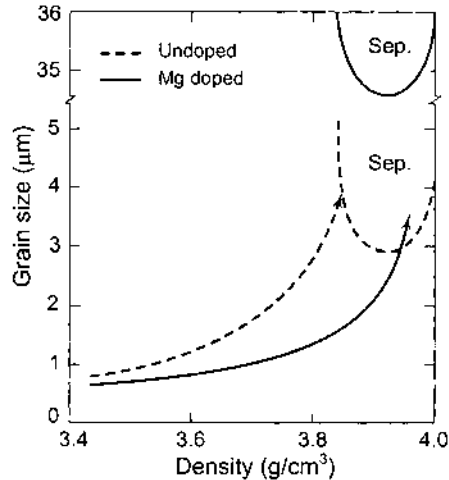


FIGURE 9.50 Grain size–density map for Al_2O_3 , illustrating the effect of raising the surface diffusion coefficient by a factor of 4, reducing the lattice diffusion coefficient by a factor of 2, and reducing the grain boundary mobility by a factor of 34. This has the effect of flattening the grain size–density trajectory and raising the separation region to larger grain sizes, thereby making it possible to sinter to full density. (From Ref. 89.)

9.10 FABRICATION PRINCIPLES FOR CERAMICS WITH CONTROLLED MICROSTRUCTURE

Most applications of ceramics require products with high density and controlled (small) grain size (90). The discussion of the previous section indicates that when suitable processing procedures are employed, such an end point is achievable through fabrication routes that have the effect of increasing the ratio of the densification rate to the grain growth (coarsening) rate or avoiding the separation region (abnormal grain growth). The principles governing these fabrication routes are discussed here, whereas the technology will be considered in Chapter 12.

Sintering with an External Pressure

When compared to sintering, hot pressing produces an increase in the driving force for densification. For an equivalent microstructure, the dependence of the densification rate on the driving force can be written

$$\dot{\rho}_{hp} \sim (\Sigma + p_a) \quad \dot{\rho}_s \sim \Sigma \quad (9.106)$$

where the subscripts hp and s refer to hot pressing and sintering, respectively, Σ is the sintering stress, and p_a is the applied pressure. Since the grain boundary mobility is unaltered,

$$\dot{G}_{hp} \approx \dot{G}_s \quad (9.107)$$

For $p_a \gg \Sigma$, we find that $(\dot{p}/\dot{G})_{hp} \gg (\dot{p}/\dot{G})_s$. According to this discussion, the effectiveness of hot pressing for the production of high density coupled with small grain size arises from the ability to increase \dot{p}/\dot{G} . For MgO-doped Al_2O_3 , the measured trajectories for the grain size versus density are shown in Fig. 9.51 for hot pressing and for sintering. The flatter trajectory for the case of hot pressing is consistent with the present discussion.

Use of Dopants

The role of dopants in sintering is fairly complex, and we shall consider this topic further in Chapter 11. We found that dopants that segregate to the grain boundary can reduce the boundary mobility by the solute drag effect, so in this case $\dot{G}_{\text{doped}} < \dot{G}_{\text{undoped}}$. Dopants may also influence the densification process, but this effect is often small compared to the effect on the grain growth rate.

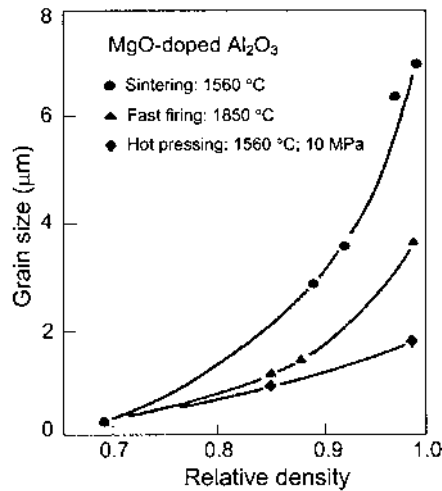


FIGURE 9.51 Experimental results for microstructural development in Al_2O_3 doped with 200 ppm MgO, showing the grain size versus density trajectories for fabrication by hot pressing, conventional sintering, and fast firing. (From Ref. 90.)

Under these conditions, the effectiveness of dopants arises from the ability to reduce \dot{G} or equivalently to increase $\dot{\rho}/\dot{G}$.

Use of Inclusions

Fine, inert inclusions, as we observed earlier, exert a drag on the grain boundary and, if the drag is large enough, may pin the boundary. They often appear not to have any significant influence on the diffusional transport of matter leading to densification. As in the case of dopants, the effectiveness of inclusions can be interpreted in terms of a decrease in \dot{G} or, equivalently, to increase $\dot{\rho}/\dot{G}$.

Uniform Packing of Fine Particles

Uniformly compacted fine powders have small pores with low coordination number (i.e., $N < N_c$). The densification rate for such a system is higher than for a similar system with heterogeneous packing. Furthermore, if the particle size distribution is narrow, the driving force for grain growth due to the curvature of the boundary is small. The effectiveness of this route can therefore be interpreted in terms of an increase in $\dot{\rho}/\dot{G}$.

Controlling the Firing Schedule

For powder systems in which the activation energy for densification is significantly greater than for grain growth (Fig. 9.52), fast heat-up to a high enough temperature where $\dot{\rho} > \dot{G}$ can provide an effective fabrication route often referred to as *fast firing*. For MgO-doped Al_2O_3 , the grain size versus density trajectory during fast firing is compared with those for hot pressing and sintering in Fig. 9.51. In this case, the benefit of fast firing over the more conventional sintering route is clear.

Liquid Phase Sintering

A second phase that forms a liquid at the firing temperature can provide a fast diffusion path for densification but grain growth by the Ostwald ripening process may also be enhanced. In this case, high density is normally accompanied by appreciable grain growth. This commonly used fabrication approach is the subject of the next chapter.

To summarize, the separation region (abnormal grain growth) that we are also trying to avoid is a moving target which depends on the porosity. Another complication is that the models used for predicting the separation region assume an idealized geometry of uniform pore size and grain size. In practice, a range of pore sizes and grain sizes exist in any given microstructure, and abnormal grain growth can occur with only *local* separation of the pore from the boundary (i.e., it is not required for all the pores to separate as assumed in the models). Generally, the sintering techniques that produce a reduction of the grain growth rate or an enhancement of the densification rate, coupled with forming methods

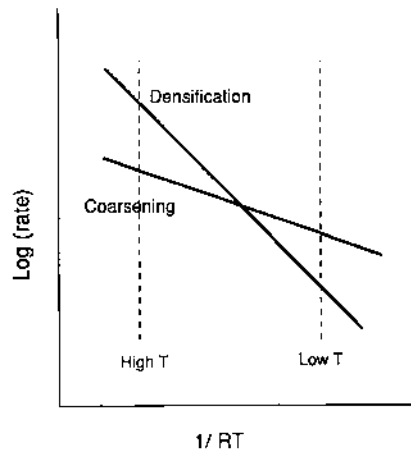


FIGURE 9.52 Under conditions where the densification mechanism has a higher activation energy than the coarsening mechanism, a fast heating rate to high firing temperatures (fast firing) can be beneficial for the achievement of high density.

that produce a homogeneous microstructure of fine pores and small interpore separation are beneficial for achieving high density.

9.11 CONCLUDING REMARKS

In this chapter we outlined the basic principles that govern microstructural development during solid-state sintering of polycrystalline ceramics. Simple models allow the derivation of equations for the kinetics of normal grain growth, but they commonly analyze a system consisting of an isolated grain boundary or a single grain and neglect the topological requirements of space filling. Computer simulations are playing an increasing role in exploring the interplay between the kinetics of grain growth and the topological requirements of space filling and provide additional insight into the grain growth process. Abnormal grain growth cannot be explained in terms of the reduction of a uniform grain boundary energy. True abnormal grain growth is believed to occur when the local driving force is higher than that resulting from the geometry or when the boundary mobility of the growing grain is higher than that of ordinary boundaries. A considerable gap exists between the theoretical understanding of microstructural evolution and the practical application to real powder systems. However, the simple models provide useful guidelines for the control of the microstructure during sintering. High density coupled with controlled grain size is achievable during sintering using

techniques that decrease the rate of grain growth (coarsening) or increase the densification rate coupled with the use of forming methods that produce a homogeneous green microstructure of fine pores with small interpore distances. Finally, if solid-state sintering is inadequate for achieving the desired end point density, then liquid phase sintering, the subject of the next chapter, provides an effective fabrication route.

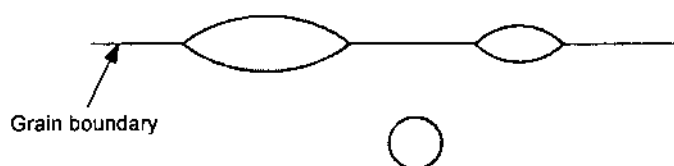
PROBLEMS

- 9.1 Distinguish between *normal* and *abnormal* grain growth. Why is it important to control normal grain growth and avoid abnormal grain growth for the achievement of high density during sintering?
- 9.2 For a dense, pure polycrystalline ZnO in which the grain growth follows normal, parabolic kinetics, the average grain size after annealing for 120 min at 1200°C is found to be 5 μm . Annealing for 60 min at 1400°C gives an average grain size of 11 μm . If the average grain size at time 0 is 2 μm , estimate what the average grain size will be after annealing for 300 min at 1300°C.
- 9.3 A dense, pure polycrystalline MgO has an average grain size of 1 μm , and the grain growth follows normal, parabolic kinetics. Estimate what the average grain size will be after 5 h annealing at 1700°C, given that the grain boundary diffusion coefficient is $D_{gb} = 10^{-8} \text{ cm}^2/\text{sec}$, the grain boundary width $\delta_{gb} = 0.5 \text{ nm}$, and the grain boundary energy $\gamma_{gb} = 0.5 \text{ J/m}^2$.

If some SiO_2 is present, leading to the formation of a continuous, liquid film with a thickness of 50 nm at the grain boundaries, estimate the change in the boundary mobility if the diffusion coefficient through the liquid D_L is

 - a. Equal to D_{gb}
 - b. Equal to $100D_{gb}$.
- 9.4 Consider the grain boundary between two spherical particles with approximately the same radius. In one case, both particles are single crystalline. In the other case, one particle is polycrystalline and the second particle is single crystalline. Compare the grain growth phenomena that may be expected to occur in the two cases.
- 9.5 Compare the densification of a homogeneously packed powder compact of 5 μm single crystalline particles with the densification of a compact of 5 μm agglomerates consisting of 0.5 μm single crystalline particles. Assume the particles have the same chemical composition.
- 9.6 Compare the conditions that control the stability of a pore in a polycrystalline ceramic with those for a pore in a glass.
- 9.7 A dense Al_2O_3 ceramic (grain size = 1 μm) contains 10 vol% of fine ZrO_2 particles that are uniformly distributed at the grain boundaries. If the particle size of the ZrO_2 is 0.2 μm , and the grain boundary energy is 0.5 J/m^2 , estimate the maximum pinning force that the ZrO_2 particles can exert on unit area of the grain boundary. If the ceramic is annealed at a high enough temperature (e.g., 1600°C), discuss the main features of the grain growth phenomena that may be expected to occur.

- 9.8 Derive the equation in Table 9.2 for the pore mobility when the pore migration is controlled by vapor transport.
- 9.9 According to the sintering equations, grain growth during sintering leads to a reduction of the densification rate. Can grain growth actually lead to densification of ceramic powder compacts? Explain your answer.
- 9.10 For a similar packing arrangement of the grains, will an increase in the dihedral angle enhance or retard pore elimination? Explain.
- 9.11 Consider a polycrystalline ceramic with pores of various sizes situated at the grain boundaries and within the grains, as sketched schematically as follows:



- a. Use arrows to sketch the possible atomic transport paths from the grain boundaries to the pores.
- b. Which pore will disappear first? Which pore will disappear last? Explain your answer.
- c. If the three pores are close enough so that the diffusion distances between the pores are relatively small, will there be any matter transported between the pores? Use arrows to show the direction of matter transport and explain your answer.

REFERENCES

1. Brook, R. J. In *Treatise on Materials Science and Technology*. Vol. 9: Ceramic Fabrication Processes; Wang, F. F. W. ed.; Academic: New York, 1976, pp. 331–364.
2. Burke, J. E. General Electric Research and Development Center. Report No. 68-C-363; Schenectady: New York, October 1968.
3. Kingery, W. D.; Bowen, H. K.; Uhlmann, D. R. *Introduction to Ceramics*; 2nd ed.; Wiley: New York, 1976.
4. Greenwood, G. W. *Acta Metall.* 1956, Vol. 4, 243.
5. Wagner, C. Z. *Electrochem.* 1961, Vol. 65, 581.
6. Lifshitz, I. M.; Slyozov, V. V. *Phys. Chem. Solids.* 1961, Vol. 19, 35.
7. Fischmeister, H.; ; Grimvall, G. *Mater. Sci. Res.* 1973, Vol. 6, 119.
8. Ardell, A. J. *Acta Metall.* 1972, Vol. 20, 61.
9. Davies, C. K. L.; Nash, P.; Stevens, R. N. *Acta Metall.* 1980, Vol. 28, 179.
10. Brailsford, A. D.; Wynblatt, P. *Acta Metall.* 1979, Vol. 27, 489.
11. Enomoto, Y.; Kawasaki, K.; Tokuyama, M. *Acta Metall.* 1987, Vol. 35, 915.
12. Smith, C. S. In *Metal Interfaces*; ASM: Cleveland, OH, 1952, pp. 65–113.
13. Atkinson, H. V. *Acta Metall.* 1988, Vol. 36, 469.
14. Burke, J. E.; Turnbull, D. *Prog. Metal Phys.* 1952, Vol. 3, 220.
15. Hillert, M. *Acta Metall.* 1965, Vol. 13, 227.

16. Feltham, P. *Acta Metall.* 1957, Vol. 5, 97.
17. Louat, N. P. *Acta Metall.* 1974, Vol. 22, 721.
18. Rhines, F. N.; Craig, K. R. *Metall. Trans.* 1974, Vol. 5A, 413.
19. Doherty, R. D. *Metall. Trans.* 1975, Vol. 6A, 588.
20. Weaire, D.; Kermode, J. P. *Phil. Mag.* 1983, Vol. B47, L29; 1983, Vol. B48, 245; 1984, Vol. B50, 379.
21. Anderson, M. P.; Srolovitz, D. J.; Grest, G. S.; Sahni, P. S. *Acta Metall.* 1984, Vol. 32, 783.
22. Srolovitz, D. J.; Anderson, M. P.; Sahni, P. S.; Grest, G. S. *Acta Metall.* 1984, Vol. 32, 793.
23. Srolovitz, D. J.; Grest, G. S.; Anderson, M. P. *Acta Metall.* 1985, Vol. 33, 2233.
24. Thompson, C. V.; Frost, H. J.; Spaepen, F. *Acta Metall.* 1987, Vol. 35, 887.
25. Rollet, A. D.; Srolovitz, D. J.; Anderson, M. P. *Acta Metall.* 1989, Vol. 37, 1227.
26. Yang, W.; Chen, L.; Messing, G. L. *Mater. Sci. Eng.* 1995, Vol. A195, 179.
27. Kunaver, U.; Kolar, D. *Acta Metall.* 1998, Vol. 46, 4629.
28. Harmer, M. P. *Ceramic Trans.* 1990, Vol. 7, 13.
29. Berry, K. A.; Harmer, M. P. *J. Am. Ceram. Soc.* 1986, Vol. 69, 143.
30. Handwerker, C. A.; Dynys, J. M.; Cannon, R. M.; Coble, R. L. *J. Am. Ceram. Soc.* 1990, Vol. 73, 1371.
31. Bennison, S. J.; Harmer, M. P. *J. Am. Ceram. Soc.* 1983, Vol. 66, C90.
32. Horn, D. S.; Messing, G. L. *Mater. Sci. Eng.* 1995, Vol. A195, 169.
33. Powers, J. D.; Glaeser, A. M. In *Sintering Technology*; German, R. M., Messing, G. L., Cornwall, R. M. eds.; Marcel Dekker: New York, 1995, pp. 333–340.
34. Bateman, C. A.; Benison, S. J.; Harmer, M. P. *J. Am. Ceram. Soc.* 1989, Vol. 72, 1241.
35. Matsuzawa, S.; Mase, S. U. S. Patent No, 4,339,301, 1981.
36. Yamamoto, T.; Sakuma, K. *J. Am. Ceram. Soc.* 1994, Vol. 77, 1107.
37. Scott, C.; Strok, J.; Levinson, L. U. S. Patent No, 5,549,746, 1996.
38. Li, T.; Scotch, A. M.; Chan, H. M.; Harmer, M. P.; Park, S. E.; Shrout, T. E.; Michael, J. R. *J. Am. Ceram. Soc.* 1998, Vol. 81, 244.
39. Becher, P. F. *J. Am. Ceram. Soc.* 1998, Vol. 81, 2821; 2831.
40. Cao, J. J.; Moberly-Chan, J. J.; De Jonghe, L. C.; Gilbert, C. J.; Ritchie, R. O. *J. Am. Ceram. Soc.* 1996, Vol. 79, 461.
41. Huang, T.; Rahaman, M. N.; Mah, T.-I.; Parthasarathay, T. A. *J. Mater. Res.* 2000, Vol. 15, 718.
42. Seabaugh, M. M.; Kerscht, I. H.; Messing, G. L. *J. Am. Ceram. Soc.* 1997, Vol. 80, 1181.
43. Horn, J. A.; Zhang, S. C.; Selvaraj, U.; Messing, G. L.; Trolier-McKinstry, S. J. *Am. Ceram. Soc.* 1999, Vol. 82, 921.
44. Yan, M. F.; Cannon, R. M.; Bowen, H. K. In *Ceramic Microstructures '76*; Fulrath, R. M., Pask, J. A. eds.; Westview Press: Boulder, CO, 1977, pp. 276–307.
45. Smith, C. S. *Trans. AIME.* 1948, Vol. 175, 15.
46. Gladman, T. *Proc. Roy. Soc.* 1966, Vol. A294, 298.
47. Haroun, N. A. *J. Mater. Sci. Lett.* 1980, Vol. 15, 2816.
48. Louat, N. *Philos. Mag. A.* 1983, Vol. 47, 903.

49. Nes, E.; Ryum, N.; Hunderi, O. *Acta Metall.* 1985, Vol. 33, 11.
50. Srolovitz, D. J.; Anderson, M. P.; Grest, G. S.; Sahni, P. S. *Acta Metall.* 1984, Vol. 32, 1429.
51. Doherty, R. D.; Srolovitz, D. J.; Rollett, A. D.; Anderson, M. P. *Scripta Metall.* 1987, Vol. 21, 675.
52. Anderson, M. P.; Grest, G. S.; Doherty, R. D.; Li, K.; Srolovitz, D. J. *Scripta Metall.* 1989, Vol. 23, 753.
53. Green, D. J. *J. Am. Ceram. Soc.* 1982, Vol. 65, 610.
54. Lange, F. F.; Hirlinger, M. J. *Am. Ceram. Soc.* 1984, Vol. 67, 164.
55. Hori, S.; Kurita, R.; Yoshimura, M.; Somiya, S. *J. Mater. Sci. Lett.* 1985, Vol. 4, 1067.
56. Kibbel, B.; Heuer, A. H. *J. Am. Ceram. Soc.* 1986, Vol. 69, 231.
57. Lange, F. F.; Yamaguchi, T.; Davis, B. I.; Morgan, P. E. D. .
58. Okada, K.; Sakuma, T. *Br. Ceram. Trans.* 1994, Vol. 93, 71.
59. Lange, F. F.; Hirlinger, M. J. *Am. Ceram. Soc.* 1987, Vol. 70, 827.
60. Stearns, L. C.; Harmer, M. P. *J. Am. Ceram. Soc.* 1996, Vol. 79, 3013; 3020.
61. Cahn, J. W. *Acta Metall.* 1962, Vol. 10, 789.
62. Lucke, K.; Stuwe, H. P. In *Recovery, and Recrystallization of Metals*; Himmel, L. ed.; Gordon and Breach: NY, 1963, pp. 171–210.
63. Hillert, M.; Sundman, B. *Acta Metall.* 1976, Vol. 24, 731.
64. Glaeser, A. M.; Bowen, H. K.; Cannon, R. M. *J. Am. Ceram. Soc.* 1986, Vol. 69, 119.
65. Chen, P.-L.; Chen, I.-W. *J. Am. Ceram. Soc.* 1994, Vol. 77, 2289.
66. Rahaman, M. N.; Zhou, Y.-C. *J. Europ. Ceram. Soc.* 1995, Vol. 15, 939.
67. Coble, R. L. U.S. Patent No. 3,026,210, 1962.
68. Brook, R. J.; Tuan, W. H.; Xue, L. A. *Ceramic Trans.* 1988, Vol. 1B, 811.
69. Rahaman, M. N.; Manalart, R. J. *Europ. Ceram. Soc.* 1998, Vol. 18, 1063.
70. Rahaman, M. N.; De Jonghe, L. C.; Voight, J. A.; Tuttle, B. A. *J. Mater. Sci.* 1990, Vol. 25, 737.
71. Jorgensen, P. J.; Anderson, R. C. *J. Am. Ceram. Soc.* 1967, Vol. 50, 553.
72. Prochazka, S.; Scanlan, R. M. *J. Am. Ceram. Soc.* 1975, Vol. 58, 72.
73. Yan, M. F. *J. Mater. Sci. Eng.* 1981, Vol. 48, 53.
74. Gupta, T. K. *J. Am. Ceram. Soc.* 1972, Vol. 55, 276.
75. Kingery, W. D.; Francois, B. *J. Am. Ceram. Soc.* 1965, Vol. 48, 546.
76. Coleman, S. C.; Beer#aae, W. B. *Phil. Mag.* 1975, Vol. 31, 1403.
77. Rhines, F. N.; DeHoff, R. T. In *Materials Science Research. Vol. 16: Sintering and Heterogeneous Catalysis*; Kuczynski, G. C., Miller, A. E., Sargent, G. A. eds.; Plenum: New York, 1984, pp. 49–61.
78. Kingery, W. D.; Francois, B. In *Sintering and Related Phenomena*; Kuczynski, G. C., Hooton, N. A., Gibbon, C. F. eds.; Gordon and Breach: New York, 1967, pp. 4717–498.
79. Cannon, R. M. Unpublished work. On the Effects of Dihedral Angle and Pressure on the Driving Forces for Pore Growth or Shrinkage.
80. Greskovich, C.; Lay, W. J. *Am. Ceram. Soc.* 1972, Vol. 55, 142.
81. Edelson, L. H.; Glaeser, A. M. *J. Am. Ceram. Soc.* 1988, Vol. 71, 225.

82. Shewmon, P. G. Trans. AIME. 1964, Vol. 230, 1134.
83. Brook, R. J. J. Am. Ceram. Soc. 1969, Vol. 52, 56.
84. Handwerker, C. A.; Cannon, R. M.; Coble, R. L. Advances in Ceramics. 1984, Vol. 10, 619.
85. Carpay, F. M. A. In Ceramic Microstructures '76; Fulrath, R. M., Pask, J. A. eds.; Westview Press: Boulder, CO, 1977, pp. 261–275.
86. Hsueh, C. H.; Evans, A. G.; Coble, R. L. Acta Metall. 1982, Vol. 30, 1269.
87. Sakarcı, M.; Hsueh, C. H.; Evans, A. G. J. Am. Ceram. Soc. 1983, Vol. 66, 456.
88. Yan, M. F.; Cannon, R. M.; Bowen, K. K. Mater. Sci. Eng. 1983, Vol. 60, 275.
89. Bennison, S. J.; Harmer, M. P. J. Am. Ceram. Soc. 1990, Vol. 73, 833.
90. Brook, R. J. Proc. Brit. Ceram. Soc. 1982, Vol. 32, 7.

10

Liquid-Phase Sintering

10.1 INTRODUCTION

Our discussion of the sintering process has so far been concerned with solid-state sintering in which the material remains entirely in the solid state. However, in many ceramic systems the formation of a liquid phase is commonly used to assist in the sintering and microstructural evolution. Usually the purpose of *liquid-phase sintering* is to enhance densification rates, achieve accelerated grain growth, or produce specific grain boundary properties. The distribution of the liquid phase and of the resulting solidified phases produced on cooling after densification is critical to achieving the required properties of the sintered material. Commonly, the amount of liquid formed during sintering is small, typically less than a few volume percent (vol%), which can make precise control of the liquid composition difficult. In some systems, such as Al_2O_3 , the amount of liquid phase can be very small and so difficult to detect that many studies that were believed to involve solid-state sintering actually involved liquid silicate phases, as later revealed by careful high-resolution transmission electron microscopy.

Liquid-phase sintering is particularly effective for ceramics such as Si_3N_4 and SiC that have a high degree of covalent bonding and are therefore difficult to densify by solid-state sintering. The process is also important when the use of solid-state sintering is too expensive or requires too high a fabrication temperature. However, the enhanced densification rates achieved by liquid-forming additives are only of interest if the properties of the fabricated ceramic remain within the required limits. A disadvantage of liquid-phase sintering is that the liquid phase used to promote sintering commonly remains as a glassy intergranular

phase that may degrade high temperature mechanical properties such as creep and fatigue resistance.

Some examples of ceramic liquid-phase sintering systems and their applications are given in Table 10.1. For consistency, we use the following nomenclature to describe the systems in liquid-phase sintering: the particulate solid forming the major component is written first while the liquid-producing component is written in brackets. In this nomenclature, Si_3N_4 sintered in the presence of a liquid phase produced by the addition of MgO is written $\text{Si}_3\text{N}_4(\text{MgO})$.

A related process is *activated sintering* in which minor amounts of additives that segregate strongly to the grain boundaries can significantly enhance mass transport rates along the grain boundary, giving rise to accelerated densification even at temperatures well below that for liquid formation in the system. In many systems, there is no clear difference in principles between activated sintering and liquid-phase sintering, except that for the activated system, the amount of additive is fairly small so that the presence of a liquid grain boundary film can be difficult to detect.

If sufficient liquid is present (on the order of 25–30 vol%), rearrangement of the solid phase coupled with liquid flow can lead to a fully dense material. Such large volume fractions of liquid are commonly used in traditional, clay-based ceramics such as porcelains and in cemented carbides. In the traditional ceramics, the liquid phases are molten silicates that remain as a glassy phase after cooling, giving the fabricated materials a glassy appearance. The ceramics are referred to as *vitrified*, and the sintering process is referred to as *vitrification*.

TABLE 10.1 Examples of Common Ceramic Liquid-Phase Sintering Systems

Ceramic system	Additive content (wt %)	Application	Reference
$\text{Al}_2\text{O}_3(\text{talc})$	~5	Electrical insulators	1
$\text{MgO}(\text{CaO-SiO}_2)$	<5	Refractories	2
$\text{MgO}(\text{LiF})$	<3	Refractories	3
$\text{ZnO}(\text{Bi}_2\text{O}_3)$	2–3	Electrical varistors	4,5
$\text{BaTiO}_3(\text{TiO}_2)$	<1	Dielectrics	6
$\text{BaTiO}_3(\text{LiF})$	<3	Dielectrics	7,8
$\text{UO}_2(\text{TiO}_2)$	~1	Nuclear ceramics	9
$\text{ZrO}_2(\text{CaO-SiO}_2)$	<1	Ionic conductors	10
$\text{Si}_3\text{N}_4(\text{MgO})$	5–10	Structural ceramics	11,12
$\text{Si}_3\text{N}_4(\text{Y}_2\text{O}_3\text{-Al}_2\text{O}_3)$	5–10	Structural ceramics	12,13
$\text{SiC}(\text{Y}_2\text{O}_3\text{-Al}_2\text{O}_3)$	5–10	Structural ceramics	14
$\text{WC}(\text{Ni})$	~10	Cutting tools	51

10.2 ELEMENTARY FEATURES OF LIQUID-PHASE SINTERING

10.2.1 Enhancement of Densification

Compared to solid-state sintering, the presence of the liquid phase leads to enhanced densification through (1) *enhanced rearrangement* of the particulate solid and (2) *enhanced matter transport* through the liquid. Figure 10.1 shows a sketch of an idealized two-sphere model in which the microstructural aspects of liquid-phase sintering are compared with those of solid-state sintering. In liquid-phase sintering, if, as we assume, the liquid wets and spreads to cover the solid surfaces, the particles will be separated by a liquid bridge. The friction between the particles is significantly reduced so that they can rearrange more easily under the action of the compressive capillary stress exerted by the liquid. In solid-state sintering by, for example, grain boundary diffusion, an important parameter that controls the rate of diffusion is the product of the grain boundary diffusion coefficient D_{gb} and the grain boundary thickness δ_{gb} . In liquid-phase sintering, the corresponding parameter is the product of the diffusion coefficient D_L of the solute atoms in the liquid and the thickness of the liquid bridge δ_L . Since δ_L is typically many times greater than δ_{gb} and diffusion through a liquid is much faster than in solids, the liquid therefore provides a path for enhanced matter transport.

10.2.2 Driving Force for Densification

Assuming as above that the liquid wets and spreads over the solid surfaces, the solid–vapor interface of the particulate system will be eliminated and pores will form in the liquid. The reduction of the liquid–vapor interfacial area provides a driving force for shrinkage (densification) of the system. For a spherical pore of

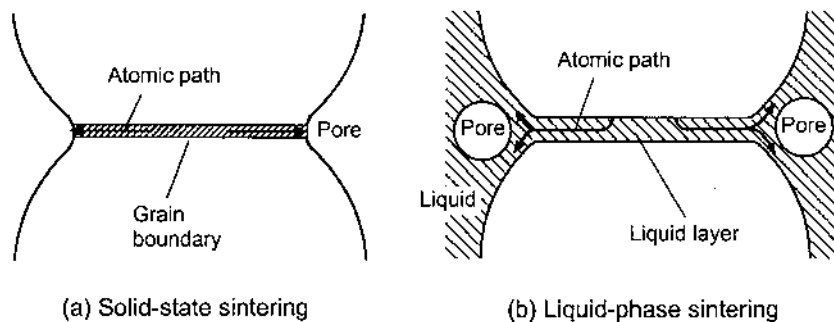


FIGURE 10.1 Sketch of an idealized two-sphere model comparing the microstructural aspects of (a) solid-state sintering with (b) liquid-phase sintering.

radius r in a liquid, the pressure difference across the curved surface is given by the equation of Young and Laplace:

$$\Delta p = -\frac{2\gamma_{lv}}{r} \quad (10.1)$$

where γ_{lv} is the specific surface energy of the liquid–vapor interface. The pressure in the liquid is lower than that in the pore, and this generates a compressive *capillary stress* on the particles. This compressive stress due to the liquid is equivalent to placing the system under an external hydrostatic pressure, the magnitude of which is given by Eq. (10.1). Taking $\gamma_{lv} \approx 1 \text{ J/m}^2$ and $r \approx 0.5 \text{ }\mu\text{m}$ gives $\Delta p \approx 4 \text{ MPa}$. Pressures of this magnitude can provide an appreciable driving force for sintering.

10.2.3 Formation of the Liquid Phase

For liquid-phase sintering, the green body is commonly formed from a mixture of two powders: a major component and an additive phase. On heating, the additive melts or reacts with a small part of the major component to form a *eutectic liquid*. The formation of the liquid phase by melting of the additive is fairly common in metallic systems, e.g., Fe(Cu) and W(Ni), whereas in ceramic systems, the formation of a eutectic liquid is more common, e.g., MgO(CaO-SiO₂) and ZnO(Bi₂O₃). For systems that rely on the formation of a eutectic liquid, *phase diagrams* play a key role in the selection of the additive and in the choice of the firing conditions. Despite the presence of a viscous liquid between the particles, the structure does not collapse unless the volume of liquid is very large. The relatively large capillary stress produced by the liquid holds the solid particles together. The effective viscosity of the system is, however, much lower than that of a similar system without the liquid phase.

In most systems, the liquid persists throughout the sintering process, and its volume does not change appreciably. This situation is sometimes referred to as *persistent liquid-phase sintering*. On cooling, the liquid commonly forms a glassy grain boundary phase, which, as outlined earlier, may degrade the high temperature mechanical properties. In a small number of systems, the liquid may be present over a major portion of the firing process but then disappears by (1) incorporation into the solid phase to produce a *solid solution*, e.g., Si₃N₄(Al₂O₃-AlN); (2) *crystallization* of the liquid, e.g., Si₃N₄(Al₂O₃-Y₂O₃); or (3) *evaporation*, e.g., BaTiO₃(LiF). The term *transient liquid-phase sintering* is used to describe the sintering in which the liquid phase disappears prior to the completion of firing. The interest in ceramics for mechanical engineering applications at high temperatures has led to the investigation of transient liquid-phase sintering in a few Si₃N₄ systems. However, the enhanced sensitivity of the system to the process variables makes microstructural control difficult in most cases. In this book, the

term liquid-phase sintering will refer most generally to the case of a persistent liquid. A distinction between persistent and transient liquid-phase sintering will be made only when it is required.

10.2.4 Microstructures

In addition to any porosity that may be present, the microstructure of the ceramic product produced by liquid-phase sintering consists of two phases: (1) the crystalline grains and (2) the grain boundary phase resulting from the liquid. Unless it is crystallizable, the grain boundary phase is commonly amorphous. As discussed later, depending on the interfacial tensions, it may penetrate the grain boundaries completely so that the grains are separated from one another by a fairly thin layer ($\approx 1\text{--}5\text{ nm}$), or it may only partially penetrate the grain boundaries.

Depending on the composition of the particulate solid and the liquid phase, a variety of grain shapes, ranging from nearly equiaxial grains to elongated grains with curved sides or straight (faceted) sides are observed. For systems with isotropic interfacial energies, when the amount of liquid is moderate (above $\sim 5\text{ vol\%}$), grains with a fairly rounded shape are observed (Fig. 10.2a) whereas for higher liquid content, the grain shape becomes spheroidal. For low volume fraction of liquid (less than $2\text{--}5\text{ vol\%}$), the grains undergo considerable changes in shape and develop a morphology in which the contact regions between neighboring grains are relatively flat (Fig. 10.2b). The shape changes allow the grains to pack more efficiently, a phenomenon usually described as grain shape accommodation. As outlined in Chapter 9, anisotropic abnormal grain growth can occur in systems with nonisotropic interfacial energies. The grains may take up a prismatic shape when the liquid content is high (Figure 10.2c), whereas at lower liquid content elongated grains with curved sides or plate-like grains with straight (faceted) sides may be observed (Fig. 10.2d).

10.3 STAGES OF LIQUID-PHASE SINTERING

In most liquid-phase sintering systems, chemical reactions between the particulate solid and the liquid are relatively weak, so that the interfacial energies have a dominant effect on the rate of sintering. Under these conditions, as illustrated in Fig. 10.3, liquid-phase sintering is generally regarded as proceeding in a sequence of dominant stages (15,16):

1. Redistribution of the liquid and *rearrangement* of the particulate solid under the influence of capillary stress gradients
2. Densification and grain shape accommodation by *solution-precipitation*
3. *Final-stage sintering* driven by the residual porosity in the liquid.

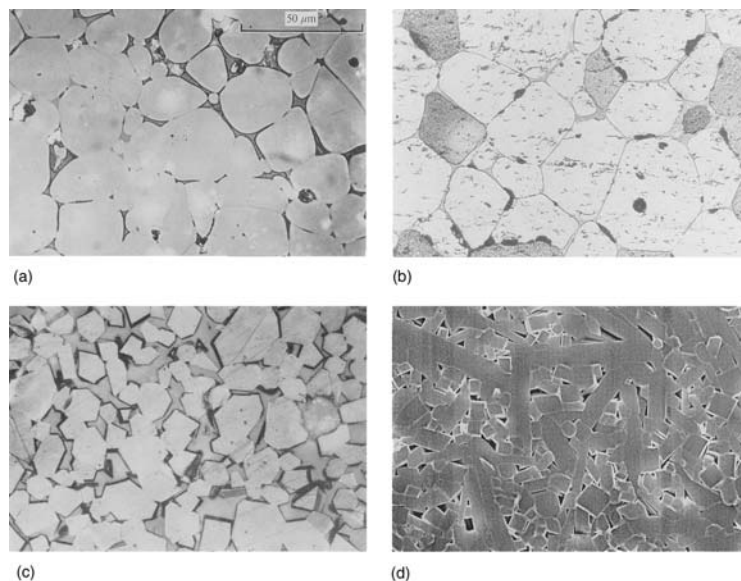


FIGURE 10.2 Commonly observed microstructures of ceramics produced by liquid-phase sintering. (a) Rounded grains in a moderate amount of liquid (> 5 vol%); (b) grains with flat contact surfaces in a low volume fraction of liquid (< 2 – 5 vol%); (c) prismatic grains dictated by anisotropic interfacial energy with a moderate to high liquid volume (> 10 vol%); (d) elongated grains with flat or curved sides resulting from anisotropic interfacial energy with a low liquid content (< 2 – 5 vol%).

As the temperature of the green body is raised, solid-state sintering may occur prior to the formation of the liquid, producing significant densification in some systems. Assuming good wetting between the liquid and the particulate solid, further densification occurs as a result of the capillary force exerted by the liquid on the particles. The particles shrink as solid dissolves in the liquid and rapidly rearrange to produce a higher packing density, releasing liquid to fill pores between the particles. Capillary stresses will cause the liquid to redistribute itself between the particles and into the small pores, leading to further rearrangement. Contact points between agglomerates will be dissolved due to their higher solubility in the liquid, and the fragments will also undergo rearrangement. Throughout the process, dissolution of sharp edges will make the particle surfaces smoother, thereby reducing the interfacial area and aiding the rearrangement of the system. Initially, rearrangement occurs rapidly, but as densification occurs, the viscosity of the system increases, causing the densification rate to decrease continuously.

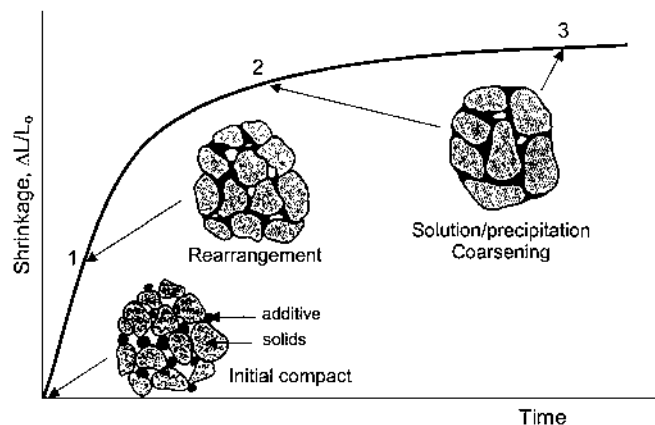


FIGURE 10.3 Schematic evolution of a powder compact during liquid-phase sintering. The three dominant stages overlap significantly.

As densification by rearrangement slows, effects dependent on the solid solubility in the liquid and the diffusivity in the liquid dominate, giving the second stage termed *solution-precipitation*. The solid dissolves at the solid-liquid interfaces with a higher chemical potential, diffuses through the liquid, and precipitates on the particles at other sites with a lower chemical potential. One type of dissolution site is the wetted contact area between the particles where the capillary stress due to the liquid or an externally applied stress leads to a higher chemical potential. Precipitation occurs at sites away from the contact area. For systems with a distribution of particle sizes, matter can also be transported from the small particles to the large particles by diffusion through the liquid, a process described as Ostwald ripening (see Chapter 9). The net result is a coarsening of the microstructure. Densification by the solution-precipitation mechanism is also accompanied by changes in the shape of the grains. When the amount of liquid is fairly large, the grains normally take up a rounded shape (Fig. 10.2a). However, for a small amount of liquid, the grains develop flat faces and assume the shape of a polyhedron to achieve more efficient packing, a process described as *grain shape accommodation* (see Fig. 10.2b).

The final stage of liquid-phase sintering is controlled by the densification of the solid particulate skeletal network. The process is slow because of the large diffusion distances in the coarsened structure and the rigid skeleton of contacting solid grains. Ostwald ripening dominates the final stage and the residual pores become larger if they contain trapped gas, leading to compact swelling. Coarsening is accompanied by grain shape accommodation, which allows more efficient

packing of the grains. Liquid may be released from the more efficiently packed regions and may flow into the isolated pores, leading to densification.

The stages of liquid phase sintering are summarized in Fig. 10.3. The extent to which each stage influences densification is dependent on the volume fraction of liquid so there are many variants in this conceptual picture. When the volume fraction of liquid is high, complete densification can be achieved by the rearrangement process alone. On the other hand, at the low liquid contents common for many systems, the solid skeleton inhibits densification, so that solution-precipitation and final stage sintering are required to achieve further densification.

10.4 THERMODYNAMIC AND KINETIC FACTORS

Production of the required microstructure in liquid phase sintering depends on several kinetic and thermodynamic factors. As discussed later, several processing parameters also influence the process.

10.4.1 Wetting and Spreading of the Liquid

Good wetting of the solid by the liquid is a fundamental requirement for liquid-phase sintering. It is generally found that liquids with a low surface tension readily wet most solids, giving a low contact angle, whereas liquids with a high surface tension show poor wetting with a large contact angle (Fig. 10.4). At a molecular level, if the cohesion between the liquid molecules is greater than the adhesion between the liquid and the solid, the liquid will not want to wet the solid.

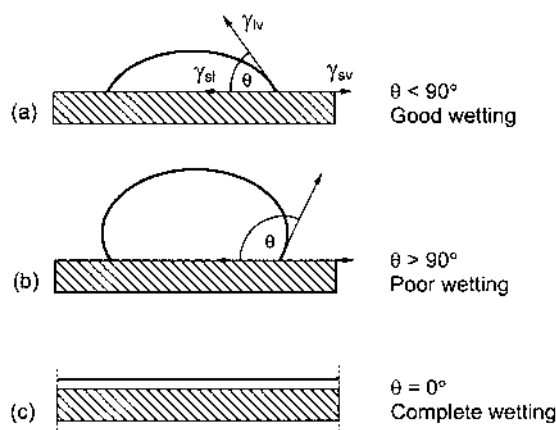


FIGURE 10.4 Wetting behavior between a liquid and a solid showing (a) good wetting, (b) poor wetting, and (c) complete wetting for a liquid with a contact angle of θ .

The degree of wetting is characterized by the contact angle θ that depends on the various interfacial energies for the solid–liquid–vapor system and is usually referred to a droplet of liquid on a flat solid surface (Fig. 10.4). If the specific energies of the liquid–vapor, solid–vapor, and solid–liquid interfaces are γ_{lv} , γ_{sv} , and γ_{sl} , respectively, then by the principle of virtual work

$$\gamma_{sv} = \gamma_{sl} + \gamma_{lv} \cos \theta \quad (10.2)$$

This equation, derived by Young and by Dupré, is what we would obtain by taking the horizontal components of the interfacial tensions. The surface energies of many inorganic melts, such as silicates, are often in the range of 0.1–0.5 J/m², with a value of ~ 0.3 J/m² commonly cited for molten silicates, and the surface energies of liquid metals and metal oxides as high as 2 J/m². The change in surface energy with temperature for melts such as silicates is not well documented. Careful measurements in the range of 1300–1500°C indicate that the surface energy of a calcium aluminosilicate melt (62 wt% SiO₂, 15 wt% Al₂O₃, 23 wt% CaO) increases slowly with temperature and can be represented by

$$\gamma_{lv} = 0.293 + 0.67 \times 10^{-4} (T - 273.2) \quad (10.3)$$

where γ_{lv} is in J/m² and T is the absolute temperature (17). Compositional changes also modify the surface energy. Table 10.2 gives the interfacial energies of a number of materials.

The geometries shown in Fig. 10.4 ignore the complication that for effective liquid-phase sintering, the solid must have some solubility in the liquid. This solubility effect leads to detailed wetting geometries or to liquid distribution that requires modification of the simple equation of Young and Dupré. Complete equilibrium must include a force-balance in both dimensions as well as the attainment of constant curvature surfaces. These effects have been examined by Cannon et al. (18), and Fig. 10.5 shows some of the configurational changes when the solubility of the solid in the liquid is taken into account.

Spreading refers to the kinetic process in which the liquid distributes itself to cover the surfaces of the particulate solid. It is important in the rearrangement stage soon after the formation of the liquid. For spreading to occur, the total interfacial energy must be reduced. For an infinitesimal change in the contact area between the solid and the liquid (Fig. 10.4), spreading will occur if

$$\gamma_{lv} + \gamma_{sl} - \gamma_{sv} = 0 \quad (10.4)$$

Thus a spreading liquid has contact angle of zero.

10.4.2 Dihedral Angle

Consider a liquid in contact with the corner of the grains. As sketched in Fig. 10.6 for the two-dimensional situation, grooves are formed where the grain boundaries

TABLE 10.2 Measured Solid–Vapor, Liquid–Vapor, and Solid–Liquid Interfacial Energies for Various Materials

	Temperature (°C)	Interfacial Energy (J/m ²)
Solids		
Al ₂ O ₃	1850	0.905
MgO	25	1.000
TiC	1100	1.190
NaCl (100)	25	0.300
0.20 Na ₂ O–0.80 SiO ₂	1350	0.380
Cu	1080	1.430
Ag	750	1.140
Fe (γ phase)	1350	2.100
Liquids		
Water	25	0.072
Al ₂ O ₃	2080	0.700
MgO	2800	0.660
B ₂ O ₃	900	0.080
Bi ₂ O ₃	825	0.213
FeO	1420	0.585
0.13 Na ₂ O–0.13 CaO–0.74 SiO ₂	1350	0.350
0.15 Al ₂ O ₃ –0.23 CaO–0.62 SiO ₂	1400	0.387
0.30FeO–0.21 CaO–0.49 SiO ₂	1400	0.396
Cu	1120	1.270
Ag	1000	0.920
Fe	1535	1.880
Solid–Liquid		
Al ₂ O ₃ (s)–silicate glaze(l)	1000	<0.700
Al ₂ O ₃ (s)–Ag(l)	1000	1.770
Al ₂ O ₃ (s)–Fe(l)	1570	2.300
MgO(s)–Ag(l)	1300	0.850
MgO(s)–Fe(l)	1725	1.600
SiO ₂ (glass)–Cu(l)	1120	1.370

Source: Ref. 9.

intersect the surface of the liquid. The dihedral angle is defined as the angle between the solid-liquid interfacial tensions. Applying a force balance and rearranging, we obtain

$$\cos \frac{\Psi}{2} = \frac{\gamma_{ss}}{2\gamma_{sl}} \quad (10.5)$$

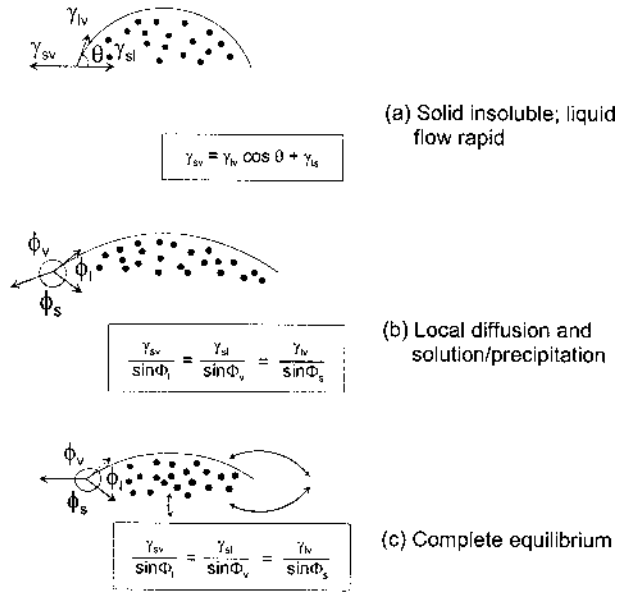


FIGURE 10.5 Shape changes associated with partial solubility of the solid in the liquid (18). (Courtesy of R. M. Cannon.)

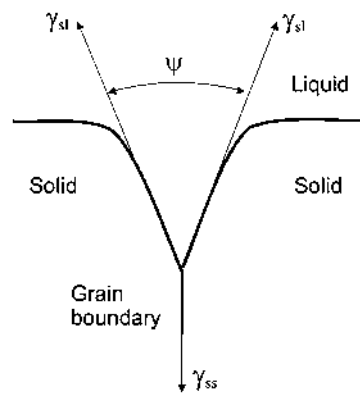


FIGURE 10.6 Dihedral angle ψ for a liquid at a grain boundary.

The solid–solid interfacial tension γ_{ss} is the same as the interfacial tension in the grain boundary γ_{gb} defined earlier in solid-state sintering.

Liquid Penetration of the Grain Boundary

The variation of the dihedral angle ψ as a function of the ratio γ_{ss}/γ_{sl} is sketched in Fig. 10.7. For $\gamma_{ss}/\gamma_{sl} < 2$, the dihedral angle takes values between 0 and 180° and the liquid does not completely penetrate the grain boundary. In particular, when the ratio γ_{ss}/γ_{sl} is small, liquid penetration of the grain boundary is limited, so solid-state processes can be significant. The condition $\gamma_{ss}/\gamma_{sl} = 2$ represents the limiting condition for complete penetration of the grain boundary by the liquid. For $\gamma_{ss}/\gamma_{sl} > 2$, no value of ψ satisfies Eq. (10.5), and this represents the condition for complete penetration of the grain boundary. One consequence is the lack of rigidity of the system. Physically, the condition $\gamma_{ss}/\gamma_{sl} > 2$ means that the sum of the specific energies associated with the two solid–liquid interfaces is less than that of the solid–solid interface, so penetration of the boundary leads to an overall decrease in energy.

Shape of the Liquid and the Grains

The dihedral angle affects the shapes of the grains and the liquid. If it is assumed that no porosity exists in the structure, then the equilibrium shape of the liquid phase can be calculated (19,20). Much earlier, Smith (21) showed that the equilibrium distribution of second phases in a granular structure can be explained on the assumption that at three-grain junctions, the interfacial tensions should be in

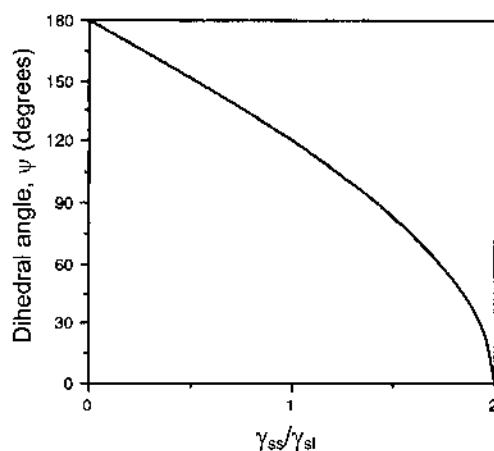


FIGURE 10.7 Variation of the dihedral angle ψ with the ratio of the solid–solid interfacial tension γ_{ss} to the solid–liquid interfacial tension γ_{sl} .

a state of balance. In two dimensions, Fig. 10.8 shows in an idealized form the shapes a small volume of liquid phase must have if it appears at the corners of three grains.

To obtain a more realistic idea of the shape of the liquid phase in the structure, we must consider the three-dimensional situation (Fig. 10.9). For $\psi = 0$, the liquid completely penetrates the grain boundary and no solid-solid contact exists. As ψ increases, the penetration of the liquid phase between the grains should decrease, whereas the amount of solid-solid contacts (i.e., grain boundary area) should increase. However, for values of ψ up to 60° , the liquid should still be capable of penetrating indefinitely along the three-grain edges, and the structure should therefore consist of two continuous interpenetrating phases. When ψ is greater than 60° , the liquid should form isolated pockets at the corners of four grains. The microstructural features obtained for various values of the dihedral angle are summarized in Table 10.3. It should be remembered that these equilibrium liquid shapes represent idealizations, so local departures from them will occur in real systems.

10.4.3 Effect of Solubility

The two solubilities to be considered are the solid solubility in the liquid and the liquid solubility in the solid. Good solid solubility in the liquid leads to densifica-

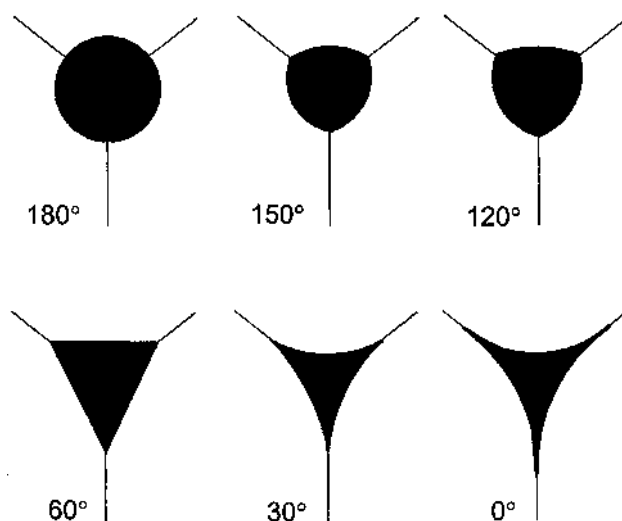


FIGURE 10.8 Effect of the dihedral angle on the idealized shape (in two dimensions) of the liquid at the corners of three grains.

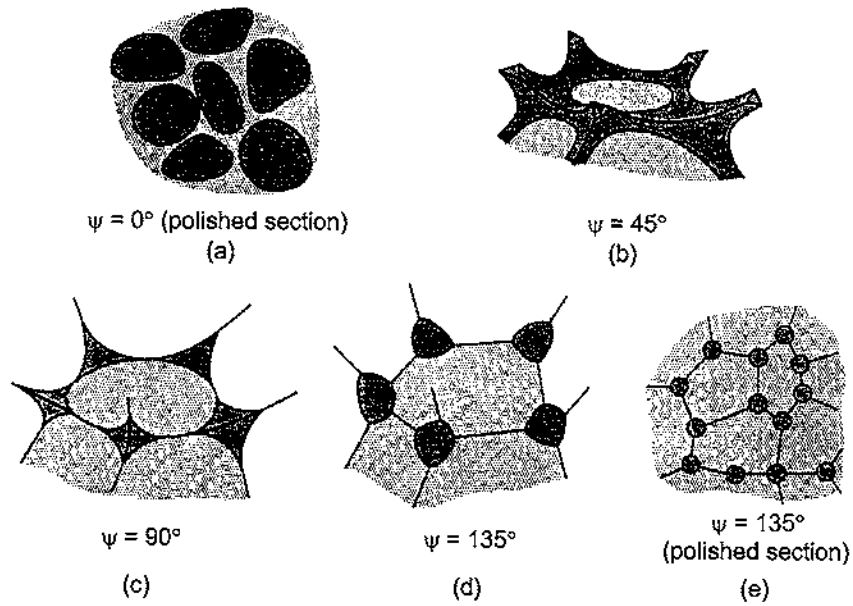


FIGURE 10.9 Idealized liquid-phase distribution (in three dimensions) for selected values of the dihedral angle. (From Ref. 9.)

TABLE 10.3 Microstructural Features for Two-Phase Ceramics Produced by Liquid-Phase Sintering for Various Ratios of the Interfacial Energies γ_{ss}/γ_{sl} and the Corresponding dihedral angles ψ

γ_{ss}/γ_{sl}	ψ	Microstructure
≥ 2	0°	All grains separated by liquid phase
$\sqrt{3}-2$	$0-60^\circ$	Continuous liquid phase penetrating all three-grain junctions; partial penetration of the grain boundaries by the liquid
$1-\sqrt{3}$	$60-120^\circ$	Isolated liquid phase partially penetrating the three-grain junctions
≤ 1	$\geq 120^\circ$	Isolated liquid phase at four-grain junctions

tion and is essential for liquid phase sintering. On the other hand, a high liquid solubility in the solid should be avoided because it leads to a transient liquid phase and swelling of the compact. Transient liquid-phase sintering, as outlined earlier, has been used successfully for a few systems, but in general, the process is difficult to control. The effect of solubility on densification and compact swelling is illustrated in Fig. 10.10.

Particle size has an effect on solubility. Following Eq. (9.3) for the relationship between solute concentration and particle radius, and taking the solubility as equivalent to the concentration, we have

$$\ln \left(\frac{S}{S_0} \right) = \frac{2\gamma_{sl}\Omega}{kTa} \quad (10.6)$$

where S is the solubility of a particle with a radius a in the liquid, S_0 is the equilibrium solubility of the solid in the liquid at a planar interface, γ_{sl} is the specific energy of the solid–liquid interface, Ω is the atomic volume, k is the Boltzmann constant, and T is the absolute temperature. According to Eq. (10.6), the solubility increases with decreasing particle radius, so matter transport will occur

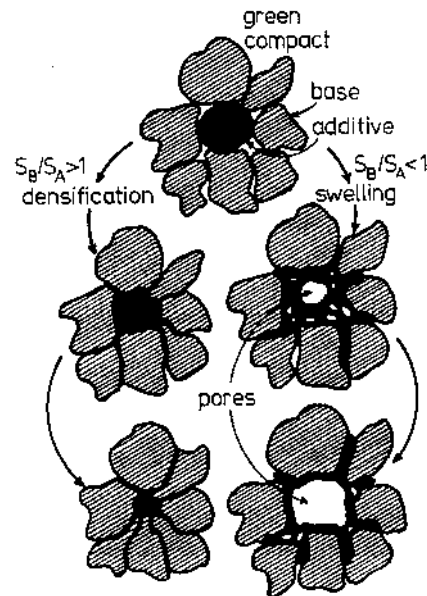


FIGURE 10.10 Schematic diagram comparing the effects of solubility on densification or swelling during liquid-phase sintering. (From Ref. 15.)

from small particles to large particles, leading to Ostwald ripening. In addition, asperities have a small radius of curvature and they tend to dissolve. Pits, crevices, and necks between the particles have negative radii of curvature, so solubility is diminished and precipitation is enhanced in those regions.

10.4.4 Capillary Forces

For a liquid that completely wets the solid, the pressure deficit in the liquid, given by Eq. (10.1), leads to a large compressive stress on the particles. In general, the magnitude and nature of the stress will depend on several factors such as the contact angle, the volume of liquid, the separation of the particles, and the particle size. To get an estimate of how these variables influence the capillary force exerted by the liquid, let us consider an idealized model consisting of two spheres of the same radius, a , separated by a distance h by a liquid with a contact angle θ (Fig. 10.11). The shape of the liquid meniscus is called a nodoid, and an analytical solution for the shape is known in terms of elliptical integrals. However, the calculations of the meniscus shape and the capillary force are complicated. As an approximation, we shall use the circular shape approximation in which the liquid meniscus is assumed to be part of a circle. With this approximation, the pressure difference across the liquid–vapor meniscus is given by

$$\Delta p = \gamma_{lv} \left(\frac{1}{Y} - \frac{1}{r} \right) \quad (10.7)$$

where Y and r are the principal radii of curvature of the meniscus.

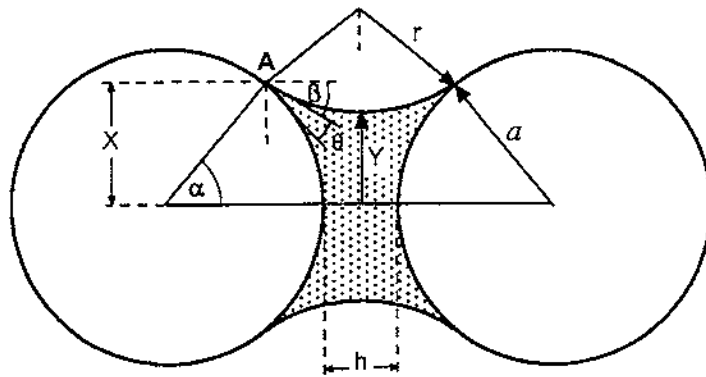


FIGURE 10.11 Geometrical parameters for an idealized model of two spheres separated by a liquid bridge.

The force acting on the two spheres is the sum of the contributions from (1) the pressure difference Δp across the liquid–vapor meniscus and (2) the surface tension of the liquid (19,23). It is commonly evaluated at the point A in Fig. 10.11. In this case, the force equation is

$$F = -\pi X^2 \Delta p + 2\pi X \gamma_{lv} \cos \beta \quad (10.8)$$

where F is taken to be positive when the force is compressive. Some of the earlier papers in the literature include only the Δp term in Eq. (10.8), but Heady and Cahn (22) showed that the Eq. (10.8) is the correct expression for F . Substituting for Δp and putting $X = a \sin \alpha$, Eq. (10.8) becomes

$$F = -\pi a^2 \gamma_{lv} \left(\frac{1}{Y} - \frac{1}{r} \right) \sin^2 \alpha + 2\pi a \gamma_{lv} \sin \alpha \cos \beta \quad (10.9)$$

The distance of separation between the spheres is

$$h = 2[r \sin \beta - a(1 - \cos \alpha)] \quad (10.10)$$

and the angles are related by

$$\alpha + \beta + \theta = \frac{\pi}{2} \quad (10.11)$$

Substituting for β in Eq. (10.10) and rearranging gives

$$r = \frac{h + 2a(1 - \cos \alpha)}{2 \cos(\theta + \alpha)} \quad (10.12)$$

The positive radius of curvature of the meniscus is given by

$$Y = a \sin \alpha - r[1 - \sin(\theta + \alpha)] \quad (10.13)$$

Substituting for r from Eq. (10.12) gives

$$Y = a \sin \alpha - \frac{h + 2a(1 - \cos \alpha)}{2 \cos(\theta + \alpha)} [1 - \sin(\theta + \alpha)] \quad (10.14)$$

The volume of the liquid bridge is

$$V = 2\pi(r^3 + r^2 Y) \left\{ \cos(\theta + \alpha) - \left[\frac{\pi}{2} - (\theta + \alpha) \right] \right\} + \pi Y^2 r \cos(\theta + \alpha) \quad (10.15)$$

A situation of interest is the solution of Eq. (10.8) for F as a function of the interparticle distance h for a given volume fraction of liquid. Figure 10.12 shows the calculated values for F between two tungsten spheres separated by a liquid copper bridge as a function of h for several values of V/V_0 , where V_0 is the volume of a tungsten sphere (24). The results are shown for two extreme values of the contact angle: $\theta = 8^\circ$ and $\theta = 85^\circ$. In the calculations, the surface energy of liquid copper was taken as 1.28 J/m^2 . For $\theta = 8^\circ$, the capillary force is large and compressive for all amounts of liquid and decreases strongly with increasing values of h (Fig. 10.12a). The dependence of F on the volume of liquid is also reversed for large values of h . For $\theta = 85^\circ$, F is negative (repulsive) for small values of h but compressive for large separations. An equilibrium separation defined by the condition $F = 0$ will be attained (Fig. 10.12b).

An important result arising from these calculations is that very different rearrangement processes can be expected for low and for high contact angles. For efficient rearrangement and the achievement of high density, the contact angle must be kept low.

10.4.5 Effect of Gravity

Because of the relatively low effective viscosity of powder compacts containing a liquid phase, the weight of the system itself can cause significant distortion, particularly when a significant amount of liquid is present ($>5\text{--}10 \text{ vol}\%$). The effect of kinetic and microstructural factors on distortion during liquid-phase sintering has been studied and macroscopic models to predict the role of parameters such as compact mass, green density, particulate solid content, and dihedral angle on distortion of liquid-phase sintered heavy metal alloys have been developed (25–28). In practice, judicious support for large objects is necessary (29).

An additional effect of gravity is the possibility of liquid redistribution, leading to particle settling or liquid drainage. Solid–liquid separation or segregation is particularly important for systems where the amount of liquid is high and where a significant density difference exists between the particulate solid and the liquid phase as, for example, in the case of cemented carbides and heavy metal alloys (30). The heavier particulate solid settles toward the bottom, leaving the lighter liquid at the top. The solid–liquid separation leads to distortion of the object and to large differences in the microstructure from the top to the bottom of the object. The effects have been examined under conditions of microgravity (31). The particulate solid and liquid do not separate as they do under gravity. However, for high liquid content, the solid is still not dispersed throughout the liquid even in microgravity. Instead, the solid particles agglomerate, as shown in Fig. 10.13 for a tungsten heavy metal alloy. Since this is a metallic system, surface charge effects are not expected to be present. The particles are propelled as a result of uneven dissolution and precipitation rates along their surfaces,

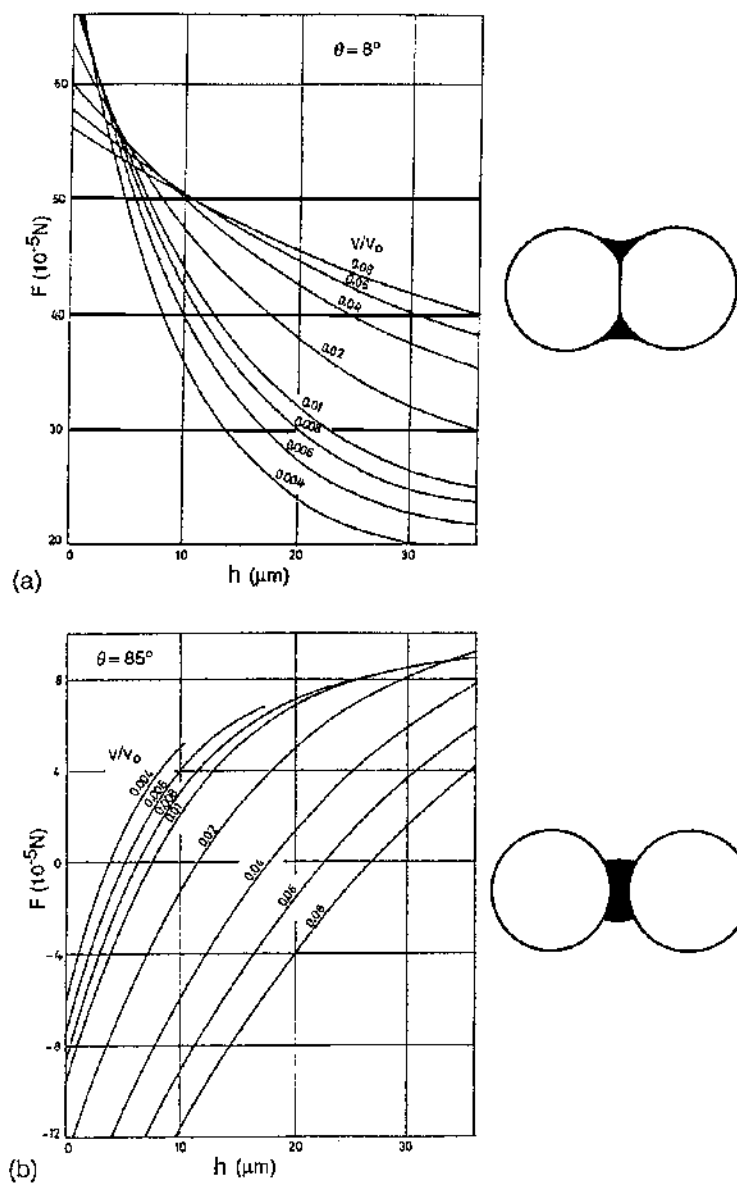


FIGURE 10.12 The calculated capillary force acting between two tungsten spheres separated by a liquid copper bridge as a function of the interparticle distance for several values of the liquid volume V normalized to the volume of a tungsten sphere V_0 at two extreme values of the contact angle. (a) $\theta = 8^\circ$; (b) $\theta = 85^\circ$. (From Ref. 24.)

leading to collision and joining. It is possible that a liquid film may be present at the contact areas between the particles, but this has not yet been determined.

10.5 GRAIN BOUNDARY FILMS

It is often assumed in the theoretical analysis of liquid-phase sintering that the composition and structure of the grain boundary liquid phase is constant. However, this is not always the case. A wetting liquid layer, as described earlier, leads to the development of a compressive capillary force, which is equivalent to placing the system under a fairly large hydrostatic compression. The evolution of the intergranular liquid layer under the influence of the capillary force as well as other forces has been the subject of recent investigation.

After the rearrangement stage, we may envisage a situation where densification occurs by the solution-precipitation mechanism, and the liquid layer separating the grains becomes progressively thinner with time. Assuming that there is no repulsion between the grain surfaces, we would eventually reach a stage where the liquid capillary becomes so narrow that liquid flow is very difficult. The solution-precipitation can still continue but at a reduced rate. Kinetically, a competition is set up between the rate at which the thickness of the liquid layer becomes thinner by viscous flow and the rate of densification. This type of argument appears to point to the development of a finite thickness of the liquid layer when densification is completed because liquid flow through the capillary becomes very slow.

Observations by high-resolution transmission electron microscopy often reveal an amorphous film, commonly a silicate glass, with a thickness of 0.5–2

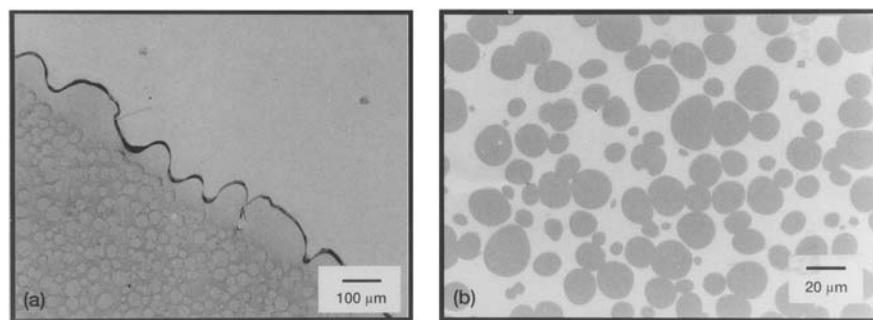
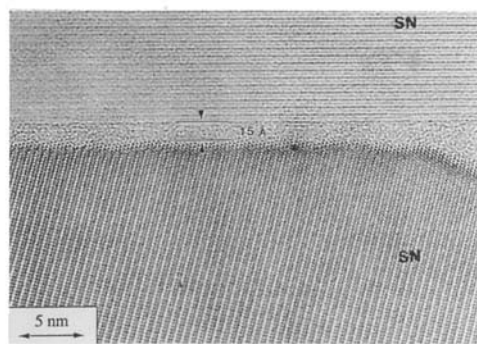
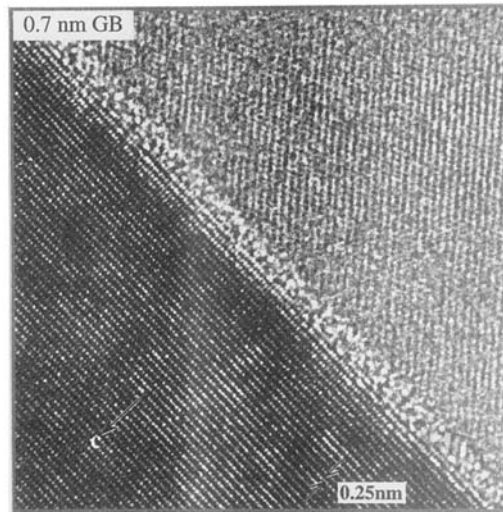


FIGURE 10.13 Micrographs of W(15.4 wt% Ni + 6.6 wt% Fe) after liquid-phase sintering for 1 min in microgravity at 1507°C. (a) Low magnification view of sample edge and wavy solidified liquid; (b) high magnification view of sample interior showing grain agglomeration. (Courtesy of R. M. German.)

nm between the grains in many ceramics that have been fabricated by liquid-phase sintering. Examples include Si_3N_4 , SiC , ZnO varistor materials, and Al_2O_3 (Fig. 10.14). There is evidence that the thickness of the intergranular film has a constant, *equilibrium* value from one boundary to another in any given material, regardless of the volume fraction of the silicate glass (the excess glass is located elsewhere, such as three- and four-grain junctions).

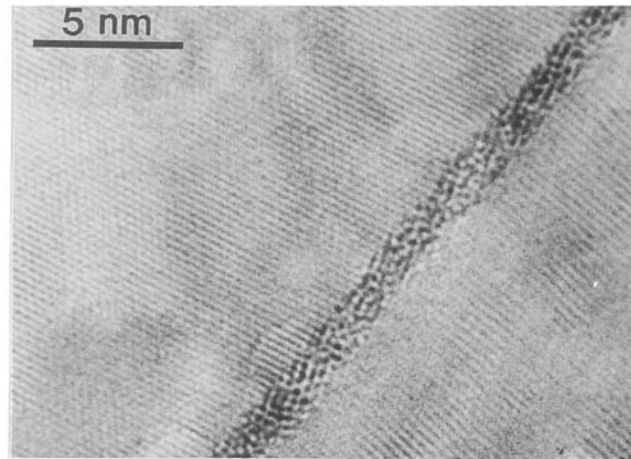


(a) $\text{Si}_3\text{N}_4(\text{Y}_2\text{O}_3)$: 1.5 nm

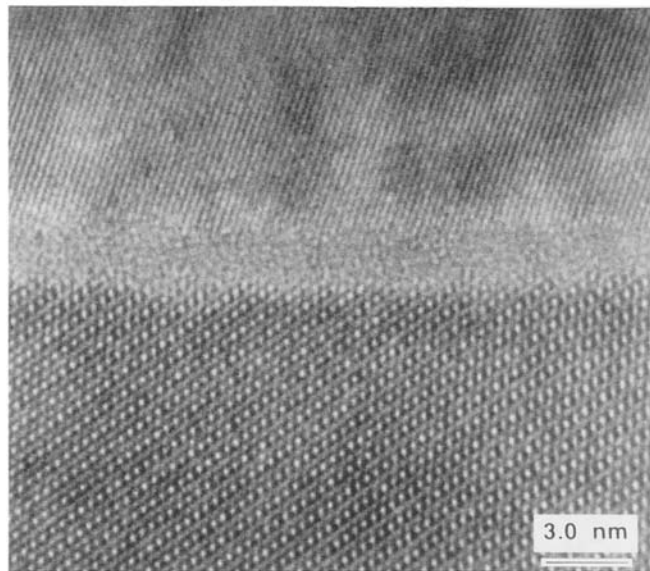


(b) $\text{SiC}(\text{Al} + \text{B} + \text{C})$: 0.7 nm

FIGURE 10.14ab Amorphous grain boundary film with a constant equilibrium thickness in (a) $\text{Si}_3\text{N}_4(\text{Y}_2\text{O}_3)$ (Courtesy of M. Cinibulk); (b) $\text{SiC}(\text{Al} + \text{B} + \text{C})$ (Courtesy of L. C. De Jonghe);



(c) $\text{ZnO}(\text{Bi}_2\text{O}_3)$: 1.5 nm



(b) $\text{Al}_2\text{O}_3(\text{CaO-SiO}_2)$: 1.5 nm

FIGURE 10.14cd (c) $\text{ZnO}(\text{Bi}_2\text{O}_3)$ (Courtesy Y.-M. Chiang); (d) $\text{Al}_2\text{O}_3(\text{CaO-SiO}_2)$ (Courtesy of F. L. Riley).

Lange (32) applied a theory developed for flat plates separated by a liquid layer to calculate the rate of thinning by viscous flow of a liquid layer separating two spherical particles undergoing liquid phase sintering. The rate of approach of two plates separated by a Newtonian viscous liquid is (33):

$$\frac{dh}{dt} = -\frac{2\pi h^5}{3\eta A^2 h_0^2} F \quad (10.16)$$

where h is the thickness of the liquid layer at time t , h_0 is the initial thickness of the layer, F is the compressive force exerted on the plates, η is the viscosity of the liquid, and A is the contact area between the liquid and the plate. To apply Eq. (10.16) to the case of liquid-phase sintering, let us consider the model shown in Fig. 10.15 for two spheres held together by the capillary force due to a liquid bridge. Instead of asking whether the liquid will be squeezed out or not, it is more convenient to determine how long it will take for the liquid to be squeezed out. Putting $y = h/h_0$ in Eq. (10.16) and integrating, the time for y to approach zero is

$$t_f = \frac{3\eta A^2}{8\pi h_0^2 F} \left(\frac{1}{y^4} - 1 \right) \quad (10.17)$$

This equation shows that $t_f = \infty$ for $y = 0$. Therefore within any experimental time frame, some liquid is predicted to remain between the particles. Further

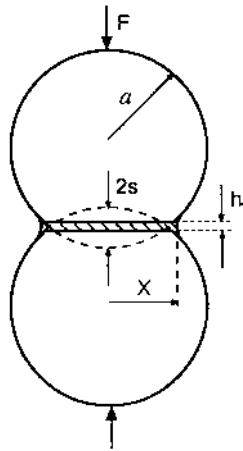


FIGURE 10.15 Parameters of an idealized two-sphere model separated by a liquid layer of thickness h used to analyze the change in the thickness of the layer during sintering.

analysis of the problem to take into account the approach of the particle centers due to densification indicates that for a wetting liquid, although the thickness decreases progressively with time, a layer of finite thickness always remains between the particles within any experimental time frame. However, when the liquid layer becomes very thin (in the nanometer range), effects other than viscous flow become dominant. These effects include structural and chemical forces as well as charge interactions.

Clarke (34) proposed an explanation for the *equilibrium* thickness of the intergranular film in terms of a balance between the attractive van der Waals forces between the grains and short-range repulsive forces due to the resistance to deformation of the silicate liquid. The repulsive forces, referred to as *disjoining* or *steric* forces, are attributed to the structural ordering of the silica tetrahedra of the intergranular film at the crystalline grain surfaces. The idea of a structural disjoining pressure is not new, having been introduced by Derjaguin and Churaev (35).

The assumption in the present system is that for microscopic thicknesses of the silicate phase, the structure of the liquid is not random, as might be expected for bulk volumes of the liquid, but instead exhibits a form of spatially varying orientation order close to each grain. If the correlation length associated with orientational fluctuations is ξ , then it is assumed that the orientational order imposed on the liquid phase structure by the grains will extend a distance ξ into the liquid. Assuming that the grains have flat sides and are separated by a distance h , the disjoining force (per unit area of the boundary) is given by the expression (34):

$$F_s = \frac{\alpha\eta_0^2}{\sinh^2(h/2\xi)} \quad (10.18)$$

where $\alpha\eta_0^2$ corresponds to the free energy difference between the intergranular film with and without ordering.

Clarke et al. (36) later explored the possibility of an electrical double-layer contributing to the repulsion, thereby assisting in the stabilization of the film thickness. This double-layer repulsion is identical in origin to that in the DLVO theory of colloid stability (Chapter 4). Assuming that the grains have flat, parallel faces separated by a distance h , the expression for the double-layer repulsion is

$$F_R = \frac{8kT}{\pi z^2 b_L h^2} \left(\tanh \frac{ze\phi_o}{4kT} \right)^2 (Kh)^2 \exp(-Kh) \quad (10.19)$$

where k is the Boltzmann constant, T is the absolute temperature, z is the valence of the charge-determining ions, e is the electronic charge, ϕ_o is the

surface potential, K is the inverse Debye length, and b_L is the *Bjerrum length* given by

$$b_L = \frac{e^2}{4\pi\epsilon\epsilon_0 kT} \quad (10.20)$$

where ϵ is the dielectric constant of the liquid medium and ϵ_0 is the permittivity of vacuum.

The attractive van der Waals force between the grains (assumed to have flat sides and separated by a distance h), found from Chapter 4, is given by

$$F_A = -\frac{A}{6\pi h^3} \quad (10.21)$$

where A is the Hamaker constant. At equilibrium, the overall force balance is satisfied:

$$F_R + F_S = F_A + p_C \quad (10.22)$$

where p_C is the compressive capillary pressure that acts to draw the grains together.

Much of the data required to evaluate the contributions of the van der Waals, disjoining, and electrical double-layer forces are not available, but equilibrium separation distances estimated from the theory are in qualitative agreement with observations. For Si_3N_4 doped with Ca (37), measurements appear to indicate that the equilibrium film thickness initially decreases with Ca concentration but then increases (Fig. 10.16). This variation in the film thickness has been qualitatively explained in terms of the balance of the van der Waals attraction, the repulsive disjoining force and the electrical double-layer repulsion, as illustrated schematically in Fig. 10.17. In the undoped Si_3N_4 , it is assumed that there is no net electrical charge, so the equilibrium thickness is controlled by the van der Waals and steric forces only, and the grain boundary film is idealized as a pure silica network structure (Fig. 10.17a). The addition of Ca^{2+} to the intergranular phase can have a dual effect. It may disrupt the silica network and the ordering imposed by the Si_3N_4 grains, thereby reducing the magnitude of the disjoining force (represented schematically in Fig. 10.17b). The addition of Ca^{2+} also provides a charged species to the system and, provided it adsorbs to the grain surfaces, may provide a double-layer repulsion (Fig. 10.17c). Since Ca^{2+} is known to be a potent silica network modifier, it may be expected that the strongest effect is to reduce the disjoining force. Further additions of Ca^{2+} may be expected to enhance the double-layer repulsion, thereby leading to an increase in the film thickness.

A problem with the force-balance explanation for the equilibrium film thickness in Ca-doped Si_3N_4 is that later studies reveal no clear evidence for

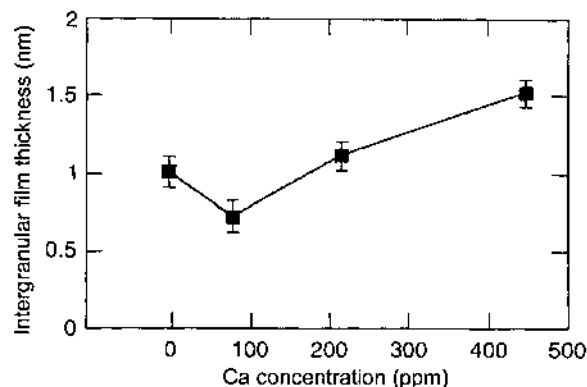


FIGURE 10.16 Equilibrium grain boundary thickness measured by HREM plotted versus the bulk calcium doping level in silicon nitride. (From Ref. 37.)

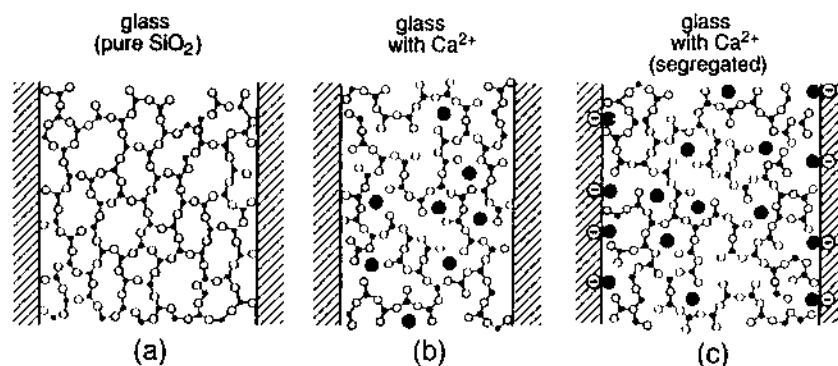


FIGURE 10.17 Model for force balance in Ca-doped silicon nitride. (From Ref. 37.)

Ca^{2+} segregation at the grain boundaries (38). The Ca^{2+} concentration appears to be constant along the length and thickness of the film. Based on these studies, it was suggested that the increase in the film thickness with Ca^{2+} concentration (Fig. 10.16) could be due to a reduction of the attractive van der Waals force rather than an increase in the electrical double-layer repulsion. For the Ca-doped Si_3N_4 system, it is also observed that for a given material (with a fixed Ca^{2+} concentration), the composition of the grain boundary film is different from that of the liquid in the three- or four-grain junction or even from boundary to boundary [Fig. 10.18]. This compositional variation is also observed in several other sys-

tems (39) and may be more common rather than an exception. Since the film composition should dictate the balance of forces and, hence, the film thickness, the nearly constant film thickness in a given material indicates that the origins of the compositional variation from boundary to boundary may be located elsewhere.

Another explanation, based on *thermodynamics*, has been proposed for the ZnO(Bi₂O₃) system in which a thin amorphous film (1.0–1.5 nm) is also observed at the grain boundaries (40). It is claimed that the thin amorphous film may represent the minimum free-energy configuration for the interface. This would be the case if the free energy of the grain boundary containing the amorphous film is lower than the sum of the crystal–crystal grain boundary energy and the free energy for accommodating the grain boundary glass as a solid solution or nonwetting secondary phase. In this case, it would not be energetically favorable to remove the intergranular amorphous film by crystallization or dewetting.

Grain boundary films in ceramics are not just restricted to the thin equilibrium films discussed so far. In a variety of other ceramics, thicker glass films (10 nm to several microns) are also observed, which have a significant effect on microstructure and properties. These thicker films represent a different regime of behavior and may vary in thickness with the volume fraction of liquid and from one boundary to another in a given sample of material.

10.6 THE BASIC MECHANISMS OF LIQUID-PHASE SINTERING

We now go on to examine in more detail the basic mechanisms and processes occurring in liquid-phase sintering. For convenience, the discussion is divided

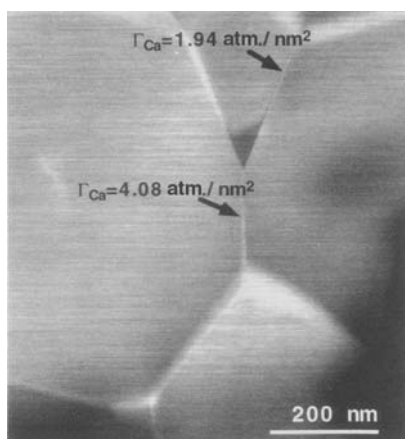


FIGURE 10.18 STEM image showing two neighboring grain boundary films with remarkably different calcium excess in calcia-doped silicon nitride. (From Ref. 38.)

into three main parts related to the three stages of liquid-phase sintering, but it should be remembered that there is some degree of overlap between the successive stages.

10.6.1 Stage 1: Rearrangement and Liquid Redistribution

The relatively large capillary pressures developed for liquid-phase sintering of fine particles cause rapid particle rearrangement when the viscosity of the system is still very low. However, other processes may accompany rearrangement which have important consequences for liquid-phase sintering. Capillary pressure gradients will cause liquid to flow from regions with large pores to regions with smaller pores, leading to redistribution of the liquid.

10.6.1.1 Liquid Redistribution

Experimental observations indicate that considerable redistribution of the liquid may occur during liquid-phase sintering. Perhaps the most dramatic evidence for such redistribution comes from the experiments of Kwon and Yoon (41) who investigated the sintering of fine tungsten powder containing coarse nickel particles that melt to form the liquid phase. As shown in Fig. 10.19, sequential filling of the pores occurs in such a way that the small pores are filled first and the larger pores later. A difficulty with modeling the process is that the local liquid surface curvature depends sensitively on the local geometry, so quantitative statements can only be made for highly idealized microstructures.

Liquid redistribution was analyzed by Shaw (42) for a two-dimensional model of circular particles. The approach involves a determination of the equilibrium distribution of the liquid in different packing arrangements of particles under the condition that the chemical potential of the liquid in all the pores in a particle array is the same at equilibrium. The chemical potential of an atom under the surface of a liquid-vapor meniscus with an average radius of curvature r is

$$\mu = \mu_o + \frac{\gamma_{lv}\Omega}{r} \quad (10.23)$$

where μ_o is the chemical potential of an atom under a flat surface, γ_{lv} is the liquid-vapor surface energy and Ω is the atomic volume. The condition that the chemical potential must be the same is therefore equivalent to the radius of the liquid menisci being the same.

For a regular array of circles (with threefold coordinated pores) in which no shrinkage occurs, Fig. 10.20 shows two possible ways in which the liquid will distribute itself. At small volume fractions, the liquid will be distributed evenly in the necks between the particles (Fig. 10.20a). Increasing the volume of liquid

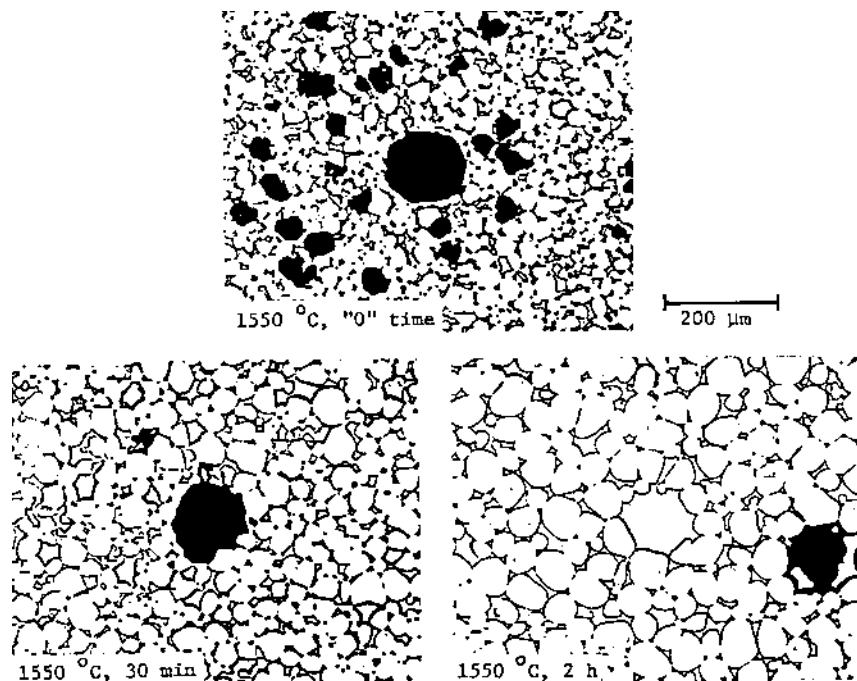


FIGURE 10.19 The change in microstructure during liquid-phase sintering of a mixture of fine ($10\ \mu\text{m}$) W powder, 2 wt% of $30\ \mu\text{m}$ Ni spheres and 2 wt% $125\ \mu\text{m}$ Ni spheres, showing sequential filling of the pores. (From Ref. 41.)

will cause the necks to fill with liquid until some critical volume fraction is reached when, instead of filling each pore evenly, the liquid prefers to adopt a distribution (driven by minimization of surface area) in which a certain fraction of the pores is completely filled and the remainder of the liquid is in isolated necks (Fig. 10.20b). Altering the amount of liquid in this regime has no effect on the amount of liquid situated at the necks but simply alters the fraction of pores that are filled. Increasing the contact angle decreases the range of liquid volume over which the liquid is evenly distributed in the necks.

An important finding of the analysis is the way in which an initially inhomogeneously distributed liquid will redistribute itself in the two-dimensional array. For low liquid content where the liquid is situated at isolated necks, there is always a force driving the liquid to redistribute itself homogeneously. In the second regime, where some of the pores are filled, it is immaterial which pores fill with liquid as long as the correct fraction of pores is filled. Consequently,

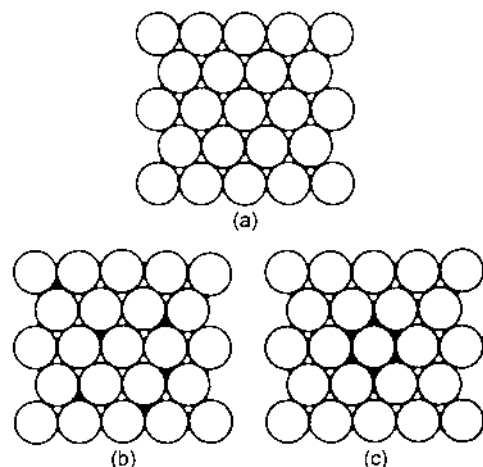


FIGURE 10.20 Possible equilibrium configurations that can be adopted by a liquid in a close-packed array of particles. (a) Isolated necks filled with liquid, (b) fraction of pores completely filled with liquid, and (c) same as (b) but with inhomogeneous liquid distribution. (From Ref. 42.)

once an inhomogeneous distribution such as that in Fig. 10.20c forms, there is no driving force to redistribute the liquid homogeneously.

A model consisting of an array of circles containing pores with threefold and sixfold coordination (Fig. 10.21), while simple in geometry, can provide some insight into how a liquid will redistribute itself in the practical situation of an inhomogeneously packed powder system. The free energy calculations can be used to construct a diagram such as that shown in Fig. 10.22 showing the distribution of the liquid in the array. The diagram shows the fraction of particles surrounding sixfold coordinated pores as a function of the volume fraction of the liquid. Four regions can be distinguished in addition to the shaded region to the right of the diagram corresponding to the case where the pores are completely filled.

To illustrate the significance of Fig. 10.22, let us consider a structure containing a fixed fraction of particles at six-fold coordinated pores and consider how the pores will fill as the volume of liquid is increased. For low volume fraction, the liquid is situated only at isolated necks between the particles. Each point in this region lies on a tie line representing liquid-filled necks at threefold coordinated pores at the bottom of the diagram and liquid-filled necks at sixfold coordinated pores at the top of the diagram. The tie lines connect systems in which the chemical potential of the liquid is the same in the two types of pores.

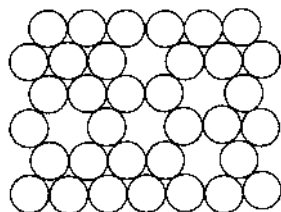


FIGURE 10.21 Example of a two-dimensional arrangement of pores that contains three-fold and sixfold coordinated pores. (From Ref. 42.)

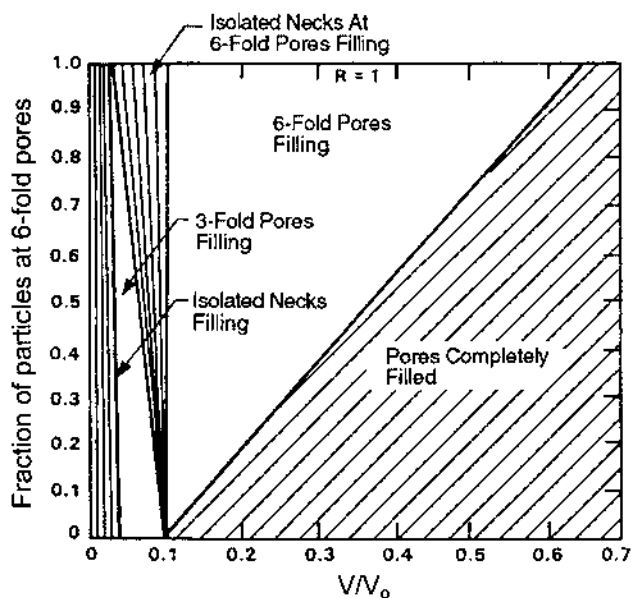


FIGURE 10.22 Liquid distribution diagram for a particle array which contains three-fold and sixfold coordinated pores. (From Ref. 42.)

As the volume fraction of liquid is increased, we enter the second region in which it becomes energetically more favorable to fill threefold coordinated pores than to continue filling the necks between the particles. In this region, the liquid content between the necks remains constant and the increase in the liquid volume goes into filling the threefold coordinated pores. When the third region is reached, all the threefold coordinated pores are filled with liquid and an increase in liquid

volume goes into filling the necks between particles surrounding the sixfold coordinated pores. Finally, in the fourth region, the sixfold coordinated pores become completely filled. When the analysis is extended to include the effect of shrinkage on the liquid distribution, the results show the general sequence of behavior described for the simple mode.

The analysis shows that the pores in the simple model fill sequentially. If we extend the results to the more complex situation of a powder compact with a distribution of pore sizes, the same behavior of sequential filling of the pores is expected to occur. The pores with the smallest coordination number will be the first to fill because such pores have high surface to volume ratio, so a given volume of liquid eliminates more solid–vapor interfacial area. If there is sufficient liquid, the pores with higher coordination number start to fill. However, the pore filling leads to a percolation problem, and the liquid might not have access to all small pores, so some may be empty while large pores start to fill.

The concerns about the homogeneity of the starting powder compact discussed earlier in the book for solid-state sintering also apply to liquid-phase sintering. It is desirable to start with a compact that is packed homogeneously to produce pores with a narrow distribution of sizes, in which the major component and the additive are mixed homogeneously to provide a homogeneous distribution of the liquid phase. Heterogeneous packing leads to sequential filling of the pores so that the larger pores are filled later in the firing process, thereby producing regions that are enriched with the liquid composition. Inhomogeneous mixing leads to an inhomogeneous liquid distribution such that there is no driving force for redistribution of the liquid. Also, using large particles to create the liquid phase (as in Fig. 10.19) leaves huge voids when the particles melt, and the liquid invades the smaller pores. The optimum situation is to start with particles that are pre-coated with the liquid-forming additive. Methods by which particles can be coated include fluidized bed vapor deposition and precipitation from solution (see Chapter 2).

10.6.1.2 Particle Rearrangement

After formation of the liquid, particle rearrangement of the initial network is rapid, occurring in as little as a few minutes. Rearrangement leads to initial densification for a wetting liquid and also determines the initial microstructure of the sintering compact, which affects further densification and microstructure development. Whereas several theoretical and experimental approaches have been used to investigate the process (24,43–46), the analysis of rearrangement in a randomly packed array of particles is a difficult problem, and an understanding of the process in real systems is limited. Computational approaches to rearrangement have been made recently (47) but the significance of the predictions require further evaluation.

Kingery (43) used an empirical approach in which the surface tension forces driving densification are balanced by the viscous forces resisting rearrangement and derived a simple kinetic relationship for the variation of the shrinkage with time:

$$\frac{\Delta L}{L_0} \sim t^{1+y} \quad (10.24)$$

where ΔL is the change in length, L_0 is the original length, and y is a positive number less than one. Whereas Eq. (10.24) does not appear to be unreasonable, experimental verification has not been convincing.

Huppmann and Riegger (19,45) analyzed the capillary forces between particles separated by a liquid bridge (see Fig. 10.12) and compared the results of their analysis with data for Cu-coated W spheres in which the Cu melted to form a homogeneous distribution of the liquid phase between the particles. For close-packed planar arrangements of the spheres, good agreement between the calculations and the data is obtained. However, for randomly packed arrays, local densification occurred, leading to opening of large pores (Fig. 10.23). Less densification than that predicted by the model was observed.

For a system of polycrystalline particles, the overall rearrangement process can consist of two stages, referred to as primary rearrangement and secondary rearrangement. *Primary rearrangement* describes the rapid rearrangement, soon after the formation of the liquid, of the polycrystalline particles under the surface tension forces of the liquid bridge. As described earlier, if $\gamma_{ss}/\gamma_{sl} > 2$, the liquid can penetrate the grain boundaries between the particles in the polycrystals, and

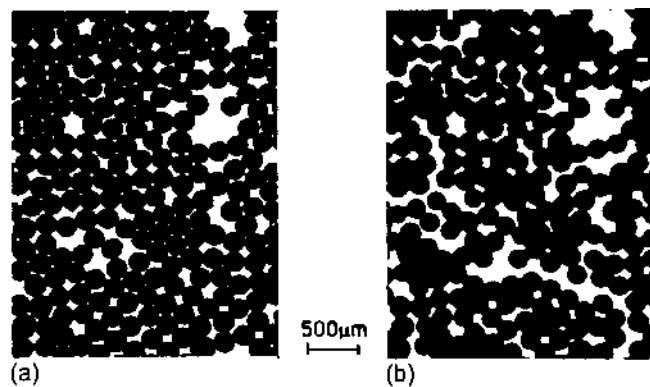


FIGURE 10.23 Planar array of copper-coated tungsten spheres before (left) and after (right) liquid-phase sintering. (From Ref. 24.)

fragmentation of the polycrystalline particles will occur. *Secondary rearrangement* describes the rearrangement of these fragmented particles. Since it depends on the rate at which the grain boundaries are dissolved away, secondary rearrangement occurs more slowly than primary rearrangement. The two types of rearrangement are sketched in Fig. 10.24.

If sufficient liquid is present, rearrangement alone may lead to a fully dense material. The relative amounts of solid and liquid for this to occur depends on the rearranged density of the particulate solid. As an example, let us consider a powder compact with a relative density of 60% (porosity = 40%), consisting of a major component and a liquid-producing additive. After formation of the liquid, suppose that the solid particles rearrange to form 64% of the final product (i.e., a packing density close to that for dense random packing of monosize spheres). For a liquid volume fraction greater than 36%, full densification is achieved by rearrangement alone. When the liquid content is less than 36%, full densification requires the occurrence of additional processes, e.g., solution-precipitation. The volumetric shrinkage due to rearrangement as a function of liquid volume is

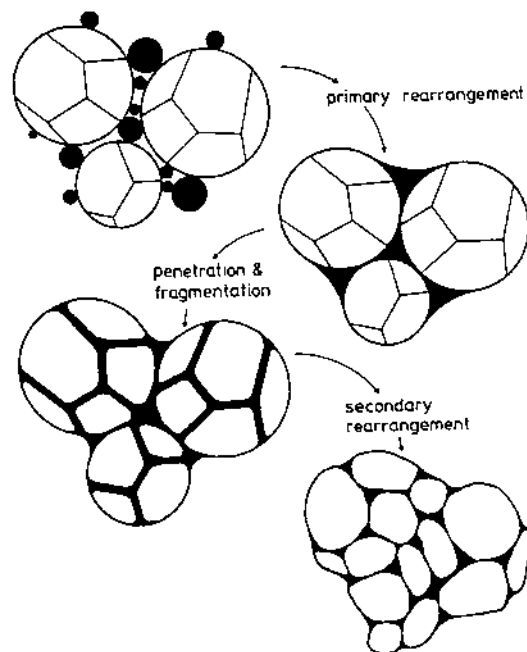


FIGURE 10.24 Schematic diagram illustrating fragmentation and rearrangement of polycrystalline particles. (From Ref. 15.)

shown in Fig. 10.25. The results in the figure imply that rearrangement to a denser packing is possible with an arbitrarily small amount of liquid, but in practice it is commonly observed that rearrangement is difficult when the liquid volume is small (less than 2–3 vol%), particularly if the solid particles have irregular shapes.

10.6.2 Stage 2: Solution-Precipitation

In stage 2, rearrangement decreases considerably and the *solution-precipitation* mechanism becomes dominant. The major processes that occur by the solution-precipitation mechanism are densification and coarsening. They occur concurrently and may be accompanied by *grain shape accommodation* if the liquid volume is small. In addition to solution-precipitation, *coalescence* of small grains with contacting large grains also contributes to coarsening and grain shape accommodation. There are two models for densification, referred to in this book as (1) densification by contact flattening and (2) densification accompanied by Ostwald ripening.

10.6.2.1 Densification by Contact Flattening

Densification by contact flattening was described by Kingery (43). As a result of the compressive capillary force of a wetting liquid, the solubility at the

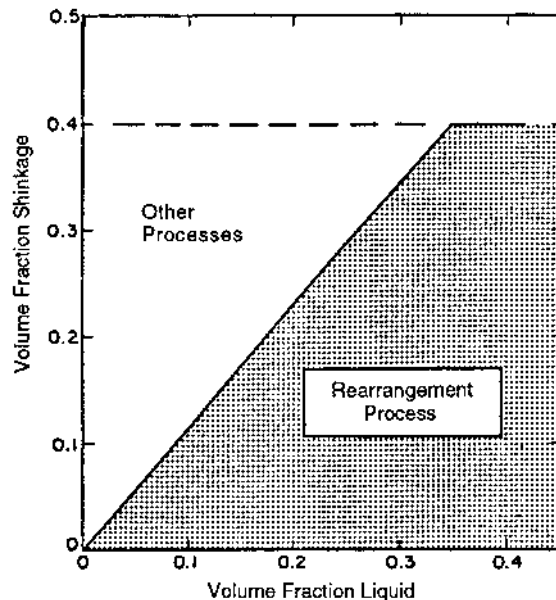


FIGURE 10.25 Fractional shrinkage due to the rearrangement process for different liquid contents. (From Ref. 43.)

contact points between the particles is higher than that at other solid surfaces. This difference in solubility (or chemical potential) leads to matter transport away from the contact points, thereby allowing center-to-center approach under the action of the surface tension forces and the formation of a flat contact zone (Fig. 10.26). As the radius of the contact zone increases, the stress along the interface decreases and densification slows. The rate of matter transport is controlled by the slower of the two mechanisms: (1) diffusion through the liquid and (2) the interface reaction leading to solution into the liquid or precipitation onto the particle surfaces.

Kingery assumed a model consisting of two spherical particles of the same radius a , for which the geometrical parameters are similar to those outlined in Fig. 8.10. If each sphere is dissolved away along the center-to-center line by a distance h to give a circular contact area of radius X , then

$$h \approx \frac{X^2}{2a} \quad (10.25)$$

The volume of material removed from each sphere is given by $V \approx \pi X^2 h/2$, and using Eq. (10.25), this becomes

$$V \approx \pi a h^2 \quad (10.26)$$

Rate control by diffusion through the liquid

Kingery adopted a diffusional flux equation similar to that assumed by Coble for the intermediate stage of solid-state sintering (see Chapter 8). In this case, the flux from the boundary per unit thickness is given by

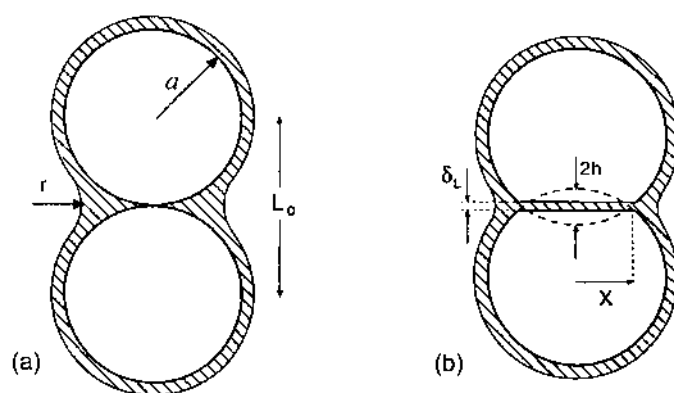


FIGURE 10.26 Idealized two-sphere model for densification by contact flattening.

$$J = 4\pi D_L \Delta C \quad (10.27)$$

where D_L is the diffusion coefficient for the solute atom in the liquid and ΔC is the solute concentration difference between that at the contact area C and that at a flat, stress-free surface C_o . If the thickness of the liquid bridge is δ_L , the rate of removal of the solid is

$$\frac{dV}{dt} = \delta_L J = 4\pi D_L \delta_L \Delta C \quad (10.28)$$

As outlined in Chapter 7, if C is small, we can write

$$\frac{\Delta C}{C_o} = \frac{p\Omega}{kT} \quad (10.29)$$

where p is the local stress on an atom, Ω is the atomic volume, k is the Boltzmann constant, and T is the absolute temperature. The capillary pressure Δp due to a spherical pore in the liquid is given by Eq. (10.1), and as described earlier, this capillary pressure is equivalent to an externally applied hydrostatic pressure that would have to be applied to the particulate system in order that the resulting interparticle force is equal to that produced by the liquid bridge. Because the contact area is less than that of the external area, the local pressure is magnified at the contact area. Assuming a simple force balance, as discussed earlier for the stress intensification factor in solid-state sintering, the local pressure p at the contact area is given by

$$pX^2 = k_1 \Delta p a^2 \quad (10.30)$$

where k_1 is a geometrical constant. Substituting for Δp and X from Eqs. (10.1) and (10.25) gives

$$p = k_1 \frac{\gamma_{lv} a}{rh} \quad (10.31)$$

Assuming that the radius of the pore is proportional to the sphere radius, i.e., $r \approx k_2 a$, where k_2 is assumed to remain constant during sintering, Eq. (10.31) becomes

$$p = \frac{k_1}{k_2} \frac{\gamma_{lv}}{h} \quad (10.32)$$

From Eqs. (10.28), (10.29) and (10.32) we obtain

$$\frac{dV}{dt} = \frac{4\pi k_1 D_L \delta_L C_o \Omega \gamma_{lv}}{k_2 h k T} \quad (10.33)$$

But dV/dt is also equal to $2\pi ah \, dh/dt$ from Eq. (10.26), so Eq. (10.33) can also be written

$$h^2 dh = \frac{2k_1 D_L \delta_L C_0 \Omega \gamma_{lv}}{k_2 a k T} dt \quad (10.34)$$

Integrating and applying the boundary condition that $h = 0$ at $t = 0$, Eq. (10.34) gives

$$h = \left(\frac{6k_1 D_L \delta_L C_0 \Omega \gamma_{lv}}{k_2 a k T} \right)^{1/3} t^{1/3} \quad (10.35)$$

Since $h/a = -\Delta L/L_0 = -(1/3)\Delta V/V_0$ (for small $\Delta L/L_0$), where $\Delta L/L_0$ and $\Delta V/V_0$ are the linear shrinkage and the volumetric shrinkage of the powder compact, respectively, we can write

$$-\frac{\Delta L}{L_0} = -\frac{1}{3} \frac{\Delta V}{V_0} = \left(\frac{6k_1 D_L \delta_L C_0 \Omega \gamma_{lv}}{k_2 a^4 k T} \right)^{1/3} t^{1/3} \quad (10.36)$$

When diffusion through the liquid is the rate-controlling mechanism, the shrinkage is predicted to be proportional to the one-third power of the time and inversely proportional to the four-thirds power of the initial particle size. It is also predicted to increase with the one-third power of the thickness of the intergranular liquid layer.

Rate control by phase boundary reaction

When the phase boundary reaction leading to dissolution of the solid into the liquid is the rate-controlling mechanism, the volumetric rate of material transfer is assumed to be directly proportional to the contact area, times a rate constant for the phase boundary reaction, times the increase of the activity of the solid at the contact area due to the capillary pressure; that is,

$$\frac{dV}{dt} = k_3 \pi X^2 (a - a_0) = 2\pi k_3 h a (C - C_0) \quad (10.37)$$

where k_3 is the reaction rate constant and the activities a and a_0 are taken to be equal to the concentrations. Following the steps outlined above for the case of diffusion control, the shrinkage is given by

$$-\frac{\Delta L}{L_0} = -\frac{1}{3} \frac{\Delta V}{V_0} = \left(\frac{2k_1 k_3 C_0 \Omega \gamma_{lv}}{k_2 a^2 k T} \right)^{1/2} t^{1/2} \quad (10.38)$$

In this case, the shrinkage is predicted to be proportional to the square root of the time and inversely proportional to the initial particle radius.

10.6.2.2 Densification Accompanied by Ostwald Ripening

The second mechanism of densification is based on the observations by Yoon and Huppmann (48) for liquid-phase sintering of W(Ni) powder mixtures. In an idealized model (Fig. 10.27), dissolution of the small grains and precipitation on the large grains away from the contact points lead to center-to-center approach of the large grains (i.e., to shrinkage). In this way, densification is accompanied by Ostwald ripening. Densification by dissolution of the small grains and precipitation on the large grains depends on the particle size distribution and other factors. Theoretical analysis of the shrinkage rate is difficult, but one estimate (19,50) based on diffusion-controlled Ostwald ripening leads to a form similar to that predicted by the contact flattening model:

$$-\frac{\Delta L}{L_0} = -\frac{1}{3} \frac{\Delta V}{V_0} = \left(\frac{48 D_L C_0 \Omega \gamma_{lv}}{a^3 k T} \right)^{1/3} t^{1/3} \quad (10.39)$$

10.6.2.3 Comparison with Experimental Data

Experimental data often show reasonable agreement with the predicted dependence of the shrinkage on the one-third power of time, which is taken to indicate a *diffusion-controlled* solution-precipitation mechanism (19,52). In several stud-

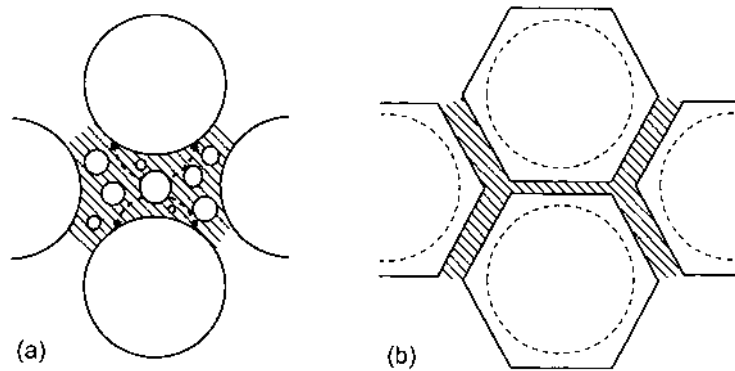


FIGURE 10.27 Schematic diagram illustrating densification accompanied by Ostwald ripening. Grain shape accommodation can also occur when the liquid volume fraction is low.

ies, the fitting of the data to determine the time dependence of the shrinkage appears somewhat arbitrary. The time at which solution-precipitation is assumed to begin has a significant effect on the exponent and this time is often difficult to determine because of the overlap with the previous rearrangement stage. In practice, the shrinkage data can normally be fitted with a curve having a smoothly varying slope instead of a line having a fixed slope equal to the predicted value.

In view of the initially high capillary forces exerted on small grain contacts, it appears reasonable that Kingery's contact flattening model is initially important. The model can also account for the phenomenon of grain shape accommodation. On the other hand, observations with real powder systems, which normally have a distribution of particle sizes, show that densification correlates with the onset of coarsening in the solution-precipitation stage and the dissolution of the small grains. This observed coarsening cannot be explained by Kingery's model. Densification accompanied by coarsening is clearly observed in the experiments by Yoon and Huppmann (48) who studied the sintering of a mixture of coarse, single crystal, spherical tungsten particles (200–250 μm in diameter), fine tungsten particles (average size $\approx 10 \mu\text{m}$), and fine nickel powder that melts to form the liquid phase. When the tungsten dissolves in the molten nickel and precipitates out, the precipitated material is not pure tungsten but a solid solution containing a small amount of nickel ($\sim 0.15 \text{ wt}\%$). By etching in Murakami's solution, the precipitated tungsten can be distinguished from the pure tungsten. Figure 10.28 shows the microstructure, after sintering at 1670°C for 3, 20, 120, and 360 min, of a powder mixture that contained 48 wt% large tungsten spheres, 48 wt% fine tungsten particles, and 4 wt% nickel. The microstructures show that the fine tungsten particles dissolve and precipitate on the coarse tungsten spheres. These observations, coupled with the measured decrease in porosity of the system with time, clearly indicate that Ostwald ripening accompanies shrinkage.

Figure 10.28 also indicates that the precipitated tungsten does not grow uniformly around the large tungsten spheres but that it occurs preferentially in the regions where no neighboring large grains impede it. The coarsened large tungsten spheres develop flat faces and assume the shape of a polyhedron, so densification and coarsening for this powder composition are accompanied by grain shape accommodation. The occurrence of accommodation indicates that Kingery's contact flattening mechanism is active, but there is no clear indication as to which mechanism causes shrinkage.

10.6.2.4 Grain Shape Accommodation

Grain shape accommodation is clearly observed in the micrographs of Fig. 10.28 for the W(Ni) system containing 4 wt% Ni. However, many microstructures of materials produced by liquid-phase sintering also show rounded (spheroidal) grains. As an example, Fig. 10.29 shows the microstructure for the same W(Ni) system described in Fig. 10.28 but with a higher amount of liquid (14 wt% Ni).

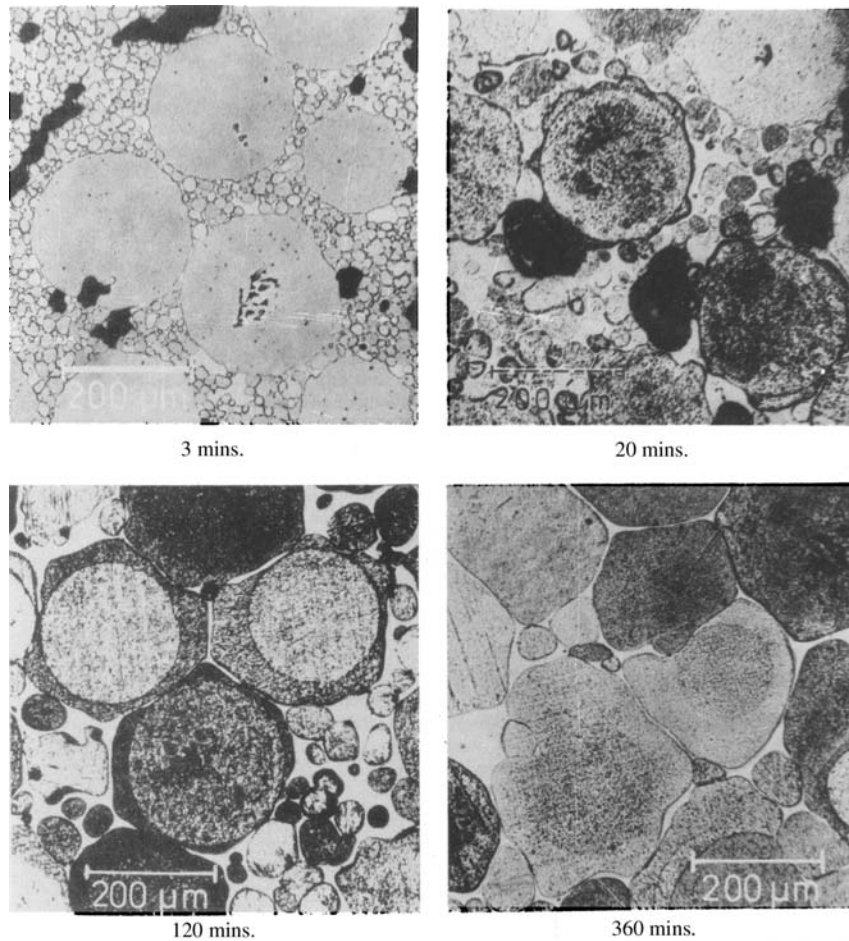


FIGURE 10.28 The microstructures of a mixture of 48 wt% large W spheres, 48 wt% fine W powder, and 4 wt% Ni after sintering for various times at 1670°C. (From Ref. 48.)

It is clear from Figs. 10.28 and 10.29 that the volume fraction of liquid is a key factor in determining whether grain shape accommodation will occur.

The occurrence of grain shape accommodation is normally favored when the amount of liquid is relatively small. In this case, the liquid is insufficient to completely fill the voids between the grains as long as the grains take up a rounded or spheroidal shape. Grain shape accommodation produces a polyhedral grain

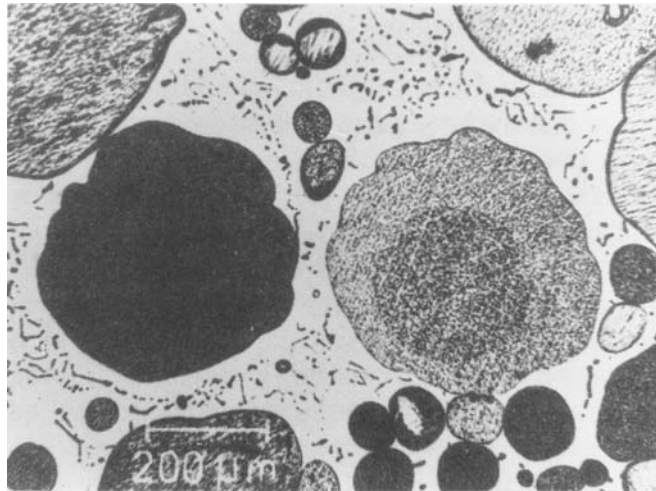


FIGURE 10.29 The microstructure of a mixture of 43 wt% large W spheres, 43 wt% fine W powder and 14 wt% Ni after sintering for 60 min at 1670°C. (From Ref. 48.)

shape with flat contact surfaces, and this leads to a more efficient packing of the grains. Liquid released from the well-packed regions can flow into the pores.

Grain shape accommodation will occur if it leads to a decrease in the energy of the system. Compared to a sphere with the same volume, the polyhedral grain shape has a higher surface area. If grain shape accommodation is to occur, the decrease in the interfacial energy associated with the filling of the pores must overcome the increase in the interfacial energy associated with the development of the polyhedral grain shape. For a large amount of liquid, the capillary pressure is low, so the driving force for contact flattening and shape accommodation is significantly reduced, and the spheroidal grain shape is maintained.

10.6.2.5 Coalescence

Grains pulled into contact by a wetting liquid can lead to coarsening by coalescence (53). As sketched in Fig. 10.30, a possible mechanism for coalescence involves contact formation between the grains, neck growth, and migration of the grain boundary. Coalescence can occur by several mechanisms, such as solid-state grain boundary migration, liquid-film migration, and solution-precipitation through the liquid (Fig. 10.31). When the dihedral angle is low, the liquid partially penetrates the grain boundary and movement of the boundary will involve initially an increase in the grain boundary energy. Coalescence is therefore impeded but solution-precipitation from the small grain to the large grain can act to eliminate

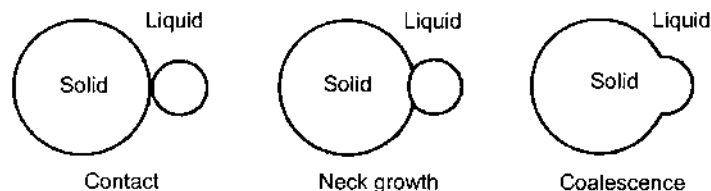


FIGURE 10.30 Schematic diagram illustrating grain growth by coalescence of small and large grains.

the energy barrier. For larger dihedral angles, where the liquid penetration of the boundary is significantly reduced, coalescence may become energetically favorable. The process is enhanced when the difference between the particle sizes becomes greater, so the conditions are most favorable for coalescence in the early portion of the solution-precipitation stage. Whereas coalescence by solid-state migration of the boundary has been reported in a few metallic systems (54), the occurrence of the process is probably low.

In systems where no solid-solid contact exists, coalescence may be possible by migration of the liquid film separating the grains. This mechanism has been found to occur in a few metallic systems and is normally referred to as directional grain growth. The coalescence process is not driven by a reduction in interfacial energy but by a reduction in chemical energy. Yoon and Huppmann (55) observed that when single-crystal W spheres are sintered in the presence of liquid Ni, one W sphere grows at the expense of its neighbor (Fig. 10.32a). An electron microprobe

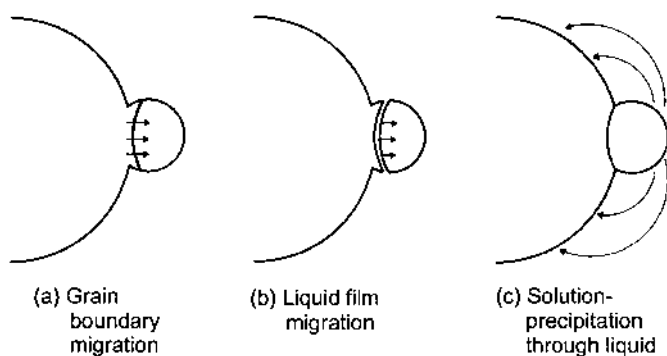


FIGURE 10.31 Three possible mechanisms of coalescence between contacting grains. (a) solid-state grain boundary migration; (b) liquid-film migration; (c) solution-precipitation through the liquid.

analysis shows that the shrinking grain consists of pure tungsten, while the precipitated material on the growing grain is a solid solution of tungsten containing 0.15 wt% nickel (Fig. 10.32b). This compositional difference between the pure W and the solid solution provides a large decrease in chemical energy, which more than offsets the increase in the interfacial energy.

10.6.3 Stage 3: Ostwald Ripening

In stage 3, densification slows considerably and microstructural coarsening clearly becomes the dominant process. For $\gamma_{ss}/\gamma_{sl} > 2$, the grains are completely separated by a liquid layer, the thickness of which, as discussed earlier, may decrease asymptotically. When the dihedral angle is greater than zero, solid-solid contacts lead increasingly to the formation of a rigid skeleton that inhibits the elimination of the isolated pores present in the liquid phase. With the development of the solid-solid contacts, solid-state sintering and coarsening take place but matter transport through the liquid is much faster, so solution-precipitation can still dominate over solid-state transport processes.

10.6.3.1 Densification by Pore Filling

When the volume of the liquid phase is fairly low, solution-precipitation and grain shape accommodation lead to a slow, continuous elimination of the isolated

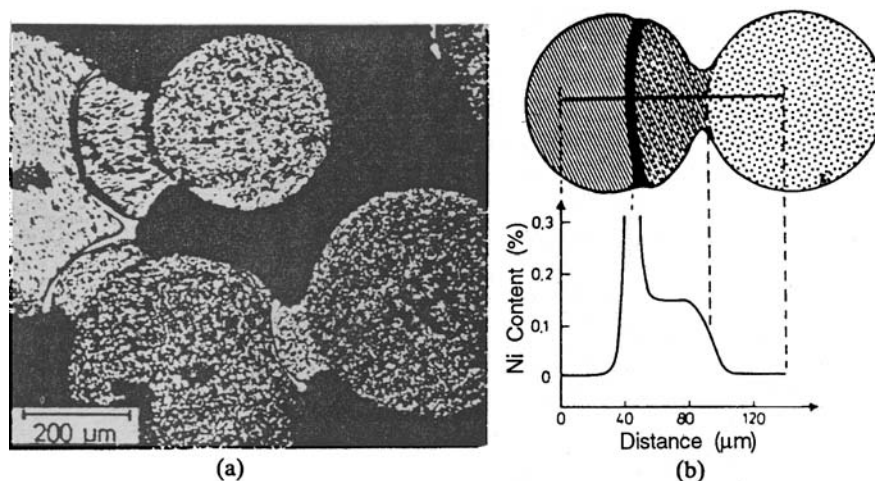


FIGURE 10.32 Directional grain growth during liquid-phase sintering of single-crystal W spheres with nickel at 1640°C, showing (a) the microstructure and (b) the microprobe analysis. (From Ref. 55.)

porosity. In some cases, continued densification of the solid skeletal network can lead to partial expulsion of the liquid phase. For a larger volume of liquid, Kang et al. (56) have shown that the filling of the isolated pores may occur in a discontinuous manner. The filling of the pores appears to be determined by grain growth rather than by grain shape accommodation. In the experiments, Kang et al. studied the shape change of grains surrounding large, isolated pores in the Mo(Ni) system. The sample was heated for 30 min at 1460°C and cooled. By repeating the sintering process three times, the shape of the growing grains after each heating cycle was revealed by ghost boundaries formed within the grains as a result of strong etching. As shown in Fig. 10.33a, the grains surrounding the pore grow laterally along the pore surface (see, for example, the grains labeled A and B), so it is clear that the pore is not filled continuously by matter deposited on its surface. The pore can remain roughly unchanged for an extended period of sintering, but at some point, when the size of the grains surrounding the pore reaches a critical value, the pore is filled rapidly.

As sketched in Fig. 10.34, a large pore remains unfilled because of preferential wetting of the necks between the particles. As the grains grow, the liquid reaches a favorable condition for filling the pore as determined by the curvature of the liquid–vapor meniscus (19,58). From Fig. 10.35, the radius of curvature of the meniscus is given by

$$r_m = a \frac{(1 - \cos \alpha)}{\cos \alpha} \quad (10.40)$$

where a is the radius of the grain (assumed to be spherical), so r_m increases with the grain size. For a contact angle of zero, the critical point for pore filling occurs when r_m becomes equal to the pore radius r , because after this point r_m can only decrease, leading to a reduction in the capillary pressure surrounding the pore. Liquid is drawn from the numerous menisci at the surface of the sample, whose radii change only very slightly because the volume of liquid required to fill the pore is small. If the contact angle is greater than zero, r_m must exceed r for pore filling to occur.

After pore filling (Fig. 10.33b), the etch boundaries of the grain labeled C reveal that the grains grow preferentially into the pocket of liquid, thereby leading to a more rounded grain shape. The growth of the grains into the liquid pocket also has the effect of improving the homogeneity of the microstructure because the size of the heterogeneity (i.e., the liquid pocket) is reduced.

Gases trapped in the isolated pores during final stage densification can prevent complete filling of the pores. As discussed in Chapter 12, sintering in a gaseous atmosphere that is not soluble in the liquid leads to trapped gases in the pores, so densification stops when the increasing gas pressure in the shrinking pores equals the sintering stress, resulting in a limiting final density. Prolonged

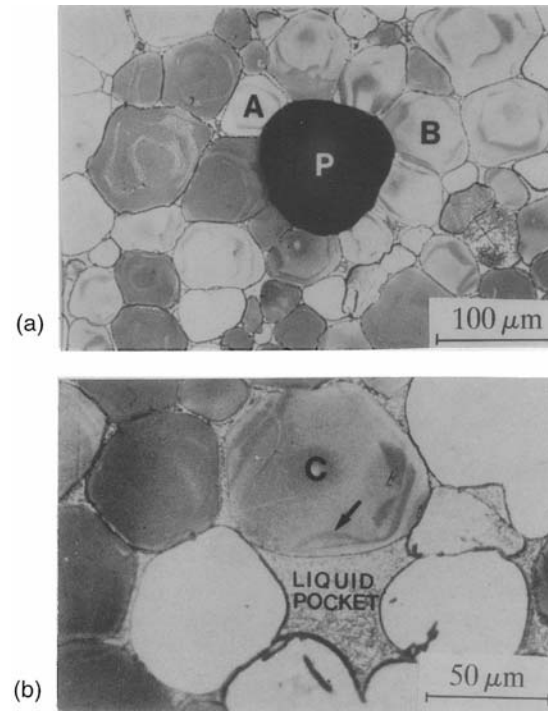


FIGURE 10.33 Microstructures of a Mo (4 wt% Ni) system showing (a) lateral growth of grains (such as A and B) around a pore (P) for a specimen sintered in three cycles (for 30 min in each cycle) at 1460°C; (b) after pore filling, preferential growth of a grain (C) into a liquid pocket formed at a pore site, resulting in a more homogeneous microstructure in a specimen sintered in three cycles (60, 30 and 30 min) at 1460°C. (From Ref. 56.)

sintering, leading to pore growth by coalescence or by Ostwald ripening, results in a reduction of the sintered density. These problems can be alleviated by sintering in a vacuum or in a gaseous atmosphere that is soluble in the liquid.

10.6.3.2 Microstructural Coarsening

Coarsening by the Ostwald ripening mechanism was suggested as early as the 1930s to account for the significant grain growth observed in the liquid-phase sintering of heavy metals. Following the theoretical analysis of the process by Lifshitz, Slyozov and Wagner, referred to as the *LSW theory* (see Chapter 9), several studies have been made to compare coarsening data obtained in liquid-phase sintering with the theory. According to the LSW theory, as well as modified

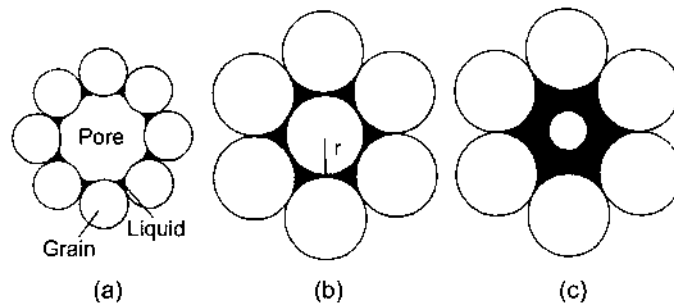


FIGURE 10.34 Pore filling during grain growth. A large pore is stable until grain growth increases the liquid meniscus radius sufficiently for capillary refilling of the pore. (From Ref. 57.)

analyses that take into account varying volume fraction of precipitates, the growth of the average grain size G with time t is given by

$$G^m = G_0^m + Kt \quad (10.41)$$

where G_0 is the initial value grain size, K is a temperature-dependent parameter, and the exponent m is dependent of the rate controlling mechanism: $m = 3$ when diffusion through the liquid is rate-controlling whereas $m = 2$ for rate control by the interface reaction.

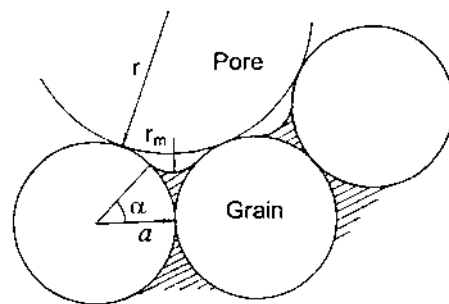


FIGURE 10.35 Calculation model for pore refilling based on spherical grains surrounding the pore. Pore refilling depends on the liquid meniscus radius exceeding the pore radius. (From Ref. 57.)

The grain growth exponent m is found to be close to 3 for many ceramic and metallic systems, indicating that diffusion-controlled coarsening is commonly active. An example is the work of Buist et al. (2) who investigated the growth of periclase (MgO), lime (CaO), and corundum (α -Al₂O₃) grains in a variety of liquid-phase compositions for a liquid content of 10–15 vol%. Typical microstructures of the sintered samples are shown in Fig. 10.36. In all cases, a grain growth exponent very close to 3 was observed. Figure 10.37 shows the data for the growth of periclase grains in four different liquids corresponding to systems with the compositions given in Table 10.4. Despite the difference in the composition of the liquids, the results show good agreement with the cubic growth law.

The solubility of the solid in the liquid and the diffusion of the solute atoms through the liquid are expected to increase with temperature in accordance with the Arrhenius relationship, so the rate of coarsening increases with temperature, as can be observed from Fig. 10.37. An increase in the dihedral angle produces a reduction in the area of the solid in contact with the liquid and a consequent increase in the grain boundary area. Because matter transport through the liquid is faster than by solid-state diffusion, a reduction in the solid–liquid contact area is expected to lower the rate of matter transport by solution-precipitation, thereby leading to a reduction in the grain growth rate. Figure 10.38 shows that the measured grain growth rate constant for liquid-phase sintered MgO compositions (Table 10.4) decreases with increasing dihedral angle. The microstructures of the compositions 2 and 3 should also be compared. Under nearly identical conditions, composition 3 with the lower dihedral angle shows a larger grain size and less solid-solid contacts (Fig. 10.36B) than composition 2 with the higher dihedral angle (Fig. 10.36C).

Decreasing volume fraction of liquid has the effect of raising the rate of grain growth (59), which is consistent with diffusion through the liquid

TABLE 10.4 Parameters for the Liquid-Phase Sintering of MgO^a in Four Different Liquids at 1550 and 1725°C

Number	Composition (wt %)	Dihedral Angle		Vol% Liquid	
		1550°C	1725°C	1550°C	1725°C
1	85 MgO(15 CaMgSiO ₄)	25	25	15	15
2	80 MgO(15 CaMgSiO ₄ ·5Cr ₂ O ₃)	40	30	16	15
3	80 MgO(15 CaMgSiO ₄ ·5Fe ₂ O ₃)	20	20	16	16
4	85 MgO(15 Ca ₂ Fe ₂ O ₅)	15	15	11	12

^a See Figs. 10.36–10.38.

Source: Ref. 2.

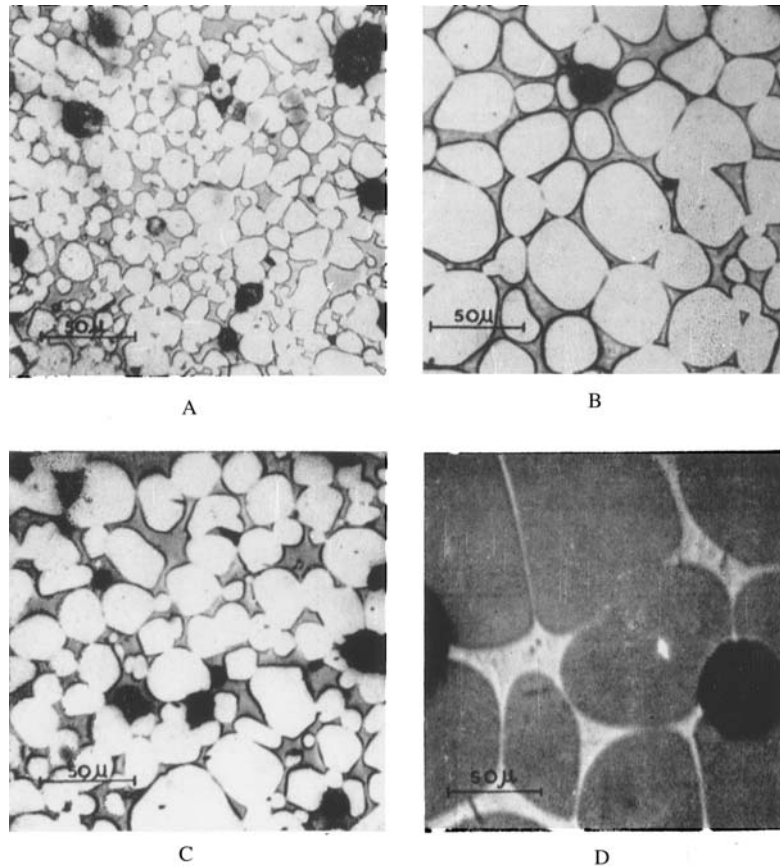


FIGURE 10.36 Microstructures of (A) composition 3 (see Table 10.4) after sintering for 0.5 h at 1550°C, showing rounded grains in a silicate matrix; (B) composition 3 after sintering for 8 h at 1550°C; (C) composition 2 after sintering for 8 h at 1550°C; (D) a composition of 85 wt% CaO (15 wt% $\text{Ca}_2\text{Fe}_2\text{O}_5$) after firing for 8 h at 1550°C, showing rounded grains in a ferrite matrix. (The very dark areas are pores, some of which contain Araldite.) (From Ref. 2.)

being the rate-controlling mechanism. With decreasing liquid volume, the diffusion distance decreases, so matter transport is faster, leading to an increase in the growth rate. Several theories have been proposed to explain the dependence of grain growth on the volume fraction of liquid (15). These analyses result in the same functional dependence of the grain size on time [Eq. (10.41)]

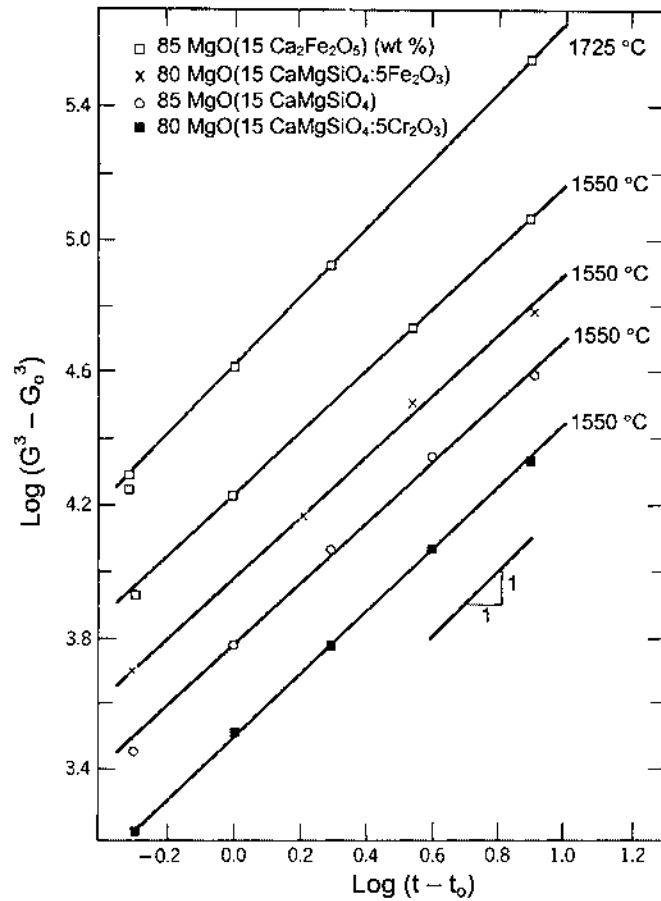


FIGURE 10.37 Plots of $\log (G^3 - G_0^3)$ against $\log(t - t_0)$ for systems containing periclase grains and liquid (see Table 10.4) at the sintering temperatures shown. G and G_0 are the mean grain diameters (in μm) at times t and t_0 (in hours). (From Ref. 2.)

but with a modified rate constant to account for the shorter diffusion distance with decreasing liquid volume. The most successful modification gives (60)

$$K = K_I + \frac{K_L}{V_L^{2/3}} \quad (10.42)$$

where $K_I + K_L$ represents the rate constant at infinite dilution, K_L is a microstructure-dependent parameter, and V_L is the volume fraction of liquid.

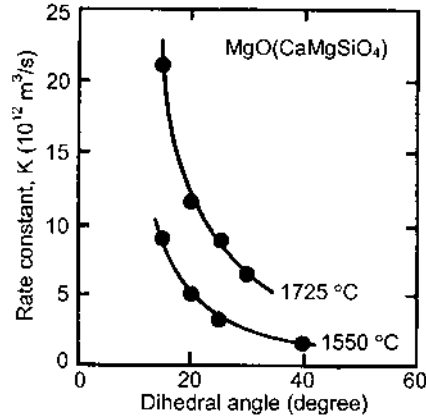


FIGURE 10.38 Effect of dihedral angle on the grain growth rate constant. (From Ref. 2.)

10.7 HOT PRESSING WITH A LIQUID PHASE

Densification in the presence of a liquid phase can also be used with hot pressing. The chemical potential of the atoms under the contact surfaces increases with the applied stress, so matter transport from the contact regions to the pores is enhanced, thereby leading to an increase in the densification rate. Hot pressing with a liquid phase was used by Bowen et al. (61) to densify Si_3N_4 powder containing MgO as the liquid-producing additive, which reacts with the SiO_2 -rich surface layer on the Si_3N_4 powder to produce a eutectic liquid at $\sim 1550^\circ\text{C}$. The measured densification kinetics are consistent with a solution-precipitation mechanism in which diffusion through the liquid is rate-controlling, and they can be described by an equation similar to Coble's equation for grain boundary diffusion-controlled solid-state sintering (see Chapter 8) provided that (1) the grain boundary thickness δ_{gb} is replaced by the thickness of the liquid layer δ_L , (2) the grain boundary diffusion coefficient D_{gb} is replaced by the diffusion coefficient for the solute in the liquid D_L , and (3) the solid-vapor interfacial energy γ_{sv} is replaced by the liquid-vapor interfacial energy γ_{lv} . When the applied pressure p_a is much greater than the capillary pressure due to the liquid meniscus, the densification rate can be written

$$\frac{1}{\rho} \frac{d\rho}{dt} = \frac{AD_L\delta_L\Omega}{G^3kT} p_a \phi \quad (10.43)$$

where A is a geometrical constant (equal to 47.5 for the intermediate stage of sintering), Ω is the atomic volume of the rate controlling species, G is the grain

size, k is the Boltzmann constant, T is the absolute temperature, and ϕ is the stress intensification factor.

Figure 10.39 shows an example of the data used to test the validity of Eq. (10.43) for the hot pressing of $\text{Si}_3\text{N}_4(\text{MgO})$ at 1650°C . After some threshold MgO content of ~ 1 wt%, the densification rate at a fixed relative density (0.70) increases linearly with the amount of MgO additive. If the MgO reacts with the available SiO_2 on the Si_3N_4 grains to form a composition close to the MgSiO_3 – SiO_2 eutectic, then the amount of liquid phase is approximately proportional to the MgO content. The thickness of the liquid layer is proportional to the amount of liquid and thus to the amount of MgO, so Fig. 10.39 indicates that the densification rate is proportional to δ_L .

10.8 USE OF PHASE DIAGRAMS IN LIQUID-PHASE SINTERING

Phase equilibrium diagrams (or simply phase diagrams) play an important role in the selection of powder compositions and sintering conditions for liquid-phase sintering. Whereas the diagrams give the phases present under *equilibrium* conditions, the reaction kinetics during liquid-phase sintering are often too fast for equilibrium to be achieved, so the phase diagrams should therefore serve only as a guide.

For a binary system consisting of a major component (or base B) and a liquid-producing additive A, the first task is to determine which additives will

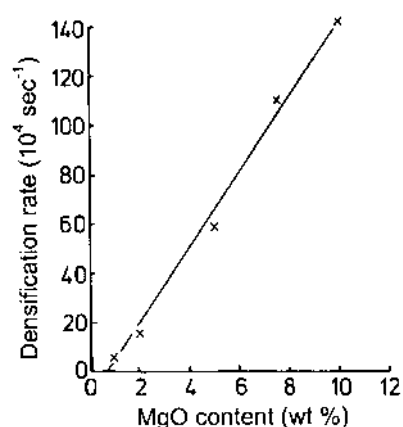


FIGURE 10.39 Densification rate at a relative density of 0.70 versus MgO additive content for hot pressing of the $\text{Si}_3\text{N}_4(\text{MgO})$ system at 1650°C (61). (Courtesy of R. J. Brook.)

form a liquid phase with the major component and under what conditions. For most systems, phase diagrams will be available in reference books (62), but if the desired diagram or region of the diagram is not available, considerable time is required to construct it. Figure 10.40 shows an idealized binary phase diagram that indicates the desirable composition and temperature characteristics for liquid-phase sintering. In addition to the solubility requirements discussed earlier, a desirable feature is a large difference in melting temperature between the eutectic and the base B. The composition of the system should also be chosen away from the eutectic composition so that the liquid volume increases slowly with temperature, thereby preventing the sudden formation of all of the liquid at or near the eutectic temperature. In practice, a typical sintering temperature would be chosen somewhat above the eutectic temperature with a composition in the (L + S₂) region.

Zinc Oxide

Zinc oxide is liquid-phase sintered with ~ 0.5 mol% of Bi₂O₃ (and small additions of other oxides) for the production of varistors. The phase diagram for the ZnO(Bi₂O₃) system (Fig. 10.41) shows the formation of a Bi-rich liquid phase above the eutectic temperature of 740°C (63). Samples that have been quenched from the sintering temperature show a liquid film that completely penetrates the

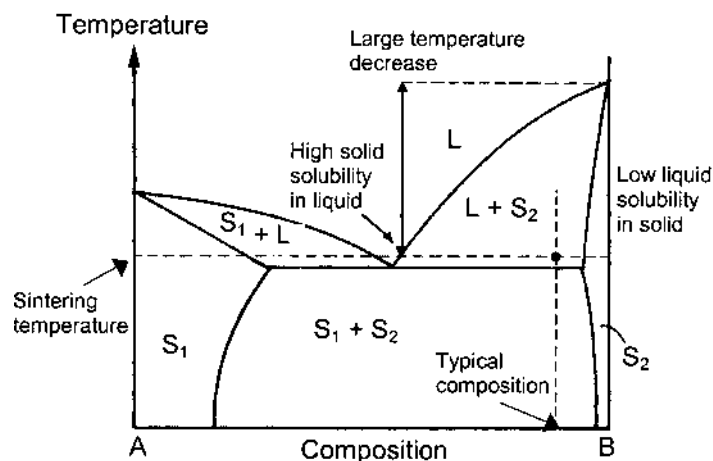


FIGURE 10.40 Model binary phase diagram showing the composition and sintering temperature associated with liquid phase sintering in the L + S₂ phase field. The favorable characteristics for liquid-phase sintering include a suppression of the melting temperature, high solid solubility in the liquid, and low liquid solubility in the solid. (From Ref. 16.)

grain boundaries (Fig. 10.14c), indicating a zero dihedral angle. However, during slow cooling, the liquid and solid compositions change, with precipitation of the principal phase, leading to a substantial increase in the dihedral angle and to a nonwetting configuration (Fig. 10.42).

Silicon Nitride

Silicon nitride is one of the ceramics best suited for mechanical engineering applications at high temperatures. The crystal structure of Si_3N_4 has a high degree of covalent bonding, so diffusional mass transport by solid-state diffusion is very slow. Si_3N_4 powders are therefore normally converted into a dense body by liquid-phase sintering. Much of the progress made in the fabrication and application of Si_3N_4 can be traced to careful work in the construction and use of phase diagrams.

Si_3N_4 powders commonly contain 1–5 wt% SiO_2 as a surface oxidation layer. At a high enough temperature, an oxide additive reacts with the SiO_2 to form a silicate liquid that aids densification. On cooling, the silicate liquid often forms an amorphous intergranular glass. MgO (5–10 wt%) was one of the first successful additives used in the fabrication of Si_3N_4 . It forms a eutectic liquid with SiO_2 at $\sim 1550^\circ\text{C}$, but the sintering temperature can be anywhere between 100–300°C higher than the eutectic temperature. Figure 10.43a shows the identi-

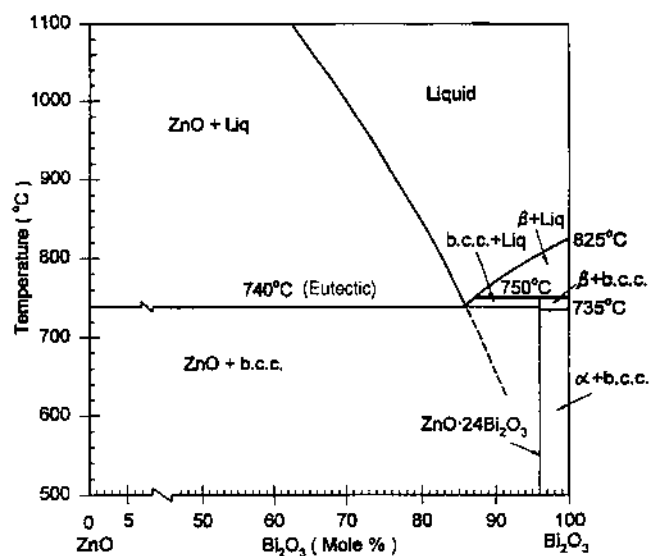


FIGURE 10.41 ZnO-Bi₂O₃ phase diagram showing limited solid solubility of Bi₂O₃ in ZnO and the formation of a eutectic containing 86 mol% Bi₂O₃ at 740°C. (From Ref. 63.)

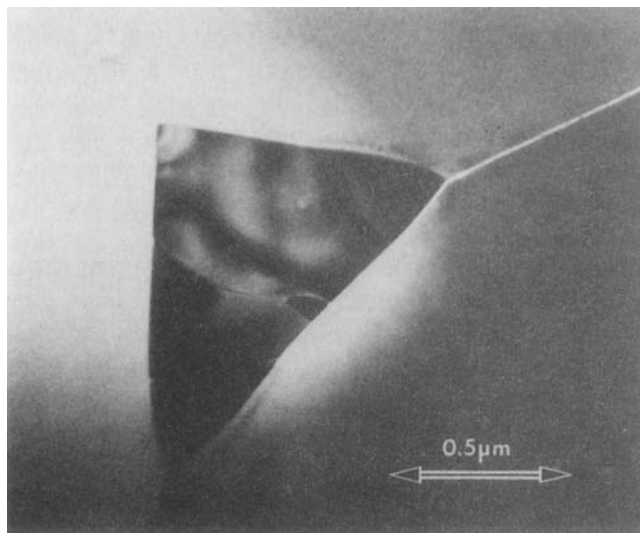


FIGURE 10.42 ZnO-Bi₂O₃ varistor composition, annealed for 43.5 h at 610°C resulting in a nonwetting secondary phase. (Courtesy of Y.-M. Chiang.)

fied tie-lines in the subsolidus system Si₃N₄-SiO₂-MgO and the compositions used in their identification (64). If equilibrium could be achieved during cooling, the fabricated materials would contain two phases if the composition lies on the tie lines or three phases if the composition lies within one of the compatibility triangles: Si₃N₄ + MgO + Mg₂SiO₄ or Si₃N₄ + Si₂N₂O + Mg₂SiO₄. Commonly, all of the magnesium is incorporated into the continuous glassy phase shown in Fig. 10.44a, so only two phases are observed. The glassy phase has a relatively low softening temperature, and this causes a severe reduction in the high temperature creep resistance of the material.

The use of Y₂O₃ as the additive instead of MgO leads to the formation of a eutectic liquid at a higher temperature (~1660°C). Whereas higher sintering temperatures need to be used, an improvement in the high temperature creep resistance of the fabricated material is also observed. The phase relations for the Si₃N₄-SiO₂-Y₂O₃ system are shown in Fig. 10.43b along with the compositions used in their identification (65). The system contains three quaternary Y-Si-O-N compounds compatible with Si₃N₄ that crystallize on cooling. Figure 10.44b shows the Y₂Si₃O₃N₄ phase that crystallized on cooling at a three (or four) grain junction for a material with a composition on the Si₃N₄-Y₂Si₃O₃N₄ tie-line. It is separated from the surrounding Si₃N₄ grains by a thin residual glass film. The conversion of the glassy phase to a crystalline phase leads to a significant

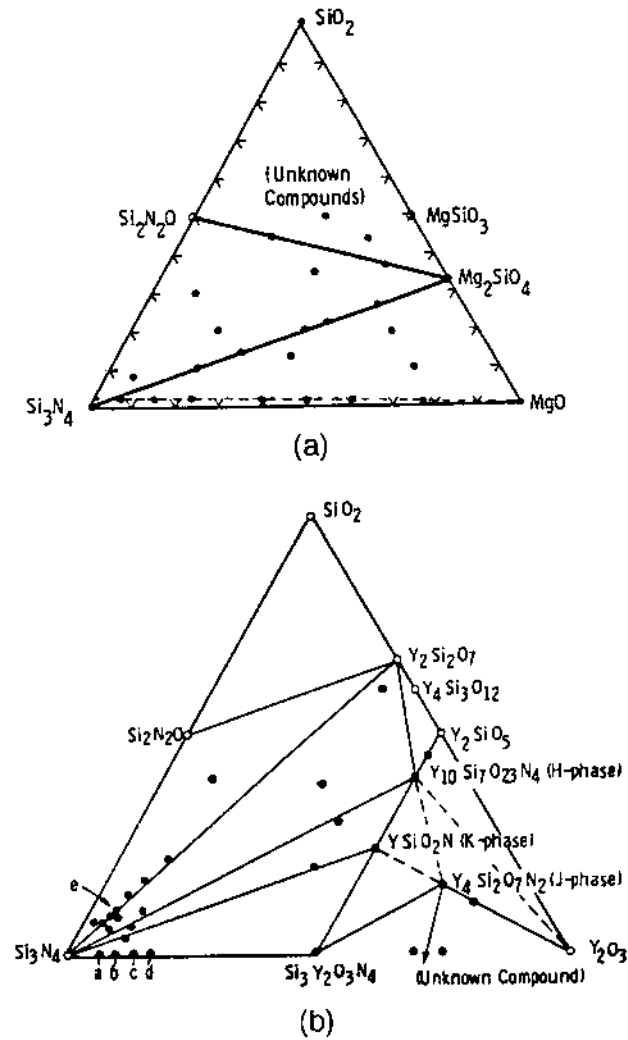


FIGURE 10.43 Experimental phase relations in (a) the system Si_3N_4 - SiO_2 - MgO determined from specimens hot pressed between 1500 and 1750°C and (b) the system Si_3N_4 - SiO_2 - Y_2O_3 determined from specimens hot pressed between 1600 and 1750°C. The filled circles represent the compositions examined. (From Refs. 64 and 65.)

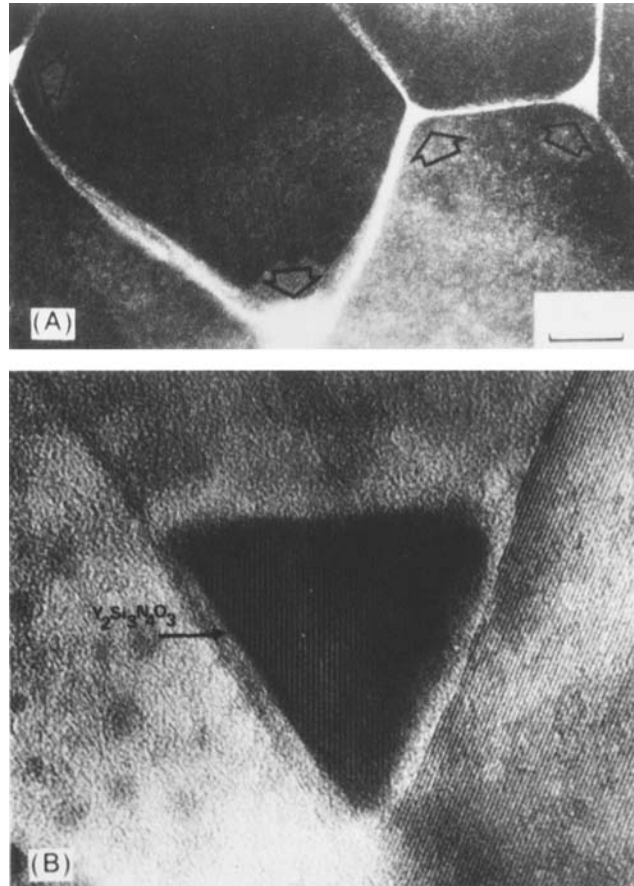


FIGURE 10.44 Transmission electron micrographs of (A) commercial sample of hot pressed $\text{Si}_3\text{N}_4(\text{MgO})$, showing continuous glassy phase between $\beta\text{-Si}_3\text{N}_4$ grains (dark-field, bar = 50 nm) and (B) hot pressed $\text{Si}_3\text{N}_4(\text{Y}_2\text{O}_3)$ showing $\text{Y}_2\text{Si}_3\text{O}_3\text{N}_4$ grain surrounded by $\beta\text{-Si}_3\text{N}_4$ grains, with a glass phase between the crystalline phases (lattice fringe spacing for the $\beta\text{-Si}_3\text{N}_4$ grain at lower left is 0.663 nm). (Courtesy of D. R. Clarke.)

improvement in the creep resistance. Many Si_3N_4 ceramics are now sintered with an additive consisting of a combination of Y_2O_3 and Al_2O_3 (19,13). On cooling, the liquid phase crystallizes to an yttrium-aluminum garnet phase. The fabricated Si_3N_4 shows improved high temperature creep resistance as well as better oxidation resistance compared to the material fabricated with Y_2O_3 alone as the additive.

10.9 ACTIVATED SINTERING

When powder compacts containing minor amounts of a eutectic-forming additive are sintered, enhanced densification rates, compared to the pure powder, may be observed well *before* the eutectic temperature is reached. This effect is commonly referred to as *activated sintering*. Examples are found in the sintering of MgF_2 with CaF_2 additive (66), Al_2O_3 with CaO (67), ZnO with Bi_2O_3 (68), as well as several metallic systems such as W with Pd , Ni , Pt , Co , or Fe (69). Figure 10.45 shows the shrinkage and grain size for pure MgF_2 with up to 5 wt% CaF_2 during constant heating rate sintering. In this system, the eutectic temperature is 980°C , while the melting points of CaF_2 and MgF_2 are 1410°C and 1252°C , respectively. Enhanced densification rates are observed as much as 200°C below the eutectic temperature. The enhancing effect appears noticeable when as little as 0.1 wt% CaF_2 is added and saturates above 1 wt%. Grain growth rates are increased as a result of the CaF_2 addition, but at 900°C they are still relatively modest.

Generally, there is no clear difference in principles involved in activated sintering and liquid phase sintering other than the activated system having a small concentration of additive (typically < 1 wt%) and a sintering temperature below the eutectic temperature (70). In some systems showing enhanced subeutectic densification, the presumption that no liquid is present may be in error due to

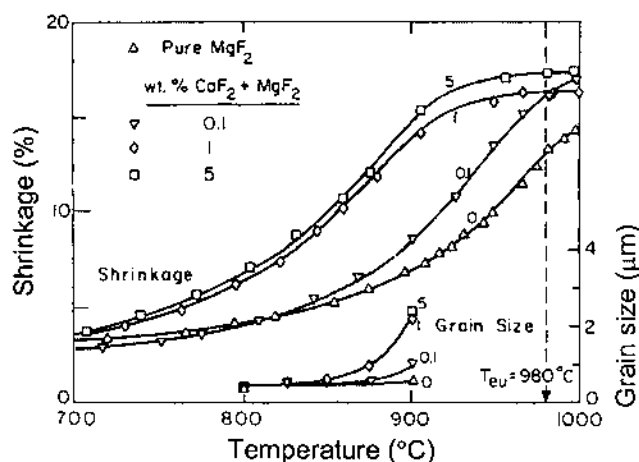


FIGURE 10.45 Shrinkage and grain size data for pure MgF_2 powder compacts with up to 5 wt% CaF_2 during constant heating rate sintering at $4.5^\circ\text{C}/\text{min}$. The eutectic temperature is 980°C and theoretical density corresponds to 20.1% shrinkage (66). (Courtesy of L. C. De Jonghe.)

impurities that lower the solidus temperature below the apparent eutectic temperature of the system and difficulties in detecting the liquid film.

Whereas the process of activated sintering is not clear, the enhanced subeutectic densification rates are often observed in systems where the additive segregates strongly to the grain boundary, presumably enhancing grain boundary transport rates significantly. The additive must also form a low-melting phase or eutectic with the major component and must also have a large solubility for the major component. This phenomenon may be understood if one considers that diffusion rates scale approximately as the absolute temperature of the melting point of a solid. If the grain boundaries are rich in the eutectic forming additive, then their relative melting points should be considerably below that of the major component, and their transport rates should be accordingly enhanced.

In ZnO with Bi_2O_3 additive, Bi-enriched intergranular amorphous films (~ 1 nm thick) are observed to form concurrently with activated sintering (Fig. 10.46) and accelerated mass transport through these amorphous films has been suggested to be responsible for the activated sintering in this system (68). It is possible that intergranular films of a similar nature may also be responsible for the enhanced subeutectic densification in other systems, but experimental observations are currently lacking. Studies on the activated sintering of W indicate that diffusion through the intergranular is the rate-limiting step. Figure 10.47 shows that the degree of activated sintering depends on the additive, which results from the different activation energies for diffusion of W through the activator-rich intergranular phase (69).

10.10 VITRIFICATION

Vitrification, as outlined earlier, is the term used to describe liquid-phase sintering where densification is achieved by the viscous flow of a sufficient amount of liquid to fill up the pore spaces between the solid grains (72). The driving force for vitrification is the reduction of solid–vapor interfacial energy due to the flow of the liquid to cover the solid surfaces. Vitrification is the common firing method for traditional clay-based ceramics, sometimes referred to as silicate systems. The process involves physical and chemical changes (e.g., liquid formation, dissolution, crystallization) as well as shape changes (e.g., shrinkage and deformation). A viscous silicate glass forms at the firing temperature and flows into the pores under the action of capillary forces but also provides some cohesiveness to the system to prevent significant distortion under the force of gravity. On cooling, a dense solid product is produced, with the glass gluing the solid particles together.

The Controlling Parameters

The amount of liquid formed at the firing temperature and the viscosity of the liquid must be such that the required density (commonly full density) is achieved

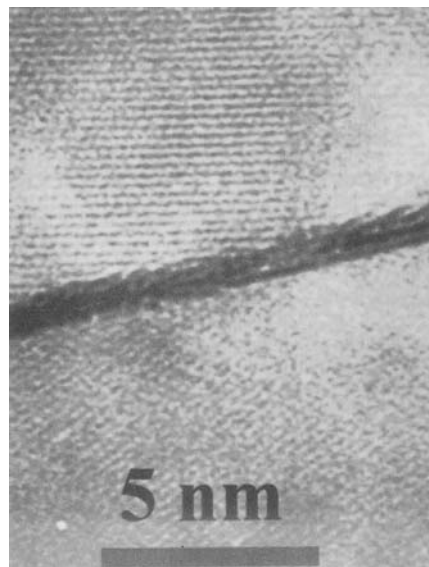


FIGURE 10.46 High resolution electron micrograph of Bi-enriched intergranular amorphous film in ZnO 0.58 mol% Bi_2O_3 sintered at $4^\circ\text{C}/\text{min}$ and air-quenched from 700°C (68). (Courtesy of Y.-M. Chiang.)

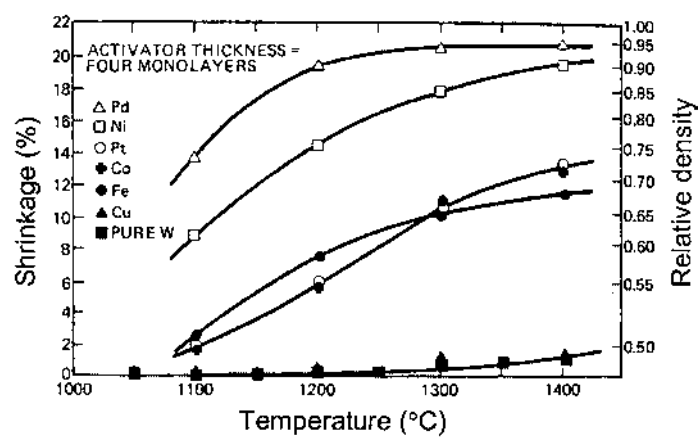


FIGURE 10.47 Activated sintering data for W particles treated with various transition metal additives. In each case the W was sintered for 1 h in hydrogen at the indicated temperature after being combined with one of the additives. (From Ref. 69.)

within a reasonable time without the sample deforming under the force of gravity. As outlined earlier, the amount of liquid required to produce full densification by vitrification depends on the packing density achieved by the solid grains after rearrangement. In real powder systems, the use of a particle size distribution to improve the packing density coupled with the occurrence of a limited amount of solution-precipitation means that the amount of liquid required for vitrification is commonly 25–30 vol%. As discussed earlier for liquid-phase sintering, the formation of the liquid must be controlled to prevent sudden formation of a large volume of liquid that will lead to distortion of the body under the force of gravity. The composition of the system should be chosen away from any eutectic composition.

We require a high enough densification rate of the system so that vitrification is completed within a reasonable time (less than a few hours) as well as a high ratio of the densification rate to the deformation rate so that densification is achieved without significant deformation of the article. These requirements determine, to a large extent, the firing temperature and the composition of the powder mixture that control the viscosity of the liquid. The models for viscous sintering of a glass predict that the densification rate depends on three major variables: the surface tension γ_{sv} of the glass, the viscosity η of the glass, and the pore radius r (Chapter 8). Assuming that r is proportional to the particle radius a , then the dependence of the densification rate on these parameters can be written

$$\dot{\rho} \sim \frac{\gamma_{sv}}{\eta a} \quad (10.44)$$

In many silicate systems, the surface tension of the glassy phase does not change significantly with composition and the change in surface tension within the limited range of firing temperatures is also small. On the other hand, the particle size has a significant effect, with the densification rate increasing inversely as the particle size. However, by far the most important variable is the viscosity. The dependence of the viscosity of a glass on temperature is well described by the *Vogel-Fulcher equation*:

$$\eta = \eta_0 \exp\left(\frac{C}{T - T_0}\right) \quad (10.45)$$

where T is the absolute temperature and η_0 , C , and T_0 are constants. This dependence is very strong; for example, the viscosity of soda-lime glass can decrease typically by a factor of ~ 1000 for an increase in temperature of only $\sim 100^\circ\text{C}$. The glass viscosity also changes significantly with composition. The rate of densification can therefore be increased significantly by changing the composition,

increasing the temperature, or some combination of these to reduce the viscosity. However, the presence of a large volume of liquid during vitrification means that if the viscosity is too low, the sample will deform easily under the force of gravity. Thus the rate of densification relative to the rate of deformation must also be considered. If the ratio of the densification rate to the deformation rate is large, densification without significant deformation will be achieved.

The deformation rate is related to the applied stress, σ , and the viscosity by the expression

$$\dot{\epsilon} = \frac{\sigma}{\eta} \quad (10.46)$$

The force due to gravity exerted on a particle of mass m is given by $W = mg$, where g is the acceleration due to gravity. The mass of the particle varies as a^3 and the area over which the force acts is proportional to the area of the particle, i.e., to a^2 . The stress therefore varies as a . The ratio of the densification rate to the deformation rate varies according to

$$\frac{\dot{\rho}}{\dot{\epsilon}} \sim \frac{1}{\eta a} \frac{\eta}{a} \sim \frac{1}{a^2} \quad (10.47)$$

According to this equation, the ratio of densification rate to the deformation rate of the system is enhanced as the particle size decreases. Therefore, the best way to achieve high densification without significant deformation is to use fine particle size. Many successful silicate systems satisfy this requirement in that the compositions contain a substantial amount of clays that are naturally fine grained.

Vitrification of Silicate Systems

Triaxial porcelain compositions are an important silicate system produced by vitrification. They are commonly prepared from powder mixtures containing three components with a typical composition being:

- 50 wt% clay. For a clay consisting of predominantly the mineral kaolinite, with a formula $\text{Al}_2(\text{Si}_2\text{O}_5)(\text{OH})_4$, composition of the clay corresponds to ~ 45 wt% Al_2O_3 and ~ 55 wt% SiO_2 .
- 25 wt% feldspar. Feldspar is an alkali-containing mineral that acts as a flux. The alkali (often K^+) serves to lower the temperature at which the viscous liquid forms. A common feldspar has the formula, KAlSi_3O_8 .
- 25 wt% silica, present as quartz. The quartz acts as a filler to reduce the amount of shrinkage during firing and also serves to reduce the thermal expansion coefficient of the porcelain.

This and similar compositions lie in the primary mullite phase field in the ternary $\text{K}_2\text{O-SiO}_2\text{-Al}_2\text{O}_3$ phase diagram (Fig. 10.48). Typical firing conditions

are in the range 1200–1400°C. Between 1200 and 1600°C, the equilibrium phases are mullite and liquid. An isothermal section of the phase diagram (Fig. 10.49) shows the equilibrium phases at 1200°C. At this temperature, the liquid has the composition of ~75 wt% SiO₂, ~12.5 wt% K₂O, and ~12.5 wt% Al₂O₃. In practice, the approach to equilibrium is incomplete, and only a small part of the SiO₂ present as quartz enters the liquid phase. The amount of SiO₂ that dissolves does not have a large effect on the amount and composition of the liquid. The cooled material contains mullite grains, a glass, and residual quartz particles. Triaxial porcelains are white, dense, and translucent and are used for the production of pottery, tiles, and insulators.

10.11 CONCLUDING REMARKS

Liquid-phase sintering is a common sintering process used in the production of a wide variety of ceramic materials. The liquid enhances densification through easier rearrangement of the grains and faster matter transport through the liquid. Liquid-phase sintering is divided conceptually into three overlapping stages de-

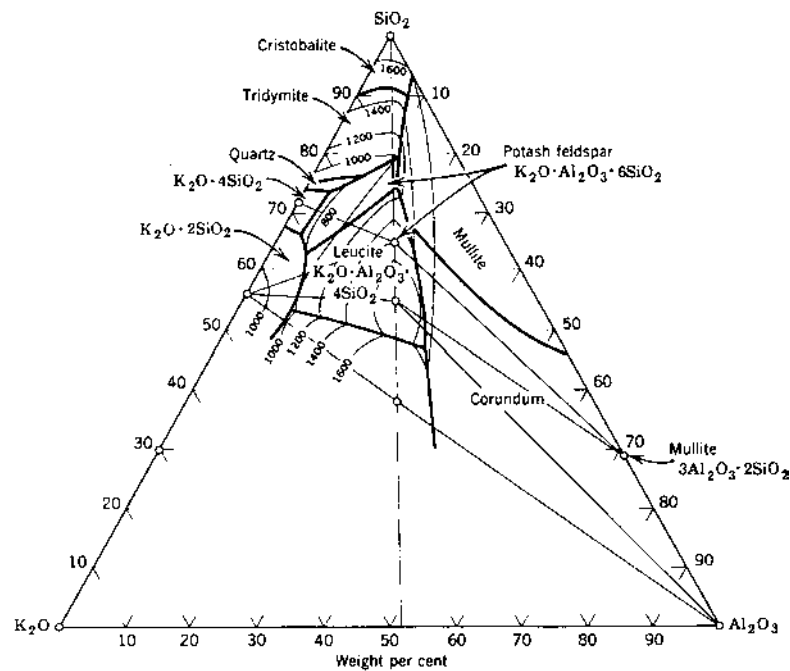


FIGURE 10.48 Phase relations for the ternary system K₂O-Al₂O₃-SiO₂. (From Ref. 71.)

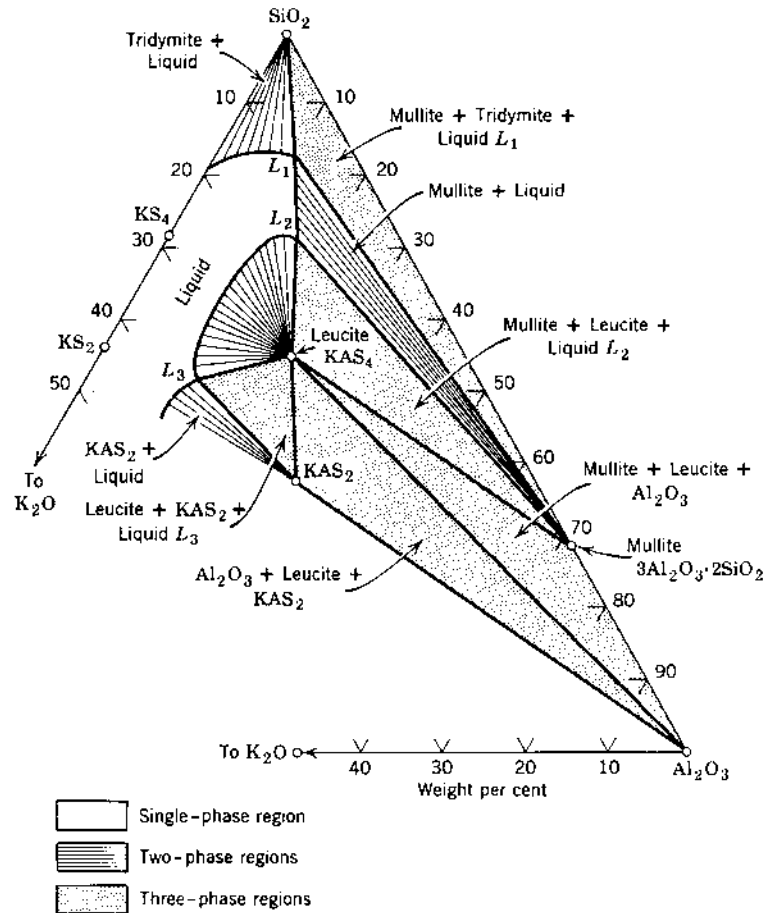


FIGURE 10.49 Isothermal cut in the $\text{K}_2\text{O}-\text{Al}_2\text{O}_3-\text{SiO}_2$ phase diagram at 1200°C . (From Ref. 9.)

finer in terms of the dominant mechanism operating in each stage: rearrangement (stage 1), solution precipitation (stage 2), and Ostwald ripening (stage 3). Rearrangement is typically fast, and following its completion, models have been proposed to predict the shrinkage of the system as a function of time. The kinetics of densification are of interest because together with grain growth, they form an integral part of microstructural evolution. Successful exploitation of liquid-phase sintering is dependent on controlling several material and processing parameters and requires a low contact angle, low dihedral angle, high solid solubility of the

solid in the liquid, homogeneous packing of the particulate solid, homogeneous distribution of the liquid-producing additive, and fine particle size. Phase diagrams play an important role in the selection of compositions and sintering conditions for liquid-phase sintering. Liquid films that appear to have an equilibrium thickness have been observed at the grain boundaries in several ceramics, and this equilibrium film thickness has been explained in terms of charge interactions between surfaces, as well as structural and chemical forces. A process that is related to liquid-phase sintering is activated sintering, in which minor amounts of additives segregate to the grain boundaries and can enhance densification rates well below any eutectic temperature in the system. If sufficient liquid is present, rearrangement by itself can lead to a fully dense material. This type of liquid-phase sintering, referred to as vitrification, is often used in the production of traditional clay-based ceramics.

PROBLEMS

- 10.1 For each of the stages associated with classic liquid-phase sintering, give the name of the stage, the dominant processes, and the main microstructural changes.
- 10.2 Determine the range of contact angles for the following conditions:
 - a. $\gamma_{lv} = \gamma_{sv} < \gamma_{sl}$
 - b. $\gamma_{lv} > \gamma_{sv} > \gamma_{sl}$
 - c. $\gamma_{lv} > \gamma_{sv} = \gamma_{sl}$
- 10.3 Given the following interfacial energies (in units of J/m²) for liquid-phase sintering: $\gamma_{sv} = 1.0$; $\gamma_{lv} = 0.8$; $\gamma_{ss} = 0.75$; and $\gamma_{sl} = 0.35$, determine:
 - a. The solid–liquid contact angle
 - b. Whether the liquid will penetrate the grain boundaries.
- 10.4 State the relationship showing how the dihedral angle ψ is related to the values of the grain boundary energy γ_{ss} and the solid–liquid interfacial energy γ_{sl} for a polycrystalline solid in contact with a liquid.
 Consider two spheres with the same radius a in contact during liquid-phase sintering. Derive an expression for the equilibrium radius of the neck X formed between the spheres when the dihedral angle is ψ . Using the relationship between the dihedral angle and the interfacial energies, plot a graph of the ratio X/a versus γ_{ss}/γ_{sl} .
- 10.5 Wetting of the solid by the liquid phase is a necessary criterion for efficient liquid-phase sintering. Discuss the wetting phenomena that are generally relevant to the liquid-phase sintering of ceramic systems.
- 10.6 Amorphous films with an equilibrium thickness of 0.5–2 nm are often observed between the grains in ceramics that have been fabricated by liquid-phase sintering. Discuss the explanations that have been put forward for the stabilization of the film thickness.
- 10.7 Briefly discuss whether each of the following factors is likely to promote shrinkage or swelling during the initial stage of liquid-phase sintering:

- a. High solid solubility in the liquid.
 - b. Low liquid solubility in the solid.
 - c. Large contact angle.
 - d. Small dihedral angle.
 - e. High green density of the compact.
 - f. Large particle size of the liquid-producing additive.
- 10.8 Derive Eq. (10.38) for the shrinkage during the solution-precipitation stage of liquid-phase sintering when the phase boundary reaction is the rate controlling mechanism.
- 10.9 Estimate the factor by which the densification rate during hot pressing is increased by the presence of a liquid phase relative to a similar system without a liquid phase in which densification occurs by a grain boundary diffusion mechanism. Assume that a continuous wetting grain boundary film with a thickness $\delta_L = 50$ nm forms during liquid-phase sintering and the diffusion coefficient through the liquid $D_L = 100 D_{gb}$, where D_{gb} is the diffusion coefficient for grain boundary diffusion in the absence of the liquid.
- 10.10 Discuss how each of the following variables is expected to influence the densification and microstructural evolution during liquid-phase sintering of Si_3N_4 :
- a. The composition of the liquid-producing additive
 - b. The volume fraction of the liquid phase
 - c. The sintering temperature
 - d. The particle size of the Si_3N_4 powder
 - e. The applied pressure

REFERENCES

1. Kim, H. Y.; Lee, J.-A.; Kim, J. J. J. Am. Ceram. Soc. 2000, Vol. 83, 3128.
2. Buist, D. S.; Jackson, C.; Stephenson, I. M.; Ford, W. F.; White, J. Trans. Br. Ceram. Soc. 1965, Vol. 64, 173.
3. Hart, P. E.; Atkin, R. B.; Pask, J. A. J. Am. Ceram. Soc. 1970, Vol. 53, 83.
4. Dey, D.; Bradt, R. C. J. Am. Ceram. Soc. 1992, Vol. 75, 2529.
5. Kim, J.; Kimura, T.; Yamaguchi, T. J. Am. Ceram. Soc. 1989, Vol. 72, 1541.
6. Hennings, D.; Janssen, R.; Reynen, P. J. L. J. Am. Ceram. Soc. 1987, Vol. 70, 23.
7. Guha, J. P.; Anderson, H. U. J. Am. Ceram. Soc. 1986, Vol. 69, C193.
8. Hausonne, J. M.; Desgardin, G.; Bajolet, P.; Raveau, B. J. Am. Ceram. Soc. 1983, Vol. 77, 801.
9. Kingery, W. D.; Bowen, H. K.; Uhlmann, D. R. Introduction to Ceramics; 2nd ed.; Wiley: New York, 1976.
10. Brook, R. J. In Advances in Ceramics, Vol. 3, Science and Technology of Zirconia; Heuer, A. H., Hobbs, L. W. eds.; The American Ceramic Society: Westerville, OH, 1981, pp. 272–285.
11. Terwilliger, G. R.; Lange, F. F. J. Mater. Sci. 1975, Vol. 10, 1169.
12. Riley, F. L. J. Am. Ceram. Soc. 2000, Vol. 83, 245.
13. Suttor, D.; Fischman, G. S. J. Am. Ceram. Soc. 1992, Vol. 75, 1063.
14. Kim, D.-H.; Kim, C. H. J. Am. Ceram. Soc. 1990, Vol. 73, 1431.

15. German, R. M. *Liquid Phase Sintering*; Plenum Press: New York, 1985.
16. German, R. M. *Sintering Theory and Practice*; Wiley: New York, 1996.
17. Weirauch, D. A., Jr.; Ziegler, D. P. 12th University Conference on Glass Science; Alfred: New York, 1993.
18. Cannon, R. M.; Saiz, E.; Tomsia, A. P.; Carter, W. C. *Mater. Res. Soc. Symp. Proc.* 1995, Vol. 357, 279.
19. Beeré, W. *Acta Metall.* 1975, Vol. 23, 131.
20. Park, H. H.; Yoon, D. N. *Met. Trans. A.* 1985, Vol. 16, 923.
21. Smith, C. S. *Trans. AIME.* 1948, Vol. 175, 15.
22. Heady, R. B.; Cahn, J. W. *Metall. Trans.* 1970, Vol. 1, 185.
23. Hwang, K. S.; German, R. M.; Lenel, F. V. *Metall. Trans.* 1987, Vol. 18A, 11.
24. Huppmann, W. J.; Riegger, H. *Acta Metall.* 1975, Vol. 23, 965.
25. Kippshut, C. M.; Bose, A.; German, R. M. *Metall. Trans. A.* 1988, Vol. 19A, 1905.
26. Mani, S. S.; German, R. M. *Advances in Powder Metallurgy—1990*; Metal Powder Industries Federation: Princeton, NJ, 1990, pp. 453–468.
27. Raman, R.; German, R. M. *Metall. Mater. Trans. A.* 1995, Vol. 26A, 653.
28. Upadhyaya, A.; German, R. M. *Metall. Mater. Trans. A.* 1998, Vol. 29A, 2631.
29. Norton, F. H. *Elements of Ceramics*; Addison-Wesley: Reading, MA, 1974.
30. German, R. M. *Metall. Mater. Trans. A.* 1995, Vol. 26A, 279.
31. German, R. M.; Liu, Y. J. *Mater. Synthesis & Processing.* 1996, Vol. 4, 23.
32. Lange, F. F. J. *Am. Ceram. Soc.* 1982, Vol. 65, C23.
33. Eley, D. D. *Adhesion*; Oxford University Press: 1961, pp. 118–120.
34. Clarke, D. R. J. *Am. Ceram. Soc.* 1987, Vol. 70, 15.
35. Derjaguin, B. V.; Churaev, N. V. J. *Colloid Interface Sci.* 1974, Vol. 49, 249.
36. Clarke, D. R.; Shaw, T. M.; Philipse, A. P.; Horn, R. G. J. *Am. Ceram. Soc.* 1993, Vol. 76, 1201.
37. Tanaka, I.; Kleebe, H.-J.; Cinibulk, M. K.; Bruley, J.; Clarke, D. R.; Ruhle, M. J. *Am. Ceram. Soc.* 1994, Vol. 77, 911.
38. Gui, H.; Pan, X.; Cannon, R. M.; Ruhle, M. J. *Am. Ceram. Soc.* 1998, Vol. 81, 3125.
39. Brydson, R.; Chen, S.-C.; Riley, F. L.; Milne, S. J.; Pan, X.; Ruhle, M. J. *Am. Ceram. Soc.* 1998, Vol. 81, 369.
40. Wang, H.; Chiang, Y. -M. J. *Am. Ceram. Soc.* 1998, Vol. 81, 89.
41. Kwon, O.-J.; Yoon, D. N. *Internat. J. Powder Metall. & Powder Technol.* 1981, Vol. 17, 127.
42. Shaw, T. M. J. *Am. Ceram. Soc.* 1986, Vol. 69, 27.
43. Kingery, W. D. J. *Appl. Phys.* 1959, Vol. 30, 301.
44. Kang, S.-J. L.; Kaysser, W. A.; Petzow, G.; Yoon, D. N. *Powder Metall.* 1984, Vol. 27, 97.
45. Huppmann, W. J.; Riegger, H.; Kaysser, W. A.; Smolej, V.; Pejovnik, S. Z. *Metallk.* 1979, Vol. 70, 707.
46. Fortes, M. A. *Powder Metall. Internat.* 1982, Vol. 14, 96.
47. Lee, S.-M.; Chaix, J.-M.; Martin, C. L.; Allibert, C. H.; Kang, S. -J. L. *Metals and Materials.* 1999, Vol. 5, 197.
48. Yoon, D. N.; Huppmann, W. J. *Acta Metall.* 1979, Vol. 27, 693.
49. Takajo, S.; Kaysser, W. A.; Petzow, G. *Acta Metall.* 1984, Vol. 32, 107.

50. Vorhees, P. W. *Ann. Rev. Mater. Sci.* 1992, Vol. 22, 197.
51. Kingery, W. D.; Niki, E.; Narasimhan, M. D. *J. Am. Ceram. Soc.* 1961, Vol. 44, 29.
52. Huppmann, W.; Riegger, H. *Internat. J. Powder Met. Powder Technol.* 1977, Vol. 13, 243.
53. Kaysser, W. A.; Takajo, S.; Petzow, G. *Acta Metall.* 1984, Vol. 32, 115.
54. Huppmann, W. J.; Petzow, G. In *Mater. Sci. Res. Vol. 13: Sintering Processes*; Kuczynski, G. C. ed.; Plenum: New York, 1980, pp. 189–201.
55. Yoon, D. N.; Huppmann, W. J. *Acta Metall.* 1979, Vol. 27, 973.
56. Kang, S.-J. L.; Kim, K.-H.; Yoon, D. N. *J. Am. Ceram. Soc.* 1991, Vol. 74, 425.
57. Park, H.-H.; Cho, S.-J.; Yoon, D. N. *Met. Trans. A.* 1984, Vol. 15A, 1075.
58. Park, H.-H.; Kwon, O.-J.; Yoon, D. N. *Met. Trans. A.* 1986, Vol. 17A, 1915.
59. Kang, T.-K.; Yoon, D. N. *Met. Trans. A.* 1978, Vol. 9A, 433.
60. German, R. M. *Metall. Mater. Trans. A.* 1995, Vol. 26A, 279.
61. Bowen, L. J.; Weston, R. J.; Carruthers, T. G.; Brook, R. J. *J. Mater. Sci.* 1978, Vol. 13, 341.
62. Levin, E. M.; Robbins, C. R.; McMurdie, H. W. *Phase Diagrams for Ceramists*; The American Ceramic Society: Columbus, OH, 1964.
63. Safronov, G. M.; Batog, V. N.; Steoanyuk, T. V.; Fedorov, P. M. *Russian J. Inorg. Chem.* 1971, Vol. 16, 460.
64. Lange, F. F. *J. Am. Ceram. Soc.* 1978, Vol. 61, 53.
65. Lange, F. F.; Singhal, S. C.; Kuznicki, R. C. *J. Am. Ceram. Soc.* 1977, Vol. 60, 249.
66. Hu, S. C.; De Jonghe, L. C. *Ceramics International.* 1983, Vol. 9, 123.
67. Wu, S. J.; De Jonghe, L. C.; Rahaman, M. N. *J. Am. Ceram. Soc.* 1985, Vol. 68, 385.
68. Luo, J.; Wang, H.; Chiang, Y. -M. *J. Am. Ceram. Soc.* 1999, Vol. 82, 916.
69. German, R. M.; Munir, Z. A. *Metall. Trans. A.* 1976, Vol. 7A, 1873.
70. German, R. M. *Sci. Sintering.* 1983, Vol. 15, 27.
71. Schairer, J. F.; Bowen, N. L. *Am. J. Sci.* 1947, Vol. 245, 199.
72. Cambier, F.; Leriche, A. In *Materials Science and Technology*; Vol. 17B, Brook, R. J. ed.; VCH: New York, 1996, pp. 123–144.

11

Special Topics in Sintering

11.1 INTRODUCTION

The effects of variables such as grain size, temperature, and applied pressure on sintering are well understood. For powder systems that approach the assumptions of the theoretical models (i.e., homogeneously packed spherical particles with a narrow size distribution), the sintering kinetics can be well described by the models. However, some important issues remain and these need to be examined in terms of their ability to limit the attainment of high density with controlled microstructure.

A continuous second phase in polycrystalline ceramics, such as a continuous pore phase or fibers in a composite may undergo capillary-induced shape changes leading to breakup and the formation of discrete pores or particles. Since the physical distribution of secondary phases has important consequences for the properties of ceramics, the *morphological stability* of continuous phases in ceramics is of considerable interest. An analysis by Rayleigh (1) permits a qualitative understanding of many of these phenomena.

The structure of real powder compacts is never completely homogeneous. Various types of *inhomogeneities* (such as variations in packing density, a distribution of pore sizes, and a distribution of particle sizes) lead to *differential densification* during sintering, where different regions of the powder compact sinter at different rates. Differential densification leads to the development of *transient stresses* that reduce the densification rate and to the growth of *microstructural flaws* that limit the properties of the fabricated ceramic. The quantification and control of inhomogeneities in the powder compact as well as techniques for limiting the magnification of inhomogeneities during sintering form key issues for microstructural control.

In composites, inhomogeneities are a necessary feature of the microstructural design of the material. *Rigid inclusions* such as particles, platelets, or fibers are incorporated into the material to improve its properties, but they invariably create severe problems for sintering by retarding the densification of the powder matrix. The retardation of densification is often observed to be much more severe in polycrystalline matrices than in glass matrices. Key issues in the sintering of powder compacts with rigid inclusions include the mechanisms responsible for the reduced densification and how the sintering difficulties can be alleviated.

The sintering of *adherent films* on a rigid substrate is required in several important applications. The substrate provides an external constraint, preventing shrinkage in the plane of the substrate, and all shrinkage occurs in the direction perpendicular to the plane of the film. Tensile stresses develop in the plane of the film which lower the densification rate of the constrained film relative to that of a free, unconstrained film, and if high enough, the stresses can lead to delamination of the film from the substrate or to cracking of the film. The *dimensional stability* of thin polycrystalline films must also be considered because under certain conditions they may become unstable and break up into islands, thereby uncovering the substrate.

Solid solution additives or dopants provide an effective approach for the fabrication, by sintering, of ceramics with high densities and controlled grain size, but as discussed in Chapter 9, the role of the dopant is not well understood. This gap in understanding limits the applicability of the approach. The major roles of the dopant and the parameters that control the effectiveness of a dopant in a given role form important issues in the solid solution additive approach.

In the production of multicomponent ceramics from a mixture of powders, a *chemical reaction* occurring between the starting materials during sintering can introduce further problems for microstructural control. *Crystallization* of an amorphous material during sintering can also lead to sintering difficulties. The parameters that control the separate processes and the interaction of densification with a chemical reaction or with crystallization must be understood to provide a basis for selecting the appropriate processing conditions for sintering.

11.2 RAYLEIGH INSTABILITY AND MICROSTRUCTURAL EVOLUTION

Rayleigh analyzed the morphological instability of cylindrical fluid jets under the influence of surface tension forces in 1878 (1) and found that an infinitely long cylindrical jet will eventually break up into a row of spherical droplets (Fig. 11.1), in much the same way as when a narrow stream of water flows from a faucet. This type of breakup, referred to as *Rayleigh instability*, is driven by a reduction in surface energy and is based on the fact that a sphere has a lower surface area than a cylinder of the same volume. Because mass must be redistri-

buted during the breakup, the fluid jet does not progress directly to a single sphere, but instead breaks up into multiple spheres, limited in number by the consideration that there exists a maximum number of spheres with total surface area lower than that of a cylinder with the same volume.

The Rayleigh analysis indicates that for a cylinder of radius r_0 subject to infinitesimal periodic perturbations with a wavelength λ in the axial direction (Fig. 11.1a), the amplitude of the perturbation will increase, due to reduction in specific surface energy, only when λ is greater than $2\pi r_0$ (the circumference of the cylinder). Growth of the perturbations with $\lambda > \lambda_{\min} (= 2\pi r_0)$ eventually leads to the formation of one spherical particle per wavelength increment of the cylinder. The Rayleigh analysis also indicates that the rate at which the amplitude of the perturbation develops reaches a maximum value when $\lambda = 9.02r_0$. This value of λ , denoted λ_{\max} , dominates the periodicity of the breakup, so the spacing of the resulting spherical particles should coincide closely with λ_{\max} . For the case when $\lambda < \lambda_{\min}$, the cylinder is stable and the infinitesimal perturbation readjusts itself with time.

Capillary-driven morphological instability has been studied for several different geometries. Nichols and Mullins (2) analyzed the stability of an infinitely long cylinder under isotropic surface energy and found that the kinetics of breakup depend on the matter transport mechanism by which the perturbation grows. For matter transport by surface diffusion, λ_{\max} is equal to $\sqrt{2}\lambda_{\min}$, whereas for lattice diffusion, λ_{\max} is equal $2.1\lambda_{\min}$. Nichols (3) extended this work to cylinders with finite length and hemispherical ends. The analysis indicates that a minimum length $L_{\min} = (7.2/\pi)\lambda_{\min}$ is necessary for ovulation (formation of more than one discrete sphere), whereas cylinders with lengths less than L_{\min} are predicted to eventually spheroidize (form a single sphere). Stüwe and Kolednik (4) analyzed the disintegration by surface diffusion of a long cylindrical pore and found a λ_{\max}

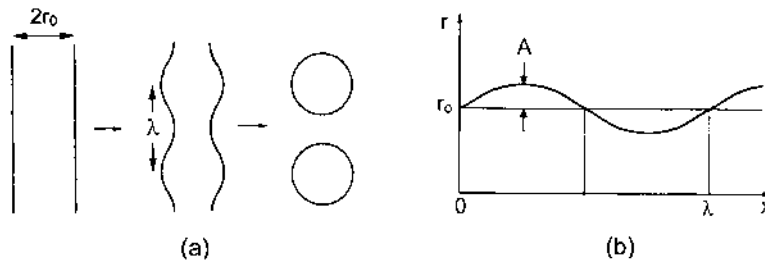


FIGURE 11.1 (a) Rayleigh instability in a cylindrical fluid (or solid) of radius r_0 subject to radial fluctuations of amplitude λ . The cylinder breaks up into a line of spheres when the amplitude of the fluctuation becomes sufficiently large. (b) Geometrical parameters in the analysis of break-up phenomena in a cylindrical material.

value identical to that obtained by Nichols and Mullins for surface diffusion-dominated growth. They also estimated a time for disintegration of the cylindrical pore into discrete spherical pores, which, for the case when the volume of the cylinder remains constant (no densification) is given by

$$\tau \approx \frac{kT}{D_s \gamma_{sv}} \left(\frac{z^4}{z^2 - 4\pi^2} \right) \left(\frac{r_0}{\delta} \right)^4 \ln \frac{r_0}{A_0} \quad (11.1)$$

where k is the Boltzmann constant; T is the absolute temperature; D_s is the surface diffusion coefficient; γ_{sv} is the specific energy of the solid–vapor interface; $z = \lambda/r_0$, where λ is the wavelength of the perturbation and r_0 is the initial radius of the cylindrical pore; δ is the diameter of an atom; and A_0 is the initial amplitude of the perturbation (Fig. 11.1b). For a given pore radius r_0 , the key factors determining τ are D_s and the ratio (r_0/A_0) .

Complicating effects arise when the continuous second phase is located along three-grain junctions in polycrystalline materials. The dihedral angle ψ that characterizes the intersection of the second phase with the grain boundary has a strong influence on the morphological stability of the continuous second phase (5–8). If ψ is close to 180° , the second phase will behave like a cylinder and will break up to form spheres as outlined above for the Rayleigh analysis. As ψ decreases, λ_{\min} increases and the second phase becomes increasingly stable against breakup (Fig. 11.2). The value of λ_{\min} tends to infinity as ψ approaches 60° when the curvature of the second phase at the three-grain junction vanishes, so the second phase is stable against perturbations of any wavelength (7).

The morphology and spatial distribution of a second phase can have important consequences for the microstructural evolution and properties of a material, so factors influencing the morphological stability of continuous second phases may become important considerations in materials design. A wide range of microstructural phenomena involving capillary-induced shape changes has been analyzed and modeled in terms of the Rayleigh instability, including fibers in composites (9); the healing of cracks introduced as a result of thermal shock (10) or by scoring and welding of bicrystals (11); pore channels formed during wire sintering experiments (2); and potassium-filled bubbles in tungsten wire (4). As discussed later for the breakup of a thin adherent film on a substrate to form islands (see Sect. 11.5), whereas the details may be different, the basic principle governing the breakup is the same.

Morphological instability effects can also arise in microstructures produced by solid-state and liquid-phase sintering. In solid-state sintering, the transition from the intermediate to the final stage involves the change in pore morphology from a continuous pore network to one in which the pores are isolated or closed. The dihedral angle is commonly large (on the order of 120°), so the continuous pore channels are expected to be unstable against breakup. Rayleigh instability

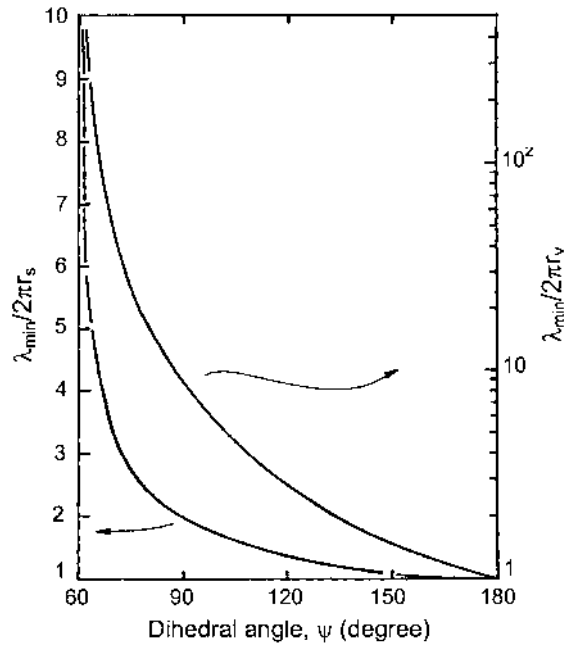


FIGURE 11.2 Dihedral angle dependence of λ_{\min} , the minimum wavelength perturbation capable of increasing in magnitude, compared with values obtained assuming a cylindrical pore geometry. Cylindrical pores of radius r_v and r_s have respective volumes and surface curvatures equivalent to those of pore characterized by a dihedral angle of ψ . (From Ref. 7.)

processes have been proposed as a potential mechanism for the transition from the intermediate to the final state microstructure, but the evidence for their occurrence is very limited. The most convincing of this limited evidence comes from an examination of the fractured surfaces of MgO hot pressed to $\sim 99\%$ of the theoretical density, which appears to show a few continuous pore channels resembling those that would be expected to develop during the growth of morphological perturbations (Fig. 11.3). Real powder compacts contain pores with nonuniform cross sections and a distribution of dihedral angles, which would influence the pore closure conditions and sizes. Pores with smaller average radius, larger amplitude of perturbation [Eq. (11.1)], and a larger dihedral angle at the grain boundary are expected to close more rapidly and at a lower density, thereby influencing the development of microstructural inhomogeneities.

In liquid-phase sintered materials, a continuous glassy phase is often present along the grain boundaries. However, liquid-phase sintering requires a low dihed-



FIGURE 11.3 Scanning electron micrograph of pore channels in MgO with well-defined perturbations (arrowed). (From Ref. 12.)

ral angle (zero in the ideal case), so the continuous glassy phase at the grain boundaries is expected to be stable against breakup and remains interconnected.

11.3 INHOMOGENEITIES AND THEIR EFFECTS ON SINTERING

The structure of real powder compacts, as outlined before, is never completely homogeneous. The characteristics of the powder and the forming method control the extent of the structural inhomogeneities in the green compact. In general, we can expect various types of structural inhomogeneity such as variations in packing density, a distribution in pore sizes, and a distribution in particle sizes. If the powder contains impurities, chemical inhomogeneity in the form of variations in composition will also be present. A common feature of such inhomogeneities is that they become exaggerated during sintering, often leading to a reduction of the densification rate and to the development of large pores or cracklike voids during sintering. Key issues include an understanding of how inhomogeneities influence sintering and how their effects on sintering can be controlled.

11.3.1 Differential Densification

Structural inhomogeneities lead to some regions of the powder compact densifying at different rates from other regions, a process referred to as *differential*

densification. The regions densifying at different rates interact with each other, and this interaction leads to the development of *transient stresses* during sintering. The stresses are said to be transient because they diminish rapidly when the densification is complete or when the sample is cooled to temperatures where no densification takes place, but in many cases, some residual stress may remain after densification. The development of transient stresses during sintering is analogous to the development of thermal stresses in materials that differ in thermal expansion coefficients. In sintering, the volumetric strain rate takes the place of the thermal strain.

Stresses due to differential densification have been analyzed for a model consisting of a spherical inhomogeneity surrounded by a uniform powder matrix (13,14). The stress system is analogous to that of a thermal stress problem in which a spherical core is surrounded by a cladding with a different thermal expansion coefficient. If the inhomogeneity (e.g., a hard, dense agglomerate) shrinks more slowly than the surrounding matrix, a hydrostatic backstress is generated in the matrix. This backstress opposes the sintering stress and leads to a reduction in the densification rate of the powder matrix (Fig. 11.4a). Differential densification may also lead to the growth of pre-existing flaws in the body. For the case of the spherical inhomogeneity that shrinks more slowly than the powder matrix, a circumferential (or hoop) stress is also set up in the matrix, which can lead to the growth of cracklike voids in the body (Fig. 11.4b). Microstructural flaws can also be produced if the inhomogeneity shrinks faster than the surrounding matrix. In this case, the inhomogeneity can shrink away from the matrix, thereby creating a circumferential void (Fig. 11.4c). Flaws such as those sketched in Fig. 11.4b and c have been observed in some sintered articles produced from heterogeneous powder compacts (15).

Another type of microstructural flaw produced by differential densification has been observed in irregular two-dimensional arrays of monosize copper spheres (16). An example of the microstructural evolution in such arrays is shown in Fig. 11.5. A detailed statistical analysis of the evolution of a similar type of array revealed that rearrangement of the particles occurred as a result of differential densification (17). The regions that densify faster exert tensile stresses on the neighboring regions densifying more slowly. If the stresses are larger than, and opposed to, the sintering stress, pores at that location will grow rather than shrink despite the fact that the compact undergoes an overall shrinkage. In three dimensions, movement of the particles is more constrained because of the higher coordination number, so particle rearrangement due to differential densification is expected to be lower than that observed in the two-dimensional arrays.

11.3.2 Control of Inhomogeneities

It is clear from Figs. 11.4 and 11.5 that differential densification can have a significant effect on densification and microstructural evolution. To reduce the

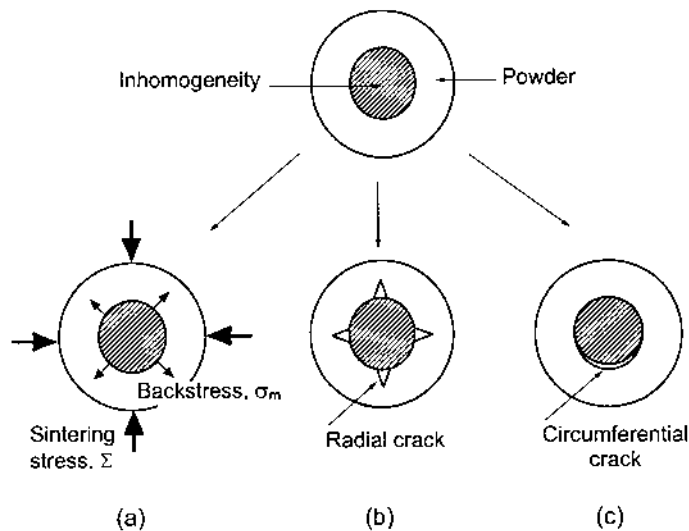


FIGURE 11.4 Schematic diagram illustrating the effects of inhomogeneities in a powder compact. (a) Reduced densification and (b) the growth of radial flaws due to an inhomogeneity that sinters more slowly than the surrounding region; (c) a circumferential flaw due to an inhomogeneity that sinters at a faster rate than the surrounding region.

undesirable effects of differential densification, we must reduce the extent of inhomogeneity present in the green compact through control of the powder quality and the forming method. Important issues in the control of inhomogeneities in the green compact are (1) the quantification of the extent of inhomogeneity in a powder compact, (2) methods for reducing or averting inhomogeneities, and (3) mechanisms for reversing structural inhomogeneities.

The quantification of inhomogeneities may allow us to determine what level of inhomogeneity can be tolerated in a given process. However, such quantification is difficult and has only been discussed at a very qualitative level. The inhomogeneity depends on the scale of observation in that the structure appears more uniform as the scale of observation becomes coarser.

One approach to reducing structural inhomogeneities in a powder compact involves the application of pressure during the compaction stage (e.g., by cold isostatic pressing) or during sintering (e.g., by hot pressing). Another approach is to attempt to produce a uniform pore size that is smaller than the particle size through colloidal consolidation or other methods. This approach has shown clear benefits, as exemplified by the work of Rhodes (18) and Yeh and Sacks (19) in which the effect of particle packing on sintering was investigated. Using the

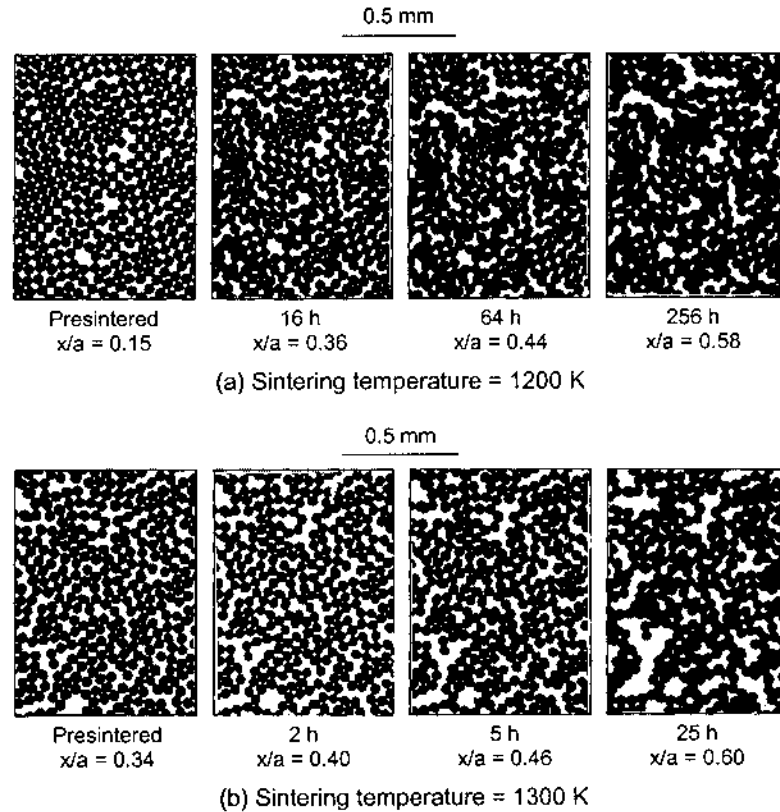


FIGURE 11.5 Evolution of the structure of two planar arrays of copper spheres during sintering. Two different starting densities, expressed as x/a , are shown, where x is the neck radius between particles of radius a . (From Ref. 16.)

same Al_2O_3 powder, which had a fairly narrow size distribution, Yeh and Sacks prepared powder compacts by slip casting a well-stabilized suspension (pH 4) and a flocculated suspension (pH 9). The structural variation in the two types of powder compacts is shown in Fig. 11.6. During sintering under the same conditions (1340°C), the more homogeneous compact with the higher packing density (pH 4) had a higher densification rate and reached a higher density when compared to the less homogeneous compact (Fig. 11.7).

11.3.3 Correction of Inhomogeneities

Faced with the problem of inhomogeneities normally present in real powder compacts, it is worth examining (1) whether sintering procedures are available

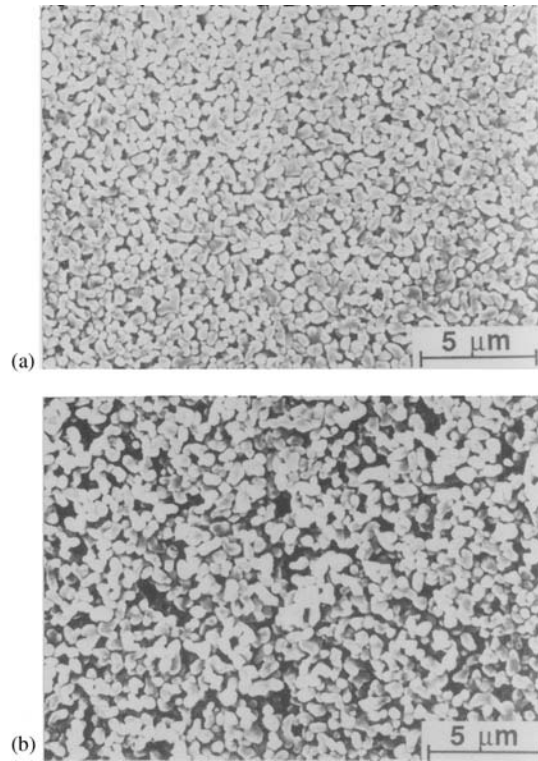


FIGURE 11.6 Scanning electron micrographs of the top surfaces of slip-cast samples of Al₂O₃ formed from (a) well-dispersed (pH 4) and (b) flocculated (pH 9) suspensions. Note the difference in packing homogeneity between the samples. (From Ref. 19.)

for reversing such inhomogeneities and (2) the extent to which the inhomogeneity can be reversed by each procedure.

A common type of inhomogeneity present in powder compacts consists of agglomerates that lead to density variations and to a distribution in the pore sizes. At one extreme of the pore size range, we have pores that are large compared to the grain size of the powder system, which would normally be characteristic of the pores between the agglomerates. These pores are surrounded by a large number of grains, so that the pore coordination number N , defined as the number of grains surrounding the pore, is large. At the other extreme, small pores with a low coordination number N will exist, which would be characteristic of the pores in the well-packed regions of the agglomerates. As discussed in Chapter 9, pores with N greater than some critical value N_C will grow whereas those with $N <$

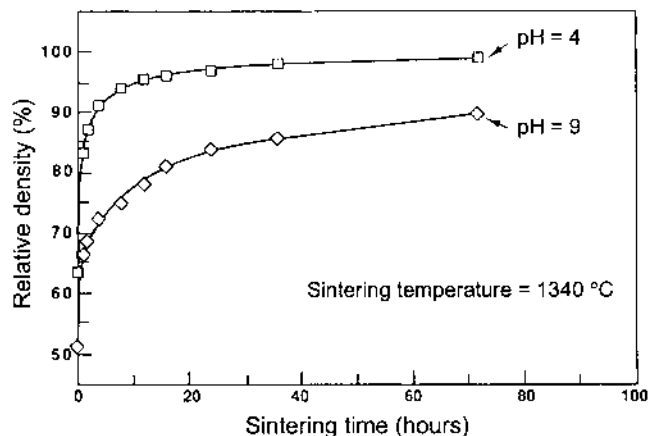


FIGURE 11.7 Relative density versus sintering time at 1340°C for the two samples described in Fig. 11.6. The sample with the more homogeneous packing (prepared from the suspension at pH 4) has a higher density at any given time. (From Ref. 19.)

N_C will shrink. An important question relating to the correction of inhomogeneities during sintering is whether the growth of the large pores can be reversed, thereby reversing the progress toward a more heterogeneous structure.

As sketched in Fig. 11.8, assuming that the grains grow faster than the pore, grain growth can eventually lead to a situation where N for the large pore becomes less than N_C . When this situation occurs, shrinkage of the large pore will occur and the progress toward a wide distribution in pore sizes (i.e., increased inhomogeneity) will be reversed. This suggests that normal grain growth might be beneficial for the sintering of heterogeneous powder compacts since it leads to a reduction in N (20). (Abnormal grain growth should still be avoided in this concept.) However, we must also consider the kinetics of achieving the required density. Whereas grain growth can indeed lead to a reduction in N , the kinetics of densification can be decreased so drastically by the larger grains that no long-term benefit for densification is achieved (21).

Although significant grain growth seriously reduces the ability to attain a high final density, the ability of a *limited* amount of grain growth to homogenize a microstructure has been clearly demonstrated (22). Figure 11.9 shows a sequence of microstructures of an MgO powder compact sintered at 1250°C to various densities. The initial compact contains clearly identifiable large pores in a fine-grained matrix. As sintering proceeds, grain growth and pore coalescence causes the microstructure to become more homogeneous. At a relative density of ~ 0.65 , grain growth has proceeded to such an extent that it becomes thermo-

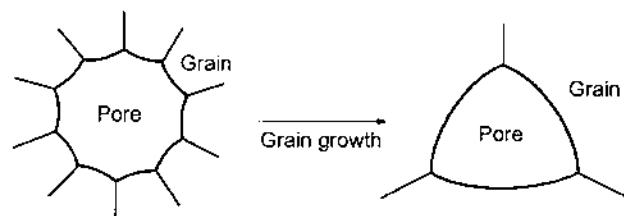


FIGURE 11.8 Schematic diagram illustrating the reduction in the pore coordination number as a result of normal grain growth.

dynamically feasible for the large pores in the original compact to shrink. The onset of shrinkage of the large pores coincides with an increase in the measured densification rate of the compact (Fig. 11.10). Densification is relatively fast in this system, so that the sacrifice in the densification rate produced by the limited grain growth to improve the homogeneity still leaves reasonable sintering rates to achieve a high final density.

A limited amount of precoarsening (i.e., coarsening at temperatures lower than the onset of densification) can also improve the microstructural homogeneity of powder compacts, providing benefits for densification and microstructural control during subsequent sintering. The overall sintering procedure, consisting of a precoarsening step followed by the sintering step, is referred to as *two-step sintering*. It has been successfully applied to powder compacts of MgO, ZnO, and Al_2O_3 (23,24). As an example, Al_2O_3 powder compacts precoarsened for 50 h at 800°C have a more uniform pore size distribution when compared to the green compact (Fig. 11.11). In subsequent sintering, the microstructure develops in a more homogeneous manner, leading to a higher final density, a smaller average grain size, and a narrower distribution of grain sizes (Fig. 11.12). During the precoarsening step, coarsening by surface diffusion, vapor transport, or a combination of these two mechanisms leads to a more uniform microstructure by an Ostwald ripening process. This improvement in the microstructural homogeneity more effectively offsets the sacrifice in the initial densification rate due to the precoarsening. Enhanced neck formation during precoarsening also produces a stronger compact that is better able to resist differential densification. The combination of a more uniform microstructure and a stronger compact produced by the precoarsening step is responsible for the microstructural refinement in the subsequent sintering step.

Another example where some homogenization of the microstructure has been observed comes from the sintering of compacts formed from mixtures of powders with particles of two different sizes, i.e., powders with a *bimodal* particle size distribution (25). If each fraction in the mixture is considered to densify in

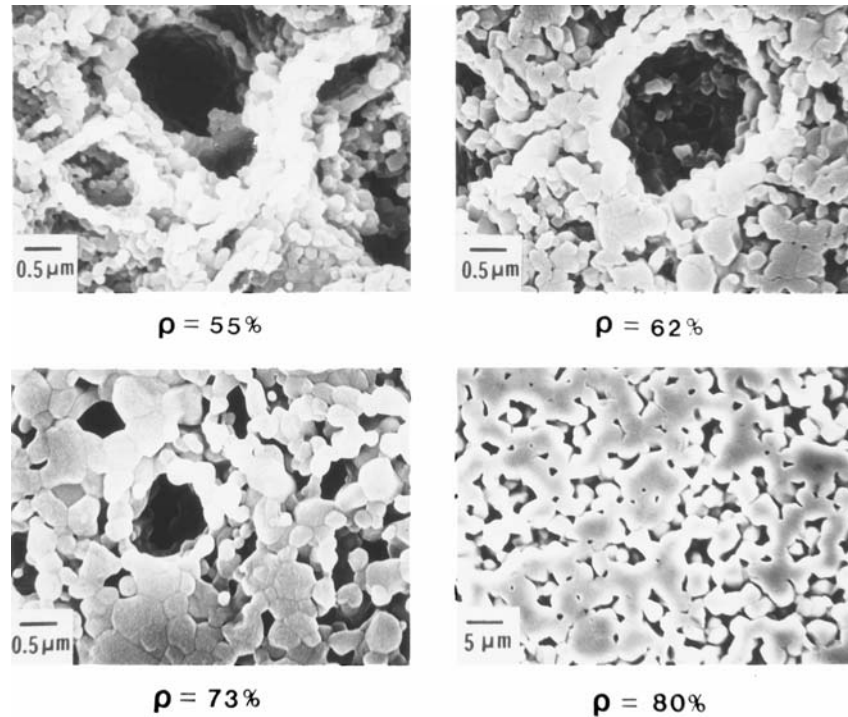


FIGURE 11.9 Microstructural evolution of an inhomogeneous MgO powder compact sintered to various densities at 1250°C. Note the trend towards homogenization of the microstructure. (From Ref. 22.)

the same way as it would independently of the other, we may expect the densification of the mixture to obey a simple rule of mixtures, in which the densification of the overall system is some weighted average of the densification of the separate powder fractions. For Al_2O_3 powder in which the particle size of the coarse fraction was ~ 10 times that of the fine fraction, the densification behavior was indeed found to approximately obey a rule of mixtures. An interesting observation was that grain growth occurred only in the fine powder fraction, thereby allowing the microstructure to become more homogeneous than that of the initial powder compact.

Whereas a limited amount of coarsening can serve to improve the microstructural homogeneity during sintering, perhaps the most effective approach, described later in the chapter, involves the use of solid solution additives (dopants).

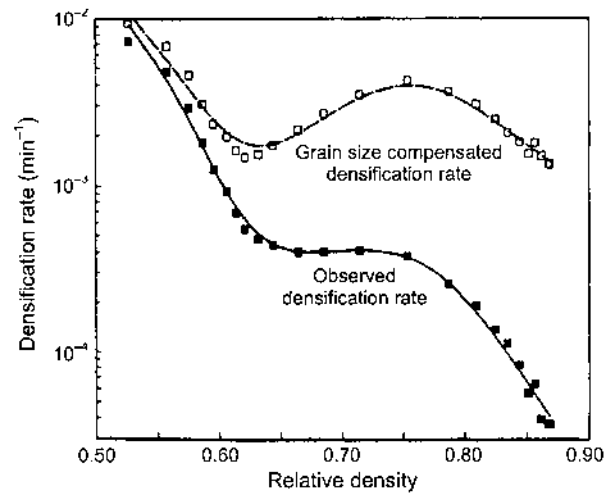


FIGURE 11.10 Observed densification rate and the grain size compensated densification rate versus relative density for the powder compact described in Fig. 11.9. The grain size compensated densification rate is a measure of the densification rate at roughly the same grain size (equal to the initial grain size). After sufficient grain growth and microstructural homogenization ($\rho \approx 0.65$), the large pores originally present in the powder compact can shrink, leading to an increase in the densification rate. (From Ref. 22.)

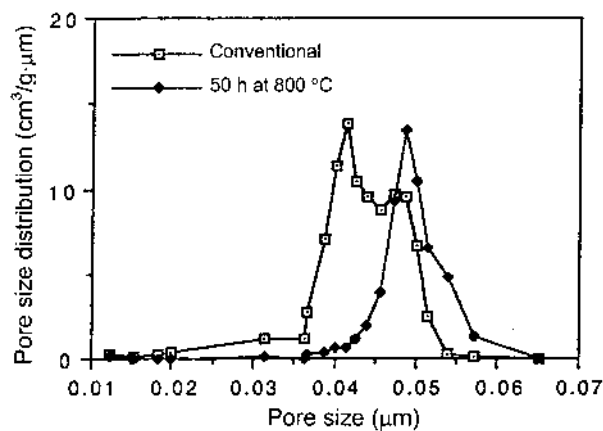


FIGURE 11.11 Pore-size distribution as a function of pore size obtained from mercury porosimetry for Al_2O_3 powder compacts heated at $10^\circ\text{C}/\text{min}$ to 800°C (conventional) and a similar compact heated for 50 h at 800°C . (From Ref. 24.)

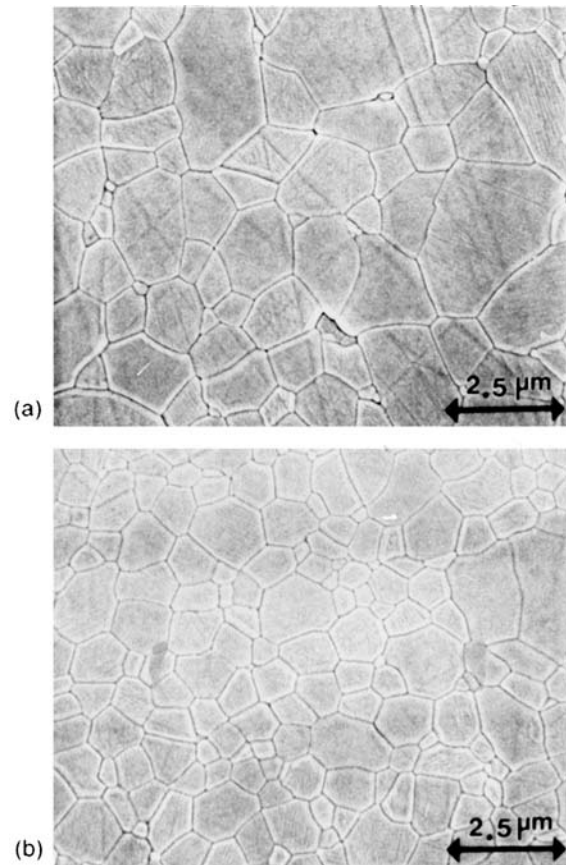


FIGURE 11.12 Scanning electron micrographs of Al₂O₃ compacts after sintering at 4°C/min to 1450°C. (a) Conventional sintering (relative density = 0.98; grain size = $1.5 \pm 0.2 \mu\text{m}$) and (b) two-step sintering with a pre-coarsening step (relative density = 0.99; grain size = $1.2 \pm 0.1 \mu\text{m}$).

11.4 CONSTRAINED SINTERING I: RIGID INCLUSIONS

Every system is constrained to some extent. For example, the sintering of a pure single-phase powder is constrained by inhomogeneities (such as agglomerates) present in the powder compact. However, the term *constrained sintering* is commonly taken to describe sintering in which the constraint is deliberately imposed and is a necessary feature of the system. An identical system in which the con-

straint is absent is taken to be the *free* or unconstrained system. The constraint may be internal to the sintering system, as exemplified by ceramic matrix composites in which a dense, rigid second phase in the form of particles, whiskers, platelets, or continuous fibers is incorporated into the powder matrix (Fig. 11.13a) or external to the sintering system, as found in the sintering of a thin adherent film on a rigid substrate (Fig. 11.13b) or the sintering laminated substrates for electronic applications (Fig. 11.13c).

We start our discussion of constrained sintering by considering the case of composites. In the overall fabrication route, the reinforcing phase is commonly incorporated into the powder matrix and the mixture is formed into a shaped article that is then densified to produce the final, dense article. A key issue for achieving the required density and microstructure of the composite is the influence of the rigid reinforcing phase on the sintering of the porous powder matrix. To simplify the treatment, we adopt a model system in which the reinforcing phase consists of dense, rigid inclusions that are spherical in shape and randomly distributed in a fine-grained, porous matrix.

Volume Fraction of Inclusions

The volume fraction of the inclusions is a key parameter that influences the sintering (and properties) of composites. It is defined as the volume of the inclu-

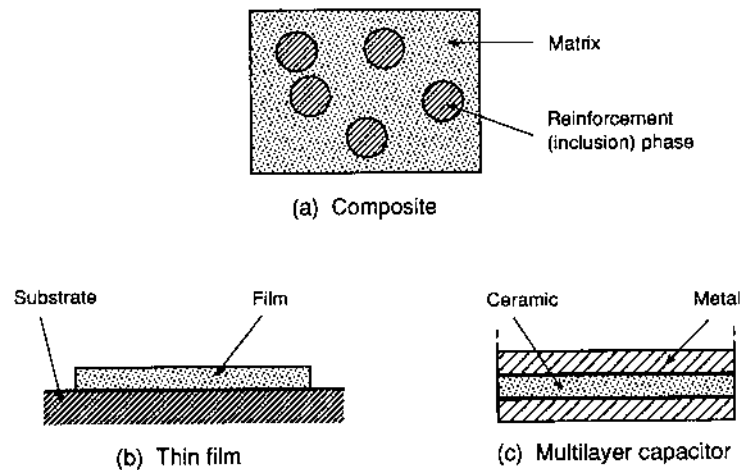


FIGURE 11.13 Examples of constrained sintering: (a) a composite in which inclusions prevent the powder matrix from sintering freely; (b) an adherent thin film for which sintering in the plane of the film is inhibited by the substrate; (c) a multilayer in which the layers sinter at different rates.

sions divided by the total volume of the composite (solid plus pores). Suppose that the composite consists of a porous powder matrix with a relative density ρ_m and rigid, fully dense inclusions (relative density $\rho_i = 1$). As the system densifies (Fig. 11.14), the total volume decreases so that the volume fraction of the inclusions increases. Commonly, the volume fraction of the inclusions v_f is determined on the basis of the fully dense composite, such that

$$v_f + v_{mf} = 1 \quad (11.2)$$

where v_{mf} is the volume fraction of the matrix in the fully dense composite. If v_i is the volume fraction of the inclusions when the relative density of the matrix is ρ_m (< 1), then v_i is related to v_f by

$$v_i = \frac{\rho_m}{\rho_m + (1 - v_f)/v_f} \quad (11.3)$$

Therefore, knowing v_f we can determine v_i at any value of ρ_m .

Densification Rate of the Composite and the Matrix

Normally we measure the density of the composite, but in many cases we may need to determine the density of the matrix phase of the composite in order to compare its densification kinetics with those of the free matrix. If D_c and D_m are the densities (i.e., mass/volume) of the composite and the matrix, respectively, then by simple geometry we can show that

$$D_m = D_c \frac{(D_{co} - v_{io}D_i)}{(D_{co} - v_{io}D_c)} \quad (11.4)$$

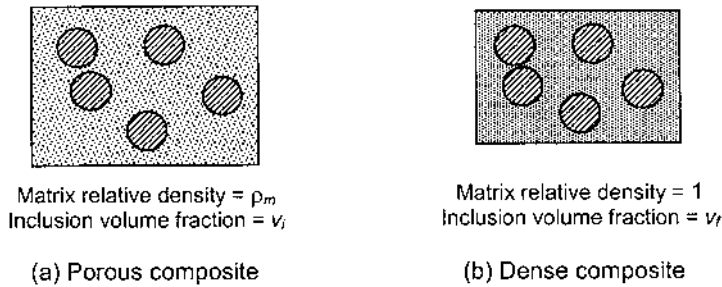


FIGURE 11.14 Matrix and inclusion parameters in the sintering of composites.

where D_i is the density of the inclusions and D_{co} and v_{io} are the initial values of D_c and v_i , respectively. Differentiating Eq. (11.4) followed by some manipulation gives

$$\frac{1}{D_m} \frac{dD_m}{dt} = \frac{1}{D_c} \frac{dD_c}{dt} \left(\frac{D_{co}}{D_{co} - v_{io} D_c} \right) \quad (11.5)$$

If ρ_c and ρ_m are the relative densities of the composite and the matrix respectively, Eq. (11.5) can be written

$$\frac{1}{\rho_m} \frac{d\rho_m}{dt} = \frac{1}{\rho_c} \frac{d\rho_c}{dt} \left(\frac{\rho_{co}}{\rho_{co} - v_{io} \rho_c} \right) \quad (11.6)$$

Equations (11.5) and (11.6) allow for the determination of the matrix densification rate from the measured densification rate of the composite.

11.4.1 The Rule of Mixtures

The rule of mixtures assumes the densification of the composite to be a weighted average of the independent densification rates of the matrix and of the inclusions; that is, it assumes that in the composite, each phase densifies in the same way as it would independently by itself. If, for example, we consider the *linear* densification rate $\dot{\epsilon}$, defined as one-third the *volumetric* densification rate $(1/\rho)dp/dt$, then according to the rule of mixtures

$$\dot{\epsilon}_c^m = \dot{\epsilon}_{fm} (1 - v_i) + \dot{\epsilon}_i v_i = \dot{\epsilon}_{fm} (1 - v_i) \quad (11.7)$$

where $\dot{\epsilon}_c^m$ is the composite densification rate predicted by the rule of mixtures, $\dot{\epsilon}_{fm}$ is the densification rate of the free matrix, and $\dot{\epsilon}_i$ is the densification rate of the inclusions, taken to be zero. According to Eq. (11.7), the ratio $\dot{\epsilon}_c^m/\dot{\epsilon}_{fm}$ varies linearly as $1 - v_i$.

When the sintering data for ceramic matrices with controlled amounts of rigid inclusions are compared with the predictions of the rule of mixtures, drastic deviations are found, particularly for polycrystalline powder matrices. Figure 11.15 shows the sintering data for a polycrystalline ZnO powder matrix (particle size $\approx 0.4 \mu\text{m}$) with different amounts of coarse, inert SiC inclusions (size $\approx 14 \mu\text{m}$) (26). The inclusions severely reduce the densification of the composite relative to that for the free ZnO matrix, and for inclusion volume fractions v_i greater than $\sim 20 \text{ vol\%}$, densification is almost completely inhibited. Data for a soda-lime glass powder (particle size $\approx 4 \mu\text{m}$) containing controlled amounts of coarse, inert SiC inclusions (particle size $\approx 35 \mu\text{m}$) are shown in Fig. 11.16 (27). The

effect of the inclusions on densification is considerably less severe than that for the polycrystalline ZnO matrix.

The data of Figs. 11.15 and 11.16 can be manipulated to produce results suitable for comparison with the predictions of the rule of mixtures. The procedure is to fit smooth curves to the data and differentiate to find the densification rate at any time. Figure 11.17 shows the results of the comparison. Drastic deviations are observed for the ZnO matrix composite for v_i as low as 3–6 vol%. The glass matrix composite shows good agreement with the predictions of the rule of mixtures for v_i less than ~20 vol% but the deviations become increasingly severe at higher v_i values.

Faced with the data showing drastic deviations from the predictions, it may be argued that the rule of mixtures is inadequate to describe the data because the assumptions are too simplistic. For example, it ignores key factors such as the following:

1. *Transient stresses* due to differential sintering between the inclusions and the matrix may arise, and if large enough, they can reduce the densification rate and cause microstructural damage.
2. The inclusions will interfere and eventually form a touching, *percolating network* at some critical value of v_i . The formation of a network will inhibit densification, and if the network is rigid enough densification may stop completely.

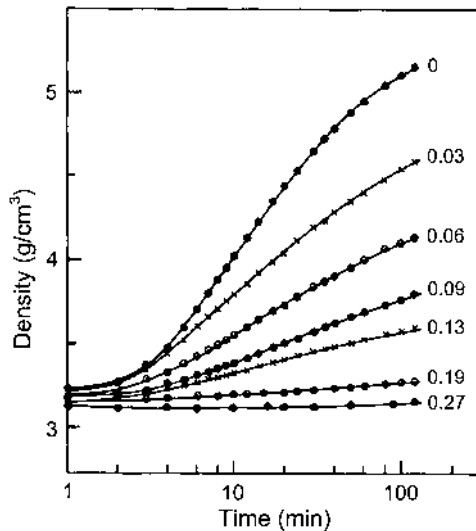


FIGURE 11.15 Density versus sintering time at 700°C for a polycrystalline ZnO powder containing different volume fractions of rigid SiC inclusions. (From Ref. 26.)

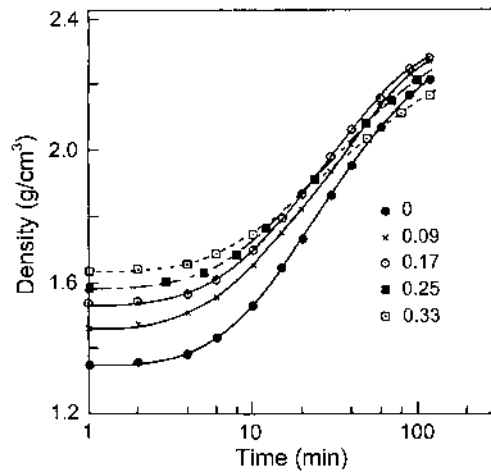


FIGURE 11.16 Density versus sintering time at 600°C for a soda-lime glass powder containing different volume fractions of rigid SiC inclusions. (From Ref. 27.)

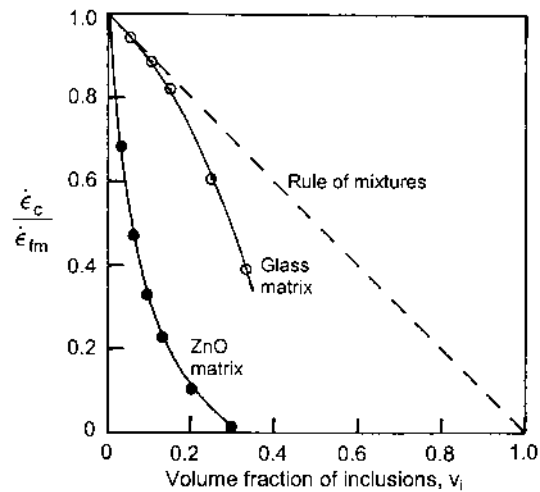


FIGURE 11.17 Comparison of the sintering data for the composites described in Figs. 11.15 and 11.16 with the predictions of the rule of mixtures. The densification rate of the composite relative to that for the free matrix is plotted versus the volume fraction of inclusions. Note the strong deviation from the predictions of the rule of mixtures for the ZnO matrix even at fairly small inclusion content.

We briefly analyze the influence of these two factors for explaining the drastic deviations from the rule of mixtures. In addition, the presence of the inclusions may disrupt the *packing* of the matrix phase in the regions surrounding the inclusions, and these packing inhomogeneities can also inhibit densification, particularly in the case of polycrystalline matrices.

11.4.2 Transient Stresses During Sintering

11.4.2.1 Composite Sphere Model

In order to determine the stresses that arise during sintering, a geometrical model must be assumed. For well-dispersed inclusions, a model that has been commonly used is the *composite sphere*, in which the core represents the inclusion and the cladding represents the porous matrix. As sketched in Fig. 11.18, the composite containing a volume fraction v_i of inclusions is conceptually divided into composite spheres, each having a volume fraction v_i of core. We can consider a single composite sphere, with the assumption that the properties of the composite sphere are representative of the whole composite. When the inclusion is much larger than the particle size of the matrix, as in most practical composites, the matrix can be regarded, to a good approximation, as a continuum. With this assumption, phenomenological constitutive equations can be used for the matrix and microscopic considerations can be neglected.

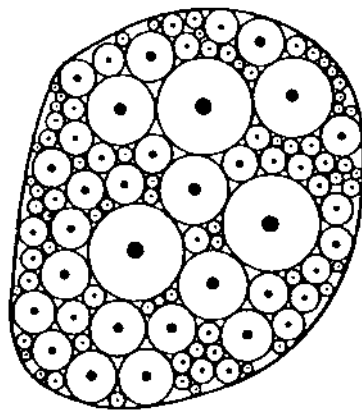


FIGURE 11.18 The composite sphere model. A composite containing spherical inclusions is conceptually divided into composite spheres (cross-sectional view). The core of each sphere is an inclusion and the outer radius of the cladding of the sphere is chosen such that each sphere has the same volume fraction of inclusion as the whole body.

11.4.2.2 Stress Components

A shrinking cladding (matrix) around a core (inclusion) gives rise to (1) compressive stresses within the core and (2) a compressive radial stress and tangential tensile stresses within the cladding (28). If σ_r , σ_θ and σ_ϕ are the components of the stress in spherical coordinates (Fig. 11.19), all three stress components in the inclusion are equal:

$$\sigma_{ri} = \sigma_{\theta i} = \sigma_{\phi i} = \sigma_i \quad (11.8)$$

where σ_i is the mean hydrostatic stress in the inclusion. Therefore, the inclusion is under purely hydrostatic stresses. In the convention that compressive stresses and strains are negative quantities, σ_i is negative. The stresses in the matrix are given by

$$\sigma_{rm} = -\frac{v_i \sigma_i}{(1 - v_i)} \left(1 - \frac{b^3}{r^3} \right) \quad (11.9)$$

$$\sigma_{\theta m} = \sigma_{\phi m} = -\frac{v_i \sigma_i}{(1 - v_i)} \left(1 + \frac{b^3}{r^3} \right) \quad (11.10)$$

where a and b are the inner and outer radii, respectively, of the composite sphere and v_i is the volume fraction of inclusions, given by

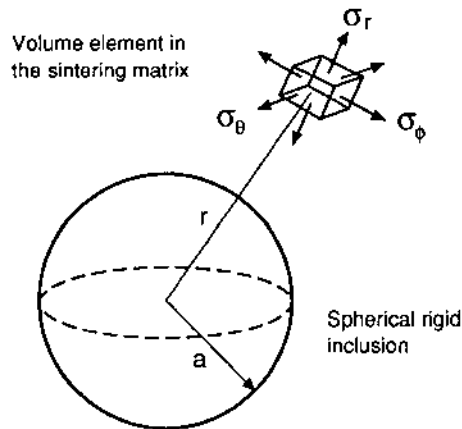


FIGURE 11.19 The stress components in a volume element at a distance r in the sintering matrix of a composite sphere. The radius of the inclusion is a , and the outer radius of the cladding (the matrix) is b .

$$v_i = \frac{a^3}{b^3} \quad (11.11)$$

The stresses in the matrix have their maximum values at the inclusion–matrix interface ($r = a$) and decrease as $1/r^3$. If $\sigma_{rm}(a)$ is the radial stress and $\sigma_{\theta m}(a)$ is the tangential (hoop) stress in the matrix at the interface, then from Eqs. (11.9)–(11.11) we obtain

$$\sigma_{rm}(a) = \sigma_i \quad (11.12)$$

$$\sigma_{\theta m}(a) = -\sigma_i \frac{1 + 2v_i}{2(1 - v_i)} \quad (11.13)$$

The mean hydrostatic stress in the matrix is

$$\sigma_m = \frac{1}{3}(\sigma_{rm} + \sigma_{\theta m} + \sigma_{\phi m}) = -\sigma_i \left(\frac{v_i}{1 - v_i} \right) \quad (11.14)$$

According to this equation, the mean hydrostatic stress in the matrix is uniform, i.e., it is independent of r . Furthermore, the matrix is under both hydrostatic and tangential stresses. Since σ_i is compressive (negative), σ_m is tensile (positive) so it opposes the compressive sintering stress. Because of this opposition to the sintering stress, σ_m is often called a *backstress*.

11.4.2.3 Effect of Transient Stresses on Sintering

The densification rate of the matrix is affected by the hydrostatic component of the stress in the matrix. For a free matrix, the linear densification rate (or strain rate) can be written [see Eq. (8.116)]

$$\dot{\epsilon}_{fm} = \frac{\Sigma}{K_m} \quad (11.15)$$

where Σ is the sintering stress and K_m is the densification or bulk viscosity. Both $\dot{\epsilon}_{fm}$ and Σ are negative quantities. For the matrix phase of the composite, the linear densification rate is

$$\dot{\epsilon}_m = \frac{\Sigma + \sigma_m}{K_m} = \frac{1}{K_m} \left[\Sigma - \sigma_i \left(\frac{v_i}{1 - v_i} \right) \right] \quad (11.16)$$

The backstress σ_m opposes Σ so it reduces the densification rate of the matrix. The tensile hoop stress $\sigma_{\theta m}$ may influence the growth of radial cracks in the matrix (see Fig. 11.4b). According to Eq. (11.16), if the transient stresses were the only significant factor, the important effects on sintering would be determined

by the value of σ_i . The calculation of σ_i therefore forms an important part in many analyses.

11.4.2.4 Calculation of Transient Stresses and Strain Rates

When one region of a sample (e.g., the matrix) shrinks at a different rate from a neighboring region (e.g., the inclusion), transient stresses are generated. Viscous flow (or creep) will always seek to relieve the stresses, so it is reasonable to assume that the calculation of the stresses would require a time-dependent, *viscoelastic* solution, where the response of the material to a stress consists of an elastic strain and a time-dependent strain due to viscous flow. However, the elastic strain is much smaller than the strains observed during sintering, so the observed deformation results almost entirely from viscous flow. A viscoelastic solution is not necessary. Instead, we can consider only the purely *viscous* response of the porous sintering material.

Viscoelastic models (14,29) have been developed for sintering with rigid inclusions, and they predict large values for the interfacial stresses and backstresses, with σ_i as high as 100 times Σ . The models assume that the materials show *linear* viscoelastic behavior and utilize the *viscoelastic analogy* (30,31) for calculating the time-dependent stresses and strain rates from the elastic solutions. However, Bordia and Scherer (32) have pointed out the inadequacy of applying the viscoelastic analogy to sintering materials that often do not show linear viscoelastic behavior. Because of the difficulties with the viscoelastic analysis, Scherer (33) developed a model based on the purely viscous response of the sintering material. In this case, the calculation of the time-dependent stresses and strain rates are greatly facilitated by assuming the *elastic-viscous analogy*, where the equations for the time-dependent viscous response are found from those for the elastic solution (30). As described below, Scherer's model predicts relatively small backstresses.

11.4.2.5 Scherer's Model for Sintering with Rigid Inclusions

The first stage in the calculation is to choose a constitutive equation that relates the applied stresses to the resulting strains. For an elastic material, the behavior is described by two independent elastic constants, such as the shear modulus G and the bulk modulus K . The constitutive equation for an isotropic linear elastic solid has the form (28)

$$\epsilon_x = \epsilon_f + \frac{1}{E} \left[\sigma_x - \nu (\sigma_y + \sigma_z) \right] \quad (11.17a)$$

$$\varepsilon_y = \varepsilon_f + \frac{1}{E} [\sigma_y - \nu(\sigma_x + \sigma_z)] \quad (11.17b)$$

$$\varepsilon_z = \varepsilon_f + \frac{1}{E} [\sigma_z - \nu(\sigma_x + \sigma_y)] \quad (11.17c)$$

where ε_x , ε_y , and ε_z are the strains, and σ_x , σ_y , and σ_z are the stresses in the x , y , and z directions; E is the Young's modulus; ν is the Poisson's ratio; and ε_f is the free strain, i.e., the strain which would be produced in the absence of local stresses. The Young's modulus E and Poisson's ratio ν are an alternative pair of elastic constants that are related to G and K by

$$G = \frac{E}{2(1 + \nu)} \quad K = \frac{E}{3(1 - 2\nu)} \quad (11.18)$$

For an isotropic, linearly viscous, incompressible material, the constitutive equation is easily obtained from Eq. (11.17) by invoking the elastic-viscous analogy: the strain is replaced by the strain rate, E is replaced by the shear viscosity η , and ν becomes $1/2$ (for an incompressible material), giving (for the x direction)

$$\dot{\varepsilon}_x = \dot{\varepsilon}_f + \frac{1}{3\eta} \left[\sigma_x - \frac{1}{2}(\sigma_y + \sigma_z) \right] \quad (11.19)$$

where the dot denotes the derivative with respect to time. For a porous material, Eq. (11.19) must be modified to allow for the compressibility of the pores; that is

$$\dot{\varepsilon}_x = \dot{\varepsilon}_f + \frac{1}{E_m} \left[\sigma_x - \nu_m(\sigma_y + \sigma_z) \right] \quad (11.20)$$

where E_m is the uniaxial viscosity of the matrix, which varies from 0 to 3η as the relative density of the matrix ρ_m goes from 0 to 1, and ν_m is the Poisson's ratio of the matrix, which varies from 0 to $1/2$ as ρ_m goes from 0 to 1. As ρ_m approaches 1, Eq. (11.20) becomes identical to Eq. (11.19). By analogy with Eq. (11.18), the shear viscosity G_m and the bulk viscosity K_m are related by

$$G_m = \frac{E_m}{2(1 + \nu_m)} \quad K_m = \frac{E_m}{3(1 - 2\nu_m)} \quad (11.21)$$

Examination of Eqs. (11.20) and (11.21) indicates that the solutions for the sintering material are obtained from those for the elastic material, Eqs. (11.17) and (11.18), by replacing G and K by G_m and K_m , respectively, and replacing the strains by the strain rates.

For the composite sphere model, the sintering problem of mismatched shrinkage rates is analogous to the problem of thermal expansion mismatch. By adopting the elastic solution for the thermal stress problem and using the elastic-viscous analogy to transform it to the time-dependent solution for the sintering problem, the following equations are obtained for the stresses and strain rates:

$$\sigma_i = (1 - v_i) K_{cs} \dot{\epsilon}_{fm} \quad (11.22)$$

$$\sigma_m = \left[\left(\frac{a}{r} \right)^3 - v_i \right] K_{cs} \dot{\epsilon}_{fm} \quad (11.23)$$

$$\sigma_{\theta m} = - \left[\frac{1}{2} \left(\frac{a}{r} \right)^3 + v_i \right] K_{cs} \dot{\epsilon}_{fm} \quad (11.24)$$

where a is the inner radius of the composite sphere, v_i is the volume fraction of inclusions, and K_{cs} is given by

$$K_{cs} = \frac{1}{1/(4G_m) + v_i/(3K_m)} \quad (11.25)$$

The free strain rate (i.e., the linear densification rate) is given by

$$\dot{\epsilon}_{fm} = \frac{1}{3} \left(\frac{\Sigma}{K_m} \right) \quad (11.26)$$

The hydrostatic backstress can be calculated from Eqs. (11.22), (11.25), and (11.26), giving

$$\frac{\sigma_m}{\Sigma} = - \frac{v_i}{v_i + 3K_m/4G_m} \quad (11.27)$$

According to this equation, as v_i approaches zero, so does σ_m . Furthermore, K_m and G_m are positive so that σ_m is always smaller than Σ .

The stress in the inclusion can be compared with the sintering stress by using Eqs. (11.22), (11.25) and (11.26):

$$\frac{\sigma_i}{\Sigma} = \frac{1 - v_i}{v_i + 3K_m/4G_m} \quad (11.28)$$

Using Eq. (11.21), as v_i approaches zero, the stress in an isolated inclusion is

$$\frac{\sigma_i}{\Sigma} = \frac{2(1 - v_m)}{1 + v_m} \quad (11.29)$$

This equation shows that σ_i/Σ can be greater than 2 only when $\nu_m < 0$. Negative values of the Poisson's ratio have not been observed experimentally so the absolute *maximum* value of σ_i predicted by Scherer's model is therefore 2Σ . The maximum stresses in the matrix occur at the interface between the matrix and the inclusion. The radial stress $\sigma_{rm}(a) = \sigma_i$, so it is also predicted to be less than 2Σ . The circumferential or hoop stress is found from Eqs. (11.24)–(11.26) to be

$$\frac{\sigma_{\theta m}(a)}{\Sigma} = -\frac{1/2 + \nu_i}{\nu_i + 3K_m/4G_m} \quad (11.30)$$

When ν_i approaches zero, Eq. (11.30) becomes

$$\frac{\sigma_{\theta m}(a)}{\Sigma} = -\frac{1 - 2\nu_m}{1 + \nu_m} \quad (11.31)$$

This equation shows that $\sigma_{\theta m}(a)$ can be no greater in magnitude than Σ unless $\nu_m < 0$, so the viscous analysis of Scherer predicts transient stresses that are considerably smaller than those calculated by viscoelastic models mentioned earlier.

The effect of the transient stresses on the densification rate of the composite can also be calculated from Scherer's model. The linear densification rate of the composite is predicted to be

$$\dot{\epsilon}_c = \frac{(1 - \nu_i)K_{cs}\dot{\epsilon}_{fm}}{4G_m} \quad (11.32)$$

Another way to express the results is to consider the densification rate of the composite relative to that predicted by the rule of mixtures. Using Eqs. (11.7), (11.25), and (11.32), this ratio is given by

$$\frac{\dot{\epsilon}_c}{\dot{\epsilon}_c^{rm}} = \frac{1}{1 + \nu_i(4G_m/3K_m)} \quad (11.33)$$

Since the denominator is always greater than 1, this equation predicts that the linear densification rate is lower than that predicted by the rule of mixtures. From Eq. (11.21), the ratio $4G_m/3K_m$ is given by

$$\frac{4G_m}{3K_m} = \frac{2(1 - 2\nu_m)}{1 + \nu_m} \quad (11.34)$$

The maximum value of this ratio is 2, which occurs when $\nu_m = 0$, so for ν_i less than ~ 0.10 , the composite densification rate is predicted to deviate from the rule of mixtures by not more than $\sim 10\%$.

Scherer also considered a *self-consistent model* in which a microscopic region of the matrix is regarded as an island of sintering material in a continuum (the composite) that contracts at a slower rate (34). The mismatch in sintering rates causes stresses that influence the densification rate of each region. It is found that the equations for the self-consistent model differ from those of the composite sphere model only in that the shear viscosity of the matrix G_m is replaced by the shear viscosity of the composite G_c . Taking Eq. (11.33), the corresponding equation for the self-consistent model is therefore

$$\frac{\dot{\epsilon}_c}{\dot{\epsilon}_c^{rm}} = \frac{1}{1 + v_i (4G_c/3K_m)} \quad (11.35)$$

An approximation to G_c can be obtained from the Hashin-Shtrikman equation (35), which, for a viscous matrix, is given by

$$G_c = G_m \left[1 + \frac{15}{2} \left(\frac{v_i}{1 - v_i} \right) \left(\frac{1 - v_m}{4 - 5v_m} \right) \right] \quad (11.36)$$

In the case of viscous sintering where the matrix phase of the composite is a glass, explicit expressions can be derived for the moduli and Poisson's ratio (36). Poisson's ratio is given to a good approximation by

$$v_m = \frac{1}{2} \left(\frac{\rho_m}{3 - 2\rho_m} \right)^{1/2} \quad (11.37)$$

where ρ_m is the relative density of the matrix, and the uniaxial viscosity is given by

$$E_m = \frac{3\eta\rho_m}{3 - 2\rho_m} \quad (11.38)$$

where η is the viscosity of the glass.

Using Eqs. (11.34) and (11.37), the ratio $4G_m/3K_m$ can be calculated in terms of the relative density of the matrix and this ratio can be substituted into Eqs. (11.28), (11.29), and (11.35) to calculate the stresses and densification rates for the composite sphere model. Alternatively, for the self-consistent model, G_c can be found from Eq. (11.36), and the same procedure repeated to determine the stresses and strain rates. Figure 11.20 shows the predicted values for $\dot{\epsilon}_c/\dot{\epsilon}_c^{rm}$ as a function of the relative density of the matrix for the composite sphere and self-consistent models. For v_i less than ~ 20 vol%, the predictions for the two models are almost identical, but they deviate significantly for much higher values of v_i . When v_i is less than ~ 10 – 15 vol%, the predicted values of $\dot{\epsilon}_c/\dot{\epsilon}_c^{rm}$ are not

very different from 1, and the rule of mixtures is accurate enough for these values of v_i .

An experimental test of Scherer's theory made using the data in Fig. 11.16 for glass matrix composites indicates that the theory performs well for v_i less than ~ 15 vol% but significantly underestimates the effects of the inclusions at higher values of v_i (Fig. 11.21). The agreement is less satisfactory for polycrystalline matrix composites. The results indicate that other factors must also play a role in hindering the sintering rates.

11.4.3 Percolation and Network Formation

As the volume fraction of inclusions increases, we reach a stage where the inclusions become so numerous that they form enough inclusion-inclusion contacts to produce a continuous network extending all the way across the sample. The network of inclusions is said to percolate through the sample, rather like water percolating through ground coffee in a coffee maker. The stage where the inclusions first form a percolating network is called the percolation threshold.

The formation of a continuous network of inclusions has important consequences for sintering as well as for other properties of the system. If the inclusions

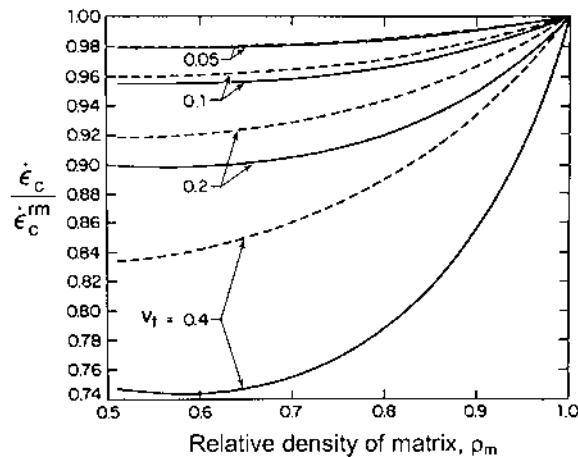


FIGURE 11.20 Comparison of the predictions of Scherer's theory of sintering with rigid inclusions with the predictions of the rule of mixtures. The linear strain rate of the composite normalized by the strain rate from the rule of mixtures [Eq. (11.7)] is plotted versus the relative density of the matrix for the indicated volume fraction of inclusions v_i . The dashed curves represent the composite sphere model [Eq. (11.33)], and solid curves, the self-consistent model [Eq. (11.35)]. (From Ref. 33.)

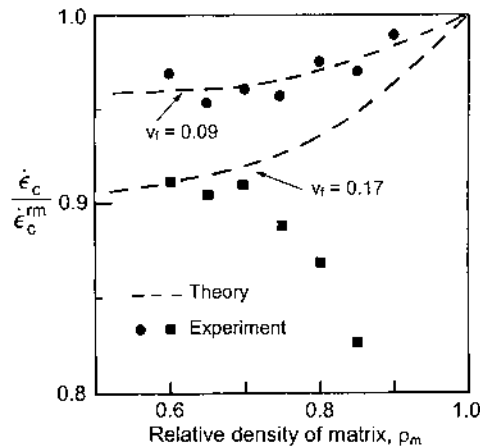


FIGURE 11.21 Comparison of the sintering data for the glass matrix composites described in Fig. 11.16 with the predictions of Scherer's theory for sintering with rigid inclusions [Eq. (11.35)]. The linear strain rate of the composite normalized by the strain rate from the rule of mixtures is plotted versus the relative density of the matrix ρ_m for the indicated volume fraction of inclusions v_f . Note the deviation starting near $\rho_m = 0.75$ for the composite with $v_f = 0.17$. (From Ref. 27.)

are electrically conducting, the structure can carry an electric current as soon as the percolating network forms (Fig. 11.22). If the contacts between the inclusions are rigid, the structure will be mechanically rigid. This is important for sintering because the increased stiffness of the structure will retard sintering, and if the structure is completely rigid, sintering will stop. The models considered so far neglect the formation of a percolating network of inclusions.

11.4.3.1 The Concept of Percolation

Percolation has been considered in some detail by Zallen (37). The concept of percolation is illustrated in Fig. 11.23 using a triangular, two-dimensional lattice (38). If we place particles on sites at random, larger and larger clusters of adjoining particles will be formed as the number of particles increases. Eventually, one of these clusters, referred to as the *percolating cluster* or the *spanning cluster*, becomes large enough to extend all the way across the lattice. The fraction of sites that must be filled before the percolating cluster appears is called the *percolation threshold*, p_c .

The percolation threshold depends on the shape and dimensionality of the lattice. For the triangular lattice shown in Fig. 11.23, the percolation threshold is reached when half of the sites is occupied, i.e., $p_c = 0.5$, whereas $p_c = 0.593$

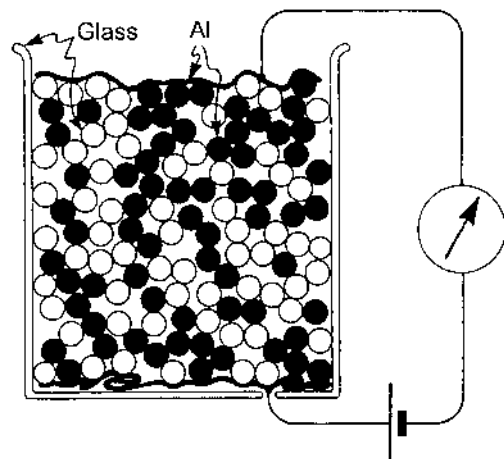


FIGURE 11.22 Sketch of an experiment to illustrate some elementary aspects of percolation in a mixture of aluminum and glass balls. When the percolation threshold for the aluminum balls is reached, the system will conduct an electrical current. (From Ref. 37.)

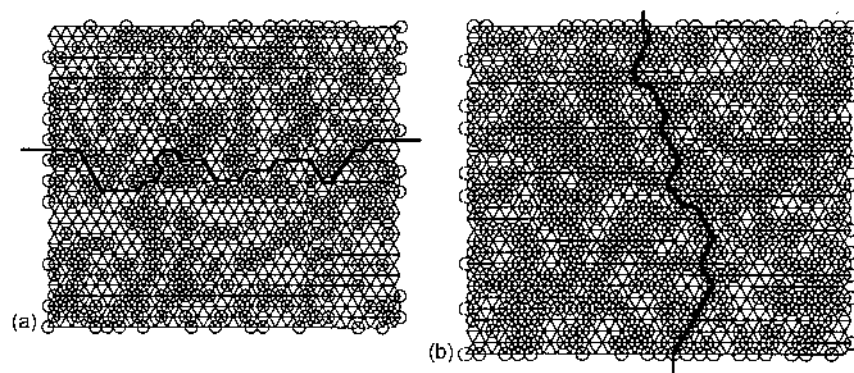


FIGURE 11.23 Illustration of percolation on a triangular lattice. When 40% of the sites are filled, no single cluster of particles extends all the way across the lattice, as indicated by the thick line in (a). When $>50\%$ of the sites are filled, a "spanning cluster" appears; then as indicated by the thick line in (b), there is a path of occupied sites completely crossing the lattice. (From Ref. 38.)

for a square, two-dimensional lattice, and $p_c = 0.311$ for a cubic lattice. For a powder system undergoing sintering, no lattice is present, but it has been shown that p_c occurs at a certain volume fraction (or area fraction in two dimensions) regardless of the nature of the lattice. In three dimensions, the percolation threshold is reached when the volume fraction of particles is ~ 16 vol% even when no lattice is present. If, for example, glass balls are mixed with aluminum balls as sketched in Fig. 11.22, the structure will become electrically conducting when the aluminum balls occupy ~ 16 vol% of the space. If the glass balls and the aluminum balls are of the same size, percolation will occur when the number fraction of the aluminum balls is ~ 0.27 . This is because the particles occupy $\sim 64\%$ of the total volume of the structure (the packing density for dense random packing) and the volume fraction of the aluminum balls (0.27×0.64) must equal 0.16. If glass and aluminum balls of the same size were placed at random on a simple cubic lattice, percolation will occur when the number fraction of the aluminum balls is ~ 0.311 because in this case, the packing density for the simple cubic lattice is 0.52 and 0.52×0.311 is approximately 0.16. The percolation threshold of ~ 0.16 applies to equiaxial particles in a random arrangement. This value will change if the particles agglomerate or repel one another. The value of p_c also depends on the aspect ratio and orientation of the particles. It decreases with increasing aspect ratio but increases if the particles become aligned.

11.4.3.2 Effect of Percolation on Sintering

The effect of percolation on the rigidity of the composite is an important factor since this will influence the sintering kinetics. If the inclusions bond together on contact, the rigidity of the composite will increase dramatically near the percolation threshold, and the sintering rate will show a corresponding decrease. Even before the percolation threshold, large clusters of inclusions will form and these will have a significant effect locally, even before the overall stiffening produced by the percolating cluster.

As the results of Fig. 11.16 indicate, it is not impossible to densify composites with an inclusion volume fraction greater than the percolation threshold (~ 16 vol%). In fact some practical composites with an inclusion content significantly greater than the percolation threshold can be sintered to almost full density. The reason is that the inclusions do not bond together to form a rigid network. In many cases, particularly for glass matrices and systems with a significant amount of liquid phase at the sintering temperature, the glass or the liquid phase wets the contacts between the inclusions, providing a lubricating layer. When the inclusion–inclusion contacts are wetted, the stage where the system becomes fairly rigid, referred to as the *rigidity threshold*, is expected to occur at inclusion contents significantly higher than the percolation threshold.

To summarize, the nature of the interactions between the inclusions will have a significant effect on sintering. If the inclusions form strong bonds on

contact (e.g., if they are not wetted by the matrix) or interlock (e.g., because of surface roughness), the densification rate will be reduced significantly near the percolation threshold. On the other hand, if the contacts between the inclusions are lubricated, higher inclusion contents can be accommodated without a drastic reduction in the densification rate.

11.4.3.3 Numerical Simulations

Numerical simulations can be extremely valuable in exploring the effects of particle interactions on the sintering of composites, as demonstrated by Scherer and Jagota (38–40), who used a finite element method to simulate the sintering of viscous matrices containing rigid inclusions. In a three-dimensional packing of spherical particles, randomly selected particles are assigned to be inclusions and the rest are chosen to be matrix particles with the same size and surface tension as the inclusions. As sketched in Fig. 11.24, the composite contains three types of contacts: inclusion–inclusion (i–i), matrix–matrix (m–m), and inclusion–matrix (i–m). The results of the finite element simulation are found to depend on (1) the degree of bonding between the inclusions and (2) the ratio N of the viscosity of the inclusions to the viscosity of the matrix particles. For rigid inclusions ($N = 10^6$) that form strong inclusion–inclusion bonds and for wetted inclusion–matrix contacts, Fig. 11.25 shows the results of a finite element simulation, plotted in the form of the ratio $4G_c/3K_m$ versus the volume fraction of inclusions. Near the percolation threshold, the viscosity rises sharply by a factor of $\sim 10^6$ characteristic of the inclusions themselves. Also shown for comparison are the predictions of two other models that were described earlier: the Hashin-Shtrikman model [Eq. (11.36)] and the self-consistent model. These two models do not account for the rapid rise in the viscosity near the percolation threshold. They do show a rapid rise in the viscosity reminiscent of a percolation threshold but it appears at too high a volume fraction.

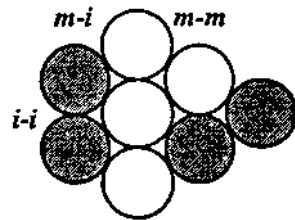


FIGURE 11.24 Contacts between inclusions (shaded) and matrix particles (white). (From Ref. 39.)

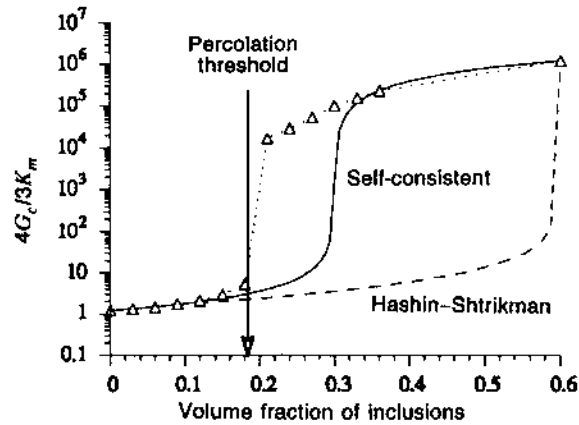


FIGURE 11.25 Shear viscosity of the composite, G_c , normalized by the bulk viscosity of the matrix, K_m , as a function of the volume fraction of inclusions (0.6 times the number fraction). Calculations by finite element method (Δ), self-consistent model (solid line), and Hashin-Shtrikman lower bound (dashed line) are shown. (From Ref. 39.)

11.4.4 Factors Influencing the Sintering of Ceramic Composites

When the effects of transient stresses and network formation between the inclusions are taken into account, the models appear to provide a reasonably good description of viscous sintering with rigid inclusions. The agreement is, however, less satisfactory for the sintering of polycrystalline matrices with rigid inclusions. The most likely reasons are that the packing of the matrix in the regions immediately surrounding the inclusions is disrupted and, more importantly, that the formation of a rigid skeletal network of inclusions effectively obstructs densification.

Based on observations of the microstructural evolution of Al_2O_3 matrix composites containing ZrO_2 inclusions and numerical analysis of the transient stresses due to differential densification between the matrix and the inclusions, Sudre et al. (41a–c) proposed a model to explain the significantly reduced sintering of polycrystalline matrices containing rigid inclusions. Figure 11.26 shows a sketch of the important features of the model. The stress field due to differential densification leads to premature densification in certain regions between the inclusions and these regions support grain growth (Fig. 11.26a). For multiple inclusions (Fig. 11.26b), the premature densification and associated grain growth lead to the development of a dense annulus that resists densification, so severely reduced

densification rates can occur even for a fairly sparse network of nontouching inclusions when the inclusion volume fraction is low.

The importance of network formation and packing inhomogeneities has been clearly demonstrated by Kapolnek and De Jonghe (42) and Hu and Rahaman (43) in sintering experiments using inclusions that were uniformly coated with the matrix phase. In the experiments by Hu and Rahaman, composites consisting of a polycrystalline ZnO matrix and inert, rigid inclusions of ZrO_2 were prepared by two separate methods. In one method, the matrix and inclusions were mixed mechanically in a ball mill and in the other, individual ZrO_2 inclusions were coated with the required thickness of ZnO powder by chemical precipitation from solution. The mechanically mixed powder and the coated powder were consolidated and sintered under nearly identical conditions. Figure 11.27 shows

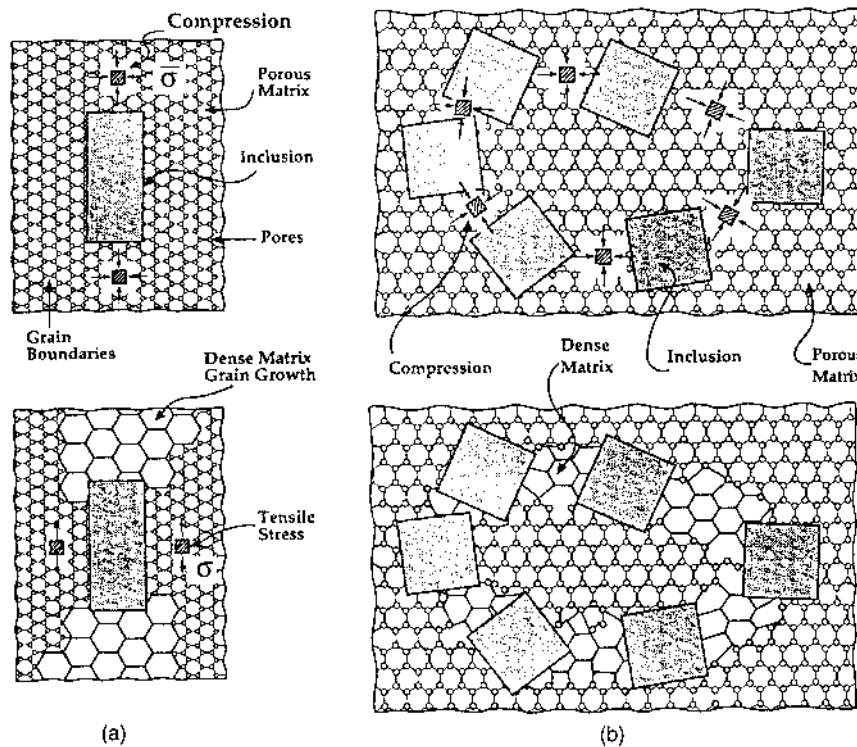


FIGURE 11.26 Schematic diagrams illustrating the sequence of events leading to the retardation of sintering and damage in bodies containing inclusions. (a) single inclusion; (b) multiple inclusions. (From Ref. 41a–c.)

a sketch comparing the inclusion distribution in the matrix for the two methods. An important feature is that for the coated powder, the inclusions are separated from one another by a layer of matrix so that network formation is minimized, and that each inclusion is surrounded by a homogeneous layer of matrix so that packing inhomogeneities, especially in the matrix immediately surrounding the inclusions, is significantly reduced. The densification of the coated powder is very close to that for an *unreinforced* ZnO containing no inclusions and, as shown in Fig. 11.28, significantly better than the mechanically mixed powder. Improved packing of the matrix phase immediately surrounding the inclusions is also found for composites formed from the coated powders (43). By severely reducing the sintering impediments through the use of coated powders, dense composites with up to 35–40 vol% of particulate, whisker, or platelet reinforcement have been prepared by conventional sintering (Fig. 11.29).

11.5 CONSTRAINED SINTERING II: ADHERENT THIN FILMS AND MULTILAYERS

Many applications, particularly in the areas of electronic and optical ceramics, require the deposition of a porous thin film on a substrate by techniques such as casting, spraying, dip coating, or spin coating, after which the film is dried and sintered to produce the required microstructure. Commonly the film adheres to the substrate but is too thin to cause it to deform, so the substrate can be considered to be rigid. If the film remains attached to the substrate during sintering and does not crack, shrinkage in the plane of the substrate is inhibited, and stresses arise in the film and the substrate. Far from the edges, all of the shrinkage occurs in the direction perpendicular to the plane of the film (Fig. 11.30). The stress in the film is essentially a tensile stress that maintains strain compatibility with the substrate, subjecting the film to simultaneous creep. This is analogous to the

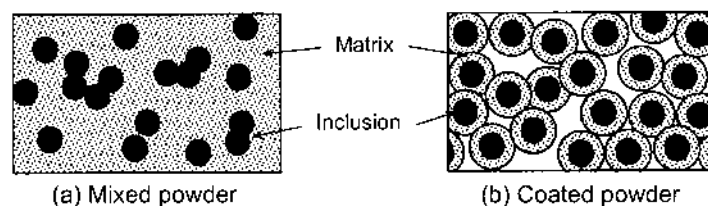


FIGURE 11.27 Schematic diagrams illustrating the distribution of inclusions (cross-sectional view) in composites formed from (a) a mixture of the inclusions and powder matrix prepared by ball-milling and (b) coated inclusions prepared by chemical precipitation.

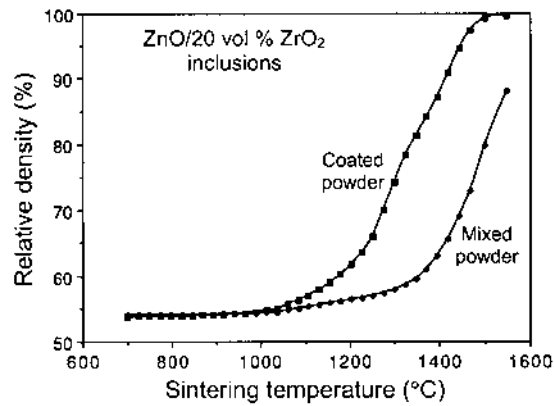


FIGURE 11.28 Data for relative density versus temperature during sintering at a constant heating rate ($5^{\circ}\text{C}/\text{min}$) for composites formed from coated powders and from mechanically mixed powders. The system consisted of a ZnO matrix and 20 vol% ZrO_2 inclusions. Note the significantly higher density of the composite formed from the coated powders. (From Ref. 43.)

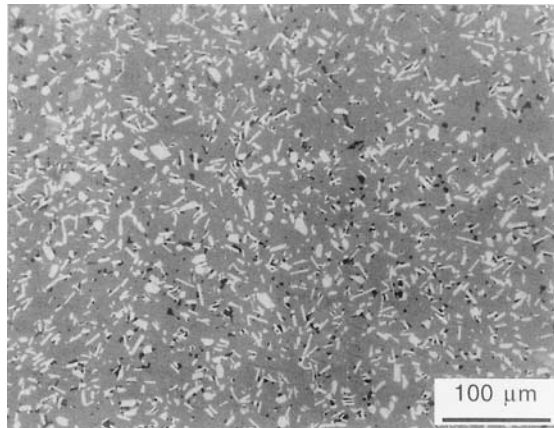


FIGURE 11.29 Optical micrograph of the polished surface of an $\text{Al}_2\text{O}_3/20 \text{ vol}\% \text{ SiC}$ platelet composite produced by conventional sintering of coated powders, showing a fairly uniform distribution of the platelets (light phase) in a dense matrix (dark phase). The very dark areas are pores, some of which are caused by pullout of platelets during polishing.

stress in a sandwich seal caused by mismatch in the thermal expansion coefficients in the layers (44). Compared to the free film, the stresses in the constrained film reduce the densification rate and can also lead to the growth of flaws.

11.5.1 Models for Constrained Sintering of Thin Films

Models for constrained sintering of thin adherent films on rigid substrates have been developed by Bordia and Raj (45) and Scherer and Garino (46). Both models consider the film to be a homogeneous continuum. The model of Bordia and Raj suffers from inconsistencies that are similar in nature to those outlined earlier for the viscoelastic models of sintering with rigid inclusions. Scherer and Garino assumed that the sintering rate of the film can be described by a constitutive relation for a porous, viscous body. By analogy with Eq. (11.20), the sintering rate along the orthogonal x , y , and z directions (see Fig. 11.30) can be written

$$\dot{\epsilon}_x = \dot{\epsilon}_f + \frac{1}{E_p} [\sigma_x - \nu_p (\sigma_y + \sigma_z)] \quad (11.39a)$$

$$\dot{\epsilon}_y = \dot{\epsilon}_f + \frac{1}{E_p} [\sigma_y - \nu_p (\sigma_x + \sigma_z)] \quad (11.39b)$$

$$\dot{\epsilon}_z = \dot{\epsilon}_f + \frac{1}{E_p} [\sigma_z - \nu_p (\sigma_x + \sigma_y)] \quad (11.39c)$$

where $\dot{\epsilon}_x$, $\dot{\epsilon}_y$, $\dot{\epsilon}_z$ and σ_x , σ_y , σ_z are the linear densification rates and stresses in the x , y , and z directions, respectively; $\dot{\epsilon}_f$ is the linear densification rate of the free or unconstrained film; E_p is the uniaxial viscosity; and ν_p is the Poisson's

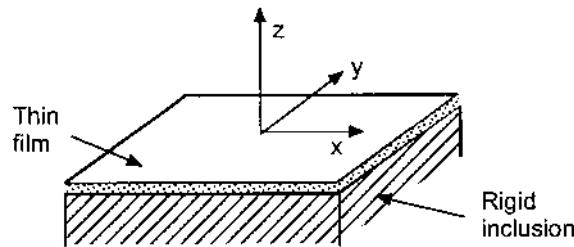


FIGURE 11.30 Geometry of a thin film attached to a rigid substrate. No shrinkage occurs in the plane of the film (xy plane); all of the shrinkage occurs in the direction perpendicular to the plane of the film (the z direction).

ratio of the porous film. As written, Eq. (11.39) is not based on any microstructural model, but a model must be chosen so that $\dot{\epsilon}_f$, E_p , and ν_p can be specified. Since there is no deformation of the film in the x and y directions, $\epsilon_x = \epsilon_y = 0$. Also there is no constraint in the z direction so that $\sigma_z = 0$. Putting $\sigma_x = \sigma_y = \sigma$, Eq. (11.39) gives

$$\sigma = -\frac{E_p \dot{\epsilon}_f}{1 - \nu_p} \quad (11.40)$$

and

$$\dot{\epsilon}_z = \left(\frac{1 + \nu_p}{1 - \nu_p} \right) \dot{\epsilon}_f \quad (11.41)$$

The volumetric densification rate is given by

$$\frac{\dot{\rho}}{\rho} = -\frac{\dot{V}}{V} = \dot{\epsilon}_x + \dot{\epsilon}_y + \dot{\epsilon}_z \quad (11.42)$$

where ρ is the relative density, V is the volume, and the dot denotes the derivative with respect to time. Using Eq. (11.41) and putting $\dot{\epsilon}_x = \dot{\epsilon}_y = 0$, the densification rate of the constrained film is

$$\left(\frac{\dot{\rho}}{\rho} \right)_c = - \left[\frac{1 + \nu_p}{3(1 - \nu_p)} \right] 3\dot{\epsilon}_f \quad (11.43)$$

Since the densification rate of the unconstrained film is given by

$$\left(\frac{\dot{\rho}}{\rho} \right)_u = -3\dot{\epsilon}_f \quad (11.44)$$

the function of ν_p in the square brackets of Eq. (11.43) represents the amount by which the densification rate of the film is retarded by the substrate.

For amorphous films where sintering occurs by viscous flow, Scherer's cylinder model described in Chapter 8 can be used to determine the terms E_p , $\dot{\epsilon}_f$, and ν_p (36). It is found that the term in the square brackets of Eq. (11.43) is always < 1 for $\rho < 1$, so that the constrained film is predicted to sinter at a slower rate than the unconstrained film. After integration, the results can be plotted as relative density versus dimensionless time (Fig. 11.31). Starting from the same initial density, ρ_0 , the constrained film takes a longer time to reach a given density than does an unconstrained film of the same material. For example, for $\rho_0 =$

0.5, the constrained film takes $\sim 25\%$ longer than the unconstrained film to reach theoretical density.

The stress in the film during sintering can be found from Eq. (11.40) and the equations for E_p , ϵ_f and ν_p . The equation can be written

$$\sigma = \frac{\gamma_{sv}}{l_0 \rho_0^{1/3}} f(\rho) \quad (11.45)$$

where γ_{sv} is the surface tension of the glass, l_0 is the length of the unit cell for Scherer's cylinder model (see Fig. 8.15), ρ_0 is the initial density, and $f(\rho)$ is a function of the density of the film. This function reaches a maximum of ~ 1 at $\rho \approx 0.81$. The maximum stress is therefore

$$\sigma_{\max} = \frac{\gamma_{sv}}{l_0 \rho_0^{1/3}} \quad (11.46)$$

For a polymeric silica gel prepared by the hydrolysis of silicon tetraethoxide, $\gamma_{sv} \approx 0.25 \text{ J/m}^2$, $l_0 \approx 10 \text{ nm}$ and $\rho_0 \approx 0.50$, so that $\sigma_{\max} \approx 30 \text{ MPa}$. This value of σ_{\max} is on the order of the stresses used in hot pressing (but it is tensile in nature). If the film is not strong enough to withstand such high tensile stresses, cracking will result. For a colloidal silica gel, the corresponding values are $\gamma_{sv} \approx 0.25 \text{ J/m}^2$, $l_0 \approx 100 \text{ nm}$, $\rho_0 \approx 0.25$, and $\sigma_{\max} \approx 3 \text{ MPa}$; that is, the maximum stress is considerably smaller.

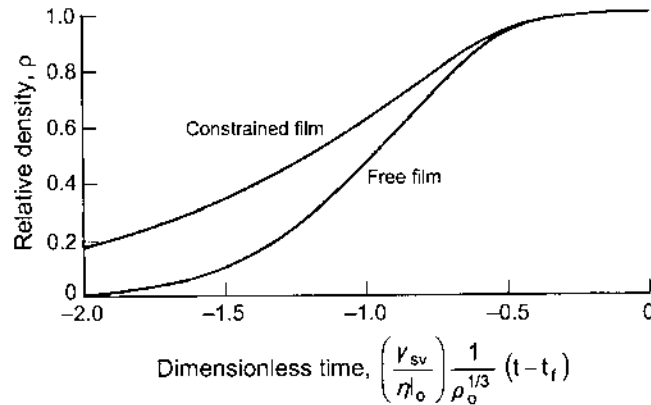


FIGURE 11.31 Predictions of the model of Scherer and Garino for the sintering of a constrained film and a free film. The constrained film is predicted to sinter more slowly than the free film. (From Ref. 46.)

11.5.2 Experimental Observations of Sintering of Thin Films

Garino and Bowen (47) studied the sintering of constrained and free films of soda-lime-silica glass, polycrystalline ZnO, and polycrystalline Al_2O_3 and compared their data with the predictions of Scherer and Garino's model. Constrained films (100–200 μm thick) were prepared by casting powder slurries onto a substrate. After drying, the shrinkage was measured using a laser reflectance apparatus sketched in Fig. 11.32. Free films were obtained by breaking off small pieces of the dried films from the substrate and the shrinkage of these films was measured from scanning electron micrographs taken at various stages of sintering.

Figure 11.33 shows the data for the volumetric shrinkage of the free film and the constrained film of the glass powder at 650°C. The data for the free film are well fitted by Scherer's cylinder model for the viscous sintering of glass. Scherer and Garino's model gives a good fit to the data for the constrained film for shrinkages up to ~25% but overestimates the shrinkage at higher values.

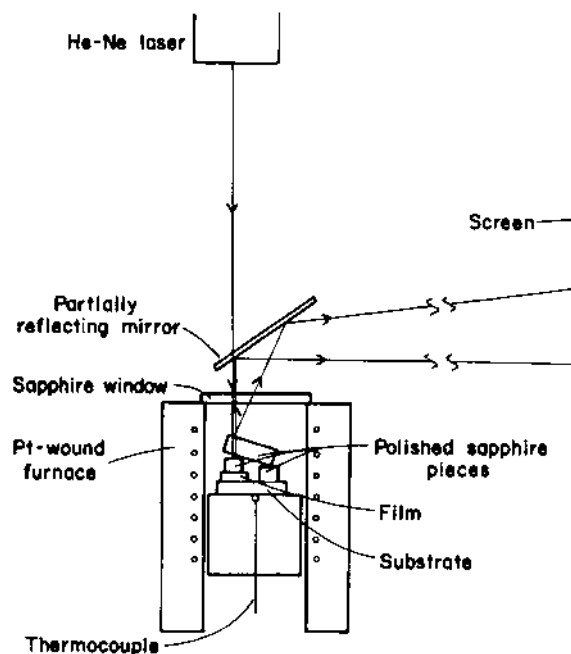


FIGURE 11.32 Schematic diagram of a laser reflectance apparatus used to measure the in situ shrinkage of an adherent film during sintering. (From Ref. 47.)

When the constrained film is sintered for times longer than those shown in the figure, the density is found to increase steadily and eventually reach the same final value as the free film.

The data for the sintering of the polycrystalline ZnO films are shown in Fig. 11.34. In this case, the constrained film sinters considerably more slowly than the free film and even after prolonged sintering does not reach the same end-point density as the free film. Instead, the shrinkage reaches a steady value that is considerably lower than that reached by the free film. The data for the Al_2O_3 films showed trends similar to those for the ZnO films.

The data of Figs. 11.33 and 11.34 indicate that the constrained sintering of polycrystalline films is qualitatively different from that of glass films. The reason for this difference is not clear, but two factors require consideration. The first factor is coarsening, which plays no part in the sintering of glassy films. Grain growth can be accounted for in Scherer and Garino's model but this modification still does not provide an adequate representation of the data for the polycrystalline films. The second factor is differential densification. Whereas microstructural observations of the polycrystalline films show features (e.g., large pores surrounded by dense regions) that are characteristic of differential densification, theories indicate that differential densification in a film is possible only if the adhesion fails (48).

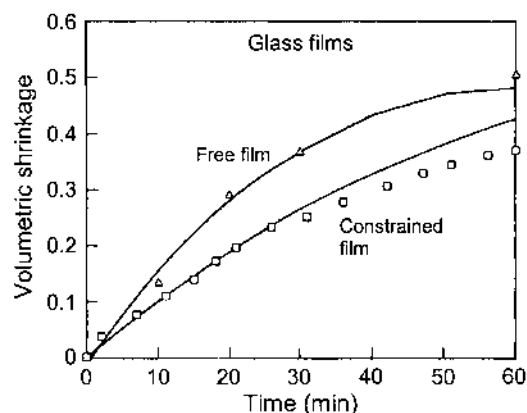


FIGURE 11.33 Isothermal shrinkage data for constrained and free glass films sintered at 650°C. The curve through the data for the free film represents the best fit to the data using Scherer's model for viscous sintering. The curve through the data for the constrained film represents the fit to the data by the thin-film model of Scherer and Garino using the fitting constants derived from the fit to the free-film data. (From Ref. 47.)

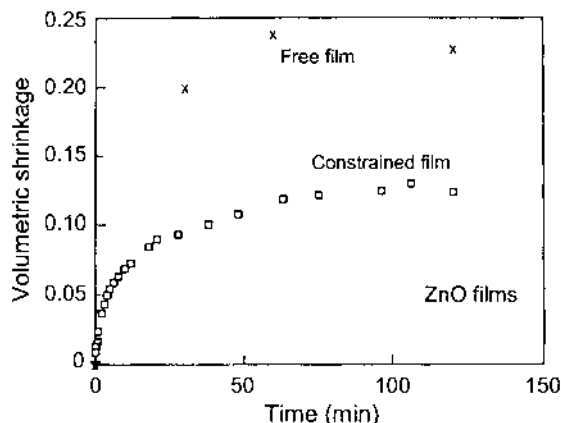


FIGURE 11.34 Shrinkage data for constrained and free films of ZnO during sintering at 778°C. (From Ref. 47.)

11.5.3 Crack Growth and Damage in Constrained Sintering of Films

As discussed earlier, the stresses generated in adherent films during constrained sintering can be substantial. If the film is sufficiently thin, the stress distribution normal to the plane of the film surface can be considered uniform. The interfacial adhesion or shear strength must be sufficiently high to support the force balance. For a fixed interfacial strength, a *critical film thickness* is found above which the interface can no longer support the tensile stress, resulting in interface failure, such as *delamination*. Typically for the sintering of particulate films on rigid substrates, this critical thickness is $<50\ \mu\text{m}$ but can be much less when large densification strains or weak interfaces are involved (49). For polymeric films prepared by sol-gel processing, the critical thickness is commonly $<1\ \mu\text{m}$. An example of a cracked and delaminated sol-gel film after sintering is shown in Fig. 11.35.

Failure by cracking can also be initiated in the film itself by the growth of pre-existing flaws during sintering. These flaws are known to occur readily during the drying of sol-gel or particulate films deposited by colloidal processing. An analysis of the mechanics of sintering constrained films predicts that a pre-existing crack will grow only under certain conditions that depend on the crack length, film thickness, and interfacial adhesion between the film and the substrate (48). In the theory, the effects of film thickness and interfacial adhesion are treated in terms of a single parameter, referred to as a *friction parameter*. The predictions of the theory, summarized in terms of a crack growth map (Fig 11.36), indicate



FIGURE 11.35 Delamination of a sintered zirconia thin film produced by a sol–gel method on a nanoporous alumina substrate. (Courtesy of L. C. De Jonghe.)

that regardless of the interfacial adhesion or film thickness, a pre-existing crack will grow only if the crack length is above a critical value (*vertical line*), whereas no crack will grow if the interfacial adhesion is large enough or the film thickness small enough such that the friction parameter is below a certain critical value (*horizontal line*). Experiments with glass films indicate that cracking occurs above a certain film thickness that is in good agreement with the theory (50). The critical parameters are more difficult to predict for polycrystalline films, but in general, a higher critical thickness for crack propagation results from careful drying prior to sintering, a homogeneous green structure, a high packing density, better interfacial adhesion, reducing the creep viscosity relative to the densification viscosity, and low sintering rates at low sintered densities.

11.5.4 Constrained Sintering of Multilayers

Adherent multilayers, formed from thick films of conductors, resistors, and dielectrics, constitute an important segment of the microelectronics industry because they serve as interconnecting substrates for integrated circuits. An important step in the manufacture of the multilayered packages is the *cosintering* (or *cofiring*) of the metal–ceramic multilayered structure (51). When the different layers sinter at different rates, transient stresses are generated that hinder the densification of the individual layers and can lead to the growth of microstructural flaws (e.g., cracking and delamination) as well as to anisotropic shrinkage (e.g., warping of the multilayered structure). In practice, the problems of reduced sintering, microstructural damage and warping are commonly minimized by matching the sintering rates of the layers through control of the powder characteristics, particle packing in the green system, and the sintering schedule. However, a clearer under-

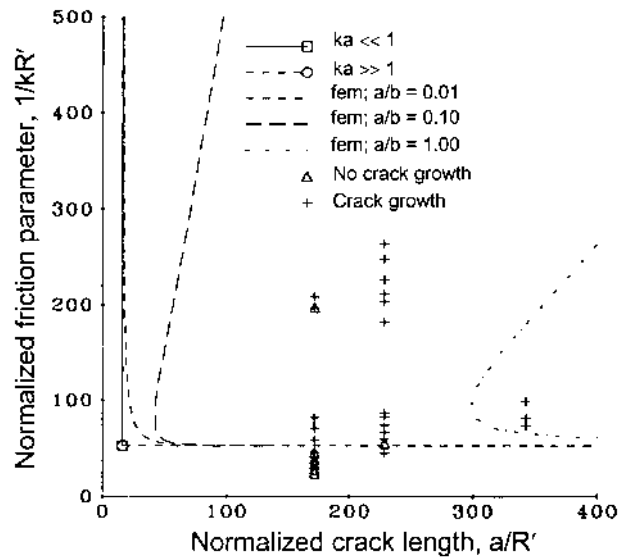


FIGURE 11.36 Crack growth map for a sintering film. The region enclosed toward the origin represents conditions under which pre-existing cracks do not extend. The symbols (+ and Δ) represent experimental data from glass films on a platinum substrate. (From Ref. 50.)

standing of these problems can be achieved by analyzing the development of the transient stresses and their effects on the sintering of the multilayered structure.

Figure 11.37 shows the data for the unconstrained shrinkage of thick films of gold particles and ceramic particles consisting of a mixture of cordierite and glass (52). When the two layers are bonded together and cosintered, the sintering of the gold is constrained by the ceramic film, leading to tensile stresses in the gold film and warping toward the gold. Later, as the ceramic film tries to shrink, it is constrained by the gold. The stresses in the films and their influence on the densification and warping of the composite structure during cosintering can be analyzed using an approach similar to that of Scherer and Garino (46), outlined earlier for the constrained sintering of films. As indicated by Eq. (11.43), the key parameters required for the analysis are the free sintering rates and the constitutive properties (shear and bulk viscosities) of the individual films. Scherer's model (36) provides an adequate representation of the constitutive properties for glasses but the models proposed for other materials are often inadequate (32). For the system described in Fig. 11.37, the use of models to account for the shear and bulk viscosities provides a reasonable description of the constrained sintering

of the composite structure. In general, more accurate values found by direct measurement should be used.

Polycrystalline films in a multilayered structure are observed to be more prone to the development of microstructural flaws than glass films during cosintering (53), so it is particularly important to minimize the presence of processing flaws in the polycrystalline layer during forming. When it does not lead to a deterioration in the properties of the multilayered system, the incorporation of a glassy second phase improves the stress relaxation in the polycrystalline film and can serve to alleviate the development of flaws.

11.6 THIN FILMS: GRAIN GROWTH AND DIMENSIONAL STABILITY

An understanding of grain growth in thin films is important because grain size, grain size distribution, and grain orientation can strongly influence the properties of polycrystalline films. Factors controlling the dimensional stability of thin films are also important because under certain conditions, films have been observed to break up into a group of islands thereby uncovering the substrate.

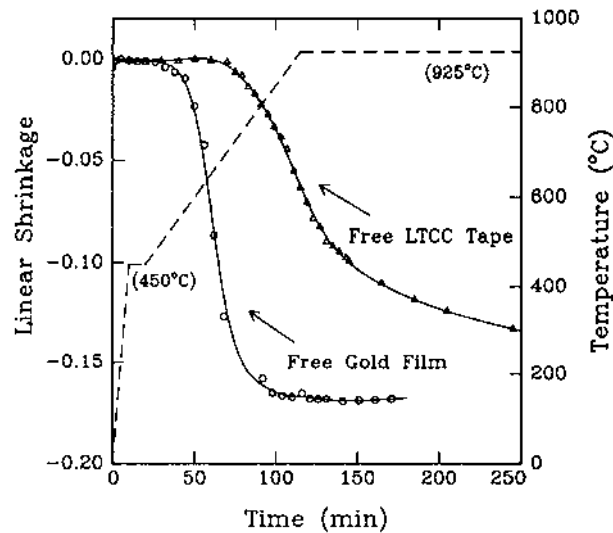


FIGURE 11.37 Shrinkage kinetics for unconstrained thick film of gold particles and LTCC tape consisting of cordierite and glass particles. The data points are fitted with smooth curves. (From Ref. 52.)

11.6.1 Grain Growth

If the initial grain size of a dense, adherent film is smaller than the film thickness, grain growth often leads to the rapid development of a grain structure with an average grain size larger than or comparable to the film thickness. The grain boundaries fully traverse the thickness of the film, leading to the development of a columnar microstructure. The occurrence of subsequent grain growth primarily by grain boundary motion in directions lying in the plane of the film can, in principle, be modeled as a two-dimensional process. Computer simulations of such two-dimensional grain growth were described in Chapter 9 but the application of such models to thin films is not straightforward. In thin films, grain growth is not truly a two-dimensional process. The film has free surfaces that provide additional constraints on the shape of a grain boundary and its motion.

The two main types of grain growth can also occur in thin films. *Normal* grain growth in thin films is found to stagnate when the average grain size (or grain diameter) is 2–3 times the film thickness (54,55), and this is often referred to as the *specimen thickness effect*. The grain size distribution in the stagnant structure can be well fitted by a *lognormal distribution*. After stagnation, any further grain growth occurs by *abnormal* growth whereby a small fraction of the grains grow at the expense of the majority of the grains. These abnormal grains develop a new population distinct from the original normal grain population. They can grow to impingement, resulting in films with grain sizes that are many times larger than the film thickness.

Mullins (56) proposed that the stagnation of grain growth in films is due to grain-boundary grooving at the junctions where the grain boundaries meet the free surfaces. The action of the grain boundary grooves to restrain grain growth may be understood by considering a flat boundary that is perpendicular to the plane of the film, running from a groove at the bottom surface to a groove on the top surface. Migration of the boundary would require an increase in its area, making the process energetically unfavorable. By incorporating the effects of grain boundary grooving into a model for two-dimensional grain growth, Frost et al. (57) accounted for the stagnation of normal grain growth and the resulting log normal distribution of grain sizes, as well as the scaling relationship between the average grain size of the stagnant structure and the film thickness.

As discussed in Chapter 9, several factors can contribute to the growth of abnormal grains, including anisotropies in the grain boundary energy and mobility. For thin films, anisotropies in *surface energy* (or interfacial energy) can also contribute to abnormal grain growth. When the grains become larger than the film thickness, the area of the free surface of the film becomes comparable to the area of the grain boundaries. If there is sufficient anisotropy in the surface free energy, then the minimization of surface free energy becomes an important driving force for grain boundary migration. Grains with orientations having low

surface energies are favored during growth and may escape from the pinning effects of grain boundary grooving and become abnormal grains. The effects of variations in the driving force for grain growth due to variations in the surface free energy of the different grains was analyzed using a two-dimensional grain growth model. The grain boundary velocity v_b is the sum of the contributions from the grain boundary curvature and the surface free energy difference, given by

$$v_b = M_b \gamma_{gb} (\kappa + \Gamma) \quad (11.47)$$

where M_b is the boundary mobility, γ_{gb} the grain boundary energy (per unit area), κ is the curvature of the boundary, and Γ is defined as

$$\Gamma = \frac{2\Delta\gamma_{sv}}{h\gamma_{gb}} \quad (11.48)$$

where $\Delta\gamma_{sv}$ is the difference in the surface free energy, and h is the film thickness. By coupling the stagnation of normal grain growth with an additional driving force due to surface free-energy difference, the results for the evolution of the grain structure are found to closely resemble experimentally observed grain growth in thin films (57). Figure 11.38 shows the results for the evolution of the microstructure in which 5% of the grains initially present were given an additional driving force of $\Gamma = 0.732$ (in units of the curvature $1/\sqrt{A_0}$, where A_0 is initial area of the grain) at a normalized time $\tau = 0.1$, coupled with a stagnation condition in which the critical curvature for boundary motion κ_{crit} is equal to $0.4/\sqrt{A_0}$ (i.e., v_b is zero below κ_{crit}). There is some general growth initially, but by $\tau = 2$, the normal grains are beginning to reach stagnation. Most of the abnormal grains, however, overcome the stagnation and continue to grow, giving rise to the transient development of a *bimodal* grain size distribution, until the entire field is taken over at $\tau = 8$. At this stage, there is no additional driving force for the boundaries between the abnormal grains, so growth of the abnormal grains stagnates.

It is found that surface free-energy differences $\Delta\gamma_{sv}$ of only a few percent should be sufficient to trigger abnormal grain growth. In this case, thin film systems that develop a bimodal grain size distribution are expected to have nearly isotropic surface free energies for most grain orientations. According to Eq. (11.48), the rate of abnormal grain growth should be higher for thinner films. However, the final grain size after abnormal grain growth should be greater in thicker films.

In many systems, particularly in the case of metallic films, the film is deposited at a temperature that is different from the temperature at which grain growth occurs. Because the film and the substrate will in general have different coefficients of thermal expansion, the films are subjected to a biaxial stress (or

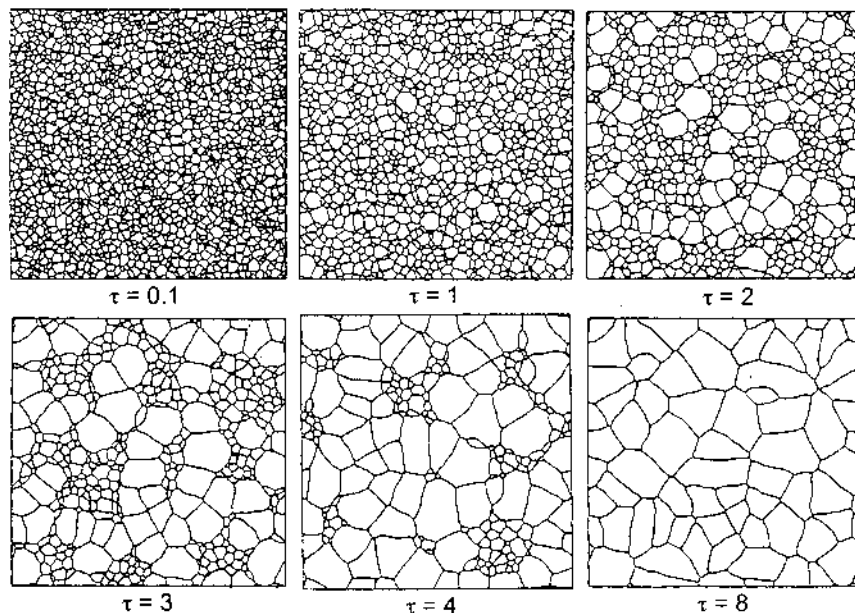


FIGURE 11.38 Evolution of the structure in a thin film in which 5% of the grains initially present were given an additional driving force of $\Gamma = 0.732$. The stagnation condition is $\kappa_{\text{crit}} = 0.4/\sqrt{A_0}$, where A_0 is the initial area of the grain, and τ is the normalized time. (From Ref. 57.)

strain) in the plane of the film during grain growth. The difference in *strain energy* between adjacent grains can also provide an additional driving force for abnormal grain growth (58).

To summarize, grain boundary drag and stagnation, coupled with variations in a volumetric energy term (surface, interface, and strain energy) lead to abnormal grain growth in thin polycrystalline films. A bimodal grain size distribution results from a restraining effect on most boundaries coupled with a volumetric energy term that favors the growth of a subpopulation of grains.

11.6.2 Dimensional and Morphological Stability

A factor that must be considered for thin films is their stability against shape changes, particularly those shape changes that tend to break up the continuous film into a group of islands. As an example, Fig. 11.39 shows the breakup of an Y_2O_3 -stabilized ZrO_2 film (8 mol% Y_2O_3) that was prepared by spin coating of mixed solutions of zirconium acetate and yttrium nitrate onto single-crystal Al_2O_3

substrates (59). After pyrolysis at 1000°C to decompose the metal salts, sintering at 1400°C produced nearly fully dense polycrystalline films, which on further heating started to break up into islands, thereby uncovering the substrate. This instability is driven by capillarity (surface tension) due to the thermodynamic requirement of minimization of the interfacial energy. A necessary condition is that the film–substrate interface has a higher specific energy than the substrate surface.

Films are stable against small perturbations but can become unstable against large-amplitude perturbations such as pinholes. Holes with radii smaller than a critical value shrink, whereas holes with radii larger than the critical value grow, eventually leading to the breakup of the film into islands with a size determined by the surface energies (60). A polycrystalline microstructure is particularly susceptible to breakup. Grain boundaries and three-grain junctions lead to the development of large perturbations that may eventually intersect the substrate and cause the film to break up into islands.

To see how these perturbations originate, we start with the well-known observation that a groove forms where the grain boundary intercepts the free surface, with the equilibrium angle at the root of the groove being the dihedral angle ψ given by $\cos(\psi/2) = \gamma_{gb}/2\gamma_{sv}$ (see Fig. 8.4). Assuming that the film consists of uniform grains with an initial size $G = 2R$ and thickness a and that the minimum energy surface shape is a spherical cap meeting the grain boundary at the equilibrium angle (Fig. 11.40), then the requirement that the film volume is conserved yields an equilibrium groove depth d , measured relative to the surface of the flat film, given by (52)

$$d = R \frac{2 - 3\cos\theta + \cos^3\theta}{3\sin^3\theta} \quad (11.49)$$

where $\theta = \pi/2 - \psi/2$. This result shows that the grain boundary groove will go to a finite depth after an infinite time of annealing. It is possible to determine the conditions under which the groove will intercept the substrate by putting $d \geq a$, giving

$$\frac{R}{a} \geq \frac{3\sin^3\theta}{2 - 3\cos\theta + \cos^3\theta} \quad (11.50)$$

The critical value of the grain radius to the film thickness $(R/a)_c$ above which the grain boundary groove intercepts the substrate is plotted in Fig. 11.41. The value of $(R/a)_c$ tends to infinity as θ goes to zero, so the grain boundary groove will never intercept the substrate for finite R and a . As θ goes to its maximum value of $\pi/2$, $(R/a)_c$ tends toward 3/2. In particular, for $\theta = 30^\circ$ (corresponding to $\psi = 120^\circ$), $(R/a)_c$ is on the order of 7. Thus, for grain sizes larger than the film

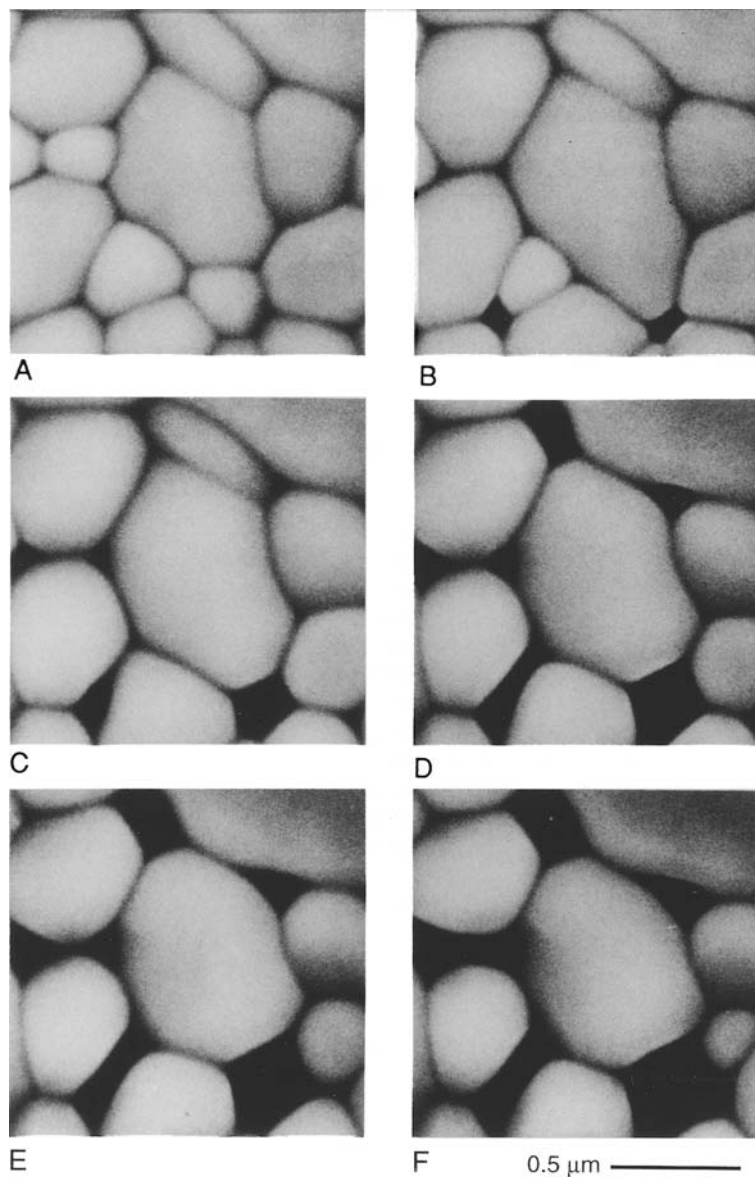


FIGURE 11.39 Microstructural evolution of a ZrO_2 (8 mol% Y_2O_3) thin film during heat treatment at 1400°C for the following times in hours: (A) 1, (B) 2, (C) 3, (D) 4, (E) 5 and (F) 6. (From Ref. 59.)

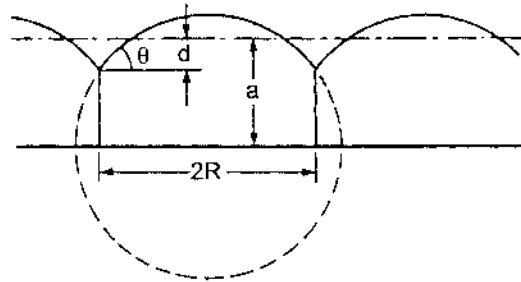


FIGURE 11.40 The equilibrium grain boundary groove configuration for a grains with a circular cross section. The shape of the surface is a spherical cap that intersects the grain boundary at an angle $\theta = 90^\circ - \pm \psi/2$, where ψ is the equilibrium dihedral angle. The grain diameter is $2R$, the film thickness is a , and the equilibrium groove depth, measured with respect to the flat film, is d . (From Ref. 60.)

thickness, grain boundary grooves can reach the substrate, resulting eventually in island formation.

Miller et al. (59) analyzed the breakup phenomena observed in Fig. 11.39 by considering the free energy changes associated with the spheroidization of the grains and the uncovering of the substrate. The total energy of the surfaces and interfaces can be expressed by

$$E = A_{sv}\gamma_{sv} + A_{gb}\gamma_{gb} + A_i\gamma_i + A_{sub}\gamma_{sub} \quad (11.51)$$

where A_{sv} is the solid–vapor interfacial area of the film, A_{gb} is the grain boundary area, A_i is the film–substrate interfacial area, A_{sub} is the substrate–vapor interfacial area, and γ_{sv} , γ_{gb} , γ_i , γ_{sub} are the corresponding interfacial energies. By evaluating E to determine its minimum value as a function of the configuration of the film, the most stable configuration can be found. The results of such calculations can be represented in terms of a diagram, referred to as an equilibrium configuration diagram, showing the minimum energy configuration for any desired values of G/a , ψ , and θ . As an example, the results of the minimum energy configuration are shown in Fig. 11.42 where G/a is plotted as a function of θ for $\psi = 120^\circ$. The diagram is divided into three regions, showing the conditions for the completely covered substrate, the uncovered substrate and the partially connected film (corresponding to the situation where the grain boundary just intercepts the substrate).

11.7 SOLID SOLUTION ADDITIVES AND THE SINTERING OF CERAMICS

As outlined in Chapter 9, the use of *solid solution additives* (also referred to as *dopants*) provides a very effective approach for the fabrication, by sintering, of

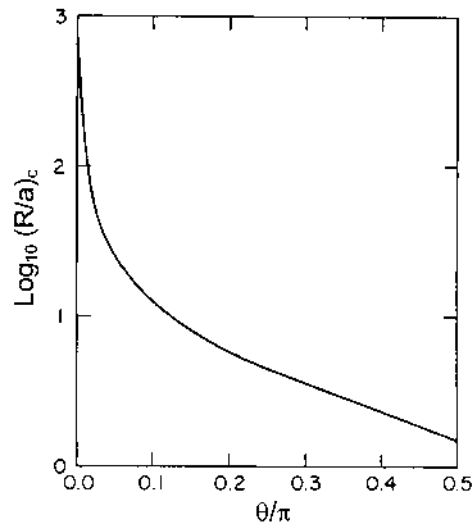


FIGURE 11.41 The critical ratio of the grain radius to the film thickness $(R/a)_c$, above which grain boundary grooving will lead to film rupture, versus the equilibrium groove angle θ . The parameters R , a , and θ are defined in Fig. 11.40. (From Ref. 60.)

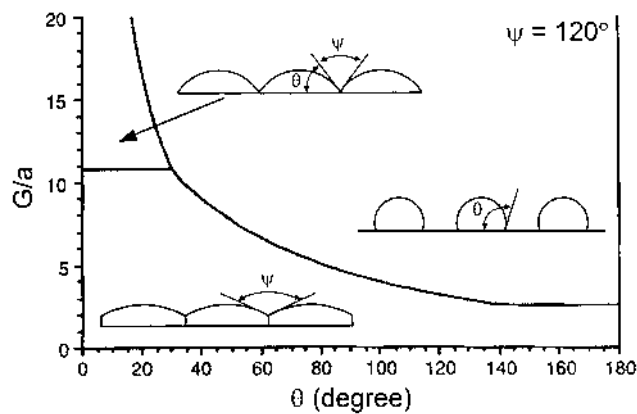


FIGURE 11.42 Two-dimensional equilibrium configuration diagram for the sintering of a thin film. The ratio of the grain diameter G to the film thickness a is plotted versus the contact angle θ for an equilibrium dihedral angle $\psi = 120^\circ$. (From Ref. 59.)

ceramics with high density and controlled grain size. The most celebrated example of this approach was reported by Coble (61), who showed in 1961 that small additions of MgO (0.25 wt%) to Al_2O_3 produced polycrystalline translucent alumina with theoretical density (Lucalox). Figure 11.43 illustrates the effect of the MgO additive. Since Coble's work, many examples of the effectiveness of the solid solution approach can be found in the ceramic literature (see Table 9.1 for a selected list).

A problem with the solid solution approach is that apart from a few recognized systems, the role of the dopant is not understood very well. The main reason for this gap in our understanding is that dopants can often display a variety of functions, which makes understanding of the dopant role difficult. As a result, the selection of additives has remained largely empirical. An additive can influence both the *kinetic* and *thermodynamic* factors in sintering. As discussed in Chapter 7, an additive can alter the defect chemistry of the host, thereby changing the diffusion coefficient for transport of ions through the lattice D_l . *Segregation* of the additive can alter the structure and composition of surfaces and interfaces, thereby altering the grain boundary diffusion coefficient D_{gb} , the surface diffusion coefficient D_s , and the diffusion coefficient for the vapor phase D_g (i.e., the evaporation/condensation process). Segregation can also alter the interfacial energies, so the additive can also act thermodynamically to change the surface energy γ_{sv} and the grain boundary energy γ_{gb} . Another consequence of segregation, as described in Chapter 9, is that the additive can alter the intrinsic grain boundary mobility, M_b .

In principle, an additive will influence each of these factors to a certain extent. In a general sense, an effective additive is one that alters many phenomena in a favorable way but few phenomena in an unfavorable one. Practically, it is commonly found that when a dopant is effective for sintering, its major role is the ability to significantly reduce M_b .

11.7.1 Effect of Additives on Kinetic Factors

Whereas an additive can alter each of the diffusion coefficients for matter transport (D_l , D_{gb} , D_s , and D_g), historically the major emphasis has been placed on the ability of the additive to alter D_l through its effect on the defect chemistry of the host. To determine how an additive will influence D_l , the defect chemistry of the host must be known. Specifically, we must know the nature of the rate-controlling species (anion or cation), the type of defect (vacancy or interstitial), and the state of charge of the defect. In practice, this information is known in only a very few cases. To illustrate the approach, let us consider Al_2O_3 , a system that has been widely studied. According to Kroger (62), the intrinsic defect structure consists of cationic Frenkel defects:



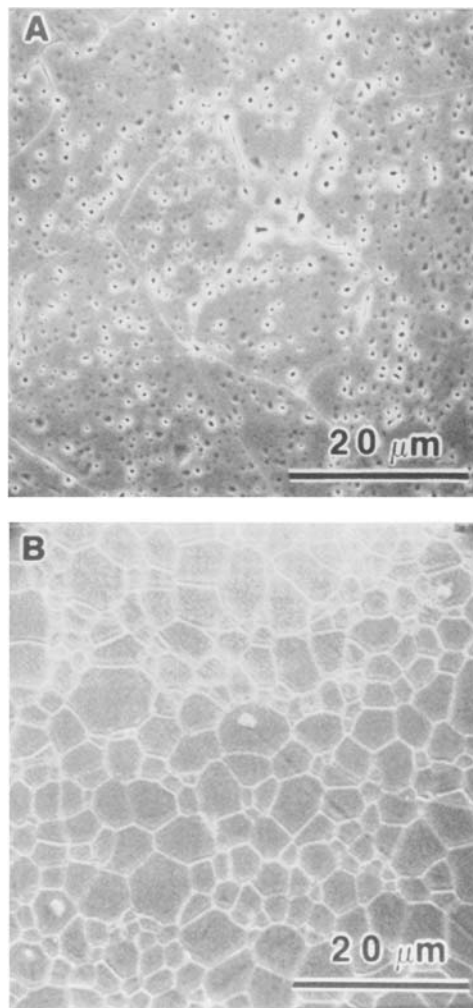
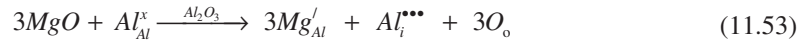


FIGURE 11.43 Microstructures of sintered Al_2O_3 . (A) undoped material showing pore-grain boundary separation and abnormal grain growth; (B) MgO-doped material showing high density and equiaxial grain structure. (From Ref. 81.)

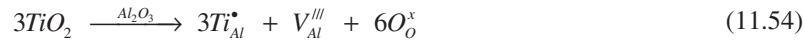
It has also been suggested that the diffusion of aluminum ions control the rate of densification, with the faster diffusion of oxygen ions occurring along the grain boundary. Based on Eq. (11.52), we may assume that the rate-controlling process is the diffusion of triply charged aluminum interstitial ions. A possible defect reaction for the incorporation of MgO into the Al_2O_3 lattice is



According to this equation, the effect of MgO would be to increase the densification rate through an increase in the concentration of aluminum interstitial ions.

Let us now consider an alternative situation, by supposing that the densification rate is controlled by the diffusion of triply-charged aluminum vacancies. In this case, the creation of aluminum interstitials by Eq. (11.53) leads to a reduction in the concentration of aluminum vacancies by Eq. (11.52) and a corresponding reduction in the densification rate.

If instead of MgO we use TiO_2 as a dopant, a possible defect reaction for the incorporation into Al_2O_3 is



According to this equation, if the rate-controlling process is the diffusion of aluminum vacancies, the addition of TiO_2 would increase the densification rate through an increase in the aluminum vacancy concentration.

As this example of Al_2O_3 shows, if we know the intrinsic defect structure of the host, it is possible to select dopants to increase D_l . However, this single factor of an increase in D_l is insufficient to guarantee an effective additive. There are cases, such as TiO_2 -doped Al_2O_3 , where the dopant produces an increase in D_l but the attainment of theoretical density is not realized. Other possible functions of the additive must be examined.

An additive can also act favorably to *decrease* the surface diffusion coefficient D_s , but this by itself is also insufficient to guarantee the achievement of theoretical density. The reason why we require a decrease (rather than an increase) in D_s can be argued as follows: A decrease in D_s reduces the rate of coarsening, thereby increasing the densification rate. Therefore, the pore size r will be smaller at any given stage of microstructural development (e.g., grain size). Because of its strong dependence on r [see Eq. (9.81)], the pore mobility M_p increases considerably and prevents separation of the pores from the boundary, so abnormal grain growth is eliminated. The diffusion distance for matter transport into the pores is kept small, thereby improving the probability of achieving high density.

11.7.2 Effect of Additives on Thermodynamic Factors

The effects of dopants on γ_{sv} and γ_{gb} have been investigated in only a few instances. In one of the most detailed studies, Handwerker et al. (63) measured

the effect of MgO doping on the distribution of dihedral angles in Al_2O_3 from grain boundary grooves on polished and thermally etched samples. We recall that the dihedral angle provides a measure of the ratio γ_{gb}/γ_{sv} . As Fig. 11.44 shows, the MgO dopant reduces the width of the distribution without significantly affecting the mean value (117°). The reduction in the spread of the dihedral angles can be interpreted qualitatively to mean that local variations in the driving force for sintering and coarsening are reduced, so a more homogeneous microstructure is favored. An improvement in the microstructural homogeneity, we will recall, favors the attainment of a higher density at a given stage of microstructural development and reduces the possibility of initiating abnormal grain growth. The dihedral angle results therefore indicate that a function of MgO dopant in Al_2O_3 is to reduce the consequences of microstructural inhomogeneity.

11.7.3 Segregation of Additives

The solute drag mechanism proposed by Cahn (64) was discussed in Chapter 9 as an important approach for reducing the intrinsic grain boundary mobility M_b , and it was recognized that the effectiveness of the method depends critically on the ability of the solute to segregate at the grain boundaries. An extensive review of grain boundary segregation in ceramics was published in 1974 by Kingery (65). The major driving forces leading to segregation of an

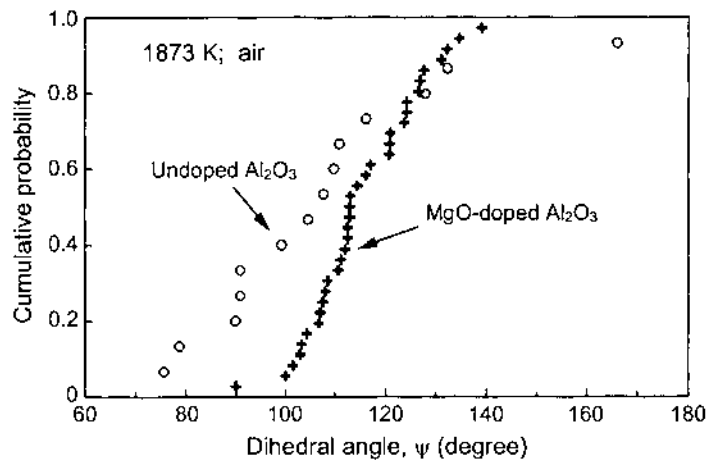


FIGURE 11.44 Cumulative distribution of dihedral angles in undoped Al_2O_3 and MgO-doped Al_2O_3 . (From Ref. 63.)

equilibrium concentration of solute at the grain boundaries in ceramics are the reduction in the *elastic strain energy* due to a difference in size between the solute and the host atom for which it substitutes and the *electrostatic potential* of interaction between aliovalent solutes and charged grain boundaries. Segregation driven by elastic strain energy is limited to the *core* of the grain boundary, typically to a width of <1 nm. In contrast, for segregation driven by the electrostatic interaction, a compensating *space charge layer* adjacent to the charged grain boundaries produces a greater width of segregation (typically 1 to a few tens of nanometers). Coupling of the elastic strain and electrostatic effects as well as dipolar effects can also influence segregation (66).

Elastic Strain Energy

When the radius of the solute ion a_s is different from that of the host a , substitution leads to a misfit in the lattice Δa defined by

$$\frac{\Delta a}{a} = \frac{a_s - a}{a} \quad (11.55)$$

The misfit produces an increase in the elastic strain energy of the lattice given by (67):

$$U_o = \frac{6\pi a^3 B_s (\Delta a / a)^2}{1 + 3B_s / 4\mu_h} \quad (11.56)$$

where B_s is the bulk modulus of the solute and μ_h is the shear modulus of the host crystal. According to this equation, the strain energy is proportional to the square of the misfit. Appendix D provides a list of ionic radii that can be used to estimate the misfit.

If the grain boundary is regarded as a thin region of disorder between the crystalline grains, it may be expected that there will be some fraction of sites at the boundary where the energy associated with the addition of solute ions is small. Segregation of the solute ions to the grain boundary region therefore provides partial relaxation of the elastic strain energy in the lattice of the grains. We may expect that the extent of segregation would depend on the difference in energy $\Delta G_a = E_l - E_b$ for the solute at the boundary E_b and in the lattice, E_l . It is evident that segregation is increasingly favored for larger values of ΔG_a since this represents a greater reduction in the free energy of the system. Furthermore, ΔG_a will have some spatial dependence because the structural disorder varies with distance from the center of the boundary. Details of the spatial dependence are not clear, but it is not believed to extend more than a few lattice spacings from the center of the boundary.

McLean (68) showed that the segregated solute concentration at the grain boundary C_{gb} is related to the solute concentration in the lattice C_o by:

$$C_{gb} = C_o \exp\left(\frac{\Delta G_a}{RT}\right) \quad (11.57)$$

where R is the gas constant and T is the temperature. By annealing Al_2O_3 samples at several temperatures, quenching the samples and using Auger electron spectroscopy to measure the Ca content at the grain boundaries, Johnson (69) found that Eq. (11.57) provided a good description of Ca segregation in Al_2O_3 when $\Delta G_a \approx 117$ kJ/mol. A simple model in which ΔG_a is assumed to be proportional to U_o , and hence to $(\Delta a/a)^2$, provides a qualitative description of the segregation of isovalent solutes.

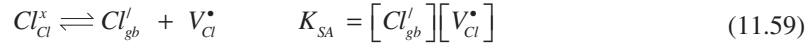
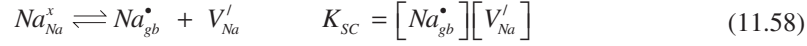
Electrostatic Interaction and the Space Charge Concept

Since Frenkel (70) first proposed that a *surface charge* and a compensating *space charge* could develop in ionic crystals in which the formation energy for cation defects differs from that for anion defects, the results have been generalized to include the charge distribution at other lattice discontinuities such as *grain boundaries* and *dislocations* (71–73). We can see how this charge (or potential) develops by considering the formation of a Schottky defect in an ionic solid such as NaCl (see Fig. 7.3). The energy of formation of a Schottky defect can be separated into energies of formation of the individual cation and anion vacancy, defined as the energy required to bring the ion to the lattice discontinuity (e.g., the grain boundary). For example, we can express this as $g_s = g_{vNa} + g_{vCl}$ for the case of NaCl. The energy of formation of the cation defect is likely to be different from that for the anion defect, and on heating, this will determine the defect concentration at the grain boundary.

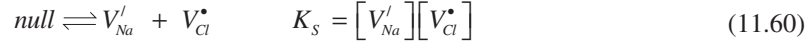
On the other hand, the bulk of the crystal must be electrically neutral, and the defect concentration is determined by the principle of electroneutrality. Thus differences in the formation energies of the individual defects cause the defect concentration at the grain boundary to be different from that in the bulk. The grain boundary can carry a net charge, and to retain electroneutrality of the system, this net charge is balanced by an adjacent *space charge* layer that decays with distance typically on the order of up to a few tens of nanometers. At equilibrium, there exists an electrical potential difference between the grain boundary and the bulk, and its interaction with charged solute ions can cause segregation at the grain boundary.

To get an idea of the variation of the potential and defect concentration in the space charge layer, let us consider NaCl, for which such effects have been examined in some detail (65). In the simplest formulation, it is assumed that the grain boundaries act as perfect sources and sinks for vacancies so that vacancies

can be readily created or destroyed. If Schottky defects dominate, then the equilibration of the cation and anion with the grain boundary can be represented by the following defect reactions:



If the ions transported to the grain boundary are assumed to simply extend the perfect lattice, then the Schottky reaction is recovered:



In NaCl, g_{vNa} is estimated to be one half g_{vCl} , so the grain boundary is enriched in the cation $[Na_{gb}^{\bullet}]$ and, through the Schottky equilibrium [Eq. (11.60)], is depleted in $[Cl_{gb}']$ at the same time. The grain boundary has a positive charge due to the excess cations, and this is compensated by a space charge that has an excess negative charge. The variation of the electrical potential and the defect concentration is summarized in Fig. 11.45a. The defect concentration varies with distance in the space charge layer according to the spatially varying potential $V(x)$ and is given by

$$[V_{Na}'] = \exp\left(\frac{-g_{vNa} + eV(x)}{kT}\right) \quad (11.61)$$

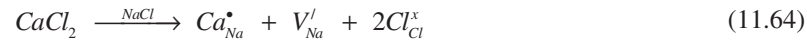
$$[V_{Cl}^{\bullet}] = \exp\left(\frac{-g_{vCl} - eV(x)}{kT}\right) \quad (11.62)$$

where e is the electronic charge, k is the Boltzmann constant, and T is the absolute temperature. It has been estimated that $g_{vNa} = 0.65$ eV and $g_{vCl} = 1.21$ eV, and since the electroneutrality condition $[V_{Na}'] = [V_{Cl}^{\bullet}]$ holds far from the grain boundary, from Eqs. (11.61) and (11.62) it is found that the electrostatic potential between the grain boundary and the bulk of the crystal is

$$V_{\infty} = \frac{1}{2e}(g_{vNa} - g_{vCl}) = -0.28V \quad (11.63)$$

This estimate shows that the potential is not trivial in magnitude.

The space charge potential changes when the bulk concentrations of the defects are altered by solutes or nonstoichiometry. Taking the case where an aliovalent dopant such as $CaCl_2$ is present in NaCl, the defect reaction for the incorporation of the dopant can be written



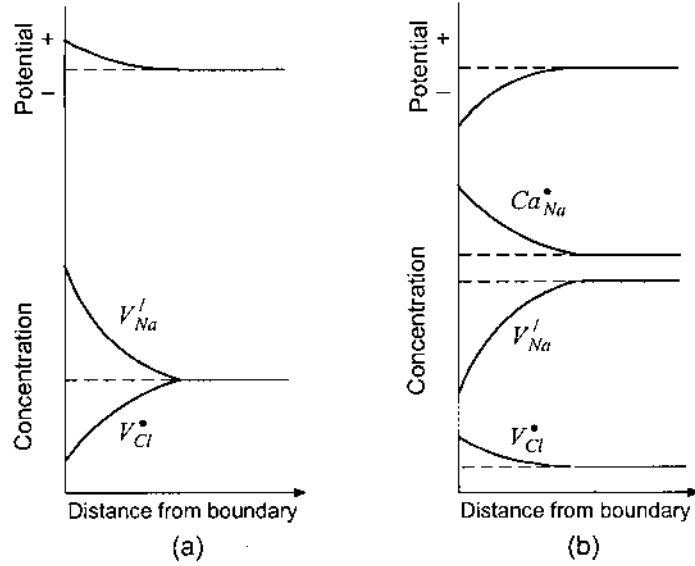


FIGURE 11.45 Schematic variations of the electrostatic potential and defect concentration as a function of distance from the grain boundary for (a) undoped NaCl and (b) NaCl doped with CaCl_2 .

Additional cation vacancies are generated in the bulk of the lattice and on equilibration, this leads to a reduction in the concentration of the Na^+ ions at the grain boundary, resulting in an excess of Cl^- at the boundary. We recall from Chapter 7 that the defect concentrations produced by impurities and dopants are normally much larger than those for intrinsic defects, so the overall effect is a reversal in the sign of the electrostatic potential. The resulting negative electrostatic potential of the boundary will cause the Ca ion with the positive effective charge to segregate at the grain boundary as a space charge to maintain the electroneutrality of the bulk of the crystal. The variation of the electrostatic potential and the defect concentration for Ca-doped NaCl are summarized in Fig. 11.45b. The cation vacancy concentration still varies according to Eq. (11.61), and far from the boundary, it can be written as

$$[V_{\text{Na}}^I] = [Ca_{\text{Na}}^{\bullet}] = \exp\left(\frac{-g_{V_{\text{Na}}} + eV_{\infty}}{kT}\right) \quad (11.65)$$

so the potential difference between the grain boundary and the bulk is given by

$$V_{\infty} = \frac{1}{e} \left(g_{V_{Na}} + kT \ln [Ca_{Na}^{\bullet}] \right) \quad (11.66)$$

This voltage is positive for reasonable values of the dopant cation concentration.

Using a similar argument, it can be shown that the addition of extrinsic chlorine vacancies to the lattice will result in a reduction of anions from the grain boundary, giving rise to a larger negative potential V_{∞} than for the intrinsic case. Thus, at a given temperature, the potential can vary from negative to positive depending on the defect concentration. At some defect concentration, the potential is zero, and this point is referred to as the *isoelectric point*, which is analogous to the isoelectric point discussed in Chapter 4 for colloidal suspensions. The isoelectric point depends on the defect concentration as well the temperature, as can be deduced from Eq. (11.66) for NaCl. The existence of the isoelectric point has been confirmed by direct observation of the migration of low-angle grain boundaries in NaCl bicrystals maintained in an electric field (74). The results in Fig. 11.46 for NaCl bicrystals with a bulk impurity content of ~ 2 ppm show that the boundary migration is reversed in experiments at 600°C and at 640°C, indicating an isoelectric point between these two temperatures.

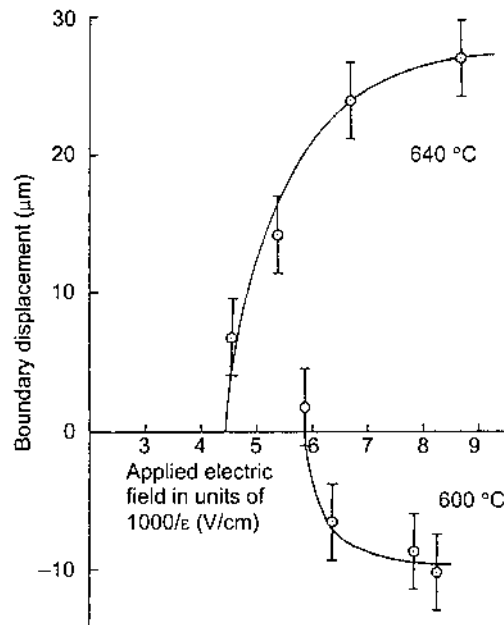


FIGURE 11.46 Migration of pure tilt low-angle grain boundary in NaCl as a function of applied electric field. The change in the direction of motion between 600°C and 640°C reflects a change in the sign of the boundary electrical potential. (From Ref. 74.)

In oxides, there are observations that appear to support the space charge concept in several systems, including Al_2O_3 (75), MgO (76), ZrO_2 (77), TiO_2 (78a,b), BaTiO_3 (79), and MgAl_2O_4 (80). The effects are particularly clear in the case of TiO_2 . A detailed study of the solute segregation indicates that the electrostatic potential at the grain boundary (and, hence, the segregation of aliovalent solutes) depends on the doping level, the temperature, and the oxygen partial pressure. As illustrated in Fig. 11.47, for TiO_2 doped simultaneously with an acceptor (Al) and a donor (Nb), the Al-rich samples show Al segregation and Nb depletion, consistent with a positive boundary and a negative space charge layer (negative V_∞). On the other hand, Nb-rich samples show Nb segregation and Al depletion. No detectable segregation or depletion is found for a slightly Nb-rich sample (Fig. 11.47B), and this composition appears to be near the isoelectric point at 1350°C . Above this temperature, Al segregation was observed whereas below this temperature, Nb segregation was observed. Determination of the potential difference V_∞ between the grain boundary and the bulk (Fig. 11.48) indicates that the isoelectric point is slightly to the donor-doped side. This is because TiO_2 is somewhat nonstoichiometric, and at high temperatures there is sufficient intrinsic reduction even in oxidizing atmospheres, that some donor doping is required to compensate for the defects introduced by reduction.

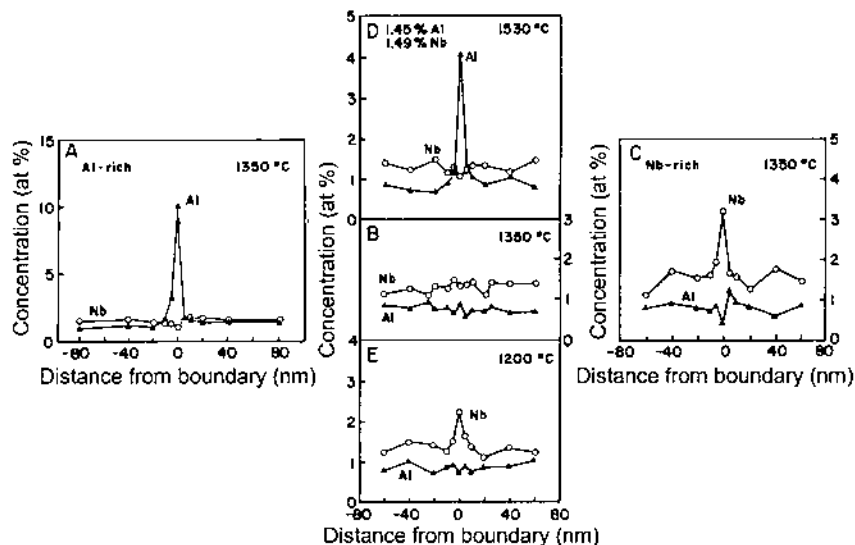


FIGURE 11.47 Scanning transmission electron microscope measurements of the solute distribution across grain boundaries in TiO_2 doped simultaneously with varying concentrations of Al and Nb. (B) represents a sample very close to the isoelectric point. (From Ref. 78a,b.)

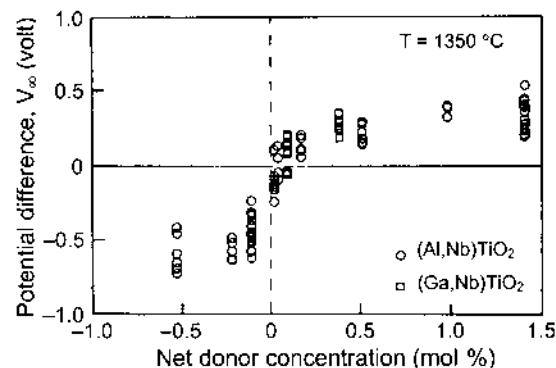


FIGURE 11.48 Potential difference V_∞ between the grain boundary and the bulk in TiO_2 . (From Ref. 78a,b.)

11.7.4 The Role of MgO in Al_2O_3

Since the work of Coble in 1961, the MgO -doped Al_2O_3 system has represented one of the most celebrated examples of the effectiveness of the solid solution approach to microstructure control. Whereas the dramatic effect of MgO on the sintered microstructure of Al_2O_3 was easily reproduced (see Fig. 11.43), understanding the *mechanism* by which MgO acts proved to be more difficult despite numerous investigations. One of the main obstacles in the earlier work has been the use of powders containing impurities that have tended to mask the true effect of MgO . However, as described in a thorough review by Bennison and Harmer (81), the dopant role in this system is now fairly well understood, at least at a phenomenological level.

The specific mechanisms by which MgO has been suggested to act are as follows:

1. MgO reacts with Al_2O_3 to form fine second phase particles of MgAl_2O_4 , due to an excess of MgO above the solid solution limit, which pin the boundaries by a Zener-type mechanism and prevent abnormal grain growth.
2. MgO in solid solution segregates at the grain boundaries and reduces the boundary mobility by a solute-drag mechanism, thereby preventing abnormal grain growth because the pores can remain attached to the boundary.
3. MgO in solid solution enhances the densification rate through an increase in the lattice diffusion coefficient for Al ions that are believed to be the rate-controlling diffusing species [see, Eq. (11.53)]. (The

oxygen ions are assumed to diffuse more rapidly along the grain boundaries.) The faster densification allows the achievement of full density prior to the onset of abnormal grain growth.

4. MgO lowers the dihedral angle by changing the relative values of the grain boundary energy and the surface energy. For a pore of constant volume, the reduction in the dihedral angle causes a greater area of the boundary to be intersected by the pore (see Fig. 8.28), so the drag force on the boundary is enhanced.
5. MgO enhances the rate of surface diffusion in Al_2O_3 , thereby enhancing the pore mobility through its dependence on the surface diffusion coefficient [see Eq. (9.81)], allowing the pores to migrate with the boundary and avoiding abnormal grain growth.

In a classic experiment, Johnson and Coble (82) proved that mechanism 1 was not necessary for the achievement of theoretical density, so this mechanism can be ruled out. In the experiment, an undoped Al_2O_3 powder compact was sintered in close proximity to a pre-equilibrated two-phase mixture of MgAl_2O_4 spinel and Al_2O_3 . The experiment was designed to allow transfer of MgO from the spinel/alumina compact to the undoped Al_2O_3 compact in concentrations below the solid solubility limit. It produced an Al_2O_3 pellet with a fully dense, fine-grained, MgO-doped outer surface and a core devoid of MgO, consisting of abnormal grains and entrapped porosity. Mechanism 5 by itself cannot lead to an enhancement of densification. An increase in the surface diffusion coefficient leads to enhanced coarsening of the microstructure (increase in the pore size and grain size), so the pore mobility and the densification rate actually decrease at any given density.

The current understanding is that MgO additions affect *all* the key parameters controlling the sintering of Al_2O_3 to some extent (i.e., D_l , D_{gb} , D_s , γ_{gb}/γ_{sv} , and M_b), so mechanisms 2 to 5 are all influenced to some degree (83a,b). The extent to which Al_2O_3 responds to MgO doping appears to depend on the concentration and composition of the background impurities in the powder. Surface diffusion appears to increase slightly, while lattice diffusion or grain boundary diffusion can be increased or decreased slightly. However, the single most important effect of MgO doping is the ability to significantly reduce the grain boundary mobility through a solute drag mechanism (i.e., mechanism 2). The consequence of this significantly reduced mobility is a reduced tendency for abnormal grain growth to occur (see Fig. 9.50).

The important role of MgO as a *microstructural homogenizer* to reduce anisotropies in the surface and grain boundary energies and mobilities and to stabilize the microstructure against the consequences of inhomogeneous densification has also been recognized. As described earlier (see Sec. 11.7.2), the effect of MgO in narrowing the distribution of dihedral angles without significantly

altering the mean value in Al_2O_3 can be interpreted as effectively reducing local variations in the driving force for sintering and grain growth, thereby promoting a more uniform development of the microstructure.

Baik et al. (84a–c) studied the segregation of Ca and Mg at free surfaces of sapphire (single-crystal Al_2O_3) and at the grain boundaries of polycrystalline Al_2O_3 . Strong Mg segregation occurs at several surfaces of sapphire, but the segregation of Ca is strongly dependent on the surface orientation. In the experiments with polycrystalline Al_2O_3 , powder compacts were doped with controlled amounts of CaO (100 ppm) or MgO (300 ppm) or with a combination of CaO (100 ppm) and MgO (300 ppm). With CaO alone, segregation is *anisotropic*, with only some grain boundaries enriched with a high concentration of Ca. On the other hand, for the sample doped with both CaO and MgO, the distribution of the Ca in the grain boundaries is more homogeneous. Assuming that MgO segregation at grain boundaries is as effective as that observed at the surfaces of sapphire, these observations may explain the effectiveness of MgO (solute drag mechanism) and the ineffectiveness of CaO (anisotropic segregation) as a grain growth inhibitor in Al_2O_3 .

Variations in the packing density of the green body, we will recall, give rise to differential densification in which the densely-packed regions undergo local densification, resulting in the development of dense, pore-free regions in an otherwise porous microstructure. These dense regions are better able to support grain growth and commonly form the sites for the initiation of abnormal grain growth. Consistent with its ability to reduce the grain boundary mobility in Al_2O_3 , MgO is found to suppress grain growth within the dense regions, thus allowing the porous regions to densify without the occurrence of abnormal grain growth (85,86). The role of MgO can be interpreted as stabilizing the microstructure against the consequences of inhomogeneous densification.

Another feature related to microstructural homogenization is the sintering of Al_2O_3 in the presence of a small amount of liquid phase. Many Al_2O_3 powders contain small amounts of SiO_2 and other impurities that form a silicate liquid phase, leading to the growth of anisotropic (faceted) abnormal grains (see Sec. 9.6). MgO additions suppress the development of such abnormal grains and produce more uniform microstructures (Fig. 11.49). Kaysser et al. (87) performed experiments in which controlled amounts of anorthite glass was added to Al_2O_3 powders containing a small amount of SiO_2 impurity and large sapphire spheres were included to seed abnormal grain growth. Rapid growth of anisotropic grains occurs for the undoped Al_2O_3 and any anisotropy of the seed crystal is hard to detect. With 0.1 wt% MgO, the matrix grains are fine and equiaxial in shape whereas the seed crystal grows abnormally but in an isotropic manner. With 0.9 wt% anorthite, the seed crystal grows abnormally with faceting along the basal planes and the addition of 0.1 wt% MgO is unable to suppress the faceting. The

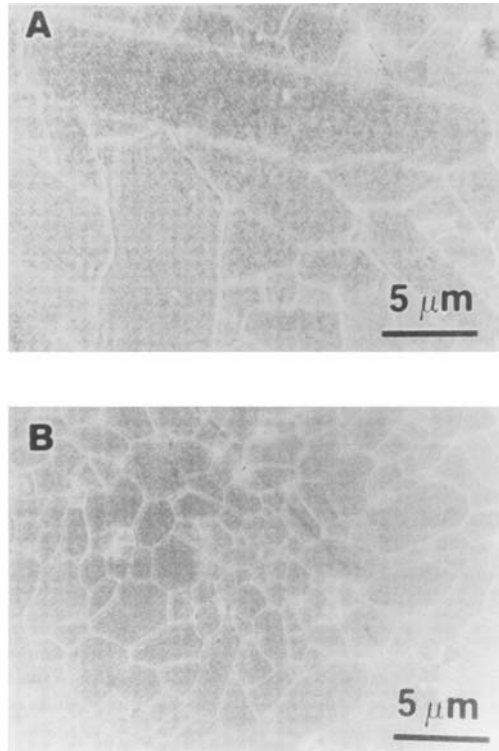


FIGURE 11.49 Microstructures of (A) dense undoped Al_2O_3 and (B) dense MgO-doped Al_2O_3 . Note the MgO addition leads to a more uniform grain structure and a smaller grain size. (From Ref. 81)

results indicate that abnormal grain growth in systems containing a liquid can be caused by anisotropic growth of boundaries containing intergranular liquid films.

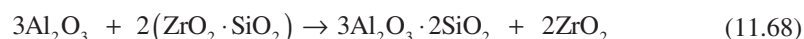
11.8 SINTERING WITH CHEMICAL REACTION: REACTION SINTERING

Reaction sintering, sometimes referred to as *reactive sintering*, is a particular type of sintering process in which the chemical reaction of the starting materials and the densification of the powder compact are both achieved in a single heat treatment step. These systems can be divided into two main classes depending on whether single-phase solids or composites are produced. For a powder compact consisting of a mixture of two reactant powders, the simplest example of reaction

sintering is shown in Eq. (11.67) and Fig. 11.50a. During sintering, reaction between two starting powders A (e.g., ZnO) and B (e.g., Fe₂O₃) and densification occur to produce a polycrystalline, *single-phase* solid C (e.g., ZnFe₂O₄):



A more complex example of reaction sintering is shown in Eq. (11.68) and Fig. 11.50b. Reaction between two starting powders D (e.g., Al₂O₃) and E (e.g., zircon, ZrSiO₄) and densification occur to produce a *composite* solid consisting of two phases F (mullite, 3Al₂O₃·2SiO₂) and G (ZrO₂):



A variation of this second class of reaction sintering system is obtained when one of the product phases, G, say, is a liquid. This occurs when the sintering temperature is above the eutectic temperature and corresponds to the process of *liquid phase sintering* discussed in detail in Chapter 10. Here, we will confine our discussion of reaction sintering mainly to systems in which the products are solids at the sintering temperature.

The energy changes for chemical reaction are much larger than those for surface area changes, (see Chapter 7) and it would be very desirable if the free energy of the reaction could be used to drive the densification process. Unfortunately, there is no evidence that the energy of the reaction can act directly as a driving force for densification. Reaction sintering has the benefit of eliminating the pre-reaction (or calcination) step in the formation of solids with complex

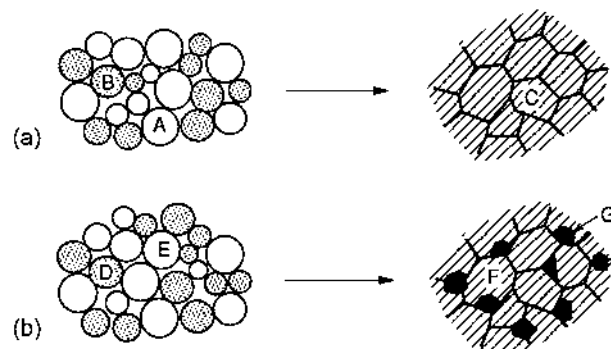


FIGURE 11.50 Schematic diagram illustrating the production of (a) a single-phase solid, C, by reaction sintering of a compacted mixture of two powders, A and B; (b) a composite solid, consisting of a matrix, F, and inclusions, G, by reaction sintering of a compacted mixture of two powders, D and E.

composition. Taking ZnFe_2O_4 as an example, the conventional route for producing a dense polycrystalline solid involves calcinations of a loose mixture of ZnO and Fe_2O_3 powders to form a single-phase ZnFe_2O_4 powder, milling the calcined powder to break down agglomerates, followed by powder compaction and sintering. In reaction sintering, the reaction and densification occurs in the same heating cycle, so the calcination and subsequent milling steps in the conventional route are eliminated.

In practice, reaction sintering has several shortcomings, so the process finds little use in the production of single-phase solids. As outlined earlier, the reactions involve energy changes that are considerably larger than the changes in surface energies, and as a result, they can lead to microstructures that inhibit densification. An example of such a microstructure is shown in Fig. 11.51 for the $\text{CaO-Al}_2\text{O}_3$ system (88). Other shortcomings include the risk of chemically inhomogeneous products due to incomplete reaction and difficulties in controlling the microstructure as a result of the added complexity introduced by the reaction.

11.8.1 Influence of Process Variables

Depending on the processing conditions such as particle size, temperature, heating rate, and applied pressure, reaction and densification can occur in sequence or concurrently or in some combination of the two. Qualitatively, it is convenient to consider the reaction and the densification as two separate processes and to develop principles that allow predictions of the influence of key process variables which are useful for the design of reaction sintering processes (89,90).

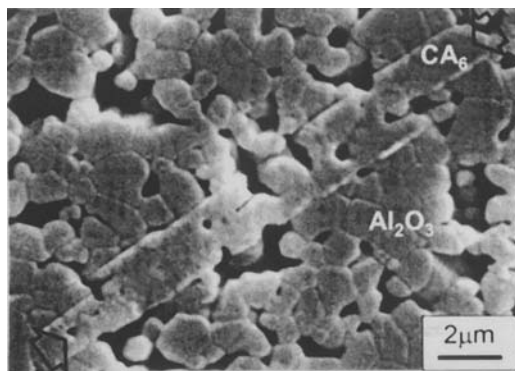


FIGURE 11.51 Scanning electron micrograph of calcium hexa-aluminate (CA_6 arrowed) formed during the densification of Al_2O_3 powder mixed with 5 wt% CaO powder, after 20 h at 1330°C . The plate-shape CA_6 phase replicates the porous Al_2O_3 matrix during solid-state reaction/grain growth and inhibits densification. (From Ref. 88.)

Particle Size of Reacting Powders

Herring's scaling laws predict the effect of particle size on the rate of matter transport during sintering (Chapter 8). The densification rate varies with particle (or grain) size G according to $1/G^4$ for grain boundary diffusion and $1/G^3$ for lattice diffusion. For the reaction, if the product forms coherently on the surface of the particles [see Fig. 2.10 and Eq. (2.16)], the reaction rate varies as $1/G^2$, but if the product does not form coherently, then the rate is expected to vary as $1/G$. Both the densification rate and the reaction rate increase with decreasing particle size (Fig. 11.52), but because of the stronger size dependence, the densification mechanism is more strongly influenced than the reaction mechanism. A reduction in the particle size increases the densification rate relative to the reaction rate.

Sintering Temperature

While densification and reaction will most likely occur by different mechanisms, they both involve diffusion and are therefore expected to be thermally activated, so the rates have an Arrhenius dependence on temperature. The dependence of the densification rate and the reaction rate on temperature is sketched in Fig. 11.53, where it is assumed that the activation energy for densification is greater than that for the reaction. In this case, increasing the temperature leads to an increase in the densification rate relative to the reaction rate.

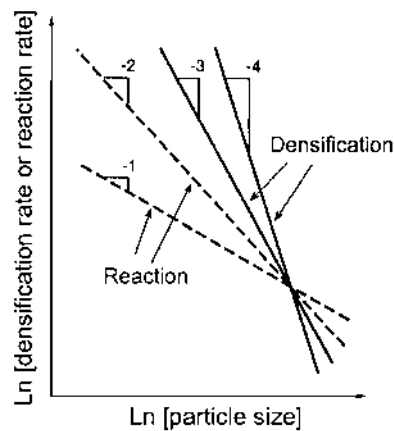


FIGURE 11.52 Predicted effect of particle size on the rates of densification and reaction during reaction sintering of a powder mixture. Smaller particle size enhances the rate of densification relative to the rate of reaction. (From Ref. 90.)

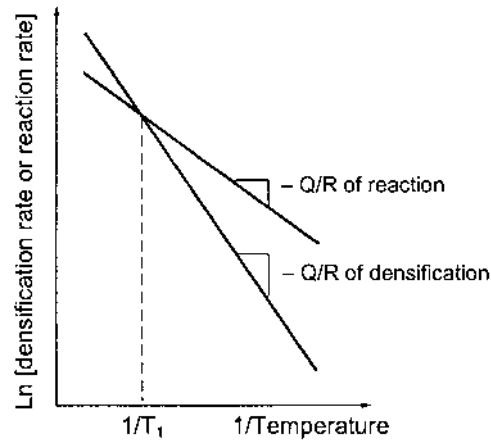


FIGURE 11.53 Predicted effect of sintering temperature on the rates of densification and reaction during reaction sintering of a powder mixture when the activation energy for densification is greater than that for the reaction. Higher sintering temperature enhances the densification rate relative to the reaction rate. (From Ref. 90.)

Applied Pressure

The application of an external pressure p_a increases the driving force for densification (Chapter 8). The effect of applied pressure on the reaction rate is difficult to predict, but because of the strong effect on the densification process, the role of applied pressure is likely to lie in its ability to accelerate the densification process, rather than in any effect on the reaction. In practice, hot pressing provides one of the surest ways to adjust the relative rates of densification and reaction in the desired direction.

Processing Trajectories in Reaction Sintering

Three different trajectories in reaction sintering are sketched in Fig. 11.54, depending on the relative rates of densification and reaction. When the reaction rate is much faster than the densification rate (curve A), the reaction occurs predominantly before any significant densification, and thus, densification must be achieved for a microstructure consisting of the fully reacted powder. Curve C shows the trajectory when the reaction rate is much slower than the densification rate, and in this case, densification occurs without any significant reaction, so the reaction process must be carried out in a fully dense microstructure. Curve B represents the trajectory for a system where the reaction rate is comparable to the densification rate.

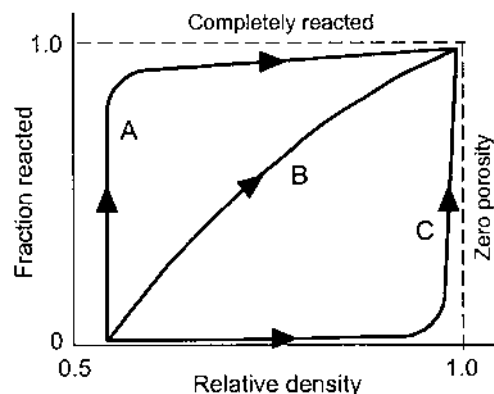


FIGURE 11.54 Sketch showing three different processing trajectories in reaction sintering. Curve A is the trajectory for a system in which the reaction rate is much faster than the densification rate; curve B is for a system where the reaction rate and densification rate are of roughly the same magnitude; for the system following trajectory C, the densification rate is much faster than the reaction rate. (From Ref. 90.)

The conceptual arguments for the effect of the process variables lead to the conclusion that the best trajectory for reaction sintering is one where densification is completed before the reaction can significantly interfere with the microstructural development (Curve C), assuming that there is no deleterious differences in molar volumes between the reactants and the product. However, it is often not possible to achieve this processing trajectory simply by reducing the particle size or optimizing the sintering temperature.

11.8.2 Experimental Observations of Reaction Sintering

Systems in which two simple oxides react to form a complex oxide are useful models for investigating the production of *single-phase ceramics* by reaction sintering because of the available data on the reaction mechanisms (91) and the relative simplicity of the reactants and product. Two examples are the formation of zinc ferrite by Eq. (11.67) and the formation of zinc aluminate spinel by the reaction between ZnO and Al₂O₃ powders,



These two systems have important similarities and differences and serve to illustrate the importance of the reaction process on the densification and microstruc-

tural evolution. For both systems, the molar volume of the reactants is almost equal to that of the product. The reaction is rapid, being completed prior to any significant densification, so the processing trajectory follows curve A (Fig. 11.54) instead of the more favorable curve C.

The observed reaction sintering results for these two systems show significant differences. For the ZnO-Fe₂O₃ system (92), the reaction produces little change in the volume of the powder compact. Despite the less favorable processing trajectory, high final densities (> 95% of the theoretical) are achieved, which are comparable to the final densities achieved in the sintering of single-phase ZnFe₂O₄ powder compacts (Fig. 11.55). For the ZnO-Al₂O₃ system, the compact expands by 25–30 vol% during the reaction (Fig. 11.56), and densification is significantly lower than that for a single-phase ZnAl₂O₄ powder compact (93).

The origins of the significantly different sintering behavior observed for the ZnO-Fe₂O₃ and ZnO-Al₂O₃ systems appear to reside in the microstructural changes produced as a result of the reaction process. These microstructural changes may, in turn, be related to the different reaction *mechanisms* in the two systems. At temperatures used in sintering, the reaction between ZnO and Fe₂O₃ occurs by a Wagner counter-diffusion mechanism where the cations migrate in opposite directions and the oxygen ions remain essentially stationary. The product is expected to form on both the ZnO and the Fe₂O₃ particles, causing little disruption of the particle packing, so the subsequent densification is not significantly affected. The reaction between ZnO and Al₂O₃ is not as clear but is believed to

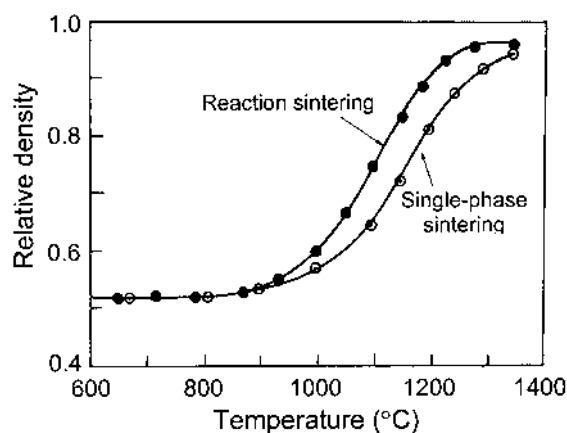


FIGURE 11.55 Relative density versus temperature for the reaction sintering of ZnO-Fe₂O₃ powder mixtures and for the sintering of a single phase ZnFe₂O₄ powder. The samples were heated at a constant rate of 5°C/min. (From Ref. 92.)

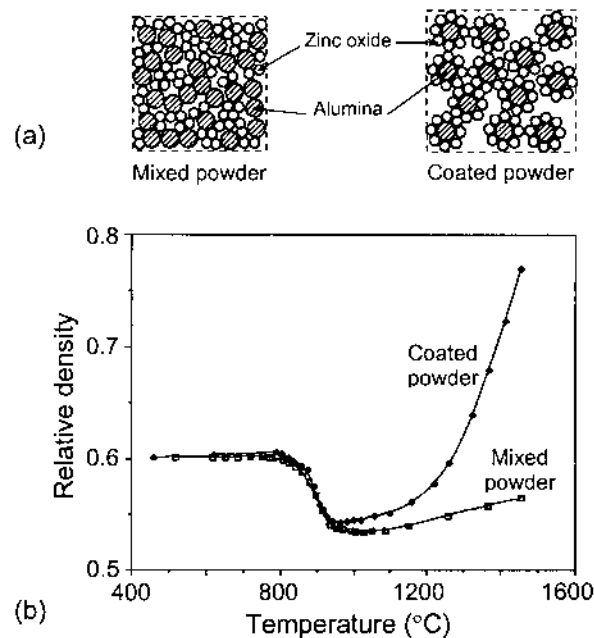


FIGURE 11.56 Effect of reactant powder distribution on densification during reaction sintering of ZnO–Al₂O₃ powders. (a) Sketch illustrating the distribution (cross-sectional view) of the ZnO and Al₂O₃ powders in compacts formed from mechanically mixed powders and from coated powders; (b) sintering data showing significantly enhanced densification for the coated powders. (From Ref. 93.)

occur by a solid-state mechanism in which the one-way diffusion of Zn²⁺ ions through the ZnAl₂O₄ product layer is rate controlling or by a gas-solid reaction between ZnO vapor and Al₂O₃ (91). In either case, the product is expected to form predominantly on the percolating network of original Al₂O₃ particles which inhibits subsequent densification. The sintering can, however, be improved. One way is to apply pressure during the subsequent sintering stage to break down the network and improve the particle packing. Another way is to modify the particle packing of the initial powder compact to reduce the disruption caused by the reaction. Coating the Al₂O₃ particles with ZnO (as opposed to the normal mechanical mixing of the powders), leads to enhanced densification rates (Fig. 11.56), which can approach that for the single-phase ZnAl₂O₄ powder.

Because of the difficulties commonly encountered in the production of single-phase ceramics with high density by reaction sintering, it appears that the process might be better applied to the fabrication of *composites*, since this class

of materials requires inhomogeneity as a microstructural characteristic. Displacement reactions such as that described by Eq. (11.68) have been the subject of research for the fabrication of ZrO_2 toughened ceramics. Different accounts of the reaction and densification sequence have been reported for this system. The work of Claussen and Jahn (94) provides an example of reaction sintering in which the reaction is delayed until after the densification is completed. Using a two-stage heating schedule (Fig. 11.57), it was possible to achieve nearly full densification at $\sim 1450^\circ\text{C}$, while the reaction between zircon and Al_2O_3 subsequently initiated and proceeded to completion at $\sim 1600^\circ\text{C}$. The resulting composite consists of a fine dispersion of monoclinic and tetragonal ZrO_2 in a mullite matrix (Fig. 11.58). The data of Di Rupo et al. (95) show that the densification and reaction processes occur simultaneously during hot pressing and sintering at 1450°C , whereas Yangyun and Brook (90) report a type of behavior which is intermediate between those observed by Claussen and Hahn and by Di Rupo et al. These different results are most probably a consequence of differences in the composition and particle size of the starting powders. The starting powders have different impurity levels and have been milled to varying extent. The powders that densify first appear to have a finer grain size and a higher level of impurity.

Reaction sintering involving displacement reactions has also been investigated as a processing route for the production of ceramic–metal composites in which the metal phase serves to improve the fracture toughness of the ceramic.

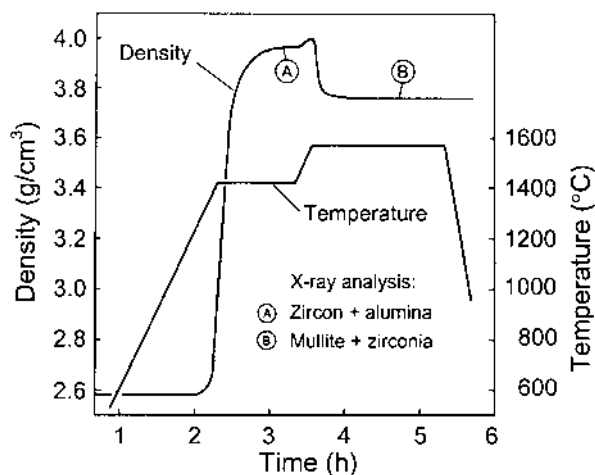


FIGURE 11.57 Sintering and reaction schedule for reaction sintering of zircon– Al_2O_3 powder mixtures. At A, only zircon and Al_2O_3 are detected by x-ray analysis; at B, the reaction to produce mullite and ZrO_2 is completed. (From Ref. 94.)

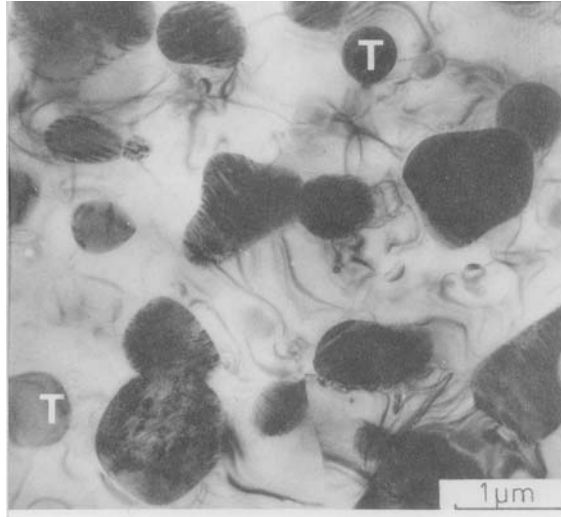


FIGURE 11.58 Bright field transmission electron micrograph of a ZrO_2 -mullite material produced by reaction sintering of zircon- Al_2O_3 powder mixtures. The material was annealed for 1 h. Larger twinned particles are monoclinic ZrO_2 and the smaller particles (T) are tetragonal ZrO_2 . Note the considerable stress contours in the mullite matrix. (From Ref. 94.).

An example is the production of Ni-reinforced Al_2O_3 from mixtures of Al and NiO powders, where the following reaction takes place:



Densities of 96–98% of the theoretical have been achieved for this system at sintering temperatures of 1600–1700°C (96).

An interesting exploitation of the reaction sintering concept is the formation of single-phase mullite and SiC-reinforced mullite composites from Al_2O_3 and SiC particles coated with an amorphous silica layer (Fig. 11.59). This process, developed by Sacks et al. (97) and referred to as *transient viscous sintering*, involves rapid densification due to viscous flow of the interparticle silica glass, while the subsequent reaction at a higher temperature between the Al_2O_3 cores and the silica glass produces the required mullite phase or SiC-reinforced mullite.

11.9 VISCOUS SINTERING WITH CRYSTALLIZATION

Sol-gel techniques discussed in Chapter 5 can be used to prepare porous gels in the form of a film or monolithic solid or fine powders, which are commonly

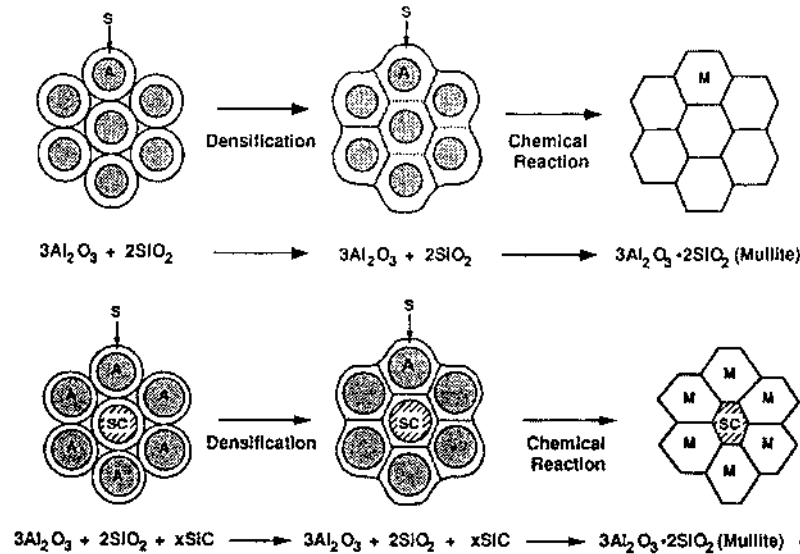


FIGURE 11.59 Schematic illustration of transient viscous sintering for the formation of (top) single-phase mullite and (bottom) mullite–SiC composite. (From Ref. 97.)

amorphous. If the composition is crystallizable, during the conversion of the dried gel or compacted powder to a dense ceramic by viscous sintering, it is possible that *crystallization* and densification can occur in sequence, in combination, or in some combination of the two. For the same chemical compound, the crystalline phase has a considerably higher viscosity than the amorphous phase, so the sintering of a polycrystalline material is significantly more difficult than the amorphous phase. This argument suggests that the most favorable processing trajectory for amorphous materials is the achievement of full density prior to any significant crystallization. In Fig. 11.54, if we replace reaction with crystallization, the most favorable processing trajectory is path C.

11.9.1 Effect of Process Variables

By analogy with our earlier discussion of reaction sintering, it is convenient to consider the crystallization and the densification as two separate processes and to develop principles that allow qualitative predictions of the influence of key process variables on the relative rates of densification and crystallization.

Viscosity

The viscosity can be altered by changes in the firing temperature or in the chemical composition of the glass, but it is more meaningful to consider the influence of

the viscosity on sintering and crystallization instead of the separate variables of temperature or composition. The rate of viscous sintering is inversely proportional to the viscosity of the glass η (Chapter 8). If η is constant, as in sintering at a fixed temperature, the extent of densification after a time t is proportional to t/η . When η changes with time, as in sintering at a constant heating rate, the extent of densification is proportional to $\int dt/\eta$. The effect of viscosity on the kinetics of crystallization has been considered by Zarzycki (98). For a fixed number of nuclei formed and when the thermodynamic barrier to formation of a nucleus is constant, Zarzycki showed that the extent of crystallization also depends on the quantity t/η or, if η changes with time, on $\int dt/\eta$. Since the extent of densification and crystallization depends on the same function of the viscosity, any factor that changes the viscosity influences both processes in such a way that the volume fraction of crystals is exactly the same by the time a given density is reached. Changes in the viscosity cannot therefore be used to vary the extent of densification relative to crystallization.

Pore Size

The crystallization process does not depend on the microstructure of the glass, but according to viscous sintering theories (Chapter 8), the densification rate is inversely proportional to the pore size r . Small pores favor rapid sintering without affecting the driving force for crystallization. The reduction in the pore size provides one of the most effective methods for increasing the ratio of the densification rate to the crystallization rate. In practice, however, the pores cannot be made too small (e.g., less than ~ 5 nm) because the sintering rate may become so rapid that full density is achieved prior to complete burnout of the organic constituents present in materials prepared, for example, by sol-gel processing. The impurities remaining in the dense solid can lead to a substantial deterioration of the properties.

Applied Pressure

Applied pressure can be very effective for increasing the densification rate if it is significantly higher than the sintering stress Σ (Chapter 8). For pores with a radius r , the sintering stress can be taken to be $\approx \gamma_{sv}/r$, where γ_{sv} is the specific surface energy of the solid-vapor interface. Taking $\gamma_{sv} \approx 0.25$ J/m² and $r \approx 10$ nm gives $\Sigma \approx 25$ MPa, a value that is comparable to the pressures available in hot pressing. We would therefore expect that hot pressing would have a significantly greater effect for larger pore sizes. The applied pressure generally has little effect on crystallization, but in some cases the effect of pressure on the crystallization process cannot be ignored. Crystallization often leads to a reduction in specific volume and the application of an applied pressure can accelerate the process.

Heating Rate

Densification depends on viscous flow but crystallization depends on two kinetic steps, nucleation and growth. The nucleation depends on the viscosity but also

on the undercooling; so increasing the heating rate at lower temperatures where the nucleation rate of the crystals is fast can delay the onset of crystallization. In this way, higher density can be achieved for a given amount of crystallization.

11.9.2 Analysis of Viscous Sintering with Crystallization

There are two main approaches for analyzing how the occurrence of crystallization can influence the densification process. In one approach, put forward by Uhlmann et al. (99), the results are represented in terms of *time-temperature-transformation* (TTT) diagrams to show the conditions of temperature and time under which crystallization and densification will occur. TTT diagrams have long been used by metallurgists to show the influence of thermal history on phase transformations, particularly in steels. In the other approach, developed by Scherer (100), the crystals formed during sintering are considered to be *rigid inclusions* in a viscous sintering matrix, and their effect on densification is analyzed by adapting the theory of sintering with rigid inclusions discussed earlier.

TTT Diagrams

An example of a TTT diagram for the crystallization of a glass is sketched in Fig. 11.60. The curve is typically C-shaped and shows the times for the beginning (and sometimes the end) of crystallization at a given temperature. If sintering is to be completed prior to crystallization, the conditions must be chosen to remain to the left of the curve C_S representing the onset of crystallization. The nose of the curve, denoted by T_{\max} , represents the maximum crystallization rate.

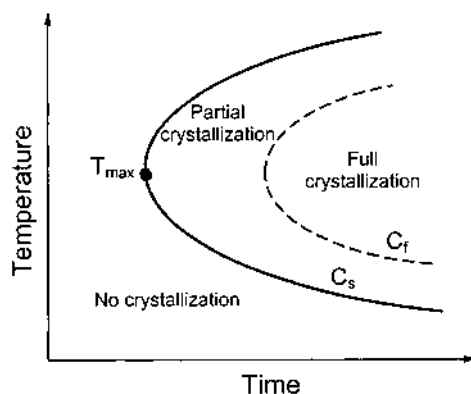


FIGURE 11.60 Sketch illustrating the regions in a time-temperature-transformation (TTT) diagram for the crystallization of an amorphous material.

In constructing the TTT diagram (101), if it is assumed that the nucleation and growth rates are constant, which is applicable when the volume crystallized is small, the volume fraction of crystals produced by a given thermal history can be calculated by Avrami's equation (102),

$$v = 1 - \exp\left(-\frac{\pi I_v u^3 t^4}{3}\right) \approx \frac{\pi I_v u^3 t^4}{3} \quad (11.71)$$

where I_v is the rate of crystal nucleation, u is the rate of crystal growth, t is the time, and the approximation applies when the volume crystallized is small. The determination of v from Eq. (11.71) relies on theories or measured values for I_v and u . According to the classical theory, the nucleation rate, defined as the number of stable nuclei produced per unit volume of untransformed material per unit time varies according to (103)

$$I_v \sim \exp\left(-\frac{\Delta G^* + \Delta G_n}{kT}\right) \quad (11.72)$$

where ΔG^* is the free energy for the formation of a nucleus, ΔG_n is the free energy of activation for atomic migration across the interface between the nucleus and the untransformed material, k is the Boltzmann constant, and T is the absolute temperature. As the temperature decreases below the liquidus, the nucleation rate increases rapidly because the thermodynamic driving force increases. The rate eventually decreases again because of the decreasing atomic mobility. This variation leads to the C-shaped TTT curve (Fig. 11.60) with a maximum crystallization rate at T_{max} . Below T_{max} , the crystal growth rate can be approximated by

$$u \sim T \exp\left(-\frac{\Delta G_c}{kT}\right) \quad (11.73)$$

where ΔG_c is the free energy of activation for atomic migration across the interface between the crystal and the uncrystallized material. It is generally assumed that $\Delta G_n \approx \Delta G_c$ and that both are equal to the activation energy Q for viscous flow defined by

$$\eta = \eta_0 \exp \frac{Q}{RT} \quad (11.74)$$

where η_0 is a constant and R is the gas constant. Substituting for Q in Eqs. (11.72) and (11.73) to determine I_v and u , followed by substitution of these quantities into Eq. (11.71) gives

$$v \sim \left(\frac{t}{\eta}\right)^4 T^3 \exp\left(-\frac{\Delta G^*}{kT}\right) \quad (11.75)$$

For a spherical nucleus, ΔG^* is given by

$$\Delta G^* = \frac{(16\pi/3)\gamma_{sl}^3}{(\Delta G_v)^2} \quad (11.76)$$

where γ_{sl} is the energy of the crystal–liquid interface and ΔG_v is the free energy change per unit volume crystallized.

Considering now the densification process, the time to reach full density during sintering by viscous flow is given approximately by [see Eq. (8.65)]

$$t_f \approx \frac{\eta}{\gamma_{sv} N^{1/3}} \approx \left(\frac{4\pi}{3}\right)^{1/3} \left(\frac{\eta r}{\gamma_{sv}}\right) \quad (11.77)$$

Thus, t_f can be found if the pore radius r , the specific surface energy of the glass–vapor interface γ_{sv} , and η are known.

Figure 11.61 shows an example of a TTT curve for silica gel, which was constructed by using viscosity data obtained from sintering studies by Sacks and Tseng (104) as well as viscosity data for conventional dry silica to find I_v and u and substituting into Eq. (11.71) to find the condition for a given volume fraction v of crystals. The value $v = 10^{-6}$ was taken to represent the onset of crystallization. The figure shows two TTT curves, one for “wet” silica with a high hydroxyl content and the other for dry silica. The viscosity of the “wet” silica is so much lower than that of the dry silica that the TTT curve for the wet silica is shifted significantly to lower times at any temperature. The curves show reasonable agreement with the crystallization data of Sacks and Tseng.

Using Eq. (11.77) to determine t_f , the dashed curves in Fig. 11.61 represent the time to reach full density at each temperature for two assumed values of the pore size of 5 nm and 500 nm. If the sintering curve does not cross the crystallization curve, then densification can be completed before detectable crystallization occurs. Consistent with the earlier discussion, gels with smaller pores are seen to sinter faster, so they are less likely to crystallize before the completion of sintering.

Analysis in Terms of Sintering with Rigid Inclusions

The approach based on TTT diagrams is valid only if the volume fraction of crystals is small. For higher volume fraction, the presence of the crystals influences the sintering rate and this must be taken into account. Scherer (100) analyzed the effect of crystallization on the sintering of an amorphous matrix as a case of sintering with rigid inclusions which was discussed earlier in this chapter.

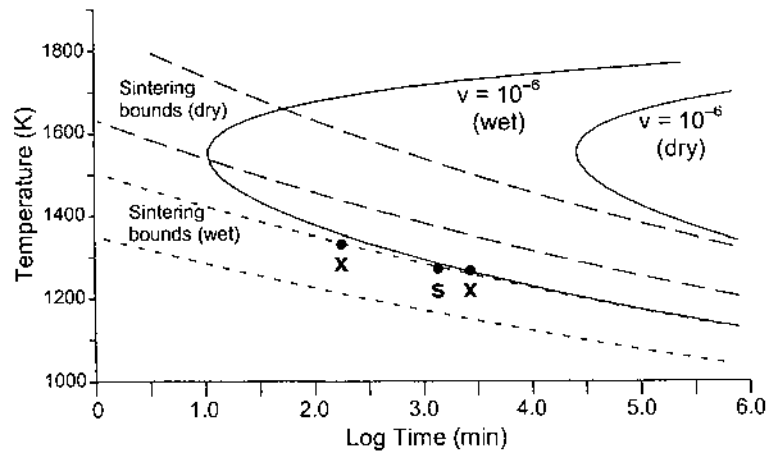


FIGURE 11.61 Sintering (dashed line) and crystallization (solid line) curves for dry silica and for “wet” silica with a higher hydroxyl content. The lower viscosity of the “wet” silica leads to a shift of the curves to lower times at any temperature. x marks treatments that resulted in crystallization with little sintering and s marks treatments that produced sintered glasses free of crystallinity. (From Ref. 99.)

Compared to the earlier discussion, the size and volume fraction of the crystals (i.e., the inclusions) increase during sintering and must be included in the analysis.

The effect of crystallization on sintering depends on where the crystals are formed and on the nature of the crystallization process. Scherer considered the case where the nucleation rate is relatively low and the growth rate is high. As sketched in Fig. 11.62, the crystals grow to a size that is large compared to the scale of the gel microstructure, so the volume fraction of the crystals formed can be easily calculated. It is easily recognized from Fig. 11.62 that if crystallization occurs prior to significant densification, considerable porosity will be trapped within the crystalline zone and the achievement of high density will be severely limited.

Because the effects become less difficult to predict than the more realistic case of constant heating rate sintering, we shall limit our discussion to isothermal sintering. The linear densification rate of the free matrix (i.e., the glass) can be found from the models for viscous sintering described in Chapter 8. The Mackenzie and Shuttleworth equation is used because of its simple form, giving

$$\dot{\epsilon}_{fm} = \frac{1}{2} \left(\frac{4\pi}{3} \right)^{1/3} \left(\frac{\gamma_{sv} N^{1/3}}{\eta} \right) \left(\frac{1}{\rho} - 1 \right)^{2/3} \quad (11.78)$$

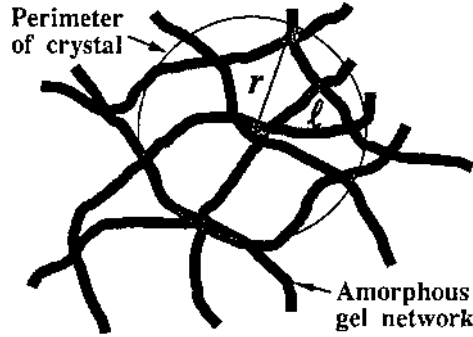


FIGURE 11.62 Schematic diagram illustrating the crystallization of an amorphous gel network when the nucleation rate is low and the growth is fast. Individual crystals are large compared to the scale of the gel structure. For a crystal to grow to a radius of r , it must trace a path of length l . (From Ref. 100.).

where γ_{sv} is the energy of the solid–vapor interface, N is the number of pores per unit volume of the solid phase, and ρ is the relative density of the glass. The linear densification rate of the composite containing a volume fraction v of crystals is assumed to follow Eq. (11.35) for the self-consistent model:

$$\dot{\epsilon}_c = \frac{(1 - v)\dot{\epsilon}_{fm}}{1 + v(4G_c/3K_m)} \quad (11.79)$$

Since the shrinkage of the body results entirely from the densification of the matrix, we also have that

$$\dot{\epsilon}_c = (1 - v)\frac{1}{3\rho}\left(\frac{d\rho}{dt}\right) \quad (11.80)$$

Equating the right-hand sides of Eqs. (11.79) and (11.80) and substituting for $\dot{\epsilon}_{fm}$ from Eq. (11.78) give

$$\frac{d\rho}{d\theta} = \frac{3}{2}\left(\frac{4\pi}{3}\right)^{1/3}\left(\frac{\rho^{1/3}(1 - \rho)^{2/3}}{1 + v(4G_c/3K_m)}\right) \quad (11.81)$$

where

$$\theta = \left(\frac{\gamma_{sv}N^{1/3}}{\eta}\right)t \quad (11.82)$$

The evaluation of Eq. (11.81) requires making some assumptions about the rheology of the system. Scherer assumed a relationship that follows from the self-consistent theory:

$$1 + v \left(\frac{4G_c}{3K_m} \right) = \frac{(1 + v_c)(1 - v)}{1 + v_c - 3(1 - v_c)v} \quad (11.83)$$

where v_c is the Poisson's ratio of the composite, given approximately by

$$v_c = \frac{v}{5} + \left(\frac{1 - v}{2} \right) \left(\frac{\rho}{3 - 2\rho} \right)^{1/2} \quad (11.84)$$

Assuming homogeneous nucleation and growth where I_v and u are constant, Scherer derived the following equation for v in terms of a parameter C and a function of the density:

$$v = 4C\rho \int_0^\theta \exp \left[-4C \int_{\theta'}^\theta \rho(\theta'') \theta''^3 d\theta'' \right] \theta'^3 d\theta' \quad (11.85)$$

where

$$C = \frac{(\pi/3)I_v u^3}{\gamma_{sv} N^{1/3} / \eta} \quad (11.86)$$

Using Eq. (11.77) for t_f , we find that C is also given by

$$C = \frac{\pi}{3} I_v u t_f^4 \quad (11.87)$$

Comparison of this equation with Eq. (11.71) shows that C is the volume fraction of crystals that appear during the time required for complete densification of the free matrix.

Taking fixed values of C , the parameters v and ρ can be found by numerically evaluating Eqs. (11.81) and (11.71). The results show that the densification behavior is highly dependent on C . For low values of C , the porosity can be eliminated (Fig. 11.63a). However, for larger values of C , substantial porosity gets trapped within the crystals (Fig. 11.63b). When v reaches ~ 50 vol%, densification of the matrix virtually stops because the glass is held in the interstices of the network of crystals. The matrix crystallizes completely, trapping residual porosity of ~ 10 vol%. Densification is predicted to stop when $v \approx 50$ vol% because Eq. (11.83) gives a sort of percolation threshold at ~ 50 vol%. However,

we know that the threshold occurs earlier, so densification is arrested at a smaller volume fraction of crystals.

11.9.3 Experimental Observations of Sintering with Crystallization

The inhibiting effects of crystallization prior to full densification have been observed for many compositions (101). In the case of alkali silicate gels, the crystallization rate is so fast that it is easier to prepare dense glasses by the more traditional melting route. Panda et al. (105a,b) found that a cordierite-type glass can be sintered to full density during constant heating rate sintering at two different heating rates, 0.2°C/min and 2.0°C/min, but later the shear viscosity reached a steady value as the glass crystallized. On the other hand, an aluminosilicate glass shows only limited sinterability when heated at 0.2°C/min because crystallization occurs prior to the glass reaching full density. Increasing the heating rate to 2.0°C/min delays the onset of crystallization, and the glass can be sintered to full density.

Mullite aerogels prepared by supercritical drying have a low initial relative density $\rho_0 \approx 0.05$, and these gels are difficult to densify, reaching a final relative density ρ_f of only ~ 0.50 after sintering at 5 °C/min to 1250°C (106). If the supercritically dried gel is first compacted to an initial density $\rho_0 \approx 0.50$, then a final density $\rho_f \approx 0.97$ is obtained under the same sintering conditions. The difficulty in densifying the low-density aerogel is attributed to the relatively large pores that lower the densification rate relative to the crystallization rate. Appreciable crystallization occurs and prevents the sample from reaching a high density.

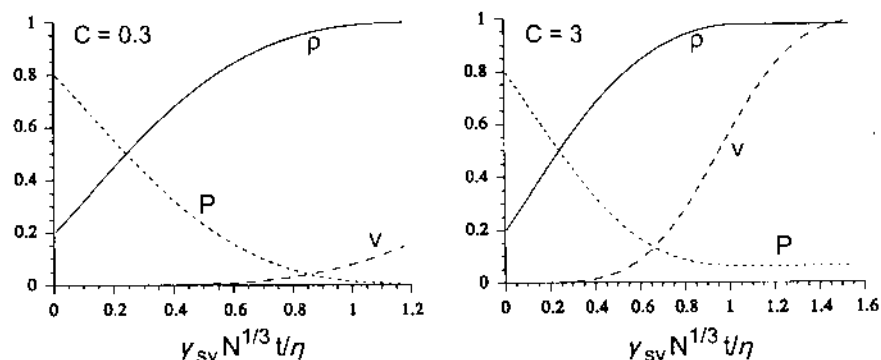


FIGURE 11.63 Predicted effect of crystallization on the sintering of an amorphous gel. The density of the matrix ρ , volume fraction of crystals v , and the porosity P are plotted versus reduced time for a gel with initial relative density of 0.2. Calculations are shown for two values of the parameter C : (a) $C = 0.3$ and (b) $C = 3.0$. (From Ref. 100.)

Amorphous TiO_2 films prepared by sol–gel processing reached a final density $\rho_f \approx 0.70$ after sintering at $1^\circ\text{C}/\text{min}$ to 750°C (107a,b). The low final density is attributed to the inhibiting effects of crystallization. When the film is heated rapidly to avoid excessive nucleation at lower temperatures, densification is completed prior to extensive crystallization, and a dense material is obtained which can be subsequently crystallized. Microstructural analysis reveals that the films stop densifying when the volume fraction of the crystals reaches a certain value, most likely corresponding to the percolation threshold. High heating rates (up to $60^\circ\text{C}/\text{min}$) delay the onset of crystallization, resulting in the production of films with higher density.

11.10 CONCLUDING REMARKS

In this chapter, we considered several important issues that are not taken into account in the simple sintering models. Rayleigh instability effects can arise and influence the morphological stability of continuous second phases in microstructures produced by solid-state and liquid-phase sintering. Inhomogeneities in a powder compact are a common source of problems for sintering, leading to differential densification which can severely retard the sintering rate and cause the growth of microstructural flaws. Whereas a few techniques may reverse the deterioration in the microstructure, the most practical approach is to minimize the extent of inhomogeneities in the green compact by careful processing (e.g., by colloidal methods).

In composites, rigid inclusions such as reinforcing particles, platelets or fibers can severely retard the sintering rate of a powder matrix, particularly in the case of a polycrystalline matrix. Realistic models predict that the transient stresses due to differential shrinkage between the inclusions and the sintering matrix are small. The major impediments to densification appear to be the formation of a rigid percolating network of the inclusion phase and, to a lesser extent, packing inhomogeneities. The sintering of thin films attached to a rigid substrate is impeded by transient stresses caused by the constrained sintering in the plane of the film. Continuum models provide an adequate explanation of the sintering of amorphous films. The sintering of polycrystalline films is qualitatively different from the sintering of amorphous films and is not adequately described by the models. Constrained sintering is also important in the cosintering (or cofiring) of multilayered structures for several industrial applications, such as the manufacture of the multilayered packages for the electronics industry.

Grain boundary drag and stagnation, coupled with variations in a volumetric energy term (surface, interface, and strain energy) lead to abnormal grain growth and the development of a bimodal grain size distribution in thin polycrystalline films. These films are also susceptible to breakup, forming islands and uncovering the substrate. Grain boundaries and three-grain junctions form the main sources

of perturbations that may eventually intersect the substrate and cause the film to break up.

We discussed the present understanding of the role of solid solution additives (dopants) in the sintering of ceramics, using MgO-doped Al_2O_3 as a special example. Whereas an effective dopant can potentially influence all of the kinetic and thermodynamic factors in sintering, its most dominant role appears to be a reduction in the grain boundary mobility by a solute drag mechanism. This mechanism is critically dependent on solute segregation at the grain boundaries which, in turn, is controlled by electrostatic effects due to a space charge layer and by elastic strain energy effects.

The principal processing parameters that control reaction sintering and viscous sintering with crystallization were considered. For such systems, successful fabrication generally depends on the ability to achieve a processing path in which full densification occurs prior to the reaction (reaction sintering) or in which full densification occurs prior to crystallization (viscous sintering).

PROBLEMS

- 11.1 Explain why a long narrow cylinder of any material or a long narrow cylindrical pore is unstable and will tend to break up into a row of spheres. Show that there exists a maximum number of spheres into which the cylindrical material or pore will break up. If the radius of the cylinder is r_0 , determine the radius of the sphere for this maximum number of spheres.
- 11.2 Is grain growth beneficial for sintering? Explain your answer.
- 11.3 Compare the sintering of a powder with a broad particle size distribution with that for a compact with a narrow size distribution when the average particle size of the two powders is the same.
- 11.4 Derive Eq. (11.3) for the volume fraction of rigid inclusions in a porous powder matrix. If the volume fraction of inclusions in the fully dense matrix $v_f = 0.20$, plot the inclusion volume fraction of the porous composite v_i as a function of the relative density of the matrix ρ_m for values of ρ_m in the range 0.5–1.0.
- 11.5 Derive Eqs. (11.4) to (11.6) relating the matrix and composite density and densification rates.
- 11.6 The sintering of Al_2O_3 powder compacts formed from a mixture of coarse and fine powders follows approximately the rule of mixtures (see Ref. 25). However, the sintering of compacts consisting of a fine Al_2O_3 powder matrix and coarse, rigid inclusions of ZrO_2 is significantly lower than the predictions of the rule of mixtures (see Ref. 41). Discuss the reasons for the difference in sintering behavior between these two systems.
- 11.7 Derive Eq. (11.7) giving a relationship for the rule of mixtures in terms of the linear densification rates.
- 11.8 Compare the grain growth phenomena that can occur in a bulk polycrystalline solid and in a thin, adherent polycrystalline film.

- 11.9 Pinholes can often occur in thin films deposited on a substrate by techniques such as evaporation, solution-based methods, and sputtering. Assuming that the pinholes have a circular cross section and the film is amorphous, determine the conditions under which the pinholes will grow or shrink, in terms of the relative values of the interfacial energies, if the film is annealed at a high enough temperature for mass transport to occur.
- 11.10 Derive Eq. (11.49) for the equilibrium groove depth of an adherent polycrystalline film. For a dihedral angle of 120° , use Eq. (11.49) to determine the critical value of the grain diameter to the film thickness above which the grain boundary groove intercepts the substrate. How does this value compare with the results of the minimum energy configuration calculations in Fig. 11.42.
- 11.11 For ZrO_2 , assuming that anion vacancies are the dominant point defects and that the formation energy of an anion vacancy is smaller than that for a cation vacancy, sketch schematically the variation of the electrostatic potential and the defect concentration as functions of the distance from the grain boundary.
Repeat the procedure for CaO-doped ZrO_2 , assuming that the defect concentrations produced by the dopant are significantly larger than those generated thermally.
- 11.12 An early explanation for the role of MgO in the sintering of Al_2O_3 is that MgO enhances the rate of surface diffusion in Al_2O_3 , thereby enhancing the pore mobility, allowing the pores to migrate with the boundary, and avoiding abnormal grain growth. Explain the flaw in this explanation.
Briefly explain what you believe to be the current understanding of the role of MgO in the sintering of Al_2O_3 .
- 11.13 Consider the reaction between equimolar mixtures of ZnO and Al_2O_3 to form ZnAl_2O_4 spinel. The molar volume of the reactants is approximately equal to that of the product. Experimentally, when equimolar mixtures of ZnO and Al_2O_3 powders with approximately the same particle size are reaction sintered, a volume expansion of 20–30% is observed (see Fig. 11.56). Suggest possible explanations for the origins of the significant volume expansion.

REFERENCES

1. Rayleigh, Lord; Proc. London Math. Soc. 1879, Vol. 10, 4–13.
2. Nicholls, F. A.; Mullins, W. W. Trans. AIME. 1965, Vol. 233, 1840; J. Appl. Phys. 1965, Vol. 36, 1826.
3. Nichols, F. A. J. Mater. Sci. 1976, Vol. 11, 1077.
4. Stüwe, H. P.; Kolednik, O. Acta Metall. 1988, Vol. 36, 1705.
5. Beeré, W. Acta Metall. 1975, Vol. 23, 131; J. Mater. Sci. 1973, Vol. 8, 1717.
6. Tucker, M. O.; Turnbull, J. A. Proc. Roy. Soc. Lond. A. 1975, Vol. 343, 299.
7. Carter, W. C.; Glaeser, A. M. J. Am. Ceram. Soc. 1984, Vol. 67, C124.
8. Carter, W. C.; Glaeser, A. M. Acta Metall. 1987, Vol. 35, 237.
9. Stapley, A. J.; Beevers, C. J. J. Mater. Sci. 1973, Vol. 8, 1296.
10. Gupta, T. K. J. Am. Ceram. Soc. 1978, Vol. 61, 191.
11. Yen, C. F.; Coble, R. L. J. Am. Ceram. Soc. 1972, Vol. 55, 507.
12. Drory, M. D.; Glaeser, A. M. J. Am. Ceram. Soc. 1985, Vol. 68, C14.

13. Evans, A. G. J. *Am. Ceram. Soc.* 1982, Vol. 65, 497.
14. Raj, R.; Bordia, R. K. *Acta Metall.* 1984, Vol. 32, 1003.
15. Lange, F. F. J. *Am. Ceram. Soc.* 1983, Vol. 66, 396.
16. Exner, H. E. *Reviews on Powder Metallurgy and Physical Ceramics.* 1979, Vol. 1, 1.
17. Weiser, M. W.; De Jonghe, L. C. J. *Am. Ceram. Soc.* 1986, Vol. 69, 822.
18. Rhodes, W. H. J. *Am. Ceram. Soc.* 1981, Vol. 64, 19.
19. Yeh, T-S.; Sacks, M. D. *Ceramic Trans.* 1990, Vol. 7, 309.
20. Lange, F. F. J. *Am. Ceram. Soc.* 1984, Vol. 67, 83.
21. Harmer, M. P.; Zhao, J. In *Materials Science Research. Vol. 21: Ceramic Microstructures '86: Role of Interfaces*; Pask, J. A., Evans, A. G. eds.; Plenum Press: New York, 1987, pp. 455–464.
22. Lin, M.; Rahaman, M. N.; De Jonghe, L. C. J. *Am. Ceram. Soc.* 1987, Vol. 70, 360.
23. Chu, M.-Y.; De Jonghe, L. C.; Lin, M. K. F.; Lin, F. J. T. *Am. Ceram. Soc.* 1991, Vol. 74, 2902.
24. Lin, F. J. T.; De Jonghe, L. C.; Rahaman, M. N. *Am. Ceram. Soc.* 1997, Vol. 80, 2269; 2891.
25. Smith, J. P.; Messing, G. L. *Am. Ceram. Soc.* 1984, Vol. 67, 238.
26. De Jonghe, L. C.; Rahaman, M. N.; Hsueh, C. H. *Acta Metall.* 1986, Vol. 34, 1467.
27. Rahaman, M. N.; De Jonghe, L. C. *Am. Ceram. Soc.* 1987, Vol. 70, C-348.
28. Timoshenko, S. P.; Goodier, J. N. *Theory of Elasticity*; 3rd ed.; McGraw Hill: New York, 1970.
29. Hsueh, C. H.; Evans, A. G.; Cannon, R. M.; Brook, R. J. *Acta Metall.* 1986, Vol. 34, 927.
30. Scherer, G. W. *Relaxation in Glass and Composites*; Wiley-Interscience: New York, 1986.
31. Christiansen, R. M. *Theory of Viscoelasticity, An Introduction*; Academic: New York, 1982.
32. Bordia, R. K.; Scherer, G. W. *Acta Metall.* 1988, Vol. 36, 2393–2416.
33. Scherer, G. W. *Am. Ceram. Soc.* 1987, Vol. 70, 719.
34. Scherer, G. W. *Am. Ceram. Soc.* 1984, Vol. 67, 709.
35. Hashin, Z.; Shtrikman, S. J. *Mech. Phys. Solids.* 1963, Vol. 11, 127.
36. Scherer, G. W. *Non-Cryst. Solids.* 1979, Vol. 34, 239.
37. Zallen, R. *The Physics of Amorphous Solids*; Wiley: New York, 1983, Chap. 4.
38. Scherer, G. W. *Ceramic Bulletin.* 1991, Vol. 70, 1059.
39. Scherer, G. W.; Jagota, A. In *Ceramic Transactions*; Vol. 19, Sacks, M. D. ed.; American Ceramic Society: Westerville, OH, 1991, pp. 99–109.
40. Jagota, A.; Scherer, G. W. *Am. Ceram. Soc.* 1993, Vol. 76, 3123.
- 41a. Sudre, O.; Lange, F. F. *Am. Ceram. Soc.* 1992, Vol. 75, 519.
- 41b. Sudre, O.; Bao, G.; Fan, B.; Lange, F. F.; Evans, A. G. *Am. Ceram. Soc.* 1992, Vol. 75, 525.
- 41c. Sudre, O.; Lange, F. F. *Am. Ceram. Soc.* 1992, Vol. 75, 3241.
42. Kapolnek, S.; De Jonghe, L. C. *Europ. Ceram. Soc.* 1991, Vol. 7, 345.
43. Hu, C. L.; Rahaman, M. N. *Am. Ceram. Soc.* 1992, Vol. 75, 2066; 1993, Vol. 76, 2549; 1994, Vol. 77, 815.

44. Hagy, H. E.; Smith, A. F. J. *Can. Ceram. Soc.* 1969, Vol. 38, 63.
45. Bordia, R. K.; Raj, R. J. *Am. Ceram. Soc.* 1985, Vol. 68, 287.
46. Scherer, G. W.; Garino, T. J. J. *Am. Ceram. Soc.* 1985, Vol. 68, 216.
47. Garino, T. J.; Bowen, H. K. J. *Am. Ceram. Soc.* 1987, Vol. 70, C315; 1990, Vol. 73, 251.
48. Jagota, A.; Hui, C. Y. *Mech. Mater.* 1990, Vol. 9, 107; 1991, Vol. 11, 221.
49. Hu, M.; Thouless, M.; Evans, A. G. *Acta Metall.* 1988, Vol. 36, 1301.
50. Bordia, R. K.; Jagota, A. J. *Am. Ceram. Soc.* 1993, Vol. 76, 2475.
51. Kumar, A. H.; Tummala, R. R. *Int. J. Hybrid Microelectronics.* 1991, Vol. 14, 137.
52. Lu, G.-Q.; Sutterlin, R. C.; Gupta, T. K. J. *Am. Ceram. Soc.* 1993, Vol. 76, 1907.
53. Cheng, T.; Raj, R. J. *Am. Ceram. Soc.* 1989, Vol. 72, 1649.
54. Beck, P. A.; Holtzworth, M. L.; Sperry, P. R. *Trans. AIME.* 1949, Vol. 180, 163.
55. Palmer, J. E.; Thompson, C. V.; Smith, H. I. J. *Appl. Phys.* 1987, Vol. 62, 2492.
56. Mullins, W. W. *Acta Metall.* 1958, Vol. 6, 414.
57. Frost, H. J.; Thompson, C. V.; Walton, D. T. *Acta Metall. Mater.* 1990, Vol. 38, 1455; 1992, Vol. 40, 779.
58. Carel, R.; Thompson, C. V.; Frost, H. J. *Acta Mater.* 1996, Vol. 44, 2479.
59. Miller, K. T.; Lange, F. F.; Marshall, D. B. J. *Mater. Res.* 1990, Vol. 5, 151.
60. Srolovitz, D. J.; Safran, S. A. J. *Appl. Phys.* 1986, Vol. 60, 247–260.
61. Coble, R. L. J. *Appl. Phys.* 1961, Vol. 32, 793, U. S. Patent # 3,026,210, March 1962.
62. Kroger, F. A. J. *Am. Ceram. Soc.* 1983, Vol. 66, 730.
63. Handwerker, C. A.; Dynys, J. M.; Cannon, R. M.; Coble, R. L. J. *Am. Ceram. Soc.* 1990, Vol. 73, 1365; 1990, Vol. 73, 1371.
64. Cahn, J. W. *Acta Metall.* 1962, Vol. 10, 789.
65. Kingery, W. D. J. *Am. Ceram. Soc.* 1974, Vol. 57, 1; 1974, Vol. 57, 74.
66. Yan, M. F.; Cannon, R. M.; Bowen, H. K. J. *Appl. Phys.* 1983, Vol. 54, 764.
67. Eshelby, J. D. In *Solid State Physics*; Vol. 3, Seitz, F., Turnbull, D. eds.; Academic: New York, 1956, p.79.
68. McLean, D. *Grain Boundaries in Metals*. Clarendon Press: Oxford, 1957.
69. Johnson, W. C. *Metall. Trans.* 1977, Vol. 8A, 1413.
70. Frenkel, J. *Kinetic Theory of Liquids*; Oxford University Press: New York, 1946.
71. Lehovec, K. J. *Chem Phys.* 1953, Vol. 21, 1123.
72. Eshelby, J. D.; Newey, C. W. A.; Pratt, P. L.; Lidiard, A. B. *Philos. Mag.* 1958, Vol. 8, 75.
73. Kliever, K. L.; Koehler, J. S. *Phys. Rev. A.* 1965, Vol. 140, 1226.
74. Schwensfeir, R. J., Jr.; Elbaum, C. J. *Phys. Chem. Solids.* 1967, Vol. 28, 597.
75. Li, C.-W.; Kingery, W. D. In *Advances in Ceramics*; Vol. 10, Kingery, W. D. ed.; American ceramic Society: Columbus, OH, 1984, pp. 368–378.
76. Chiang, Y. M.; Hendrickson, A. F.; Kingery, W. D.; Finello, D. J. *Am. Ceram. Soc.* 1981, Vol. 64, 385.
77. Hwang, S.-L.; Chen, I. -W. J. *Am. Ceram. Soc.* 1990, Vol. 73, 3269.
- 78a.Ikeda, J. A. S.; Chiang, Y. -M. J. *Am. Ceram. Soc.* 1993, Vol. 76, 2437.
- 78b.Ikeda, J. A. S.; Chiang, Y. -M.; Garratt-Reed, A. J.; Vander Sande, J. B. J. *Am. Ceram. Soc.* 1993, Vol. 76, 2447.
79. Chiang, Y.-M.; Takagi, T. J. *Am. Ceram. Soc.* 1990, Vol. 73, 3278.

80. Chiang, Y.-M.; Kingery, W. D. J. Am. Ceram. Soc. 1990, Vol. 73, 1153.
81. Bennison, S. J.; Harmer, M. P. Ceramic Trans. 1990, Vol. 7, 13.
82. Johnson, W. C.; Coble, R. L. J. Am. Ceram. Soc. 1978, Vol. 61, 110.
- 83a. Bennison, S. J.; Harmer, M. P. J. Am. Ceram. Soc. 1985, Vol. 68, C22; 1990, Vol. 73, 833.
- 83b. Berry, K. A.; Harmer, M. P. J. Am. Ceram. Soc. 1986, Vol. 69, 143.
- 84a. Baik, S. J. Am. Ceram. Soc. 1986, Vol. 69, C101.
- 84b. Baik, S.; White, C. L. J. Am. Ceram. Soc. 1987, Vol. 70, 682.
- 84c. Baik, S.; Moon, J. H. J. Am. Ceram. Soc. 1991, Vol. 74, 819.
85. Harmer, M. P.; Bennison, S. J.; Narayan, C. Mater. Sci. Res. 1983, Vol. 15, 309.
86. Shaw, N. J.; Brook, R. J. J. Am. Ceram. Soc. 1986, Vol. 69, 107.
87. Kaysser, W. A.; Sprissler, M.; Handwerker, C. A.; Blendell, J. E. J. Am. Ceram. Soc. 1987, Vol. 70, 339.
88. Wu, S. J.; De Jonghe, L. C.; Rahaman, M. N. J. Am. Ceram. Soc. 1985, Vol. 68, 385.
89. Kolar, D. Sci. Ceram. 1981, Vol. 11, 199.
90. Yangyun, S.; Brook, R. J. Sci. Sintering. 1985, Vol. 17, 35.
91. Schmalzried, H. Solid State Reactions; Academic Press: New York, 1974.
92. Rahaman, M. N.; De Jonghe, L. C. J. Am. Ceram. Soc. 1993, Vol. 76, 1739.
93. Hong, W. S.; De Jonghe, L. C.; Yang, X.; Rahaman, M. N. J. Am. Ceram. Soc. 1995, Vol. 78, 3217.
94. Claussen, N.; Jahn, J. J. Am. Ceram. Soc. 1980, Vol. 63, 228.
95. Di Rupo, E.; Gilbert, E.; Carruthers, T. G.; Brook, R. J. J. Mater. Sci. 1979, Vol. 14, 705.
96. Tuan, W. H.; Brook, R. J. J. Europ. Ceram. Soc. 1992, Vol. 10, 95.
97. Sacks, M. D.; Bozkurt, N.; Scheiffele, G. W. J. Am. Ceram. Soc. 1991, Vol. 74, 2428.
98. Zarzycki, J. In Advances in Ceramics; Vol. 4, American Ceramic Society: Columbus, OH, 1982, pp. 204–216.
99. Uhlmann, D. R.; Zelinski, B. J.; Silverman, L.; Warner, S. B.; Fabes, B. D.; Doyle, W. F. In Science of Ceramic Chemical Processing; Hench, L. L., Ulrich, D. R. eds.; Wiley: New York, 1986, pp. 173–183.
100. Scherer, G. W. Mater. Res. Soc. Symp. Proc. 1990, Vol. 180, 503.
101. Brinker, C. J.; Scherer, G. W. Sol-Gel Science; Academic Press: New York, 1990, Chap. 11.
102. Avrami, M. J. Chem. Phys. 1939, Vol. 7, 1103; 1940, Vol. 8, 212; 1941, Vol. 9, 177.
103. Christian, J. W. The Theory of Phase Transformations in Metals and Alloys; 2nd ed.; Pergamon Press: New York, 1975.
104. Sacks, M. D.; Tseng, T. -Y. J. Am. Ceram. Soc. 1984, Vol. 69, 532.
- 105a. Panda, P. C.; Raj, R. J. Am. Ceram. Soc. 1989, Vol. 72, 1564.
- 105b. Panda, P. C.; Mobley, W. M.; Raj, R. J. Am. Ceram. Soc. 1989, Vol. 72, 2361.
106. Rahaman, M. N.; De Jonghe, L. C.; Shinde, S. L.; Tewari, P. H. J. Am. Ceram. Soc. 1988, Vol. 71, C338.
- 107a. Keddle, J. L.; Giannelis, E. P. J. Am. Ceram. Soc. 1991, Vol. 74, 2669.
- 107b. Keddle, J. L.; Braun, P. V.; Giannelis, E. P. J. Am. Ceram. Soc. 1994, Vol. 77, 1592.

12

Densification Process Variables and Densification Practice

12.1 INTRODUCTION

Processing prior to sintering, as discussed in detail earlier, has a significant effect on the microstructure of the fabricated ceramic. However, assuming that proper powder preparation and consolidation procedures are in effect, successful fabrication is still dependent on the ability to control the microstructure through manipulation of the process variables in the sintering stage. A wide variety of sintering techniques have been developed to obtain ceramics with the required density, microstructure and composition. In general, these methods involve the manipulation of some combination of the heating schedule, atmosphere, and applied pressure.

Sintering in which no external pressure is applied to the body is referred to as *conventional*, *free*, or *pressureless sintering*. Conventional sintering is the preferred method because it is more economical, but the additional driving force available in sintering with the application of pressure (referred to as *pressure sintering*) often guarantees the attainment of high density and a fine-grained microstructure. Heating of the powder compact is commonly achieved with electrical resistance furnaces that allow temperatures as high as $\sim 2500^{\circ}\text{C}$ to be attained. The heating schedule can be simple, as in isothermal sintering where the temperature is increased monotonically to a sintering hold temperature and then lowered to room temperature, or have a complex temperature-time relationship.

Control of the sintering atmosphere is also important, and precise control of the oxygen or nitrogen partial pressure as a function of temperature may in some cases be beneficial or essential. Ferrites, for example, form an important class of ceramics where atmosphere control is essential for developing optimum

magnetic properties. The atmosphere is important for controlling processes such as decomposition, evaporation of volatile constituents, and vapor transport. It can also influence the oxidation number of atoms (particularly those of the transition elements) and the stoichiometry of the solid. Insoluble gases trapped in closed pores may hinder the final stages of densification or lead to swelling of the compact after densification and in these cases, a change of the sintering atmosphere or the use of vacuum is indicated.

The use of *microwave* energy for heating and sintering ceramics has attracted increasing attention within the last 10–15 years. This method of heating is fundamentally different from that in conventional furnaces in that heat is generated internally by interaction of microwaves with the material. It is effective for heating ceramic bodies rapidly, and some studies have shown considerable enhancement of sintering with microwave heating. However, the achievement of sufficiently uniform heating can be difficult.

Pressure sintering is commonly used for the production of high cost ceramics and prototype ceramics where high density must be guaranteed. It also provides an effective additional variable for the study of sintering mechanisms. In ceramics, the main pressure sintering methods are *hot pressing* in which the pressure is applied uniaxially to the powder in a die and, to a lesser extent, *hot isostatic pressing* in which the pressure is applied isostatically by means of a surrounding gas.

12.2 CONVENTIONAL SINTERING

A variety of furnaces are available commercially to provide the heating schedule and atmosphere used in conventional sintering. Sizes range from those for small, research-type powder compacts to large furnaces that can accommodate parts several feet in diameter for industrial production. We also need to have measures for the sintering process to provide the data for understanding sintering and for optimizing the process variables in practical sintering.

12.2.1 Measurement Techniques

The most common types of sintering furnaces are electrical resistance furnaces in which a current carrying resistor, commonly called the *furnace element* or *winding*, provides the source of heat. In addition to size and cost, important considerations in the selection of a furnace are the maximum temperature capability and the atmosphere in which it can be operated for extended periods. Table 12.1 provides a selected list of common furnace elements. Several metal alloys (e.g., nichrome) can be used as furnace elements for temperatures up to $\sim 1200^{\circ}\text{C}$ in both oxidizing and reducing atmospheres. For extended use in air, other furnace elements can deliver higher temperatures: e.g., Pt (up to $\sim 1400^{\circ}\text{C}$); SiC (1450°C);

MoSi₂ (1600°C); LaCrO₃ (1750°C). For higher temperatures, furnace elements consisting of various refractory metals (e.g., Mo, W, and Ta) can be used in vacuum, inert, or reducing atmospheres up to ~2000°C. At these high temperatures, the metallic elements must not be exposed to atmospheres containing carbon or nitrogen because they readily form carbides and nitrides, which reduce the life of the element considerably. Graphite elements, heated electrically or by induction, can provide temperatures up to ~2800°C in inert or reducing atmospheres. For extended use of graphite elements above ~2000°C, high purity He gas from which the trace impurities of oxygen have been removed (e.g., by passing the gas through an oxygen getter prior to entering the furnace) provides a useful atmosphere.

A temperature controller forms an integral part of most furnaces to take the system through the required heating cycle. In many cases it is also necessary to have fairly precise control of the sintering atmosphere around the powder compact or to use a sintering atmosphere that is not compatible with the furnace element. For laboratory-scale experiments, a tube furnace (Fig. 12.1) can often provide the desired temperature and atmosphere control. Silica tubes can be used for temperatures up to ~1100°C, whereas high purity Al₂O₃ tubes can be used up to temperatures in the range of 1600–1800°C, but the low thermal shock resistance of Al₂O₃ limits its maximum heating or cooling rate to 10–20°C/min depending on the thickness of the tube.

Several techniques are available to monitor sintering but, in practice, a few selected measurements prove to be most useful. These might include measurement of the shrinkage or density and, if necessary, the surface area or neck radius as a function of sintering time or temperature to allow an examination of the sintering kinetics. Additional information from the microstructure, such as the grain size and grain size distribution, the pore size distribution, as well as the concentration and distribution of second phases (including porosity) are required to understand the events occurring during sintering.

TABLE 12.1 Heating Elements Commonly Used in Electrical Resistance Furnaces

Material	Maximum temperature (°C)	Furnace atmosphere
Nichrome	1200	Oxidizing; inert; reducing
Pt	1400	Oxidizing
SiC	1450	Oxidizing
MoSi ₂	1600	Oxidizing
LaCrO ₃	1750	Oxidizing
Mo, W, Ta	2000	Vacuum; inert; reducing ^a
C (graphite)	2800	Inert; reducing ^b

^a Atmospheres containing nitrogen or carbon must be avoided above ~1500°C.

^b Vacuum may be used below ~1500°C.

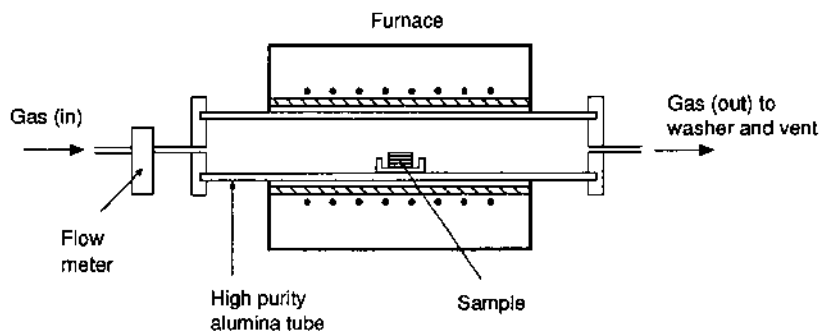


FIGURE 12.1 Schematic diagram of a tube furnace used for controlled atmosphere sintering.

The shrinkage can be determined directly by measuring the initial dimensions (e.g., length and diameter for a cylindrical pellet) and the dimensions after a given time t (or temperature T). The *linear shrinkage* is defined as $\Delta L/L_0$, where L_0 is the initial length, and $\Delta L = L - L_0$, where L is the length after time t . In this definition, $\Delta L/L_0$ is negative for sintering, but commonly, the negative sign is ignored and the magnitude is reported. The density can be determined from the mass and dimensions (volume) for a sample with a regular shape or by the Archimedes method.

To provide data for the sintering kinetics, it is required to measure the density or shrinkage at several times (or temperatures), giving a plot of density or shrinkage versus sintering time (or temperature). This can be very time consuming. For laboratory-scale experiments, the technique of *dilatometry* provides continuous monitoring of the linear shrinkage of the powder compact over the complete sintering schedule. A variety of dilatometers are available commercially for providing the required accuracy in shrinkage measurement as well as control of the temperature and atmosphere. The equipment is identical to that commonly used to measure the thermal expansion coefficient of solids (Fig. 12.2). The change in length of the powder compact is monitored by a linear voltage displacement transducer (LVDT), the output of which is collected using a computer. Commonly, the shrinkage $\Delta L/L_0$ is plotted as a function of time or temperature. If the mass of the powder compact remains constant and the shrinkage is isotropic, the relative density can be determined from the shrinkage data using the equation

$$\rho = \frac{\rho_0}{(1 - \Delta L/L_0)^3} \quad (12.1)$$

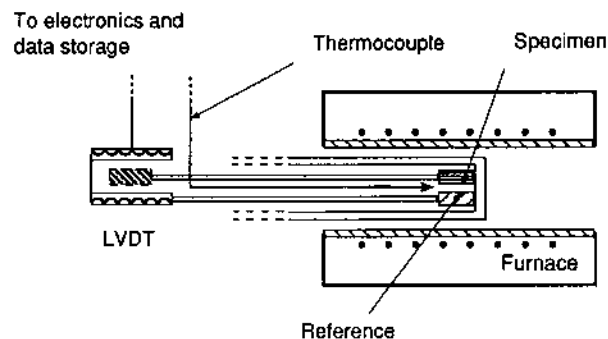


FIGURE 12.2 Schematic diagram of a dual push-rod dilatometer for continuous monitoring of shrinkage kinetics.

where ρ_0 is the initial relative density of the compact, commonly determined from the mass and dimensions.

It is often useful to determine the densification rate $\dot{\rho}$, defined as $(1/\rho) d\rho/dt$. The procedure involves fitting a smooth curve through the density data and differentiating with respect to time to find the slope at any instant. As an example of the valuable information that can be obtained economically with a dilatometer, Fig. 12.3a shows the shrinkage data for a ZnO powder compact ($\rho_0 = 0.52$) that was sintered at a constant heating rate of $5^\circ\text{C}/\text{min}$ to $\sim 1100^\circ\text{C}$ and the corresponding density data determined using Eq. (12.1). In this case, the data show that shrinkage (or densification) starts at $\sim 500^\circ\text{C}$ and is almost completed at $\sim 1000^\circ\text{C}$. The maximum in the densification rate occurs at $\sim 800^\circ\text{C}$ (Fig. 12.3b), corresponding to a density of ~ 0.80 .

Grain size has a strong influence on the sintering kinetics, so measurements of the average grain size and the distribution of grain sizes are almost always necessary. These data are commonly obtained by *quantitative microscopy* on polished and etched sections of pellets that have been sintered to several representative times or temperatures in the sintering schedule. Measurements of the average pore size and the pore size distribution are also valuable. They are often performed using *mercury porosimetry* (see Chapter 3) for samples sintered to representative times or temperatures.

12.2.2 Heating Schedule

Heating schedules can be simple, as in sintering studies involving *isothermal sintering* or *constant heating rate sintering* of single-phase powders in laboratory-scale experiments, or have a more complex temperature–time relationship, as in

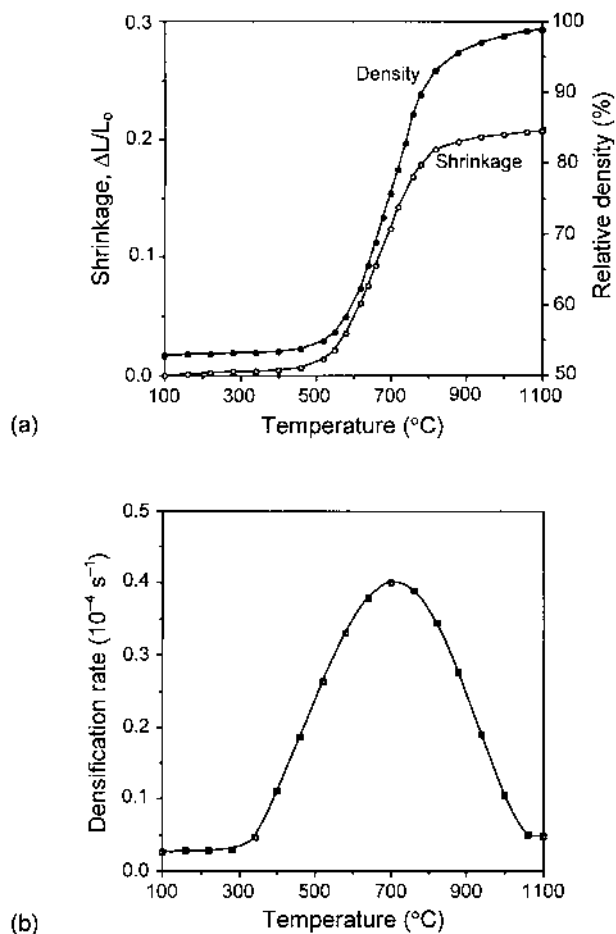


FIGURE 12.3 Sintering curves for ZnO in air during constant heating rate sintering at 5°C/min obtained from the dilatometric shrinkage curve showing (a) the shrinkage and density as a function of temperature and (b) the densification rate as a function of temperature.

the sintering of ceramics for industrial applications. A general heating schedule is shown in Fig. 12.4.

Stage 1. Binder burnout

In this stage, removal of volatile materials such as adsorbed water, and the conversion of additives such as metal organic compounds or organic binders take place.

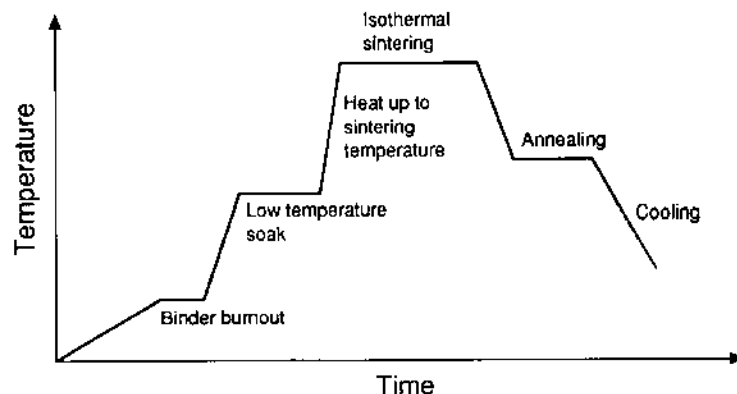


FIGURE 12.4 Sketch of a general heating schedule.

The heat-up rate is often slow and carefully controlled, often $<2^{\circ}\text{C}/\text{min}$, since rapid heating may cause boiling and evaporation of organic additives, leading to swelling and even cracking of the specimen. Typically, the hold temperature in this stage is, at most, $400\text{--}500^{\circ}\text{C}$.

Stage 2. Low-temperature soak

Stage 2 can be included to promote chemical homogenization or the reaction of powder components. The hold temperature is commonly below that for the onset of measurable sintering. Chemical homogenization may, for example, involve a solid-state reaction in which a small amount of dopant is incorporated into the powder or a reaction leading to the formation of a liquid phase.

Stage 3. Heat-up to the sintering temperature

This stage involves heat-up to the isothermal sintering temperature. The heating rate is limited by the sample size and the thermal characteristics of the furnace. For large bodies, the heat-up times can stretch for many hours to avoid temperature gradients that could lead to cracking or to avoid the formation of a dense outer layer on an incompletely densified core, as would result from differential densification. In laboratory-scale experiments with small specimens, it is often observed that a faster heating rate in this stage enhances the densification in the subsequent isothermal sintering stage. A possible explanation of this observation is that the coarsening of the powder during the heat-up is reduced due to the shorter time taken to reach the isothermal sintering temperature, thereby resulting in finer microstructure at the start of isothermal sintering.

Stage 4. Isothermal sintering

The isothermal sintering temperature is chosen to be as low as possible yet compatible with the requirement that densification be achieved within a reasonable time (typically less than 24 h). Higher sintering temperatures lead to faster densification, but the rate of coarsening also increases. The increased coarsening rate may lead to abnormal grain growth where pores are trapped inside large grains. Whereas densification proceeds faster, the final density may be limited. Figure 12.5 shows qualitatively some possible sintering profiles for different sintering temperatures.

Stage 5. Annealing

An additional hold stage may be included prior to final cool-down of the material to relieve thermal stresses, to allow for precipitation of second phases, or to modify the chemical composition or the microstructure. Annealing to reduce thermal stresses is common in systems that contain a glassy matrix or that undergo a crystallographic transformation involving a volume change. Modification of the chemical composition and the microstructure is common in many functional ceramics such as ferrites (discussed later). In structural ceramics, a good example of the use of an annealing step to modify the microstructure is the crystallization of the glassy grain boundary phase in Si_3N_4 to improve the high temperature creep resistance (see Chapter 10).

Stage 5. Cool down to room temperature

The cooling rate can be fairly fast for relatively small articles but is much slower for large articles to prevent large temperature gradients that can lead to cracking.

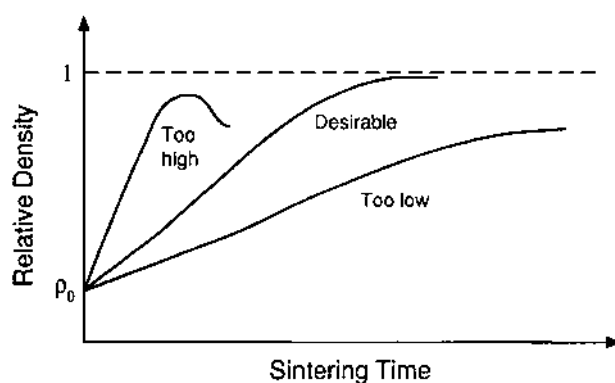


FIGURE 12.5 Sketch of sintering curves to illustrate the selection of an optimum isothermal sintering temperature.

When compositional or microstructural modification must be achieved, the cooling rate needs to be carefully controlled. As discussed later, some functional ceramics (e.g., ferrites) also require that the cooling be carried out in a controlled atmosphere to control the stoichiometry and microstructure.

The cooling rate can influence the precipitation of second phases and their distribution in the fabricated article. Strontium-doped TiO_2 provides a good example of this type of effect (1). The solubility limit of Sr in TiO_2 is slightly less than 0.5 mol% at 1400°C. Even for concentrations below the solubility limit, cooling from 1400°C leads to the precipitation of SrTiO_3 at the grain boundaries. This precipitation is probably due to the segregation of Sr ions that have a large size misfit in the TiO_2 lattice. The morphology of the precipitates depends on the cooling rate. Well below the solubility limit (0.2 mol% Sr), slow cooling from 1400°C leads to the precipitation of fine discrete particles. On the other hand, if the same composition is cooled rapidly to room temperature, no second phase is formed. Near the solubility limit (0.5 mol%), slow cooling leads to the precipitation of a continuous second phase between 1400°C and 1250°C, but this breaks up on further cooling below 1200°C to produce discrete particles.

Isothermal Sintering

In isothermal sintering (Fig. 12.6), the temperature is increased monotonically to a fixed sintering temperature, maintained at this temperature for the required time, and finally lowered to room temperature. This is the most common heating schedule. The holding time is often long compared to the heat-up time and generally, the isothermal sintering temperature should be significantly above the intended service temperature of the article. As outlined earlier, the heat-up time is limited by the sample size and by the characteristics of the furnace. Considerable densification and microstructural changes can occur during the heat-up stage of isothermal sintering but these changes are often ignored in sintering studies. The data for this nonisothermal stage are also unsuitable for comparison with the predictions of sintering models that assume idealized isothermal conditions.

Constant Heating Rate Sintering

In this case, the sample is heated at a constant rate to a specified temperature and immediately cooled (Fig. 12.6). Provided that the sintering mechanisms do not change over the temperature range and the activation energies for densification and coarsening are available, constant heating rate experiments may be simpler to analyze theoretically than the isothermal experiments because ideal isothermal sintering is not possible (2,3). The heating rate is limited by the sample size and the characteristics of the furnace. High heating rates are commonly most useful in laboratory-scale experiments.

Effect of Heating Rate on Sintering

As discussed in Chapter 11, manipulation of the heating rate can be useful in cases where a reaction or crystallization occurs during sintering. The heating rate

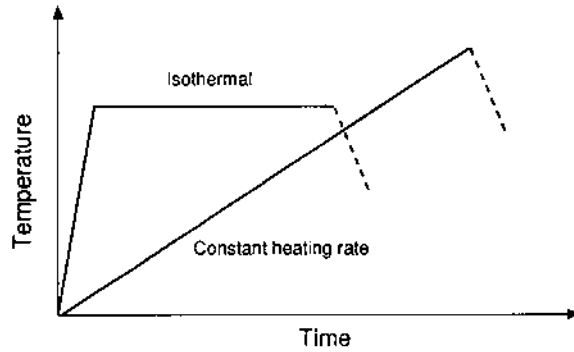


FIGURE 12.6 Sketch of the temperature–time schedule for isothermal sintering and constant heating rate sintering.

can also influence the sintering and microstructural evolution of single-phase ceramics that do not undergo reaction or crystallization.

Amorphous materials

In the case of amorphous materials, coarsening is absent and viscous flow is the dominant densification mechanism. The influence of heating rate is dependent on the structure of the amorphous material. The initial stage sintering of powders prepared from *melted glass* show good agreement with the predictions of Frenkel's model (see Chapter 8) when the viscosity η is described by a single-valued function of temperature,

$$\eta = \eta_0 \exp \frac{Q}{RT} \quad (12.2)$$

where η_0 is a constant, Q is the activation energy, R is the gas constant, and T is the absolute temperature (4). For a broader range of density, Scherer's cylinder model provides a good representation of the sintering kinetics. With increasing heating rate, the shrinkage or densification curves for glass powders shift to higher temperatures. This is because at a higher heating rate the glass has less time for densification at a given temperature.

The densification of *gels* during constant heating rate sintering depends on the gel structure (5,6). *Particulate gels* show behavior similar to that for compacts formed from powders of melted glass. The viscosity can be described by a single-valued function of temperature, and the sintering data can be well represented by the theories for viscous sintering. On the other hand, *polymeric gels* do not show good agreement with the theoretical predictions, regardless of the geometri-

cal model used. As an example, Fig. 12.7 shows a comparison of the shrinkage data with the predictions of Scherer's cylinder model (see Chapter 8) for a multi-component gel sintered at heating rates of 0.5, 1, and 3°C/min. The predicted values were calculated by assuming a constant activation energy for viscous flow (~ 500 kJ/mol) throughout the densification process. The approach fails because the viscosity of the gels is not a single-valued function of the temperature. The apparent activation energy depends on the hydroxyl content of the gel, which varies with temperature and time, so the viscosity changes with time and temperature. The densification kinetics therefore depend on the thermal history and not just the current temperature.

The effect of heating rate is of considerable interest and importance for the sintering of gels. Particulate gels, as outlined earlier, show normal behavior where the shrinkage curves shift to higher temperatures with increasing heating rate. For polymeric gels, the behavior depends on the interplay between the hydroxyl content of the gel (which influences the viscosity) and the time available for sintering. It is commonly observed that above a certain value of the heating rate, the shrinkage curves shift to *lower* temperatures with increasing heating rate. This is because the more rapidly heated gel retains more hydroxyl groups, which lower the viscosity and offset the shorter time available for sintering. Isothermal sintering of polymeric gels leads to a rapid increase in the viscosity, so the densification rate decreases drastically. It is therefore advantageous to increase the temperature continuously during sintering so that the rising temperature compensates for the loss of hydroxyl groups and the corresponding increase in the viscosity. The faster the heating rate, the lower the temperature at which densification is completed. However, this applies when crystallization does not interfere with the densification. Extremely fast heating rates can lead to undesirable effects such as incomplete burnout of the organics and trapped gases that expand and cause cracking or bloating of the article. The maximum heating rate must be determined empirically for each gel.

Polycrystalline materials

The constant heating rate sintering of polycrystalline materials is complicated, even for the initial stage, by the occurrence of multiple mechanisms (7). For a wider range of density, the simultaneous occurrence of densification and coarsening must be taken into account. Lange (8) studied the sintering of Al_2O_3 powder compacts at constant heating rates of 2.5 to 20°C/min up to 1500°C and found that for each heating rate, the densification strain rate increased to a maximum at a relative density of ~ 0.8 , followed by a decrease at higher density. It was suggested that densification processes dominated at relative densities below ~ 0.8 , whereas coarsening dominated above this relative density.

The sintering and microstructural evolution of ZnO powder compacts was studied by Chu et al. (9) over a wide range of constant heating rates (0.5 to 15°C/

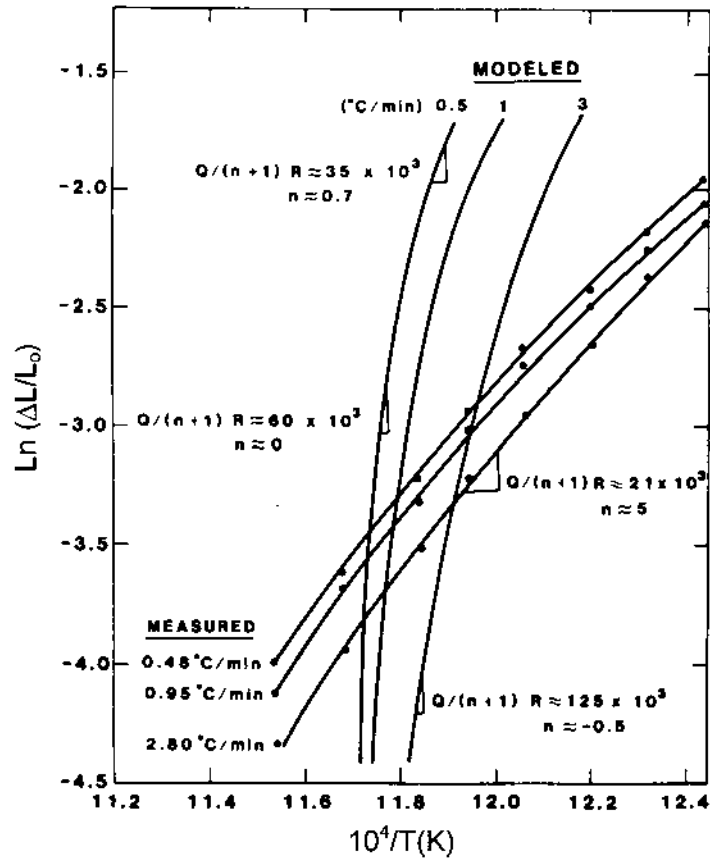


FIGURE 12.7 Natural logarithm of the shrinkage versus the reciprocal of the temperature for a multicomponent gel during constant heating rate sintering: calculated curves (MODELED) and measured data (MEASURED). (From Ref. 5.)

min). The data for the relative density ρ versus temperature T show that the curves are clustered within a fairly narrow band (Fig. 12.8). An interesting observation is that the derivative of the densification strain with respect to T , that is $(1/\rho) d\rho/dT$, for this range of constant heating rates falls on the same *master curve* (Fig. 12.9). A similar observation was made by Lange (8) for the Al_2O_3 data described earlier.

In constant heating rate sintering, the sintering temperature T and the sintering time t are related through the heating rate α by the equation

$$T = \alpha t + T_0 \quad (12.3)$$

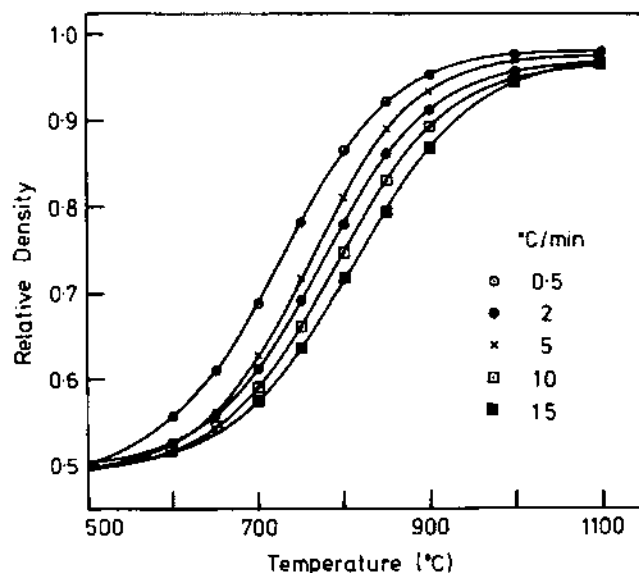


FIGURE 12.8 Relative density versus temperature for ZnO powder compacts with the same initial density (0.50 ± 0.01), sintered at constant heating rates of 0.5–15°C/min. (From Ref. 9.)

where T_0 is an initial temperature. Differentiating Eq. (12.3) gives

$$dT = \alpha dt \quad (12.4)$$

According to Eq. (12.4), the densification rate ($1/\rho$) $d\rho/dt$ can be obtained from the data of Fig. 12.9 by multiplying by α . As Fig. 12.10 shows, the densification rate increases with increasing heating rate. Higher heating rates also lead to a finer grain size (Fig. 12.11). As an indication of the change in grain size, scanning electron micrographs of the compacts sintered to 1100°C show that the grain size is reduced by a factor of ~ 2 when the heating rate is increased from 0.5°C/min to 5°C/min (Fig. 12.12).

A representation of constant heating rate data should take into account the simultaneous occurrence of densification and coarsening. As a first approximation, we can modify the theoretical equations for isothermal sintering to account for the effect of changing temperature on the densification and coarsening processes. Following Eq. (8.118), the linear densification rate (equal to one third the volumetric densification rate) can be written

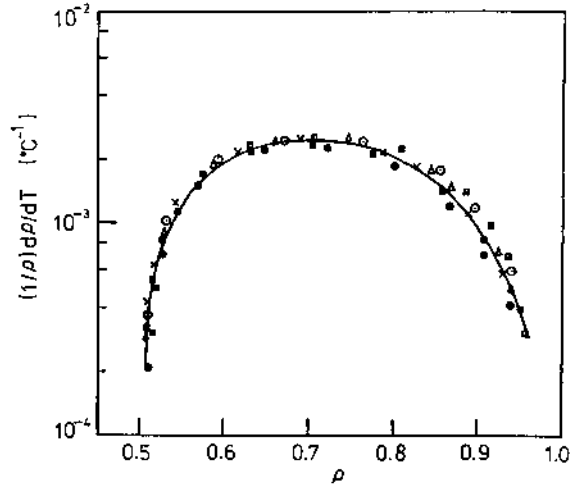


FIGURE 12.9 Change in the densification strain per unit change in temperature as a function of density, determined from the data of Fig. 12.8. The data for the different heating rates fall on the same master curve. (From Ref. 9.)

$$\dot{\epsilon}_\rho = \frac{H_l D(T) \phi^{(m+1)/2} \Sigma}{G^m(T, t) kT} \quad (12.5)$$

where $\dot{\epsilon}_\rho$ is now a function of both temperature and time, H_l is a constant, the diffusion coefficient D is now a function of temperature, ϕ is the stress intensity factor, Σ is the sintering stress, $G(T, t)$ represents a coarsening function that depends on temperature and time, k is the Boltzmann constant, and m is an integer that depends on the diffusion mechanism ($m = 2$ for lattice diffusion and $m = 3$ for grain boundary diffusion). The diffusion coefficient can be written

$$D(T) = D_0 \exp\left(-\frac{Q_d}{RT}\right) \quad (12.6)$$

where D_0 is a constant, R is the gas constant, and Q_d is the activation energy for the densification process. The coarsening function may be expected to have the same form as the grain growth equation [Eq. (9.37)] and for isothermal sintering at a given T can be written as

$$G^m(t) = G_o^m + A \exp\left(-\frac{Q_c}{RT}\right) t \quad (12.7)$$

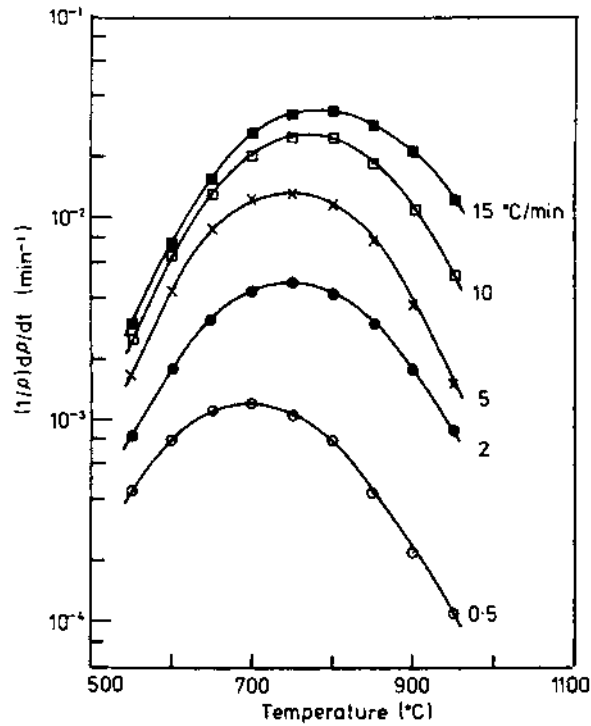


FIGURE 12.10 Densification rate versus temperature determined from the data of Fig. 12.8. Above $\sim 700^\circ\text{C}$, the rate is approximately proportional to the heating rate. (From Ref. 9.)

where G_0 is the initial grain size, A is a constant, and Q_c is the activation energy for the coarsening process. For constant heating rate sintering, Eq. (12.7) can be modified to give the grain size at any temperature and time history:

$$G^m(T, t) = G_0^m + A \int_{t_0}^t \exp\left(-\frac{Q_c}{RT}\right) dt \quad (12.8)$$

Substituting for dt from Eq. (12.4) gives

$$G^m(T, t) = G_0^m + \frac{A}{\alpha} \int_{T_0}^T \exp\left(-\frac{Q_c}{RT}\right) dT \quad (12.9)$$

Since the integral is a function of T only, when $G^m \gg G_0^m$, Eq. (12.9) can be written in the form

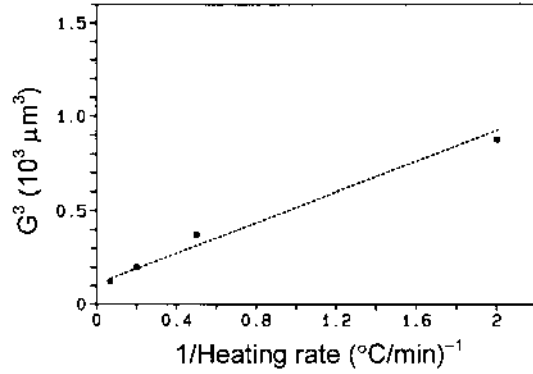


FIGURE 12.11 Cube of the final grain size versus the inverse of the heating rate for ZnO. (From Ref. 9.)

$$G^m \approx \frac{1}{\alpha} F_1(T) \quad (12.10)$$

where $F_1(T)$ is a function of temperature only. At any temperature, G^m is proportional to $1/\alpha$, and when $m = 3$, the grain size data in Fig. 12.11 satisfy this relation.

The densification rate follows from Eq. (12.5) for the known relationship for $G(T, t)$. When $G^m \gg G_0^m$, Eq. (12.10) can be used and the densification rate becomes

$$\dot{\epsilon}_p \approx \alpha F_2(T) \quad (12.11)$$

where $F_2(T)$ is a function of temperature only. The densification rate at any temperature is predicted to be proportional to the heating rate α , which is consistent with the data shown in Fig. 12.10 for T greater than $\sim 700^\circ\text{C}$. To find the density, Eq. (12.11) must be integrated, giving

$$\frac{1}{3} \int_{\rho_0}^{\rho} \frac{d\rho}{\rho} \approx \alpha \int_{t_0}^t F_2(T) dt \quad (12.12)$$

Substituting for dt from Eq. (12.4) gives

$$\frac{1}{3} \ln \frac{\rho}{\rho_0} \approx \int_{T_0}^T F_2(T) dT \quad (12.13)$$

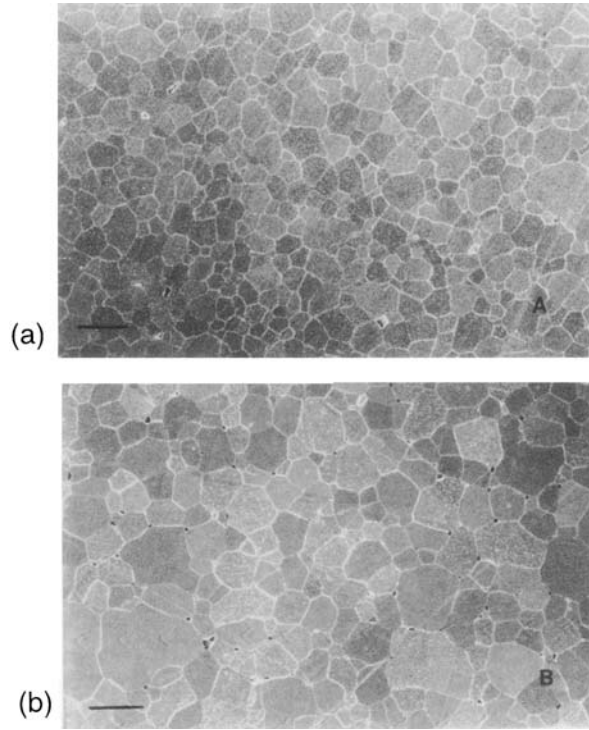


FIGURE 12.12 Scanning electron micrographs of polished and etched surfaces of ZnO powder compacts sintered to 1100°C at constant heating rates of (a) 5°C/min and (b) 0.5°C/min. (From Ref. 9.)

According to this equation, for compacts with the same green density ρ_0 , the density at any temperature is independent of the heating rate and is a function of the temperature only. This result shows good agreement with the density data in Fig. 12.8.

Master Sintering Curve

Experimentally, it is found that Σ is approximately constant and that ϕ is a function of the density only (see Chapter 8). For a given powder consolidated to a given green microstructure, if it is assumed that the grain size is dependent on the sintered density only, then, with slight rearrangement, Eq. (12.5) becomes

$$\frac{k}{H_1 D_0 \Sigma} \int_{\rho_0}^{\rho} \frac{G^m(\rho)}{3\rho\phi^{(m+1)/2}(\rho)} d\rho = \int_{t_0}^t \frac{1}{T} \exp\left(-\frac{Q_d}{RT}\right) dt \quad (12.14)$$

The integral on left-hand side of Eq. (12.14) contains density-dependent terms only and can be taken to quantify the effects of the microstructure on densification, whereas the right-hand side depends only on Q and the temperature–time schedule. Putting

$$F(\rho) = \frac{k}{H_1 D_o \Sigma} \int_{\rho_o}^{\rho} \frac{G^m(\rho)}{3\rho\phi^{(m+1)/2}(\rho)} d\rho \quad (12.15)$$

and

$$\Theta(T, t) = \int_{t_o}^t \frac{1}{T} \exp\left(-\frac{Q_d}{RT}\right) dt \quad (12.16)$$

then Eq. (12.14) can be written

$$F(\rho) = \Theta(T, t) \quad (12.17)$$

The relationship between ρ and $F(\rho)$ is referred to as the *master sintering curve*.

One way to construct a master sintering curve is to determine the grain size–density trajectory and the relationship for $\phi(\rho)$, followed by integration of the combined functions in Eq. (12.15). A simpler procedure is to make use of the equality in Eq. (12.17). This is the approach taken by Su and Johnson (10) who used a different formulation of the sintering model equation corresponding to Eq. (12.5). The master sintering curve can be constructed from a series of sintering experiments for different times or temperatures. Each experiment gives the measured value of ρ and the corresponding value of $\Theta(T, t)$ found by performing the integration shown in Eq. (12.16) for the temperature–time schedule if Q is known or can be approximated. The most economical method of generating the master sintering curve is to perform constant heating rate sintering experiments at four or five heating rates using a dilatometer. Figure 12.13 shows the master sintering curve determined from the data for ZnO shown in Fig. 12.8.

Once the master sintering curve has been determined for a particular powder system, it can be used to predict the sintering behavior of similar powder compacts under arbitrary temperature–time schedules. In this way, it can serve a useful function for designing sintering schedules to reach a required final density. However, the limitations of the procedure should be understood if it to be used effectively in practice. The procedure can be applied only to compacts of the same starting powder which have been consolidated to the same green density by the same forming method. It is also assumed that the grain size and geometrical parameters are dependent on the density only and that one diffusion mechanism dominates in the sintering process.

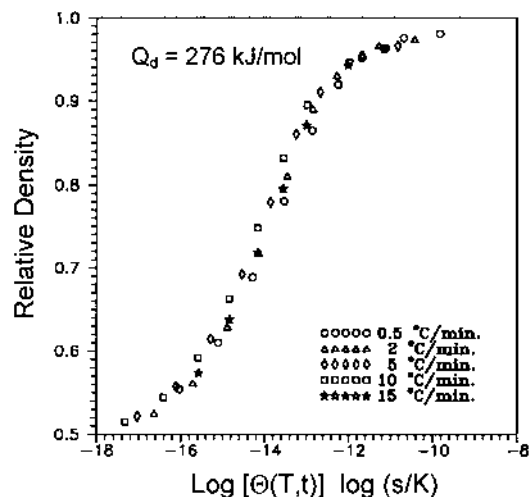


FIGURE 12.13 Master sintering curve for ZnO constructed from the data in Fig. 12.8. (From Ref. 10.)

Multistage Sintering

Multistage sintering, involving the introduction of extended temperature plateaus or more complex temperature–time schedules, is often used in practice to achieve specific chemical or microstructural features. An example is the sintering of the ion-conducting ceramic sodium beta-alumina, in which the sintering schedule consists of two separate peak temperatures (11). Optimum results for the microstructure and strength are obtained in this case by reducing the sintering temperature by $\sim 150^\circ\text{C}$ after reaching the first peak temperature of $\sim 1500^\circ\text{C}$.

As described in Chapter 11, the use of a *two-step sintering* technique by Lin et al. (12) and Chu et al. (13) produced a reduction in the average grain size and an improvement in the microstructural homogeneity of ZnO, MgO, and Al_2O_3 . The first stage consists of an extended hold at a temperature below the onset of shrinkage (50 h at 800°C for Al_2O_3) where the occurrence of a limited amount of coarsening, presumably by surface diffusion or vapor transport, has the effect of improving the homogeneity of the porous powder compact. In the second stage, sintering of the homogenized microstructure at normal temperatures results in the refinement of the microstructure. Excessive coarsening in the first stage should be avoided, and this is commonly achieved through trial and error to determine the optimum conditions of time and hold temperature.

Fast Firing

Fast firing is an example of heating cycle control where the powder compact is subjected to short firing at high temperature (e.g., 10 min at 1800–1900°C for Al_2O_3). The process has been shown to be effective for achieving high density and fine grain size in several ceramics (e.g., Al_2O_3 and BaTiO_3) but because of the rapid heating, the process is suitable only for the production of small or thin-walled articles. The powder compact is pushed through a short (5–10 cm) hot zone in a tube furnace, such as that shown in Fig. 12.1, at constant speeds ranging from ~ 0.25 to ~ 20 cm/min. The temperature of the hot zone and the speed at which the sample is pushed through determine the rate of heating of the sample.

The concept underlying fast firing, put forward by Brook (14), was outlined in Chapter 9. The most favorable situation is one where the activation energy for densification is greater than that for coarsening, so that at higher temperatures the densification rate is faster than the coarsening rate. The faster the sample is heated through the low temperature region where the ratio of densification rate to coarsening rate is unfavorable, the better the expected result. The argument therefore is for the use of rapid heating and short firing times at high temperature.

To predict which powder systems are expected to benefit from the use of fast firing, it is necessary to know the controlling mechanism for the processes of densification and coarsening and, in addition, to have reliable data for the activation energies for the appropriate diffusion coefficients. In most cases, this information is unavailable or incomplete. The best way to determine the effectiveness of the fast firing technique is therefore to try it. However, some data can be found for a few systems and it is worth considering the effectiveness of fast firing in these systems.

For Al_2O_3 , the densification mechanism for fine powders at moderate to high temperatures is that of lattice diffusion of the cation with an activation energy of 580 kJ/mol. The surface diffusion activation energies derived from sintering studies are relatively low (230–280 kJ/mol). On this basis, fast firing should work for Al_2O_3 . In practice, fast firing is indeed found to be effective for the production of Al_2O_3 with high density and fine-grained microstructure, as the data in Fig. 9.51 show (15).

For MgO , activation energies for surface diffusion range from 360 to 450 kJ/mol and those for cation lattice diffusion (believed to be the rate controlling densification mechanism) range from 150 to 500 kJ/mol. The activation energies for lattice diffusion determined from sintering studies cover a narrower range (250 to 500 kJ/mol) but are still not precise enough to avoid an overlap with the surface diffusion values. As the grain size increases, densification by oxygen diffusion in the grain boundary is believed to become significant. The activation energy for the oxygen diffusion mechanism is in the range of 250 to 300 kJ/mol, which is significantly lower than that for surface diffusion. For densification

controlled by the grain boundary diffusion of oxygen, firing to higher temperature will clearly lead to a reduction in ratio of the densification rate to the coarsening rate (an effect opposite to the one desired). While the information for the rate controlling mechanism and activation energies are fairly imprecise, experiments show that fast firing is ineffective for MgO. This finding is consistent with the general argument.

Fast firing has also been used successfully to produce dense BaTiO_3 ceramics with a fine-grained microstructure (16). The fast fired samples contained smaller grains at a given density compared with those prepared by conventional sintering (Fig. 12.14). For this system, information on the mechanisms of densification and coarsening and the activation energies is incomplete.

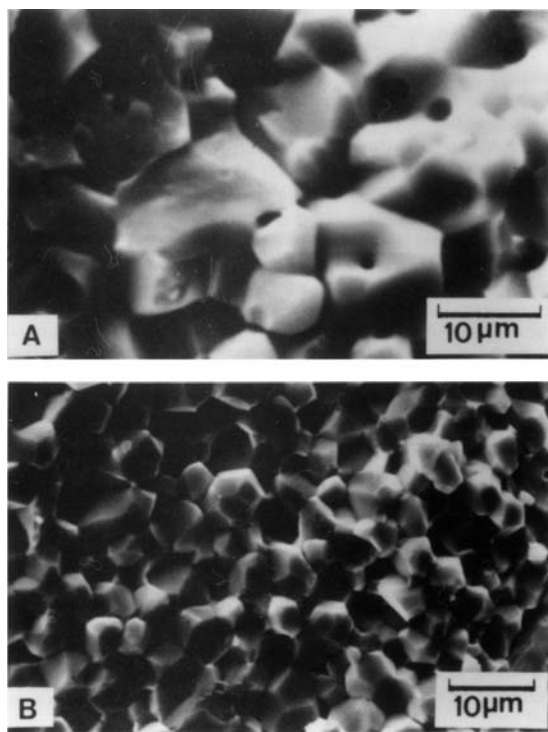


FIGURE 12.14 Scanning electron micrographs of the fractured surfaces of BaTiO_3 materials containing 2 mol% excess BaO (A) conventionally sintered at 1370°C for 26 h and (B) fast-fired at 1470°C for 5 min. (From Ref. 16.)

Rate-Controlled Sintering

In rate-controlled sintering, the densification rate is coupled with the temperature control of the sintering furnace in such a way as to keep the shrinkage rate (or densification rate) at a constant value or below a given value (17,18). The result is a fairly complicated temperature schedule that at times approaches the multi-staged sintering schedules. Whereas the underlying mechanisms of rate-controlled sintering are not fully understood, beneficial effects on microstructure have been reported for several ceramics, including cases where chemical reactions occur during densification (19,20). Manipulation of the temperature schedule is necessarily limited by the thermal impedance of the sintering furnace and by the size of the ceramic sample.

12.2.3 Sintering Atmosphere

The sintering atmosphere can have several important effects on densification and microstructural development during sintering, and in many instances, it can have a decisive effect on the ability to reach high density with controlled grain size. Atmosphere is not directly considered in the sintering models, but the theories can provide a basis for understanding the effects arising from atmospheric conditions. The important effects are associated with both physical phenomena, as in the case of the atmospheric gas trapped in isolated pores in the final stage of sintering, and chemical phenomena, particularly when the volatility, ionic oxidation state, and defect chemistry of the system can be modified.

Gases in Pores

In the final stage of sintering, gas from the atmosphere (or from volatile species in the solid) gets trapped when the pores pinch off and become isolated. At the point when the pores become isolated, the pressure of the trapped gas is equal to the pressure of the sintering atmosphere. Further sintering is influenced by the solubility of the gas atoms in the solid, as has been demonstrated by Coble (21) in the sintering of Al_2O_3 . Coble found that that MgO-doped Al_2O_3 can be sintered to theoretical density in vacuum or in an atmosphere of H_2 or O_2 , which diffuse out to the surface of the solid, but not in He, Ar, or N_2 (or, therefore, air), which have a limited solubility in Al_2O_3 .

Information on the diffusivity of gases in ceramics is normally not available, so it is difficult to predict the effects of a given gas trapped in the pores. However, interstitial diffusion is expected to be more favorable for smaller molecules (e.g., H_2 and He) than for larger ones (e.g., Ar and N_2). Diffusion of larger molecules may occur by a vacancy mechanism, but this will depend on the stoichiometry of the solid. Diffusion along the disordered grain boundaries can provide an easier

path for smaller as well as larger molecules. Whenever it can be used, vacuum sintering (at least to the onset of pore closure) eliminates the problem of trapped gases.

When the gas has a high solubility in the solid, the densification rate is unaffected by the gas trapped in the pores because rapid diffusion through the lattice or along the grain boundaries can occur during shrinkage. For an insoluble gas, as shrinkage of the isolated pores takes place, the gas is compressed and its pressure increases. Shrinkage stops when the gas pressure becomes equal to the driving force for sintering. Assuming for simplicity that the pores are spherical, the limiting density is reached when the gas pressure p in the pores is given by

$$p = \frac{2\gamma_{sv}}{r} \quad (12.18)$$

where γ_{sv} is the specific energy of the solid–vapor interface, and r is the limiting pore size. For an idealized microstructure in which the solid phase is a continuum and the pores have the same radius r , the limiting porosity P can be easily estimated. Applying the gas law $p_1V_1 = p_2V_2$ to the initial situation (when the pores just become isolated) and to the limiting situation (when shrinkage stops) gives

$$p_o N \left(\frac{4}{3} \pi r_o^3 \right) = p N \left(\frac{4}{3} \pi r^3 \right) \quad (12.19)$$

where N is the number of pores per unit volume, p_o is the pressure of the sintering atmosphere, and r_o is the radius of the pores when they become isolated. Substituting for p from Eq. (12.18) gives

$$p_o r_o^3 = 2\gamma_{sv} r^2 \quad (12.20)$$

The porosity P_o when the pores become isolated and the limiting porosity P are related by

$$\frac{P_o}{P} = \frac{r_o^3}{r^3} \quad (12.21)$$

Substituting for r from Eq. (12.20), after some rearrangement, Eq. (12.21) gives

$$P = P_o \left(\frac{p_o r_o}{2\gamma_{sv}} \right)^{2/3} \quad (12.22)$$

According to this equation, the limiting porosity is controlled essentially by the pressure of the sintering atmosphere and by the radius of the pores when they become pinched off. In practice, sintering in a vacuum (where applicable) and

homogeneous packing of fine particles (giving fine pores) can improve the final density.

For a slightly soluble gas trapped in the pores, the diffusivity of the gas in the solid becomes low enough that it cannot escape to the surface in the time scale for sintering, but it is possible that diffusion of the gas between neighboring pores can occur. In this case, the final stage sintering can be idealized as follows. After the pores become isolated, densification will become progressively slower because of the increasing gas pressure in the shrinking pores. Eventually a limiting density will be reached at which densification almost stops because the gas pressure in the pores is equal to the driving force for sintering. Any further changes during sintering will be controlled by the exchange of gases between the neighboring pores. In general, there will be a distribution of pore sizes in the solid. Considering a small pore near a large pore (Fig. 12.15), initially, when the limiting density is reached, the pressure p_l in the large pore is given by

$$p_l = \frac{n_l kT}{V_l} = \frac{2\gamma_{sv}}{r_l} \quad (12.23)$$

where n_l is the number of molecules of gas in the large pore of radius r_l and volume V_l . Because of the higher gas pressure in the small pore, there will be a net diffusion of gas molecules from the small pore to the large pore. If n_s molecules of gas are transferred to the large pore, the new gas pressure in the large pore is

$$p'_l = \frac{(n_l + n_s)kT}{V_l} > \frac{2\gamma_{sv}}{r_l} \quad (12.24)$$

Since the gas pressure becomes greater than the driving force for sintering, the large pore must expand. The expansion of the large pore is greater than the

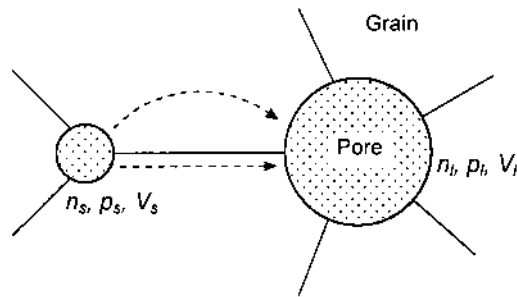


FIGURE 12.15 Sketch showing the parameters for two neighboring pores filled with a slightly soluble gas. A net diffusion of gas occurs from the small pore to the large pore.

shrinkage of the small pore so that the overall result is an increase in porosity. For this system, the densification behavior goes through a maximum, as sketched in Fig. 12.16. This decrease in density after the maximum value is referred to as *swelling* (or bloating).

For polycrystalline solids, additional effects must be considered. The location of the pores will influence the gas diffusion path. When the pores are located within the grains, diffusion will depend on the gas solubility in the crystal lattice. For the more common case in which the pores are located at the grain boundaries, diffusion of the gas through the disordered grain boundary region provides an important additional path.

When microstructural coarsening occurs with a slightly soluble or insoluble gas trapped in the pores, pore coalescence can also lead to swelling. Consider two spherical pores of radius r_1 , each containing n_1 molecules of an insoluble (or slightly soluble) gas. At the limiting situation when shrinkage stops, the gas pressure in each pore is given by

$$p_1 = \frac{2\gamma_{sv}}{r_1} = \frac{n_1 kT}{V_1} \quad (12.25)$$

The volume of the pore V_1 is equal to $(4/3)\pi r_1^3$, and substituting into Eq. (12.25) gives

$$r_1 = \left(\frac{3n_1 kT}{8\pi\gamma_{sv}} \right)^{1/2} \quad (12.26)$$

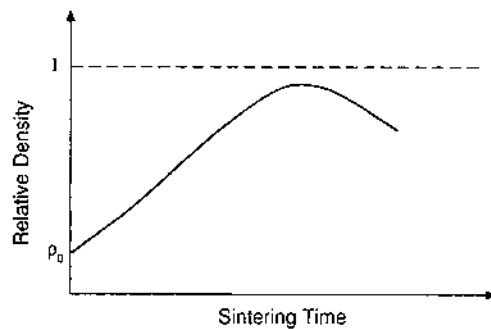


FIGURE 12.16 Schematic diagram showing the densification of a powder compact with a slightly soluble gas in the pores. The density goes through a maximum with time, as a result of sintering with the trapped gas in the pores.

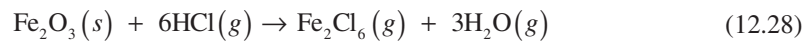
When the two pores coalesce as a result of grain growth to form a single pore with a radius r_2 , this pore contains $2n_1$ molecules of gas and the limiting condition when it stops shrinking is given by

$$r_2 = \left(\frac{6n_1 kT}{8\pi\gamma_{sv}} \right)^{1/2} \quad (12.27)$$

Equations (12.26) and (12.27) show that $r_2 = \sqrt{2}r_1$, so the volume V_2 , is $2\sqrt{2}V_1$, which is greater than $2V_1$, the original volume of the two pores. This means that after coalescence, the pore will expand, giving rise to swelling and a decrease in density, as sketched in Fig. 12.16. Swelling is also commonly observed when relatively dense ceramics, previously hot pressed in a carbon die (or furnace), are annealed in an oxidizing furnace (22). Carbon and sulfur impurities react with O_2 gas diffusing along the grain boundaries from the atmosphere to form insoluble gases such as CO, CO_2 , and SO_2 , and the pressures generated by these gases are high enough to produce voids in the structure.

Vapor Transport

The heating schedule, as described earlier, provides an important process parameter for controlling the relative rates of densification and coarsening during sintering. Enhanced vapor transport, produced by changing the composition or partial pressure of the gas in the sintering atmosphere, can provide another key process parameter for microstructural control, as demonstrated by the work of Readey et al. (23–26), who studied the sintering of several oxides in reducing atmospheres. The gas in the atmosphere reacts with the powder to produce gaseous species that enhance vapor transport. An example is the sintering of ferric oxide, Fe_2O_3 , in an atmosphere of HCl gas. The reaction can be described as follows:



The gaseous Fe_2Cl_6 produced in the reaction leads to enhanced vapor transport. Figure 12.17 shows the data for the shrinkage as a function of time at $1000^\circ C$ for various partial pressures of HCl. Densification decreases as the partial pressure of the HCl and, hence, the rate of vapor transport increase. For HCl pressures in excess of 10^{-2} MPa (0.1 atmosphere), shrinkage is almost completely inhibited. As Fig. 12.18 shows, the decrease in densification is caused by coarsening of the microstructure.

Water Vapor in the Sintering Atmosphere

Several studies have shown that water vapor in the atmosphere can also lead to a modification of the densification to coarsening ratio. For Al_2O_3 , it was found that when compared to sintering in dry H_2 , sintering in H_2 containing water vapor

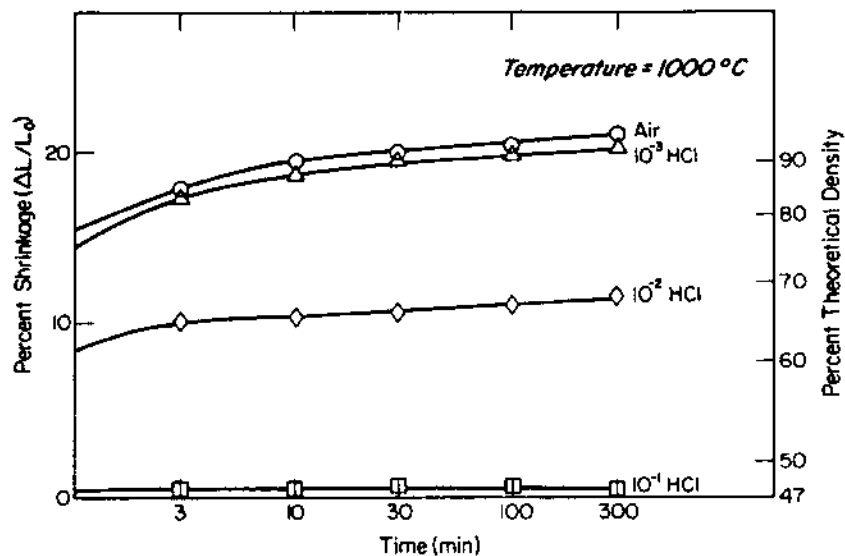


FIGURE 12.17 Shrinkage versus time for Fe_2O_3 powder compacts sintered at 1000°C in different partial pressures of HCl. (From Ref. 23.)

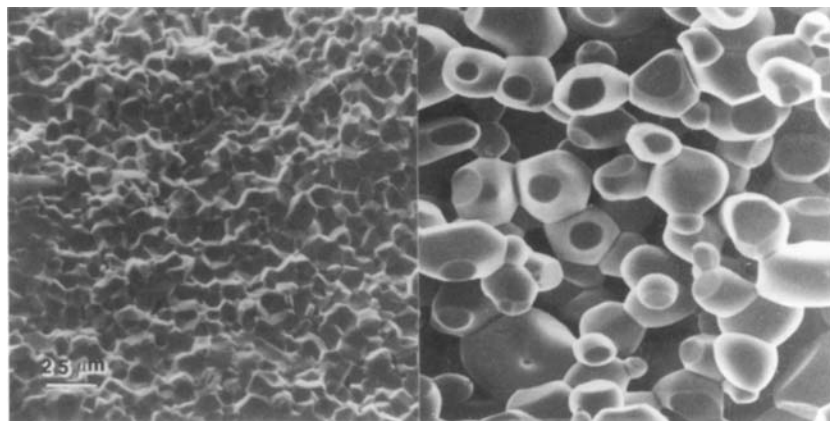


FIGURE 12.18 Scanning electron micrographs of fractured surfaces of Fe_2O_3 powder compacts sintered for 5 h at 1200°C in air (left) and 10% HCl (right). (From Ref. 23.)

enhanced the densification rate but reduced the coarsening rate during final stage densification (27). The overall result is an enhancement of the densification to coarsening ratio in H_2 containing water vapor, so the grain size versus density trajectory is displaced to higher density for a given grain size.

In the case of MgO, the rates of densification and coarsening are both found to be enhanced by water vapor in the sintering atmosphere. Figure 12.19 shows the densification data for MgO powder compacts at various temperatures in static dry air and in flowing water vapor (28). A comparison of the data at any given temperature shows faster densification in water vapor. The trajectories for grain size versus relative density for undoped MgO obtained in the same experiments (Fig. 12.20) show that water vapor causes a slight enhancement in the grain size at any density in the intermediate stage (relative density $\rho \approx 0.72$ –0.85) but a reduction at higher density. The increased coarsening rate in MgO appears to be caused by enhanced surface diffusion (29), but the mechanism for the enhanced densification is unclear. Changes in the diffusivity and the interfacial energies (surface and grain boundary energies) appear to be the key factors responsible for the enhanced densification.

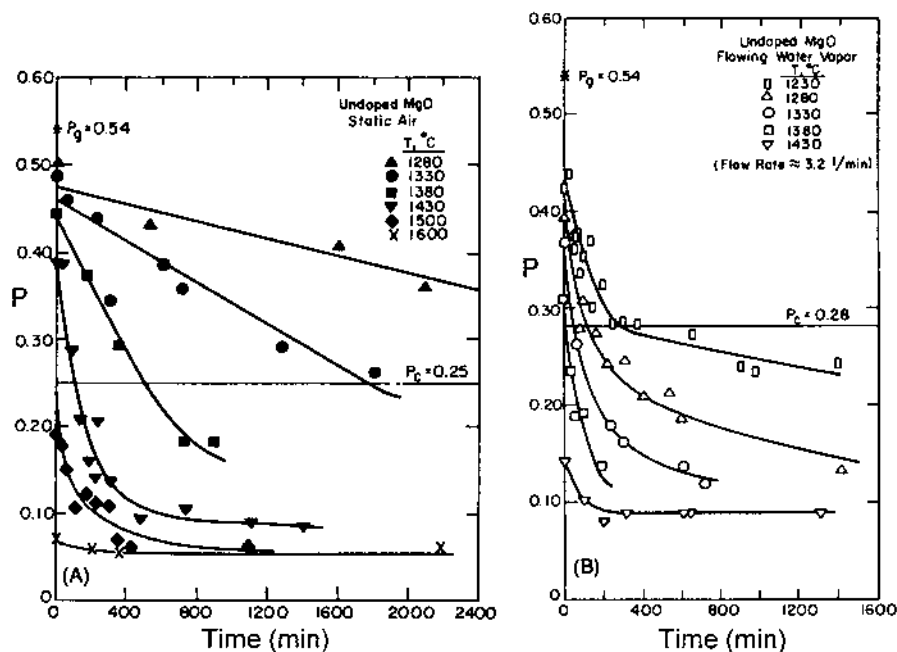


FIGURE 12.19 Porosity versus time for MgO powder compacts sintered at different temperatures in (A) static air and (B) flowing water vapor. (From Ref. 28.)

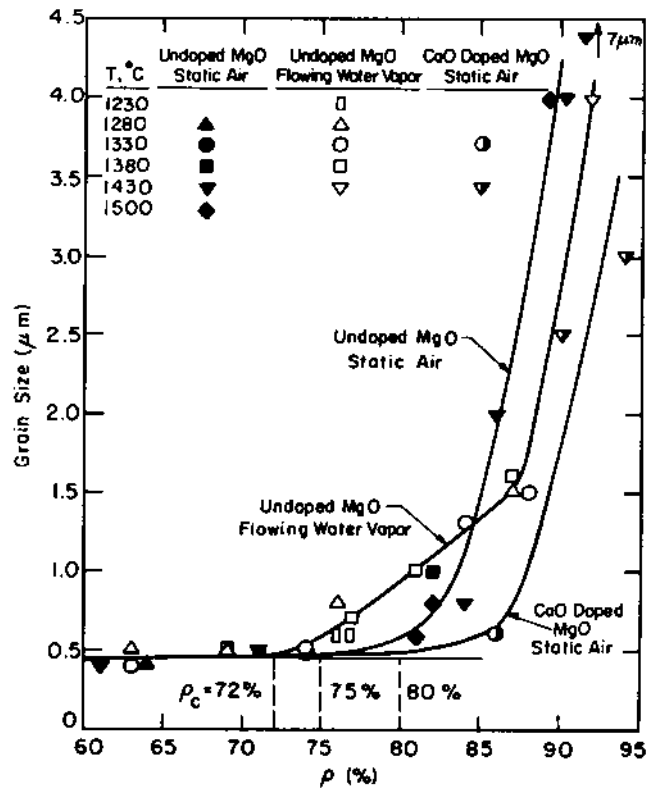


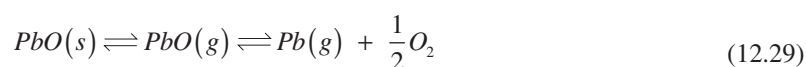
FIGURE 12.20 Grain size versus relative density for MgO powder compacts sintered in air and in flowing water vapor and for CaO-doped MgO powder compacts in static air. (From Ref. 28.)

Volatilization and Decomposition

For some powder compositions, such as sodium β -alumina and lead-based electroceramics, evaporation of volatile components (e.g., Na and Pb) can occur during sintering, thereby making it difficult to control the chemical composition and the microstructure of the sintered material. A common solution is to surround the powder compact with a coarse powder having the same composition as the compact, which leads to the establishment of an equilibrium partial pressure of the volatile component, thereby reducing the tendency for evaporation from the powder compact. As an example of this approach, Fig. 12.21 shows a schematic illustration of the system used for the sintering of sodium β -alumina in a labora-

tory scale experiment. The ceramic is a good ionic conductor at temperatures even below 300°C and is used as a solid electrolyte in sodium-sulfur batteries that have electrodes of molten sulfur and sodium polysulfides. The sample surrounded by the coarse powder is encapsulated in an alumina or platinum tube. The alumina tube is much cheaper than the platinum, but due to the reaction with the powder, it can be used only a few times before falling apart. For extended use, platinum may have an advantage in overall cost.

Evaporation of PbO in lead-based electroceramics can be represented as (30)



Lead is poisonous, so that in addition to controlling the lead loss, the evaporated lead must be contained. In practice, this is achieved by surrounding the sample with lead-based powder compositions (31), such as a mixture of PbO and PbZrO₃ for lead-lanthanum-zirconium titanate (PLZT), to provide a positive vapor pressure in a closed Al₂O₃ crucible (Fig. 12.22). With the controlled atmosphere apparatus, PLZT can be sintered to full density (Fig. 12.23), yielding materials with a high degree of transparency.

For many systems, sintering must be carried out at temperatures where the decomposition of the powder becomes important. If the rate of decomposition is high, the porosity generated by the weight loss limits the attainment of high density. Generally, the weight loss during sintering should be kept below a few percent if high density is to be achieved. Silicon nitride (Si₃N₄) is a good example of a system in which the effects of decomposition are important. It shows significant decomposition at the high temperatures (1700–1900°C) required for densification. The decomposition reaction can be written as

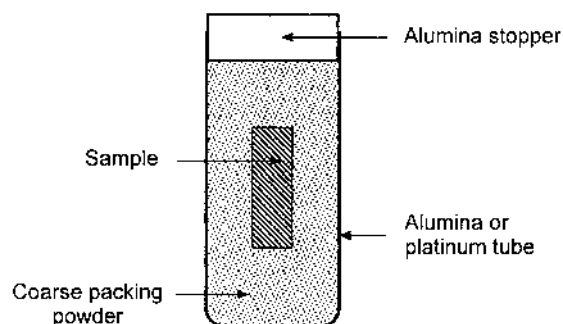


FIGURE 12.21 Laboratory scale apparatus for the sintering of sodium β-alumina.

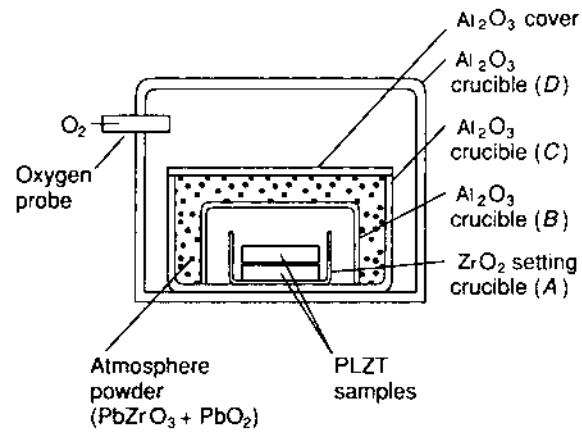


FIGURE 12.22 Apparatus for the sintering of lead lanthanum zirconium titanate (PLZT) in controlled atmosphere. (From Ref. 31.)

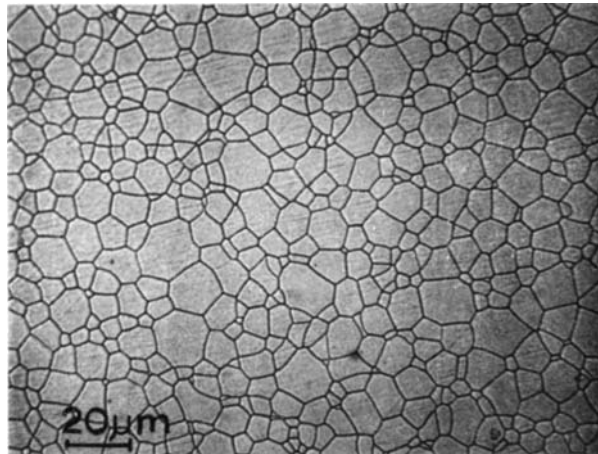


FIGURE 12.23 Scanning electron micrograph of PLZT microstructure produced by sintering in controlled atmosphere. (From Ref. 31.)

The vapor pressure of the N_2 gas generated by the decomposition is ~ 0.1 atmosphere at 1700°C and increases to ~ 1 atmosphere at 1875°C , so significant weight loss can occur if the decomposition is not controlled. One solution is to surround the sample with a powder of the same composition in a closed graphite crucible under N_2 gas at normal atmospheric pressure. A better method involves raising the N_2 gas pressure in the sintering atmosphere (to values of 10–20 atm or higher) so that the reaction in Eq. (12.30) is driven to the left (32). Nitrogen gas has a fairly high solubility in Si_3N_4 so that the unfavorable sintering effects produced by gasses trapped in pores are avoided even for such high gas pressures.

Oxidation Number

The sintering atmosphere influences the oxidation state of certain cations, particularly those of the transition elements (e.g., Cr), and control of the oxidation state has been shown to have a significant effect on the densification of chromium-containing oxides (33–36). Figure 12.24 shows the porosity of three chromites as a function of oxygen partial pressure in the atmosphere after sintering for 1 h at temperatures in the range 1600 – 1740°C . The chromites show little densification if the oxygen partial pressure is greater than $\sim 10^{-10}$ atm, but relative densities of 99% or greater are obtained by sintering in an oxygen partial pressure of $\sim 10^{-12}$ atm when the Cr ion is stabilized in its trivalent state (as Cr_2O_3). At oxygen partial pressures greater than $\sim 10^{-12}$ atm, Cr_2O_3 becomes unstable and vaporizes as CrO_2 or CrO_3 , and the high vapor pressure enhances evaporation/condensation processes, leading to neck growth and coarsening but little densification.

The *valence* of an atom is equal to the number of bonds it forms in the most satisfactory formulation of the substance. For example, the valence of the oxygen atom is 2. On the other hand, *oxidation number* (or oxidation state) is based on an ionic view of the substance and is the charge on an atom in the most plausible ionic formulation of the substance. Often the valence and the magnitude of the oxidation number are the same, as in MgO , in which the oxidation state of the oxygen atom is -2 . However, many atoms form stable compounds where the oxidation state is different from the valence. In the case of Cr, the principal oxidation numbers of the chromium atom are $+6$ (for example, in CrO_3), $+4$ (CrO_2), $+3$ (Cr_2O_3), $+2$ (CrO), and 0 (Cr metal). The oxidation number of the Cr atom changes readily from $+6$ in an atmosphere with a high oxygen partial pressure to $+4$, $+3$, $+2$, and finally 0 as the oxygen partial pressure decreases. Each oxidation state, except for the $+3$ state, corresponds to an oxide with a fairly high vapor pressure, so in the case of Cr_2O_3 , sintering must be carried out in an atmosphere in which Cr atoms are maintained in the $+3$ oxidation state if high density is to be achieved.

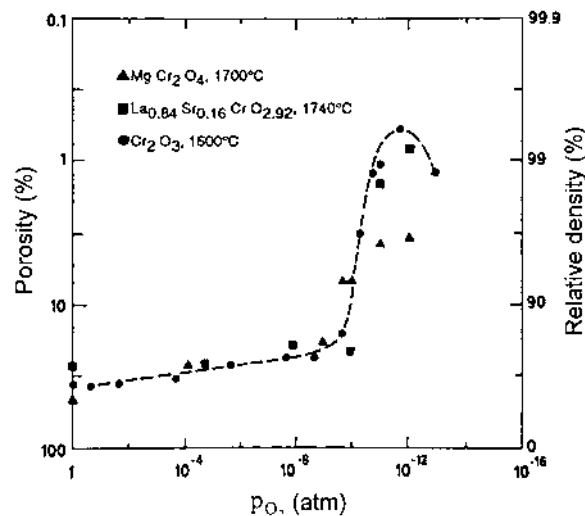


FIGURE 12.24 Final porosity versus oxygen partial pressure in the atmosphere for sintered chromites. (From Ref. 35. Courtesy of H. U. Anderson.)

The conditions for thermal stability of a substance can be calculated from standard thermochemical data. The results are most usefully plotted on an *Ellingham diagram*. Figure 12.25 shows an example of the calculations for the chromium oxide system (34). The standard free energy of formation (per mole of oxygen) for three oxides is plotted versus temperature. Also shown (on the right) are the oxygen partial pressure (in atmospheres) in equilibrium with the reactions and the partial pressures of the gas mixtures (H_2 –water vapor and CO – CO_2) required to produce the desired oxygen partial pressure. For example, Fig. 12.25 indicates that at 1600°C (the vertical line), the oxygen partial pressure must not be below $10^{-11.7}$ (or 2×10^{-12}) atm if reduction of Cr_2O_3 to Cr is to be avoided (the lowest diagonal line). The maximum density in Fig. 12.24 (99.4% of the theoretical value) is achieved when the oxygen partial pressure is $\sim 2 \times 10^{-12}$ atmosphere, a value that corresponds to the equilibrium partial pressure of oxygen between Cr_2O_3 and Cr.

As shown in Fig. 12.24, the oxidation state control used for the sintering of Cr_2O_3 can also be applied to other chromites. However, the dramatic effects of oxidation state control observed for the chromites have not been repeated for other ceramic systems, so the approach appears to have limited applicability. The use of TiO_2 as a dopant (37) allows the sintering of Cr_2O_3 to be carried out at a significantly higher oxygen partial pressure and (10^{-1} atm) and at a lower temperature (1300°C). The mechanism by which TiO_2 operates to modify the sintering

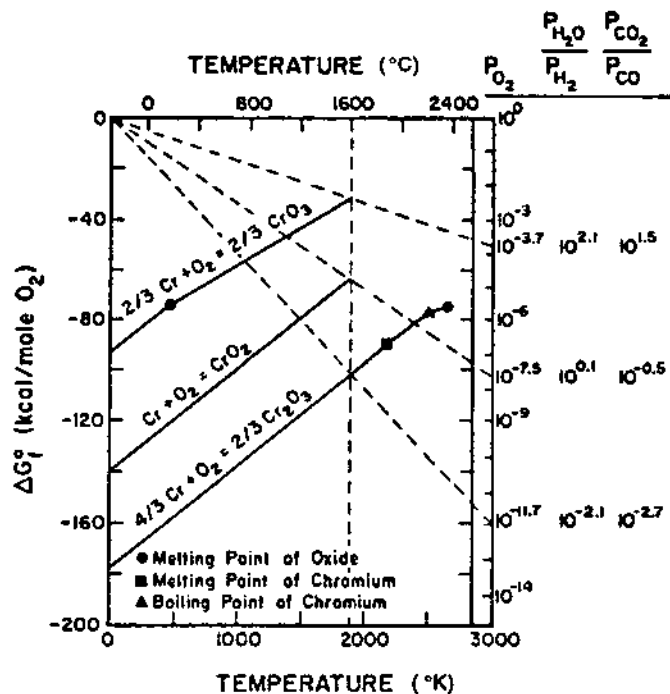


FIGURE 12.25 Standard free energy of formation of chromium oxides as a function of temperature. (From Ref. 34. Courtesy of P. D. Ownby.)

is not clear, but it has been suggested that the Ti^{4+} ions replace the Cr ions that are in an oxidation state greater than 3, thereby suppressing the formation of the volatile oxides CrO_2 and CrO_3 . Another suggestion is the addition of TiO_2 to Cr_2O_3 leads to the formation of chromium vacancies that enhance the sintering rate.

Atmosphere control is also particularly important in the sintering of ferrites for magnetic applications, such as manganese-zinc ferrites and nickel-zinc ferrites, both of which have the spinel crystal structure (38). In addition to limiting the evaporation of the volatile Zn component, the atmospheric conditions must also be controlled to give the right concentration of ferrous iron in the sintered material for achieving the required magnetic properties. The general formula of the stoichiometric compounds can be written $M_{1-x}Zn_xFe_2O_4$, where M represents Ni or Mn. Commercial compositions are often nonstoichiometric and must be carefully formulated to produce the desired properties. The nickel-zinc ferrites, with the general formula, $Ni_{1-x}Zn_xFe_{2-y}O_4$, are formulated with a deficiency of

iron (with y in the range $0 < y < 0.025$) to keep the sensitivity high and the magnetic loss low. The oxidation number of $+2$ is the most stable for both Ni and Zn. The $+3$ state for Fe is stable only if there is a slight deficiency of iron (or excess of oxygen). Nickel-zinc ferrites can therefore be sintered under a wide variety of oxidizing atmospheres (e.g., air or oxygen).

The manganese-zinc system provides an additional degree of complexity in the sintering of ferrites with the spinel structure. The spinel phase is stable only over a certain range of atmosphere and temperature conditions. These ferrites, with the general formula $\text{Mn}_{1-x}\text{Zn}_x\text{Fe}_{2+y}\text{O}_4$, are formulated with an excess of iron ($0.05 < y < 0.20$). The concentration of Fe in the $+2$ oxidation state (i.e., “ferrous iron”) is critical to the achievement of the desired properties of low magnetic loss and a maximum in the magnetic permeability. To produce the desired concentration of ferrous iron ($\text{Fe}^{2+}/\text{Fe}^{3+} \approx 0.05/2.00$), a two-stage firing schedule is employed (Fig. 12.26). The sample is first sintered at a temperature ($1250\text{--}1400^\circ\text{C}$) in an atmosphere of high oxygen partial pressure (0.3 to 1 atm) to minimize the evaporation of zinc. In this stage the densification and grain growth are essentially completed. In the second stage, the sample is annealed at a lower temperature ($1050\text{--}1200^\circ\text{C}$) in an atmosphere with fairly low oxygen partial pressure (50–100 ppm) to establish the desired concentration of ferrous iron. Figure 12.27 shows the compositional path followed in the sintering schedule. During the first stage of the sintering schedule, the ferrite has a composition corresponding to S. In the second stage, equilibrium is quickly reached because of the fairly high annealing temperature; the ferrite attains a different composition (corresponding to A) that depends on the temperature and atmosphere of annealing. Further cooling along C represents additional compositional changes if equilibrium is reached. In practice, with the cooling rates used and the decreasing temperature, the composition does not change significantly on cooling.

Defect Chemistry and Stoichiometry

The sintering behavior of the highly stoichiometric oxides (e.g., Al_2O_3 and ZrO_2) shows little dependence on the oxygen partial pressure over a wide range of values. For other oxides, particularly the transition metal oxides, the oxygen partial pressure can have a significant influence on the concentration and type of lattice defects and, hence, the stoichiometry of the compound. The sintering of these oxides would therefore be expected to depend significantly on the oxygen partial pressure in the atmosphere. Oxygen ions have a significantly larger ionic radius than most cations and are often less mobile, so the diffusion of oxygen ions may often control the sintering rate. Thus an atmosphere that produces an increase in the oxygen vacancy concentration may often enhance sintering. In practice, it is difficult to separate the effects of defect chemistry and stoichiometry

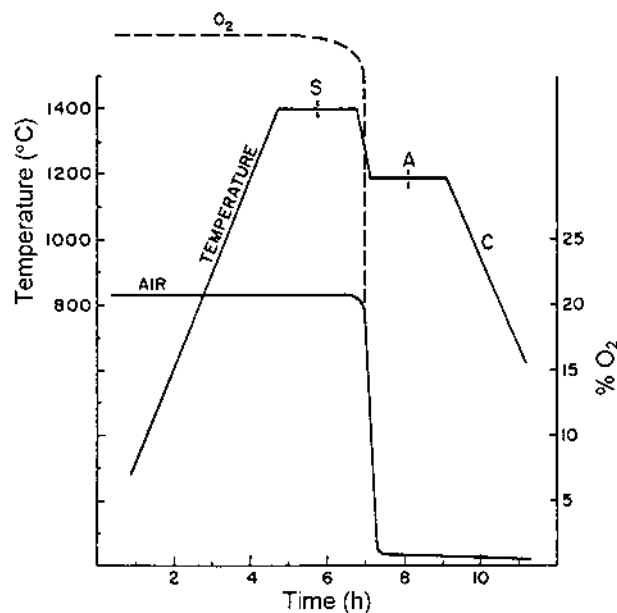


FIGURE 12.26 Schematic firing cycle for manganese zinc ferrites. (From Ref. 38.)

from the those of the nondensifying mechanisms (e.g., vapor transport and surface diffusion) brought about by the change in the atmosphere.

Reijnen (39) found that the sintering of NiFe_2O_4 and NiAl_2O_4 is severely retarded for powder compositions with an excess of Fe or Al and explained the behavior in terms of a reduction in the oxygen vacancy concentration. The densification and grain growth behavior of Fe_3O_4 as a function of oxygen partial pressure was studied by Yan (40) at three different temperatures. The type and concentration of the lattice defects may be expected to vary over the wide range of oxygen partial pressure used in the experiments, but the sintered density is found to be insensitive to the atmosphere (Fig. 12.28a). On the other hand, as shown in Fig. 12.28b, the oxygen partial pressure has a significant effect on the grain growth. High oxygen partial pressure leads to small grain size whereas the grain size is much larger at low oxygen partial pressure. The mechanism is not very clear, but it has been suggested that oxygen lattice diffusion controls the pore mobility. Since oxygen lattice diffusion is faster at lower oxygen partial pressure, an increase in the pore mobility leads to faster grain growth if the boundary mobility is controlled by the pore motion.

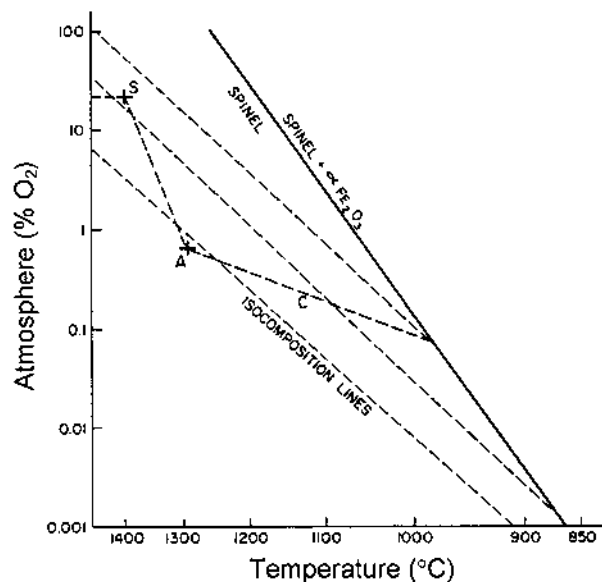


FIGURE 12.27 Schematic representation of the stoichiometry path followed during the firing of manganese zinc ferrites. (From Ref. 38.)

12.2.4 Production of Controlled Sintering Atmospheres

Atmospheres with a variety of compositions and oxygen partial pressures may be required for sintering, and it may also be necessary to control the rate of gas flow through the furnace. In most cases the required gas composition is available commercially (e.g., O_2 , air, N_2 , Ar, He, and H_2). Normally, Ar or He is used to provide an inert atmosphere, but the commercial gases contain a small amount of oxygen (10–100 ppm) and may need to be purified by passing through an oxygen getter prior to entering the furnace. Nitrogen is a common atmosphere for the sintering of nitrides (e.g., Si_3N_4), but some care must be exercised in its use at very high temperatures. It reacts with refractory metal windings and heat shields to form nitrides, thereby shortening the life of the furnace, and it also reacts with graphite to produce poisonous gases. Hydrogen is fairly explosive and must be handled carefully. However, inert gases such as He and Ar containing less than 5% H_2 are not explosive and can be handled safely.

Atmospheres with high oxygen partial pressure can be achieved with O_2 or air, whereas mixtures of O_2 and an inert gas (He, Ar, or N_2) can provide atmospheres with an oxygen partial pressure down to $\sim 10^{-2}$ atm. Lower oxygen

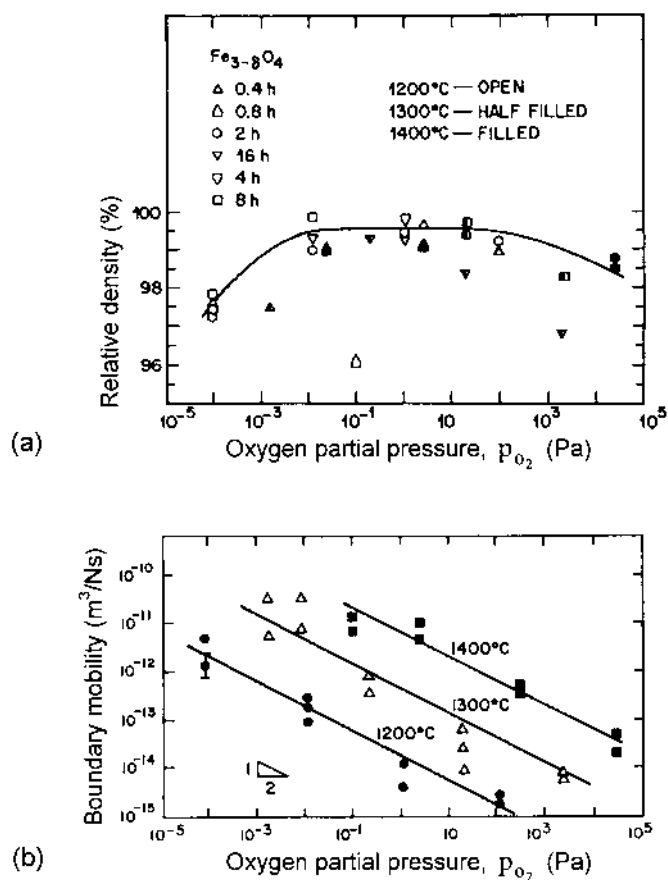


FIGURE 12.28 Data for (a) the relative density and (b) the boundary mobility as a function of the oxygen partial pressure in the atmosphere during the sintering of Fe_3O_4 powder compacts under the conditions of time and temperature indicated. (From Ref. 40.)

partial pressures (below $\sim 10^{-4}$ atm) is commonly obtained by flowing mixtures of gases such as H_2 -water vapor or CO - CO_2 . Care must be exercised in the handling of both gas mixtures because H_2 is explosive and CO is poisonous, so it must be vented properly. Mixing of CO - CO_2 gas is performed prior to admission of the gas into the furnace (e.g., by passing the gases in the correct proportions through a column containing glass beads), and the total gas flow through the furnace must be adjusted to a fixed rate. For control of the oxygen partial pressure with H_2 - H_2O mixtures, H_2 is bubbled through a gas washer containing distilled water at a fixed temperature.

The equilibrium oxygen partial pressure of a mixture at any given temperature is calculated using standard thermodynamic equations and appropriate thermochemical data (41). For example, if an oxygen partial pressure of $10^{-11.7}$ atm at 1600°C is required (as indicated in Fig. 12.25), this can be obtained by establishing the equilibrium



The reaction arises from the following two reactions:



where ΔG° is the standard free energy change for the reaction. For the reaction described by Eq. (12.31), we obtain

$$\Delta G^\circ = -282,400 + 86.81T \text{ J} \quad (12.34)$$

Putting $\Delta G^\circ = -RT \ln K_p$, where K_p is the equilibrium constant for the reaction and $T = 1873\text{K}$ gives $\ln K_p = 7.70$. The equilibrium constant is also given by

$$K_p = \frac{P_{\text{CO}_2}}{P_{\text{CO}}(P_{\text{O}_2})^{1/2}} \quad (12.35)$$

Substituting $p_{\text{O}_2} = 10^{-11.7}$ atm and $\ln K_p = 7.70$ into Eq. (12.35) gives

$$\frac{P_{\text{CO}_2}}{P_{\text{CO}}} = 10^{-2.5} \quad (12.36)$$

The value in Eq. (12.36) is very close to that indicated in Fig. 12.25. For the same p_{O_2} of $10^{-11.7}$ atm at 1600°C using the reaction



it can be shown that

$$\frac{P_{\text{H}_2\text{O}}}{P_{\text{H}_2}} = 10^{-1.9} \quad (12.38)$$

Thus, if in the $\text{H}_2\text{-H}_2\text{O}$ mixture, $p_{\text{H}_2} = 1$ atm, then $p_{\text{H}_2\text{O}}$ must equal 0.013 atm, which is the saturated vapor pressure of water at 11.1°C . The required gas mixture can be produced by bubbling H_2 gas through pure water at 11.1°C , thereby saturating the hydrogen with water vapor. When the reaction equilibrium is established at 1600°C , the oxygen partial pressure in the furnace will be $10^{-11.7}$ atm.

12.3 MICROWAVE SINTERING

Since about 1970, there has been a growing interest in the use of microwaves for heating and sintering ceramics. The principles and application of the method in the processing and sintering of ceramics and other materials have been the subject of several review articles (42,43) and conference proceedings (44,45). Microwave heating is fundamentally different from conventional heating in which electrical resistance furnaces are typically used (Fig. 12.29). In microwave heating, heat is generated internally by interaction of the microwaves with the atoms, ions, and molecules of the material. Heating rates in excess of $1000^\circ\text{C}/\text{min}$ can be achieved, and significantly enhanced densification rates have been reported. However, the control of microwave sintering can be difficult. The shape of the ceramic body affects the local heating rates significantly, and the microwave frequency can play a significant role in the temperature gradients that develop in the body; so achieving sufficiently uniform heating is not straightforward.

12.3.1 Interaction of Microwaves with Matter

Microwaves are electromagnetic waves with a frequency in the range of 0.3–300 GHz or, equivalently, with a wavelength in the range of 1 mm to 1 m, which is

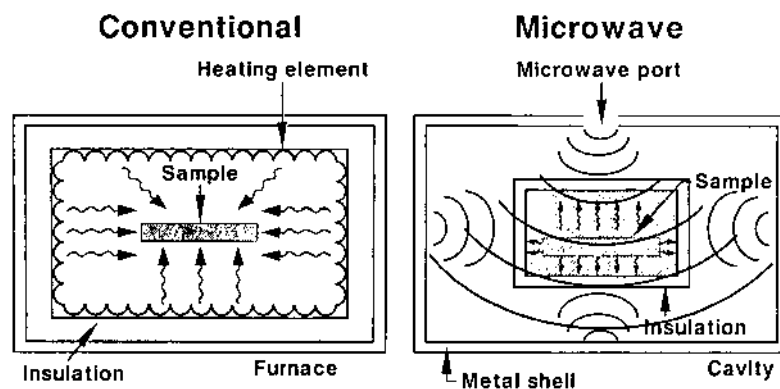


FIGURE 12.29 Heating patterns in conventional and microwave furnaces. (From Ref. 42.)

a wavelength range of the same order as the linear dimensions of most practical ceramics. In common with other electromagnetic waves, microwaves have electrical and magnetic field components, an amplitude and phase angle, and the ability to propagate (i.e., to transfer energy from one point to another). These properties govern the interaction of microwaves with materials and produce heating in some materials.

As sketched in Fig. 12.30, depending on the electrical and magnetic properties of the material, microwaves can be transmitted, absorbed, or reflected (42). Microwaves penetrate metals only in a thin skin (on the order of $1\text{ }\mu\text{m}$), so metals can be considered to be opaque to microwaves or to be good reflectors of microwaves. Most electrically insulating (or dielectric) ceramics such as Al_2O_3 , MgO , SiO_2 , and glasses are transparent to microwaves at room temperature, but when heated above a certain critical temperature T_c , they begin to absorb and couple more effectively with microwave radiation. Other ceramics, such as Fe_2O_3 , Cr_2O_3 , and SiC , absorb microwave radiation more efficiently at room temperature. The addition of a microwave-absorbing second phase to ceramics that are microwave transparent can greatly enhance the interaction of the system with microwaves.

The degree of interaction between the microwave electric and magnetic field components with the dielectric or magnetic material determines the rate at

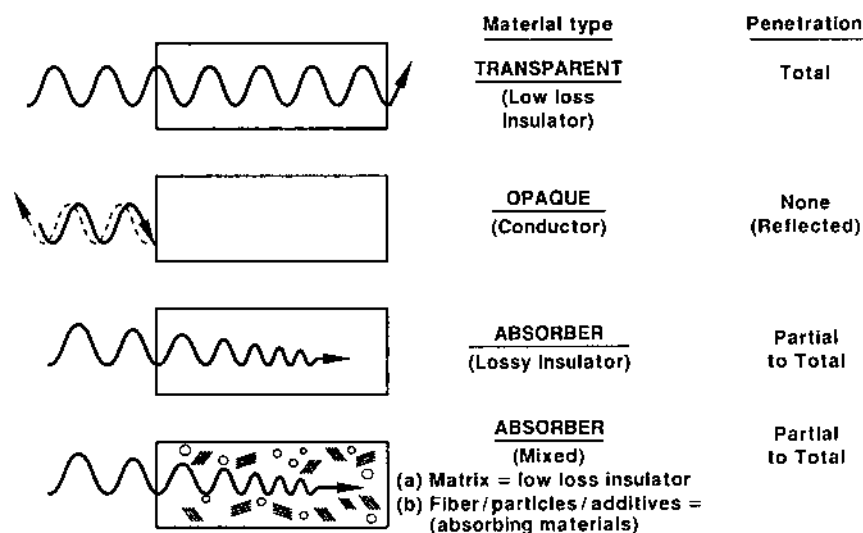


FIGURE 12.30 Schematic diagram illustrating the interaction of microwaves with materials. (From Ref. 42.)

which energy is dissipated in the material by various mechanisms. The properties of the material that are most important for the interaction are the *permittivity* ϵ for a dielectric material and the *permeability* μ for a magnetic material. Commonly the relative permittivity ϵ_r (also called the *dielectric constant*), equal to ϵ/ϵ_0 , and the relative permeability μ_r , equal to μ/μ_0 , are used, where ϵ_0 is the permittivity and μ_0 the permeability of vacuum. In alternating fields, the behavior is best described with the help of complex quantities. For example, in the case of the permittivity, we can write

$$\epsilon_r^* = \epsilon_r' - j\epsilon_r'' \quad (12.39)$$

where ϵ_r^* is the complex relative permittivity, the prime and double prime represent the real and imaginary parts of the complex relative permittivity, and $j = \sqrt{-1}$. When microwaves penetrate the material, the electromagnetic field induces motion in the free and bound charges (e.g., electrons and ions) and in dipoles. The induced motion is resisted because it causes a departure from the natural equilibrium of the system, and this resistance, due to frictional, elastic, and inertial forces, leads to the dissipation of energy. As a result, the electric field associated with the microwave radiation is attenuated and heating of the material occurs. The loss tangent, $\tan \delta$, defined by

$$\tan \delta = \frac{\epsilon_r''}{\epsilon_r'} \quad (12.40)$$

is used to represent the losses arising from all mechanisms. The average power dissipated per unit volume of the material is given by

$$W = \pi E_0^2 f \epsilon_0 \epsilon_r'' = \pi E_0^2 f \epsilon_0 \epsilon_r' \tan \delta \quad (12.41)$$

where E_0 is the amplitude of the electric field, given by $E = E_0 \exp j\omega t$, and f is the frequency, equal to $\omega/2\pi$. According to Eq. (12.41), the power absorbed by the material depends on (1) the frequency and the square of the amplitude of the electric field and (2) the dielectric constant and the loss tangent of the material. In practice, these quantities are interdependent, so it is difficult to alter one without affecting the others. Nevertheless, Eq. (12.41) shows, in a general way, the important parameters that control the power absorbed.

Since the electric field is attenuated as the microwaves propagate through the material, the depth of penetration of the microwaves into the material is an important parameter. If any linear dimension of the material is greater than the depth of penetration, uniform heating cannot be expected to occur. A few different parameters are used in the literature as a measure of the depth of penetration. The *skin depth* D_s , commonly used for metals, gives the distance into the material

at which the electric field falls to $1/e$ of its original value, where e is the base of the natural logarithm (equal to 2.718). It is given by

$$D_s = \frac{c}{\sqrt{2}\pi f (\epsilon'_r)^{1/2} \tan \delta} \quad (12.42)$$

where c is the speed of light. For metals, D_s is on the order of $1\text{ }\mu\text{m}$ at microwave frequencies whereas for insulating materials such as Al_2O_3 , D_s is on the order of 1 m. For a given material, Eq. (12.42) shows that the skin depth decreases with increasing frequency of the microwave radiation. Another version of the skin depth, often referred to as the *penetration depth*, gives the depth D_p at which the power is reduced to half of its value at the surface of the material. It is given by

$$D_p \approx \frac{c}{10f (\epsilon'_r)^{1/2} \tan \delta} \quad (12.43)$$

Equations (12.41) to (12.43) show that the most important material parameters that govern its interaction with microwave radiation are the dielectric constant ϵ'_r and the loss tangent $\tan \delta$. During microwave heating, both ϵ'_r and $\tan \delta$ change with temperature and knowledge of these changes is important for controlling microwave sintering. Figures 12.31 and 12.32 show the variation in ϵ'_r and $\tan \delta$ for several ceramics during microwave heating at 8–10 GHz. Except for Al_2O_3 , the ϵ'_r values do not change significantly whereas the $\tan \delta$ values are far more affected. For materials such as Al_2O_3 , BN, SiO_2 , and glass ceramics, $\tan \delta$ initially increases slowly with temperature until some critical temperature T_c is reached. Above T_c , the materials couple more effectively with the microwave radiation and $\tan \delta$ increases fairly rapidly with temperature.

To overcome the problem of inefficient microwave heating at lower temperatures, the materials can be heated conventionally to T_c when the microwaves couple more effectively with the sample to produce the rapid heating and high sintering temperatures. Another approach involves partially coating the internal surfaces of a refractory cavity with a thin paste of SiC. When a microwave field is applied, the microwaves penetrate the walls of the refractory cavity and interact with the highly absorbing SiC. The heat generated by the SiC heats the sample by radiation to T_c at which point the microwaves couple more effectively with the sample.

12.3.2 Microwave Sintering Techniques

Microwave sintering of ceramics is quite straightforward. The ceramic body, usually contained in nonabsorbing or weakly absorbing insulation such as loose, nonconducting powder, is placed within a microwave cavity. It is possible to use

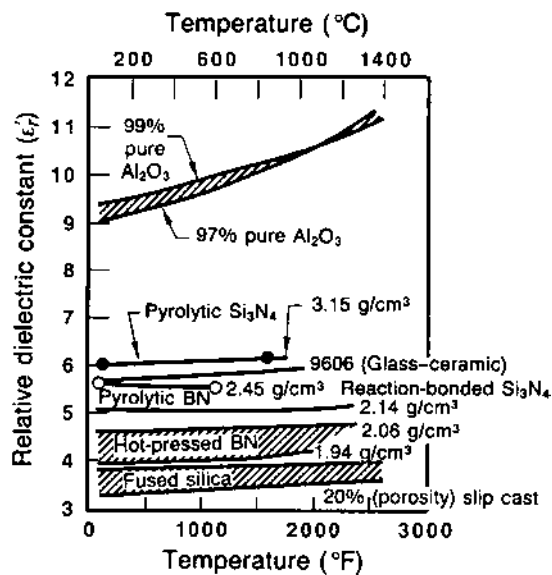


FIGURE 12.31 Dielectric constant (at a frequency of 8–10 GHz) versus temperature for some ceramics. (From Ref. 42.)

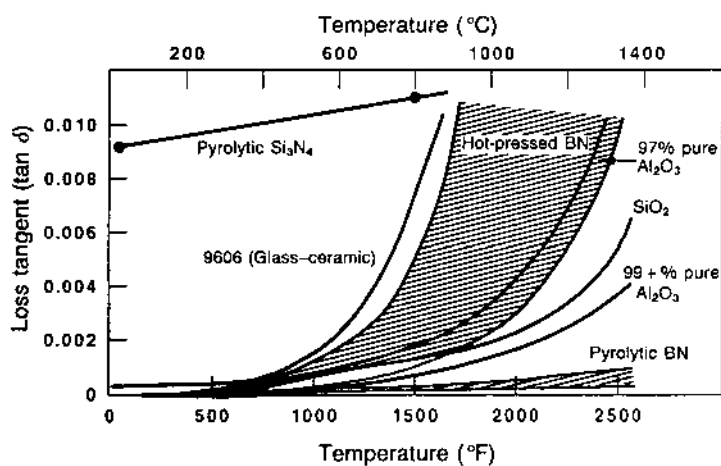


FIGURE 12.32 Dielectric loss tangent (at a frequency of 8–10 GHz) versus temperature for some ceramics. (From Ref. 42.)

a simple consumer microwave oven to achieve densification if the ceramic body is properly insulated (46), but achieving sufficiently uniform heating is difficult. Figure 12.33 shows the main components of laboratory-scale equipment for microwave sintering of ceramics (47). The microwave generator is a key element in the system. Most generators are operated at a frequency of ~ 2.45 GHz, but a combination of frequencies ranging between ~ 2.45 and 85 GHz has been proposed as providing more uniform heating (48). Continuous microwave sintering has been reported, in which samples are passed through the microwave cavity (49).

Control of Microwave Sintering

During microwave heating, the absorption of electromagnetic energy raises the temperature of the entire sample but heat loss from the surface causes the exterior to become cooler than the interior. Thus, in ceramics with poor thermal conductivity, large *temperature gradients* can develop in the body. The shape of the ceramic body and the microwave frequency strongly influence the temperature gradients and achieving sufficiently uniform heating of the body can be difficult. These thermal gradients, which are not as severe in conventional sintering, lead to undesirable density gradients during microwave sintering. At high heating rates commonly available with microwave sintering, these gradients lead to nonuniform properties and even cracking of the sample. Increased localized heating can also lead to *thermal runaway* when the temperature of the sample increases rapidly, resulting in melting of the sample.

The energy absorption during microwave sintering is proportional to the volume of the body, but the heat loss is proportional to the surface area, so the

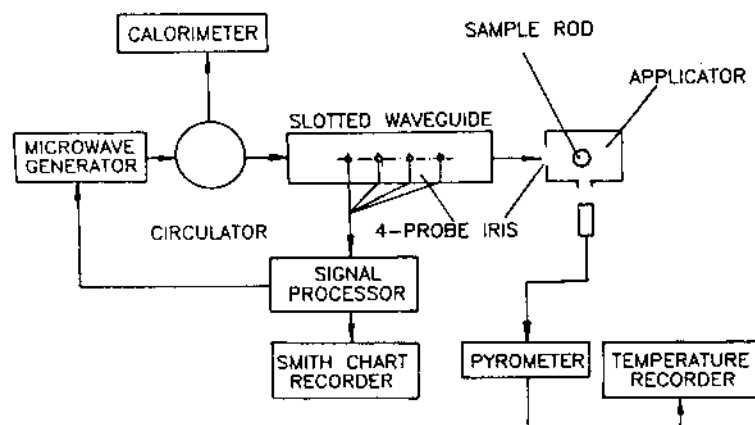


FIGURE 12.33 Schematic diagram of a microwave sintering system. (From Ref. 47.)

temperature gradient should depend on the surface to volume ratio. Ceramic components often have complex shapes, in which case the different regions, having different surface to volume ratios, would be subjected to different internal temperature gradients (50). One approach for alleviating the temperature gradients involves insulating the sample using a non absorbing or weakly-absorbing powder.

The microwave frequency also plays a significant role in the temperature gradients that can develop within the ceramic body (48). At lower temperatures when $\tan \delta$ is small and at lower microwave frequencies (2.45 GHz), the skin depth D_s is commonly larger than the sample dimensions [Eq. (12.42)], so a quasi-homogeneous energy absorption is expected inside the sample. At higher temperatures and frequencies, D_s can become smaller than the sample dimensions, so heating is concentrated at the surface. Thus another approach to reducing the thermal gradients is to simultaneously apply two microwave sources operating at widely separated frequencies (e.g., 2.45 and 30 GHz). By independently adjusting the power of each source, it is possible to control the rate and spatial distribution of the energy absorption within the sample.

Accurate measurement of the temperature in microwave sintering presents more difficulties than in conventional sintering. Because of interference from the microwave field, thermocouples cannot be relied upon to function properly (51). The presence of thermocouples during microwave heating of low and medium loss ceramics ($\tan \delta < 0.1$) can locally distort the electromagnetic field and can lead to enhanced energy absorption, enhanced heat loss by conduction, and even thermal runaway. To avoid these difficulties as well as serious error in the temperature measurement, a noncontact sensing system such as an optical pyrometer should be used whenever it is possible.

12.3.3 Microwave Sintering of Ceramics

Microwave heating has been used in the sintering of a variety of ceramics (42–45) and interest in the technique is growing. The most detailed studies of microwave sintering has been carried out with Al_2O_3 , and the results allow a meaningful comparison of the sintering characteristics in microwave heating with those obtained for similar samples in conventional heating. The data show a significant enhancement of the sintering and grain growth rates when microwave heating is used, but the mechanisms responsible for this enhancement is unclear.

Figure 12.34 shows the data of Janney and Kimrey (52) for the densification of MgO-doped Al_2O_3 powder compacts during sintering by microwave heating (28 GHz) and by conventional heating. Similar green compacts (relative density (≈ 0.55)) were used in the experiments, and they were heated at the same rate ($50^\circ\text{C}/\text{min}$) to the required temperature followed by isothermal sintering for 1 h. The conventional sintering data are in good agreement with those obtained by

others in similar experiments with the same powder. In contrast, the microwave sintered compacts show significantly enhanced sintering rates. Shrinkage starts below $\sim 900^{\circ}\text{C}$ and relative densities greater than 90% are achieved at temperatures as low as 950°C . As outlined earlier, accurate temperature measurement and control are commonly more difficult in microwave sintering. However, it appears unlikely that such a large reduction in the temperature (300–400°C) required to achieve a given density could be attributable to errors in temperature measurement. Activation energy data determined from the densification rates at different isothermal temperatures (Fig. 12.35) show that the value for microwave sintering (170 kJ/mol) is considerably lower than that in conventional sintering (575 kJ/mol).

In a subsequent set of experiments (53), the grain growth kinetics of fully dense MgO-doped Al_2O_3 samples, fabricated by hot pressing, were measured during microwave heating (28 GHz) and conventional heating. The general evolution of the microstructure is roughly similar with both types of heating, and the normal grain growth kinetics can be well described by a cubic law. However, as the data in Fig. 12.36 show, the grain growth kinetics is considerably enhanced in microwave heating. The activation energy for grain growth in microwave heating (480 kJ/mol) is found to be $\sim 20\%$ lower than that in conventional heating (590 kJ/mol). [These activation energies are expected to be appropriate to grain growth in Al_2O_3 controlled by fine second phase MgAl_2O_4 particles in the grain boundary because the MgO concentration used in the experiments (0.1 wt%) is

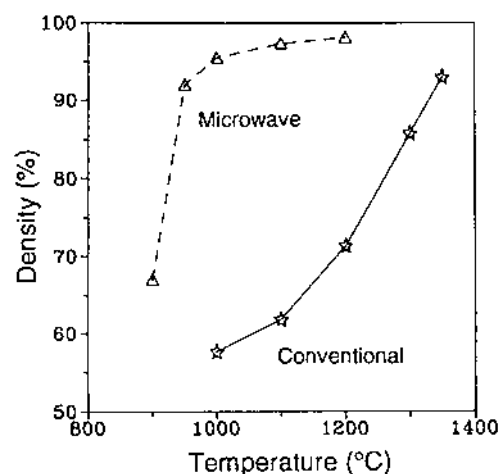


FIGURE 12.34 Relative density versus temperature for MgO-doped Al_2O_3 powder compacts during sintering by microwave heating and by conventional heating. (From Ref. 52.)

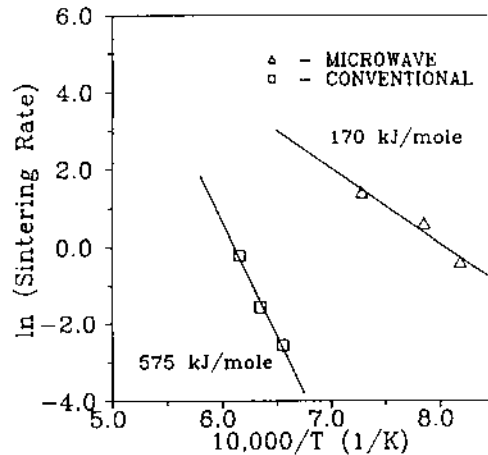


FIGURE 12.35 Arrhenius plot of the densification rate data (at a relative density of 0.80) for MgO-doped Al_2O_3 for sintering by microwave heating and by conventional heating. (From Ref. 52.)

significantly higher than the solid solubility limit for MgO in Al_2O_3 (~ 0.025 wt%).]

Measurements of the rate of oxygen diffusion in sapphire (single-crystal Al_2O_3) with an ^{18}O tracer indicate that the diffusion coefficient for microwave heating is ~ 2 times the value for conventional heating (52). Furthermore, the activation energy for diffusion in microwave heating (410 kJ/mol) is considerably lower than that for conventional heating (710 kJ/mol). This enhanced oxygen diffusion in sapphire indicates that neither free surfaces nor grain boundaries, as would be present in polycrystalline materials, are essential for the enhancement of diffusion.

12.3.4 Plasma Sintering

A variation of microwave sintering is sintering in a *plasma* generated in a microwave cavity or by a radio frequency induction-coupled method (54–58). High heating rates (on the order of $100^\circ\text{C}/\text{min}$) and rapid sintering (linear shrinkage rates of up to 3% per second) can be achieved without specimen damage for small-diameter rods and tubes. As an example, Henrichsen et al. (58) achieved full densification for tubular specimens by translating the tube at a rate of 25 mm/min through an egg-shaped plasma with a height of ~ 50 mm. A schematic of the method is shown in Fig. 12.37.

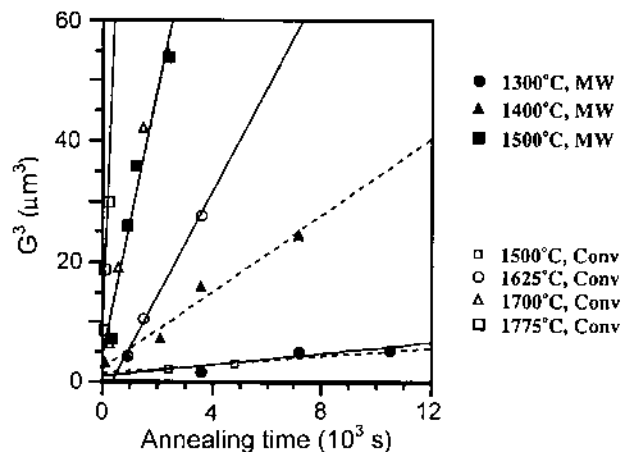


FIGURE 12.36 Grain growth kinetics of fully dense, hot-pressed MgO-doped Al_2O_3 during annealing by microwave heating and by conventional heating. The data follow a cubic growth law in both cases, but grain growth is faster in microwave heating. (From Ref. 53.)

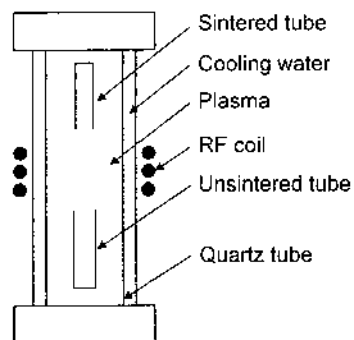


FIGURE 12.37 Schematic of plasma sintering apparatus.

Significantly enhanced densification has been reported in plasma sintering for a variety of ceramics but the mechanisms are not clear. In microwave-induced plasma sintering of Al_2O_3 , Su and Johnson (57) found significantly enhanced densification rates when compared to conventional sintering under the same time-temperature schedule. These results indicate that, besides the rapid heating rate achievable in a plasma, an *athermal* effect caused by the plasma itself also

contributes to the enhanced sintering. Su and Johnson attribute this athermal effect in Al_2O_3 to an increase in the concentration of Al interstitials. Diffusion of Al interstitials along grain boundaries is believed to be the dominant sintering mechanism; so the higher Al interstitial concentration contributes to the enhanced sintering in the plasma.

Plasma Assisted Sintering

Several attempts have been made at increasing the heating rates, giving rise to terms such as *superfast* or *ultrafast* sintering. One method, referred to as *spark plasma sintering*, involves passing a dc current pulse through a powder compact contained in a graphite die, under an applied pressure of 30–50 MPa (Fig. 12.38). Specimen temperatures are difficult to assess in this method and are usually measured using an optical pyrometer focused on the graphite die wall. Both the die and the specimen are heated by the current pulse. Heating rates in excess of $600^\circ\text{C}/\text{min}$ have been reported. The high heating rates are thought to be caused, in part, by spark discharges generated in the voids between the particles. Remarkably high densification rates may be achieved under such conditions, with minimal grain growth. This approach is particularly useful in producing dense ceramic bodies from nanosized powders (59,60). The specimen shapes that can be prepared by spark plasma sintering are limited to simple shapes such as discs that can be contained in the compression die.

A related method is a thermal explosive forming, in which a reactive mixture of components (*e.g.*, Ti and C), is heated up in a die and then ignited by passing an electrical current pulse. The process may perhaps be regarded as a self-propagating high temperature synthesis under pressure. Formation of dense boride, nitride, and carbide composites has been reported (61).

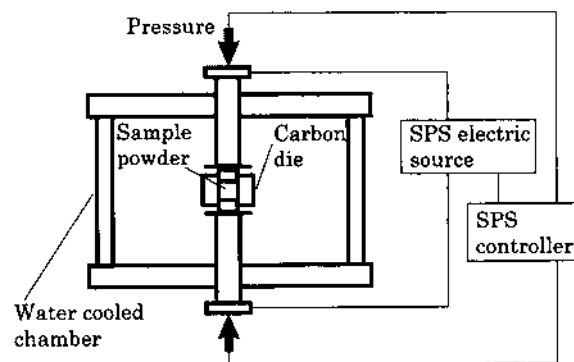


FIGURE 12.38 Schematic of spark plasma sintering (SPS) apparatus.

12.4 PRESSURE SINTERING

Sintering with an externally applied pressure is often referred to as *pressure sintering* or *pressure-assisted sintering*. The method is particularly important for preparing dense samples of ceramics with a high degree of covalent bonding (such as SiC and Si₃N₄) and ceramic matrix composites, which are commonly difficult to densify by conventional sintering. There are three principal ways in which the pressure is applied to the sample, giving rise to

1. Hot pressing, where the pressure is applied uniaxially to the powder in a die
2. Sinter forging, which is similar to hot pressing but without confining the sample in a die
3. Hot isostatic pressing, where the pressure is applied isostatically by means of a gas

Hot pressing is the most widely used of the three methods, whereas sinter forging sees little use in ceramic fabrication.

A key advantage of pressure sintering is the ability to significantly enhance the densification rate relative to the coarsening rate (see Chapter 8), thereby guaranteeing, in most cases, the attainment of high density and fine grain size. Since most properties normally improve with high density and fine grain size, superior properties are achieved. The enhancement of the densification rate also means that a lower sintering temperature or a shorter sintering time can be used in hot pressing when compared to conventional sintering. The significantly lower sintering temperature can be important for systems that contain volatile components or suffer from decomposition at higher temperatures. In research studies, pressure sintering is well suited to the production of prototype materials for the investigation of microstructure-property relations. Pressure sintering also provides an additional variable that is very effective for the study of the mechanisms of sintering. It will be recalled that the kinetic data in conventional sintering are often difficult to interpret because of the simultaneous occurrence of multiple mechanisms. Pressure sintering significantly enhances the densification mechanisms, so that the interference from the nondensifying mechanisms becomes much less.

A disadvantage of pressure sintering is the high cost of production, so in industrial applications, the method is used only for the production of specialized, high-cost ceramics where high density must be guaranteed. Pressure sintering cannot be easily automated, and in the cases of hot pressing and sinter forging, the method is commonly limited to the fabrication of relatively simple shapes. Whereas complex shapes can be produced by hot isostatic pressing, shape distortion can be a problem. Pressure sintering also has a size limitation. Large articles

(e.g., greater than ~ 1 m) have been produced industrially but the equipment becomes highly specialized and expensive.

12.4.1 Hot Pressing

Equipment and Die Materials

Figure 12.39 shows a schematic diagram of the main features of a laboratory-scale hot press (62). Heat and pressure are applied to a sample, in the form of a powder or a green compact, in a die. Depending on the furnace, operating temperatures in excess of 2000°C can be used, whereas typical operating pressures range from ~ 10 to ~ 75 MPa. Table 12.2 provides some information on the die materials that have been used in hot pressing (63). Graphite is the most common die material because it is relatively inexpensive, is easily machined, and has excellent creep resistance at high temperatures. For pressures below ~ 40 MPa, standard graphite can be used, whereas for higher pressures, specialty graphite and more expensive refractory metal and ceramic dies can be used. Graphite oxidizes slowly below $\sim 1200^{\circ}\text{C}$ so it can be exposed to an oxidizing atmosphere for short periods only. Above $\sim 1200^{\circ}\text{C}$, it must be used in an inert or reducing atmosphere. A common problem is the reactivity of graphite towards other ceramics, which leads to a deterioration of the contact surfaces of the die or to sticking of the sample to the die wall. This problem can be alleviated by coating the contact surfaces of the die with boron nitride if the temperature remains below $\sim 1350^{\circ}\text{C}$. Above this temperature, the boron nitride can react with graphite. Lining the graphite die with graphite foil is also useful for prolonging the life of the die.

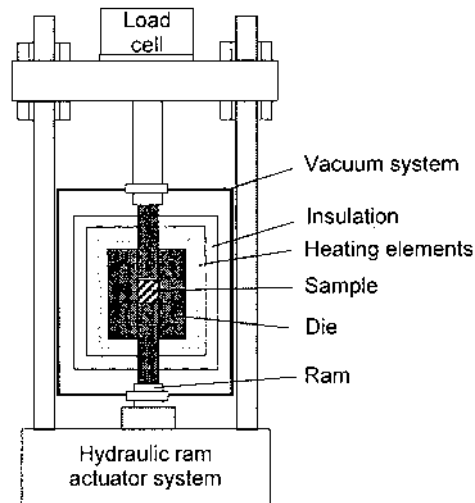


FIGURE 12.39 Schematic of the hot pressing process.

TABLE 12.2 Die Materials for Hot Pressing

Material	Maximum temperature (°C)	Maximum pressure (MPa)	Comments
Nimonic alloys	1100	High	Creep and erosion problems
Mo (or Mo alloys)	1100	20	Oxidation unless protected
W	1500	25	Oxidation unless protected
Al ₂ O ₃	1400	200	Expensive, brittle
BeO	1000	100	Expensive, brittle
SiC	1500	275	Expensive, brittle
TaC	1700	55	Expensive, brittle
WC, TiC	1400	70	Expensive, brittle
TiB ₂	1200	100	Expensive, brittle
Graphite (standard)	2500	40	Severe oxidation above 1200°C
Graphite (special)	2500	100	Severe oxidation above 1200°C

Source: Ref. 63.

The standard laboratory process leads to the production of simple shapes, such as discs. A variation allowing for some shape flexibility was developed by Lange and Terwilliger (64). In this method, the green body is packed in coarse powder in the hot pressing die, developing a roughly isostatic pressure on the sample. More complex hot pressing systems have also been developed, such as a multibore machine for hot pressing nuclear reactor pellets (65).

Process Variables

The simplest procedure, often used in laboratory studies when kinetic data are required, is to apply the required pressure to the powder in the die and release the pressure prior to heating. The system is heated fairly rapidly and on reaching the sintering temperature, the pressure is re-applied to the powder. After densification is completed, the pressure is released and the system is cooled to room temperature. More commonly in fabrication experiments, a moderate pressure (10–20 MPa) is applied to the system from the start and upon reaching the sintering temperature, the pressure is increased to the required value (40–50 MPa). The rate of densification can be deduced by following the ram displacement. Typically, the sintering temperature is chosen to achieve full densification in ~30 min to 2 h. Some guidance for selecting the appropriate hot pressing temperature may be obtained from pressure sintering maps (66), but trial and error is more reliable. An applied pressure is often maintained during the cool-down period. A schematic of the pressure–temperature treatment is shown in Fig. 12.40.

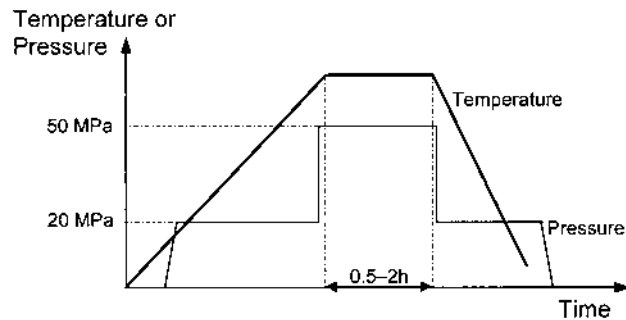


FIGURE 12.40 Schematic pressure-temperature schedule for hot pressing with a high-strength graphite die.

Because of the significant axial strain in hot pressing, texture may develop in the final microstructure. For powders that contain elongated particles, rotation of the particles under the action of the applied stress is an important mechanism for texture development (67). Texturing may also develop for equiaxial particles, and this can be seen as follows. Since the die walls are fixed, the compaction of the powder during hot pressing occurs only in the direction of the applied pressure. As sketched in Fig. 12.41, a representative element of the powder (e.g., three grains) will undergo the same relative shape changes as the overall compact. Thus, the grains become flatter in the direction of the applied pressure.

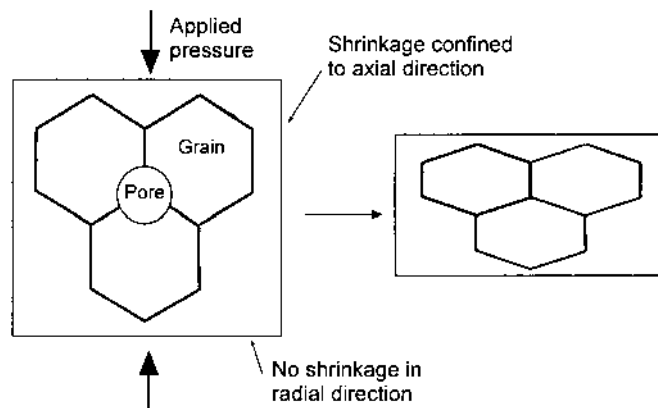


FIGURE 12.41 Schematic diagram illustrating the development of microstructural texturing during hot pressing.

Hot pressing is less effective for very fine powders, particularly when they are well compacted prior to hot pressing, because the sintering stress for these powders can be greater than the pressure that the hot pressing die can tolerate. Benefits may however still be derived when the applied pressure enhances the rearrangement process or assists in the collapse of large pores. Insoluble gases trapped in residual pores can lead to swelling of the ceramic at elevated service temperatures, but this problem can be alleviated by hot pressing in a vacuum. Swelling can also occur in oxidizing atmospheres at elevated service temperatures if the ceramic is contaminated with carbonaceous impurities by hot pressing in graphite dies. For some powders, particularly those of highly covalent materials where solid-state diffusion is slow, it may still be difficult to achieve full densification by hot pressing. As in the conventional sintering route, additives can also be used in hot pressing to aid the densification process.

Analysis of Hot Pressing Data

Data for the densification kinetics during hot pressing can be determined from measurements of the change in the height of the sample as a function of time under known conditions of pressure, isothermal firing temperature, and particle size of the powder. Commonly, the change in height is monitored continuously by measuring the ram displacement using a dial gage or a linear voltage displacement transducer. For a cylindrical die cavity with a constant cross-sectional area A_0 and assuming that the mass of the powder m_0 is constant, the density of the sample at time t is given by $d = m_0/A_0L$, where L is the height of the sample. If d_f and L_f are the final density and height, respectively, of the hot pressed disk, then $d_f = m_0/A_0L_f$. Combining these two equations gives $\rho = \rho_f L_f/L$, where ρ is the relative density at time t and ρ_f is the final relative density of the hot pressed sample. Since $L = L_f + \Delta L$, where ΔL is the change in length of the sample, the relative density as a function of time can be determined from the data for ΔL as a function of time coupled with the measured values of L_f and ρ_f . In laboratory experiments, hot pressing data are often acquired at a given isothermal temperature for known values of the applied pressure. The most useful representation of the data is in terms of plots showing (1) the relative density ρ versus $\log t$, and (2) the densification rate, defined as $(1/\rho) d\rho/dt$, versus ρ , for the applied pressures used. An example of the analysis of hot pressing data along these lines is given in Ref. 68.

As discussed in Chapter 8, the hot pressing models predict that the densification rate can be written in the general form

$$\frac{1}{\rho} \frac{d\rho}{dt} = \frac{AD\phi^{(m+n)/2}}{G^m kT} (p_a^n + \Sigma) \quad (12.44)$$

where A is a constant, D is the diffusion coefficient for the rate controlling species, G is the grain size, k is the Boltzmann constant, T is the absolute temperature,

ϕ is the stress intensification factor that is a function of density only, p_a is the applied stress, Σ is the sintering stress, and the exponents m and n depend on the mechanism of sintering (Table 8.7). According to Eq. (12.44), a plot of the data for log (densification rate) versus log (applied pressure) gives the exponent n that can be used to determine the mechanism of densification. For the commonly used pressure range in hot pressing (20–50 MPa), data for most ceramics give $n \approx 1$, indicating that the densification process is diffusion controlled. This finding is not surprising in view of the impediments to dislocation motion caused by the strong bonding in most ceramics and the fine grain size that favors diffusional mechanisms. Using starting powders with different particle sizes, data for the densification rate at a given density and applied pressure versus the grain size can be used to determine the exponent m , thus providing additional information on the densification mechanism. For diffusional mechanisms, because of the larger grain size exponent ($m = 3$) and the generally lower activation energy for grain boundary diffusion, finer powders and lower hot pressing temperatures favor grain boundary diffusion over lattice diffusion ($m = 2$).

Reactive Hot Pressing

Reactive hot pressing of a mixture of powders has been used successfully to produce composites (69,70). Densification is more readily achieved in this case when compared to the *reaction sintering* process described in Chapter 11, and this is due to the enhanced driving force for densification as well as the ability of the applied pressure to break down unfavorable microstructural features produced by the reaction, such as particle–particle bridges that constrain sintering.

A related process is *hydrothermal hot pressing*, in which powders are compacted under hydrothermal conditions. The powder is essentially mixed with a small amount of water and compacted in an autoclave at temperatures above the boiling point of water, typically between 100 and 350°C. The design of the system should allow for fluid to leave the sample (71), and any residual water present in the sample after hydrothermal hot pressing is removed by drying. Ceramics such as hydroxyapatite (72) and amorphous titania (73) have been compacted in this way.

12.4.2 Sinter Forging

Sinter forging, also referred to as *hot forging*, is similar to hot pressing but without the sample confined in a die (Fig. 12.42). Typically, a green compact or a partially sintered compact is heated while applying a uniaxial stress (74,75). The applied uniaxial stress p_z gives rise to a hydrostatic component $p_z/3$ that provides an additional driving force for sintering, so Eq. (12.44) can also be used to predict the densification rate in sinter forging if p_a is replaced by $p_z/3$. There is also a shear component of the applied uniaxial stress which causes creep of the sample.

The high shear strains in sinter forging can serve to reduce processing flaws in the body by rearrangement of the grains during the initial and intermediate stage of sintering, thereby producing a more homogeneous microstructure (76–78).

Uniaxial strains in the direction of the applied stress are significantly larger than in hot pressing, and these large strains have been used effectively to produce texturing (grain alignment) in some ferroelectric ceramics to develop anisotropic dielectric properties (79,80). For fine powders, use can be made of possible superplastic deformation modes in sinter forging to enhance texturing (81). During the process, the strain rate has to be limited to avoid damaging the sample.

12.4.3 Hot Isostatic Pressing

Equipment

In hot isostatic pressing, sometimes abbreviated *HIP*, the preconsolidated powder is tightly enclosed in a glass or metal container (sometimes referred to as a can) that is sealed under a vacuum and placed in a pressure vessel (Fig. 12.43). Alternatively, the sample can be predensified to the closed porosity stage by conventional sintering, in which case the can is not needed in the subsequent HIP stage. The pressurizing gas is introduced by means of a compressor to achieve a given initial gas pressure (a few thousand psi), and the sample is heated to the sintering temperature. During this time the gas pressure increases further to the

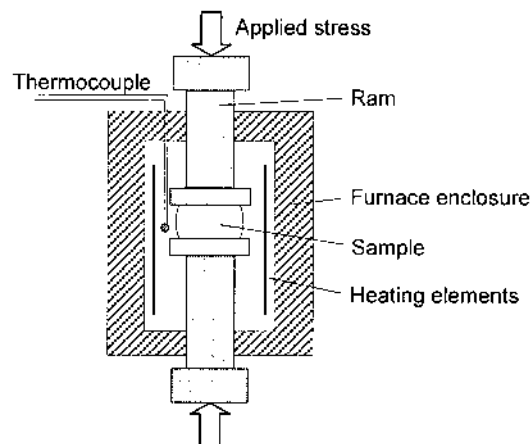


FIGURE 12.42 Schematic of the sinter forging process.

required value and the can collapses around the sample, thereby acting to transmit the isostatic pressure to the sample.

A schematic diagram of a pressure vessel containing a sample for HIP is shown in Fig. 12.44. The pressure vessel is typically of the cold-wall design, in which the furnace is thermally insulated from the wall of the vessel and flowing water provides external cooling. It is penetrated, normally through the end closures, to supply power and control instrumentation to the furnace. Electrical resistance furnaces (e.g., graphite or Mo) and inert pressurizing gases (Ar or He) are commonly used. Depending on the furnace, HIP systems designed for use with inert gases can routinely be operated at temperatures up to $\sim 2000^{\circ}\text{C}$ and pressures up to ~ 200 MPa (30,000 psi). Systems for use with reactive gases (e.g., O_2 or N_2) are also available, but the temperature and pressure capability are significantly lower. The quality of the ceramics produced by HIP is perhaps the highest obtainable by any other pressure sintering method, because externally heated dies cannot withstand the high pressures that can be applied in HIP.

Process Variables

The densification of metal powders by HIP may sometimes involve filling the loose powder into a deformable metal container, but this method is unsuitable for most ceramic powders. Because of their fine size and low poured (or tap) density, considerable deformation and distortion of the material occurs during

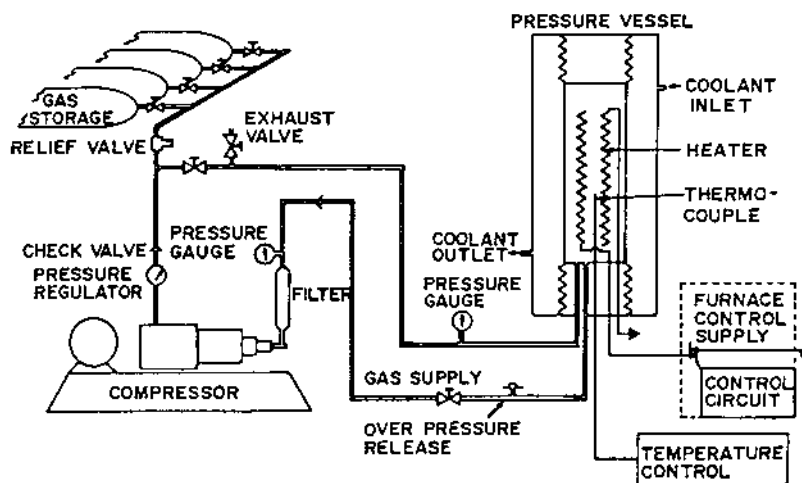


FIGURE 12.43 Simplified schematic diagram of a system used for a hot isostatic pressing. (From Ref. 82.)

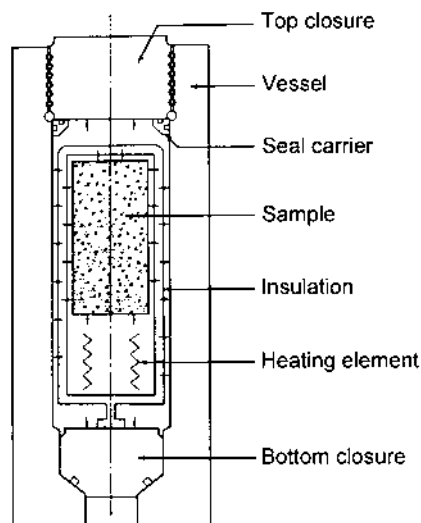


FIGURE 12.44 Schematic diagram of a pressure vessel with a sample for hot isostatic pressing. (Courtesy of ASEA Autoclave Systems Inc., Columbus, OH.)

HIP. Most ceramic powders are first consolidated to form a shaped green article and, if required, lightly presintered to develop some strength for handling prior to HIP. As outlined earlier, the shaped green article can be encapsulated in a glass or metal can, or sintered to closed porosity, prior to HIP. Compacts with open porosity cannot be densified without the encapsulation because the pressurizing gas in the pores resists the sintering stress. The materials commonly used for encapsulation consist of a thin walled metal can (e.g., Mo or Ta) or a glass can. Following densification, the can is removed mechanically or chemically (by dissolution). The method in which the powder compact is sintered to closed porosity and then subjected to HIP is sometimes referred to as *sinter/HIP*. The main objective in sinter/HIP is to remove the residual porosity without significant coarsening, which can often be difficult to accomplish in conventional sintering.

The selection of the encapsulation route or the sinter/HIP route is often governed by the quality of the fabricated article and the cost. If significant coarsening occurs during the sintering step of the sinter/HIP route, the microstructure can be considerably coarser than that of a similar article produced by the encapsulation route. Dimension control of the fabricated article may however be better in sinter/HIP because of the small shrinkage during the HIP stage. Reaction of the ceramic with the can often leads to degradation of the sample surface, so some surface machining may be necessary with the encapsulation route. The sinter/HIP route

eliminates the cost of encapsulation, but the time required for the overall sintering plus HIP steps is longer than that for HIP of the encapsulated green article.

Because the green body can be shaped during forming or machined to the desired shape, dense bodies with complex shapes can be produced by HIP (Fig. 12.45), which provides one of the most important advantages over hot pressing. However, inhomogeneous densification during HIP can lead to undesirable shape changes such as distortion. Inhomogeneous densification may be caused by inadequate processing of the green article (as discussed earlier in the book) or by inadequate HIP practice, such as nonuniformity of the temperature and pressure over the dimensions of the sample. Temperature gradients are a common source of problems, particularly for large articles. As in conventional sintering, when the temperature of the powder compact is raised, heat diffuses inward from the surface. If heat flow through the compact is slow (as in most ceramic powders), a temperature gradient is set up. In most HIP operations, the sample is under a pressure during heat-up which causes the hotter surface layer to densify faster than the interior, giving rise to a dense skin. Heat conduction through the dense skin is faster than through the less dense interior, further adding to the temperature difference between the surface and the interior. Under certain circumstances, a densification front develops and propagates inward. This leads to large shape changes of the article, which is no longer identical to that of the original article.

An analysis of a one-dimensional model for coupled heat flow and densification in a powder compact shows that the tendency towards shape distortion can be characterized by a dimensionless factor that measures the ratio of the densification rate to the heat-transfer rate (84). When this ratio is <1 , densification

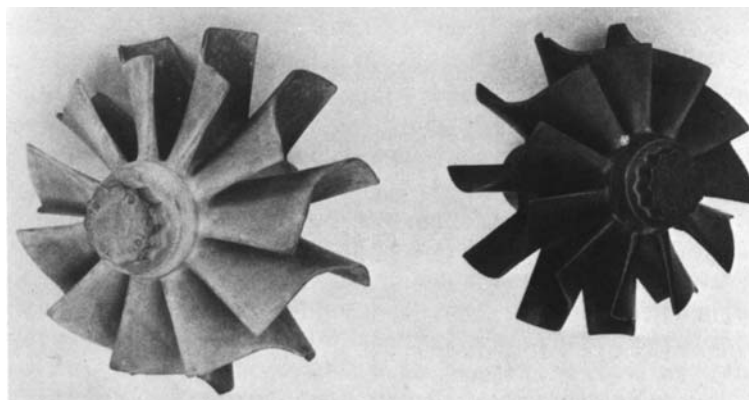


FIGURE 12.45 Turbocharger impeller, formed by injection molding (left) and densified to full density by hot isostatic pressing (right). (From Ref. 83.)

is nearly uniform, but when it is >1 , there is a tendency for a densification front to form and propagate inwards from the surface. Extension of the ideas from one to three dimensions produces new complications. As sketched in Fig. 12.46 for a cylindrical shape, when densification is uniform, the cylinder (as expected) shrinks uniformly but when nonuniform densification takes place, a dense shell forms around the cylinder. Pressure can be transmitted to the inner core only if the cylindrical shell creeps inwards, a process which can be slow. A larger part of the pressure is carried by the shell, and the densification of the core all but ceases.

The problem of shape distortion caused by temperature gradients can be alleviated by allowing the sample to equilibrate at the firing temperature before applying the full pressure, but this may be impractical in the simpler HIP equipment or may lead to a significant drop in the temperature if a large volume of gas is admitted quickly to the autoclave. The problem may also be reduced by using the sinter/HIP route.

Kinetics and Mechanisms

Because of the nature of the HIP process, kinetic data are not easy to obtain. Data for most ceramics are limited to values for the final density after a specified isothermal firing time under a given pressure. As in the case of hot pressing, the nondensifying mechanisms are not enhanced by the applied pressure and can often be neglected. Particle rearrangement, which contributes to densification

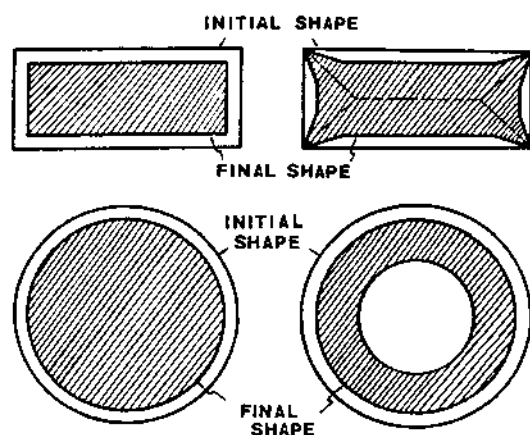


FIGURE 12.46 Consequences of inhomogeneous densification during hot isostatic pressing of an encapsulated cylindrical powder compact: (top) shape change and (bottom) density gradients with residual porosity and internal stress. (From Ref. 84.)

during the initial stage, is usually ignored because of the transient nature of the contribution and the difficulty of analyzing the process. The much higher applied pressure means that, in metals, plastic deformation plays a more important role in HIP than in hot pressing. Instantaneous plastic yielding of the metallic powder particles at their contact points will be more significant in the early stages of HIP. Plastic yielding is still expected to be unlikely for most ceramic powders, so for polycrystalline ceramics the possible mechanisms that need to be considered are lattice diffusion, grain boundary diffusion, and plastic deformation by dislocation motion (power law creep).

Constitutive equations have been developed for the various mechanisms of densification during HIP (85). Using available data for the material parameters, these equations have been used to predict the relative contribution of each mechanism to densification. The procedure follows along the same lines discussed in Chapter 8 for the construction of the sintering diagrams. The results are plotted on HIP diagrams that show the conditions of dominance for each mechanism. Figure 12.47 shows the HIP diagram for Al_2O_3 powder with a particle size of $2.5\mu\text{m}$. As might be expected for this material, densification is predicted to occur predominantly by diffusion.

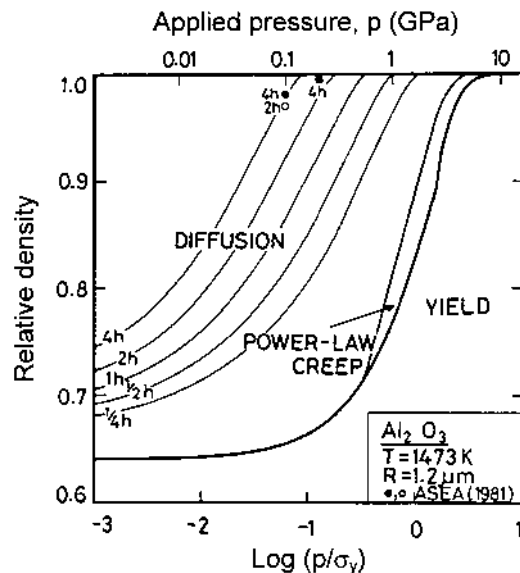


FIGURE 12.47 A hot isostatic pressing (HIP) map for α -alumina powder with a particle size of $2.5\mu\text{m}$ at 1473K . (From Ref. 85.)

12.5 CONCLUDING REMARKS

In this chapter, we considered the main methods for the densification of ceramic powder compacts by conventional sintering, where sintering is performed without the application of an external pressure, and by pressure sintering, where an external pressure is applied to the sample during sintering. Heating of the sample during sintering is commonly achieved using electrical resistance furnaces with heat transferred from the furnace elements to the sample. In recent years, microwave sintering, in which the sample is heated internally by microwave radiation, has attracted some interest. The control of microwave sintering is more complicated than in conventional sintering, but experiments have shown considerable enhancement of sintering when microwave heating is used. Compared to pressure sintering, conventional sintering is the preferred method for densification because it is economical. However, when it is difficult or impossible to produce high density by conventional sintering, pressure sintering is used. The quality of the ceramic article produced by pressure sintering is often superior to that obtained in conventional sintering. Even with proper powder preparation and consolidation procedures, successful fabrication is still dependent on the ability to control the microstructure through manipulation of the process variables during sintering. In conventional sintering, the main process variables are the heating cycle (temperature–time schedule) and the sintering atmosphere. Proper manipulation of these two variables can provide considerable benefits for densification. Applied pressure provides an additional variable that is not only effective for enhancing densification but also useful for studying the mechanisms of sintering.

PROBLEMS

- 12.1 Derive the following elementary relations for the isotropic sintering of a power compact:
 - a. $\rho = \rho_0/(1 - \Delta L/L_0)^3$
 - b. $\Delta\rho/\rho = \Delta V/V_0$where ρ is the relative density, L is the length, and V is the volume of the compact at any time; ρ_0 , L_0 , and V_0 are the initial values and $\Delta\rho$, ΔL , and ΔV represent the changes in the parameters.
- 12.2 Consider the constant heating rate sintering of a ceramic powder compact. How would an increase in the heating rate from 1°C/min to 20°C/min be expected to influence the sintering behavior when:
 - a. Coarsening is insignificant.
 - b. Coarsening is significant.
- 12.3 Plot the limiting porosity in a powder compact as a function of the grain size (in the range of 0.1 to 100 μm) when sintering is carried out in an insoluble gas at atmospheric pressure. Assume that the pore size is one third the grain

size and that the specific surface energy of the solid–vapor interface is 1 J/m^2 .

- 12.4 When sintered in an oxygen atmosphere at 1700°C for a few hours, an MgO-doped Al_2O_3 powder compact (starting particle size $\approx 0.2 \text{ }\mu\text{m}$) reaches theoretical density with an average grain size of $\sim 10 \text{ }\mu\text{m}$. However, when sintered under similar conditions in air (1 atm pressure), the compact reaches a limiting density of 95% of the theoretical. At the end of the intermediate stage when the pores become pinched off, the average grain size and average pore size are found to be $2 \text{ }\mu\text{m}$ and $0.5 \text{ }\mu\text{m}$, respectively. Estimate the average grain size and average pore size when the sample sintered in air reaches its limiting density, stating any assumptions that you make.

Further sintering of the sample in air leads to grain growth with pore coalescence, with the pores reaching an average size of $4 \text{ }\mu\text{m}$. Will the porosity be different? Explain. If the porosity is different, estimate how different.

- 12.5 When a CeO_2 powder (starting particle size $\approx 20 \text{ nm}$) is sintered at a constant heating rate of 5°C/min in air, the compact reaches a limiting density of $\sim 95\%$ of the theoretical at $\sim 1300^\circ\text{C}$, after which the density decreases at higher temperatures. Discuss the factors that may be responsible for preventing the achievement of full density. What steps may be taken to achieve a density close to the theoretical value for this system?
- 12.6 In the sintering of Cr_2O_3 powder, the procedure adopted by a student calls for the powder to remain as Cr_2O_3 at all times above 800°C , never changing to Cr or CrO_2 . The student decides to employ a flowing mixture of H_2 and water vapor for atmosphere control. Using the data in Fig. 12.25 (or otherwise), plot the limits of the $\text{H}_2/\text{H}_2\text{O}$ ratio in the sintering atmosphere as a function of the temperature for the experiment.
- 12.7 Determine the skin depth for Al_2O_3 for microwave sintering at 1250°C when the microwave generator is operated at a frequency of (a) 2.5 GHz and (b) 85 GHz , assuming that the dielectric constant and $\tan \delta$ values for Al_2O_3 at 1250°C are 10 and 0.005, respectively.

Discuss qualitatively the expected temperature distribution in a ceramic body with a linear dimension of 30 cm during microwave sintering at each frequency. How can the temperature distribution in the body be made more uniform?

- 12.8 A student is given the task of sintering a fine-grained BaTiO_3 powder (average particle size $\approx 0.1 \text{ }\mu\text{m}$; purity $>99.9\%$) to a density greater than 98% of the theoretical value and with an average grain size not greater than $1 \text{ }\mu\text{m}$. Discuss how the student should attempt to accomplish the task.
- 12.9 Estimate the factor by which the driving force for densification is enhanced by hot pressing with an applied pressure of 40 MPa , relative to conventional sintering, when the particle size of the powder is (a) $20 \text{ }\mu\text{m}$ and (b) 20 nm . Assume that the pore size is one third the particle size and the specific surface energy of the solid–vapor interface is 1 J/m^2 .

REFERENCES

1. Ling, H. C.; Yan, M. F. J. *Mater. Sci.* 1983, Vol. 18, 2688.
2. Woolfrey, J. L.; Bannister, M. J. J. *Am. Ceram. Soc.* 1972, Vol. 55, 390.
3. Bannister, M. J. J. *Am. Ceram. Soc.* 1968, Vol. 51, 548.
4. Cutler, I. B. J. *Am. Ceram. Soc.* 1969, Vol. 52, 14.
5. Brinker, C. J.; Scherer, G. W.; Roth, E. P. J. *Non-Cryst. Solids.* 1985, Vol. 72, 345.
6. Brinker, C. J.; Scherer, G. W. *Sol-Gel Science*; Academic: New York, 1990, Chap. 11.
7. Young, W. S.; Cutler, I. B. J. *Am. Ceram. Soc.* 1970, Vol. 53, 659.
8. Lange, F. F. *Ceramic Trans.* 1989, Vol. 1, 1069.
9. Chu, M. Y.; Rahaman, M. N.; De Jonghe, L. C.; Brook, R. J. J. *Am. Ceram. Soc.* 1991, Vol. 74, 1217.
10. Su, H.; Johnson, D. L. J. *Am. Ceram. Soc.* 1996, Vol. 79, 3211.
11. Duncan, J. H.; Bugden, W. G. *Proc. Brit. Ceram. Soc.* 1981, Vol. 31, 221.
12. Lin, F. J. T.; De Jonghe, L. C.; Rahaman, M. N. J. *Am. Ceram. Soc.* 1997, Vol. 80, 2269.
13. Chu, M.-Y.; De Jonghe, L. C.; Lin, M. F. K.; Lin, F. J. T. J. *Am. Ceram. Soc.* 1991, Vol. 74, 2902.
14. Brook, R. J. *Proc. Br. Ceram. Soc.* 1982, Vol. 32, 7.
15. Harmer, M. P.; Brook, R. J. J. *Br. Ceram. Soc.* 1981, Vol. 80, 147.
16. Mostaghaci, H.; Brook, R. J. *Trans. Br. Ceram. Soc.* 1983, Vol. 82, 167.
17. Huckabee, M. L.; Hare, T. M.; Palmour, H., III. In *Processing of Crystalline Ceramics*; Palmour, H., Davis, R. F., Hare, T. M. eds.; Plenum Press: New York, 1978, pp. 205–215.
18. Huckabee, M. L.; Paisley, M. J.; Russell, R. L.; Palmour, H., III. *J. Am. Ceram. Soc.* 1994, Vol. 73, 82.
19. Agarwal, G.; Speyer, R. F. J. *Mater. Res.* 1996, Vol. 11, 671.
20. Ragula, A. V. *Nanostructured Materials.* 1998, Vol. 10, 349.
21. Coble, R. L. J. *Am. Ceram. Soc.* 1962, Vol. 45, 123.
22. Bennison, S. J.; Harmer, M. P. J. *Am. Ceram. Soc.* 1985, Vol. 68, 591.
23. Readey, D. W. *Ceramic Trans.* 1990, Vol. 7, 86.
24. Quadir, T.; Readey, D. W. J. *Am. Ceram. Soc.* 1989, Vol. 72, 297.
25. Lee, J.; Readey, D. W. *Mater. Sci. Res.* 1984, Vol. 18, 145.
26. Readey, M. J.; Readey, D. W. J. *Am. Ceram. Soc.* 1987, Vol. 70, C358.
27. Thompson, A. M.; Harmer, M. P. J. *Am. Ceram. Soc.* 1993, Vol. 76, 2248.
28. Wong, B.; Pask, J. A. J. *Am. Ceram. Soc.* 1979, Vol. 62, 141.
29. Anderson, P. J.; Morgan, P. L. *Trans. Faraday Soc.* 1964, Vol. 60, 930.
30. Northrop, D. A. J. *Am. Ceram. Soc.* 1967, Vol. 50, 441; 1968, Vol. 51, 357.
31. Snow, G. S. J. *Am. Ceram. Soc.* 1973, Vol. 56, 479.
32. Mitomo, M. J. *Mater. Sci.* 1976, Vol. 11, 1103.
33. Ownby, P. D.; Jungquist, G. E. J. *Am. Ceram. Soc.* 1972, Vol. 55, 433.
34. Ownby, P. D. *Mater. Sci. Res.* 1973, Vol. 6, 431.
35. Anderson, H. U. J. *Am. Ceram. Soc.* 1974, Vol. 57, 34.

36. Anderson, H. U. *Mater. Sci. Res.* 1978, Vol. 11, 469.
37. Callister, W. D.; Johnson, M. L.; Cutler, I. B.; Ure, R. W., Jr. *J. Am. Ceram. Soc.* 1979, Vol. 62, 208.
38. Reynolds, T., III. In *Treatise on Materials Science and Technology*; Vol. 9, Wang, F. F. Y. ed.; Academic Press: New York, 1976, pp. 199–215.
39. Reijnen, P. In *Reactivity of Solids*; Mitchell, J. W., DeVries, R. C., Roberts, R. W., Cannon, P. eds.; Wiley: New York, 1969, pp. 99–114.
40. Yan, M. F. *J. Am. Ceram. Soc.* 1980, Vol. 63, 443.
41. Gaskell, D. R. *Introduction to Metallurgical Thermodynamics*; 2nd ed.; McGraw-Hill: New York, 1981.
42. Sutton, W. H. *Am. Ceram. Soc. Bulletin.* 1989, Vol. 68, 376.
43. *MRS Bulletin.* November 1993, Vol. 18.
44. *Materials Research Society Symposium Proceedings. Microwave Processing of Materials I–V*; Materials Research Society: Pittsburg, PA.
45. *Ceramic Transactions. Microwaves: Theory and Applications in Materials Processing I–IV*; American Ceramic Society: Westerville, OH.
46. Fang, Y.; Agrawal, D. K.; Roy, D.; Roy, R. J. *Mater. Res.* 1994, Vol. 9, 180.
47. Tian, Y. L.; Johnson, D. L. *Ceramic Trans.* 1987, Vol. 1, 925.
48. Birnboim, A.; et al. *J. Am. Ceram. Soc.* 1998, Vol. 81, 1493.
49. Cheng, J.; Agrawal, D.; Roy, R.; Jayan, P. S. *J. Mater. Processing Technol.* 2000, Vol. 108, 26.
50. Birnboim, A.; Carmel, Y. *J. Am. Ceram. Soc.* 1999, Vol. 82, 3024.
51. Pert, E.; et al. *J. Am. Ceram. Soc.* 2001, Vol. 84, 1981.
52. Janney, M. A.; Kimrey, H. D. *Mater. Res. Soc. Symp. Proc.* 1991, Vol. 189, 215.
53. Janney, M. A.; Kimrey, H. D.; Schmidt, M. A.; Kiggans, J. O. *J. Am. Ceram. Soc.* 1991, Vol. 74, 1675.
54. Johnson, D. L.; Rizzo, R. A. *Am. Ceram. Soc. Bulletin.* 1980, Vol. 59, 467.
55. Kim, J. S.; Johnson, D. L. *Am. Ceram. Soc. Bulletin.* 1983, Vol. 62, 620.
56. Kemer, E. L.; Johnson, D. L. *Am. Ceram. Soc. Bulletin.* 1985, Vol. 64, 1132.
57. Su, H.; Johnson, D. L. *J. Am. Ceram. Soc.* 1996, Vol. 79, 3199.
58. Henriksen, M.; Hwang, J.; Dravid, V. P.; Johnson, D. L. *J. Am. Ceram. Soc.* 2000, Vol. 83, 2861.
59. Gao, L.; Shen, Z.; Miyamoto, H.; Nygren, M. *J. Am. Ceram. Soc.* 1999, Vol. 82, 1061.
60. Takeuchi, T.; Tabuchi, M.; Kageyama, H. *J. Am. Ceram. Soc.* 1999, Vol. 82, 939.
61. Gutmanas, E.; Gotman, I. *J. Europ. Ceram. Soc.* 1999, Vol. 19, 2381.
62. Vasilos, T.; Spriggs, R. M. *Prog. Ceram. Sci.* 1966, Vol. 4, 95.
63. Briggs, J. In *Concise Encyclopedia of Advanced Ceramic Materials*; Brook, R. J. ed.; Pergamon: Oxford, 1991, pp. 219–222.
64. Lange, F. F.; Terwilliger, G. R. *Am. Ceram. Soc. Bulletin.* 1973, Vol. 52, 573.
65. Rigby, F. *Proc. Brit. Ceram. Soc.* 1981, Vol. 31, 249.
66. Wilkinson, D. S.; Ashby, M. F. *Mater. Sci. Res.* 1975, Vol. 10, 473.
67. Kimura, T.; Yoshimoto, T.; Iida, N.; Fujita, Y.; Yamaguchi, T. *J. Am. Ceram. Soc.* 1989, Vol. 82, 85.

68. Vieira, J. M.; Brook, R. J. *J. Am. Ceram. Soc.* 1984, Vol. 67, 245.
69. Zhang, G.-J.; Deng, Z.-Y.; Kondo, N.; Yang, J.-F.; Ohji, T. *J. Am. Ceram. Soc.* 2000, Vol. 83, 2330.
70. Wen, G.; Li, S. B.; Zhang, B. S.; Guo, Z. X. *Scripta. Materialia.* 2000, Vol. 43, 853.
71. Yamasaki, N.; Yanagisawa, K.; Nishioka, M.; Kanahara, S. *J. Mater. Sci. Lett.* 1986, Vol. 5, 355.
72. Hosoi, K.; Hashida, T.; Takahashi, H.; Yamasaki, N.; Korenaga, T. *J. Am. Ceram. Soc.* 1996, Vol. 79, 2271.
73. Yanagisawa, K.; Ioku, K.; Yamasaki, N. *J. Am. Ceram. Soc.* 1997, Vol. 80, 1303.
74. He, Y. J.; Winnubst, A. J. A.; Verweij, A.; Burggraaf, A. J. *J. Mater. Sci.* 1994, Vol. 29, 6505.
75. Winnubst, A. J. A.; Boutz, M. M. R. *Key Eng. Mater.* 1998, Vol. 153–154, 301.
76. Venkatachari, K.; Raj, R. *J. Am. Ceram. Soc.* 1987, Vol. 70, 514.
77. Panda, P. C.; Wang, J.; Raj, R. *J. Am. Ceram. Soc.* 1988, Vol. 71, C507.
78. Mayo, M. J.; Hague, D. C. *Mater. Sci. Forum.* 1994, Vol. 170–172, 141.
79. Takenaka, T.; Sakata, K. *Jpn. J. Appl. Phys.* 1980, Vol. 19, 31.
80. Knickerbocker, J. U.; Payne, D. A. *Ferroelectrics.* 1981, Vol. 37, 733.
81. Kondo, N.; Suzuki, Y.; Ohji, T. *J. Am. Ceram. Soc.* 1999, Vol. 82, 1067.
82. Wills, R. R.; Brockway, M. C.; McCoy, L. G. *Mater. Sci. Res.* 1984, Vol. 17, 559.
83. Larker, H. T. *Mater. Sci. Res.* 1984, Vol. 17, 571.
84. Li, W.-B.; Ashby, M. F.; Easterling, K. E. *Acta Metall.* 1987, Vol. 35, 2831.
85. Arzt, E.; Ashby, M. F.; Easterling, K. E. *Metal. Trans.* 1983, Vol. 14A, 211.

Appendix A

Physical Constants

Velocity of light, c	$2.998 \times 10^8 \text{ m s}^{-1}$
Permittivity of vacuum, ϵ_0	$8.854 \times 10^{-12} \text{ F m}^{-1}$
Permeability of vacuum, $\mu_0 = 1/\epsilon_0 c^2$	$1.257 \times 10^{-6} \text{ H m}^{-1}$
Elementary charge, e	$1.602 \times 10^{-19} \text{ C}$
Planck constant, h	$6.626 \times 10^{-34} \text{ J s}$
Avogadro number, N_A	$6.022 \times 10^{23} \text{ mol}^{-1}$
Atomic mass unit, $m_u = 10^{-3}/N_A$	$1.661 \times 10^{-27} \text{ kg}$
Mass of electron, m_e	$9.110 \times 10^{-31} \text{ kg}$
Mass of proton, m_p	$1.673 \times 10^{-27} \text{ kg}$
Mass of neutron, m_n	$1.675 \times 10^{-27} \text{ kg}$
Faraday constant, $F = N_A e$	$9.649 \times 10^4 \text{ C mol}^{-1}$
Rydberg constant, R_∞	$1.097 \times 10^7 \text{ m}^{-1}$
Bohr magneton, μ_B	$9.274 \times 10^{-24} \text{ J T}^{-1}$
Gas constant, R	$8.314 \text{ J K}^{-1} \text{ mol}^{-1}$
Boltzmann constant, $k = R/N_A$	$1.381 \times 10^{-23} \text{ J K}^{-1}$
Gravitational constant, G	$6.67 \times 10^{-11} \text{ N m}^2 \text{ kg}^{-2}$
Stefan-Boltzmann constant, σ	$5.670 \times 10^{-8} \text{ W m}^{-2} \text{ K}^{-4}$
Standard volume of ideal gas, V_o	$22.414 \times 10^{-3} \text{ m}^3 \text{ mol}^{-1}$
Acceleration due to gravity, g (at sea level and zero degree latitude)	9.780 m s^{-2}

Appendix B

SI Units—Names and Symbols

Quantity	Unit	Symbol	Relation to other units
<i>Base units</i>			
Length	meter	m	
Mass	kilogram	kg	
Time	second	s	
Electric current	ampere	A	
Temperature	kelvin	K	
Amount of substance	mole	mol	
Luminous intensity	candela	cd	
<i>Supplementary units</i>			
Plane angle	radian	rad	
Solid angle	steradian	sr	
<i>Derived units with special names</i>			
Frequency	hertz	Hz	s^{-1}
Temperature	degree Celsius	$^{\circ}\text{C}$	$T(^{\circ}\text{C}) = T(\text{K}) - 273.2$
Force	newton	N	kg m s^{-2}
Pressure and stress	pascal	Pa	N m^{-2}
Energy	joule	J	N m
Power	watt	W	J s^{-1}
Electric charge	coulomb	C	A s
potential	volt	V	J C^{-1}
resistance	ohm	Ω	V A^{-1}
capacitance	farad	F	C V^{-1}
Magnetic flux	weber	Wb	V s
flux density	tesla	T	Wb m^{-2}
Inductance	henry	H	V s A^{-1}
Luminous flux	lumen	lm	cd sr

Appendix C

Conversion of Units and Decimal Fractions and Multiples

CONVERSION OF UNITS

Length	1 micron (μm) = 10^{-6} m 1 ångström (\AA) = 10^{-10} m 1 inch (in) = 25.4 mm
Mass	1 pound (lb) = 0.454 kg
Volume	1 liter (l) = 10^{-3} m ³
Density	1 gm cm ⁻³ = 10^3 kg m ⁻³
Force	1 dyne = 10^{-5} N
Angle	1° = 0.01745 rad
Pressure and stress	1 lb in ⁻² (psi) = 6.89×10^3 Pa 1 bar = 10^5 Pa 1 atmosphere (atm) = 1.013×10^5 Pa 1 torr = 1 mm Hg = 133.32 Pa
Energy	1 erg = 10^{-7} J 1 calorie = 4.1868 J 1 electron volt (eV) = 1.6022×10^{-19} J
Viscosity	
dynamic	1 poise = 0.1 Pa s
kinematic	1 stokes = 10^{-4} m ² s ⁻¹

DECIMAL FRACTIONS AND MULTIPLES

Fraction	Prefix	Symbol	Multiple	Prefix	Symbol
10^{-3}	milli	m	10^3	kilo	k
10^{-6}	micro	μ	10^6	mega	M
10^{-9}	nano	n	10^9	giga	G
10^{-12}	pico	p	10^{12}	tera	T
10^{-15}	femto	f	10^{15}	peta	P
10^{-18}	atto	a	10^{18}	exa	E

Appendix D

Ionic Crystal Radii (in units of 10^{-10} m)

Coordination number = 6											
Ag ⁺	Al ³⁺	As ⁵⁺	Au ⁺	B ³⁺	Ba ⁺	Be ²⁺	Bi ³⁺	Bi ⁵⁺	Br ⁺	C ⁴⁺	Ca ²⁺
1.15	0.54	0.46	1.37	0.27	1.35	0.45	1.03	0.76	1.96	0.16	1.00
Cd ²⁺	Ce ⁴⁺	Cl [−]	Co ²⁺	Co ³⁺	Cr ²⁺	Cr ³⁺	Cr ⁴⁺	Cs ⁺	Cu ⁴	Cu ²⁺	Cu ³⁺
0.95	0.87	1.81	0.75	0.55	0.80	0.62	0.55	1.67	0.77	0.73	0.54
Dy ³⁺	Er ³⁺	Eu ³⁺	F [−]	Fe ²⁺	Fe ³⁺	Ga ³⁺	Gd ³⁺	Ge ⁴⁺	Hf ⁴⁺	Hg ²⁺	Ho ³⁺
0.91	0.89	0.95	1.33	0.78	0.65	0.62	0.94	0.53	0.71	1.02	0.90
I [−]	In ³⁺	K ⁺	La ³⁺	Li ⁺	Mg ²⁺	Mn ²⁺	Mn ⁴⁺	Mo ³⁺	Mo ⁴⁺	Mo ⁶⁺	N ⁵⁺
2.20	0.80	1.38	1.03	0.76	0.72	0.83	0.53	0.69	0.65	0.59	0.13
Na ⁺	Nb ⁵⁺	Nd ³⁺	Ni ²⁺	Ni ³⁺	O ^{2−}	OH ⁺	P ⁵⁺	Pb ²⁺	Pb ⁴⁺	Rb ⁺	Ru ⁴⁺
1.02	0.64	0.98	0.69	0.56	1.40	1.37	0.38	1.19	0.78	1.52	0.62
S ^{2−}	S ⁶⁺	Sb ³⁺	Sb ⁵⁺	Sc ³⁺	Se ^{2−}	Se ⁶⁺	Si ⁴⁺	Sm ³⁺	Sn ⁴⁺	Sr ²⁺	Ta ⁵⁺
1.84	0.29	0.76	0.60	0.75	1.98	0.42	0.40	0.96	0.69	1.18	0.64
Te ^{2−}	Te ⁶⁺	Th ⁴⁺	Ti ²⁺	Ti ³⁺	Ti ⁴⁺	Tl ⁺	Tl ³⁺	U ⁴⁺	U ⁵⁺	U ⁶⁺	V ²⁺
2.21	0.56	0.94	0.86	0.67	0.61	1.50	0.89	0.89	0.77	0.73	0.79
V ⁵⁺	W ⁴⁺	W ⁶⁺	Y ³⁺	Yb ³⁺	Zn ²⁺	Zr ⁴⁺					
0.54	0.66	0.60	0.90	0.87	0.74	0.72					
Coordination number = 4											
Ag ⁺	Al ³⁺	As ⁵⁺	B ³⁺	Be ²⁺	C ⁴⁺	Cd ²⁺	Co ²⁺	Cr ⁴⁺	Cu ⁺	Cu ²⁺	F ⁺
1.00	0.39	0.34	0.11	0.27	0.15	0.78	0.58	0.41	0.60	0.57	1.31
Fe ²⁺	Fe ³⁺	Ga ³⁺	Ge ⁴⁺	Hg ²⁺	In ³⁺	Li ⁴⁺	Mg ²⁺	Mn ²⁺	Mn ⁴⁺	Na ⁺	Nb ⁵⁺
0.63	0.49	0.47	0.39	0.96	0.62	0.59	0.57	0.66	0.39	0.99	0.48
Ni ²⁺	O ^{2−}	P ⁵⁺	Pb ²⁺	S ⁶⁺	Se ⁶⁺	Sn ⁴⁺	Si ⁴⁺	Ti ⁴⁺	V ⁵⁺	W ⁶⁺	Zn ²⁺
0.55	1.38	0.17	0.98	0.12	0.28	0.55	0.26	0.42	0.36	0.42	0.60

(continued)

Coordination number = 8

Bi^{3+}	Ce^{4+}	Ca^{2+}	Ba^{2+}	Dy^{3+}	Gd^{3+}	Hf^{4+}	Ho^{3+}	In^{3+}	Na^{+}	Nd^{3+}	O^{2+}
1.17	0.97	1.12	1.42	1.03	1.05	0.83	1.02	0.92	1.18	1.11	1.42
Pb^{2+}	Rb^{+}	Sr^{2+}	Th^{4+}	U^{4+}	Y^{3+}	Zr^{4+}					
1.29	1.61	1.26	1.05	1.00	1.02	0.84					

Coordination number = 12

Ba^{2+}	Ca^{2+}	La^{3+}	Pb^{2+}	Sr^{2+}
1.61	1.34	1.36	1.49	1.44

Source: Shannon, R. D. *Acta Crystallographica*, 1976, Vol. A32, 751.

Appendix E

Density and Melting Point of Some Elements, Ceramics, and Minerals

Chemical formula	Density (g/cm ³)	Melting point (°C)	Common names
Al	2.70	660	Aluminum
AlN	3.255	2000 ^d	Aluminum nitride
Al ₂ O ₃	3.986	2053	Alumina; corundum
Al ₂ O ₃ •H ₂ O	3.44	—	Aluminum monohydrate; boehmite
	3.40	—	Diapsore
Al ₂ O ₃ •3H ₂ O	2.53	—	Aluminum trihydroxide; bayerite
	2.42	—	Gibbsite
Al ₂ O ₃ •SiO ₂	3.25	—	Sillimanite
	3.59	—	Kyanite
	3.15	—	Andalusite
3Al ₂ O ₃ •2SiO ₂	3.16	1850	Mullite
Al ₂ O ₃ •2SiO ₂ •2H ₂ O	2.65	—	Kaolinite
Al ₂ O ₃ •2SiO ₂ •4H ₂ O	2.62	—	Halloysite
Al ₂ O ₃ •4SiO ₂ •2H ₂ O	2.78	—	Pyrophyllite
Al ₂ O ₃ •TiO ₂	3.70	1200 ^d	Aluminum titanate
B ₄ C	2.50	2350	Boron carbide
BN	2.270	2500 ^s	Boron nitride (hexagonal)
	3.470		Boron nitride (cubic)
B ₂ O ₃	2.55	450 ^d	Boric oxide
BaO	5.72	1972	Barium oxide (cubic)

(continued)

Chemical formula	Density (g/cm ³)	Melting point (°C)	Common names
BaO•Al ₂ O ₃ •2SiO ₂	3.25	—	Barium feldspar; celsian
BaTiO ₃	6.02	1625	Barium titanate
BeO	3.01	2577	Beryllium oxide; bromelite
C	3.513	4400	Diamond
	2.2	4480	Graphite
CaCO ₃	2.71	900 ^d	Calcium carbonate; calcite
	2.83	825 ^d	Aragonite
CaCO ₃ •MgCO ₃	2.86	750 ^d	Dolomite
CaF ₂	3.18	1418	Calcium fluoride; fluorite
CaO	3.34	2898	Calcium oxide; lime
Ca(OH) ₂	2.2	580 ^d	Calcium hydroxide; slaked lime
CaO•Al ₂ O ₃	2.98	1605	Calcium aluminate
CaO•2Al ₂ O ₃	2.91	1720	Calcium dialuminate
CaO•6Al ₂ O ₃	3.69	1840	Calcium hexaluminate
CaO•Al ₂ O ₃ •2SiO ₂	2.76	1551	Anorthite; lime feldspar
CaO•MgO•2SiO ₂	3.30	1391	Diopside
2CaSO ₄ •H ₂ O	—	160 ^d	Plaster of Paris
CaSO ₄ •2H ₂ O	2.32	160 ^d	Gypsum
CaO•SiO ₂	2.92	1540	Calcium metasilicate; wollastonite
CaO•TiO ₂	3.98	1975	Calcium metatitanate; perovskite
CeO ₂	7.65	2400	Cerium (IV) oxide
Ce ₂ O ₃	6.2	2210	Cerium (III) oxide
Cr ₂ O ₃	5.22	2329	Chromium oxide
Cu	8.96	1085	Copper
CuO	6.30–6.45	1326	Cupric oxide; tenorite
Cu ₂ O	6.00	1235	Cuprous oxide; cuprite
FeO	6.0	1377	Ferrous oxide; wuestite
Fe ₂ O ₃	5.25	1565	Ferric oxide; hematite
Fe ₃ O ₄	5.17	1597	Ferroso-ferric oxide; magnetite
FeS ₂	5.02	>600 ^d	Iron disulfide; pyrite
FeTiO ₃	4.72	~1470	Ilmenite
K ₂ O	2.35	350 ^d	Potash
K ₂ O•Al ₂ O ₃ •4SiO ₂	2.49	1686	Leucite
K ₂ O•Al ₂ O ₃ •6SiO ₂	2.56	—	Orthoclase; microcline; potash feldspar
K ₂ O•3Al ₂ O ₃ •6SiO ₂ •2H ₂ O	2.80–2.90	—	Mica; muscovite
LaCrO ₃	6.70		Lanthanum chromite
LaMnO ₃	5.70		Lanthanum manganite

Density and Melting Point of Some Elements, Ceramics, and Minerals 857

Chemical formula	Density (g/cm ³)	Melting point (°C)	Common names
La ₂ O ₃	6.51	2304	Lanthanum oxide; lanthana
LiF	2.64	848	Lithium fluoride
Li ₂ O	2.013	1570	Lithium oxide; lithia
Li ₂ O•Al ₂ O ₃ •4SiO ₂	3.13	—	Spodumene (alpha)
	2.40	—	Spodumene (beta)
Li ₂ O•Al ₂ O ₃ •8SiO ₂	2.42	—	Petalite
MgCO ₃	3.05	540 ^d	Magnesium carbonate; magnesite
MgO	3.581	2850	Magnesia; periclase
MgO•Al ₂ O ₃	3.55	2135	Magnesium aluminate; spinel
2MgO•2Al ₂ O ₃ •5SiO ₂	2.60	—	Cordierite (beta)
Mg(OH) ₂	2.37	350 ^d	Brucite
MgO•SiO ₂	3.19	1550 ^d	Magnesium metasilicate; clinostatite
2MgO•SiO ₂	3.21	1900	Magnesium orthosilicate; fosterite
3MgO•4SiO ₂ •H ₂ O	2.71	—	Talc; soapstone
MoSi ₂	6.24	2030	Molybdenum disilicide
NaCl	2.17	800	Sodium chloride
Na ₂ O	2.27	1132 ^d	Sodium oxide; soda
Na ₂ O•Al ₂ O ₃ •2SiO ₂	2.61	1526	Nephelite
Na ₂ O•Al ₂ O ₃ •4SiO ₂	3.34	1000	Jadeite
Na ₂ O•Al ₂ O ₃ •6SiO ₂	2.63	1100	Albite; soda feldspar
Na ₂ O•SiO ₂	2.40	1088	Sodium metasilicate
Na ₂ O•2SiO ₂		875	Sodium disilicate
Nb ₂ O ₅	4.55	1500	Niobia
NiO	6.72	1955	Nickel oxide; bunsenite
PbO	9.35	—	Litharge (transforms to massicot)
	9.64	897	Massicot
PbO ₂	9.64	300 ^d	Lead dioxide; plattnerite
Pb ₃ O ₄	8.92	830	Red lead
PbS	7.60	1114	Lead sulfide; galena
PbTiO ₃	7.9	1290	Lead titanate
Si	2.329	1414	Silicon
SiC	3.217	2700	Silicon carbide
Si ₃ N ₄	3.184	1900 ^d	Silicon nitride
SiO ₂	2.648	—	α-Quartz (transforms to β-quartz)
	2.533	—	β-Quartz (transforms to tridymite)
	2.265	—	Tridymite (transforms to cristobalite)
	2.334	1722	Cristobalite
	2.196	—	Silica (vitreous)
SrTiO ₃	5.10	2080	Strontium titanate

(continued)

Chemical formula	Density (g/cm ³)	Melting point (°C)	Common names
TiB ₂	4.52	3200	Titanium diboride
TiC	4.910	3000	Titanium carbide
TiO ₂	4.23	1840	Titania; rutile
	3.89	—	Anatase (transforms to rutile)
	4.14	—	Brookite (transforms to rutile)
UO ₂	10.97	2825	Uranium dioxide; urania
WC	15.6	2785	Tungsten carbide
Y ₂ O ₃	5.03	2438	Yttrium oxide; yttria
3Y ₂ O ₃ •5Al ₂ O ₃	4.55	1970	Yttrium aluminum garnet
ZnO	5.606	1975	Zinc oxide; zincite
ZnO•Al ₂ O ₃	4.50		Zinc aluminate
ZnS	4.09	1700	Zinc sulfide; wurtzite
	4.04	1700	Sphalerite
ZrB ₂	6.09	3245	Zirconium diboride
ZrO ₂	5.56	—	Zirconia (monoclinic)
	6.10	—	Zirconia (tertragonal)
	5.68–5.91	2680	Zirconia (cubic)
ZrO ₂ •SiO ₂	4.60	2250	Zirconium orthosilicate; zircon

^d decomposition; ^s sublimation

Appendix F

Aperture Size of U.S. Standard Wire Mesh Sieves (ASTM E 11:87)

Aperture size (mm/ μ m)	Sieve number	Aperture size (μ m)	Sieve number
5.6 mm	3.5	300	50
4.75	4	250	60
4.00	5	212	70
3.35	6	180	80
2.80	7	150	100
2.36	8	125	120
2.00	10	106	140
1.70	12	90	170
1.40	14	75	200
1.18	16	63	230
1.00	18	53	270
850 μ m	20	45	325
710	25	38	400
600	30	32	450
500	35	25	500
425	40	20	635
355	45		

Index

- Acheson process, 77
- Activated sintering, 673–677
- Activation energy, 444, 446, 613
- Activity, 454
 - relation to concentration, 454
- Additives
 - forming, 344–360
 - grain growth control, 585
 - liquid-phase sintering, 621
- Adsorption from solution
 - ions, 194–197
 - polyelectrolytes, 224–226
 - polymers, 212–215
 - surfactants, 349–350
- Agglomerates, 31, 50, 127
 - effects on packing, 343
 - effects on sintering, 693, 696
- Aggregate, 128
- Aging of gels, 19, 279
- Alkoxides (*see* Metal alkoxides)
- Alkyl ammonium acetate, 351
- Aluminum oxide
 - activation energies, 798
 - bayerite, 266
 - boehmite, 266
 - composites
 - $\text{Al}_2\text{O}_3/\text{Al}$, 11–12
 - $\text{Al}_2\text{O}_3/\text{ZrO}_2$, 13–14
- [Aluminum oxide]
 - defect reactions, 433, 740–742
 - dihedral angle, 743
 - extrusion, 393
 - fast firing, 798
 - gels, 305–307
 - grain boundary film, 640
 - grain growth
 - solute drag, 750
 - Zener pinning, 580
 - hot isostatic pressing, HIP map, 840
 - hot pressing, deformation map, 522
 - microwave sintering, 824–826
 - powders
 - Bayer process, 99
 - from solution, 89
 - pressure casting, 380
 - reaction bonding, 13–14
 - single crystal conversion, 572
 - sintering
 - $\text{Al}_2\text{O}_3/\text{ZrO}_2$ composite, 720
 - atmosphere, 800
 - effects of packing, 694–695
 - grain size/density data, 612
 - microstructural map, 611
 - role of MgO , 750–752
 - thin films, 727

- [Aluminum oxide]
 - slip casting, 374
 - solute segregation, 745
 - suspensions, 224–227
 - tape casting, 383
 - two-step sintering, 698
- Ambipolar diffusion, 462–466
- Arrhenius relation, 70, 559
- Atmosphere
 - controlled O₂ partial pressure, 815
 - effects on decomposition, 70–71
 - effects on sintering
 - β -Al₂O₃, 808
 - Fe₃O₄, 814
 - ferrites, 813
 - gases in pores, 800–804
 - PLZT, 808
 - Si₃N₄, 808
 - swelling, 803
 - translucent Al₂O₃, 800
 - effects on vapor transport, 804
 - oxidation number, 810
 - water vapor, 804
- Auger electron spectroscopy, 170–172
- Avrami equation, 766
- Ball milling (*see also* Comminution)
 - dry milling, 56–57
 - effects of dispersant, 57
 - grinding medium, 58
 - milling rate, 58
 - wet milling, 56–57
- Barium titanate
 - fast firing, 799
 - powder synthesis
 - coprecipitation, 93
 - hydrothermal, 94
 - single crystal conversion, 572
 - tape casting, 383
- Bayer process, 99
- BET surface area, 148
- Binders
 - binder removal (*see* Debinding)
 - cellulose, 355–356
 - extrusion, 393
 - injection molding, 397
- [Binders]
 - slip casting, 374
 - sodium silicate, 359
 - spray drying, 361
 - synthetic, 354
 - tape casting, 383
 - viscosity grade, 356–358
 - water-soluble, 358
- Bjerrum length, 642
- Boltzmann distribution, 158
- Boltzmann equation, 216
- Bonding
 - coordinate, 349
 - hydrogen, 351
- Bragg's law, 163
- Bridging flocculation, 214, 220
- Brouwer diagram, 439–440
- Brownian motion, 128, 145, 190, 234
- Calcination, 64 (*see also* Decomposition, Solid-state reactions)
- Capillary
 - condensation, 150
 - hysteresis, 152
 - stress (pressure), 19, 284
- Carman-Kozeny equation, 287, 376
- Carter equation, 75
- Casting methods
 - pressure casting, 379–381
 - slip casting, 373–379
 - tape casting, 381–85
- Cation exchange capacity, 193
- Ceramics
 - advanced, 1, 50
 - applications, 4–5
 - fabrication methods, 3–35
 - traditional, 1, 49
- Chemical potential, 451–458
- Chemical vapor deposition, 6–9
- Chemical vapor infiltration, 9–10
- Citrate gel method, 108
- Coagulation, 207
- Coalescence
 - grain, 660–661
 - pore, 588

- Coarsening (*see also* Ostwald ripening)
 - liquid-phase sintering, 665
 - LSW theory, 546–554
 - particles, 85–86
 - porous compacts, 540, 542, 586
- Coated particles
 - sintering, 721
 - synthesis, 95–98
- Coatings (*see* Films)
- Coble creep, 517
- Cold isostatic pressing, 371–372
- Colloids (*see also* Suspensions)
 - coagulation, 207
 - definition, 128
 - electrostatic stabilization, 191–208
 - electrosteric stabilization, 222–227
 - flocculation, 206, 208
 - lyophilic, 183
 - lyophobic, 183
 - peptization, 206
 - steric stabilization, 211–222
 - types, 182
- Comminution, 52–61
 - agitated ball mills (attrition mills), 60
 - ball milling, 55–61
 - jet mills, 55
 - vibratory ball mills, 59
- Compaction (*see* Die compaction)
- Composite particles (*see* Coated particles)
- Composites
 - chemical vapor infiltration, 9–10
 - constrained sintering, 701–724
 - directed metal oxidation, 11–12
- Composite sphere model, 707
- Composition-depth profiling, 170
- Constitutive equation
 - incompressible viscous solid, 711
 - porous elastic solid, 710
 - porous viscous solid, 711, 724
- Constrained sintering
 - effects of rigid inclusions, 701–722
 - composite sphere model, 707
 - numerical simulations, 719–720
 - percolation, 715–719
 - rule of mixtures, 704
 - [Constrained sintering]
 - Scherer theory, 710–715
 - self-consistent model, 714
 - transient stresses, 707–709
 - multilayers, 730–732
 - thin films, 722–730
 - models, 724–726
 - experimental data, 727
 - crack growth and damage, 729
- Conventional sintering (*see also* Sintering)
 - effects of heating rate
 - gels, 788–789
 - polycrystalline ceramics, 789–795
 - furnaces, 780
 - heating elements, 781
 - heating schedule, 783–800
 - measurement techniques, 780–783
 - multistage sintering, 797
- Coprecipitation, 92–93
- Correlation factor, 451
- Coulter counter, 142
- Creep
 - equation for porous solids, 535
 - equations for dense solids, 517
 - mechanisms, 517
 - strain rate, 528
 - viscosity, 529
- Critical moisture content, 408
- Critical point
 - drying, 283
 - fluids, 297
- Crystallization
 - effects on sintering, 762–772
 - kinetics, 766–767
- Curvature
 - effect on chemical potential, 458, 546
 - effect on sintering stress, 526
 - effect on solubility, 548, 634
- Darcy's law, 287, 373
- Debinding, 409–418
 - capillary flow, 410–411
 - solvent extraction, 411
 - thermal debinding
 - models, 413–416

- [Debinding]
 - oxidative degradation, 415–416
 - stages and mechanisms, 412
 - thermal degradation, 413–415
- Debye forces, 184
- Debye-Hückel approximation, 200
- Debye length, 201
- Decomposition
 - carbonates, 64–71
 - effects of atmosphere, 70–71
 - kinetics, 65–71
 - mechanisms, 67
 - thermodynamics, 64–66
- Defects in crystals
 - Brouwer diagram, 439–440
 - defect chemistry, 431–441
 - defect concentration, 434
 - defect reactions, 432–433
 - electronic defects, 432
 - extrinsic defects, 431
 - Frenkel defect, 435
 - intrinsic defects, 431
 - Kroger-Vink notation, 431–432
 - nonstoichiometry, 436
 - oxidation reaction, 437
 - point defects, 431–441
 - reduction reaction, 437
 - Schottky defect, 434
 - solute incorporation, 438–440
 - types, 430
- Deflocculants (*see* Dispersants)
- Densification (*see also* Sintering)
 - simultaneous grain growth, 602–611
- strain rate
 - linear, 524, 528
 - volumetric, 528, 534
- viscosity, 524
- Density
 - apparent, 156
 - green, 418
 - packing, 328, 330
 - relative, 499
 - tap, 332
- Depletion stabilization, 221
- Desintering (*see* Swelling)
- Die compaction, 360–371
 - defects, 371
 - die filling, 262
 - die wall friction, 366
 - ejection, 370
 - equation, 364
 - granules, 362, 368
 - lubricants, 360
 - particles, 365–367
 - stages, 362–363
- Diffusion in solids
 - ambipolar diffusion, 462–466
 - Fick's laws, 441
 - flux equations, 459
 - flux of atoms, 460
 - flux of vacancies, 460
 - mechanisms, 446–450
 - random diffusion, 444
- Diffusion coefficient, 441
 - data, 447
 - temperature dependence, 446
 - types, 450–451
- Diffusivity (*see* Diffusion coefficient)
- Dihedral angle
 - Al_2O_3 , 743
 - influence on morphological stability, 690
 - liquid-phase sintering, 628–632
 - solid-state sintering, 475, 591
- Dilatometry, 782
- Dip coating, 316–318
- Directed metal oxidation, 11–12
- Directional grain growth, 661
- Disjoining forces, 286, 642
- Dispersants, 347–353
 - extrusion, 393
 - gel casting, 387
 - inorganic, 348
 - organic, 349–353
 - slip casting, 374
 - spray drying, 361
 - tape casting, 383
- Dispersion forces, 184
- DLVO theory, 203
- Doctor blade process (*see* Tape casting)

- Domains, 228, 331
- Dopant (*see also* Solid solution additive)
 - acceptor, 438
 - aliovalent, 438
 - donor, 438
- Drying control chemical additives, 19, 295
- Drying of gels
 - conventional drying, 281–296
 - chemical additives, 19, 295
 - cracking, 293–295
 - driving force, 282
 - drying stresses, 292
 - evaporation rate, 292
 - funicular liquid, 290
 - pendular liquid, 291
 - shrinkage, 20, 281
 - stages, 281
 - structural changes, 297–298
 - warping, 291
 - supercritical drying, 296–297
 - critical point, 296
 - fluids, 297
- Drying of granular ceramics
 - cracking and warping, 408–410
 - granular layers, 405–407
 - granular solids, 407–409
 - high humidity drying, 409
 - shrinkage, 408
- Elastic-viscous analogy, 710
- Electrical double layer
 - charge distribution, 198–199
 - Debye-Hückel approximation, 200
 - Debye length, 201
 - DLVO theory, 203
 - Gouy-Chapman equation, 201
 - repulsion, 203–205
 - surface charge, 202–203
- Electrokinetic phenomena, 209
- Electrophoresis, 209–211
- Electrophoretic deposition, 388–391
- Electrophoretic mobility, 210
- Electrostatic stabilization, 191–208
- Electrosteric stabilization, 222–227
- Equilibrium constant
 - chemical reaction, 434
 - defect reaction, 434–440
- ESCA (*see* X-ray photoelectron spectroscopy)
- Euler equation, 554
- Evaporation/condensation (*see* Vapor transport)
- Extrusion, 391–394
 - co-extrusion, 394–396
 - compositions, 393
 - defects, 394–395
 - mechanics, 393
- Fabrication methods
 - chemical vapor deposition, 6–9
 - chemical vapor infiltration, 9–10
 - directed metal oxidation, 11–12
 - firing of compacted powders, 28–35
 - glass ceramic route, 27
 - melt casting, 27
 - polymer pyrolysis, 21–26
 - reaction bonding, 12–16
 - sol-gel process, 17–20
- Fast firing, 613, 798
- Fick's laws of diffusion, 441
- Films
 - breakup phenomena, 735–738
 - constrained sintering, 722–730
 - crack growth and damage, 729
 - delamination, 729
 - diamond, 7–9
 - dip coating, 316–318
 - drying, 320, 406
 - grain boundary films, 639–645
 - grain growth, 733–735
 - specimen thickness effect, 733
 - spin coating, 318–320
- Firing (*see* Sintering)
- Floc, 128
- Flocculation of suspensions
 - bridging, 214
 - depletion, 222
 - kinetics, 208
- Flux
 - diffusion, 441
 - flow of liquid, 287

- Forces between particles
 - nonretarded, 185
 - retarded, 185
 - van der Waals, 184–187
- Forming
 - cold isostatic pressing, 371–372
 - die compaction, 360–371
 - electrophoretic deposition, 388–391
 - extrusion, 391–394
 - gel casting, 385–388
 - injection molding, 396–399
 - pressure casting, 379–381
 - slip casting, 373–379
 - solid free-form fabrication, 399–405
 - tape casting, 381–385
- Fractal dimension, 270
- Free sintering (*see* Conventional sintering)
- Freeze drying, 106–107
- Frenkel
 - defect, 435
 - energy balance concept, 490
 - model for viscous sintering, 489
- Funicular liquid, 290
- Furnaces, 780, 782
 - elements, 781
- Gas adsorption, 150–152
- Gates–Gaudin–Schuhman equation, 136
- Gel casting, 385–388
- Gel point, 275
- Gels (*see also* Sol-gel process)
 - aerogel, 250
 - aging, 19, 279
 - crystallization, 304, 771–772
 - drying, 19, 279–299
 - gel point, 275
 - multicomponent gels, 307–315
 - particulate, 248, 250–252
 - polymeric, 248, 252–254
 - sintering, 299–304, 788–789
 - xerogel, 249
- Gibbs free energy, 452–455
- Glass (*see also* Viscous sintering)
 - phases in ceramics, 645, 672, 675
 - viscosity, 679, 766, 788
- Glass ceramics, 27
- Glass transition temperature, 251, 355, 359, 369
- Glycine nitrate process, 108
- Gouy–Chapman equation, 201
- Grain boundary
 - diffusion, 449
 - energy, 573
 - films, 639–645
 - glassy phases, 645
 - migration, 542
 - mobility
 - intrinsic mobility, 557, 585
 - solute drag, 585
 - data, 575
 - parameters, 600
 - sliding, 520–521
 - solute segregation, 582
 - space charge, 745–750
 - structure, 570
 - thickness, 542
 - velocity, 557
- Grain growth (*see also* Coarsening)
 - abnormal grain growth, 567–573
 - causes of abnormal growth, 570
 - computer simulation, 568–570
 - definition, 543
 - single crystal conversion, 572
 - anisotropic grain growth, 572
 - control of grain growth
 - effect of fine inclusions, 574–580
 - effect of solutes, 580–585
 - definition, 541
 - dense solids, 556–573
 - driving force, 542
 - effects on densification, 546
 - effects on properties, 545
 - kinetic equations, 559, 561, 602
 - normal grain growth
 - Burke and Turnbull model, 557
 - computer simulations, 563–567
 - definition, 543
 - mean field theories, 559–561
 - topological analysis, 561–563

- [Grain growth]
 - porous solids, 585–593, 597–602
 - templated grain growth, 573
 - thin films, 733–735
 - very porous solids, 594–597
 - with pore coalescence, 588
- Grain shape accommodation, 658–660
- Granules, 128
 - characteristics, 361–362
 - die compaction, 362, 368
 - hardness, 368
 - spray drying, 103, 361
- Green body
 - density variation, 367
 - microstructure, 418
- Grinding (*see* Comminution)
- Hamaker constant, 186, 189
 - effect of intervening medium, 189, 190
 - Lifshitz theory, 188
 - measurement, 188
 - microscopic approach, 188
- Hashin–Shtrikman equation, 714
- Heating
 - furnace elements, 781
 - microwave, 818–824
 - rate, 787
 - schedule for sintering
 - constant heating rate, 783, 787
 - general schedule, 784–787
 - isothermal sintering, 783, 787
- Helmholtz–Smoluchowski equation, 210
- Henry’s equation, 211
- Herring scaling laws, 477–482
 - application to Al_2O_3 , 482
- Hofmesiter series, 348
- Homogeneity
 - chemical composition, 30
 - particle mixing, 75
 - particle packing, 328, 343
- Homogenizers, 360
- Hot forging (*see* Sinter forging)
- Hot isostatic pressing
 - equipment, 835
 - HIP diagrams, 840
 - mechanisms, 839
 - process variables, 836–839
 - sinter/HIP process, 837
- Hot pressing
 - data analysis, 833
 - deformation maps, 522
 - die materials, 831
 - driving force, 429, 515–516
 - equations, 518–520
 - equipment, 830
 - hydrothermal hot pressing, 834
 - mechanisms, 520–522
 - models, 515–518
 - process variables, 831–832
 - reactive hot pressing, 834
- Hydrolysis reactions
 - aqueous silicates, 254–260
 - forced hydrolysis, 89
 - metal alkoxides, 86–88, 265–266
 - powder synthesis, 93–95
 - salt solutions, 89–92
 - silicon alkoxides, 266–270
- Hydrothermal hot pressing, 834
- Hydrothermal powder synthesis, 93–95
- Impurity drag (*see* Solute drag)
- Inclusions
 - effects on grain growth, 574–580
 - effects on sintering, 701–722
- Inhomogeneities
 - control of inhomogeneities, 693
 - correction during sintering, 695–701
 - effects on particle packing, 696
 - effects on sintering, 692–701
 - differential densification, 692
 - transient stresses, 693
 - microstructural flaws, 693
- Injection molding, 396–399
 - binder system, 396–397
 - compositions, 398

- Interfacial energy, 629
- Ionic crystal radius, 853–854
- Ionic mobility, 463
- Isoelectric point, 195
 - space charge potential, 748
 - suspensions, 195
 - data for oxides, 196
- Isomorphic substitution, 193
- Isostatic pressing (*see* Cold isostatic pressing)

- Jander equation, 75
- Jet mill, 55

- Keesom forces, 183
- Kelvin equation, 78, 150
- Krieger–Dougherty equation, 235
- Kroger–Vink notation, 431–432

- LaMer diagram, 84, 97
- Langmuir adsorption isotherm, 148
- Lattice diffusion, 448–449
- Law of mass action, 434
- Lewis acid, 215, 349
- Lewis base, 215, 349
- Light scattering, 143
- Liquid-phase sintering
 - capillary forces, 635–637, 651
 - coalescence, 660–661
 - coarsening (*see also* Ostwald ripening)
 - dependence on liquid content, 666
 - grain growth kinetics, 665
 - dihedral angle effects, 628–632, 666
 - directional grain growth, 661
 - driving force, 622
 - effects of applied pressure, 668–670
 - effects of gravity, 637
 - grain boundary films, 639–645
 - grain shape accommodation, 658–660
 - mechanisms, 645–668
 - microstructures, 625
 - pore filling, 662–665
 - rearrangement, 646–652
- [Liquid-phase sintering]
 - liquid redistribution, 646–650
 - primary rearrangement, 651
 - secondary rearrangement, 651
- Si_3N_4 , 671
- Solubility, 632–634
- solution–precipitation, 652–662
- spreading of liquid, 628
- stages, 624–627
- swelling, 634
- transient liquid, 623
- use of phase diagrams, 670–673
- wetting, 627–628
- ZnO , 671
- Lognormal distribution function, 135
- London forces (*see* Dispersion forces)
- LSW theory, 546–554
- Lubricants, 360, 397

- Mackenzie and Shuttleworth model, 504
- Magnesium oxide
 - activation energies, 798
 - Brouwer diagram, 440
 - defect reactions, 438–439
 - fast firing, 798
 - hot pressing, 512
 - liquid-phase sintering, 621, 666
 - sintering
 - effect of inhomogeneities, 697
 - effect of water vapor, 806
- Master sintering curve, 795–796
- Mechanochemical synthesis, 61–63
- Menhaden fish oil, 349
- Mercury porosimetry, 153–155, 783
- Metal alkoxides
 - aluminum alkoxides, 266
 - boron alkoxides, 266
 - definition, 260
 - double alkoxides, 263
 - hydrolysis and condensation, 265
 - molecular complexity, 263
 - polymerization, 265
 - preparation, 260–263
 - properties, 263–266
 - silicon alkoxides, 266–267
 - transesterification, 262

- Metal-organic compounds, 260
- Microscopy
 - atomic force (AFM), 167
 - optical, 137
 - quantitative, 783
 - scanning electron (SEM), 168
 - scanning tunneling (STM), 167
 - transmission electron (TEM), 168
- Microstructure, 35–41
 - consolidated suspensions, 227–230
 - definition, 2
 - diagrams (maps)
 - grain size versus pore size, 605
 - grain size versus density, 610, 611
 - effects of impurities, 37, 51
 - flaws, 39–41
 - glass ceramics, 28
 - green body, 418
 - liquid-phase sintering, 36, 624
 - Rayleigh instability effects, 688–692
 - solid-state sintering, 35, 37
 - triaxial whiteware, 38
- Microwave sintering, 818–826
 - Al₂O₃, 824–826
 - equipment, 821
 - principles, 818–821
 - temperature control, 823
- Milling (*see* Comminution)
- Mixing, 75
- Mobility
 - grain boundary, 557, 575, 585
 - pore, 598–600
- Modulus
 - bulk modulus, 711
 - shear modulus, 711
 - Young's, 711
- Moisture content
 - definition, 407
 - critical, 408
- Nabarro-Herring creep, 517
- Newtonian viscosity, 231–232
- Nonretarded forces, 185
- Normal distribution function, 134
- Nucleation and growth
 - crystals in glass, 766
 - heterogeneous nucleation, 78, 96
 - homogeneous nucleation, 78
 - liquid from vapor, 78–80
 - particles from solution, 80–84
- Oleic acid, 351
- Optical atomic spectroscopy, 156–161
- Organic additives in processing
 - binders, 353–359
 - dispersants, 347–353
 - lubricants, 360
 - plasticizers, 359
 - solvents, 345–347
- Organometallic compounds, 260
- Osmotic pressure, 286
- Ostwald ripening
 - liquid-phase sintering, 656,
 - LSW theory, 546–554
 - particle growth, 85
- Oxidation number, 810
 - sintering of Cr₂O₃, 811
- Packing of particles
 - Andreasen equation, 341
 - binary mixtures, 334–339
 - continuous size distribution, 341–342
 - coordination number, 330
 - dense random, 333
 - domains, 228, 331
 - effects on sintering, 694–696
 - loose random, 333
 - monosize particles, 332–334
 - packing density, 328, 330
 - packing homogeneity, 328, 343
 - particles and short fibers, 338–339
 - random, 331–344
 - regular, 330–331
 - ternary and multiple mixtures, 339
- Particles (*see also* Powders)
 - aspect ratio, 136
 - coated particles, 95–98
 - definition, 128
 - porosity, 149–156
 - shape, 136

- [Particles]
 - size, 129–133
 - definition, 130
 - size distribution, 133–136
 - Gates-Gaudin-Schuhman, 136
 - lognormal, 135
 - normal, 134
 - Rosin-Rammler, 135
 - size measurement, 137–146
 - types, 127–128
- Pechini method, 108
- Peclet number, 234
- Pendular liquid, 291
- Penetration depth, 821
- Peptization, 206
- Percolation
 - effects on sintering, 715–719
 - gelation, 278
 - percolating cluster, 716
 - threshold, 278, 716
- Phase diagrams
 - $K_2O-Al_2O_3-SiO_2$, 681, 682
 - liquid-phase sintering, 671
 - $Si_3N_4-SiO_2-MgO$, 674
 - $Si_3N_4-SiO_2-Y_2O_3$, 674
 - $ZnO-Bi_2O_3$, 672
- Plasma sintering, 826–828
- Plasticity
 - forming methods, 391
 - hot isostatic pressing, 840
 - hot pressing, 520
 - suspensions, 194, 232
- Plasticizers, 359
- Point defects (*see* Defects in crystals)
- Point of zero charge, 195
- Poiseuille's equation, 15
- Poisson's equation, 199
- Poisson's ratio, 711
- Poly(acrylic acid), 223, 353, 354
- Polycarbosilane, 23
- Polyelectrolytes, 222
 - adsorption from solution, 224–226
 - dissociation, 223
 - effects on suspension rheology, 238
 - stabilization of suspensions, 225–227
- Polyethylene, 413
- Poly(ethylene glycol), 354
- Polyethyleneimine, 353, 354
- Poly(ethylene oxide), 354
- Poly(ethylene oxide)/polystyrene, 214
- Polyisobutylene succinamide, 351
- Polymeric stabilization (*see* Steric stabilization)
- Polymer pyrolysis, 21–26
- Polymers
 - block copolymers, 214
 - end-to-end distance, 213
 - homopolymers, 213
 - preceramic, 21
- Poly(methacrylic acid), 223, 353, 354
- Poly(methyl methacrylate), 354, 413
- Polysilazane, 25
- Poly(vinyl alcohol), 354
- Poly(vinyl butyral), 354, 417
- Poly(vinyl pyrrolidone), 354
- Poly(vinyl pyrrolidone)/polystyrene, 214
- Pore
 - coalescence, 588
 - coordination number, 591
 - evolution during sintering, 586–590
 - migration, 598
 - mobility, 598–600
 - parameters, 600
 - shrinkage, 476, 590–592
 - stability, 590–593
 - velocity, 598
- Pore–boundary interactions
 - kinetics, 600–601
 - thermodynamics, 590–593
- Porosity
 - closed porosity, 587
 - measurement
 - gas adsorption, 149–152
 - mercury porosimetry, 153–155
 - pycnometry, 156
 - open porosity, 587
- Powders (*see also* Particles)
 - desirable characteristics, 50–51
 - granulation, 106, 361

- [Powders]
 - synthesis methods, 53
 - chemical methods, 62–118
 - mechanical methods, 52–63
- Precipitation from solution
 - heterogeneous, 96
 - homogeneous, 77–84
 - hydrothermal, 93–95
 - powder synthesis, 86–107
- Precursors
 - metal alkoxides, 17, 260–266
 - metal-organic polymers, 21
 - preceramic polymers, 21
 - BN/B₄C, 25–26
 - SiC, 22–24
 - Si₃N₄, 24–25
- Pressure casting, 379–381
- Pressureless sintering (*see* Conventional sintering)
- Pycnometry, 156
- Random diffusion, 444
- Rate-controlled sintering, 800
- Rate controlling mechanism, 465
- Rayleigh instability, 688–692
- Reactions
 - decomposition, 64–71
 - defect, 432–433
 - gas-phase, 110–118
 - solid-state, 71–76
 - solution reactions, 86–100, 109
- Reaction sintering, 754–762
 - ceramic–metal composites, 762
 - process variables, 755–757
 - process trajectories, 757–758
 - zircon–Al₂O₃, 761
 - ZnO–Al₂O₃, 758–760
 - ZnO–Fe₂O₃, 758–760
- Reactive hot pressing, 834
- Rearrangement
 - hot isostatic pressing, 839
 - hot pressing, 520
 - liquid-phase sintering, 626, 646–652
 - two-dimensional arrays, 651
- Retarded forces, 185
- Reynolds number, 141
- Rheology, 230 (*see also* Viscosity)
- Rigidity threshold, 718
- Rosin–Rammler equation, 135
- Rule of mixtures, 704
- Schottky defect, 434
- Schulze–Hardy rule, 348
- Secondary ion mass spectrometry (SIMS), 174–176
- Sedimentation, particle size measurement, 140
- Segregation
 - solute at grain boundary, 582
 - in suspensions, 379, 385
- Self-consistent model, 714, 769, 770
- Shrinkage (*see also* Sintering)
 - linear, 524, 528
 - measurement, 782
 - volumetric, 528, 534
- Sieves
 - mesh number, 859
 - particle size measurement, 139
- Silanol group, 254
- Silicon carbide
 - CVD reactions, 7
 - fibers, 23–24
 - grain boundary film, 640
 - polymer precursors, 22–24
 - powder synthesis
 - Acheson process, 77
 - vapor-phase reactions, 115–118
 - reaction bonding, 15–16
- Silicon dioxide
 - CVD reactions, 7
 - gels, 254–260, 266–279
 - isoelectric point, 196
 - powders
 - flame synthesis, 114
 - solubility, 258
 - Stober process, 85–87
 - suspensions, 238–240

- Silicon nitride
 - CVD reactions, 7
 - decomposition, 808
 - gas pressure sintering, 810
 - hot pressing, 668–670
 - liquid-phase sintering, 671–673
 - microstructure, 36, 675
 - phase diagram, 674
 - polymer precursors, 24–25
 - powders, 109–118
 - properties, 111
 - synthesis, 109–118
 - reaction bonding, 13
 - surface characterization, 169, 173, 177
- Sinter forging, 834
- Sintering
 - activated, 673–677
 - atmosphere effects, 800–815
 - constant heating rate, 783, 787
 - constrained, 701–732
 - conventional, 779, 780–815
 - diagrams (maps), 511–514
 - heating rate dependence, 787–795
 - heating schedule, 783–787
 - isothermal, 783, 787
 - liquid-phase, 620–673
 - microwave, 818–826
 - multistage, 797
 - parameters, 426
 - plasma sintering, 826–828
 - pressure, 779, 829–840
 - rate-controlled, 800
 - reaction, 754–762
 - solid-state, 470–535
 - two-step sintering, 698
 - viscous, 489, 498, 504
 - vittrification, 677–681
- Sintering stress, 524–530
 - measurement, 527–530
- Skin depth, 820
- Slip casting, 373–379
 - compositions, 374
 - defects, 379
 - mechanics, 373–376
- Sodium oleate, 351
- Sodium silicate, 348, 359
- Sol, 17
- Sol-gel process (*see also* Gels)
 - advantages, 20
 - Al₂O₃ gels, 305–307
 - applications, 315–323
 - aqueous silicates, 254–260
 - disadvantages, 20
 - fibers, 320–322
 - films and coatings, 316–321
 - glass monoliths, 322
 - multicomponent gels, 307–315
 - porous materials, 323
 - silicon alkoxides, 266–279
 - hydrolysis and condensation, 267–270
 - polymer growth, 270–278
 - gelation, 278–279
 - powders, 107
- Solid free-form fabrication, 399–405
 - direct ink-jet printing, 405
 - fused deposition modeling, 403
 - laminated object manufacturing, 402–403
 - robocasting, 405
 - selective laser sintering, 403–404
 - stereolithography, 401–402
 - three-dimensional printing, 404
- Solid solution additives (dopants)
 - grain growth control, 585
 - role in sintering, 740–743
 - role of MgO in Al₂O₃, 750–752
 - segregation at grain boundaries
 - elastic strain, 744
 - space charge concept, 745
- Solid-state reactions, 64–76
 - calcinations, 64
 - decomposition, 64–71
 - powders, 74–76
 - solid solution formation, 71–76
 - reaction mechanisms, 73
 - parabolic growth law, 73
- Solid-state sintering
 - analytical models, 482–506
 - coarsening, 470, 476

- [Solid-state sintering]
 - densification, 470
 - diagrams (maps), 511–514
 - driving force, 427–429
 - effects of grain boundaries, 473–476
 - general sintering equation, 535
 - mechanisms, 471–473
 - numerical simulation, 506–508
 - phenomenological equations, 510–511
 - scaling laws, 477–482
 - stages of sintering, 483–485
 - two-sphere model, 486–487
- Solubility
 - amorphous silica, 258
 - effect of curvature, 548, 634
 - liquid–phase sintering, 632
- Solute
 - drag, 580–585
 - segregation, 582
- Solvents, 345–347
- Space charge concept, 745–750
 - defect concentration, 746–747
 - electrostatic potential, 747
 - isoelectric point, 748–749
 - in oxides, 749
- Spark plasma sintering, 828
- Spectroscopy
 - atomic absorption, 157
 - atomic emission, 157
 - Auger electron, 170–172
 - X-ray fluorescence, 160
 - X-ray photoelectron, 172–174
- Spin coating, 318–320
- Spray drying
 - solutions, 100–102
 - suspensions, 103
- Spray pyrolysis, 102–105
- Stearic acid, 351
- Steric stabilization, 211–222
 - adsorption of polymers, 212–215
 - bridging flocculation, 220
 - critical flocculation temperature, 218
 - effect of solvent, 217
 - repulsion, 219
 - theta temperature, 218
- Stern layer, 201–202
- Stober process, 86
- Stoichiometry, 813
- Stokes
 - diameter, 130
 - equation, 141
 - law, 140
- Stokes-Einstein equation, 145, 234
- Stress
 - capillary, 19, 284
 - drying, 292
 - hydrostatic, 708–709
 - sintering, 524–530
 - thermal, 693, 712
 - transient, 707–709
- Stress intensification factor, 515, 522–525
 - measurement, 530–531
- Supercritical drying, 19, 296–97
- Surface
 - area, 146–149
 - BET method, 148
 - characterization, 164–177
 - charge, 191–198, 202
 - chemistry, 168–176
 - curvature, 427
 - energy
 - silica gel, 726
 - silicate melts, 628
 - solids and liquids, 629
 - structure, 167–168
 - tension, common solvents, 346
- Surface diffusion, 450
- Surfactant, 346, 349
- Suspensions (*see also* Colloids)
 - rheology, 230–243
 - zeta potential, 209–211
- Swelling (*see also* Desintering)
 - liquid-phase sintering, 634
 - gases in pores, 803
- Syneresis, 279
- Tap density, 332

- Tape casting, 381–385
 - casting parameters, 383–385
 - defects, 385
 - slurry composition, 383
- Temperature
 - sintering, 786
 - wet bulb, 289
- Tetraethoxysilane (TEOS), 266–268
- Tetrakaidecahedron, 494
- Texture, 572, 832
- Thermal debinding (*see* Debinding)
- Theta temperature, 218
- Thin films (*see* Films)
- Titanium dioxide
 - CVD reaction, 7
 - electrophoretic mobility, 212
 - grain growth during sintering, 586
 - isoelectric point, 196, 212
 - monodisperse particles, 42, 85
 - powder synthesis
 - flame synthesis, 114
 - Stober process, 85, 87
 - sintering
 - sol-gel film, 772
 - monodisperse powder, 41–43
 - solute segregation, 749
 - space charge concept, 749
 - surface charge, 212
- Tracer diffusion coefficient, 443
- Transport coefficient, 459
- Transient liquid-phase sintering, 623
- Triaxial whiteware, 680
- TTT diagram, 765–768

- Uranium dioxide
 - open and closed porosity, 587
 - pore coalescence, 586

- Vacancy
 - chemical potential, 454
 - diffusion, 448
 - equilibrium concentration, 460
 - flux, 460
- van der Waals forces, 183–187

- Vapor–phase reactions, 110–118
- Vapor pressure
 - Kelvin equation, 461–462
- Vapor transport
 - effects on sintering, 804
 - mechanism, 472
- Viscoelastic analogy, 710
- Viscosity (*see also* Rheology)
 - Bingham, 232
 - bulk viscosity, 711
 - Einstein equation, 235
 - gel point, 275
 - glass, 679, 766, 788
 - intrinsic, 236
 - Krieger-Dougherty equation, 235
 - measurement, 233
 - molecular weight dependence, 277
 - Newtonian, 231–232
 - non-Newtonian, 231–232
 - relative, 235
 - rheopectic, 233
 - shear thickening (dilatant), 232
 - shear thinning (pseudoplastic), 232
 - shear viscosity, 711
 - temperature dependence, 679, 766, 788
 - thixotropic, 233
 - uniaxial viscosity, 711
- Viscous sintering
 - coated particles, 509
 - effect of crystallization, 765–772
 - Frenkel energy balance concept, 490
 - Frenkel model, 489–491
 - heating rate dependence, 788–789
 - Mackenzie and Shuttleworth model, 504
 - numerical simulation, 508–509
 - rigid inclusions, 706, 710–714, 767
 - Scherer model, 498–501
 - with crystallization, 762–772
 - experimental data, 771–772
 - process variables, 763–764
 - TTT diagrams, 765–767

- Vitrification, 677–681
 - controlling parameters, 678–680
 - silicate systems, 680
- Vogel-Fulcher equation, 679
- Volume diffusion (*see* Lattice diffusion)
- Wet-bulb temperature, 289
- Wetting
 - contact angle, 282, 346
 - surfactant, 346
- X-ray diffraction (XRD), 162–164
 - Bragg's law, 163
 - Rietveld method, 164
- X-ray fluorescence (XRF), 160–162
- X-ray line broadening, 145–146
 - Scherer equation, 145
- X-ray photoelectron spectroscopy (XPS), 172–174
- Yield stress, 232
- Young and Dupré equation, 628
- Young and Laplace equation, 153, 526
- Young's modulus, 711
- Zener relationship, 577
- Zeta potential, 209–211
- Zinc oxide
 - activated sintering, 677
 - constrained sintering
 - thin film, 728
 - ZnO–SiC composite, 704–705
 - ZnO–ZrO₂ composite, 721
 - conventional sintering
 - effect of heating rate, 789–795
 - grain boundary film, 640, 677
 - liquid-phase sintering, 671
 - master sintering curve, 796
 - reaction sintering
 - ZnO–Al₂O₃, 758–760
 - ZnO–Fe₂O₃, 758–760
 - sintering of thin films, 728–729